Dissertation zur Erlangung des Doktorgrades
der Fakultät für Chemie und Pharmazie
der Ludwig-Maximilians-Universität München

Conditional probes and fluorogenic reagents for manipulating and imaging biology

Philipp Mauker

aus

München, Deutschland

2025

Erklärung

Diese Dissertation wurde im Sinne von § 7 der Promotionsordnung vom 28. November 2011 von Herrn Prof. Dr. Oliver Thorn-Seshold betreut.

Eidesstattliche Versicherung

Diese Dissertation wurde eigenständig und ohne unerlaubte Hilfe erarbeitet.

München, 27.01.2026

_____

Philipp Mauker

Dissertation eingereicht am:	22.10.2025
1. Gutachter:	Prof. Dr. Oliver Thorn-Seshold
2. Gutachter:	Dr. Pavel Kielkowski
Mündliche Prüfung am:	23.01.2026

Abstract

This thesis focuses on the development of chemical molecular tools to visualise and manipulate biological systems, aiming to study the role of proteins and biochemical analytes in health and disease. The first part develops fluorogenic xanthene probes for imaging membrane damage (**Paper 1**) and enzyme activity (**Paper 2**). The second part (**Paper 3**) develops a cageable HaloTag ligand that selectively ligates to the HaloTag protein only after activation by light or a biochemical stimulus.

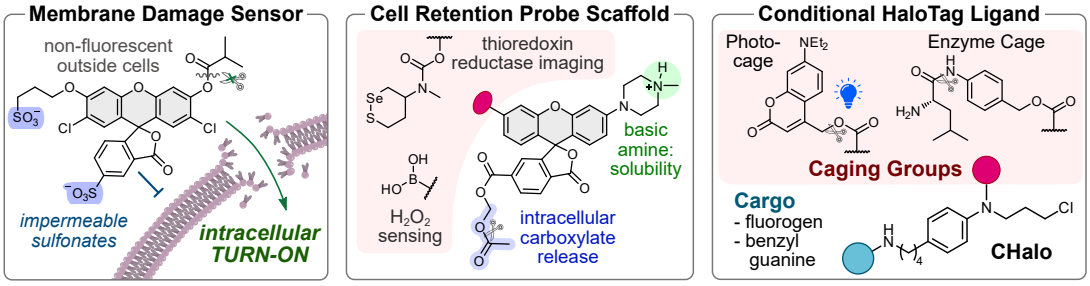

Fluorogenic Probes

Paper 1: Damage to cell membranes plays a key role in diverse pathologies, including bacterial infections and multiple sclerosis. DNA-intercalating fluorogens are commonly used to detect such damage, but they can be toxic and are restricted to identifying permeabilisation in cell volumes that contain a nucleus. To overcome these limitations, this work develops disulfonated fluorogenic probes that selectively label the *entire cytosol* of damaged cells, with near zero background fluorescence for sensitive detection. These probes reliably reveal membrane damage induced by biological, biochemical, or physical means and are compatible with multicolour microscopy. Their advantages over DNA fluorogens are demonstrated by imaging neuronal axon damage *in vitro* and discriminating membrane damage at single-cell resolution in *Drosophila* wound models *in vivo*.

Paper 2: Fluorogenic bioactivity probes are powerful tools for research and diagnostics, widely used to study enzyme activity in disease contexts or for fluorescence assisted surgery. While these probes must be membrane permeable to efficiently enter cells, often their fluorescent products also leak out, leading to signal loss, poor cell-by-cell resolution, and low sensitivity for low-turnover processes. Prior cell-retention strategies are typically inefficient or disrupt native biology through non-specific alkylation or precipitation. To overcome this, Paper 2 screened charge- and polarity-based designs and identified a rhodol scaffold that can switch from cell-permeable to cell-retained states. This modular scaffold is compatible with sensing diverse species (e.g. glutathione, thioredoxin reductase, hydrogen peroxide), and releases a bright, soluble, cell-retained fluorophore enabling sensitive, cell-resolved activity imaging.

Conditional HaloTag Ligand

Paper 3: The HaloTag self-labelling protein system enables the covalent attachment of diverse chemical reagents to fusion proteins of interest (POIs). It is widely used for fluorogenic imaging, analyte sensing, or for tethering to increase local reagent concentrations. However, its utility has been limited by the lack of control: existing ligands only link chemical and biological components *unconditionally*. This absence of ligands that can respond to a (bio-)chemical stimulus, is a major design and performance gap in the HaloTag toolbox. Paper 3 (and the Patent) introduce a conditional HaloTag ligand that ligates only after uncaging e.g. by light or enzymatic activity. This new ligand expands the HaloTag system with new capabilities: (1) photo-triggered fluorogenic reagents enable spatiotemporally precise protein labelling, (2) photo-triggered heterodimerisers allow light-controlled protein recruitment forcing two POIs into proximity, and (3) enzyme-triggered fluorogens permit durable recording and ratiometric quantification of enzyme activities (e.g. peptidases, oxidoreductases) in ways that should prove easily multiplexable.

Overall, this thesis develops molecular tools for probing and manipulating biological systems with unprecedented precision. The fluorogenic probes enhance the sensitivity for studying membrane integrity and enzyme activity, while the conditional HaloTag ligand brings programmable control to one of the most widely used protein labelling systems. This sets the stage for dissecting cellular processes with spatial and temporal precision, advancing basic research and translational applications.

Kurzzusammenfassung

Diese Dissertation beschreibt die Entwicklung chemischer Werkzeuge zur Visualisierung und Manipulation biologischer Systeme, um die Rolle von Proteinen und biochemischen Analyten im Kontext von Krankheiten zu untersuchen. Der erste Teil behandelt fluorogene Xanthen-Sonden zur Detektion von Membranschäden (**Publikation 1**) und Enzymaktivität (**Publikation 2**). Der zweite Teil (**Publikation 3**) stellt einen aktivierbaren HaloTag-Liganden vor, der selektiv nach Aktivierung mit Licht oder einem biochemischen Stimulus an das HaloTag-Protein bindet.

Fluorogene Fluoreszenzsonden

Publikation 1: Schäden an Zellmembranen spielen eine zentrale Rolle bei vielen Erkrankungen, etwa bei bakteriellen Infektionen oder Multipler Sklerose. Bisher verwendete DNA-interkalierende Fluorogene zur Detektion solcher Schäden sind nur eingeschränkt nutzbar, aufgrund ihrer Toxizität und da sie auf die Identifizierung von Permeabilisierung in Zellvolumina mit Zellkern beschränkt sind. Um diese Limitierungen zu überwinden, wurden in dieser Arbeit disulfonierte fluorogene Sonden entwickelt, die das gesamte Zytosol geschädigter Zellen mit minimalem Hintergrundsignal markieren. Sie ermöglichen eine empfindliche Detektion von Membranschäden, sind kompatibel mit Mehrfarbenmikroskopie und erlauben unter anderem die Sichtbarmachung neuronaler Axonschäden *in vitro* sowie die Analyse von Membranschäden auf Einzelzellebene in *Drosophila*-Wundmodellen *in vivo*.

Publikation 2: Fluorogene Bioaktivitätssonden sind wichtige Werkzeuge in Forschung und Diagnostik, die zur Untersuchung von Enzymaktivitäten in der Grundlagenforschung oder für fluoreszenzgestützte Chirurgie weitverbreitet eingesetzt werden. Während diese Sonden selbst membrangängig sein müssen, um effizient in Zellen zu gelangen, diffundieren auch ihre fluoreszenten Produkte häufig wieder heraus, was zu Signalverlust, geringer zellulärer Auflösung und niedriger Sensitivität bei langsam ablaufenden Prozessen führt. Bisherige Strategien zur Zellretention sind meist ineffizient oder beeinflussen die native Zellbiologie durch unspezifische Alkylierung oder Kristallbildung. In Publikation 2 wurden daher ladungs- und polaritätsbasierte Designs untersucht und ein modulares Rhodol-Gerüst identifiziert, das zwischen membrangängigem und zellretiniertem Zustand umschalten kann. Diese modulare Plattform erlaubt die Detektion verschiedener Spezies (z. B. Glutathion, Thioredoxin Reduktase, Wasserstoffperoxid) und liefert zellretinierte, helle Signale für zellaufgelöste Aktivitätsmessungen.

Aktivierbarer HaloTag Ligand

Publikation 3: Das HaloTag-System ermöglicht die kovalente Verbindung chemischer Reagenzien mit gewünschten Fusionsproteinen. Seine Anwendung wurde jedoch bisher durch das Fehlen von Kontrolle über diese Bindung eingeschränkt: Bestehende Liganden koppeln chemische und biologische Komponenten *bedingungslos*. Publikation 3 stellt einen konditionalen HaloTag-Liganden vor, der erst nach Aktivierung – etwa durch Licht oder enzymatische Aktivität – binden kann. Dieser neue Ligand erweitert das HaloTag-System um mehrere neue Funktionen: (1) lichtaktivierbare fluorogene Reagenzien ermöglichen eine räumlich und zeitlich präzise Proteinmarkierung, (2) lichtgesteuerte Heterodimerisierer erlauben die kontrollierte Rekrutierung von Proteinen, um zwei Proteine gezielt in räumliche Nähe zu bringen, und (3) enzymaktivierte Fluorogene ermöglichen die Aufzeichnung und ratiometrische Quantifizierung von Enzymaktivitäten (z. B. Peptidasen, Oxidoreduktasen).

Insgesamt entwickelt diese Arbeit molekulare Werkzeuge zum präzisen Visualisieren und Manipulieren biologischer Systeme. Die fluorogenen Sonden verbessern die Sensitivität zur Untersuchung von Membranintegrität und Enzymaktivität, während der aktivierbare HaloTag-Ligand eine programmierbare Kontrolle in das am weitesten verbreiteten Proteinmarkierungssystem einführt. Damit schafft diese Dissertation neue Möglichkeiten zur räumlich und zeitlich aufgelösten Analyse zellulärer Prozesse.

Content Overview

Parts of this work have been published in peer-reviewed journals

1) **Paper 1** (first author, *JACS*, **2024**):
Mauker, P.[#]; Beckmann[#], D.; Kitowski, A.; Heise, C.; Wientjens, C.; Davidson, A. J.; Wanderoy, S.; Fabre, G.; Harbauer, A. B.; Wood, W.; Wilhelm, C.; Thorn-Seshold, J.; Misgeld, T.; Kerschensteiner, M.; Thorn-Seshold, O.
Fluorogenic Chemical Probes for Wash-Free Imaging of Cell Membrane Damage in Ferroptosis, Necrosis, and Axon Injury.
J. Am. Chem. Soc. **2024**, *146* (16), 11072–11082. https://doi.org/10.1021/jacs.3c07662

2) **Paper 2** (first author, *Chemical Science*, **2025**):
Mauker, P.; Dessen-Weissenhorn, L.; Zecha, C.; Vepřek, N. A.; Brandmeier, J. I.; Beckmann, D.; Kitowski, A.; Kernmayr, T.; Thorn-Seshold, J.; Kerschensteiner, M.; Thorn-Seshold, O.
A Modular Scaffold for Cellularly-Retained Fluorogenic Probes for Sensitive Cell-Resolved Bioactivity Imaging.
Chem. Sci. **2025**, *16* (47), 22630–22637. https://doi.org/10.1039/D5SC05388A.

Parts of this work have been deposited on a preprint server while under scientific review

3) **Paper 3** (first author, *bioRxiv*, **2025**):
Mauker, P.; Zecha, C.; Dessen-Weissenhorn, L.; Roman-Albasini, L.; Meiring, J. C. M.; Brandmeier, J.; Beckmann, D.; Prohaska, J.; Reynders, M.; Li, Y. L.; Mrug, K.; von Schwerin, H.; Veprek, N. A.; Gaisbauer, J.; Dehmelt, L.; Nalbant, P.; Zenker, J.; Akhmanova, A.; Kerschensteiner, M.; Harbauer, A.; Thorn-Seshold, J.; Thorn-Seshold, O.
Logic-Gating the HaloTag System with Conditional-Halo-Ligator "CHalo" Reagents.
bioRxiv **2025**. https://doi.org/10.1101/2025.09.23.676741

Other published parts arising from this PhD that have not been included in this dissertation

4) **Patent**: O. Thorn-Seshold, P. Mauker; Compound, composition, kit and their use for protein labelling. Patent LU602798, **2025**. *Note*: This patent is based on the results discussed in Paper 3 and is therefore not presented separately.

5) **Paper 4***:* (*ACIE*, **2024**):
Schmitt, C.; Mauker, P.; Vepřek, N. A.; Gierse, C.; Meiring, J. C. M.; Kuch, J.; Akhmanova, A.; Dehmelt, L.; Thorn-Seshold, O.
A Photocaged Microtubule-Stabilising Epothilone Allows Spatiotemporal Control of Cytoskeletal Dynamics.
Angew. Chem. Int. Ed. **2024**, *63* (43), e202410169. https://doi.org/10.1002/anie.202410169
summary of Paper 4 on the next page.

Brief summary of <u>Paper 4</u> (not part of this thesis) and of my contributions to it:

Microtubules (MTs) are cytoskeletal structures that undergo constant assembly and disassembly, and are vital for many cellular processes including intracellular transport, cell proliferation, cell motility, and neuronal development.[1–4] Modulators of MT dynamics serve as antimitotic drugs in clinics[5,6] as well as tools for basic cytoskeleton research. However, precise spatiotemporal control of these tools is needed to better study MT functions in specific contexts which motivates the development of light-controlled MT-modulating toolsets. While many useful photoactivatable MT destabilisers have been reported by our group,[7–12] photocaged MT stabilisers were far less well developed. Photocaged taxanes were shown to release their active forms only inefficiently (either via double uncaging, or 1,2-benzoyl shift after uncaging)[13–16]; and there were only two somewhat useful photoswitchable stabilisers: photoswitchable taxanes (AzTax)[17], or photoswitchable epothilones (STEpo),[18] which both suffered from low potency and a small turn-on index of bioactivity.

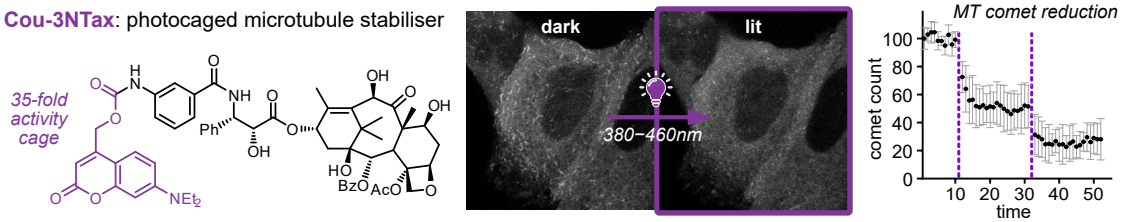

Paper 4 aimed to develop high-performance, photo-activated microtubule (MT) stabilisers to solve this unmet reagent need. My contribution to the project included the design and synthesis of a photocaged taxane derivative. This was achieved by introducing the photon-efficient *N,N*-diethylaminocoumarin photocage to 3'-*N*-aminobenzoate functionalised taxane analogues, to give **Cou-3NTax** and **Cou-4NTax**. Both reagents were efficiently photouncaged with blue light (>50% conversion). Light-activation of **Cou-3NTax** resulted in a 35-fold potency increase in cell viability assays and allowed MT stabilisation in live cell imaging. However, the low potency of **3NTax** (0.8 µM vs. ~1 nM potency for docetaxel and paclitaxel)[19] necessitated high concentrations which is problematic due to the limited aqueous solubility of taxanes. Consequently, the study focused on a highly potent and water-soluble photocaged ZK-epothilone (**CouEpo**) that was developed by my colleague Carina Schmitt.

Table of Contents

A. INTRODUCTION

1 Enzymatic and biochemical reactions define life, health and disease

The orchestrated network of dynamic chemical reactions in cells constitutes the biochemical foundation of life, and even minor and temporary imbalances can mark the difference between health and disease. These reactions are (kinetically) controlled by enzymes, which act as biological catalysts and can be regulated in response to external or internal stimuli, allowing a cell to maintain cellular homeostasis by responding to environmental changes. Enzymes work hand in hand with small molecule regulators such as hormones or secondary messengers, that can induce signalling pathways and alter enzymatic activity (e.g. by up- or down-regulation).[20] Cellular compartments provide distinct reaction environments which are optimised for their specific functions and are separated by lipid bilayer membranes (**Figure 1a**).[21,22] All these parallel reaction pathways, catalysts, and products, interact with each other to build a complex and finely balanced network (**Figure 1b**) and dysregulation of these networks can be caused by or result in pathological cell states.

Since the discovery of the first enzyme more than two centuries ago[23], we now have a much better understanding of the diversity of chemical reactions they can catalyse, and how they can function cooperatively or competitively in complex networks. Nevertheless, many enzymes remain poorly characterised.[24,25] Methods to evaluate and perturb enzymatic function in living systems are urgently needed, in order to understand their role in health and disease and to develop therapeutic strategies.[26] Genetic techniques (e.g. knock-out, mutations and RNA-mediated interference) can be used to modulate protein expression levels, and they are precise in the sense that they specifically manipulate their target protein.[27] However, expression levels are not directly proportional to protein activity (which is additionally controlled by post-translational modifications), and genetic manipulation is time-consuming and cannot be easily translated between different cell lines or organisms. A key advantage of chemical tools such as small molecule ligands and probes is that they can modulate and visualise protein activity without needing genetic manipulation, allowing easy translation between different model systems: which drastically reduces the time needed to implement and leverage new test systems.

This work focuses on the development of such *chemical tools* to probe biology.

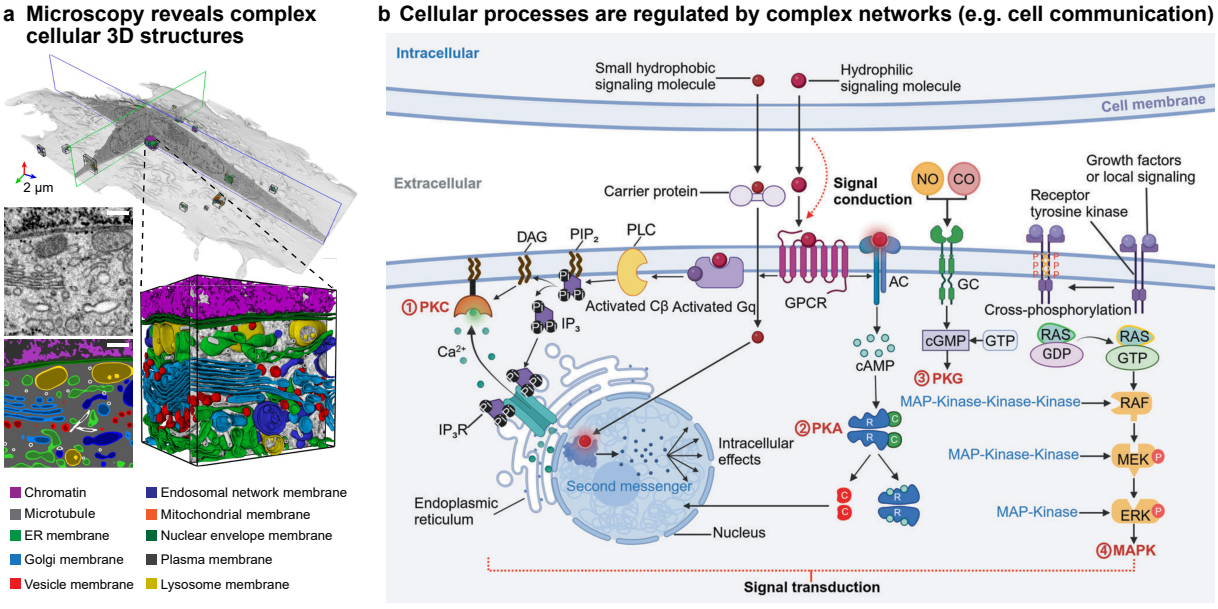

Figure 1: Complex biological structures and interaction networks require precise molecular tools to study them (a) Electron microscopy reveals the complex structural features of a cell (reprinted with permission from *Nature* **2021**, *Copyright © 2021, Springer Nature,* reference[28]). **(b)** Signalling pathway of cell-cell communication outlining the complex cellular networks of proteins, ions and second messengers that respond to a specific stimulus to generate the desired outcome (reprinted with permission from *Sig. Transduct. Target. Ther.* **2024**, *Copyright © 2024, Springer Nature,* reference[29]).

2 Fluorogenic probes for visualising biological processes

2.1 Broad meaning of the umbrella term “Chemical Probes” and focus of this work

The umbrella term *probe* is broadly used for molecules that (selectively) interact with proteins or processes of interest, to study their roles in biology either by visualising or by perturbing their native function or activity. This work focuses on **fluorogenic enzyme turnover probes**. These are probes that provide a readout for (bio)chemical reactions: often, the inactive probe molecule (“off”) is chemically converted to a fluorescent signal-generating product (“on”) by an enzyme or biochemical analyte (**Figure 2a**). Turnover probes report on enzymatic activity or analyte reactivity by generating a signal proportional to the number of activation reactions that occur. Ideally, a **fluorogenic** turn-on mechanism allows reliable quantification by suppressing all signal from non-activated probe molecules (pro-fluorophores), making these probes very sensitive as *activity* reporters.[30,31] Fluorogenic probes are the major probe class used to resolve and quantify bioactivity in cells and tissues, but there are also other readout designs like chemiluminescence[32–34] or photoacoustic probes[35] which can e.g. allow higher signal-to-noise ratios and/or deeper tissue penetration in some settings.

These **turnover probes** are the crucial focus of this thesis, thus, more detail about their design and performance is given in **Section 2.2**. Confusingly though, several other classes of reagents are also termed *probes* in different contexts e.g. in medicinal chemistry, activity-based protein profiling, and structural or anatomical microscopy. Although each class of "probe" is quite different in design and performance, it is worthwhile to introduce those briefly, before the focus moves back to turnover probes:

(1) Selective **modulators of protein function** (like inhibitors or agonists) are used as probes to answer mechanistic questions about their target (**Figure 2b**).[36] As distinct from *therapeutically effective* drugs, such modulating probes must be very *mechanistically selective* for their target protein and have a defined mode of action (avoiding polypharmacology), while the requirements towards potency, bioavailability, pharmacokinetics, and metabolic safety, are much lower. Often, probes have helped to identify new drug targets. For example, the orphan nuclear liver X receptor (LXR) agonist T0901317 revealed the role of LXR in inflammation, atherosclerosis, and Alzheimer's disease: which inspired the development of several LXR drug candidates tested in clinical trials.[37,38]

(2) **Activity-based protein profiling** (ABPP) is used to identify the target enzymes, selectivity, and binding sites, of a small molecule inhibitor by covalently reacting a probe analogue of the inhibitor, with its protein target (**Figure 2c**).[39] ABPP probes feature the ligand structure that binds to the protein, a covalent warhead, and an analysis tag (e.g. a fluorophore or clickable functionality that allows pull-down and mass spectrometry analysis). The major class of activity-based probes for protein profiling are electrophilic probes (intrinsic covalent reaction with protein nucleophile). Photoaffinity probes on the other hand rely on light-induced electrophile generation to covalently label their protein binding partners.[26]

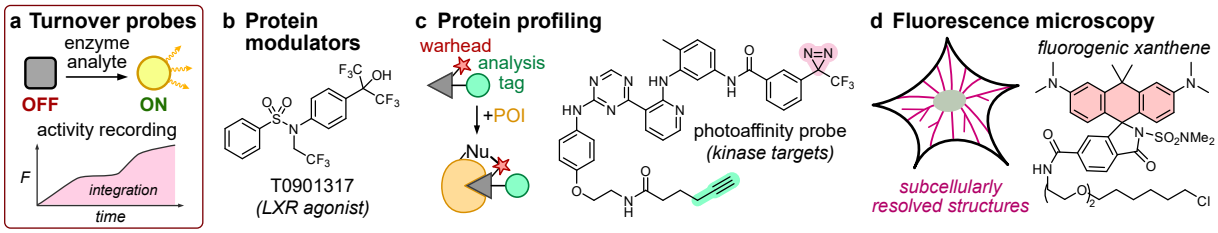

Figure 2: Example probes for different application fields. (a) General mode of action for turnover probes. **(b)** Medicinal chemistry probe T0901317[38]; **(c)** Photoaffinity probe for protein profiling[39]; **(d)** Carbopyronine-based probe for fluorescence microscopy.[40]

(3) **Fluorescence probes for microscopy** are reporters that selectively label proteins of interest, and thereby allow to visualise the localisation, abundance, (3D) structure, movement, or trafficking of proteins within live cells (**Figure 2d**). Fluorescence probes are fundamental for the structural elucidation of biology,[41] and they rely on bright fluorophores that specifically label their target with high spatial precision (often using self-labelling protein tags like HaloTag, also see **Section 4.2.1**). These probes may be permanently fluorescent, or conditionally fluorogenic: i.e., only fluorescent when bound to their target, to eliminate unwanted background signal.[40,42–44]

2.2 Functional features of fluorogenic turnover probes

Fluorogenic turnover probes are non-fluorescent pro-fluorophores that are transformed to their fluorescent fluorophore products by a specific biochemical stimulus, typically an enzyme or small molecule analyte. They comprise three general features: (1) the fluorophore that generates the detectable signal upon activation, (2) the turn-on mechanism that controls the off→on switching, and (3) the activation motif that (selectively) reacts with the target enzyme or analyte. Optionally, self-immolative spacers can be utilised to translate between the available functional groups on the fluorophore and the functionality required for the activation motif.

2.2.1 Fluorophore

A choice of fluorophore is based on many criteria, including: (1) for multi-colour imaging applications, the probe fluorophore must be spectrally distinct from other fluorophores in the setup (e.g. all other activity probes or structural stains). (2) Short-wavelength light (blue and UV) can be phototoxic for cells and must be avoided (unless only low light intensities are needed) so that the light itself does not perturb the biological system. (3) For thick tissues or *in vivo* applications, one must also consider the required light penetration. While blue light penetrates less than 1 mm into biological tissues, red and NIR light reaches up to two centimetre penetration depth.[45,46] (4) The fluorophore must be compatible with a sensitive and selective readout using the excitation light sources and emission filters of the device (e.g. microscopy, flow cytometer, plate reader). For broadest applicability in most laboratories, one should align probes with standard "channels", e.g. the GFP channel (green-fluorescent protein), which are available on almost all devices; or, for multi-colour applications, one would typically use non-standard colours which do not overlap with reporter fluorophores (potentially requiring high-end instruments that allow free choice of the excitation and emission wavelengths). (5) Low-turnover targets particularly benefit from bright fluorophores for sensitive detection and (6) if high light-intensities are used, the fluorophore must be very photostable.

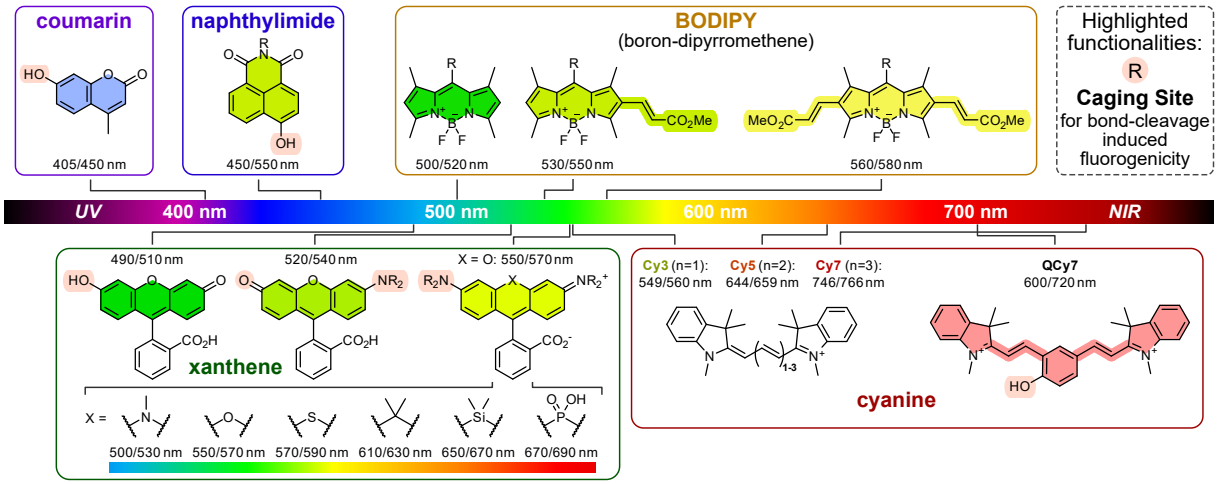

Figure 3: Fluorophores for fluorogenic probes across the visible spectrum. The fluorescence properties of fluorogenic probes are defined by the fluorophore class. Frequently used examples are coumarins, naphthylimides, BODIPYs, xanthenes or cyanines.[30,47–54]

A variety of fluorophores is available, from different dye classes and with tuneable spectral properties across the whole visible to NIR spectrum, to match most probe requirements (**Figure 3**). Classic probes use violet to blue excited coumarin[48] or naphthylimide dyes[49] but recently the focus shifted to more red-shifted fluorophore classes. These include xanthenes, boron-dipyrromethenes (BODIPYs), and cyanines, which are all easily red-shifted by extending their conjugated π-systems: e.g. with the cyanine series Cy3, Cy5, and Cy7, spanning 200 nm of the visible spectrum (green to red). [30,47,52–55] As a bright and photostable fluorophore class, xanthenes are one of the most widely used fluorophore classes in probe development and can be sub-classified depending on their xanthene donor/acceptor substitution: fluoresceins (*O,O*), rhodols (*N,O*) and rhodamines (*N,N*). Especially rhodamines have been optimised and tuned for high-performance imaging and their absorption and emission properties can be strongly modulated (over 200 nm, green to far-red) by modifying the bridging group.[51] Readers interested in (fine-)tuning xanthene fluorophore properties are referred to excellent studies by the Lavis Lab.[51,56–58]

2.2.2 Fluorescence turn-on mechanisms

Xanthenes with pendant ring nucleophiles can adopt two forms: a non-fluorescent, spirocyclised form; and a fluorescent, open form with π-conjugation across the whole xanthene core (**Figure 4a**). This **intramolecular spirocyclisation** can be utilised to create many types of activatable probes, all relying on a reaction-induced shift in the spirocyclisation equilibrium. The spirocyclisation equilibrium constant of a probe or fluorophore depends on the electrophilicity of its xanthene core (controlled by the electron-donating capacity of the donor/acceptor substituents, and the nature of the bridging group "X") relative to the nucleophilicity of its pendant-ring nucleophile, modified by local environment effects.

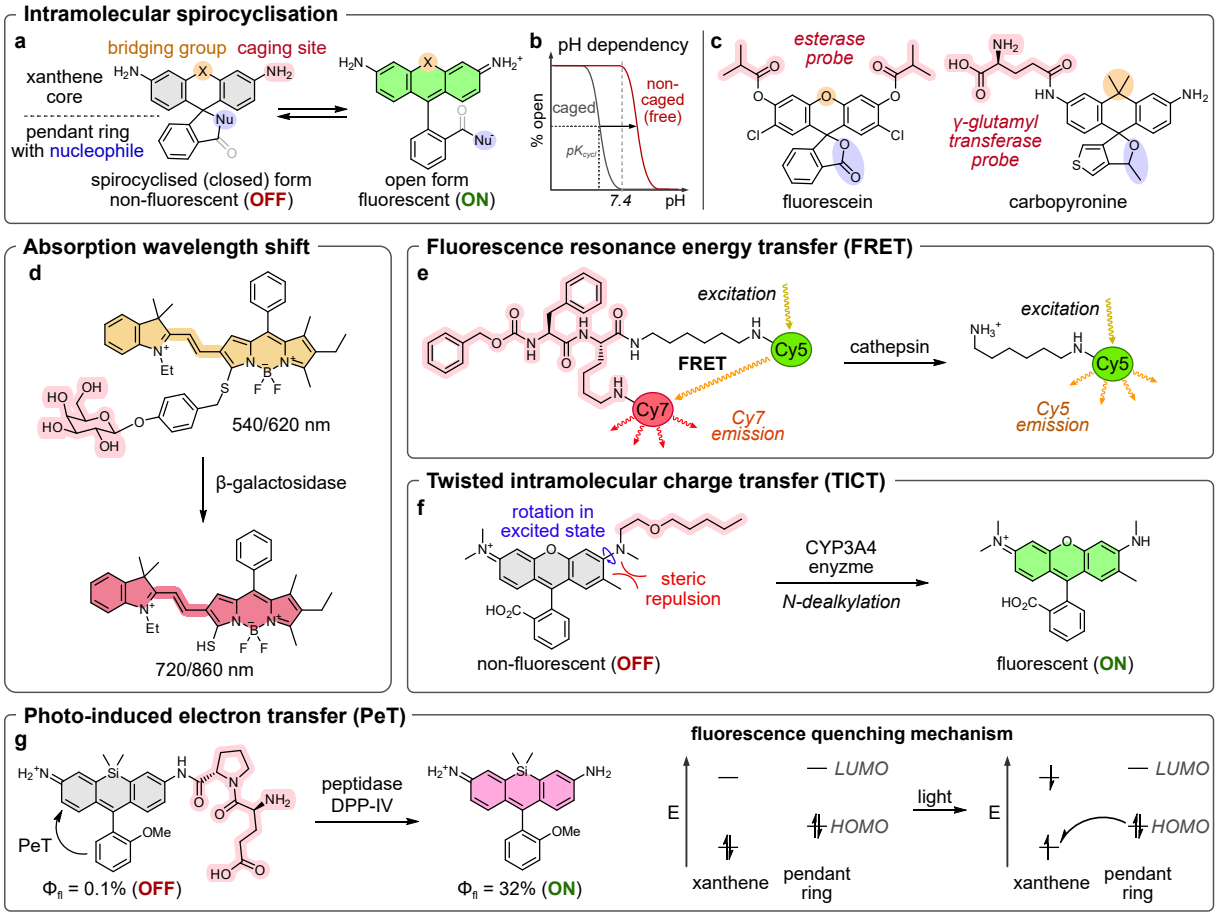

Figure 4: Turn-on mechanisms for fluorogenic probes. (a–c) Intramolecular spirocyclisation of xanthenes can be modulated by caging the aniline or phenol, and by changing the bridging group and the pendant ring nucleophile (examples: esterase[59] and γ-glutamyl transferase probes[60]). **(d)** Wavelength shift probes change their absorption maximum upon activation (example: β-galactosidase probe[61]). **(e)** Fluorescence resonance energy transfer (FRET) probes quench the fluorescence of a donor fluorophore with an acceptor fluorophore and allow ratiometric readout (example: cathepsin probe[62]). **(f)** Twisted intramolecular charge transfer (TICT) probes quench their fluorescence due to aniline bond rotation in their excited state which can be suppressed by reducing the steric repulsion (example: CYP3A4 probe[63]). **(g)** Photo-induced electron transfer (PeT) probes quench their fluorescence with a nearby electron acceptor or electron donor (shown, SiR peptidase probe[64]).

Typically, fluorogenic probes rely on reaction-based changes to either the donor/acceptor electron densities, or key local environment effects. Most simply, changing the dye's local microenvironment from low- to high-dielectric (when it switches from a free nonpolar-partitioned state to a covalently-HaloTag-bound state) can be exploited to make dyes that are fluorogenic upon HaloTag ligation: e.g. MaP dyes, or silicon rhodamines (see **Section 4.2.1**).[40,65] More commonly though, fluorogenic probes can be built when a targeted reaction transforms a fluorescein or rhodamine from an electron poor, acylated ("caged", ester or amide) probe state, into an electron richer, free ("non-caged", phenol or aniline) product state. This is accompanied by a shift of the spirocyclisation equilibrium: from a more-closed (nonfluorescent) probe state, to a more-open (fluorescent) product state. By modifying the bridging group to tune the wavelengths of excitation and emission, then adjusting the pendant ring nucleophilicity to compensate for the electrophilicity of the bridge, a range of fluorogenic probes can be rationally created to feature distinct optical properties, all while following similar molecular design principles.[30]

A convenient way of formalising the balances involved in this multi-step design and refinement process is to focus on the pH dependency of the spirocyclisation equilibria of any acylated probe and its corresponding free product, according to their conserved structural elements (bridge nature, pendant nucleophile, etc). Either molecule's equilibrium can be described with an equilibrium constant pK_{cycl} defined as the pH with 50% spirocyclisation (**Figure 4b**). When a rhodamine probe's $pK_{cycl} < pH_{bio}$ (typically ~7) but the product's $pK_{cycl} > pH_{bio}$, then the reaction-induced increase of pK_{cycl} results in fluorescence turn-on (**Figure 4b–c**). Conveniently, Urano and co-workers developed a straightforward method for designing spectrally shifted turn-on probes by reliably predicting pK_{cycl} values of unknown xanthenes with density functional theory calculations, which reduces the synthetic efforts towards new probes.[60] Whether empirically identified or rationally designed, spirocyclisation probes are a highly effective design strategy and they have become widely used for many application types – even fluorescence assisted cancer surgery in patients.[66,67] **Spirocyclisation probes are key to all projects of this thesis (Papers 1–3).**

Besides **spirocyclisation probes** which are used across all projects in this thesis, there are many other systems covered in the prior art on fluorogenic probes that are not relevant for this thesis but interesting to introduce comparatively, particularly the following four:

Chemically induced **absorption wavelength shift** probes utilise the simple effect that biochemical uncaging reactions can change the electronic properties of fluorophores thereby shifting their absorption profiles into spectral regions where their caged probes do not absorb light. Such wavelength shifts can often be achieved by donor-unmasking (deacylation or dealkylation), e.g. with far-red BODIPY dyes (**Figure 4d**)[62] or cyanines.[47] One advantage of wavelength-shift probes is their suitability as ratiometric probes (samples are excited to quantify both probe, and the released fluorophore).[30]

Fluorescence resonance energy transfer (FRET) describes the energy transfer from an excited donor-fluorophore to an acceptor chromophore with longer wavelength absorption in its close proximity. There are two types of FRET probe designs: (a) dye-quencher probes use a non-fluorescent quencher as acceptor; (b) dye-dye type probes use a second fluorophore as acceptor which allows for ratiometric signal readout (**Figure 4e**).[30] FRET probes are particularly suited for endopeptidases which can be difficult to target with other turn-on mechanisms. Elegant designs can utilise AND-gate approaches, where two acceptor chromophores are released by two different enzymes which may drastically increase the on-target selectivity, e.g. for fluorescence assisted surgery probes.[63]

Twisted intramolecular charge transfer (TICT) describes the effect that the excited state of donor-substituted fluorophores can often be quenched by intramolecular charge transfer e.g. when aniline donor substituents are twisted out of the fluorophore plane.[68] The twisting tendency depends on the electronic structure of the substituent and the steric repulsion between the “in-plane” substituent and nearby groups (steric repulsion = sr-TICT). TICT can be exploited for probes when the steric repulsion changes upon reaction (**Figure 4f**), which has been successfully utilised for the development of e.g. CYP enzyme probes with signal generation upon *N*-dealkylation.[61]

Photo-induced electron transfer (PeT) probes utilise the non-radiative deactivation of a fluorophore's singlet excited state (fluorescence quenching) by electron transfer between the excited fluorophore and a nearby electron donor or acceptor (**Figure 4g**). The HOMO energy of the fluorophore and the oxidation potential of the electron-donor/acceptor must be matched for efficient electron transfers. In PeT probes the fluorophore is often caged (e.g. by alkylation or acylation) to change its HOMO energy and ensure efficient quenching in the caged probe, while no quenching should occur in the free fluorophore.[30] The probe design can profit from density functional theory based prediction methods for HOMO energies and oxidation potentials (developed for xanthenes by Urano and co-workers).[69] While PeT probes are somewhat rare as turnover probes, they are crucial for metal ion sensing (e.g. calcium probes).[70]

2.2.3 Enzymatic or biochemical activation substrates

In general, probes release their cargo upon a chemical reaction that affects a "activation substrate" (typically a bond cleavage reaction, or an oxidation or reduction), so activating their fluorescence by the turn-on mechanisms discussed above (**Section 2.2.2**).

This section now illustrates the wide range of enzyme and biochemical activation substrate groups that are available (**Figure 5**), which allow us to study these diverse targets, and in doing so, shows the importance of activity probes for basic research and diagnostic applications. The motifs that will prove relevant to this PhD are esterases for **Paper 1**, esterases, oxidoreductases (TrxR) and hydrogen peroxide reactive boronates for **Paper 2**, and peptidases and oxidoreductases for **Paper 3**. However, all three papers have a generalist focus that is far more concerned with scaffold fluorogenicity (**Section 2.2.2**) and retention (**Section 2.4**) than with any specifics of the unmasking groups.

Hydrolases

Cells express a large pool of **peptidases** (also called proteases) with different functions and many of them are known to be dysregulated in diseased and cancerous cells which led to the development of numerous probes. Examples are probes for γ-glutamyl transferase (GGT; breast, oral and hepatic cancer)[71], leucine aminopeptidase (LAP; breast cancer)[72] or calpain-1 with a proline-arginine dipeptide probe (glioblastoma)[73]. Targeting the dysregulation of the peptidase pool, Urano and co-workers developed a screening platform with 380 mono- and dipeptide probes and tested them with clinical specimen to identify new biomarkers and to develop cancer-selective pro-drug strategies.[74] **Glycosidases** are likewise promising targets as biomarkers for metabolically active cancers cells, for example *N*-acetyl glycosidase (colon cancer)[75] or α-mannosidase (breast cancer)[76]. β-Galactosidase probes are used with the lacZ reporter gene for selective labelling of lacZ positive cells.[77] **Phosphatases** are phosphate ester hydrolysing enzymes that play key roles in disease pathogenesis and cell regulation which inspired the development of phosphate-caged probes.[31,78,79] **Esterases** are often utilised for improved drug delivery of sensors or bioactive molecules and carboxyesterase probes are used to determine the stability and esterase hydrolysis efficiency of different esters.[59] Selective esterase-ester pairs can even be used for selective delivery of bioactive molecules to specific, genetically modified cell populations in complex tissues.[80] Octanoic acid probes visualise lipase activity in bacterial pathogens like tuberculosis[81] and cyclopropanecarboxylate probes are used to image butyrylcholinesterase which is important for cholinergic neurotransmission with abnormal levels being associated with neurodegenerative diseases[82].

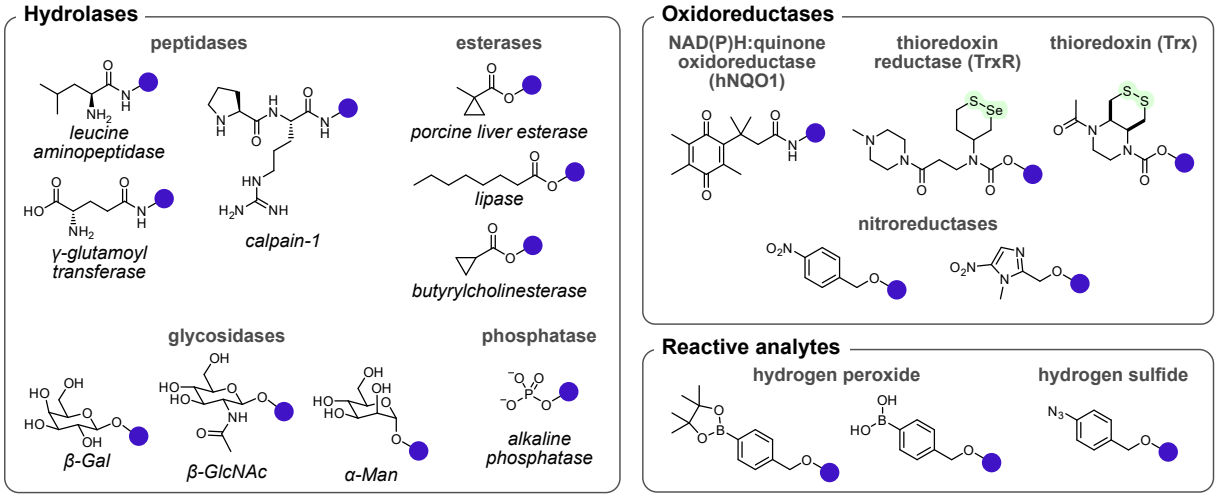

Figure 5: Enzymatic and biochemical activation substrates for fluorogenic probes. Fluorogenic probes utilise enzyme and analyte activatable motifs which are cleaved or modified upon reaction to generate a signal. The most important enzyme classes are hydrolases and oxidoreductases; commonly targeted reactive analytes are hydrogen peroxide and hydrogen sulfide (azides with questionable selectivity).

Oxidoreductases

Oxidoreductases as key moderators of cellular redox biology are associated with pathologies like cancer and inflammatory diseases and probes to study them are needed to understand their function. **NAD(P)H:quinone oxidoreductase isozyme 1** (hNQO1) is upregulated in many cancers[83] and its activity can be visualised with quinone propionate motifs.[84] **Thioredoxin** (Trx) and **thioredoxin reductase** (TrxR) are key regulators of the thiol/disulfide redox network. Only recently, the first selective probes featuring chemoselective disulfide or selenenyl sulfide motifs became available which sets the stage for a better understanding of these enzymes but also for the development of selective drugs which was hardly possible before – again underlining the importance of bioactivity probes as research tools.[85–88] Nitroreductase (NTR) is a flavin-dependent enzyme that is upregulated in hypoxic tumour environments and can be studied with nitroaryl-caged probes.[89,90]

Reactive analytes

Reactive oxygen species like **hydrogen peroxide** (H_2O_2) occur naturally as oxidative secondary messenger involved in cell signalling (typically by protein cysteine oxidation) or as an unwanted metabolic byproduct from the respiratory chain.[91] Harmful levels have been correlated to neurodegeneration, cancer, or autoimmune disorders.[92–94] In common H_2O_2 probes, aryl boronic acids (or boronate esters) are used that are converted to phenols upon reaction with H_2O_2.[95] **Hydrogen sulfide** (H_2S) on the other hand is a reductive signalling molecule involved in physiological processes such as cell growth regulation or cardiovascular protection and its dysregulation has been associated with diseases like diabetes and Alzheimer's disease. Small molecule probes detecting endogenous hydrogen sulfide use aryl azides that form anilines upon H_2S reduction.[96–98]

All these probe types have helped to understand and investigate their target enzymes and analytes, and are fundamental as basic research tools and diagnostic agents. Notably, peptidase and glycosidase probes are even used as diagnostic tools in fluorescence imaging guided surgery for detecting small cancer lesions and the borders between healthy and cancerous tissue which reduces the patient's risk of recurrence.[30,66,99] For a much broader overview of the available probe motifs, the interested reader is referred to the excellent reviews by Raines[31] and Urano[30].

2.2.4 Self-immolative spacers act as chemical adapters

Before the enzymatic or biochemical targets (discussed above) can be addressed by pairing their appropriate substrate motifs with the desired fluorophore scaffold, often, a chemical adapter is needed.

Self-immolative spacers (also called auto-immolative linkers) are chemical adapters that chemically connect the activation substrate with their cargo and spontaneously eliminate after activation.[100,101] Spacers can improve probe designs in four ways (**Figure 6a**): (1) As **translators** between functional groups released from the enzymatic activation step and needed on the released cargo, **which may not otherwise be freely compatible:** e.g connecting an amine releasing peptidase motif with a phenolic fluorophore[102]. (2) They can be utilised to reduce the steric hindrance to accelerate the enzymatic activation rate[102,103], and (3) they can act as molecular splitters which allows the use of FRET probe designs (which rely on *endo*-bond cleavage to separate acceptor and donor fluorophore) for *exo*-hydrolases like glycosidases that can only cleave terminal functionalities[104]. (4) Spacers can additionally improve the hydrolytic probe stability, e.g. by transforming phenolic esters into the less labile aliphatic esters.[59]

Two classes of spacers are mostly used: electronic cascade elimination spacers and cyclisation spacers. Famous electronic cascade elimination spacers are the (*aza*-)quinone methide type spacers which are installed as hydroxy- or aminobenzyl groups and undergo 1,4- or 1,6-elimination upon biochemically stimulated deacylation or dealkylation (**Figure 6b**). Optionally such spacers can be introduced as carbonates/carbamates to additionally eliminate carbon dioxide. Oxymethyl spacers release hemiacetals which undergo 1,2-elimination to release their activated (fluorescent) product.[59,100,101] Cyclisation spacers can form a thermodynamically favoured cyclisation product (entropically favoured) upon enzymatic release of a hydroxyl or amino group (**Figure 6c**). (2-Hydroxyphenyl)propionic acid esters undergo 6-*exo-trig* cyclisation which can be accelerated by utilising a “trimethyl lock” of three methyl groups that

pre-organise the spacer for much faster cyclisation (also called Thorpe-Ingold effect[105]).[106,107] Diamine spacers like *N*,*N*'-dimethyl-1,2-diamine or 2-(aminomethyl)piperidine spacers undergo 5-*exo*-*trig* cyclisation upon deacylation to efficiently release phenolic cargos.[101,102]

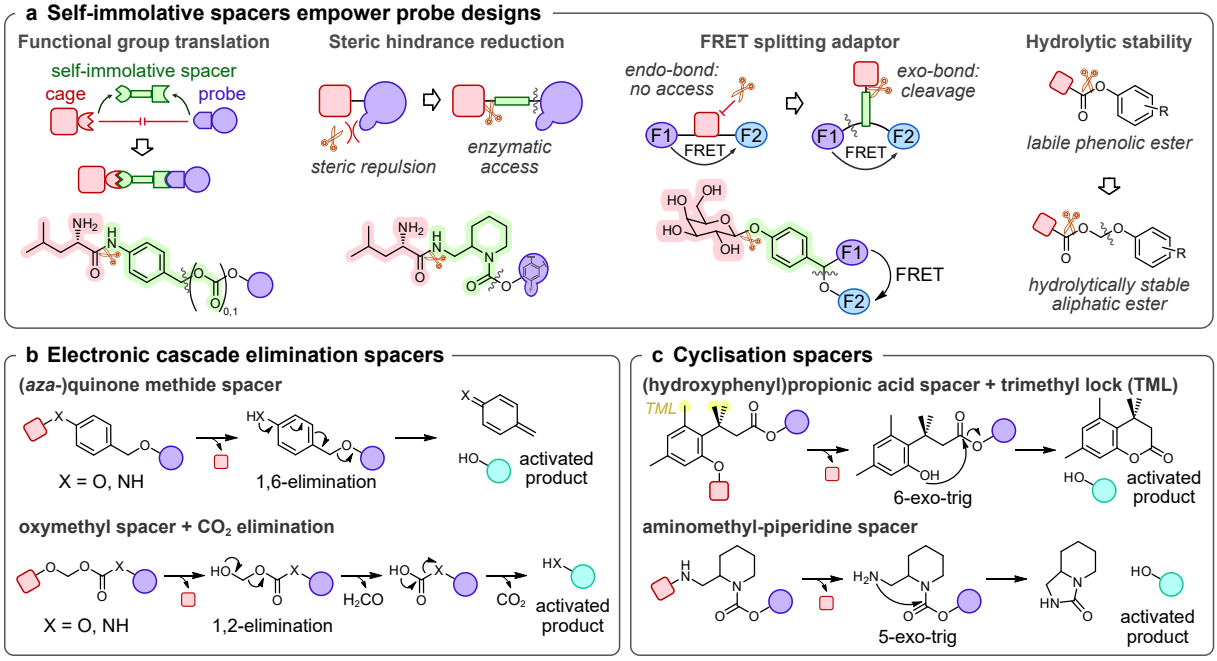

Figure 6: Self-immolative spacers are used as chemical adaptors. (a) Functional features and improvements that spacers bring to empower probe designs. **(b)** Examples of electronic cascade elimination spacers. **(c)** Examples of cyclisation spacers.

By correctly uniting the three design "modules" – fluorogenic scaffold, substrate masking group, and chemical adapter – an enormous variety of fluorogenic probes can, in theory, be created. However, there are many additional needs that must be considered before a probe can be rationally designed to deliver a satisfactory level of performance, e.g. signal background and retention.

2.3 Signal background compromises probe performance

The fluorescence signal generated from fluorogenic probes is accompanied by different types of background noise that can compromise probe performance and depends on the different instruments that are used to record probe fluorescence. Three instrumental setups are mostly used: microscopy, flow cytometry or plate reader instruments which provide different information quality and throughput.

Fluorescence microscopy is an imaging technique that gives detailed information about the fluorescence signal distribution (cell-by-cell resolution and even intracellular distribution), and can be used for real-time analysis (**Figure 7a**), though at the expense of low throughput (only few conditions per day). Notably, two types of microscopes can be used: Cheaply available epifluorescence microscopes illuminate the whole sample and collect fluorescence not only from the sample plane ("in focus") but also from the layers above and below which increases the background signal. Confocal microscopes solve this problem by point illumination and a pin hole that filters out most of the fluorescence from outside the sample plane and thereby achieve higher resolution with lower background than epifluorescence microscopes.[108] In **flow cytometry**, cell populations are analysed on a cell-by-cell basis to give a signal distribution for the whole population (**Figure 7b**). This method gives detailed information on the signal heterogeneity and removes extracellular background during sample preparation and by only quantifying the cellular fluorescence when passing through the detector. Flow cytometry allows higher throughput than microscopy (dozens to hundreds of samples per day) but has limitations as an endpoint analysis and it cannot resolve the subcellular signal distribution.[109] **Plate reader** instruments allow bulk measurements for cell populations reporting an averaged signal from all cells and the extracellular medium in a sample (**Figure 7c**). This allows to analyse activity differences of cell populations that were treated differently, e.g. with inhibitors. The method allows real-time analysis with high throughput (thousands of samples per day) but the information about signal heterogeneity within cell populations in a well is lost.

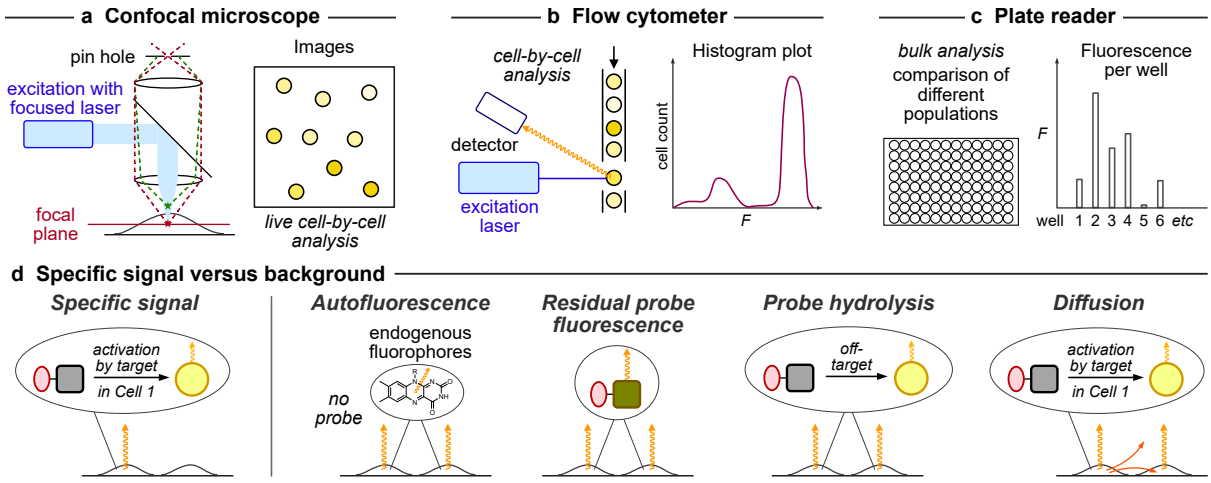

Figure 7: Different instruments record different types of signal and background. (a) Confocal microscopes record images with high resolution allowing to differentiate signal distribution with subcellular precision, **(b)** flow cytometry enables cell-by-cell analysis and **(c)** plate reader instruments are used for bulk analysis of cell populations. **(d)** Analytical methods are affected by various types of non-specific background from autofluorescence, residual probe fluorescence, unwanted probe hydrolysis and post-activation diffusion.

Signal background is the fluorescence that does not originate from the probe's target enzyme or analyte in the activating cell ("specific signal") and can reduce the imaging resolution and detection sensitivity of fluorogenic probes. There are different types of signal that contribute to this problematic background (**Figure 7d**): (1) Autofluorescence is caused by endogenous fluorophores like flavins, fatty acids and proteins and is generally unavoidable but less problematic with red-shifted fluorophores.[110] (2) Residual fluorescence from the probe (before activation) is determined by the probe's turn-on mechanism. (3) Non-specific fluorophore release can occur from spontaneous probe hydrolysis in aqueous buffer or from off-target activation by other enzymes or analytes which can result in both intracellular and extracellular background. (4) Diffusion of the released fluorophore from the activating cell to the extracellular medium or neighbouring cells is another type of background that can falsify the signal quantification by lowering the specific signal in the activating cell and falsely increasing the signal in other cells / medium.

Diligent sample preparation can help to reduce the background signal. Washing with fresh medium removes the extracellular signal at the time of washout which can significantly improve image quality and allows to only quantify cellular signal in plate reader measurements. Fixation protocols can further reduce the background by removing all non-covalently bound and non-fixable intracellular fluorophores.

2.4 Cell-retained probes increase the detection sensitivity

This section overlaps with and extends on the background discussion I wrote for Paper 2 (that developed an improved scaffold for cellularly retained probes).

Post-activation signal loss is problematic in bioactivity imaging for two reasons: fluorophore excretion to the extracellular medium reduces the absolute intracellular signal and increases the background which together drastically reduces the signal-to-noise ratio, and it sabotages cell-resolved imaging to distinguish differential cellular activity within heterogeneous cell populations (**Figure 8a**). While this is not problematic for high-turnover enzymes or analytes that generate strong signals, low-turnover processes with only slow signal generation can become invisible if fluorophore excretion is faster than probe-activation. Building up and retaining the product signal inside the activating cell in the long term is particularly important for *in vivo* work, where probe dosage cannot be high. Signal retention allows to accumulate signal and thereby freeze the activity information over time to generate a fluorescence readout that integrates the bioactivity over the whole treatment time.

Eukaryotic cells are enclosed by lipid bilayer membranes which retain cellular components such as ions and proteins, and reduce exposure to extracellular molecules.[111] Three major membrane translocation mechanisms are known: (1) Passive diffusion allows small apolar molecules to readily cross membranes while larger or more polar species such as ions and proteins are "membrane impermeable", because the energy penalty for desolvation and traversal through the lipophilic inner region of the membrane is

high.[112] (2) Selective ion channels or pumps and transporters ensure the uptake or excretion of otherwise impermeable ions and metabolites that are required by the cellular machinery. (3) Non-selective translocation via endocytic pathways allows internalisation of any external material by the uptake of extracellular medium in vesicles.[113]

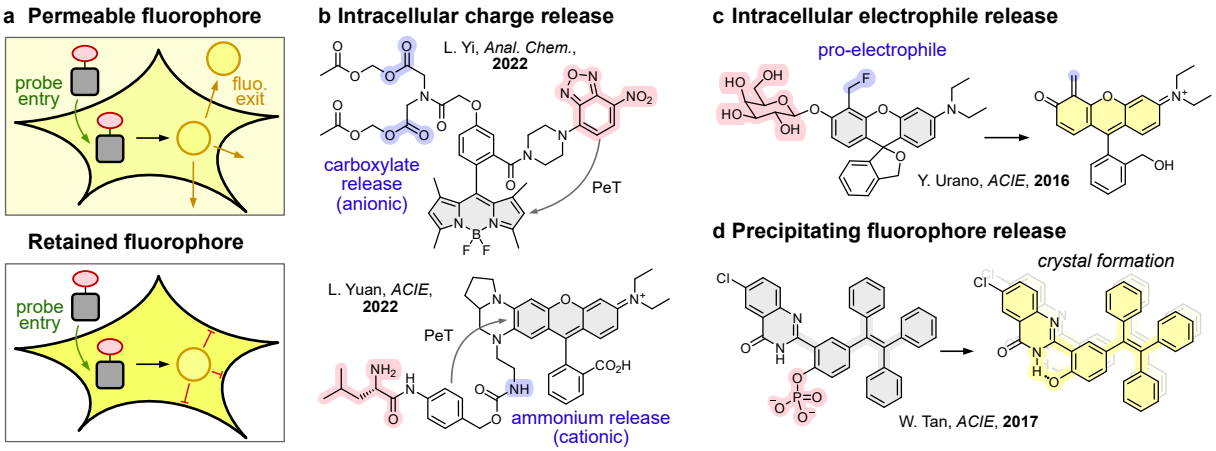

Figure 8: Cell-retained probes increase the signal-to-noise ratio. (a) Comparison of signal-to-noise ratio for permeable and retained fluorophores. **(b–d)** Retention strategies in literature: **(b)** intracellular charge release, **(c)** intracellular electrophile release, and **(d)** precipitating fluorophores.

Live cell probes must be membrane-permeable to access intracellular biochemistry. Problematically, often their fluorophore products are either similarly permeable (e.g. coumarins) and rapidly exit the cell by passive diffusion[114] or they are instead excreted by non-selective transporters (e.g. negatively charged fluorophores like fluoresceins).[115,116] This drawback of probes utilising common fluorophores (also see **Section 2.2.1**) has inspired the development of probes that release cell-retained fluorophores. Three general strategies are applied: (1) charge- and polarity-based impermeabilisation by suppression of passive membrane crossing, (2) precipitation of the released fluorophore, and (3) release of electrophiles for intracellular ligation to impermeable biomolecules (e.g. proteins or glutathione). However, all these strategies currently suffer from limitations:

Charge-based cell retention is the most broadly utilised approach (**Figure 8b**). Generally, these strategies intracellularly release either cationic (e.g. ammonium ions)[117,118] or anionic groups such as carboxylates[119], phosphonates[120] or sulfonates[121] which cannot cross lipid bilayer by passive diffusion. Usually cellular delivery of the charged functionalities is achieved by masking them as lipophilic, membrane-permeable groups (e.g. acetoxymethyl esters of carboxylates and phosphonates[119,120] or trifluoromethylbenzyl sulfonate esters[121,122]), some probes alternatively harness endocytic uptake or transporter-mediated uptake mechanisms[117,123]. Nagano and Yi developed PeT probes for nitric oxide[119] and hydrogen sulfide[52] which intracellularly release acetoxymethyl masked carboxylates but their specific designs are limited to special reaction types and cannot be utilised for simple bond-cleavage reactions which would allow modular use for many types of analytes and enzymes (see **Section 2.2.3**). Other examples by Gilbert and Chang overcome this problem by generating carboxylate-releasing phenol- and aniline-masked xanthenes for sensing hydrogen sulfide[98] and hydrogen peroxide,[124] which might be somewhat translatable to other activating triggers except that these probe designs suffer from low fluorescence brightness, low solubility, and non-specific, partial intracellular signal generation which strongly reduces any sensitivity (opposing the main goal of retained probes: increasing the sensitivity and suppressing signal background). Yuan developed PeT probes with cationic retention by releasing a basic amine for detecting hydrogen peroxide as well as leucine aminopeptidase and nitroreductase activity.[125] However, this design requires benzylic spacers whose 1,6-elimination influences signal turn-on kinetics and intracellularly releases electrophilic (*aza*-)quinone-methides which can be cytotoxic, and the net positively charged fluorophore accumulates in lysosomes after activation. Overall, previously explored charge-based retention probes come with different limitations in activation trigger modularity, fluorophore brightness, cellular uptake, release of reactive side products or undesired compartmentalisation (e.g. of basic amines to the lysosome) and the retention of negatively charged fluorophores is usually limited due to active excretion by non-specific anion transporters.[115,116]

Precipitating fluorophores accomplish intracellular fluorescence trapping by forming insoluble crystals. One example are probes based on the water-insoluble fluorophore HPQ ((2-(2'-hydroxyphenyl)-4(3*H*)-quinazolinone) that features excited-state intramolecular proton transfer (ESIPT)-based solid-state fluorescence with a large Stokes-Shift and bright signal.[126] HPQ-derived probes have been developed for alkaline phosphatase[127] and aminopeptidases[128] enabling not only cellular but even subcellular resolution of probe activation. Problematically, precipitating fluorophores come with several disadvantages: (i) their precipitation concentration threshold limits the sensitivity and renders activation below this threshold invisible, (ii) the water-insolubility of the fluorophore due to its lipophilicity and π--stacking limits the activating trigger to polar, solubilising motifs (such as phosphates or amino acids) to avoid pre-activation precipitation or membrane localisation, and (iii) the formed crystals cause inflammatory responses and are cytotoxic which perturbs biology and thus might devalue the data generated from the assay and prevent long-term imaging.[129]

Intracellular release of electrophiles for subsequent labelling of cell-impermeable biomolecules was pioneered by Urano with the development of the so-called SPiDER probes which use unreactive benzyl fluorides that only upon probe activation generate electrophilic (*aza*-)quinone-methides which react with intracellular proteins or glutathione.[130] The modularity of this strategy enabled the development of various probes for glycosidases, peptidases, nitroreductase and hydrogen peroxide with durable cellular signal retention.[71,77,89,131,132] However, the released electrophiles can alkylate their target enzyme and thereby kill its activity,[89] and the accumulation of reactive species can furthermore be toxic especially for high turnover cells.[131]

2.5 When cells cannot retain any more: membrane damage in disease contexts

The plasma membrane separates the intracellular and the extracellular space and loss of membrane integrity allows otherwise impermeable molecules to enter or exit the cell which often leads to cell death.[111] Cells with damaged membranes that are still viable are an interesting study population as they are at the verge of cell death but can still recover. This decision point between recovery and cell death is particularly relevant in the context of neurodegeneration since neurons are post-mitotic (non-dividing) cells and are therefore irreversibly lost when they die. Neuronal membrane damage is studied in the contexts of spinal cord traumata (mechanical damage) and multiple sclerosis where the immune system causes inflammatory axon damage.[133,134] Recent studies have shown that axonal membrane damage and subsequent calcium influx into these damaged neurons initiates cell death and that the calcium concentration decides over the cell fate with a window for potential cell rescue of only a few hours.[135,136] Other study fields of membrane damage include bacterial infections (e.g. with pore forming toxins like Listeriolysin *O*)[137], diseases like malaria and diabetes where membrane damage is observed in red blood cells (erythrocytes)[138,139], and phagocytic clearance of dead cells from wounded tissues[140]. In all these fields, tools to visualise the membrane damage are not only crucial to study biological responses to membrane damage but also for the development of therapeutic intervention strategies.

Current membrane damage stains are routinely used *in vitro* as live-dead stains and typically either sulfonated chromophores like Trypan Blue or cationic DNA intercalating dyes like propidium iodide or Sytox Green are used.[140–142] However, such DNA binding dyes have several drawbacks and are only used since there are no alternatives. (1) DNA intercalators can be toxic, which is acceptable for live-dead staining, but cannot be used for long-term tracking of live systems (e.g. to monitor cell development after membrane recovery).[143] (2) They can only be used if the membrane damage occurs near a nucleus but are useless when damage is far away from the nucleus as in neuronal axon damage or oligodendrocytes where cytoplasmic cell parts can be far away from the cell body and nucleus, or for erythrocytes which lack a nucleus.[135,144] (3) Nuclear stains cannot visualise the full cell volume of damaged cells which renders processes at the cell periphery invisible which is for example crucial for macrophage clearance of dead cells in wounded tissues.[140] (4) DNA intercalating dyes like propidium iodide often feature low fluorescence brightness and broad emission peaks which reduces their sensitivity and makes them incompatible with many standard fluorophores in multiplexed assays.

All these biological limitations are particularly problematic for *in vivo* imaging. The ideal membrane damage probe would non-invasively mark the cytosolic volume of damaged cells without nuclear dependency which would be valuable for studying the role of membrane damage and integrity in many diseases, e.g. from multiple sclerosis[133] to Parkinson's[134] and malaria[139].

3 Light-controlled manipulation of biology with spatiotemporal precision

3.1 Why is light a good stimulus?

Proteins can have different functions depending on the cellular growth phase, their subcellular location, or at a single time but in different tissue regions. They are often involved in complex interaction networks that are impossible to replicate in cell-free assays, particularly because often some of their interaction partners remain unidentified. Selective tools are needed to manipulate proteins directly in living cells, with spatial and temporal precision to investigate their dynamic roles.[145] Such targeted manipulation enables the analysis of downstream biological processes, the identification of participating molecules, and ultimately, the modulation of cellular dynamics for the development of therapeutic strategies.[146–149]

Permanently bioactive small molecules lack both spatial and temporal resolution since they need to distribute across all cells upon addition which is already inhomogeneous in 2D cell culture and even more problematic in 3D cultures, tissues or *in vivo*. This distribution time also hampers the temporal resolution and makes the onset time dependent on the investigated system and not a reproducible feature of the molecule across many test systems. Delivering an *inactive* molecule that can distribute homogeneously across all cells even in complex systems and then (after incubation) *activating* this molecule with a precise local stimulus greatly improves the spatiotemporal resolution.[150]

Light is the ideal activation stimulus for many such applications: on modern microscopes, light can be easily applied with extremely high spatial precision (down to ~1 µm, typical cell diameter: 10−50 µm), at any desired time (within (milli-)seconds), it is minimally invasive and easily penetrates cells in 2D and 3D cultures as well as thin tissues.[151] Red or near-infrared light can be used for applications where even lower invasiveness and deeper tissue penetration (up to 2 cm) is needed.[45] The utility of light for the precise application of biological stimuli led to the development of both optogenetic, and photopharmaceutical (small molecule) methods.[152] Although genetic methods have the advantage of acting extremely precisely on the target protein, due to genetic modifications which avoid off-target effects that are often observed for small molecule ligands, they not only suffer from poor translatability across different study systems, but are also often less photon-efficient and more susceptible to photo-bleaching: problems that partly arise from their much lower tunability compared to small molecules.[150,152,153] Photopharmacology mainly utilised bioactive small molecules that change their affinity upon illumination, split into two major compound classes: photoswitches (reversible), and photocages (irreversible) (**Figure 9**).

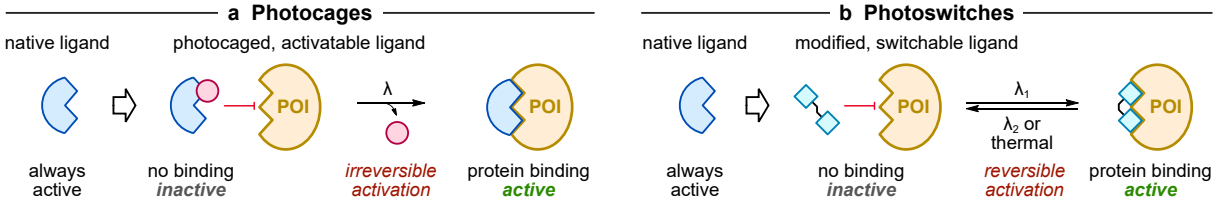

Figure 9: Pharmacologically active molecules can be converted to light-responsive ligands. (a) Photocages are photolabile groups that can be attached to bioactive molecules to suppress their protein binding affinity but can be locally cleaved by light to locally release the active ligand. **(b)** Photoswitches can be reversible isomerised from there *E* to their *Z* form with light which is exploited in photopharmacology usually by switching from a less active to a more active state (e.g. by increasing the binding affinity).

3.2 Photocaged small molecules to manipulate biological systems

Coumarin photocages are used in this thesis for light-controlled HaloTag ligation (**Paper 3**), this section additionally presents other photolabile protecting groups across the visible spectrum for comparison and examples of their use to modulate protein activity with caged ligands.

In photocaged bioactive molecules the binding affinity of a ligand is strongly reduced by the attachment of a photolabile protecting group (PPG) that is irreversibly removed upon light induced photouncaging (**Figure 9a**). Photocages are usually directly introduced to acidic functional groups by alkylation (e.g. carboxylates, phenols, phosphates, thiols) or indirectly attached to more basic functionalities via self-immolative spacers or as carbamates or carbonates (e.g. amines, aliphatic alcohols). Advantageously, many ligands can be photocaged without further modification which makes the design straightforward and avoids potency losses that are observed for photoswitchable ligands.[154,155]

The *ortho*-nitrobenzyl photocage was discovered in the 1960s. It can be removed by phototoxic UVC-UVB light (250−350 nm) following the mechanism shown in **Figure 10a**.[156,157] Since then, it has been widely used, and UVA derivatives (like alkoxy-nitroaryl groups, λ_{max} = 350 nm)[158] have also been developed. However, its harsh uncaging conditions and its cell-toxic nitrosoaryl uncaging byproducts[159] have motivated the use and development of chemically distinct, improved photocages. Today a broad palette of photolabile protecting groups with tuneable wavelengths across the whole visible to NIR spectrum is available (**Figure 10c**).[146,154,155,160] *N*,*N*-diethylaminocoumarins can be uncaged with violet and blue light (**Figure 10b**)[154,161,162] and are GFP-orthogonal (i.e. GFP imaging does not uncage them);[163] they can also be red-shifted by extending their π-system[164]. Further red-shifted xanthene[165] and boron-dipyrromethene (BODIPY)[166–168] photocages allow efficient and wavelength-tuneable cleavage with green to far-red light, which were only surpassed by the recent development of near-infrared cyanine cages[169,170]. Since the uncaging yields generally decrease upon π-extension of the chromophore, photocatalyst-assisted cleavage strategies have also been utilised to improve long-wavelength uncaging efficiency (e.g. silicon-rhodamine assisted *ortho*-nitrobenzyl cleavage with far-red light[171]).

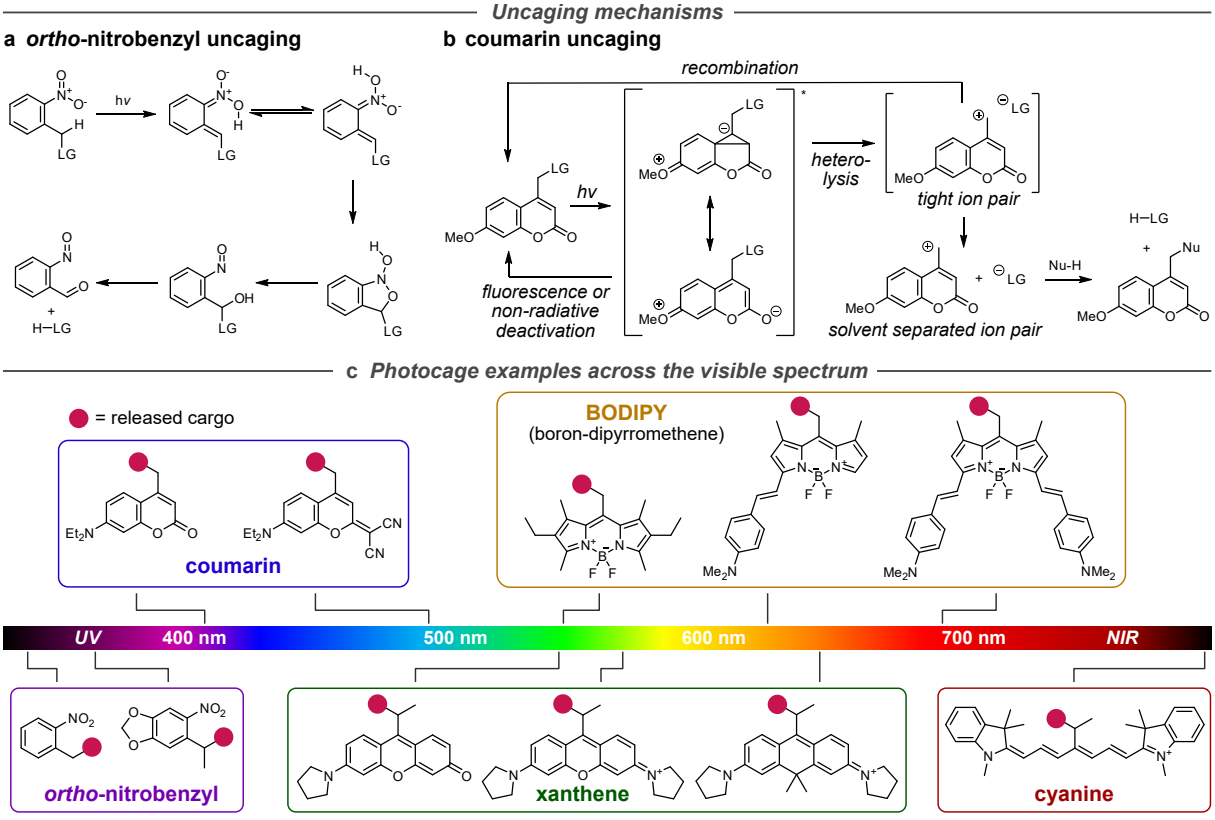

Figure 10: Photolabile protecting groups. (a−b) Photouncaging mechanisms for **(a)** *ortho*-nitrobenzyl[157] and **(b)** coumarin cages[154,161]. **(c)** Example photocage classes with uncaging wavelengths across the visible spectrum: *ortho*-nitrobenzyl, coumarin, BODIPY, xanthene and cyanine cages.[156,158,163–169]

Photocaged ligands have been published in chemical journals with a broad range of protein targets. The BODIPY-caged TRPV1 agonist *N*-vanillylnonanamide enabled light-control of the neural activity in *C. elegans*[172]. Caged versions of dopamine and etilefrine controlled the beating frequency of human cardiomyocytes[169,173]. Protein translation can be controlled with caged puromycin derivatives[174] or photocaged messenger RNA which suppresses the RNA-binding to translation initiation factors until photoactivation ("FlashCaps").[175] Photocages were also utilised to locally release gaseous signalling molecules like carbon monoxide or hydrogen sulfide.[176,177] Activatable, caged fluorophores are used in super-resolution microscopy applications,[178] and photocaged, unnatural amino acids have even been incorporated into proteins to generate e.g. a light-activatable kinase, to investigate its signalling cascade.[179]

Photocages often feature large potency increases upon uncaging. Their easy wavelength tunability allows free choice of uncaging colour to be compatible with imaging colours, and could even be used for orthogonal activation of several bioactive molecules in one system.[180] Nevertheless, photocages have some (practical) disadvantages compared to photoswitchable tools: (1) By design, photocages only allow one-directional, irreversible activation which is a major limitation for some applications such as ion channel signalling. (2) Higher light-doses are needed for uncaging (especially with red-shifted cages), and uncaging with subsequent spacer or carbon dioxide elimination steps (s-min) is much slower than photoswitching (ps). (3) Photocages are limited to nucleophilic functional groups, which are not always available on the ligand of interest, and (4) they often significantly increase the molecular weight of their ligands which can compromise aqueous solubility and cell membrane permeability. (5) Post-activation diffusion of the released active ligand limits the spatial resolution. This is equally problematic with photoswitches, but when high spatial precision is needed, photoswitches can be tuned to rapidly back-isomerise to their inactive form thermally or they can be actively deactivated in neighbouring cells by *Z*→*E* photoswitching to avoid off-target efficacy which is impossible with photocaged ligands.

3.3 Molecular photoswitches to manipulate biological systems

Photocages are the most relevant for light-induced activation in this work (**Paper 3**), but photoswitches are also broadly used in the prior art (e.g. for photopharmacology) with a different property profile compared to photocages which makes them particularly well suited for some applications.

Molecular photoswitches are molecules that reversibly undergo structural changes upon illumination with specific light wavelengths. The class of azobenzenes is their most prominent representative.[145] Azobenzene photoswitches rapidly isomerise (≤ picoseconds[181]) from their thermally stable *E* form to the metastable *Z* form with light of wavelength λ_1 which can be reverted with light of wavelength λ_2 or by thermally equilibrating to the thermodynamically favoured *E* form.[182,183] *E*→*Z* isomerisation not only changes the orientation of the aryl substituents but also the molecular shape, the distance between the phenyl rings and the dipole moment. *E*-azobenzenes are extended and planar, while the *Z* form adopts a compact, twisted 3D shape which also reduces the distance between the phenyl ring termini by ~3.5 Å and increases the overall dipole moment.[145,184] Any of these light-triggered property changes can be exploited for photopharmaceuticals where light controls the bioactivity of a small molecule drug (**Figure 9b**). There are two general strategies to develop photopharmaceuticals from permanently active ligands: bioisosteric replacement (also called "azologisation") and (azo-)extension.

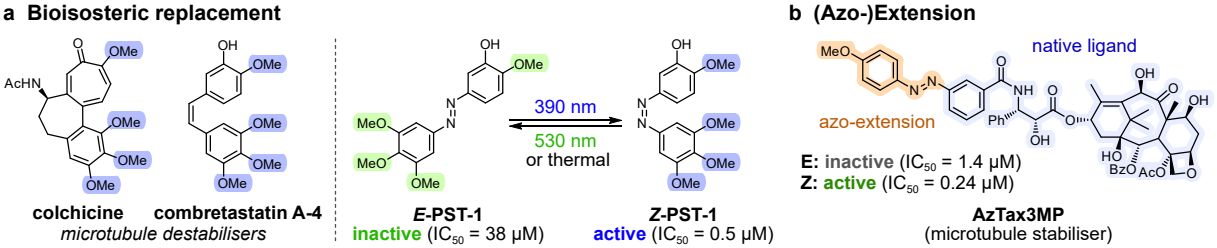

Figure 11: Design principles of photoswitchable bioactive molecules: (a) Bioisosteric replacement mimics biaryl ligands (example: the photoswitchable microtubule destabiliser PST-1 mimics combretastatin A-4[7]). (b) (Azo-)Extension designs modify known bioactive molecules with additional, photoswitchable groups (example: AzTax3MP extends the taxane core with an azobenzene group[17]).

Bioisosteric replacement substitutes parts of a ligand while mimicking its orientation and electronic structure (**Figure 11a**). One example is the photoswitchable microtubule destabiliser PST-1 which mimics combretastatin A-4 (derived from the natural product colchicine).[7] Illumination with blue light drastically changes the activity of PST-1 (80-fold difference in cytotoxicity) which can be reverted with green light. Such large potency shifts are often seen with bioisosteric replacement designs since these ligands can strongly change the orientation of protein-interacting functionalities. Since bioisosteric replacement is restricted to ligands with switch-like structural motifs (usually biaryls) other designs utilise the ligand **extension** strategy. Such designs extend the native ligand with a photoswitch in a way that does not block binding of the target protein but is still (sterically) involved in the protein interactions to ensure that switching changes the target affinity (**Figure 11b**). One example is the paclitaxel-derived microtubule stabiliser AzTax3MP which extends the taxane motif with an aryl-azo functionality to modulate its potency with light. AzTax3MP provides a five-fold potency increase upon light-activation. This gives a significantly smaller biological switching window than the replacement ligand PST-1 – a limitation that is often observed for extension designs.[150]

Photoswitchable photopharmaceuticals have been developed for a variety of protein targets.[182,185,186] **Ion channels** as transmembrane proteins are well-suited for modulation with lipophilic azobenzene photoswitches and many of them have been targeted so far: e.g. potassium channel ligands allowing optical control of neuronal firing[187], photochromic ligands of the AMPA receptor allowing vision restoration in mouse retina[188], or photoswitchable ligands for the transient receptor potential (TRP) protein family including reagents to manipulate nociception (TRPV1)[189] or digestive processes (TRPC4/5)[190]. Inhibiting **cytoskeleton** dynamics with e.g. the previously introduced PST-1 has been used to study cell division, intracellular transport, cell motility, and even mitosis *in vivo* in *C. elegans* with cellular resolution (blue illumination of the target cell, green rescue illumination of neighbouring cells).[7] The development of light-controllable PHOtochemically TArgeting Chimeras (PHOTACs) derived from the PROteolysis TArgeting Chimeras (PROTACs) has allowed to spatiotemporally activate **ubiquitylation of target proteins** for subsequent degradation by harnessing the cellular protein degradation machinery.[191] **Protein translation** has also been optically modulated with a photoswitchable puromycin derivative “puroswitch” that light-dependently induces the termination of translation at the ribosome.[192]

Although these and other photoswitchable ligands have been strongly published in chemical journals, they come with several limitations for advanced pharmacological and biological uses: (1) Photoswitchable ligands should typically be fully inactive in their *E* form and only activated upon light triggered *E*→*Z* isomerisation, to avoid spontaneous activation of the ligand due to thermal *Z*→*E* isomerisation, however, this limits the scope of ligand applications. (2) Photoisomerisation is never quantitative and therefore the “on”- and “off”-switched populations are always mixtures of both isomers which additionally limits their window of biological effect switching. Especially, incomplete *Z*→*E* back-isomerisation is problematic due to the remaining active isomer (often up to 30% depending on the switch), which inspired the development of switches with improved isomerisation efficiencies (e.g. pyrrole hemithioindigos, arylazopyrazoles or diazocines)[10,193,194] or fluorophore antenna approaches for quantitative back-switching[54,195]. (3) Photoswitches are typically isomerised with short-wavelength light which can be phototoxic and suffers from low tissue penetration, and there are only few photoswitches which successfully red-shift the isomerisation wavelengths.[54,194–196] (4) The incorporation of photoswitches into bioactive molecules usually goes along with drastic potency loss and, even more problematically, the light-induced potency differences can be small which gives experimenters only a small functional dynamic range to photocontrol the activity. Recently the concept of *efficacy switches* was introduced that allows concentration independent protein-modulation by switching from agonist to antagonist (instead of switching from low to high affinity).[190,197]

For each application, the advantages and drawbacks of photocages and photoswitches have to be compared to choose the best system (compare **Paper 4**, not included in this thesis[198]). Photocages are usually more broadly applicable to almost all bioactive molecules, while photoswitches are very limited in scope but nonetheless have some unique application areas and benefits (see **Outlook Section 9.3**).

4 Self-labelling proteins: visualising and manipulating biological systems

This section presents the prior art of self-labelling proteins (SLPs) and their ligands and exemplifies major research applications of SLPs. This widespread use motivated us to develop a cageable HaloTag ligand that only ligates to HaloTag upon uncaging by a stimulus (e.g. light or enzyme activity) which extends the current toolset and enables new applications (**Paper 3**).

4.1 Comparison of self-labelling proteins and their ligands

Self-labelling proteins (SLPs) connect the worlds of small molecule chemistry and protein biochemistry: "protein tags" are genetically fused to any protein of interest, and covalently bind to their molecular ligand motifs almost regardless of what molecular cargo the ligand motif is attached to (**Figure 12a**). This experimentally straightforward and highly protein specific approach renders SLPs invaluable for various chemical-to-biological conjugation reactions and their diverse chemical biology applications including fluorescent labelling for fluorescence microscopy, analyte sensing, chemically induced protein dimerisation, or locally increasing ligand concentrations to modulate receptors.[44] Several parameters define high-performance SLP-ligand pairs: including, (1) the ligand-protein binding reaction should be fast, (2) the ligand should be cell-membrane permeable, (3) the ligand should otherwise be biologically innocent (e.g. non-toxic), (4) the protein tag should be small to avoid drastically altering the POI properties, and (5) the tag should be well expressed and folded.[42,44]

Self-labelling proteins were developed in the early 2000s with **SNAP-tag** as the first SLP presented by the Johnsson lab in 2003. SNAP-tag is a genetically engineered variant of the human DNA repair protein O^6-alkylguanine DNA alkyl transferase which specifically reacts with O^6-benzyl guanine (BG) substrates via nucleophilic cysteine attack followed by guanine release (**Figure 12b**).[199–201] The SNAP-tag protein and its faster-ligating SNAP$_f$ variant (2−5× faster)[202,203] are comparably small (19 kDa) and the cell-free ligation rates to benzyl guanine conjugates are moderately high with low cargo dependency (10^4–10^6 M^{-1} s^{-1}).[204] Problematically, the low membrane permeability of the polar guanine ligand motif reduces the cellular ligation efficiency. This inspired the development of the more permeable O^4-benzyl-6-chloropyrimidine-2-amine (CP) ligand, which however has slower cell-free ligation kinetics (10^3–10^4 M^{-1} s^{-1}).[204,205] This major limitation was recently overcome with the development of SNAP-tag2 protein and the corresponding trifluoromethyl fluorobenzyl pyrimidine (TF) ligand, improving both the ligand permeability and the ligation rate (up to 100-fold faster than SNAP-tag).[206]

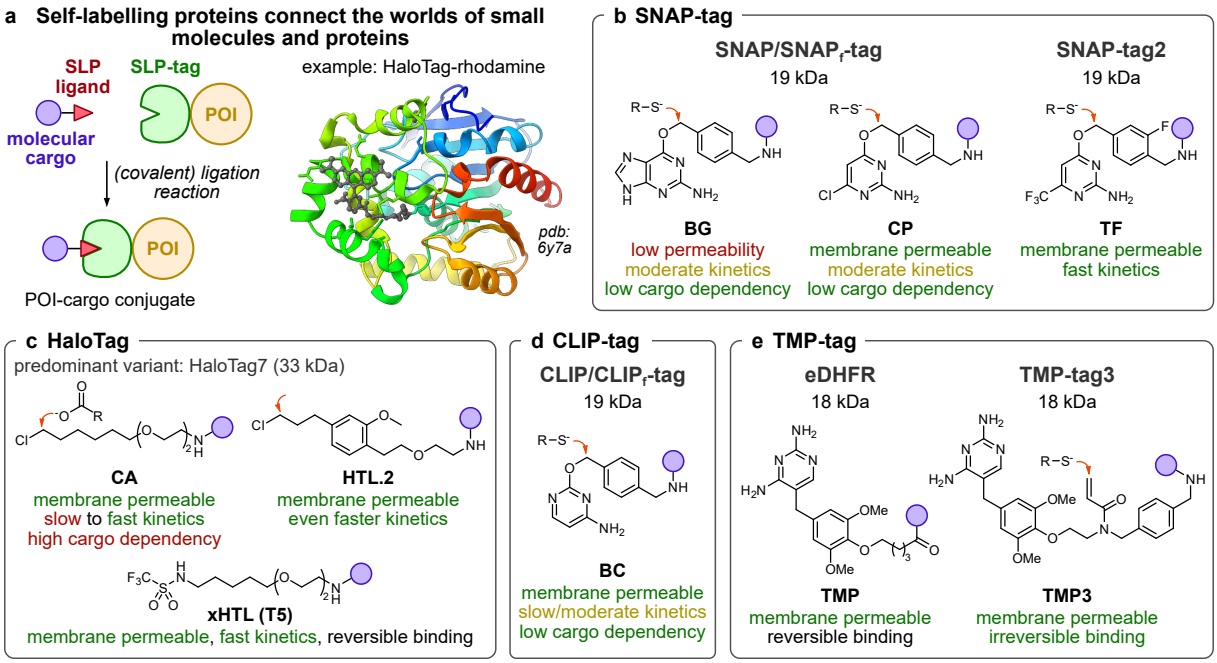

Figure 12: (a) Self-labelling proteins bring together the worlds of small molecules and proteins (HaloTag crystal structure: pdb 6y7a from ref[204]). Commonly used examples of SLPs are **(b)** SNAP-tag, **(c)** HaloTag, **(d)** CLIP-tag, and **(e)** TMP-tag which each specifically ligate to their ligands.

HaloTag is a modified variant of the bacterial dehalogenase DhaA found in *Rhodococcus rhodochrous* which naturally catalyses the hydrolysis of alkyl halides by forming an intermediate alkyl ester with the aspartate in its active centre, that is subsequently hydrolysed. The ester hydrolysis that recovers the aspartate is prevented in HaloTag due to a mutation of the basic histidine to a neutral phenylalanine rendering the aspartate alkylation irreversible and thereby covalently binding the ligand (**Figure 12c**).[207] HaloTag was first described in 2008 and is today the most widely used SLP system (with HaloTag7 as the predominant variant). The HaloTag chloroalkane ligand CA (hexyl chloride) is membrane permeable and the ligation rate can be very fast (up to 10^8 M^{-1} s^{-1} which almost reaches the diffusion limit)[204], especially with xanthene fluorophores which strongly interact with the protein surface, allowing high fluorogenicity by shifting the open-closed equilibrium from the spirocyclised to the open form upon protein binding (also see **Section 2.2.2** for xanthene spirocyclisation).[208] Microscopy applications particularly profit from these strong xanthene-protein interactions as they increase the fluorophore brightness giving up to nine-fold brighter signal than SNAP-tag with the same dyes.[209] HaloTag is well expressed in most cell lines and has a uniform negative surface charge which reduces its tendency to aggregate.[44,210] However, HaloTag is larger (33 kDa) than SNAP-tag and the ligation rate is strongly dependent on the attached cargo (rate differences 10^3–10^8 M^{-1} s^{-1})[204] making SNAP-tag the better choice for some applications. Recent developments of the improved HaloTag ligand HTL.2 enabled 45-fold faster ligation of non-xanthene cargos in cells to overcome this limitation.[211] Exchangeable HaloTag ligands (xHTLs), like the trifluorosulfonamide T5, reversible bind to HaloTag and is used for super-resolution microscopy recovering on-target fluorescence by continuously exchanging photobleached dyes.[212]

SNAP-tag and HaloTag are the most widely used self-labelling proteins but for applications requiring multiple orthogonal tags the **CLIP-tag** (or the faster $CLIP_f$-tag[202]) and its O^2-benzylcytosine (BC) ligand can be used (**Figure 12d**).[213] The protein is small (19 kDa), the BC ligand is more cell permeable than the BG SNAP-tag ligand and ligation rates are moderately fast (10^3–10^4 M^{-1} s^{-1}).[204,213] Alternatively, the **TMP-tag** (based on *Escherichia coli* dihydrofolate reductase, eDHFR) and its folate analogue ligand trimethoprim (TMP) can be used (**Figure 12e**).[214] The protein is equally small (18 kDa) and binds the TMP ligand with high affinity. However, the binding of the original eDHFR-TMP system is reversible which led to the development of covalent and fast-labelling versions (TMP-tag3) which introduce electrophilic acrylamides to react with a genetically installed cysteine on the protein surface for irreversible long-term labelling.[215,216] Although TMP has 1000-fold lower affinity towards the endogenous mammalian dihydrofolate reductase it can still have off-target effects which is particularly problematic when used at high concentrations.[214] The eDHFR system is restricted to intracellular applications as it requires a reducing environment and NADPH as a co-factor.[216]

4.2 How self-labelling proteins are used in biological research

Self-labelling proteins enabled otherwise impossible investigations across various research fields.

4.2.1 Fluorescence microscopy

Bright and photostable HaloTag binding fluorophores are widely used in **fluorescence microscopy** and have revolutionised imaging quality, particularly with the rise of the field of super-resolution microscopy (SRM) (**Figure 13a**).[217] Fluorescent protein (FP) tags (e.g. green-fluorescent protein GFP) come with several drawbacks, despite continuous development.[218,219] FPs are usually less bright and less photostable than molecular fluorophores, especially in the far-red region; they are often not resistant to fixation protocols[220]; their chromophores have to mature after protein expression which takes time and is often oxygen-dependent[221]; and wavelength tuning is much more difficult than for molecular fluorophores[51]. Many SLP binding dyes are cell permeable and can even penetrate thick tissues after fixation;[220] and the SLP's ligated colour can be easily swapped by using different dyes that ligate to the same SLP-construct instead of genetically re-engineering the protein constructs.[40,51,56,57,217] The development of environment-sensitive, fluorogenic dyes that only become fluorescent upon ligation to their SLP enabled wash-free imaging from near-zero background which further improved the image quality, especially in live cell and *in vivo* applications where washing out excess dye can be inefficient.[65] Such fluorogens often exploit interactions of the fluorophore with the protein surface (e.g. controlling spirocyclisation in

xanthenes: **Figure 13b**, also see **Section 2.2.2**); and up to 1000-fold fluorescence increases upon ligation are known.[40,217] SLPs have been used for microscopy to elucidate cellular structures and protein localisation, optionally using orthogonal SLPs for simultaneous multiplexed imaging of several protein targets in live cells[222,223], to study protein movement and trafficking[224], or to determine intracellular protein concentrations[225]. Protein turnover and half lives in live cells and *in vivo* can be investigated by pulse-chase protocols using different dye colours over time.[226,227]

4.2.2 Local, cell-type specific concentration increase

SLPs can be used to combine the efficacy of small molecule drugs with the cell type specificity of genetic tools by anchoring pharmacologically active small molecules in proximity to their target protein. Such methods locally and cell-type specifically increase drug concentrations which allows to modulate e.g. receptors in a single cell-type without effecting the same receptor in all other cell-types. Such methods have been developed for several applications, e.g.: (1) DART (Drug Acutely Restricted by Tethering) which anchors drugs to membrane bound HaloTag, drastically increasing the local concentration and effectively suppressing efficacy in other cell types without the requirement to modify the target receptor itself (**Figure 13c**);[211,228] (2) PORTL (Photoswitchable Orthogonal Remotely Tethered Ligand) is a photoswitchable modification of DART that puts receptor activity under light control (drugs can be photoswitched to turn receptor activity off and on);[229–231] (3) T-REX (Targetable Reactive Electrophiles and Oxidants) uses SLPs to tether caged electrophiles to a protein of interest (e.g. the redox protein KEAP1) which are locally released by light activation, allowing to study the downstream effects of these electrophiles with high target protein and cell-type specificity.[232,233]

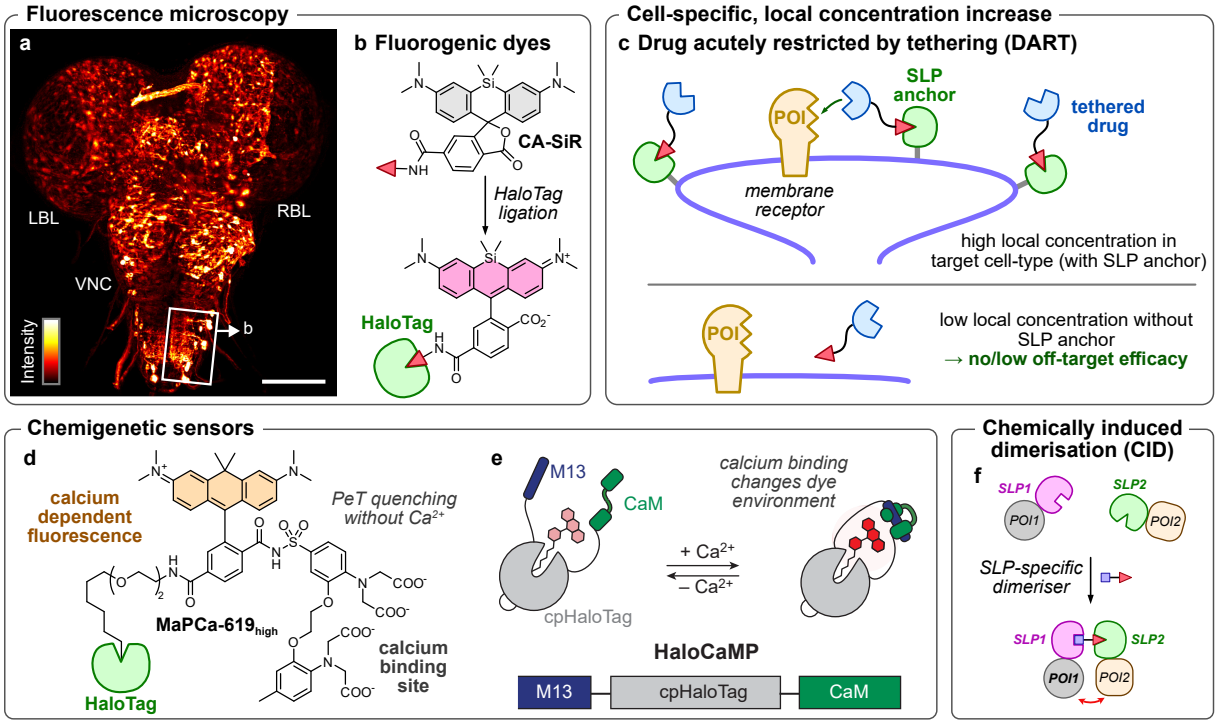

Figure 13: Self-labelling proteins advance several research areas. (a) Cell-permeable, fluorogenic and red-emitting Halo-dyes (here JF_{635}-Halo) efficiently stain complex and thick tissues and, e.g. allow *in vivo* imaging throughout the central nervous system of *Drosophila* larvae (LBL, left brain lobe; VNC, ventral nerve cord; RBL, right brain lobe, reprinted with permission from *Nat. Meth.* **2017**, *Copyright © 2017, Springer Nature,* reference[217]). **(b)** HaloTag ligation controls the spirocyclisation equilibrium of xanthene fluorophores (here CA-SiR) providing fluorogenic dyes for wash-free, background-free imaging.[65] **(c)** SLPs can increase the local concentration of drugs with cell-type specificity by tethering them to an SLP-anchor close to the target protein.[211] **(d)** Calcium sensing BAPTA-fluorophores that are only fluorescent upon HaloTag ligation allow wash-free, localised Ca^{2+} sensing.[234] **(e)** HaloCaMP senses calcium ions with a modified HaloTag-fluorophore conjugate that modulates the dye environment upon calcium binding[235] (adapted from *Annu. Rev. Biochem.* **2025**, *Copyright © 2025 by the authors,* reference[44]). **(f)** Chemical dimerisers that ligate to orthogonal SLPs can induce protein-specific heterodimerisation (chemically induced dimerisation, CID).

4.2.3 Chemigenetic sensors

Sensing second messengers like calcium ions with (sub-)cellular specificity is crucial for fundamental research (e.g. in neuronal signalling). SLPs can be used to combine the tunability and fluorescence brightness of molecular calcium sensors with the protein specificity of genetic engineering, by anchoring the sensor to localised SLPs in the desired cell compartment (**Figure 13d**).[234,236,237] Johnsson and co-workers further improved this powerful technique by developing fluorogenic sensors that are only fluorescent when they are ligated to HaloTag *and* bind calcium which even allows wash-free calcium sensing.[234] However, molecular calcium sensors usually feature tetracarboxylates, that can be delivered to cells as acetoxymethyl esters which are intracellularly cleaved by esterases, but which are inefficiently translocated from the cytosol to target compartments after carboxylate unmasking. Thus, the Johnsson lab also developed a HaloTag-based sensor called HaloCaMP, where the HaloTag is modified with two calcium binding peptide units (CaM and M13; **Figure 13e**).[235] This approach uses membrane permeable fluorogenic dyes which are ligated to HaloTag and turn fluorescent upon the local environment change when the CaM and M13 unit bind to each other when calcium is present. In the similar WHaloCaMP system the fluorescence is quenched by a nearby tryptophan before calcium binding.[238]

4.2.4 Chemically induced dimerisation

Chemically-induced protein (hetero)dimerisation (CID) is used to probe protein interaction-dependent functions like receptor signalling, or localisation-dependent single-protein functions.[239] Due to their specificity, SLPs are well-suited for chemically induced dimerisation forcing two proteins of interest into proximity via addition of a bifunctional chemical linker (**Figure 13f**). Several works used orthogonally reacting HaloTag, SNAP-tag, CLIP-tag and TMP-tag dimerisers to specifically re-locate proteins to cellular compartments, to initiate signalling pathways, or to identify native protein interaction partners.[240–244] Recent designs induce and simultaneously report successful protein dimerisation with FRET-induced fluorescence changes which allowed the investigation of proximity-induced signal transduction of receptors.[239]

SLPs can likewise be used to induce protein degradation with high specificity by recruiting an E3 ligase to a Halo-tagged protein of interest allowing to chemically knock-down specific protein targets.[245] Alternatively, HaloTag ligands were used to install adamantyl groups whose hydrophobicity mimics partially denatured proteins which leads to degradation – an approach that has even been used *in vivo*.[246]

4.3 Conditional ligation to self-labelling proteins

Self-labelling proteins (SLPs) are invaluable tools for a variety of applications by covalently connecting small molecule cargos to a protein of interest. This ligation reaction is usually *unconditional,* limiting the spatial and temporal resolution of these tools which would be needed to precisely study dynamic processes. Localisation of proteins is naturally precisely controlled by biology, and in many cases determines protein function (e.g. regulating signalling or transport). Photocaged TMP- and SNAP-tag ligands have been used with lipid-anchors to conditionally re-localise cytosolic POIs to the plasma membrane upon light activation with spatiotemporal precision[247,248] (**Figure 14a**, photocages are further discussed in **Section 3.2**). Similarly, photocaged versions of bifunctional chemical inducers of protein dimerisation can induce and subsequently end the interaction of target proteins by using “photosplittable” dimerisers (**Figure 14b**).[241,242,249–251] Light-controlled CID tools bring two major advantages: (1) spatiotemporal control to manipulate biological function and (2) avoiding the “Hook effect” caused by incomplete dimerisation due to monovalent saturation of each POI at high dimeriser concentrations. Recently, caged benzyl guanines extended conditional SNAP-tag ligation from light-triggered to biochemical uncaging with hydrogen peroxide or β-glucuronidase allowing to record and integrate bioactivity with protein anchors.[252]

So far, conditional SLP ligation has been implemented for SNAP- and TMP-tag by caging benzyl guanine (BG) and trimethoprim (TMP) which both feature cageable amines that can be utilised to suppress ligation (**Figure 14c**).[241,242,249–251] The chemically inert HaloTag ligands (**Figure 12c**) however cannot be reversibly functionalised. To date only genetic modifications of the HaloTag allow conditional ligation, by splitting the protein into two fragments, that only ligate conventional HaloTag ligands after binding to each other.[253] The Johnsson lab recently improved previous split-HaloTag approaches with a circularly

permuted HaloTag version (cpHaloΔ) which does not react with HaloTag ligands before binding the complementary small peptide Hpep. Fluorogenic Halo-dyes can be used to visualise cpHaloΔ-Hpep binding (**Figure 14d**) induced by protein-protein interactions, G-Protein Coupled Receptor activation, or increases of intracellular calcium concentrations.[254] Fine-tuning a calcium dependent protein labelling system (Caprola) yielded 15 Caprola sensors with tuned Ca^{2+}-binding affinity (ranging from 40−1000 nM) by modulating the binding affinity of cpHaloΔ with various Hpep variants, which were used to record elevated calcium levels and allowed selecting cells from heterogeneous samples for transcriptomic analysis and visualising neuronal calcium signalling in flies and zebrafish.[254]

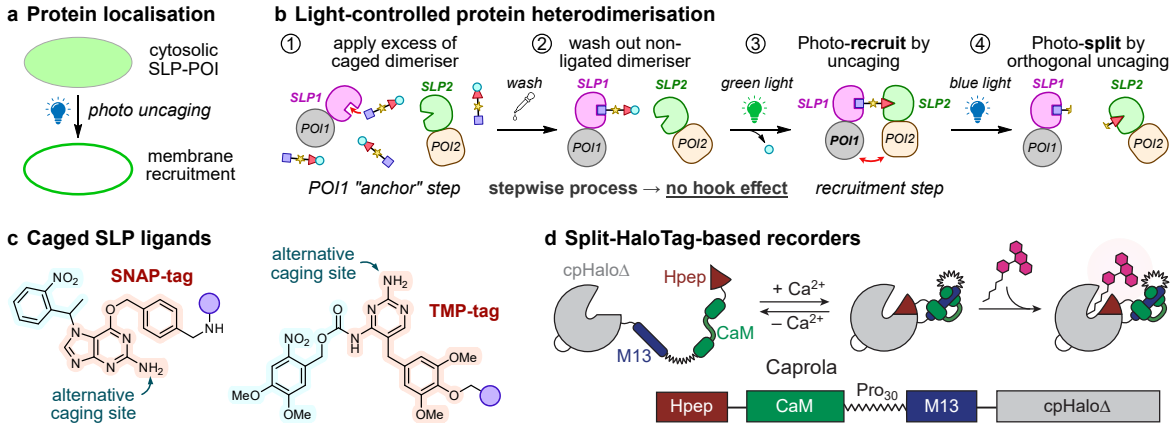

Figure 14: Conditional ligation to SLPs with caged ligands or splitSLPs. Caged SLP ligands can be used **(a)** to re-locate proteins or **(b)** to chemically induce and terminate protein-protein interactions. **(c)** Benzyl guanine and trimethoprim ligands for SNAP-tag and TMP-tag feature suitable caging sites to suppress SLP-ligation which the HaloTag ligands lack. **(d)** Split-HaloTag variants like the calcium sensor "Caprola" allow conditional HaloTag ligation upon calcium binding (adapted from *Annu. Rev. Biochem.* **2025**, *Copyright © 2025 by the authors,* reference[44]).

Conditional SLP tools enable unprecedented visualisation and manipulation of biological processes. While genetic approaches utilising split-SLPs are powerful, they require genetic modifications and cannot be easily translated between different target proteins or second messengers. Small molecules that harness the available pool of self-labelling proteins are much cheaper to engineer for new reactivities and can be directly applied to the thousands of established experimental SLP systems.[44] Such chemical tools were successfully developed for the SNAP-tag and the TMP-tag system, however, there are to date no cageable ligands available for the HaloTag system which is the most commonly used and best-performing SLP. **Paper 3** overcomes this limitation by developing a novel HaloTag ligand that can be caged to conditionally ligate to HaloTag.

B. AIMS AND OBJECTIVES OF THIS WORK

This thesis aims to develop molecular tools for visualising and precisely manipulating biological processes, focusing on three overarching goals: (1) sensitive detection of cell membrane damage, (2) sensitive and durable quantification of intracellular enzyme activity, and (3) developing a conditional HaloTag ligand (one that binds to HaloTag only in response to a chosen (bio)chemical stimulus).

Aim 1: Wash-free membrane damage probes.

Cell membrane damage plays a critical role in diverse pathological processes, including bacterial infections and multiple sclerosis. Conventional DNA-intercalating fluorogens are commonly used to detect membrane permeabilisation, but they are cytotoxic and limited to identifying damage in cell volumes that contain a nucleus. In **Paper 1**, this challenge is addressed through the development of modular, wash-free membrane damage probes that are non-fluorescent in the extracellular environment to allow imaging with near-zero background, but selectively enter membrane-compromised cells, and only there release a fluorophore. This approach avoids toxic DNA intercalation and enables sensitive marking of the *entire cytosolic volume* of damaged cells.

Aim 2: A scaffold for cell-retained fluorogenic probes for sensitive bioactivity imaging.

Fluorogenic bioactivity probes are powerful analytical tools for studying enzyme functions in disease-related contexts. While these probes must be membrane permeable to efficiently enter cells, often their fluorescent products can also rapidly leak out after activation, leading to signal loss, poor cellular resolution, and low sensitivity for low-turnover processes. Existing cell-retention strategies are inefficient or disrupt native biology through non-specific alkylation or precipitation. In **Paper 2**, this limitation is addressed by developing a general probe scaffold to generate turnover probes that are water-soluble and membrane-permeable to efficiently enter cells, fully suppress pre-activation fluorescence, and resist hydrolytic or off-target activation. Upon enzymatic turnover, these probes release a soluble, cell-retained fluorophore that enables non-invasive, sensitive, and cell-resolved quantification of bioactivity.

Aim 3: A chemically controlled HaloTag ligand for conditional covalent HaloTag ligation.

The HaloTag self-labelling protein system enables the covalent attachment of diverse chemical reagents to diverse proteins of interest, and is widely used for many applications, including fluorogenic imaging, analyte sensing, or locally increasing reagent concentrations by tethering. So far, its utility has been limited due to lack of control, since existing ligands only link chemical and biological components *unconditionally*. Split-HaloTag sensors have been engineered, that make the ligation reactivity of the protein itself conditional on a biological stimulus, which allowed "molecular recording" of some types of physiological events with unprecedented resolution. However, to date no chemical motifs exist that allow (bio)chemical control over HaloTag ligation from the reagent side. **Paper 3** addresses this by developing a cageable HaloTag ligand, CHalo, that rapidly and selectively ligates to HaloTag only after uncaging. CHalo's structure allows the modular introduction of various caging groups, which gives a range of e.g. photo- and enzyme-activated ligands. Its general and modular design should be useful for local fluorogenic labelling, conditional protein heterodimerisation with SNAP-tag, and quantitative imaging of enzymatic activity. Importantly, such a chemical tool is directly compatible with existing HaloTag fusion constructs, facilitating broad adoption without the need for genetic re-engineering.

C. RESULTS AND DISCUSSION

5 Paper 1: Fluorogenic probes for wash-free imaging of membrane damage

In this work, we rationally designed membrane-impermeable fluorogenic probes that selectively stain membrane-damaged cells. Such probes are essential for interrogating membrane integrity in various pathological contexts, including bacterial infections and neuronal damage in multiple sclerosis. Conventional DNA-intercalating fluorogens, such as propidium iodide, are limited in their applicability because they lack activation modularity, can exhibit cytotoxicity, and rely on nuclear access for signal generation. Consequently, they fail to detect membrane damage in non-nucleated cell-types (e.g. erythrocytes) or in regions distant from the nucleus (e.g. axonal damage in neurons).

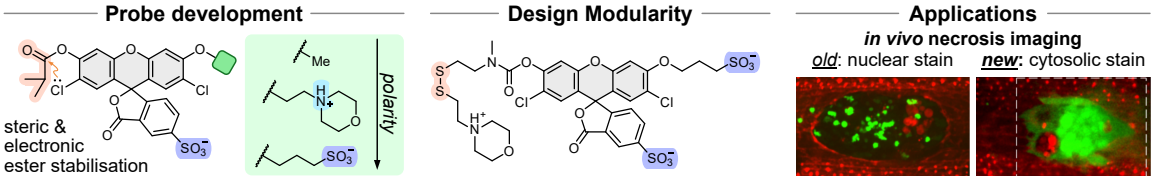

To overcome these limitations, we defined a set of design requirements for next-generation damage probes: (1) near-zero background fluorescence prior to activation, with no extracellular activation to enable wash-free imaging, (2) exclusion from cells with intact membranes, (3) efficient entry into membrane-compromised cells, (4) rapid signal generation inside damaged cells, and (5) bright, spectrally distinct fluorescence compatible with multicolour imaging.

Our probe design exploits the biophysical principle that charged molecules cannot passively diffuse across the lipophilic interior of lipid bilayer membranes due to the high desolvation energy. We therefore utilised sulfonates to achieve charge-based impermeabilisation. Fluoresceins were selected as the fluorogenic probe scaffold due to their biocompatibility, water-solubility (ensures cytosolic distribution), sharp excitation and emission spectra, synthetic accessibility, and ability to undergo full spirocyclisation of the acylated probe (resulting in no background fluorescence) yet with a strong turn-on response upon deacylation. As a general, ubiquitous intracellular trigger, we chose esterases to cleave the capping group and release the fluorophore inside damaged cells. However, we observed that sulfonated fluorescein esters were more prone to spontaneous hydrolysis in aqueous buffers than their neutral probe variants. To address this issue, we implemented previously described stabilisation strategies, combining electronic stabilisation through n→π* donation from *ortho*-chlorides with steric protection by using isobutyrate esters (instead of acetates). This approach balanced the extracellular hydrolytic stability with rapid intracellular activation by esterases.

Contrary to our initial expectations, a single sulfonate proved insufficient to fully prevent membrane permeation of otherwise lipophilic xanthene probes. We hypothesised that this permeability is due to their amphiphilic nature. To ensure complete exclusion from healthy cells, we systematically increased probe polarity, first by introducing a basic amine and finally via disulfonation. Through this optimisation, we developed the disulfonated ester probe **MDG1** (“Membrane-Damage Green 1”), which exhibited complete exclusion from healthy cells and a strong signal turn-on inside damaged cells. Then, to enhance probe stability, we exploited the modularity of the spirocyclised xanthene system and replaced the *O*-ester capping group with a more robust *N*-carbamate cap that fully resists hydrolysis in complete cell culture media (like DMEM) for hours: giving probes like **MDG2** (unmasked intracellularly by reduction of an attached disulfide). The synthesis of both disulfonated probe types posed challenges due to their acidity and polarity, which constrained solvent choice and often required the use of polar co-solvents to ensure (partial) solubility. Moreover, purification was complicated by the need to avoid ester hydrolysis during reversed-phase chromatography and subsequent product isolation from the aqueous eluents.

We validated our probes using two complementary membrane-damage models: membrane poration induced by the pore-forming bacterial toxin listeriolysin *O* (LLO), and radical-mediated damage mimicking inflammatory membrane damage. After simple 2D cell culture validation, we applied the probes to biological systems where suitable tools were previously lacking:

(1) **Ferroptosis** is a non-apoptotic form of cell death involving lipid peroxidation that compromises membrane integrity. Conventional imaging approaches detect this process indirectly with lipid peroxide-sensitive probes, whereas MDG1 enabled direct visualisation of ferroptotic membrane damage in primary T cells. (2) In **axonal membrane damage,** which is highly relevant in disease contexts such as multiple sclerosis, nuclear stains like propidium iodide are useless as the nucleus is far away from the damage site. MDG1 allowed to visualise such axonal damage, offering a sensitive tool for studying neuroinflammatory membrane disruption. (3) In **complex 3D tissues**, nuclear stains can only identify regions containing damaged cells without revealing the boundaries or identifying intact cells within the damaged region. MDG1 overcomes this limitation by staining the entire cytosolic volume of damaged cells thereby delineating both damaged and undamaged cells within the affected tissue. We demonstrated these advantages by imaging necrotic cells in *Drosophila* embryos *in vivo*.

Together, these results establish generalisable design principles for membrane-damage selective small molecules which can, in principle, be extended beyond fluorescence imaging towards the development of targeted pro-drug delivery systems for membrane-damaged pathological tissues.

Personal contributions

I co-designed target compounds and performed synthesis and structural characterisation [all precursors, probes and fluorophores], UV-vis and fluorescence spectroscopy [Fig S2ab,de,ij], cell-free assays (probe hydrolysis in different cell culture media [Figs S2gh, S16a], esterase activation [Fig S2f], GSH activation [Fig S16b], Michaelis-Menten kinetics [Fig S3]) and cell biology during the early probe design (epifluorescence microscopy and flow cytometry [with A.K., Figs 2d, S4]). I contributed to the design of all experiments and advised collaboration partners for applications in cell biology, and I coordinated data assembly, prepared all figures, and co-wrote the manuscript.

Main contributions from other authors: D.B. performed confocal microscopy, image quantification and membrane-damage assays with LLO and AAPH [Figs 2−4]; A.K. performed flow cytometry [Fig 2d]; C.W. performed cell biology for ferroptosis sensing [Fig 5]; A.J.D. performed necrosis imaging in Drosophila [Fig 6d−f]; S.W. performed *in vitro* imaging of axonal damage [Fig 6ab]; O.T.-S. co-designed target compounds and co-wrote the manuscript.

JACS
JOURNAL OF THE AMERICAN CHEMICAL SOCIETY
pubs.acs.org/JACS
Article

Fluorogenic Chemical Probes for Wash-free Imaging of Cell Membrane Damage in Ferroptosis, Necrosis, and Axon Injury

Philipp Mauker,[‡‡] Daniela Beckmann,[‡‡] Annabel Kitowski, Constanze Heise, Chantal Wientjens, Andrew J. Davidson, Simone Wanderoy, Gabin Fabre, Angelika B. Harbauer, Will Wood, Christoph Wilhelm, Julia Thorn-Seshold, Thomas Misgeld, Martin Kerschensteiner, and Oliver Thorn-Seshold*

Cite This: *J. Am. Chem. Soc.* 2024, 146, 11072−11082

ABSTRACT: Selectively labeling cells with damaged membranes is needed not only for identifying dead cells in culture, but also for imaging membrane barrier dysfunction in pathologies *in vivo*. Most membrane permeability stains are permanently colored or fluorescent dyes that need washing to remove their non-uptaken extracellular background and reach good image contrast. Others are DNA-binding environment-dependent fluorophores, which lack design modularity, have potential toxicity, and can only detect permeabilization of cell volumes containing a nucleus (i.e., cannot delineate damaged volumes *in vivo* nor image non-nucleated cell types or compartments). Here, we develop modular fluorogenic probes that reveal the whole cytosolic volume of damaged cells, with near-zero background fluorescence so that no washing is needed. We identify a specific disulfonated fluorogenic probe type that only enters cells with damaged membranes, then is enzymatically activated and marks them. The esterase probe **MDG1** is a reliable tool to reveal live cells that have been permeabilized by biological, biochemical, or physical membrane damage, and it can be used in multicolor microscopy. We confirm the modularity of this approach by also adapting it for improved hydrolytic stability, as the redox probe **MDG2**. We conclude by showing the unique performance of **MDG** probes in revealing axonal membrane damage (which DNA fluorogens cannot achieve) and in discriminating damage on a cell-by-cell basis in embryos *in vivo*. The **MDG** design thus provides powerful modular tools for wash-free *in vivo* imaging of membrane damage, and indicates how designs may be adapted for selective delivery of drug cargoes to these damaged cells: offering an outlook from selective diagnosis toward therapy of membrane-compromised cells in disease.

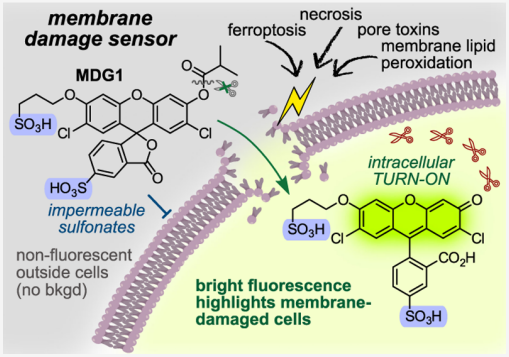

1. INTRODUCTION

Cells are enclosed by the plasma membrane, which retains cellular components, such as ions and proteins, and reduces exposure to extracellular molecules. Eukaryotic membranes are primarily bilayers of amphipathic membrane lipids that expose hydrophilic headgroups to water while aggregating their lipophilic tails.[1] While small apolar molecules readily cross membranes, larger or more polar species such as ions and proteins are "membrane-impermeable" because the energy penalty for desolvation and traversal of the lipophilic inner region of the membrane is high: i.e., they cannot cross intact membranes by passive diffusion (the mode of cellular entry that we focus on in this work).[2]

Loss of cell membrane integrity allows otherwise impermeable molecules to cross membranes.[3] The resulting osmotic and energetic imbalance, entry or mislocalization of toxic species, and aberrant signaling, can cause cellular stress and initiate cell death pathways. Membrane integrity can be impaired by a variety of physiological and pathological processes: from physical stress, e.g., mechanical injury, to chemical modification, e.g., lipid peroxidation, to protein pore formation, e.g., as induced by pyroptosis or bacterial toxins. However, membrane repair can potentially reverse cellular demise: which is particularly important in postmitotic cells such as neurons, e.g., after physical or inflammatory insults in conditions such as blunt spinal trauma or multiple sclerosis. These aspects render membrane-damaged cells a relevant study population (Supporting Notes 1−2).[4,5] As such, finding ways to selectively address cell membrane integrity with small molecules is crucial, either for detecting membrane-compromised cells on the verge of death, or for therapeutically rerouting them to survive (we refer to compromised cells as "damaged" or "leaky"). Here, we develop

Received: July 18, 2023
Revised: March 22, 2024
Accepted: March 25, 2024
Published: April 9, 2024

https://doi.org/10.1021/jacs.3c07662
J. Am. Chem. Soc. 2024, 146, 11072−11082

Journal of the American Chemical Society pubs.acs.org/JACS Article

chemistry to do this by using damaged membranes as a selective, passive entry pathway.

Impermeabilization of small molecules is often achieved by attaching "permanently" charged groups, such as sulfonates ($pK_a \approx -2$).[6] Charged imaging agents are routinely used *in vitro* for detecting leaky cell membranes for discriminating live and dead cells. For example, Trypan Blue is a polysulfonated dye used for counting dead cells, as it selectively passes leaky membranes but is excluded from healthy cells.[7] The cationic fluorophore propidium iodide (PI) is used similarly for staining dead cells in fluorescence microscopy and flow cytometry (Figure 1a).[8]

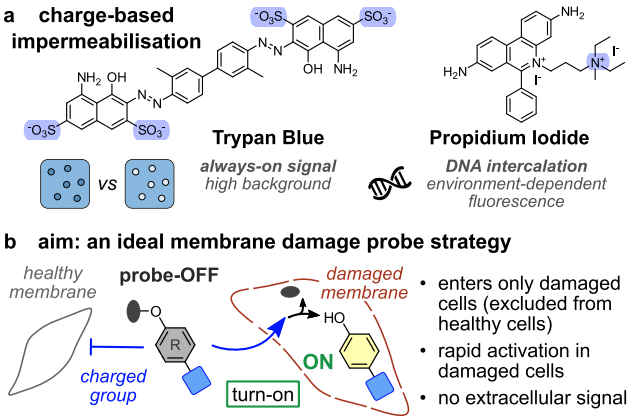

Figure 1. Cell-impermeable probes. (a) Current imaging agents for damaged membranes. (b) A goal for a damage-selective fluorogenic probe.

Conceptually, these current agents have major caveats. "Always-on" chromophores, such as Trypan Blue, require washing steps, background subtraction, and/or cell isolation to remove the signal from dye that is not taken up in cells. Environment-sensitive stains like PI, which give intracellular signal turn-on by DNA binding, bring different problems: (a) their DNA binding can be toxic,[9] which is fine for live/dead staining, but not for long-term tracking in live systems (Supporting Note 1). (b) Without a nucleus to stain, DNA-binding dyes are ineffective. Thus, erythrocytes (red blood cells, which lack a nucleus) cannot be imaged, nor can other cell types if the nucleus is far from the region undergoing membrane damage. This is biologically relevant since highly differentiated cells often suffer membrane injury far from the nucleus, for example, in the long axonal processes of neurons, where membrane integrity appears to be a key determinant of degeneration after physical nerve damage (see Section 2.7),[4] or in oligodendrocytes (which can suffer complement-induced membrane pores in autoimmune neurodegenerative diseases), where the cytoplasmic compartments of myelin-bearing processes are poorly connected to the cell body.[10] (c) DNA binders do not visualize the full intracellular volume of damaged cells but can only give a bright point at the nucleus. In complex three-dimensional (3D) tissues, they give a cloud of stained nuclei that qualitatively indicates a damaged region: but there are no sharp boundaries that delineate which cells within a damaged zone are damaged or not. Particularly, for asymmetric cells that are intergrown with each other, 3D tracing across stack images to map their nucleus to their full cytosolic volumes becomes practically impossible (Section 2.8). All of these limitations are particularly severe for *in vivo* imaging, which is unfortunate since *in vivo*-capable probes that could delineate such damaged vs nondamaged cell volumes, noninvasively and without nuclear dependency, would be valuable for studying the role of membrane damage and integrity in many diseases from multiple sclerosis[11] to Parkinson's disease[12] and malaria.[13]

Rationally exploiting membrane (im)permeabilization can also offer far more powerful applications than live/dead assays. Charged bioactive molecules are currently used to selectively address extracellular targets: to inhibit extracellularly exposed receptors,[14] photouncage signaling lipids locally at the plasma membrane,[15] or bioorthogonally label cell-surface proteins[16−18] tags. This field is also still in early stages and would benefit from more systematic evaluations: e.g., Belov et al. recently revealed that double sulfonation, which had been assumed to guarantee cell impermeability, actually does not reliably prevent cell entry for rhodamines.[19] While these methods are elegant and are starting to engage properly with membrane permeability, there remains an unmet need for generalized approaches to simultaneously mask and impermeabilize molecules, such that only intracellular reactions in permeabilized cells activate them: ideally giving "impermeable, off → ON" fluorogenic probes or prodrugs.

Fluorogenic probes are ideally nonfluorescent compounds that develop fluorescence only after activation by a target trigger. This off → ON mode could solve the problems that block current always-on membrane damage dyes from *in vivo* uses, as it eliminates nonspecific background and so maximizes their sensitivity (signal to background ratio) without requiring washout. Indeed, fluorogenic probes have become crucial tools to image and quantify biological processes noninvasively in living cells, particularly for investigating enzyme activities of peptidases, esterases, phosphatases, glycosidases, and oxidoreductases.[20−26] Cell *permeable* fluorogenic probes that become fluorescent and cell-trapped after entry are highly valued[27] and widely used, e.g., fluorogenic acetoxymethyl ethers, such as calcein-AM.[28] However, until now, there have been no modular chemical systems that are silenced and cell impermeable but likewise activate an imaging agent or release a drug upon entry.

Here, we aimed at developing fluorogenic membrane damage probes (Figure 1b), which use general chemical or biological features to meet these performance needs: (1) near-zero background fluorescence before activation, and no activation outside of cells, to enable wash-/subtraction-free imaging; (2) exclusion from cells with intact membranes; (3) entry into membrane-damaged cells; (4) rapid signal generation by enzymatic unmasking of a modular capping group; and (5) bright, tunable fluorescence with narrow spectra matching typical biological imaging settings to allow costaining with other fluorophores.

We chose xanthenes as the fluorogenic scaffold. These can be trapped by chemical capping in a completely nonfluorescent "closed" form, where π-conjugation is interrupted by spirocyclization to give a nonfluorescent probe, but then unmasked by target enzymes to reallow equilibration with the conjugated, fluorescent, quinoid "open" form. Fluorescein ester probes, for example, can be intracellularly activated in many cell types.[29] Although fluorescein acetates are famously susceptible to spontaneous hydrolysis, other esters can resist it (discussion below),[30] and a range of more stable masking groups with other enzymatic targets are known (need 1). Xanthene fluorescence is also bright, narrow, and easily tuned by substitutions, and fluorescein is compatible with standard microscopes and multiplexed imaging (need 5).

https://doi.org/10.1021/jacs.3c07662
J. Am. Chem. Soc. 2024, 146, 11072−11082

Journal of the American Chemical Society pubs.acs.org/JACS Article

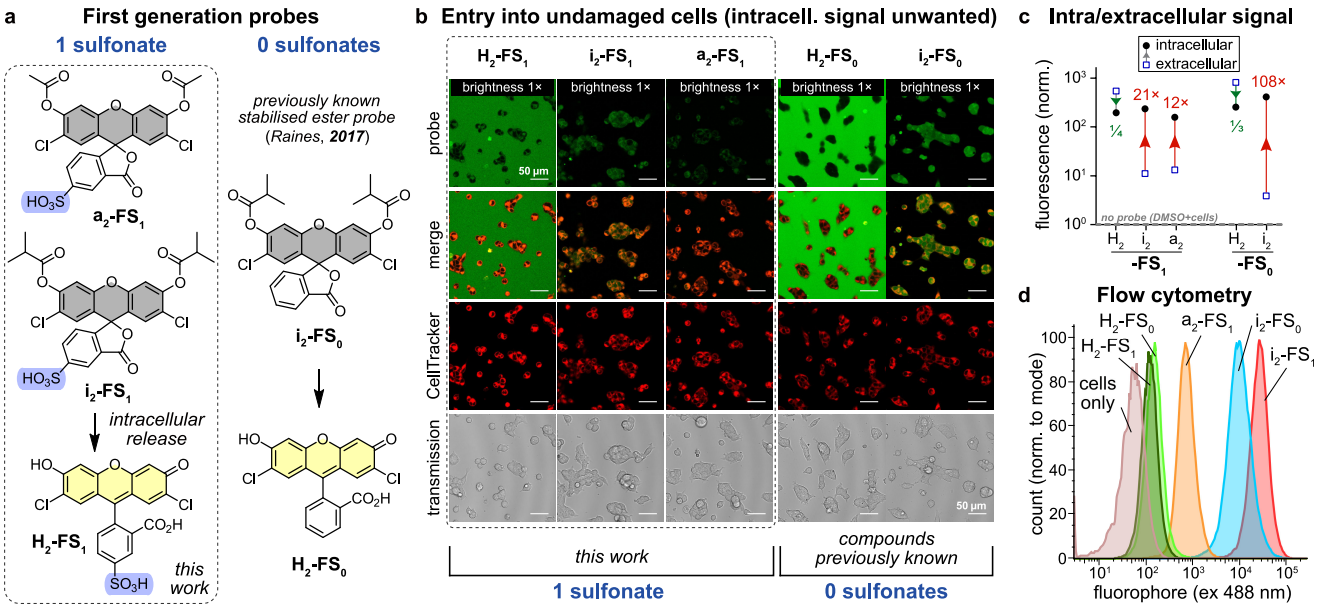

Figure 2. Cell penetration and fluorogenicity of double-capped probes or fluorophores in healthy cells. (a) Sulfonated probes $\mathbf{i_2}$-$\mathbf{FS_1}$ and $\mathbf{a_2}$-$\mathbf{FS_1}$ from the fluorophore $\mathbf{H_2}$-$\mathbf{FS_1}$ and the known reference $\mathbf{i_2}$-$\mathbf{FS_0}$ from $\mathbf{H_2}$-$\mathbf{FS_0}$. (b, c) Confocal microscopy of healthy HEK cells incubated with test compounds (5 μM) for 10 min without washing (CellTracker is a cytosolic stain; scale bars: 50 μm). (c) Image quantification for intracellular vs extracellular fluorescence (note $\log_{10}$ vertical axis; values normalized to autofluorescence of dimethyl sulfoxide (DMSO) control as 1; see also Supporting Note 3). (d) Orthogonal quantification of cellular entry-and-activation from flow cytometry of healthy HeLa cells (10 μM test compounds, 20 min of incubation). (All data: n = 3; "brightness 1×" is the adjustment relative to settings used in Figures 3 and 4).

We explored polysulfonation for cell exclusion. Tanaka et al. had reported the first cell-excluded fluorescein probe, 5-sulfofluorescein diacetate, in 1995.[31] Raines' work improving the aqueous stability of fluorescein esters[30] instead suggested to (1) switch to the 2′,7′-dichlorofluorescein scaffold ($\mathbf{H_2}$-$\mathbf{FS_0}$), where $n \rightarrow \pi^*$ donation can improve resistance to spontaneous hydrolysis; and (2) switch to isobutyrate esters, to further reduce spontaneous hydrolysis rates while retaining good intracellular enzymatic activation speed.[30] Taken together, our starting point was to test the selectivity of anionically decorated 5-sulfo-2′,7′-dichlorofluorescein esters as potentially membrane-impermeable nonfluorescent probes that should enter damaged cells and be activated therein; this should work toward a longer-term goal of similarly selective, modular prodrugs for disease modification *in vivo* (Supporting Note 2).[4,5]

2. RESULTS AND DISCUSSION

2.1. Doubly Capped Monosulfonate Probes Enter Healthy Cells. We synthesized the novel, sulfonated fluorophore 5-sulfo-2′,7′-dichlorofluorescein ($\mathbf{H_2}$-$\mathbf{FS_1}$) by adapting known procedures (compound naming scheme in Figure S1).[32] Condensing 4-chlororesorcinol with 4-sulfophthalic acid yielded 68% of the mixed 5- and 6-sulfofluoresceins. Conveniently, this could be purified to >95% purity of the 5-sulfo regioisomer by precipitation and wash/filter steps without chromatography of the very polar mixture. The absorption, excitation, and emission properties of $\mathbf{H_2}$-$\mathbf{FS_1}$ (ex/em maxima ca. 500/525 nm) match the strong fluorophore dichlorofluorescein $\mathbf{H_2}$-$\mathbf{FS_0}$ (Figure S2a–c). We synthesized the fluorogenic probes $\mathbf{i_2}$-$\mathbf{FS_1}$ and $\mathbf{a_2}$-$\mathbf{FS_1}$ (Figure 2a) by double *O*-acylation of $\mathbf{H_2}$-$\mathbf{FS_1}$ using 5–10 equiv of acid anhydride in DMF (see Supporting Information). As expected, these were locked as nonfluorescent spirolactones (Figure S2d,e).

To perform wash-free damage imaging, the probes must remain nonfluorescent outside cells by avoiding spontaneous nonenzymatic hydrolysis while also being rapidly enzymatically processed upon cellular entry to give fluorescence. We first tested the probe stability. During a typical time frame for cell experiments (15 min incubation at 37 °C), the isobutyrates of $\mathbf{i_2}$-$\mathbf{FS_1}$ were relatively stable in phosphate-buffered saline (PBS) or Hanks' balanced salt solution (HBSS) buffers (<1% activation), whereas the less sterically hindered acetates of $\mathbf{a_2}$-$\mathbf{FS_1}$ were ca. 8-fold more labile, as expected (discussion at Figure S2g,h). These observations emphasize the need for isobutyrate capping. We decided to use HBSS for cellular experiments, since it provides more nutrients than PBS and can be used as a pH-buffering medium without a CO_2 atmosphere. We then assessed probe activation by the model enzyme porcine liver esterase (PLE), showing that both probes were activated above their spontaneous hydrolysis rates (Figure S2f).

Next, we tested the exclusion of the probes from healthy cells, using confocal microscopy to localize their activated fluorescence and quantify the intracellular vs extracellular intensities (Figure 2b,c). We anticipated the probes $\mathbf{i_2}$-$\mathbf{FS_1}$ and $\mathbf{a_2}$-$\mathbf{FS_1}$, and the fluorophore $\mathbf{H_2}$-$\mathbf{FS_1}$, would be cell-excluded due to their sulfonation. We also used neutral $\mathbf{H_2}$-$\mathbf{FS_0}$ as a slow cell-entering reference fluorophore and Raines' neutral $\mathbf{i_2}$-$\mathbf{FS_0}$[30] as a reference probe with good cell penetration and enzymatic deacylation. Predictably, fluorophores $\mathbf{H_2}$-$\mathbf{FS_0}$ and $\mathbf{H_2}$-$\mathbf{FS_1}$ gave the highest extracellular signals (empty blue boxes in Figure 2c), with a lower intracellular signal (filled black circles in Figure 2c), so cells were seen as "shadow images" in microscopy (Figure 2b).

This supported that monosulfonate $\mathbf{H_2}$-$\mathbf{FS_1}$ is cell-impermeable, and we had hoped that its ester-capped probes would be also. Unexpectedly though, $\mathbf{i_2}$-$\mathbf{FS_1}$ gave almost equal intracellular fluorescence as $\mathbf{i_2}$-$\mathbf{FS_0}$, i.e., when doubly *O*-acylated to the fluorogenic spirolactone, a single sulfonate is insufficient for cell exclusion (Figure 2b,c). $\mathbf{a_2}$-$\mathbf{FS_1}$ showed a lower intracellular signal than $\mathbf{i_2}$-$\mathbf{FS_1}$, supporting that isobutyrate lipophilicity promotes cellular entry despite the sulfonate charge penalty.[33]

https://doi.org/10.1021/jacs.3c07662
J. Am. Chem. Soc. 2024, 146, 11072–11082

Journal of the American Chemical Society pubs.acs.org/JACS Article

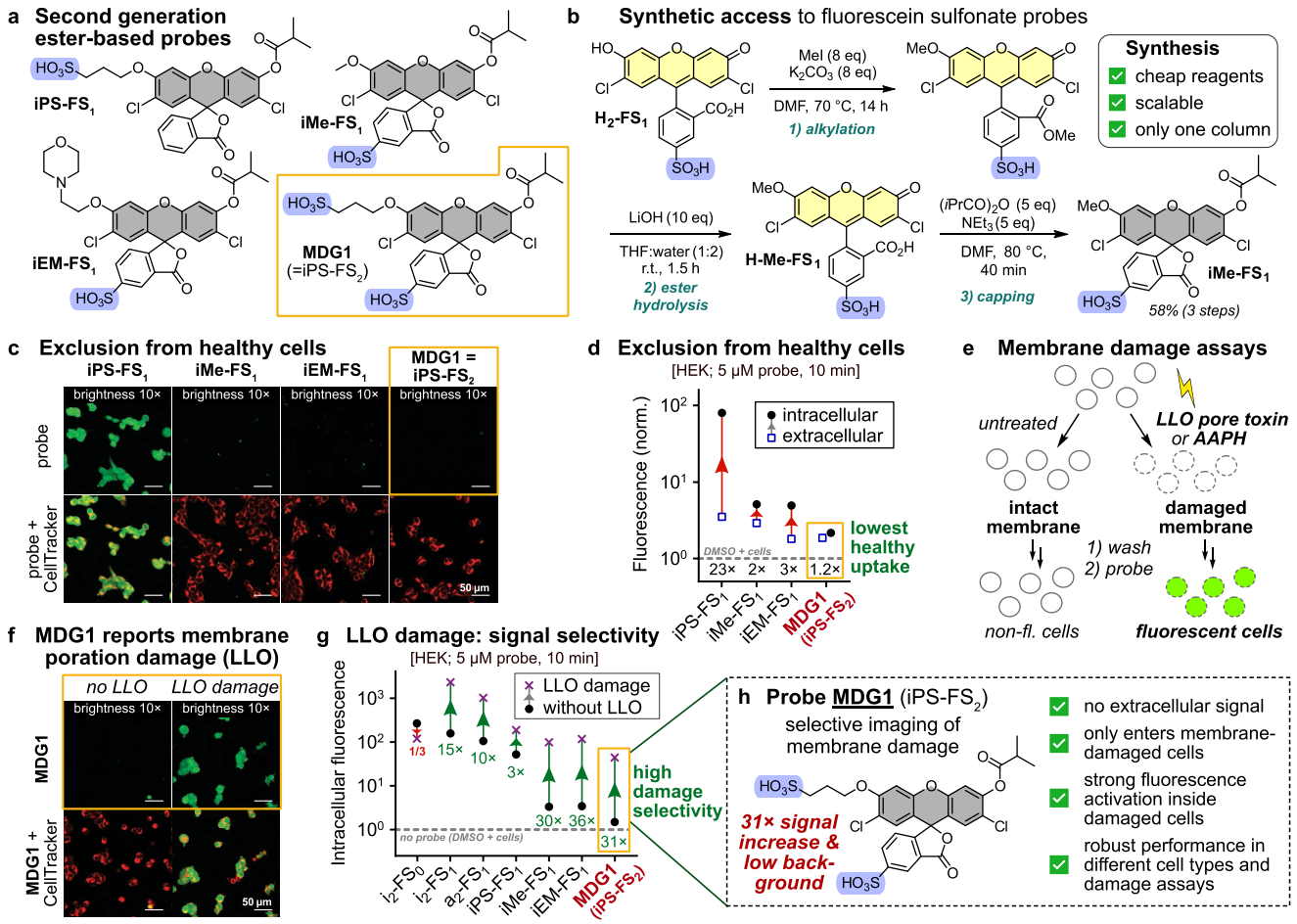

Figure 3. Monocapped fluorogenic probes that are excluded from healthy cells but enter and turn on in damaged cells. (a, b) Overview and synthetic route for monocapped probes. (c, d) Microscopy studies of healthy HEK cells treated with probes (5 μM, 10 min), quantified for intra- and extracellular fluorescence relative to no-probe control ("DMSO", set to 1). (e) Membrane damage assays. (f, g) Listeriolysin O (LLO) damage assay (HEK cells, 5 μM probe, 10 min, no washing). Intracellular fluorescence (relative to DMSO) for damaged vs undamaged cells. (h) Damage probe **iPS-FS$_2$** (**MDG1**). (Scale bars: 50 μm; "brightness 10×" is the gain relative to that in Figures 2 and 4; full legend in Supporting Note 3).

Thus, we needed to develop even more hydrophilic capped probes to enforce cell exclusion. Still, we noted two useful results: first, isobutyrate ester capping on the sulfo-dichloro-fluorescein is an excellent platform for low-background, high-sensitivity imaging as needed for damaged cell probes. The extracellular background signal from *O*-deacylation of diester **i$_2$-FS$_1$** reached only 1−2% of the signal of uncapped **H$_2$-FS$_1$**, without any washing steps before imaging (empty blue boxes, Figure 2c). Second, the microscopy quantifications in HEK cells matched qualitatively to population averages from flow cytometry over thousands of HeLa cells (Figures 2d and S4). Thus, the effect that two lipophilic *O*-capping groups can bring a monosulfonated spirocyclized probe across the membrane[34] for intracellular activation is conserved across different cell types. The flow cytometry data are monomodal, supporting the idea that a single mechanism is responsible for entry: a result that is encouraging for further tuning.

2.2. Capped Disulfonate Probe MDG1 Is Excluded by Healthy Cells. To tune membrane permeability via increasingly polar spiro probes while keeping the stability of the isobutyrate cap strategy, we *O*-alkylated one xanthene phenol before installing a single isobutyrate ester, resulting in monocapped probes (Figure 3a). For increasingly polar *O*-alkyl moieties on the **FS$_1$** scaffold, we used methyl (**iMe-FS$_1$**), amine (β-ethylmorpholino **iEM-FS$_1$**), or sulfonate (γ-propylsulfonate **iPS-FS$_2$**), and we controlled for monosulfonate position by comparing **iMe-FS$_1$** (on the pendant ring) with **iPS-FS$_1$** (on the *O*-alkyl chain; Figure 3a). The probe syntheses were run to avoid chromatography (strategy adapted from the literature[27,35,36]): e.g., for **iMe-FS$_1$**, **H$_2$-FS$_1$** was doubly alkylated at the carboxylate and at one phenol, then the ester was cleaved mildly with LiOH to give the monoalkylated fluorophore (**H-Me-FS$_1$**), which was then capped with isobutyric anhydride to afford the probe in good yield (58% over three steps, Figure 3b).

The optical properties of the monoalkylated fluoresceins were slightly different from symmetric fluoresceins (Figure S2a,b): they have two absorption maxima, ca. 460 and 485 nm, with 4-fold weaker absorbance at 485 nm, and their fluorescence quantum yields (λ_{max} ca. 525 nm) are reduced from ∼0.8 to ∼0.2, which are expected results[37] for the unsymmetric chromophore (discussion at Figure S2). Due to this intensity difference, their microscopy images are displayed at different brightness to keep focus on the key feature, that is, their exclusion from healthy cells relative to their signal in damaged cells. All probes and fluorophores were photostable (Figure S2c), and all probes were stable enough in handling to ensure <5% ester cleavage in stocks (Figure S2d,e). The monocapped probes were enzymatically activated to maximum 5−10× faster

https://doi.org/10.1021/jacs.3c07662
J. Am. Chem. Soc. 2024, 146, 11072−11082

Journal of the American Chemical Society pubs.acs.org/JACS Article

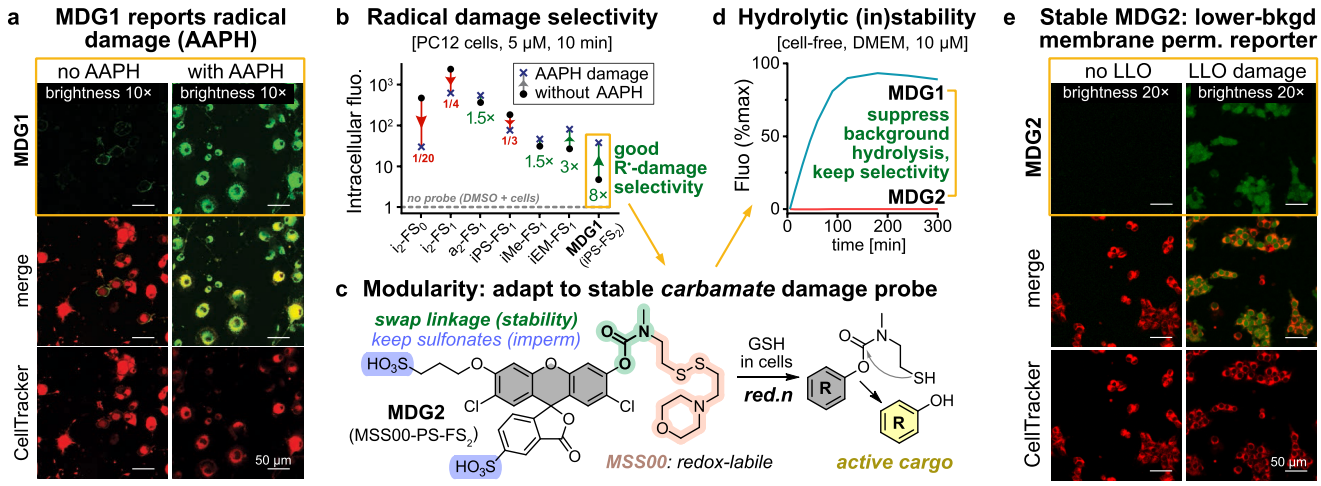

Figure 4. Scope for fluorogenic membrane damage probes. (a, b) Nonspecific membrane damage (polyunsaturated fatty acid (PUFA) peroxidation) was induced by the radical initiator 2,2′-azobis(2-amidinopropane) (AAPH). **MDG1** images, and quantified intracellular fluorescence for all probes (PC12 cells). (c−e) **MDG2**, with a GSH-labile reduction trigger attached as a phenolic carbamate, has far less spontaneous hydrolysis in extracellular medium than **ester MDG1** but retains the damage-selective performance in the LLO assay (HEK cells). (All: 5 μM probe for 10 min, no wash; scale bars: 50 μm; "brightness 10/20×" is the gain relative to settings in Figures 2 and 3; full legend in Supporting Note 3).

than doubly capped probes (expected, as a single ester cleavage gives the full signal, whereas, for double capping, the first and second cleavages affect fluorescence differently; see Figure S2f). The hydrolytic stability of the ester probes was good in PBS, limited in HBSS, and poor in Dulbecco's modified Eagle's medium (DMEM); therefore, we continued using HBSS for cellular membrane damage assays (Figure S2g,h).

As expected, the fluorophore cores that are released after ester cleavage were excluded from healthy cells (Figure S5). However, the unwanted entry of the intact probes into healthy cells was only avoided by high polarity, e.g., with the disulfonated **iPS-FS$_2$** that gave nearly no intracellular fluorescence above background (Figure 3c,d). (Of the monosulfonates, **iEM-FS$_1$**/**iMe-FS$_1$** gave <3-fold higher intracellular than extracellular signal; for **iPS-FS$_1$**, the ratio was 23-fold.) Importantly, these microscopy results were matched on a population level and tested quantitatively by flow cytometry (Figure S4c,d). PerMM molecular dynamics simulations[38,39] also support that **iPS-FS$_2$** ($\log P_{erm} = -9.45$) should have much lower healthy cell permeability than **iPS-FS$_1$** ($\log P_{erm} = -5.11$; see the Supporting Information in Table S2).

Since **iPS-FS$_2$** was later confirmed as our best ester-based probe, we renamed it **MDG1**: for Membrane Damage Green 1.

2.3. Capped Disulfonate MDG1 Is a Damage-Selective Reporter. To investigate probe uptake and activation in damaged cells, we first used the pore-forming bacterial protein listeriolysin O (LLO) to induce membrane damage (Figure 3e).[40] We chose LLO as a model as it induces small-diameter pores that are suitable for small molecule uptake[41] by a well-studied mechanism of action.[42] Microscopy showed that all sulfonated probes had a higher intracellular signal with LLO than without, but only **MDG1** (=**iPS-FS$_2$**) was suitable as a selective probe for wash-free imaging of damaged cells since it was the only probe with both near-zero extracellular background and a high ratio of the signal in LLO-damaged vs healthy cells (>30×) (Figures 3f−h and S5−S7).

We next tested if **MDG1** would also report on radical damage to membrane integrity since we were interested in targeting membrane-damaged axons as are found in inflammatory lesions in models of multiple sclerosis.[4,5] Although the cause of this damage is unknown, such lesions have high loads of reactive oxygen and nitrogen species,[43] and it is speculated that permeabilization results from lipid peroxidation (Supporting Note 2). We therefore treated the neuronal cell line PC12[44] with the radical-generating initiator 2,2′-azobis(2-amidinopropane) (**AAPH**) to peroxidize membrane lipids.[45] Again, **MDG1** was excluded from healthy cells yet stained AAPH-damaged cells, with the highest selectivity of all probes (8-fold selectivity, Figure 4a,b; see Figure S8). Thus, the disulfonate **MDG1** became our best esterase probe for charge-based discrimination of membrane damage, as it is most reliably excluded from intact cells across different cell lines, while showing strong signal turn-on in damaged cells (the different subcellular signal distributions in AAPH- vs LLO-damaged cells are a result of the damage treatments, not the cell lines; see Figure S10).

Then, we assessed practical aspects of using **MDG1** across biological assays. Three key results are: (a) **MDG1**-probed cells can be imaged for times longer than the 10 min needed for optimal loading. Damaged cells remain clearly marked for at least 2 h in wash-free imaging despite slow rises of extracellular background (Figure S11). This makes **MDG1** useful to study, e.g., longer damage response time courses. (b) **MDG1**-probed cells can be fixed and analyzed posthoc, eliminating the need for live-cell microscopy setups (Figure S14). The signal does drop with washing (rate depends on damage type—LLO: rapid loss; AAPH: partial retention; Figure S12), but since washing is not needed, we recommend simply avoiding wash steps in either live or fixed imaging (Figures S12 and S14). (c) Membrane resealing after stress can also be investigated using **MDG1** by adding the probe after different post-stress recovery times (Figure S13) to report on membrane integrity recovery.

2.4. Design Modularity Allows Tuning Probe Stability and Scope. The design of this system is intentionally modular, in that the probe's impermeabilization is ensured by the fluorophore so that the trigger can be chosen freely. We aim at alternative fluorogenic triggers for two reasons: (1) to identify more extracellularly robust triggers that withstand cell culture media over longer imaging time courses, and may resist extracellular processing *in vivo*, as more performant and applicable damage imaging probes; and (2) to work toward

https://doi.org/10.1021/jacs.3c07662
J. Am. Chem. Soc. 2024, 146, 11072−11082

Journal of the American Chemical Society pubs.acs.org/JACS Article

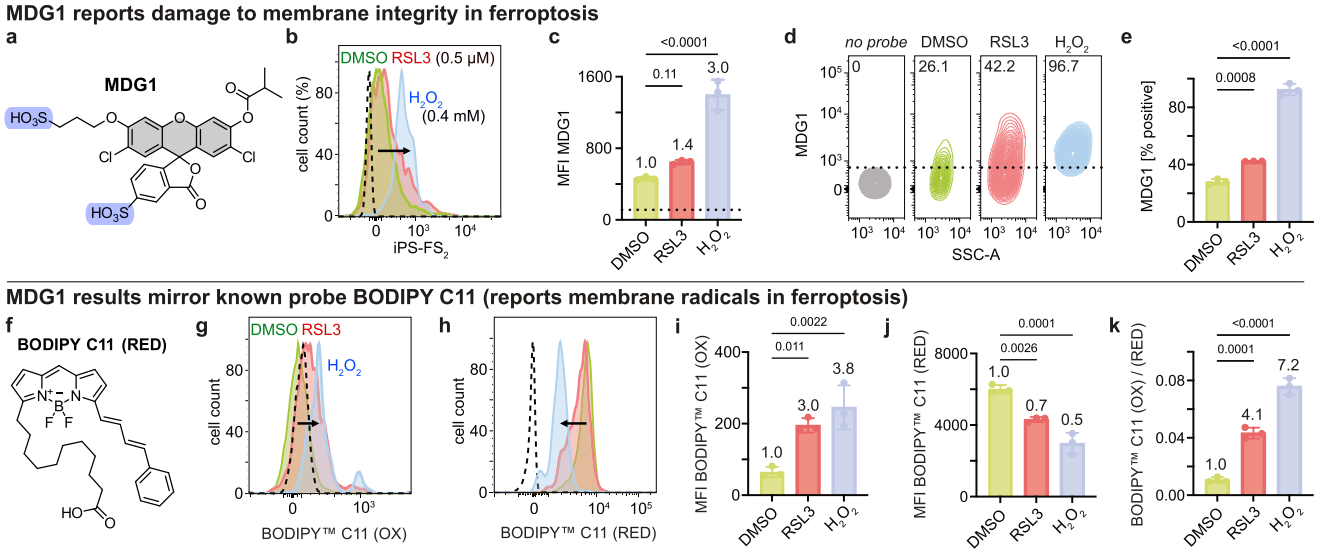

Figure 5. Sensing membrane damage in ferroptosis. (a–k) T-cells were isolated from a culture of total lung lymphocytes, optionally pretreated with RSL3 or H_2O_2, then treated for 1 h with probes **MDG1** (50 μM) or **BODIPY-C11** (RED) (250 μM), and analyzed by flow cytometry. (a–e) Cells pretreated with H_2O_2 are strongly marked by **MDG1**; control cells are not (b, d). (f–k) **BODIPY-C11** also reveals cells pretreated with H_2O_2, although it needs ratiometric evaluation of the oxidized/reduced fluorescence intensities (k) to do so (full legend in Supporting Note 3).

molecular imaging of specific enzymes, either on the surface of healthy cells, or within damaged cells.

In this study, we explored one approach for extracellularly robust probes using an intracellularly reducible disulfide trigger[46] that adapts onto the scaffold as the tertiary carbamate probe **MDG2**. This ought to be far more hydrolytically resistant than the ester cap of **MDG1** yet also effectively cleaved by thiols upon cellular entry (Figure 4c). Indeed, no undesired **MDG2** activation was observed over 5 h in DMEM medium (Figures 4d and S16a), but even 0.1 mM GSH rapidly activated it (Figure S16b; intracellular [GSH] ~ 1–5 mM[47]). **MDG2** was as well-excluded from healthy cells as **MDG1** (Figures 4e and S17), with good signal increase in damaged cells (LLO: 8-fold; AAPH: 3-fold; Figure S17). Though its intracellular fluorescence increases ca. 3 times more slowly than with ester probe **MDG1**, the far greater extracellular stability of **MDG2** permits application at higher concentration and/or for longer, if needed.

Taken together, the monocapped disulfonate fluorogen "**MDG**" design is a synthetically accessible, biochemically flexible, and reliable platform for small molecule probes that discriminate for damaged cells.

2.5. Comparison to Size-Based Cell Exclusion. An alternative approach for fluorogenic probes to report on cell membrane damage might be to develop macromolecular probes that are excluded from passively entering healthy cells on the basis of size, but may still enter more porous cells. Healthy cells do perform active macromolecular uptake by varied mechanisms, which can prevent size-based exclusion from being completely effective (see, e.g., ref 48). Nevertheless, although the focus of this work was on small molecule probes, we tested this approach (Supporting Information, section Dextrans).

In brief, we first tested commercially available, permanently fluorescent 6–2000 kDa dextrans in an AAPH assay, and saw slightly increased uptake after damage (Figure S15). To adapt them into no-wash turn-on probes, we required fluorogenic dextrans; but these are barely reported (the first monofunctional fluorogenic dextran was only published in 2018[48]) and are not commercially available. We therefore prepared monoisobutyrate-capped, chloro-stabilized fluorogenic fluorescein NHS ester **NHS-i-Flu**, assuming that its one-step off/on unmasking would make it more suitable for quantification than the previous double-capped[48] fluorogenic dextran. Fina Biosolutions LLC (MD) conjugated this NHS ester to 70 kDa dextran; however, carefully controlled AAPH assays did not indicate sufficient damage-dependent cellular entry (Figure S15). This suggests that the background rates of active uptake of macromolecules by healthy cells are too high, compared to any damage-induced changes in their passive membrane permeability, for such large carriers to be a robust approach to probe membrane integrity. We thus continued with charge-based exclusion of **MDG1/2**.

2.6. Membrane Biology Part 1: Cellular Ferroptosis. Ferroptosis is a nonapoptotic form of cell death first described by Stockwell in 2012,[49] where radical chain reactions with (poly)unsaturated fatty acids in membrane lipids, mediated by molecular oxygen, form lipid hydroperoxides that lead to catastrophic loss of membrane integrity and ultimately to cell death. Several cellular mechanisms suppress ferroptosis. These include the reductase GPx4 that reduces lipid hydroperoxides to unreactive alcohols to stop propagation;[50,51] thus, GPx4 inhibitors, e.g., RSL3, can be useful as ferroptosis inducers. Chemical methods such as H_2O_2 overload also induce lipid peroxidation by Fenton chemistry, albeit intervening at a different stage of the cascade.[52]

Typically, ferroptosis is imaged by proxy, using reactive membrane-integrating probes that intercept oxygen-centered radicals (**BODIPY-C11**,[53] Figure 5f) or that react with hydroperoxide products (e.g., phosphine "Liperfluo"). However, neither type directly reveals the biologically relevant result of ferroptosis, which is the loss of membrane integrity. Since they alter peroxidation biochemistry, these probe types are also invasive and have biological limitations;[53] as **BODIPY-C11** needs ratiometric measurement, it blocks two imaging channels.

Since the redox-independent probe **MDG1** can instead directly report on membrane integrity loss, we tested whether it could provide an alternative strategy for ferroptosis imaging. To this end, we challenged T-cells isolated from mouse lungs

https://doi.org/10.1021/jacs.3c07662
J. Am. Chem. Soc. 2024, 146, 11072–11082

Journal of the American Chemical Society pubs.acs.org/JACS Article

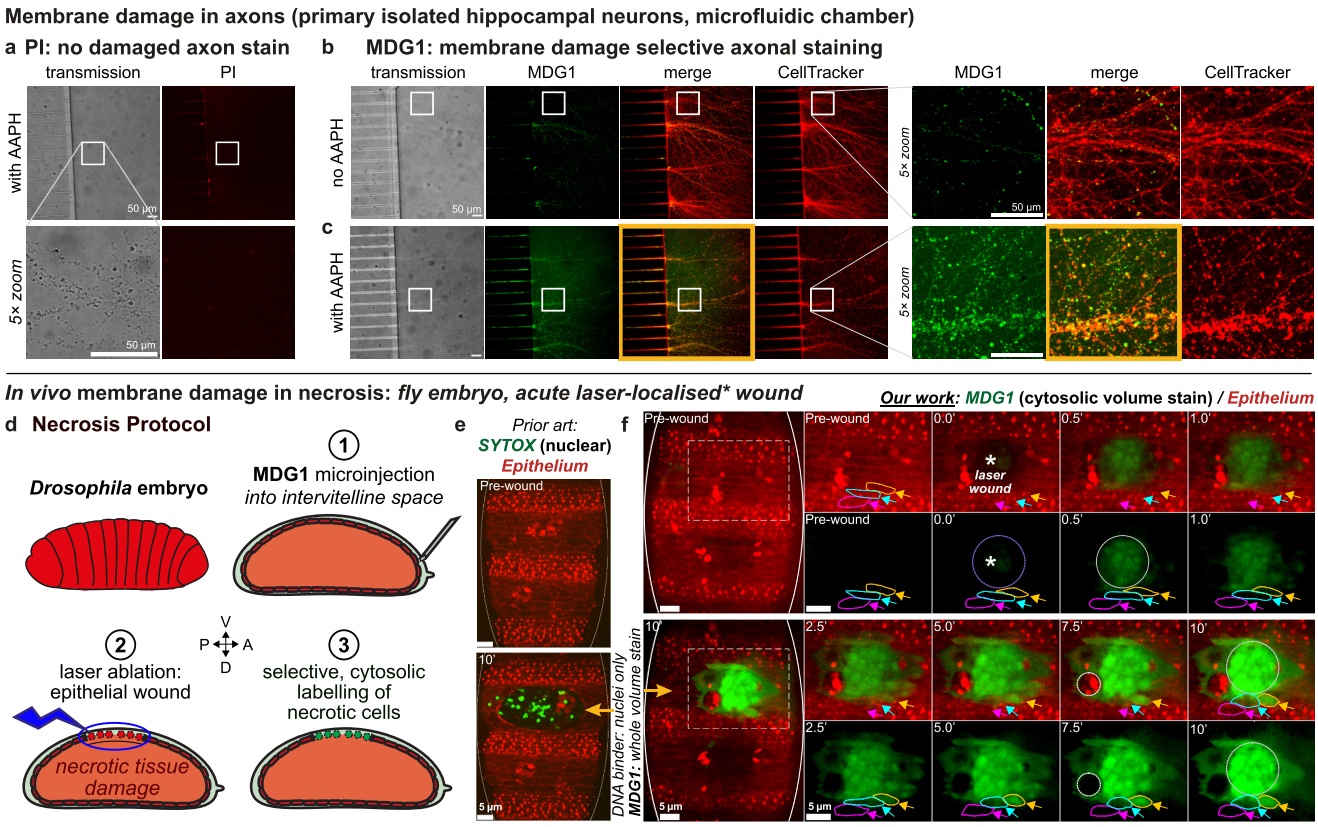

Figure 6. Sensing membrane damage in axons, and necrotic tissue *in vivo*. (a–c) The membrane-damaged axons of primary mouse hippocampal neurons are selectively stained by **MDG1** (25 μM, 15 min) after damage by AAPH (300 mM, 90 min); but this axonal membrane damage cannot be revealed by the (nuclear) stain PI (full data in Figures S22 and S23; scale bars = 50 μm). (d–f) After treating live Drosophila embryo with **MDG1** or reference stain **SYTOX Green**, local necrotic damage was triggered by local laser wounding (at asterisk) of the ventral epithelium (mCherry-moesin cell surface marker in red), and probe fluorescence was imaged (green). Cells in the laser focus (violet ring at time 0.0′) rapidly take up and activate the probe (time 0.5′); most cells that contact the damage focus are also labeled later (e.g., yellow- and cyan-ringed epithelial cells), but neighboring undamaged cells remain dark (e.g., magenta-ringed epithelial cell, or macrophage indicated by gray ring at time 7.5′). (Time in min, scale bar 5 μm; full legend in Supporting Note 3; high-resolution images in Figure S19 and Movie S1).

with RSL3 or H_2O_2 to induce ferroptotic lipid peroxidation and then probed them with **MDG1**. Flow cytometry showed strong challenge-dependent signal enhancement (Figure 5a–e), which corresponded well to a **BODIPY-C11** proxy readout of peroxidation (Figure 5f–k; controls of cell-type-dependent exclusion from undamaged cells in Figure S18). Although such a match is not strictly needed, since these probes measure different biological/biochemical aspects, the similarity of their responses is highly satisfying.

2.7. Membrane Biology Part 2: Axonal Damage. Sensitive fluorescence imaging of membrane damage is most often done using DNA-binding nuclear stains, such as propidium iodide. However, nuclear stains directly reveal membrane disintegration only close to the nucleus, which is not always enough for biological applications. For instance, loss of axonal membrane integrity can be an early hallmark of inflammatory axon damage, e.g., in multiple sclerosis.[11,12] Since the neuronal cell body (soma) that contains the nucleus typically resides far away from the site of axonal injury, nuclear staining is often not practical; similar considerations apply for imaging damage to distal dendrites, e.g., in the cortex, where even with well-performing two-photon microscopy, the somata of deeper layer neurons can be hard to reach, while their apical dendrites, where, e.g., damage from superficial traumatic or inflammatory lesions is concentrated, are easily observable.[54] Neuroscience is not the only field in which the current nuclear staining methods have limits in detecting membrane permeabilization; e.g., some cell types, such as erythrocytes, do not even have nuclei that could be a staining target, even though tracing damage to their membranes is important for studying diseases such as malaria[13] and diabetes.[55] Here, we focus on identifying axon damage as a highly relevant and unique application for **MDG** probes that will be indicative of other applications in neuroscience.

For axonal assays, we isolated primary mouse hippocampal neurons and cultured them in microfluidic devices to separate the cell body (somatic chamber) from the axon (axonal chamber). After damaging the axons with AAPH, we applied imaging agents. Nuclear stains such as PI did not reveal damaged axons (Figure 6a). However, **MDG1** clearly traced damaged axons (yellow in merge panels, Figure 6c), leaving undamaged axons almost nonfluorescent (Figure 6b). We thereby provide the first imaging agent that enables bright, wash-free fluorogenic imaging of axonal membrane damage, against low nonspecific and nondamage background: a valuable tool for studying axonal damage in a broad range of neurological conditions.[5]

2.8. Membrane Biology Part 3: *In Vivo* Imaging of Necrosis. The requirements for a probe to succeed *in vivo*, i.e., in a live intact animal (3D system), are much more stringent than in two-dimensional (2D) cell culture. In culture, all cells contact a vast reservoir of solution, where convective currents

https://doi.org/10.1021/jacs.3c07662
J. Am. Chem. Soc. 2024, 146, 11072–11082

resupply fresh probe while diluting away any fluorophore that is activated and/or released from a cell; this can make fluorescence appear more cell-localized than is the underlying chemistry. However, both resupply and dilution are limited in 3D; so, for a probe to label damaged cells *in vivo* robustly in a cell-resolved manner, the probe's entry, activation, and retention, must be efficient and exceptionally selective for damaged cells (full exclusion from healthy cells and minimal activation in the extracellular space). We now tested the cell resolution of **MDG1** in a demanding *in vivo* assay.

Acute necrotic injury can be induced *in vivo* with high spatial precision by laser ablation. Drosophila embryos are well-studied and ethically acceptable model organisms in which to probe it. Traditional laser damage assays with live Drosophila embryos microinject cell-impermeable chemical dyes into the intervitelline space (a fluid layer surrounding the epithelium)[56] and then image their fluorescence signal following laser ablation (Figure 6d), typically observing the accumulation of membrane-impermeable DNA-binding fluorophores, such as SYTOX (structure in Figure S20)[57] or PI in the nuclei of necrotic cells. Again, the drawback of these DNA stains is that they only visualize where the nuclei of damaged cells are, but do not give information about cellular shape and boundaries, or the extent of the damaged zone *in vivo* (Figure S21). By contrast, we expected that by revealing the entire cytosolic volume of necrotic cells, **MDG1** would offer advantages compared to nuclear stains, e.g., helping to determine the boundaries of necrotic zones across stacks of 2D image slices, which do not necessarily each map the nucleus together with accessible cell outline markers, as well as highlighting whether nondamaged cells are present in the damage zone or enter it over time. We thus compared nuclear SYTOX Green (Figure 6e) to our probe **MDG1** in embryonal damage assays (Figure 6f).

Time-lapse microscopy of embryos pretreated with **MDG1** before local laser ablation revealed outstanding performance (Figure 6f). Cells in the laser focus, which are visible since their red cell outline marker[58] is photobleached by the laser at time 0, were durably labeled by **MDG1** fluorescence within just 30 s (time 0.5 min, Figure 6f). Cells contacting the damage focus were also labeled, at a predictably slower rate: consistent with the hypothesis that localized loss of membrane integrity even at one side or tip of the cell can be detected by **MDG1** (yellow/cyan-marked cells at 5 min, Figure 6f). Pleasingly, viable cells neighboring the damage zone remained completely nonfluorescent (magenta-indicated epithelial cell at 5 min), with macrophages infiltrating the damage zone even appearing as "shadow images" (gray-indicated macrophage at 7.5 min, Figure 6f). Against this sharply spatially defined pool of fluorescent damaged cells, all other nondamaged cells and areas remained nonfluorescent throughout the imaging experiment, supporting that **MDG1** is a highly sensitive as well as selective probe for robust, fluorogenic imaging of cell membrane damage *in vivo* (further detail in Figure S19, Supporting Note 3, and Movie S1).

Taken together, we believe that noninvasive fluorogenic reagents, such as **MDG1**, which directly and selectively reveal the membrane permeabilization that is a driving force in ferroptosis, necrosis, bacterial toxicity, axonal degeneration, and in a host of other pathological situations, may find broad applications in biophysics, cellular, and *in vivo* biology.

3. CONCLUSIONS

We have harnessed molecular charges and polarity in a modular fluorogenic probe design to develop a reliable platform for probing cell membrane integrity. We aimed for "no-wash" molecular imaging probes that are excluded from healthy cells yet enter cells with compromised membranes, whereupon their fluorescence is activated from near-zero background. The disulfonated fluorogenic **MDG** probe type we identified, covering the ester probe **MDG1** or the reducible probe **MDG2**, will enable noninvasive tracking and quantification of the induction of membrane permeability or the recovery of membrane integrity across a range of biological or chemical stressors or diseases. The probes can be used robustly in various cell biology applications and *in vivo*. Finally, the way that they reveal the cytosolic volume of damaged cells is a useful advance compared to traditional nuclear damage stains, such as PI or Sytox, since it allows **MDGs** to reveal cellular damage far from the nucleus (e.g., axonal damage, as relevant to neurodegeneration), as well as to highlight nondamaged cells within damaged zones as "shadow images" even in *in vivo* settings.

We see at least four open avenues for development. The extracellular stability of the carbamate **MDG2** offers an intriguing lead for no-wash *in vivo* imaging of membrane damage after chemical improvements, such as by (a) tuning the fluorophore toward red/NIR operation, e.g., by adaptation to Si-rhodols,[59,60] and (b) improving the intracellular turn-on speed, which is set by the choice of trigger.[61] The disease model scope for which membrane permeability probes are appropriate reporters, can also be more widely explored. Using cell-excluded probes on healthy cells to perform molecular imaging of their cell-surface enzymology is an interesting prospect, particularly for redox biochemistry.[62] Finally, the opportunities to harness similar chemical design principles to selectively deliver pharmacologically active agents (instead of fluorophores) which could ameliorate disease states characterized by increased membrane permeability, are alluring for translational research.

Conceptually, permeability studies of stepwise-tuned sets of chemical probes, such as the ones devised here, can also reveal useful lessons for chemical biology. One point we raise is that the 3D placement of the sulfonates in **MDG1/2**, far from each other along orthogonal vectors, was actively chosen to avoid an overall head/tail surfactant structure that could cause membranolytic stress. However, as pointed out by a colleague, the cell entry of these disulfonate probes may still involve them inducing mild membrane stress, which only integrity-compromised cells are unable to resist. That would make their design more actively involved in achieving their biological readout than a picture of "*n* charges per *m* aromatic rings," suggesting opportunities for nuanced research.

With many avenues for chemical, biochemical, biological, biophysical, and translational explorations now opening up, we look forward to the further development and applications of these deceptively simple chemical tools for probing the integrity of lipid bilayer membranes.

■ ASSOCIATED CONTENT

Supporting Information

The Supporting Information is available free of charge at https://pubs.acs.org/doi/10.1021/jacs.3c07662.

Synthesis, analysis, biochemical and cell biological evaluations (PDF)

Time-lapse imaging of fly embryo laser damage, corresponding to Figure 6 (AVI)

https://doi.org/10.1021/jacs.3c07662
J. Am. Chem. Soc. 2024, 146, 11072−11082

AUTHOR INFORMATION

Corresponding Author

Oliver Thorn-Seshold − *Department of Pharmacy, Ludwig-Maximilians University of Munich, 81377 Munich, Germany;* orcid.org/0000-0003-3981-651X; Email: oliver.thorn-seshold@cup.lmu.de

Authors

Philipp Mauker − *Department of Pharmacy, Ludwig-Maximilians University of Munich, 81377 Munich, Germany*

Daniela Beckmann − *Institute of Clinical Neuroimmunology, LMU University Hospital, Ludwig-Maximilians University of Munich, 81377 Munich, Germany; Biomedical Center (BMC), Faculty of Medicine, Ludwig-Maximilians University of Munich, 82152 Martinsried, Germany*

Annabel Kitowski − *Department of Pharmacy, Ludwig-Maximilians University of Munich, 81377 Munich, Germany*

Constanze Heise − *Department of Pharmacy, Ludwig-Maximilians University of Munich, 81377 Munich, Germany*

Chantal Wientjens − *Immunopathology Unit, Institute of Clinical Chemistry and Clinical Pharmacology, Medical Faculty, University Hospital Bonn, University of Bonn, 53127 Bonn, Germany*

Andrew J. Davidson − *Institute for Regeneration and Repair, The University of Edinburgh, Edinburgh EH16 4UU, U.K.*

Simone Wanderoy − *University Hospital, Technical University of Munich, 81675 Munich, Germany; Max Planck Institute for Biological Intelligence, 82152 Martinsried, Germany*

Gabin Fabre − *Pharmacology & Transplantation, UMR 1248 INSERM, University of Limoges, 87000 Limoges, France*

Angelika B. Harbauer − *Max Planck Institute for Biological Intelligence, 82152 Martinsried, Germany; Munich Cluster for Systems Neurology (SyNergy), 81377 Munich, Germany; Institute of Neuronal Cell Biology, Technical University of Munich, 80802 Munich, Germany*

Will Wood − *Institute for Regeneration and Repair, The University of Edinburgh, Edinburgh EH16 4UU, U.K.*

Christoph Wilhelm − *Immunopathology Unit, Institute of Clinical Chemistry and Clinical Pharmacology, Medical Faculty, University Hospital Bonn, University of Bonn, 53127 Bonn, Germany*

Julia Thorn-Seshold − *Department of Pharmacy, Ludwig-Maximilians University of Munich, 81377 Munich, Germany;* orcid.org/0000-0002-4879-4159

Thomas Misgeld − *Munich Cluster for Systems Neurology (SyNergy), 81377 Munich, Germany; Institute of Neuronal Cell Biology, Technical University of Munich, 80802 Munich, Germany; German Center for Neurodegenerative Diseases (DZNE), 81377 Munich, Germany*

Martin Kerschensteiner − *Institute of Clinical Neuroimmunology, LMU University Hospital, Ludwig-Maximilians University of Munich, 81377 Munich, Germany; Biomedical Center (BMC), Faculty of Medicine, Ludwig-Maximilians University of Munich, 82152 Martinsried, Germany; Munich Cluster for Systems Neurology (SyNergy), 81377 Munich, Germany*

Complete contact information is available at: https://pubs.acs.org/10.1021/jacs.3c07662

Author Contributions

‡‡P.M. and D.B. contributed equally to this work.

Funding

This research was supported by funds from the German Research Foundation (DFG: SFB 1032 project B09 number **201269156**, SFB TRR 152 project P24 number **239283807**, SPP 1926 project number **426018126**, and Emmy Noether grant **400324123** to O.T.-S.; high-resolution microscopy instrumentation grant INST95/1755-1 FUGG, ID **518284373** to T.M.; TRR 274/2 project C02—ID **408885537** to M.K. and T.M.; TRR 128 projects B10 and B13, and TRR 152 project P27—ID **239283807** to M.K.); T.M. was further supported by the German Center for Neurodegenerative Diseases (DZNE); and M.K. and T.M. were further supported by the Munich Center for Systems Neurology (SyNergy EXC 2145; Project ID **390857198**).

Notes

The authors declare no competing financial interest.

ACKNOWLEDGMENTS

The authors acknowledge support from the Joachim Herz Foundation (Research Fellowships to P.M. and J.T.-S.); the Studienstiftung des Deutschen Volkes (Ph.D. scholarships to P.M. and D.B.); and the Munich Graduate School of Systemic Neurosciences (D.B.). They thank Dr. Andrew Lees (Fina Biosolutions LLC, MD) for many helpful discussions while planning and designing dextran conjugates. They thank Dr. Lees and Dr. Samson Gebretnsae (Fina Biosolutions LLC, MD) for performing all custom syntheses of dextran conjugates. They thank Alexander Sailer and Adrian Müller-Deku (LMU) for initial work on fluorescein diacetate NHS ester conjugations to aminodextrans; Bekkah Bingham (LMU) for chromatographic analysis of the integrity of fluorescein diacetate in dextran conjugates; and Philip Woelfle (LMU) for initial testing of dextran conjugates. They are grateful to Henrietta Lacks, now deceased, and to her surviving family members for their contributions to biomedical research.

REFERENCES

(1) Bretscher, M. S.; Raff, M. C. Mammalian Plasma Membranes. *Nature* **1975**, *258* (5530), 43−49.

(2) Yang, N. J.; Hinner, M. J. Getting Across the Cell Membrane: An Overview for Small Molecules, Peptides, and Proteins. *Methods Mol. Biol.* **2015**, *1266*, 29−53.

(3) Jimenez, A. J.; Maiuri, P.; Lafaurie-Janvore, J.; Divoux, S.; Piel, M.; Perez, F. ESCRT Machinery Is Required for Plasma Membrane Repair. *Science* **2014**, *343* (6174), No. 1247136.

(4) Witte, M. E.; Schumacher, A.-M.; Mahler, C. F.; Bewersdorf, J. P.; Lehmitz, J.; Scheiter, A.; Sánchez, P.; Williams, P. R.; Griesbeck, O.; Naumann, R.; Misgeld, T.; Kerschensteiner, M. Calcium Influx through Plasma-Membrane Nanoruptures Drives Axon Degeneration in a Model of Multiple Sclerosis. *Neuron* **2019**, *101* (4), 615−624.e5.

(5) Williams, P. R.; Marincu, B.-N.; Sorbara, C. D.; Mahler, C. F.; Schumacher, A.-M.; Griesbeck, O.; Kerschensteiner, M.; Misgeld, T. A Recoverable State of Axon Injury Persists for Hours after Spinal Cord Contusion in Vivo. *Nat. Commun.* **2014**, *5* (1), No. 5683.

(6) Guthrie, J. P. Hydrolysis of Esters of Oxy Acids: pKa Values for Strong Acids; Brønsted Relationship for Attack of Water at Methyl; Free Energies of Hydrolysis of Esters of Oxy Acids; and a Linear Relationship between Free Energy of Hydrolysis and pKa Holding over a Range of 20 pK Units. *Can. J. Chem.* **1978**, *56* (17), 2342−2354.

(7) Strober, W. Trypan Blue Exclusion Test of Cell Viability. *Curr. Protoc. Immunol.* **1997**, *21* (1), A.3B.1−A.3B.2.

(8) Suzuki, T.; Fujikura, K.; Higashiyama, T.; Takata, K. DNA Staining for Fluorescence and Laser Confocal Microscopy. *J. Histochem. Cytochem.* **1997**, *45* (1), 49−53.

(9) Biebricher, A. S.; Heller, I.; Roijmans, R. F. H.; Hoekstra, T. P.; Peterman, E. J. G.; Wuite, G. J. L. The Impact of DNA Intercalators on DNA and DNA-Processing Enzymes Elucidated through Force-Dependent Binding Kinetics. *Nat. Commun.* **2015**, *6* (1), No. 7304.
(10) Snaidero, N.; Möbius, W.; Czopka, T.; Hekking, L. H. P.; Mathisen, C.; Verkleij, D.; Goebbels, S.; Edgar, J.; Merkler, D.; Lyons, D. A.; Nave, K.-A.; Simons, M. Myelin Membrane Wrapping of CNS Axons by PI(3,4,5)P3-Dependent Polarized Growth at the Inner Tongue. *Cell* **2014**, *156* (1), 277−290.
(11) Friese, M. A.; Schattling, B.; Fugger, L. Mechanisms of Neurodegeneration and Axonal Dysfunction in Multiple Sclerosis. *Nat. Rev. Neurol.* **2014**, *10* (4), 225−238.
(12) Cheng, H.-C.; Ulane, C. M.; Burke, R. E. Clinical Progression in Parkinson Disease and the Neurobiology of Axons. *Ann. Neurol.* **2010**, *67* (6), 715−725.
(13) Mohandas, N.; An, X. Malaria and Human Red Blood Cells. *Med. Microbiol. Immunol.* **2012**, *201* (4), 593−598.
(14) Walker, J. R.; Hall, M. P.; Zimprich, C. A.; Robers, M. B.; Duellman, S. J.; Machleidt, T.; Rodriguez, J.; Zhou, W. Highly Potent Cell-Permeable and Impermeable NanoLuc Luciferase Inhibitors. *ACS Chem. Biol.* **2017**, *12* (4), 1028−1037.
(15) Nadler, A.; Yushchenko, D. A.; Müller, R.; Stein, F.; Feng, S.; Mulle, C.; Carta, M.; Schultz, C. Exclusive Photorelease of Signalling Lipids at the Plasma Membrane. *Nat. Commun.* **2015**, *6* (1), No. 10056, DOI: 10.1038/ncomms10056.
(16) Poc, P.; Gutzeit, V. A.; Ast, J.; Lee, J.; Jones, B. J.; D'Este, E.; Mathes, B.; Lehmann, M.; Hodson, D. J.; Levitz, J.; Broichhagen, J. Interrogating Surface versus Intracellular Transmembrane Receptor Populations Using Cell-Impermeable SNAP-Tag Substrates. *Chem. Sci.* **2020**, *11* (30), 7871−7883.
(17) Birke, R.; Ast, J.; Roosen, D. A.; Lee, J.; Roßmann, K.; Huhn, C.; Mathes, B.; Lisurek, M.; Bushiri, D.; Sun, H.; Jones, B.; Lehmann, M.; Levitz, J.; Haucke, V.; Hodson, D. J.; Broichhagen, J. Sulfonated Red and Far-Red Rhodamines to Visualize SNAP- and Halo-Tagged Cell Surface Proteins. *Org. Biomol. Chem.* **2022**, *20* (30), 5967−5980.
(18) Jonker, C. T. H.; Deo, C.; Zager, P. J.; Tkachuk, A. N.; Weinstein, A. M.; Rodriguez-Boulan, E.; Lavis, L. D.; Schreiner, R. Accurate Measurement of Fast Endocytic Recycling Kinetics in Real Time. *J. Cell Sci.* **2019**, *133* (2), No. jcs231225.
(19) Kim, D.; Stoldt, S.; Weber, M.; Jakobs, S.; Belov, V. N.; Hell, S. W. A Bright Surprise: Live-Cell Labeling with Negatively Charged Fluorescent Probes Based on Disulfonated Rhodamines and HaloTag. *Chemistry−Methods* **2023**, *3*, No. e202200076.
(20) Chyan, W.; Raines, R. T. Enzyme-Activated Fluorogenic Probes for Live-Cell and in Vivo Imaging. *ACS Chem. Biol.* **2018**, *13* (7), 1810−1823.
(21) Lippert, A. R.; Van de Bittner, G. C.; Chang, C. J. Boronate Oxidation as a Bioorthogonal Reaction Approach for Studying the Chemistry of Hydrogen Peroxide in Living Systems. *Acc. Chem. Res.* **2011**, *44* (9), 793−804.
(22) Albers, A. E.; Dickinson, B. C.; Miller, E. W.; Chang, C. J. A Red-Emitting Naphthofluorescein-Based Fluorescent Probe for Selective Detection of Hydrogen Peroxide in Living Cells. *Bioorg. Med. Chem. Lett.* **2008**, *18* (22), 5948−5950.
(23) Gruber, T. D.; Krishnamurthy, C.; Grimm, J. B.; Tadross, M. R.; Wysocki, L. M.; Gartner, Z. J.; Lavis, L. D. Cell-Specific Chemical Delivery Using a Selective Nitroreductase−Nitroaryl Pair. *ACS Chem. Biol.* **2018**, *13* (10), 2888−2896.
(24) Li, L.; Ge, J.; Wu, H.; Xu, Q.-H.; Yao, S. Q. Organelle-Specific Detection of Phosphatase Activities with Two-Photon Fluorogenic Probes in Cells and Tissues. *J. Am. Chem. Soc.* **2012**, *134* (29), 12157−12167.
(25) Chao, T.-Y.; Raines, R. T. Fluorogenic Label to Quantify the Cytosolic Delivery of Macromolecules. *Mol. Biosyst.* **2013**, *9* (3), 339−342.
(26) Tian, L.; Yang, Y.; Wysocki, L. M.; Arnold, A. C.; Hu, A.; Ravichandran, B.; Sternson, S. M.; Looger, L. L.; Lavis, L. D. Selective Esterase−Ester Pair for Targeting Small Molecules with Cellular Specificity. *Proc. Natl. Acad. Sci. U.S.A.* **2012**, *109* (13), 4756−4761.
(27) Li, X.; Higashikubo, R.; Taylor, J.-S. Use of Multiple Carboxylates to Increase Intracellular Retention of Fluorescent Probes Following Release From Cell Penetrating Fluorogenic Conjugates. *Bioconjugate Chem.* **2008**, *19* (1), 50−56.
(28) Kaneshiro, E. S.; Wyder, M. A.; Wu, Y.-P.; Cushion, M. T. Reliability of Calcein Acetoxy Methyl Ester and Ethidium Homodimer or Propidium Iodide for Viability Assessment of Microbes. *J. Microbiol. Methods* **1993**, *17* (1), 1−16.
(29) Rotman, B.; Papermaster, B. W. Membrane Properties of Living Mammalian Cells as Studied by Enzymatic Hydrolysis of Fluorogenic Esters. *Proc. Natl. Acad. Sci. U.S.A.* **1966**, *55* (1), 134−141.
(30) Chyan, W.; Kilgore, H. R.; Gold, B.; Raines, R. T. Electronic and Steric Optimization of Fluorogenic Probes for Biomolecular Imaging. *J. Org. Chem.* **2017**, *82* (8), 4297−4304.
(31) Tsuji, T.; Kawasaki, Y.; Takeshima, S.; Sekiya, T.; Tanaka, S. A New Fluorescence Staining Assay for Visualizing Living Microorganisms in Soil. *Appl. Environ. Microbiol.* **1995**, *61* (9), 3415−3421.
(32) Woodroofe, C. C.; Lim, M. H.; Bu, W.; Lippard, S. J. Synthesis of Isomerically Pure Carboxylate- and Sulfonate-Substituted Xanthene Fluorophores. *Tetrahedron* **2005**, *61* (12), 3097−3105.
(33) Kand, D.; Liu, P.; Navarro, M. X.; Fischer, L. J.; Rousso-Noori, L.; Friedmann-Morvinski, D.; Winter, A. H.; Miller, E. W.; Weinstain, R. Water-Soluble BODIPY Photocages with Tunable Cellular Localization. *J. Am. Chem. Soc.* **2020**, *142* (11), 4970−4974.
(34) Ye, R.; Ren, C.; Shen, J.; Li, N.; Chen, F.; Roy, A.; Zeng, H. Molecular Ion Fishers as Highly Active and Exceptionally Selective K^+ Transporters. *J. Am. Chem. Soc.* **2019**, *141* (25), 9788−9792.
(35) Li, X.; Taylor, J. S. General Strategy for the Preparation of Membrane Permeable Fluorogenic Peptide Ester Conjugates for in Vivo Studies of Ester Prodrug Stability. *Bioorg. Med. Chem.* **2004**, *12* (3), 545−552.
(36) Krafft, G. A.; Sutton, W. R.; Cummings, R. T. Photoactivable Fluorophores. 3. Synthesis and Photoactivation of Fluorogenic Difunctionalized Fluoresceins. *J. Am. Chem. Soc.* **1988**, *110* (1), 301−303.
(37) Liu, C.; Pan, J.; Li, S.; Zhao, Y.; Wu, L. Y.; Berkman, C. E.; Whorton, A. R.; Xian, M. Capture and Visualization of Hydrogen Sulfide by a Fluorescent Probe. *Angew. Chem., Int. Ed.* **2011**, *50* (44), 10327−10329.
(38) Lomize, A. L.; Pogozheva, I. D. Physics-Based Method for Modeling Passive Membrane Permeability and Translocation Pathways of Bioactive Molecules. *J. Chem. Inf. Model.* **2019**, *59* (7), 3198−3213.
(39) Lomize, A. L.; Hage, J. M.; Schnitzer, K.; Golobokov, K.; LaFaive, M. B.; Forsyth, A. C.; Pogozheva, I. D. PerMM: A Web Tool and Database for Analysis of Passive Membrane Permeability and Translocation Pathways of Bioactive Molecules. *J. Chem. Inf. Model.* **2019**, *59* (7), 3094−3099.
(40) Köster, S.; van Pee, K.; Hudel, M.; Leustik, M.; Rhinow, D.; Kühlbrandt, W.; Chakraborty, T.; Yildiz, Ö. Crystal Structure of Listeriolysin O Reveals Molecular Details of Oligomerization and Pore Formation. *Nat. Commun.* **2014**, *5* (1), No. 3690.
(41) Murakami, M.; Kano, F.; Murata, M. LLO-Mediated Cell Resealing System for Analyzing Intracellular Activity of Membrane-Impermeable Biopharmaceuticals of Mid-Sized Molecular Weight. *Sci. Rep.* **2018**, *8* (1), No. 1946.
(42) Repp, H.; Pamukçi, Z.; Koschinski, A.; Domann, E.; Darji, A.; Birringer, J.; Brockmeier, D.; Chakraborty, T.; Dreyer, F. Listeriolysin of Listeria Monocytogenes Forms Ca2+-Permeable Pores Leading to Intracellular Ca2+ Oscillations. *Cell. Microbiol.* **2002**, *4* (8), 483−491.
(43) Ohl, K.; Tenbrock, K.; Kipp, M. Oxidative Stress in Multiple Sclerosis: Central and Peripheral Mode of Action. *Exp. Neurol.* **2016**, *277*, 58−67.
(44) Greene, L. A.; Tischler, A. S. Establishment of a Noradrenergic Clonal Line of Rat Adrenal Pheochromocytoma Cells Which Respond to Nerve Growth Factor. *Proc. Natl. Acad. Sci. U.S.A.* **1976**, *73* (7), 2424−2428.
(45) Miki, M.; Tamai, H.; Mino, M.; Yamamoto, Y.; Niki, E. Free-Radical Chain Oxidation of Rat Red Blood Cells by Molecular Oxygen

https://doi.org/10.1021/jacs.3c07662
J. Am. Chem. Soc. 2024, 146, 11072−11082

and Its Inhibition by α-Tocopherol. *Arch. Biochem. Biophys.* **1987**, *258* (2), 373−380.
(46) Felber, J. G.; Zeisel, L.; Poczka, L.; Scholzen, K.; Busker, S.; Maier, M. S.; Theisen, U.; Brandstädter, C.; Becker, K.; Arnér, E. S. J.; Thorn-Seshold, J.; Thorn-Seshold, O. Selective, Modular Probes for Thioredoxins Enabled by Rational Tuning of a Unique Disulfide Structure Motif. *J. Am. Chem. Soc.* **2021**, *143* (23), 8791−8803.
(47) Hwang, C.; Sinskey, A. J.; Lodish, H. F. Oxidized Redox State of Glutathione in the Endoplasmic Reticulum. *Science* **1992**, *257* (5076), 1496−1502.
(48) Chyan, W.; Kilgore, H. R.; Raines, R. T. Cytosolic Uptake of Large Monofunctionalized Dextrans. *Bioconjugate Chem.* **2018**, *29* (6), 1942−1949.
(49) Dixon, S. J.; Lemberg, K. M.; Lamprecht, M. R.; Skouta, R.; Zaitsev, E. M.; Gleason, C. E.; Patel, D. N.; Bauer, A. J.; Cantley, A. M.; Yang, W. S.; Morrison, B.; Stockwell, B. R. Ferroptosis: An Iron-Dependent Form of Nonapoptotic Cell Death. *Cell* **2012**, *149* (5), 1060−1072.
(50) Conrad, M.; Pratt, D. A. The Chemical Basis of Ferroptosis. *Nat. Chem. Biol.* **2019**, *15* (12), 1137−1147.
(51) Mannes, A. M.; Seiler, A.; Bosello, V.; Maiorino, M.; Conrad, M. Cysteine Mutant of Mammalian GPx4 Rescues Cell Death Induced by Disruption of the Wild-Type Selenoenzyme. *FASEB J.* **2011**, *25* (7), 2135−2144.
(52) Takashi, Y.; Tomita, K.; Kuwahara, Y.; Roudkenar, M. H.; Roushandeh, A. M.; Igarashi, K.; Nagasawa, T.; Nishitani, Y.; Sato, T. Mitochondrial Dysfunction Promotes Aquaporin Expression That Controls Hydrogen Peroxide Permeability and Ferroptosis. *Free Radical Biol. Med.* **2020**, *161*, 60−70.
(53) Macdonald, M.; Murray, I.; Axelsen, P. Mass Spectrometric Analysis Demonstrates That BODIPY 581/591 C11 Overestimates and Inhibits Oxidative Lipid Damage. *Free Radical Biol. Med.* **2007**, *42* (9), 1392−1397.
(54) Jafari, M.; Schumacher, A.-M.; Snaidero, N.; Ullrich Gavilanes, E. M.; Neziraj, T.; Kocsis-Jutka, V.; Engels, D.; Jürgens, T.; Wagner, I.; Weidinger, J. D. F.; Schmidt, S. S.; Beltrán, E.; Hagan, N.; Woodworth, L.; Ofengeim, D.; Gans, J.; Wolf, F.; Kreutzfeldt, M.; Portugues, R.; Merkler, D.; Misgeld, T.; Kerschensteiner, M. Phagocyte-Mediated Synapse Removal in Cortical Neuroinflammation Is Promoted by Local Calcium Accumulation. *Nat. Neurosci.* **2021**, *24* (3), 355−367.
(55) Turpin, C.; Catan, A.; Guerin-Dubourg, A.; Debussche, X.; Bravo, S. B.; Álvarez, E.; Elsen, J. V. D.; Meilhac, O.; Rondeau, P.; Bourdon, E. Enhanced Oxidative Stress and Damage in Glycated Erythrocytes. *PLoS One* **2020**, *15* (7), No. e0235335.
(56) Lawrence, P. A.; Bodmer, R.; Vincent, J.-P. Segmental Patterning of Heart Precursors in Drosophila. *Development* **1995**, *121* (12), 4303−4308.
(57) Raymond, M. H.; Davidson, A. J.; Shen, Y.; Tudor, D. R.; Lucas, C. D.; Morioka, S.; Perry, J. S. A.; Krapivkina, J.; Perrais, D.; Schumacher, L. J.; Campbell, R. E.; Wood, W.; Ravichandran, K. S. Live Cell Tracking of Macrophage Efferocytosis during Drosophila Embryo Development in Vivo. *Science* **2022**, *375* (6585), 1182−1187.
(58) Millard, T. H.; Martin, P. Dynamic Analysis of Filopodial Interactions during the Zippering Phase of Drosophila Dorsal Closure. *Development* **2008**, *135* (4), 621−626.
(59) Ito, H.; Kawamata, Y.; Kamiya, M.; Tsuda-Sakurai, K.; Tanaka, S.; Ueno, T.; Komatsu, T.; Hanaoka, K.; Okabe, S.; Miura, M.; Urano, Y. Red-Shifted Fluorogenic Substrate for Detection of lacZ-Positive Cells in Living Tissue with Single-Cell Resolution. *Angew. Chem., Int. Ed.* **2018**, *57* (48), 15702−15706.
(60) Grimm, J. B.; Brown, T. A.; Tkachuk, A. N.; Lavis, L. D. General Synthetic Method for Si-Fluoresceins and Si-Rhodamines. *ACS Cent. Sci.* **2017**, *3* (9), 975−985.
(61) Zeisel, L.; Felber, J. G.; Scholzen, K. C.; Schmitt, C.; Wiegand, A.; Komissarov, L.; Arnér, E. S. J.; Thorn-Seshold, O. Piperazine-Fused Cyclic Disulfides Unlock High-Performance Bioreductive Probes of Thioredoxins and Bifunctional Reagents for Thiol Redox Biology. *J. Am. Chem. Soc.* **2024**, *146* (8), 5204−5214.
(62) Coelho, F.; Saidjalolov, S.; Moreau, D.; Thorn-Seshold, O.; Matile, S. Inhibition of Cell Motility by Cell-Penetrating Dynamic Covalent Cascade Exchangers: Integrins Participate in Thiol-Mediated Uptake. *JACS Au* **2023**, *3* (4), 1010−1016.

https://doi.org/10.1021/jacs.3c07662
J. Am. Chem. Soc. 2024, 146, 11072−11082

6 Paper 2: A general probe motif for sensitive, signal-retained imaging

In this work, we developed a general and modular scaffold for cell-retained fluorogenic probes that enable sensitive imaging of biochemical activities in living cells. Fluorogenic probes are invaluable tools for studying such activities in disease contexts or for fluorescence assisted surgery. Many established probes reliably quantify enzymatic activity in cell-free assays; but when used instead in cells, their fluorescent products often diffuse out or are actively exported. This leads to progressive signal loss, poor cell-by-cell resolution, and reduced sensitivity as the rate of signal loss sets a lower limit for the enzyme activity that can even be detected, rendering low-turnover processes effectively invisible. Existing strategies to retain fluorescent products, such as charge-based impermeabilisation, intracellular precipitation, or alkylation-based covalent trapping, each suffer from major drawbacks, including insufficient retention, lack of design modularity, cytotoxicity, or interference with the biological process under investigation. We therefore set out to develop a modular probe scaffold that overcomes these limitations.

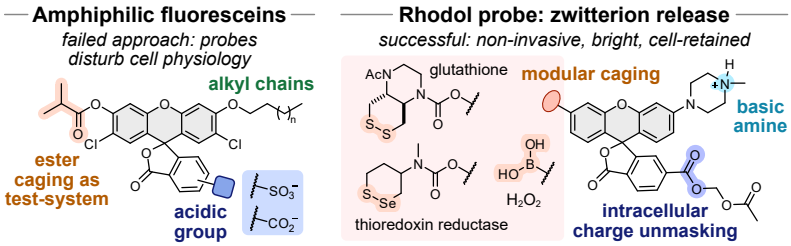

Our design was guided by four key criteria: (1) aqueous solubility for reproducible handling and bioavailability, (2) efficient cell entry by passive diffusion, (3) complete suppression of background fluorescence prior to activation, and (4) robust post-activation retention of a soluble, cytosolic fluorophore.

Building on observations from our work on membrane-damage probes, where mono-sulfonated fluorescens showed uptake into healthy cells, we initially explored amphiphilic sulfo- and carboxyfluoresceins as potential scaffolds. Literature reports suggested that medium-length lipid substituents could enhance both cellular uptake and intracellular retention of small molecules. Based on this, we designed a series of ester-caged, *O*-alkylated fluorescein probes with systematically varied alkyl chain lengths (from C4−C10). Testing these probes in cells revealed a clear relationship between alkyl chain length, signal intensity and subcellular distribution. Long *n*-decyl probes produced only weak membrane-localised fluorescence, whereas the *n*-butyl probe generated a moderate and homogeneously distributed intracellular signal that was retained for hours. Replacing the permanently charged sulfonate with a reversibly deprotonated carboxylate further enhanced cellular uptake, resulting in ca. 20-fold higher fluorescence intensity while maintaining cytosolic signal retention.

However, further investigation revealed a fundamental flaw in the amphiphilic design. In salt buffers (used to prevent hydrolysis of the ester test probes), strong intracellular fluorescence coincided with signs of cellular distress (manifested as rounding and blebbing) which we initially attributed to the simplified medium. When we instead tested the cognate but hydrolytically stable carbamate-caged probes in complete cell culture media (like DMEM), cells remained healthy but showed no intracellular signal. We concluded that the apparent uptake in PBS resulted from probe-induced membrane disruption under nutrient-poor conditions rather than genuine permeability. Thus, amphiphilic, lipidated probes were deemed unsuitable for non-invasive probe design and were abandoned.

We then initiated a new probe scaffold design cycle that avoids anionic groups (to permit cell entry) and amphiphilic membrane disruption, while ensuring aqueous solubility with a reversibly protonatable amine. We replaced the fluorescein core with a rhodol motif to additionally improve photostability, brightness, and pH-independence, and systematically varied its functionalities by combining (1) either an apolar piperidine or a basic piperazine as *N*-substituent, and (2) optionally, a carboxylate or an acetoxymethyl masked carboxylate (which intracellularly releases a carboxylate). As observed for the fluorescein analogues, negatively charged carboxylates were membrane impermeable and produced no cellular signal, while amine-only probes entered cells but failed to retain their fluorescence after activation. Only the bis-functionalised rhodol, featuring both a basic amine and a masked carboxylate, achieved stable intracellular retention across multiple cell lines which validated the utility of zwitterionic fluorophores for

cytosolic signal retention. This resulting scaffold, termed **TraG** (Trappable Green), achieves intracellular retention by simultaneously preventing cell excretion from passive diffusion and active transporters.

To demonstrate the modularity of the TraG scaffold, we adapted it to two representative activation systems: an analyte probe for hydrogen peroxide, and an enzyme activity probe for thioredoxin reductase (TrxR). Both probes produced bright, cytosolically distributed, and retained fluorescence after activation. In particular, the TrxR probe outperforms the established RX1 probe (which relies on fluorophore precipitation), by avoiding cytotoxicity and improving sensitivity. Unlike RX1, which requires a threshold concentration for precipitation-based detection, the TraG probe enabled linear signal generation from TrxR activity at much lower probe concentrations.

In summary, the TraG scaffold establishes a versatile and non-invasive platform for fluorogenic bioactivity imaging with robust intracellular signal retention. It combines low background fluorescence, aqueous solubility, rapid cell uptake, and sustained intracellular retention with flexible chemical modularity, allowing immediate adaptation to a wide range of activation substrates. The durable and non-toxic staining not only enhances the probe sensitivity but also enables new applications for imaging, tracking and selecting cells with high enzymatic activity for downstream analyses (e.g. by flow cytometry cell sorting).

Personal contributions

I independently co-designed target compounds (lipidated fluoresceins, acetoxymethyl masked rhodols) and performed synthesis and structural characterisation [all precursors, probes and fluorophores], UV-vis and fluorescence spectroscopy [Fig 3b, Figs S20−22, Table S1], cell-free assays (probe hydrolysis in different cell culture media [Figs S23−24], esterase activation [Fig S25], glutathione activation[Fig S26], hydrogen peroxide activation [Figs S27−28]) and cell biology (early epifluorescence microscopy for the lipidated sulfo- and carboxy-fluoresceins, image analysis [Figs S4cd, S5c−e, S6bc+e, S9, S10]). I contributed to the design of all experiments and advised colleagues and collaborators for cell biology applications; I coordinated data assembly, prepared all figures, and co-wrote the manuscript.

Main contributions from other authors: L.D.-W. performed cell biology, confocal and epifluorescence microscopy [Figs 2e, 4c] and cell-free probe characterisation [Fig 4b]; C.Z. performed cell biology and cell retention plate reader assays [Fig 2cd]; D.B. performed cell biology, confocal microscopy and image quantification for the hydrogen peroxide sensor (HEK cells and macrophages) [Figs 3c−g]; N.A.V. performed cell biology and confocal microscopy with lipidated fluoresceins; J.I.B. supported with rhodol probe synthesis; O.T.-S. co-designed target compounds and co-wrote the manuscript.

Chemical Science

ROYAL SOCIETY OF CHEMISTRY

EDGE ARTICLE

View Article Online
View Journal | View Issue

Cite this: *Chem. Sci.*, 2025, **16**, 22630

All publication charges for this article have been paid for by the Royal Society of Chemistry

A modular scaffold for cellularly-retained fluorogenic probes for sensitive cell-resolved bioactivity imaging

Philipp Mauker,[ab] Lucas Dessen-Weissenhorn,[b] Carmen Zecha,[b] Nynke A. Vepřek,[b] Julia I. Brandmeier,[b] Daniela Beckmann,[cd] Annabel Kitowski,[b] Tobias Kernmayr,[b] Julia Thorn-Seshold,[ae] Martin Kerschensteiner[cdf] and Oliver Thorn-Seshold *[a]

Here, we develop a general design for high-quality fluorogenic activity probes to quantify biochemical processes within live cells, *via* the release of a fully cell-retained, bright fluorescent soluble product upon reaction. Live cell probes must be membrane-permeable to access intracellular biochemistry, but often that means their fluorophore products are similarly permeable resulting in rapid signal loss from the activating cell, which limits their cell-by-cell resolution as well as their sensitivity for quantifying low-turnover processes. Current strategies to retain fluorescent products within cells usually disrupt native biology *e.g.* by non-specific alkylation or solid precipitation. Here, scanning charge- and polarity-based approaches to swap from permeable to cell-retained states, we developed a bright fluorogenic rhodol-based platform, Trappable Green (**TraG**), balancing all key requirements for signal integration (rapid probe entry, but effective product retention, across many cell lines) and being modular so it can be adapted to quantify many biochemical target types (examples shown here include probes for GSH, TrxR, and H_2O_2). The simple and rugged **TraG** scaffold can now permit straightforward implementation in a range of cell-retained enzyme activity probes, which will enable more accurate cell-resolved imaging as well as higher-sensitivity integration of low-turnover processes, without the drawbacks of alkylation or precipitation-based strategies.

Received 18th July 2025
Accepted 13th October 2025

DOI: 10.1039/d5sc05388a

rsc.li/chemical-science

Introduction

Imaging and quantifying biological activity are key challenges in basic and applied research. Focusing on enzyme activity rather than mRNA or protein levels takes post-translational regulation mechanisms into account (PTMs, compartmentalisation, chaperoning), and allows researchers to correctly interpret biochemistry in action. Fluorogenic probes are, ideally, non-fluorescent probes that only generate a fluorescent product after activation by their specific biochemical target or enzyme. They have become crucial tools for sensitive and non-invasive bioactivity imaging, especially in lysates: with probes for peptidases, esterases, phosphatases, glycosidases, and oxidoreductases,[1–7] or reactive analytes such as hydrogen peroxide and hydrogen sulfide,[8,9] in widespread use.

Sensitive, cell-resolved detection is crucial for longitudinally visualising bioactivity during assay time courses, and for understanding the heterogeneity of cell populations. However, fluorogenic probes often encounter a major problem in live cells and tissues: the signal of their fluorescent products becomes diffuse or is lost over time. Apolar, membrane-permeable fluorophores such as coumarins can rapidly exit the cell across the plasma membrane by passive diffusion,[10] while negatively charged fluorophores such as fluoresceins are instead excreted from cells by active transport.[11,12] This post-activation signal loss sabotages cell-resolved activity imaging, and lowers the sensitivity and reliability of signal quantification (higher and time-dependent background signal). Moreover, the *rate* of signal loss sets a lower limit on the enzyme activity or analyte concentration that can be detected. For *in vivo* work, where probe dosage must be low, or for imaging low-turnover processes, or for situations demanding high sensitivity and quantitative reliability, building up and retaining the product signal inside the activating cell in the long term is a crucial challenge for probe design.

[a]*Faculty of Chemistry and Food Chemistry, Dresden University of Technology, Dresden 01069, Germany. E-mail: oliver.thorn-seshold@tu-dresden.de*
[b]*Department of Pharmacy, LMU Munich, Munich 81377, Germany*
[c]*Institute of Clinical Neuroimmunology, LMU University Hospital, LMU Munich, Munich 81377, Germany*
[d]*Biomedical Center (BMC), Faculty of Medicine, LMU Munich, Martinsried 82152, Germany*
[e]*Faculty of Medicine, University Hospital Dresden, Dresden University of Technology, Dresden 01307, Germany*
[f]*Munich Cluster for Systems Neurology (SyNergy), Munich 81377, Germany*

View Article Online
Edge Article Chemical Science

The importance of retaining the fluorescence signal within cells has driven three probe designs for signal trapping (full discussion in Fig. S3). (1) Charge/polarity-based product impermeabilization usually suppresses passive membrane transit with ionic motifs, *e.g.* carboxylates,[13] phosphonates,[14] sulfonates,[15] or tetraalkylammoniums.[16,17] To deliver probes into the cell in the first place, intracellularly-cleaved lipophilic masking groups[13–15,18] (*e.g.* carboxylates masked as acetoxymethyl esters,[9,13,19,20] or amines as carbamates[21]), endocytosis (*e.g.* by cell-penetrating peptides),[22] or transporter-mediated uptake[16] are often used. None of these approaches has been developed to a state of general applicability; however, typical issues include activation triggers that are not modular; product fluorophore dimness; slow cellular uptake; release of reactive side products; and/or unwanted compartmentalisation. (2) Water-insoluble solid-state fluorophores can be released as reaction products that precipitate as fluorescent cellularly-trapped crystals (*e.g.* the ELF-97 probe, releasing an HPQ fluorophore).[23–25] Yet, crystal deposits cause inflammatory responses and are cytotoxic,[26] perturbing biology or preventing longitudinal imaging; moreover, these probes are insensitive at low turnover since the precipitation threshold must be crossed before any signal is seen; also, these probes are rarely well-soluble (mirroring the product insolubility). (3) Products that alkylate cell-impermeable biomolecules can be released: a cell retention strategy pioneered by Urano with *e.g.* SPiDER probes (non-reactive benzylfluoride probes are enzymatically triggered to give electrophilic quinone methide products that rapidly react with proteins or GSH, enabling long-term signal retention).[6,27–30] However, they can also alkylate their target enzyme,[30] induce electrophile stress responses, or accumulate toxic effects,[28] especially in high-turnover cells.

There are many requirements that must be balanced to deliver a good probe for high-sensitivity enzyme imaging in live cells. Fig. 1 shows the major needs, *e.g.* (a) good aqueous solubility of the probe, for reproducible handling, high bioavailability, and to avoid aggregation or sequestration; (b) probe robustness, *i.e.* no occurrence of non-specific (background) product release; (c) reliably effective cell entry across cell lines (*e.g.* by passive diffusion); (d) linear fluorescence signal (*e.g.* targets activate fluorescence by just one reaction site per probe molecule); (e) high signal turn-on ratio: the probe is very dark under typical imaging conditions, and the released product is very bright; (f) effective cell retention of the product, allowing long-term signal integration; (g) the fluorophore and probe byproducts must not risk perturbing biology in the long term (unlike precipitating or alkylating probes). Ideally, the probe design would also be modular, *i.e.* easily chemically adaptable to image enzymes with various reactivity classes. Considering that none of the prior strategies meets all eight of these requirements (discussion in Fig. S3), we set out to develop a probe design that does. We chose *O*-unmasking of a phenolic fluorophore for activation, a reaction that is applicable for many types of molecular imaging. We now outline the development of a generalised probe design for high-sensitivity enzyme imaging with a cell-retained product that meets all these requirements.

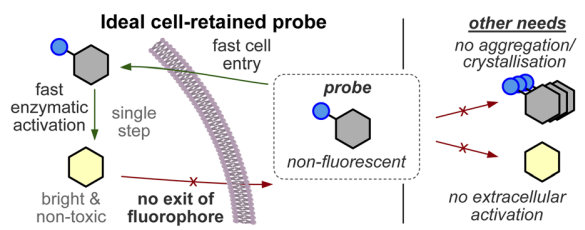

Fig. 1 Desirable features for a sensitive, quantitative, cell-retained fluorogenic probe.

Results and discussion

Design strategy

Facing an eight-factor optimization problem, the challenge was to identify key needs for each factor, choose "good enough" solutions for each (where these already exist) that do not push the other factors out of scope, and focus on the balance of properties that is needed for successful performance overall. For example, ensuring both aqueous solubility and membrane permeability requires a probe with balanced polarity, and sparing use of polar groups *e.g.* carboxylates or amines. The choice of fluorophore influences the efficiency of fluorescence suppression in its masked probe form (*e.g.* up to 100% suppression for spirocyclised xanthenes), the signal activation linearity (*e.g.* 1 or 2 activating reaction sites), and the brightness of the released fluorophore (functionalisation). We prioritised combining known and new strategies to reach a modularly applicable platform that delivers a well-performing probe independent of the chosen biochemical target, and selected the permeable-probe-to-retained-product transition as the key chemical challenge that might need chemical tuning.

Design 1: lipidated charged fluoresceins (Fig. S4–S7)

We first focused on using synthetically accessible *O*-masked fluorogenic probe designs to test which physicochemical features would ensure good cell entry and cell retention and left the other requirements for later. Fluorescein spirolactone *O*-alkylated *O*′-esters are a convenient fluorogenic test system with only one reaction site,[31] and we had previously noted that some monosulfonated fluorescein diesters were surprisingly capable of cell entry despite their charge.[32] We now took these known systems and measured their cell retention after washing, under standard conditions, which was promising for the diester (**i_2-FS**, which has two activation sites which is undesired due to non-linear signal response upon de-acylations (only 10% signal upon the first ester cleavage); Fig. S4) though poor for the monoester (**iPS-F**, one activation site, desirable linear response). Following the notion that medium-length lipids enhance the cell uptake and retention of natural products,[33] we next synthesised a set of more lipid-like *O*-alkylated sulfonated fluorescein monoester probes (**iC4-FS–iC10-FS**, for C4–C10 alkyl; for all structures, see Fig. S1). All lipidated designs gave good product retention after washing (Fig. S5bd), but the absolute cellular signal was low, which we attributed to poor cellular

View Article Online
Chemical Science Edge Article

uptake due to the sulfonate (Fig. S5c; their signal distribution also varied from uniform **C4-FS** to membrane-only **C10-FS**; Fig. S5e). Deleting the sulfonate to raise permeability was a failure (**iC4-F**: no signal seen in cells (Fig. S6e) or in cell-free esterase assays (Fig. S25)), illustrating the importance of solubility for bioavailability. Using a reversibly ionisable carboxylate in **iC4-FC** ($pK_a \approx 4.3$) instead of the sulfonate gave 20-fold higher cellular signal intensity than **iC4-FS**, yet kept its good post-wash retention and uniform signal distribution (Fig. S6). However, we had noted significant cellular distress (rounding and blebbing) with all FS- and FC-ester probes so far. To allow testing the probes in more complete cell media (DMEM with FCS instead of HBSS), we switched the trigger group from an *O*-isobutyrate ester to a hydrolytically robust, reductively cleavable *O*-carbamate (**GL-C4-FC**; Fig. S24 and S26). We then found that the pairing of a strong signal with cell blebbing had been caused by the combination of the lipidated FS/FC probes with the salt buffer solution that had been needed to avoid isobutyrate ester hydrolysis. In more complete buffer (DMEM), cell morphology stayed healthy, and no signal was seen (Fig. S6f and S7). We imagine that the membrane stress of the amphipathic FS/FC probes, plus the lack of nutrients in salt buffer, disrupted membranes enough for the charged probes to enter cells[34] (details in Fig. S6), indicating that amphipathic probes are unsuitable for non-invasive cell imaging.

Design 2: charge-balanced rhodol probes (Fig. 2a)

From our experience with the **FS/FC** lipidated fluorescein probes, we concluded that amphipathic anionic designs are unsuited for good cell entry and retention. We also prioritised probe solubility, and hydrolytically stable *O*-carbamate probes that could be studied in complete cell culture media. We thus switched to rhodol scaffolds, since rhodols can be *O*-acylated to give nonfluorescent (fully spirolactone) probes, but can be much brighter than *O*′-alkyl fluoresceins (limit: $\sim 7 \times 10^3$ L mol^{-1} cm^{-1}, Table S1), and their fluorescence is more photostable and is constant over the pH range 4–10.[35] We then synthesised a set of six reductively-activated[36] "GL-Rho" probes: with (1) either an apolar piperidine (**Rho**) or a basic piperazine (**Rho-A**) as an *N*-substituent; and (2) optionally, a 6-carboxylate (**C**) or its masked, membrane-permeable acetoxymethyl (AM) ester (**C^m**) (Fig. 2a). The rhodol fluorophores were accessed from the fluorescein ditriflates by one-sided Buchwald–Hartwig coupling, followed by triflate hydrolysis with LiOH or TBAF. These were transformed into fluorogenic probes by a one-pot sequence, converting their phenolic –OH to

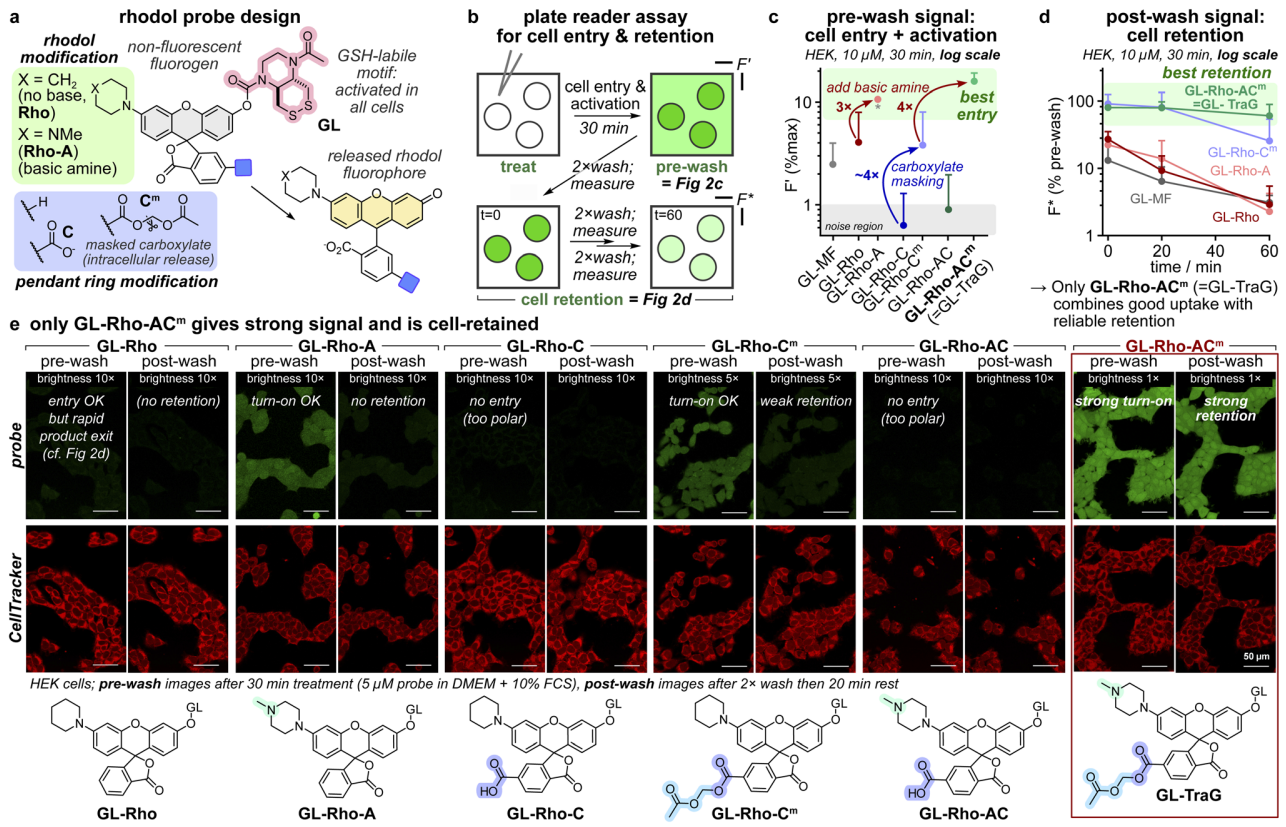

Fig. 2 The rhodol probe design Rho-AC^m (=Trappable Green: TraG) delivers strong intracellular signal activation and retention. (a) Probe panel overview. (b) Plate reader assay for cell entry, activation, and retention. (c) Entry and activation in HEK293T cells (10 μM probe, DMEM with 10% FCS, 30 min treatment; *F*′ is fluorescence as a % of full activation of the whole well; error bars: SD; biological replicates normalised to **GL-Rho-A** (marked with an asterisk); $n = 3$; error bars: SD; the methyl fluorescein probe **GL-MF** (ref. 36) is a non-rhodol benchmark for entry and retention, see Fig. S1). (d) Cell retention (conditions as in c; *F** is fluorescence as a % of pre-wash value; error bars = SD). (e) Cell turn-on and retention assayed by confocal microscopy (conditions as in c except with a 5 μM probe; scale bars: 50 μm; full data in Fig. S9a).

View Article Online
Edge Article Chemical Science

a pentafluorophenyl carbonate, then acylating the GSH-labile **GL** disulfide motif (later deprotecting and optionally masking the 6-carboxylates).

The optical properties of the rhodol products varied somewhat, with excitation maxima at 490–530 nm, Stokes shifts of ~25 nm (emission maxima at 515–560 nm), and extinction coefficients of 3–6 × 10^4 L mol^{-1} cm^{-1}. Fluorescence quantum yields varied from 4–64%, with piperazinyl products **H-Rho-A** and **H-Rho-AC** being the brightest, as expected[37] (~3 × 10^4 L mol^{-1} cm^{-1}; Fig. S21 and Table S1). Importantly for high sensitivity, all probes were non-fluorescent, with outstanding probe/product signal turn-on ratios of up to ~550 (Fig. S21); the piperazinyl probes were particularly efficiently activated by their target GSH (Fig. S26); and the carbamates of all probes were hydrolytically stable for hours in FCS-supplemented DMEM, for long term cell experimentation (Fig. S24).

Probe selection: disulfide reduction sensing (Fig. 2b–e)

We then tested cell entry, activation, and signal retention in HEK cells (Fig. 2b). Cell entry and activation was moderate for piperidinyl **GL-Rho**, but 3× higher for the basic piperazinyl (**GL-Rho-A**; Fig. 2c). Adding a carboxylate blocked cellular uptake (**GL-Rho-C**/**GL-Rho-AC**); masking it as an acetoxymethyl ester (**GL-Rho-C^m**/**GL-Rho-AC^m**) let the probes reach the same signal as that of **GL-Rho**/**GL-Rho-A**. Importantly, probe treatment does not impair cell morphology, and uptake occurs homogeneously in healthy cells with uniform cellular distribution of the product signal (Fig. S9a and 10). We then subjected cells to three cycles of "wash, measure, and wait", to monitor intracellular signal retention. The rhodol product from **GL-Rho**/**GL-Rho-A** leaked out rapidly from cells, but an added carboxylate (**GL-Rho-C^m**/**GL-Rho-AC^m**) greatly enhanced cell retention, particularly for **GL-Rho-AC^m** where cells stayed bright despite three medium exchanges over 1 h (Fig. 2d). We used confocal microscopy to complement these plate reader assays. **GL-Rho-A**, **GL-Rho-C^m**, and **GL-Rho-AC^m** indeed show cell entry and activation, while **GL-Rho-C** and **GL-Rho-AC** do not (Fig. 2e). Only **GL-Rho-AC^m** had strong post-wash signal retention (Fig. 2e and S9ab) and gave good performance in HeLa, MEF, and A549 cell lines (Fig. S11, strong retention in HeLa cells, weaker in A549 cells).

The **Rho-AC^m** scaffold features fast cell entry and signal generation, plus good post-wash intracellular signal retention, by combining a basic amine with a masked, intracellularly-revealed carboxylate. The combination of high fluorogenicity with good cell retention allows sensitive cell-resolved imaging either without washing, or with washing (even after a significant delay). Its aqueous solubility avoids aggregation effects; the full spirocyclisation of the probe state (before reaction) plus its biochemical robustness allow zero-background imaging; and with the high brightness of the released fluorophore, its signal turn-on ratio is strong (170×). The probe rapidly enters different cell lines where its phenolic single activation site is efficiently activated and provides linear signal turn-on for reliable signal quantification to give a uniform cellular signal. Crucially, neither the probe nor the fluorophore causes apparent cellular harm (and toxic crystal formation or non-specific bioconjugation are avoided), supporting that the data acquired during longitudinal imaging or enzyme activity integration can be reliably interpreted. We thus considered that this design combines all eight desirable design features (see Introduction) within one probe scaffold. Since the **Rho-AC^m** scaffold showed the best performance, we renamed it Tra ppable G reen (**TraG**), and to test the versatility of **TraG** as a modular platform, we now evaluated two additional types of **TraG** activity probes.

Modularity test 2: hydrogen peroxide sensing (Fig. 3)

Hydrogen peroxide (H_2O_2) is a major physiological messenger with baseline levels that fuel cell signalling and metabolic function,[38] but which can also be created as an unwanted metabolic byproduct at harmful levels that have been correlated to neurodegeneration, cancer, or autoimmune disorders.[39–41] Sensitive and linearly-responsive tools are needed to resolve and study its multiple roles. The most common small molecule probes for sensing H_2O_2 exposure use arylboronic acids that H_2O_2 converts to phenols.[8] Signal integration is crucial for sensitively detecting low H_2O_2 concentrations, so cell retained probes (*e.g.* SPiDER: intracellular quinone-methide trapping) have been utilised despite their moderate cell-toxicity.[19,28,42]

We hoped that a **TraG**-based design could deliver a more biocompatible cell-retained H_2O_2 sensor (Fig. 3a), and considered that a boronate's oxidation-hydrolysis mechanism (instead of the previous carbamate cyclisation mechanism) would be a good test of the modularity of the **TraG** platform. As the common pinacol boronate diester was hydrolytically unstable during purification (as reported elsewhere[43]), we applied the probe as a free boronic acid (membrane permeable, pK_a ≈ 8–9 (ref. 44)). This **HP-TraG** probe gave linear signal generation with H_2O_2 (Fig. 3b), with up to 48-fold turn-on (Fig. S22). Loading it into HEK cells (15 min), then washing and extracellularly administering 25–100 μM H_2O_2 gave H_2O_2-dependent intracellular fluorescence signals with a high turn-on index (up to a 7-fold increase, Fig. 3c and d) that were cell-retained for >2 h after washing off the extracellular medium (Fig. 3e and f). Finally, we used **HP-TraG** for imaging endogenous H_2O_2 in Hoxb8-derived macrophages[45] after activation with phorbol 12-myristate 13-acetate (PMA).[46] The **HP-TraG** signal increases by 60% upon PMA treatment, *i.e.* sensitively detecting both the low endogenous baseline and the slightly increased H_2O_2 concentrations upon activation (1–4 μM in macrophages[47]), again with strong post-wash signal retention (Fig. 3g and S14). Thus, the **TraG** cell-retained fluorogenic design adds a useful new hydrogen peroxide sensor to the toolbox of chemical biology that gives strong performance (rapid, H_2O_2-dependent intracellular signal) while overcoming the drawbacks of cell-reactive quinone methides as trapping agents.

Modularity test 3: TrxR enzyme imaging (Fig. 4)

Mammalian thioredoxin reductase (TrxR) is a key enzyme that uses NADPH to reduce thioredoxins, which drive hundreds of redox reactions involved in metabolism, protein folding, and signaling.[48,49] TrxR is also one of just 25 selenoproteins in the human proteome; its selenium is needed so that its activity is

View Article Online
Chemical Science Edge Article

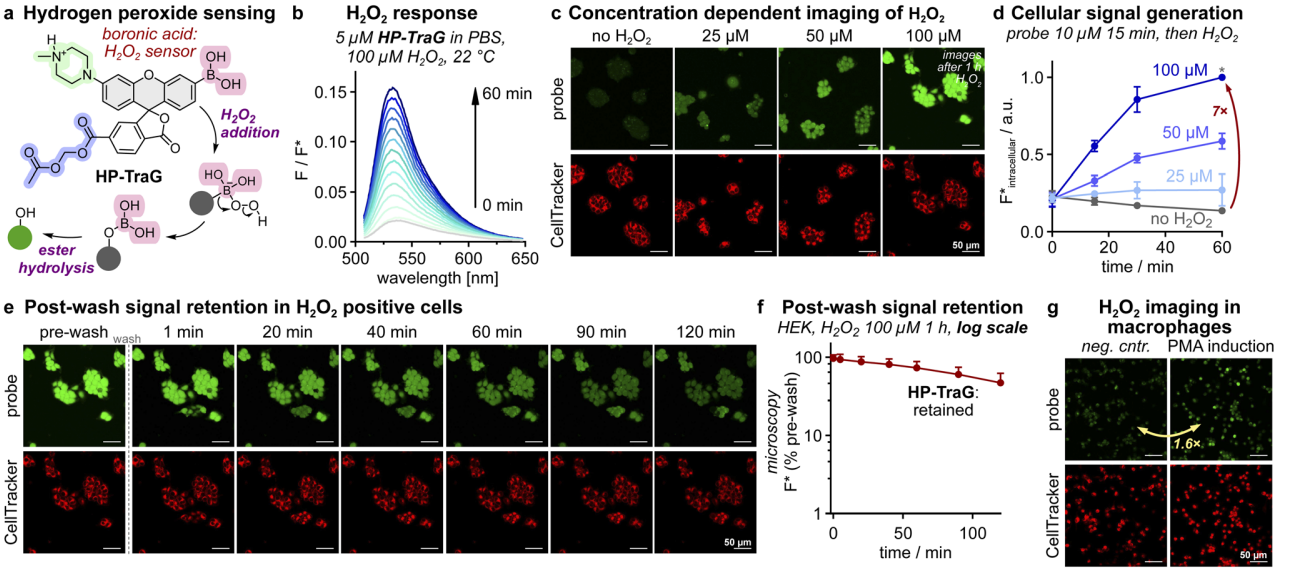

Fig. 3 H_2O_2 sensing with HP-TraG. (a) Structure and mechanism of **HP-TraG**. (b) Cell-free H_2O_2 response (5 µM in PBS, 100 µM H_2O_2 over 60 min). (c and d) [H_2O_2]-dependent activation in HEK cells (15 min **HP-TraG** loading (10 µM), washing, then 60 min H_2O_2 treatment; full images in Fig. S12; panel d: intracellular signal quantified from microscopy; *biological replicates benchmarked to the 100 µM value at 1 h; $n = 3$; error bars: SD). (e and f) Post-wash intracellular signal retention (HEK cells treated as in c and d, with 100 µM H_2O_2 for 1 h and then washed and imaged; full images in Fig. S13; $n = 3$; error bars: SD). (g) Hoxb8-derived macrophages loaded with **HP-TraG** (10 µM for 15 min) and then treated with phorbol 12-myristate 13-acetate (PMA, 1.6 µM for 1 h) and then imaged (ratio quantified from images; full images in Fig. S14) (all scale bars: 50 µm).

resilient against biochemical damage.[50] TrxR is a difficult target for molecular imaging due to its low expression level (*ca.* ≤20 nM) *vs.* high levels of chemically similar thiol off-targets (>10 µM).[51] Only activity imaging can map TrxR function, since its activity is decoupled from mRNA levels (Se incorporation is regulated post-transcriptionally), and antibodies do not distinguish non-functional or non-Se forms. The first and only TrxR-selective probe for live cell activity imaging, RX1, was published in 2022,[52] and is used for redox biology studies and high-throughput screening.[53] RX1's target specificity stems from its cyclic selenenylsulfide, a substrate that is selectively reduced by TrxR then cyclises to release its phenolic cargo HPQ (Fig. 4a). The precipitating and thus cellularly retained solid-state fluorophore HPQ was chosen for signal accumulation to overcome low TrxR levels. However, high probe dosage and long incubation times were needed to surpass the precipitation threshold (K_S), and the crystalline HPQ precipitates that generate signal also stimulate inflammatory responses and are toxic to cells. A soluble cell-retained fluorophore product could solve both drawbacks, giving a more biocompatible probe (lower dosage that is less cellularly damaging but still a quantifiable signal) that is also faster to quantify (since K_S need no longer be overcome). Thus, we patched RX1's selenenylsulfide onto our rhodol scaffold, hoping the resulting probe **TR-TraG** would keep TrxR selectivity while accessing the advantages of cell-retained soluble fluorophores.

In cell-free experiments, **TR-TraG** was activated by even 20 nM TrxR1 (vicinal selenolthiol); cell-free selectivity was decent over vicinal dithiols (resisting thioredoxin 1 up to 300 nM, though resistance to glutaredoxin 1 was lower), and outstanding over monothiol GSH (1000 mol eq. of GSH reach only ~15% activation after 4 h, *i.e.* the level reached by 0.002 mol eq. of TrxR after 0.5 h; Fig. S15). Pleasingly, in cellular assays, the **TR-TraG** signal mainly depended on TrxR activity: inhibition with electrophile TRi-1 (ref. 54) (HeLa and A549 cells, Fig. S16) or genetic knockout (in MEF cells,[55] Fig. S17) largely controlled its signal. Thus, the selenenylsulfide substrate does set the probe's target-selectivity. We next examined some systematic benefits of the soluble cell-retained design.

A major technical drawback of precipitating fluorophores is their non-linear fluorescence response. In each cell, the released fluorophore concentration has to surpass K_S (HPQ: ~2 µM) before the true signal starts to be observable, whereas soluble fluorophores are theoretically detectable with linear activation response from the first molecule released. Plate reader assays with precipitating fluorophores also suffer from inter-cell variability since turnover must reach *ca.* $2K_S$ in the majority of cells before the overall signal becomes linear, again, an issue that does not affect soluble probes. Finally, probe quenching in precipitation-based systems is often incomplete: even quenching one fluorescence channel (*e.g.* HPQ: ESIPT quenching by *O*-masking) does not suppress all channels (weak long-wavelength tail of normal emission, Fig. S18b, 45 min), whereas xanthene spirocyclisation quenching can be complete. All these advantages were evident when comparing **TR-TraG** and RX1 in cellular assays. **TR-TraG** builds up signal linearly from time zero, proportional to its dosage, reaching a usefully quantifiable signal even at ≤1 h at 3 µM (Fig. 4b); while the RX1 signal starts only at >3 h at 100 µM, with no true signal at lower times or doses. Such high RX1 exposure is incompatible with assays in tissues due to limited, variable biodistribution, a limitation that **TR-TraG** escapes. The rhodol's reproducible

View Article Online
Edge Article Chemical Science

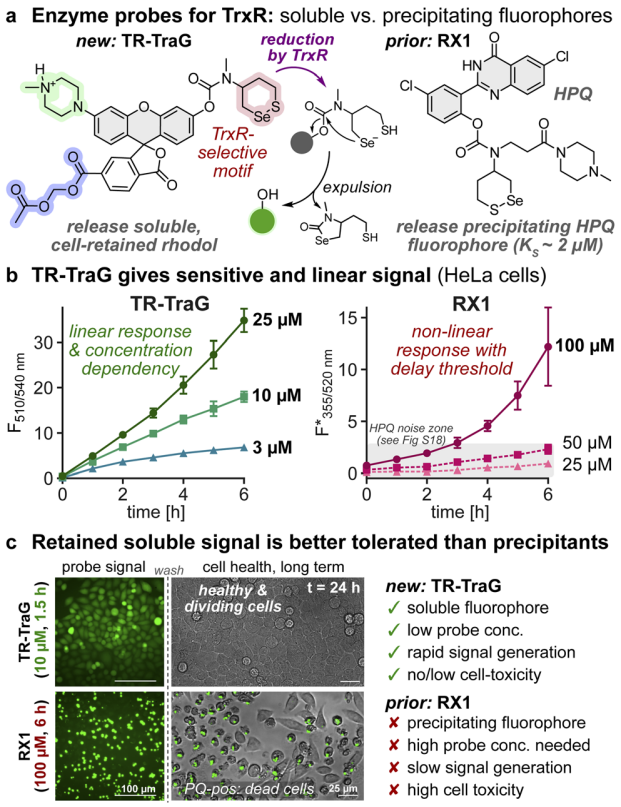

Fig. 4 The TraG probe design can be modularly equipped with enzyme activation motifs to address different targets. (a) The TrxR1 probe **TR-TraG** (releases soluble **H-TraG**) compared to known probe **RX1** (precipitating fluorophore). (b) Cellular concentration-dependent fluorescence generation of **RX1** and **TR-TraG** in HeLa cells ($n = 3$; error bars: SD). (c) Microscopy of HeLa cells treated with **TR-TraG** (10 µM) or **RX1** (100 µM) for 6 h, then washed, and kept for 24 h to assess cell viability; PQ precipitates correlate to dead cell morphology (full data in Fig. S18 and S19).

signal (Fig. S16) also contrasts to the highly variable signal of RX1[52] which results from its sensitivity to precipitation effects.

A major biological problem with precipitating fluorophores is that they cause cellular stress and cytotoxicity, which limit or prevent long-term experiments and *in vivo* assays.[26] Typical ways to run high-powered assays, *e.g.* first imaging and sorting by FACS to stratify cell populations, then further cultivation or parameter testing, are thus impossible. The rhodol **TR-TraG** instead allowed high-quality cell-resolved imaging at order(s) of magnitude lower probe exposure (10 µM, 90 min) than RX1 (100 µM, 6 h; see Fig. S18), which should already result in far lower biological stress from the probe. Yet, we attribute the major difference to product exposure. Cells treated with **TR-TraG** were healthy and continued dividing to confluency over 24 h (as did untreated controls), whereas RX1-treated cells that formed PQ crystals were essentially dead (with no escape even after probe removal and culture for 24 h in fresh media; Fig. 4c, S18 and 19). Thus, **TraG** type probes will likely enable long-term cell tracking by bioactivity, *e.g.* using FACS to resolve and study cell subpopulations: which at least in the context of TrxR probes is a novel and urgently needed advancement.

Conclusions

We designed a novel, modularly applicable fluorogenic probe scaffold for flexible use in sensitive biochemical activity imaging at low probe doses, which results in the linear generation of a biocompatible, cell-retained, bright fluorescence signal from the released fluorophore **H-TraG** (=H-Rho-AC) (λ_{ex} 504 nm, λ_{em} 531 nm, $\varepsilon_{\lambda_{ex}} = 51\,000\ M^{-1}\ cm^{-1}$). The combination of a basic amine and an intracellularly unmasked carboxylate on the spirocyclised rhodol precursor allows rapid cell loading and retention of the probe, as well as excellent post-wash retention of the fluorescent open-form rhodol product generated by *O*-unmasking, across different cell lines (hours in HEK and HeLa cells, up to 1 h in MEF, A549, and Hoxb8-derived macrophages). That the piperazine-rhodol seems to escape significant signal loss by passive diffusion or by active transport contributes to the reliability of signal detection and confidence in signal quantification, even after long "post-wash" incubation times as would be encountered in multi-step cell biology assays (such as cell population sorting) or in situations with wash-in/wash-out (such as ADME kinetics during *in vivo* enzyme activity imaging). The signal is uniformly distributed across the whole cell with no compartmental accumulation, which is a further advantage for *in vivo* imaging in 3D environments.

Previous approaches to ensure cellular signal retention and thus biochemical activity integration have greatly relied on releasing precipitating fluorophore or intracellular alkylator products, which have biological as well as technical disadvantages. Here, we combine known and new strategies to design the modular, broadly applicable **TraG** probe platform, which distinguishes itself from known retention strategies since it has good performance with respect to all eight features required for live cell probes (including but not only the degree of cell retention) in one scaffold.

We applied our modular scaffold to generate two activity sensor probes showing the superior performance that a soluble fluorophore probe can achieve with a well-tempered cell-entry/exit profile. (1) The hydrogen peroxide sensor **HP-TraG** senses exogenous and endogenous hydrogen peroxide in cells, adding a novel and milder cell-retained H_2O_2 probe to the probe toolbox. (2) **TR-TraG** images the cellular enzyme activity of thioredoxin reductase 1 (TrxR1) and outperforms the current probe RX1 in multiple respects: it more rapidly reaches higher sensitivity quantification, even at vastly lower probe loading, and delivers beneficial linear signal development, as well as allowing long-term cellular viability. Nevertheless, the modular performance of this system, with two probes of rather different overall polarity that are taken up efficiently and perform strongly across multiple cell lines, promises the straightforward design and generation of a variety of other phenol-releasing probes centred on this scaffold (*e.g.* for *O*-unmasking by glycosidases or phosphatases, or by peptidases *via* self-immolative spacers), which can improve the sensitivity and biocompatibility of long-term-compatible cellular and *in vivo* molecular imaging.

View Article Online
Chemical Science Edge Article

Source of biological samples

Human cervical cancer cell line (HeLa): ACC 57 (German Collection of Microorganisms and Cell Cultures DSMZ); human embryonic kidney cell line (HEK293): ACC 305 (German Collection of Microorganisms and Cell Cultures DSMZ); human lung cancer cell line (A549): CCL-185 (American Type Culture Collection ATCC).

Author contributions

P. M. performed synthesis, chemical analysis, enzymatic cell-free studies, cell biology, and coordinated data assembly. L. D.-W., C. Z., N. A. V., D. B. and A. K. performed cell biology. L. D.-W., N. A. V. and D. B. performed confocal microscopy, image analysis and quantification. J. I. B. and T. K. performed synthesis. J. T.-S. and M. K. supervised cell biology and confocal microscopy. P. M. and O. T.-S. designed the concept and experiments. O. T. -S. supervised all other experiments. P. M. and O. T.-S. co-wrote the manuscript with input from all authors.

Conflicts of interest

The authors declare no competing financial interests.

Abbreviations

A549	human lung cancer cell line
ADME	absorption, distribution, metabolism, and excretion
AM	acetoxymethyl ester
DMEM	Dulbecco's modified Eagle's medium (cell culture media)
ESIPT	excited state intramolecular proton transfer
FACS	fluorescence-activated cell sorting (by flow cytometry)
FCS	foetal calf serum
Hoxb8	macrophage precursor cell line
HPQ	2-(2′-hydroxyphenyl)-4(3*H*)-quinazolinone (fluorophore)
GSH	glutathione
HEK	human embryonic kidney cell line HEK293T
HeLa	human cervical cancer cell line
K_S	solubility limit
MEF	mouse embryonic fibroblast cell line
PBS	phosphate buffered saline (buffer)
PMA	phorbol 12-myristate 13-acetate
RX1	molecular probe for TrxR1 activity with a cell-retained signal based on HPQ release and precipitation
SPiDER	molecular probe scaffold with cell retention of a signal based on enzymatic unfurling of an alkylating *ortho*-quinone methide
TBAF	tetra*n*butylammonium fluoride
TrxR	the mammalian selenoenzyme thioredoxin reductase 1

Data availability

The data supporting this article have been included as part of the supplementary information (SI). Supplementary information: synthesis, analysis, biochemistry, and cell biology, incl. design and performance of lipidated fluorescein probes (Fig. S4–S8), rhodol probes (Fig. S9–S18), photocharacterisations (Fig. S20–S22 and Table S1), and cell-free assays (Fig. S23–S28) (PDF). See DOI: **https://doi.org/10.1039/d5sc05388a**.

Acknowledgements

The authors acknowledge support from the German Research Foundation (DFG; Emmy Noether grant 400324123 to O.T.-S.); the Joachim Herz Foundation (Research Fellowships to P. M. and J. T.-S.); the Studienstiftung des Deutschen Volkes (PhD scholarships to P. M. and D. B.); and the Munich Graduate School of Systemic Neurosciences (D. B.). We thank Lukas Zeisel and Jan Felber (TUDD, LMU) for synthesising the dithiane bioreductive activation triggers for GL- and TR-probes. We thank Markus Conrad (TUM) for the kind gift of the validated TrxR knockout MEF cell line (generation and validation reported in ref. 55). We are grateful to Dr Johannes Morstein (Caltech) for collegial discussions around cellular uptake, retention, and localisation.

References

1 W. Chyan and R. T. Raines, *ACS Chem. Biol.*, 2018, **13**, 1810–1823.
2 A. R. Lippert, G. C. Van de Bittner and C. J. Chang, *Acc. Chem. Res.*, 2011, **44**, 793–804.
3 A. E. Albers, B. C. Dickinson, E. W. Miller and C. J. Chang, *Bioorg. Med. Chem. Lett.*, 2008, **18**, 5948–5950.
4 T. D. Gruber, C. Krishnamurthy, J. B. Grimm, M. R. Tadross, L. M. Wysocki, Z. J. Gartner and L. D. Lavis, *ACS Chem. Biol.*, 2018, **13**, 2888–2896.
5 L. Li, J. Ge, H. Wu, Q.-H. Xu and S. Q. Yao, *J. Am. Chem. Soc.*, 2012, **134**, 12157–12167.
6 H. Ito, Y. Kawamata, M. Kamiya, K. Tsuda-Sakurai, S. Tanaka, T. Ueno, T. Komatsu, K. Hanaoka, S. Okabe, M. Miura and Y. Urano, *Angew. Chem., Int. Ed.*, 2018, **57**, 15702–15706.
7 L. Tian, Y. Yang, L. M. Wysocki, A. C. Arnold, A. Hu, B. Ravichandran, S. M. Sternson, L. L. Looger and L. D. Lavis, *Proc. Natl. Acad. Sci. U. S. A.*, 2012, **109**, 4756–4761.
8 M. S. Messina, G. Quargnali and C. J. Chang, *ACS Bio Med Chem Au*, 2022, **2**, 548–564.
9 K. G. Fosnacht, M. D. Hammers, M. S. Earp, A. K. Gilbert and M. D. Pluth, *Chem.–Asian J.*, 2022, **17**, e202200426.
10 B. G. Rosser, S. P. Powers and G. J. Gores, *J. Biol. Chem.*, 1993, **268**, 23593–23600.
11 H. Sun, D. R. Johnson, R. A. Finch, A. C. Sartorelli, D. W. Miller and W. F. Elmquist, *Biochem. Biophys. Res. Commun.*, 2001, **284**, 863–869.
12 S. E. Bresler, V. M. Bresler, E. N. Kazbekov, A. A. Nikiforov and N. N. Vasilieva, *Biochim. Biophys. Acta, Biomembr.*, 1979, **550**, 110–119.

View Article Online
Edge Article Chemical Science

13 S. Izumi, Y. Urano, K. Hanaoka, T. Terai and T. Nagano, *J. Am. Chem. Soc.*, 2009, **131**, 10189–10200.
14 J. L. Turnbull, B. R. Benlian, R. P. Golden and E. W. Miller, *J. Am. Chem. Soc.*, 2021, **143**, 6194–6201.
15 S. T. Caldwell, S. N. O'Byrne, C. Wilson, F. Cvetko, M. P. Murphy, J. G. McCarron and R. C. Hartley, *Chem. Commun.*, 2021, **57**, 3917–3920.
16 T. Fukuda, S. Yokomizo, S. Casa, H. Monaco, S. Manganiello, H. Wang, X. Lv, A. D. Ulumben, C. Yang, M.-W. Kang, K. Inoue, M. Fukushi, T. Sumi, C. Wang, H. Kang, K. Bao, M. Henary, S. Kashiwagi and H. Soo Choi, *Angew. Chem., Int. Ed.*, 2022, **61**, e202117330.
17 S. Jia, E. Y. Lin, E. B. Mobley, I. Lim, L. Guo, S. Kallepu, P. S. Low and E. M. Sletten, *Chem*, 2023, **9**, 3648–3665.
18 L. Rusha and S. C. Miller, *Chem. Commun.*, 2011, **47**, 2038–2040.
19 B. C. Dickinson, J. Peltier, D. Stone, D. V. Schaffer and C. J. Chang, *Nat. Chem. Biol.*, 2011, **7**, 106–112.
20 H. Ye, L. Sun, Z. Pang, X. Ji, Y. Jiao, X. Tu, H. Huang, X. Tang, Z. Xi and L. Yi, *Anal. Chem.*, 2022, **94**, 1733–1741.
21 G. Jiang, X.-F. Lou, S. Zuo, X. Liu, T.-B. Ren, L. Wang, X.-B. Zhang and L. Yuan, *Angew. Chem., Int. Ed.*, 2023, e202218613.
22 X. Li, R. Higashikubo and J.-S. Taylor, *Bioconjugate Chem.*, 2008, **19**, 50–56.
23 Y. Liu, C. Xu, H.-W. Liu, L. Teng, S. Huan, L. Yuan and X.-B. Zhang, *Anal. Chem.*, 2021, **93**, 6463–6471.
24 Z. Huang, E. Terpetschnig, W. You and R. P. Haugland, *Anal. Biochem.*, 1992, **207**, 32–39.
25 H.-W. Liu, K. Li, X.-X. Hu, L. Zhu, Q. Rong, Y. Liu, X.-B. Zhang, J. Hasserodt, F.-L. Qu and W. Tan, *Angew. Chem., Int. Ed.*, 2017, **56**, 11788–11792.
26 S. R. Mulay, J. Desai, S. V. Kumar, J. N. Eberhard, D. Thomasova, S. Romoli, M. Grigorescu, O. P. Kulkarni, B. Popper, V. Vielhauer, G. Zuchtriegel, C. Reichel, J. H. Bräsen, P. Romagnani, R. Bilyy, L. E. Munoz, M. Herrmann, H. Liapis, S. Krautwald, A. Linkermann and H.-J. Anders, *Nat. Commun.*, 2016, **7**, 10274.
27 R. Obara, M. Kamiya, Y. Tanaka, A. Abe, R. Kojima, T. Kawaguchi, M. Sugawara, A. Takahashi, T. Noda and Y. Urano, *Angew. Chem., Int. Ed.*, 2021, **133**, 2153–2157.
28 H. Iwashita, E. Castillo, M. S. Messina, R. A. Swanson and C. J. Chang, *Proc. Natl. Acad. Sci. U. S. A.*, 2021, **118**, e2018513118.
29 H. Kashima, M. Kamiya, F. Obata, R. Kojima, S. Nakano, M. Miura and Y. Urano, *Chem. Commun.*, 2021, **57**, 5802–5805.
30 S. Wang, W. Tan, W. Lang, H. Qian, S. Guo, L. Zhu and J. Ge, *Anal. Chem.*, 2022, **94**, 7272–7277.
31 W. Chyan, H. R. Kilgore, B. Gold and R. T. Raines, *J. Org. Chem.*, 2017, **82**, 4297–4304.
32 P. Mauker, D. Beckmann, A. Kitowski, C. Heise, C. Wientjens, A. J. Davidson, S. Wanderoy, G. Fabre, A. B. Harbauer, W. Wood, C. Wilhelm, J. Thorn-Seshold, T. Misgeld, M. Kerschensteiner and O. Thorn-Seshold, *J. Am. Chem. Soc.*, 2024, **146**, 11072–11082.
33 J. Morstein, A. Capecchi, K. Hinnah, B. Park, J. Petit-Jacques, R. C. Van Lehn, J.-L. Reymond and D. Trauner, *J. Am. Chem. Soc.*, 2022, **144**, 18532–18544.
34 J. Pfeffermann, R. Yadav, T. Glasnov, O. Thorn-Seshold and P. Pohl, *bioRxiv preprint*, 2025, DOI: **10.1101/2025.01.13.632814**.
35 M. D. Hammers, M. J. Taormina, M. M. Cerda, L. A. Montoya, D. T. Seidenkranz, R. Parthasarathy and M. D. Pluth, *J. Am. Chem. Soc.*, 2015, **137**, 10216–10223.
36 L. Zeisel, J. G. Felber, K. C. Scholzen, C. Schmitt, A. J. Wiegand, L. Komissarov, E. S. J. Arnér and O. Thorn-Seshold, *J. Am. Chem. Soc.*, 2024, **146**, 5204–5214.
37 Z. Ye, W. Yang, C. Wang, Y. Zheng, W. Chi, X. Liu, Z. Huang, X. Li and Y. Xiao, *J. Am. Chem. Soc.*, 2019, **141**, 14491–14495.
38 H. Sies, V. V. Belousov, N. S. Chandel, M. J. Davies, D. P. Jones, G. E. Mann, M. P. Murphy, M. Yamamoto and C. Winterbourn, *Nat. Rev. Mol. Cell Biol.*, 2022, **23**, 499–515.
39 M. T. Lin and M. F. Beal, *Nature*, 2006, **443**, 787–795.
40 H. J. Forman and H. Zhang, *Nat. Rev. Drug Discovery*, 2021, **20**, 689–709.
41 E. C. Cheung and K. H. Vousden, *Nat. Rev. Cancer*, 2022, **22**, 280–297.
42 E. W. Miller, B. C. Dickinson and C. J. Chang, *Proc. Natl. Acad. Sci. U. S. A.*, 2010, **107**, 15681–15686.
43 S. E. Caldwell, I. R. Demyan, G. N. Falcone, A. Parikh, J. Lohmueller and A. Deiters, *Bioconjugate Chem.*, 2025, **36**, 540–548.
44 K. A. Kurnia, W. Setyaningsih, N. Darmawan and B. Yuliarto, *J. Mol. Liq.*, 2021, **326**, 115321.
45 V. Redecke, R. Wu, J. Zhou, D. Finkelstein, V. Chaturvedi, A. A. High and H. Häcker, *Nat. Methods*, 2013, **10**, 795–803.
46 R. Huang, L. Zhao, H. Chen, R.-H. Yin, C.-Y. Li, Y.-Q. Zhan, J.-H. Zhang, C. Ge, M. Yu and X.-M. Yang, *PLoS One*, 2014, **9**, e96246.
47 J. M. Slauch, *Mol. Microbiol.*, 2011, **80**, 580–583.
48 C. G. Miller, A. Holmgren, E. S. J. Arnér and E. E. Schmidt, *Free Radical Biol. Med.*, 2018, **127**, 248–261.
49 E. S. J. Arnér and A. Holmgren, *Eur. J. Biochem.*, 2000, **267**, 6102–6109.
50 A. P. Lothrop, G. W. Snider, E. L. Ruggles and R. J. Hondal, *Biochemistry*, 2014, **53**, 554–565.
51 L. Zeisel, M. S. Maier and O. Thorn-Seshold, *Synthesis*, 2023, **55**, 1385–1393.
52 L. Zeisel, J. G. Felber, K. C. Scholzen, L. Poczka, D. Cheff, M. S. Maier, Q. Cheng, M. Shen, M. D. Hall, E. S. J. Arnér, J. Thorn-Seshold and O. Thorn-Seshold, *Chem*, 2022, **8**, 1493–1517.
53 F. H. Abdalbari and C. M. Telleria, *Discover Oncol.*, 2021, **12**, 1–18.
54 W. C. Stafford, X. Peng, M. H. Olofsson, X. Zhang, D. K. Luci, L. Lu, Q. Cheng, L. Trésaugues, T. S. Dexheimer, N. P. Coussens, M. Augsten, H.-S. M. Ahlzén, O. Orwar, A. Östman, S. Stone-Elander, D. J. Maloney, A. Jadhav, A. Simeonov, S. Linder and E. S. J. Arnér, *Sci. Transl. Med.*, 2018, **10**, eaaf7444.
55 M. Conrad, *Biochim. Biophys. Acta Gen. Subj.*, 2009, **1790**, 1575–1585.

7 Paper 3: A novel, cageable HaloTag ligand for conditional covalent binding

In this work, we rationally designed a caged, chemically controlled HaloTag ligand that enables conditional and stimulus-responsive HaloTag labelling. The HaloTag self-labelling protein system allows covalent attachment of diverse chemical moieties to fusion proteins for fluorescence microscopy, analyte sensing or chemically induced protein dimerisation (CID). However, its utility has so far been constrained by the lack of control as existing ligands covalently link chemical and biological components unconditionally. Recent advances, such as split-HaloTag constructs (e.g. CaProLa), have demonstrated conditional reactivity linked to biological events (such as calcium spikes), thereby enabling recordings of cell physiology with unprecedented precision. Nonetheless, no small molecule based conditional HaloTag ligand has been available to date. Such a chemical motif would offer substantial advantages: it would be faster to engineer for new reactivities, cheaper to translate between biological models, and could be directly applied to the thousands of established HaloTag systems.

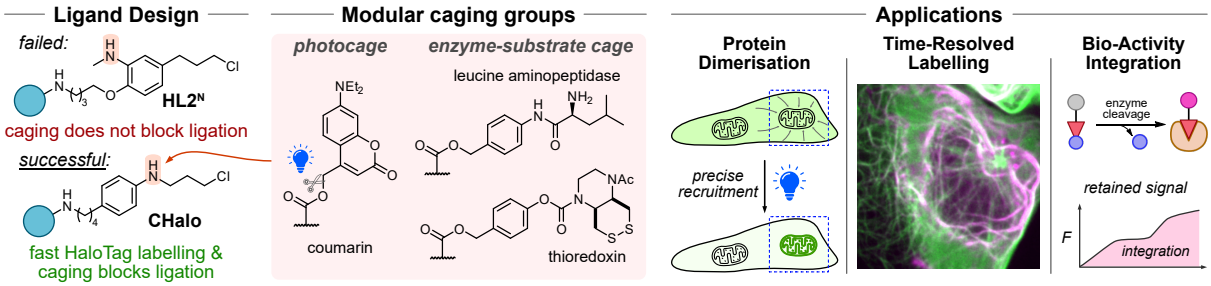

To fill this gap, we set out to develop this useful, missing conditional HaloTag ligator modality. HaloTag reacts with linear chain substrates like the chloroalkane motif “CA” that insert into the active site tunnel for covalent attachment. As the ether chain of the CA ligand lacks suitable caging sites, we designed aniline ligands based on the recently published methoxy-benzene ligand HTL.2, placing the cageable aniline 6 atoms from the chloride producing the $HL2^N$ ligand. $HL2^N$ efficiently ligated to HaloTag, but against our expectations, its coumarin caged derivative failed to fully suppress binding, despite the steric bulk of the caging group. Thus, we re-designed the ligand and moved the cageable aniline closer to the chloride to afford the CHalo ligand, in which the aniline is positioned only 3 atoms away from the chloride. While free CHalo reagents again ligated efficiently, its caged derivatives fully suppress binding over hours, thereby meeting the *off→on* performance required for logic-gated HaloTag applications. Kinetic analysis with purified HaloTag protein showed fast ligation rates (~10^6 M^1s^{-1}), only 10–50-fold slower than the parent CA ligand. Often the effective ligation rates in cellular applications are reduced by low membrane permeability or low aqueous solubility, but cellular CHalo labelling was only 5-fold slower than CA labelling rendering it a suitable ligand for high-performance applications.

Application 1: Functionalisation of CHalo with fluorogenic silicon-rhodamine (SiR) dyes produced fluorogenic, covalent stains for far-red protein imaging. Caged CHalo-SiR reagents exhibited negligible background fluorescence and a strong fluorescence turn-on upon uncaging and HaloTag ligation. We utilised this feature to develop the photocaged Cou-CHalo-SiR for spatio-temporally precise and durable protein labelling triggered by blue-light uncaging. Notably, Cou-CHalo-SiR is unaffected by GFP imaging wavelengths (>470 nm), enabling spatiotemporally controlled and background-free fluorogenic labelling as demonstrated for microtubules.

Application 2: Beyond photoactivation, the CHalo-SiR design enables enzyme substrate-caged probes that record enzymatic activity as durable fluorescence signals through irreversible HaloTag labelling thereby “recording” the enzymatic event. This concept leverages the diverse HaloTag systems and animal models already available while maintaining the modularity and adaptability of small molecule probes. Utilising leucine aminopeptidase and thioredoxin activation substrates, we demonstrated that CHalo-SiR reagents generate bright, cell-retained fluorescence with linear signal intensity over a 100-fold concentration range. Thus, CHalo reagents set the stage for probes that enable *in vivo* enzyme activity recording/imaging, with quantitative, cell-retained information – without perturbing native biology.

Application 3: Finally, we extended the CHalo concept to chemically-induced protein heterodimerisation (CID), a strategy used to study interaction-dependent functions like receptor signalling and localisation-dependent protein functions. We developed a photocaged CHalo dimeriser conjugated to a SNAP-tag ligand on the opposite side. This design overcomes key limitations of current CID strategies, including incomplete dimerisation due to monovalent saturation, lack of photochemical control, or reversible target binding. Using this reagent, we achieved rapid photo-induced re-localisation of a cytosolic HaloTagged protein to a mitochondrial SNAP-tag partner. The Cou-CHalo-BG reagent should allow photo-recruiting any HaloTag protein to any SNAP-tag target, paving the way for future “recruiter-splitter” systems that allow on-demand disconnection.

The CHalo motif thus establishes a chemically logic-gated HaloTag ligand architecture that unites small-molecule precision with HaloTag versatility and genetic specificity. Its modular design provides a general framework for conditional protein labelling, enabling new capabilities in spatio-temporally controlled labelling, enzyme activity recording and inducible protein interaction studies.

Personal contributions

I co-designed target compounds, performed synthesis and structural characterisation [all precursors, ligands, probes and reagents], UV-vis and fluorescence spectroscopy [Figs S10b−d+fg, S15, Table S1], and cell-free assays (photolysis experiments for photocaged CHalo reagents [Figs S7e, S10k, S26a], HaloTag ligation kinetics [Fig S10i], spirocyclisation of CHalo-SiR depending on the dielectric constant of the solvent [Fig S10e], light-dependent HaloTag ligation [Fig S10l] and quantification of in-gel fluorescence [Figs S6e, S7d, S8b, S10h, S11, S12b, S13b, S14b,d]). I contributed to the design of all experiments and advised colleagues and collaboration partners for applications in cell biology, and I coordinated data assembly, prepared all figures, and co-wrote the manuscript.

Main contributions from other authors: C.Z. and L.D.-W. performed cell-free ligation experiments and quantification during the ligand design cycles; J.C.M.M. performed fluorogenic microtubule-labelling with Cou-CHalo-SiR [Fig 2a−c]; D.B. performed confocal microscopy, image analysis and quantification for Leu-CHalo-SiR [Fig 2d−f]; L.R.-A. performed live cell photo-heterodimerisation with Cou-CHalo-SiR [Fig 2j−l]; J.T.-S. performed redox probe cellular assays with SS66T/SS66C-CHalo-SiR [Fig 2gi]; J.I.B. supported with precursor synthesis; J.P.P. synthesised SS66T/SS66C-CHalo-SiR, supported by M.R.; O.T.-S. designed the study, co-designed target compounds and co-wrote the manuscript.

Logic-gating the HaloTag system with Conditional-Halo-ligator 'CHalo' reagents

Philipp Mauker[1,2], Carmen B.J. Zecha[2], Lucas Dessen-Weissenhorn[2], Luciano Román-Albasini[3], Joyce C.M. Meiring[4], Julia I. Brandmeier[2], Daniela Beckmann[5,6], Jan P. Prohaska[1], Martin Reynders[1], Yi Louise Li[7], Kristina Mrug[8], Hannah von Schwerin[2], Nynke A. Vepřek[2], Julia F. Gaisbauer[2], Leif Dehmelt[9], Perihan Nalbant[8], Jennifer Zenker[7], Anna Akhmanova[4], Martin Kerschensteiner[5,6,10], Angelika B. Harbauer[3,11], Julia Thorn-Seshold[2,12], Oliver Thorn-Seshold[1,*]

[1] Faculty of Chemistry and Food Chemistry, Dresden University of Technology, Dresden, DE.
[2] Department of Pharmacy, LMU Munich, Munich, DE.
[3] Max Planck Institute for Biological Intelligence; Martinsried, DE.
[4] Division of Cell Biology, Neurobiology and Biophysics, Department of Biology, Utrecht University, Utrecht, NL.
[5] Institute of Clinical Neuroimmunology, LMU University Hospital, LMU Munich, Munich, DE.
[6] Biomedical Center (BMC), Faculty of Medicine, LMU Munich, Martinsried, DE.
[7] Australian Regenerative Medicine Institute, Monash University, Clayton, Victoria, AU.
[8] Faculty of Biology, University of Duisburg-Essen, Essen, DE.
[9] Department of Chemistry and Chemical Biology, Technical University Dortmund, Dortmund, DE.
[10] Munich Cluster for Systems Neurology (SyNergy), Munich, DE.
[11] Technical University of Munich, Institute of Neuronal Cell Biology; Munich, DE.
[12] Institute for Clinical Chemistry, Medical Faculty, Dresden University of Technology, Dresden, DE.
* Corresponding Author: oliver.thorn-seshold@tu-dresden.de

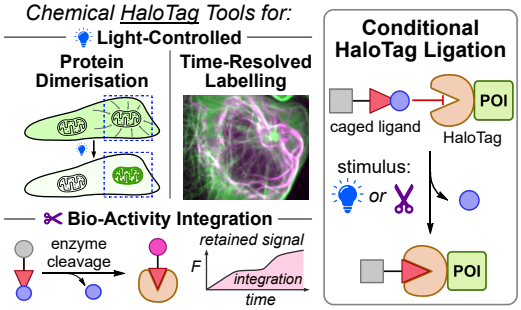

Abstract: HaloTag proteins spontaneously ligate onto any chemical reagent featuring a chloroalkane motif (**CA**). We introduce the conditional **CHalo** motif, which ligates to HaloTag only after uncaging by light or enzymes. (1) Photo-triggered **CHalo** fluorogenic reagents allow spatiotemporally-specific labeling; (2) photo-triggered **CHalo** heterodimerisers can photocontrol protein recruitment; and (3) enzyme-triggered **CHalo** reagents can durably record diverse enzyme activities, and multiplexing them should allow quantitative ratiometric recording of multiple activities in parallel. **CHalo** thus permits manifold extensions to the HaloTag technology.

Introduction (Fig. 1a-c)

HaloTag, SNAP-tag, and CLIP-Tag self-labelling proteins empower *chemical biology* by mediating the ligation of diverse *chemical* reagents to diverse *biological* targets (fusion proteins of interest, POIs). HaloTag is used throughout cell and *in vivo* biology,[1] to visualise POIs with fluorogenic reagents (Halo-SiR), or to functionalise them as sensors (WHalo-CaMP), drug targets (T-REX, DART), or for degradation.[2] Nonetheless, the utility of HaloTag was limited because it links the chemical and biological worlds *unconditionally*. Split-HaloTag sensors were recently engineered so their ligating reactivity is *conditional* on a biological event (calcium spike, GPCR-arrestin binding), making them "molecular activity recorder" proteins (CaProLa) that can reveal biology with unprecedented resolution.[3]

A major cognate gap in the HaloTag toolbox remains: no *chemical motif* was known, that would ligate to HaloTag conditional on a (bio)chemical stimulus. Such a Conditional HaloTag Ligator motif could be immensely useful: e.g. with enzymatic activity as the stimulus, to durably record bioactivity with dyes (molecular imaging; **Fig. 1a**); or light as a spatiotemporally precise stimulus to track defined pools of POIs (photoactivated labelling; **Fig. 1b**) or trigger protein-protein interactions (photoactivated heterodimerisation; **Fig. 1c**). Compared to protein tools, it is much cheaper to engineer small molecules for new reactivities, faster to translate them between biological models, and it is feasible to apply several different chemical reagents in parallel to acquire multi-dimensional data (multiplexing). Conditional HaloTag Ligator reagents could also be applied directly into the thousands of established experimental HaloTag systems.[1] We aimed to synthesise this useful, missing Conditional HaloTag Ligator modality (**Fig. 1d**).

Development of the CHalo platform (Fig. 1d-g)

HaloTag ligates linear chain substrates like the "chloroalkane" motif (CA, **Fig. 1e-g**)[4] that insert down a protein tunnel.[5] We expected that adding a cage group on the chain would stop insertion: thus ligation would only be possible after a stimulus removes the cage. Since the ether chains of known HaloTag motifs like CA have no potential caging sites, we designed alternative motifs with anilines for flexible caging as stimulus-responsive carbamates (e.g. photocages, enzyme cages, bioorthogonal cages; **Supplementary Note 3**, **Fig. S9**). We first adapted Tadross' methoxybenzene **HTL.2**[6] (**Fig. 1e**) as isosteric **HL2^{N}** (cageable nitrogen 6 atoms from the chlorine; **Fig. S6**) which ligated very efficiently, but *N*-caging did not block ligation. After several redesign cycles we discovered **CHalo** (cageable nitrogen 3 atoms from chlorine, i.e. closest possible; **Fig. 1d**; **Supplementary Note 1**). Uncaged **CHalo** reagents can ligate very efficiently (~10^6 $M^{-1}s^{-1}$), only 10-fold slower than cognate CA reagents[5] (**Fig. S10h–j**; **Supplementary Note 4**); while crucially, carbamate-**Caged-CHalo** did not ligate (<1% over 100 min; **Fig. S7cd**; **Supplementary Note 2**). **CHalo** thus fits the "off/ON" need for logic-gated HaloTag uses (**Fig. 1a–c**).

Uncaging CHalo-SiR triggers strongly SiR-fluorogenic HaloTag ligation

Silicon-rhodamines (SiR: e.g. SiR-Halo/CA-SiR, Halo-JF646, etc; **Fig. 1f**) are valued for low-photodamage, far-red tracking of HaloTag proteins, with low background since they are fluorogenic upon HaloTag ligation.[2,7] Ligated **CHalo-SiR** reached the same fluorescence brightness as ligated CA-SiR, though with even larger fluorogenicity (lower background; **Fig. S10bc**, **Supplementary Note 4**). Crucially, **caged-CHalo-SiR** reagents had as low background fluorescence as non-ligated CHalo-SiR (**Fig. S10fg**). Thus, **caged-CHalo-SiR** reagents should be highly fluorogenic upon uncaging then ligation, and should be bright enough for any settings that CA-SiR can be used in.

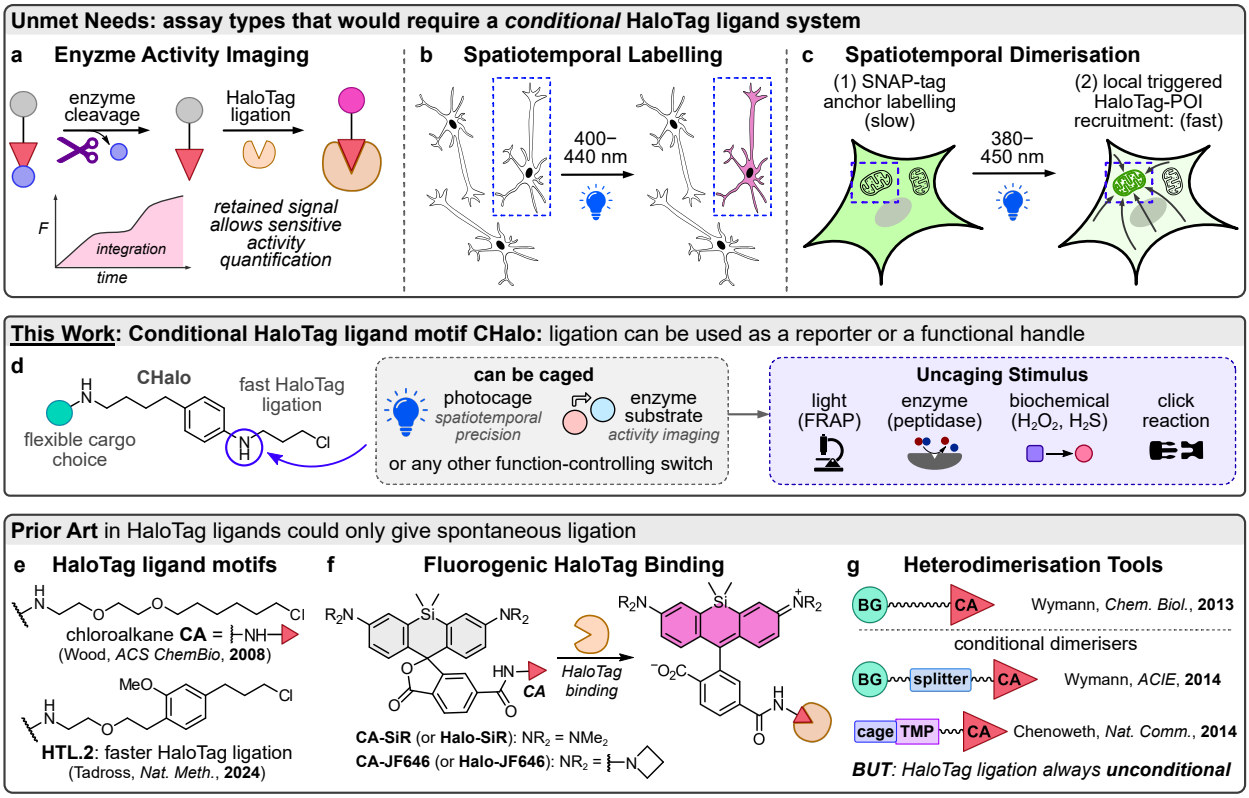

Fig. 1 | CHalo aims to unlock conceptually new chemigenetic assays for biology. a-c, Logic-gated HaloTag applications that would require a conditional HaloTag ligand. **d**, **CHalo** uses aniline uncaging to control its ligation to HaloTag. **e-g**, Prior HaloTag ligator motifs, popular reagents, and heterodimerisers.

CHalo reagents equip HaloTag to apply or record biological and biochemical stimuli

Using HaloTag as an "all-purpose anchor protein" to durably mark cells or proteins at a specific time or region, or upon specific stimuli, is attractive for tracing cell dynamics, trafficking, history, and fates (**Fig. 1a**). There are crucial differences between ligation prior to stimulus response (prior art), or ligation downstream of the stimulus (CHalo). Prior ligation uses HaloTag as a single-purpose anchor, focusing on its fusion protein: suiting e.g. high-resolution localisation (HaloTag-reactive caged-fluorophores like PaX[8] or PA-JF549).

Downstream ligation instead focuses on the uncaging step: e.g. durably transducing or quantifying stimuli. We now showcase these new features with a set of CHalo reagents (**Fig. 2**). Conceptually, it should also allow "multipurpose" HaloTag assays: applying multiple CHalo reagents together, to record or transduce multiple stimuli in parallel, via one HaloTag type. These may be particularly attractive to quantitatively and ratiometrically record several enzyme activities at once (**Supplementary Note 5**).

Photocaged-CHalo-SiR is a fluorogenic label for HaloTag (Fig. 2a-c)

We created the coumarin-photocaged ligator-fluorogen reagent **Cou-CHalo-SiR** for spatiotemporally-photolocalised, durable cell marking (**Fig. 2a**). **Cou-CHalo-SiR** does not ligate HaloTag and is unaffected by GFP imaging (>470 nm); but violet light uncages it efficiently (ca. 50% conversion by 10 mJ/mm^2 at 400-440 nm, **Fig. S10k**), enabling fluorogenic ligation (**Fig. S10l**). In cells, **Cou-CHalo-SiR** photolabels specific POIs, with temporal control (ligation half-times ca. 1 minute after uncaging, **Fig. 2c**) and minimal background (**Fig. 2b**, **Movie S1**: StableMARK-Halo, marker of stable microtubule subfraction; SiR-based background signal discussed at **Fig. S17**).

More generally, **photocaged-CHalo-Fluorogen** reagents will be high-sensitivity fluorogenic HaloTag labels that are compatible with multicolour as well as "multipurpose" multiplexed assays (**Supplementary Note 5**).

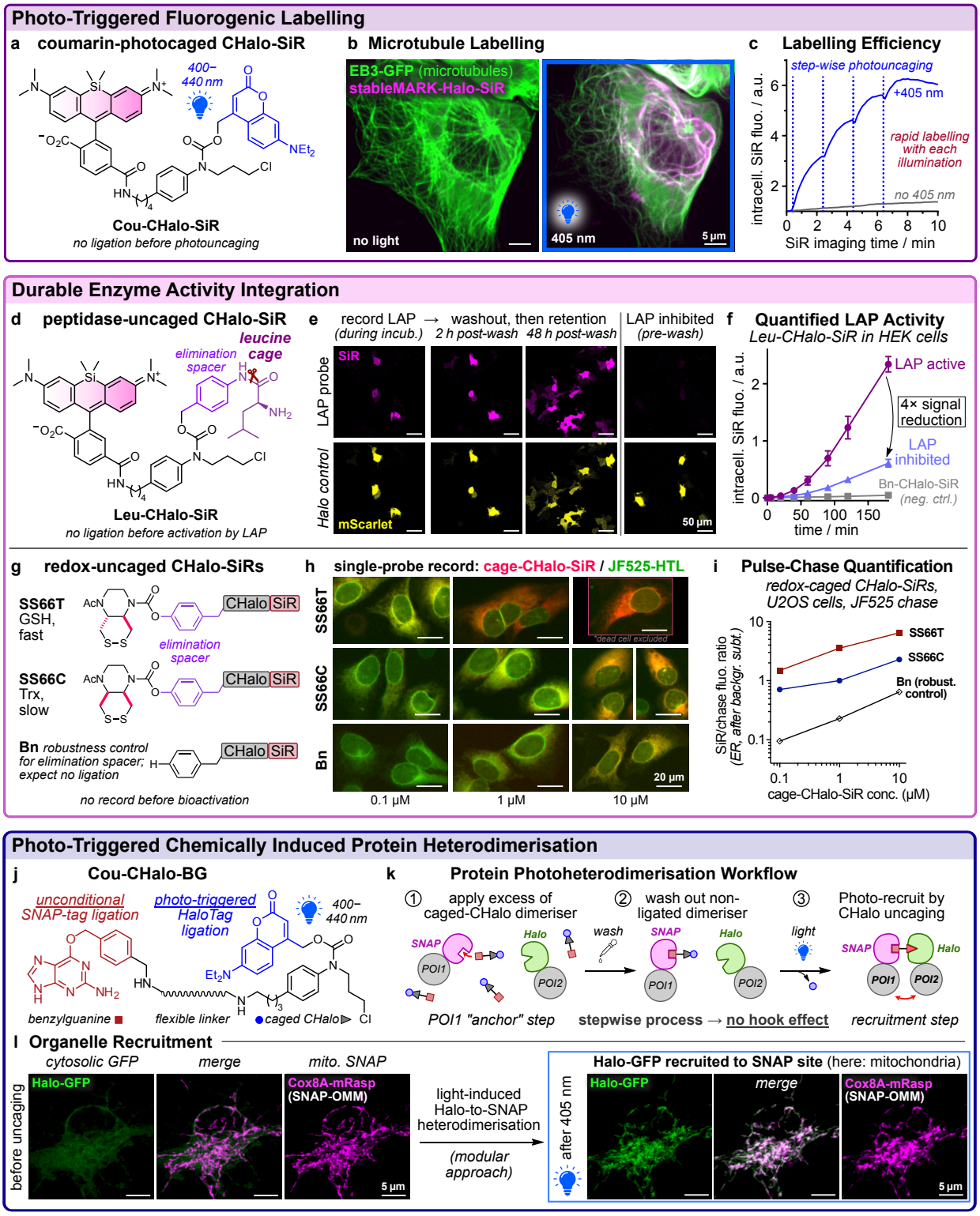

Fig. 2 | CHalo unlocks logic-gated HaloTag applications. a-c, Photoactivated label **Cou-CHalo-SiR**: temporally resolved photouncaging then HaloTag ligation activates red fluorescence (here: labelling StableMARK-Halo, a marker for stable microtubules, in U2OS cells; EB3-GFP overe xpressed to reveal the total microtubule network; 5 µM Cou-CHalo-SiR for 5 min; then 405 nm flashes; **Movie S1**). **d-f**, Model enzyme activity probe **Leu-CHalo-SiR**: durable imaging of leucine aminopeptidase activity (HEK cells with cytosolic HaloTag:mScarlet, 1 µM probe, 3 h; then 2× wash; optional pretreatment with inhibitor bestatin, 100 µM, 30 min). **g-i**, Bioreduction probes **SS66T-CHalo-SiR** (nonspecific, thiols) and **SS66C-CHalo-SiR** (thioredoxin) can be recorded and benchmarked by chase labelling to give coherent relative activities despite separate cell populations, over 100-fold differences of probe concentrations, and >20-fold different intrinsic activity levels (U2OS cells with HaloTag-Sec61 (ER-localised recorder) and GFP-NUP98 (nuclear marker, green), 0.1-10 µM SiR probes [red], 16 h; then chase with JF525-HTL [green], 1 µM). **j-l**, Photoactivated Halo-to-SNAP heterodimeriser **Cou-CHalo-BG**: modular, irreversible protein photoheterodimerisation (here: mouse primary neurons; mitochondrial SNAP-OMM anchor and mito-mRaspberry marker (magenta), cytosolic GFP-HaloTag target (green); SNAP labelled first (5 µM, 1 h) then 3× wash, 405 nm photoactivation, 5 min incubation, and re-imaged; **Movie S2**).

Substrate-caged-CHalo-SiR probes are fluorogenic enzyme activity recorders (Fig. 2d-i)

There are no general platforms for sensitive fluorogenic chemical probes to allow *in vivo* enzyme activity integration and imaging, with durably quantitative cell-retained information, that do not impact native biology.[9] Using enzyme activity to unleash CHalo ligation could leverage the diverse HaloTag systems and animal models already available,[1] while harnessing the advantages of small molecule enzyme probes[10] (e.g. unimpeded enzyme rates; **Supplementary Note 5**), but allowing clean persistent signal trapping.

Our test leucine-peptidase probe **Leu-CHalo-SiR** (**Fig. 2d**) gave excellent cellular signal retention over hours after washing (**Fig. 2e**), and plausible controls (signal low with peptidase inhibitor, no signal for no-peptide control **Bn-CHalo-SiR**; **Fig. 2ef**). This promises that CHalo can harness known substrate-mimic probe designs, including the use of chemical adapters to access diverse reactivities (**Fig. S9c**),[11] but now converting them into durably trapped biologically innocent integrators: a meaningful step towards high-sensitivity enzyme imaging *in vivo*.

We next tested intracellular redox-activated fluorogenic probes, based on bioreductive unmasking of either the thioredoxin-selective cyclic disulfide **SS66C**[12,13] or its essentially glutathione (GSH)-reporting diastereomer **SS66T**[12,13] (**Fig. 2g**). As a step towards quantitative comparisons of recorded signals, we followed pulse labelling with these slow-turnover probes by chase labelling with the rapidly-labelling green fluorogenic ligand JF525-HTL; and we used image segmentation to focus on recorder regions (endoplasmic reticulum) while excluding non-ligated intracellular background (**Fig. 2h**). These data showed excellent linearity in the recorded signals over a ca. 100-fold concentration range (**Fig. 2i**), and were coherent with the specific activities expected (**SS66T**: high; **SS66C**: moderate; control **Bn** that can only be activated by unwanted hydrolysis: low). This suggests that CHalo-based recording may be able to reliably integrate and quantify even low enzymatic turnovers (low probe concentration and low activity), which has traditionally proved challenging for small molecule probes; and by recording a chemically different class of bioactivity, it underlines the modular applicability of the CHalo motif.

Modular phototargeted SNAP/Halo heterodimerisation (Fig. 2j-l)

Chemically-induced protein (hetero)dimerisation (CID) is useful to probe interaction-dependent functions like receptor signaling, or single-protein functions dependent on localisation.[14] SNAP-tag and HaloTag are proving valuable for covalent CID, complementing earlier noncovalent interaction domains (FKBP-FRB, eDHFR).[15] Yet, because POI1-to-POI2 ligand designs suffer "hook effect" problems (incomplete dimerisation due to monovalent saturation of each POI), stepwise POI1-labelling / washout / POI2-labelling strategies are crucial.[16] These require POI2-labelling to be unmasked upon external stimulus, typically photouncaging;[17] but no photocaged[18] SNAP-to-Halo designs are known.

CHalo solves the missing need for a modular, effective, photocaged SNAP-to-Halo double-covalent CID reagent. **Cou-CHalo-BG** performs the slower[5] benzylguanine-SNAP-ligation first; then, after washout of unligated reagent, photouncaging allows HaloTag ligation (**Fig. 2j-k**). This allowed rapidly relocalising a cytosolic HaloTagged POI1 to a mitochondrial SNAP-tag in primary mouse neurons (**Fig. 2l**, **Fig. S26b**). **Cou-CHalo-BG** should be useful to photo-recruit *any* HaloTag protein to *any* SNAP-tag target; multiplexing analogues with spectrally distinct cages (**Fig. S9b**) could colour-code recruitment to various targets (e.g. Cage[2]-CHalo-TMP; Cage[3]-CHalo-CLIP); and recruiter-splitters[19] could disconnect them on demand. The broad implementation of HaloTag tools may make such recruiters, which CHalo now unlocks, of particular practical impact.

Conclusion

In conclusion, we developed the CHalo chemical motif which now allows diverse functional applications of the ubiquitous HaloTag protein. Recording enzyme activity, tracking protein pools, and recruiting proteins on demand, are three impactful examples of *chemigenetic logic-gating* that CHalo/HaloTag can deliver. In principle, almost any stimulus which cleaves a bond in a small molecule substrate can be used to activate the ligation; any HaloTagged protein can be targeted; and almost any chemical cargo can be delivered, including ligation-activated molecules (e.g. fluorogenic labels). We expect that CHalo can unite the broad availability of HaloTag models with the diversity of logic-gated chemistry to achieve substantial biological impact. We are particularly interested in multi-reagent/single-anchor assays, e.g. for "rainbow" ratiometric parallel recording with single cell resolution, since these should be able to test whether multiple enzymes' activities are locked or are uncoupled (in physiological, or in challenged, stressed, or pathological conditions). Such quantitative multidimensional data should particularly impact systems biology, while more broadly empowering biochemistry and quantitative biology studies both *in vitro* and *in vivo*.

References

(1) Porzberg, N.; Gries, K.; Johnsson, K. Exploiting Covalent Chemical Labeling with Self-Labeling Proteins. *Annu. Rev. Biochem.* **2025**, *94*, 29–58. https://doi.org/10.1146/annurev-biochem-030222-121016.

(2) Deo, C.; Abdelfattah, A. S.; Bhargava, H. K.; Berro, A. J.; Falco, N.; Farrants, H.; Moeyaert, B.; Chupanova, M.; Lavis, L. D.; Schreiter, E. R. The HaloTag as a General Scaffold for Far-Red Tunable Chemigenetic Indicators. *Nat. Chem. Biol.* **2021**, *17* (6), 718–723. https://doi.org/10.1038/s41589-021-00775-w.

(3) Huppertz, M.-C.; Wilhelm, J.; Grenier, V.; Schneider, M. W.; Falt, T.; Porzberg, N.; Hausmann, D.; Hoffmann, D. C.; Hai, L.; Tarnawski, M.; Pino, G.; Slanchev, K.; Kolb, I.; Acuna, C.; Fenk, L. M.; Baier, H.; Hiblot, J.; Johnsson, K. Recording Physiological History of Cells with Chemical Labeling. *Science* **2024**, *383* (6685), 890–897. https://doi.org/10.1126/science.adg0812.

(4) Merrill, R. A.; Song, J.; Kephart, R. A.; Klomp, A. J.; Noack, C. E.; Strack, S. A Robust and Economical Pulse-Chase Protocol to Measure the Turnover of HaloTag Fusion Proteins. *J. Biol. Chem.* **2019**, *294* (44), 16164–16171. https://doi.org/10.1074/jbc.RA119.010596.

(5) Wilhelm, J.; Kühn, S.; Tarnawski, M.; Gotthard, G.; Tünnermann, J.; Tänzer, T.; Karpenko, J.; Mertes, N.; Xue, L.; Uhrig, U.; Reinstein, J.; Hiblot, J.; Johnsson, K. Kinetic and Structural Characterization of the Self-Labeling Protein Tags HaloTag7, SNAP-Tag, and CLIP-Tag. *Biochemistry* **2021**, *60* (33), 2560–2575. https://doi.org/10.1021/acs.biochem.1c00258.

(6) Shields, B. C.; Yan, H.; Lim, S. S. X.; Burwell, S. C. V.; Cammarata, C. M.; Fleming, E. A.; Yousefzadeh, S. A.; Goldenshtein, V. Z.; Kahuno, E. W.; Vagadia, P. P.; Loughran, M. H.; Zhiquan, L.; McDonnell, M. E.; Scalabrino, M. L.; Thapa, M.; Hawley, T. M.; Field, G. D.; Hull, C.; Schiltz, G. E.; Glickfeld, L. L.; Reitz, A. B.; Tadross, M. R. DART.2: Bidirectional Synaptic Pharmacology with Thousandfold Cellular Specificity. *Nat. Methods* **2024**, *21* (7), 1288–1297. https://doi.org/10.1038/s41592-024-02292-9.

(7) Lukinavičius, G.; Umezawa, K.; Olivier, N.; Honigmann, A.; Yang, G.; Plass, T.; Mueller, V.; Reymond, L.; Corrêa Jr, I. R.; Luo, Z.-G.; Schultz, C.; Lemke, E. A.; Heppenstall, P.; Eggeling, C.; Manley, S.; Johnsson, K. A Near-Infrared Fluorophore for Live-Cell Super-Resolution Microscopy of Cellular Proteins. *Nat. Chem.* **2013**, *5* (2), 132–139. https://doi.org/10.1038/nchem.1546.

(8) Lincoln, R.; Bossi, M. L.; Remmel, M.; D'Este, E.; Butkevich, A. N.; Hell, S. W. A General Design of Caging-Group-Free Photoactivatable Fluorophores for Live-Cell Nanoscopy. *Nat. Chem.* **2022**, *14* (9), 1013–1020. https://doi.org/10.1038/s41557-022-00995-0.

(9) Mauker, P.; Dessen-Weissenhorn, L.; Zecha, C.; Vepřek, N.; Brandmeier, J. I.; Beckmann, D.; Kitowski, A.; Kernmayr, T.; Thorn-Seshold, J.; Kerschensteiner, M.; Thorn-Seshold, O. Cellularly-Retained Fluorogenic Probes for Sensitive Cell-Resolved Bioactivity Imaging. *bioRxiv* **2025**. https://doi.org/10.1101/2025.04.17.649302.

(10) Chyan, W.; Raines, R. T. Enzyme-Activated Fluorogenic Probes for Live-Cell and in Vivo Imaging. *ACS Chem. Biol.* **2018**, *13* (7), 1810–1823. https://doi.org/10.1021/acschembio.8b00371.

(11) Papot, S.; Tranoy, I.; Tillequin, F.; Florent, J.-C.; Gesson, J.-P. Design of Selectively Activated Anticancer Prodrugs: Elimination and Cyclization Strategies. *Curr. Med. Chem. Anticancer Agents* **2002**, *2* (2), 155–185. https://doi.org/10.2174/1568011023354173.

(12) Zeisel, L.; Felber, J. G.; Scholzen, K. C.; Schmitt, C.; Wiegand, A. J.; Komissarov, L.; Arnér, E. S. J.; Thorn-Seshold, O. Piperazine-Fused Cyclic Disulfides Unlock High-Performance Bioreductive Probes of Thioredoxins and Bifunctional Reagents for Thiol Redox Biology. *J. Am. Chem. Soc.* **2024**, *146* (8), 5204–5214. https://doi.org/10.1021/jacs.3c11153.

(13) Felber, J. G.; Kitowski, A.; Zeisel, L.; Maier, M. S.; Heise, C.; Thorn-Seshold, J.; Thorn-Seshold, O. Cyclic Dichalcogenides Extend the Reach of Bioreductive Prodrugs to Harness Thiol/Disulfide Oxidoreductases: Applications to Seco-Duocarmycins Targeting the Thioredoxin System. *ACS Cent. Sci.* **2023**, *9* (4), 763–776. https://doi.org/10.1021/acscentsci.2c01465.

(14) Broichhagen, J.; Trumpp, M.; Gatin-Fraudet, B.; Bruckmann, K.; Burdzinski, W.; Roßmann, K.; Levitz, J.; Knaus, P.; Jatzlau, J. Developing HaloTag and SNAP-Tag Chemical Inducers of Dimerization to Probe Receptor Oligomerization and Downstream Signaling. *Angew. Chem. Int. Ed.* **2025**, *64* (35), e202506830. https://doi.org/10.1002/anie.202506830.

(15) Erhart, D.; Zimmermann, M.; Jacques, O.; Wittwer, M. B.; Ernst, B.; Constable, E.; Zvelebil, M.; Beaufils, F.; Wymann, M. P. Chemical Development of Intracellular Protein Heterodimerizers. *Chem. Biol.* **2013**, *20* (4), 549–557. https://doi.org/10.1016/j.chembiol.2013.03.010.

(16) Ballister, E. R.; Aonbangkhen, C.; Mayo, A. M.; Lampson, M. A.; Chenoweth, D. M. Localized Light-Induced Protein Dimerization in Living Cells Using a Photocaged Dimerizer. *Nat. Commun.* **2014**, *5* (1), 5475. https://doi.org/10.1038/ncomms6475.

(17) Chen, X.; Venkatachalapathy, M.; Kamps, D.; Weigel, S.; Kumar, R.; Orlich, M.; Garrecht, R.; Hirtz, M.; Niemeyer, C. M.; Wu, Y.-W.; Dehmelt, L. "Molecular Activity Painting": Switch-like, Light-Controlled Perturbations inside Living Cells. *Angew. Chem. Int. Ed.* **2017**, *56* (21), 5916–5920. https://doi.org/10.1002/anie.201611432.

(18) Caldwell, S. E.; Demyan, I. R.; Falcone, G. N.; Parikh, A.; Lohmueller, J.; Deiters, A. Conditional Control of Benzylguanine Reaction with the Self-Labeling SNAP-Tag Protein. *Bioconjugate Chem.* **2025**, *36* (3), 540–548. https://doi.org/10.1021/acs.bioconjchem.5c00002.

(19) Zhang, H.; Aonbangkhen, C.; Tarasovetc, E. V.; Ballister, E. R.; Chenoweth, D. M.; Lampson, M. A. Optogenetic Control of Kinetochore Function. *Nat. Chem. Biol.* **2017**, *13* (10), 1096–1101. https://doi.org/10.1038/nchembio.2456.

(20) Thorn-Seshold, O.; Mauker, P. Compound, Composition, Kit and Their Use for Protein Labelling. Patent Application **2025**, LU602798.

Online content

All methods, additional references, reporting summaries, source data, extended data, supplementary information, acknowledgements, peer review information; details of author contributions and competing interests; and statements of data and code availability are available at *doi.org/xxxxxxxxx.* In brief, this includes the following:

Supplementary Information

Document S1: Supplementary Notes 1–5, Figures S1–S26, Table S1, chemistry, materials and methods.

Movie S1: Timelapse imaging of photo-triggered fluorogenic labelling of stable microtubules with **Cou-CHalo-SiR**, corresponding to **Fig. 2b** (**MP4**)

Movie S2: Timelapse imaging of photo-triggered HaloTag-to-SNAP-tag recruitment with **Cou-CHalo-BG**, corresponding to **Fig. 2l** (**AVI**)

Data and materials availability

All data needed to evaluate the conclusions in the paper are present in the paper and/or the Supplementary Materials, and are deposited and freely available on BioRxiv.

Author ORCiDs

Philipp Mauker: 0009-0007-8740-7864
Luciano Román-Albasini: 0000-0002-7523-5635
Joyce C. M. Meiring: 0000-0001-9166-5363
Yi Louise Li: 0009-0003-2615-3160
Kristina Mrug: 0009-0000-4363-0617
Martin Reynders: 0000-0001-7415-3649
Nynke A. Vepřek: 0000-0001-7301-265X
Julia F. Gaisbauer: 0009-0002-9428-8203
Leif Dehmelt: 0000-0002-6559-6496
Perihan Nalbant: 0000-0002-5649-5933
Jennifer Zenker: 0000-0002-9929-2909
Anna Akhmanova: 0000-0002-9048-8614
Martin Kerschensteiner: 0000-0003-4898-9383
Angelika B. Harbauer: 0000-0002-4568-9003
Julia Thorn-Seshold: 0000-0002-4879-4159
Oliver Thorn-Seshold: 0000-0003-3981-651X

Author Contributions Statement

P.M. performed synthesis, chemical analysis, photochemical evaluation, cell-free ligation experiments, analysed data and coordinated data assembly. J.T.-S. performed multiplexed cellular assays, and supervised L.D.-W. and C.Z. performing cell-free ligation experiments and quantification. J.P.P., M.R., J.I.B., H.S., and J.G. performed chemical synthesis. N.A.V. performed early cell-free ligation experiments. D.B. performed cell biology, confocal microscopy, image analysis and quantification for **Leu-CHalo-SiR**, supervised by M.K.. K.M. performed early live cell photo-heterodimerisation studies with **Cou-CHalo-BG**, supervised by P.N. and advised by L.D.. J.C.M.M. performed fluorogenic cell labelling with **Cou-CHalo-SiR**, supervised by A.A.. L.R.-A. performed live cell photo-heterodimerisation with **Cou-CHalo-BG**, supervised by A.B.H.. Y.L.L. performed mouse embryo live imaging with **Cou-CHalo-SiR**, supervised by J.Z.. O.T.-S. designed the study and the targets and supervised all other experiments. P.M. and O.T.-S. designed the experiments and co-wrote the manuscript with input from all authors.

Acknowledgements

P.M. and J.T.-S. thank the Joachim Herz Foundation for fellowship support; P.M., and D.B. thank the Studienstiftung for fellowship support; J.Z. acknowledges a Sylvia & Charles Viertel Senior Medical Fellowship; and J.P.P. thanks the Fonds der chemischen Industrie for a Kekulé fellowship. We thank Alison Tebo (Janelia) for the advice about the role of the benzamide in the ligation step, which motivated us to keep developing reagents further despite having been disappointed in the performance of **HL2^{N}** and **HL3**; Luke Lavis (Janelia) for supportive discussions about the system concept; Julien Hiblot and Kai Johnsson (Max Planck Institute) for very kind gifts of **CA**-type reagents and HaloTag plasmids; Alf Honigmann (TU Dresden) for gifts of HaloTag plasmids; Gerti Beliu for kind gifts of HTL chase ligands and plasmids; Gerti Beliu and Made Budiarta (Uni Würzburg) and Ünal Coskun (TU Dresden) for producing HaloTag protein for cell-free assays; Dr. Inmaculada Segura (LMU) for her cloning expertise; the Imaging Facility at the Max Planck Institute for Biological Intelligence, Martinsried, Germany (RRID:SCR_026797) for facility access; and Thomas Misgeld (TUM) for supportive discussions. This work was supported by grants from the German Research Foundation (DFG: Emmy Noether grant 400324123 to O.T.-S.; SPP1926 grant 426018126 to O.T.-S., P.N., and L.D.; CRC1430 project A08 grant 424228829 to P.N. and K.M.; TRR353 ID 471011418 and SPP2453 ID 541742535 to A.B.H.; grant DE 823/10-1 to L.D.); the Max Planck Society (MPRGL to A.B.H.); the European Union (ERC StG Project 101077138 — MitoPIP to A.B.H.; Synergy grant PushingCell project number 101071793 to A.A.); the Munich Center for Systems Neurology (SyNergy EXC 2145; Project ID 390857198 to A.B.H. and M.K.); the Gravitation programme IMAGINE! (project number 24.005.009 to J.C.M.M and A.A.); and the NHMRC (APP2009409 to J.Z.). The Australian Regenerative Medicine Institute is supported by grants from the State Government of Victoria and the Australian Government.

Competing Interests Statement

P.M. and O.T.-S. are coinventors on a patent application owned by TU Dresden[20] that discloses structures included in this paper. The other authors declare no competing interests.

D. SUMMARY AND OUTLOOK

8 Summary

This thesis develops three types of molecular tools to visualise and manipulate biological systems, enabling new ways of studying the role of proteins and biochemical analytes in health and disease:

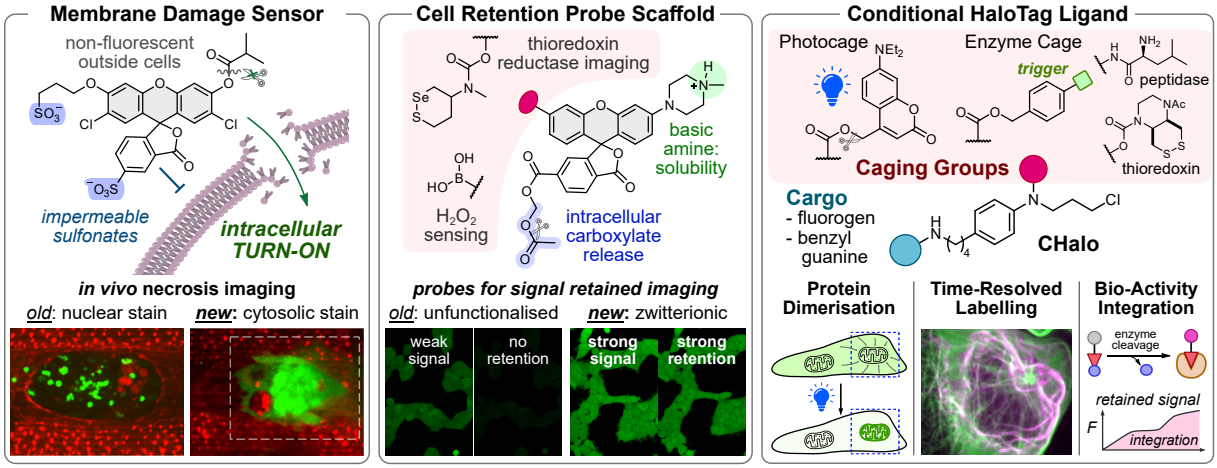

Membrane Damage Imaging: Damage to cell membranes plays a key role in diverse pathologies, including bacterial infections and multiple sclerosis. DNA-intercalating fluorogens are commonly used to detect such damage, but they can be toxic and are restricted to identifying permeabilisation in cell volumes that contain a nucleus. To overcome these limitations, this work develops disulfonated fluorogenic probes that selectively label the *entire cytosol* of damaged cells, with near zero background fluorescence for sensitive detection. These probes reliably reveal membrane damage induced by biological, biochemical, or physical means and are compatible with multicolour microscopy. Their advantages over DNA fluorogens are demonstrated by imaging neuronal axon damage *in vitro* and discriminating membrane damage with single-cell resolution in *Drosophila* wound models *in vivo*.

Cell Retention Probe Scaffold: Fluorogenic bioactivity probes are powerful research tools, widely used to study enzyme activity in disease contexts or for fluorescence assisted surgery. While these probes must be membrane permeable to efficiently enter cells, often their fluorescent products also leak out, leading to signal loss, poor cell-by-cell resolution, and low sensitivity for low-turnover processes. Prior cell-retention strategies are inefficient or disrupt native biology through non-specific alkylation or precipitation. To overcome this, Paper 2 screened charge- and polarity-based designs and identified a rhodol scaffold that can switch from cell-permeable to cell-retained states. The cell-retained product is a bright, soluble fluorophore; and the modular probe design enables sensitive, cell-resolved activity imaging that is compatible with sensing diverse species (e.g. glutathione, thioredoxin reductase, hydrogen peroxide).

Conditional HaloTag Ligand: The HaloTag self-labelling protein system enables the covalent attachment of diverse chemical reagents to fusion proteins of interest (POIs). It is widely used for fluorogenic imaging, analyte sensing, or for tethering to increase local reagent concentrations. However, its utility has been limited by the lack of control as existing ligands link chemical and biological components *unconditionally*. The absence of ligands that can respond to a chemical stimulus, is a major design and performance gap in the HaloTag toolbox. Paper 3 introduces a conditional HaloTag ligand that ligates only after uncaging e.g. by light or enzymatic activity. This new ligand expands the HaloTag system with new capabilities: (1) photo-triggered fluorogenic reagents enable spatiotemporally precise protein labelling, (2) photo-triggered heterodimerisers allow light-controlled protein recruitment forcing two POIs into proximity, and (3) enzyme-triggered fluorogens permit durable recording and ratiometric quantification of enzyme activities (e.g. peptidases, oxidoreductases) in ways that should prove easily multiplexable.

Overall, these molecular tools allow probing and manipulating biological systems with unprecedented precision, setting the stage for dissecting various cellular processes with spatial and temporal precision in basic research and translational applications.

9 Outlook

A critical appraisal of the biological performance of the reagents created in this PhD suggests many productive avenues for further chemical development. I will highlight 13 of them within this section.

9.1 Membrane damage probes

Paper 1 presents the first fluorogenic membrane-damage probes capable of staining the entire cytosol of membrane-compromised cells. The ester-caged probe MDG1 was successfully applied to visualise cell damage caused by oxidative stress, toxin-induced pore formation, and ferroptosis across various cell types, including primary mouse neurons *in vitro* and necrotic cells in fly embryos *in vivo*. However, these experiments required the use of simple salt buffers (PBS or HBSS), as the phenolic esters of MDG1 rapidly hydrolysed in nutrient-supplemented cell culture media such as DMEM. This limitation prevents the use of MDG1 in more complex biological contexts where such media or physiological fluids are essential, for example, when studying neuronal axon damage in models of multiple sclerosis or spinal cord injury *in vivo*. More generally, we can state that an ideal membrane damage probe should be hydrolytically stable and detect even small cytosolic volumes (such as thin axons) with zero background. Three main factors limit MDG1 from meeting these requirements: (a) its hydrolytic instability leads to background fluorescence in the extracellular medium, (b) the low brightness of the released fluorophore diminishes the on-target signal, and (c) post-activation cell-exit of the fluorophore reduces the intracellular signal while increasing the extracellular background. **Paper 1** partially addressed the challenge of hydrolytic instability through an alternative probe activation strategy, developing a reductively activated, linear disulfide probe (MDG2), in which the fluorophore is carbamate caged and released via intramolecular cyclisation upon glutathione reduction. MDG2 is hydrolytically stable in DMEM for hours but suffered from limited cellular signal: only up to eight-fold increase in damaged over healthy cells, compared to more than 30-fold increase observed for MDG1. This reduced turn-on efficiency likely results from slower activation kinetics of MDG2, as rapid intracellular signal generation is essential to outcompete fluorophore excretion. **I now propose four avenues for future probe improvement**:

(1) Alternative caging strategies that enable hydrolytic stability *and* fast fluorophore release would be the highest priority for continuing work in this topic. Two possibilities might be: (a) **acetoxymethyl ether caging**, giving aliphatic esters that are much more resistant to spontaneous hydrolysis than the phenolic esters[255] of MDG1, while still allowing rapid cargo release; (b) **bicyclic disulfides** ensure much faster cyclisation than linear disulfides due to thiol pre-organisation[87] and the subsequent fluorophore release can be enhanced by acidifying the phenolic leaving group with *ortho*-fluoride substituents, which should produce substantially higher signal intensities in damaged cells than MDG2 (**Figure 15a**).

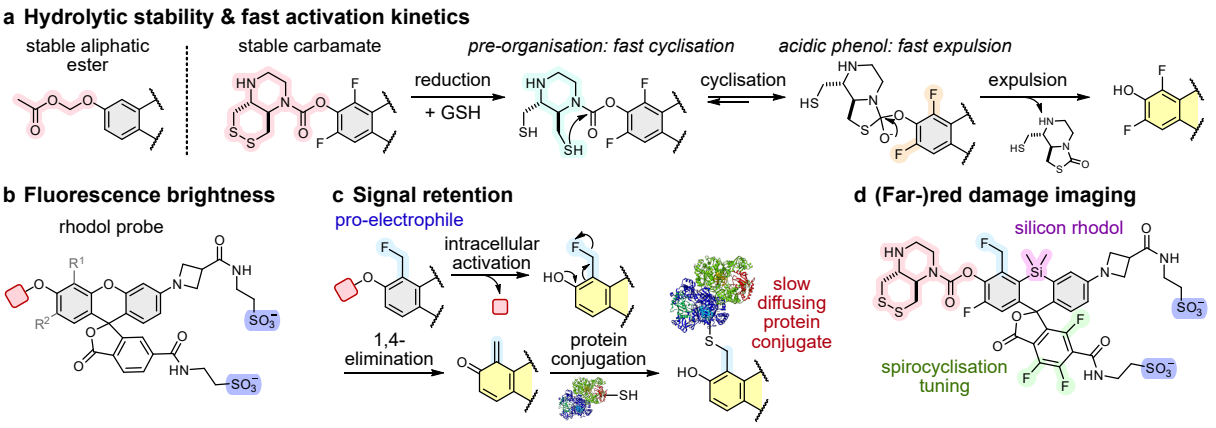

Figure 15: Proposed steps towards high-performance membrane damage probes for *in vivo* applications. **(a)** Hydrolytically stable masking groups like acyloxymethyl ethers or carbamates, to suppress non-specific, extracellular signal background. **(b)** Sulfonated rhodol probes which are brighter than *O*-alkylated fluoresceins and can increase the signal-to-noise ratio. **(c)** Pro-electrophile probes that intracellularly alkylate proteins upon uncaging, for durable signal retention inside damaged cells. **(d)** Red-shifted silicon-rhodol probes that may better reveal membrane damage in thick tissues due to the deeper tissue penetration of (far-)red light.

(2) Enhancing **fluorophore brightness** can further improve probe sensitivity by increasing the fluorescence intensity per released fluorophore, thereby efficiently surpassing the autofluorescence threshold and yielding higher turn-on ratios. The current MDG probe designs are based on *O*-alkylated

fluoresceins which exhibit ca. ten-fold lower brightness compared to unmodified fluoresceins.[256] In contrast, rhodols can be functionalised at the aniline substituent without brightness loss[257], which could be exploited for brighter, disulfonated membrane damage probes (**Figure 15b**).

(3) **Post-activation signal loss** is generally unavoidable in the context of plasma membrane damage, as disruption of the lipophilic bilayer compromises the separation between intra- and extracellular environments. Therefore, even otherwise impermeable molecules can both enter and exit damaged cells, thereby reducing probe sensitivity. Small molecules typically exhibit ca. ten-fold faster diffusion rates than macromolecules such as proteins[258], and in pathological contexts, membrane damage often manifests not as discrete pores but as heterogeneous membrane disorganisation which allows crossing of small, charged molecules while still restricting the permeability of larger macromolecules.[135,136] To counteract signal loss, intracellular protein conjugation could be exploited to enhance signal retention. Urano and co-workers pioneered this concept employing fluoromethyl groups to generate electrophilic quinone methides upon uncaging which rapidly anchor to intracellular, membrane-impermeable proteins via thiol conjugation (see **Section 2.4**).[130] I propose to utilise this strategy for membrane damage probes with prolonged intracellular retention (**Figure 15c**). Alternatively, sulfonated dyes that are fluorogenic upon HaloTag ligation (previously used for extracellular HaloTag labelling[259,260]) could be repurposed to covalently label membrane-compromised cells. Such durable labelling would not only enhance detection sensitivity but also enable post-recovery studies by allowing the tracking of previously damaged cells or their isolation for metabolomic and proteomic analyses.

(4) The modular probe design should enable **spectral tuning** of the xanthene fluorophore through modification of the bridging atom, giving access to red-fluorescent probes like carbo-rhodols (~590/610 nm)[261] or silicon-rhodols (~610/630 nm)[77] (**Figure 15d**). For these red-shifted xanthene probes, careful adjustment of the open-close equilibrium will be essential to ensure complete transition from the spirocyclised to the open form upon uncaging which can be achieved, e.g., by fluorination of the pendent ring or the xanthene core.[51,57] Bright, red-shifted probes would allow damage imaging in complex or thick tissues where deeper light penetration is required compared to conventional 2D cell culture. Additionally, the availability of spectral probe variants would enable the investigation of membrane re-sealing dynamics by sequential staining in different colours. Such experiments could identify compromised cells at each time point, thereby enabling comparisons of membrane recovery and post-damage behaviour as a function of the duration of the membrane damage.

Each of these four proposed strategies is logically precedented by **Paper 1**'s design logic, syntheses, or results, and could deliver substantial benefits in probe performance in cell culture or *in vivo* settings.

9.2 Cell retention probes

Most research groups developing fluorogenic turnover probes currently focus on the design of enzyme-specific activation substrates, while comparatively little emphasis has been given on optimising the cell-retention properties of the released fluorophore. Indeed, the field is still dominated by a few **well-characterised, bright, but non-retained** green to yellow probe scaffolds based on fluoresceins, rhodols and rhodamines. Yet, cellular signal retention is a crucial feature that determines probe sensitivity and single-cell resolution. Although several cell-retention probe designs have been reported, each exhibits drawbacks and lacks the versatility needed for broad utility (see **Section 2.4**). **Paper 2** takes the first step toward addressing this gap through the development of a green-fluorescent rhodol scaffold (TraG) that serves as a general motif for phenol-releasing probes with improved signal retention.

(5) One valuable next step would be to establish a **systematic library of cell-retained scaffolds** spanning the visible to near-infrared spectrum, compatible with the diverse activation substrates previously reported (**Section 2.2.3**) that release phenol or aniline fluorophores. Such a library would allow straightforward design of reliably quantifiable probes "for any enzyme, in any colour": whose scaffold ensures they are soluble, membrane permeable, and release bright cell-retained fluorophores. The development of this scaffold library could substantially accelerate the progress toward those next-generation probes.

To develop such a versatile platform, I propose modifying the TraG scaffold to enable modular, convergent assembly of the functional units: fluorophore, activation substrate, and intracellular trapping

functionalities. This could be achieved by merging the solubilising amine and the acetoxymethyl carboxylate into a single "**trapping group**" (**Figure 16a**). This design would intracellularly generate a zwitterionic fluorophore as the TraG scaffold (which is crucial for reliable signal retention) while simplifying the synthesis by separately preparing the trapping group (**Figure 16b**) and the substrate caged fluorogens which are then connected via mild amide coupling at the final synthetic step (**Figure 16c**). This approach offers several advantages: Separating fluorophore caging from introducing the trapping group (a) **shortens the synthetic route**, which is particularly important for red-shifted xanthene probes (e.g. silicon or carbon bridges: X = $SiMe_2$, CMe_2), and (b) improves the activation **substrate compatibility**, which is limited in TraG probes due to the late-stage alkylation of the carboxylate with acetoxymethyl bromide. This approach could also be extended conveniently to aniline-releasing rhodamine probes (**Figure 16d**). Again, these probes must ensure quantitative uncaging-induced conversion from spirocyclised to open forms, by appropriately tuning the xanthene electrophilicity and pendent ring nucleophilicity, e.g. via fluorination (see **Section 2.2.2**).[51,57,60,67,262] Colour tuning in this modular scaffold would enable flexible matching of probe spectra to experimental requirements (e.g. parallel imaging with fluorescent proteins), simultaneous quantification of different enzymatic activities, or deep-tissue and *in vivo* applications with far-red probes. Systematically providing the key parameters for these cell-retained analogues (signal retention in different cell lines, typical turn-on ratios, and synthetic access) could facilitate rapid adoption of these better-quantifiable scaffolds to generate probes with much higher biological performance.

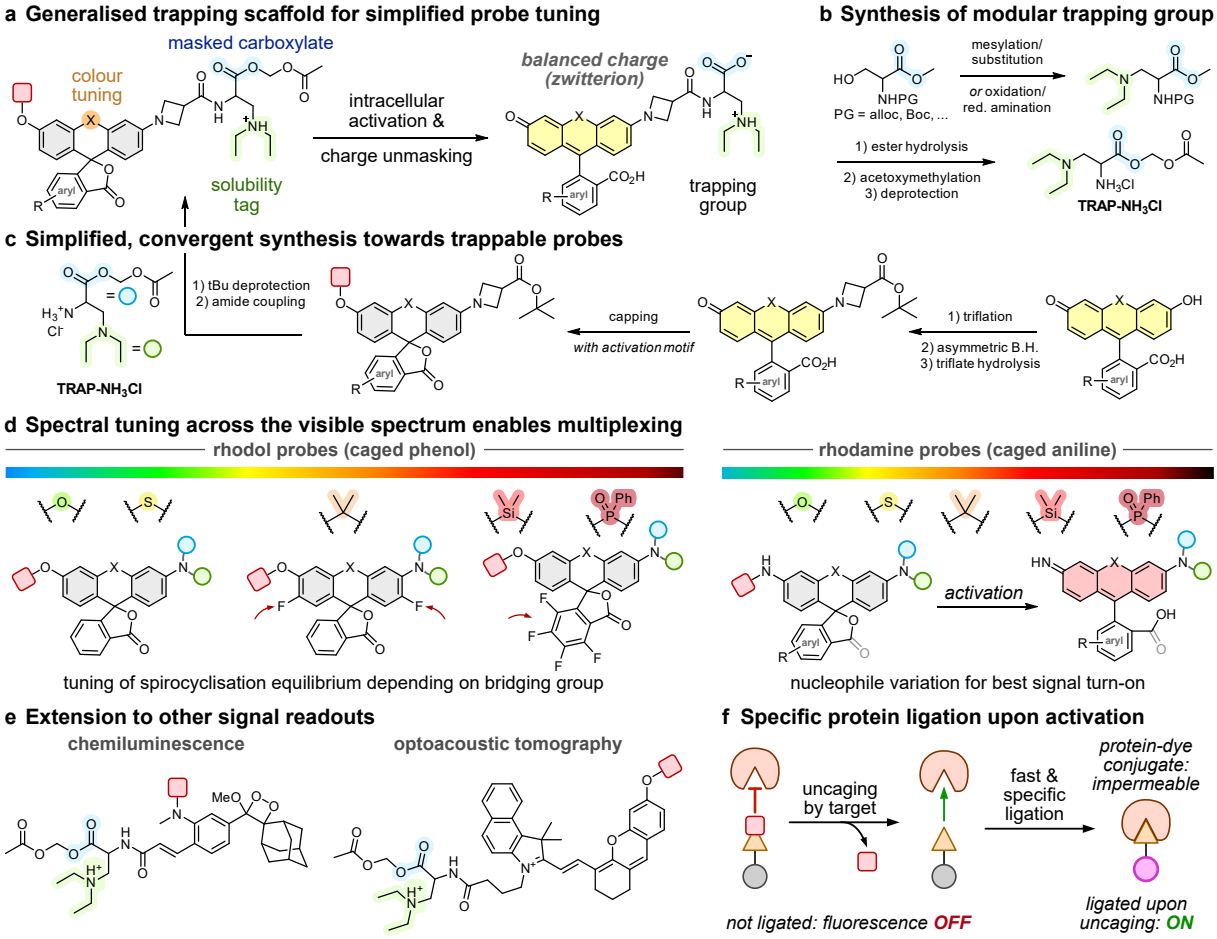

Figure 16: Towards generally applicable, multicolour cell-retained probes. (a–c) Optimised probe design with straightforward synthetic access. **(d)** Spectral tuning of bright xanthene fluorophores enables multiplexed activity imaging and flexible choice of the uncaging substrates (rhodols: phenol release, rhodamines: aniline release). **(e)** A charge-unmasking, zwitterionic trapping group can be utilised for other reporter molecules for chemiluminescence or multispectral optoacoustic tomography. **(f)** Protein-specific ligation upon uncaging is a clean and biologically innocent method for cell-retained fluorogenic probes that can utilise cagable ligands for self-labelling proteins.

(6) The development of a modular **trapping group** as outlined above, combining the features required for reliable intracellular retention, would also allow translation to **other probe scaffolds and modalities**. For example, **chemiluminescent** probes (e.g. aryl-1,2-dioxetanes) emit light upon chemical excitation, thus achieving very high signal-to-noise ratios by avoiding background noise (from autofluorescence in

fluorescence imaging).[32–34,263] **Optoacoustic tomography** represents another non-invasive imaging technique capable of deep-tissue penetration. This method uses laser pulses to excite chromophores and detects ultrasound-frequency thermoelastic pressure waves that are generated during non-radiative, thermal relaxation of the chromophore (e.g. with cyanine dyes).[264,265] By incorporating a general trapping group, it should be possible to generate signal-retained chemiluminescence and optoacoustic probes (**Figure 16e**), extending the retention strategy beyond conventional fluorescence imaging.

Although **Paper 2** significantly improved cellular signal retention via charge-based membrane impermeabilisation, and even if the previous two outlook projects are tackled, this charge-based strategy is likely to always suffer from two major drawbacks: (a) signal retention is not long-term (only a few hours) due to imperfect suppression of passive diffusion and active transporters that can export small molecules like charged fluorophores;[115,116] (b) intracellular trapping occurs independently of probe activation, as the trapping group generates its zwitterion in all cells via esterase-mediated unmasking. While this is advantageous in well-perfused cultures and tissues, this indiscriminate trapping is particularly problematic *in vivo*, as the probe amount available to target cells can be low and non-specific accumulation may lead to toxic concentrations. Urano's quinone-methide releasing fluoromethyl probes (see **Section 2.4**) address this issue by simultaneously activating fluorescence and electrophilicity upon enzymatic activation, only trapping the released fluorophore inside the activating cells. However, quinone-methides can be cytotoxic and often perturb cellular biology.[89,131]

To overcome those limitations, cell-retained probes that generate a **protein-reactive ligand upon** uncaging, which only fluoresces upon covalent binding to a *specific* protein, would seem ideal. Self-labelling proteins are well-suited for this approach, as they covalently react with non-natural ligands without disrupting native biology, while rendering the bound fluorophore membrane-impermeable and thereby cell-trapped (**Figure 16f**). The lack of suitable **cageable, fast-ligating ligand-fluorogens** had previously prevented SLP use for probe designs – a barrier that was now overcome by the cageable HaloTag ligand in **Paper 3**. Outlook **Section 9.3** (**Figure 18**) now goes beyond that paper's results to describe how enzyme-triggered HaloTag ligation could enable sensitive, cell-resolved imaging of *multiple* enzyme activities in parallel.

9.3 Conditional HaloTag ligands

Design optimisation

Paper 3 develops the first cageable HaloTag ligand (CHalo) and demonstrates its utility for spatiotemporally controlled fluorogenic labelling, protein heterodimerisation, and enzyme activity imaging. Several design optimisations could further enhance CHalo performance and enable new applications:

(7) A key performance parameter of self-labelling protein (SLP) ligands is their **ligation kinetics**. Direct comparison of the xanthene-conjugate CHalo-SiR with the conventional chloroalkane ligand (CA-SiR) revealed approximately 10−50-fold slower ligation rates. Rapid ligation can be important for spatially resolved activation experiments in which HaloTag ligation must be faster than post-activation diffusion and potential cell-exit of the ligand. Slow ligation rates reduce the spatial resolution as labelling occurs in neighbouring cells, thus requiring higher photouncaging light doses to achieve sufficient signal, and they decrease the sensitivity of enzyme probes when only a fraction of the ligand binds HaloTag in the activating cell. Thus, improving the CHalo ligation rates should be a priority for future endeavours.

Analysis of the crystal structure of HaloTag and its CA ligand suggests strategies to achieve this goal as the ligand shows a distinct ligand orientation inside the binding pocket, with an overall linear chain and bonds 4−6 adopting a *syn*-conformation (**Figure 17a**). Tadross and co-workers demonstrated that restricting this bond orientation via an aryl ring, and filling empty space in the protein pocket with a methoxy substituent can substantially accelerate binding kinetics (up to 45-fold for non-xanthene cargos with HTL.2, **Figure 17b**).[211] In contrast, the initial CHalo ligand, developed in **Paper 3**, positions the aryl ring one methylene unit further from the chloride and lacks substituents to fully occupy the binding pocket (**Figure 17c**), suggesting that ligation could be enhanced by repositioning the aryl ring closer to the chloride and/or introducing suitable aryl substituents (**Figure 17d**). I propose systematic screening for

aryl substituents at different positions to identify CHalo variants with ligation rates comparable to (or faster than) the CA ligand, ideally with lower substrate dependency.

(8) Beyond theoretical labelling kinetics measured in cell-free assays at low concentrations (typically 10−50 nM), **effective HaloTag labelling** in cells is often limited by poor membrane permeability or low **aqueous solubility**.[40] The caged **CHalo-SiR** fluorogens are relatively lipophilic due to spirocyclisation and are thus expected to be membrane permeable. However, aqueous solubility of such lipophilic reagents is low, resulting in aggregation in our experiments (even below 1 µM), reducing the imaging quality and experimental reproducibility. A recent study claims that the cargo benzamide can be alkylated without impairing kinetics[260], which – if true – could enable the introduction of a basic amine (**Figure 17e**) to ensure solubility at relevant concentrations while maintaining membrane permeability.

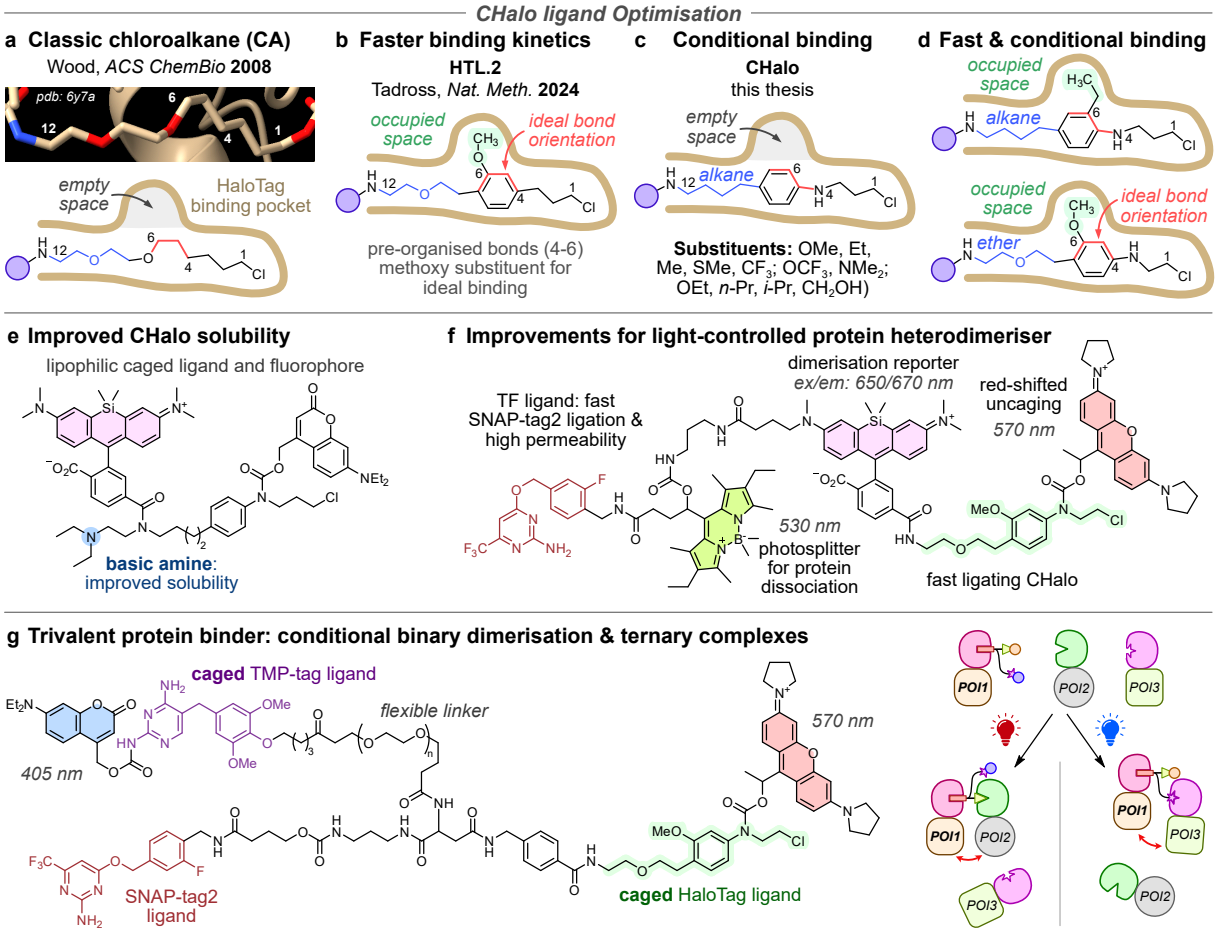

Figure 17: Property optimisation of (caged) CHalo reagents. (a–d) Design optimisation of the CHalo ligand towards even higher HaloTag ligation rates. **(e)** Basic amines can improve the CHalo solubility that compromises especially caged-fluorogen performance. **(f)** Improved CHalo protein heterodimerisers could implement red-shifted photocages to activate HaloTag ligation, a fluorogenic silicon-rhodamine to report successful HaloTag binding, the membrane permeable and fast-ligating TF ligand (for SNAP-tag2) and a wavelength-orthogonal photosplitter to induce protein dissociation. **(g)** Trivalent protein binders with orthogonally caged SLP ligands can be used for conditional binary dimerisation and the formation of ternary protein complexes.

(9) The **photouncaging efficiency** could be improved using cages that transiently generate secondary cations upon uncaging. That steric repulsion should suppress the recombination of the contact ion pair[162] (**Section 3.2**), while also reducing side-reactions of the CHalo aniline with the coumaryl cation (that resulted in significant formation of coumaryl-alkylated CHalo in our cell-free photouncaging assays).

(10) The light activated **protein heterodimeriser** developed in **Paper 3** could also be modified for broader applications (**Figure 17f**). (a) The SNAP-tag ligand benzyl guanine (BG) suffers from low membrane permeability and moderate ligation rates. Implementing the recently published, more **permeable SNAP-tag2 ligand TF**, which achieves up to 100-fold faster SNAP ligation[206], would enhance the performance of a second-generation CHalo dimeriser. (b) Introducing a fluorogenic silicon-rhodamine would allow fluorescence **reporting of successful HaloTag ligation**. (c) A "**photosplitter**" could be

used for light-controlled dissociation, by employing two photocages with distinct uncaging wavelengths: CHalo uncaging with long-wavelength light followed by photo-splitting with shorter wavelengths, enabling reversible control over protein interactions. (d) The **linker length and flexibility** of the dimeriser should be varied, over a library of dimerisers. Users should then test these varying linkers for their precise protein pair, to individually balance proximity and flexibility, optimising interactions at the desired site. (e) Future designs could extend the CHalo dimeriser to trivalent SLP-ligands with two of three ligands orthogonally photocaged (**Figure 17g**). This would enable **conditional binary dimerisation** (POI1&POI2 *or* POI1&POI3) or, potentially, photo-controlled formation of ternary protein complexes (POI1-POI2-POI3) if suitably permissive ligation/binding domains can be addressed with long linkers.

Towards non-invasive, durable and multiplexed enzyme activity imaging

Paper 2 introduces a charge-based strategy for cellular signal retention of fluorogenic turnover probes to visualise and quantify enzymatic and analyte bioactivity. While this approach significantly enhances probe performance, charged small molecules inherently face limits to long-term retention due to slow passive diffusion and active transporters.[115,116] In contrast, macromolecular impermeabilisation offers much greater durability, a principle exploited in Urano's quinone-methide releasing fluoromethyl probes.[130] These probes rapidly label intracellular protein thiols preventing post-activation fluorophore leakage and thereby achieve single-cell resolution. However, their toxicity and potential interference with the activating enzyme, potentially disturbing the biological system they aim to study, make them invasive. **Enzyme-caged CHalo-fluorogens** address this problem by coupling enzymatic activation with specific, covalent HaloTag labelling providing a non-invasive, cell-retained readout (**Figure 18a**). Until now, turnover probes could not exploit self-labelling protein chemistry because cageable *and* fast ligating ligands were unavailable. **Paper 3** resolves this issue by developing the first cageable HaloTag ligand featuring fast ligation rates (~10^6 $M^{-1}s^{-1}$) and demonstrates the utility of enzyme-caged **CHalo-SiR** reagents for activity imaging of leucine aminopeptidase, thioredoxin, and the reductant glutathione. Faster ligating CHalo ligands (see **Figure 17a–d**) should further improve signal capture and cellular resolution by efficiently trapping released fluorogens within the activating cell before they diffuse away.

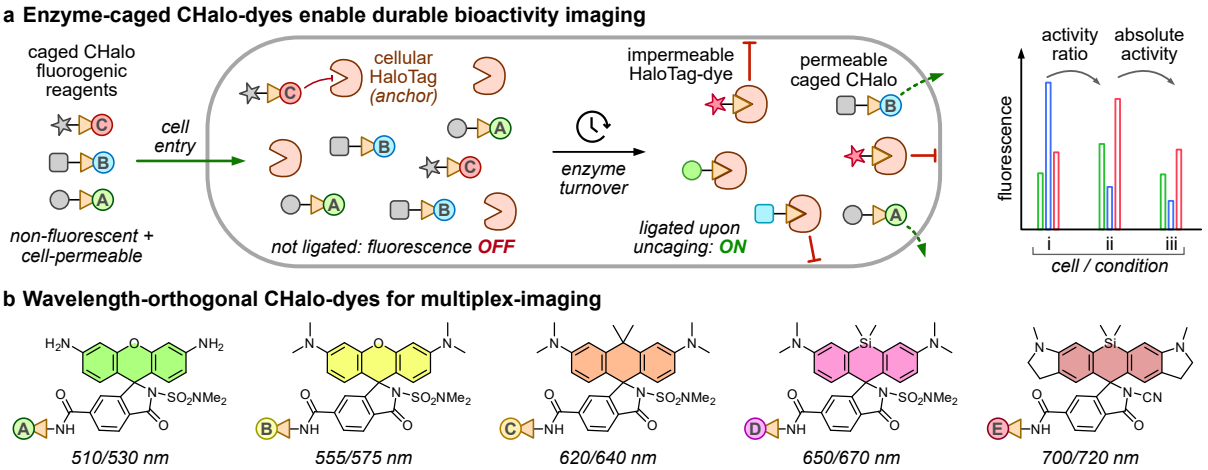

Figure 18: Enzyme-caged CHalo fluorogens enable durable and parallel enzyme activity imaging. (a) Schematic overview of multi-enzyme imaging with orthogonally caged, fluorogenic CHalo-dyes that ligate to HaloTag upon enzymatic turnover and thereby become membrane impermeable and fluorescent – allowing ratiometric sensing of bioactivity (relative and absolute activity differences) with single-cell resolution. **(b)** Green to far-red xanthene fluorophores can be used as bioactivity recorders and tuning their spirocyclisation equilibrium improves their membrane permeability and fluorogenicity for wash-free, zero-background imaging.

(11) Future work should expand this concept from single-colour imaging to **multi-colour enzyme activity profiling**, enabling simultaneous and ratiometric quantification of different enzyme activities in parallel (**Figure 18a**). Such a system would combine the advantages of the HaloTag platform, with those of fluorogenic dye ligation and enzyme-selective activation substrates: (a) HaloTag serves as an intracellular anchor, retaining activated ligands; (b) a palette of bright, fluorogenic dyes spanning the visible spectrum is available, all of which are fully spirocyclised (non-fluorescent) in aqueous media and become fluorescent only upon HaloTag ligation (**Figure 18b**);[40] (c) since benzyl caging of the CHalo fully suppresses ligation, previously established activation substrates (see **Section 2.2.3**) can be

immediately integrated via benzylic 1,6-elimination spacers (see **Section 2.2.4**); (d) ratiometric readouts of enzyme activity (activity X relative to activity Y) could be almost independent of the probe-mix concentration applied and the incubation time in the assay: making it particularly suitable for *in vivo* applications where probe distribution is inhomogeneous and time-variant.

Such multiplexed CHalo imaging would enable the study of *relative* enzyme activities within interconnected pathways, for example assessing the dynamic changes of redox enzymes like thioredoxin reductase relative to thioredoxin during the cell cycle, monitoring glycosidases' activities under metabolic stress, or comparing peptidases' activities in cancerous versus healthy tissues. Ultimately, CHalo probes can provide a general, non-invasive framework for highly sensitive and quantitative activity imaging.

Photoswitchable HaloTag ligands for reversible activation

Photocaged CHalo reagents enable local activation of HaloTag ligation, but the precision achieved is limited due to post-activation ligand diffusion, which competes with the local labelling. While diffusion is less problematic for anchored heterodimerisers bound to (membrane) proteins, it remains a major limitation for purely small molecule reagents like CHalo fluorogens, where rapid dye diffusion prevents (sub-)cellular resolution. Improving the ligation kinetics could partially solve this problem if reaction rates approach diffusion rates (as observed for the fastest HaloTag dye CPY-CA[204]). However, since photouncaging is irreversible, diffusion of the activated ligand inevitably results in off-target labelling.

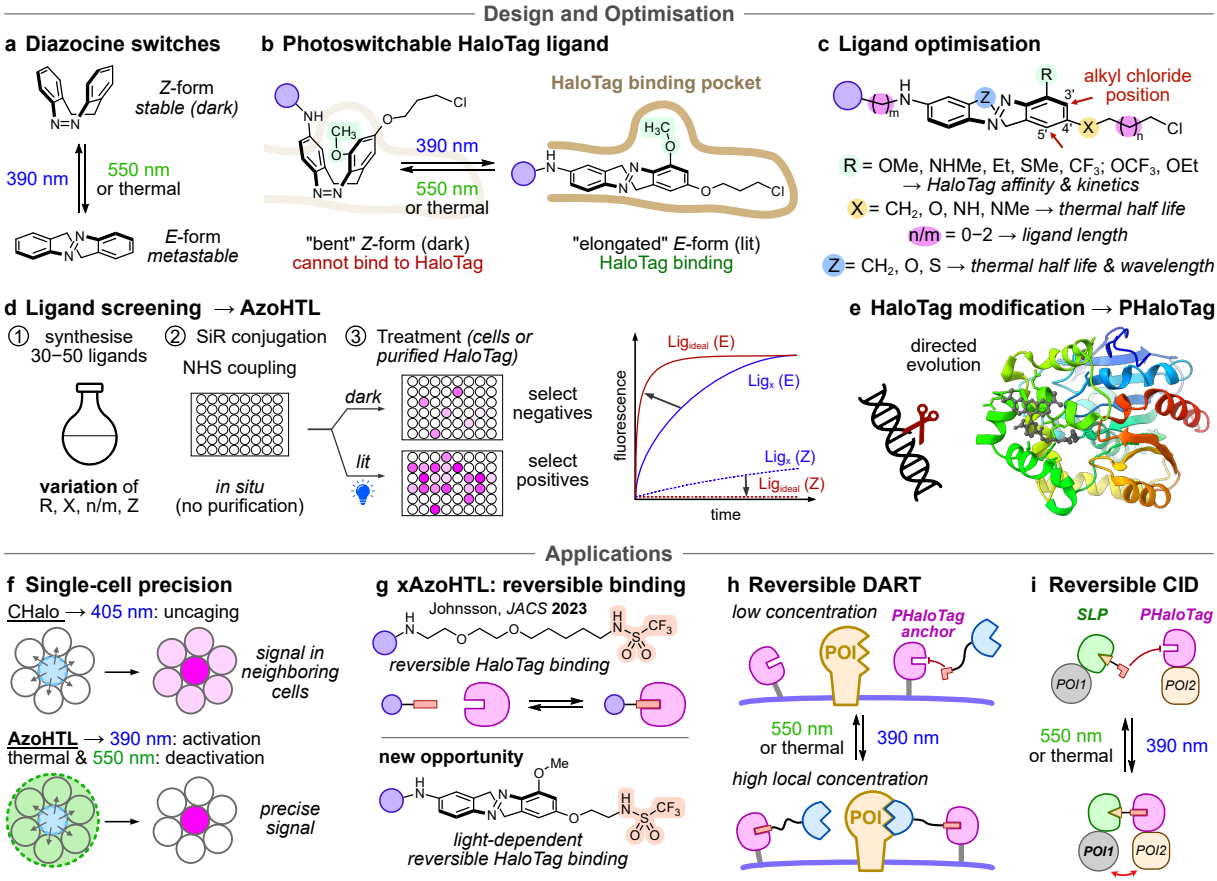

Figure 19: Towards reversibly light-activatable and reversibly binding HaloTag ligands. (a−b) Diazocine photoswitch based HaloTag ligands adopt elongated structures upon blue-light illumination to penetrate into the HaloTag protein tunnel and are quantitatively back-isomerised to their "bent", thermally stable *Z*-form which should not be able to bind HaloTag. **(c−d)** Photoswitchable HaloTag ligands (AzoHTLs) can be modified at several sites and their structure should be optimised by screening various linker lengths, chloroalkane attachment sites, functionalisations to ideally fit the HaloTag binding pocket and bridging atoms. **(e)** Protein engineering by directed evolution may be required for fast binding of active (*E*)-AzoHTL and full binding suppression of inactive (*Z*)-AzoHTL to provide a new, optimised HaloTag variant for photoswitchable ligation (PHaloTag). **(f)** AzoHTL-dye conjugates can enable local labelling with single-cell precision by suppressing off-target ligation in neighbouring cells via fast thermal relaxation or deactivation with green light (rescuing these cells from the active reagent). **(g)** Photoswitchable AzoHTLs can utilise reversible HaloTag ligand structures that do not covalently label the protein[212] to enable photoswitchable, reversible HaloTag binding that could be applied to **(h)** reversible DART (drug acutely restricted by tethering) or **(i)** reversible CID (chemically induced protein heterodimerisation).

(12) A conceptually superior solution could utilise **reversible ligand activation**, enabling precise local labelling when ligands spontaneously revert to their inactive form outside the illuminated region or can be switched off by a secondary light stimulus. Photoswitches fulfil these criteria by reversibly adopting distinct conformations upon illumination (**Figure 19a**, see also **Section 3.3**). A photoswitchable HaloTag ligand could therefore be designed to fit into the HaloTag binding pocket only in its elongated, light-activated form, while the "bent" dark-state conformation prevents ligation. Bridged azobenzenes (or diazocines) represent ideal photoswitches for this strategy as they adopt a bent *Z*-form in the dark and convert to a linear *E*-form upon blue-light illumination, which can be quantitatively reversed with green light (**Figure 19b**).[266,267] Such an "**AzoHTL**" ligand would bind to HaloTag in a light-dependent manner. I propose screening different ligand structures to optimise "lit" ligation rates and "dark" suppression of the binding by varying the aryl substituents (to fully fill the space in the protein binding pocket), the alkyl chain lengths (*m, n*), and alkyl chloride attachment sites on the aryl ring (**Figure 19c**). The thermal relaxation rates can be tuned by modifying the bridging atoms "X" and "Z" (with thermal half-times ranging from minutes to days).[268,269] To optimise performance, this small ligand library (30−50 compounds) can be coupled to fluorogenic SiR dyes and screened for labelling efficiencies in both lit and dark state either with purified HaloTag protein or with HaloTag expressing cells which would additionally select for cellular uptake (**Figure 19d**). If none of the AzoHTL ligands both fully suppresses HaloTag ligation prior to activation *and* rapidly ligates after illumination, mutagenesis and directed evolution could generate an optimised photoswitch-binding HaloTag variant (**PHaloTag**) with high specificity for the best-performing AzoHTL (**Figure 19e**). Photoswitchable AzoHTL ligands would provide a **reversibly activatable but irreversibly binding** SLP system enabling precise and durable local labelling, potentially with subcellular resolution, either with a diazocine that rapidly relaxes to its *Z*-form thermally or by applying green light outside the region of interest to back-isomerise the ligand (**Figure 19f**).

(13) Alternatively, building on the known exchangeable HaloTag ligands (xHTLs)[212], a **reversibly activatable and reversibly binding** ligand (**xAzoHTL**) can be designed by replacing the chloride with a non-covalent binding group such as the trifluoromethyl sulfonamide of the T5 ligand (**Figure 19g**).Unlike the AzoHTL-chloride, which ligates permanently and covalently to HaloTag, xAzoHTL would reversibly and non-covalently dock to HaloTag in its light-activated form and dissociate upon backswitching to its inactive form. This could enable a range of new applications, including fully reversible, spatially controlled protein labelling; light-dependent receptor modulation by tethering agonists to HaloTag to increase the local concentration (DART, **Figure 19h**); or reversible chemically induced dimerisation of proteins (CID, **Figure 19i**). Such reversible CIDs could, for example, allow to study the effects of temporary induction of protein degradation or phosphorylation with kinases. Crucially, these reversible HaloTag ligands would not only enable previously inaccessible applications but also leverage the widespread use of HaloTag-fusion proteins for immediate implementation in existing experimental systems.

9.4 Next steps for these conditional probes and fluorogenic reagents

Among the various opportunities arising from this work, future efforts should prioritise the optimisation of the conditional HaloTag ligand CHalo, as it represents the most versatile and impactful direction for further development, addressing even some key limitations of the cell-retention probes developed in Paper 2. Improving its ligation kinetics will be particularly critical to unlock its full potential, since labelling speed ultimately determines overall experimental performance. In parallel, the development of a reversible AzoHTL ligand could elevate the HaloTag chemistry into a fully stimulus-responsive system, paving the way for real-time chemical control of protein behaviour in complex biological environments.

E. APPENDIX

10 Supporting information

Supporting information for Paper 1

Supporting information to the publication: “Fluorogenic Chemical Probes for Wash-free Imaging of Cell Membrane Damage in Ferroptosis, Necrosis, and Axon Injury” (pages 72−131).

Supporting information for Paper 2

Supporting information to the publication: “A Modular Scaffold for Cellularly-Retained Fluorogenic Probes for Sensitive Cell-Resolved Bioactivity Imaging” (pages 132−209).

Supporting information for Paper 3

Supporting information to the publication: “Logic-gating the HaloTag system with Conditional-Halo-ligator 'CHalo' reagents” (pages 210−340).

Supplementary Information to

Fluorogenic chemical probes for wash-free imaging of cell membrane damage in ferroptosis, necrosis, and axon injury

Philipp Mauker[1,#], Daniela Beckmann[2,3#], Annabel Kitowski[1], Constanze Heise[1], Chantal Wientjens[4], Andrew J. Davidson[5], Simone Wanderoy[6,7], Gabin Fabre[8], Angelika B. Harbauer[7, 9,10] , Will Wood[5], Christoph Wilhelm[4], Julia Thorn-Seshold[1], Thomas Misgeld[9,10,11], Martin Kerschensteiner[2,3,9], Oliver Thorn-Seshold[1,*]

[1] Department of Pharmacy, Ludwig-Maximilians University of Munich, Butenandtstr. 7, 81377 Munich, DE.

[2] Institute of Clinical Neuroimmunology, LMU University Hospital, Ludwig-Maximilians University of Munich, Marchioninistr. 15, 81377 Munich, DE.

[3] Biomedical Center (BMC), Faculty of Medicine, Ludwig-Maximilians University of Munich, Grosshaderner Str. 9, 82152 Martinsried, DE.

[4] Immunopathology Unit, Institute of Clinical Chemistry and Clinical Pharmacology, Medical Faculty, University Hospital Bonn, University of Bonn, Venusberg-Campus 1, 53127 Bonn, DE.

[5] Institute for Regeneration and Repair, The University of Edinburgh, Edinburgh BioQuarter, 5 Little France Drive, Edinburgh, EH16 4UU, UK

[6] University Hospital, Technical University of Munich, Ismaninger Straße 22, 81675 Munich, DE

[7] Max Planck Institute for Biological Intelligence, Am Klopferspitz 18, 82152 Martinsried, DE

[8] Pharmacology & Transplantation, UMR 1248 INSERM, Univ. Limoges, 87000 Limoges, FR

[9] Munich Cluster for Systems Neurology (SyNergy), Feodor-Lynen-Str. 17, 81377 Munich, DE.

[10] Institute of Neuronal Cell Biology, Technical University of Munich, Biedersteiner Straße 29, 80802 Munich, DE.

[11] German Center for Neurodegenerative Diseases (DZNE), Feodor-Lynen-Str. 17, 81377 Munich, DE.

[#] The two first authors contributed equally to this work. *Corresponding author.

Table of Contents

Author Contributions: P.M. performed synthesis, chemical analysis, enzymatic cell-free studies, cell biology, flow cytometry, coordinated data assembly and co-wrote the manuscript. D.B. performed cell biology, confocal microscopy and image analysis / quantification. A.K. and C.H. performed cell biology and flow cytometry. C. Wientjens performed cell biology for ferroptosis sensing. A.D. performed necrosis imaging in Drosophila. S.W. performed axonal imaging in microfluidics chambers. G.F. performed PerMM permeation coefficient calculations. J.T.-S., C. Wilhelm, T.M. and M.K. supervised cell biology. W.W. supervised necrosis imaging in Drosophila. A.B.H. supervised axonal imaging in microfluidics chambers. T.M. and M.K. supervised confocal microscopy. T.M., M.K. and O.T.-S. designed the concept and experiments. O.T.-S. supervised all other experiments and co-wrote the manuscript with input of the other authors. Correspondence and requests for materials should be addressed to O.T.-S.

ACKNOWLEDGMENT: We acknowledge support from the Joachim Herz Foundation (Research Fellowships to P.M. and J.T.-S.); from the Studienstiftung des Deutschen Volkes (PhD scholarships to P.M. and D.B.); and the Munich Graduate School of Systemic Neurosciences (D.B.). We thank Dr. Andrew Lees (Fina Biosolutions LLC, MD, USA) for many helpful discussions while planning and designing dextran conjugates. We thank Dr. Lees and Dr. Samson Gebretnsae (Fina Biosolutions LLC, MD, USA) for performing all custom syntheses of dextran conjugates. We thank Alexander Sailer and Adrian Müller-Deku (LMU) for initial work on fluorescein diacetate NHS ester conjugations to aminodextrans; Bekkah Bingham (LMU) for chromatographic analysis of the integrity of fluorescein diacetate in dextran conjugates; and Philip Woelfle (LMU) for initial testing of dextran conjugates. We are grateful to Henrietta Lacks, now deceased, and to her surviving family members for their contributions to biomedical research.

1 Overview of all fluorogenic probes and fluorophores

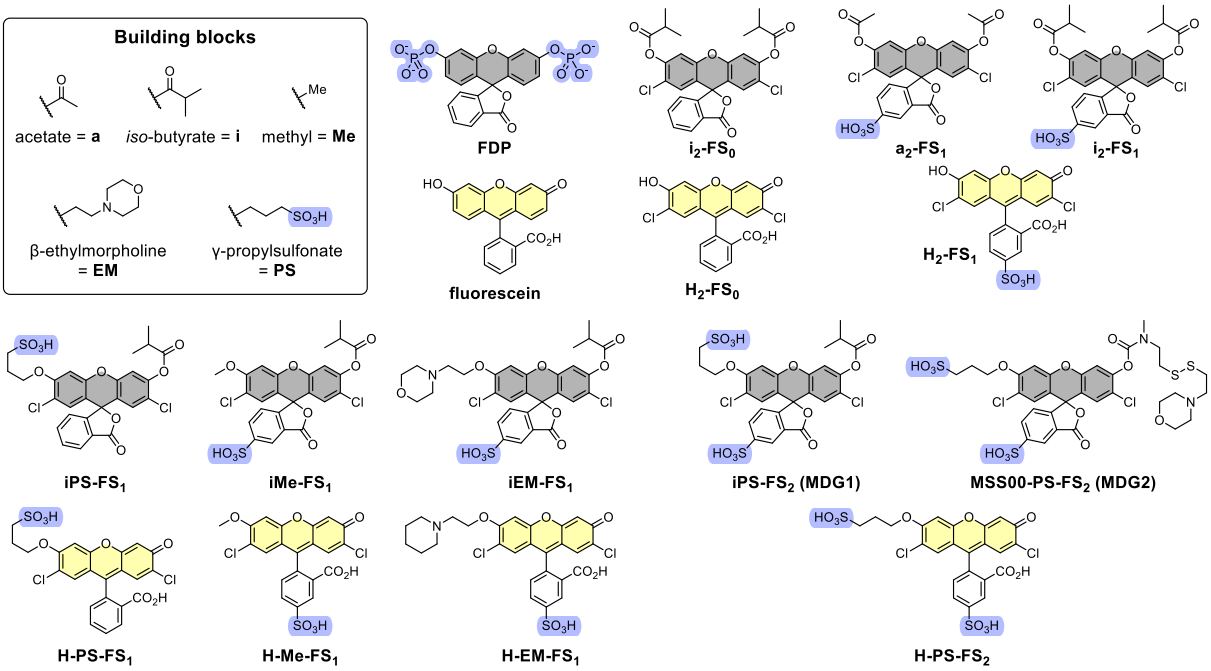

Figure S1: Structure overview of all probes and fluorophores and their naming rationale.

2 Photocharacterisation and cell free stability / esterase characterisation

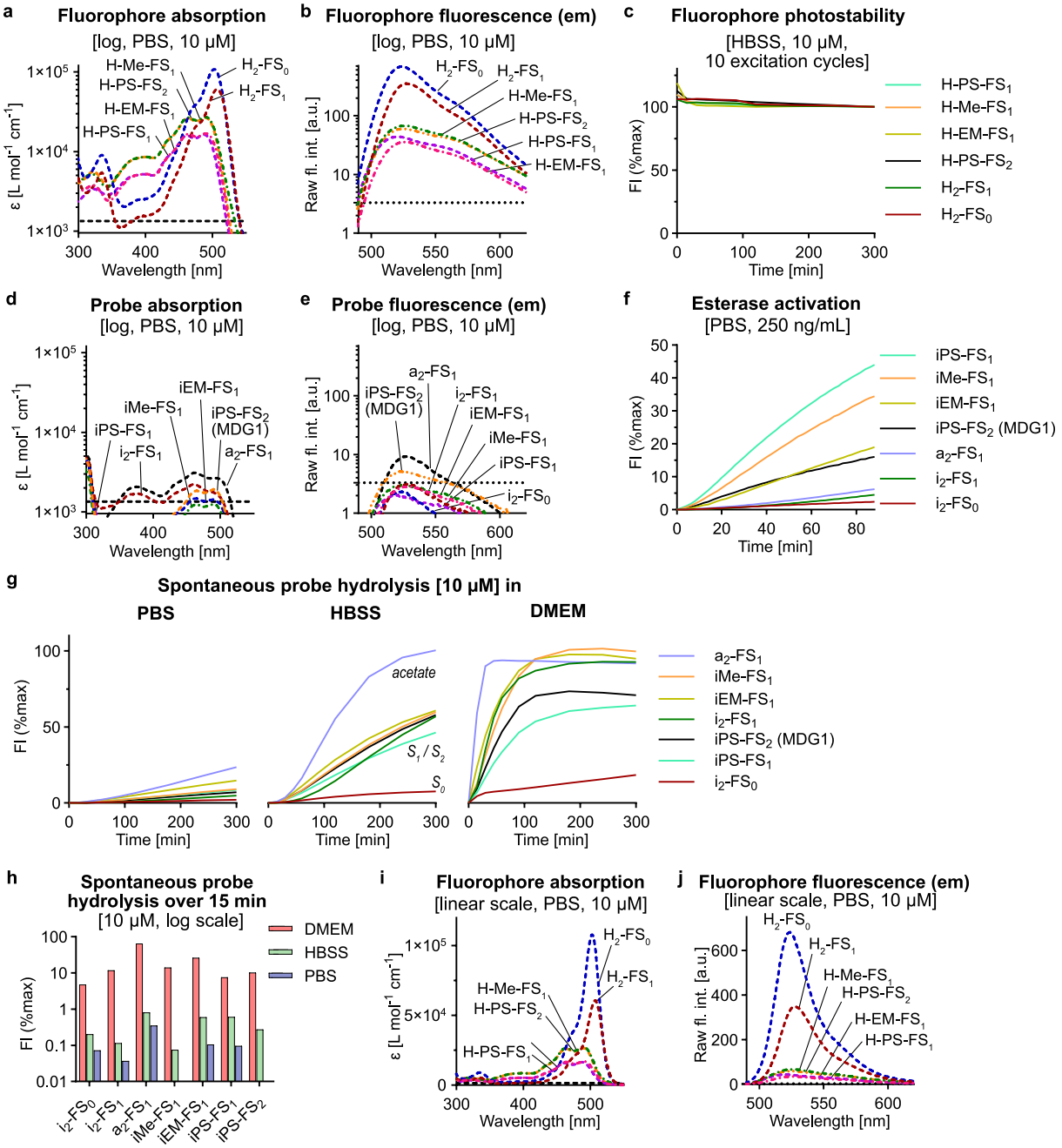

Figure S2: **Photocharacterisation, probe stability towards hydrolysis and *in vitro* activation by esterase (a)** UV-vis absorption spectra of fluorophores (10 µM in PBS); **(b)** fluorescence emission spectra (excitation: 485 nm) of the fluorophores (10 µM in PBS); **(c)** photostability of the fluorophores during plate-reader imaging (10 acquisitions over 6 h). **(d)** UV-vis absorption spectra of probes (10 µM in PBS); **(e)** fluorescence emission spectra (excitation: 485 nm) of the probes (10 µM in PBS); **(f)** time-course of probe activation by porcine liver esterase (250 ng/mL, probe conc.: 10 µM in PBS). **(g)** spontaneous probe hydrolysis time-courses in DMEM, PBS and HBSS (probe conc.: 10 µM); **(h)** summary of spontaneous probe hydrolysis after 15 min in DMEM, HBSS and PBS (probe conc.: 10 µM). **(i)** UV-vis absorption spectra of fluorophores (10 µM in PBS); **(j)** fluorescence emission spectra with linear vertical scale (excitation: 485 nm) of the fluorophores with linear vertical scale (10 µM in PBS). Note logarithmic vertical scales in panels **a-e and h**, vertical dashed line marks 5% level of H-Me-FS$_1$ fluorescence / extinction coefficient.

Regarding fluorescence properties: H_2-FS_0 shows one absorption peak with a maximum at 503 nm in PBS (pH = 7.4) whereas **H_2-FS_1** is red-shifted slightly to 507 nm as expected for electron withdrawing substituents such as the sulfonate.[1]

Quantum yields of the novel fluorophores were determined the following equation (Resch-Genger and co-workers[2]):

$$\Phi_{f,x} = \Phi_{f,st} \cdot \frac{F_x}{F_{st}} \cdot \frac{1 - 10^{-A_{st}(\lambda_{ex})}}{1 - 10^{-A_x(\lambda_{ex})}} \cdot \frac{n_x(\lambda_{em})^2}{n_{st}(\lambda_{em})^2}$$

Fluorescein was used as a reference fluorophore with a quantum yield of $\Phi_{f,st}$ = 0.85 (in PBS, pH=7.4).[3]

Compound	Quantum yield
H_2-FS_0	0.78
H_2-FS_1	0.75
H-Me-FS_1	0.24
H-EM-FS_1	0.18
H-PS-FS_1	0.23
H-PS-FS_2	0.22

Regarding enzymatic turn-on: To be detectable, the probes must be rapidly enzymatically processed upon cellular entry to generate a fluorescent signal. We assessed probe activation by the model enzyme porcine liver esterase (PLE, 250 ng/mL, 15 U/mg) in PBS as the least hydrolysing buffer (**Fig S2f**). All probes are activated above spontaneous hydrolysis in PBS proving the activation by esterases as desired, but clear differences between the two probe classes are observed: all mono-capped probes are activated much faster than the doubly capped probes (in terms of percentage maximum fluorescence) which stems from their different activation profiles discussed above representing a key advantage of mono-capped probes. Michaelis-Menten kinetics measurements (**Fig S3**) show that our sulfonated probes have similar substrate affinity as the non-sulfonated control **i_2-FS_0** (K_m values range from 10 to 36 µM) and around 10-fold higher turnover numbers.

Regarding spontaneous probe hydrolysis: We expected our sulfonated probes to be less hydrolytically stable than their non-sulfonated analogues, due to a lower tendency to aggregate and potentially to local pH depression, which both should enhance hydrolytic reactivity. We examined the probe stabilities in PBS, the standard cell culture medium DMEM (without FCS) and HBSS. PBS is a very simple cell buffer containing sodium and potassium chloride as well as sodium hydrogen- and dihydrogen-phosphates. The HBSS we used contains the same ingredients (in different amounts) plus additional salts (calcium and magnesium chloride and sulfate, sodium hydrogencarbonate), as well as glucose, to ensure longer cell viability in experiments as compared to PBS, although we expected that the stronger Lewis acids could better promote ester hydrolysis. The cell culture medium DMEM additionally contains amino acids, which we expected to give even higher ester cleavage by trans-acylation, as well as vitamins (we did not supplement it with FCS). We thus expected PBS to show the lowest spontaneous probe hydrolysis and DMEM to show the highest, while cellular viability during longer-term experiments should increase in the same order.

Indeed, the hydrolysis time-courses show that sulfonated probes are hydrolysed faster than non-sulfonated; and that the acetate probe (**a_2-FS_1**) is much more labile than any isobutyrate probe (**Fig S2g**). After 15 min incubation at 37 °C which is a typical timeframe for cell experiments, all sulfonated probes show high hydrolysis in DMEM (70% for **a_2-FS_1**, 5-25% for isobutyrate probes) which is strongly reduced in HBSS (<1% activation) and in PBS there is almost no activation (<0.1% activation except for **a_2-FS_1**) (**Fig S2h**).

For all cellular experiments, we now used HBSS by default as it offers low hydrolysis of chloro-stabilised isobutyrates with better cell viability maintenance than PBS.

Michaelis-Menten kinetics

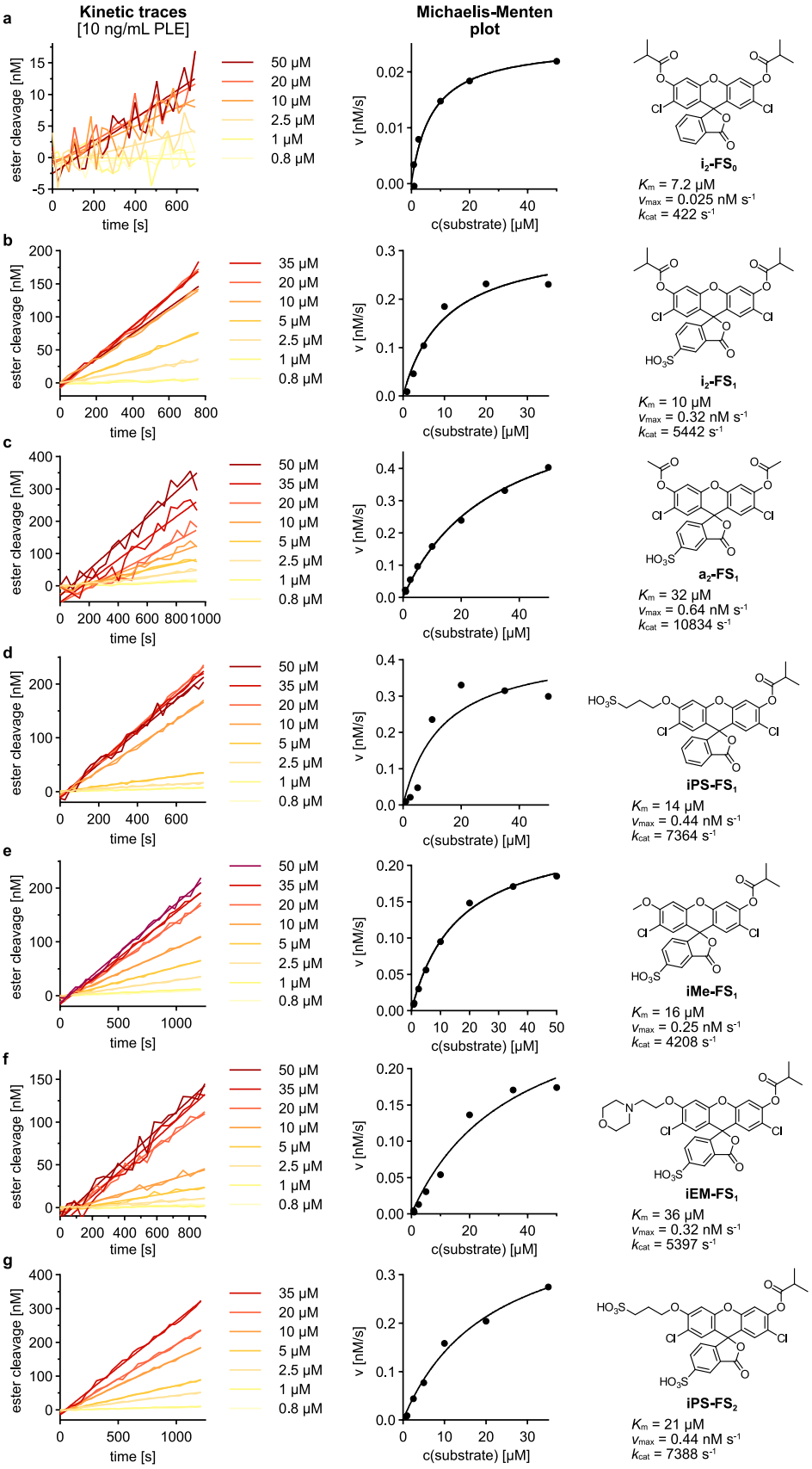

Figure S3: Kinetic traces and Michaelis-Menten plots for probe activation with porcine liver esterase (10 ng/mL, 229 U/mg) in PBS (pH = 7.4). Interestingly, sulfonation of the probes caused an up to ~10-fold apparent increase in enzymatic turnover (k_{cat}) compared to the non-sulfonated **i_2-FS$_0$**, though we presume this reflects a greater availability of the probe in the aqueous assay rather than an enzyme preference (**Figure S3**).

3 Supporting Notes

3.1 Supporting Note 1 - Cell-Impermeable Stains and Fluorogenic Probes

Always-On Imaging Agents vs Fluorogenic Probes: Permanently fluorescent, cell-excluded compounds can be useful *in vitro* stains for cells with leaky membranes, since low-background images can be taken by exchanging the extracellular medium before imaging and/or by background-subtracting the homogenous signal of the extracellular medium. However, for *in vivo* imaging, “washing out” free probe is usually impossible so a high background signal remains, and this background signal usually cannot be compensated away due to its inhomogeneous 3D distribution. In this situation, fluorogenic probes offer a key advantage. Due to their fluorescence switch-on, true off→on fluorogenic probes can give high signal-to-background ratios and therefore be useful for wash-free *in vivo* imaging, as long as they are suitably stable in the extracellular medium, and as long as they are retained in those cells which originally activated them.

Other Factors, Propidium iodide (PI): Conceptually, PI achieves fluorescence turn-on by DNA-intercalation, not by enzymatic bond cleavage: so, its "impermeable-off→entered-activated" switch concept is not transferable to other types of bioactives or imaging agents or even to other situations such as cell surface imaging. Even as a stain for permeabilised cells, it is optically limited in even its cellular applications, due to poor fluorescence brightness, and broad spectral peaks which makes it incompatible with many other dyes. Biologically, the DNA intercalation of PI becomes problematic when not used for live/dead staining but for live cell imaging of cells which are damaged but not necessarily dead yet, particularly in an *in vivo* context where washout of PI that has not been spontaneously uptaken cannot be ensured before endocytosis causes nonspecific uptake, and where PI's bioactivity as a DNA intercalator is then unacceptable over the longer experimental timescales of useful studies, due to its slow/very slow excretion.

Phosphates as a non-general impermeabilising capping group: The dianion fluorescein diphosphate (**FDP**) is an example of an impermeabilised probe, that natively addresses cell-surface enzymes. Its two charged phosphates that also serve as fluorescence blocking groups are activated by enzymatic triggers (phosphatases); however, suitable phosphatases act at the cell surface of all healthy cells, whereupon the more lipophilic fluorescein product can then enter the cell or disengage to diffuse away into the medium; and this activation is therefore not selective for damaged cells. Due to the 2D activation surface, the activation of **FDP** is also comparably slow; and even after cellular uptake, the released fluorophore can diffuse back out of the cell which reduces the observed intracellular over extracellular fluorescence intensities.

Evaluation of a membrane damage probe by confocal microscopy: Our membrane damage probe evaluation goal for *healthy cell* treatments was to assess (a) intracellular signal, that quantifies how much probe undesirably entered healthy cells and was activated by deacylation, i.e. a "false positive" signal for a membrane damage probe; to (b) extracellular signal, that quantifies spontaneous probe hydrolysis in the medium, which is also undesirable since this sets the background level against which a probe must provide higher signal for damaged cells.

3.2 Supporting Note 2 - The Biology of Membrane-Damaged Cells

Cell membrane integrity can be damaged by a variety of physiological and pathological processes: from physical stress (e.g. mechanical injury) to chemical modification (e.g. peroxidation), or protein pore formation (e.g. programmed cell death, or insertion of bacterial toxins). All of these impair the separation of intracellular and extracellular spaces and allow otherwise membrane-impermeable species to cross membranes.[4,5]

Membrane-damaged cells are an interesting study population as they find themselves at the crossroads between cell death and survival: they can either heal and recover, or else they will die. This crossroads is especially relevant in the context of neurodegeneration since neurons are post-mitotic (non-dividing) cells and can therefore not be replaced by new cells once lost. For example, two recent studies have shown that the degeneration of axons (long-distance neuronal projections) can be initiated by loss of plasma membrane integrity.[6,7] In the mouse models of traumatic spinal cord contusion injury (SCCI) and of neuroinflammatory axon degeneration in multiple sclerosis (*Experimental Autoimmune Encephalomyelitis*, EAE), membrane-damaged axons entered a meta-stable state from which they could completely recover (by re-establishing membrane-integrity and calcium homeostasis) or else proceed to axonal fragmentation (irreversible disintegration). Diagnostic and therapeutic interventions in such situations could therefore make great use of probes that can selectively label these meta-stable membrane-damaged axons: which, for example, PI cannot do, but **MDG1** can (**Fig 6** and **Fig S22-23**); and particularly, could make use of similar *platform chemistries* as used in **MDG1**, to create pro-regenerative drugs or prodrugs that are selectively targeted at membrane-damaged cells: which the modularity of the **MDG** design was intended to enable.

Even more broadly than the cases of traumatic and inflammatory neurological conditions, studying membrane-compromised cells on the verge of cell death, or therapeutically promoting their survival, would be helpful in a variety of physiological and pathological situations (beyond axon degeneration): and for this, strategies to target them selectively with small molecules are needed. Initially, to investigate probe uptake and activation in damaged cells, we used the pore-forming bacterial toxin listeriolysin O (LLO) to induce

membrane damage (**Fig 3e**). LLO protein is secreted by bacteria to penetrate the host cell by ring-oligomerisation on the target membrane where a subsequent conformational change leads to pore formation.[8]

Next however, we followed our main longterm motivation which had been to develop turn-on membrane-damage probes for selective targeting of (membrane-)damaged axons as are commonly found in inflammatory lesions in mouse models of multiple sclerosis as well as in traumatic SCCI (although note, axonal membrane damage in SCCI is caused mechanically, a route of lesion formation is not addressed in this study).[6,7] We thus examined a neuronal cell line PC12, derived from rat pheochromocytoma, that can be differentiated into neurite-extending neurons using neuronal growth factor.[9] Although the origin of altered axonal membrane permeability in the neuroinflammatory lesions of multiple sclerosis is unknown, we speculated that it may either be mediated by a protein pore as employed by cytotoxic immune cells or cell-autonomous cell death pathways, or else, since inflammatory lesions feature high levels of reactive oxygen and nitrogen species[10,11], may be the consequence of plasma membrane lipid peroxidation. Since LLO had already modelled membrane damage by insertion of protein pores, we now decided to test the robustness of our approach by modelling lipid peroxidation. To this end, PC12 cells were treated with 2,2'-azobis(2-amidinopropane) bis(HCl) salt (**AAPH**), a free-radical generating azo compound which can peroxidise membrane lipids experimentally.[12]

Note that the choice of model system affects the absolute values of any readout, which is why we compare multiple cell lines and damage models, as well as the more realistic embryo, to study the performance of our conditionally cell-excluded fluorogens. For example, fluorescence microscopy reveals different degrees of cell-exclusion from healthy vs damaged PC12 cells than found in HEK and HeLa cells (see **Fig S8** for further discussion): e.g. **MDG1** is efficiently excluded from healthy PC12 cells, but strongly stains AAPH-damaged cells with eight-fold higher cell-fluorescence as shown by confocal imaging (**Fig 4a,b**; we speculate that the "signal enhancement" in the AAPH assay may be lower than in the LLO assay because peroxidative-type damage does not create such enormous structured voids for the probe to permeate through). While the absolute values for a compound in any particular model system should not be assumed to translate to others, we believe that where relative orders of results are consistent across multiple cell lines and damage models, these are predictive of general effects.

3.3 Supporting Note 3 - Full Figure Legends

Note to Legend for Figure 2c: *The intracellular fluorescence quantified for the active fluorophores H_2-FS_1 and H_2-FS_0 is somewhat higher than expected in this procedure, because automatic recognition of intracellular vs extracellular space using the CellTracker channel is imperfect (pixel overlaps)*.

Note to Figures 2c, 3d, 3g, 4b*: for clarity, the n≥3 datapoints underlying the means are shown in* ***Figure S25****, and the main text panels are kept purposefully sparse to focus on the magnitude and direction of the fold-change vectors involved (extra/intracellular signal in* ***2c****; healthy/damaged signal in* ***3d,3g,4b****).*

Figure 3: Fluorogenic probes that are excluded from healthy cells but enter and are then activated inside damaged cells. (a-b) Overview and typical synthetic route for mono-capped mono/bis-anionic fluorescein probes. **(c)** Confocal microscopy images of HEK cells treated with **iMe-FS_1**, **iEM-FS_1**, **iPS-FS_1** and **iPS-FS_2** (=**MDG1**) (5 µM, 10 min) (*n* = 3); **(d)** quantified intracellular and extracellular fluorescence for **iMe-FS_1**, **iEM-FS_1**, **iPS-FS_1** and **iPS-FS_2** (=**MDG1**) (5 µM, 10 min) in HEK cells, dashed line marks auto-fluorescence (DMSO control) (*n* = 3); **(e)** Membrane damage assay overview. **(f)** Confocal microscopy images of HEK cells either untreated (without LLO) or pre-treated with LLO (0.2 µg/mL) for 5 min followed by **MDG1** treatment (5 µM). Images taken 10 min after probe application without prior washing (*n* = 3). **(g)** Quantified intracellular fluorescence for each probe (5 µM, 10 min, non-wash) for healthy and LLO damaged HEK cells (*n* = 3); **(h)** Chemical structure of **MDG1**. *Scale bar: 50 µm*. *Note*: "Brightness 10×" indicates images are adjusted as compared to brightness in Fig. 2.

Figure 4: Biological and chemical scope of the fluorogenic cell-excluded probe concept. (a-b) Works for nonspecific oxidative AAPH-induced membrane damage (PUFA peroxidation). Confocal microscopy images of PC12 cells either untreated (without AAPH) or treated with AAPH (300 mM) for 90 min followed by probe treatment (5 µM). Images taken 10 min after probe application without prior washing (*n* = 3). **(b)** Quantified intracellular fluorescence for each probe (5 µM, 10 min, without washing) with and without pre-treatment with AAPH (300 mM, 90 min) (*n* = 3); **(c-e) Other fluorogenic triggers can be modularly introduced to tune probe performance. (c)** Applying a GSH-labile redox trigger to our modular impermeable fluorophore system for intracellular fluorescence turn-on; **(d)** Spontaneous probe hydrolysis of ester probe **MDG1** and redox probe **MDG2** in standard cell culture medium DMEM; **(e)** Confocal microscopy images of HEK cells either untreated (without LLO) or treated with LLO (0.2 µg/mL) for 5 min followed by probe treatment (5 µM). Images taken 10 min after probe application without prior washing (*n* = 3). *Scale bar: 50 µm*.

Figure 5: (a-k) Sensing membrane damage in ferroptosis (T-cells in a culture of total lung lymphocytes; optional pre-treatment with RSL3 (0.5 µM) or hydrogen peroxide (0.4 mM)). (a) Chemical structure of **MDG1**. **(b)** Histograms of the mean fluorescence intensity (MFI) of **MDG1** (administered at 50 µM for 30 min), in optionally pre-treated T cells, as assessed by flow cytometry. **(c)** Quantified MFI of **MDG1** of the histogram plots shown in panel **a**. **(d)** Contour plots of **MDG1** fluorescence vs. SSC-A pre-gated on T cells ($TCRb^+$) showing the gating on damage positive cells (**MDG1**$^+$). **(e)** Quantification of **MDG1**$^+$ cells. **(f)** Chemical structure of the administered **BODIPY-C11** (RED) (reduced form). **(g-h)** Histograms of the MFI of **(g) BODIPY-C11** (OX) fluorescence and **(h) BODIPY-C11** (RED) fluorescence, following administration of **BODIPY-C11** (RED) (250 µM for 1 h). **(i-j)** Quantified MFI of **BODIPY-C11** (OX and RED) of the histogram plots shown in panels **g-h**. **(k)** Ratio of the MFI of **BODIPY-C11** (OX) divided by (MFI of **BODIPY-C11** (RED) plus MFI of **BODIPY-C11** (OX)), used as a proxy for the amount of lipid peroxidation, and thus as an indication of ferroptosis.

Figure 6: (a-c) Selective staining of AAPH damaged (300 mM, 90 min) E16.5 mouse hippocampal neuronal axons in microfluidic devices with MDG1 (25 µM, 15 min). There is significantly increased axonal fluorescence in damaged vs undamaged cells. For full figure with controls see **Fig S23**; scale bar = 50 µm. **(d-f) Sensing membrane damage in necrosis in live *Drosophila* embryo.** The epithelial cell-surface-marker mcherry-Moesin (red channel) is used to outline epithelial cells; three cells of interest are annotated with the magenta, cyan and yellow arrows/outlines. Note also the presence of several macrophages which clear apoptotic epithelial cells by ingestion (so at the start of imaging they have collected multiple red-fluorescent conglomerates within themselves). **MDG1** was microinjected into the intervitelline space, then local necrotic tissue damage was triggered by local laser wounding using laser ablation at time zero (focal area indicated with asterisk), and probe fluorescence was imaged over the following minutes. **(d)** Experimental setup. **(e-f)** The ventral epithelium of the embryo was laser-wounded, resulting in expansion then rebound of the targeted tissue area (note slight movement of cells between frames), in local photobleaching of the mCherry-Moesin marker (dark zone already at the "time zero" frame collected immediately after wounding), and in necrotic cellular damage at the target site. Cells that had been entirely within the original damage zone are most rapidly and strongly labelled by **MDG1** activation (green channel); cells that had been partially covered by or contacting the damage zone are also labelled (e.g. yellow- and cyan-indicated epithelial cells); cells that were not contacting the damage zone are not labelled (e.g. magenta-indicated epithelial cell). Note also the two macrophages at centre-left (containing ingested mCherry conglomerates) which are not laser-damaged, and therefore are not labelled (they show up as shadows in the green channel). Images shown are Z-projections to account for curvature of the organism. Time shown in minutes; scale bars 5 µm; "A/P/V/D" indicates anterior / posterior / ventral / dorsal.

4 Biological characterisation

4.1 Exclusion of probes and fluorophores from healthy HeLa and HEK cells

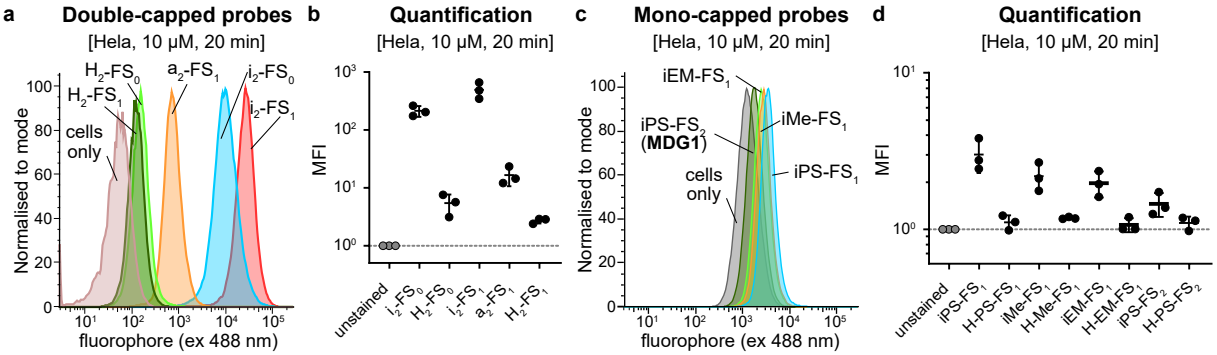

Figure S4: Flow cytometry analysis of cell penetration of the probes and fluorophores into healthy HeLa cells. **(a)** Histogram plots of cellular fluorescence (of fluorescein) for the doubly capped probes after treatment of HeLa cells for 20 min (probe conc.: 10 µM); **(b)** Mean fluorescence intensities (MFI) of doubly capped probes and fluorophores (norm. to DMSO control, *n* = 3); **(c)** Histogram plots of cellular fluorescence (of fluorescein) for the mono-capped probes after treatment of HeLa cells for 20 min (probe conc.: 10 µM); **(d)** Mean fluorescence intensities of mono-capped probes and fluorophores (norm. to DMSO control, *n* = 3).

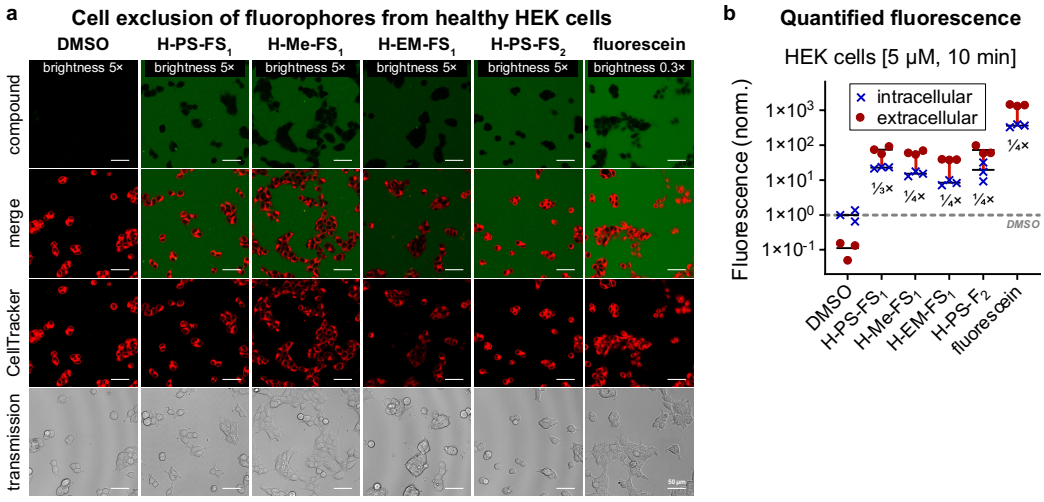

Figure S5: **Microscopy and quantification of cell exclusion of sulfonated fluorophores into healthy HEK cells; (a)** Confocal microscopy images of HEK cells after treatment with fluorophores (5 µM) for 10 min (non-wash, CellTracker™ CMTPX Red for cell staining) (*n* = 3); **(b)** quantified intracellular and extracellular fluorescence intensities (compound treatment: 5 µM, 10 min, non-wash) in HEK cells, horizontal line marks auto-fluorescence (DMSO control) (*n* = 3). *Scale bar: 50 µm*.

Note that the small, but real, differences in cell-uptake of the fluorophores (compare **Fig S4d**) cannot be seen by imaging because of the extremely bright extracellular signal, which is the major reason we focus on turn-on probes.

Table S1: Normalised cellular fluorescence values quantified from microscopy images for the cell penetration into healthy HEK cells (normalised to DMSO control (intracellular), n = 3).

Compound	Intracellular fluorescence			Extracellular fluorescence			Mean (intra)	Mean (extra)	Ratio intra/extra
i_2-FS_0	417	526	301	4.75	2.93	3.81	415	3.83	108
i_2-FS_1	325	213	171	4.16	20.49	8.57	236	11.1	21.3
a_2-FS_1	167	124	190	9.43	16.8	13.2	160	13.1	12.2
iPS-FS_1	84.6	85.7	70.9	3.57	3.07	3.94	80.4	3.53	22.8
iMe-FS_1	4.42	5.51	5.01	2.35	2.63	3.75	4.98	2.91	1.71
iEM-FS_1	4.43	4.32	6.27	1.57	1.58	2.20	5.01	1.78	2.81
iPS-FS_2	1.92	2.89	1.61	1.94	1.76	1.87	2.14	1.86	1.15
FDP	9.60	21.5	14.7	10.5	8.85	11.4	15.3	10.3	1.49
fluorescein	362	398	323	1308	1467	1401	361	1392	0.26
H_2-FS_0	212	278	240	727	867	889	243	828	0.29
H_2-FS_1	235	158	195	517	571	513	196	534	0.37
H-PS-FS_1	23.0	23.5	21.5	90.7	56.7	74.1	22.7	73.9	0.31
H-Me-FS_1	12.9	17.7	15.1	60.4	69.8	53.6	15.2	61.3	0.25
H-EM-FS_1	7.02	8.26	10.0	39.7	38.7	37.9	8.4	38.8	0.22
H-PS-FS_2	9.10	17.2	32.0	60.0	59.0	97.9	19.4	72.3	0.27
DMSO	1.36	0.99	0.65	0.13	0.16	0.05	**1**	0.11	8.86

4.2 Permeability Calculations

Table S2: Permeability coefficients of fluorogenic chemical probes calculated with PerMM using the plasma membrane model.

Molecule	$LogP_{erm}$ ($cm.s^{-1}$)	
	Closed form	*Open form*
Fluorescein	-4.00	-4.57
H_2-FS_0	-4.46	-5.15
H-PS-FS_1	-6.72	-7.26
H-PS-FS_2	-11.28	-11.35
i_2-FS_0	-0.37	
iPS-FS_1	-5.11	
iPS-FS_2	-9.45	

Permeability coefficient calculations using PerMM[13,14] (**Table S2**) show that the number of sulfonates in fluorogenic probes has a drastic effect on cell penetration, as observed experimentally. Each additional sulfonate moiety lowers the permeation coefficient by 2 to 5 log units. Probes with no sulfonates are permeable, while those with 2 are impermeable. Interestingly, isobutyrate ester capping has a double effect: (i) in the closed form, it increases the permeability coefficient by 2 log units per isobutyrate, compared to the uncapped structure (due to hydrophobicity), and (ii) by preventing the opening of the spirocycle, it avoids the increase in polarity that the uncapped forms undergo upon adopting the open form and revealing the carboxylic acid moiety, (decreased permeability coefficient by 0.7 log units). These are coherent with the results of **Figure 2**. Therefore, both uncapping of the probe and the associated ring opening of the product fluorophore render the product significantly more impermeable to passive diffusion than the probe. The dichlorination of **H_2-FS_0** (c.f. fluorescein) also slightly lowers its permeation coefficient by about 0.5 log units.

The conformations of the probes were built and minimized using Avogadro software, MMF94s forcefield and the steepest-descent algorithm. Permeability coefficients were calculated with PerMM[13,14] server at 298K with pH = 7.4, with the drag optimization method, and including deionization energy for ionizable molecules. The pK_a of the sulfonic acids was set to −2.8, taken from benzenesulfonic acid[15]. The pK_a of the carboxylic acid of the open forms was set to 4.5, taken from fluorescein[16]. To compare with experiments on cells, the values presented in **Table S2** are taken from the plasma membrane model of PerMM.

4.3 LLO Damage Assay

4.3.1 Entry of probes into LLO-damaged HEK cells

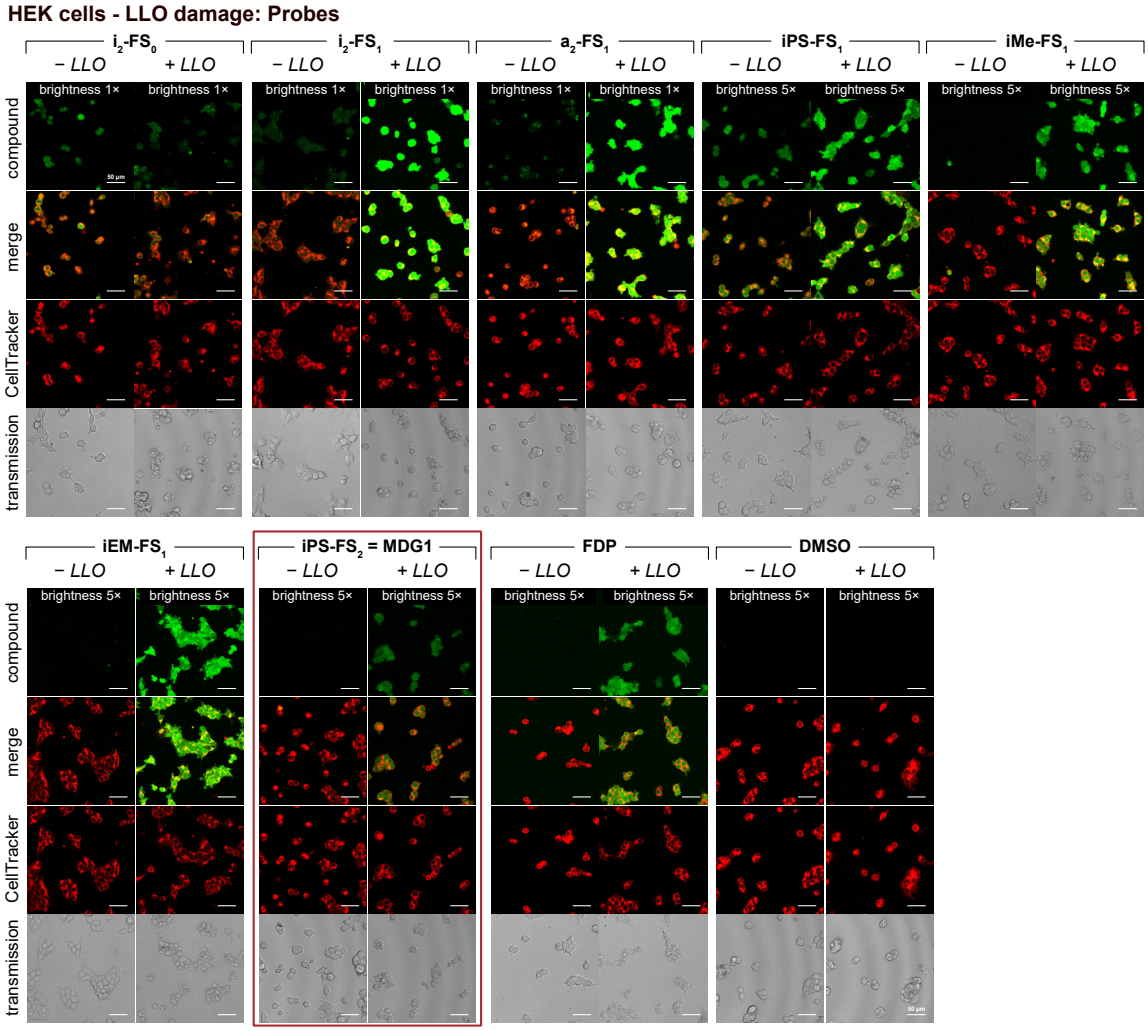

Figure S6: Probe uptake in LLO-damaged HEK cells. Confocal microscopy images for turn-on probes of HEK cells pre-treated with LLO (0.2 mg/mL) for 5 min followed by probe treatment (5 µM). Images taken 10 min after probe application without prior washing (n = 3). *Scale bar: 50 µm*.

Detailed discussion of probe uptake

Quantifying the intracellular fluorescence reveals significant differences between the probes (also see **Fig 3g**). The membrane permeable probe **H_2-FS$_0$** shows lower fluorescence with LLO than without which could be explained by faster signal loss due to excretion of the released fluorophore **H_2-FS$_0$** through the created pores. **i_2-FS$_1$**, which is also permeable to healthy cells, on the other hand shows even higher signal generation in damaged cells. We reason that this mono-sulfonated probe already features very low permeability because of the polar sulfonate but very fast intracellular signal generation (see above: faster esterase activation and lower hydrolytic stability). Thus, we suspect that the better cell penetration into LLO-damaged cells outcompetes the signal loss of the released fluorophore. Also, the membrane-permeable probes **a_2-FS$_1$** and **iPS-FS$_1$** show moderate signal increase with LLO. However, all these membrane permeable probes are not suitable for membrane-damage imaging from low background as they already give high fluorescence with healthy cells (besides their moderate uptake ratios). For this goal the cell-excluded probes **iMe-FS$_1$**, **iEM-FS$_1$** and **iPS-FS$_2$** (=**MDG1**) are more suited. Quantification shows around 30-fold signal increase in damaged cells for all three probes making them valuable tools to distinguish healthy from membrane-damaged cells with high contrast and sensitivity by far outperforming commercially available **FDP** (only 7-fold increase). **iPS-FS$_2$** (=**MDG1**) reveals the best performance as it features the lowest fluorescence in healthy cells enabling the highest sensitivity. The permanently fluorescent fluorophores show high extracellular fluorescence and can only penetrate into permeabilised cells (**Fig S7**).

4.3.2 Entry of fluorophores into LLO-damaged HEK cells

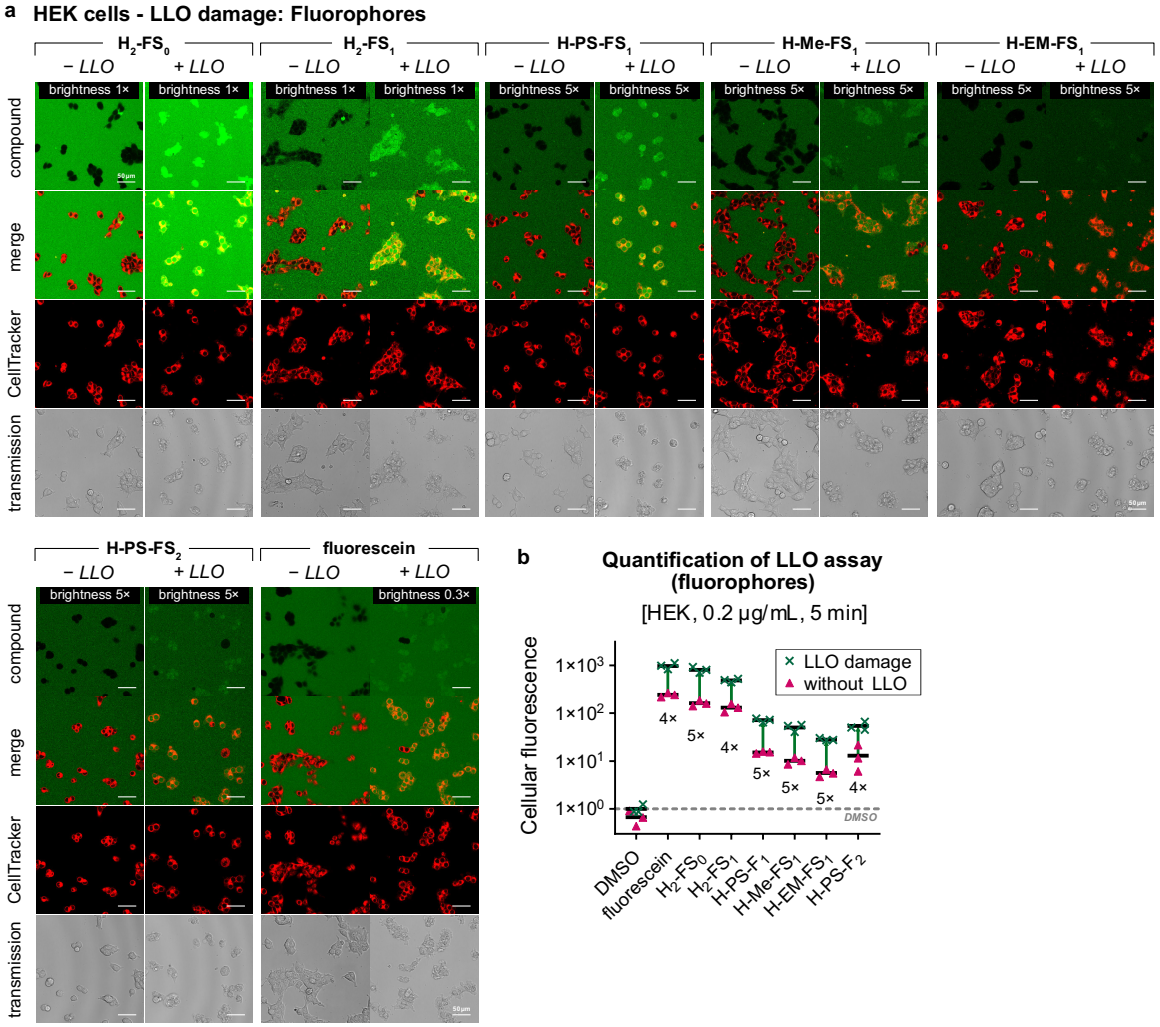

Figure S7: Fluorophore uptake in LLO-damaged HEK cells. (a) Confocal microscopy images for fluorophores of HEK cells pre-treated with LLO (0.2 mg/mL) for 5 min followed by probe treatment (5 µM). Images taken 10 min after probe application without prior washing (n = 3). **(b)** Quantified intracellular fluorescence for each fluorophore (5 µM, 10 min, non-wash) for healthy and LLO damaged HEK cells (n = 3). *Scale bar: 50 µm.*

4.3.3 Data (normalised): Exclusion or entry into LLO-damaged HEK cells

Table S3: Normalised intracellular fluorescence values quantified from microscopy images for the LLO membrane damage assay in HEK cells (normalised to DMSO control with LLO (such that its intracellular fluorescence value is 1), n = 3).

Compound	+LLO			−LLO			Mean (+LLO)	Mean (−LLO)	Ratio +/−LLO
i_2-FS_0	85.3	117	142	280	352	202	115	278	0.41
i_2-FS_1	3391	1416	2251	218	143	115	2353	158	14.9
a_2-FS_1	957	1122	1038	112	83	127	1039	107	9.67
iPS-FS_1	204	174	178	56.7	57.5	47.5	185	53.9	3.44
iMe-FS_1	89.4	102	111	2.97	3.69	3.36	101	3.34	30.2
iEM-FS_1	109	120	132	2.97	2.90	4.20	121	3.36	36.0
iPS-FS_2	48.3	43.6	43.0	1.29	1.94	1.08	45.0	1.44	31.3
FDP	77.8	58.5	66.1	6.43	14.4	9.85	67.5	10.2	6.59
fluorescein	986	1106	834	242	267	217	976	242	4.03
H_2-FS_0	803	920	704	142	187	161	809	163	4.96
H_2-FS_1	493	526	442	157	106	131	487	131	3.71
H-PS-FS_1	77.3	64.3	73.2	15.4	15.7	14.4	71.6	15.2	4.72
H-Me-FS_1	54.3	56.6	40.6	8.62	11.9	10.1	50.5	10.2	4.96
H-EM-FS_1	30.1	27.5	27.0	4.70	5.54	6.71	28.2	5.65	4.99
H-PS-FS_2	45.3	50.3	66.3	6.10	11.5	21.4	53.9	13.0	4.15
DMSO	1.25	0.88	0.88	0.91	0.66	0.43	**1**	0.67	1.49

4.4 AAPH Damage Assay

4.4.1 Entry of probes into AAPH-damaged PC12 cells

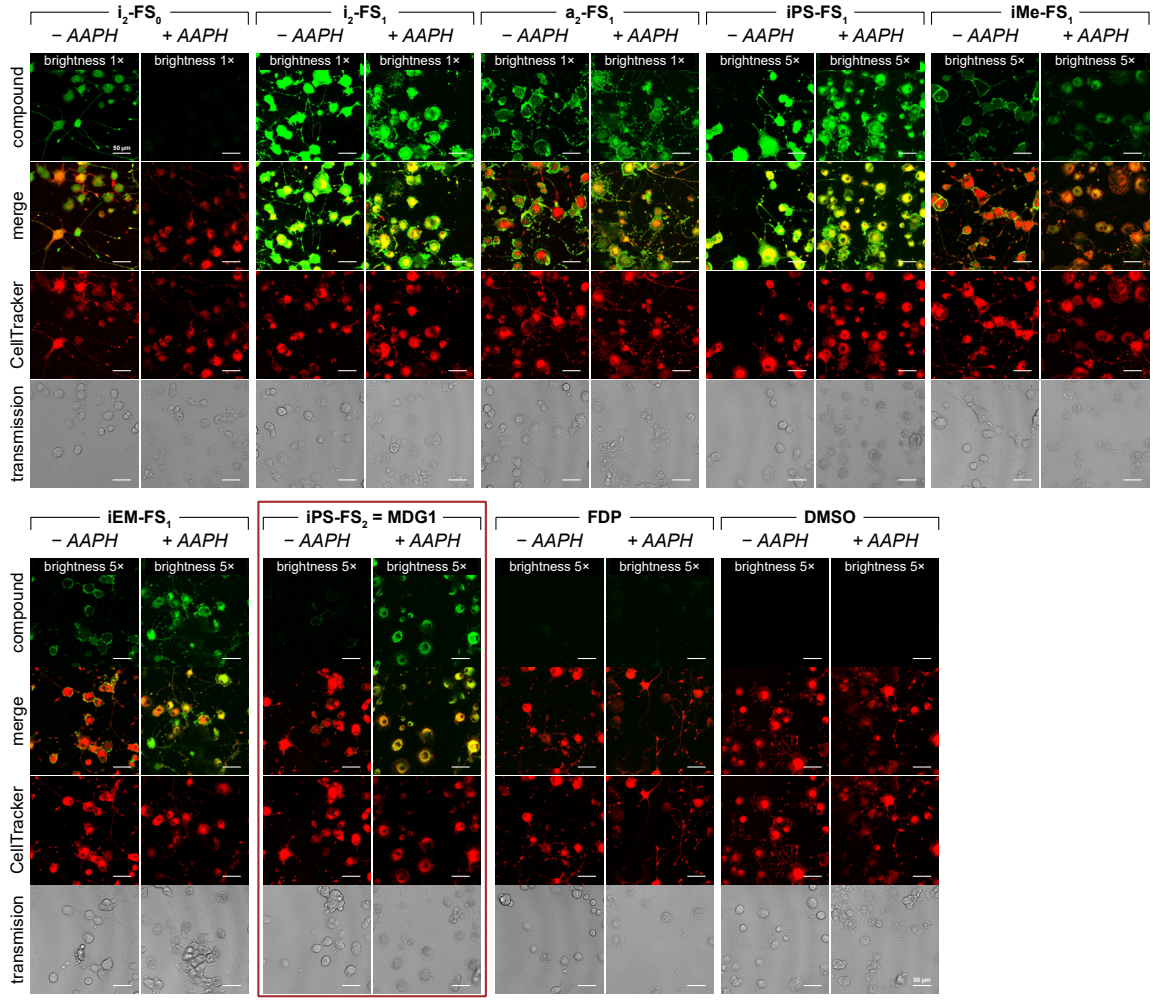

Figure S8: Probe uptake in AAPH-damaged PC12 cells. Confocal microscopy images for turn-on probes of PC12 cells pre-treated with AAPH (300 mM) for 90 min followed by probe treatment (5 µM). Images taken 10 min after probe application without prior washing (*n* = 3). *Scale bar: 50 µm*.

Note: we interpret the **i_2-FS$_0$** result of lower fluorescence in treated than in untreated cells as indicating that its leak-out after activation is more severe from damaged than healthy cells, matching the trend from the LLO assay.

Fluorescence microscopy reveals different degrees of cell-exclusion from healthy PC12 cells which deviate from the ones found in HEK and HeLa cells. Lipophilic mono-sulfonates (**i_2-FS$_1$**, **a_2-FS$_1$**, **iPS-FS$_1$**) are well permeable as observed before, but interestingly **i_2-FS$_1$** is even brighter than its non-sulfonated parent **i_2-FS$_0$** in healthy PC12 cells (**Fig S8, Fig 4b**). The more polar mono-capped probes (**iMe-FS$_1$**, **iEM-FS$_1$**) turned out to be significantly more permeable than in HEK and HeLa cells, suggesting cell-type specific differences in membrane permeability. The more polar disulfonated **MDG1** however was efficiently excluded by healthy PC12 cells. The higher fluorescence in healthy cells brings along low turn-on ratios (low selectivity) for all probes except for **MDG1** (which also performed best in the LLO assay). The permanently fluorescent fluorophores are again excluded from healthy cells but penetrate into leaky cells as expected for the more polar open-form fluoresceins (**Fig S9**).

4.4.2 Entry of fluorophores into AAPH-damaged PC12 cells

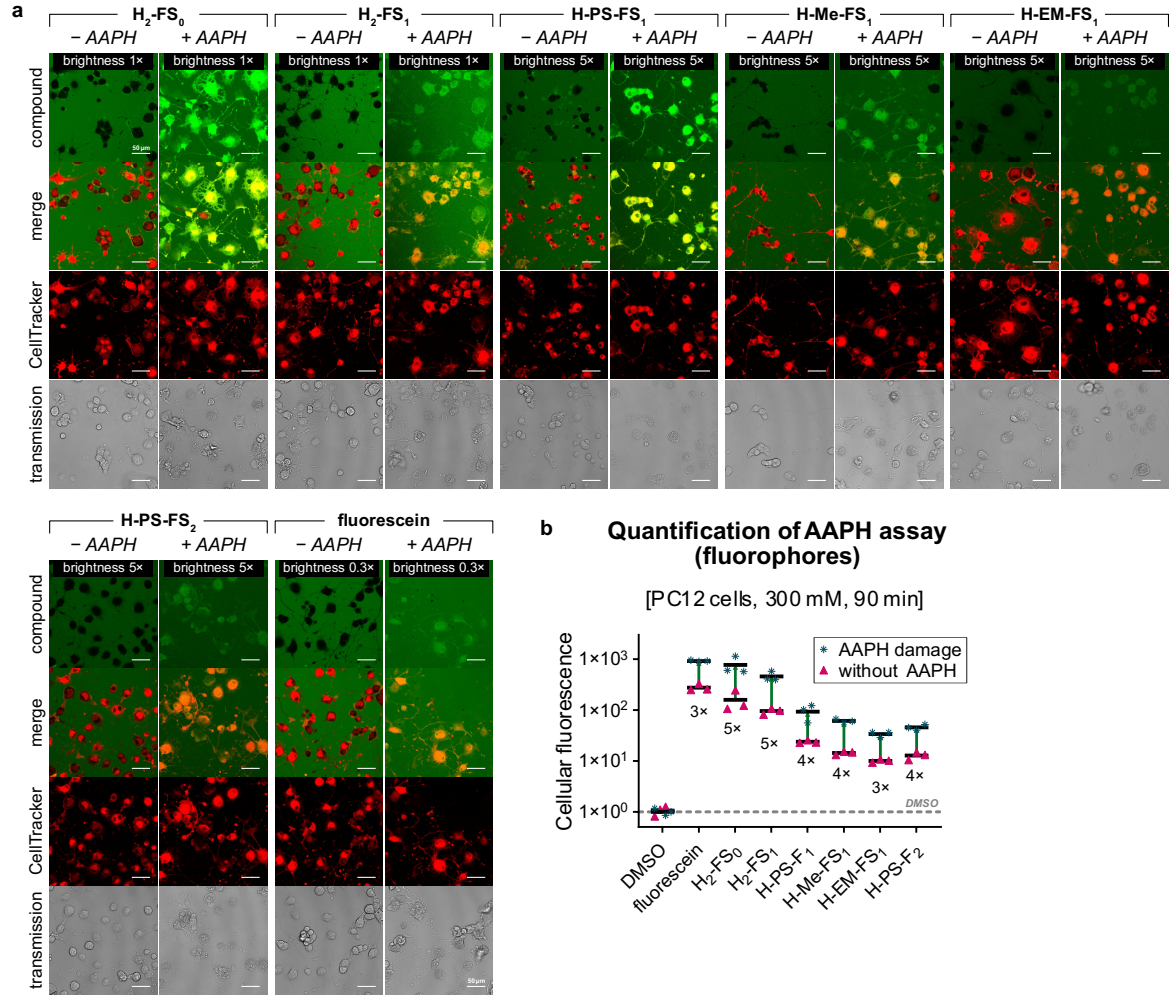

Figure S9: Fluorophore uptake in AAPH-damaged PC12 cells. (a) Confocal microscopy images for fluorophores of PC12 cells pre-treated with AAPH (300 mM) for 90 min followed by probe treatment (5 µM). Images taken 10 min after probe application without prior washing (n = 3). **(b)** Quantified intracellular fluorescence for each fluorophore (5 µM, 10 min, non-wash) for healthy and AAPH damaged PC12 cells (n = 3). *Scale bar: 50 µm*.

4.4.3 Data (normalised): Exclusion or entry into AAPH-damaged PC12 cells

Table S4: Normalised intracellular fluorescence values quantified from microscopy images for the AAPH membrane damage assay (normalised to DMSO control (+AAPH), n = 3).

Compound	+AAPH			−AAPH			Mean (+AAPH)	Mean (−AAPH)	Ratio +/−AAPH
i_2-FS_0	52.4	23.7	14.1	643	476	310	30.1	476	0.06
i_2-FS_1	717	823	332	2633	2668	1865	624	2389	0.26
a_2-FS_1	390	871	390	243	512	335	550	363	1.51
iPS-FS_1	82.2	95.5	55.6	141	259	155	77.8	185.2	0.42
iMe-FS_1	57.7	31.2	48.8	34.1	34.8	28.8	45.9	32.5	1.41
iEM-FS_1	62.7	116.0	63.0	27.1	34.5	20.6	80.6	27.4	2.94
iPS-FS_2	40.7	45.8	26.6	3.97	5.35	5.18	37.7	4.83	7.80
FDP	20.4	13.3	24.0	5.57	4.12	7.52	19.2	5.74	3.35
fluorescein	920	901	955	256	250	328	925	278	3.33
H_2-FS_0	1151	604	569	246	106	123	775	158	4.90
H_2-FS_1	411	576	395	82.1	97.2	107	460	95.4	4.83
H-PS-FS_1	122	101	56.0	22.8	25.7	23.1	93.1	23.9	3.90
H-Me-FS_1	66.8	57.2	59.8	15.3	13.2	14.7	61.3	14.4	4.26
H-EM-FS_1	36.2	29.0	36.2	10.1	10.8	9.2	33.8	10.0	3.36
H-PS-FS_2	45.0	52.4	40.0	10.5	14.8	13.2	45.8	12.8	3.57
DMSO	0.99	1.17	0.84	0.82	1.26	1.10	**1**	1.06	0.95

4.4.4 Subcellular distribution of compounds: nuclear exclusion in AAPH assays

We observe that the fluorescent product from **MDG1** activation is cytosolic but excluded from the nucleus in AAPH-damaged PC12 cells, whereas it can be found in the cytosol and the nucleus of LLO-damaged HEK cells. This raises the question whether this is a cell-type- or treatment-specific effect.

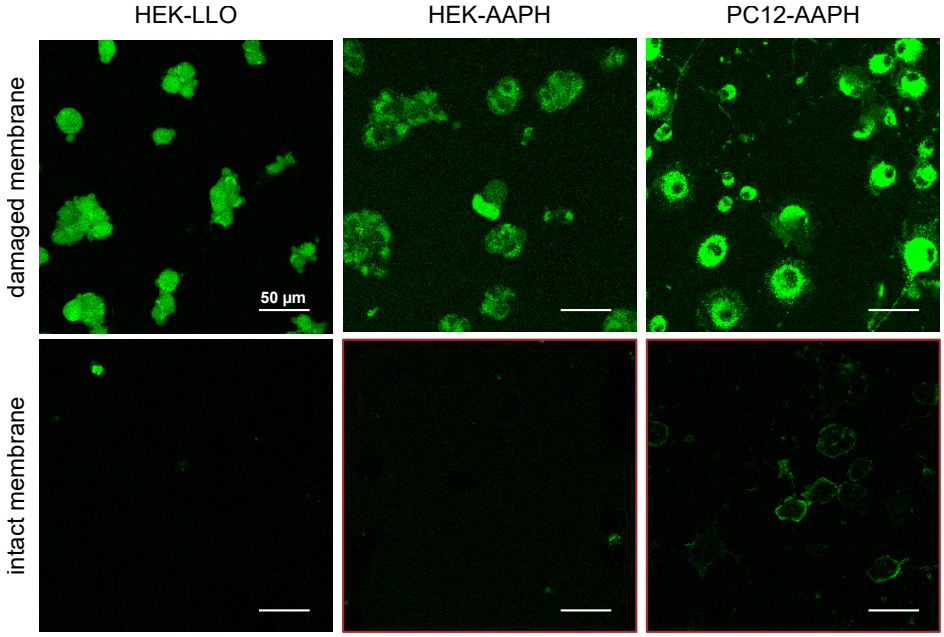

Figure S10: AAPH damage in HEK or PC12 cells leads to the dye product being excluded from the nucleus, whereas LLO assays show the dye in the nucleus. Confocal microscopy images of HEK cells pre-treated with LLO (0.2 mg/mL) for 5 min and HEK and PC12 cells pre-treated with AAPH (300 mM) for 90 min followed by **iPS-FS_2** treatment (5 µM) for 10 min*;* Please note: Images were taken with different acquisition parameters. They were put together to visualize subcellular compound distribution. A *quantitative* comparison is only possible between corresponding damage and control conditions, not between HEK-LLO / HEK-AAPH and PC12-AAPH. *Scale bar: 50 µm*.

All tested compounds that enter the cytosol of healthy or LLO-damaged HEK cells also enter the nucleus (see **FigS5**, **S6**), whereas the results are more complex for PC12 cells (see **FigS7, S8**). Here, compounds that are able to enter undamaged cells (notably **i_2-FS_0**, **i_2-FS_1** and **iPS-FS_1**) also enter the nucleus, whereas nuclear exclusion in at least a subset of cells can be observed for all compounds in the AAPH-damaged condition.

This includes nuclear exclusion of compounds that readily stain nuclei of healthy PC12 cells and suggests this being a treatment-specific, not a cell-type-specific, effect. To test this, we treated HEK cells with AAPH and applied **MDG1** (**Fig S10**). The AAPH-damaged HEK cells display cytoplasmic uptake but nuclear exclusion of **MDG1**, thus resembling AAPH-damaged PC12 cells and differing from LLO-damaged HEK-cells. This supports that nuclear exclusion is due to AAPH treatment (i.e. selective permeabilisation of the plasma, not nuclear, membrane) and is independent of cell type.

4.5 Wash-free imaging over longer times

When imaging **MDG1**-treated cells for much longer than our 10 min standard procedure, a slow but continuous increase in extracellular background fluorescence is seen, even in HBSS. This increase is most likely caused by non-enzymatic ester hydrolysis in the extracellular medium, since its rate is similar to that in HBSS stability assay (**Fig S2**), and since fluorophore leakage from (even damaged) cells into the medium has negligible contribution to the background increase (see **section 4.5**). However, this extracellular background remains much lower than specific cellular signal over hours, so damaged cells remain brightly labelled and well distinguishable from background. For LLO-damaged HEK cells, the signal peaks shortly after addition then drops slightly to plateau at around 75% of the peak fluorescence; whereas for AAPH-damaged PC12 cells we observe continuous signal increase over at least 2 h (**Fig S11**). The signal-to-background performance of the probe, and the "best timepoint to read out", are therefore dependent on the type of membrane damage. For an optimal signal-to-background ratio, we recommend short **MDG1** incubation times.

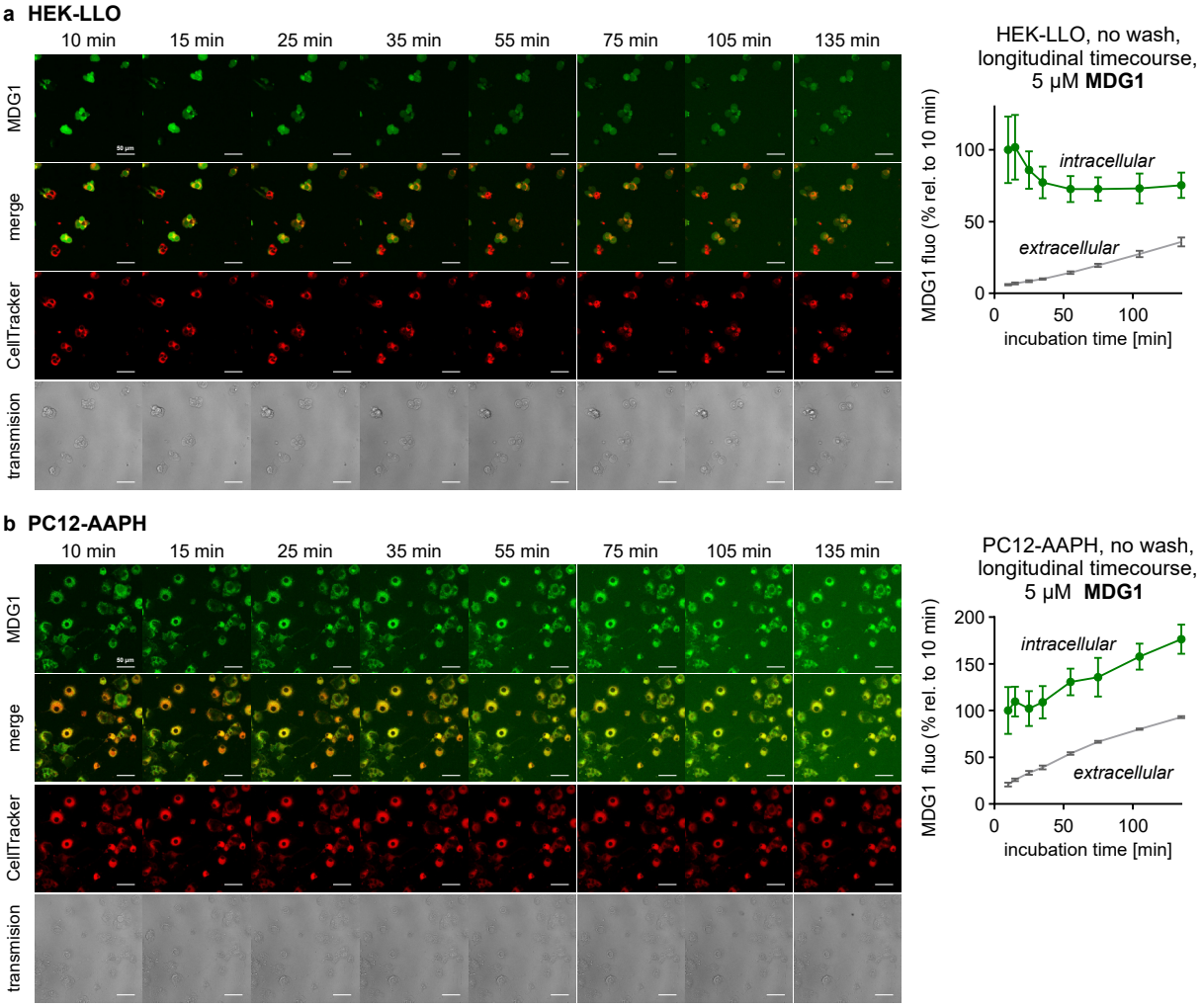

Figure S11: Longer time period live-cell imaging with MDG1. (a) Confocal microscopy images of HEK cells pre-treated with LLO (0.2 mg/mL) for 5 min, then treated with **MDG1** (5 µM, medium change). Images were taken longitudinally at different timepoints of **MDG1** incubation without washing; **(b)** Confocal microscopy images of PC12 cells pre-treated with AAPH (300 mM) for 90 min, washed (2×), then treated with **MDG1** (5 µM). Images were taken longitudinally at different timepoints of **MDG1** incubation without washing; *Note: 100% in graphs refers to the mean intracellular fluorescence after 10 min; Scale bar: 50 µm.*

4.6 Cell Retention of the fluorophore product from MDG1

4.6.1 Post-wash cell retention in live-cell imaging

MDG1 was designed to probe membrane damage in wash-free setups by generating *and then retaining* fluorescence inside cells, while remaining dark in the extracellular space so that washing would not be needed. To investigate just the cellular retention of the probe after activation, we performed a washing assay (although this is not the intended use of the probe), in which we removed the extracellular probe / fluorophore after 10 min of incubation with probe, washed, and then replaced the medium with a second round, of fresh HBSS. In this setup, we observe a marked loss of intracellular signal within the first 20 min post-wash for both cell- and damage-types. While the fluorescence is lost almost completely in LLO-treated HEK cells, around one third of the signal is retained long-term in AAPH treated PC12 cells. The amount leaked out from cells (volume ca. 2000 μm^3/cell; ca. 20,000 cells/well) is however then diluted in the extracellular medium (ca. 300 µL) and in confocal (**Fig S12**), this dilution prevents it being detected as extra background in the medium. Considering our mode of membrane-damage selectivity, which is enabled by charge-based impermeabilization to intact lipid bilayers, this leak-out especially with long-lasting LLO pores is not surprising, since **MDG1**'s released fluorophore is deliberately designed not to covalently react with intracellular proteins or other structures, so as to avoid potentially unwanted biological effects. It is therefore expected that the released fluorophore can also reverse-cross damaged membranes to leave the cell. Naturally, this makes **MDG1** a poor choice for post-wash imaging under fresh aqueous medium after more than 20 min of wash-time; but (a) it works well in wash-free imaging for which it was designed (see also **section 4.4**) and (b) complementary probes with post-reaction intracellularly-trapped fluorophores for post-wash imaging are being addressed in separate, ongoing work.

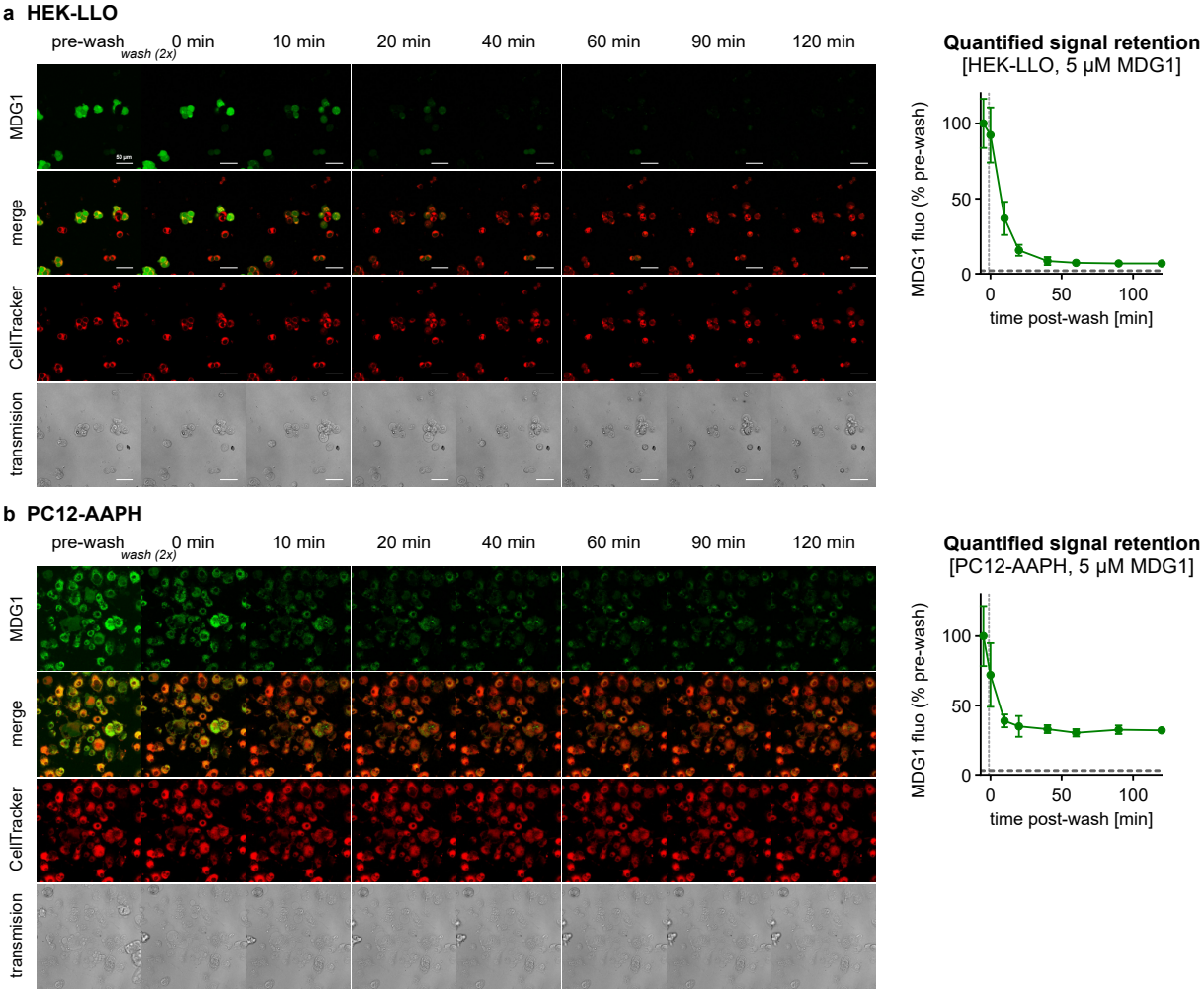

Figure S12: Post-wash signal retention in MDG1 live-cell imaging setup. (a) Confocal microscopy images of HEK cells pre-treated with LLO (0.2 mg/mL) for 5 min, then treated with **MDG1** (10 min, 5 µM, medium change), then washed and incubated in fresh HBSS. Images were taken once pre-wash and at several timepoints post-wash (n = 3) (Note: in the top-right cell cluster a new cell moves into the focal plane at the 10 min image time point); **(b)** Confocal microscopy images of PC12 cells pre-treated with AAPH (300 mM) for 90 min, then washed/probed/washed. Images were taken once pre-wash and at several timepoints post-wash (n = 3). *Note: 100% in graphs refers to the mean intracellular fluorescence before washing off the **MDG1**; dashed line in graphs indicates autofluorescence of damaged cells without **MDG1**; Scale bar: 50 µm.*

4.6.2 Resealing of LLO-damaged HEK and AAPH-damaged PC12 cells

Given the differences in longer-term cell retention between HEK-LLO and PC12-AAPH assays (**Fig S11**), we examined whether these may be due to different degrees of *repair* of membrane damage. We therefore damaged HEK cells with LLO, or PC12 cells with AAPH, then washed off the damage agent, left the cells to recover for various lengths of **recovery time**, and *then* added **MDG1** (**Fig S13**). Both cell types show significant membrane repair (less dye uptake with longer recovery times). LLO-damaged HEK cells reveal strong repair for the first 40 min then plateau, resulting in around 40% of potential maximum intracellular fluorescence thereafter. AAPH-damaged PC12 cells on the other hand show slower repair that continues over the 2 h recovery time range investigated, and (coincidentally) also reach down to ca. 40% of their maximum fluorescence intensity within 2 h recovery. It should also be remembered that as the membrane repairs, *fresh probe will more slowly penetrate into the cells*. We expect these repair kinetic profiles to be partly responsible for dye retention in our assays since the damage agents are always washed out from the assay before applying probes; but these experiments do not explain the degree of difference in long-term dye retention between HEK-LLO and PC12-AAPH assays. Rather, the time-course of signal loss shown in 4.5.1 likely results from a combination of the rates of probe entry, dye exit, and ongoing membrane repair: e.g. in the case of HEK cells porated with LLO, most dye has already diffused out of the cells before membrane repair starts, while in the case of PC12 cells treated with AAPH, membrane repair seems to curtail dye exit.

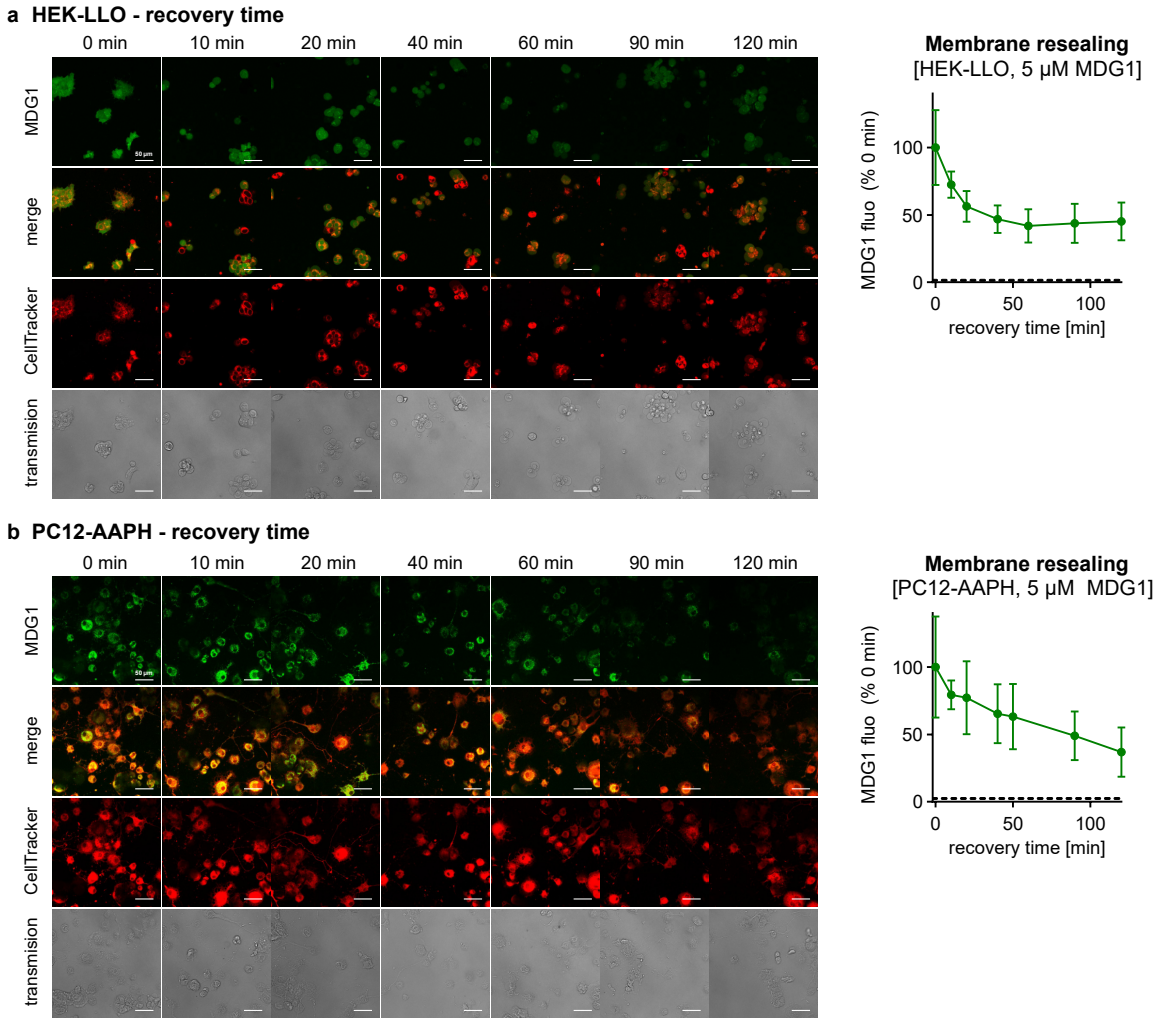

Figure S13: Resealing of LLO-damaged HEK and AAPH-damaged PC12 cells. (a) Confocal microscopy images of HEK cells pre-treated with LLO (0.2 mg/mL) for 5 min, allowed to recover for X min, followed by **MDG1** treatment (10 min, 5 µM) (n = 3); **(b)** Confocal microscopy images of PC12 cells pre-treated with AAPH (300 mM) for 90 min, allowed to recover for X min, followed by **MDG1** treatment (10 min, 5 µM) (n = 3); *Note: 100% in graphs refers to the mean intracellular fluorescence obtained with 0 min recovery time between damaging treatment and iPS-FS$_2$ incubation; dashed line in graphs indicates autofluorescence of damaged cells without iPS-FS$_2$; Scale bar: 50 µm.*

4.6.3 Ability to image MDG1-treated damaged cells after fixation

MDG1 was designed and characterised as a wash-free probe for the visualisation of membrane damage in live-cell imaging. However, imaging of PFA-fixed cells mounted onto microscope slides is a simpler approach and more accessible to many laboratories. We therefore investigated the fixability of our probe.

MDG1 is not itself fixable because it does not feature any fixable functional groups such as free amines. Nevertheless, we investigated if it is *effectively* fixable due to its impermeability to cell membranes that remain mostly intact during PFA fixation. As membranes were damaged with AAPH beforehand, we expected substantial leak-out of dye (lower signal) similar to our observations in the retention assay (see **section 4.5.1**). Since AAPH-damaged cells also have relatively high autofluorescence in the green channel after PFA fixation, we increased the concentration of **MDG1** to 50 µM to ensure strong signal would be present.

We tested imaging both immediately after fixing and mounting, or after leaving mounted cells for 24 h. Our observations in fixed cells replicate those of live-cell imaging experiments:

(1) we observe **no cytosolic staining of cells with healthy membranes,** only the characteristic ring-shaped plasma membrane staining which can arise from probe hydrolysis and then fluorophore insertion into the outer leaflet (columns 1-2 in **Fig S14**).

(2) AAPH-damaged cells have strong cytosolic fluorescence, indicating probe entry, reaction, and retention during the fixation / storage process (columns 3-4 in **Fig S14**).

Slides imaged 24 h after fixation have less bright cells than those imaged immediately, as expected.

At both 0 h and 24 h, differentiation between healthy versus damaged cells is unequivocal (**Fig S14**) due to the characteristic dye distributions either throughout the cytosol (damage) or only on the plasma membrane (healthy). Since the auto-detection cell mask routine we used for *highly conservative* image quantification integrates over the whole membrane, the auto-analysis pixel integration results for undamaged cells would be high (relative fluorescence intensities on the same scale as in **Fig S14** are 13 / 10 (0 / 24 h)); but since these do not represent the *true intracellular fluorescence* intensities that are intended to be captured by analysis, they are not plotted on that graph.

In summary, **MDG1** was designed to serve in live-cell no-wash imaging, where it does show the best results, but if the dye concentration is increased and signal-to-background losses are tolerated, it can also be visualised after PFA fixation in some settings (e.g. not for LLO-damaged HEK cells, where we could not see significant staining of the damaged cells after fixation, as is consistent with a more severe and long-lasting degree of membrane poration, that may even be fixed in place by PFA, similar to the complete signal loss seen in post-wash live-cell imaging of LLO-damaged HEK cells). We also observed that the choice of mounting medium has a strong impact on AAPH-induced autofluorescence, which can be a limiting factor for these experiments (data not shown) - an observation that is not entirely suprising, as, depending on the composition of the mounting medium, membranes can be further degraded.

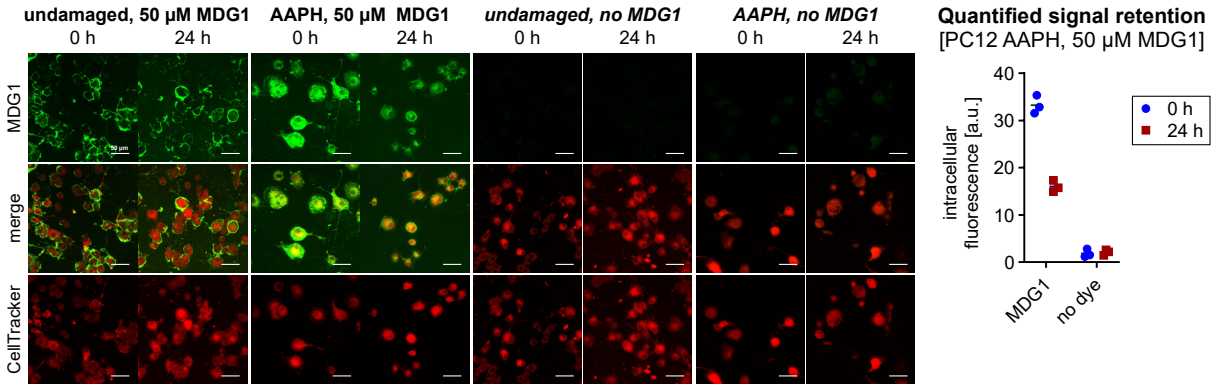

Figure S14: Imaging of MDG1 in PFA-fixed cells. Confocal microscopy images of PC12 cells pre-treated with AAPH (300 mM) for 90 min followed by **MDG1** treatment (50 µM, 10 min) and subsequent PFA fixation. Quantification of the intracellular fluorescence directly after fixation and mounting (0 h) and after 24 h (n = 3); *Scale bar: 50 µm*.

4.7 Dextran conjugates: rationale and performance

An alternative approach for fluorogenic probes to selectively report on cell membrane damage might be to develop macro-molecular probes without specific uptake mechanisms, that are excluded from healthy cells on the basis of their size (rather than their polarity), yet passively enter more porous damaged cells. Although the focus of this work was on small molecule probes, we briefly tested the accessibility of this approach.

Intensely fluorescent, cell-excluded macromolecular reporters (typically bearing several fluorophores per macromolecule) are useful for e.g. anatomical tracking of blood vessels or cell surface labelling. Dextrans are biologically "innocent" platform macromolecules that can be obtained commercially in good size purity from low kDa up to mid MDa and bearing a large range of fluorophores or reactive functional groups with various degrees of labelling.

Initial testing of permanently fluorescent dextrans indicated increased PC12 cellular uptake following membrane damage by AAPH treatments (radical PUFA peroxidation), for commercial, permanently fluorescent dextran sizes 6-120 kDa, with peak effect around 40-70 kDa (assessed after washing to remove the cell-excluded dextran fraction).

Since washing brings complications in 2D cell culture and cannot be performed *in vivo*, we then wished to test fluorogenic dextrans in a no-wash protocol; however, these are barely reported (first monofunctional fluorogenic dextran only published in 2018[17]) and there are no commercial suppliers. We therefore prepared the isobutyrate-capped, chloro-stabilised fluorogenic fluorescein NHS ester **NHS-i-Flu** because we expected commercially available fluorescein diacetate to be labile to spontaneous hydrolysis at pH~7.4 based on the observations of Raines and others.[18] We chose a mono- capped probe since its simple off/on unmasking may make it more suitable for quantification than the known doubly-capped probe.[17] Fina Biosolutions LLC (MD, USA) performed custom conjugation of **NHS-i-Flu** to 70 kDa dextran (**i-Flu-AmDex**), however, followup testing of this custom-made fluorogenic **NHS-i-Flu**-derived dextran did not indicate any increase of cellular entry (and intracellular activation and retention) following AAPH damage (**Fig S15**); and results in the same assay without washing contraindicated any significant increase of uptaken signal from the permanently fluorescent carboxyfluorescein-derived dextrans (**Fig S15**: 70 kDa; also tested: 10, 40, 2000 kDa).

Therefore, these investigations into damage-selectivity of macromolecular uptake were not continued.

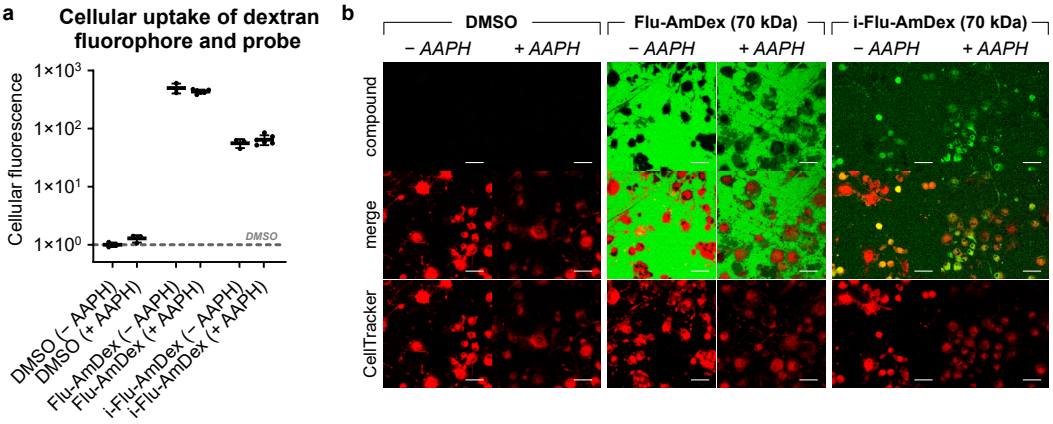

Figure S15: Initial results for dextran conjugates. (a) Quantified intracellular signal from permanently fluorescent, fluorescein dextran conjugate after washing (shown: 70 kDa) and from **NHS-i-Flu**-derived fluorogenic dextran conjugates (20 µM, 20 min, without washing) with and without pre-treatment with AAPH (300 mM, 90 min). **(b)** Confocal microscopy images of PC12 cells either untreated (without AAPH) or treated with AAPH (300 mM) for 90 min followed by treatment with dextran-conjugates (20 µM). Images taken 20 min after probe application without prior washing. *Scale bar: 50 µm*

4.8 Concept adaptation into the disulfide-reduction probe MDG2

4.8.1 Probe stability and GSH activation

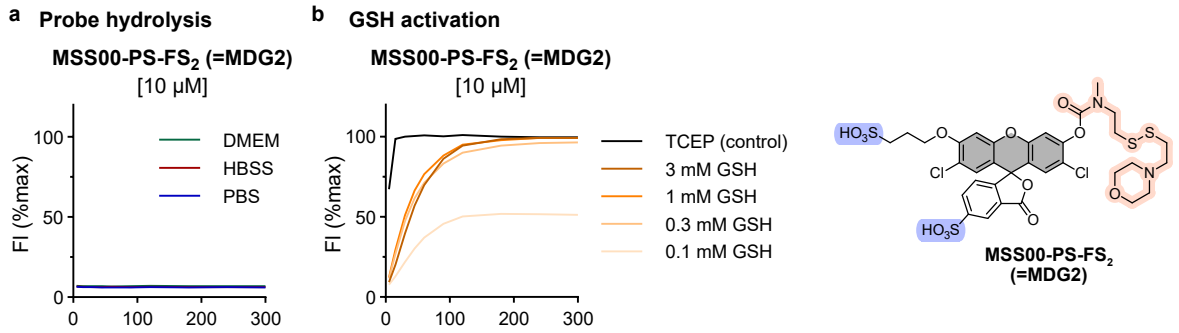

Figure S16: Hydrolytic stability and GSH activation of MSS00-PS-FS$_2$ (=MDG2). (a) Probe hydrolysis of **MDG2** in PBS, HBSS and DMEM over 5 h (probe concentration 10 µM); **(b)** GSH activation time-course over 5 h for **MDG2** with different GSH concentrations (probe concentration: 10 µM).

4.8.2 Exclusion or entry into membrane damaged cells

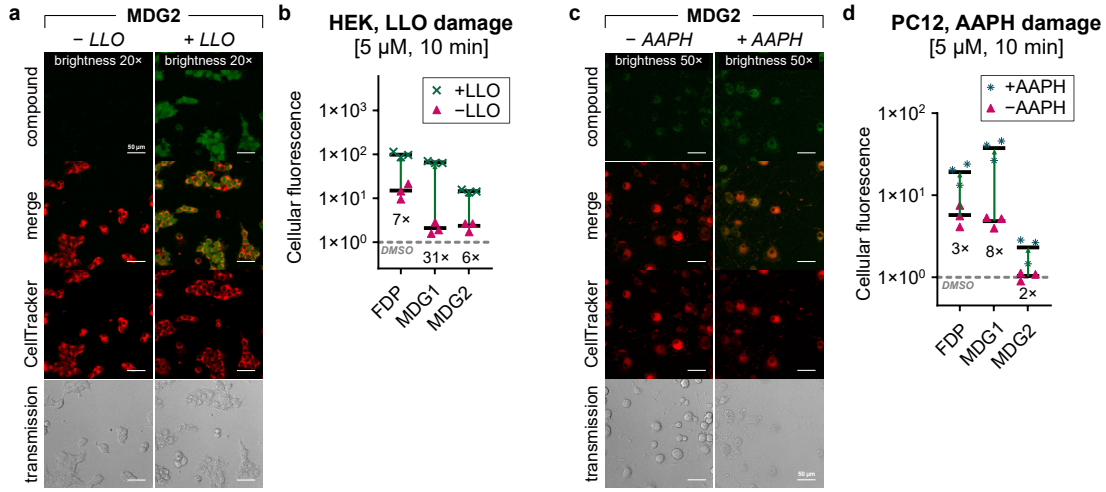

Figure S17: Membrane damage selectivity of MDG2: (a) Confocal microscopy images for **MDG2** of HEK cells pre-treated with LLO (0.2 mg/mL) for 5 min followed by probe treatment (5 µM). Images taken 10 min after probe application without prior washing (n = 3). **(b)** Quantified intracellular fluorescence for each fluorophore (5 µM, 10 min, non-wash) for healthy and LLO damaged HEK cells (n = 3). **(c)** Confocal microscopy images of PC12 cells either untreated (without AAPH) or treated with AAPH (300 mM) for 90 min followed by probe treatment (5 µM). Images taken 10 min after probe application without prior washing (n = 3). **(d)** Quantified intracellular fluorescence for each probe (5 µM, 10 min, without washing) with and without pre-treatment with AAPH (300 mM, 90 min) (n = 3). *Scale bar: 50 µm.*

4.8.3 Data (normalised): Exclusion or entry into LLO-damaged HEK cells

Table S5: Normalised intracellular fluorescence values quantified from microscopy images for the LLO membrane damage assay in HEK cells (normalised to DMSO control with LLO (such that its intracellular fluorescence value is 1), n = 3).

Compound	+LLO			−LLO			Mean (+LLO)	Mean (−LLO)	Ratio +/−LLO
MSS00-PS-FS$_2$	14.4	13.5	15.8	1.73	2.66	2.66	14.6	2.35	6.21
DMSO	1.25	0.88	0.88	0.91	0.66	0.43	**1**	0.67	1.49

4.8.4 Data (normalised): Exclusion or entry into AAPH-damaged PC12 cells

Table S6: Normalised intracellular fluorescence values quantified from microscopy images for the AAPH membrane damage assay (normalised to DMSO control (+AAPH), n = 3).

Compound	+AAPH			−AAPH			Mean (+AAPH)	Mean (−AAPH)	Ratio +/−AAPH
MSS00-PS-FS$_2$	2.65	2.83	1.46	1.09	1.12	0.898	2.31	1.04	2.23
DMSO	0.99	1.17	0.84	0.82	1.26	1.10	**1**	1.06	0.95

4.9 Cell-type-resolved features of MDG1 (healthy cells, whole lung culture)

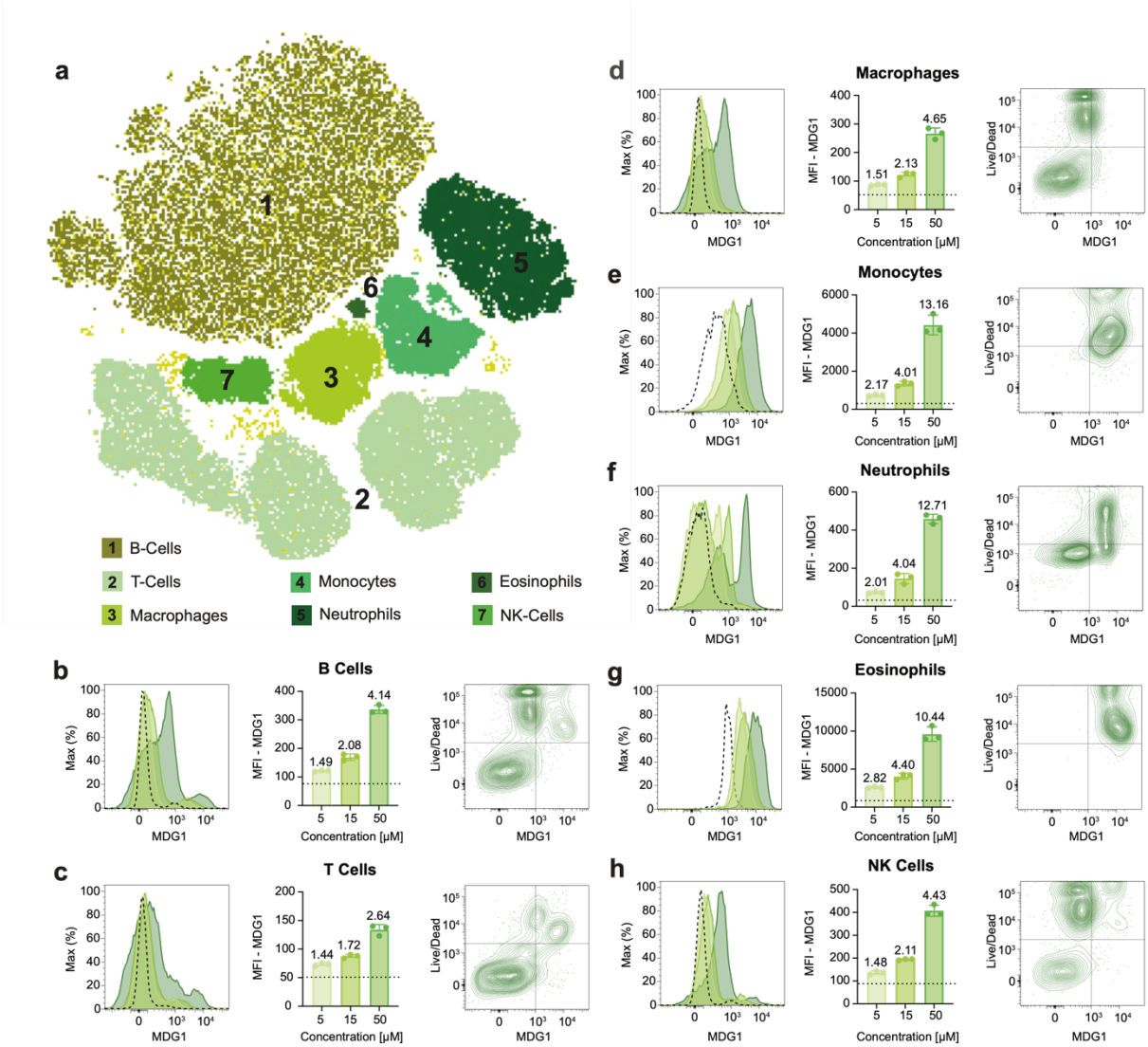

Figure S18: Plausibility comparison of MDG1 vs "Live/Dead" staining, in whole lymphocyte culture. The cells were incubated with **MDG1** followed by surface staining to identify the different cell types. **(a)** tSNE showing the different cell clusters of the whole lymphocyte culture. **(b-h)** Histograms of the cellular fluorescence intensity and barcharts of the quantified mean fluorescence intensity (MFI) with **MDG1** (5 µM, 15 µM and 50 µM), and contour plots (50 µM **MDG1** vs. Live/Dead (DAPI)) in **(b)** B cells, **(c)** T cells, **(d)** macrophages, **(e)** monocytes, **(f)** neutrophils, **(g)** eosinophils, and **(h)** NK cells. Dotted lines in the histogram indicate the control without **MDG1** stain (commonly called "fluorescence minus one", FMO). The values above the bars indicate the ratio, **MDG1** signal divided by FMO background. All data was assessed by flow cytometry and analysed with the FlowJo software. As these are mostly healthy cells, we do not expect large signal to FMO ratios, except for cells that have highly active uptake (so monocytes, neutrophils and eosinophils were not surprising). The most important features we wanted to evaluate were, for those cells that do *not* have high active uptake, (1) whether cells that have high Live/Dead stain readouts (i.e. permeable cells) would be reliably identified by **MDG1**: i.e. contour clouds for cells with high Live/Dead values are always to the right of the cloud with the lowest Live/Dead values, which was indeed observed; (2) whether the **MDG1** vs. Live/Dead contour plots could indicate cell permeability/uptake information that single-axis histograms do not resolve: which was also observed (see e.g. the plots for B cells and T cells).

4.10 Necrosis imaging in the fly

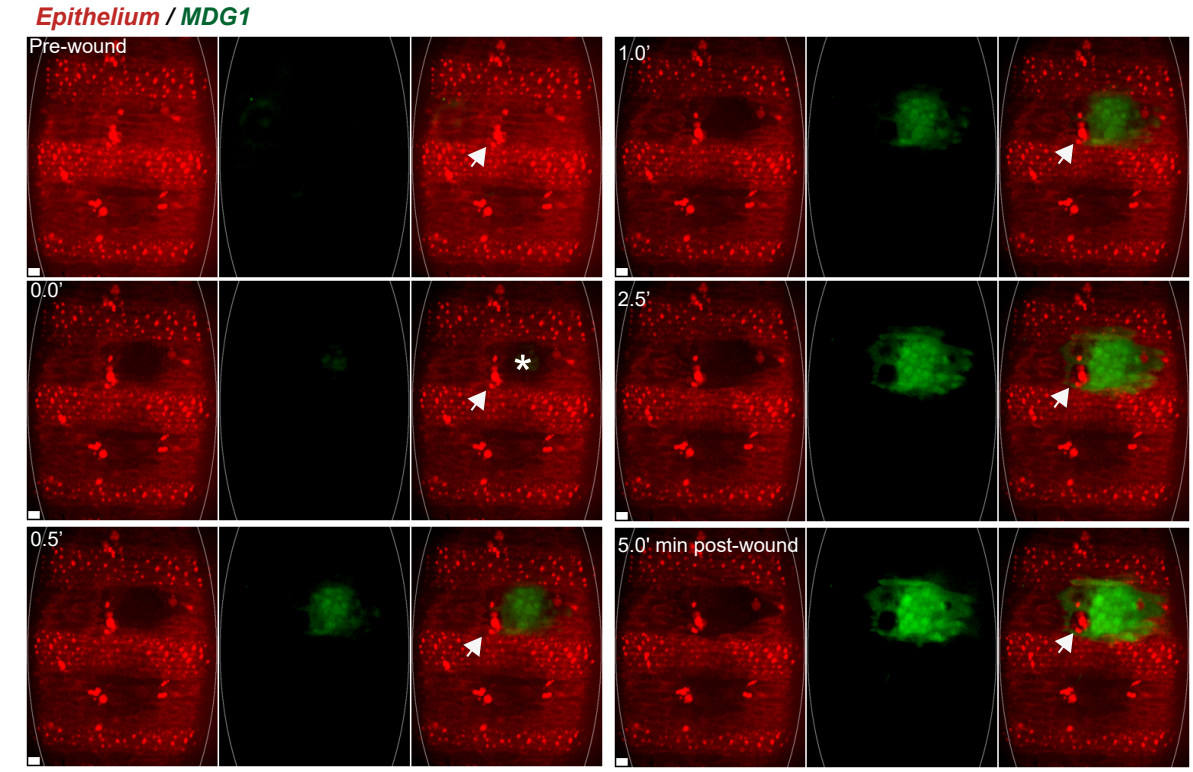

Figure S19: **MDG1 labels *in vivo* necrotic tissue damage within wounded *Drosophila* embryo.** Ventral epithelium (mcherry-Moesin, red channel, oval outline) of *Drosophila* embryo was locally wounded using laser ablation (asterisk). Laser-wounding results in necrotic tissue damage, which was rapidly labelled with previously microinjected **MDG1** (green). Time = minutes, scale bars = 10 µm. For further details, see **Fig 6** and its full legend (**Supporting Note 3**). Note also the two macrophages at centre-left (containing ingested mCherry conglomerates) which are not laser-damaged, and therefore are not labelled (they show up as shadows in the green channel); the larger of the two is indicated with the white arrowhead, the smaller is directly above it.

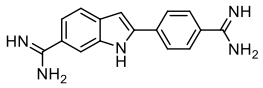

Sytox Green

Figure S20: Structure of Sytox Green.

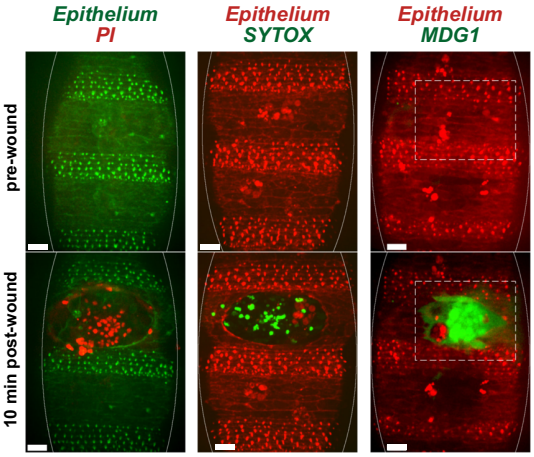

Figure S21: Direct comparison of the membrane-damage staining of PI, Sytox Green and MDG1 in necrotic tissue damage within wounded *Drosophila* embryo. Ventral epithelium (green channel for PI, red channel for Sytox and MDG1, oval outline) of *Drosophila* embryo was locally wounded using laser ablation. Laser-wounding results in necrotic tissue damage, which was rapidly labelled with previously microinjected PI (red, nuclear staining), Sytox Green (green, nuclear staining) or **MDG1** (green, cytosolic staining of the whole wounded area). Note the way that **MDG1** highlights the presence of non-damaged macrophages within the damage zone, which PI cannot reveal. Scale bars = 10 µm.

4.11 Axonal imaging of neuronal cultures in microfluidic chambers

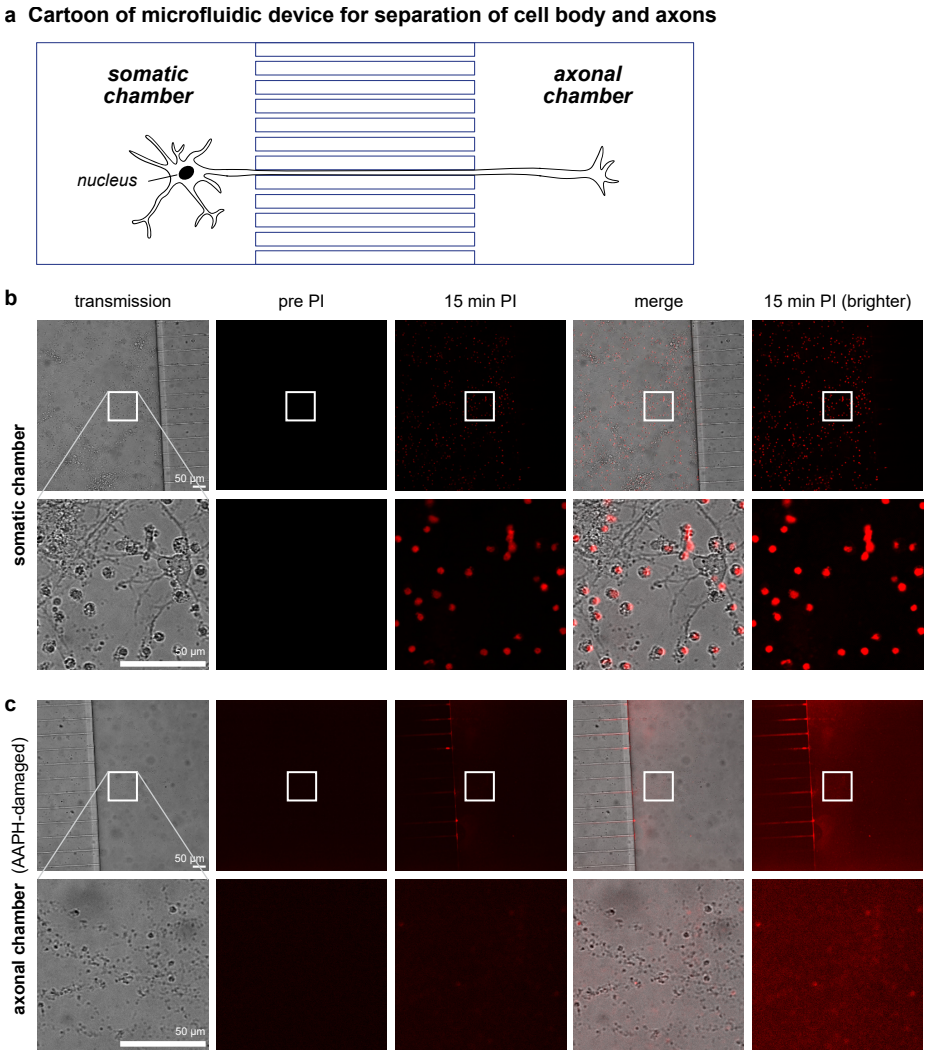

Figure S22: Propidium iodide (PI) stains the nuclei of damaged neurons but does not label membrane-compromised axons (here shown by the separation between the somatic and axonal chambers). (a) Cartoon of how neurons grow in the microfluidic device that models the physiological separation of cell body and axonal terminals: a widely used and accepted *in vitro* model of soma-axon separation.[22,23] E16.5 primary hippocampal neurons are harvested from mice, and placed in the somatic chamber of the microfluidic device. About half the cells grow healthily, and during culturing over weeks they grow axons through the channels into the axonal chamber. *(The other half of the cells within the somatic chamber are damaged or dying from the harvesting and seeding process, which is why they can be stained by PI in the somatic chamber: see panel **b** (rounded-up structures in the zoomed-in transmission image), but these are not expected to grow axons into the axonal chamber (therefore no strong staining with **MDG1** is expected in the axonal chamber without additional damage in this compartment).* Cells are then treated and imaged. **(b-c)** Neurons were damaged in the axonal compartment only by treatment with AAPH (90 min, 300 mM) in the axonal chamber, then treated with PI in both chambers (3.3 µg/mL). Images were taken before, and 15 min after, PI addition. **(b)** In the somatic chamber, PI stains the dying or damaged neurons: as expected, the staining is only visible in the nuclei (which are in the somatic chamber). **(c)** In the axonal chamber, there is no PI stain that can reveal AAPH-damaged axons. Even when the brightness of the PI channel is greatly increased (right column), no damaged axon structures are visible, only background (compare to CellTracker images in **Fig S23**). Scale bars = 50 µm; lower-row images are zoomed-in areas from the corresponding upper rows.

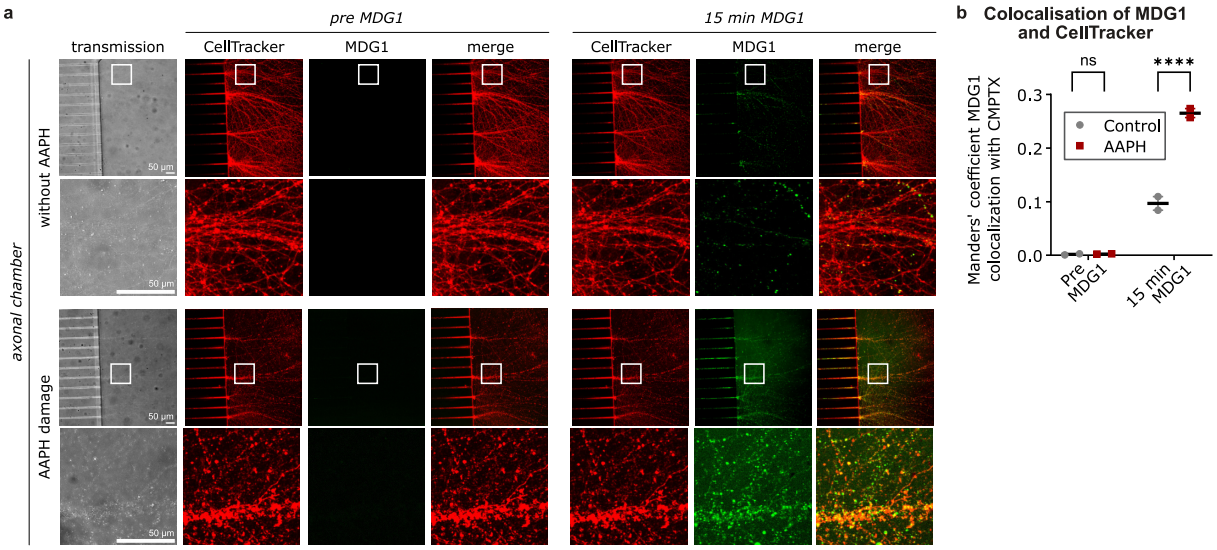

Figure S23: AAPH-damaged axons show increased MDG1 signal compared to undamaged axons. Hippocampal neurons were grown in microfluidic devices as per **Fig S22**. Cells were stained red by CMTPX CellTracker; AAPH damage was induced in the axonal chamber; and then **MDG1** was applied (25 µM); images were taken before or 15 min after **MDG1** application. **(a)** While at 15 min after dye application there is only a minor co-localization of the **MDG** signal with axons without AAPH damage, with AAPH damage there is a marked increase in the co-localization between **MDG1** signal and axons (yellow pixels in the *15 min, merge* images at bottom right). **(b)** Mander's coefficient for the co-localisation of **MDG1** to CellTracker, depending on AAPH treatment. AAPH-damaged axons have substantially higher colocalization of **MDG1** pixels to CellTracker pixels than non-damaged axons. This supports that their much brighter overall **MDG1** signal is indeed due to more dye being activated within axons, rather than extracellularly (NB: **MDG1** brightness is the same across all images). Scale bar = 50 µm.

5 Biological materials and methods

5.1 Cell lines

HeLa cells were obtained from German Collection of Microorganisms and Cell Cultures (DSMZ Cat No. ACC 57) and grown in Dulbecco's modified Eagle's medium (DMEM, Sigma-Aldrich, D1145) supplemented with 10% heat-inactivated fetal bovine serum (Sigma-Aldrich, F0804), penicillin (100 U/mL) and streptomycin (100 µg/mL) (Sigma-Aldrich, P4333) at 37°C and 5% CO_2. Cell growth was monitored using an inverted microscope (Nikon Eclipse Ti).

HEK 293T cells were obtained from ATCC (Cat. No. crl-3216) and grown in DMEM (ThermoFisher 21885108) supplemented with 10% FBS (Biochrom S0615) and 1% Penicillin/Streptomycin (ThermoFisher 15140122) at 37°C and 5% CO_2. Cell growth was monitored using an inverted microscope (Leica DMi1).

PC12 cells were obtained from Sigma-Aldrich (Cat. No. 88022401) and grown in RPMI (ThermoFisher 61870010) supplemented with 10% Horse Serum (Sigma-Aldrich H1138), 5% FBS and 1% Penicillin/Streptomycin at 37°C and 5% CO_2. Cell growth was monitored using an inverted microscope (Leica DMi1).

5.2 Cell-free characterisation

Plate reader instrument

Raw fluorescence readout of cell-free activity was performed with a FluoStar Omega plate reader from BMG Labtech, Ortenburg (Germany), set to ex: 485bp10 and em: 520lp. All plate reader experiments were performed in black 96 well plates.

Cell media for probe stability assay

- Phosphate buffered saline (PBS) from Sigma Aldrich (Cat. No. D8537)
- Hanks´ balanced salt solution (HBSS) from Sigma Aldrich (Cat. No. H6648)
- Dulbecco´s modified eagle´s medium from Sigma Aldrich (Cat. No. D1145) without FBS supplementation

Probe stability assay

Water (10 µL) was placed in a black 96 well plate and the probes/fluorophores were added from a 1 mM stock solution in DMSO (1 µL) (water stock for **H-PS-FS$_2$** and **iPS-FS$_2$** = **MDG1**). Then the different media PBS, HBSS or DMEM (89 µL) were added to the probes with a multipipette (for smallest possible differences in the starting time) to reach a final concentration of 10 µM. All samples in technical duplicates. The fluorescence intensity in each well was measured with the plate reader at different time-points (0 min, 15 min, 30 min, 1 h, 2 h, 3 h, 4 h, 5 h, 6 h). Between measurements the samples were incubated at 37 °C under air atmosphere. At the end of the experiment, a piperidine solution (50 mM, 100 µL) was added to each well to determine the maximum intensity in each well. The recorded data were background subtracted (fluorescence at 0 min) and normalised to their maximum fluorescence (determined after 2 h incubation with piperidine).

Esterase assay

PBS (49 µL) was placed in a black 96 well plate and the probes/fluorophores were added from a 1 mM stock solution in DMSO (1 µL) (water stock for **H-PS-FS$_2$** and **iPS-FS$_2$** = **MDG1**). Porcine liver esterase (lyophilised powder, ≥15 units/mg, purchased from Sigma Aldrich, Cat.-No.: E3019) was diluted in PBS to give a stock solution of 500 ng/mL. The esterase stock solution was added to the probes with a multipipette (for smallest possible differences in the starting time) to reach a final probe/fluorophore concentration of 10 µM and a esterase concentration of 250 ng/mL (all samples in technical duplicates). The probes/fluorophores were placed in the pre-heated plate reader and incubated at 37 °C for the whole experiment. The fluorescence intensity in each well was measured every two minutes for the total duration of 90 min. At the end of the experiment, a piperidine solution (50 mM, 100 µL) was added to each well to determine the maximum intensity in each well. The recorded data were background subtracted (fluorescence at 0 min) and normalised to their maximum fluorescence (determined after 2 h incubation with piperidine).

Michaelis-Menten kinetics

PBS (75 µL, pH=7.4) was placed in a black 96 well plate, porcine liver esterase (PLE, ammonium sulfate suspension, 229 U/mg; Sigma Aldrich, Cat.-No.: E2884) was added (final concentration: 10 ng/mL) and the mixture was warmed to 37 °C. The probes were added from 5X DMSO stocks and the fluorescence intensitiy was measured in the pre-heated plate reader at 37 °C for 20 min. The corresponding fluorophores were measured (10 µM) for calculating the conversion rates. All probes were parallelly measured without PLE in PBS only for background subtraction of spontaneous hydrolysis. For double ester probes the generated signal was corrected by a factor of 10 to account for the mono-activation of the probe which gives circa 10% of the fluorescence of the fluorophore.

5.3 Flow cytometry

Instrument and data analysis

Flow cytometry experiments were performed on a LSR Fortessa flow cytometer (Becton Dickinson) run by BD FACSDiva software (version 8.0.1). 20,000 events per technical replicate were analysed. Channel 530/30 was used for probe/fluorophore quantification and channel 780/60 was used for Zombie NIR Dye quantification. FlowJo software from BD (version 10.8.1) was used for data analysis. Live/dead gating was performed from the heat-treated cells (for gating settings see **Fig S24**) and only live cells were used for fluorescence evaluation. All quantified fluorescence values were normalised to the auto-fluorescence of untreated cells (DMSO control).

Sample preparation

HeLa cells were seeded in 24-well plates (250.000 cells / well) and cultured in DMEM for 16 h. The medium was removed and the cells were carefully rinsed with HBSS (3 × 250 µL). The probes and fluorophores were prepared in HBSS from DMSO stocks (final compound concentration: 10 µM, final DMSO concentration: 1 %) and added to the cells (250 µL each). The plate was incubated at 37 °C under air atmosphere for 20 min. Then the medium was removed, the cells were trypsinised with 1 × Trypsin in PBS and centrifuged for 5 min at 500g. The supernatant was removed and the cells were resuspended in PBS (200 µL; + 1% FBS; + 1:200 Zombie NIR Fixable Dye from BioLegend®, cat.-no.: 423105) and placed on ice until measurement at the flow cytometer.

Live/dead control: these cells were not incubated with a probe/fluorophore but heated to 70 °C for 3 min in HBSS before applying the Zombie staining. Otherwise, the cells were treated like all other conditions.

5.4 Confocal microscopy

Instrument

Confocal imaging was performed at the Core Facility Bioimaging of the LMU Biomedical Center with an inverted Leica SP8X microscope, equipped with Argon laser, WLL2 laser (470 - 670 nm) and acusto-optical beam splitter. Live cells were recorded at 37 °C and kept in Hank's Balanced Salt Solution (HBSS, ThermoFisher 14025092) for the duration of the assay for minimal spontaneous hydrolysis of the probes and to allow incubation without CO_2. The same instrument was used to record fixed cells mounted onto slides.

Acquisition Settings

General Settings: Images were acquired with a 20× 0.75NA objective and additional optical zoom of 2×. Image pixel size was 284×284 nm. The following fluorescence settings were used: probes/fluorophores (from here on comprehensively referred to as "compounds", excitation 488 nm (Argon), emission 500 – 540 nm) and CellTracker (excitation 594 nm (WLL), emission 605 – 645 nm). Recording was performed sequentially to avoid bleed-through. Compounds and CellTracker were recorded with hybrid photo detectors (HyDs), a transmitted light image was generated with a conventional photomultiplier tube. The microscope was programmed to take three images of different fields of view per condition tested (fixed cell imaging: three images per coverslip), which were focused using reflection-based adaptive focus control.

Standard compound uptake assay protocol: The scan was started after 10 min of compound incubation. Bias deriving from time delays between compounds imaged in different wells was minimised by permutation of the positioning of compounds between replicates. The time-delay between LLO- or AAPH-treated cells and their respective sham-treated controls was constant (2.5 min) due to the setup of the plate.

To account for vast brightness differences between the compounds, which were larger than the dynamic range of the detectors, brighter compounds were detected using narrower and red-shifted emission windows. H_2-FS_1, i_2-FS_1 and a_2-FS_1 were detected at 580 - 585 nm or 560 - 565 nm for HEK-LLO and PC12-AAPH assays respectively. H_2-FS_0, i_2-FS_0, fluorescein and FDP were detected at 545 - 570 nm or 550 - 565 nm for HEK-LLO and PC12-AAPH assays respectively. The normalisation factor was determined by taking a sequential scan of both detection windows (original 500 – 540 nm and red-shifted window) at low 488 nm Argon laser power.

Wash-free imaging over longer time-period: Additional scans of the same fields of view were started at 15, 25, 35, 55, 75, 105 and 135 min of compound incubation.

Post-wash cell retention live-cell imaging: The pre-wash scan was started after 10 min of compound incubation as usual. Washing was performed and additional scans of the same fields of view were started at 0, 10, 20, 40, 60, 90 and 120 min post-wash.

Resealing assays: For each well, images were taken after 10 min of compound incubation.

Fixed cell assays: The slides were imaged directly after fixation and mounting and again about 24 h later.

Sample preparation

Live cell assays were performed in 8-well glass bottom chambered coverslips (ibidi 80827). For fixed cell assays, 12 mm diameter coverslips (ethanol washed and autoclaved) were placed in 24-well plates. For HEK cell assays, coverslips were coated one day before experiment by applying a 0.1 mg/mL poly-D-lysine (Sigma-Aldrich P7280) solution for 2 h at 37°C. HEK cells were seeded into the coated wells at a density of 30.000 cells per cm². For PC12 cell assays, coverslips were coated six days before the experiment by applying a 0.1 mg/ml poly-D-lysine solution for 2 h at 37°C, followed by collagen IV (Sigma-Aldrich H4417) coating at 0.1 µg / cm^2 and 37°C overnight. PC12 cells were separated by drawing them ten times through a 30 G needle and then seeded into the coated wells at a density of 10.000 cells per cm². Two hours after seeding, medium was changed to differentiation medium (RPMI supplemented with 1% Horse Serum, 1% Penicillin/Streptomycin and 100 ng/ml ß-NGF (ThermoFisher 13257-019)). Medium was again changed to fresh differentiation medium 48 – 72 h after seeding.

5.4.1 LLO and AAPH damage assay procedures

HEK-LLO live cell assays were performed with the following timeline: To stain all cells irrespectively, HEK cells were incubated with 0.5 µM CellTracker™ Red CMTPX Dye (ThermoFisher C34552) at 37 °C for 15 min. Medium was then changed to ice cold HBSS containing 0.2 µg/ml lysteriolysin O (LLO, abcam ab83345) or ice cold HBSS only for control wells. Cells were incubated on ice for 5 min. Medium was then changed to 5 µM compound solutions prepared with 37 °C warm HBSS and chambered coverslips were subsequently put onto the microscope stage (37 °C).

PC12-AAPH live cell assays were performed with the following timeline: To stain all cells irrespectively, PC12 cells were incubated with 0.5 µM CellTracker™ Red CMTPX Dye at 37 °C for 15 min. Medium was then changed to HBSS containing 300 mM AAPH (Cayman Chemical Cay82235-10) and 100 ng/ml ß-NGF or HBSS with ß-NGF only for control wells. Cells were incubated at 37°C on the microscope stage for 90 min. Cells were then 1x washed with HBSS and medium subsequently changed to 5 µM compound solutions.

Altered timeline for post-wash cell retention assays: An additional wash step was introduced after the end of the confocal scan started at 10 min compound incubation. The complete medium was removed and replaced by 37 °C warm HBSS. The washing was performed twice.

Altered timeline for resealing assays: The timeline was followed as described above for only one well (0 min recovery time) for all other wells medium was changed to 37 °C warm HBSS after LLO-/AAPH-incubation (in case of AAPH after additional HBSS wash step as described above). The medium change to 5 µM compound solutions occurred at different timepoints (10, 20, 40, 60, 90, 120 min recovery time measured from the end of LLO-/AAPH incubation) for one well at a time.

PC12-AAPH fixed cell assays were performed with the following timeline: All conditions were performed in duplicates. To stain all cells irrespectively, PC12 cells were incubated with 2 µM CellTracker™ Red CMTPX Dye in PC12 growth medium at 37 °C, 5% CO_2 for 15 min. Medium was then changed to PC12 growth medium containing 300 mM AAPH (Cayman Chemical Cay82235-10) and 100 ng/ml ß-NGF or PC12 growth medium with ß-NGF only for control wells. Cells were incubated at 37°C, 5% CO_2 for 90 min. Cells were then 1x washed with PBS and subsequently incubated with 50 µM compound in PBS or PBS only for control wells at 37°C, 5% CO_2 for 10 min. Cells were washed with cold PBS and then incubated with 4% paraformaldehyde (PFA) for 10 min at room temperature. PFA was washed away twice with PBS. For mounting, a small drop of Vectashield® Antifade Mounting Medium (Vector Laboratories, H-1000) was placed on the slide and the coverslip positioned on it face-down. Excess mounting medium was carefully removed. Samples were left to dry for around 10 min and the remaining salt film removed with ethanol before imaging.

5.4.2 Image analysis

Images were analysed using Fiji ImageJ. Based on the CellTracker channel, in which all cells are stained irrespective of membrane damage, images were segmented using the “Trainable Weka Segmentation” plugin. For resealing assays the segmentation was performed on the compound channel for reasons outlined below. The classifier was trained individually for every single image. The plugin generates a mask that defines two regions: Intracellular and extracellular. The intracellular region of interest (ROI) was then eroded by 10 pixels to exclude the periphery of cells (where they are very thin and show low signal for both CellTracker and compounds) from analysis. The resulting mask was then applied to the compound channel, to obtain an intracellular and extracellular mean fluorescence intensity value.

For bright compound detected with red-shifted emission windows, these intensity values had to be multiplied with a normalisation factor which was obtained by measuring and averaging over mean fluorescence intensity of ten cells in original vs red-shifted detection window, thus obtaining a mean normalisation factor.

For the standard uptake assay, values were normalised to intracellular value of DMSO control. For wash-free imaging over longer time-period, values were normalised to the mean 10 min incubation time value. For post-wash cell retention live-cell imaging, values were normalised to the mean pre-wash value. For resealing assays, values were normalised to the mean 0 min recovery time value.

Images were excluded from analysis if they were out of focus, showed less than three cells, overgrown cells (> 66% of area covered by cells) or an intolerable amount of dead cells or debris. If more than one image had to be excluded, the complete replicate (LLO- or AAPH- and sham-treated condition) was repeated for the affected compound.

Data was plotted using GraphPad Prism. The same primary data was used for to quantify intra-/extracellular distribution of compounds in healthy HEK cells (sham-treated) and to compare compound uptake into LLO- vs sham-treated cells (intracellular values used only). Likewise, intracellular quantification values were used to compare compound uptake into AAPH- vs sham-treated cells. For all resulting plots, one data point represents one replicate (mean over three fields of view) unless noted otherwise.

Altered segmentation for resealing assays: For the resealing assay, segmentation was not performed on the CellTracker channel, but on the compound channel. This was done to exclude cells that had never been damaged (from here on referred to as “undamaged cells”) from analysis. The reason why this was necessary for this experiment but not for others is that while in all HEK-LLO assays a small proportion of cells remains undamaged (i.e. not taking up compound while neighbouring cells do), the resealing assay with its delayed medium change to compound leads to increasing detachment of damaged cells towards later timepoints while the undamaged cells stay attached. This biases the cell distribution towards a higher proportion of undamaged cells towards later analysis timepoints. This bias can be circumvented by segmentation on the compound channel, thus excluding undamaged cells. A limitation of this approach is, that it also excludes completely resealed cells from analysis. Using a two-dye approach in which we incubated cells with Cadaverine-AlexaFluor594 at 0 min recovery time and the same cells with **MDG1** after longer recovery times, we could estimate that the number of completely resealed cells is below 3% and thus negligible for resealing analysis (data not shown). For comparability reasons, the segmentation on compound channel was also performed for the PC12-AAPH resealing assay although the described bias does not exist there.

5.5 Ferroptosis sensing, isolated mouse lung lymphocytes

Mice

C57BL/6 (WT) were bred in-house and maintained at in-house facilities. All mice were kept under specified pathogen free (SPF) conditions. All procedures were performed according to ethical protocols approved by the local and regional ethics committees.

Whole lymphocyte culture

Lungs were isolated, diced and digested with Liberase TL (0.25 mg/mL, Roche) and DNase I (1 mg/mL, Sigma) for 1 h at 37 °C. Lung cells were purified using a 37.5% Percoll gradient and red blood cell lysis was performed with Ammonium-Chloride-Potassium (ACK) lysing buffer. The single cell suspension was plated in 96-well U bottom plates with 3 x 10^5 cells per well in RPMI medium supplemented with 3% FCS. Cells were then treated with RSL3, H_2O_2, or left untreated (PBS control) for 24 h at 37 °C.

Flow cytometry

To probe for signal from **MDG1** or BODIPY, total lung lymphocytes were incubated with **MDG1** (50 µM in FCS-free RPMI) for 30 min at 37 °C or with BODIPY- C11 (RED) (250 µM in FCS-free RPMI) (Image-iT® Lipid Peroxidation Sensor Kit, Fisher Scientific) for 1 h at 37 °C. To stain for surface markers fluorochrome-conjugated antibodies against the following surface antigens were used: CD45, CD11b, CD11c, Ly6G, Ly6C, SiglecF, F4/80, CD64, CD19, TCRb, CD4, CD8, CD44, NK1.1. DAPI (1:10000 from 5 mg/mL stock; at 4 °C for 20 min) was used to exclude dead cells. After washing the cells were resuspended in 50 µL FACS buffer and subsequently analysed using a BD LSR Fortessa.

5.6 Necrosis sensing, live fly embryo

; e22c-gal4, uas-mcherry-moesin[19,20] (SYTOX and MDG1) *or ; ubi-gma*[21] (PI) *Drosophila* embryos were collected in cell strainers (Falcon), dechorionated with bleach (Jangro), and washed with water. Embryos (stage 15) were mounted ventral side up on scotch tape stuck down on a glass slide, then dechorionated in box with silica beads for 25-30 min. A droplet of VOLTALEF oil (VWR) was added to each embryo, following which **MDG1** (10 mM in water) or SYTOX™-Green (Invitrogen, Thermo Fisher Scientific, diluted 1:50, (0.6 µM) with PBS) or neat Propidium Iodide (eBioscienceTM, Thermo Fisher Scientific, 0.02 mg/mL) was microinjected at 300 hPa into the intervitelline space surrounding the head of the embryo using an InjectMan4® microinjector (Eppendorf) and a FemtoJet injectman rig (Eppendorf) fitted with Femto tips (Eppendorf). A bridging glass cover slip was sealed over the top of the embryos, supported by two coverslips either side of the embryos. These were imaged live on an inverted spinning disc confocal microscope (Perkin Elmer Ultraview) with a plan-apochromat 63× objective (NA 1.4) and a Hamamatsu C9100-14 camera, and Volocity acquisition software (Perkin Elmer). Epithelial wounds were generated using a nitrogen-pumped Micropoint ablation laser tuned to 435 nm (single photon mode, focused within the epithelial layer at the area indicated by the asterisk; Andor Technologies). All images shown are z-projections.

The full imaging time-course is shown as the channel merge in **Movie S1**, with annotated still image zooms in **Fig 6**, and with larger resolution images of the first five minutes in **Fig S19**. For further details see the full legend to **Fig 6**, given in **Supporting Note 3**.

5.7 Axonal imaging of neuronal cultures in microfluidic chambers

RD450 microfluidic chambers (Microfluidic Neuron Device XONA Microfluidics Cat# RD450) were assembled and neurons were seeded as described previously.[22] Briefly, the devices were sterilized using 70% ethanol. Once dry, the devices were assembled in 6-well glass bottom plates coated overnight with 20 mg/mL poly-L-Lysine and 3.5 mg/mL laminin that had been thrice washed with distilled water and dried. Dissection of E16.5 mouse hippocampal neurons were done as described previously.[23] Following dissociation, hippocampal neurons were pelleted at 4000g for 4 min and resuspended at a final concentration of 400k in Neuronal Basal + PSG + B27. 10 µL were plated into the somal compartment and incubated at 37°C in 5% CO2 for 15 min before filling the wells up with Neuronal Basal + PSG + B27. 50% of the medium was replaced every 2-3 days with fresh Neuronal Basal + PDG + B27. For MDG1 experiments, prior to imaging, 5 µM CMTPX were mixed in Neuronal Basal + PSG + B27 and added to the top somal and axonal well of DIV8-9 neurons and incubated at 37°C in 5% CO_2 for 15 min for an even distribution and rinsed twice with Neuronal Basal + PSG + B27 (no CMTPX staining was performed for PI experiments). This was followed by a 90 min incubation at 37 °C in 5% CO_2 of 300 mM AAPH mixed in Neuronal Basal + PSG + B27 added to the top axonal well. To ensure proper osmotic pressure, 150 µL was added to the top axonal well for even distribution between the axonal wells, whereas 120µL Neuronal Basal + PSG + B27 was added to both somal wells. At the microscope, all four wells were washed with imaging media HBSS three times and pre-images were acquired at a Nikon Ti2 spinning disk microscope using 20x/air objective. The HBSS was then replaced with HBSS containing 25 µM MGD1 or 3.3 µg/mL PI and the chosen ROIs were imaged at 5 and 15 min following the addition of MGD1.

Analysis of MGD1 staining in neuronal cultures: 5 ROIs (100 µm × 100 µm) were chosen per image timeframe. For **MGD1** fluorescent intensity measurements, the images were subjected to maximum projection and the average integrated density was acquired. Co-localization was analysed in z-stack images using the JACoP plugin and the Mander's coefficients were exported to Excel and plotted in GraphPad.

6 Synthetic Chemistry

6.1 Chemistry methods and techniques

6.1.1 Analytical methods

High resolution mass spectrometry (**HRMS**) was conducted using two different instruments: (1) a *Thermo Finnigan LTQ FT Ultra FourierTransform* ion cyclotron resonance spectrometer from *ThermoFisher Scientific GmbH* applying electron spray ionisation (ESI) with a spray capillary voltage of 4 kV at temperature 250 °C with a method dependent range from 50 to 2000 u and (2) a *Finnigan MAT 95 from Thermo Fisher Scientific* applying electron ionisation (EI) at a source temperature of 250 °C and an electron energy of 70 eV with a method dependent range from 40 to 1040 u.

Nuclear magnetic resonance (**NMR**) spectroscopy was performed using different instruments: (1) a *Bruker Avance* (600/150 MHz, with TCI cryoprobe) or (2) a *Bruker Avance III HD Biospin* (400/100 MHz, with BBFO cryoprobe^{TM}) from Bruker Corp. either at 400 MHz or 500 MHz or (3) a Bruker Avance III HD (800 MHz, with cryoprobe). NMR-spectra were measured at 298 K, unless stated otherwise, and were analysed with the program *MestreNova 12* developed by *MestreLab Ltd.* ^{1}H-NMR spectra chemical shifts (δ) in parts per million (ppm) relative to tetramethylsilane (δ = 0 ppm) are reported using the residual protic solvent ($CHCl_3$ in $CDCl_3$: δ = 7.26 ppm, DMSO-d_5 in DMSO-d_6: δ = 2.50 ppm, CHD_2OD in CD_3OD: δ = 3.31 ppm) as an internal reference. For ^{13}C-NMR spectra, chemical shifts in ppm relative to tetramethylsilane (δ = 0 ppm) are reported using the central resonance of the solvent signal ($CDCl_3$: δ = 77.16 ppm, DMSO-d_6: δ = 39.52 ppm, CD_3OD: δ = 49.00 ppm) as an internal reference. For ^{1}H-NMR spectra in addition to the chemical shift the following data is reported in parenthesis: multiplicity, coupling constant(s) and number of hydrogen atoms. The abbreviations for multiplicities and related descriptors are s = singlet, d = doublet, t = triplet, q = quartet, or combinations thereof, m = multiplet and br = broad. When rotamers were observed in the NMR spectra, the corresponding signals are separated by a slash ("/"). Where known products matched literature analysis data, only selected data acquired are reported.

Analytical high performance liquid chromatography (**HPLC**) analysis was conducted either using an *Agilent 1100* system from *Agilent Technologies Corp.,* Santa Clara (USA) equipped with a DAD detector and a *Hypersil Gold* HPLC column from *ThermoFisher Scientific GmbH*, Dreieich (Germany) or a *Agilent 1200 SL* system *Agilent Technologies Corp.,* Santa Clara (USA) equipped with a DAD detector, a *Hypersil Gold* HPLC column from *ThermoFisher Scientific GmbH*, Dreieich (Germany) and consecutive low-resolution mass detection using a LC/MSD IQ mass spectrometer applying ESI from *Agilent Technologies Corp.,* Santa Clara (USA). For both systems mixtures of water (analytical grade, 0.1 % formic acid) and MeCN (analytical grade, 0.1 % formic acid) were used as eluent systems.

UV-Vis spectra were recorded on an Cary 60 UV-Vis spectrophotometer from *Agilent Technologies Inc*., Santa Clara (USA) using 1 cm quartz or PMMA cuvettes. The scan rate was set to 600 nm/min and 2.5 nm slit width was used. Unless stated otherwise, the probes and fluorophores were dissolved in PBS (pH = 7.4, 1 % DMSO) at 10 µM concentration.

Fluorescence spectroscopy was performed on a Cary Eclipse Fluorescence Spectrometer from *Agilent Technologies Inc*., Santa Clara (USA) using quartz cuvettes. 480 nm light was used for excitation and spectra were recorded from 490−620 nm. The scan rate was set to 120 nm/min and 5 nm slit width was used. Unless stated otherwise, the probes and fluorophores were dissolved in PBS (pH = 7.4, 1 % DMSO) at 10 µM concentration.

6.1.2 Synthetic techniques

Unless stated otherwise, all reactions were performed without precautions in regard to potential air- and moisture-sensitivity and were stirred with Teflon-coated magnetic stir bars. For work under inert gas (nitrogen) atmosphere, a Schlenk apparatus equipped with a liquid nitrogen trap and a high vacuum pump from Vacuubrand GmbH, Wertheim (Germany) were used. For solvent evaporation a *Laborota 400* from Heidolph GmbH, Schwabach (Germany) equipped with a vacuum pump was used. Flash column chromatography was conducted with a Biotage® Isolera One Chromatograph with Biotage® Sfär Silica D columns (10 g or 25 g silica) for normal-phase (np) chromatography or with Biotage® Sfär C18 D columns (12 g or 30 g silica) or Phenomenex AQ C18 spherical 20-35 µm columns (12 g) for reversed-phase (rp) chromatography. Reactions were monitored by thin layer chromatography (TLC) on TLC plates (*Si 60 F254 on aluminium sheets*) provided by Merck GmbH and visualised by UV irradiation and by analytical HPLC.

Chemicals

All chemicals, which were obtained from Sigma-Aldrich, TCI, Alfa Aesar, Acros, abcr or carbolution were used as received and without purification. Tetrahydrofuran (THF), dichloromethane (DCM) and dimethylformamide (DMF) were provided by Acros and were stored under argon atmosphere and dried over molecular sieves. TLC control, extractions and column chromatography were conducted using distilled, technical grade solvents. Whenever the term *hexanes* is used, the applied solvent actually comprised isomeric mixtures of hexane (2-methylpentane, 3-methylpentane, 2,2-dimethylbutane, 2,3-dimethylbutane).

6.2 Synthetic procedures

6.2.1 Literature procedures

The following molecules were synthesised according to literature procedures:

- **i_2-FS$_0$**[24]
- 4-(2-iodoethyl)morpholine[25]
- MSS00·HCl[26]

Synthetic Note: The mono-capped probes were synthesised by a route designed for simplicity and to avoid chromatography (**Fig 3b**). For example, **H_2-FS$_1$** was doubly alkylated at both the carboxylate and the phenol, then the ester was cleaved mildly with LiOH in THF/water at room temperature, to return the mono-alkylated fluorophores (e.g. **H-Me-FS$_1$, Fig 3b**); using typical conditions such as sodium hydroxide in methanol required heating and resulted in significant decomposition of the fluorescein core to the corresponding benzophenones. These mono-alkylated fluorophores were capped with isobutyric anhydride, affording the probes in good yield after the first and only column chromatography (e.g. **iMe-FS$_1$**, 58% over three steps, **Fig 3b**). Pure reference samples of uncapped, mono-alkylated fluorophores (e.g. **H-Me-FS$_1$**) could also be obtained by re-cleaving these probes with sodium hydroxide at room temperature within five minutes.

6.2.2 Symmetric Fluorophores and Probes [non- or bis-acylated]

5-Sulfo-2′,7′-dichlorofluorescein (H_2-FS$_1$)

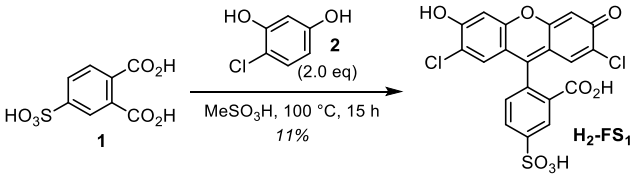

H_2-FS$_1$ was prepared adapting a previously described procedure.[27] Sodium hydroxide (2M, aq., 50 mL, 100 mmol, 3.3 eq) was added to 4-sulfophthalic acid (**1**, 50% in water, 11.4 mL, 30.0 mmol, 1.0 eq) until the solution was basic (checked by pH paper). The mixture was evaporated affording a purple solid which was dissolved in methanesulfonic acid (60 mL). 4-Chlororesorcinol (**2**, 8.67 g, 60.0 mmol, 2.0 eq) was added. The reaction mixture was heated to 100 °C for 15 h, poured into ice water (200 mL) and stirred at r.t. for 15 min. The suspension was filtered, and the wet precipitate was suspended in acetone (130 mL) and heated to reflux for 2 h. The suspension was filtered affording regioisomerically pure **H_2-FS$_1$** (1.51 g, 3.14 mmol, 11%) as orange solid (isomeric ratio >20:1). *Note*: *the acetone filtrate can be evaporated to afford a regioisomeric mixture of 5- and 6-sulfofluoresceins. Filtering the precipitated reaction mixture directly without acetone suspension increases the yield to 68% (isomeric mixture 1:1).*

TLC R_f = 0.70 (*rp,* 40% MeCN); **^{1}H-NMR** (400 MHz, DMSO-d_6): δ (ppm) = 11.10 (s, br, 1H), 8.08 (s, 1H), 8.01 (d, J = 7.7 Hz, 1H), 7.28 (d, J = 7.8 Hz, 1H), 6.90 (s, 2H), 6.71 (s, 2H); **^{13}C-NMR** (101 MHz, DMSO-d_6): δ (ppm) = 168.0, 155.2, 151.6, 150.6, 150.0, 133.2, 128.4, 125.7, 123.8, 121.6, 116.4, 110.2, 103.7, 81.4; **HRMS** (ESI−): m/z calc. for $C_{20}H_9Cl_2O_8S^-$ [M−H]$^-$: 478.9401, found: 478.9398.

5-Sulfo-2′,7′-dichlorofluorescein diacetate (a_2-FS$_1$)

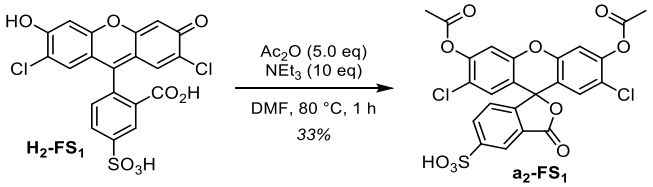

a_2-FS$_1$ was prepared adapting a previously described procedure.[27] **H_2-FS$_1$** (100 mg, 208 µmol, 1.0 eq) was dissolved in dry DMF (5 mL) and triethylamine (0.37 mL, 2.08 mmol, 10 eq) and acetic anhydride (0.10 mL, 1.04 mmol, 5.0 eq) were added. The reaction mixture was heated to 80 °C for 30 min, then the volatiles were removed *in vacuo*. The crude product was purified by column chromatography (reversed phase, 5→40% MeCN (0.1% FA)). From the product column fractions the acetonitrile was removed *in vacuo* (*Note*: 40 °C water bath, not higher to avoid probe hydrolysis) and the remaining water was lyophilised over night to afford **a_2-FS$_1$** (39 mg, 69.0 µmol, 33%) as light yellow solid.

TLC R_f = 0.48 (*rp,* 40% MeCN); **^{1}H-NMR** (400 MHz, DMSO-d_6): δ (ppm) = 8.13 (s, 1H), 8.02 (d, J = 7.8 Hz, 1H), 7.57 (s, 2H), 7.44 (d, J = 7.8 Hz, 1H), 7.14 (s, 2H), 2.35 (s, 6H); **^{13}C-NMR** (101 MHz, DMSO-d_6): δ (ppm) = 168.1, 167.7, 151.3, 150.9, 149.3, 148.3, 133.4, 128.8, 125.4, 123.9, 122.0, 121.9, 117.6, 113.3, 79.7, 20.4; **HRMS** (ESI−): m/z calc. for $C_{24}H_{13}Cl_2O_{10}S^-$ [M−H]$^-$: 562.9612, found: 562.9624.

5-Sulfo-2´,7´-dichlorofluorescein diisobutyrate (i_2-FS_1)

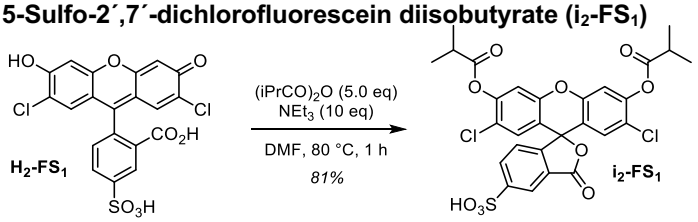

i_2-FS_1 was prepared adapting a previously described procedure.[27] **H_2-FS_1** (2.19 g, 4.55 mmol, 1.0 eq) was dissolved in dry DMF (25 mL) and TEA (7.74 mL, 45.5 mmol, 10 eq) and isobutyric anhydride (15.6 mL, 91.0 mmol, 5.0 eq) were added. The reaction mixture was heated to 80 °C for 1 h, then the volatiles were removed *in vacuo*. The crude product was purified by column chromatography (reversed phase, 5→50% MeCN (0.1% FA)). To the product fractions, sodium hydrogencarbonate was added until pH = 7 was reached, then DCM was added, the layers were separated and the aq. layer was extracted with DCM. The combined organic layers were dried over sodium sulfate, filtered and concentrated affording **i_2-FS_1** (1.38 g, 3.69 mmol, 81%) as colourless solid.

TLC R_f = 0.22 (*rp,* 40% MeCN); **^{1}H-NMR** (400 MHz, DMSO-d_6): δ (ppm) = 8.13 (d, J = 1.7 Hz, 1H), 8.03 (dd, J = 8.0, 1.5 Hz, 1H), 7.57 (s, 2H), 7.44 (d, J = 8.0 Hz, 1H), 7.15 (s, 2H), 2.91 (hept, J = 7.0 Hz, 2H), 1.28 (d, J = 7.0 Hz, 12H); **^{13}C-NMR** (101 MHz, DMSO-d_6): δ (ppm) = 174.2, 168.1, 151.7, 151.3, 149.8, 148.7, 133.8, 129.3, 125.8, 124.3, 122.5, 122.4, 118.0, 113.7, 80.2, 33.8, 19.1; **HRMS** (ESI−): m/z calc. for $C_{28}H_{21}Cl_2O_{10}S^-$ $[M-H]^-$: 619.0238, found: 619.0248.

6.2.3 General Procedure for mono-capped probes and fluorophores

The mono-capped probes were synthesised in three steps from **H_2-FS_1** by alkylation with the respective halide, ester cleavage with lithium hydroxide and capping with isobutyric anhydride (adapted from Woodroofe *et al.*[27]). The pure fluorophores were obtained by cleaving purified probe with sodium hydroxide in methanol/water.

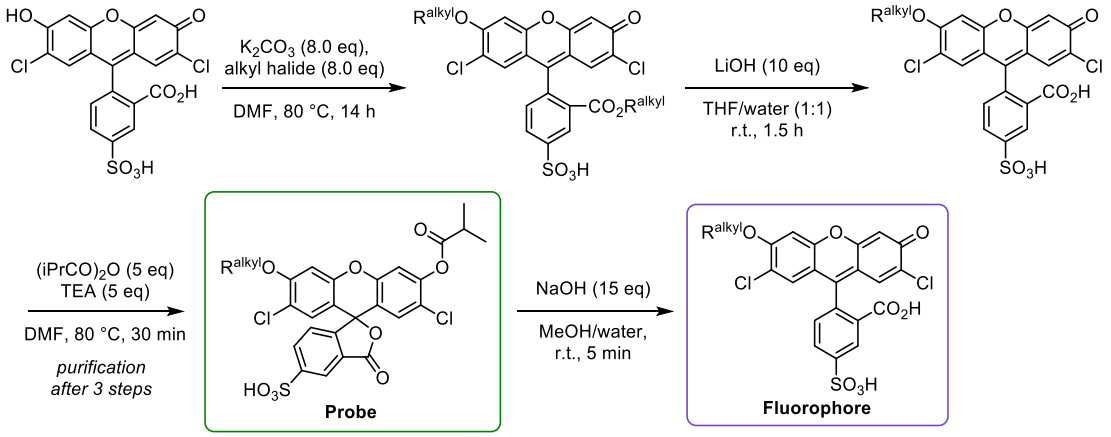

General Procedure A: mono-capped probes

H_2-FS_1 (1.0 eq) was dissolved in anhydrous DMF (0.01−0.04 M). Potassium carbonate (8.0 eq) and the respective **alkyl halide** (8.0 eq) were added and the reaction was heated 80 °C for 2.5−21 h until full conversion to the dialkyl-product (monitored by HPLC/MS). The solvent was removed *in vacuo* and the crude product was dissolved in THF/water (~0.02 M). Lithium hydroxide (10 eq) was added and the reaction mixture was stirred at r.t. for 1.5 h. Then aqueous hydrochloric acid (2 M, 12 eq) was added to acidify the solution (checked by pH paper) and the volatiles were removed *in vacuo* affording the crude alkylated fluorophore which was dissolved in DMF (~0.02 M). Triethylamine (5.0 eq) and isobutyric anhydride (5.0 eq) were added and the reaction mixture was heated to 80 °C for 30 min. The volatiles were removed *in vacuo* and the crude product was purified by reversed-phase flash column chromatography (acetonitrile/water, 0.1% FA). From the column fractions containing the product, the acetonitrile was removed at the rotary evaporator (bath temperature: 40 °C to avoid probe hydrolysis), then the aqueous solution was lyophilised overnight.

Notes: (1) If the probe can not be afforded in the desired purity by this procedure, we recommend capping the purified fluorophores (see General Procedure B). (2) For **iPS-FS_2** (=**MDG1**) this procedure was adapted due to lower solubility in organic solvents.

General Procedure B: mono-alkylated fluorophores

The corresponding probe (1.0 eq) was dissolved in methanol (~0.02 M). Sodium hydroxide (aqueous, 2 M, 15 eq) was added and the reaction mixture was stirred at r.t. for 5 min. Hydrochloric acid (aqueous, 2 M, 20 eq) was added to acidify the solution and the volatiles were removed *in vacuo*. The crude product was purified by reversed-phase flash column chromatography (acetonitrile/water, 0.1% FA). The solvent of the product fractions was removed *in vacuo*.

Notes: We found that the purification of the fluorophores was simplest to perform by preparing the probes in three steps only purifying the product and then cleaving the probe to the fluorophore again.

6.2.4 7'-*O*-alkylated-2'-*O*-acylated [mono-capped] fluorogenic probes

iMe-FS$_1$

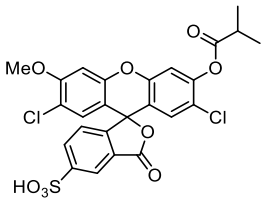

Prepared according to General Procedure A from **H$_2$-FS$_1$** (60 mg, 125 µmol, 1.0 eq) and methyl iodide (62 µL, 997 µmol, 8.0 eq). Reaction time for alkylation: 14 h. Ester cleavage in THF/water = 1:1. Purification of the probe by rp-column chromatography: 10→50% MeCN.

The product **iMe-FS$_1$** (41.0 mg, 72.5 µmol, 58% (3 steps)) was obtained as light yellow solid.

TLC R_f = 0.33 (*rp,* 40% MeCN); **^{1}H-NMR** (400 MHz, DMSO-d$_6$): δ (ppm) = 8.12 (d, J = 11.6 Hz, 1H), 8.01 (dd, J = 8.0, 1.2 Hz, 1H), 7.52 (s, 1H), 7.35 (d, J = 8.0 Hz, 1H), 7.19 (s, 1H), 7.12 (s, 1H), 6.89 (s, 1H), 3.96 (s, 3H), 2.99 – 2.84 (m, 1H), 1.27 (d, J = 7.0 Hz, 6H); **^{13}C-NMR** (101 MHz, DMSO-d$_6$): δ (ppm) = 174.2, 168.2, 156.9, 151.9, 151.3, 150.5, 150.0, 148.6, 133.8, 129.3, 128.7, 125.9, 124.2, 122.3, 122.2, 118.2, 118.0, 113.5, 111.2, 101.8, 80.7, 57.4, 33.8, 19.1; **HRMS** (ESI−): m/z calc. for $C_{25}H_{17}Cl_2O_9S^-$ $[M-H]^-$: 562.9975, found: 562.9979.

iEM-FS$_1$

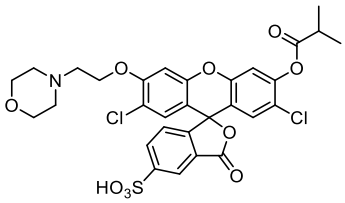

Prepared according to General Procedure A from **H$_2$-FS$_1$** (80 mg, 166 µmol, 1.0 eq) and 4-(2-iodoethyl)morpholine (321 mg, 1.33 mmol, 8.0 eq). Reaction time for alkylation: 16 h. Ester cleavage in THF/water = 1:2. Purification of the probe by rp-column chromatography: 5→60% MeCN.

The product **iMe-FS$_1$** (56.0 mg, 84.3 µmol, 51% (3 steps)) was obtained as off-white solid.

TLC R_f = 0.33 (*rp,* 40% MeCN); **^{1}H-NMR** (400 MHz, DMSO-d$_6$): δ (ppm) = 9.86 (s, br, 1H), 8.12 – 8.10 (m, 1H), 8.02 (dd, *J* = 8.0, 1.5 Hz, 1H), 7.52 (s, 1H), 7.35 – 7.30 (m, 2H), 7.17 (s, 1H), 6.95 (s, 1H), 4.56 (s, 2H), 3.99 (s, 2H), 3.66 (s, 8H), 2.92 (hept, J = 7.0 Hz, 1H), 1.27 (d, J = 7.0 Hz, 6H); **^{13}C-NMR** (101 MHz, DMSO-d$_6$): δ (ppm) = 174.2, 168.2, 155.2, 151.9, 151.3, 150.3, 149.9, 148.6, 133.8, 129.4, 128.9, 125.9, 124.1, 122.4, 122.3, 118.2, 118.1, 113.5, 112.2, 102.9, 80.5, 64.9, 63.9, 63.8, 52.7, 33.8, 19.1; **HRMS** (ESI+): m/z calc. for $C_{30}H_{28}Cl_2NO_{10}S^+$ $[M+H]^+$: 664.0805, found: 664.0809.

iPS-FS$_1$

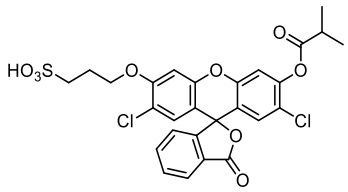

Prepared according to General Procedure A from **H$_2$-FS$_0$** (60 mg, 150 µmol, 1.0 eq) and sodium 3-bromopropane-1-sulfonate (269 mg, 1.20 mmol, 8.0 eq). Reaction time for alkylation: 21 h. Ester cleavage in THF/water = 1:4. Purification of the probe by rp-column chromatography: 10→60% MeCN.

The product **iPS-FS$_1$** (21.0 mg, 42.1 µmol, 28% (3 steps)) was obtained as light orange solid.

TLC R_f = 0.36 (*rp,* 40% MeCN); **^{1}H-NMR** (400 MHz, DMSO-d$_6$): δ (ppm) = 8.04 (d, J = 7.5 Hz, 1H), 7.83 (t, *J* = 7.2 Hz, 1H), 7.77 (t, *J* = 7.4 Hz, 1H), 7.53 (s, 1H), 7.42 (d, *J* = 7.5 Hz, 1H), 7.17 (s, 1H), 7.01 (s, 1H), 6.81 (s, 1H), 4.29 (m, 2H), 2.91 (hept, *J* = 7.0 Hz, 1H), 2.60 (m, 2H), 2.06 (m, 2H), 1.26 (d, *J* = 7.0 Hz, 6H); **^{13}C-NMR** (101 MHz, DMSO-d$_6$): δ (ppm) = 173.8, 168.2, 155.8, 151.5, 150.1, 149.7, 148.1, 136.1, 130.8, 128.6, 128.1, 125.6, 125.4, 124.1, 121.6, 118.0, 117.8, 113.2, 110.8, 101.9, 80.4, 68.5, 47.7, 33.3, 25.0, 18.7; **HRMS** (ESI+): m/z calc. for $C_{27}H_{23}Cl_2O_9S^+$ [M+H]$^+$: 593.0434, found: 593.0430.

iPS-FS$_2$ (=**MDG1**)

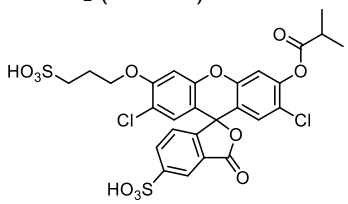

Prepared according to General Procedure A from **H$_2$-FS$_1$** (400 mg, 831 µmol, 1.0 eq) and 1,3-propanesultone (812 mg, 6.65 mmol, 8.0 eq) and heated to 100 °C for 7 h. Ester cleavage in water (no THF). Purification of the probe by rp-column chromatography: 5→40% MeCN.

The product **iPS-FS$_2$** (136 mg, 0.202 mmol, 24% (3 steps)) was obtained as light yellow solid.

TLC R_f = 0.62 (*rp,* 40% MeCN); **^{1}H-NMR** (400 MHz, D$_2$O/DMSO-d$_6$ 2:1): δ (ppm) = 8.24 (s, 1H), 8.06 (d, J = 8.1 Hz, 1H), 7.33 – 7.27 (m, 2H), 7.04 (s, 1H), 6.97 (s, 1H), 6.82 (s, 1H), 4.14 (t, J = 6.0 Hz, 2H), 2.89 – 2.75 (m, 3H), 2.15 – 2.05 (m, 2H), 1.17 (d, J = 7.0 Hz, 6H).; **^{13}C-NMR** (101 MHz, D$_2$O/DMSO-d$_6$ 2:1): δ (ppm) = 177.6, 170.5, 157.4, 154.6, 151.7, 151.3, 149.8, 148.6, 135.0, 130.1, 129.6, 127.3, 126.1, 125.5, 124.0, 123.6, 119.8, 118.3, 111.3, 103.5, 83.5, 69.4, 49.1, 35.1, 25.6, 19.8; **HRMS** (ESI−): m/z calc. for $C_{27}H_{21}Cl_2O_{12}S_2^-$ [M−H]$^-$: 670.9857, found: 670.9864.

6.2.5 2'-*O*-[mono]alkylated fluorophores

H-Me-FS$_1$

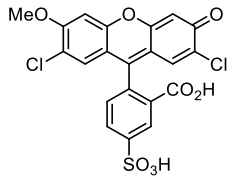

Prepared according to General Procedure B from **iMe-FS$_1$** (26 mg, 46.4 µmol, 1.0 eq). Purification by rp-column chromatography: 5→40% MeCN.

The product **H-Me-FS$_1$** (14 mg, 28.3 µmol, 61%) was obtained as orange solid.

TLC R_f = 0.48 (*rp,* 40% MeCN); **^{1}H-NMR** (400 MHz, DMSO-d$_6$): δ (ppm) = 11.11 (s, br, 1H), 8.08 (d, J = 1.4 Hz, 1H), 8.00 (dd, J = 7.9, 1.5 Hz, 1H), 7.28 (d, J = 7.9 Hz, 1H), 7.20 (s, 1H), 6.93 (s, 1H), 6.83 (s, 1H), 6.75 (s, 1H), 3.94 (s, 3H); **^{13}C-NMR** (101 MHz, DMSO-d$_6$): δ (ppm) = 168.4, 156.7, 155.7, 152.1, 151.1, 150.8, 150.3, 133.7, 128.9, 128.6, 126.1, 124.2, 122.0, 117.5, 117.0, 111.5, 110.6, 104.0, 101.8, 81.6, 57.3; **HRMS** (ESI−): m/z calc. for $C_{21}H_{11}Cl_2O_8S^-$ [M−H]$^-$: 492.9557, found: 492.9559.

H-EM-FS$_1$

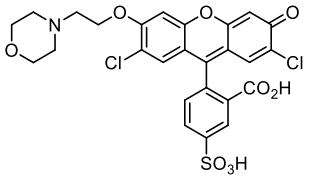

Prepared according to General Procedure B from **iEM-FS$_1$** (56 mg, 84.3 µmol, 1.0 eq). Purification by rp-column chromatography: 5→40% MeCN.

The product **H-EM-FS$_1$** (42 mg, 70.7 µmol, 84%) was obtained as red solid.

TLC R_f = 0.48 (*rp,* 40% MeCN); **^{1}H-NMR** (400 MHz, DMSO-d$_6$): δ (ppm) = 11.11 (s, 1H), 9.89 (s, br, 1H), 8.09 (d, J = 1.4 Hz, 1H), 8.02 (dd, J = 8.0, 1.5 Hz, 1H), 7.33 (s, 1H), 7.24 (d, J = 8.0 Hz, 1H), 6.93 (s, 1H), 6.88 (s, 1H), 6.79 (s, 1H), 4.55 (s, 2H), 3.99 (s, 2H), 3.67 (s, 8H); **^{13}C-NMR** (101 MHz, DMSO-d$_6$): δ (ppm) = 167.9, 155.3, 154.7, 151.6, 150.7, 150.2, 149.8, 133.3, 128.5, 128.4, 125.6, 123.6, 121.7, 117.3, 116.6, 112.0, 110.1, 103.5, 102.6, 81.0, 64.3, 63.4, 54.8, 52.2; **HRMS** (ESI−): m/z calc. for $C_{26}H_{20}Cl_2NO_9S^-$ [M−H]$^-$: 592.0241, found: 592.0244.

H-PS-FS$_1$

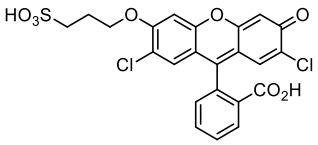

Prepared according to General Procedure B from **iPS-FS$_1$** (19 mg, 32.0 µmol, 1.0 eq). Purification by rp-column chromatography: 10→40% MeCN.

The product **H-PS-FS$_1$** (16 mg, 30.6 µmol, 95%) was obtained as orange solid.

TLC R_f = 0.59 (*rp,* 40% MeCN); **^{1}H-NMR** (400 MHz, methanol-d$_4$): δ (ppm) = 11.13 (s, br, 1H), 8.02 (d, J = 7.5 Hz, 1H), 7.82 (t, J = 7.4 Hz, 1H), 7.75 (t, J = 7.4 Hz, 1H), 7.36 (d, J = 7.6 Hz, 1H), 7.18 (s, 1H), 6.94 (s, 1H), 6.75 (s, 1H), 6.67 (s, 1H), 4.27 (t, J = 6.3 Hz, 2H), 2.59 (t, J = 7.3 Hz, 2H), 2.10 – 1.98 (m, 2H); **^{13}C-NMR** (101 MHz, methanol-d$_4$): δ (ppm) = 168.3, 155.5, 155.2, 151.6, 150.4, 150.0, 136.0, 130.6, 128.2, 128.0, 125.8, 125.1, 124.0, 117.2, 116.4, 111.1, 110.4, 103.7, 102.0, 81.3, 68.4, 47.7, 24.9; **HRMS** (ESI−): m/z calc. for $C_{23}H_{15}Cl_2O_8S^-$ [M−H]$^-$: 520.9870, found: 520.9878.

H-PS-FS$_2$

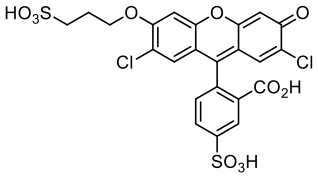

Prepared according to General Procedure B from **iPS-FS$_2$** (69 mg, 103 µmol, 1.0 eq). Purification by rp-column chromatography: 2→10% MeCN.

The product **H-PS-FS$_2$** (24 mg, 39.8 µmol, 39%) was obtained as orange solid.

TLC R_f = 0.85 (*rp,* 40% MeCN); **^{1}H-NMR** (400 MHz, D$_2$O): δ (ppm) = 8.49 (s, 1H), 8.15 (d, J = 8.7 Hz, 1H), 7.45 (d, J = 8.1 Hz, 1H), 6.89 (s, 1H), 6.83 (s, 1H), 5.69 (s, 1H), 5.63 (s, 1H), 3.42 – 3.24 (m, 2H), 2.95 – 2.85 (m, 2H), 2.16 – 1.98 (m, 2H).; **^{13}C-NMR** (101 MHz, D$_2$O): δ (ppm) = 169.6, 155.6, 155.2, 152.5, 150.0, 150.0, 145.5, 133.3, 128.3, 128.2, 127.0, 125.1, 123.4, 118.2, 117.7, 109.8, 109.7, 102.7, 100.0, 91.1, 67.3, 47.5, 24.0; **HRMS** (ESI−): m/z calc. for $C_{23}H_{15}Cl_2O_{11}S_2^-$ [M−H]$^-$: 600.9438, found: 600.9443.

6.2.6 Reducible disulfide probe

MSS00-PS-FS$_2$ (=MDG2)

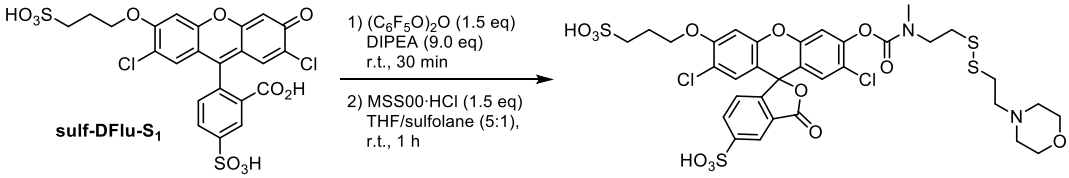

H-PS-FS$_2$ (10 mg, 16.6 µmol, 1.0 eq) was dissolved in THF (3.0 mL) and sulfolane (0.6 mL). DIPEA (25 µL, 149 µmol, 9.0 eq) and bis(pentafluorophenyl) carbonate (10 mg, 24.9 µmol, 1.5 eq) were added and the reaction mixture was stirred at r.t. for 30 min. The redox trigger **MSS00·HCl** (13 mg, 41.5 µmol, 2.5 eq) was added and the reaction was stirred at r.t. for 1 h. The volatiles were removed *in vacuo* and the crude product was purified by reversed-phase-AQ flash column chromatography (5→30% MeCN, acetonitrile/water, 0.1% FA). The product (4.8 mg, 5.57 µmol, 34%) was obtained as colourless solid.

TLC R_f = 0.72 (*rp,* 40% MeCN); **^{1}H-NMR** (800 MHz, DMSO-d$_6$) δ 8.20 (s, 1H), 8.07 (d, J = 7.9 Hz, 1H), 7.39/7.34 (2 × s, 1H), 7.32 (d, J = 7.6 Hz, 1H), 7.12/7.11 (2 × s, 1H), 6.94 (s, 1H), 6.82 (s, 1H), 4.21 – 4.17 (m, 2H), 3.97 – 3.85 (m, 2H), 3.77 – 3.67 (m, 1H), 3.66 – 3.55 (m, 3H), 3.41 – 3.31 (m, 4H), 3.03/2.91 (2 × s, 3H), 3.02 – 2.92 (m, 6H), 2.77 – 2.73 (m, 2H), 2.09 (p, J = 6.6 Hz, 2H).; **^{13}C-NMR** (201 MHz, DMSO-d$_6$) δ = 168.6, 156.2, 153.5/153.1, 152.7/152.7, 150.4, 149.9, 149.2/149.0, 148.9, 133.9, 128.7/128.6, 128.4, 125.9/125.9, 124.6, 122.6, 122.5, 118.4, 117.1, 113.7/113.4, 110.4, 102.3, 81.6, 68.5, 63.6, 55.6/55.5/55.4/51.7, 48.1, 47.9, 47.0, 36.2, 35.4/35.2, 35.2/34.8/32.9/32.5, 30.4/30.3, 26.2, 24.7.; **HRMS** (ESI−): m/z calc. for $C_{33}H_{33}Cl_2N_2O_{13}S_4^-$ [M−H]$^-$: 863.0248, found: 863.0242.

6.2.7 Esterase-labile fluorogenic probe for attachment onto macromolecules

Dichlorofluorescein isobutyrate NHS-ester (NHS-i-Flu)

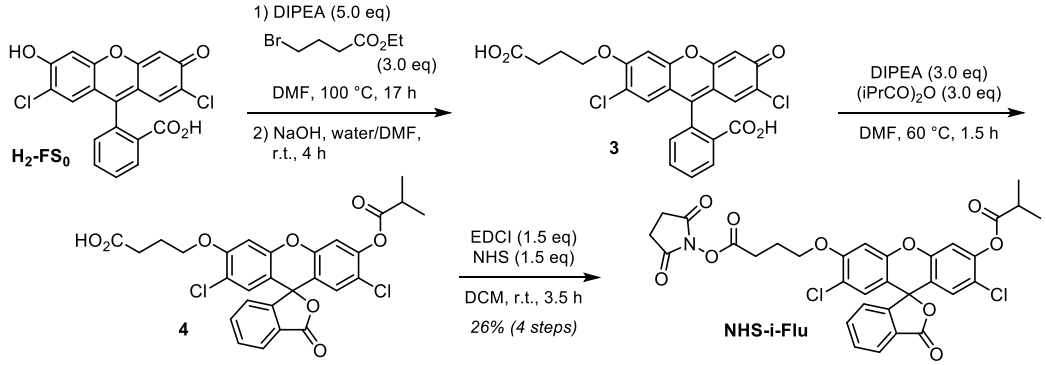

2´,7´-Dichlorofluorescein (**H$_2$-FS$_0$**, 600 mg, 1.50 mmol, 1.0 eq) was dissolved in dry DMF (20 mL). DIPEA (1.27 mL, 7.48 mmol, 5.0 eq) and ethyl 4-bromobutyrate (0.64 mL, 4.49 mmol, 3.0 eq) were added and the reaction mixture was heated to 100 °C for 17 h. After allowing the reaction mixture to cool to r.t., aqueous sodium hydroxide solution (2M, 12 mL, 16 eq) was added and the mixture was stirred for another 4 h. Then hydrochloric acid (2M, 14 mL, 19 eq) was added and the volatiles were removed *in vacuo*.

The crude **3** was dissolved in dry DMF (14 mL), DIPEA (0.51 mL, 2.99 mmol, 3.0 eq) and isobutyric anhydride (0.50 mL, 2.99 mmol, 3.0 eq) were added and the reaction mixture was heated to 60 °C for 1.5 h. Water (120 mL) and DCM (120 mL) were added, the layers were separated and the aqueous layer was extracted with DCM (1 × 120 mL). The organic layer was dried over sodium sulfate, the desiccant was filtered off and the solvent was removed *in vacuo*. Reversed-phase column chromatography (acetonitrile/water, 0.1% FA, 10→50% MeCN) was used to semi-purify **4**, which was directly used for the NHS-ester formation.

4 was dissolved in DCM (10 mL) and *N*-hydroxysuccinimide (259 mg, 2.25 mmol, 1.5 eq) and EDCI (431 mg, 2.25 mmol, 1.5 eq) were added. The reaction mixture was stirred at r.t. for 3.5 h, then the reaction mixture was diluted with DCM (20 mL) and water (20 mL), the layers were separated and the aqueous layer was extracted with DCM (2 × 20 mL). The crude product was purified by column chromatography (iso-hexanes/EtOAc, 40→100% EtOAc). **NHS-i-Flu** (255 mg, 0.393 mmol, 26%) was obtained as colourless solid.

TLC R_f = 0.36 (*np, iso*-hexanes/EtOAc); **^{1}H-NMR** (400 MHz, $CDCl_3$): δ (ppm) = 8.03 (d, J = 7.3 Hz, 1H), 7.75 – 7.62 (m, 2H), 7.15 (d, J = 7.5 Hz, 1H), 7.09 (s, 1H), 6.82 (s, 1H), 6.79 (s, 1H), 6.73 (s, 1H), 4.15 (t, J = 5.9 Hz, 2H), 2.91 – 2.78 (m, 7H), 2.27 (p, J = 6.7 Hz, 2H), 1.36 – 1.29 (m, 6H); **^{13}C-NMR**(101 MHz, $CDCl_3$): δ (ppm) = 174.2, 169.2, 168.8, 168.2, 155.8, 152.0, 150.4, 150.0, 148.4, 135.7, 130.5, 129.0, 128.7, 126.0, 125.5, 124.0, 122.3, 119.0, 117.7, 112.7, 111.3, 101.4, 81.2, 67.3, 34.1, 27.5, 25.6, 24.2, 19.0; **HRMS** (EI+): m/z calc. for $C_{32}H_{25}Cl_2NO_{10}^+$ [M]$^{+}$: 653.0856, found: 653.0855.

7 Raw biological assay data

Table S7: Cellular fluorescence values quantified from microscopy images for the cell penetration into healthy HEK cells (n = 3).

Compound	Intracellular fluorescence			Extracellular fluorescence			Mean (intra)	Mean (extra)	Ratio intra/extra
i_2-FS_0	411	517	296	4.68	2.88	3.75	408	3.77	108
i_2-FS_1	319	209	168	4.095	20.2	8.43	232	10.9	21.3
a_2-FS_1	165	122	187	9.28	16.5	13.0	158	12.9	12.2
iPS-FS_1	83.3	84.4	69.7	3.516	3.022	3.878	79.1	3.47	22.8
iMe-FS_1	4.35	5.42	4.93	2.31	2.59	3.69	4.90	2.86	1.71
iEM-FS_1	4.36	4.25	6.17	1.54	1.56	2.16	4.93	1.75	2.81
iPS-FS_2	1.89	2.85	1.59	1.91	1.73	1.84	2.11	1.83	1.15
FDP	9.44	21.2	14.5	10.4	8.71	11.2	15.0	10.1	1.49
fluorescein	356	391	318	1287	1444	1379	355	1370	0.26
H_2-FS_0	209	274	236	715	854	874	240	814	0.29
H_2-FS_1	231	155	192	509	562	504	193	525	0.37
H-PS-FS_1	22.7	23.1	21.1	89.3	55.8	72.9	22.3	72.7	0.31
H-Me-FS_1	12.6	17.4	14.8	59.5	68.7	52.7	15.0	60.3	0.25
H-EM-FS_1	6.91	8.13	9.85	39.0	38.1	37.3	8.30	38.1	0.22
H-PS-FS_2	8.95	16.9	31.4	59.1	58.1	96.4	19.1	71.2	0.27
DMSO	1.34	0.98	0.64	0.13	0.15	0.05	0.98	0.11	8.86

Table S8: Intracellular fluorescence values quantified from microscopy images for the LLO membrane damage assay (n = 3).

Compound	+LLO			−LLO			Mean (+LLO)	Mean (−LLO)	Ratio +/−LLO
i_2-FS_0	125	172	208	411	517	296	169	408	0.41
i_2-FS_1	4977	2079	3305	319	209	168	3454	232	14.9
a_2-FS_1	1406	1646	1523	165	122	187	1525	158	9.67
iPS-FS_1	299	256	261	83.3	84.4	69.7	272	79.1	3.44
iMe-FS_1	131	149	163	4.35	5.42	4.93	148	4.90	30.2
iEM-FS_1	160	177	194	4.36	4.25	6.17	177	4.93	36.0
iPS-FS_2	70.90	63.98	63.17	1.89	2.85	1.59	66.02	2.11	31.3
FDP	114	85.82	97.07	9.44	21.18	14.47	99.05	15.0	6.59
fluorescein	1447	1624	1225	356	391	318	1432	355	4.03
H_2-FS_0	1178	1351	1033	209	274	236	1187	240	4.96
H_2-FS_1	723	772	650	231	155	192	715	193	3.71
H-PS-FS_1	114	94.45	107	22.65	23.11	21.14	105	22.3	4.72
H-Me-FS_1	79.6	83.1	59.6	12.6	17.4	14.8	74.1	15.0	4.96
H-EM-FS_1	44.2	40.4	39.6	6.91	8.13	9.85	41.4	8.30	4.99
H-PS-FS_2	66.5	73.8	97.3	8.95	16.9	31.4	79.2	19.1	4.15
DMSO	1.83	1.29	1.29	1.34	0.98	0.64	1.47	0.98	1.49

Table S9: Intracellular fluorescence values quantified from microscopy images for the AAPH membrane damage assay (n = 3).

Compound	+AAPH			−AAPH			Mean (+AAPH)	Mean (−AAPH)	Ratio +/−AAPH
i_2-FS_0	49.5	22.4	13.3	608	450	293	28.4	450	0.06
i_2-FS_1	678	778	314	2490	2523	1764	590	2259	0.26
a_2-FS_1	369	824	369	230	484	317	520	344	1.51
iPS-FS_1	77.7	90.3	52.5	134	245	147	73.5	175	0.42
iMe-FS_1	54.5	29.5	46.1	32.2	32.9	27.2	43.4	30.8	1.41
iEM-FS_1	59.3	110	59.6	25.6	32.7	19.5	76.2	25.9	2.94
iPS-FS_2	38.5	43.3	25.1	3.75	5.06	4.90	35.6	4.57	7.80
FDP	19.3	12.5	22.7	5.27	3.90	7.11	18.2	5.43	3.35
fluorescein	870	852	903	242	236	310	875	263	3.33
H_2-FS_0	1088	571	538	232	100	116	733	149	4.90
H_2-FS_1	389	544	373	77.7	91.9	101	435	90.23	4.83
H-PS-FS_1	115	95.9	53.0	21.6	24.3	21.8	88.1	22.6	3.90
H-Me-FS_1	63.2	54.1	56.6	14.5	12.4	13.9	57.9	13.6	4.26
H-EM-FS_1	34.2	27.4	34.2	9.58	10.2	8.74	31.9	9.50	3.36
H-PS-FS_2	42.5	49.6	37.8	9.89	14.0	12.5	43.3	12.1	3.57
DMSO	0.94	1.10	0.80	0.77	1.19	1.04	0.95	1.00	0.95

8 Gating, controls, full-data images

8.1 Flow cytometry (undamaged HeLa cells): Gating and controls

Gating used for graphs shown in **Fig 2** and **Fig S4**:

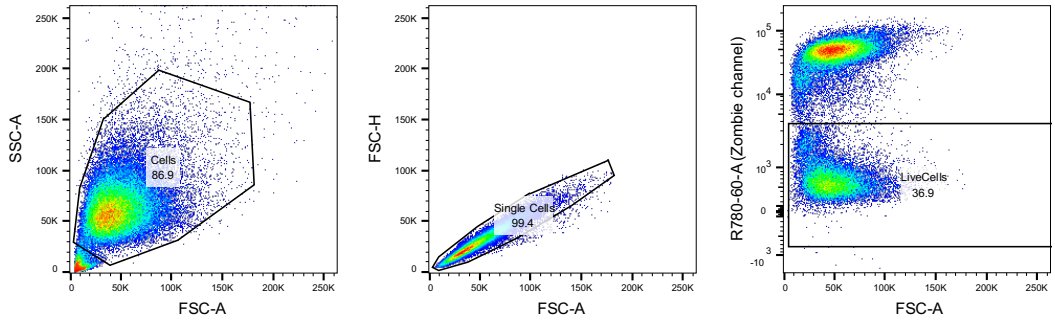

Figure S24: Gating and control samples for flow cytometry analysis of the probe and fluorophore permeability.

8.2 Cell exclusion/uptake panels from main text figures, with all datapoints

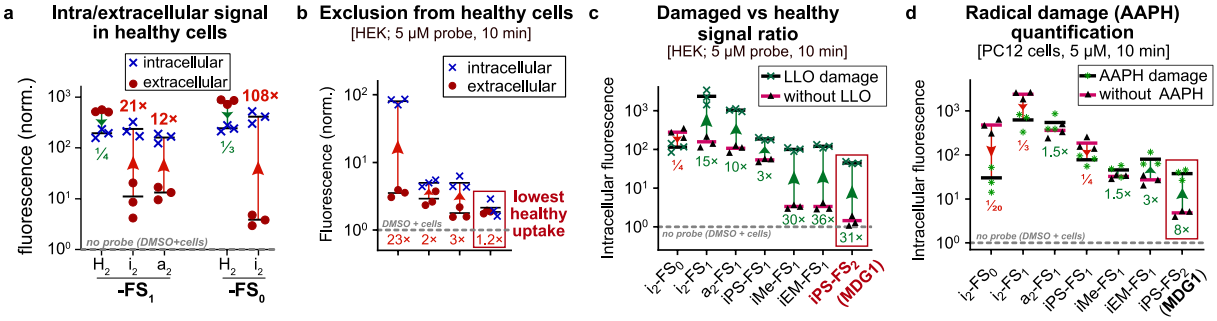

Figure S25: Cell uptake panels: (a) from **Figure 2c; (b)** from **Figure 3d; (c)** from **Figure 3g; (d)** from **Figure 4b**.

References

(1) Grimm, J. B.; Tkachuk, A. N.; Xie, L.; Choi, H.; Mohar, B.; Falco, N.; Schaefer, K.; Patel, R.; Zheng, Q.; Liu, Z.; Lippincott-Schwartz, J.; Brown, T. A.; Lavis, L. D. A General Method to Optimize and Functionalize Red-Shifted Rhodamine Dyes. *Nat. Methods* **2020**, *17* (8), 815–821. https://doi.org/10.1038/s41592-020-0909-6.

(2) Würth, C.; Grabolle, M.; Pauli, J.; Spieles, M.; Resch-Genger, U. Relative and Absolute Determination of Fluorescence Quantum Yields of Transparent Samples. *Nat Protoc* **2013**, *8* (8), 1535–1550. https://doi.org/10.1038/nprot.2013.087.

(3) Zhang, X.-F.; Zhang, J.; Liu, L. Fluorescence Properties of Twenty Fluorescein Derivatives: Lifetime, Quantum Yield, Absorption and Emission Spectra. *J. Fluoresc.* **2014**, *24* (3), 819–826. https://doi.org/10.1007/s10895-014-1356-5.

(4) Conrad, M.; Pratt, D. A. The Chemical Basis of Ferroptosis. *Nat. Chem. Biol.* **2019**, *15* (12), 1137–1147. https://doi.org/10.1038/s41589-019-0408-1.

(5) Jimenez, A. J.; Maiuri, P.; Lafaurie-Janvore, J.; Divoux, S.; Piel, M.; Perez, F. ESCRT Machinery Is Required for Plasma Membrane Repair. *Science* **2014**, *343* (6174). https://doi.org/10.1126/science.1247136.

(6) Witte, M. E.; Schumacher, A.-M.; Mahler, C. F.; Bewersdorf, J. P.; Lehmitz, J.; Scheiter, A.; Sánchez, P.; Williams, P. R.; Griesbeck, O.; Naumann, R.; Misgeld, T.; Kerschensteiner, M. Calcium Influx through Plasma-Membrane Nanoruptures Drives Axon Degeneration in a Model of Multiple Sclerosis. *Neuron* **2019**, *101* (4), 615-624.e5. https://doi.org/10.1016/j.neuron.2018.12.023.

(7) Williams, P. R.; Marincu, B.-N.; Sorbara, C. D.; Mahler, C. F.; Schumacher, A.-M.; Griesbeck, O.; Kerschensteiner, M.; Misgeld, T. A Recoverable State of Axon Injury Persists for Hours after Spinal Cord Contusion in Vivo. *Nat. Commun.* **2014**, *5* (1), 5683. https://doi.org/10.1038/ncomms6683.

(8) Köster, S.; van Pee, K.; Hudel, M.; Leustik, M.; Rhinow, D.; Kühlbrandt, W.; Chakraborty, T.; Yildiz, Ö. Crystal Structure of Listeriolysin O Reveals Molecular Details of Oligomerization and Pore Formation. *Nat. Commun.* **2014**, *5* (1), 3690. https://doi.org/10.1038/ncomms4690.

(9) Greene, L. A.; Tischler, A. S. Establishment of a Noradrenergic Clonal Line of Rat Adrenal Pheochromocytoma Cells Which Respond to Nerve Growth Factor. *PNAS* **1976**, *73* (7), 2424–2428. https://doi.org/10.1073/pnas.73.7.2424.

(10) Ohl, K.; Tenbrock, K.; Kipp, M. Oxidative Stress in Multiple Sclerosis: Central and Peripheral Mode of Action. *Exp. Neurol.* **2016**, *277*, 58–67. https://doi.org/10.1016/j.expneurol.2015.11.010.

(11) Haider, L.; Fischer, M. T.; Frischer, J. M.; Bauer, J.; Höftberger, R.; Botond, G.; Esterbauer, H.; Binder, C. J.; Witztum, J. L.; Lassmann, H. Oxidative Damage in Multiple Sclerosis Lesions. *Brain* **2011**, *134* (Pt 7), 1914–1924. https://doi.org/10.1093/brain/awr128.

(12) Miki, M.; Tamai, H.; Mino, M.; Yamamoto, Y.; Niki, E. Free-Radical Chain Oxidation of Rat Red Blood Cells by Molecular Oxygen and Its Inhibition by α-Tocopherol. *Arch. Biochem. Biophys.* **1987**, *258* (2), 373–380. https://doi.org/10.1016/0003-9861(87)90358-4.

(13) Lomize, A. L.; Pogozheva, I. D. Physics-Based Method for Modeling Passive Membrane Permeability and Translocation Pathways of Bioactive Molecules. *J. Chem. Inf. Model.* **2019**, *59* (7), 3198–3213. https://doi.org/10.1021/acs.jcim.9b00224.

(14) Lomize, A. L.; Hage, J. M.; Schnitzer, K.; Golobokov, K.; LaFaive, M. B.; Forsyth, A. C.; Pogozheva, I. D. PerMM: A Web Tool and Database for Analysis of Passive Membrane Permeability and Translocation Pathways of Bioactive Molecules. *J. Chem. Inf. Model.* **2019**, *59* (7), 3094–3099. https://doi.org/10.1021/acs.jcim.9b00225.

(15) Guthrie, J. P. Hydrolysis of Esters of Oxy Acids: pKa Values for Strong Acids; Brønsted Relationship for Attack of Water at Methyl; Free Energies of Hydrolysis of Esters of Oxy Acids; and a Linear Relationship between Free Energy of Hydrolysis and pKa Holding over a Range of 20 pK Units. *Can. J. Chem.* **1978**, *56* (17), 2342–2354. https://doi.org/10.1139/v78-385.

(16) Sjöback, R.; Nygren, J.; Kubista, M. Absorption and Fluorescence Properties of Fluorescein. *Spectrochim. Acta, Part A* **1995**, *51* (6), L7–L21. https://doi.org/10.1016/0584-8539(95)01421-P.

(17) Chyan, W.; Kilgore, H. R.; Raines, R. T. Cytosolic Uptake of Large Monofunctionalized Dextrans. *Bioconjugate Chem.* **2018**, *29* (6), 1942–1949. https://doi.org/10.1021/acs.bioconjchem.8b00198.

(18) Chandran, S. S.; Dickson, K. A.; Raines, R. T. Latent Fluorophore Based on the Trimethyl Lock. *J. Am. Chem. Soc.* **2005**, *127* (6), 1652–1653. https://doi.org/10.1021/ja043736v.

(19) Lawrence, P. A.; Bodmer, R.; Vincent, J.-P. Segmental Patterning of Heart Precursors in Drosophila. *Development* **1995**, *121* (12), 4303–4308. https://doi.org/10.1242/dev.121.12.4303.

(20) Millard, T. H.; Martin, P. Dynamic Analysis of Filopodial Interactions during the Zippering Phase of Drosophila Dorsal Closure. *Development* **2008**, *135* (4), 621–626. https://doi.org/10.1242/dev.014001.

(21) Kiehart, D. P.; Galbraith, C. G.; Edwards, K. A.; Rickoll, W. L.; Montague, R. A. Multiple Forces Contribute to Cell Sheet Morphogenesis for Dorsal Closure in Drosophila. *Journal of Cell Biology* **2000**, *149* (2), 471–490. https://doi.org/10.1083/jcb.149.2.471.

(22) Ashrafi, G.; Schlehe, J. S.; LaVoie, M. J.; Schwarz, T. L. Mitophagy of Damaged Mitochondria Occurs Locally in Distal Neuronal Axons and Requires PINK1 and Parkin. *Journal of Cell Biology* **2014**, *206* (5), 655–670. https://doi.org/10.1083/jcb.201401070.

(23) Harbauer, A. B.; Hees, J. T.; Wanderoy, S.; Segura, I.; Gibbs, W.; Cheng, Y.; Ordonez, M.; Cai, Z.; Cartoni, R.; Ashrafi, G.; Wang, C.; Perocchi, F.; He, Z.; Schwarz, T. L. Neuronal Mitochondria Transport *Pink1* mRNA via Synaptojanin 2 to Support Local Mitophagy. *Neuron* **2022**, *110* (9), 1516-1531.e9. https://doi.org/10.1016/j.neuron.2022.01.035.
(24) Chyan, W.; Kilgore, H. R.; Gold, B.; Raines, R. T. Electronic and Steric Optimization of Fluorogenic Probes for Biomolecular Imaging. *J. Org. Chem.* **2017**, *82* (8), 4297–4304. https://doi.org/10.1021/acs.joc.7b00285.
(25) Seltzman, H. H.; Shiner, C.; Hirt, E. E.; Gilliam, A. F.; Thomas, B. F.; Maitra, R.; Snyder, R.; Black, S. L.; Patel, P. R.; Mulpuri, Y.; Spigelman, I. Peripherally Selective Cannabinoid 1 Receptor (CB1R) Agonists for the Treatment of Neuropathic Pain. *J. Med. Chem.* **2016**, *59* (16), 7525–7543. https://doi.org/10.1021/acs.jmedchem.6b00516.
(26) Felber, J. G.; Zeisel, L.; Poczka, L.; Scholzen, K.; Busker, S.; Maier, M. S.; Theisen, U.; Brandstädter, C.; Becker, K.; Arnér, E. S. J.; Thorn-Seshold, J.; Thorn-Seshold, O. Selective, Modular Probes for Thioredoxins Enabled by Rational Tuning of a Unique Disulfide Structure Motif. *J. Am. Chem. Soc.* **2021**, *143* (23), 8791–8803. https://doi.org/10.1021/jacs.1c03234.
(27) Woodroofe, C. C.; Lim, M. H.; Bu, W.; Lippard, S. J. Synthesis of Isomerically Pure Carboxylate- and Sulfonate-Substituted Xanthene Fluorophores. *Tetrahedron* **2005**, *61* (12), 3097–3105. https://doi.org/10.1016/j.tet.2005.01.024.

9 NMR spectra

5-Sulfo-2´,7´-dichlorofluorescein (H_2-FS_1)

^{1}H-NMR

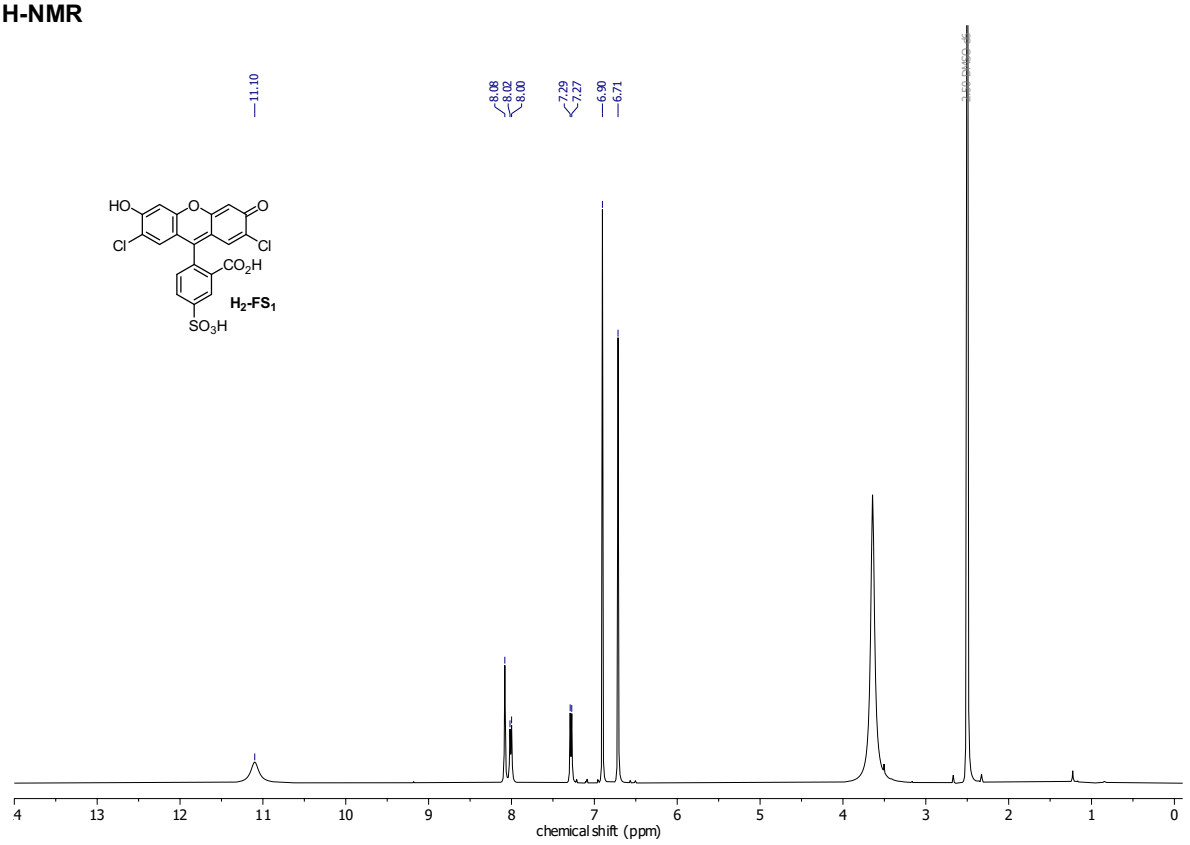

^{13}C-NMR

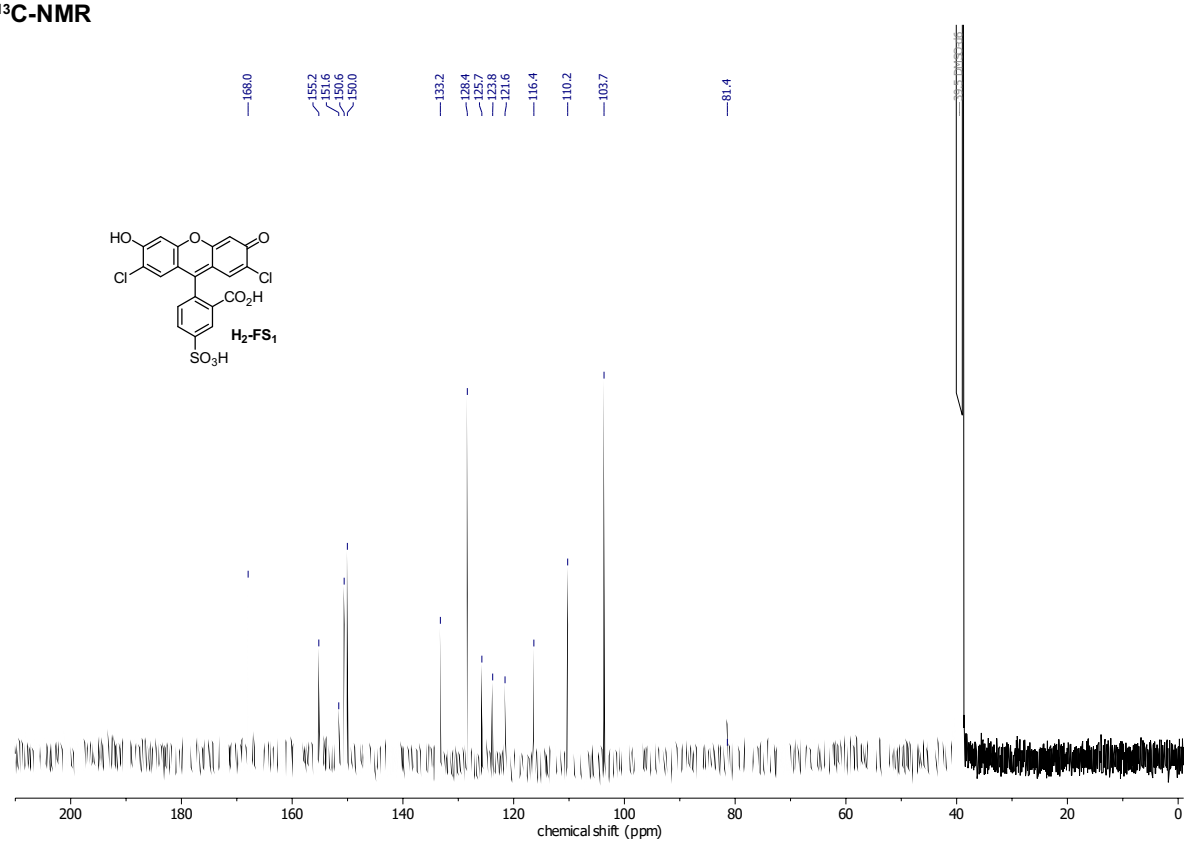

5-Sulfo-2´,7´-dichlorofluorescein diacetate (a_2-FS_1)

^{1}H-NMR

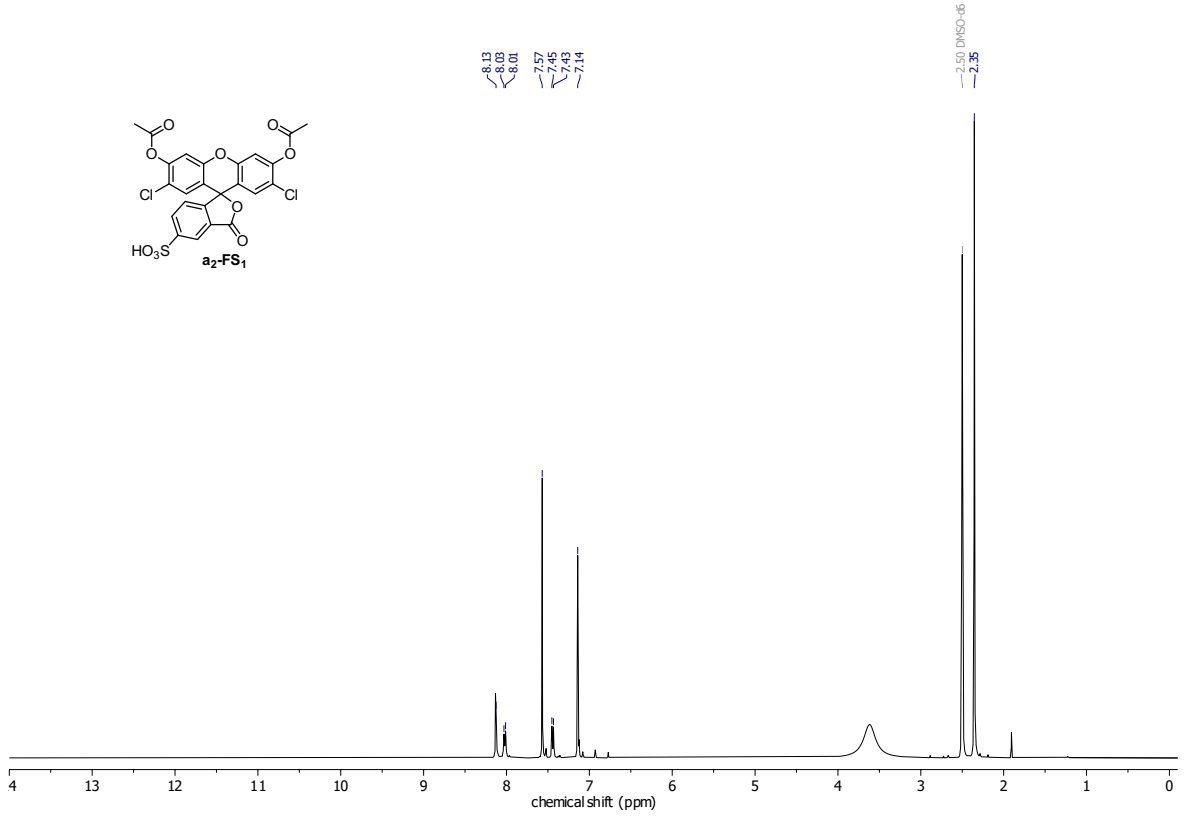

^{13}C-NMR

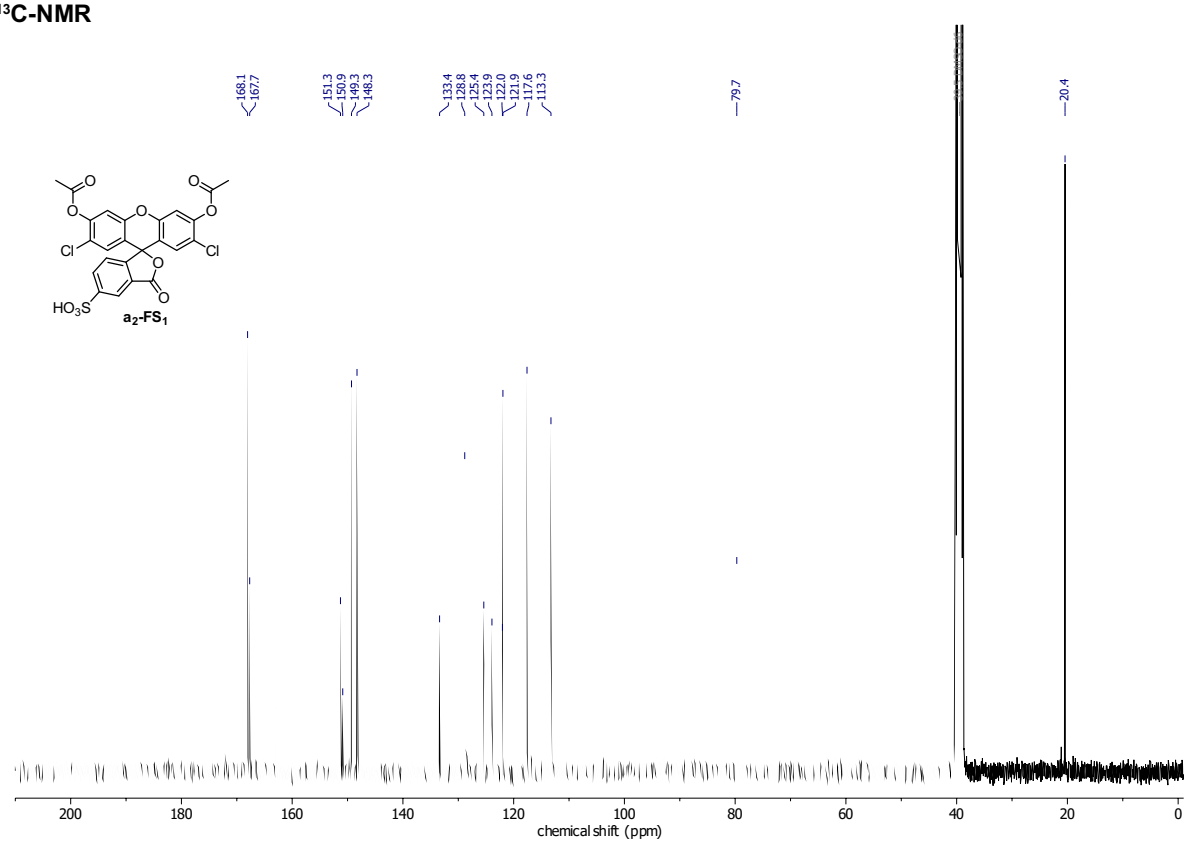

5-Sulfo-2´,7´-dichlorofluorescein diisobutyrate (i_2-FS_1)

^{1}H-NMR

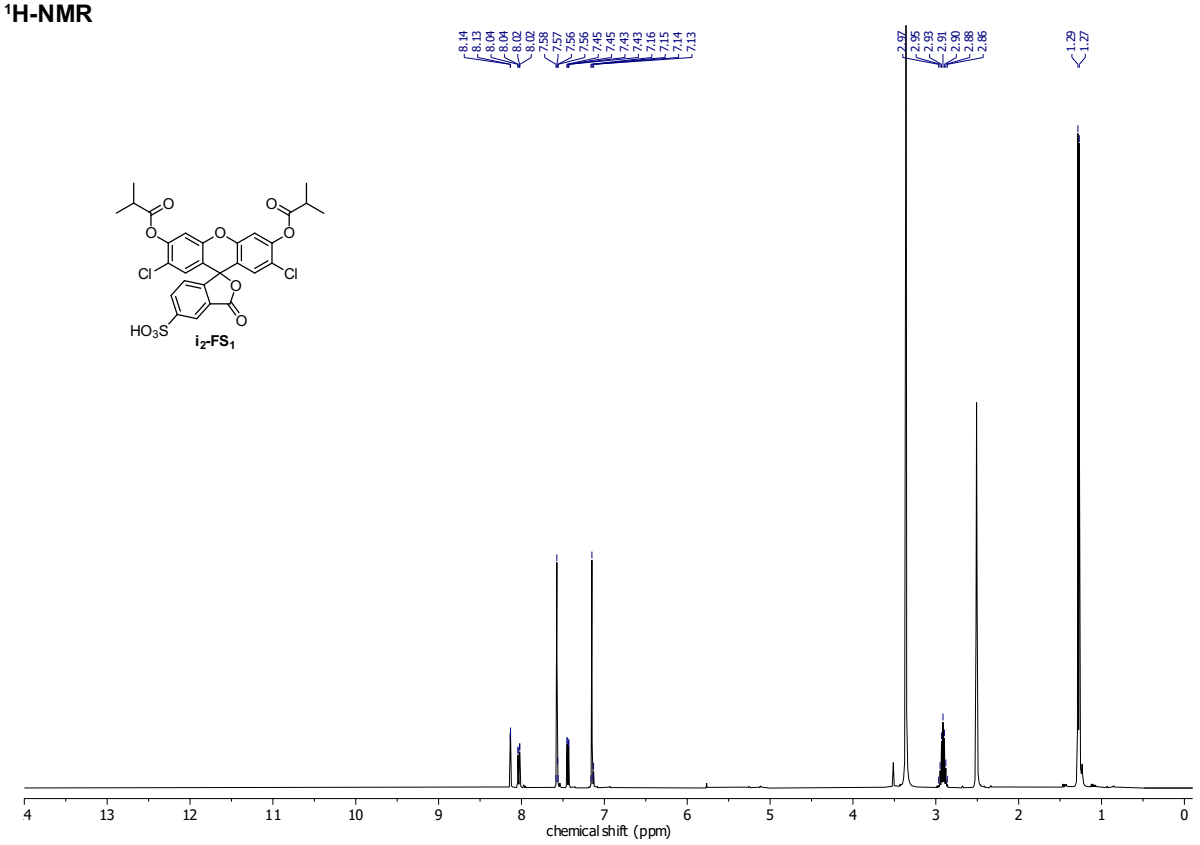

^{13}C-NMR

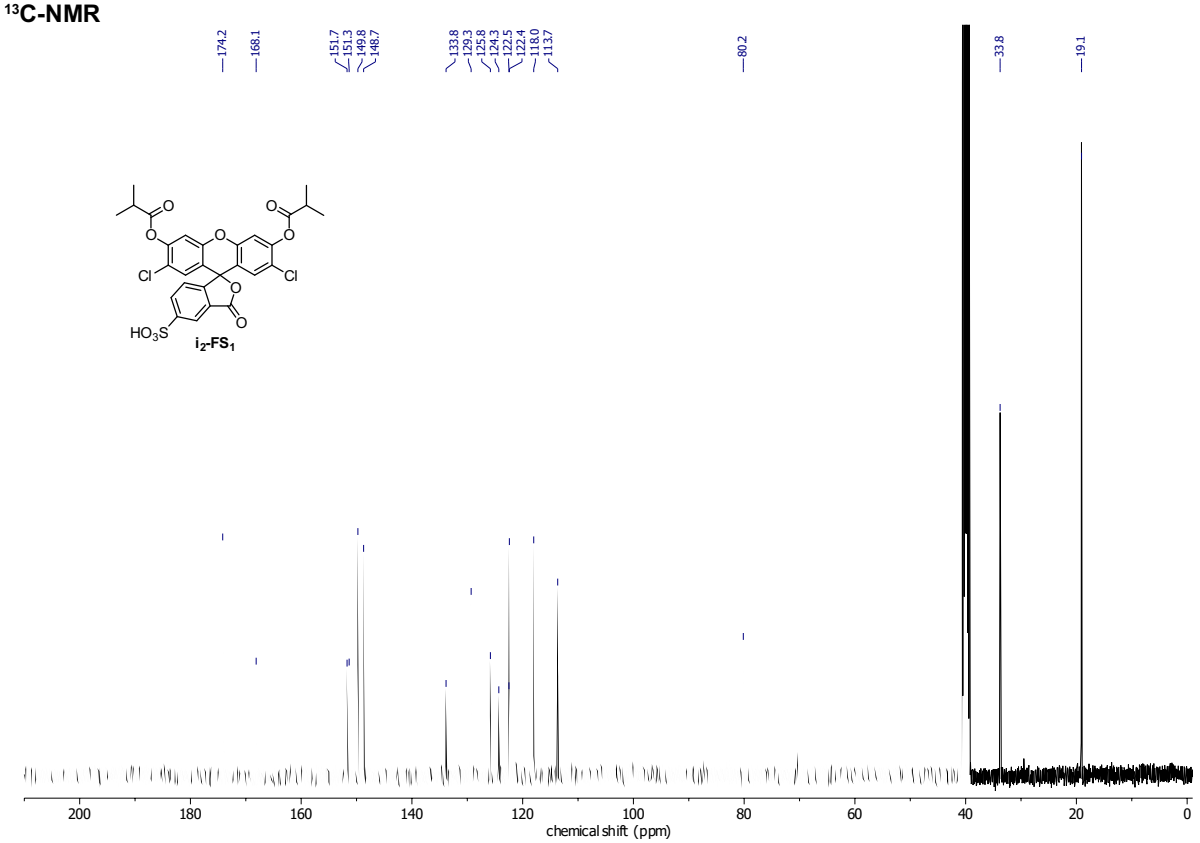

iMe-FS$_1$

^{1}H-NMR

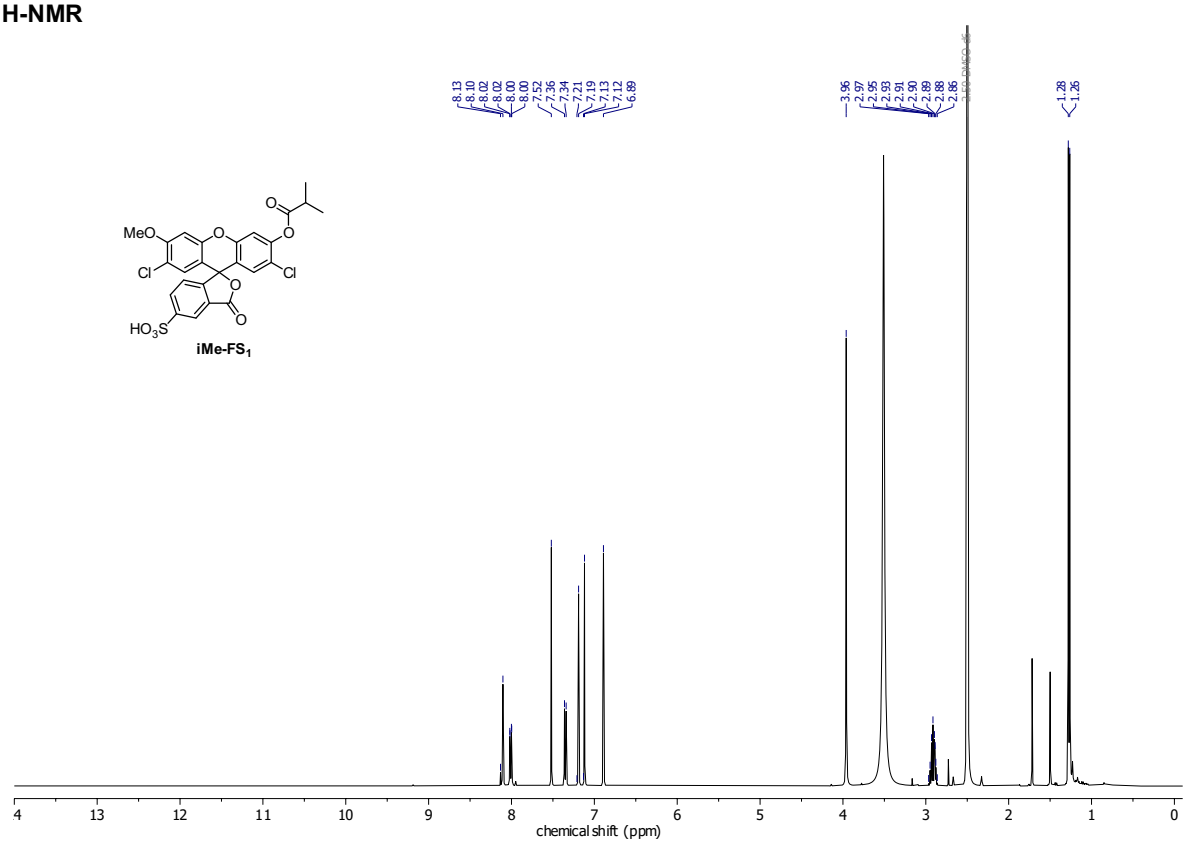

^{13}C-NMR

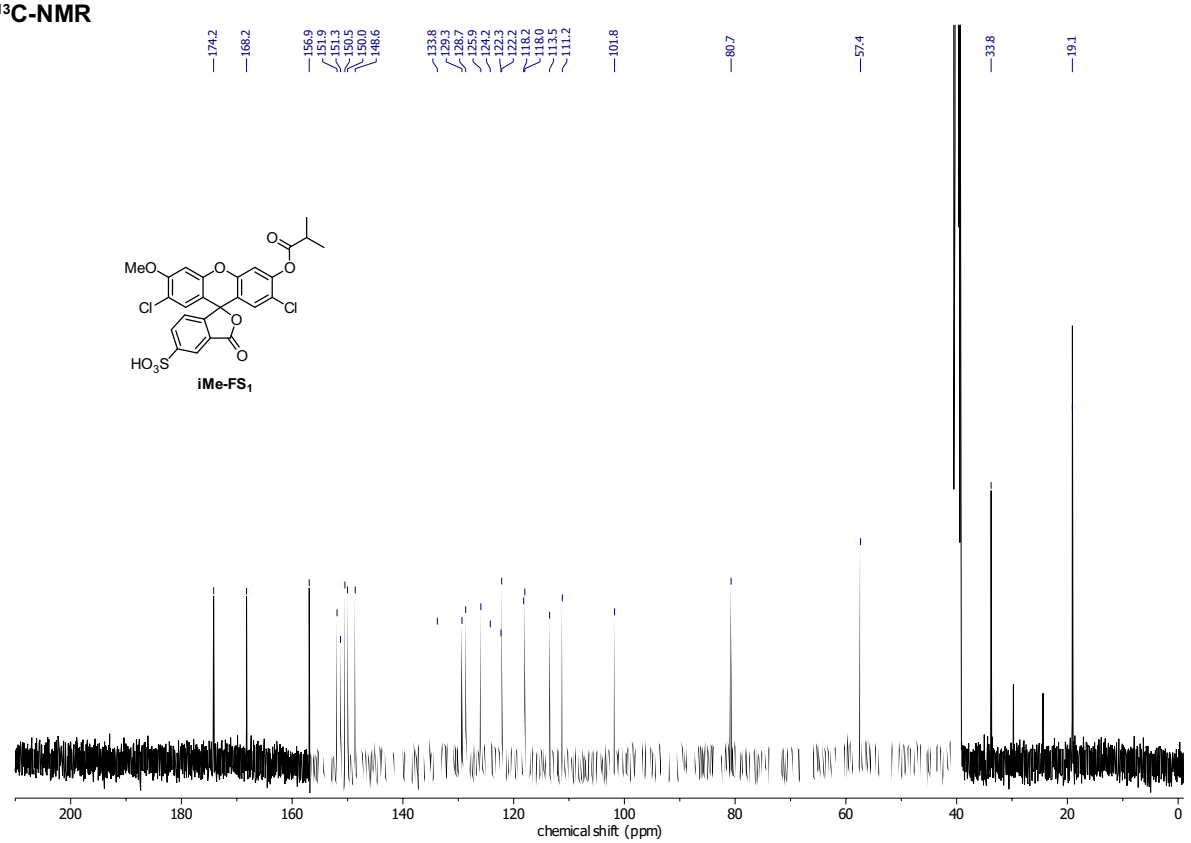

iEM-FS$_1$
^{1}H-NMR

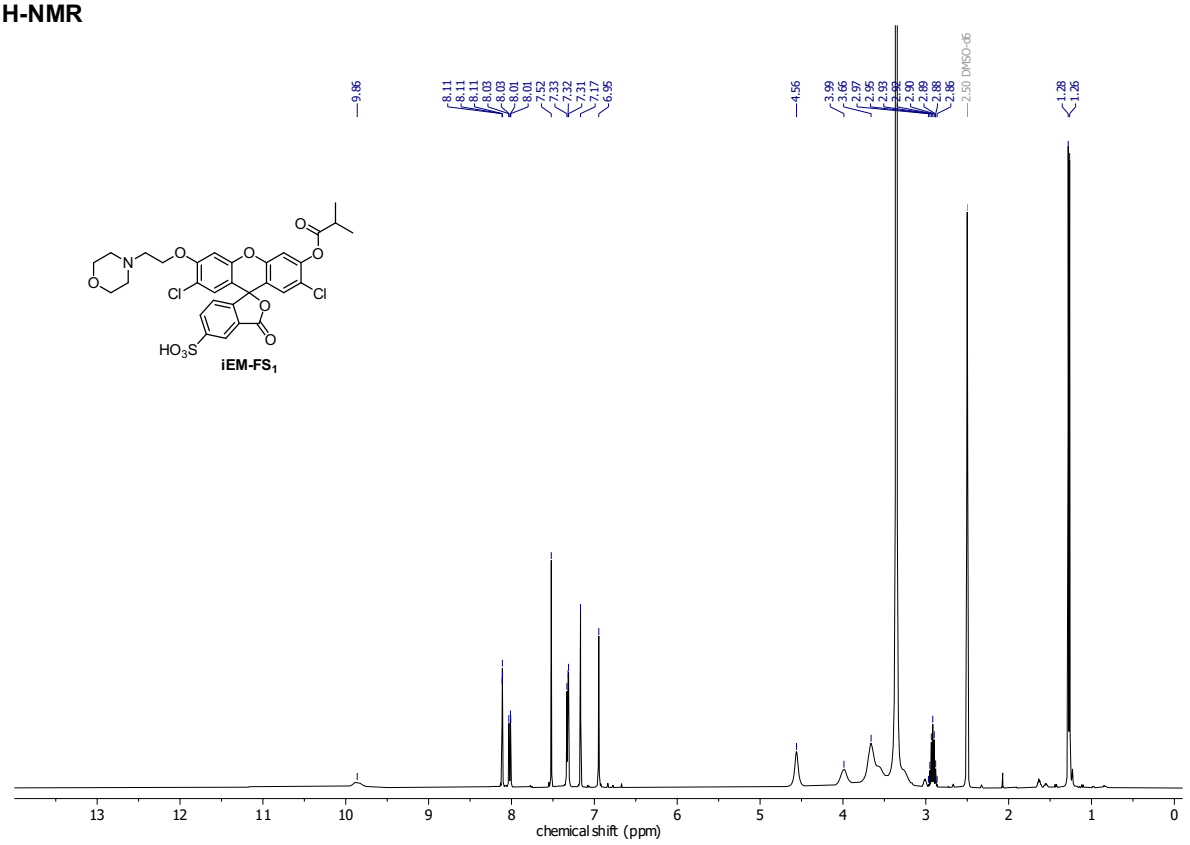

^{13}C-NMR

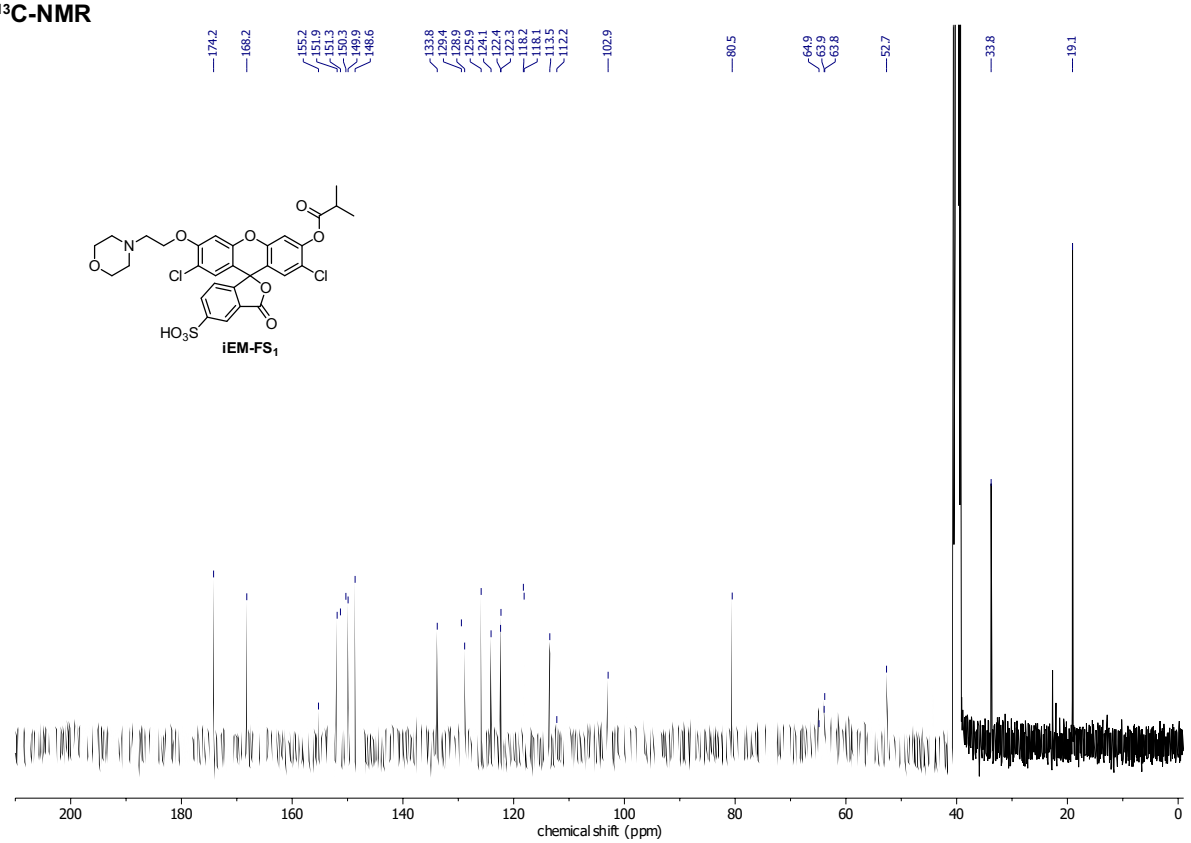

HSQC spectrum

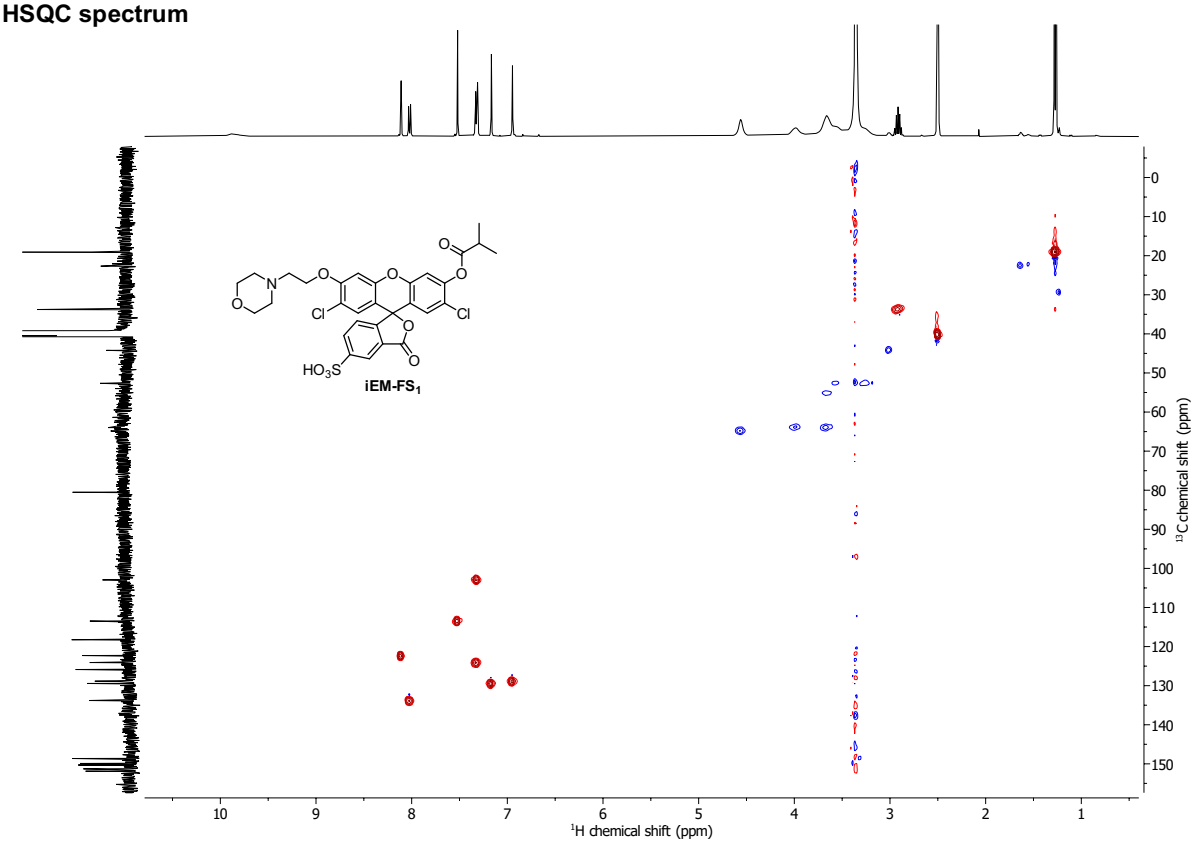

iPS-FS$_1$

^{1}H-NMR

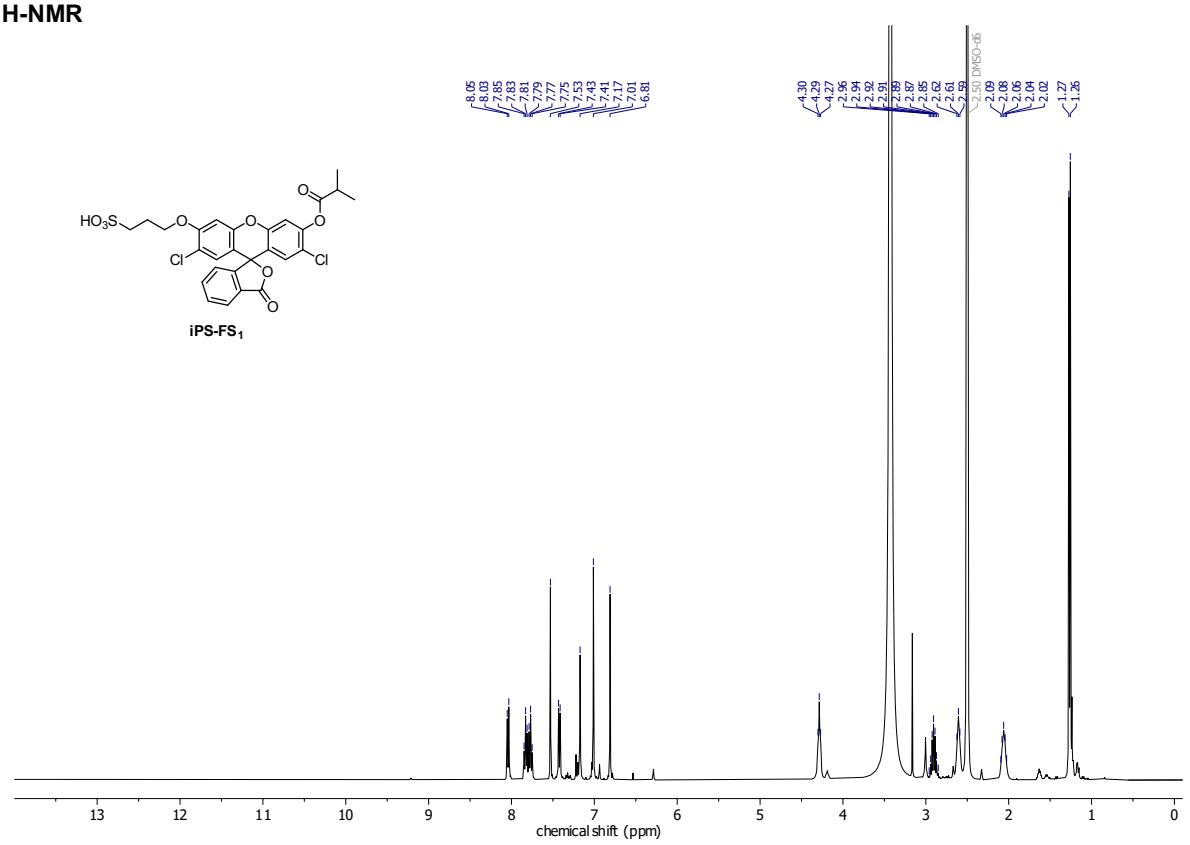

^{13}C-NMR

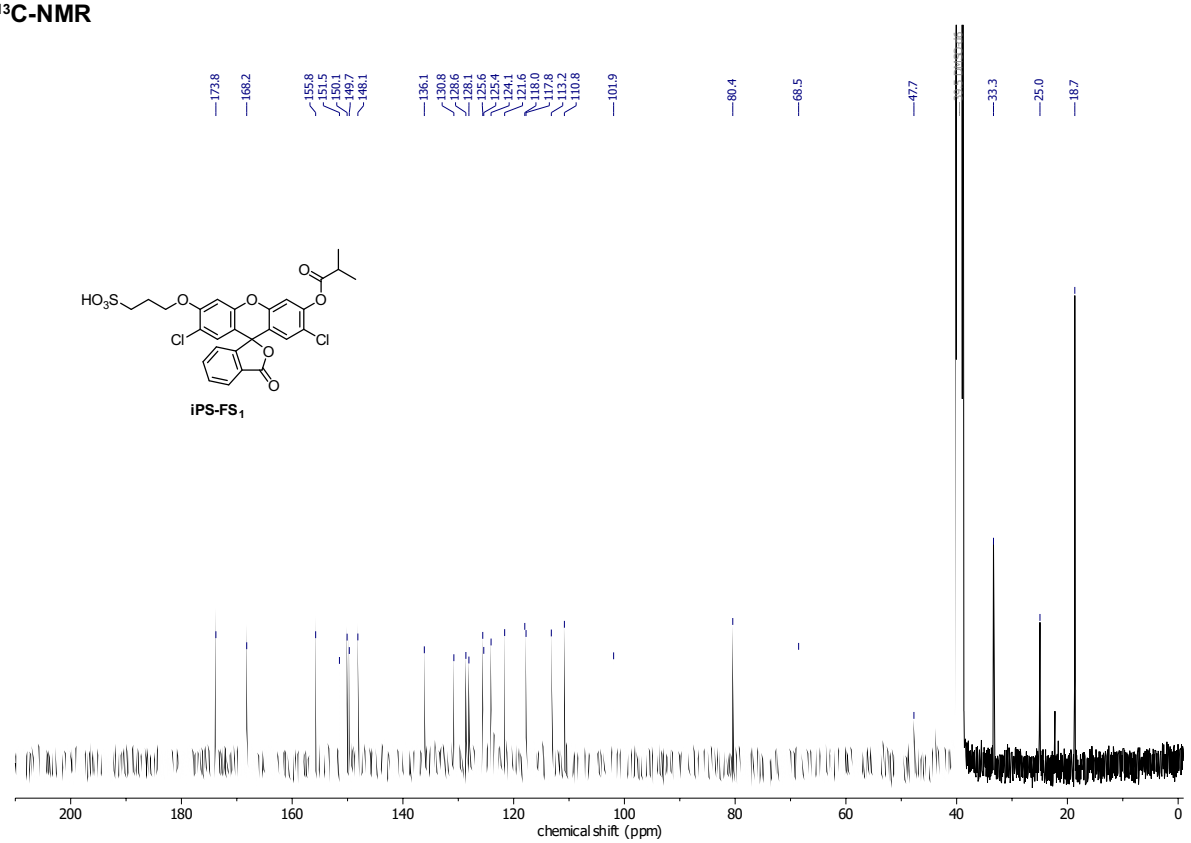

iPS-FS$_2$ (MDG1)

^{1}H-NMR

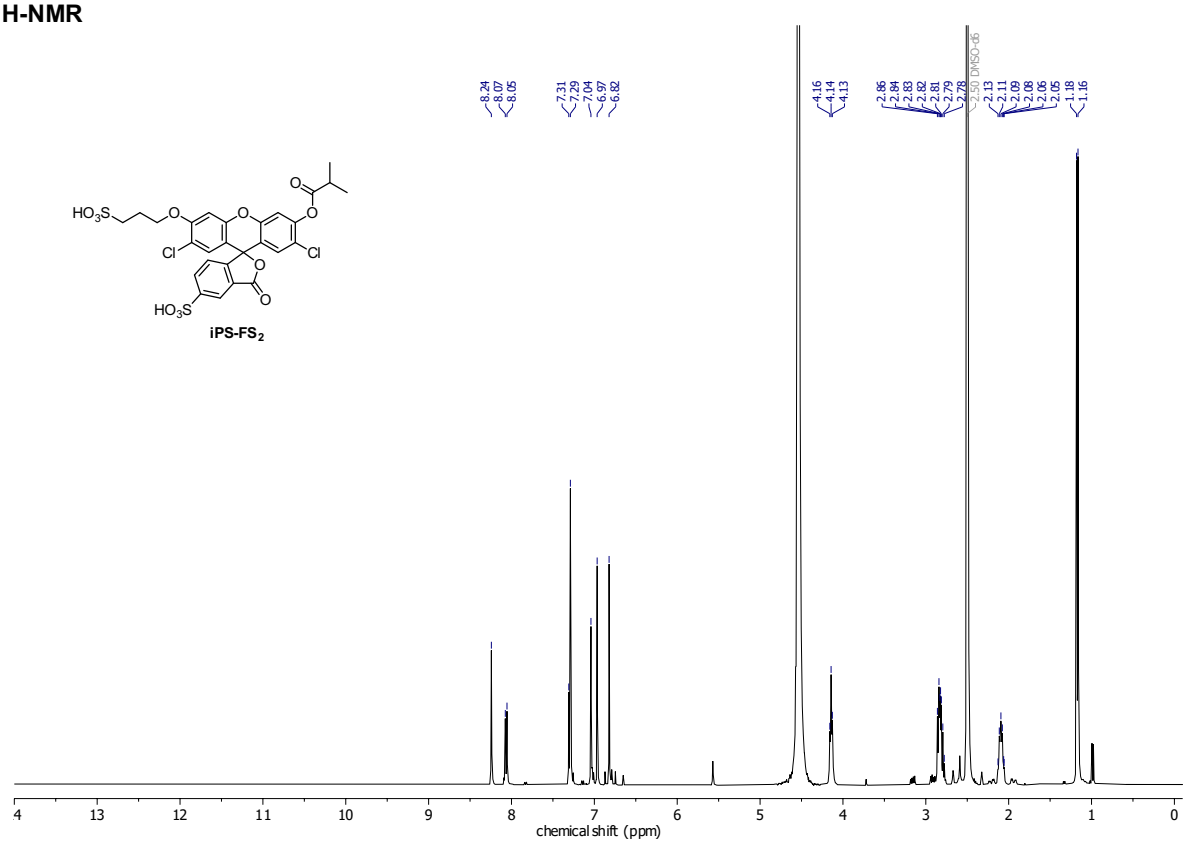

^{13}C-NMR

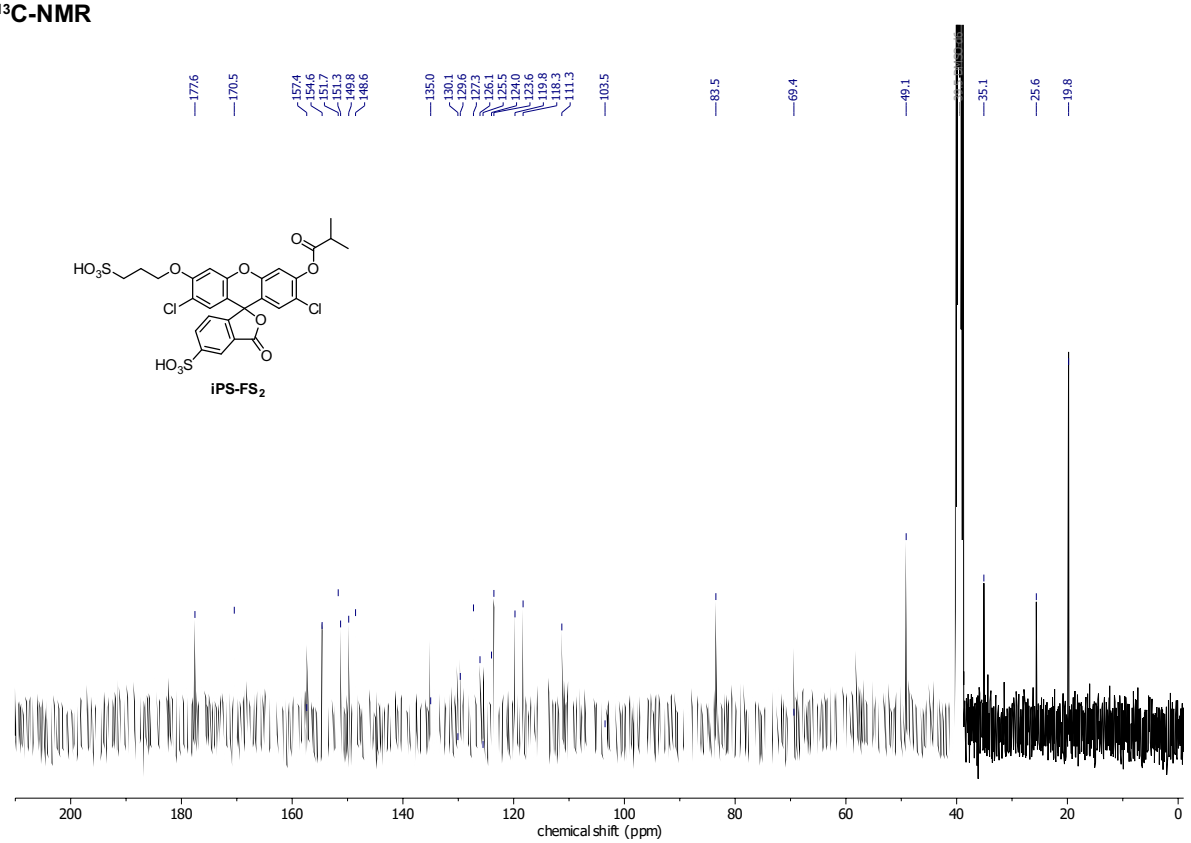

H-Me-FS$_1$

^{1}H-NMR

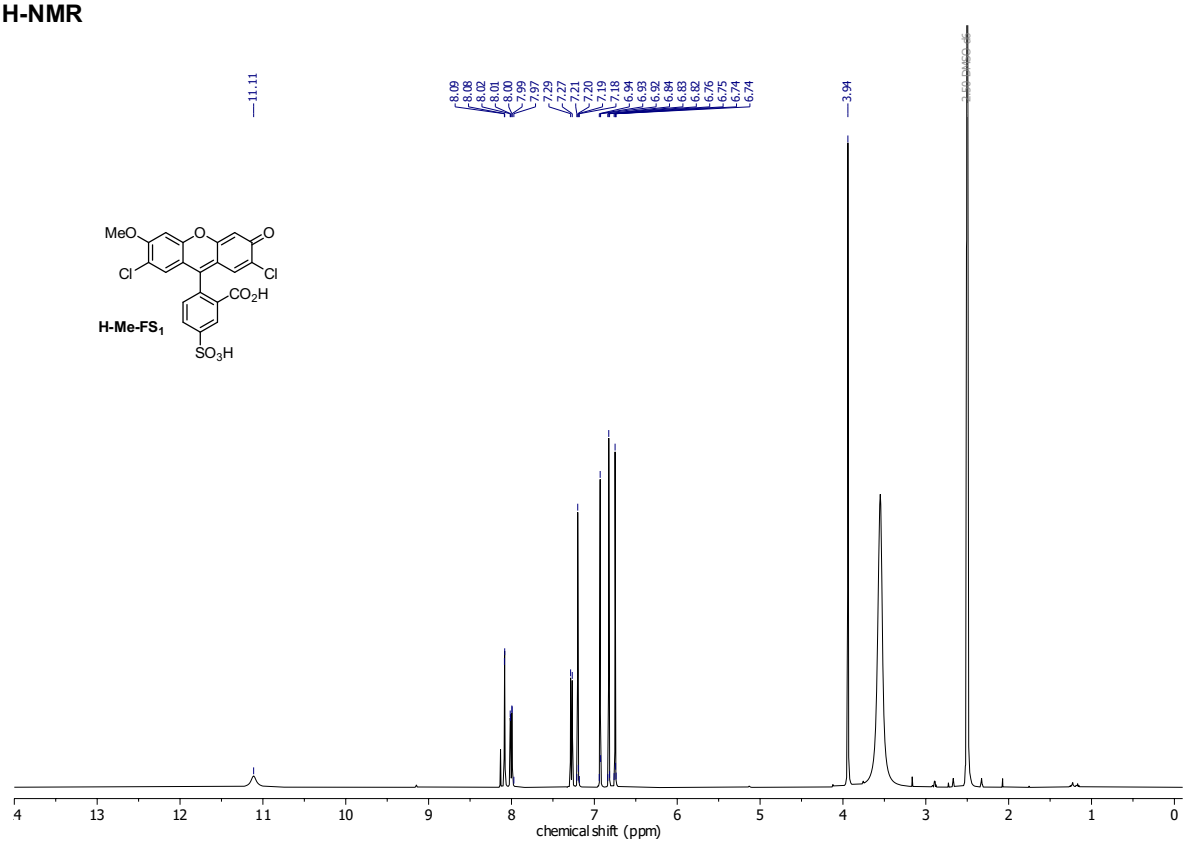

^{13}C-NMR

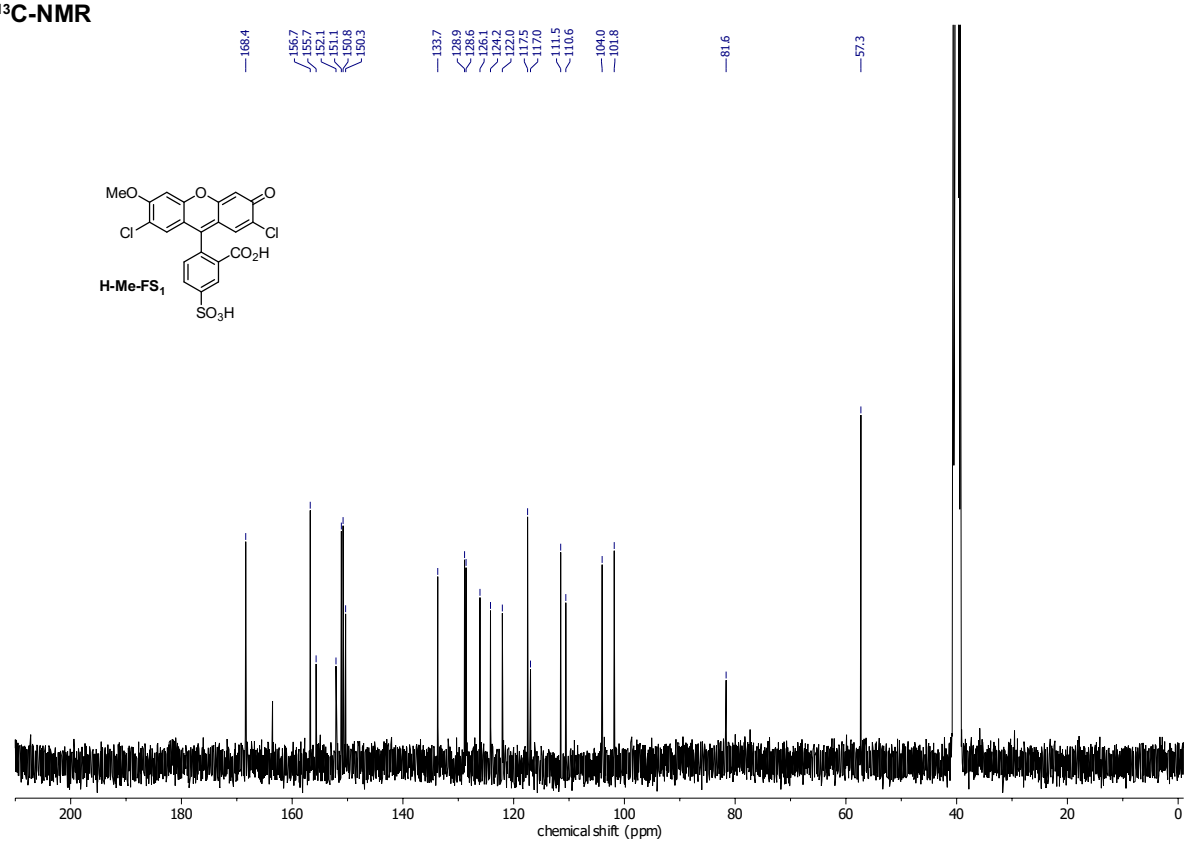

H-EM-FS$_1$

^{1}H-NMR

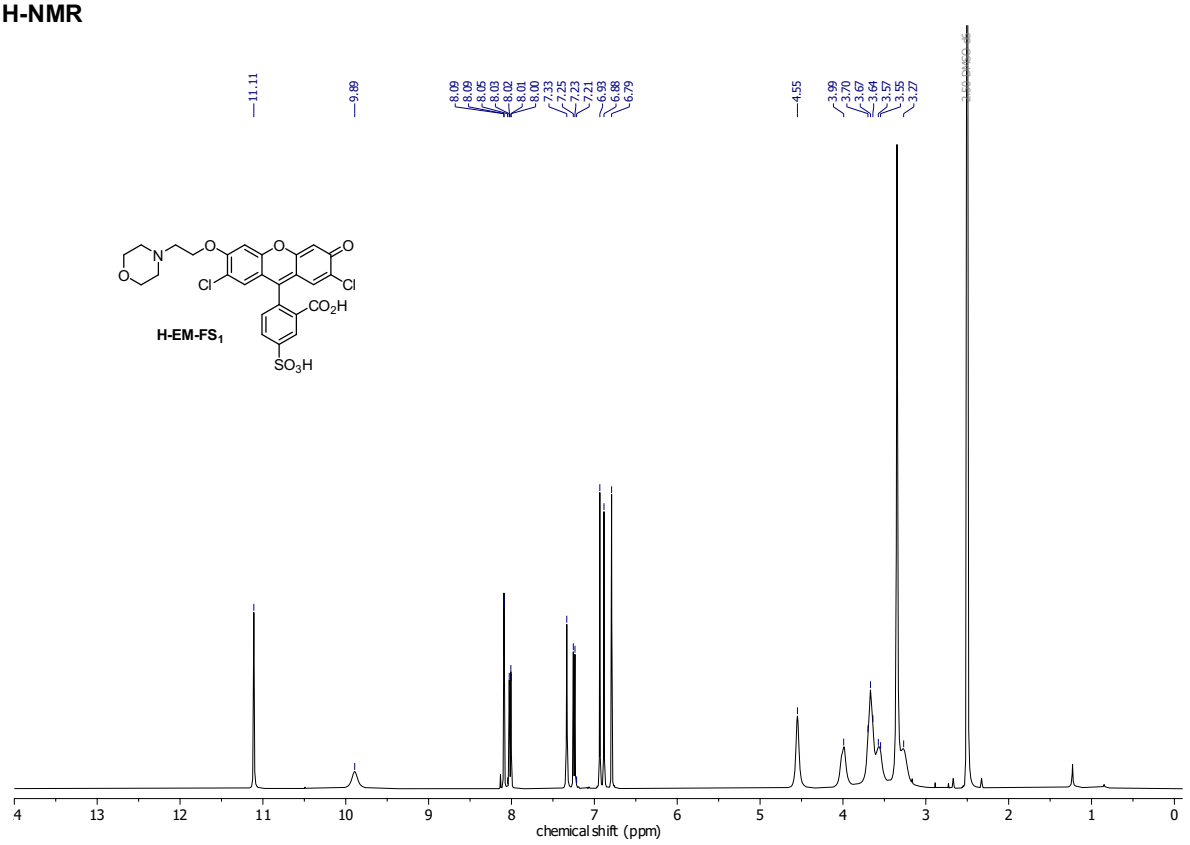

^{13}C-NMR

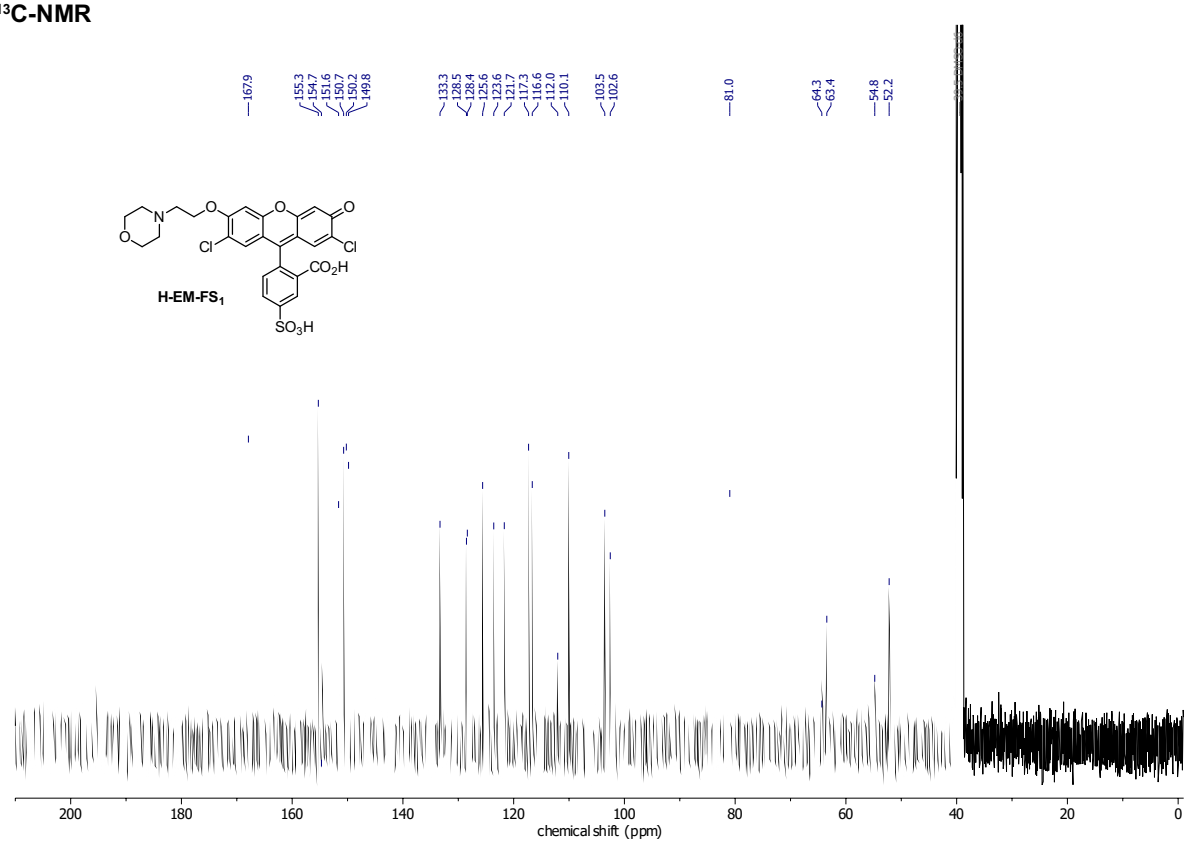

HSQC spectrum

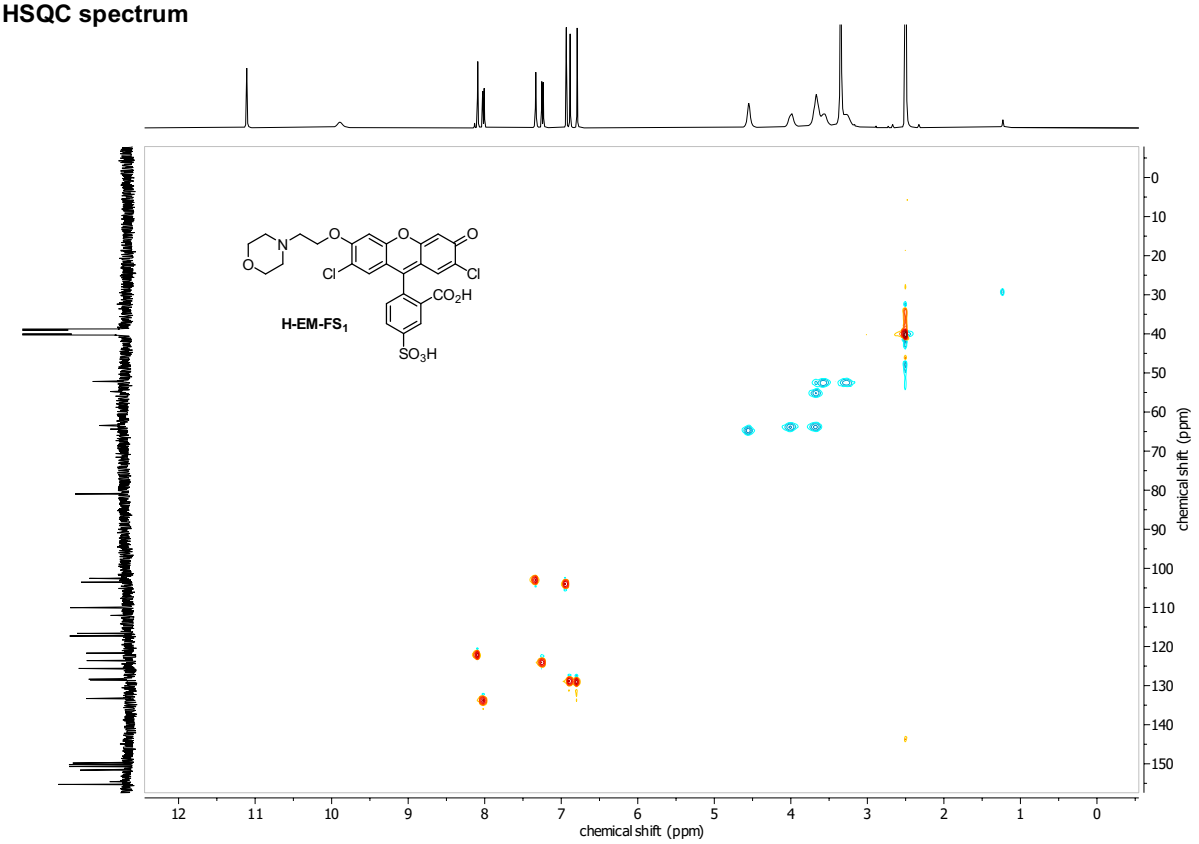

H-PS-FS$_1$

^{1}H-NMR

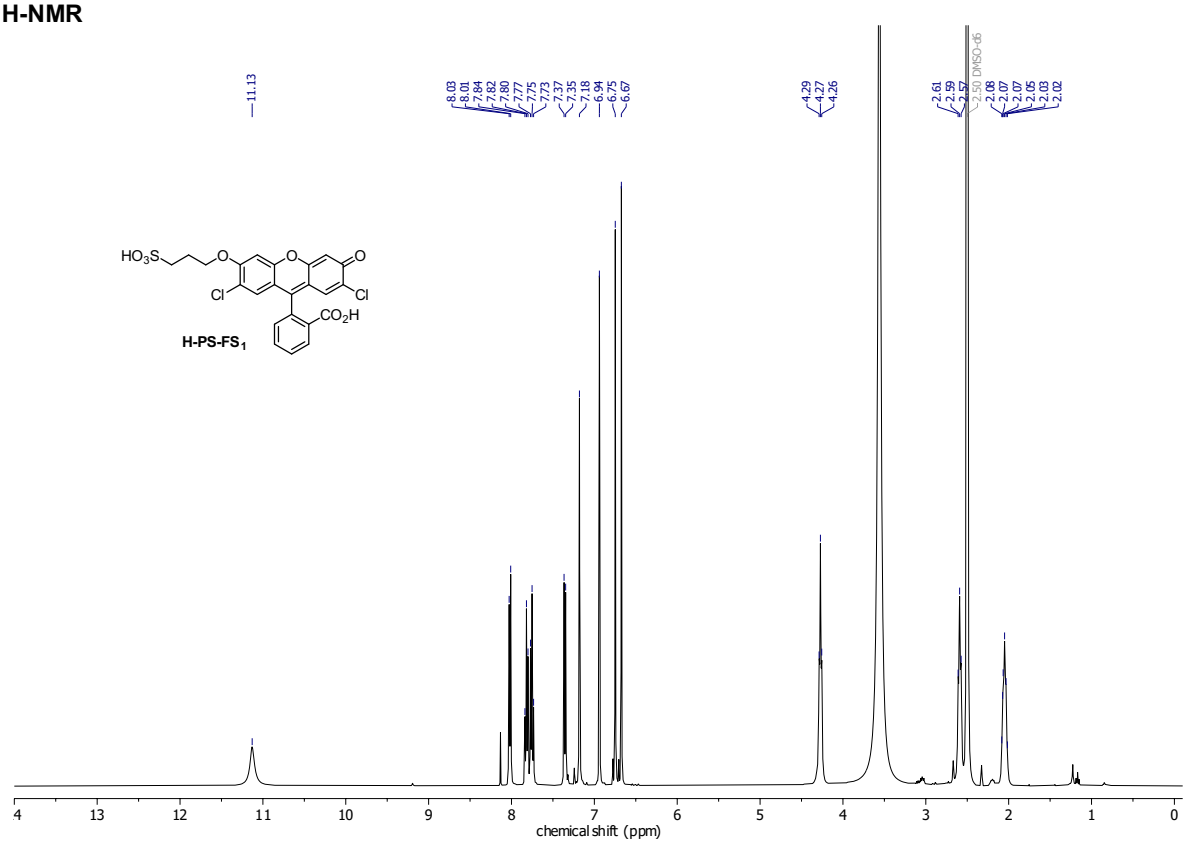

^{13}C-NMR

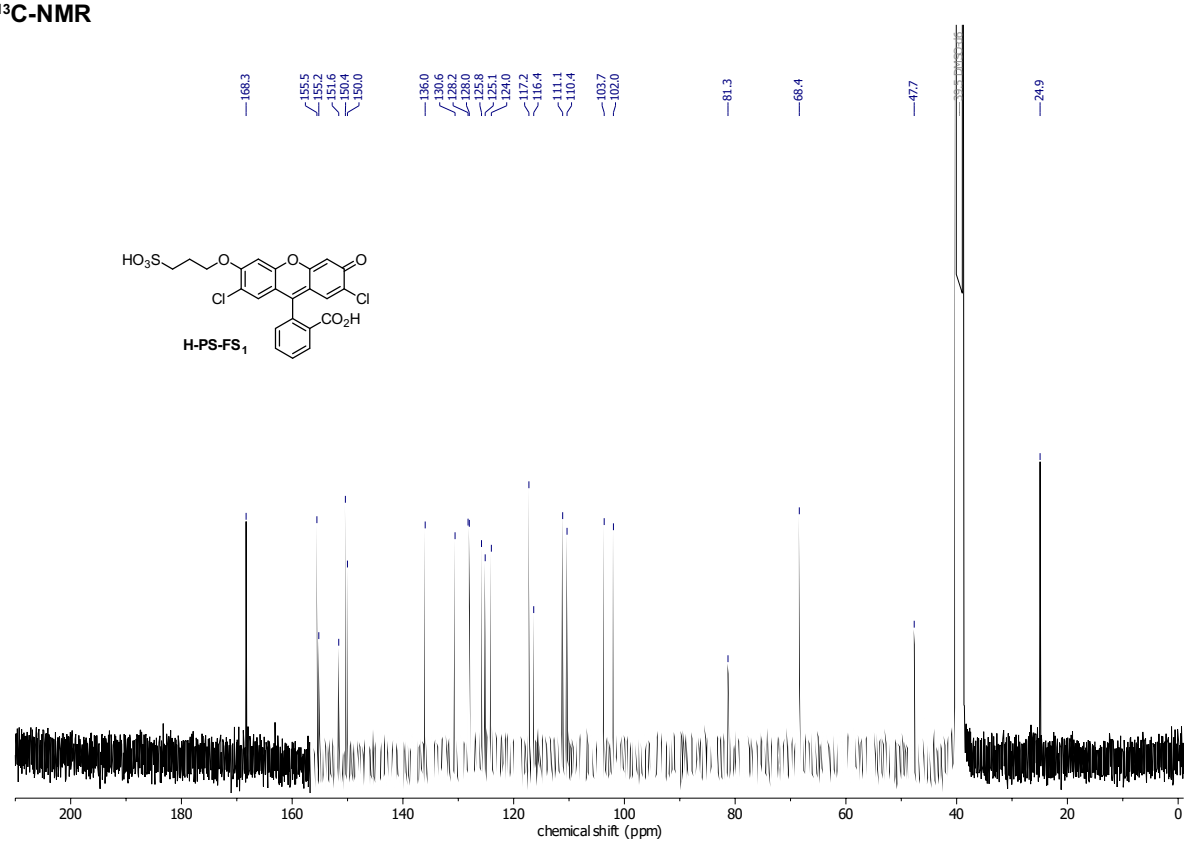

H-PS-FS$_2$

^{1}H-NMR

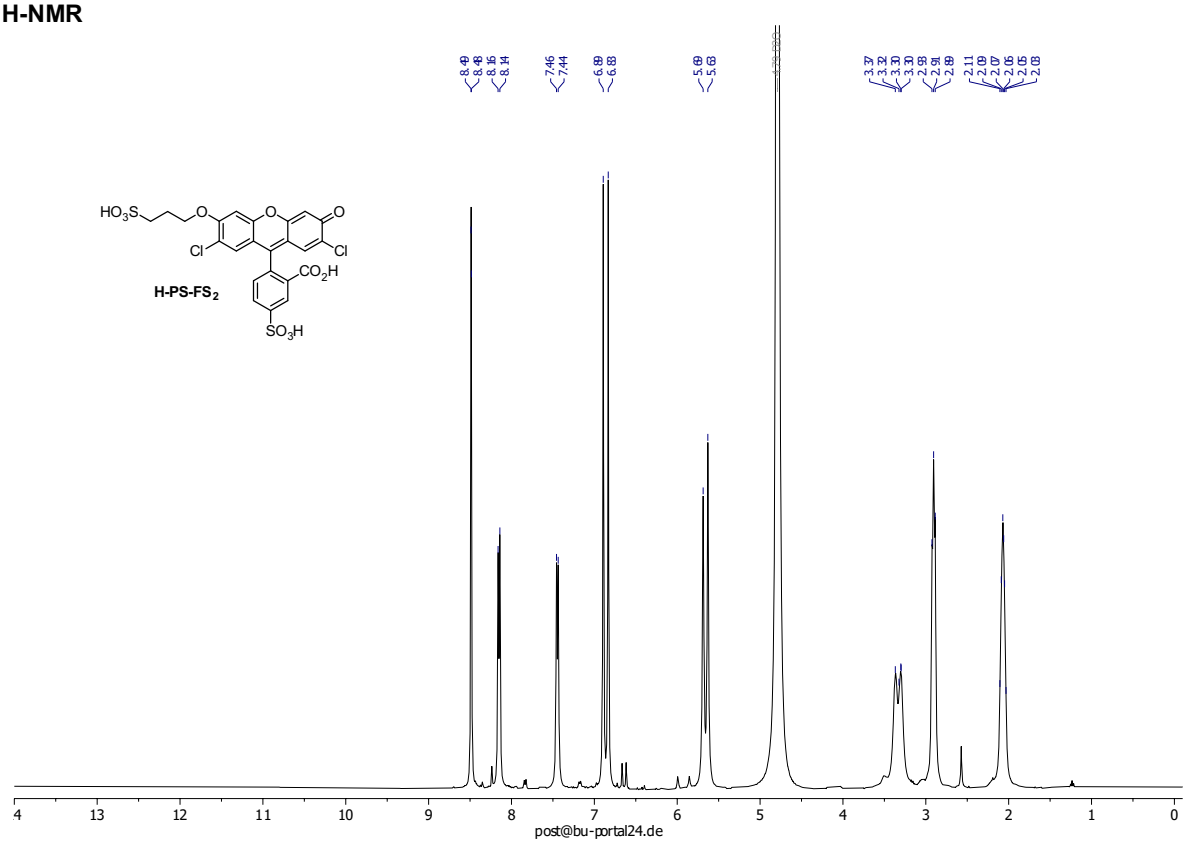

^{13}C-NMR

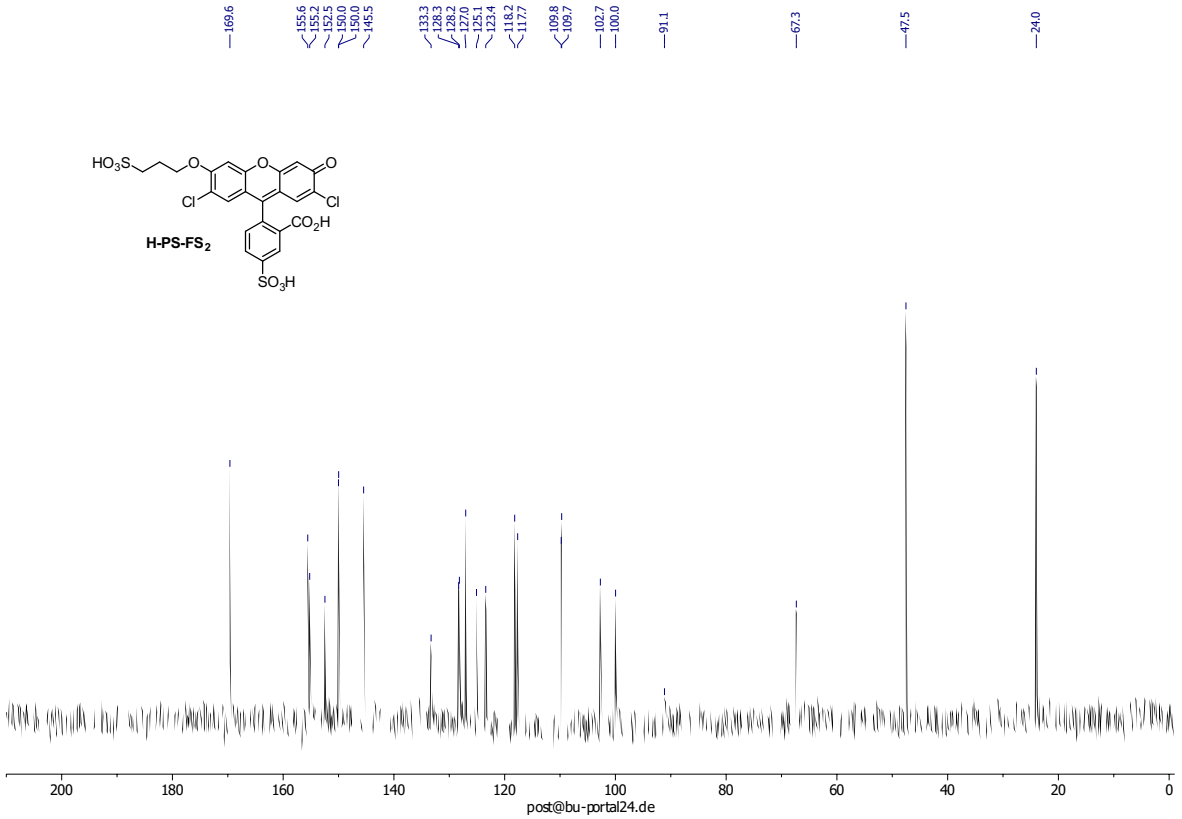

MSS00-PS-FS$_2$ (MDG2)

^{1}H-NMR

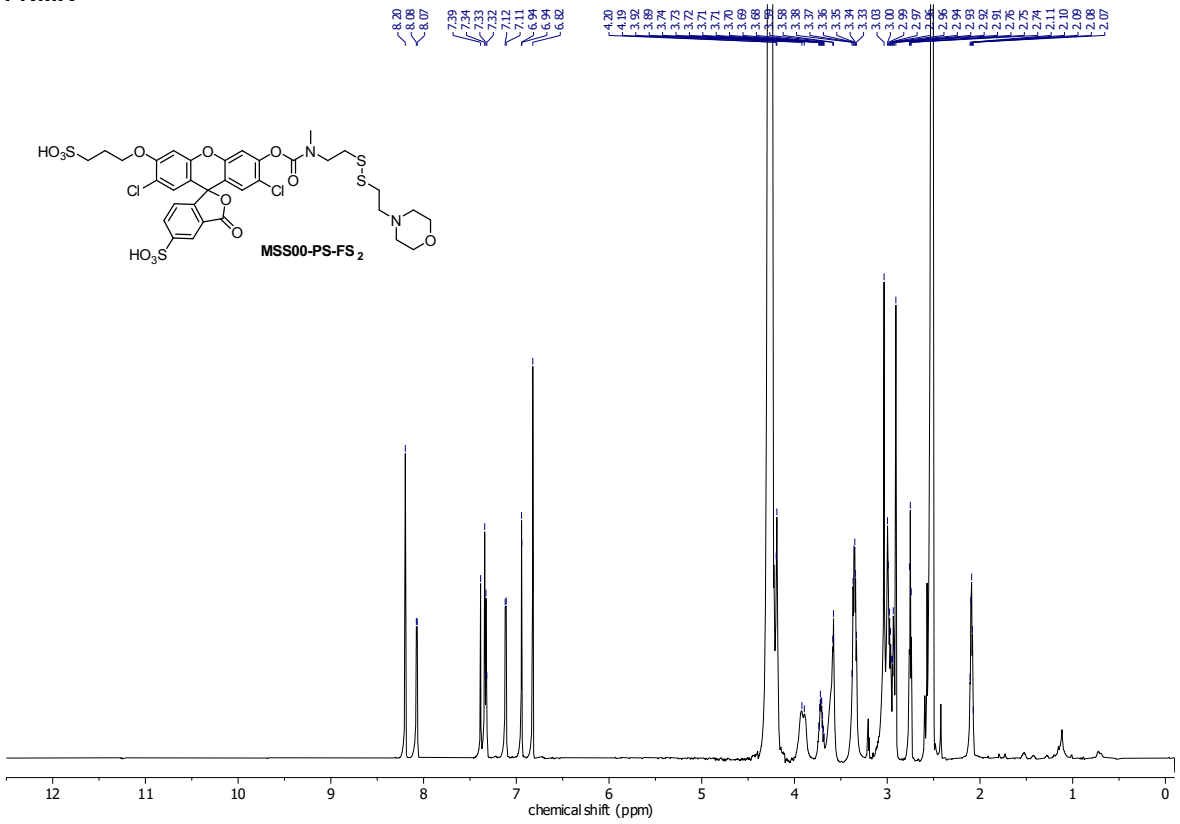

^{13}C-NMR

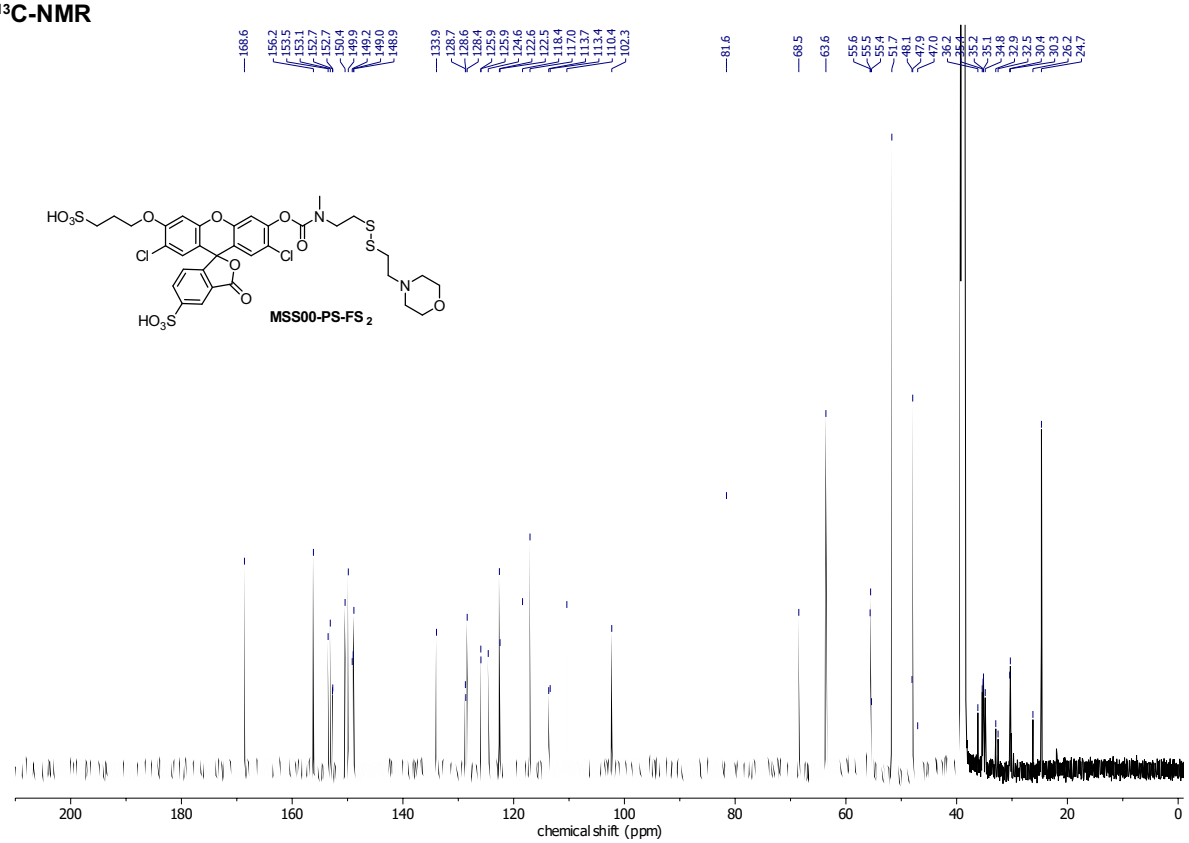

HSQC spectrum

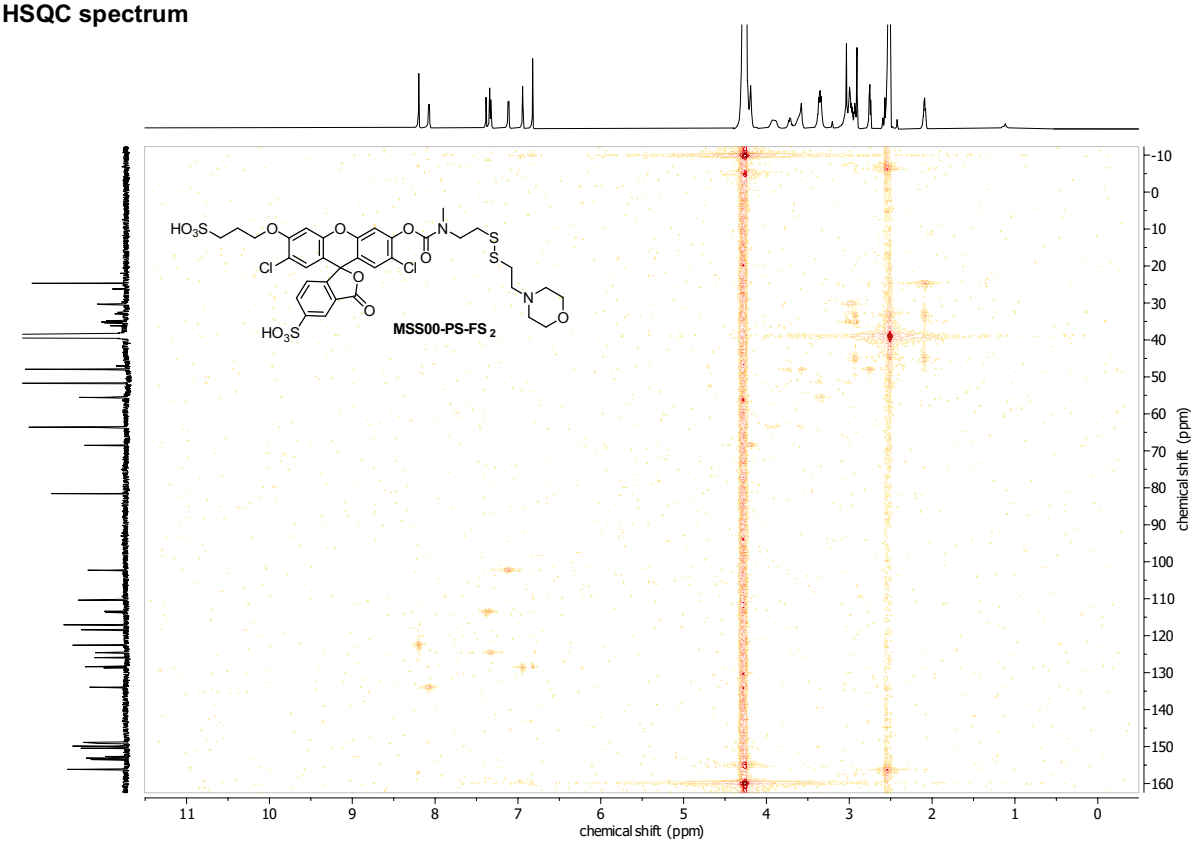

HSQC spectrum

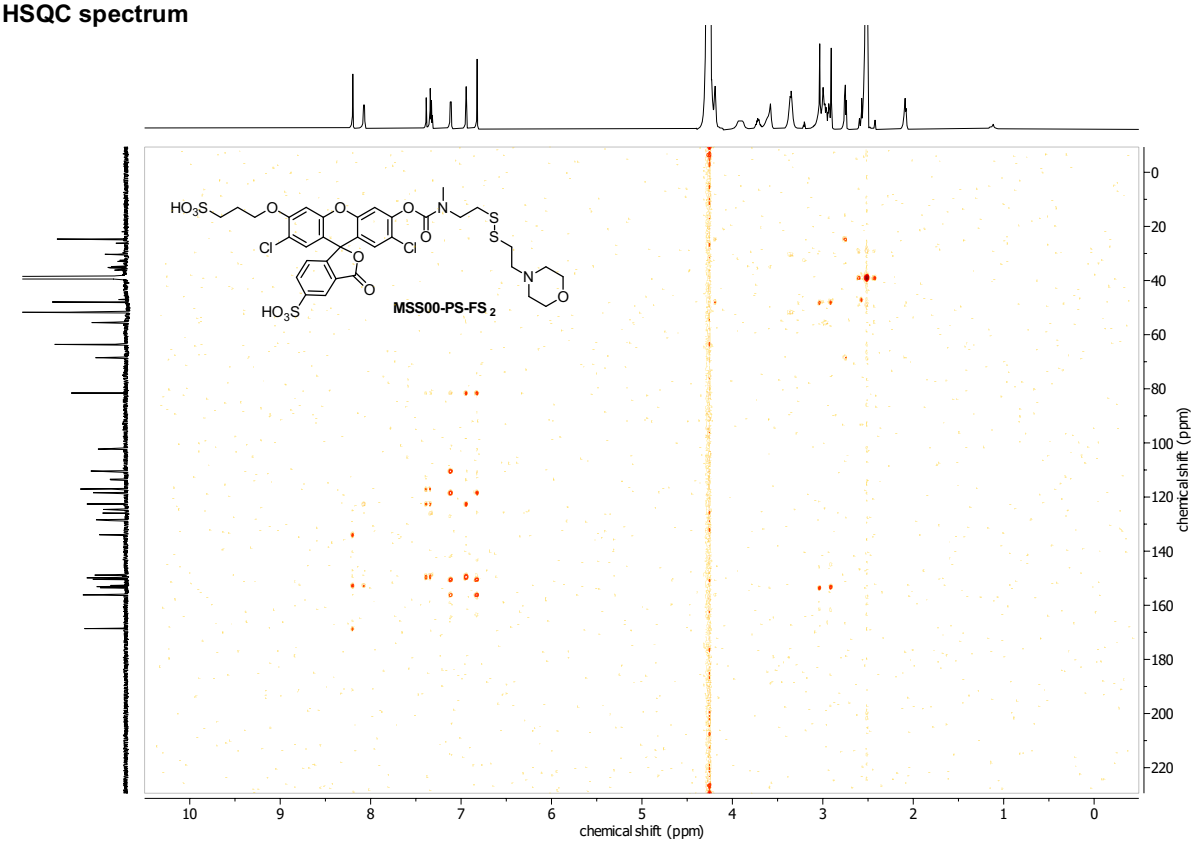

Dichlorofluorescein isobutyrate NHS-ester (NHS-iFS$_0$)

^{1}H-NMR

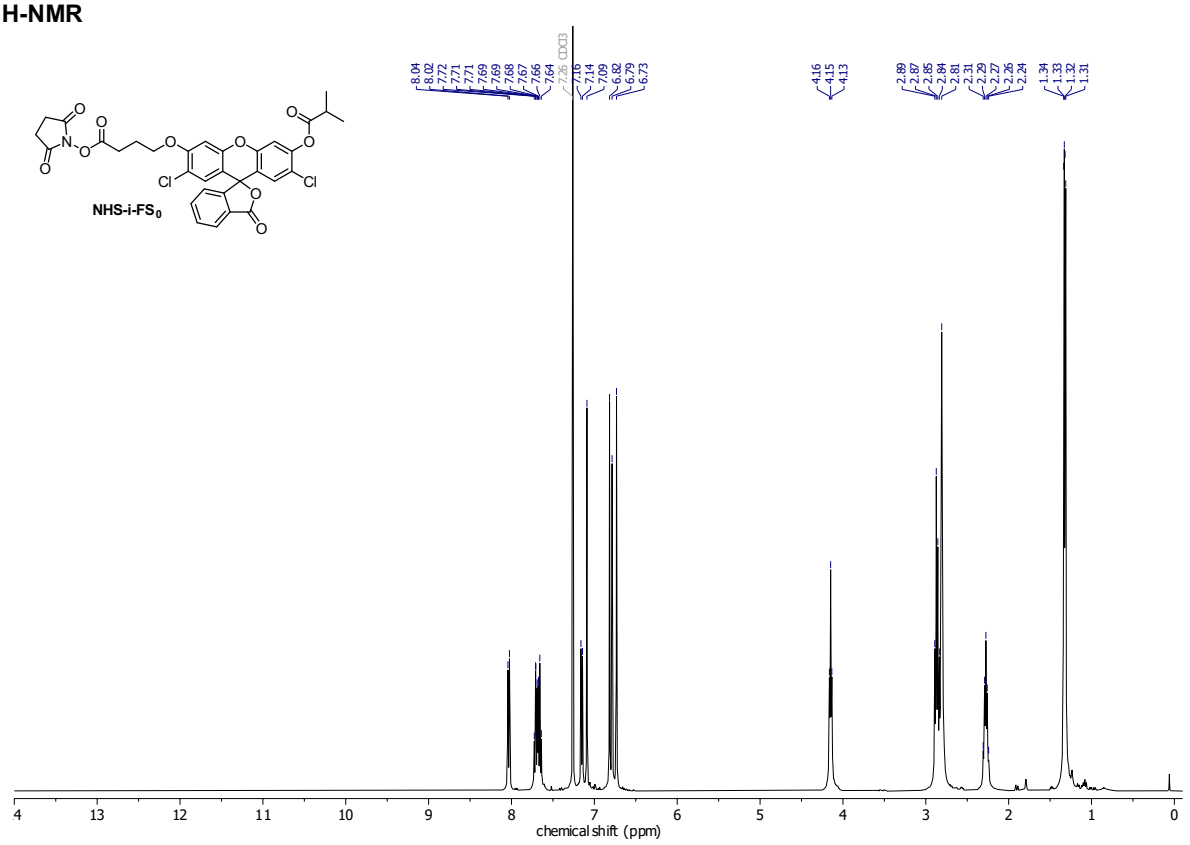

^{13}C-NMR

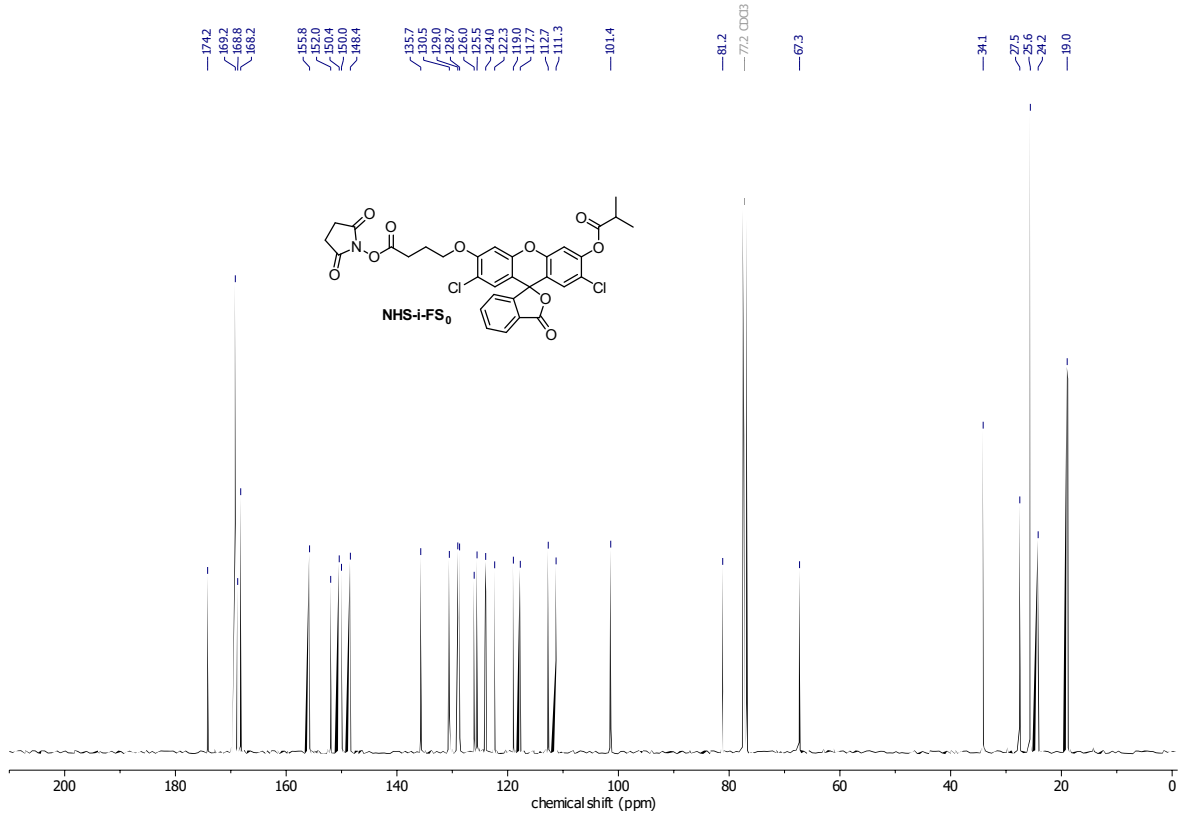

Supplementary Information to

A Modular Scaffold for Cellularly-Retained Fluorogenic Probes for Sensitive Cell-Resolved Bioactivity Imaging

Philipp Mauker[a], Lucas Dessen-Weissenhorn[b], Carmen Zecha[b], Nynke A. Vepřek[b], Julia I. Brandmeier[b], Daniela Beckmann[c][d], Annabel Kitowski[b], Tobias Kernmayr[b], Julia Thorn-Seshold[a][e], Martin Kerschensteiner[c][d][f], Oliver Thorn-Seshold*[a]

[a] P. Mauker, J. Thorn-Seshold, O. Thorn-Seshold; Faculty of Chemistry and Food Chemistry; Dresden University of Technology; Bergstrasse 66, Dresden 01069 (Germany); *E-mail: oliver.thorn-seshold@tu-dresden.de.

[b] L. Dessen-Weissenhorn, C. Zecha, N. A. Vepřek, J. I. Brandmeier, A. Kitowski, T. Kernmayr; Department of Pharmacy; Ludwig-Maximilians University of Munich; Butenandtstrasse 7, Munich 81377 (Germany).

[c] D. Beckmann, M. Kerschensteiner; Institute of Clinical Neuroimmunology, LMU University Hospital; LMU Munich; Marchioninistrasse 15, Munich 81377 (Germany).

[d] D. Beckmann, M. Kerschensteiner; Biomedical Center (BMC), Faculty of Medicine; LMU Munich; Grosshaderner Strasse 9, Martinsried 82152 (Germany).

[e] J. Thorn-Seshold; Faculty of Medicine, University Hospital Dresden; Dresden University of Technology; Fiedlerstrasse 42, Dresden 01307 (Germany).

[f] M. Kerschensteiner; Munich Cluster for Systems Neurology (SyNergy); Feodor-Lynen-Strasse 17, Munich 81377 (Germany).

Table of Contents

1 Overview of all fluorogenic probes and fluorophores

1.1 Fig S1: Fluorescein-derived probes and fluorophores

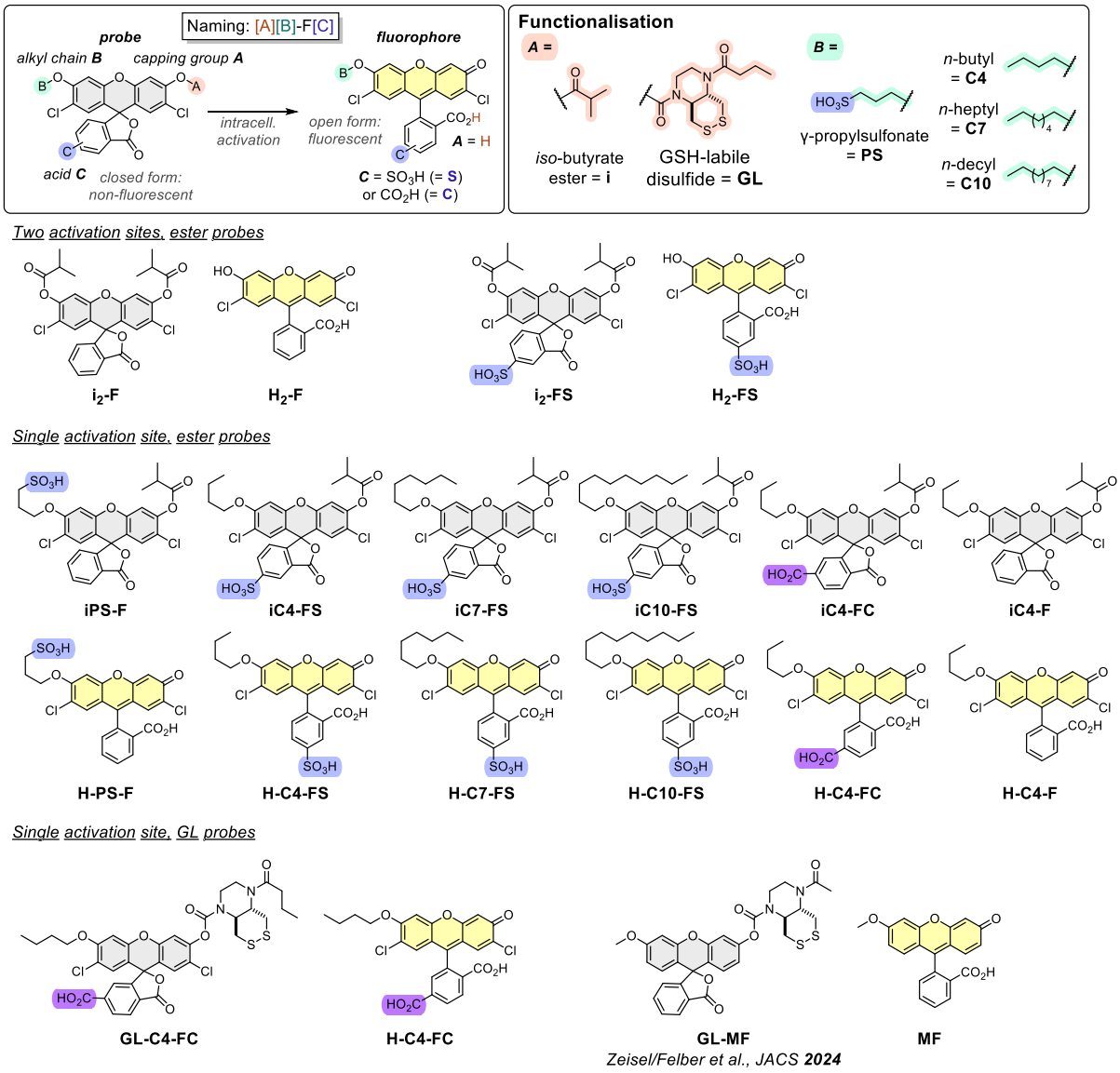

Figure S1: Compound naming rationale and structure overview of all fluorescein-derived probes and fluorophores.

1.2 Fig S2: Rhodol-derived probes and fluorophores

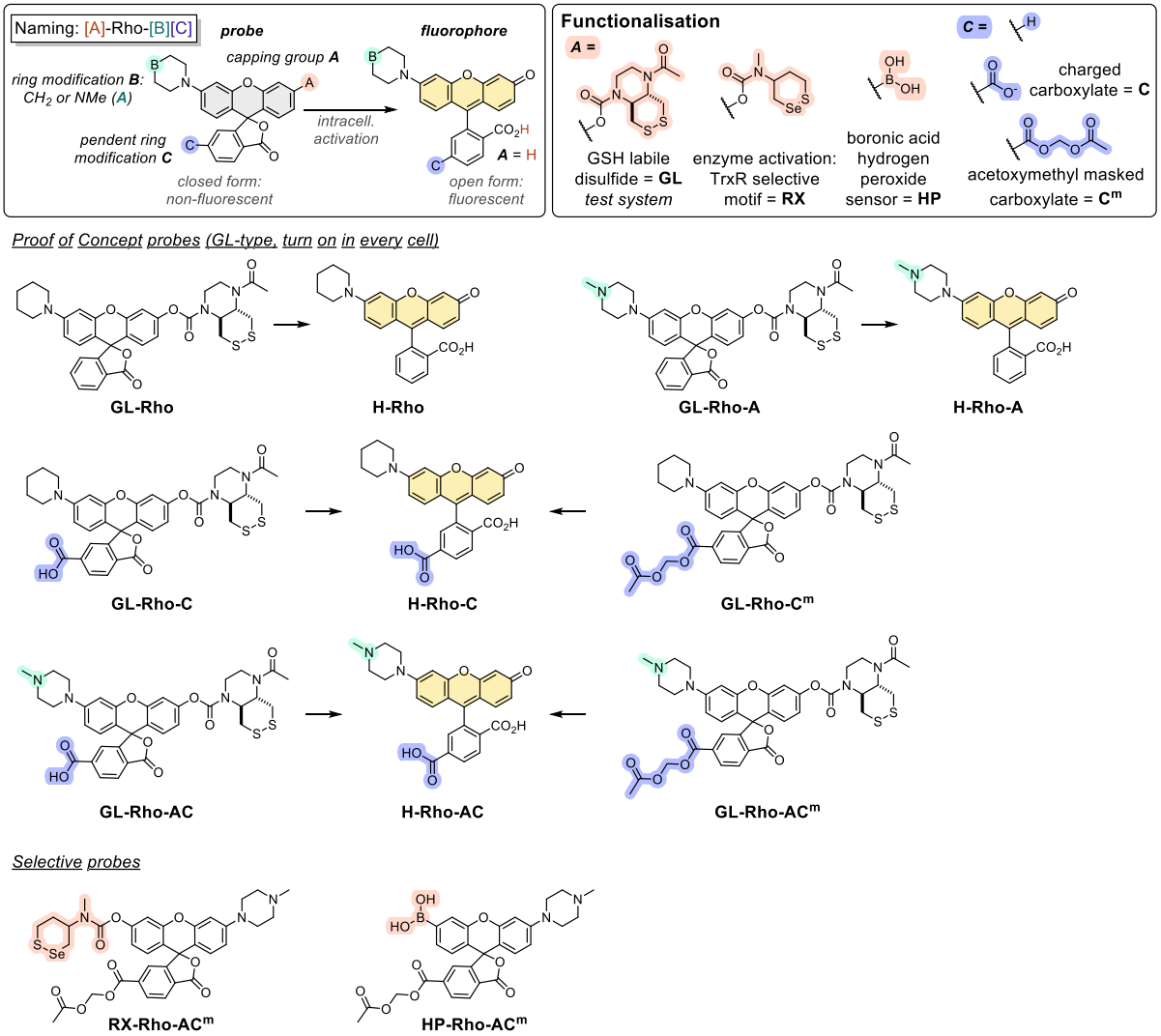

Figure S2: Compound naming rationale and structure overview of all rhodol probes and fluorophores.

2 Cell retention approaches: requirements, and prior art (Fig S3)

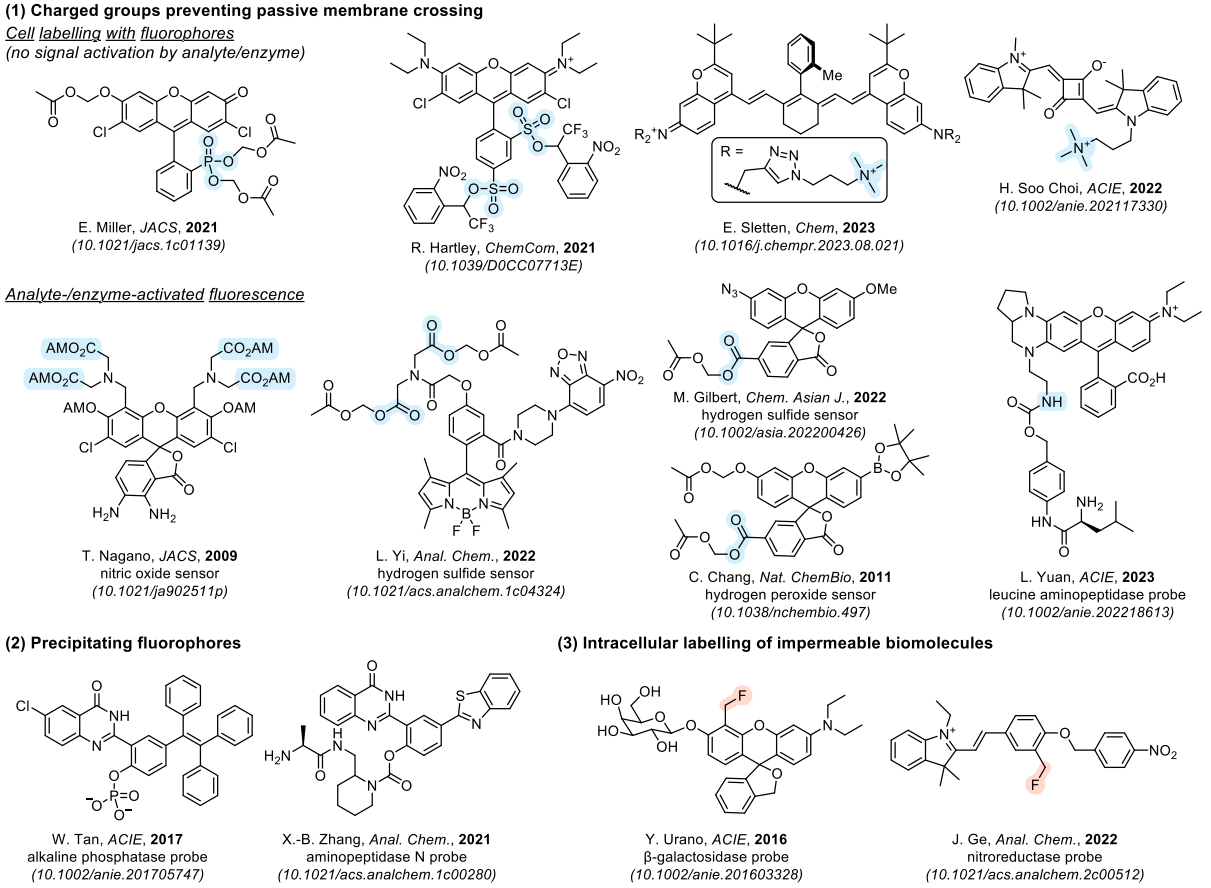

Figure S3: Strategies for intracellular fluorophore and probe signal retention used in literature.

The need for cell-retained probes has inspired many investigations of intracellular fluorophore trapping, with three general probe strategies emerging: (1) charge- and polarity-based impermeabilization by suppression of passive membrane crossing, (2) precipitation of the released fluorophore, and (3) intracellular labelling of impermeable biomolecules (e.g. proteins or glutathione) (overview of literature approaches in **Fig S3**).

(1) Charge-based cell retention is to date the most broadly utilised approach despite its limitations. Generally, these strategies use either cationic motifs such as tetraalkylammonium ions[1,2] or anionic groups such as carboxylates[3], phosphonates[4] or sulfonates[5] which cannot cross lipid bilayer by passive diffusion. The key challenge is cellular delivery of such polar groups which can be achieved in different ways: (i) cleavable masking groups that transform the charged functionality into lipophilic, membrane-permeable groups (e.g. acetoxymethyl carboxyl/phosphonate esters[3,4] or trifluoromethylbenzyl sulfonate esters[5,6]), (ii) endocytosis which can be induced by cell-penetrating peptides[7], and (iii) transporter-mediated uptake[1]. Most approaches focus on fluorophore delivery for cellular labelling and are not applicable for activity probes which generate fluorescence upon enzyme- or analyte-triggered activation. However, there are some examples investigating signal retention of activity probes which come with different limitations. Nagano and Yi developed sensors for nitric oxide[3] and hydrogen sulfide[8] which intracellularly release acetoxymethyl masked carboxylates and suppresses fluorescence by photoinduced electron transfer (PET) and FRET quenching before reacting with the analyte – an approach that limits applications to special reaction types and cannot be utilised for simple bond-cleavage reactions which would allow modular use for many types of analytes and enzymes. Other examples from Gilbert and Chang overcome this problem by generating phenol- and aniline-modified xanthenes for sensing hydrogen sulfide[9] and hydrogen peroxide[10] which would be translatable to other activating triggers but suffers from low fluorescence brightness or non-specific, partial intracellular signal generation which strongly reduces the sensitivity (opposing the goal main goal of retained probes: increased sensitivity and zero background). Yuan uses cationic retention releasing a basic amine for detecting hydrogen peroxide as well as leucine aminopeptidase and nitroreductase activity[11] and achieves signal turn on by PET quenching before activation requiring benzylic spacers whose 1,6-elimination influences signal turn-on kinetics and intracellularly releases electrophilic (aza)quinone-methides which can be cytotoxic, and the net positively charged fluorophore accumulates in lysosomes after activation. Overall, previously explored probe motifs come with different limitations in activation trigger modularity, fluorophore brightness, cellular uptake, release of reactive side products or undesired compartmentalisation (e.g. of basic amines to the lysosome).

(2) Precipitating fluorophores are a different approach to accomplish intracellular trapping of fluorescence. The water-insoluble fluorophore HPQ ((2-(2'-hydroxyphenyl)-4(3*H*)-quinazolinone) features excited-state intramolecular proton transfer (ESIPT)-based solid-state fluorescence with a large Stokes-Shift and bright signal.[12] HPQ-derived probes have been developed for alkaline phosphatase[13] and aminopeptidases[14] enabling not only cellular but even subcellular resolution of probe activation. Unfortunately, precipitating fluorophores come with several disadvantages: (i) their precipitation concentration threshold limits the sensitivity and renders activation below this threshold invisible, (ii) the water-insolubility of the fluorophore due to its lipophilicity and π--stacking limits the activating trigger to polar, solubilising motifs (such as phosphates or amino acids) to avoid pre-activation precipitation or membrane localisation, and – most problematically – (iii) the high cytotoxicity of intracellularly formed crystals which changes cell metabolism and makes visualisation of natural, biological activity impossible.

(3) Intracellular labelling of impermeable biomolecules as a cell retention approach was pioneered by Urano with the development of the so-called SPiDER probes. While previous approaches used active electrophiles to trap drugs[15] or fluorescent sensors[16], SPiDER probes are not electrophilic before activation and generate reactive quinone-methides upon activation which rapidly react with proteins and glutathione and have been successfully used for the development of glucosidase, peptidase, nitroreductase and hydrogen peroxide probes with durable cell retention.[17–21] However, the release of electrophiles can cause problems and influence the enzyme activity it is probing by reacting with the protein of interest[21] and the accumulation of reactive species can furthermore be toxic especially for high turnover cells.[19]

3 Figs S4-S6: Lipidated sulfo- and carboxyfluorescein probes

This chapter expands on the main text's shorter description of the design and performance of the failed set of lipidated fluorescein probes.

Sulfonated mono-capped fluorescein probes are not cell-retained

In a previous study we noticed that some mono-sulfonated fluoresceins can enter cells, which we used as a starting point for investigating and optimising cellular delivery and retention of such probes.[22] As an easy-to-synthesise test system for intracellular activation of phenolic probes, we used 2´,7´-dichlorofluorescein isobutyrate esters (**Fig S4a**) which are more stable against spontaneous ester hydrolysis in aqueous medium by sterical (isobutyrate vs. acetate) and electronic effects (n→π* interaction of chloride and ester) compared to ordinary fluorescein diacetate.[23] First, we investigated the previously described[22] diester **i$_2$-F** and its sulfonated analogue **i$_2$-FS** both featuring two esterase activation sites (resulting in non-linear fluorescence turn-on upon esterase activation as the first ester cleavage results in only 10% fluorescence activation with the other 90% coming from the second ester cleavage) and compared it to the sulfonated mono-ester **iPS-F** (one activation site, linear fluorescence turn-on). **i$_2$-F** releases dichlorofluorescein (**H$_2$-F**) with strong cellular signal which is actively exported from cells by anion transporters[24,25] and therefore shows reduced post-wash cell retention, its sulfonated analogue **i$_2$-FS** shows lower cellular signal but is able to escape the export pathway and is well retained after activation (**Fig S4b–d**). Unfortunately, these encouraging results did not translate to the single activation-site **iPS-F** which gives low cellular signal and is not cell retained. Thus, a different strategy was needed.

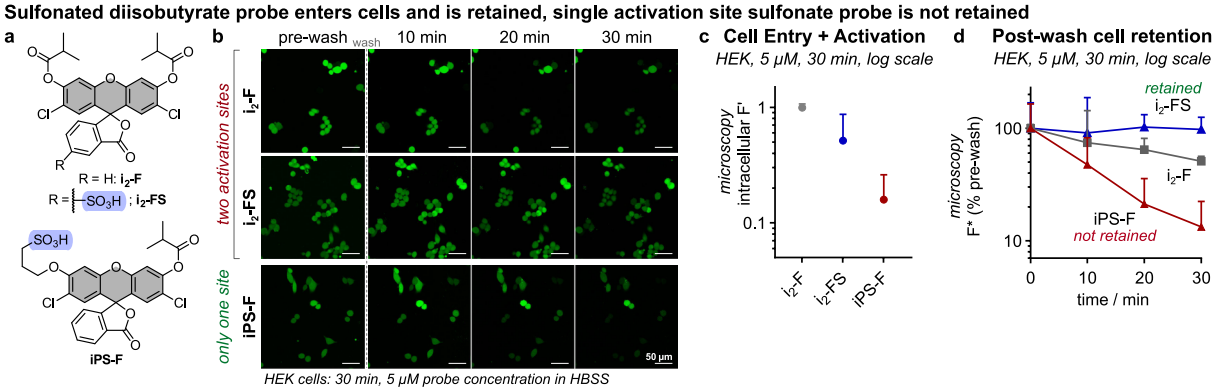

Figure S4: Sulfonated mono-capped fluorescein probes are not retained. (a) Structures of previously reported sulfonated fluorescein probes which served as entry for retention study; **(b)** Confocal microscopy: intracellular signal and post-wash retention of fluorescein diisobutyrate **i$_2$-F** compared to the sulfonated derivatives **i$_2$-FS** and **iPS-FS** (treatment with 5 µM probe in HBSS for 30 min, then wash (2× with HBSS); *scale bars: 50 µm*; transmission and CellTracker images: Fig S7); **(c)** Intracellular fluorescence signal quantified from microscopy images (treatment with 5 µM probe in HBSS for 30 min; F' is intracellular fluorescence normalized to the i$_2$-F signal; *error bars: SD*; *n*=3); **(d)** Post-wash intracellular signal retention quantified from microscopy images (treatment with 5 µM probe in HBSS for 30 min, then wash (2× with HBSS), F* is fluorescence as % of pre-wash value; *error bars: SD*; *n*=3).

Lipidated sulfonate probes can be cell-retained

Nature uses medium-length lipids to enhance cell uptake and retention of natural products.[26] Inspired by this observation, we synthesised a set of *O´*-lipidated sulfofluorescein esters with different alkyl-chain lengths (*n*-butyl, *n*-heptyl and *n*-decyl: C4, C7 and C10) aiming for signal retention by combining charge introduction with lipidation (**Fig S5a**). The *O´*-alkyl fluoresceins show expected fluorescence properties (full discussion at **Fig S20**, **Table S1**), so next we investigated their cellular performance. Depending on the lipid tail length, different cellular uptake efficiency and post-wash retention is observed: **iC4-FS** and **iC7-FS** give low but decent cellular signal which is strongly reduced for **iC10-FS** with its much longer lipid tail, but all probes retain their fluorescence after washing (**Fig S5b–d**, the **iC10-FS** fluorescence was not quantified due to membrane-anchoring). The cellular signal distribution strongly depends on the lipid length: while **iC4-FS** (short tail) gives uniform signal distribution across the whole cell, **iC10-FS** (long tail) is anchored in the plasma membrane and slowly leaks into the cell after washing which renders it useless for activity imaging. The fluorescence of **iC7-FS** (medium-length tail) is mostly found in the cytosol and excluded from the nucleus. The signal intensity trend (**Fig S5c**) and the *in vitro* esterase activation kinetics (**Fig S25**) show lower signal for longer lipids, indicating reduced solubility and/or aggregation for more lipophilic probes with increased alkyl chain length, rendering **iC4-FS** the favourite candidate for optimising the cellular uptake.

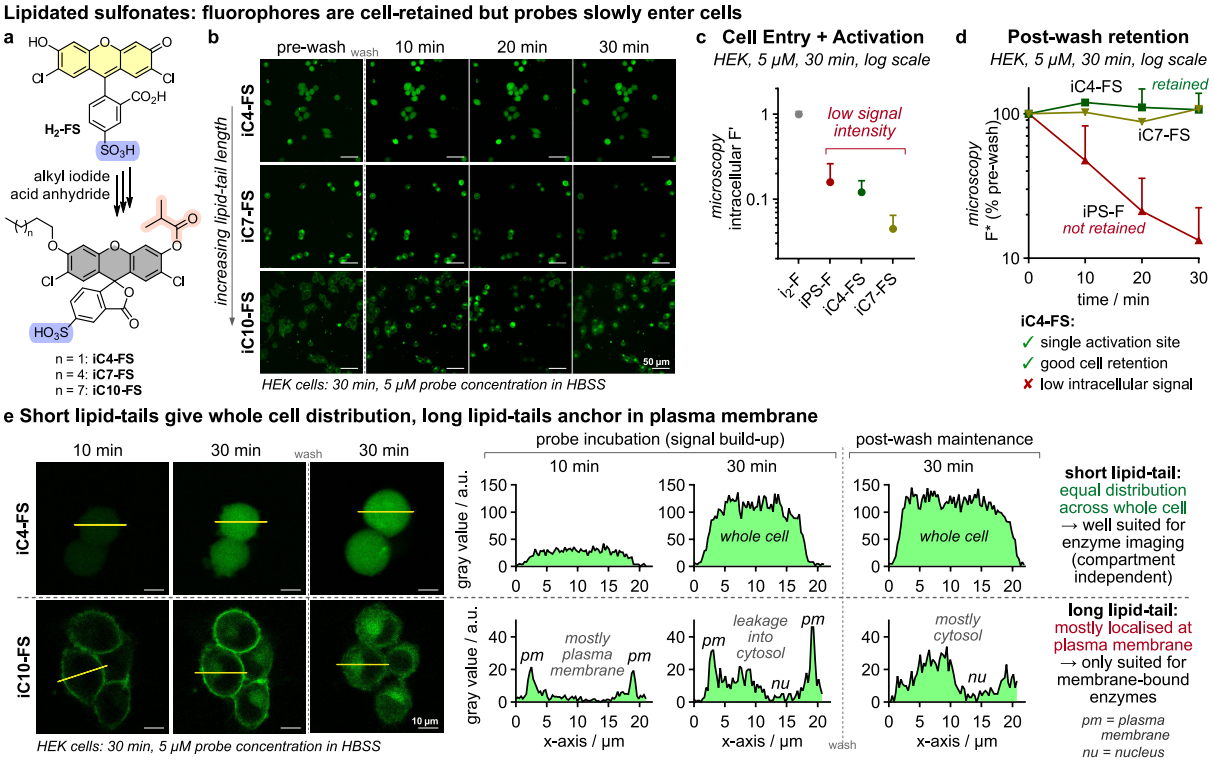

Figure S5: Lipidated sulfonated fluorescein probes are cell-retained but slowly enter cells. (a) Chemical structures and synthetic accessibility of lipidated sulfofluorescein isobutyrate probes **iC4-FS**, **iC7-FS** and **iC10-FS**; **(b)** Confocal microscopy: intracellular signal and post-wash retention of lipidated fluorescein probes (treatment with 5 µM probe in HBSS for 30 min, then wash (2× with HBSS); *scale bars: 50 µm*; transmission and CellTracker images: Fig S7); **(c)** Intracellular fluorescence signal quantified from microscopy images (treatment with 5 µM probe in HBSS for 30 min; F' is intracellular fluorescence normalized to the i_2-F signal; *error bars: SD*; *n*=3); **(d)** Post-wash intracellular signal retention quantified from microscopy images (treatment with 5 µM probe in HBSS for 30 min, then wash (2× with HBSS), F* is fluorescence as % of pre-wash value; *error bars: SD*; *n*=3); **(e)** Confocal microscopy images of intracellular signal distribution for **iC4-FS** and **iC10-FS** and quantification of the gray values distribution across one cell (treatment with 5 µM probe in HBSS for 30 min, then wash (2× with HBSS); *scale bars: 10 µm*).

Lipidated carboxylate probes appeared to improve cell uptake but were ultimately found to rely on unphysiological membrane integrity destabilisation for this uptake, which stopped our development

To improve cellular uptake, we synthesised the short lipid tail carboxylate probe **iC4-FC** (**Fig S6a**) exchanging the permanently deprotonated sulfonate **iC4-FS** ($pK_a \approx -2$)[27] for a reversibly protonatable carboxylate ($pK_a \approx 4.3$). This less polar probe promisingly gave 20-fold higher cellular signal compared to its sulfonate-version while maintaining the post-wash retention of the fluorophore and the whole-cell signal distribution (**Fig S6b–d**). These results indicated that the signal retention is caused mostly by the lipid-tail while the acid-functionality influences the cellular uptake, so we investigated the cellular performance of a C4-tail probe without a charged group **iC4-F** (**Fig S6e**). Surprisingly, we found absolutely no cellular signal development which is in line with the cell-free esterase assay which also showed no turn-on of **iC4-F** presumably due to the high lipophilicity and hence insolubility and aggregation in aqueous medium as well as potentially membrane localisation in cells which overall makes the probe biologically unavailable.

In summary, the **C4-FC** motif seemed to deliver many of the desired features of a cell-retained probe with single-site activation, rapid cell entry, post-wash signal retention and uniform distribution in the whole cell. Problematically, with our proof-of-concept probe **iC4-FC** we observed severe changes in cell morphology such as cell rounding and blebbing (**Fig S6d**, **Fig S8**) which we first attributed to the use of HBSS buffer instead of DMEM supplemented with fetal calf serum (FCS) where the cell viability is improved. We used HBSS as default medium for our ester probes since the dichlorofluorescein isobutyrates are hydrolytically unstable in supplemented (nucleophile containing) cell culturing media such as DMEM supplemented with fetal calf serum (FCS) – and the hydrolytic instability even increases with solubilised FS- and FC-type probes compared to more lipophilic probes such as **i_2-F** (see cell-free hydrolytic stability in **Fig S23**).

To avoid spontaneous probe hydrolysis in FCS-supplemented DMEM, we synthesised the hydrolytically stable carbamate probe **GL-C4-FC** which is rapidly activated by (intracellularly abundant) glutathione (GSH, intracellular concentrations ~1−5 mM[28]; cell-free GSH activation in **Fig S26**) while being stable in typical cell culture media with low GSH concentrations (cell-free stability in cell culture media: **Fig S24**). Comparing the performance of **GL-C4-FC** in HBSS and in DMEM revealed an unexpected behaviour: cells treated in HBSS are strongly fluorescent but show impaired cell morphology (rounding and blebbing) at high probe

concentration (10 µM), while negligible signal is generated when treated in DMEM where a healthy morphology is maintained. Cells cultured in either HBSS or DMEM without probe addition are also healthy, showing that HBSS itself does not impair the cells under the treatment conditons. Also, when the probe is treated in HBSS at lower concentrations (3 and 1 µM) the signal disproportionally decreases, while the cell morphology improves gradually (**Fig S8**) which clearly shows that our FS- and FC-type probes can only enter cells with disrupted membranes. Furthermore, these probes themselves damage the plasma membrane together with the simple buffer HBSS, while the nutrient-supplemented DMEM prevents the membrane disruption of the probes rendering them impermeable. We reason that the detergenic character of our negatively charged, lipidated fluoresceins together with the lack of nutrients in HBSS causes the membrane disruption which the probes rely on to enter the cells. Unfortunately, we did not see a strategy to avoid this problem with the carboxyfluorescein motif and therefore abandoned this approach and tested rhodol scaffolds instead. However, we gained some insights that guided us for the design of rhodol probes: (1) negative charges should be avoided, but if intracellularly released can assist cell retention if they are not actively translocated out of the cell by transport mechanisms; (2) solubility tags should be used to ensure bioavailability of the probe (since very lipophilic probes such as **iC4-F** are not even activated by isolated esterase); and (3) the proof-of-concept probes should allow testing in standard cell culturing media such as DMEM (with FCS), so hydrolytically stable carbamates are better suited than esters.

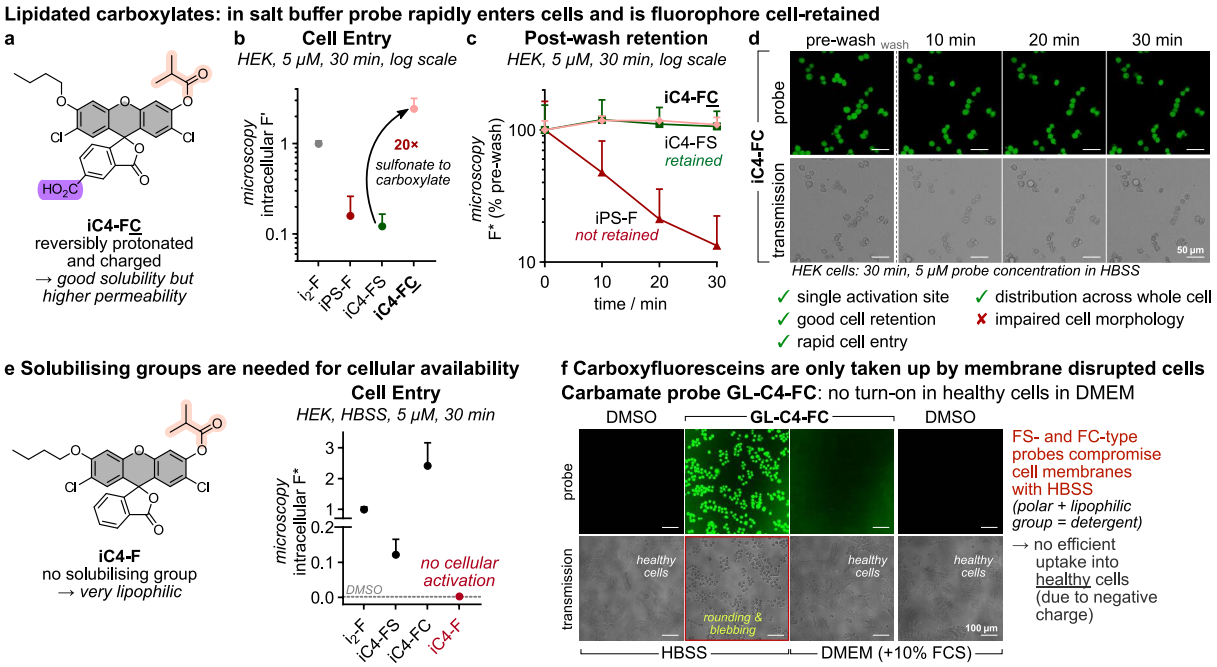

Figure S6: Lipidated carboxy-fluorescein probes rapidly enter cells and are retained. (a) Chemical structure of **iC4-FC** which is reversibly protonated and charged under physiological conditions; **(b)** Intracellular fluorescence signal quantified from microscopy images (treatment with 5 µM probe in HBSS for 30 min; F' is intracellular fluorescence normalized to the i_2-F signal; *error bars: SD*; *n*=3); **(c)** Post-wash intracellular signal retention quantified from microscopy images (treatment with 5 µM probe in HBSS for 30 min, then wash (2× with HBSS), F* is fluorescence as % of pre-wash value; *error bars: SD*; *n*=3); **(d)** Confocal microscopy: intracellular signal and post-wash retention of **iC4-FC** (treatment with 5 µM probe in HBSS for 30 min, then wash (2× with HBSS); *scale bars: 50 µm*; CellTracker images: Fig S7); **(e)** Intracellular fluorescence signal of **iC4-F** (with no solubilising groups) quantified from microscopy images (treatment with 5 µM probe in HBSS for 30 min; *error bars: SD*; *n*=3); **(f)** The hydrolytically stable carbamate probe **GL-C4-FC** only generates signal when treated in HBSS but not in DMEM (with 10% FCS) in HEK293T cells (images after 30 min probe incubation (10 µM), no washing, *scale bars: 100 µm*).

4 Supplementary Figures

4.1 Fig S7: Fluorescein probe microscopy: all channels

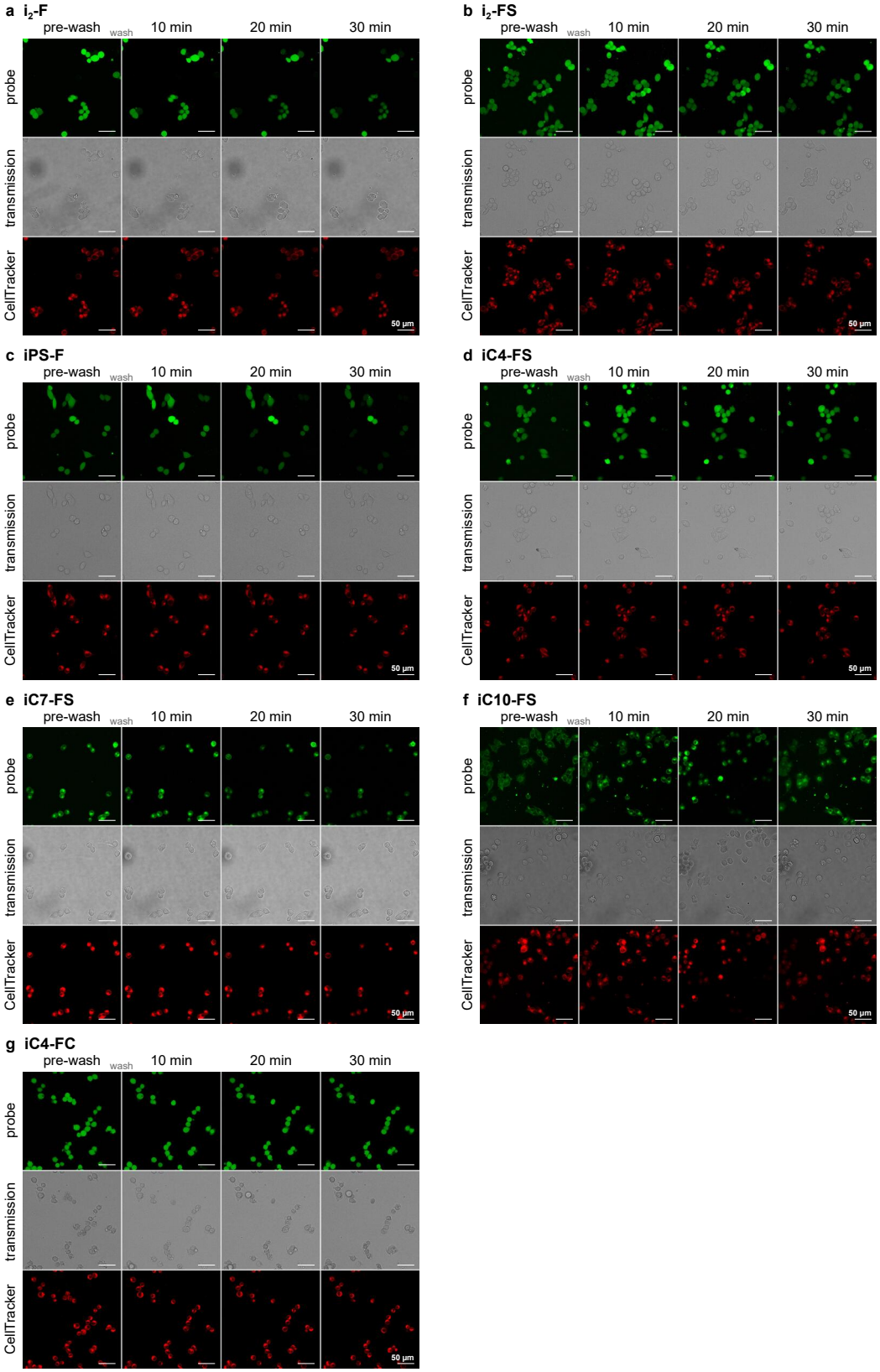

Figure S7: Full figure for confocal microscopy of fluorescein probes (all channels: probe, transmission and CellTracker Red). Cells were pre-treated with CMTPX (1µM for 30 min), then treated with the probes (5 µM probe for 30 min in HBSS) and imaged for the pre-wash image. Then the medium was removed (2× wash with HBSS) and post-wash images were acquired after 10, 20 and 30 min (*scale bars: 50 µm*).

4.2 Fig S8: Comparison of GL-C4-FS and GL-C4-FC

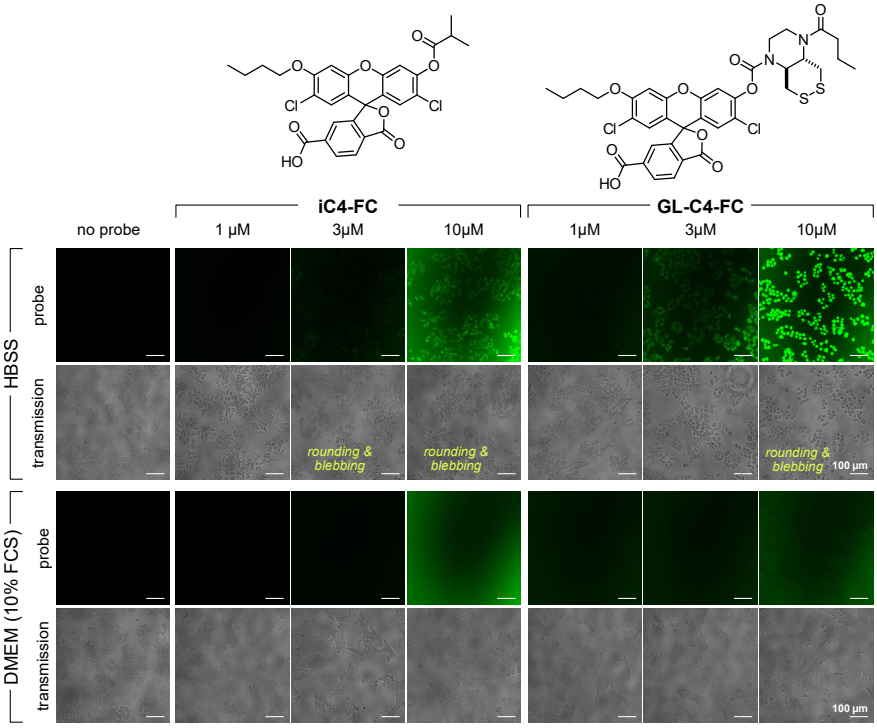

HEK cells: 30 min treatment, images taken on epifluorescence microscope

Figure S8: Comparison of the carboxyfluorescein probes iC4-FC (ester) and GL-C4-FC (hydrolytically stable carbamate) in HBSS vs. DMEM (+10% FCS) at different concentrations (1, 3 and 10 µM). Epifluorescence microscopy images of HEK293T cells treated 1–10 µM probe for 30 min in different media shows intracellular fluorescence but strongly impaired cell morphology after treatment in HBSS while cells remain healthy but non-fluorescent in DMEM (*scale bars: 100 µm*).

4.3 Fig S9: Cell entry & retention of rhodol probes

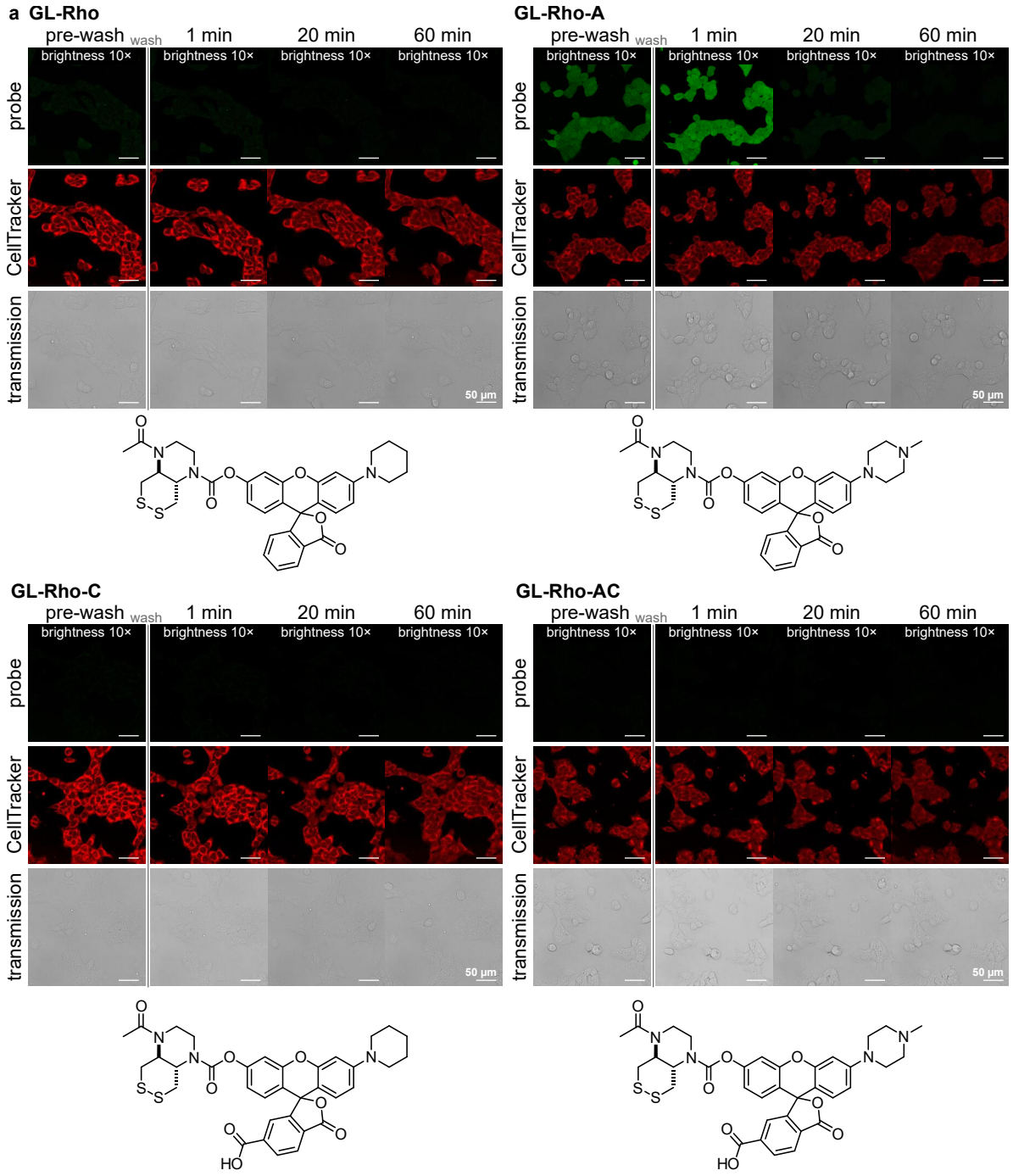

Figure S9 Part 1: Comparison of cellular turn-on and retention for all rhodol probes by confocal microscopy (full caption below at Part 2 of this figure).

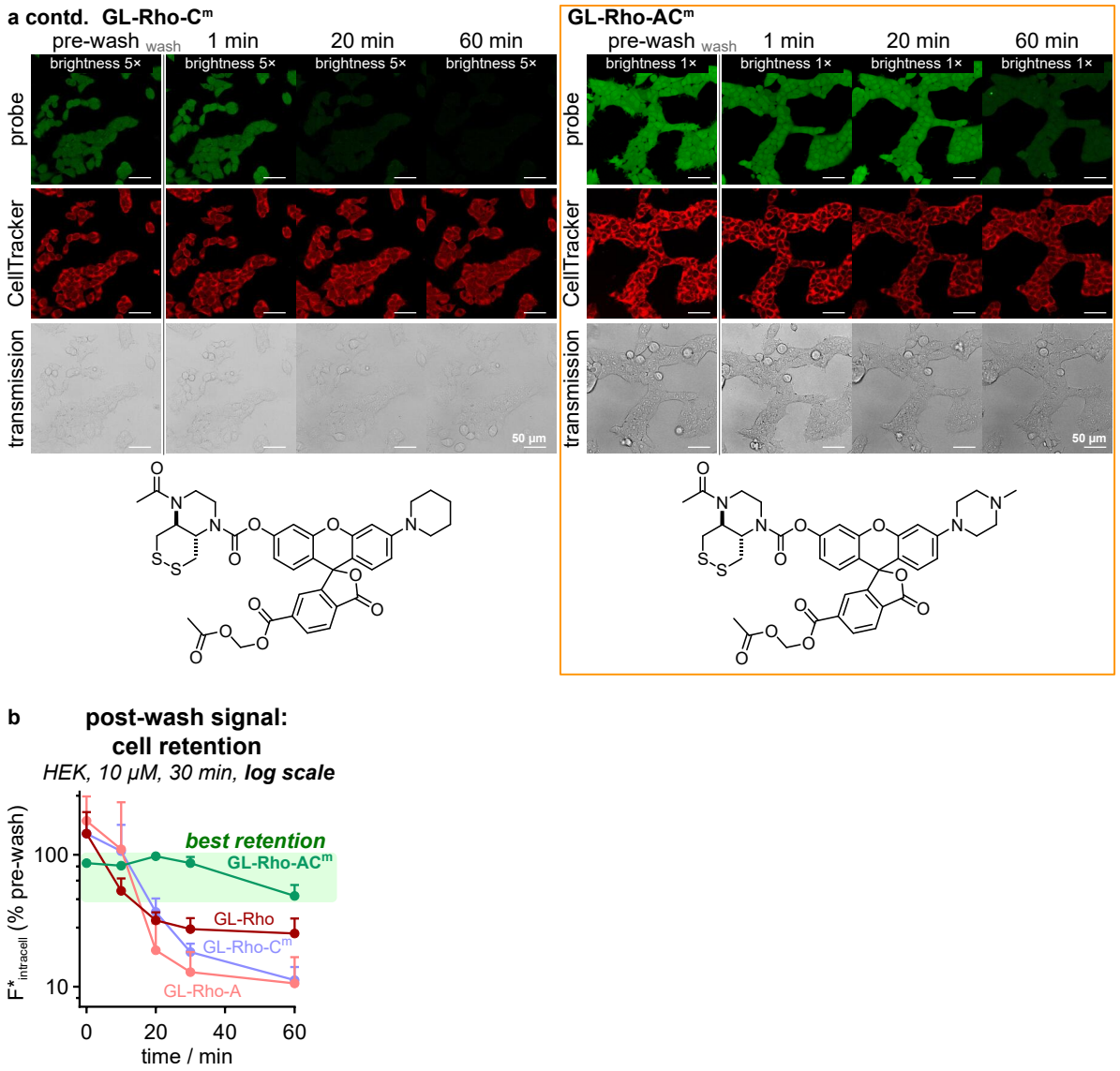

Figure S9 Part 2: Comparison of cellular turn-on and retention for all rhodol probes by confocal microscopy: (a) HEK293T cells; pre-wash images taken after 30 min treatment with 5 µM probe in DMEM (with 10% FCS); post-wash images after 2× wash with DMEM after 1, 20 and 60 min incubation (*scale bars: 50 µm*); **(b)** the intracellular fluorescence intensities were quantified to determine signal retention and are plotted in the graph below the images (n=3; error bars: SD).

Though **Fig 2c** (platereader assay, where signal is integrated over intra- and extra-cellular spaces) shows that **GL-Rho** enters cells and becomes activated, its exit (which **Fig 2d** timepoint 0 shows is ~80% complete before the cells have even been washed) is presumably too fast for any intracellular build-up to be seen in microscopy (**Fig 2d** later timepoints, and **Fig S9a**).

4.4 Fig S10: Cellular distribution of GL-Rho-AC^m signal

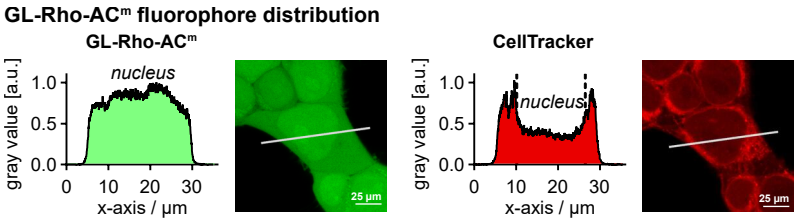

Figure S10: Cellular fluorescence distribution of GL-Rho-AC^m (after 30 min treatment, CellTracker signal for comparison (excluded from nucleus); *scale bars: 25 µm*).

4.5 Fig S11: Entry and retention across several cell lines

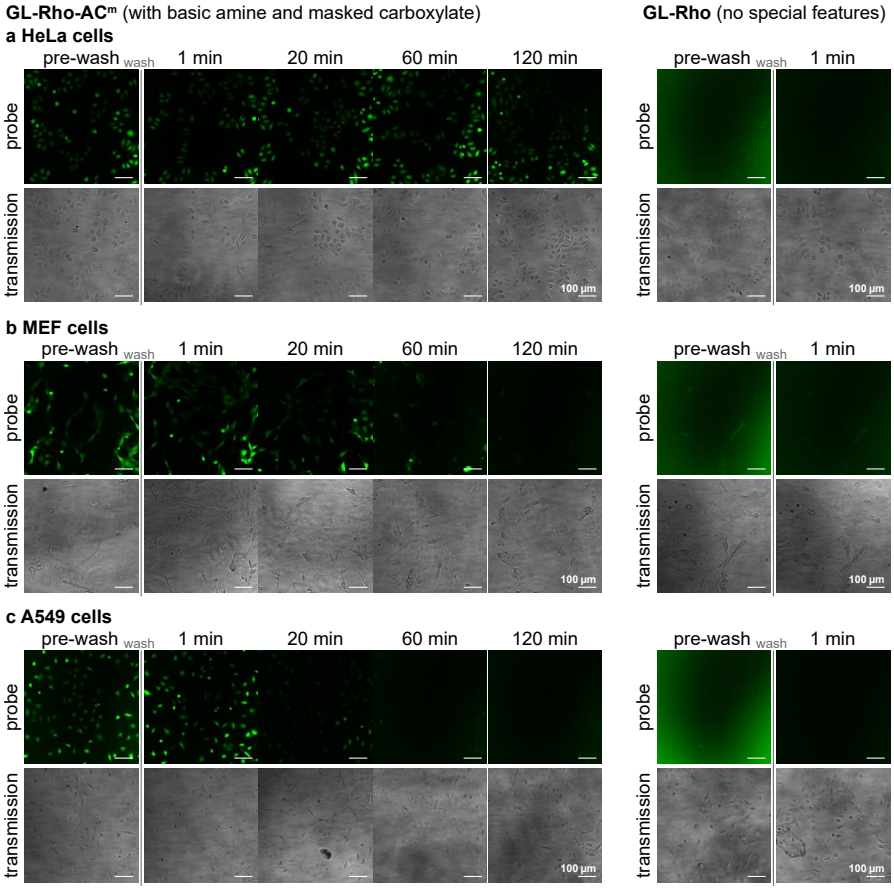

Figure S11: Post-wash signal retention of GL-Rho-AC^m compared to non-functionalised rhodol GL-Rho in different cell lines: (a) HeLa, **(b)** MEF, or **(c)** A549 cells were treated with 5 µM probe in DMEM (+10% FCS) for 30 min (pre-wash image), then washed (2× with DMEM) and imaged after again for post-wash retention for up to 2 h (*scale bars: 100 µm*).

We assume that the strong uptake across multiple cell lines of the several **TraG**-based probe expressions, which span a reasonable space of size/TPSA/polarity parameters (**GL-Rho-AC^m**, **HP-TraG**, and **TR-TraG**), indicates that cellular uptake relies mainly on passive diffusion, but it is also possible that these amine probes may profit from transporter-mediated uptake e.g. by organic cation transporters.[29,30]

4.6 Figs S12-S14: Characterisation of hydrogen peroxide sensor HP-TraG

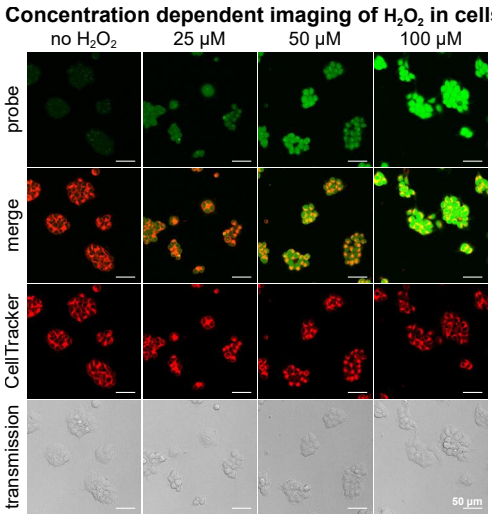

Figure S12: Full figure panel of Figure 4c. Concentration dependent activation of **HP-TraG** in cells (10 µM, 15 min loading before H_2O_2 addition, then 60 min H_2O_2 treatment; *scale bars: 50 µm*).

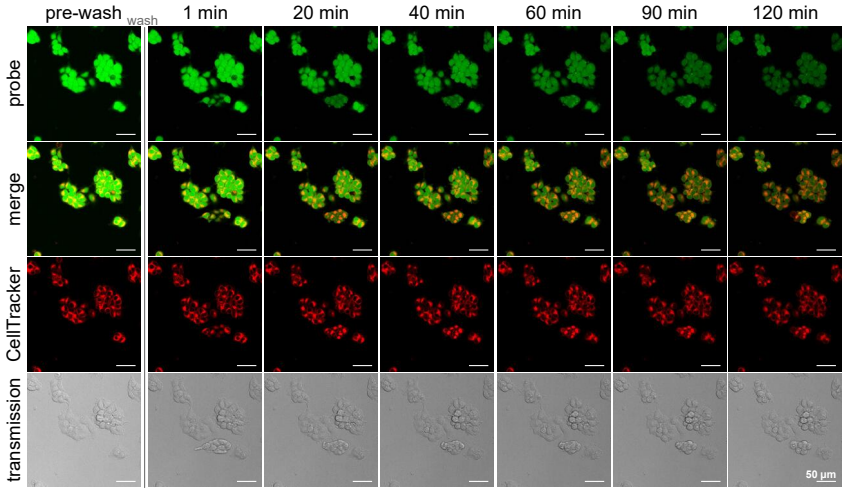

Figure S13: Full figure panel of Figure 4e. Confocal microscopy images of post-wash signal retention of **HP-TraG** (10 µM, 15 min loading before H_2O_2 addition) in HEK cells treated with H_2O_2 (100 µM for 1 h; *scale bars: 50 µm*).

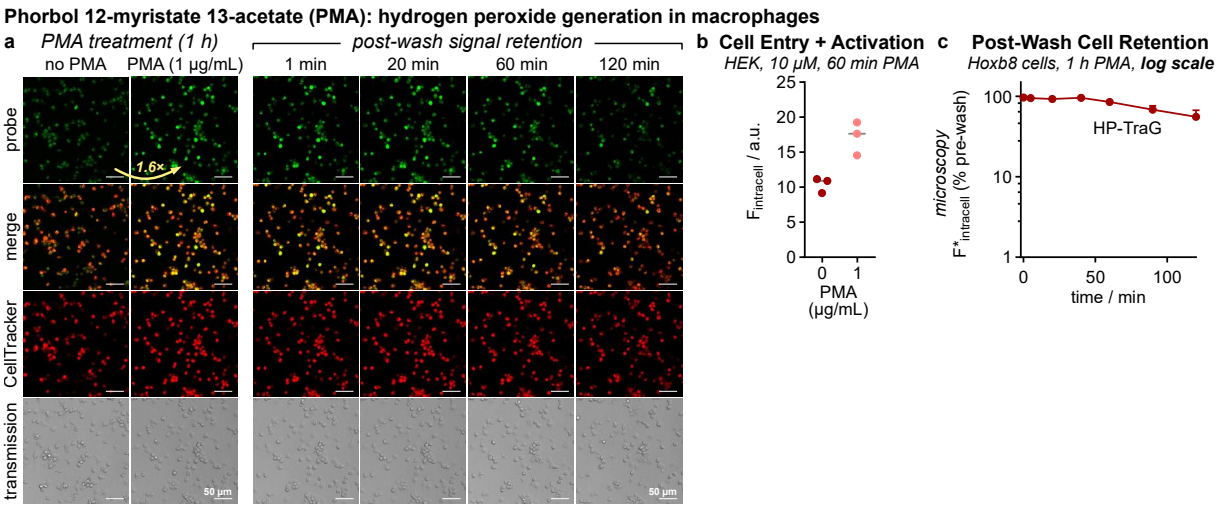

Figure S14: Hoxb8-derived macrophages activated with phorbol 12-myristate 13-acetate (PMA, 1 µg/mL, 1 h) that triggers H_2O_2 production which is visualised by **HP-TraG** (10 µM, 15 min loading before PMA addition): **(a)** microscopy images (*scale bars: 50 µm*); **(b)** intracellular **HP-TraG** signal after PMA treatment (1 h, 1 µg/mL, 10 µM probe loading for 15 min before PMA addition) and **(c)** the post-wash signal retention quantified from images in panel a (*n*=3; error bars: SD).

4.7 Fig S15-S19: Characterisation of TrxR enzyme probe TR-TraG

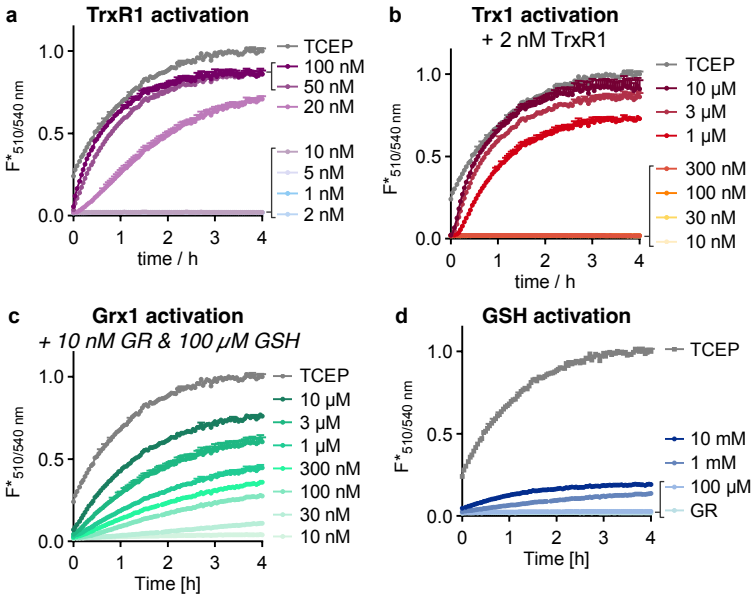

Figure S15: Activation of TR-TraG by key redox enzymes and gluthathion (GSH): (a) Target enzyme TrxR1, **(b)** Trx1 (+2 nM TrxR1 which is needed for Trx1 recovery by reduction), **(c)** Grx1 (+10 nM GR and 100 µM GSH which is needed for Grx1 recovery by reduction), and **(d)** GSH; Conditions: 10 µM **TR-TraG** in TE buffer at 37 °C for 4 h, TCEP: positive control (100 µM); NADPH co-factor concentration in all samples: 100 µM.

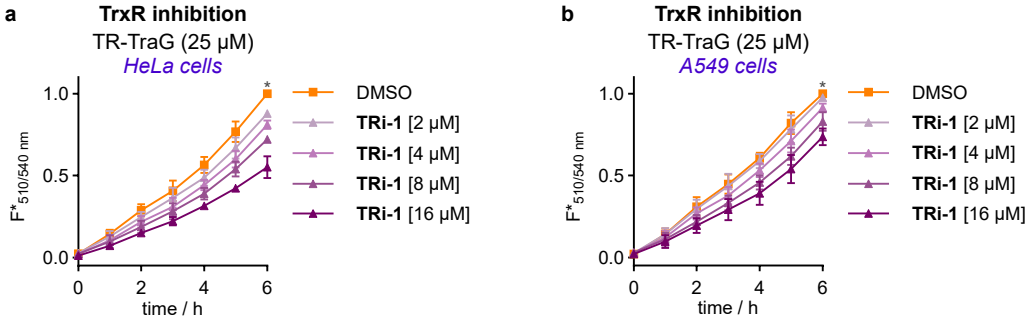

Figure S16: TrxR inhibition dependent TR-TraG signal in HeLa and A549 cells. Cells were treated with TrxR inhibitor TRi-1 at 2–16 µM for 3 h before medium exchange (2×) and probe addition (t = 0; 10 µM in DMEM (+10% FCS)), then the fluorescence was measured for 6 h (values normalised to DMSO-cells after 6 h, marked with asterisk; *error bars: SD*; *n*=3). The reproducibility of the TR-TraG fluorescence values throughout the cell culture experiments (small relative error, typ. ±<10%) contrasts to the stronger variability of the previously-published probe RX1 (typ. ±>20%)[31], which we assign to the reprodubility of its soluble (rather than precipitating) fluorogenic cargo.

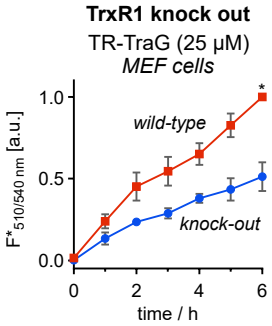

Figure S17: TR-TraG is activated in TrxR expressing MEF cells while the signal is strongly reduced when TrxR is knocked out (probe treatment at 25 µM and 37 °C in Se-supplemented DMEM (+ 10% FCS); *error bars: SD*; *individual experiments normalised to wild-type endpoint (marked with asterisk); n*=3).

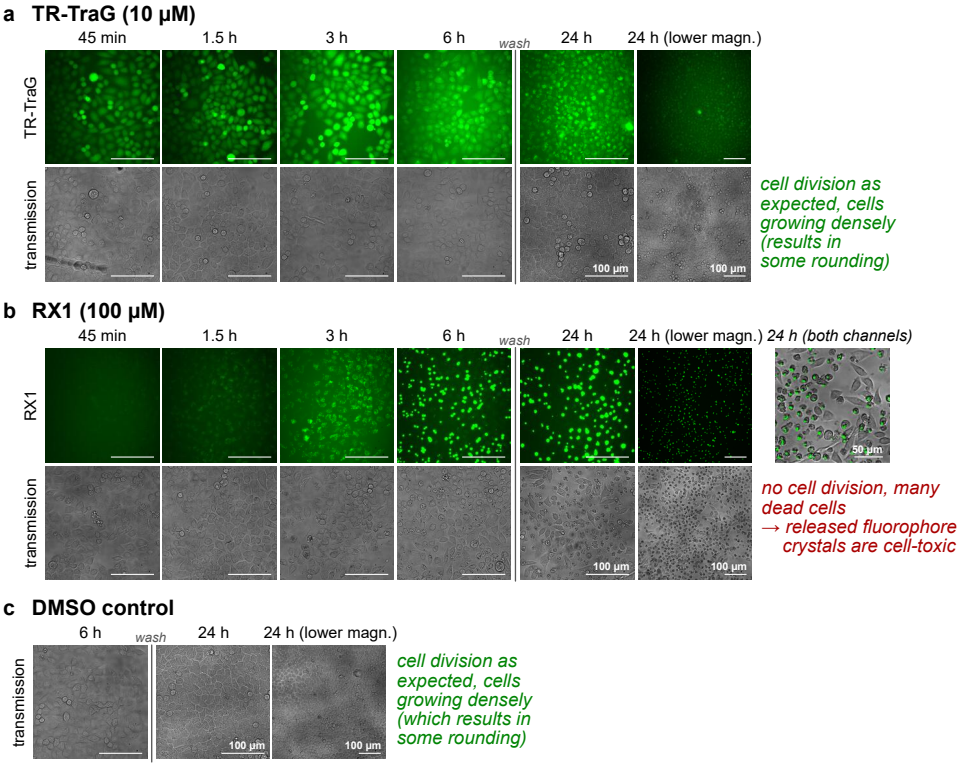

Figure S18: Full figure: comparison of TR-TraG with RX1. HeLa cells were treated with **TR-TraG** (10 µM, panel a) or **RX1** (100 µM, panel b) and imaged after 45 min and 1.5, 3 and 6 h, then washed (2×) and imaged again after 24 h to show post-treatment cell viability compared to untreated cells (DMSO control, panel c); PQ precipitates lead to morphological changes that are consistent with cell death (*scale bars: 100 µm*).

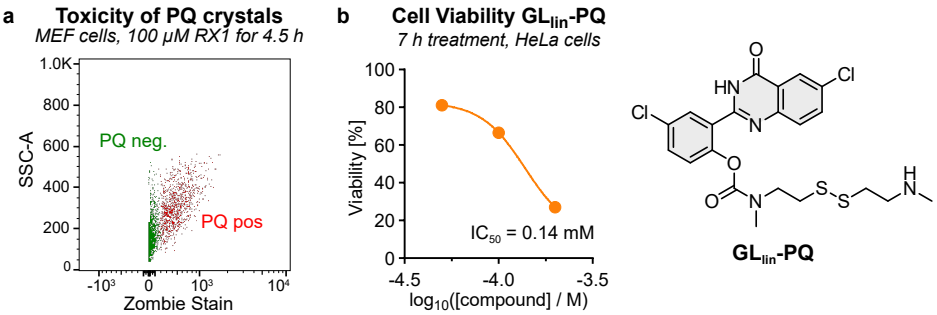

Figure S19: Cell toxicity of precipitating PQ-probes. (a) Flow cytometry analysis of MEF cells treated with RX1 (100 µM, 4.5 h) followed by Zombie live-dead staining; the cells were previously gated for PQ fluorescence. **(b)** Cell viability assay (resazurin) for HeLa cells treated with the GSH activated **GL_{lin}-PQ** (7 h treatment).

We showed the cell-toxic effects of precipitating probes using flow cytometry: MEF cells treated with RX1 for were treated with Zombie dead stain showing that all cells with PQ crystals were dead (**Fig S19a**). To prove that the correlation between dead cells and PQ staining is not caused by a higher TrxR activity in dying cells resulting in RX1 activation, we used the GSH activated probe **GL_{lin}-PQ** that is activated in all cells independent of the activity of redox enzymes like TrxR and performed a viability assay again showing the toxicity of precipitating fluorophores (IC_{50} = 0.14 mM, RX1 is typically used at concentrations of 0.1 mM).

5 Cell-free photocharacterisation, probe stability, and probe activation

5.1 Figs S20-S22: Photocharacterisation

5.1.1 Fluoresceins: Absorption and emission spectra

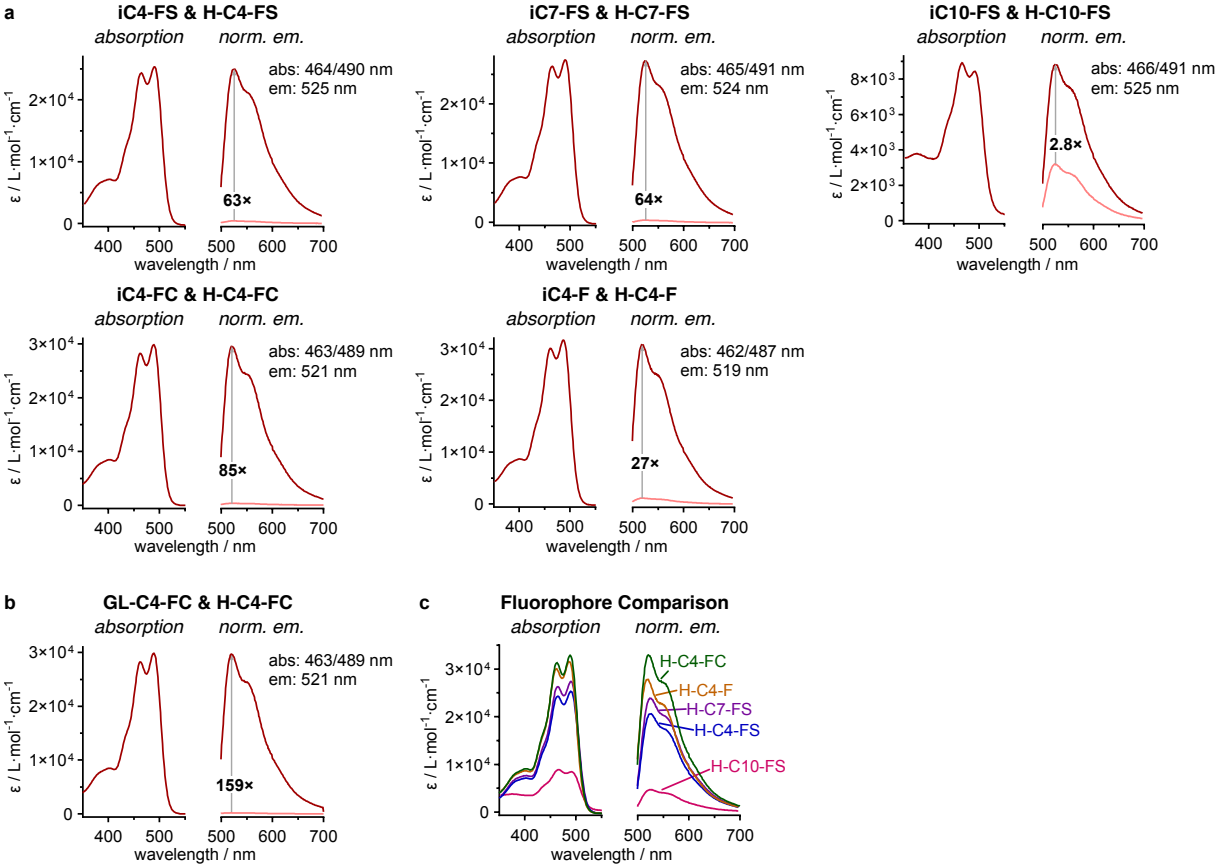

Figure S20: Absorption and emission spectra of fluorescein probes and fluorophores: **(a)** *iso*-butyrate ester probes and **(b)** GL-probe **GL-C4-FC** (10 µM in PBS, pH = 7.4; *dark red line: fluorophore; light red line: probe; grey, emission spectra: λ_{ex} = 495 nm*); **(c)** Comparison of absorption and fluorescence emission of all fluorescein fluorophores.

The monoalkylated fluoresceins have two absorption maxima at ca. 465 and 490 nm, with slight red-shifting for sulfonate and carboxylate probes as expected for electron withdrawing substituents.[32] The probes have 3-fold weaker absorbance at 485 nm compared to unmodified, symmetric fluorescein, and their fluorescence quantum yields (λ_{max} ~525 nm) are reduced from ~0.8 to ~0.2 (**Table S1**), which are expected results for the unsymmetric chromophore.[33] Very low absorption and emission is observed for the lipophilic **H-C10-FS**, presumably due to aggregation effects. All (spirocyclised) probes are non-fluorescent and feature very good turn-on ratios to the fluorophore (except **iC10-FS** with its very weak fluorescence of the fluorophore).

5.1.2 Rhodols: Absorption, excitation and emission spectra

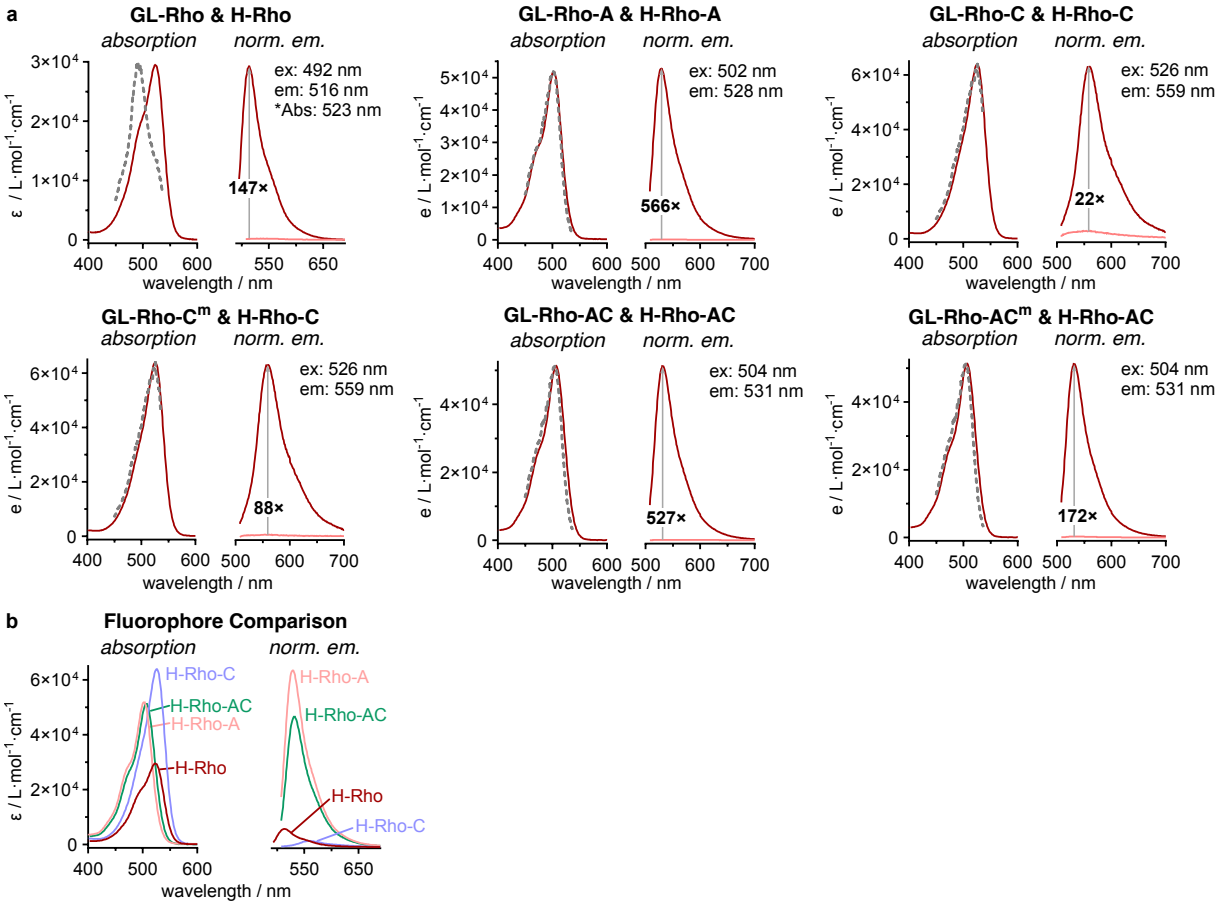

Figure S21: **(a)** Absorption, excitation and emission spectra of rhodols fluorophores and GL-probes (10 µM in PBS, pH = 7.4; *dark red line: fluorophore; light red line: probe; grey, dashed line represents excitation spectra: λ_{em} = 550 nm; emission spectra: λ_{ex} = 495 nm*); **(b)** Comparison of absorption and fluorescence emission of all rhodol fluorophores (λ_{ex} = *495 nm*).

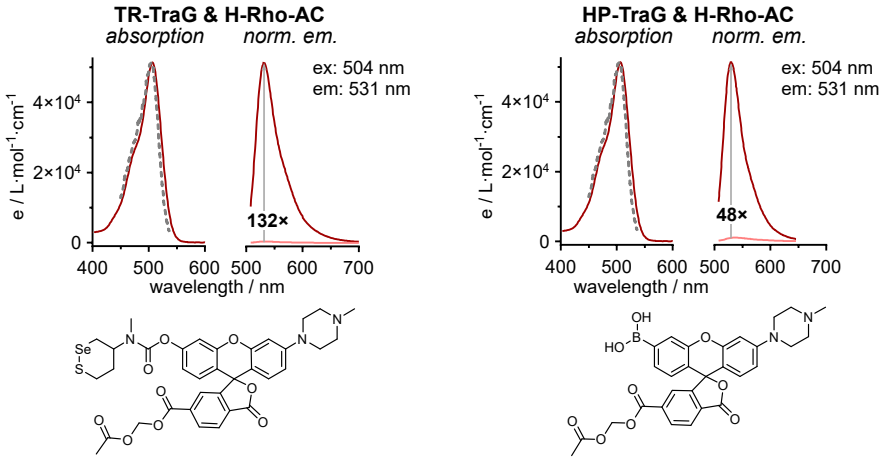

Figure S22: Absorption, excitation and emission spectra of **TR-TraG** (10 µM) and **HP-TraG** (5 µM) in PBS (pH = 7.4; *dark red line: fluorophore; light red line: probe; grey, dashed line represents excitation spectra: λ_{em} = 550 nm; emission spectra: λ_{ex} = 495 nm*).

We suppose that the lower max fluorogenicity for some of the probes derives from <2% contamination by species that can enter an open-closed equilibrium, e.g. hydrolysed or rhodamine byproducts of synthesis, that is inconvenient but also unnecessary to remove to high purity.

5.1.3 Table S1: Photophysical properties overview

	Fluorophore	$\lambda_{Abs,max}$ / nm	$\lambda_{emission,max}$ / nm	Stokes Shift / nm	$\varepsilon_{\lambda,max}$ / L mol^{-1} cm^{-1}	Φ	brightness / L mol^{-1} cm^{-1}
fluoresceins — *two activation sites*	fluorescein	490	513	23	$84 \cdot 10^3$	0.85	$72 \cdot 10^3$
	H_2-F	503	523	20	$68 \cdot 10^3$	0.78	$53 \cdot 10^3$
	H_2-FS	507	526	19	$51 \cdot 10^3$	0.75	$38 \cdot 10^3$
fluoresceins — *single activation site*	H-C4-F	487	521	34	$32 \cdot 10^3$	0.18	$5.7 \cdot 10^3$
	H-C4-FS	490	524	34	$25 \cdot 10^3$	0.16	$4.0 \cdot 10^3$
	H-C7-FS	491	523	32	$27 \cdot 10^3$	0.17	$4.7 \cdot 10^3$
	H-C10-FS	491	523	32	$8.4 \cdot 10^3$	0.09	$0.73 \cdot 10^3$
	H-C4-FC	489	521	32	$33 \cdot 10^3$	0.21	$7.1 \cdot 10^3$
rhodols — *single activation site*	H-Rho*	492*	514	22	$18 \cdot 10^3$ *	0.26	$4.7 \cdot 10^3$
	H-Rho-A	503	530	27	$52 \cdot 10^3$	0.64	$33 \cdot 10^3$
	H-Rho-C	525	560	35	$64 \cdot 10^3$	0.04	$2.6 \cdot 10^3$
	H-Rho-AC	507	531	24	$51 \cdot 10^3$	0.51	$26 \cdot 10^3$

**excitation maximum instead of absorption maximum*

Table S1: Photophysical properties of fluorescein and rhodol fluorophores.

Quantum yields of the novel fluorophores were determined the following equation (Resch-Genger and co-workers[34]):

$$\Phi_{f,x} = \Phi_{f,st} \cdot \frac{F_x}{F_{st}} \cdot \frac{1 - 10^{-A_{st}(\lambda_{ex})}}{1 - 10^{-A_x(\lambda_{ex})}} \cdot \frac{n_x(\lambda_{em})^2}{n_{st}(\lambda_{em})^2}$$

Fluorescein was used as a reference fluorophore with a quantum yield of $\Phi_{f,st}$ = 0.85 (in PBS, pH=7.4).[35]

5.2 Fig S23-S24: Cell-free probe stability in cell culture media

5.2.1 Ester probes

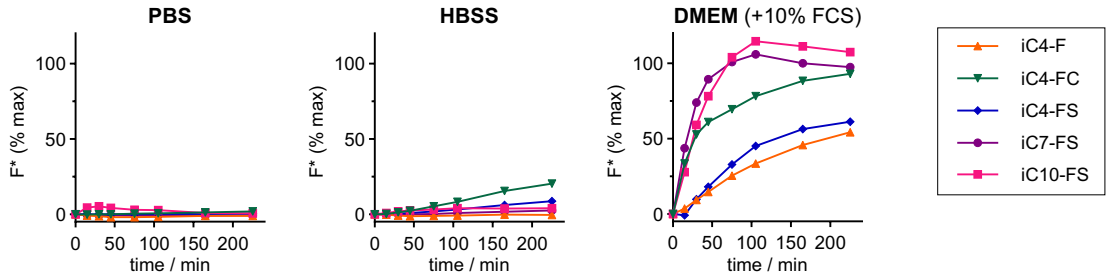

Figure S23: Probe stability in different cell culture media. Spontaneous probe hydrolysis time-courses of ester probes in PBS, HBSS and DMEM (probe conc.: 10 µM, incubation at 37 °C).

We examined the probe stabilities in PBS, HBSS and the standard cell culture medium DMEM (with 10% FCS). PBS is a very simple cell buffer containing sodium and potassium chloride as well as sodium hydrogen- and dihydrogen-phosphates. HBSS we used contains the same ingredients (in different amounts) plus additional salts (calcium and magnesium chloride and sulfate, sodium hydrogencarbonate), as well as glucose, to ensure longer cell viability in experiments as compared to PBS, although we expected that the stronger Lewis acids could better promote ester hydrolysis. The cell culture medium DMEM additionally contains amino acids, which we expected to give even higher ester cleavage by trans-acylation, as well as vitamins. We thus expected PBS to show the lowest spontaneous probe hydrolysis and DMEM to show the highest, while cellular viability during longer-term experiments should increase in the same order.

Indeed, in PBS we observe no relevant hydrolysis within 4 h, while in HBSS the least hydrophilic probes **iC4-FC** and **iC4-FS** show some activation (20 and 10% respectively) but overall the probes are very stable and within a typical imaging experiment timeframe (<60 min) the hydrolysis is very low. In FCS-supplemented DMEM however, all probes are rapidly activated, interestingly the lipophilic sulfonated probes (**iC10-FS** and **iC7-FS**) have the fastest turn-on, we assume that this is mainly due to assisted solubility by proteins and potential nucleophilic attack of protein surface amines (lysines). Therefore, we decided to perform all experiments with ester probes in HBSS.

5.2.2 GL probes

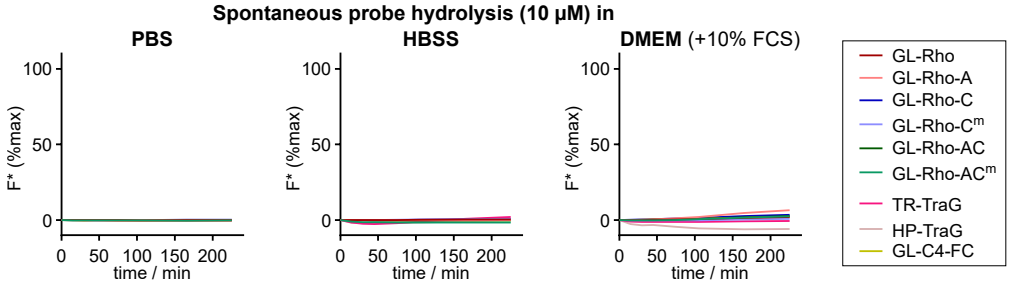

Figure S24: Probe stability in different cell culture media. Spontaneous probe hydrolysis time-courses of carbamate capped GL-probes in PBS, HBSS and DMEM (probe conc.: 10 µM, incubation at 37 °C).

We chose the GSH-labile GL-trigger for non-specific intracellular proof-of-concept probe activation as we expected much better hydrolytic stability of the carbamate (compared to the ester probes). Indeed, we observe no probe activation in PBS and HBSS within 4 h, and only negligible activation in DMEM (with 10% FCS). This allowed us to perform experiments with GL-probes in FCS-supplemented DMEM which is an ideal medium for cell viability.

5.3 Figs S25-S26: *in vitro* activation of proof-of-concept probes

5.3.1 Esterase activation of ester probes

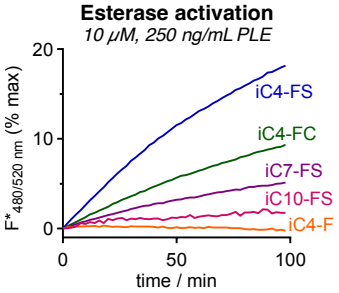

Figure S25: Esterase activation of ester probes. Time-course of probe activation by porcine liver esterase (250 ng/mL) above spontaneous hydrolysis in PBS (values were corrected for PBS activation, probe conc.: 10 µM, incubation at 37 °C).

The probes must be rapidly processed upon cellular entry to generate a fluorescent signal. We assessed probe activation by the model enzyme porcine liver esterase (PLE, 250 ng/mL) in PBS as the least hydrolysing buffer (**Fig S23**). All probes (except **iC4-F**) are activated above spontaneous hydrolysis in PBS proving the activation by esterases as desired. However, depending on the lipophilicity strong kinetics differences are observed: charged sulfonate **iC4-FS** with a short lipid tail gives rapid activation which is drastically slowed down for the longer lipid tails (**iC7-FS** and **iC10-FS**). Carboxylate **iC4-FC** is activated slower than is sulfonated version but still with good turn-on, uncharged **iC4-F** on the other hand shows no detectable signal generation, presumably due to insolubility and/or self-aggregation resulting in bio-unavailability.

5.3.2 Glutathione activation of GL-probes

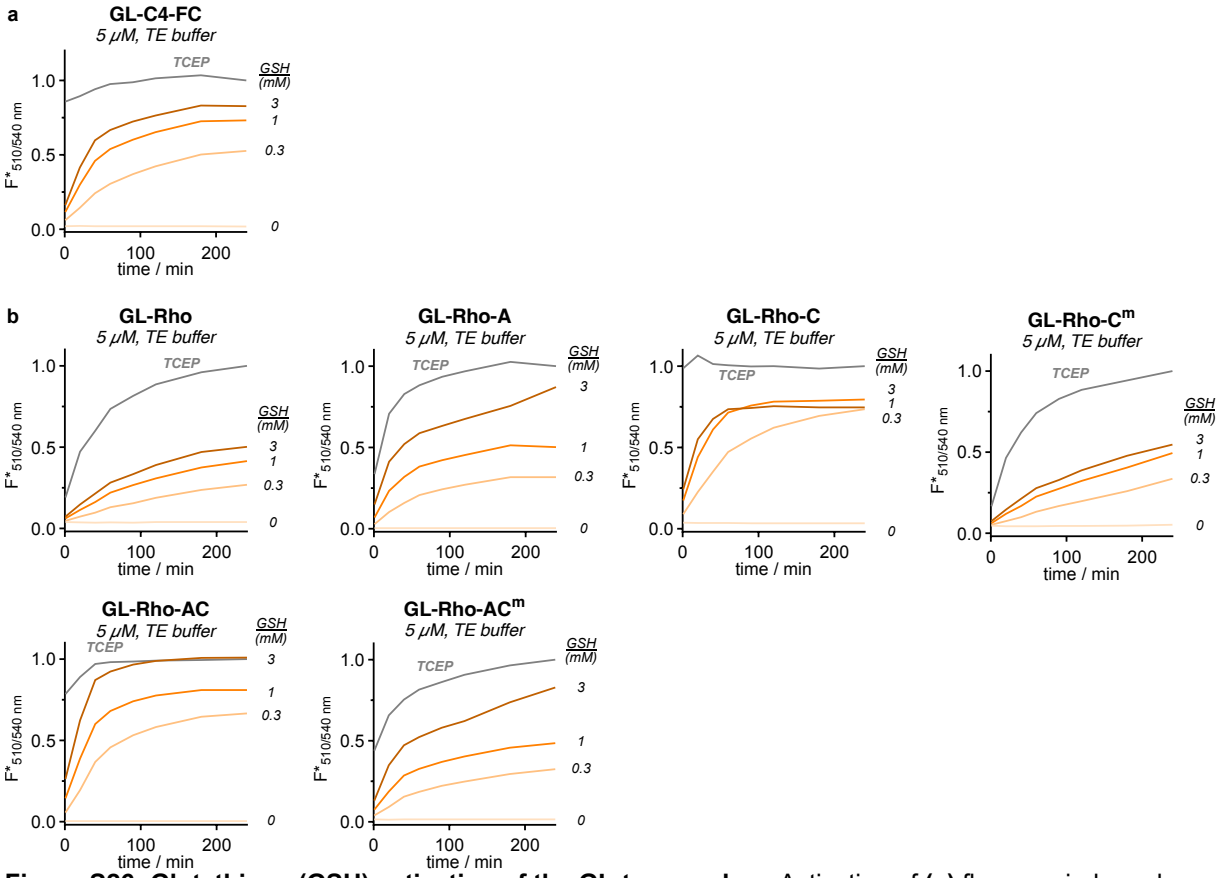

Figure S26: Glutathione (GSH) activation of the GL-type probes. Activation of **(a)** fluorescein-based **GL-C4-FC** and **(b)** rhodol-based probes **GL-Rho**, **GL-Rho-A**, **GL-Rho-C**, **GL-Rho-C^{m}**, **GL-Rho-AC** and **GL-Rho-AC^{m}** with GSH (0−3 mM) in TE buffer (pH = 7.4).

5.4 Figs S27-S28: *in vitro* activation of HP-TraG

Oxidation of HP-TraG with hydrogen peroxide

Reaction monitoring

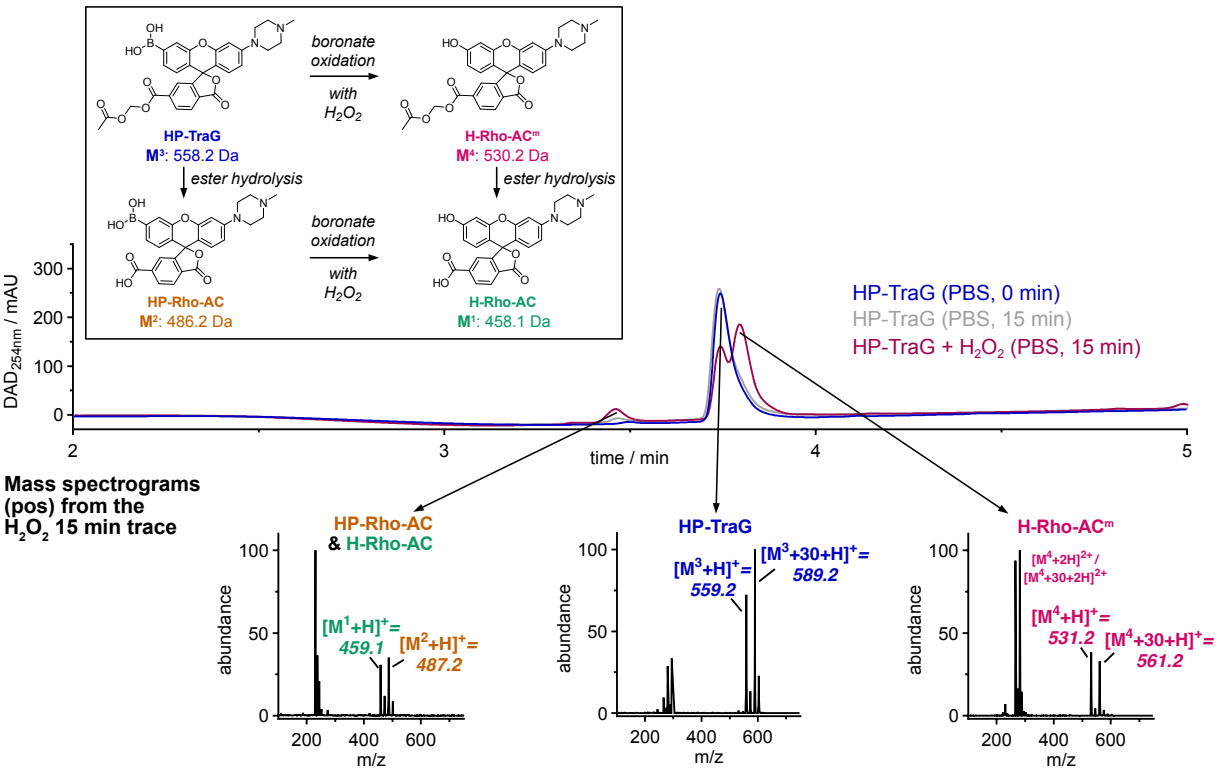

Figure S27: Oxidation of HP-TraG with hydrogen peroxide to the corresponding rhodol (50 µM probe with 500 µM H_2O_2 in PBS for 15 min at room temperature (22 °C)).

We tested the H_2O_2 sensing ability of **HP-TraG** by HPLC-MS to confirm the desired oxidation pathway. **HP-TraG** (**Fig S27**, molecule **M³**, 50 µM) was treated with 10 eq H_2O_2 (0.5 mM) in PBS and incubated at room temperature and analysed by HPLC-MS. **HP-TraG** is well oxidised to the corresponding rhodol (**M⁴**) with ca. 60% conversion after 15 min; while a small proportion of the acetoxymethyl esters of both **HP-TraG** and **M⁴** hydrolyse presumably due to H_2O_2 nucleophilicity, to give **M¹** and **M²**. This **HP-TraG** sample contained an extra, co-eluting species with an additional formaldehyde unit (m/z = x+30) which was still present in the **M⁴** oxidation product, proving that the modification was not located on the boronic acid, and it did not change the functional performance for oxidation-induced fluorogenicity (see below).

Acetoxymethyl ester cleavage by esterase (PLE)

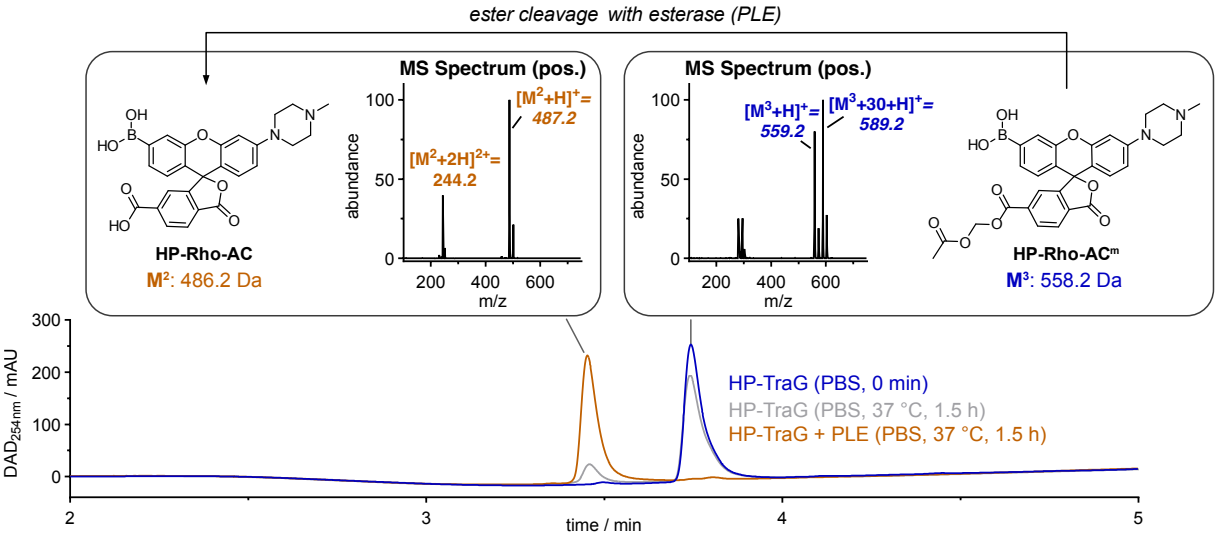

Figure S28: Acetoxymethyl ester cleavage of HP-TraG with porcine liver esterase (PLE) (50 µM probe with 60 µg/mL PLE at 37 °C for 1.5 h.

We then investigated the esterase unmasking of the acetoxymethyl ester which is required for reliable intracellular trapping of the fluorophore (**Fig S28**). **HP-TraG** (molecule **M^3**, 50 µM) was incubated with porcine liver esterase (PLE, 60 µg/mL, 15 U/mg) at 37 °C for 1.5 h which cleanly converted **HP-TraG** (as well as the M+30 impurity) into the same carboxylate **M^2** with no +30 shift in the mass spectrum. This shows that the extra formaldehyde unit in the **HP-TraG** side product is located on the pendant carboxylate, and is converted to the same boronic acid product (**M^2**) by intracellular esterases. Taken together, the *in vitro* hydrogen peroxide oxidation and the esterase catalysed ester cleavage assays show that **HP-TraG** follows the expected pathway for oxidation to the phenol, and that the co-eluting contaminant which arises during synthesis is likely to have the same cellular performance (ester cleavage to give the same cell-trapped boronate which is the active sensing species). We therefore used the mixtures with variable residual amounts of M+30 contaminant for the cellular evaluations since separation (C18 and normal-phase column chromatography) was infeasible and since the outcomes were identical.

6 Biological materials and methods

6.1 Cell culture and cell lines

Cells were grown in high glucose Dulbecco's modified Eagle's medium (DMEM, Sigma-Aldrich, D1145) supplemented with 10% heat-inactivated fetal bovine serum (Biochrom S0615), 1% L-glutamine (Sigma-Aldrich, G7513), 1 mM Sodium Pyruvate (Sigma-Aldrich, S8636) and 100 nM sodium selenite (Sigma-Aldrich, 214485-5G) at 37 °C and 5% CO_2. Washing was performed with Dulbecco's phosphate buffered saline (PBS, Sigma-Aldrich, D8537), cell detachment was performed using Trypsin-EDTA solution (Sigma-Aldrich, T4174) diluted to 1× Dulbecco's PBS (Sigma-Aldrich, D8537). Cell growth was monitored using an inverted microscope (Nikon Eclipse Ti), passage was kept between 2 and 20.

HeLa (DSMZ Cat No. ACC57) and A549 (DSMZ; ACC 107) cells were obtained from German Collection of Microorganisms and Cell Cultures. HEK293T cells were obtained from ATCC (Cat. No. crl-3216), TrxR knockout and reference mouse embryonic fibroblasts (MEF) were a kind gift from Marcus Conrad. All cell lines were tested regularly for mycoplasma contamination and only mycoplasma negative cells were used in assays.

In all experiments, probes and inhibitors were treated from DMSO stocks with 1% final DMSO concentration in the experiment (unless stated otherwise).

Cell media

- Phosphate buffered saline (PBS) from Sigma Aldrich (Cat. No. D8537)
- Hanks´ balanced salt solution (HBSS) from Sigma Aldrich (Cat. No. H6648)
- Dulbecco´s modified eagle´s medium (DMEM) from Sigma Aldrich (Cat. No. D1145), used with the following supplements (unless stated otherwise): 10% FCS (Biochrom S0615), 1 mM Sodium Pyruvate (Sigma-Aldrich, S8636) and 100 nM sodium selenite (Sigma-Aldrich,214485-5G)

6.2 Cell-free characterisation

Whole well fluorescence measurements were performed with a BMG Labtech FluoStar Omega plate reader (fluorescein settings: ex: 485bp10 and em: 520lp) or a Tecan M1000 plate reader: rhodol settings: excitation 510 nm, emission 540 nm; fluorescein settings: excitation 498 nm, emission 518 nm. All plate reader experiments were performed in coated black F-bottom 96-well plates (greiner, 655077).

Probe stability assay

Water (10 µL) was placed in a black 96 well plate and the probes/fluorophores were added from a 1 mM stock solution in DMSO (1 µL). Then the different media PBS, HBSS or DMEM (89 µL) were added to the probes with a multipipette (for smallest possible differences in the starting time) to reach a final concentration of 10 µM. All samples in technical duplicates. The fluorescence intensity in each well was measured after 1, 15, 30 min and 1, 2, 3, 4, 5, 6 h using a Tecan Infinite M1000 plate reader (fluoresceins: ex/em 480bp5/520bp5; rhodols: ex/em 510bp5/540bp5). Between measurements the samples were incubated at 37 °C under air atmosphere. At the end of the experiment, a *n*-butyl amine solution (50 mM, 100 µL) was added to each well to determine the maximum fluorescence after full probe activation in each well. The recorded data were background subtracted (fluorescence at 0 min) and normalised to their maximum fluorescence (determined after 2.5 h incubation with *n*-butylamine, corrected for concentration and pH changes by calculating the fluorescence ratio for the fluorophores upon *n*-butylamine addition).

Esterase activation of fluorescein esters

PBS (49 µL) was placed in a black 96 well plate and the probes/fluorophores were added from a 1 mM stock solution in DMSO (1 µL). Porcine liver esterase (lyophilized powder, ≥15 units/mg, purchased from Sigma

Aldrich, Cat.-No.: E3019) was diluted in PBS to give a stock solution of 500 ng/mL and warmed to 37 °C. The esterase stock solution was added to the probes with a multipipette (for smallest possible differences in the starting time) to reach a final probe/fluorophore concentration of 10 µM and an esterase concentration of 250 ng/mL (all samples in technical triplicates). The probes/fluorophores were placed in the pre-heated plate reader and incubated at 37 °C for the whole experiment. The fluorescence intensity in each well was measured every 2 min for the total duration of 100 min. At the end of the experiment, a *n*-butylamine solution (50 mM, 100 µL) was added to each well to determine the maximum fluorescence after full probe activation in each well. The recorded data were background subtracted (fluorescence at 0 min) and normalised to their maximum fluorescence (determined after 2.5 h incubation with *n*-butylamine, corrected for concentration and pH changes by calculating the fluorescence ratio for the fluorophores upon *n*-butylamine addition).

GSH activation of GL probes

The probes were placed in the respective wells of a 96-well plate (50 µL, 10 µM in TE buffer, final conc. 5 µM), then GSH (50 µL, 2× stock solutions in TE buffer, final conc 0, 0.3, 1.0, 3.0 mM) or TCEP (50 µL, 0.6 mM in TE buffer, final conc 0.3 mM; positive control for maximum activation) was added with a multipipette (for smallest possible differences in the starting time). The fluorescence intensity in each well was measured after 1, 20, 40, 60, 90, 120, 180 and 240 min using a Tecan Infinite M1000 plate reader (GL-C4-FC: ex/em 480bp5/520bp5; rhodols: ex/em 510bp5/540bp5). Between measurements the samples were incubated at 37 °C under air atmosphere. The recorded data were normalised to their maximum fluorescence (determined at the endpoint of the TCEP positive control).

6.3 Cellular characterisation

General

Whole well fluorescence measurements were performed with a FluoStar Omega plate reader from BMG Labtech, Ortenburg (Germany) (fluorescein settings: ex: 485bp10 and em: 520lp) or on a M1000 plate reader (Tecan): rhodol settings: excitation 510 nm, emission 540 nm; fluorescein settings: excitation 498 nm, emission 518 nm. All plate reader experiments were performed in coated black F-bottom 96-well plates (greiner, 655077). The data was assembled and sorted in Microsoft Excel (version 16.88) and plotted in GraphPad Prism (version 10.4.1).

Epifluorescence microscopy images were acquired on an inverted microscope (Nikon Eclipse Ti), using the CFI Plan Achro DL 10× objective (Nikon). For fluorescence images the probes were excited with a pE-4000 (CoolLED) (rhodols: ex. 490 nm at 100% intensity with 530/50 nm emission filter; RX1: ex. 365 nm with 420lp emission filter).

6.3.1 Proof-of-concept probes: uptake and retention

Comparison of FC-probe uptake in DMEM and HBSS

We compared the cellular signal generation of **GL-C4-FC** in HBSS and DMEM. HEK293T cells (10.000 cells/well) were seeded on Poly-D-Lysine (gibco, A3890401) coated clear 96-well plates (TPP, Z707902) in 100 µL. After 1 d the cells were washed (3× medium change with DMEM or HBSS respectively) and **GL-C4-FC** and **iC4-FC** were added at 1, 3 and 10 µM from 10× stock solutions using a D300e Digital Dispenser (Tecan). The probes were incubated for 30 min and imaged by epifluorescence microscopy. During incubation, cells in HBSS were kept at 37 °C under air atmosphere and cells in DMEM were kept at 37 °C under 5% CO_2 atmosphere.

Uptake and post-wash retention (plate reader)

Fluorescence measurements were performed on a M1000 plate reader (Tecan) (rhodol settings: excitation 510 nm, emission 540 nm; fluorescein settings: excitation 498 nm, emission 518 nm).

HEK293T cells (10.000 cells/well) were seeded on Poly-D-Lysine (gibco, A3890401) coated black F-bottom 96-well plates (greiner, 655077). After 1 d the medium was removed and the rhodol probes (GL-Rho-AC^m, GL-Rho, GL-Rho-A, GL-Rho-AC, GL-Rho-C^m, GL-Rho-C) and fluorescein probes (GL-MF) were added in DMEM (100 µL, probe conc. 10 µM) with a multipipette (for smallest possible differences in the starting time).

The samples were incubated at 37 °C for 30 min under 5% CO_2 and the fluorescence was measured ("pre-wash"). The cells were washed (2× medium change) and the fluorescence was measured ("0 min post-wash"). The cells were incubated at 37 °C for 60 min under 5% CO_2 and the cells were washed (2×) and measured after 20 and 60 min ("20/60 min post-wash" respectively).

Controls:
(1) Untreated cells for subtraction of the autofluorescence (of cells and medium)
(2) Probes in cell medium for subtraction of the residual probe fluorescence in DMEM (10 µM probe conc.)
(3) Full activation of probes for determination of maximum probe fluorescence: TCEP (300 µM final concentration, BLDpharm, BD155793) was added to the probes in DMEM (5 µM final probe conc.) and the fluorescence was measured after 90 min (when the signal was constant)

The raw data was assembled and sorted using Microsoft Excel. “Cell entry & activation” values were calculated from “pre-wash” fluorescence subtracted by the residual fluorescence of probes in cell medium (Control 2) which was divided by the max. fluorescence of fully activated probe (Control 3). “Cell retention” values were calculated from cellular post-wash fluorescence subtracted by the cellular autofluorescence (Control 1) which was divided by the total amount of activated probe (“pre-wash” fluorescence minus control 2). Data was plotted using GraphPad Prism. For all resulting plots, one data point represents one biological replicate.

Confocal microscopy imaging

Fluorescein probes

Instrument: Leica SP8 point scanning confocal microscope using a 20× air objective, at 2× zoom, 1024x1024 pixel, 200 Hz scan speed, Pinhole: 1.00 AU. Environmental conditions were controlled using a stage top incubator (OKO Lab H301 K-frame) at 37 °C without CO_2 (for HBSS cell medium). The fluoresceins were excited at 488 nm (10% intensity), and emission was detected at 504-548 nm using a HyD detector. Cell Tracker Red CMTPX was excited with 594 nm (1% intensity) and emission was detected at 605−645 nm using a HyD detector. All probes were imaged in 2−3 independent biological runs.

HEK293T cells were plated on poly-D-lysine coated (gibco, A3890401) 8-well imaging dishes (No. 1.5, µ-Slide, 8-well, ibidiTreat, ibidi USA Inc., Wisconsin) and left to adhere in DMEM for 16-24 h. The DMEM was removed and warm HBSS was added. Cells were kept at 37 °C without CO_2 atmosphere and treated with Cell Tracker Red (CMTPX, Invitrogen, C34552, final conc. 1 µM) in HBSS for 30 min at 37 °C. The cells were washed with warm HBSS (2× medium change), then the probes were added (2 µL from 200× stock into 400 µL HBSS on the cells, final probe conc. 5 µM). Pre-wash images were acquired after 10, 20 and 30 min, then the cells were washed with warm HBSS (3× medium change), and post-wash images were acquired every 10 min for 60 min.

Quantification of fluorescence intensity was performed using Fiji/imageJ. All cells were selected from raw, unprocessed images based on the transmitted light image and the fluorescence intensity of the probe channel was measured. All cells were selected, overlapping areas were counted only for one of the cells. Typically, more than 50 cells were selected for each compound per time point over three locations within the same well.

Rhodol probes (except HP-TraG)

Instrument: Leica SP8 point scanning confocal microscope using a water 40× objective was used, no digital zoom, 2048x2048 pixels, 200 Hz scan speed, Pinhole: 1.00 AU. Environmental conditions were controlled using a stage top incubator (OKO Lab H301 K-frame) at 37 °C with 5% CO_2. The rhodols were excited at 518 nm (0.2% intensity), and emission was detected at 523−593 nm using a HyD detector. Cell Tracker Red CMTPX was excited with 598 nm (0.5% intensity) and emission was detected at 603−789 nm using a HyD detector. All probes were imaged in three independent experiments (n = 3).

HEK293T cells were seeded at 40.000 cells/well in Poly-D-Lysine coated (gibco, A3890401) 8-well imaging dishes (No. 1.5, µ-Slide, 8-well, ibidiTreat, ibidi USA Inc., Wisconsin) in 200 µL DMEM and cultured over night. The cells were stained with CellTracker Red (CMTPX, 4 µM, Invitrogen A3890401) for 45 min. The cells were washed (2× medium change), treated with the rhodol probe (5 µM, final DMSO concentration 0.5%) for 30 min and imaged to get pre-wash images. The cells were washed to remove the extracellular probe (2× medium change) and imaged after 1, 10, 20, 30 and 60 min.

For the cellular signal distribution of **GL-Rho-AC^{m}**, representative images were taken after 30 min of probe incubation (5 µM) using a 63× oil objective with otherwise identical conditions as above.

Images were analysed using Fiji ImageJ. For cellular fluorescence quantification, images were segmented by thresholding on the CellTracker channel. The resulting mask was then applied to the probe channel to obtain a mean fluorescence intensity value. Data was plotted using GraphPad Prism.

Retention in different cell lines

Experiments were performed in high glucose DMEM. HeLa (10.000 cells/well), MEF (5.000 cells/well) and A549 (5.000 cells/well) cells were seeded on Poly-D-Lysine (gibco, A3890401) coated black, clear F-bottom 96-well-plates (greiner, 655096) in 100 µL medium. After 1 d the medium was removed and the compounds **GL-Rho-AC^{m}** and **GL-Rho** were added in DMEM (5 µM probe concentration), incubated for 30 min and pre-wash images were acquired by epifluorescence microscopy. Then the cells were washed (2× medium change with DMEM) and imaged after 1, 20, 60 and 120 min while keeping the cells at 37 °C under CO_2 atmosphere between measurements.

6.3.2 HP-TraG characterisation

General

All cells were grown at 37 °C and 5% CO_2. Cell growth was monitored using an inverted microscope (Leica DMi1). HEK 293T cells were grown in DMEM (ThermoFisher 21885108) supplemented with 10% FBS (Biochrom S0615) and 1% Penicillin/Streptomycin (ThermoFisher 15140122). Hoxb8 cells were grown in RPMI (Thermo Fisher 61870010) supplemented with 10% FBS (Biochrom S0615), 1% Penicillin/Streptomycin (ThermoFisher 15140122), 0.1% 2-Mercaptoethanol (Thermo Fisher 31350010), 1 µM β-estradiol (Sigma E2758), and supernatant from a Flt3L-producing B16 melanoma cell line to a final concentration of 35 ng/mL. For macrophage differentiation, Hoxb8 cells were grown in RPMI supplemented with 10% FBS, 1% Penicillin/Streptomycin and 10-20 ng/ml M-CSF (PeproTech 315-02) for 5 days before seeding.

Confocal live cell imaging was performed at the Core Facility Bioimaging of the Biomedical Center with an inverted Leica SP8X microscope, equipped with Argon laser, WLL2 laser (470−670 nm) and acusto-optical beam splitter. Live cells were treated and recorded at 37 °C. For the duration of the assay, cells were kept in Hank's Balanced Salt Solution (HBSS, ThermoFisher 14025092) to allow incubation without CO_2. Assays were performed in 8-well glass bottom chambered coverslips (ibidi 80827).

The microscope was programmed to take three images of different fields of view per condition and time point tested, which were focused using reflection-based adaptive focus control. Images were acquired with a 20× 0.75 objective and additional 2× optical zoom. Image pixel size was 284 nm. The following fluorescence settings were used: **HP-TraG** excitation 488 nm (Argon), emission 500−570 nm; CellTracker Red excitation 594 nm (WLL), emission 605−645 nm. Recording was performed sequentially to avoid bleed-through. **HP-TraG** and CellTracker Red were recorded with hybrid photo detectors (HyDs), a transmitted light image was generated with a conventional photomultiplier tube.

Images were analysed using Fiji ImageJ. For cellular fluorescence quantification, images were segmented by thresholding on the CellTracker channel. The resulting mask was then applied to the **HP-TraG** channel to obtain a mean fluorescence intensity value. Data was plotted using GraphPad Prism.

H_2O_2 assays with HEK cells

Chambered coverslips were coated 2 d before the experiment by applying a 0.1 mg/mL Poly-D-Lysine (Sigma-Aldrich P7280) solution for 2 h at 37 °C. HEK cells were seeded into the coated wells at a density of 20.000 cells per cm².

Cells were stained with 0.5 µM CellTracker™ Red CMTPX Dye (ThermoFisher C34552) at 37 °C for 15 min. The medium was then changed to 10 µM **HP-TraG** solution in HBSS. After 10 min loading time, pre-treatment images were recorded. After 15 min loading time, cells were washed with HBSS once and the medium then changed once more to H_2O_2 solutions of the indicated molarities in HBSS or HBSS only for the negative control wells. The different H_2O_2 concentrations were obtained by serial dilution. Images were acquired at 15, 30 and 60 min of treatment. All wells were then washed twice with HBSS and post-wash images acquired at the indicated times thereafter.

PMA assays with Hoxb8-derived macrophages

Chambered coverslips were coated one day before experiment by applying a 0.1 mg/ml Poly-D-Lysine (Sigma-Aldrich P7280) solution for 2 h at 37 °C. Hoxb8-derived macrophages were seeded into the coated wells at a density of 300.000 cells per cm² and their differentiation medium was additionally supplemented with TNF-α (10 µg/ml, PeproTech 315-01A) and IFN-γ (10 µg/mL, PeproTech 315-05) for M1 polarisation.

Cells were stained with 0.5 µM CellTracker™ Red CMTPX Dye (ThermoFisher C34552) at 37 °C for 15 min. The medium was then changed to 10 µM **HP-TraG** solution in HBSS. After 10 min loading time, pre-treatment images were recorded. After 15 min loading time, cells were washed with HBSS once and the medium then changed once more to 1 µg/ml PMA in HBSS or HBSS only for the negative control wells. Images were acquired at 15, 30 and 60 min of treatment. All wells were then washed twice with HBSS and post-wash images acquired at the indicated times thereafter.

6.3.3 TR-TraG characterisation

General cell culture

Cells were grown at 37 °C under 5% CO2 atmosphere and cell growth was confirmed using a Nikon Eclipse Ti microscope (Nikon Corp., Minato (Japan)). HeLa (DSMZ; ACC57),–cell lines were purchased from the German Collection of Microorganisms and Cell Cultures. Wildtype TrxR1 (WT) and TrxR1 knockout (KO) mouse embryonic fibroblasts (MEF) were a kind gift from Marcus Conrad (MEFs isolated from conditional TrxR1 knockout mouse embryos were immortalised by lentiviral transduction. *In vitro* deletion of TrxR1 was achieved by Tat-Cre induced recombination and verified by PCR and immunoblotting for TrxR1[36]. All cell lines are tested regularly for mycoplasma contamination and only mycoplasma negative cells are used in assays. HeLa cells were grown in Dulbecco's modified Eagle's medium (DMEM: glucose (4.5 g/L), glutamine,

pyruvate, phenol red, $NaHCO_3$ (2.7 g/L); PAN Biotech, Aidenbach (Germany)). Media were supplemented with 10% heat-inactivated fetal bovine serum, penicillin (100 U/mL), streptomycin (100 µg/mL) and optionally with Na_2SeO_3 (0–100 nM) or Na_3PO_3S (0–1.2 mM). PBS Dulbecco buffer (Merck GmbH, Darmstadt (Germany)) was used for washing and resuspending steps; TrypLETM Express (gibco Life Technologies Inc., Massachusetts (USA)) was used to detach cells from flasks or dishes.

Cell-free enzyme assays

All experiments were performed in TE buffer (Tris-HCl (50 mM), EDTA (1 mM), pH = 7.4). and in black 96-well plates (microplates, 96-well, F-bottom, black, Fluotrack, high binding; Greiner bio-one GmbH, 655077) in technical triplicates. For all measurements the fluorescence intensity was measured every 150 s at 37 °C for 4 h using a Tecan Infinite M1000 plate reader (**TR-TraG**: ex/em 510bp5/540bp5).

TrxR1

TrxR1 (40 µL from 2.5× stock in TE buffer, final conc. 1−100 nM) was placed in the respective wells, **TR-TraG** (50 µL from 2× stock in TE buffer, final conc. 10 µM) was added and the reaction was started by adding NADPH (10 µL from 1 mM stock in TE buffer, final conc. 100 µM).

Trx1

Trx1 (20 µL from 5× stock in TE buffer, final conc. 0.01−10 µM) and TrxR1 (20 µL from 5× stock in TE buffer, final conc. 20 nM) were placed in the respective wells, **TR-TraG** (50 µL from 2× stock in TE buffer, final conc. 10 µM) was added and the reaction was started by adding NADPH (10 µL from 10× stock in TE buffer, final conc. 100 µM).

Grx1

Grx1 (20 µL from 5× stock in TE buffer, final conc. 0.01−10 µM), GR (10 µL from 5× stock in TE buffer, final conc. 10 nM) and GSH (10 µL from 5× stock in TE buffer, final conc. 100 µM) were placed in the respective wells, **TR-TraG** (50 µL from 2× stock in TE buffer, final conc. 10 µM) was added and the reaction was started by adding NADPH (10 µL from 10× stock in TE buffer, final conc. 100 µM).

Controls: The following negative controls were also measured: NADPH only (100 µL NADPH at 100 µM in TE-buffer), NADPH with **TR-TraG** (100 µM NADPH with 10 µM **TR-TraG** in TE-buffer), **TR-TraG** only (10 µM in TE-buffer), **TR-TraG** with Trx1 and Grx1 without the respective reductases (10 µM Trx1/Grx1 with 10 µM **TR-TraG** in TE-buffer) and **TR-TraG** with GSH (0.1−10 mM GSH with 10 µM **TR-TraG** in TE-buffer). To determine the maximum probe fluorescence, TCEP (final concentration of 200 µM) was added to the probes.

Human recombinant thioredoxin 1 (Trx 1) (lyophilized), human recombinant glutaredoxin 1 (Grx 1) (lyophilized from 10 µL TE-buffer, pH 7.5), human thioredoxin reductase (TrxR1) (1.5 mg/mL in 50% glycerol/TE-buffer, pH 7.5) and baker's yeast glutathione reductase (GR) (100 µM in 50% glycerol/TE-buffer, pH 7.5) were a kind gift by Elias Arnér and produced as previously described.[37,38]

TRi-1 inhibition assay

The activation of **TR-TraG** was quantitatively assessed depending on TrxR inhibition with Tri-1 by microplate reader fluorescence measurement. HeLa and A549 cells were seeded at 20.000 cells/well on 96-well plates (microplates, 96-well, F-bottom, µCLEAR®, black, Fluotrack, high binding; Greiner bio-one GmbH, 655087) in 100 µL medium (DMEM, 10% FCS) and cultured over night. Then the cells were preincubated with TRi-1 (2, 4, 8 and 16 µM final concentrations from DMSO stock solutions) for 3 h, cells were washed with PBS (2×) and the probe (**TR-TraG**: 25 µM; RX1: 100 µM) was added in fresh DMEM. The fluorescence intensity was measured hourly for 6 h using a Tecan Infinite M1000 plate reader (**TR-TraG**: ex/em 510bp5/540bp5; RX1: ex/em 355bp5/520bp5). In between measurements, cells were kept at 37 °C and 5% CO_2 atmosphere.

TrxR knockout assay

TrxR knockout and reference mouse embryonic fibroblasts (MEF) were a kind gift from Marcus Conrad and generated as previously described.[39] In brief: MEFs isolated from conditional TrxR1 knockout mouse embryos, were immortalised by lentiviral transduction. *In vitro* deletion of TrxR1 was achieved by Tat-Cre induced recombination and verified by PCR and immunoblotting for TrxR1.

The activation of **TR-TraG** in TrxR-wildtype and -knockout cells (MEF cell lines) was assessed by microplate reader fluorescence measurement. Both cell lines were seeded at 20.000 cells/well on Poly-D-Lysine (gibco, A3890401) coated 96-well plates (microplates, 96-well, F-bottom, µCLEAR®, black, Fluotrack, high binding; Greiner bio-one GmbH, 655087) in 100 µL medium (DMEM, 10% FCS) and cultured over night. Then the cells were treated with **TR-TraG** at 25 µM (1% final DMSO concentration). The fluorescence intensity was measured hourly for 6 h using a Tecan Infinite M1000 plate reader (**TR-TraG**: ex/em 510bp5/540bp5; RX1: ex/em 355bp5/520bp5). In between measurements, cells were kept at 37 °C and 5% CO_2 atmosphere.

Probe dose dependent activation

The activation of **TR-TraG** and RX1 was quantitatively assessed depending on the probe concentration by microplate reader fluorescence measurement. HeLa cells were seeded at 20.000 cells/well on 96-well plates (microplates, 96-well, F-bottom, µCLEAR®, black, Fluotrack, high binding; Greiner bio-one GmbH, 655087) in 100 µL medium (DMEM, 10% FCS) and cultured over night. Then the cells were treated with **TR-TraG** at

3, 10 and 25 µM or RX1 at 25, 50 and 100 µM (1% final DMSO concentration). The fluorescence intensity was measured hourly for 6 h using a Tecan Infinite M1000 plate reader (**TR-TraG**: ex/em 510bp5/540bp5; RX1: ex/em 355bp5/520bp5). In between measurements, cells were kept at 37 °C and 5% CO_2 atmosphere.

Comparison of TR-TraG and RX1 (microcopy)

To qualitatively evaluate the effects of the **TR-TraG** and RX1 regarding signal generation and cell toxicity we imaged both probes by epifluorescence microscopy ((**TR-TraG**: ex/em 490bp5/510lp; RX1: ex/em 365bp5/410lp). HeLa cells were seeded at 20.000 cells/well on 96-well plates (microplates, 96-well, F-bottom, µCLEAR®, black, Fluotrack, high binding; Greiner bio-one GmbH, 655087) in 100 µL medium. Cells were treated with **TR-TraG** (10 µM) and RX1 (100 µM) and imaged after 45 min, 1.5 h, 3 h and 6 h. After 6 h of incubation, the were washed (2× medium change) and imaged again after 24 h.

Cell Viability

As a proxy readout for viable cells, mitochondrial diaphorase activity was quantified by measuring the reduction of resazurin (7-hydroxy-3H-phenoxazin-3-one 10-oxide) to resorufin. Cells were incubated with 20 µL of 0.15 mg mL^{-1} resazurin per well for 3 h at 37 °C. Resorufin fluorescence (excitation 544 nm, emission 590 nm) was measured using a FLUOstar Omega microplate reader (BMG Labtech). Results are represented as percent of DMSO-treated control.

Fluorescence microscopy

Intracellular PQ-OH(s) precipitation was confirmed using a Nikon Eclipse Ti2 upright microscope from Nikon Instruments Europe BV, Amsterdam (Netherlands) (ex/em 355bp50/410lp; or transmitted light, as appropriate). Images were processed using Fiji version 1.51 (ImageJ). Confocal time lapse microscopy was performed on live HeLa cells seeded in 8-well slides (ibiTreat µ ibidi slides, ibidi GmbH, Martinsried (Germany)). Slides were placed on the motorized stage of a Leica SP8 laser-scanning confocal microscope (Wetzlar, Germany), treated with SS50-PQ at 50 µM on the stage and immediately imaged for one hour with ex/em 405laser/530bp20, collecting fluorescence and brightfield images.

Flow cytometry

After treatment with probed, cells were harvested and stained with a fixable viability dye according to the manufacturer's recommendations (zombie NIR™ Fixable Viability Kit, BioLegend). Cells were fixed in 4% paraformaldehyde (PFA) in PBS for 30 min and either stored in PBS or immediately resuspended in a wash buffer containing PBS with 1% bovine serum albumin (BSA) and 1 mM EDTA. Flow cytometry was conducted at the BioMedical Centre Core Facility of the LMU Munich on a BD LSRFortessa (BD Bioscience, Heidelberg (Germany)) using the integrated BD FACS Diva software v.8.0.1. The following excitation/detection settings were used: zombie (ex/em 647laser/780bp60) and PQ fluorescence (ex/em 355laser/530bp30). Data were processed using FlowJo v.10.7.1 (BD Biosciences). An unstained sample was used to exclude cell debris and doublets. Zombie dye was used as a marker for dead or dying cells. PQ-positive gate was set so that 0% of cells were PQ-positive in an unstained sample.

7 Synthetic Chemistry

7.1 Chemistry methods and techniques

7.1.1 Analytical methods

High resolution mass spectrometry (**HRMS**) was conducted on the following instruments: (1) a *Thermo Finnigan LTQ FT Ultra FourierTransform* ion cyclotron resonance spectrometer from *ThermoFisher Scientific GmbH* applying electron spray ionisation (ESI) with a spray capillary voltage of 4 kV at temperature 250 °C with a method dependent range from 50 to 2000 u;(2) a *Finnigan MAT 95 from Thermo Fisher Scientific* applying electron ionisation (EI) at a source temperature of 250 °C and an electron energy of 70 eV with a method dependent range from 40 to 1040 u; and (3) a Waters Xevo G2-XS Q-TOF applying electron spray ionisation (ESI) with a spray capillary voltage of 2 kV at a source temperature of 140 °C with a method dependent range from 50 to 1200 u.

Nuclear magnetic resonance (**NMR**) spectroscopy was performed using the following instruments: (1) a *Bruker Avance* (600/150 MHz, with TCI cryoprobe) or (2) a *Bruker Avance III HD Biospin* (400/100 MHz, with BBFO cryoprobe™) from Bruker Corp. or (3) a Bruker Avance III HD (800 MHz, with cryoprobe) or (4) a Bruker Avance Neo (600/150 MHz, with cryoprobe). NMR-spectra were measured at 298 K, unless stated otherwise, and were analysed with the program *MestreNova 12* developed by *MestreLab Ltd.* ^{1}H-NMR spectra chemical shifts (δ) in parts per million (ppm) relative to tetramethylsilane (δ = 0 ppm) are reported using the residual protic solvent ($CHCl_3$ in $CDCl_3$: δ = 7.26 ppm, DMSO-d_5 in DMSO-d_6: δ = 2.50 ppm, CHD_2OD in CD_3OD: δ = 3.31 ppm) as an internal reference. For ^{13}C-NMR spectra, chemical shifts in ppm relative to tetramethylsilane (δ = 0 ppm) are reported using the central resonance of the solvent signal ($CDCl_3$: δ = 77.16 ppm, DMSO-d_6: δ = 39.52 ppm, CD_3OD: δ = 49.00 ppm) as an internal reference. For ^{1}H-NMR spectra in addition to the chemical shift the following data is reported in parenthesis: multiplicity, coupling constant(s) and number of hydrogen atoms. The abbreviations for multiplicities and related descriptors are s = singlet, d = doublet, t = triplet, q = quartet, or combinations thereof, m = multiplet and br = broad. When rotamers were observed in the NMR spectra, the corresponding signals are separated by a slash ("/"). Where known products matched literature analysis data, only selected data acquired are reported.

Analytical high performance liquid chromatography (**HPLC**) analysis was conducted either using an *Agilent 1100* system from *Agilent Technologies Corp.,* Santa Clara (USA) equipped with a DAD detector and a *Hypersil Gold* HPLC column from *ThermoFisher Scientific GmbH*, Dreieich (Germany) or a *Agilent 1200 SL* system *Agilent Technologies Corp.,* Santa Clara (USA) equipped with a DAD detector, a *Hypersil Gold* HPLC column from *ThermoFisher Scientific GmbH*, Dreieich (Germany) and consecutive low-resolution mass detection using a LC/MSD IQ mass spectrometer applying ESI from *Agilent Technologies Corp.,* Santa Clara (USA). For both systems mixtures of water (analytical grade, 0.1 % formic acid) and MeCN (analytical grade, 0.1 % formic acid) were used as eluent systems.

UV-Vis spectra were recorded on an Cary 60 UV-Vis spectrophotometer from *Agilent Technologies Inc*., Santa Clara (USA) using 1 cm quartz or PMMA cuvettes. The scan rate was set to 600 nm/min and 2.5 nm slit width was used. Unless stated otherwise, the probes and fluorophores were dissolved in PBS (pH = 7.4, 1 % DMSO) at 10 µM concentration.

Fluorescence spectroscopy was performed on a Cary Eclipse Fluorescence Spectrometer from *Agilent Technologies Inc*., Santa Clara (USA) using quartz cuvettes (scan rate: 120 nm/min, 5 nm slit width) or on a Tecan Infinite M1000 plate reader. Unless stated otherwise, the samples were measured at 10 µM concentration.

7.1.2 Synthetic techniques

Unless stated otherwise, all reactions were performed without precautions regarding potential air- and moisture-sensitivity and were stirred with Teflon-coated magnetic stir bars. For work under inert gas (nitrogen) atmosphere, a Schlenk apparatus and a high vacuum pump from Vacuubrand GmbH, Wertheim (Germany) were used. For solvent evaporation a *Laborota 400* from Heidolph GmbH, Schwabach (Germany) equipped with a vacuum pump was used. Flash column chromatography was conducted with a Biotage® Isolera One Chromatograph with Biotage® Sfär Silica D columns (10 g or 25 g silica) for normal-phase (np) chromatography or with Biotage® Sfär C18 D columns (12 g or 30 g silica) for reversed-phase (rp) chromatography. Reactions were monitored by thin layer chromatography (TLC) on TLC plates (*Si 60 F254 on aluminium sheets*) provided by Merck GmbH and visualised by UV irradiation and by analytical HPLC-MS. The procedures and yields are not optimised.

7.1.3 Chemicals

All chemicals, which were obtained from BLDpharm, Sigma-Aldrich, TCI, Alfa Aesar, Acros, abcr or carbolution were used as received and without purification. Tetrahydrofuran (THF), dichloromethane (DCM) and dimethylformamide (DMF) were provided by Acros and were stored under argon atmosphere and dried over molecular sieves. TLC control, extractions and column chromatography were conducted using distilled, technical grade solvents. Whenever the term *hexanes (Hex)* is used, the applied solvent actually comprised isomeric mixtures of hexane (2-methylpentane, 3-methylpentane, 2,2-dimethylbutane, 2,3-dimethylbutane).

7.2 Synthetic procedures

7.2.1 Literature procedures

The following molecules were synthesised according to literature procedures:

- **i_2-F** (Chyan *et al*.[23], compound 3b)
- **i_2-FS** (Mauker *et al*.[22], compound i_2-FS_1)
- **iPS-F** (Mauker *et al*.[22], compound iPS-FS_1)
- **GL-MF** (Zeisel, Felber *et al*.[40], compound Ac-SS66C-MF)
- **Compound 2** (Zeisel, Felber *et al*.[40], compound 7T)
- **Compound 21** (Zeisel *et al*.[31], compound S20 followed by Boc-deprotection).

7.2.2 General Procedures

General Procedure A: *O´*-alkyl fluorescein ester probes

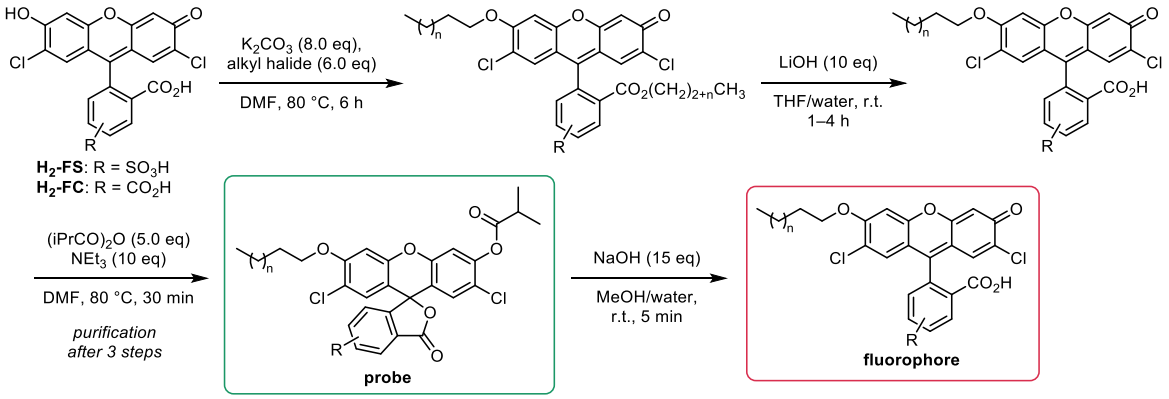

Step 1: Alkylation

H_2-FS or **H_2-FC** (1.0 eq) was dissolved in anhydrous DMF (0.02−0.15 M). Potassium carbonate (8.0 eq) and the respective **alkyl halide** (6.0 eq) were added and the reaction was heated 80 °C for 2−15 h until full conversion to the di-alkyl product (for sulfofluoresceins) or to the tri-alkyl product (for carboxyfluoresceins) (monitored by HPLC/MS). The reaction mixture was filtered to remove insoluble salts and the solvent was removed *in vacuo*.

Step 2: Ester cleavage

The crude product was dissolved in THF/water (0.004−0.05 M) (*Note: at high salt/compound concentrations THF and water are not miscible*). Lithium hydroxide (10 eq) was added and the reaction mixture was stirred at room temperature for 1−4 h. Aqueous hydrochloric acid (2 M, 12 eq) was added to acidify the solution (checked by pH paper) and the volatiles were removed *in vacuo* and optionally semi-purified by reversed-phase flash column chromatography affording the *O´*-alkylated fluorophore (*Note: acidification before evaporation is recommended to avoid decomposition of the fluorescein to the corresponding benzophenones*).

Step 3: Acylation

The crude fluorophore was dissolved in DMF (0.01−0.05 M), triethylamine (10 eq) and isobutyric anhydride (5.0 eq) were added and the reaction mixture was heated to 80 °C for 30 min. The volatiles were removed *in vacuo* and the crude product was purified by reversed-phase flash column chromatography (acetonitrile/water, 0.1% FA). From the column fractions containing the product, the acetonitrile was removed at the rotary evaporator (bath temperature: 40 °C to avoid probe hydrolysis), then the aqueous solution was lyophilised overnight.

Note: If the probe cannot be afforded in the desired purity by this procedure, we recommend capping the purified fluorophores (see General Procedure B)

General Procedure B: *O*-alkyl fluorescein fluorophores

The corresponding probe (1.0 eq) was dissolved in methanol/THF (1:1, 0.008−0.02 M). Sodium hydroxide (aqueous, 2 M, 10 eq) was added and the reaction mixture was stirred at r.t. for 5 min. Hydrochloric acid (aqueous, 2 M, 12 eq) was added to acidify the solution and the volatiles were removed *in vacuo*. The crude product was purified by reversed-phase flash column chromatography (acetonitrile/water, 0.1% FA). The solvent of the product fractions was removed *in vacuo*.

Note: We found that the purification of the fluorophores was simplest to perform by preparing the probes in three steps only purifying the product and then cleaving the probe to the fluorophore again; however, purification of the fluorophore before capping is also feasible.

General Procedure C: *O*-Aryl carbamate formation

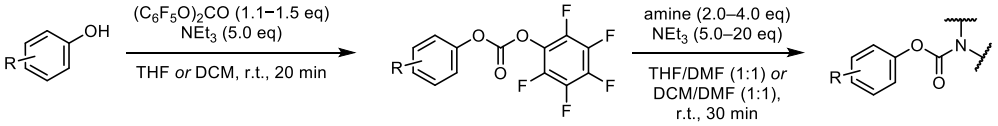

The corresponding phenol (1.0 eq) was dissolved in anhydrous THF or DCM (0.01−0.03 M) under nitrogen atmosphere, triethylamine (5.0 eq) and bis(pentafluorophenyl)carbonate (1.1−1.5 eq) were added and the reaction mixture was stirred at room temperature for 20 min. The desired amine (2.0−4.0 eq) was added as solid to the mixture, then anhydrous DMF was added. The reaction mixture was stirred at room temperature for 30 min. For isolation, the volatiles were removed *in vacuo* and the crude product was purified by reversed-phase flash column chromatography (acetonitrile/water, 0.1% formic acid).

General Procedure D: Buchwald-Hartwig cross coupling

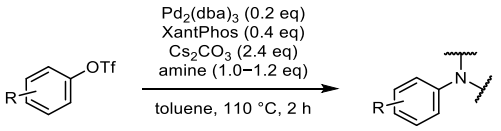

The corresponding triflate (1.0 eq) was placed in a round-bottom flask (dried in the dry-oven at 80 °C over night) and dissolved in anhydrous toluene (0.05 M) under nitrogen atmosphere. The respective amine (1.0−1.2 eq) and cesium carbonate (2.4 eq) were added and the solution was degassed by bubbling nitrogen through the solution for at least 5 min. XantPhos (20 mol%) and $Pd_2(dba)_3$ (10 mol%) were added and the reaction was heated to reflux for 2 h. The crude product was obtained by removing the volatiles *in vacuo*.

General Procedure E: Triflate cleavage with lithium hydroxide or TBAF

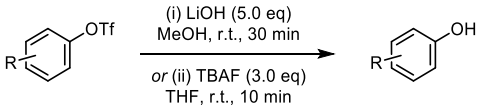

(i) The corresponding triflate was dissolved in methanol (0.07 M) and lithium hydroxide (5.0 eq) was added. The reaction mixture was stirred at room temperature for 20 min. Then aqueous HCl (2 M, 7.0 eq) was added before removing the volatiles *in vacuo*.

(ii) The corresponding triflate was dissolved in anhydrous THF (0.05−0.08 M) and TBAF (1 M solution in THF, 3.0 eq) was added. The reaction mixture was stirred at room temperature for 20 min.

General Procedure F: *tert*-Butyl carboxylate deprotection

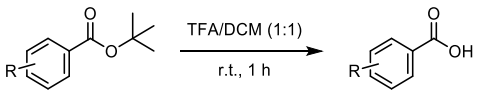

The corresponding *tert*-butyl carboxylate was dissolved in anhydrous DCM (0.01−0.02 M), trifluoroacetic acid (final solution: DCM:TFA = 1:1) was added and the reaction mixture was stirred at room temperature for 1 h. The crude product was afforded by removing the volatiles *in vacuo*.

General Procedure G: Acetoxymethylation

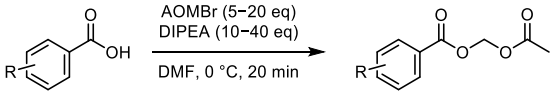

The corresponding carboxylic acid was dissolved in anhydrous DMF (0.01−0.02 M) at 0 °C, DIPEA (10−40 eq) and acetoxymethyl bromide (AOMBr, 5−20 eq) were added and the mixture was stirred at 0 °C for 20 min. The product was purified by preparative HPLC.

Note: methyl piperazine probes also form the acetoxymethyl ammonium byproduct if reacted for longer or at room temperature.

7.2.3 Proof-of-concept fluorescein probes and fluorophores

iC4-FS

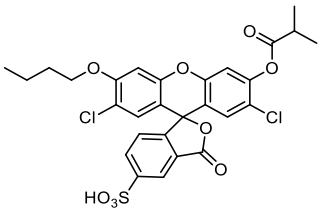

Prepared according to General Procedure A from **H_2-FS** (30 mg, 63 µmol, 1.0 eq; 0.10 M) and *n*-butyl iodide (43 µL, 0.38 mmol, 6.0 eq). Reaction time for alkylation: 6 h. Ester cleavage: 0.033 M in THF/water = 1:1 for 2 h, semi-purified by rp-column chromatography: 10→50% MeCN. Acylation: 0.01 M, purification by rp-column chromatography: 15→70% MeCN.

The product **iC4-FS** (18 mg, 30 µmol, 47% (3 steps)) was obtained as light yellow solid.

TLC *Rf* = 0.79 (*rp*, 60% MeCN)
^{1}H-NMR (400 MHz, DMSO-d_6): δ (ppm) = 8.10 (s, 1H), 8.00 (dd, J = 8.0, 1.2 Hz, 1H), 7.51 (s, 1H), 7.35 (d, J = 8.0 Hz, 1H), 7.18 (s, 1H), 7.12 (d, J = 2.4 Hz, 1H), 6.88 (s, 1H), 4.23 – 4.12 (m, 2H), 2.91 (hept, J = 6.9 Hz, 1H), 1.75 (p, J = 6.5 Hz, 2H), 1.46 (h, J = 7.3 Hz, 2H), 1.27 (d, J = 7.0 Hz, 6H), 0.94 (t, J = 7.4 Hz, 3H).
^{13}C-NMR (101 MHz, DMSO-d_6): δ (ppm) = 174.2, 168.3, 156.3, 151.9, 151.2, 150.4, 150.0, 148.6, 133.8, 129.4, 128.6, 125.9, 124.2, 122.3, 122.1, 118.2, 118.2, 113.5, 111.0, 102.3, 80.8, 69.5, 33.8, 30.8, 19.1, 19.1, 14.1.
HRMS (ESI+): m/z calc. for $C_{28}H_{25}Cl_2O_9S^+$ $[M+H]^+$: 607.0591, found: 607.0590.

iC7-FS

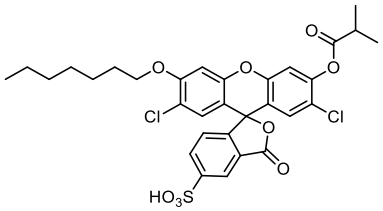

Prepared according to General Procedure A from **H_2-FS** (27 mg, 56 µmol, 1.0 eq; 0.04 M) and *n*-heptyl iodide (55 µL, 0.34 mmol, 6.0 eq). Reaction time for alkylation: 3 h. Ester cleavage: 0.02 M in THF/water = 2:1 for 3.5 h, semi-purified by rp-column chromatography: 15→70% MeCN. Acylation: 0.02 M, purification by rp-column chromatography: 30→100% MeCN.

The product **iC7-FS** (25 mg, 39 µmol, 74% (3 steps)) was obtained as light yellow solid.

TLC *Rf* = 0.67 (*rp*, 60% MeCN)
^{1}H-NMR (800 MHz, DMSO-d_6): δ (ppm) = 8.11 (s, 1H), 8.02 (d, J = 8.0 Hz, 1H), 7.51 (s, 1H), 7.35 (d, J = 7.9 Hz, 1H), 7.18 (s, 1H), 7.12 (s, 1H), 6.88 (s, 1H), 4.22 – 4.14 (m, 2H), 2.92 (hept, J = 6.8 Hz, 1H), 1.77 (p, J = 6.6 Hz, 2H), 1.44 (p, J = 7.8, 7.4 Hz, 2H), 1.35 (p, J = 7.3 Hz, 2H), 1.28 (d, J = 7.0 Hz, 6H), 1.32 – 1.21 (m, 4H), 0.87 (t, J = 6.8 Hz, 3H).
^{13}C-NMR (201 MHz, DMSO-d_6): δ (ppm) = 174.2, 168.2, 156.3, 151.9, 151.3, 150.4, 150.0, 148.6, 133.8, 129.3, 128.6, 125.9, 124.2, 122.3, 122.1, 118.2, 118.2, 113.5, 111.1, 102.3, 80.8, 69.8, 33.8, 31.7, 28.8, 28.7, 25.8, 22.5, 19.1, 14.4.
HRMS (ESI−): m/z calc. for $C_{31}H_{29}Cl_2O_9S^-$ $[M-H]^-$: 647.0915, found: 647.0917.

iC10-FS

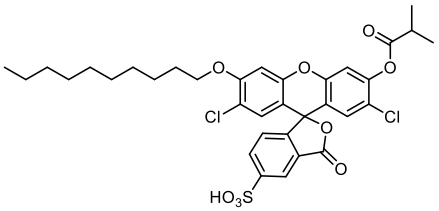

Prepared according to General Procedure A from **H_2-FS** (50 mg, 0.10 mmol, 1.0 eq; 0.02 M) and *n*-decyl iodide (0.13 mL, 0.62 mmol, 6.0 eq). Reaction time for alkylation: 2 h. Ester cleavage: 0.004 M in THF/water = 3:2 for 4 h, no purification. Acylation: 0.03 M, purification by rp-column chromatography: 40→100% MeCN.

The product **iC10-FS** (32 mg, 46 µmol, 45% (3 steps)) was obtained as colourless solid.

TLC *Rf* = 0.50 (*rp*, 60% MeCN)
^{1}H-NMR (800 MHz, DMSO-d_6): δ (ppm) = 8.10 (s, 1H), 8.01 (dd, J = 7.9, 1.2 Hz, 1H), 7.50 (s, 1H), 7.34 (d, J = 7.9 Hz, 1H), 7.17 (s, 1H), 7.11 (s, 1H), 6.87 (s, 1H), 4.21 – 4.13 (m, 2H), 2.91 (hept, J = 7.0 Hz, 1H), 1.76 (p, J = 6.6 Hz, 2H), 1.43 (p, J = 7.6, 7.2 Hz, 2H), 1.33 (p, J = 6.9 Hz, 2H), 1.27 (d, J = 7.0 Hz, 6H), 1.30 – 1.20 (m, 10H), 0.84 (t, J = 7.0 Hz, 3H).
^{13}C-NMR (201 MHz, DMSO-d_6): δ (ppm) = 174.2, 168.2, 156.3, 151.9, 151.3, 150.4, 150.0, 148.6, 133.8, 129.3, 128.6, 125.9, 124.2, 122.3, 122.1, 118.2, 118.2, 113.5, 111.1, 102.3, 80.8, 69.8, 33.8, 31.8, 29.4, 29.4, 29.1, 29.0, 28.7, 25.8, 22.6, 19.1, 14.4.
HRMS (ESI−): m/z calc. for $C_{34}H_{35}Cl_2O_9S^-$ $[M-H]^-$: 689.1384, found: 689.1387.

iC4-FC

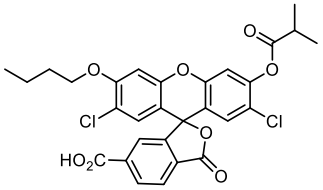

Prepared according to General Procedure A from **H_2-FC** (29 mg, 65 µmol, 1.0 eq; 0.07 M) and *n*-butyl iodide (60 µL, 0.52 mmol, 8.0 eq). Reaction time for alkylation: 3 h. Ester cleavage: 0.01 M in THF/water = 3:2 for 13 h, semi-purified by rp-column chromatography: 25→80% MeCN. Acylation: 0.01 M, purification by rp-column chromatography: 40→100% MeCN.

The product **iC4-FC** (10 mg, 17 µmol, 26% (3 steps)) was obtained as colourless solid.

TLC *Rf* = 0.41 (*rp*, 60% MeCN)
^{1}H-NMR (800 MHz, DMSO-d_6): δ (ppm) = 8.25 (d, J = 7.9 Hz, 1H), 8.11 (d, J = 7.6 Hz, 1H), 7.82 (s, 1H), 7.51 (s, 1H), 7.19 (s, 1H), 7.14 (s, 1H), 6.90 (s, 1H), 4.22 – 4.14 (m, 2H), 2.92 (hept, J = 7.0 Hz, 1H), 1.75 (p, J = 6.4 Hz, 2H), 1.47 (dt, J = 12.4, 6.2 Hz, 2H), 1.28 (d, J = 7.0 Hz, 6H), 0.95 (t, J = 7.4 Hz, 3H).
^{13}C-NMR (201 MHz, DMSO-d_6): δ (ppm) = 174.2, 168.0, 166.7, 156.3, 152.0, 150.9, 150.6, 150.1, 148.6, 131.8, 129.3, 128.8, 128.6, 125.8, 124.8, 122.1, 118.2, 118.1, 113.5, 110.9, 102.4, 81.1, 69.5, 33.8, 30.8, 19.1, 19.1, 14.1.
HRMS (ESI−): m/z calc. for $C_{29}H_{23}Cl_2O_8^-$ $[M-H]^-$: 569.0775, found: 569.0778.

iC4-F

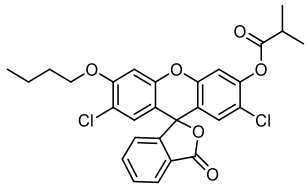

iC4-F

Prepared according to General Procedure A from **H_2-F** (82 mg, 0.20 mmol, 1.0 eq; 0.04 M) and *n*-butyl iodide (0.14 mL, 1.2 mmol, 6.0 eq). Reaction time for alkylation: 3 h. Ester cleavage: 0.01 M in THF/water = 3:2 for 13 h, semi-purified by rp-column chromatography: 10→50% MeCN. Acylation: 0.01 M, purification by np-column chromatography: Hex/EtOAc 0→20%.

The product **iC4-F** (41 mg, 78 µmol, 38% (3 steps)) was obtained as colourless solid.

TLC *Rf* = 0.26 (*np*, Hex:EtOAc 9:1)
^{1}H-NMR (400 MHz, CD_2Cl_2): *δ* (ppm) = 8.03 (dd, J = 7.3, 1.1 Hz, 1H), 7.75 (td, J = 7.5, 1.3 Hz, 1H), 7.70 (td, J = 7.5, 1.1 Hz, 1H), 7.24 – 7.18 (m, 1H), 7.14 (s, 1H), 6.87 (s, 1H), 6.86 (s, 1H), 6.77 (s, 1H), 4.12 – 4.05 (m, 2H), 2.88 (hept, J = 7.0 Hz, 1H), 1.90 – 1.79 (m, 2H), 1.53 (t, J = 8.7 Hz, 2H), 1.33 (dd, J = 7.0, 2.6 Hz, 6H), 0.99 (t, J = 7.4 Hz, 3H).
^{13}C-NMR (101 MHz, CD_2Cl_2): *δ* (ppm) = 174.5, 168.9, 156.8, 152.2, 150.9, 150.6, 148.9, 136.0, 130.8, 129.4, 128.9, 126.6, 125.7, 124.3, 122.6, 119.1, 118.3, 112.9, 111.1, 101.5, 81.5, 69.7, 34.5, 31.2, 19.5, 19.0, 19.0, 13.9.
HRMS (ESI+): m/z calc. for $C_{28}H_{24}Cl_2NaO_6^+$ $[M+Na]^+$: 549.0848, found: 549.0843.

H-C4-FS

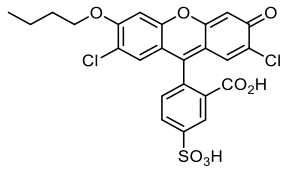

Prepared according to General Procedure B from **iC4-FS** (18 mg, 30 µmol, 1.0 eq, 0.008 M). Purification by rp column chromatography: 10→60% MeCN.

The product **H-C4-FS** (15 mg, 28 µmol, 94%) was obtained as orange solid.

TLC *Rf* = 0.71 (*rp*, 50% MeCN)
^{1}H-NMR (400 MHz, DMSO-d_6): *δ* (ppm) = 11.12 (s (br), 1H), 8.08 (s, 1H), 8.00 (d, J = 8.0 Hz, 1H), 7.28 (d, J = 7.9 Hz, 1H), 7.19 (s, 1H), 6.92 (s, 1H), 6.81 (s, 1H), 6.75 (s, 1H), 4.22 – 4.09 (m, 2H), 1.74 (p, J = 6.5 Hz, 2H), 1.45 (h, J = 7.4 Hz, 2H), 0.94 (t, J = 7.4 Hz, 3H)
^{13}C-NMR (101 MHz, DMSO-d_6): *δ* (ppm) = 168.4, 156.1, 155.7, 152.1, 151.1, 150.7, 150.4, 133.7, 128.9, 128.6, 126.1, 124.2, 122.0, 117.7, 116.9, 111.3, 110.6, 104.0, 102.4, 81.7, 69.4, 30.8, 19.1, 14.1.
HRMS (ESI−): m/z calc. for $C_{24}H_{17}Cl_2O_8S^-$ $[M-H]^-$: 535.0027, found: 535.0025.

H-C7-FS

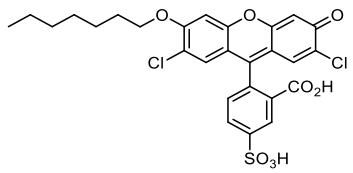

Prepared according to General Procedure B from **iC7-FS** (25 mg, 39 µmol, 1.0 eq, 0.01 M). Purification by rp column chromatography: 10→70% MeCN.

The product **H-C7-FS** (10 mg, 17 µmol, 45%) was obtained as orange solid.

TLC *Rf* = 0.66 (*rp*, 50% MeCN)
^{1}H-NMR (400 MHz, DMSO-d_6): *δ* (ppm) = 8.08 (s, 1H), 8.00 (dd, J = 8.0, 1.4 Hz, 1H), 7.27 (d, J = 7.9 Hz, 1H), 7.18 (s, 1H), 6.92 (s, 1H), 6.81 (s, 1H), 6.75 (s, 1H), 4.19 – 4.09 (m, 2H), 1.75 (p, J = 6.5 Hz, 2H), 1.48 – 1.38 (m, 2H), 1.38 – 1.30 (m, 2H), 1.30 – 1.23 (m, 4H), 0.90 – 0.81 (m, 3H).
^{13}C-NMR (101 MHz, DMSO-d_6): *δ* (ppm) = 168.0, 155.7, 155.3, 151.7, 150.6, 150.3, 149.9, 133.3, 128.5, 128.2, 125.7, 123.8, 121.6, 117.3, 116.5, 110.9, 110.2, 103.6, 102.0, 81.2, 69.3, 31.3, 28.4, 28.3, 25.4, 22.1, 14.0.
HRMS (ESI−): m/z calc. for $C_{27}H_{23}Cl_2O_8S^-$ $[M-H]^-$: 577.0496, found: 577.0496.

H-C10-FS

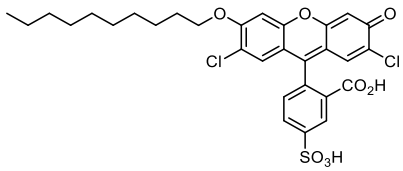

Prepared according to General Procedure B from **iC10-FS** (32 mg, 46 µmol, 1.0 eq, 0.008 M). Purification by rp column chromatography: 40→100% MeCN.

The product **H-C10-FS** (12 mg, 19 µmol, 41%) was obtained as orange solid.

TLC *Rf* = 0.50 (*rp*, 50% MeCN)
^{1}H-NMR (400 MHz, DMSO-d_6): δ (ppm) = 8.12 – 8.05 (m, 1H), 8.00 (dd, J = 8.0, 1.5 Hz, 1H), 7.26 (d, J = 7.9 Hz, 1H), 7.18 (s, 1H), 6.91 (s, 1H), 6.80 (s, 1H), 6.73 (s, 1H), 4.19 – 4.09 (m, 2H), 3.23 – 3.15 (m, 2H), 1.75 (p, J = 6.5 Hz, 2H), 1.67 – 1.55 (m, 2H), 1.48 – 1.38 (m, 2H), 1.24 (s, 6H), 0.89 – 0.80 (m, 5H).
^{13}C-NMR (101 MHz, DMSO-d_6): δ (ppm) = 168.0, 155.7, 150.7, 150.4, 150.0, 133.2, 128.4, 128.1, 125.7, 123.8, 121.7, 117.3, 117.0, 111.0, 109.8, 103.6, 101.9, 82.7, 69.3, 62.8, 31.3, 29.0, 28.7, 25.8, 25.4, 22.2, 21.7, 14.0.
HRMS (ESI−): m/z calc. for $C_{30}H_{29}Cl_2O_8S^-$ $[M-H]^-$: , found: 619.0963.

H-C4-FC

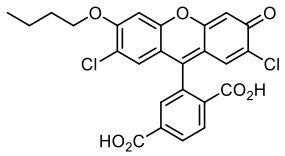

Was obtained purely during the preparation of iC4-FC according to General Procedure A from **H_2-FC** (0.30 g, 0.67 mmol, 1.0 eq, 0.07 M). Purification by rp column chromatography: 25→80% MeCN.

The product **H-C4-FC** (0.10 g, 0.21 mmol, 31%) was obtained as orange solid.

TLC *Rf* = 0.61 (*rp*, 60% MeCN)
^{1}H-NMR (400 MHz, DMSO-d_6): δ (ppm) = 11.14 (s, 1H), 8.24 (dd, J = 8.0, 1.2 Hz, 1H), 8.12 (d, J = 8.0 Hz, 1H), 7.75 (s, 1H), 7.20 (s, 1H), 6.93 (s, 1H), 6.87 (s, 1H), 6.80 (s, 1H), 4.15 (tt, J = 9.9, 5.0 Hz, 2H), 1.74 (p, J = 6.5 Hz, 2H), 1.46 (h, J = 7.4 Hz, 2H), 0.94 (t, J = 7.4 Hz, 3H).
^{13}C-NMR (101 MHz, DMSO-d_6): δ (ppm) = 168.0, 166.5, 156.1, 155.7, 152.3, 150.8, 150.4, 138.0, 131.7, 129.7, 128.9, 128.6, 126.3, 124.9, 117.7, 116.9, 111.1, 110.3, 104.0, 102.4, 82.1, 69.4, 30.8, 19.1, 14.1.
HRMS (ESI−): m/z calc. for $C_{25}H_{17}Cl_2O_7^-$ $[M-H]^-$: 499.0357, found: 499.0361.

H-C4-F

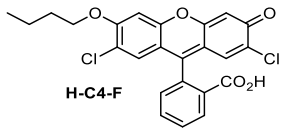

Prepared according to General Procedure B from **iC4-F** (30 mg, 57 µmol, 1.0 eq, 0.01 M). Purification by rp column chromatography: 40→100% MeCN.

The product **H-C4-F** (22 mg, 48 µmol, 85%) was obtained as orange solid.

TLC *Rf* = 0.37 (*rp*, 60% MeCN)
^{1}H-NMR (400 MHz, DMSO-d_6): δ (ppm) = 8.02 (d, J = 7.5 Hz, 1H), 7.82 (t, J = 7.2 Hz, 1H), 7.75 (t, J = 7.4 Hz, 1H), 7.33 (d, J = 7.6 Hz, 1H), 7.20 (s, 1H), 6.92 (s, 1H), 6.74 (s, 1H), 6.68 (s, 1H), 4.22 – 4.08 (m, 2H), 1.74 (p, J = 6.5 Hz, 2H), 1.52 – 1.36 (m, 2H), 0.93 (t, J = 7.4 Hz, 3H).
^{13}C-NMR (101 MHz, DMSO-d_6): δ (ppm) = 168.3, 155.6, 155.4, 151.5, 150.4, 150.1, 136.0, 130.6, 128.3, 128.0, 125.9, 125.2, 124.0, 117.2, 116.5, 111.2, 110.3, 103.6, 102.0, 81.4, 69.0, 30.4, 18.7, 13.7.
HRMS (ESI−): m/z calc. for $C_{24}H_{17}Cl_2O_5^-$ $[M-H]^-$: 455.0459, found: 455.0461.

GSH activatable fluorescein probe GL-C4-FC

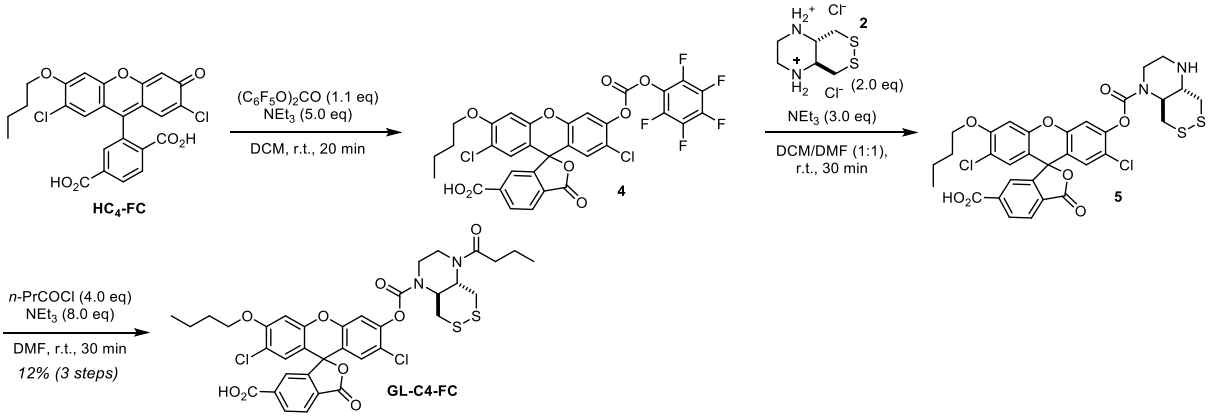

Compound **2** was prepared according to a known procedure (Zeisel, Felber *et al*.[40], compound 7T).

H-C4-FC (10 mg, 20 µmol, 1.0 eq, 0.007 M) was transformed to **5** following General Procedure C in DCM with 1.1 eq bis(pentafluorophenyl)carbonate and 2.0 eq of amine **2** with 5.0 eq triethylamine (purification: 15→100% MeCN). The semi-purified intermediate **5** was dissolved in anhydrous DMF (3 mL), triethylamine (22 µL, 0.16 mmol, 8.0 eq) and *n*-butyryl chloride (8.4 µL, 80 µmol, 4.0 eq) were added and the reaction mixture was stirred at room temperature for 30 min. The volatiles were removed *in vacuo* and the crude product was purified by preparative HPLC (acetonitrile/water, 0.1% formic acid; 50→100% MeCN, 20 min) affording **GL-C4-FC** (1.8 mg, 2.3 µmol, 12% over 3 steps) as colourless solid.

Note: dichloromethane should be used as solvent for the transformation of **H-C4-FC** to **4** since the same reagents in THF resulted in significant activation of the 6-carboxylate to form a mix of the desired carbamate and the byproducts 6-carboxy amide and both carbamate and carboxy-amide (and unreacted starting material) in equal amounts with primary/secondary amines (reaction in DMF almost cleanly affords the carboxy-amide and no carbamate).

TLC *Rf* = 0.37 (*rp*, 60% MeCN)
^{1}H-NMR (800 MHz, DMSO-d_6): δ (ppm) = 8.25 (dd, J = 7.9, 2.5 Hz, 1H), 8.11 (d, J = 7.8 Hz, 1H), 7.80 (s, 1H), 7.44 (s, 1H), 7.20 (s, 1H), 7.13 (s, 1H), 6.91 (s, 1H), 4.29 (s, 1H), 4.22 – 4.15 (m, 2H), 4.14 – 4.00 (m, 1H), 4.03 – 3.88 (m, 1H), 3.88 – 3.72 (m, 2H), 3.72 – 3.35 (m, 4H), 3.25 – 2.94 (m, 1H), 2.38 – 2.21 (m, 2H), 1.75 (p, J = 6.6 Hz, 2H), 1.51 – 1.43 (m, 4H), 0.95 (t, J = 7.4 Hz, 3H), 0.86 (t, J = 6.4 Hz, 3H).
^{13}C-NMR (201 MHz, DMSO-d_6): δ (ppm) = 172.3, 168.0, 166.5, 162.8, 156.3, 152.1, 152.1, 150.6, 150.1/150.0, 148.9, 131.9, 129.2, 129.2, 128.6, 126.3, 124.8, 122.3, 118.2, 117.8, 113.5, 110.9, 102.4, 81.1, 69.5, 58.4, 57.9, 46.8, 38.9, 38.4, 37.1, 35.2, 30.8, 19.1, 18.5, 14.2, 14.1.
HRMS (ESI−): m/z calc. for $C_{36}H_{33}Cl_2N_2O_9S_2^-$ $[M-H]^-$: 771.1010, found: 771.1022.

7.2.4 Proof-of-concept rhodol probes and fluorophores

Synthetic Route for GL-Rho

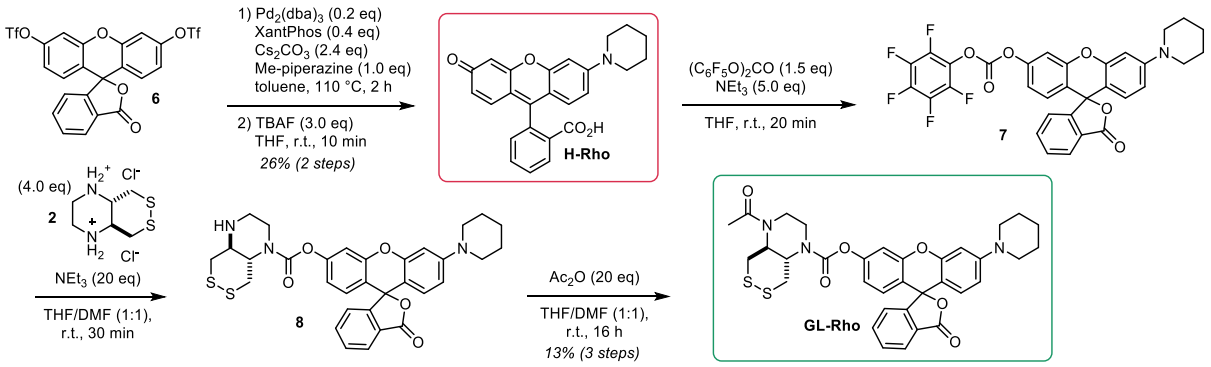

Fluorescein ditriflate **6** (He *et al.*[41], compound 3) and compound **2** (Zeisel, Felber *et al.*[40], compound 7T) were prepared according known procedures.

H-Rho

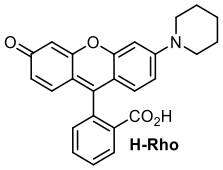

Buchwald-Hartwig coupling according to General Procedure D from fluorescein ditriflate **6** (0.15 g, 0.25 mmol, 1.0 eq, 0.05 M) with piperidine (25 µL, 0.25 mmol, 1.0 eq) followed by triflate cleavage according to General Procedure E(ii) (0.08 M). Purification by rp column chromatography: 10→45% MeCN.

The product **H-Rho** (26 mg, 66 µmol, 26% over 2 steps) was obtained as red solid.

^{1}H-NMR (400 MHz, MeOD-d_4): δ (ppm) = 8.07 (d, J = 7.3 Hz, 1H), 7.77 (td, J = 7.5, 1.3 Hz, 1H), 7.71 (td, J = 7.5, 1.1 Hz, 1H), 7.23 (d, J = 7.4 Hz, 1H), 6.86 – 6.78 (m, 2H), 6.75 – 6.68 (m, 3H), 6.60 (dd, J = 8.8, 2.3 Hz, 1H), 3.40 – 3.35 (m, 4H), 1.75 – 1.64 (m, 6H).
HRMS (ESI+): m/z calc. for $C_{25}H_{22}NO_4^+$ [M+H]$^+$: 400.1543, found: 400.1531.

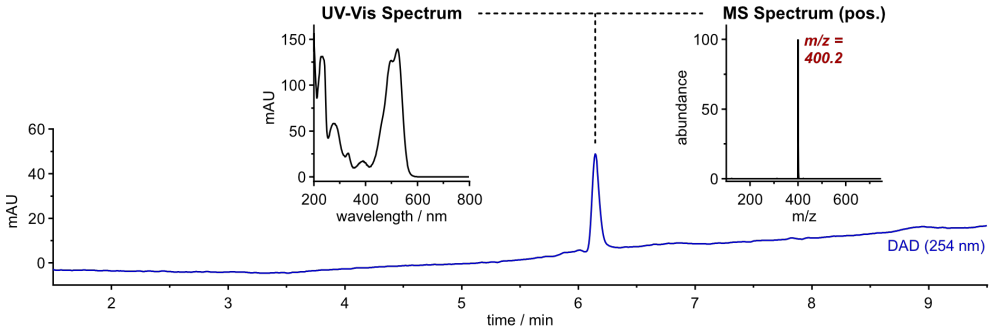

GL-Rho

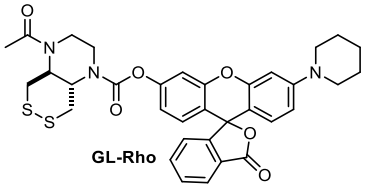

H-Rho (24 mg, 60 µmol, 1.0 eq, 0.03 M) was transformed into **8** following General Procedure C in THF with 1.5 eq bis(pentafluorophenyl)carbonate and 4.0 eq of amine **2** with 20 eq triethylamine. Then, acetic anhydride (0.11 mL, 1.2 mmol, 20 eq) was added to the reaction mixture of the intermediate product and stirred at room temperature for 16 h. The volatiles were removed *in vacuo* and the crude product was purified by preparative HPLC (acetonitrile/water, 0.1% formic acid; 20→100% MeCN, 20 min) affording **GL-Rho** (3.5 mg, 5.5 µmol, 13% over 3 steps) as light-red solid.

^{1}H-NMR (400 MHz, DMSO-d_6): δ (ppm) = 8.03 (d, J = 7.5 Hz, 1H), 7.81 (td, J = 7.5, 1.2 Hz, 1H), 7.74 (td, J = 7.5, 0.9 Hz, 1H), 7.31 (d, J = 7.6 Hz, 1H), 7.16 (s, 1H), 6.85 (t, J = 8.7 Hz, 1H), 6.80 (d, J = 8.7 Hz, 1H), 6.79 – 6.72 (m, 3H), 6.55 (d, J = 8.7 Hz, 1H), 4.27 (t, J = 10.6 Hz, 1H), 3.96 (s, 2H), 3.69 (dq, J = 35.9, 18.0 Hz, 5H), 3.26 (s, 4H), 3.05 (d, J = 11.7 Hz, 1H), 2.06 (s, 3H), 1.58 (s, 6H).
^{13}C-NMR (101 MHz, DMSO-d_6): δ (ppm) = 170.7, 169.1, 153.4, 152.8, 151.8, 136.2, 130.8, 129.4, 128.9, 126.4, 125.2, 124.5, 118.3, 116.8, 112.7, 110.5, 107.2, 101.2, 82.8, 58.9, 58.2, 48.8, 25.3, 24.4, 22.4.
HRMS (ESI+): m/z calc. for $C_{34}H_{34}N_3O_6S_2^+$ $[M+H]^+$: 644.1884, found: 644.1881.

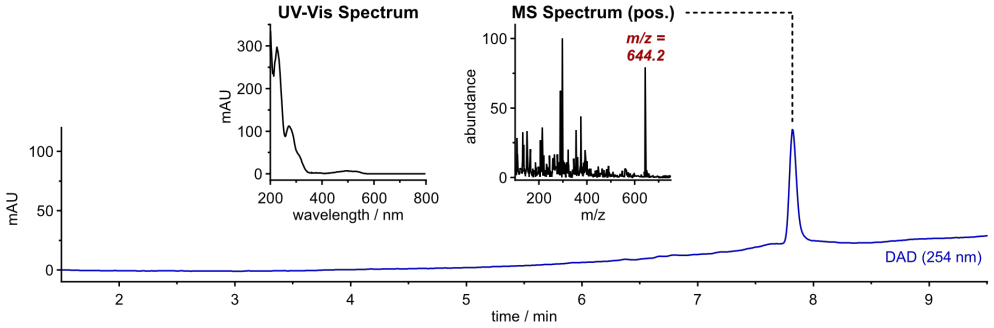

Synthetic Route for GL-Rho-A

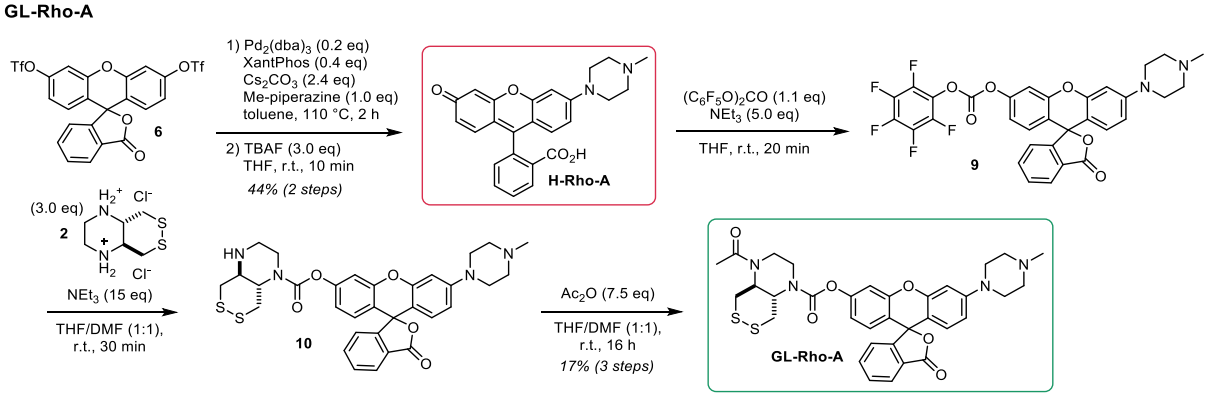

Fluorescein ditriflate (**6**) was prepared according to a known procedure (He *et al.*[41], compound 3).

H-Rho-A

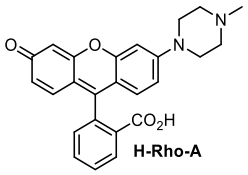

Buchwald-Hartwig coupling according to General Procedure D from fluorescein ditriflate **6** (0.15 g, 0.25 mmol, 1.0 eq, 0.05 M) with methyl piperazine (28 µL, 0.25 mmol, 1.0 eq) followed by triflate cleavage according to General Procedure E(ii) (0.08 M). Purification by rp column chromatography: 10→40% MeCN.

The product **H-Rho-A** (46 mg, 0.11 mmol, 44% over 2 steps) was obtained as red solid.

^{1}H-NMR (400 MHz, MeOD-d_4): δ (ppm) = 8.40 (s, 1H), 8.01 (d, J = 7.6 Hz, 1H), 7.77 (td, J = 7.4, 2.4 Hz, 1H), 7.70 (td, J = 7.3, 2.7 Hz, 1H), 7.19 (dd, J = 7.5, 4.1 Hz, 1H), 6.88 (dd, J = 24.0, 2.2 Hz, 1H), 6.77 (ddd, J = 11.7, 8.9, 2.3 Hz, 1H), 6.69 – 6.62 (m, 2H), 6.62 – 6.57 (m, 1H), 6.54 (dd, J = 8.7, 2.0 Hz, 1H), 3.67 – 3.58 (m, 3H), 3.44 (s, 2H), 3.26 (s, 2H), 3.14 – 3.05 (m, 2H), 2.72 (s, 2H).
HRMS (ESI+): m/z calc. for $C_{25}H_{23}N_2O_4^+$ [M+H]$^+$: 415.1652, found: 415.1641

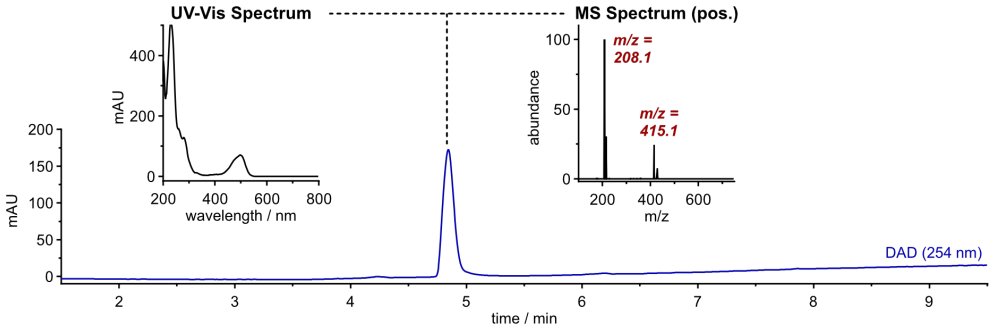

GL-Rho-A

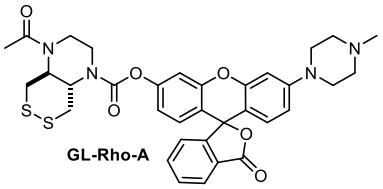

H-Rho-A (20 mg, 48 µmol, 1.0 eq, 0.02 M) was transformed into **10** following General Procedure C in THF with 1.1 eq bis(pentafluorophenyl)carbonate and 3.0 eq of amine **2** with 15 eq triethylamine. Then, acetic anhydride (34 µL, 0.36mmol, 7.5 eq) was added to the reaction mixture of the intermediate product and stirred at room temperature for 16 h. The volatiles were removed *in vacuo* and the crude product was purified by preparative HPLC (acetonitrile/water, 0.1% formic acid; 20→75% MeCN, 20 min) affording **GL-Rho-A** (5.3 mg, 8.1 µmol, 17% over 3 steps) as colourless solid.

^{1}H-NMR (400 MHz, DMSO-d_6): δ (ppm) = 8.10 (d, J = 7.5 Hz, 1H), 7.88 (t, J = 7.4 Hz, 1H), 7.81 (t, J = 7.4 Hz, 1H), 7.38 (d, J = 7.5 Hz, 1H), 7.23 (s, 1H), 6.94 (d, J = 8.4 Hz, 1H), 6.87 (dd, J = 12.2, 7.8 Hz, 3H), 6.65 (d, J = 8.8 Hz, 1H), 4.34 (t, J = 10.2 Hz, 1H), 4.04 (s, 2H), 3.87 – 3.61 (m, 4H), 3.60 – 3.45 (m, 2H), 3.12 (d, J = 12.3 Hz, 1H), 2.58 (s, 8H), 2.29 (s, 3H), 2.13 (s, 3H).
^{13}C-NMR (101 MHz, DMSO-d_6): δ (ppm) = 170.7, 169.1, 153.2, 152.8, 152.4, 152.0, 151.7, 136.2, 130.8, 129.4, 128.9, 126.3, 125.3, 124.5, 118.4, 116.8, 112.5, 110.6, 108.0, 101.3, 82.7, 59.9, 58.9, 54.8, 47.5, 46.2, 38.8, 37.3, 22.4.
HRMS (ESI+): m/z calc. for $C_{34}H_{35}N_4O_6S_2^+$ [M+H]$^+$: 659.1993, found: 659.1993

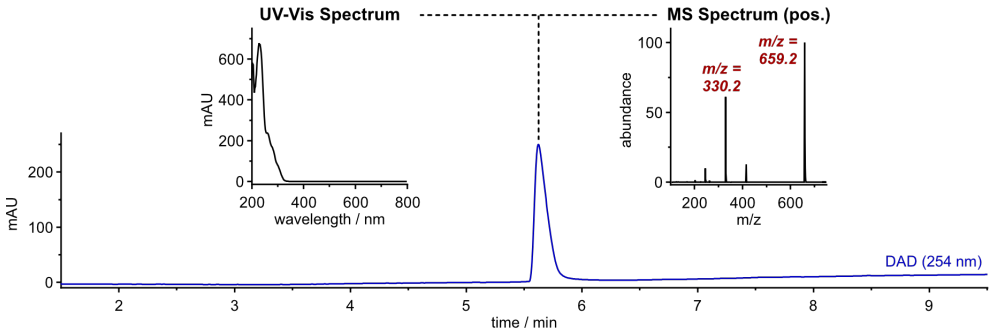

Synthetic Route for GL-Rho-C and GL-Rho-C^m

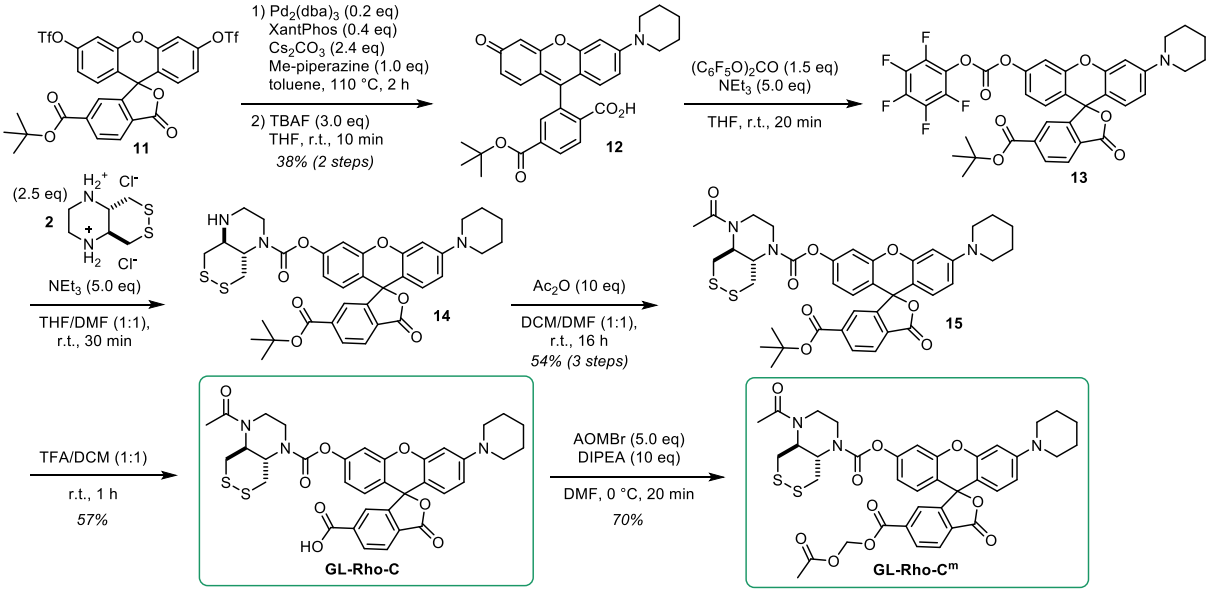

6-*tert*-Butoxycarbonylfluorescein (**11**) ditriflate was prepared according to a previously described procedure (Grimm *et al*.[42], compound S4).

Compound 12

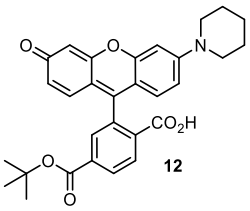

Buchwald-Hartwig coupling according to General Procedure D from ditriflate **11** (50 mg, 72 µmol, 1.0 eq, 0.04 M) with piperidine (7 µL, 72 µmol, 1.0 eq) followed by triflate cleavage according to General Procedure E(ii) (0.05 M). Semi-purification by rp column chromatography: 0→60% MeCN.

The product **12** (14 mg, 27 µmol, 38% over 2 steps) was obtained as red solid.

^{1}H-NMR (400 MHz, MeOD-d_4): δ (ppm) = 8.25 (dd, J = 8.1, 1.4 Hz, 1H), 8.12 (d, J = 8.1 Hz, 1H), 7.73 – 7.70 (m, 1H), 6.91 – 6.84 (m, 2H), 6.82 – 6.73 (m, 3H), 6.63 (dd, J = 8.9, 2.3 Hz, 1H), 3.44 (s, 4H), 1.69 (s, 6H), 1.55 (s, 9H).

LRMS (ESI+): m/z calc. for $C_{30}H_{30}NO_6^+$ $[M+H]^+$: 500.2, found: 500.2.

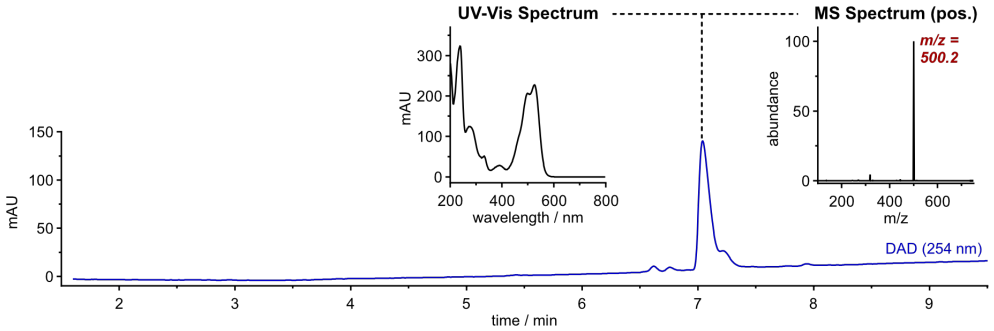

Compound 15

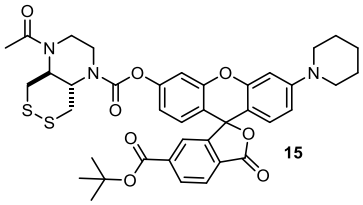

12 (5 mg, 10 µmol, 1.0 eq, 0.005 M) was transformed into **14** following General Procedure C in THF with 1.5 eq bis(pentafluorophenyl)carbonate and 2.5 eq of amine **2** with 5.0 eq triethylamine. Then, acetic anhydride (9.4 µL, 0.10mmol, 10 eq) was added to the reaction mixture of the intermediate product and stirred at room temperature for 16 h. The volatiles were removed *in vacuo* and the crude product was purified by np flash column chromatography (DCM/MeOH, 0→3% MeOH) affording **15** (4 mg, 5.4 µmol, 54% over 3 steps) as colourless solid.

TLC *Rf* = 0.70 (*np*, DCM:MeOH 19:1)
HRMS (ESI+): m/z calc. for $C_{39}H_{42}N_3O_8S_2^+$ [M+H]$^+$: 744.2408, found: 744.2396.

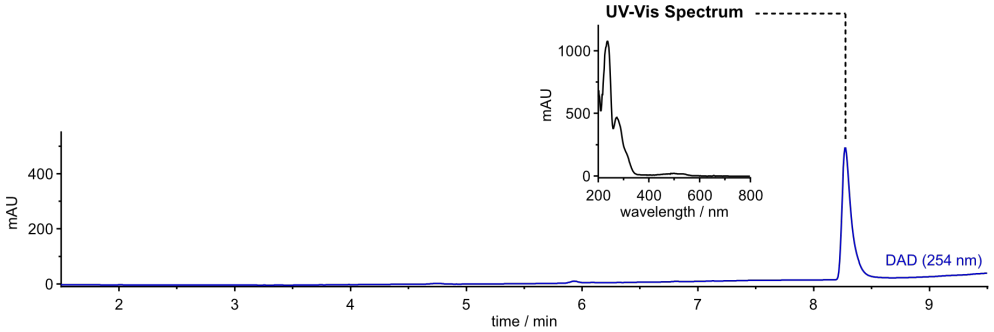

GL-Rho-C

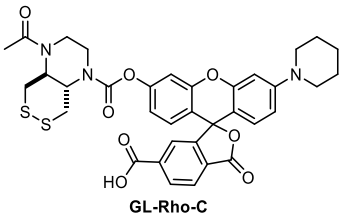

Prepared according to General Procedure F from **15** (4 mg, 5.4 µmol, 1.0 eq, 0.01 M). The crude product was purified by preparative HPLC (acetonitrile/water, 0.1% formic acid; 15→100% MeCN, 20 min) affording **GL-Rho-C** (2.1 mg, 3.1 µmol, 57%) as colourless solid.

^{1}H-NMR (800 MHz, DMSO-d_6): δ (ppm) = 8.21 (d, J = 8.1 Hz, 1H), 8.08 (d, J = 8.0 Hz, 1H), 7.64 (s, 1H), 7.16 (s, 1H), 6.87 – 6.82 (m, 2H), 6.78 (d, J = 2.5 Hz, 1H), 6.74 (dd, J = 9.0, 2.5 Hz, 1H), 6.58 (d, J = 8.9 Hz, 1H), 4.33 – 4.13 (m, 1H), 4.08 – 3.79 (m, 2H), 3.76 – 3.54 (m, 4H), 3.28 – 3.22 (m, 4H), 3.05 (d, J = 12.1 Hz, 1H), 2.05 (s, 3H), 1.61 – 1.53 (m, 6H).
^{13}C-NMR (201 MHz, DMSO-d_6): δ (ppm) = 170.1, 168.1, 166.1, 153.0, 152.5, 152.0, 151.7, 151.3, 131.0, 129.0, 128.5, 125.0, 124.2, 117.9, 115.9, 112.2, 110.1, 106.4, 100.7, 82.5, 58.4, 57.8, 48.3, 40.0, 24.8, 23.9, 21.9.
HRMS (ESI+): m/z calc. for $C_{35}H_{34}N_3O_8S_2^+$ [M+H]$^+$: 688.1782, found: 688.1765.

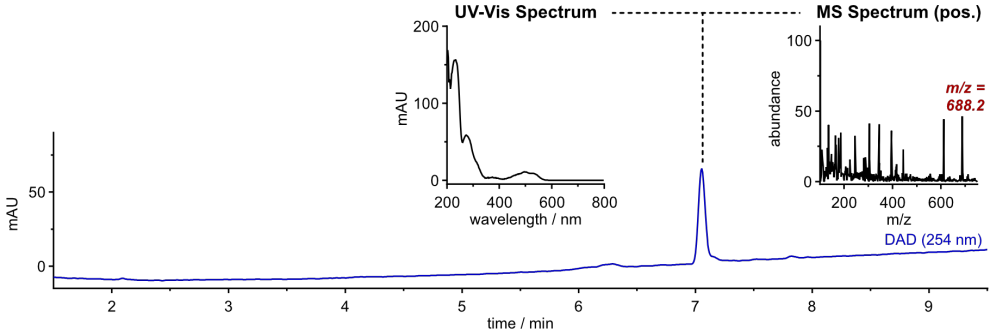

GL-Rho-C^{m}

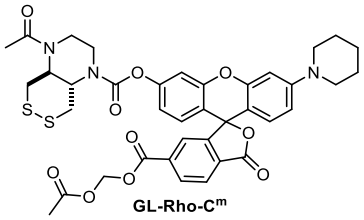

Prepared according to General Procedure G from **GL-Rho-C** (3.7 mg, 5.4 µmol, 1.0 eq, 0.01 M) with 10 eq DIPEA and 5.0 eq acetoxymethyl bromide. The crude product was purified by preparative HPLC (acetonitrile/water, 0.1% formic acid; 20→100% MeCN, 20 min) affording **GL-Rho-C^{m}** (1.6 mg, 2.1 µmol, 70%) as colourless solid.

^{1}H-NMR (800 MHz, DMSO-d_6): δ (ppm) = 8.27 (d, J = 8.1 Hz, 1H), 8.19 (d, J = 8.1 Hz, 1H), 7.75 (s, 1H), 7.17 (s, 1H), 6.88 (d, J = 8.6 Hz, 1H), 6.85 (s, 1H), 6.78 (s, 1H), 6.74 (dd, J = 9.0, 1.9 Hz, 1H), 6.60 (d, J = 8.9 Hz, 1H), 5.87 (s, 2H), 4.31 – 4.14 (m, 1H), 3.95 (s, 2H), 3.78 – 3.53 (m, 4H), 3.53 – 3.37 (m, 2H), 3.27 (s, 4H), 3.04 (d, J = 11.9 Hz, 1H), 2.06 (s, 6H), 1.57 (s, 6H).
^{13}C-NMR (201 MHz, DMSO-d_6): δ (ppm) = 169.3, 167.6, 163.4, 153.0, 152.5, 152.2, 151.7, 151.4, 135.1, 131.3, 130.3, 129.2, 128.6, 125.8, 124.7, 117.9, 115.6, 112.2, 110.1, 105.9, 100.7, 82.9, 80.1, 58.5, 57.7, 48.3, 40.0, 24.9, 23.9, 21.9, 20.5.
HRMS (ESI+): m/z calc. for $C_{38}H_{38}N_3O_{10}S_2^+$ $[M+H]^+$: 760.1993, found: 760.1996.

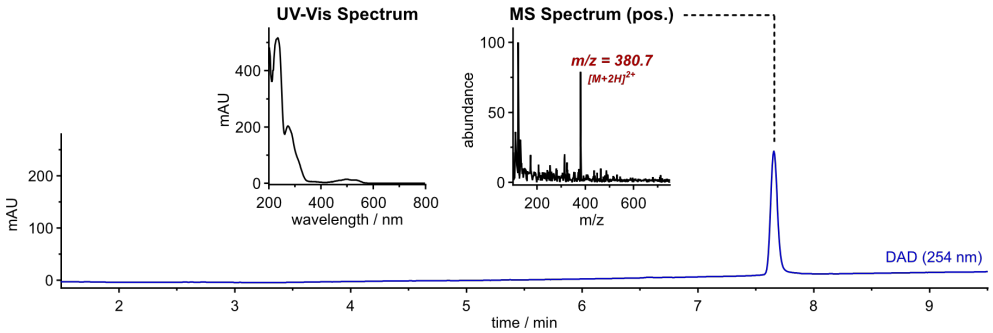

H-Rho-C

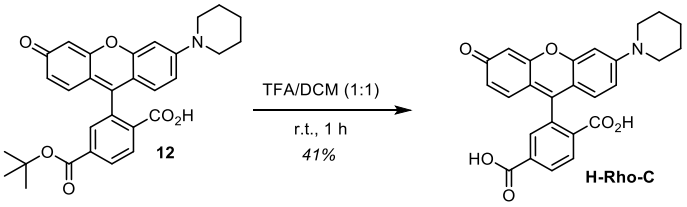

Prepared according to General Procedure F from **12** (6 mg, 12 µmol, 1.0 eq, 0.02 M). The crude product was purified by preparative HPLC (acetonitrile/water, 0.1% formic acid; 5→50% MeCN, 20 min) affording **H-Rho-C** (2.2 mg, 4.9 µmol, 41%) as red solid.

^{1}H-NMR (400 MHz, DMSO-d_6): δ (ppm) = 8.22 – 8.16 (m, 1H), 8.05 (d, J = 8.0 Hz, 1H), 7.60 (s, 1H), 6.76 (d, J = 2.4 Hz, 1H), 6.70 (dd, J = 9.0, 2.5 Hz, 1H), 6.68 (d, J = 2.3 Hz, 1H), 6.59 (d, J = 8.7 Hz, 1H), 6.57 – 6.49 (m, 2H), 3.25 (s, 4H), 1.56 (s, 6H).
^{13}C-NMR (101 MHz, DMSO-d_6): δ (ppm) = 168.2, 166.3, 159.6, 152.8, 152.1, 151.9, 140.3, 130.8, 129.2, 128.4, 124.9, 124.3, 112.6, 111.9, 109.3, 106.9, 102.2, 100.8, 83.7, 48.4, 24.8, 23.9.
HRMS (ESI+): m/z calc. for $C_{26}H_{22}NO_6^+$ $[M+H]^+$: 444.1442, found: 444.1435.

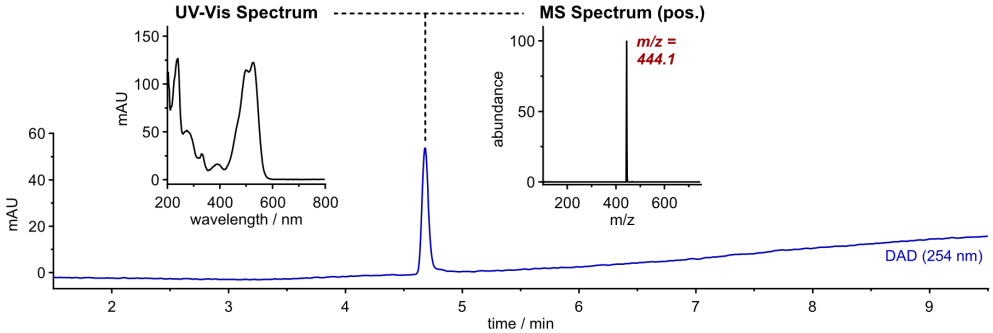

Synthetic Route for GL-Rho-AC and GL-Rho-AC^m (= GL-TraG)

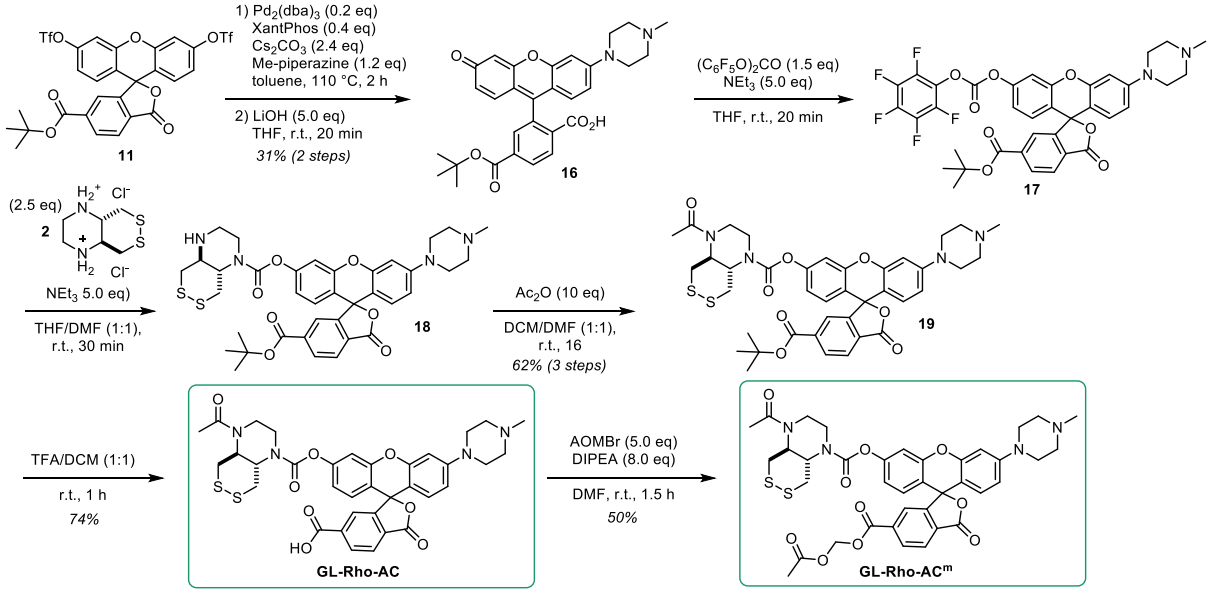

Compound 16

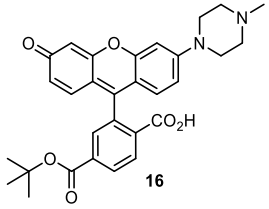

Buchwald-Hartwig coupling according to General Procedure D from triflate **11** (70 mg, 0.10 mmol, 1.0 eq, 0.05 M) with methyl piperazine (13 µL, 0.12 mmol, 1.2 eq) followed by triflate cleavage according to General Procedure E(i) (0.07 M). Purification by rp column chromatography: 2→35% MeCN.

The product **16** (16 mg, 31 µmol, 31% over 2 steps) was obtained as red solid.

TLC *Rf* = 0.43 (*np*, DCM:MeOH 4:1)
^{1}H-NMR (400 MHz, MeOD-d_4): δ (ppm) = 8.25 (dd, J = 8.0, 1.2 Hz, 1H), 8.08 (d, J = 8.0 Hz, 1H), 7.67 (s, 1H), 6.84 (d, J = 1.8 Hz, 1H), 6.75 (dd, J = 9.0, 1.9 Hz, 1H), 6.71 – 6.61 (m, 3H), 6.55 (dd, J = 8.8, 2.2 Hz, 1H), 3.47 (s, 4H), 3.28 (s, 4H), 2.86 (s, 3H), 1.52 (s, 9H).
HRMS (ESI+): m/z calc. for $C_{30}H_{31}N_2O_6^+$ $[M+H]^+$: 515.2177, found: 515.2169.

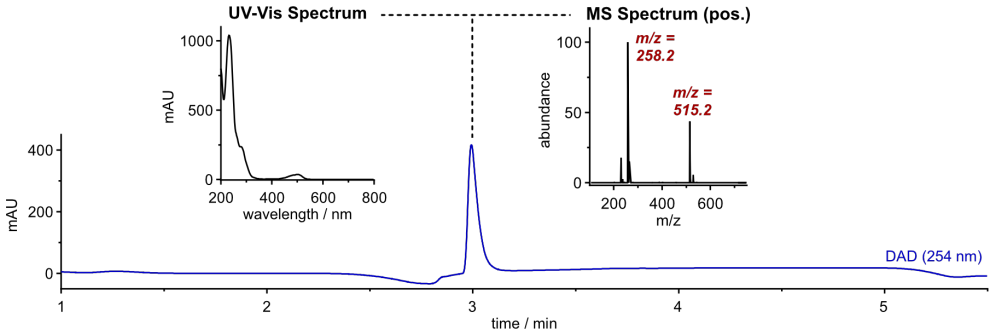

Compound 19

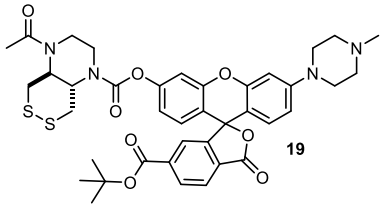

16 (30 mg, 51 µmol, 1.0 eq, 0.03 M) was transformed into **19** following General Procedure C in THF with 1.5 eq bis(pentafluorophenyl)carbonate and 2.5 eq of amine **2** with 5 eq triethylamine (purification: 15→100% MeCN). Then, acetic anhydride (16 µL, 0.17mmol, 10 eq) was added to the reaction mixture of the intermediate product and stirred at room temperature for 16 h. The volatiles were removed *in vacuo* and the crude product was was purified by np flash column chromatography (DCM/MeOH, 0→8% MeOH) affording **19** (8 mg, 11 µmol, 62% over 3 steps) as colourless solid.

TLC *Rf* = 0.40 (*np*, DCM/MeOH 19:1)
HRMS (ESI+): m/z calc. for $C_{39}H_{43}N_4O_8S_2^+$ $[M+H]^+$: 759.2517, found: 759.2499

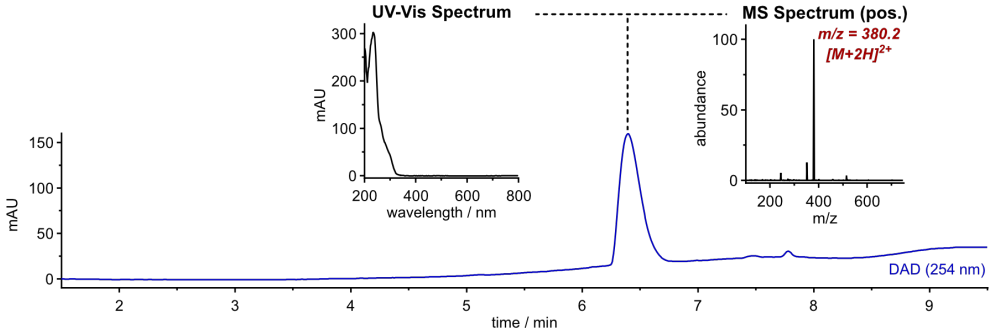

GL-Rho-AC

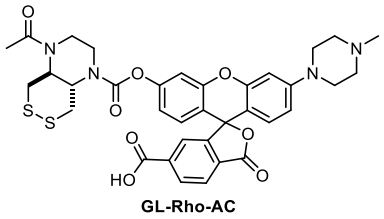

Prepared according to General Procedure F from **19** (8 mg, 11 µmol, 1.0 eq, 0.02 M). The crude product was purified by preparative HPLC (acetonitrile/water, 0.1% formic acid; 5→40% MeCN, 20 min) affording **GL-Rho-AC** (5.5 mg, 8.0 µmol, 74%) as colourless solid.

^{1}H-NMR (800 MHz, DMSO-d_6): δ (ppm) = 8.19 (d, J = 8.0 Hz, 1H), 8.05 (d, J = 7.4 Hz, 1H), 7.61 (s, 1H), 7.16 (s, 1H), 6.85 (s, 2H), 6.82 (s, 1H), 6.76 (d, J = 8.6 Hz, 1H), 6.61 (d, J = 8.8 Hz, 1H), 4.34 – 4.13 (m, 1H), 4.08 – 3.79 (m, 2H), 3.77 – 3.55 (m, 4H), 3.53 – 3.39 (m, 2H), 3.26 (s, 4H), 3.05 (d, J = 12.1 Hz, 1H), 2.59 – 2.53 (m, 4H), 2.30 (s, 3H), 2.05 (s, 3H).
^{13}C-NMR (201 MHz, DMSO-d_6): δ (ppm) = 170.1, 168.2, 166.5, 163.3, 152.6, 152.6, 152.0, 151.5, 151.2, 130.9, 129.1, 128.5, 127.7, 124.8, 124.1, 117.9, 116.0, 112.0, 110.1, 107.4, 101.0, 82.2, 58.5, 53.8, 46.6, 45.1, 36.9, 21.9.
HRMS (ESI+): m/z calc. for $C_{35}H_{35}N_4O_8S_2^+$ $[M+H]^+$: 703.1891, found: 703.1891.

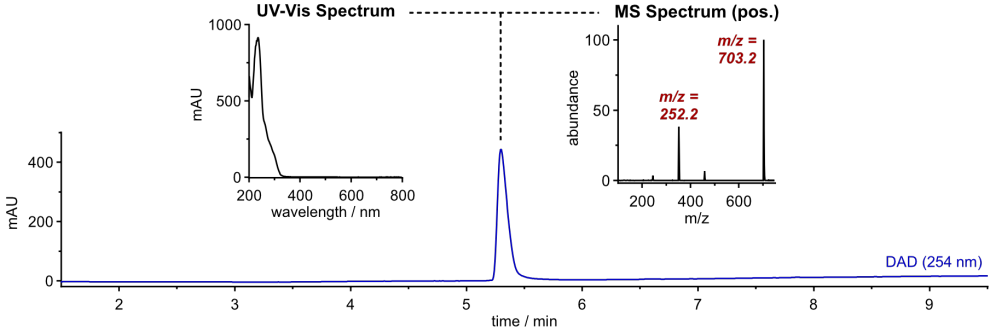

GL-Rho-AC^{m} (= GL-TraG)

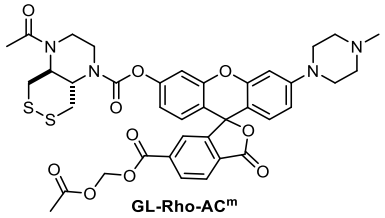

Prepared according to General Procedure G from **GL-Rho-AC** (5.5 mg, 7.8 µmol, 1.0 eq, 0.01 M) with 10 eq DIPEA and 5.0 eq acetoxymethyl bromide. The crude product was purified by preparative HPLC (acetonitrile/water, 0.1% formic acid; 10→50% MeCN, 20 min) affording **GL-Rho-AC^{m}** (2.2 mg, 2.7 µmol, 50%) as colourless solid.

TLC *Rf* = 0.24 (*np*, 3% MeOH / DCM)
^{1}H-NMR (400 MHz, DMSO-d_6): δ (ppm) = 8.27 (d, J = 8.1 Hz, 1H), 8.20 (d, J = 8.0 Hz, 1H), 7.75 (s, 1H), 7.17 (s, 1H), 6.89 (d, J = 8.6 Hz, 1H), 6.87 – 6.80 (m, 2H), 6.76 (d, J = 9.0 Hz, 1H), 6.63 (d, J = 8.9 Hz, 1H), 5.86 (s, 2H), 4.27 (t, J = 10.1 Hz, 1H), 4.09 – 3.83 (m, 2H), 3.79 – 3.52 (m, 4H), 3.24 (d, J = 4.7 Hz, 4H), 3.04 (d, J = 12.0 Hz, 1H), 2.44 – 2.39 (m, 4H), 2.21 (s, 3H), 2.06 (s, 6H).
HRMS (ESI+): m/z calc. for $C_{38}H_{39}N_4O_{10}S_2^+$ [M+H]$^+$: 775.2102, found: 775.2094

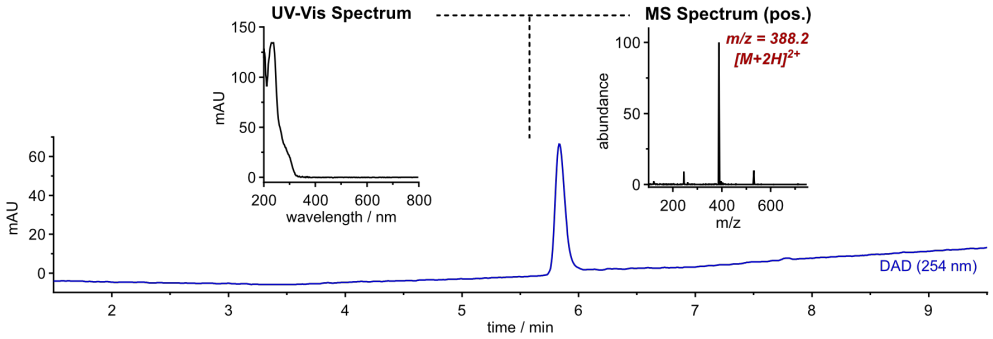

H-Rho-AC

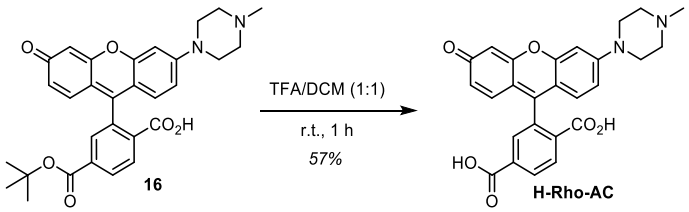

Prepared according to General Procedure F from **16** (4 mg, 7.8 µmol, 1.0 eq, 0.02 M). The crude product was purified by preparative HPLC (acetonitrile/water, 0.1% formic acid; 2→30% MeCN, 20 min) affording **H-Rho-AC** (2.0 mg, 4.4 µmol, 57%) as red solid.

^{1}H-NMR (400 MHz, DMSO-d_6): δ (ppm) = 8.18 (d, J = 9.1 Hz, 1H), 7.99 (d, J = 7.9 Hz, 1H), 7.55 (s, 1H), 6.80 (d, J = 2.3 Hz, 1H), 6.72 (dd, J = 9.0, 2.3 Hz, 1H), 6.67 (d, J = 2.2 Hz, 1H), 6.63 – 6.49 (m, 3H), 3.24 (s, 4H), 2.27 (s, 3H).
HRMS (ESI+): m/z calc. for $C_{26}H_{23}N_2O_6^+$ [M+H]$^+$: 459.1551, found: 459.1541.

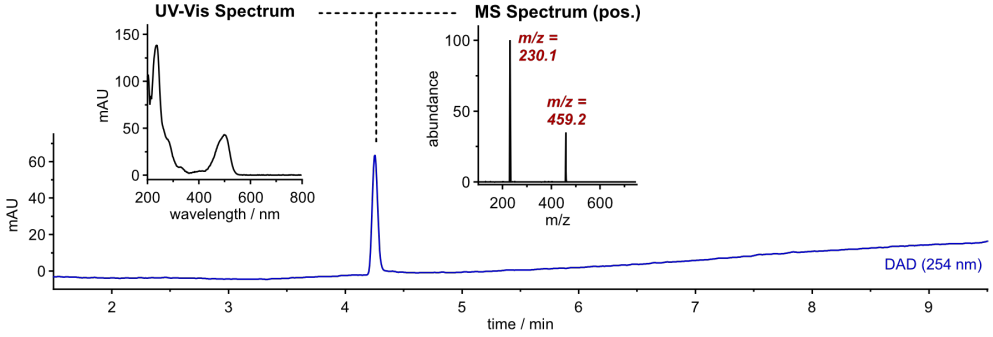

7.2.5 Hydrogen Peroxide Sensor HP-TraG

Synthetic Route for HP-TraG

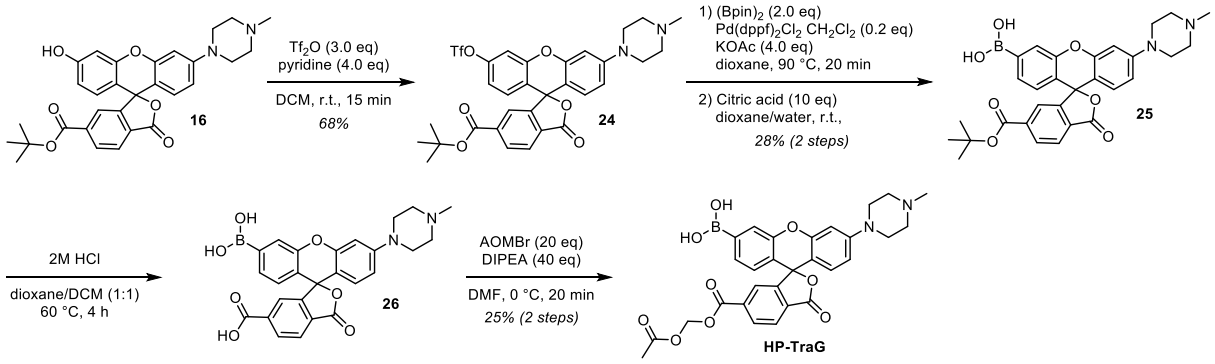

Compound 24

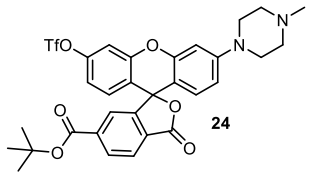

16 (8 mg, 16 µmol, 1.0 eq) was dissolved in anhydrous DCM (1.5 mL), pyridine (5 µL, 62 µmol, 4.0 eq) and trifluoromethanesulfonic anhydride (7.8 µL, 46 µmol, 3.0 eq) were added and the reaction mixture was stirred at room temperature for 15 min. The volatiles were removed *in vacuo* and the crude product was purified by rp flash column chromatography (5→60% MeCN, acetonitrile/water, 0.1% FA) to afford **24** (6.8 mg, 11 µmol, 68%) as light-red solid.

TLC *Rf* = 0.18 (*np*, 4% MeOH / DCM)
^{1}H-NMR (600 MHz, CD_2Cl_2): *δ* (ppm) = 8.25 (dd, J = 8.0, 1.3 Hz, 1H), 8.06 (dd, J = 8.0, 0.7 Hz, 1H), 7.75 (dd, J = 1.2, 0.8 Hz, 1H), 7.28 (d, J = 2.5 Hz, 1H), 6.98 (dd, J = 8.8, 2.5 Hz, 1H), 6.89 (d, J = 8.8 Hz, 1H), 6.77 (d, J = 2.3 Hz, 1H), 6.68 (dd, J = 8.9, 2.3 Hz, 1H), 6.65 (d, J = 8.8 Hz, 1H), 3.40 – 3.35 (m, 4H), 2.73 (s, 4H), 2.45 (s, 3H), 1.53 (s, 9H).
^{13}C-NMR (151 MHz, CD_2Cl_2): *δ* (ppm) = 168.4, 164.3, 153.3, 152.7, 152.7, 152.3, 150.5, 139.2, 131.6, 130.6, 129.9, 129.1, 125.4, 125.3, 120.2, 119.9, 118.0, 117.0, 112.9, 110.9, 108.3, 102.3, 82.9, 82.6, 54.7, 47.6, 45.6, 28.1.
HRMS (ESI+): m/z calc. for $C_{31}H_{30}F_3N_2O_8S^+$ $[M+H]^+$: 647.1669, found: 647.1671.

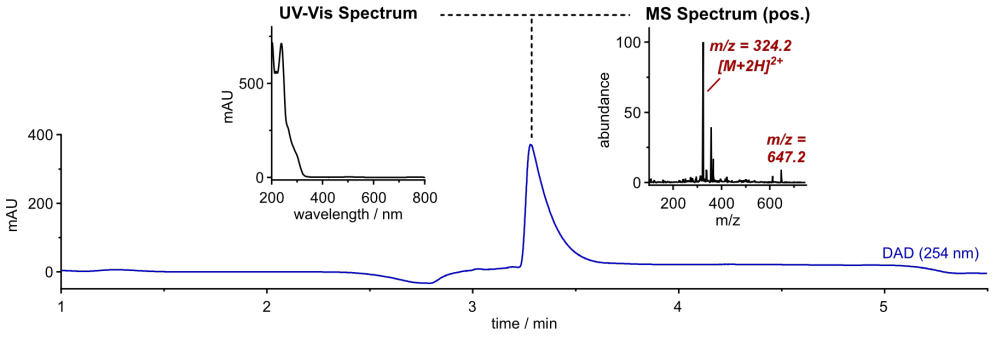

Compound 25

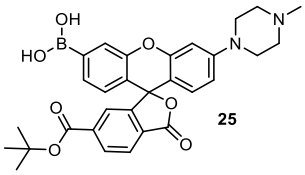

25

24 (6.8 mg, 11 µmol, 1.0 eq) was dissolved in anhydrous 1,4-dioxane (1 mL) under nitrogen atmosphere and degassed by bubbling nitrogen through the solution for 2 min. Potassium acetate (4.1 mg, 42 µmol, 4.0 eq), bis(pinacolato)diboron ($(Bpin)_2$, 5.3 mg, 21 µmol, 2.0 eq) and bis(diphenylphosphino)ferrocene)palladium(II) dichloride ($Pd(dppf)Cl_2$, 1.5 mg, 2.1 µmol, 20 mol%) were added and the mixture was degassed for 5 min. Then the reaction mixture was heated to 90 °C for 20 min and allowed to cool to room temperature. Citric acid (20 mg, 0.11 mmol, 20 eq) was dissolved in water (0.2 mL), added to the reaction mixture and heated to 40 °C for 40 min. The crude product was semi-purified by preparative HPLC (acetonitrile/water, 0.1% formic acid; 5→60% MeCN, 20 min) affording **25** (1.6 mg, 3.0 µmol, 28% over 2 steps) as light-red solid.

LRMS (ESI+): m/z calc. for $C_{30}H_{32}BN_2O_7^+$ $[M+H]^+$: 543.2, found: 543.2.

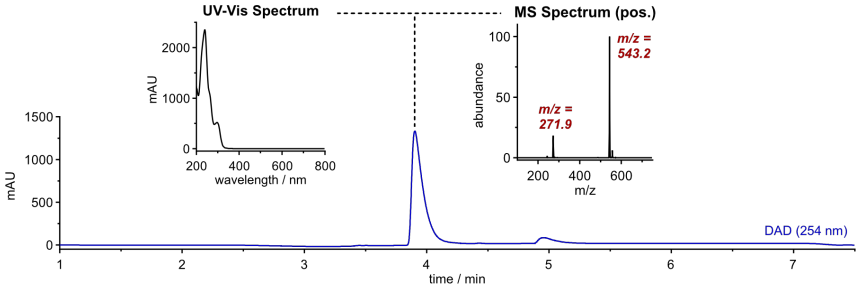

HP-TraG

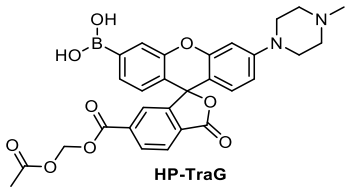

25 (1.6 mg, 3.0 µmol, 1.0 eq) was dissolved in anhydrous DCM (0.5 mL) and HCl (4 M in dioxane, 0.5 mL) was added. The reaction mixture was heated to 60 °C for 4 h and the volatiles were removed *in vacuo*. The intermediate product was acetoxymethylated without purification following General Procedure G (0.01 M) with 40 eq DIPEA and 20 eq acetoxymethyl bromide. The crude product was purified by preparative HPLC (acetonitrile/water, 0.1% formic acid; 5→40% MeCN, 20 min) affording **HP-TraG** (0.41 mg, 0.73 µmol, 25% over 2 steps) as light-red solid. The reaction can deliver a second species that contains an additional formaldehyde equivalent (m/z +30)) at the pendant carboxylate (^{1}H-NMR suggests an ortho-ester or acetoxymethoxymethyl ($AcOCH_2OCH_2O$-ester)), that cannot easily be separated from it by prep-HPLC and np-flash column chromatography, but which has identical performance with respect to hydrogen peroxide oxidation and esterase cleavage and therefore chromatographed **HP-TraG** can be used without any issues (see Figs S27−28).

^{1}H-NMR (HP-TraG): (600 MHz, DMSO-d_6): δ (ppm) = 8.47 (s, 2H), 8.31 – 8.25 (m, 1H), 8.23 – 8.17 (m, 1H), 7.70 (s, 2H), 7.45 (dd, J = 7.8, 1.0 Hz, 1H), 6.83 (d, J = 2.4 Hz, 1H), 6.80 – 6.71 (m, 2H), 6.63 (dd, J = 8.9, 2.4 Hz, 1H), 5.86 (s, 2H), 3.27 – 3.22 (m, 4H), 2.46 – 2.40 (m, 4H), 2.21 (s, 3H), 2.05 (s, 3H).

^{1}H-NMR (*side product*): (600 MHz, DMSO-d_6): δ (ppm) = 8.47 (s, 2H), 8.31 – 8.25 (m, 1H), 8.23 – 8.17 (m, 1H), 7.70 (s, 2H), 7.45 (dd, J = 7.8, 1.0 Hz, 1H), 6.83 (d, J = 2.4 Hz, 1H), 6.80 – 6.71 (m, 2H), 6.63 (dd, J = 8.9, 2.4 Hz, 1H), 5.54 (s, 2H), 5.32 (s, 2H), 3.27 – 3.22 (m, 4H), 2.46 – 2.40 (m, 4H), 2.21 (s, 3H), 1.71 (s, 3H).

HRMS (HP-TraG): (ESI+): m/z calc. for $C_{29}H_{28}BN_2O_9^+$ $[M+H]^+$: 559.1882, found: 559.1895.

HRMS (*side product*): (ESI+): m/z calc. for $C_{30}H_{30}BN_2O_{10}^+$ $[M+H]^+$: 589.1988, found: 589.2001.

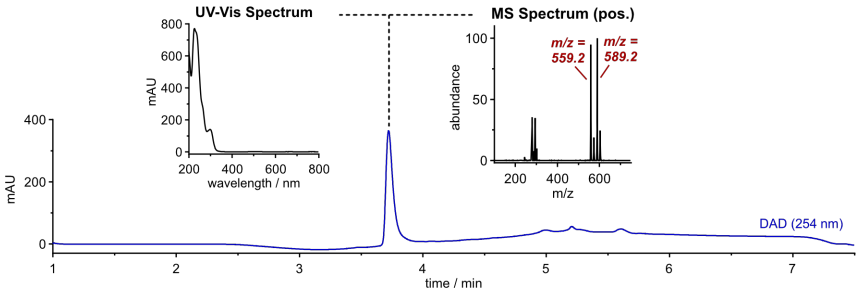

7.2.6 Enzyme Activity Probe TR-TraG

Synthetic Route for TR-TraG

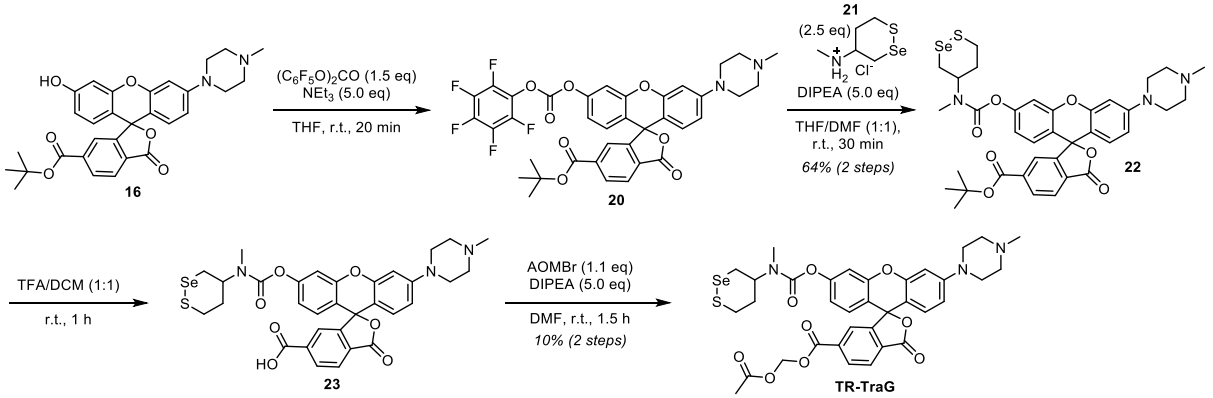

Compound **21** was prepared according to a previously described procedure (Zeisel *et al*.[31], compound S20 followed by Boc-deprotection).

Compound 22

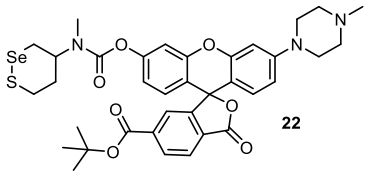

16 (30 mg, 51 µmol, 1.0 eq) was dissolved in anhydrous THF (2 mL) under nitrogen atmosphere, DIPEA (86 µL, 0.51 mmol, 10 eq) and bis(pentafluorophenyl)carbonate (30 mg, 76 µmol, 1.5 eq) were added and the reaction mixture was stirred at room temperature for 20 min. **21** (9.8 mg, 42 µmol, 2.5 eq) was added as solid to the mixture, then anhydrous DMF was added. The reaction mixture was stirred at room temperature for 30 min. The volatiles were removed *in vacuo* and the crude product was semi-purified by np flash column chromatography (DCM/MeOH, 0→6% MeOH) to afford **22** (8 mg, 11 µmol, 64% over 2 steps) as light-red solid.

TLC *Rf* = 0.41 (*np*, 8% MeOH / DCM)
HRMS (SI): m/z calc. for $C_{36}H_{40}N3O_7SSe^+$ $[M+H]^+$: 738.1747, found: 738.1726.

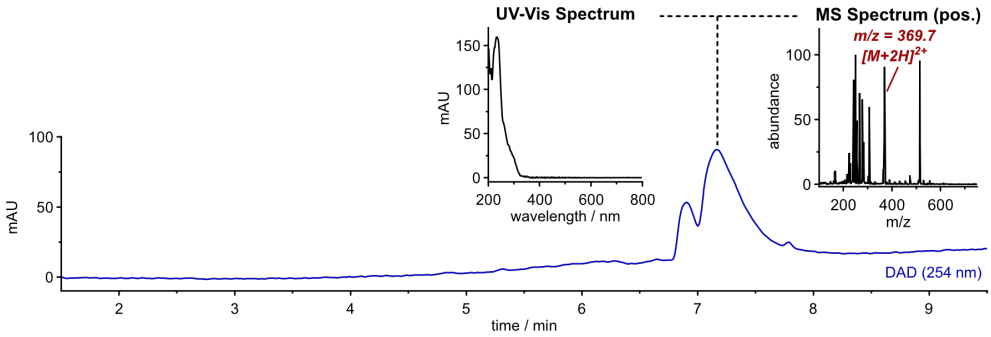

TR-TraG

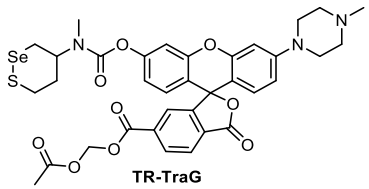

22 (8 mg, 11 µmol, 1.0 eq, 0.02 M) was deprotected according to General Procedure F. The intermediate product was acetoxymethylated without purification following General Procedure G with 10 eq DIPEA and 5.0 eq acetoxymethyl bromide. The crude product was purified by preparative HPLC (acetonitrile/water, 0.1% formic acid; 15→50% MeCN, 20 min) affording **TR-TraG** (0.82 mg, 1.1 µmol, 10% over 2 steps) as colourless solid.

^{1}H-NMR (400 MHz, MeOD-d_4): δ (ppm) = 8.49 (s, 1H), 8.34 (dd, J = 8.0, 1.3 Hz, 1H), 8.13 (d, J = 8.0 Hz, 1H), 7.83 (s, 1H), 7.15 – 7.11 (m, 1H), 6.88 – 6.83 (m, 1H), 6.82 – 6.76 (m, 2H), 6.72 (dd, J = 8.9, 2.4 Hz, 1H), 6.64 (d, J = 8.9 Hz, 1H), 5.92 (s, 2H), 4.35 (s, 4H), 4.23 (d, J = 40.6 Hz, 1H), 3.51 – 3.40 (m, 1H), 3.25 (d, J = 12.6 Hz, 1H), 3.18 – 3.09 (m, 1H), 3.01 (s, 2H), 2.92 (s, 1H), 2.65 – 2.59 (m, 5H), 2.36 (s, 3H), 2.30 (d, J = 8.7 Hz, 1H), 2.07 (s, 3H).
HRMS (ESI+): m/z calc. for $C_{35}H_{36}N_3O_9SSe^+$ $[M+H]^+$: 754.1332, found: 754.1320.

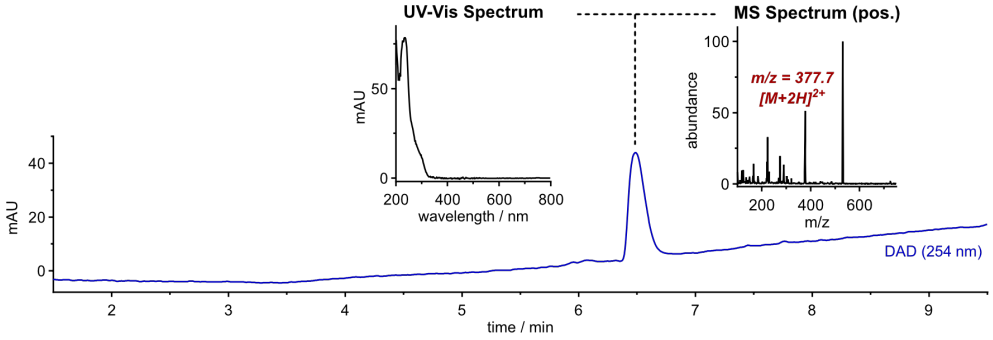

8 References

(1) Fukuda, T.; Yokomizo, S.; Casa, S.; Monaco, H.; Manganiello, S.; Wang, H.; Lv, X.; Ulumben, A. D.; Yang, C.; Kang, M.-W.; Inoue, K.; Fukushi, M.; Sumi, T.; Wang, C.; Kang, H.; Bao, K.; Henary, M.; Kashiwagi, S.; Soo Choi, H. Fast and Durable Intraoperative Near-Infrared Imaging of Ovarian Cancer Using Ultrabright Squaraine Fluorophores. *Angew. Chem. Int. Ed.* **2022**, *61* (17), e202117330. https://doi.org/10.1002/anie.202117330.

(2) Jia, S.; Lin, E. Y.; Mobley, E. B.; Lim, I.; Guo, L.; Kallepu, S.; Low, P. S.; Sletten, E. M. Water-Soluble Chromenylium Dyes for Shortwave Infrared Imaging in Mice. *Chem* **2023**, *9* (12), 3648–3665. https://doi.org/10.1016/j.chempr.2023.08.021.

(3) Izumi, S.; Urano, Y.; Hanaoka, K.; Terai, T.; Nagano, T. A Simple and Effective Strategy To Increase the Sensitivity of Fluorescence Probes in Living Cells. *J. Am. Chem. Soc.* **2009**, *131* (29), 10189–10200. https://doi.org/10.1021/ja902511p.

(4) Turnbull, J. L.; Benlian, B. R.; Golden, R. P.; Miller, E. W. Phosphonofluoresceins: Synthesis, Spectroscopy, and Applications. *J. Am. Chem. Soc.* **2021**. https://doi.org/10.1021/jacs.1c01139.

(5) Caldwell, S. T.; O'Byrne, S. N.; Wilson, C.; Cvetko, F.; Murphy, M. P.; McCarron, J. G.; Hartley, R. C. Photoactivated Release of Membrane Impermeant Sulfonates inside Cells. *Chem. Commun.* **2021**, *57* (32), 3917–3920. https://doi.org/10.1039/D0CC07713E.

(6) Rusha, L.; Miller, S. C. Design and Application of Esterase-Labile Sulfonate Protecting Groups. *Chem. Commun.* **2011**, *47* (7), 2038–2040. https://doi.org/10.1039/C0CC04796A.

(7) Li, X.; Higashikubo, R.; Taylor, J.-S. Use of Multiple Carboxylates to Increase Intracellular Retention of Fluorescent Probes Following Release From Cell Penetrating Fluorogenic Conjugates. *Bioconjugate Chem.* **2008**, *19* (1), 50–56. https://doi.org/10.1021/bc070079y.

(8) Ye, H.; Sun, L.; Pang, Z.; Ji, X.; Jiao, Y.; Tu, X.; Huang, H.; Tang, X.; Xi, Z.; Yi, L. Cell-Trappable BODIPY-NBD Dyad for Imaging of Basal and Stress-Induced H2S in Live Biosystems. *Anal. Chem.* **2022**, *94* (3), 1733–1741. https://doi.org/10.1021/acs.analchem.1c04324.

(9) Fosnacht, K. G.; Hammers, M. D.; Earp, M. S.; Gilbert, A. K.; Pluth, M. D. A Cell Trappable Methyl Rhodol-Based Fluorescent Probe for Hydrogen Sulfide Detection. *Chem. Asian J.* **2022**, *17* (16), e202200426. https://doi.org/10.1002/asia.202200426.

(10) Dickinson, B. C.; Peltier, J.; Stone, D.; Schaffer, D. V.; Chang, C. J. Nox2 Redox Signaling Maintains Essential Cell Populations in the Brain. *Nat. Chem. Biol.* **2011**, *7* (2), 106–112. https://doi.org/10.1038/nchembio.497.

(11) Jiang, G.; Lou, X.-F.; Zuo, S.; Liu, X.; Ren, T.-B.; Wang, L.; Zhang, X.-B.; Yuan, L. Tuning the Cellular Uptake and Retention of Rhodamine Dyes by Molecular Engineering for High-Contrast Imaging of Cancer Cells. *Angew. Chem. Int. Ed.* **2023**, e202218613. https://doi.org/10.1002/anie.202218613.

(12) Huang, Z.; Terpetschnig, E.; You, W.; Haugland, R. P. 2-(2′-Phosphoryloxyphenyl)-4(3*H*)-Quinazolinone Derivatives as Fluorogenic Precipitating Substrates of Phosphatases. *Anal.Biochem.* **1992**, *207* (1), 32–39. https://doi.org/10.1016/0003-2697(92)90495-S.

(13) Liu, H.-W.; Li, K.; Hu, X.-X.; Zhu, L.; Rong, Q.; Liu, Y.; Zhang, X.-B.; Hasserodt, J.; Qu, F.-L.; Tan, W. In Situ Localization of Enzyme Activity in Live Cells by a Molecular Probe Releasing a Precipitating Fluorochrome. *Angew. Chem. Int. Ed.* **2017**, *56* (39), 11788–11792. https://doi.org/10.1002/anie.201705747.

(14) Liu, Y.; Xu, C.; Liu, H.-W.; Teng, L.; Huan, S.; Yuan, L.; Zhang, X.-B. Precipitated Fluorophore-Based Molecular Probe for In Situ Imaging of Aminopeptidase N in Living Cells and Tumors. *Anal. Chem.* **2021**, *93* (16), 6463–6471. https://doi.org/10.1021/acs.analchem.1c00280.

(15) Zhang, W.; Fan, W.; Zhou, Z.; Garrison, J. Synthesis and Evaluation of Radiolabeled Phosphoramide Mustard with Selectivity for Hypoxic Cancer Cells. *ACS Med. Chem. Lett.* **2017**, *8* (12), 1269–1274. https://doi.org/10.1021/acsmedchemlett.7b00355.

(16) Rosser, B. G.; Powers, S. P.; Gores, G. J. Calpain Activity Increases in Hepatocytes Following Addition of ATP. Demonstration by a Novel Fluorescent Approach. *J. Biol. Chem.* **1993**, *268* (31), 23593–23600. https://doi.org/10.1016/S0021-9258(19)49504-5.

(17) Ito, H.; Kawamata, Y.; Kamiya, M.; Tsuda-Sakurai, K.; Tanaka, S.; Ueno, T.; Komatsu, T.; Hanaoka, K.; Okabe, S.; Miura, M.; Urano, Y. Red-Shifted Fluorogenic Substrate for Detection of lacZ-Positive Cells in Living Tissue with Single-Cell Resolution. *Angew. Chem. Int. Ed.* **2018**, *57* (48), 15702–15706. https://doi.org/10.1002/anie.201808670.

(18) Obara, R.; Kamiya, M.; Tanaka, Y.; Abe, A.; Kojima, R.; Kawaguchi, T.; Sugawara, M.; Takahashi, A.; Noda, T.; Urano, Y. γ-Glutamyltranspeptidase (GGT)-Activatable Fluorescence Probe for Durable Tumor Imaging. *Angew. Chem. Int. Ed.* **2021**, *133* (4), 2153–2157. https://doi.org/10.1002/ange.202013265.

(19) Iwashita, H.; Castillo, E.; Messina, M. S.; Swanson, R. A.; Chang, C. J. A Tandem Activity-Based Sensing and Labeling Strategy Enables Imaging of Transcellular Hydrogen Peroxide Signaling. *Proc. Natl. Acad. Sci. U.S.A.* **2021**, *118* (9), e2018513118. https://doi.org/10.1073/pnas.2018513118.

(20) Kashima, H.; Kamiya, M.; Obata, F.; Kojima, R.; Nakano, S.; Miura, M.; Urano, Y. Photoactivatable Fluorophores for Durable Labelling of Individual Cells. *Chem. Commun.* **2021**, *57* (47), 5802–5805. https://doi.org/10.1039/D1CC01488A.

(21) Wang, S.; Tan, W.; Lang, W.; Qian, H.; Guo, S.; Zhu, L.; Ge, J. Fluorogenic and Mitochondria-Localizable Probe Enables Selective Labeling and Imaging of Nitroreductase. *Anal. Chem.* **2022**, *94* (20), 7272–7277. https://doi.org/10.1021/acs.analchem.2c00512.

(22) Mauker, P.; Beckmann, D.; Kitowski, A.; Heise, C.; Wientjens, C.; Davidson, A. J.; Wanderoy, S.; Fabre, G.; Harbauer, A. B.; Wood, W.; Wilhelm, C.; Thorn-Seshold, J.; Misgeld, T.; Kerschensteiner, M.; Thorn-Seshold,

O. Fluorogenic Chemical Probes for Wash-Free Imaging of Cell Membrane Damage in Ferroptosis, Necrosis, and Axon Injury. *J. Am. Chem. Soc.* **2024**, *146* (16), 11072–11082. https://doi.org/10.1021/jacs.3c07662.
(23) Chyan, W.; Kilgore, H. R.; Gold, B.; Raines, R. T. Electronic and Steric Optimization of Fluorogenic Probes for Biomolecular Imaging. *J. Org. Chem.* **2017**, *82* (8), 4297–4304. https://doi.org/10.1021/acs.joc.7b00285.
(24) Sun, H.; Johnson, D. R.; Finch, R. A.; Sartorelli, A. C.; Miller, D. W.; Elmquist, W. F. Transport of Fluorescein in MDCKII-MRP1 Transfected Cells and Mrp1-Knockout Mice. *Biochem. Biophys. Res. Commun.* **2001**, *284* (4), 863–869. https://doi.org/10.1006/bbrc.2001.5062.
(25) Bresler, S. E.; Bresler, V. M.; Kazbekov, E. N.; Nikiforov, A. A.; Vasilieva, N. N. On the Active Transport of Organic Acids (Fluorescein) in the Choroid Plexus of the Rabbit. *Biochim. Biophys. Acta, Biomembr.* **1979**, *550* (1), 110–119. https://doi.org/10.1016/0005-2736(79)90119-6.
(26) Morstein, J.; Capecchi, A.; Hinnah, K.; Park, B.; Petit-Jacques, J.; Van Lehn, R. C.; Reymond, J.-L.; Trauner, D. Medium-Chain Lipid Conjugation Facilitates Cell-Permeability and Bioactivity. *J. Am. Chem. Soc.* **2022**. https://doi.org/10.1021/jacs.2c07833.
(27) Guthrie, J. P. Hydrolysis of Esters of Oxy Acids: pKa Values for Strong Acids; Brønsted Relationship for Attack of Water at Methyl; Free Energies of Hydrolysis of Esters of Oxy Acids; and a Linear Relationship between Free Energy of Hydrolysis and pKa Holding over a Range of 20 pK Units. *Can. J. Chem.* **1978**, *56* (17), 2342–2354. https://doi.org/10.1139/v78-385.
(28) Hwang, C.; Sinskey, A. J.; Lodish, H. F. Oxidized Redox State of Glutathione in the Endoplasmic Reticulum. *Science* **1992**, *257* (5076), 1496–1502. https://doi.org/10.1126/science.1523409.
(29) Dresser, M. J.; Leabman, M. K.; Giacomini, K. M. Transporters Involved in the Elimination of Drugs in the Kidney: Organic Anion Transporters and Organic Cation Transporters. *J. Pharm. Sci.* **2001**, *90* (4), 397–421. https://doi.org/10.1002/1520-6017(200104)90:4<397::AID-JPS1000>3.0.CO;2-D.
(30) Koepsell, H. Organic Cation Transporters in Health and Disease. *Pharmacol. Rev.* **2020**, *72* (1), 253–319. https://doi.org/10.1124/pr.118.015578.
(31) Zeisel, L.; Felber, J. G.; Scholzen, K. C.; Poczka, L.; Cheff, D.; Maier, M. S.; Cheng, Q.; Shen, M.; Hall, M. D.; Arnér, E. S. J.; Thorn-Seshold, J.; Thorn-Seshold, O. Selective Cellular Probes for Mammalian Thioredoxin Reductase TrxR1: Rational Design of RX1, a Modular 1,2-Thiaselenane Redox Probe. *Chem* **2022**, *8* (5), 1493–1517. https://doi.org/10.1016/j.chempr.2022.03.010.
(32) Grimm, J. B.; Tkachuk, A. N.; Xie, L.; Choi, H.; Mohar, B.; Falco, N.; Schaefer, K.; Patel, R.; Zheng, Q.; Liu, Z.; Lippincott-Schwartz, J.; Brown, T. A.; Lavis, L. D. A General Method to Optimize and Functionalize Red-Shifted Rhodamine Dyes. *Nat. Methods* **2020**, *17* (8), 815–821. https://doi.org/10.1038/s41592-020-0909-6.
(33) Liu, C.; Pan, J.; Li, S.; Zhao, Y.; Wu, L. Y.; Berkman, C. E.; Whorton, A. R.; Xian, M. Capture and Visualization of Hydrogen Sulfide by a Fluorescent Probe. *Angew. Chem. Int. Ed.* **2011**, *50* (44), 10327–10329. https://doi.org/10.1002/anie.201104305.
(34) Würth, C.; Grabolle, M.; Pauli, J.; Spieles, M.; Resch-Genger, U. Relative and Absolute Determination of Fluorescence Quantum Yields of Transparent Samples. *Nat Protoc* **2013**, *8* (8), 1535–1550. https://doi.org/10.1038/nprot.2013.087.
(35) Zhang, X.-F.; Zhang, J.; Liu, L. Fluorescence Properties of Twenty Fluorescein Derivatives: Lifetime, Quantum Yield, Absorption and Emission Spectra. *J. Fluoresc.* **2014**, *24* (3), 819–826. https://doi.org/10.1007/s10895-014-1356-5.
(36) Mandal, P. K.; Schneider, M.; Kolle, P.; Kuhlencordt, P.; Forster, H.; Beck, H.; Bornkamm, G. W.; Conrad, M. Loss of Thioredoxin Reductase 1 Renders Tumors Highly Susceptible to Pharmacologic Glutathione Deprivation. *Cancer Research* **2010**, *70* (22), 9505–9514. https://doi.org/10.1158/0008-5472.CAN-10-1509.
(37) Cheng, Q.; Arnér, E. S. J. Overexpression of Recombinant Selenoproteins in E. Coli. In *Selenoproteins*; Humana Press, New York, NY, 2018; pp 231–240. https://doi.org/10.1007/978-1-4939-7258-6_17.
(38) Dóka, É.; Pader, I.; Bíró, A.; Johansson, K.; Cheng, Q.; Ballagó, K.; Prigge, J. R.; Pastor-Flores, D.; Dick, T. P.; Schmidt, E. E.; Arnér, E. S. J.; Nagy, P. A Novel Persulfide Detection Method Reveals Protein Persulfide- and Polysulfide-Reducing Functions of Thioredoxin and Glutathione Systems. *Science Advances* **2016**, *2* (1), e1500968. https://doi.org/10.1126/sciadv.1500968.
(39) Mandal, P. K.; Schneider, M.; Kölle, P.; Kuhlencordt, P.; Förster, H.; Beck, H.; Bornkamm, G. W.; Conrad, M. Loss of Thioredoxin Reductase 1 Renders Tumors Highly Susceptible to Pharmacologic Glutathione Deprivation. *Cancer Research* **2010**, *70* (22), 9505–9514. https://doi.org/10.1158/0008-5472.CAN-10-1509.
(40) Zeisel, L.; Felber, J. G.; Scholzen, K. C.; Schmitt, C.; Wiegand, A. J.; Komissarov, L.; Arnér, E. S. J.; Thorn-Seshold, O. Piperazine-Fused Cyclic Disulfides Unlock High-Performance Bioreductive Probes of Thioredoxins and Bifunctional Reagents for Thiol Redox Biology. *J. Am. Chem. Soc.* **2024**, *146* (8), 5204–5214. https://doi.org/10.1021/jacs.3c11153.
(41) He, H.; Ye, Z.; Zheng, Y.; Xu, X.; Guo, C.; Xiao, Y.; Yang, W.; Qian, X.; Yang, Y. Super-Resolution Imaging of Lysosomes with a Nitroso-Caged Rhodamine. *Chem. Commun.* **2018**, *54* (23), 2842–2845. https://doi.org/10.1039/C7CC08886H.
(42) Grimm, J. B.; English, B. P.; Chen, J.; Slaughter, J. P.; Zhang, Z.; Revyakin, A.; Patel, R.; Macklin, J. J.; Normanno, D.; Singer, R. H.; Lionnet, T.; Lavis, L. D. A General Method to Improve Fluorophores for Live-Cell and Single-Molecule Microscopy. *Nat Methods* **2015**, *12* (3), 244–250. https://doi.org/10.1038/nmeth.3256.

9 NMR spectra

iC4-FS

^{1}H-NMR

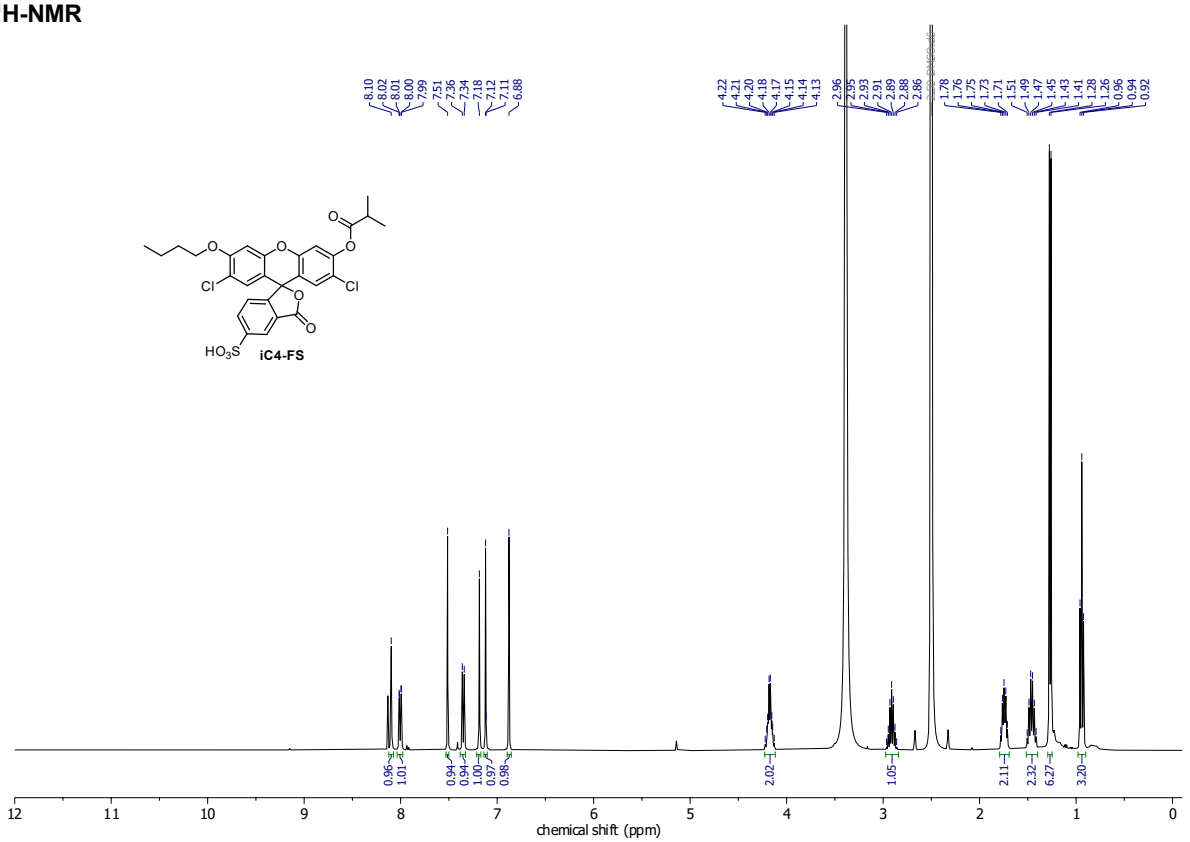

^{13}C-NMR

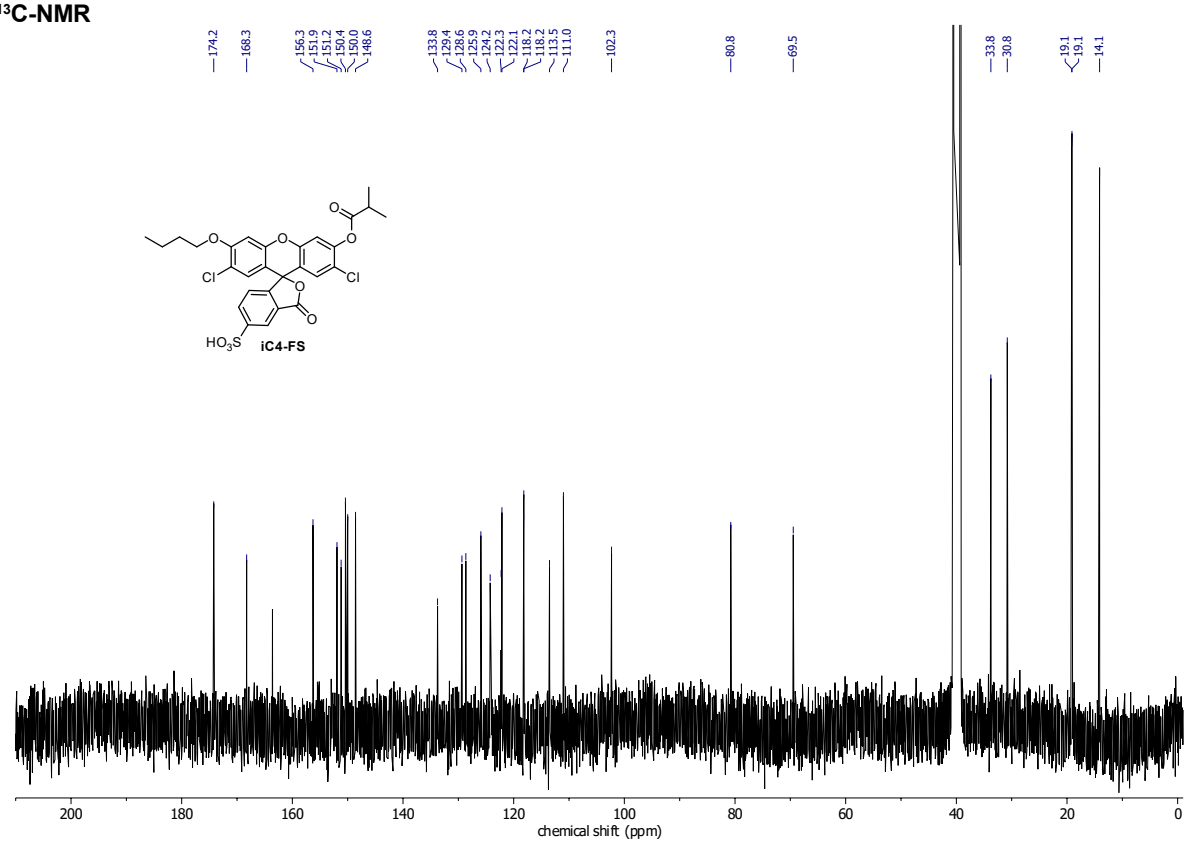

iC7-FS

^{1}H-NMR

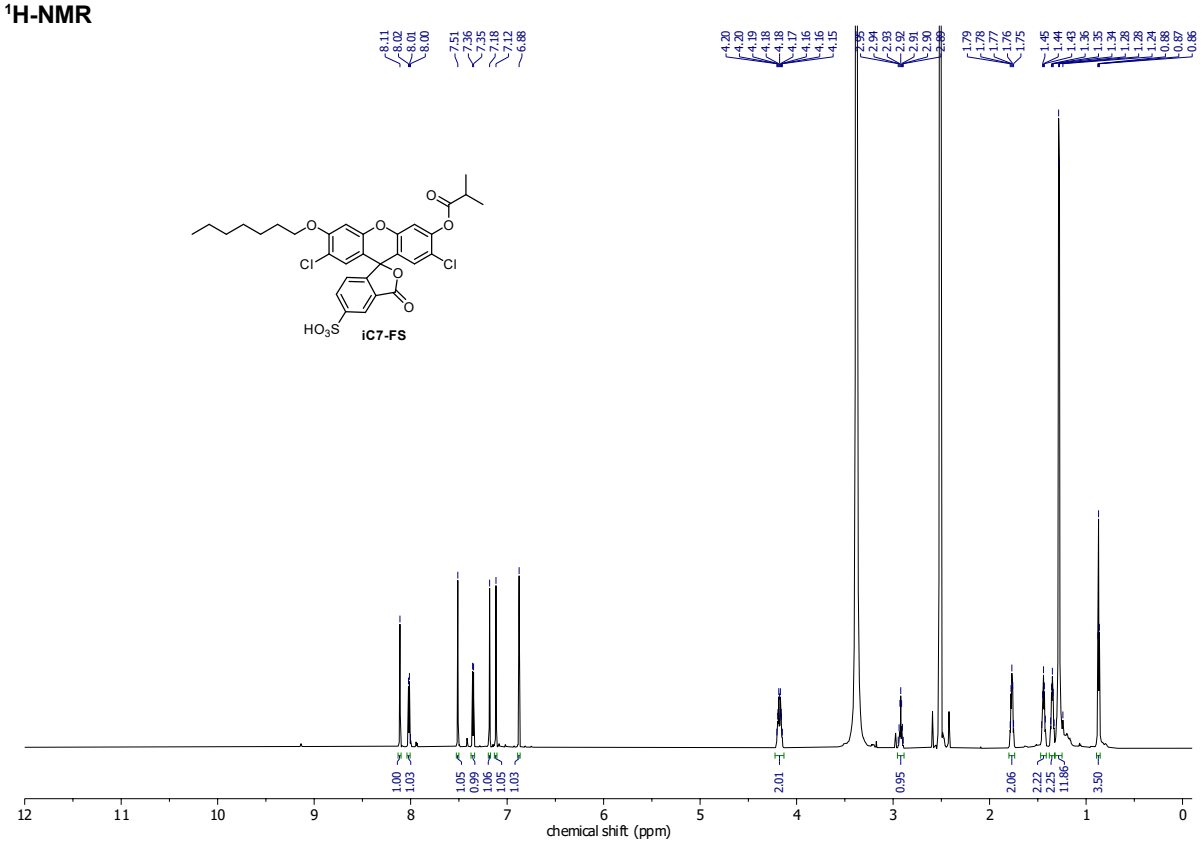

^{13}C-NMR

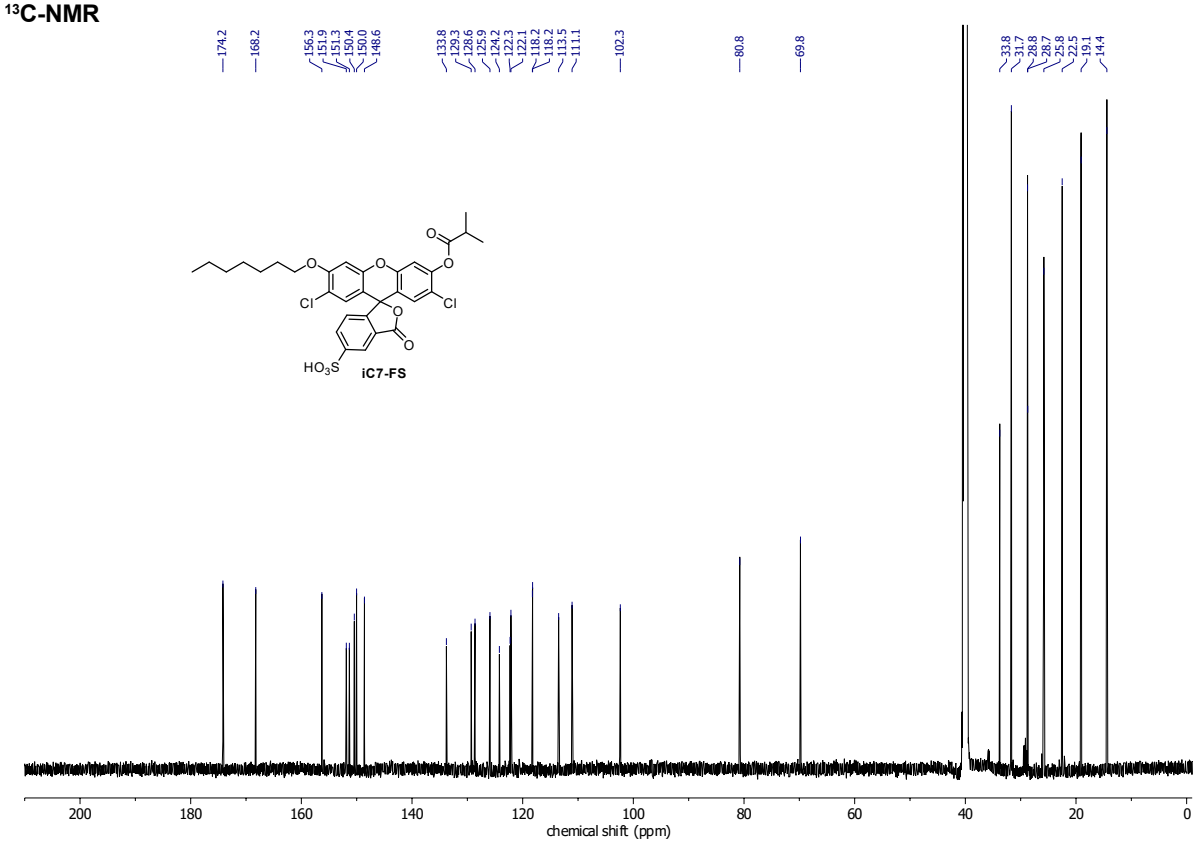

iC10-FS

^{1}H-NMR

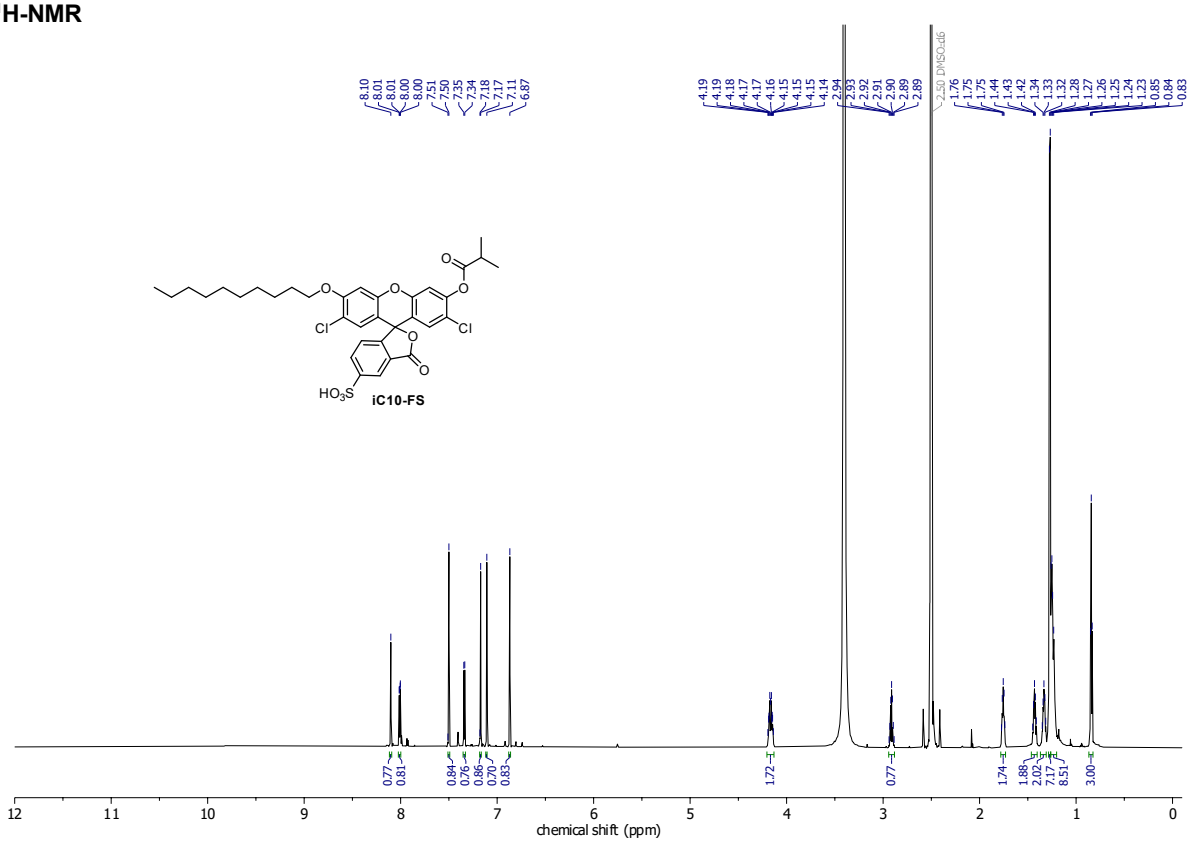

^{13}C-NMR

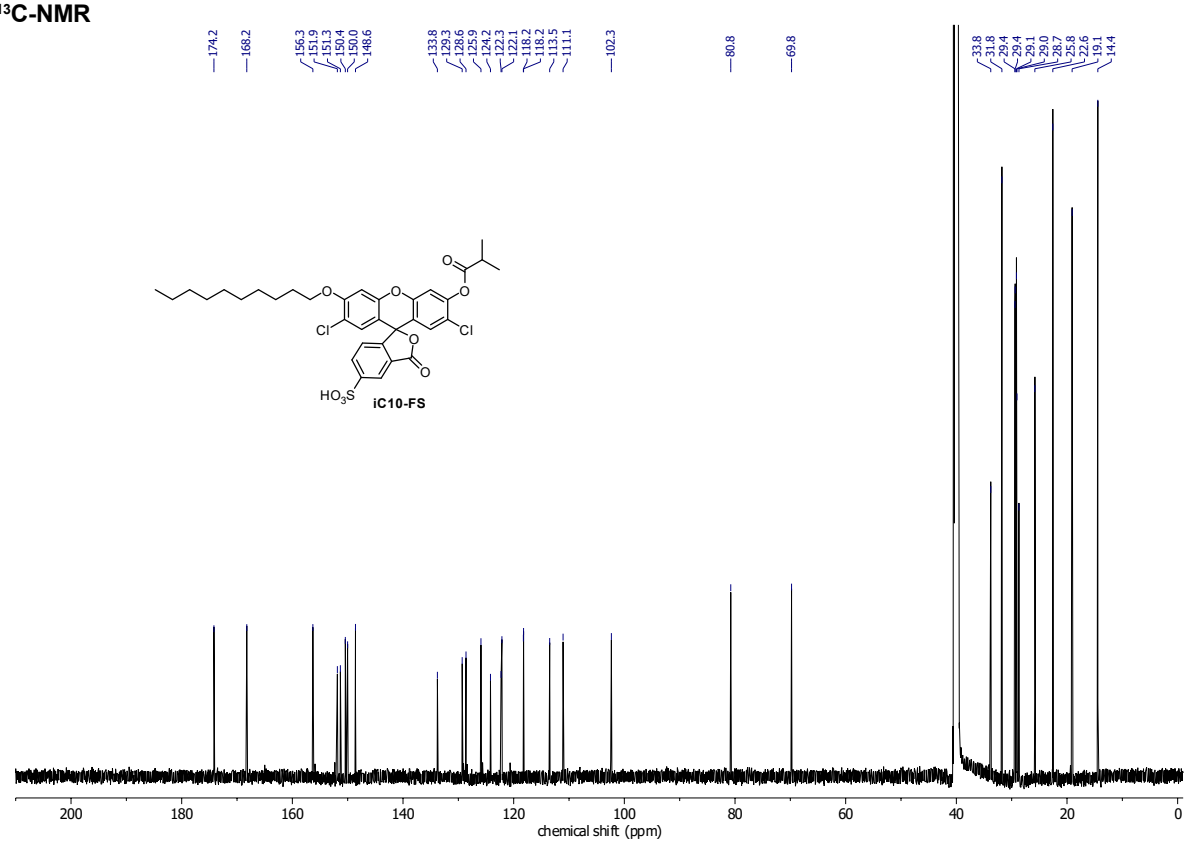

iC4-FC

^{1}H-NMR

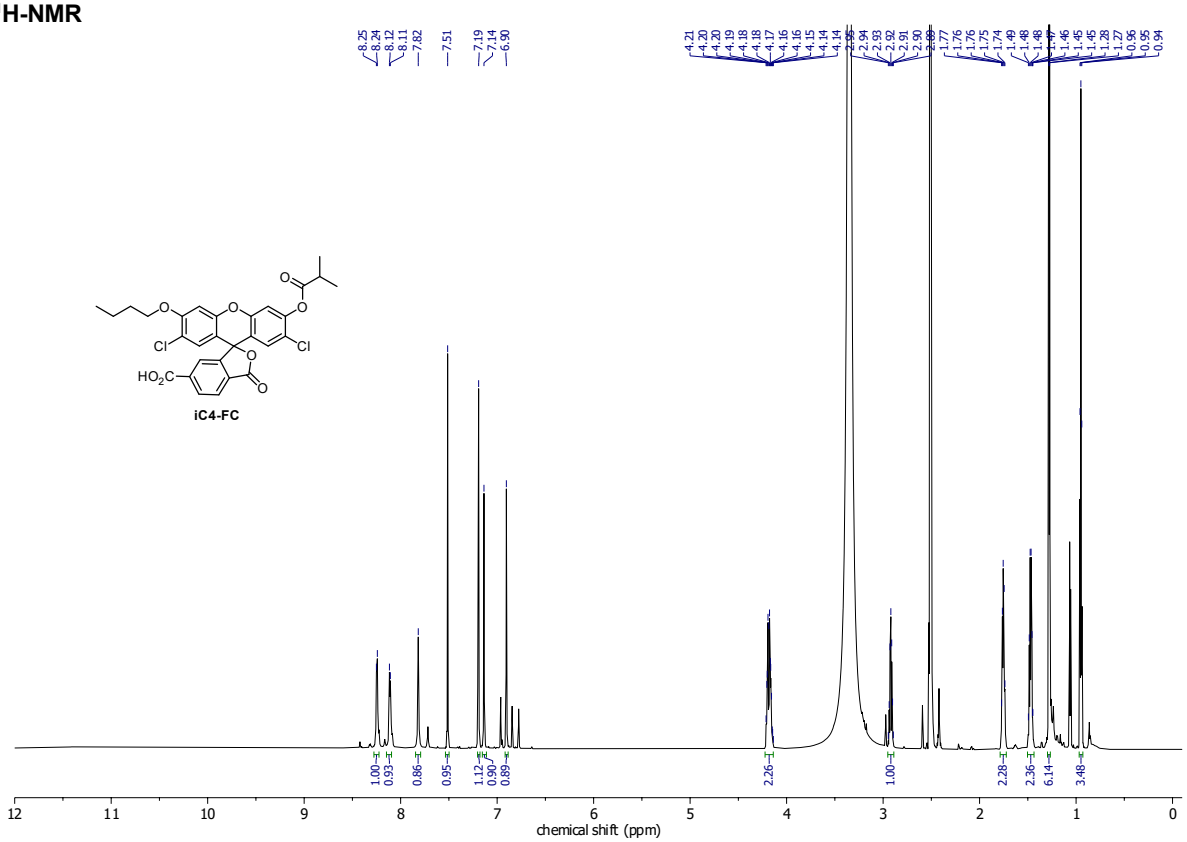

^{13}C-NMR

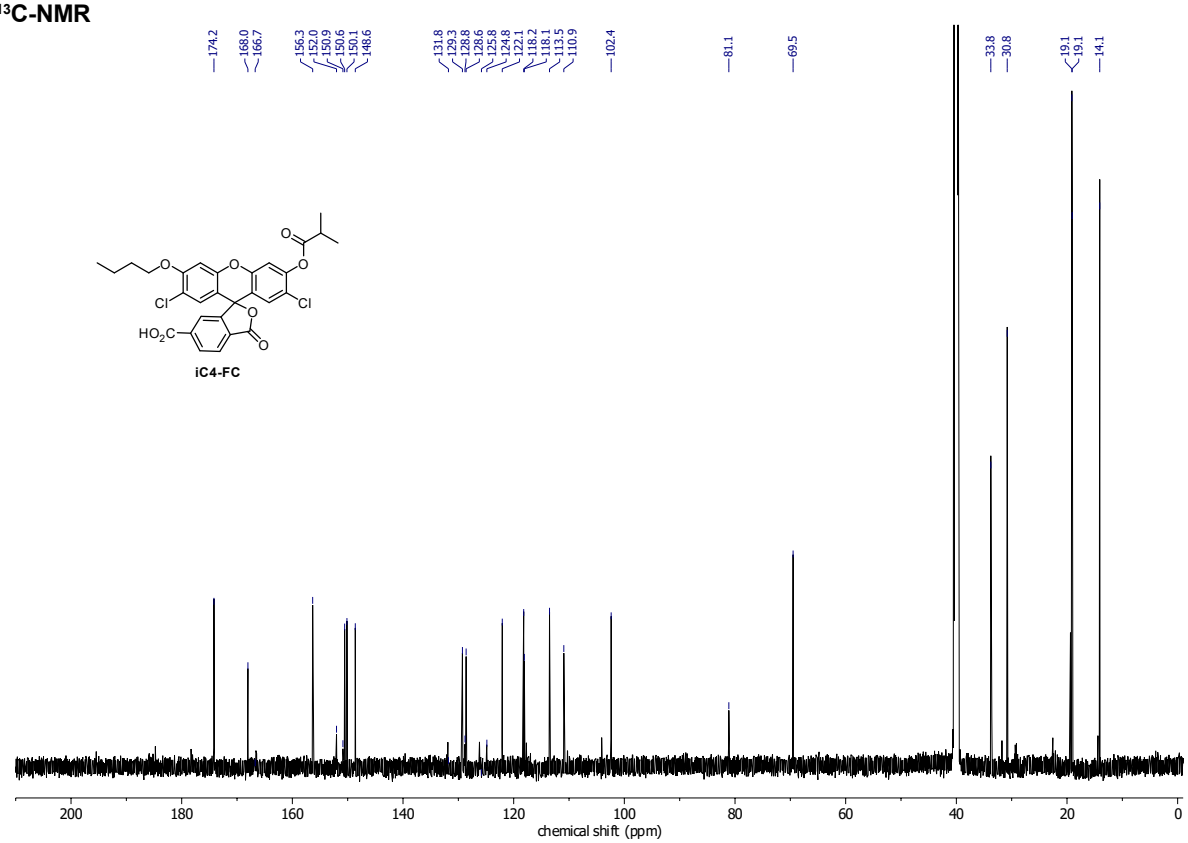

iC4-F

^{1}H-NMR

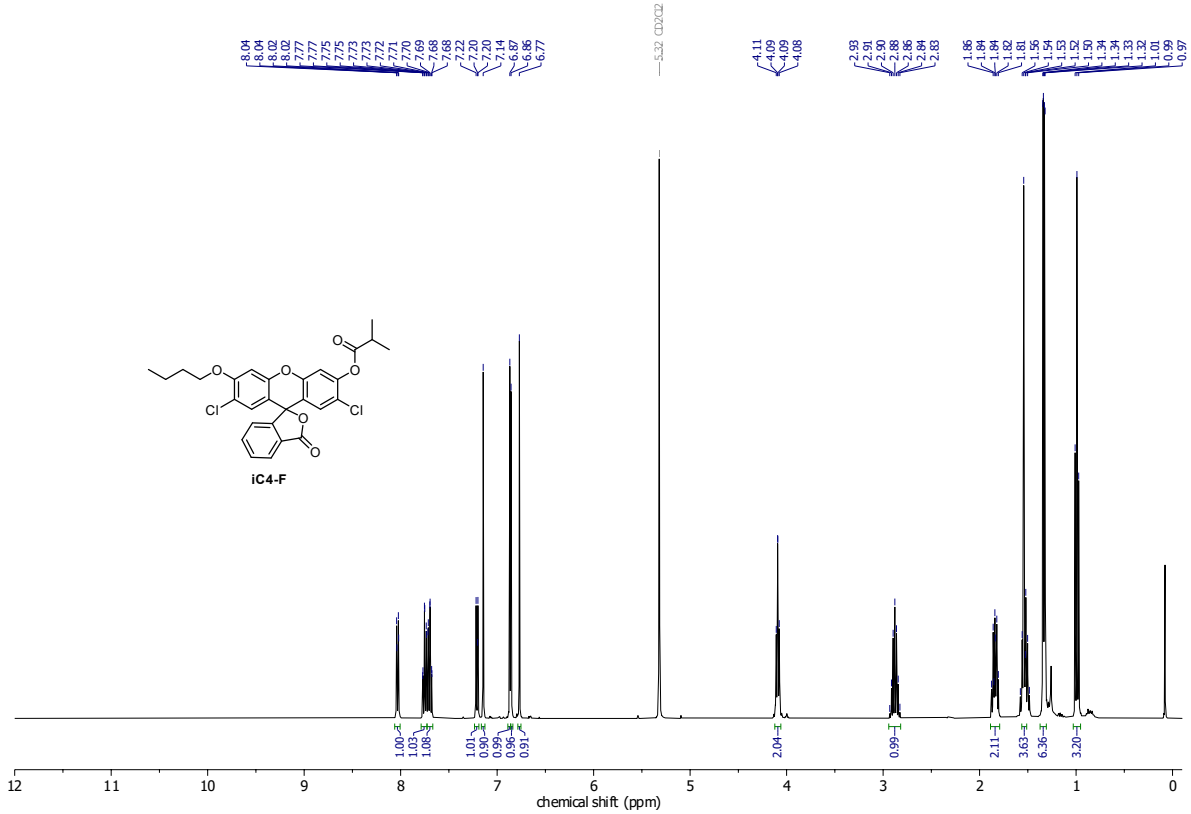

^{13}C-NMR

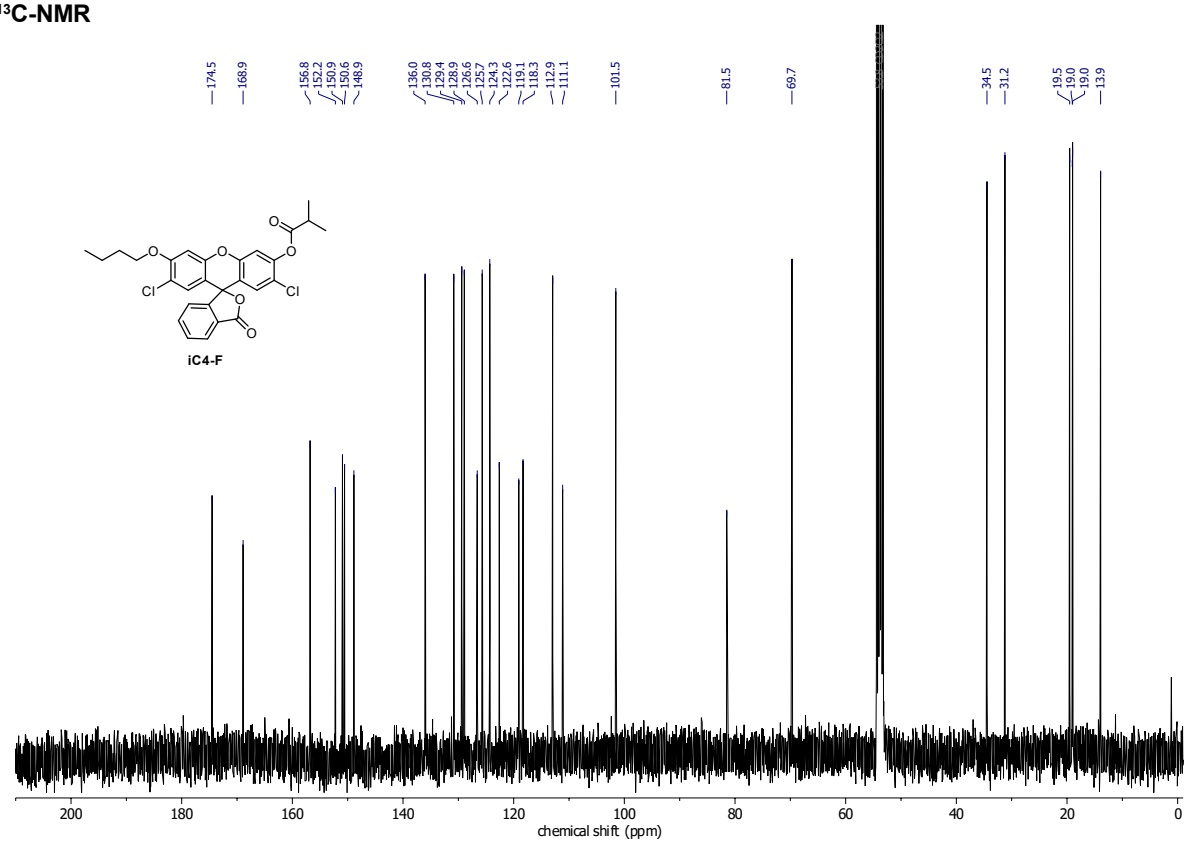

H-C4-FS

^{1}H-NMR

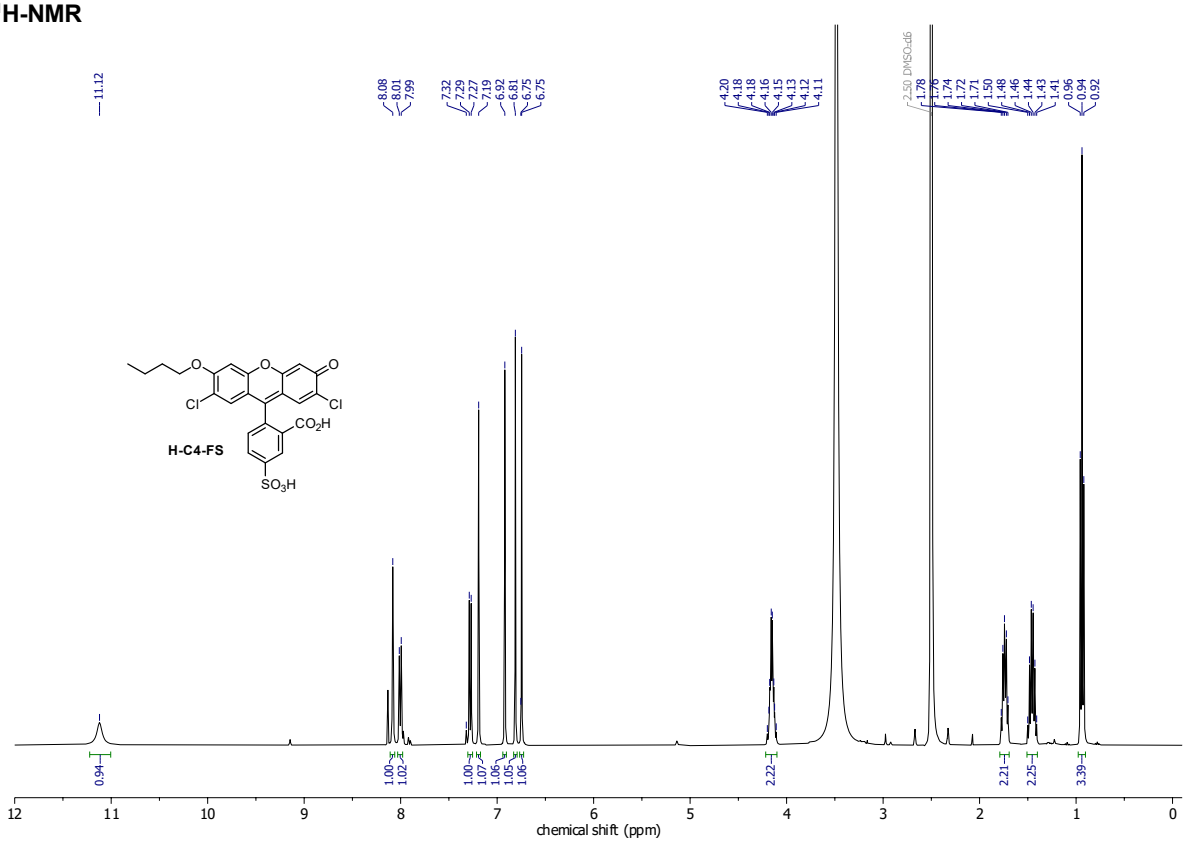

^{13}C-NMR

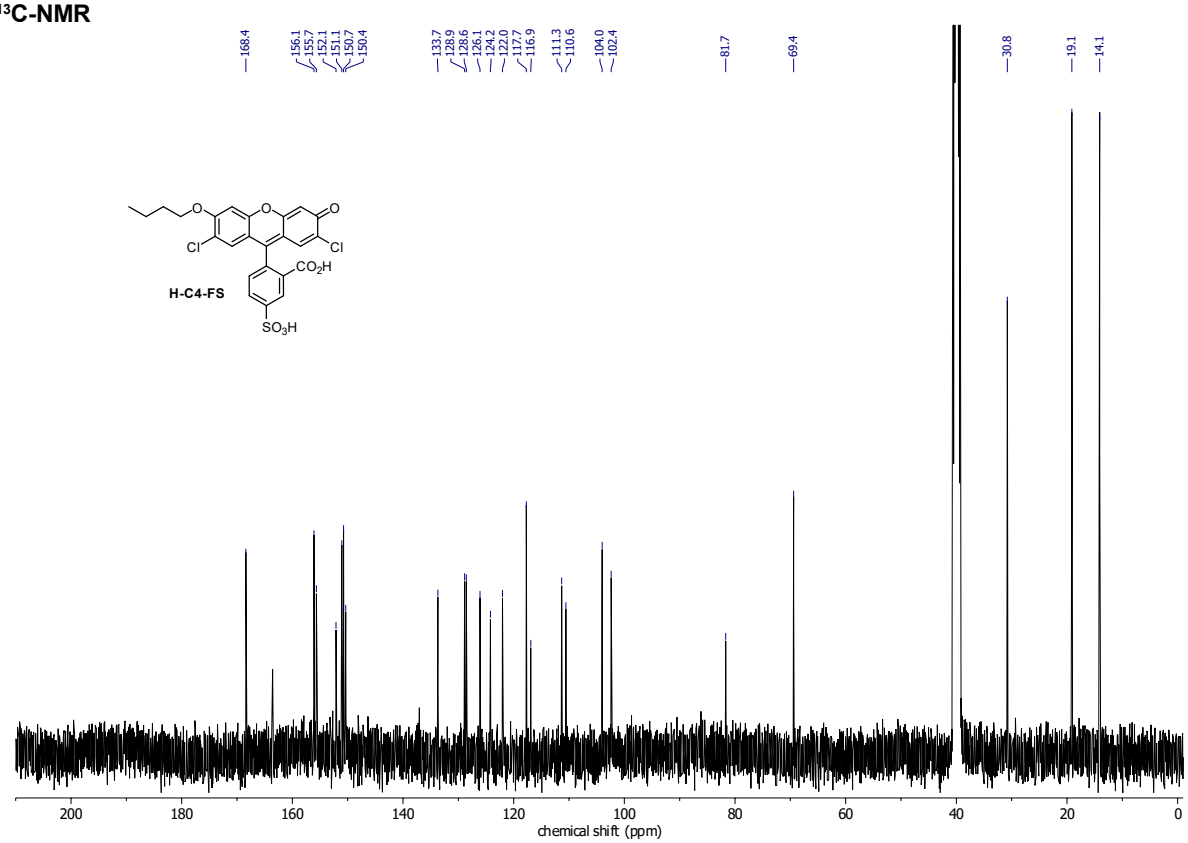

H-C7-FS

^{1}H-NMR

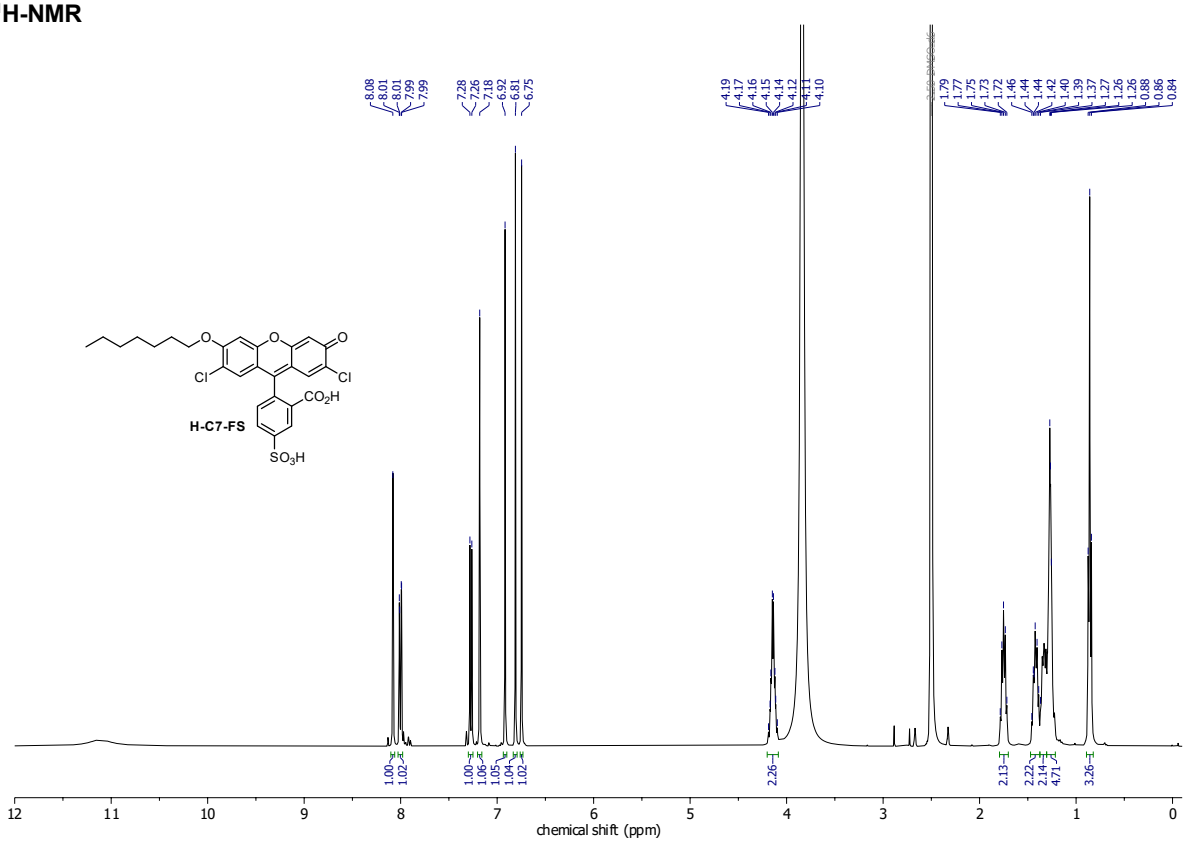

^{13}C-NMR

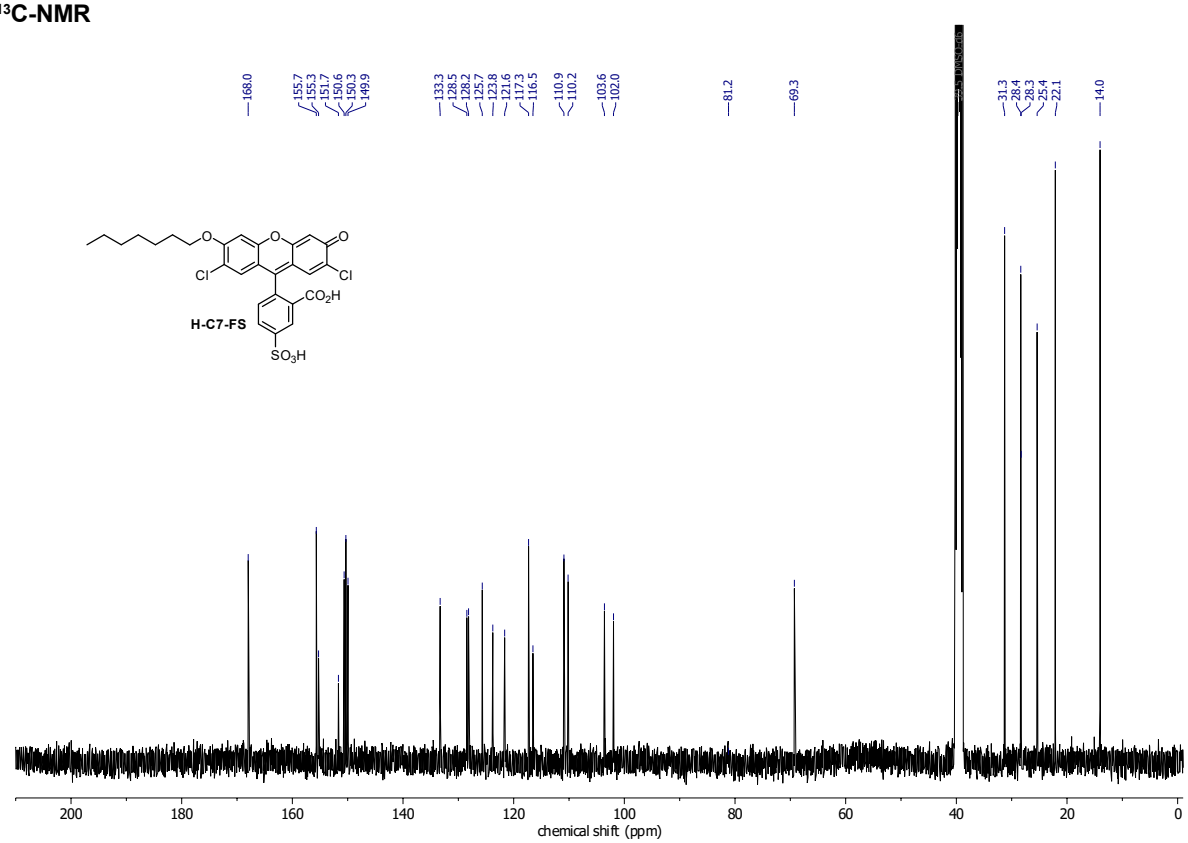

H-C10-FS

^{1}H-NMR

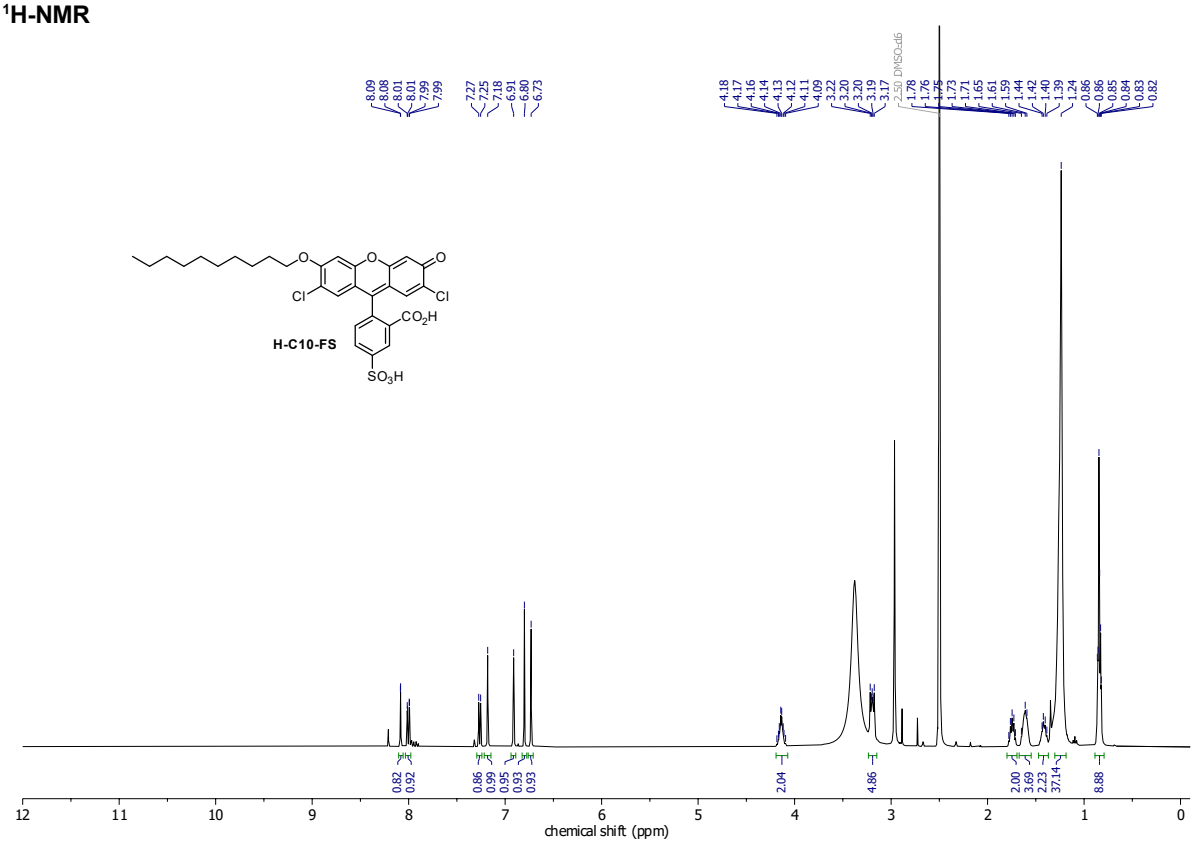

^{13}C-NMR

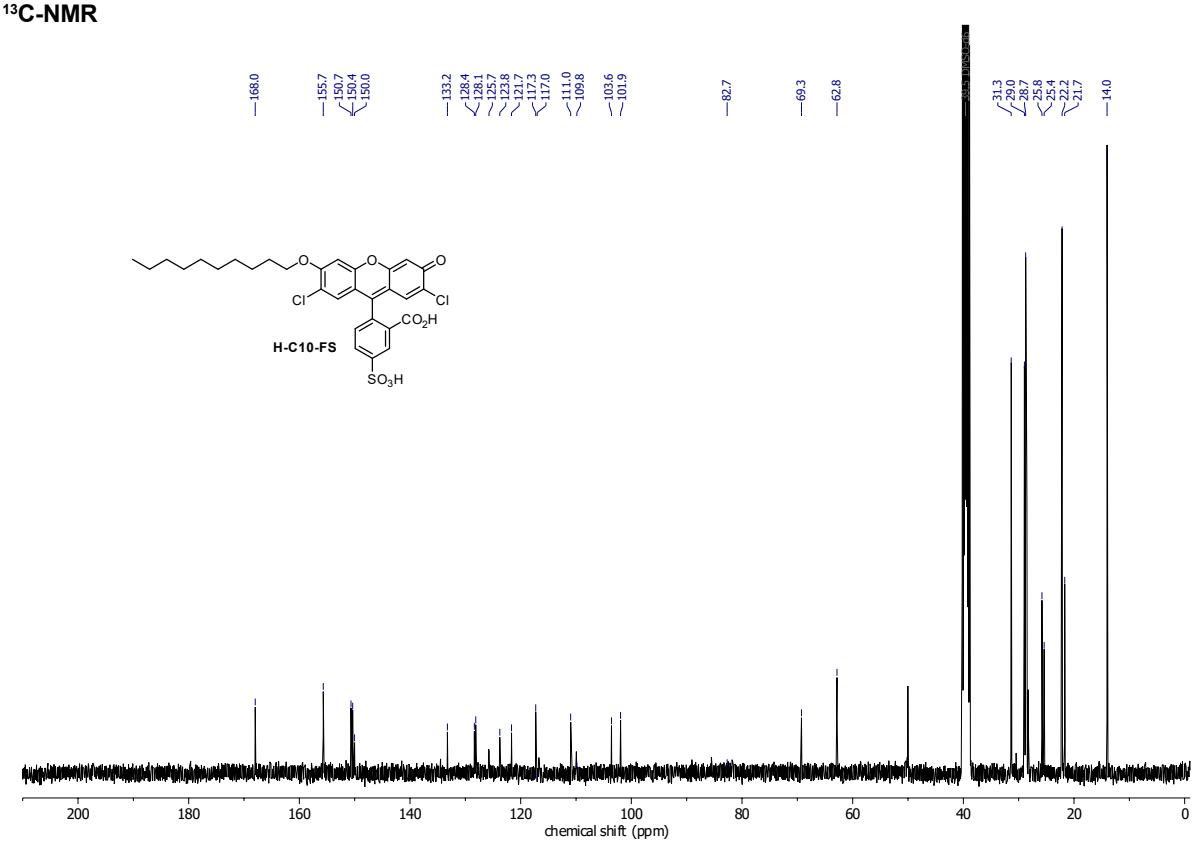

H-C4-FC

^{1}H-NMR

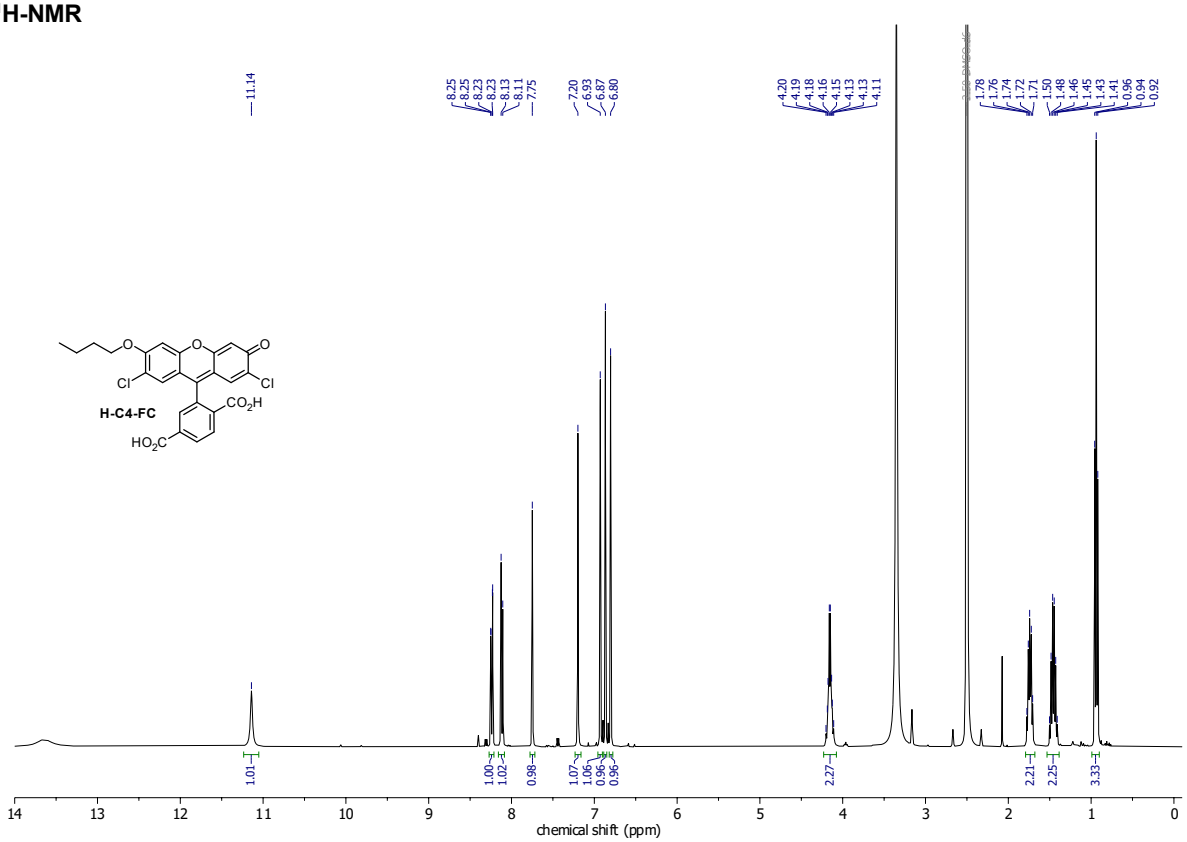

^{13}C-NMR

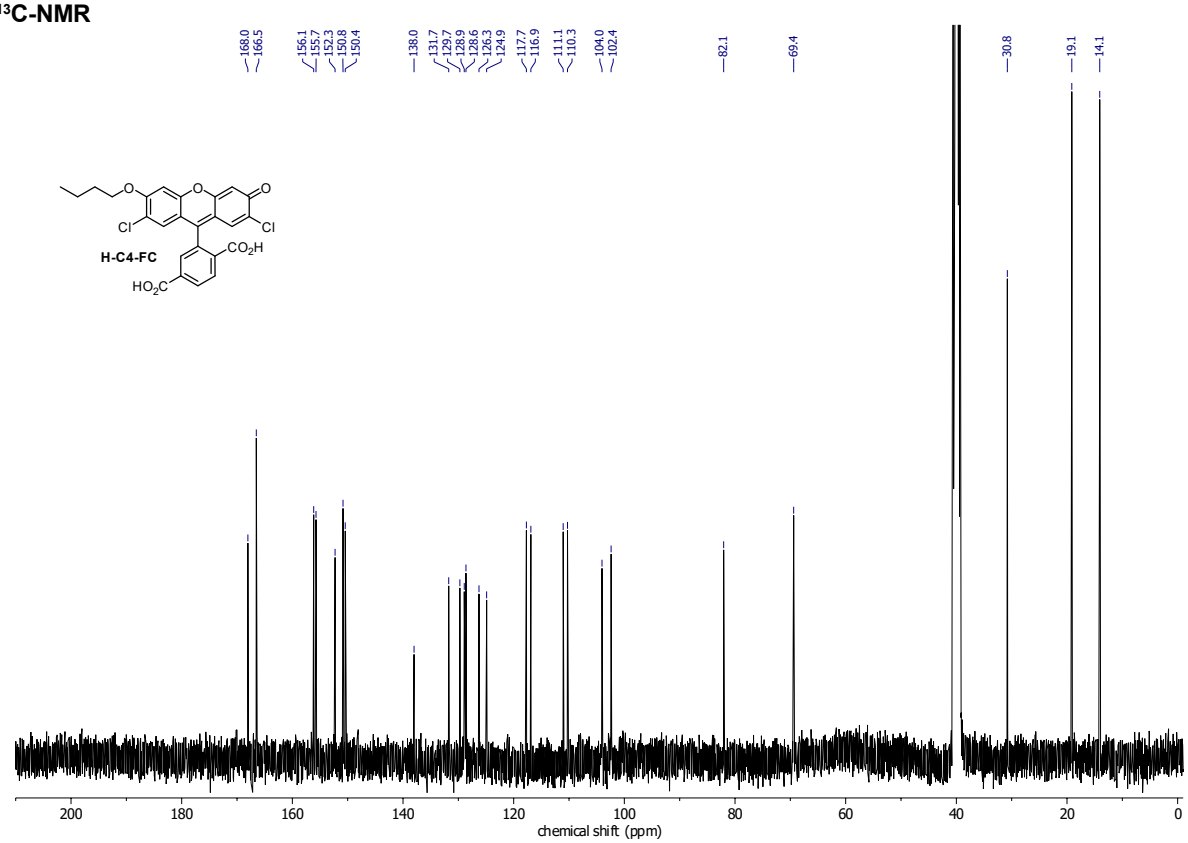

H-C4-F

^{1}H-NMR

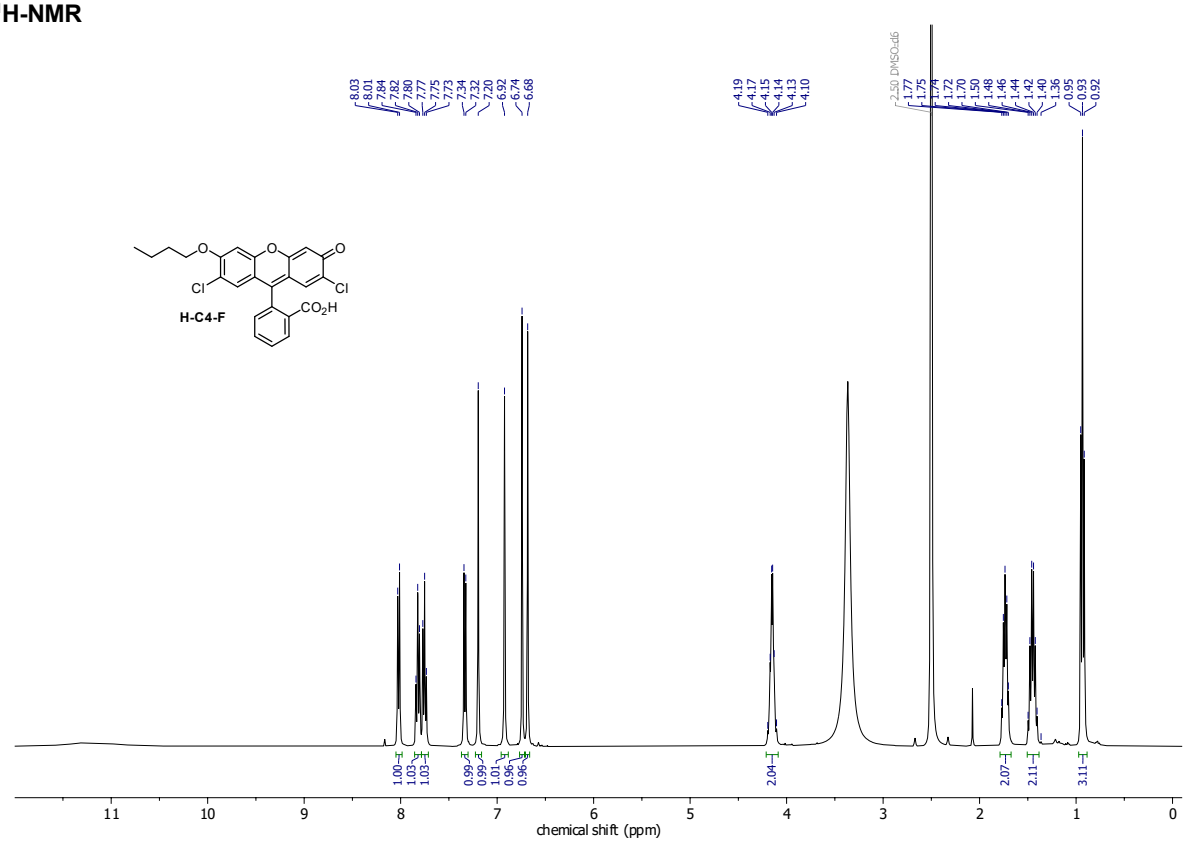

^{13}C-NMR

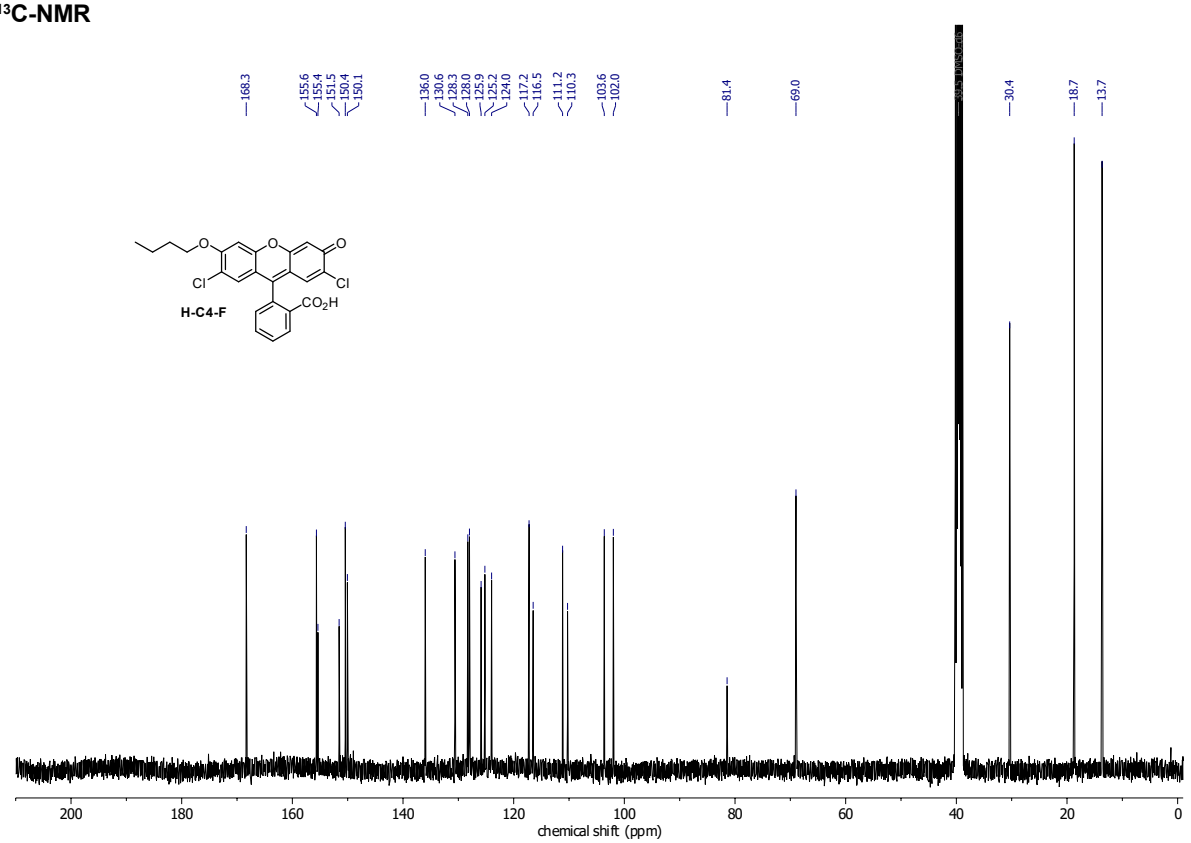

GL-C4-FC

^{1}H-NMR

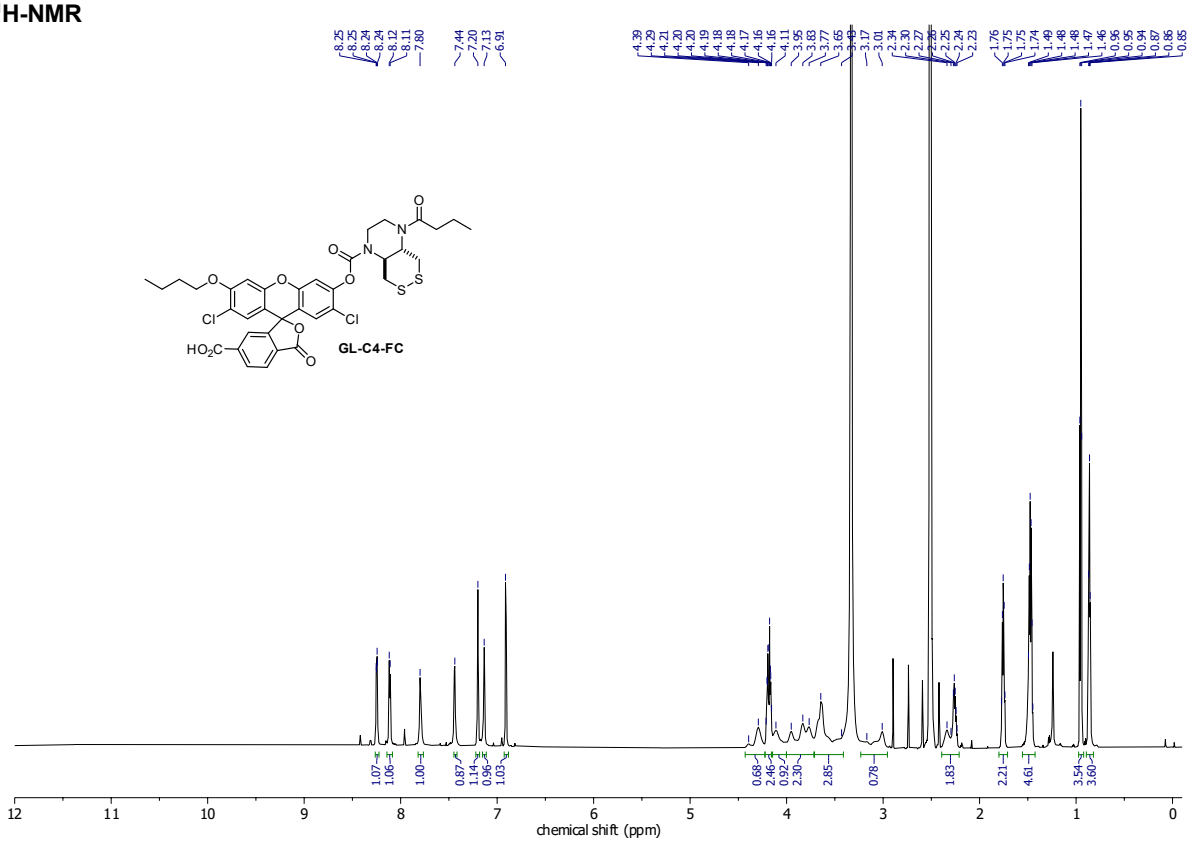

^{13}C-NMR

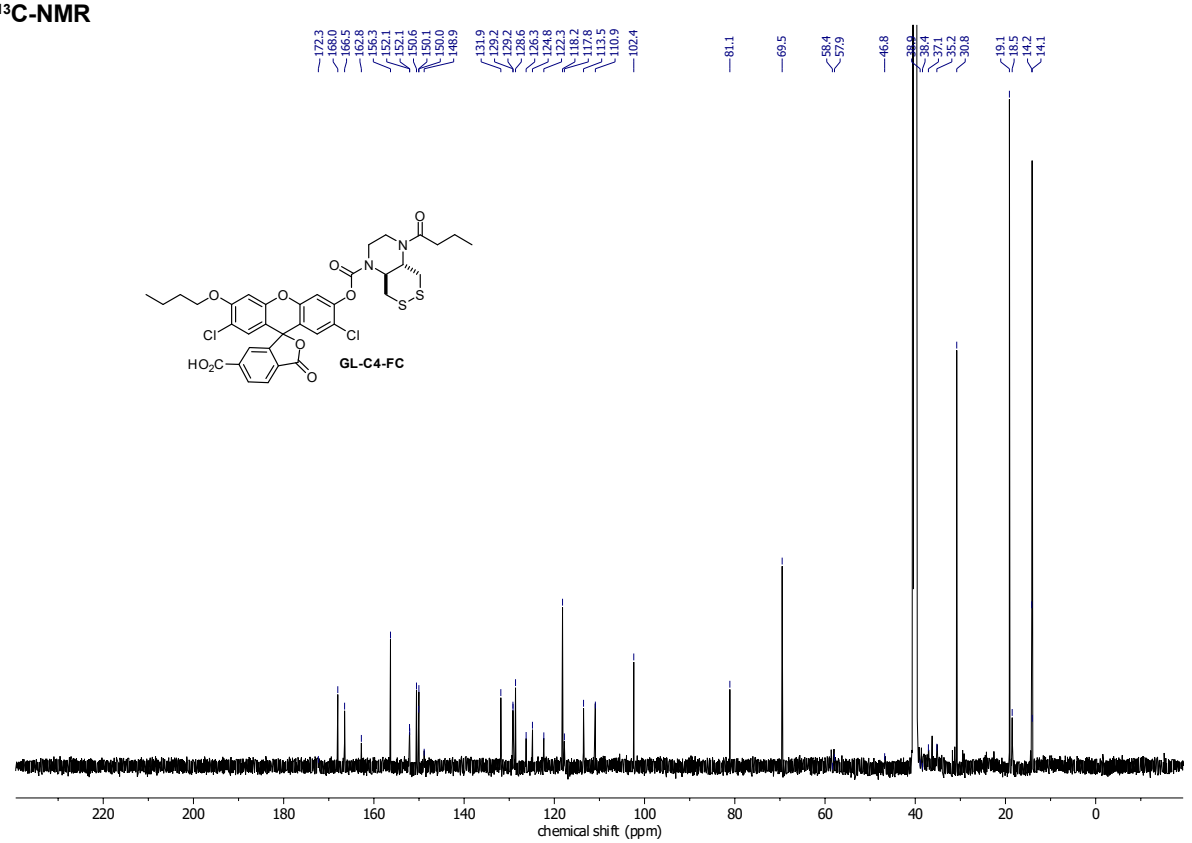

HSQC

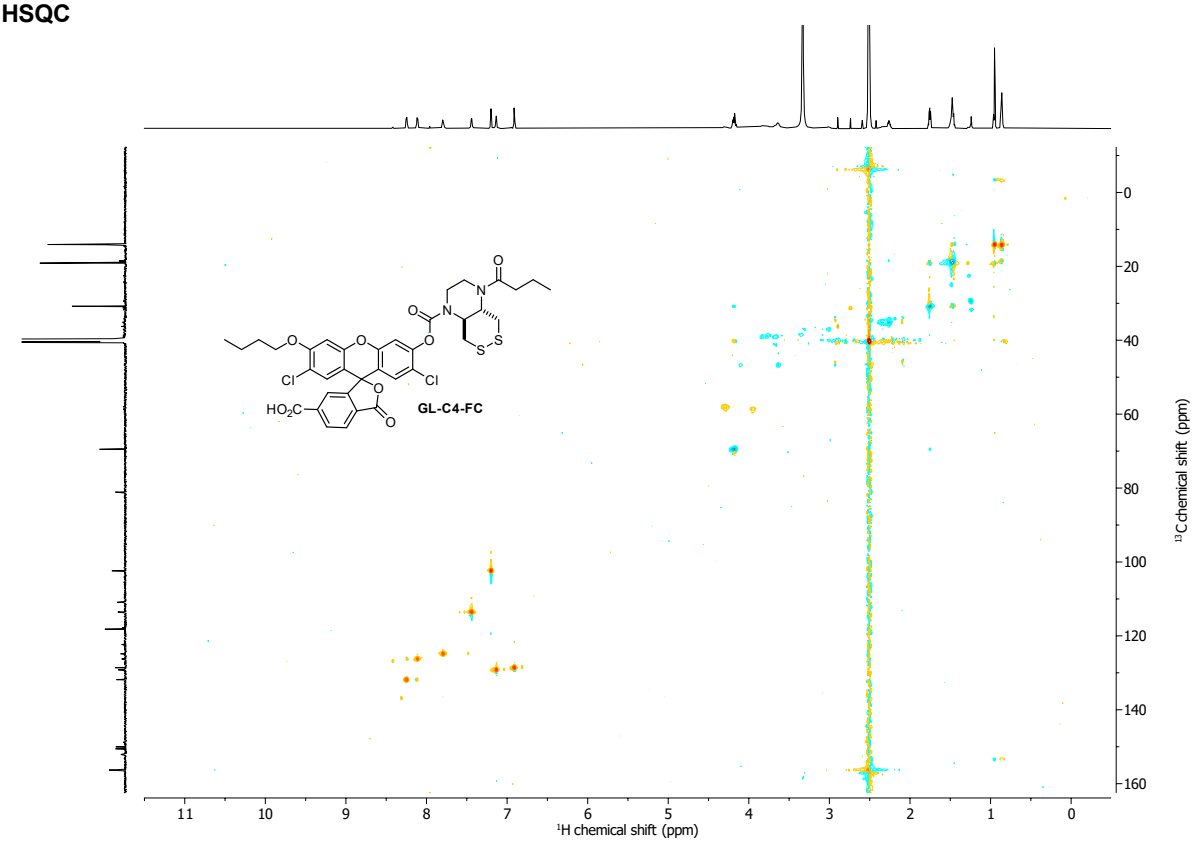
GL-C4-FC
^{1}H chemical shift (ppm)
^{13}C chemical shift (ppm)

HMBC

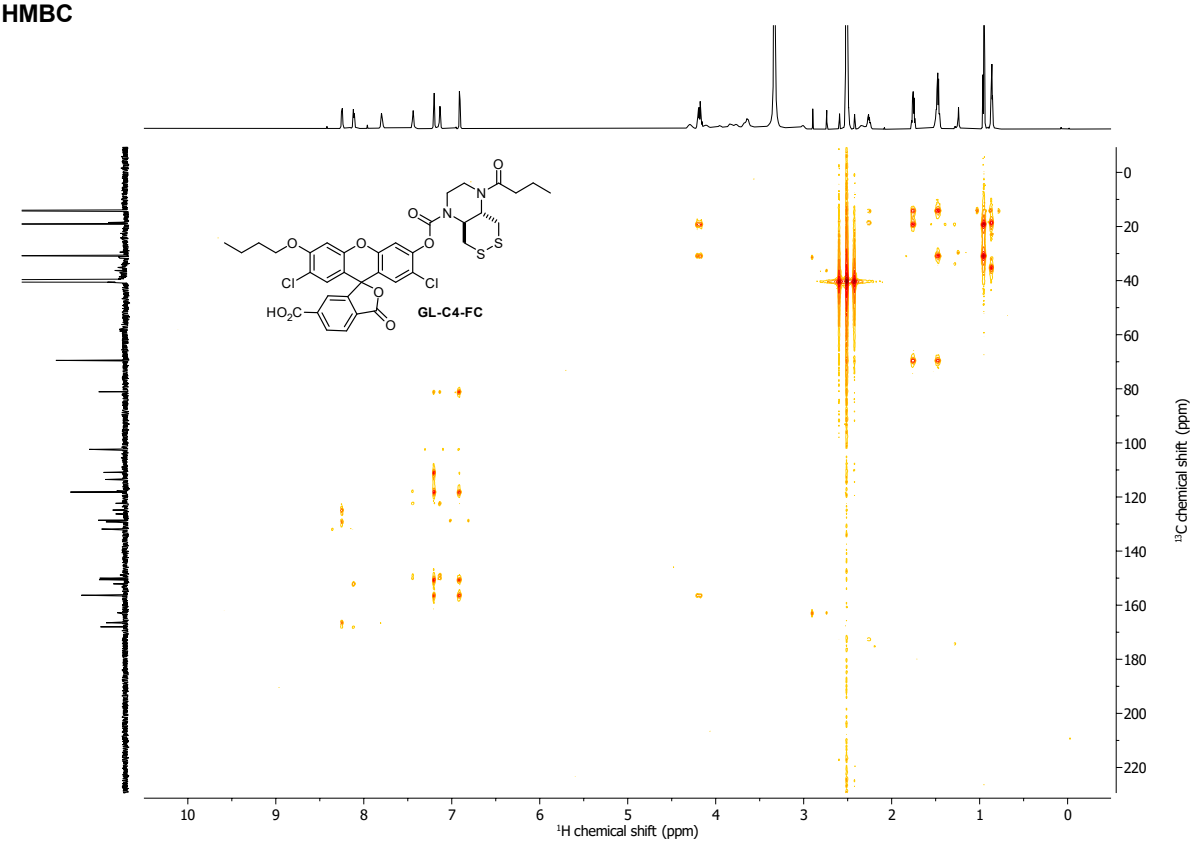
GL-C4-FC
^{1}H chemical shift (ppm)
^{13}C chemical shift (ppm)

H-Rho
^{1}H-NMR

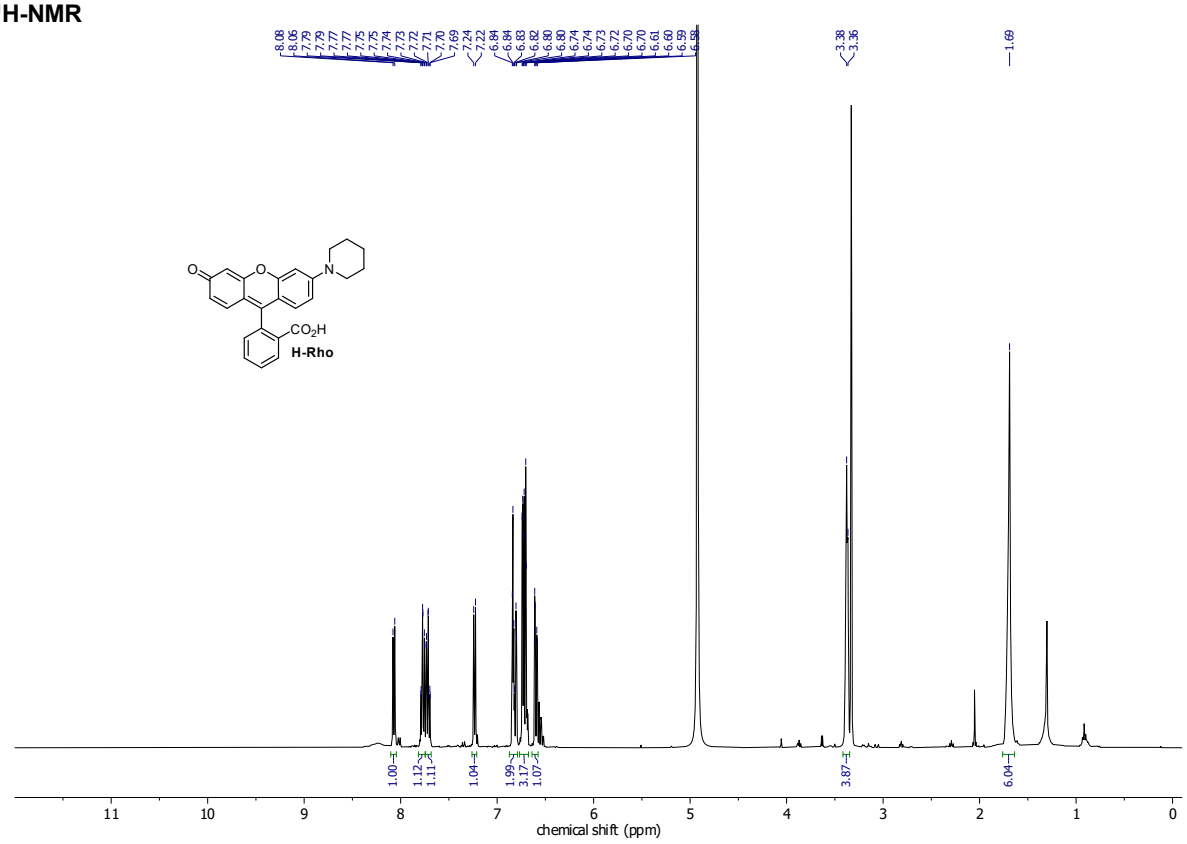
8.08
8.06
7.79
7.77
7.75
7.74
7.73
7.72
7.71
7.70
7.69
7.24
7.22
6.84
6.83
6.82
6.80
6.74
6.73
6.72
6.70
6.61
6.60
6.59
3.38
3.36
1.69
O
O
N
CO2H
H-Rho
1.00
1.12
1.11
1.04
1.99
3.17
1.07
3.87
6.04
11
10
9
8
7
6
5
4
3
2
1
0
chemical shift (ppm)

GL-Rho

^{1}H-NMR

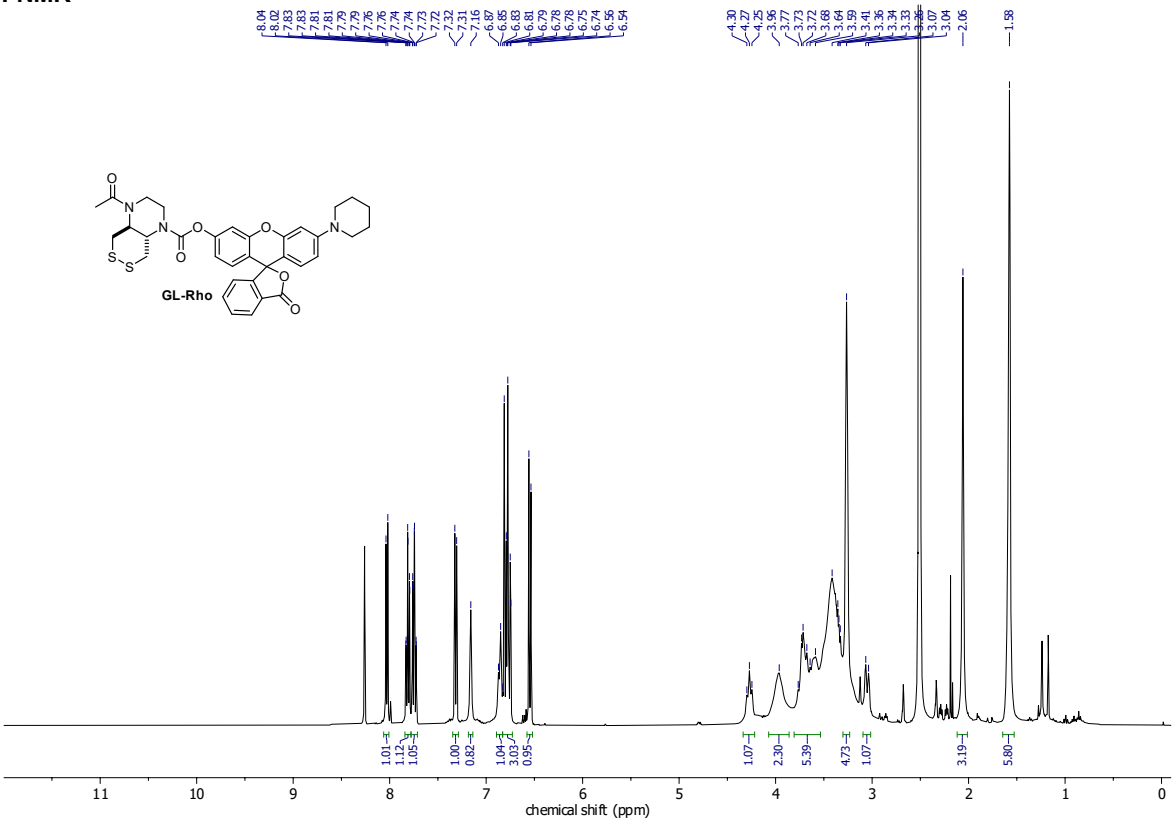

^{13}C-NMR

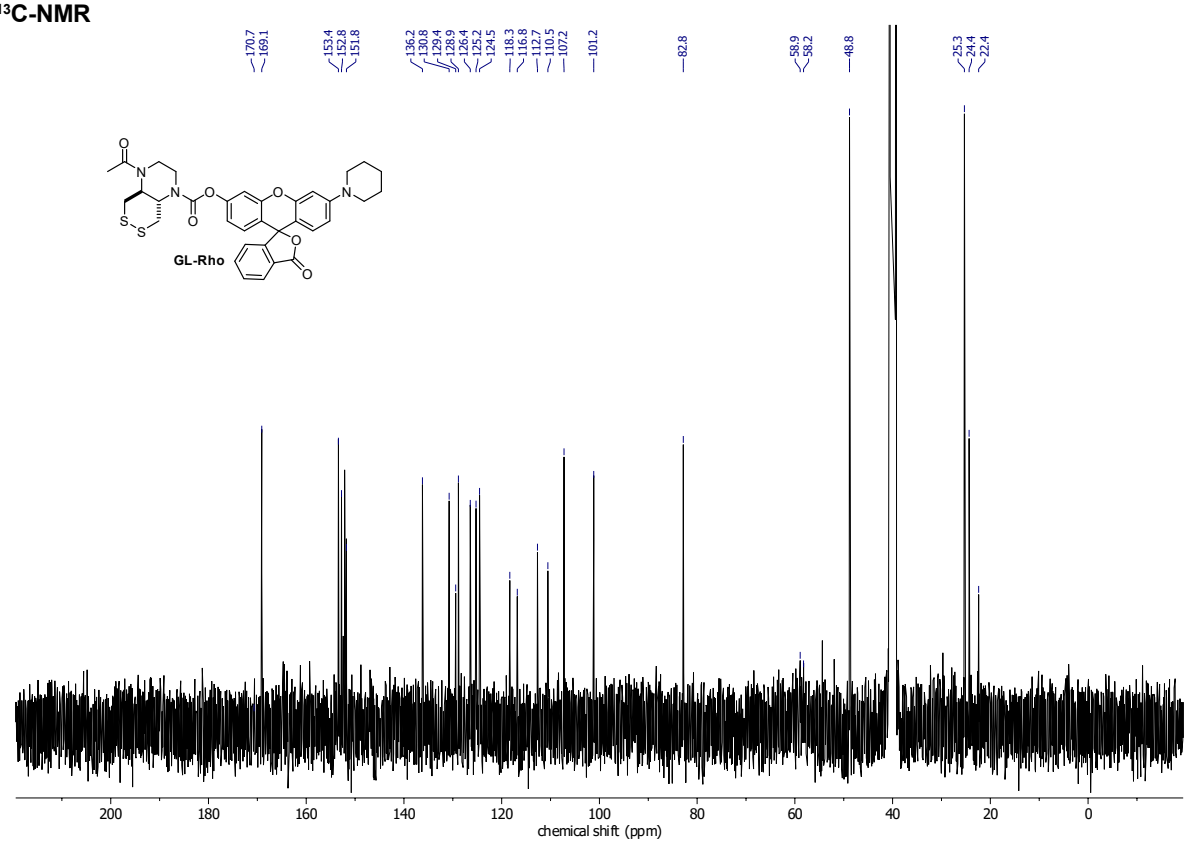

H-Rho-A
^{1}H-NMR

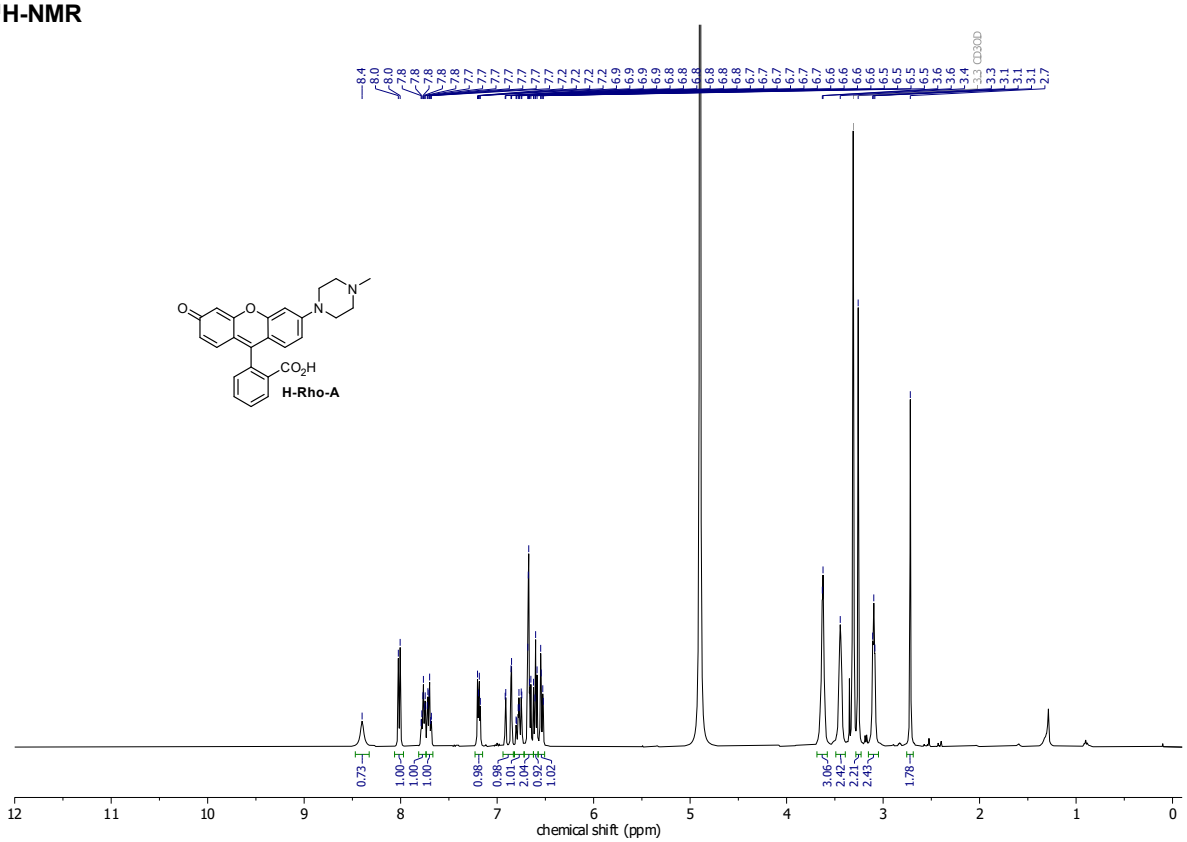

GL-Rho-A

^{1}H-NMR

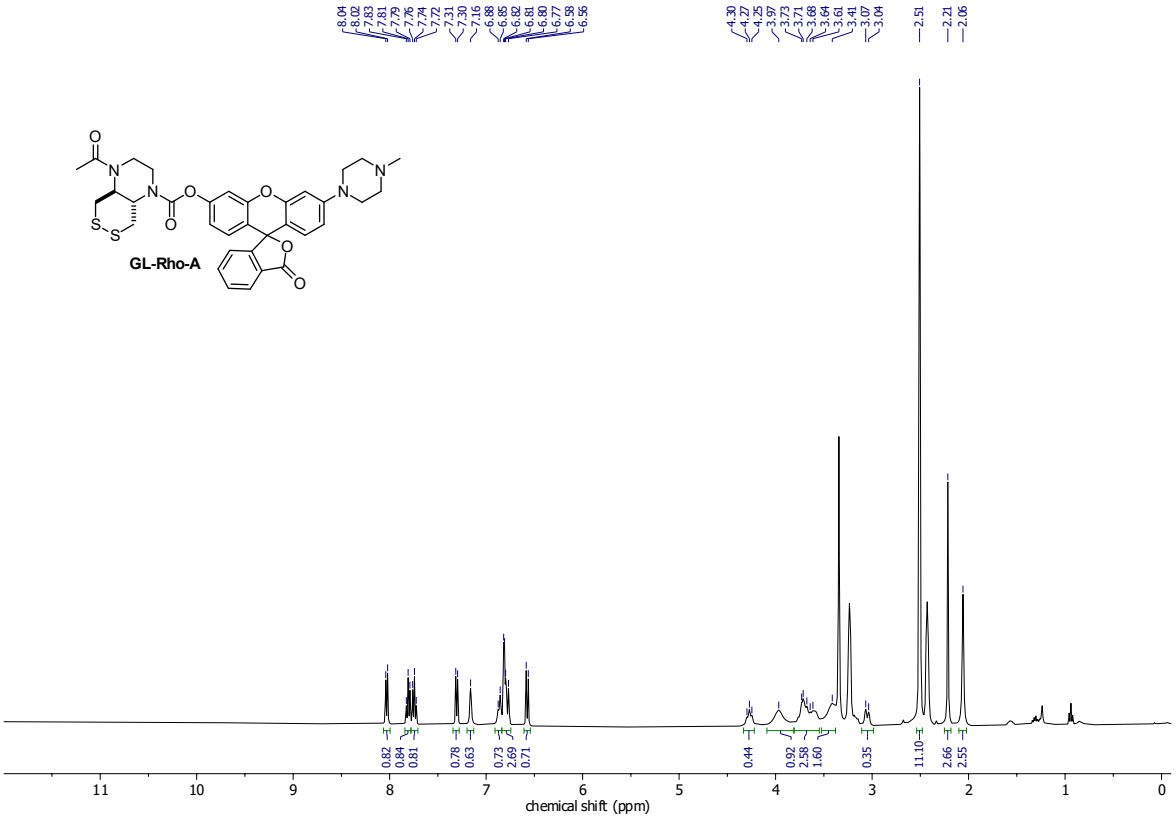

^{13}C-NMR

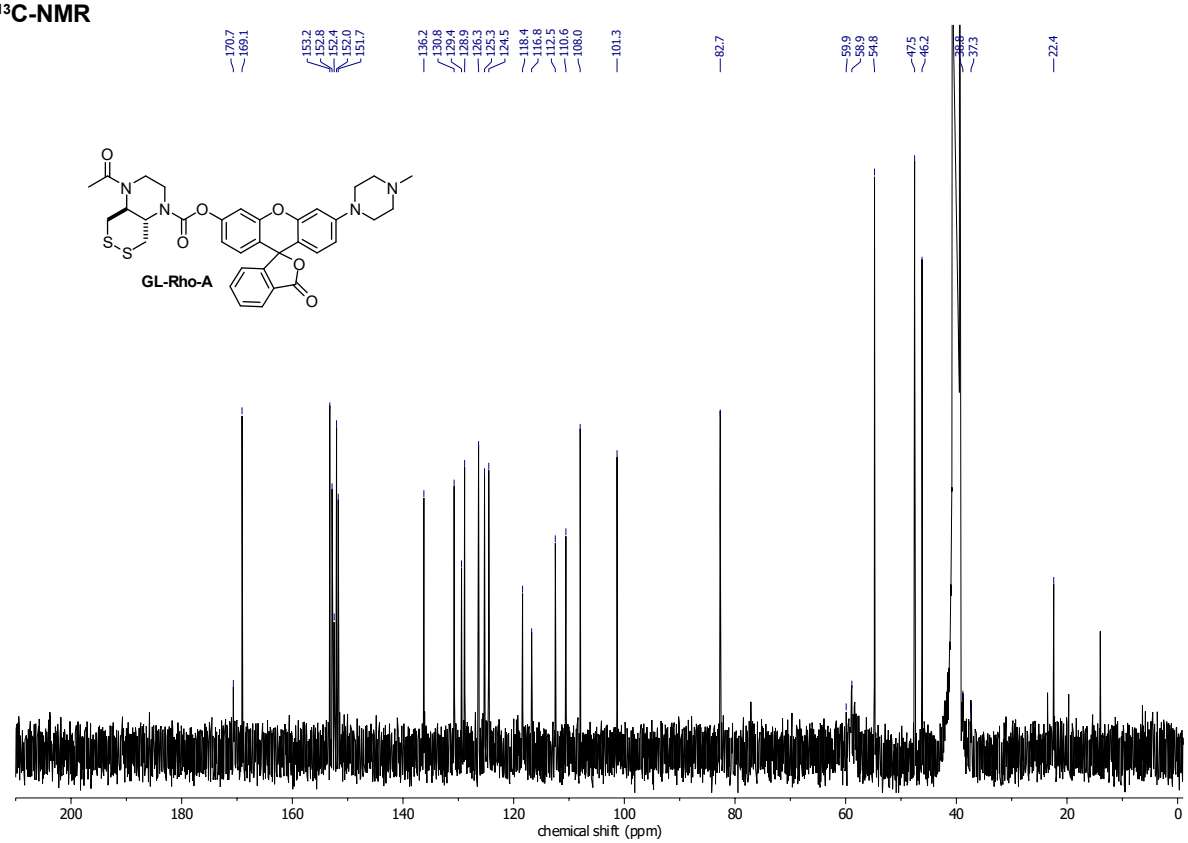

Compound 12
^{1}H-NMR

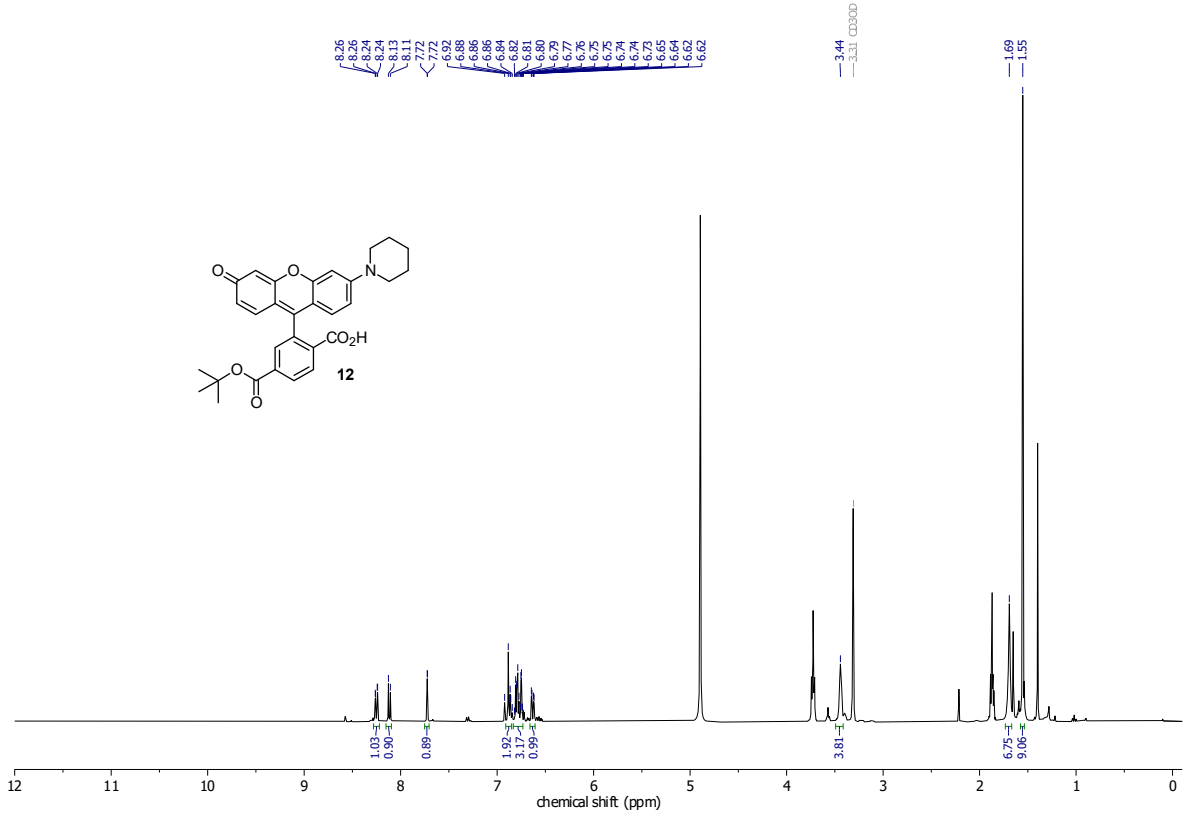

GL-Rho-C

^{1}H-NMR

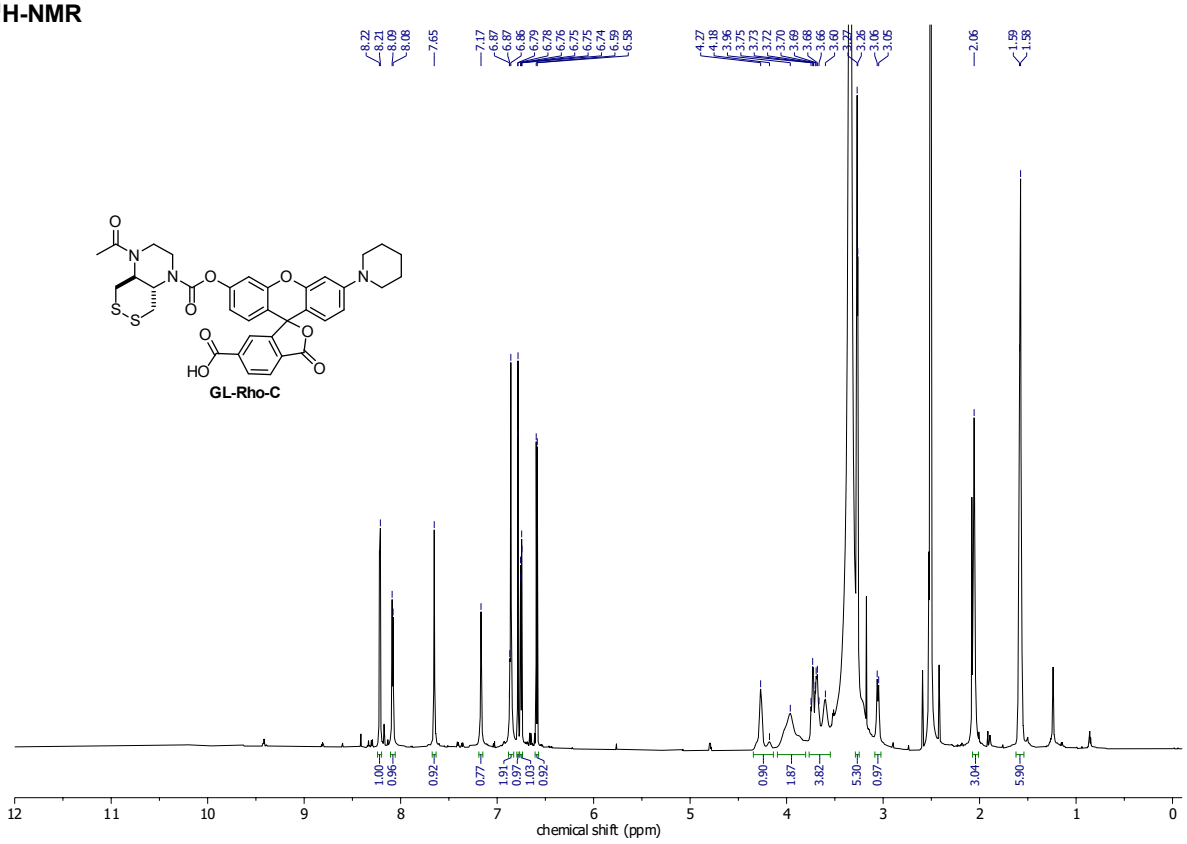

^{13}C-NMR

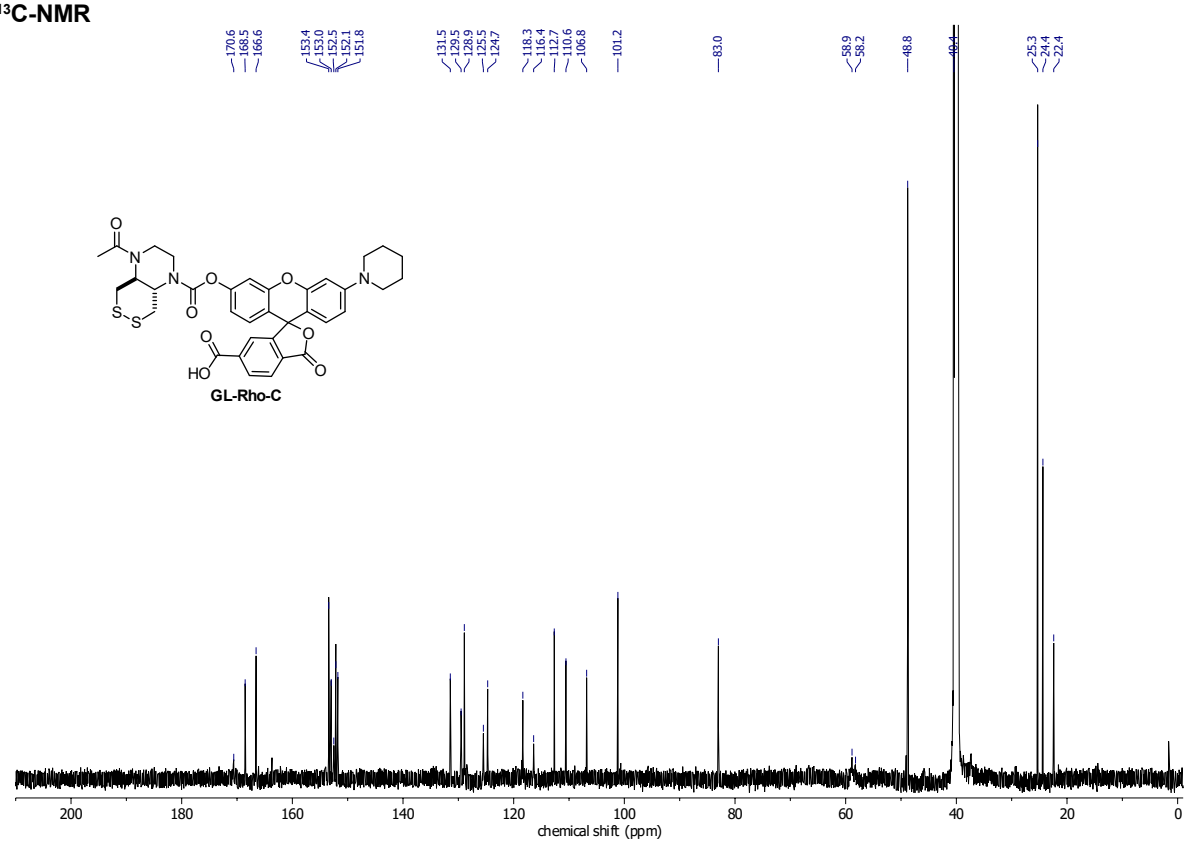

GL-Rho-C^{m}

^{1}H-NMR

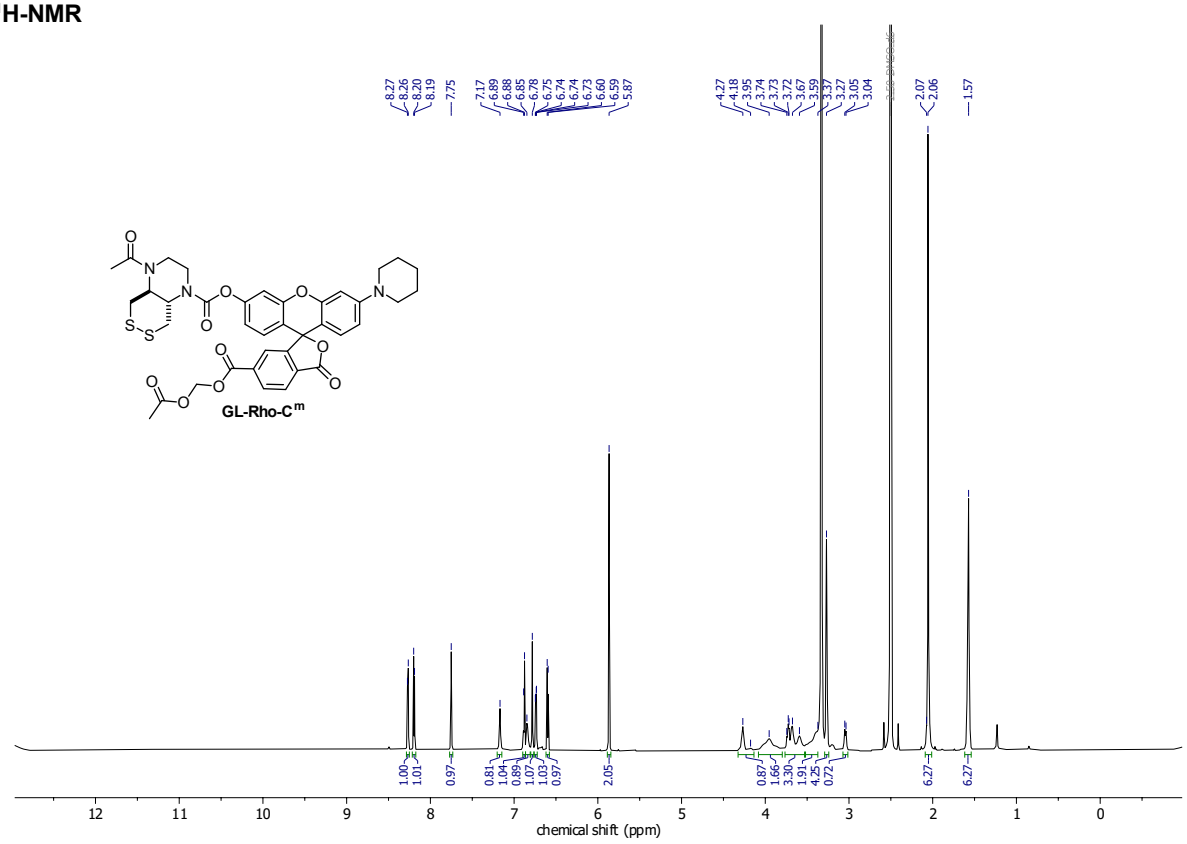

^{13}C-NMR

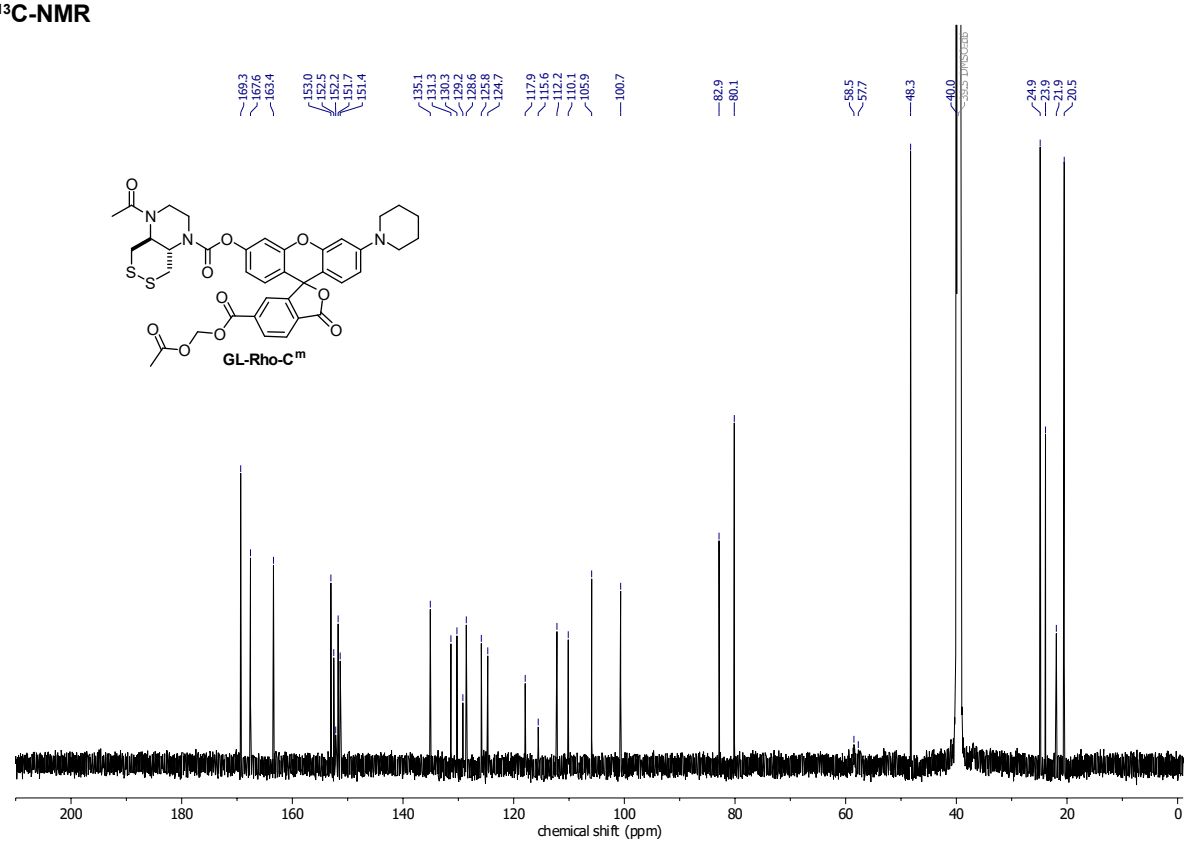

H-Rho-C

^{1}H-NMR

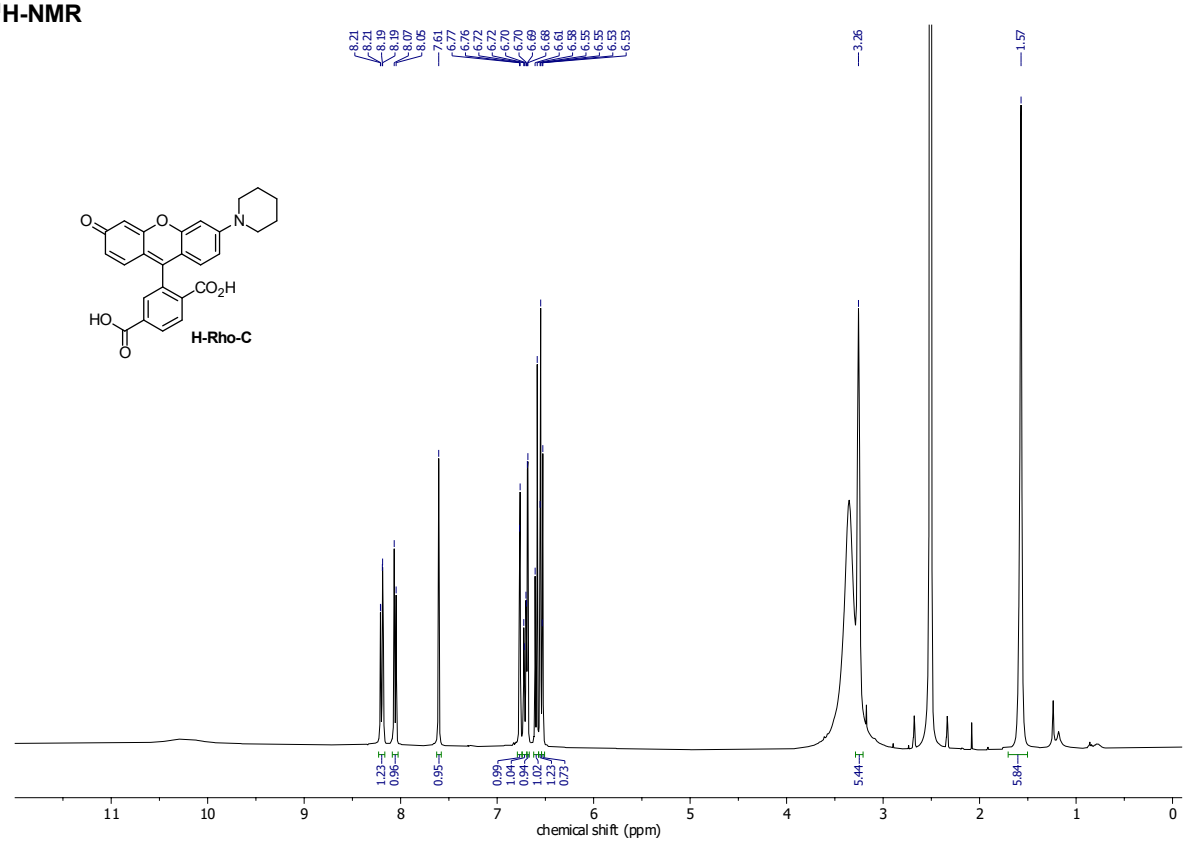

^{13}C-NMR

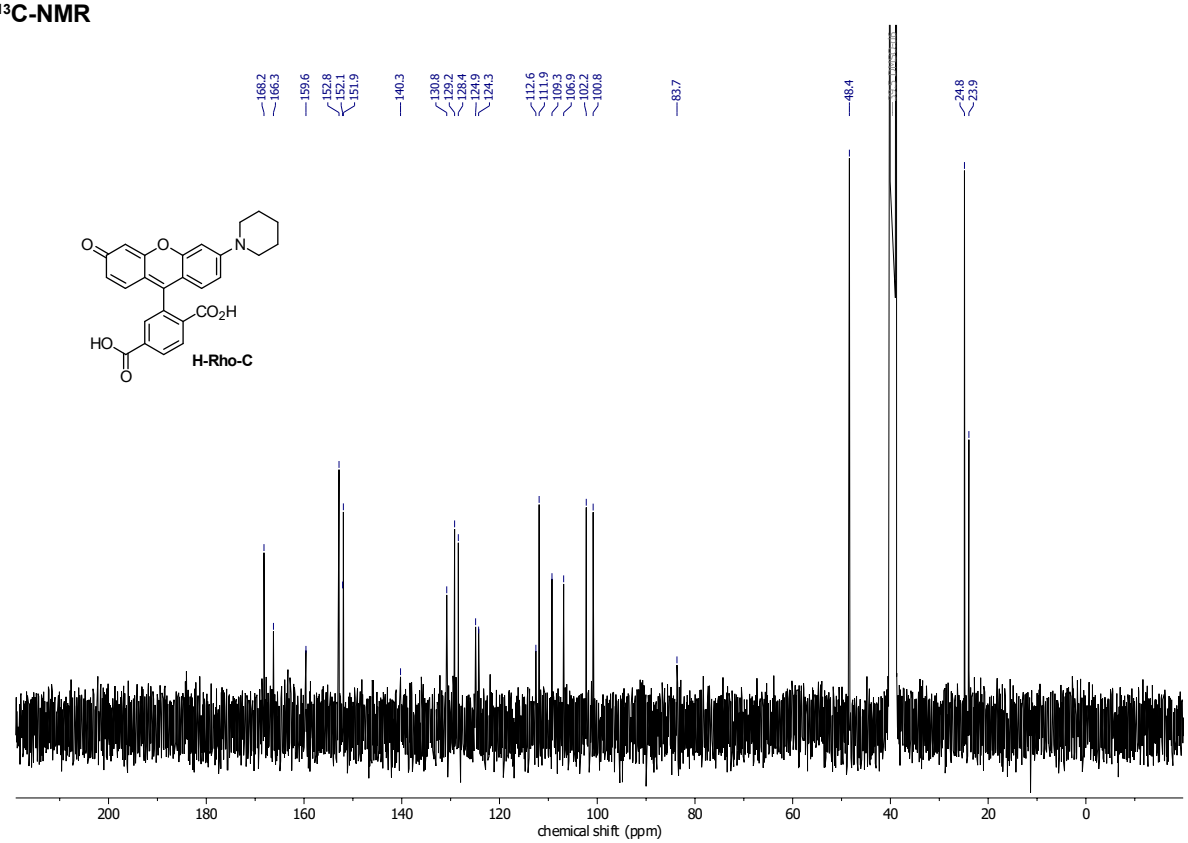

Compound 16
^{1}H-NMR

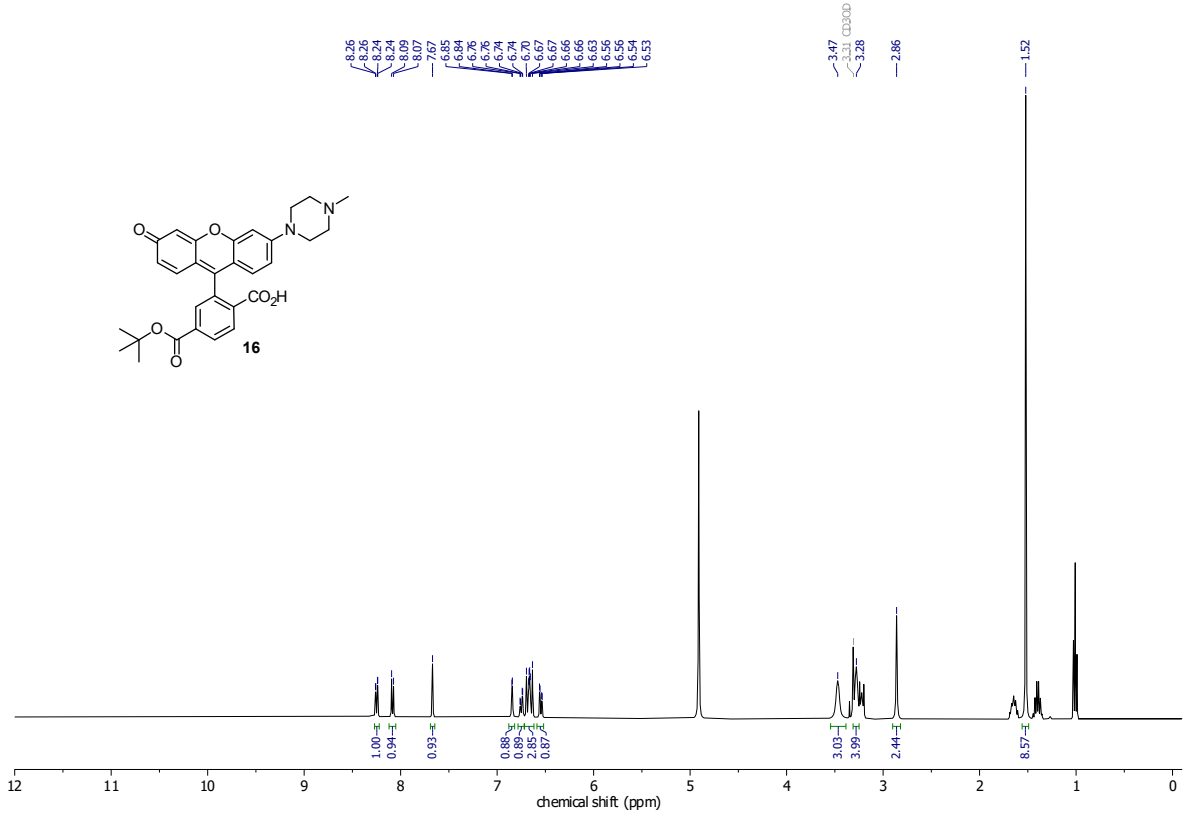

GL-Rho-AC

^{1}H-NMR

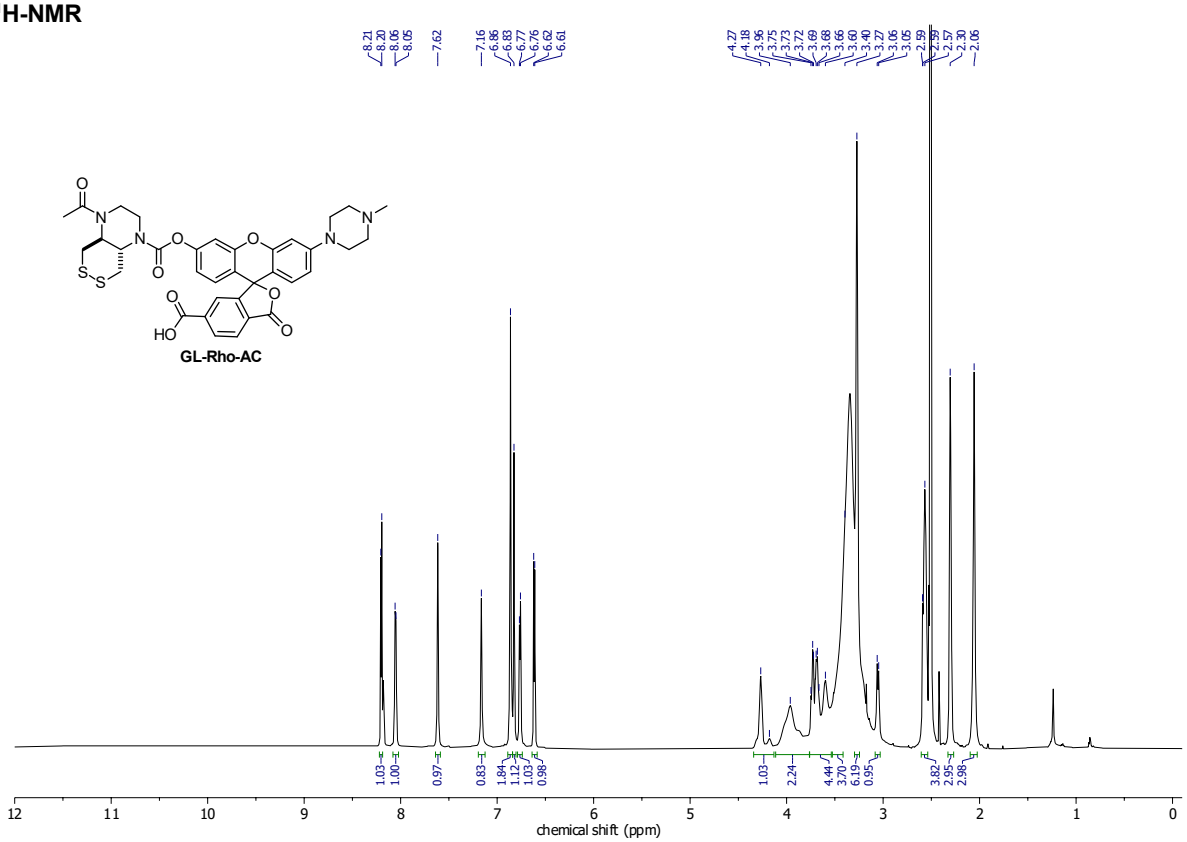

^{13}C-NMR

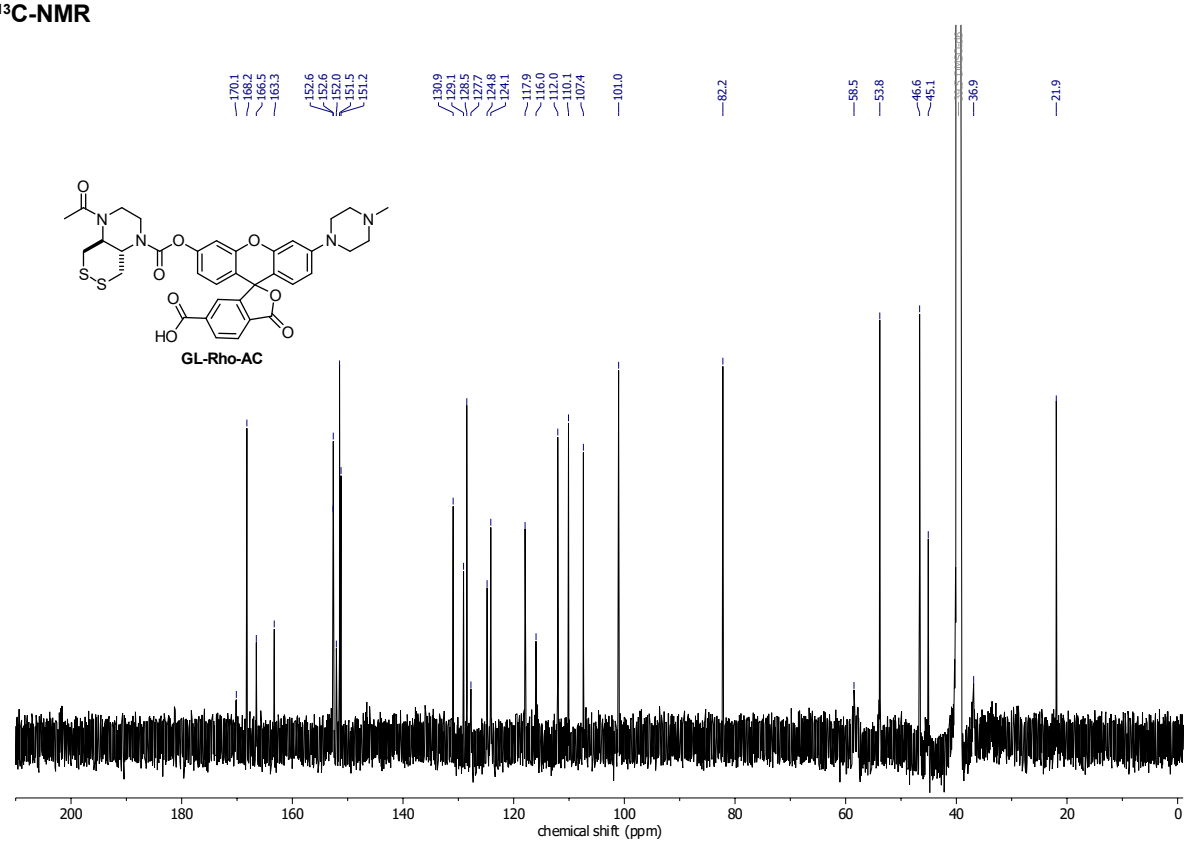

GL-Rho-AC^{m} (= GL-TraG)
^{1}H-NMR

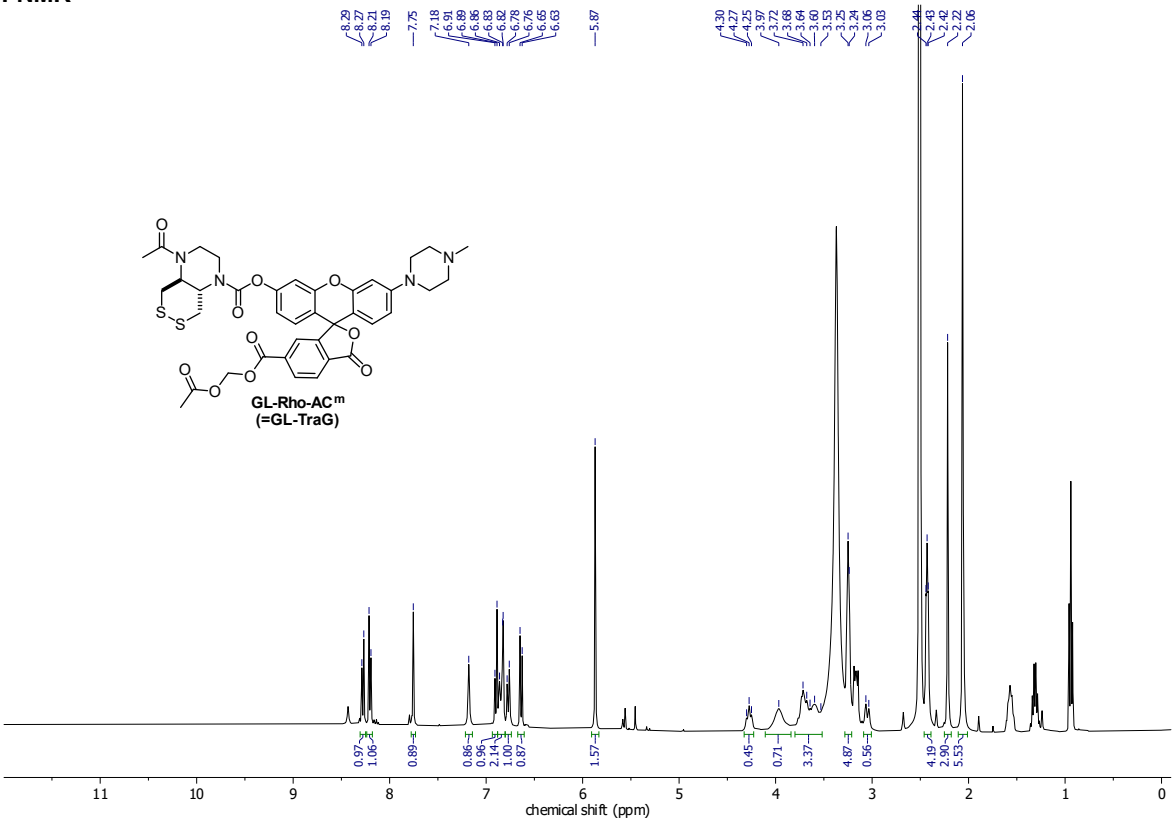

H-Rho-AC (= H-TraG)
^{1}H-NMR

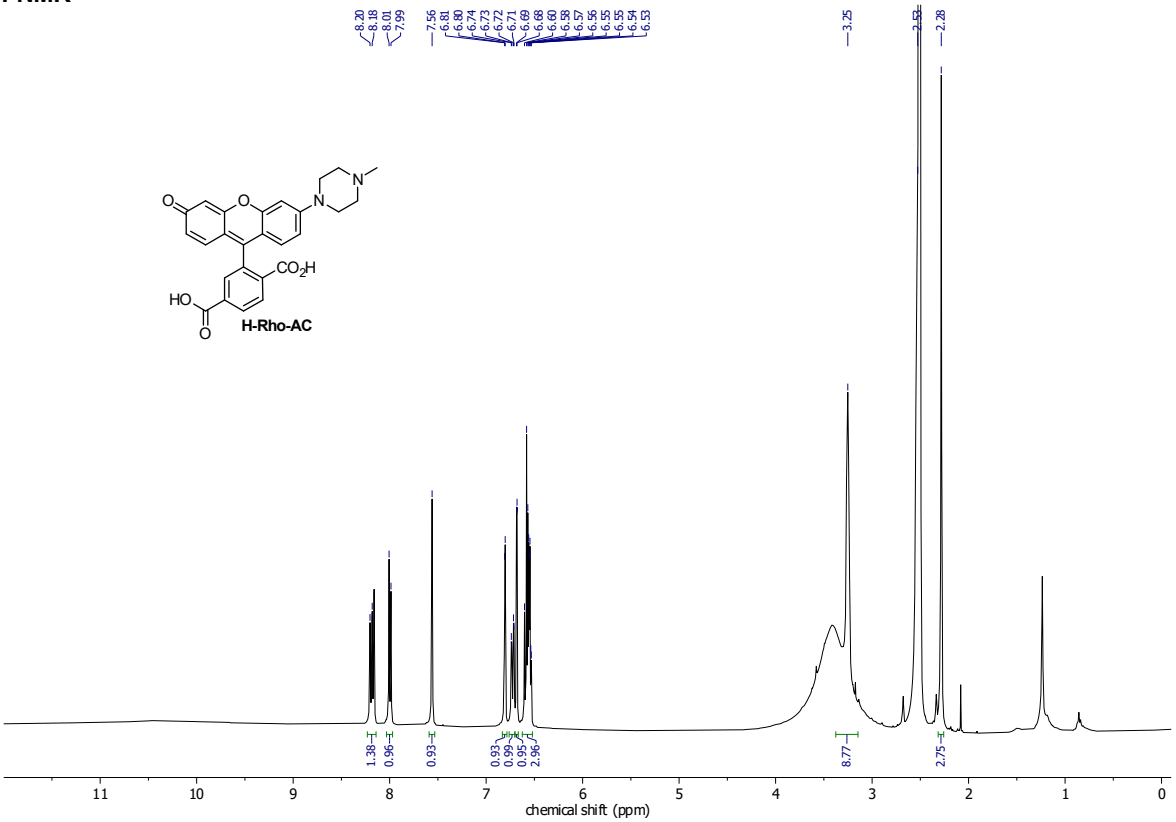

Compound 24

^{1}H-NMR

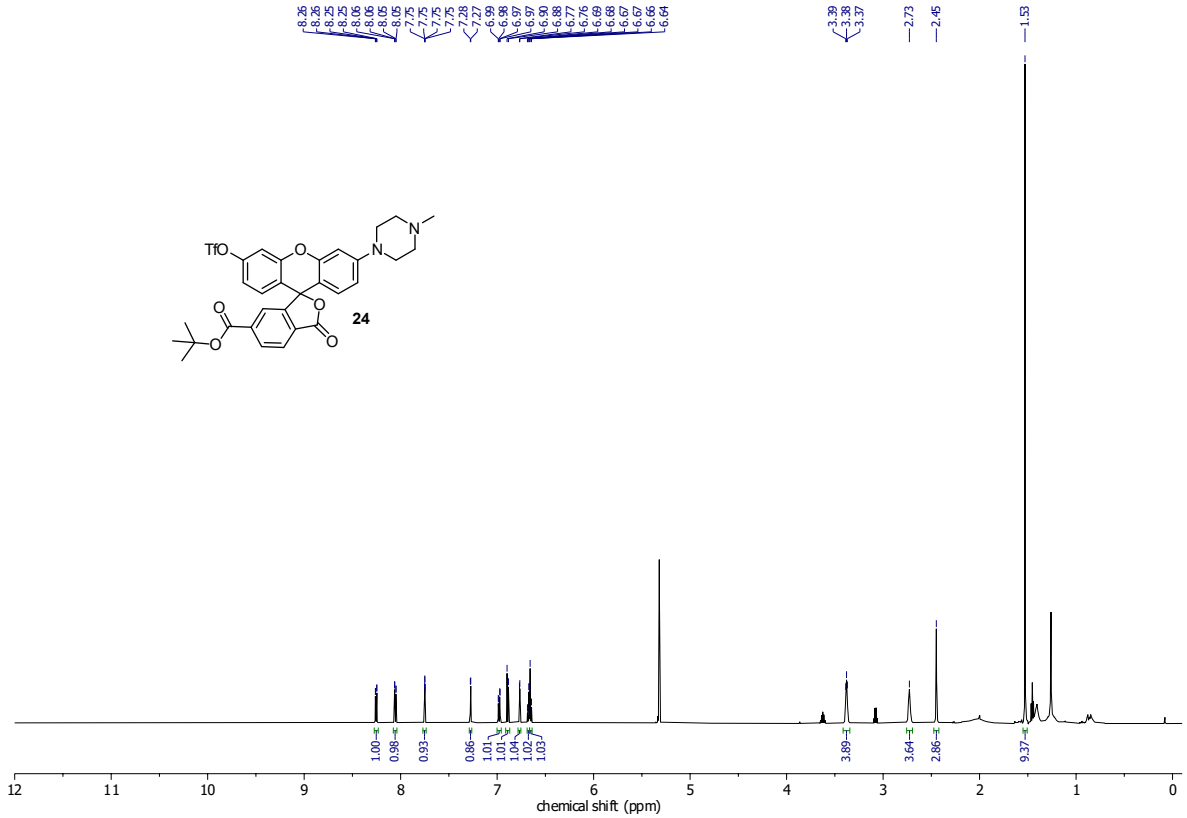

^{13}C-NMR

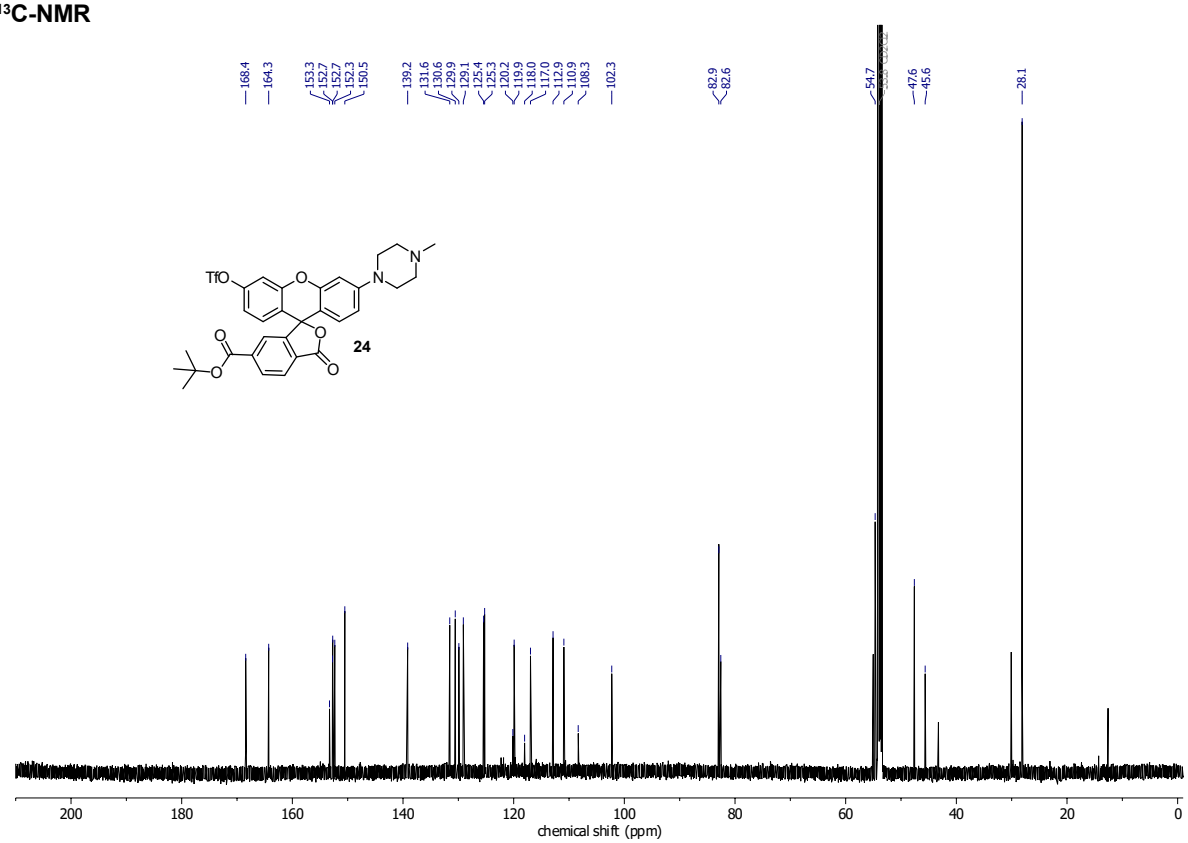

HP-TraG
^{1}H-NMR

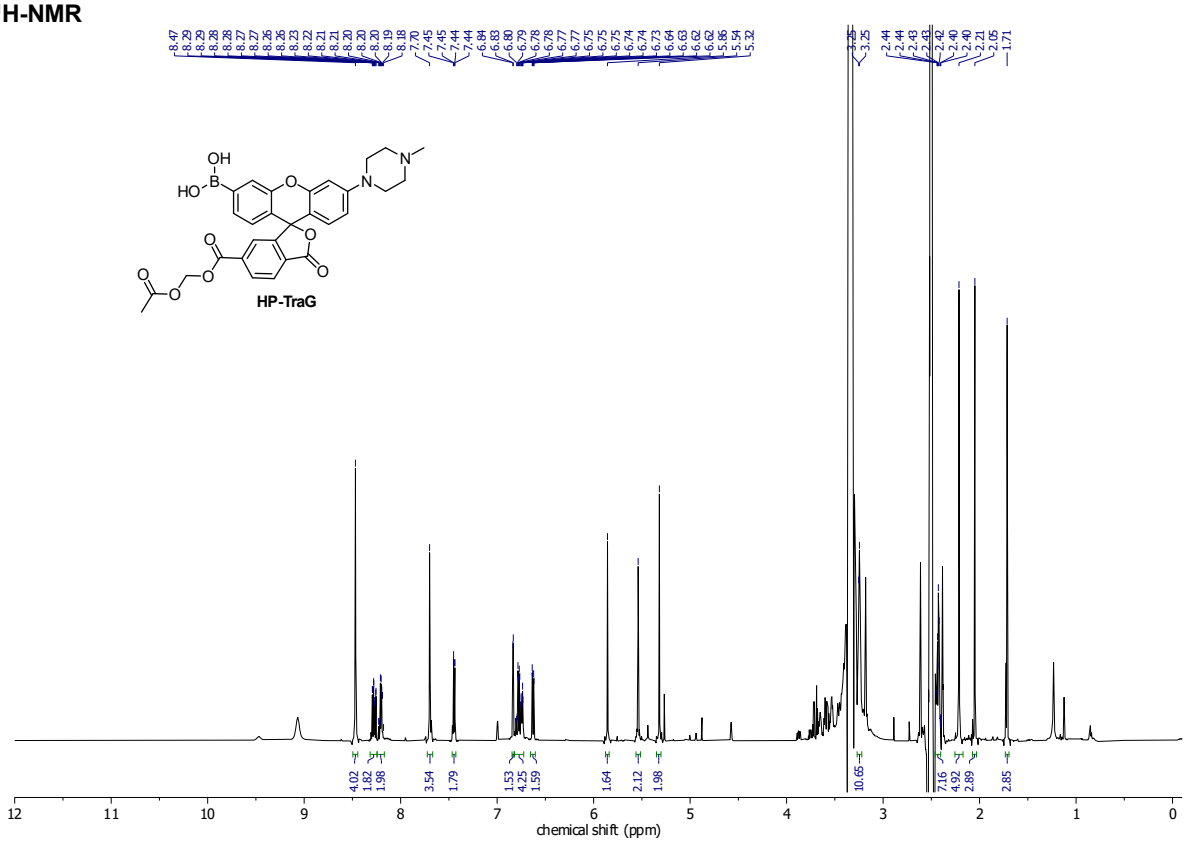

*contains other species (~50 mol%) with equal properties regarding esterase cleavage and hydrogen peroxide oxidation (see Figs26-27).

TR-TraG
^{1}H-NMR

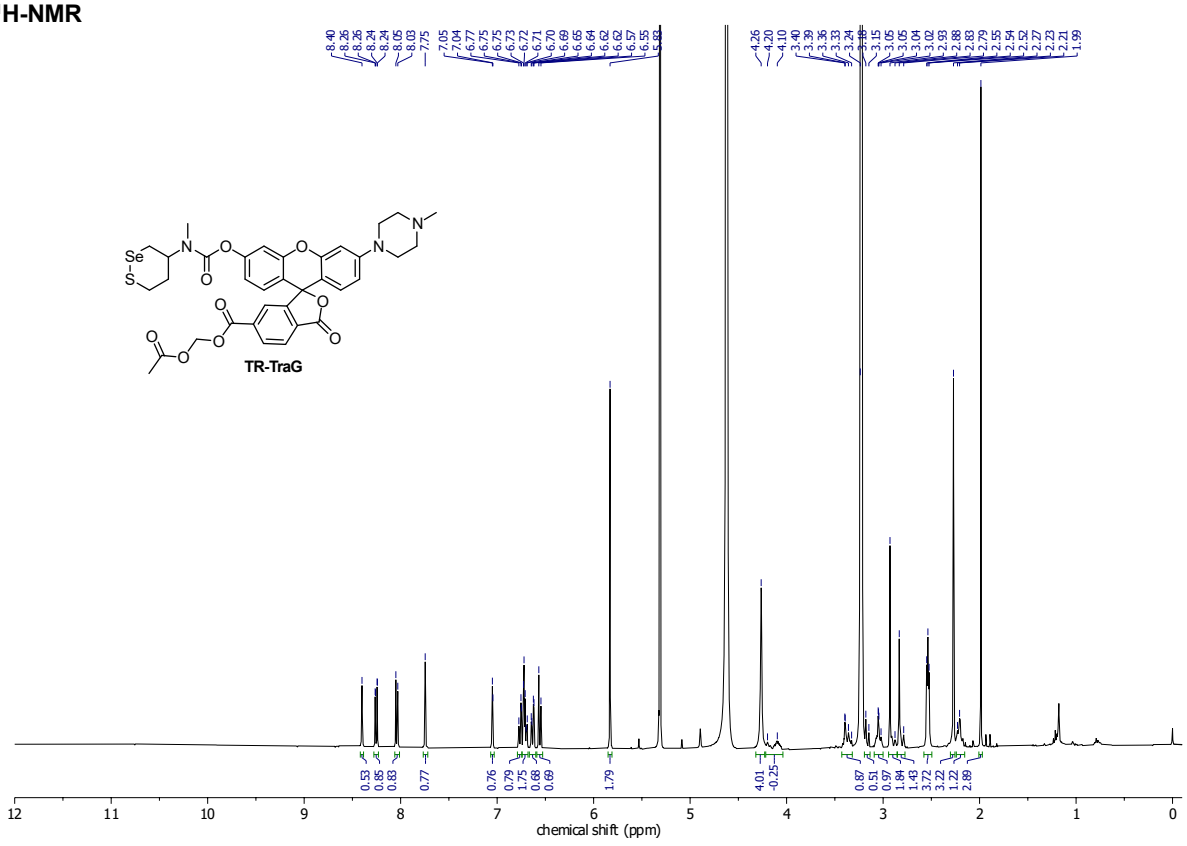

Supplementary Information to

Logic-gating the HaloTag system with Conditional-Halo-ligator 'CHalo' reagents

Philipp Mauker[1,2], Carmen B.J. Zecha[2], Lucas Dessen-Weissenhorn[2], Luciano Román-Albasini[3], Joyce C.M. Meiring[4], Julia I. Brandmeier[2], Daniela Beckmann[5,6], Jan P. Prohaska[1], Yi Louise Li[7], Kristina Mrug[8], Hannah von Schwerin[2], Nynke A. Vepřek[2], Julia F. Gaisbauer[2], Leif Dehmelt[9], Perihan Nalbant[8], Jennifer Zenker[7], Anna Akhmanova[4], Martin Kerschensteiner[5,6,10], Angelika B. Harbauer[3,11], Julia Thorn-Seshold[2,12], Oliver Thorn-Seshold[1,*]

[1] Faculty of Chemistry and Food Chemistry, Dresden University of Technology, Dresden, DE.
[2] Department of Pharmacy, LMU Munich, Munich, DE.
[3] Max Planck Institute for Biological Intelligence; Martinsried, DE.
[4] Division of Cell Biology, Neurobiology and Biophysics, Department of Biology, Utrecht University, Utrecht, NL.
[5] Institute of Clinical Neuroimmunology, LMU University Hospital, LMU Munich, Munich, DE.
[6] Biomedical Center (BMC), Faculty of Medicine, LMU Munich, Martinsried, DE.
[7] Australian Regenerative Medicine Institute, Monash University, Clayton, Victoria, AU.
[8] Faculty of Biology, University of Duisburg-Essen, Essen, DE.
[9] Department of Chemistry and Chemical Biology, Technical University Dortmund, Dortmund, DE.
[10] Munich Cluster for Systems Neurology (SyNergy), Munich, DE.
[11] Technical University of Munich, Institute of Neuronal Cell Biology; Munich, DE.
[12] Institute for Clinical Chemistry, Medical Faculty, Dresden University of Technology, Dresden, DE.

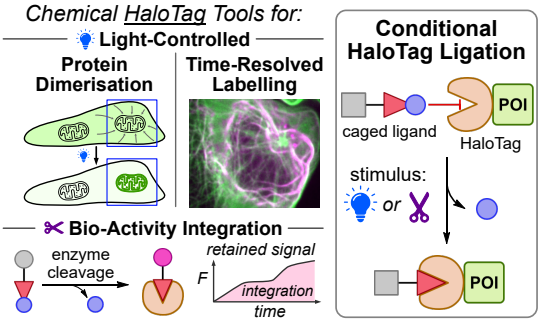

For standard reagent use guides see Supplementary Note 1 (starting on page 3). Particularly, with photocaged CHalo reagents (Cou-CHalo-SiR, Cou-CHalo-BG, etc) we strongly suggest experimenters to use red-only light sources for focusing on the microscope and for room lighting (not filtered white light bulbs).

Table of Contents

1 User Guides for Photocaged CHalo Reagents (Fig S1-S3)

We are happy to freely distribute Cou-CHalo reagents while our stocks last; we only ask receiving experimenters to send us their concentration and power integral settings / data, plus any other helpful assay or model parameters or identifiers, so that we can compile "typical benchmark settings" to recommend to the user community.

1.1 General handling

Warning: for photocaged CHalo reagents e.g. **Cou-CHalo-SiR**, **Cou-CHalo-BG**, etc, use **red-only** light sources for focusing and for transmission imaging on the microscope: since that light is focused through the objective, even minor wavelength components can reach high intensity and cause unexpected photouncaging. Red-only sources include red-emitting lasers (>630 nm) or red LEDs (typ. 630-660 nm) - these will always be good choices. Interference-filtered red-bandpass white sources *might* in principle be tolerated if the interference filtering is very effective (mileage may vary). In our experience, absorption-filtered white sources should always be avoided - such filtering is usually not >99.9% effective and the transmitted violet/blue light fraction then causes uncaging during setup that destroys reagent functionality.

Lighting in the room and during handling: Red-only LEDs for room lighting and experiment setup are very cheap; we use 3 euro red LED strips that plug into a USB socket with ca. 60 LEDs per strip (picture at right; each strip easily illuminates a workbench and/or hood; see e.g. this product link). Red-only room / handling lighting is not strictly required - as long as the light in the room / during handling is very dim (glow from computer monitor, etc), the amount of photouncaging it causes should be insignificant (note that an LED-based computer monitor can also be set to show pure red light). However, we are skeptical about "red light bulbs" that are actually absorption-filtered white light bulbs. Taken together we see no reason not to simply buy and use a USB-pluggable red LED strip for room lighting during handling.

Storage: To avoid the chemical degradation of reagent stocks during long-term storage, they should be aliquoted and then stored in the fridge/freezer (typically −20 °C; can depend on the solvent and reagent); wrapping the vials in aluminium foil will also prevent their photouncaging. For these irreversibly uncageable compounds, ideally, fresh aliquots should be used for each experiment, until the point where assays are confirmed to be working as expected and where satisfactory benchmark performance (for the compound in the assay settings) is available, so that any deviations from expected performance can be identified (although in our experience, assay problems rarely arise from stock degradation, but rather from on-stage mistakes).

Treatment: the reagents should always be added from 100X DMSO stocks (fresh dilution in two 10X steps on the experiment day), otherwise the reagents might precipitate from aqueous solutions at higher concentrations. If concentrations above 1 µM are used, experimenters should lock out for potential precipitation.

1.2 Pre-tests: plausibility, working concentration, and uncaging settings

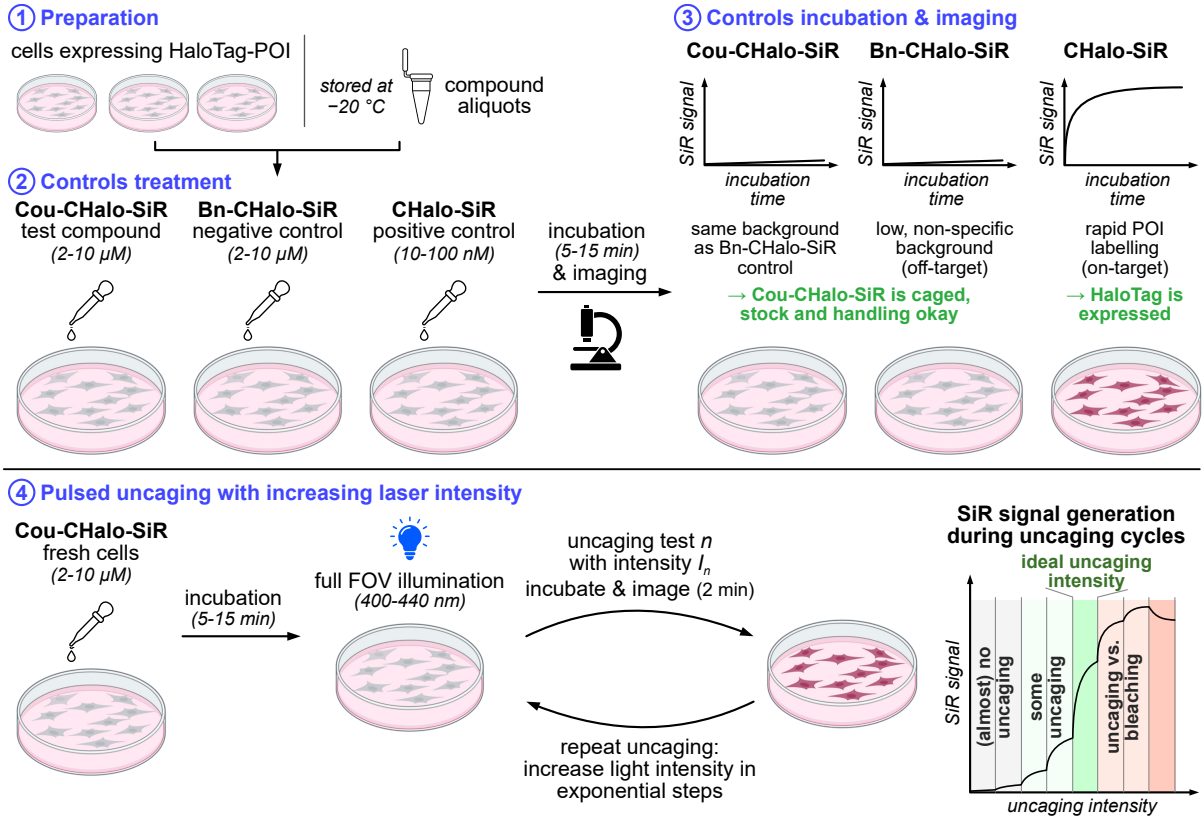

Figure S1: Experimental workflow to determine the ideal photouncaging settings using the **Cou-CHalo-SiR** fluorogenic dye with step-wise increase of the uncaging light "intensity" (in reality, the applied power integral, with units ~ µJ·µm^{-2}).

Determining the ideal photouncaging conditions with the microscope setup to be used in practice is crucial for straightforward and successful application of Cou-CHalo reagents. If too little light power is applied, local photouncaging will be insufficient; but too high light power will cause fluorophore bleaching, cellular phototoxicity, and can release too much CHalo species (i.e. allowing diffusion and out-of-target zone labelling) – finding the sweet spot is key. We recommend the following protocol to establish the uncaging conditions.

(A) Though non-ligated CHalo-SiR has zero fluorescence in cell-free buffer, subcellular compartmentalisation of any SiR reagents into mitochondria and ER gives non-specific background signals in these compartments (also see **Fig. S17**). The caged but non-activatable **Bn-CHalo-SiR** should be used as a control to report on this (expectedly minimal) non-specific "**compartment background**" signal (concentration-dependent) from CHalo-SiR and caged-CHalo-SiR reagents. Non-CHalo SiR reagents (e.g. SiR-Halo, CA-SiR, etc) can have much higher intensities of compartment background signal, and may also have slightly different localisation patterns, at the same concentration.

(B) If **Cou-CHalo-SiR** (at the same concentration) gives higher cellular signal in HaloTag-expressing cells *before uncaging* than **Bn-CHalo-SiR**, the **Cou-CHalo-SiR** must have partially degraded by losing the Cou cage, allowing it to ligate to HaloTag and generate strong ligated signal. In our experience, typically such unintentional photouncaging will have occurred on the stage during the microscopy experiment, e.g. from "white" light being focused through the objective (e.g. for a transmission image or for focussing), or from applying merely "filtered" red light where the filtering does not remove all UV/violet/blue light (instead of applying "red source" light from LEDs or lasers). In rare cases, photouncaging seems to have occurred by careless reagent stock and/or cell handling before reaching the stage (fix: handle stocks and cells under red source lighting and protect stocks from UV/violet/blue light exposure, e.g. wrapping vials in aluminium foil and storing them in the fridge/freezer).

(C) **CHalo-SiR** should be used as a positive control to find the maximum expected target-specific fluorescence, by titrating its concentration up (while comparing to the Bn-CHalo-SiR compartment background signal at the same concentration). It is also a good control for successful HaloTag-POI expression. **CHalo-SiR** is the photouncaging product from **Cou-CHalo-SiR** illumination. When **CHalo-SiR** is applied directly to cells, it ligates to HaloTag upon treatment; typically at low concentrations it will mainly give signal from the ligated product (signal/concentration gradient is high), while at intermediate concentrations all HaloTag protein will become saturated, such that at high concentrations its signal/concentration gradient matches that for the compartment background (low). In typical assays we aim to locally photogenerate an "acceptable" uncaged concentration of **CHalo-SiR** that may be in the 10-100 nM range (since photouncaging proceeds to the same percentage independent of the reagent concentration, we typically aim to minimise photodamge in these

assays by applying a rather high **Cou-CHalo-SiR** concentration and only uncaging a small percentage of it). Thus we recommend applying the **CHalo-SiR** control at concentrations from 10−100 nM, typically by using 100−500X DMSO stocks (maximum DMSO concentration in cell medium: 1%).

Experimental steps (Fig. S1):

Pre-tests: (1) Cells expressing the HaloTag-POI fusion protein and fresh stocks of **Cou-CHalo-SiR**, **Bn-CHalo-SiR** and **CHalo-SiR** are prepared. (2) The cells are treated with the respective compound (2−10 µM) and incubated for 5−15 min (*Note: all three dyes are well cell permeable allowing for short incubation times; higher concentrations of 2−10 µM should be used for **Cou-CHalo-SiR** to achieve rather high local concentrations since the photouncaging product is likewise permeable and will diffuse away from the activation site*). (3) The cells are imaged in the SiR channel (excitation: 650 nm, emission: 670 nm) during the incubation to determine the SiR signal increase. *Expected results*: **Bn-CHalo-SiR** and **Cou-CHalo-SiR** should give very low signal, that is approximately equal (minor non-specific "compartment background" signal in mitochondria and ER is expected, also see **Fig. S17**). If **Cou-CHalo-SiR** shows higher fluorescence than **Bn-CHalo-SiR**, typically the handling off- or on-stage has led to (partial) unwanted photouncaging of **Cou-CHalo-SiR**, so handling should be improved but reagent stocks are still fine (less likely: the stock used has been degraded and significant **CHalo-SiR** is now present inside it). **CHalo-SiR** should rapidly develop on-target fluorescence by ligating to HaloTag in the compartment where it is expressed (note though: signal does not *necessarily* reach plateau during the first 15 min at low concentrations).

Parameter tuning: If the pre-tests gave the expected results, experimenters can move forward to set experimental parameters for pulsed photouncaging assays. (4) A fresh well of HaloTag-POI expressing cells is treated with **Cou-CHalo-SiR** (typ. 10 µM as a start point*) for 5−15 min and then the whole field of view (FOV) is photouncaged step-wise several times (400−440 nm light) with ***significantly*** ** increasing light energies at each step, imaging the SiR channel over ca. 2 min after each uncaging step (e.g. taking 4-10 images). ***Assuming that the concentration has been well chosen****, a good uncaging energy is found by identifying which step gave the steepest specific SiR signal increase.

An expected **photouncaging** profile is shown in **Fig. S1**. Note that e.g. an uncaging light power integral of "0.1" will result in 10% photouncaging percentage that may give already e.g. 50% of maximum specific Halo-ligated signal (if Cou-CHalo-SiR concentration is 5 times higher than HaloTag concentration); but an uncaging light power integral of "1" that will result in ca. 66% uncaging (logarithmic response) but this only gives e.g. 100% of maximum specific signal (HaloTag is saturated), and any further increases in uncaging light power cannot increase the specific signal. In fact, **photobleaching** of the Halo-ligated SiR dye by the uncaging light always accompanies each uncaging step, so the total signal (at high Halo-ligation) can actually reduce with additional uncaging light.

*** Concentration:** A good control is to compare results with e.g. 3 µM and 30 µM of the Cou-CHalo-SiR reagent. The same photouncaging profile as for 10 µM should give nonlinearly scaled, but plausible, SiR signal profiles (e.g. with 30 µM, 3 fold lower uncaging light integral should be required to saturate the HaloTag and give maximum specific signal; with 3 µM, 3 fold higher light integral is required). If the concentration-comparison assays give plausible results then the 10 µM working concentration can be considered well-chosen. If not, adjust the concentration and run again.

**** Light Energy**: Ideally, the uncaging light power integrals should be scanned by logarithmic steps (1,2,4,8,16,...). Adjusting the laser intensity over a reproducible region (e.g. 2, 4, 8, 16, 32%) may be the most practical way to identify roughly the right power integral. However, ***once that power setting is found***, we strongly recommend to run a control that scans a smaller range of light power integrals by ***linearly*** adjusting the pixel dwell time over perhaps a 4-fold range, since that is an easy and reproducible way to linearly vary the applied power integral, without changing its spatial distribution, with good reproducibility. Since a "good" uncaging energy is by definition one that uncages a rather small amount of reagent (see point (C) above), that *linear* pixel dwell time scan series should be enough to deliver clear and ***linear*** **responses in HaloTag-ligated-SiR readout**, despite the complexities of e.g. photobleaching. If that linearity is not seen, saturation or thresholding effects must have been operating: thus the power integral would usually have been set vastly too high or too low, and severe photobleaching or absolute signal intensity problems may have been seen. **In such cases, the first step is to re-evaluate the working concentration**, and re-start the tuning procedure. *Nonlinearity can be a particular problem when overall HaloTag expression per cell is very low: e.g. it is easily possible that the step-wise illumination leads to HaloTag saturation after initial steps, preventing possible specific signal increase of higher light dose steps, while photobleaching starts to dominate. In that case, the photouncaging test should be repeated with a fresh well or fresh plate of cells (to avoid cases where unwanted light scattering may have photouncaged some reagent in neighbouring cells and wells), and starting from perhaps 5% of the uncaging energy that gave specific signal saturation.*

Finally: When the ideal light power integral (i.e. roughly the dwell time per pixel (ms) multiplied by energy density (W/µm^2 ***in the sample plane***)) has been identified, the experimenters should record the actual laser power for reference purposes (since the laser power can vary over time, this will allow reproducibly adjusting laser intensity for comparable future experiments). Please also send us the concentration / power integral settings that work for you, so we can add them to our **typical benchmark settings** compilation.

1.3 Light-controlled fluorogenic labelling with Cou-CHalo-SiR (typical steps)

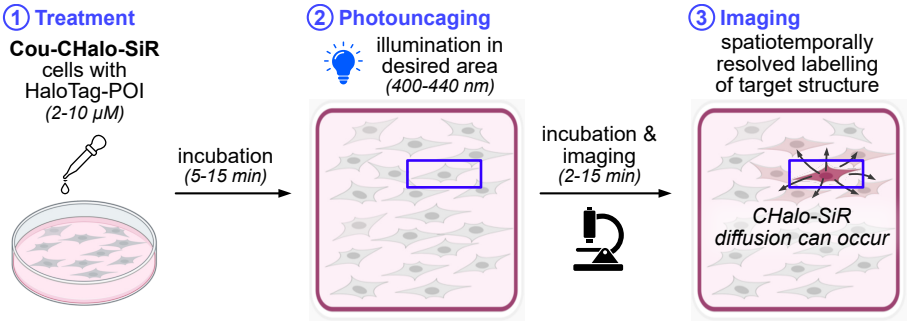

Figure S2: Experimental workflow for spatiotemporally controlled, fluorogenic HaloTag-POI labelling with **Cou-CHalo-SiR**.

Cou-CHalo-SiR can be used for spatiotemporally controlled fluorogenic labelling.

Experimental steps (Fig. S2): (1) HaloTag-POI expressing cells are treated with **Cou-CHalo-SiR** for 5−15 min (the dye is well membrane permeable). We recommend starting with 2−10 µM concentrations to achieve high local concentrations since the released photouncaging product **CHalo-SiR** is rapidly diluted due to post-activation diffusion. (2) The desired region is illuminated with identical light doses as determined in the pre-tests (**Fig. S1**) and (3) SiR channel imaging is started immediately after uncaging to observe the fluorogenic HaloTag labelling of the target protein (excitation: 650 nm, emission: 670 nm). Typically, the signal plateaus within 5 min. Due to the cell-permeability of the **CHalo-SiR** photouncaging product before it ligates, the product can diffuse away from its activation site (**do not expect subcellular spatial resolution!**), and can exit the cell in which it was activated. After cell exit, **in 2D cell culture** it probably dilutes away in the cell culture medium, particularly if convective currents assist flow; whereas if cells are located **in a gel / matrix or multicellular organism**, "dilution away" is spatially limited and one can expect substantial labelling of neighbouring cells. Therefore, a fresh well of cells should be used for every experiment to achieve ideal temporal control for the labelling. (If neighbour labelling is seen in 2D cell culture without a gel/matrix, this probably indicates that the uncaging illumination was not truly cell- or subcellularly-localised.)

1.4 Protein heterodimerisation with Cou-CHalo-BG

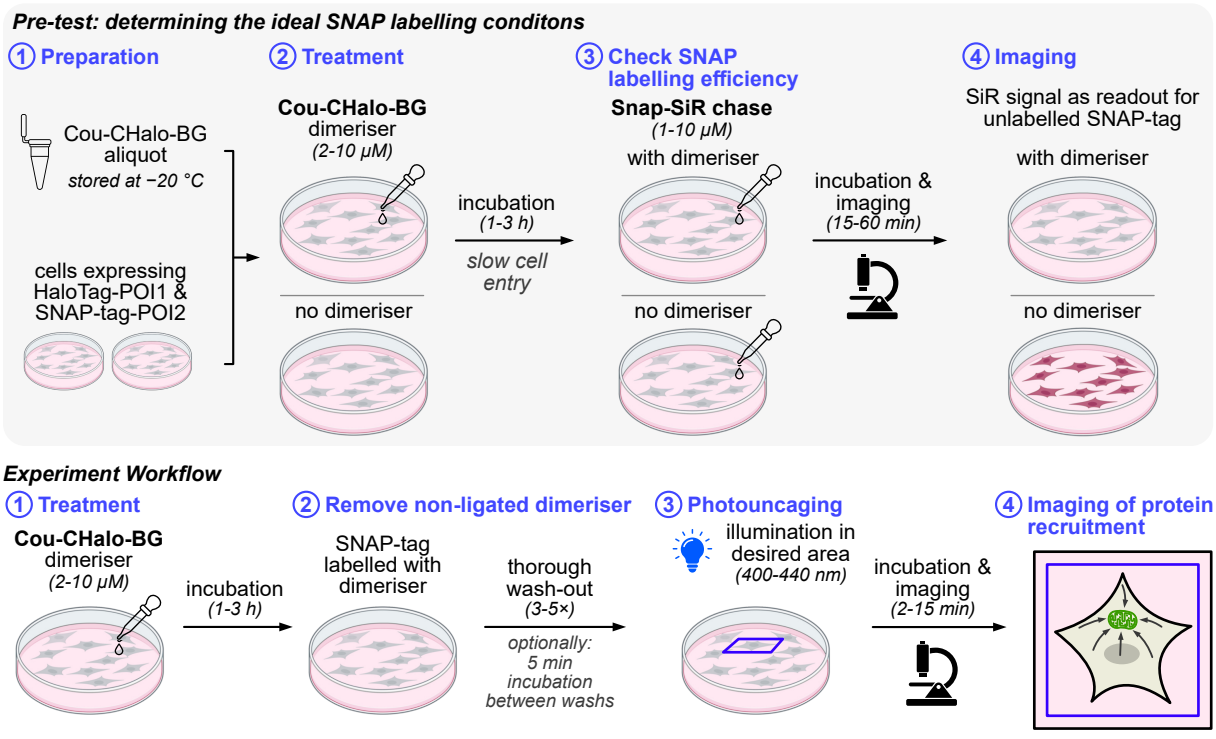

Figure S3: Experimental workflow for spatiotemporally controlled HaloTag-to-SNAP-tag protein heterodimerisation with **Cou-CHalo-BG**.

The photo-activatable SNAP-tag-to-HaloTag dimeriser **Cou-CHalo-BG** enables light-controlled protein heterodimerisation. For successful and quantitative dimerisation, efficient SNAP-tag labelling is crucial, therefore a pre-test to determine the SNAP labelling conditions should be performed.

Experimental steps (Fig. S3): (1) Cells expressing the HaloTag-POI1 and SNAP-tag-POI2 proteins are prepared (*note: for successful dimerisation, both POIs must be expressed so they share access to the same compartment: e.g. cytsol to outer mitochondrial membrane or cytosol to inner plasma membrane dimerisation is possible, but not from ER to inner mitochondrial membrane*). (2) Cells are treated with fresh aliquots of **Cou-CHalo-BG** (2−10 µM) while in parallel control cells are cultured without treatment (DMSO control). Longer incubation times (1−3 h) than with **CHalo-SiR** are needed to reach high SNAP-tag anchor labelling, due to the lower membrane permeability of **Cou-CHalo-BG** compared to the **CHalo-SiR** dyes. (3) The medium is changed to remove the dimeriser (2× wash), then a SNAP chase dye (e.g. 1−10 µM Snap-SiR) is added to both the untreated cells and the cells pre-incubated with **Cou-CHalo-BG**, and is incubated for 15−60 min (needs longer incubation than for comparable HaloTag dyes), before the cells are imaged (checks for SNAP-tag labelling efficiency, by fluorogenic SNAP-tag ligation and SiR signal generation (excitation: 650 nm, emission: 670 nm)). **Ideally**, the cells pre-treated with the dimeriser show no SiR fluorescence and the untreated cells show high signal (alternatively a strong SiR signal reduction in the dimeriser cells allows to estimate the labelled portion of the SNAP-tag). If full labelling is achieved, the loading concentration (or, if really desired, the loading time) can be reduced so that it is easier to achieve full unligated wash-out in later applications. If very low labelling is observed, the loading concentration (or, in unusual cases, just the incubation time) should be increased.

The actual experiment: After establishing a SNAP-tag labelling protocol for the **Cou-CHalo-BG** dimeriser, it can be used for light-induced SNAP-tag-to-HaloTag protein heterodimerisation. (1) Cells expressing the HaloTag-POI1 and SNAP-tag-POI2 proteins are treated with fresh aliquots of **Cou-CHalo-BG** (2−10 µM) for 1−3 h. (*Note regarding protein expression: depending on the system and the readout, the experimenter should ensure that the ratio of HaloTag-POI1 and SNAP-tag-POI2 expression is tuned to support the desired effect. For example, for our experiments for cytosolic HaloTag-GFP recruitment to mitochondrial SNAP-tag, we aimed to achieve near-quantitative re-localisation of HaloTag-GFP and thus transfected it substoichiometrically (aim: higher expression of SNAP anchor than Halo target), then specifically chose to work with cells that had dim GFP fluorescence in the hope that the SNAP expression in those cells would be higher than the HaloTag expression (though, if there had been a SNAP reporter fluorescent protein, we would have used that to get a proper Halo:SNAP expression ratio estimate, which would have allowed better experiment design)*). (2) The excess of non-ligated dimeriser is removed by thorough washing (3−5× change medium, optionally with 5 min incubation after each medium change) to avoid undesired HaloTag ligation by residual non-SNAP-tag ligated dimeriser after uncaging. (3) The desired region is illuminated with identical light doses as determined before (see **Fig. S1**) and (4) the cells are imaged to observe the induced protein recruitment. For cytosolic HaloTag-GFP recruitment to mitochondrial SNAP-tag (on the outer mito-membrane) we saw relocalisation complete within 1 min, however, heterodimerisation kinetics will strongly dependent on the nature of the two POIs selected. If no relocalisation is observed, the wash-out protocol should be improved to avoid HaloTag ligation of remaining, non-SNAP ligated dimeriser (also see main **Fig. 1**).

When the SNAP-tag anchor is prevented from freely diffusing in the cell (e.g. bound to an organelle surface or structure), subcellularly-spatially-specific uncaging should result in subcellularly-spatially-specific HaloTag recruitment.

2 Reagent Overview (Fig S4-S5)

2.1 CHalo Reagents

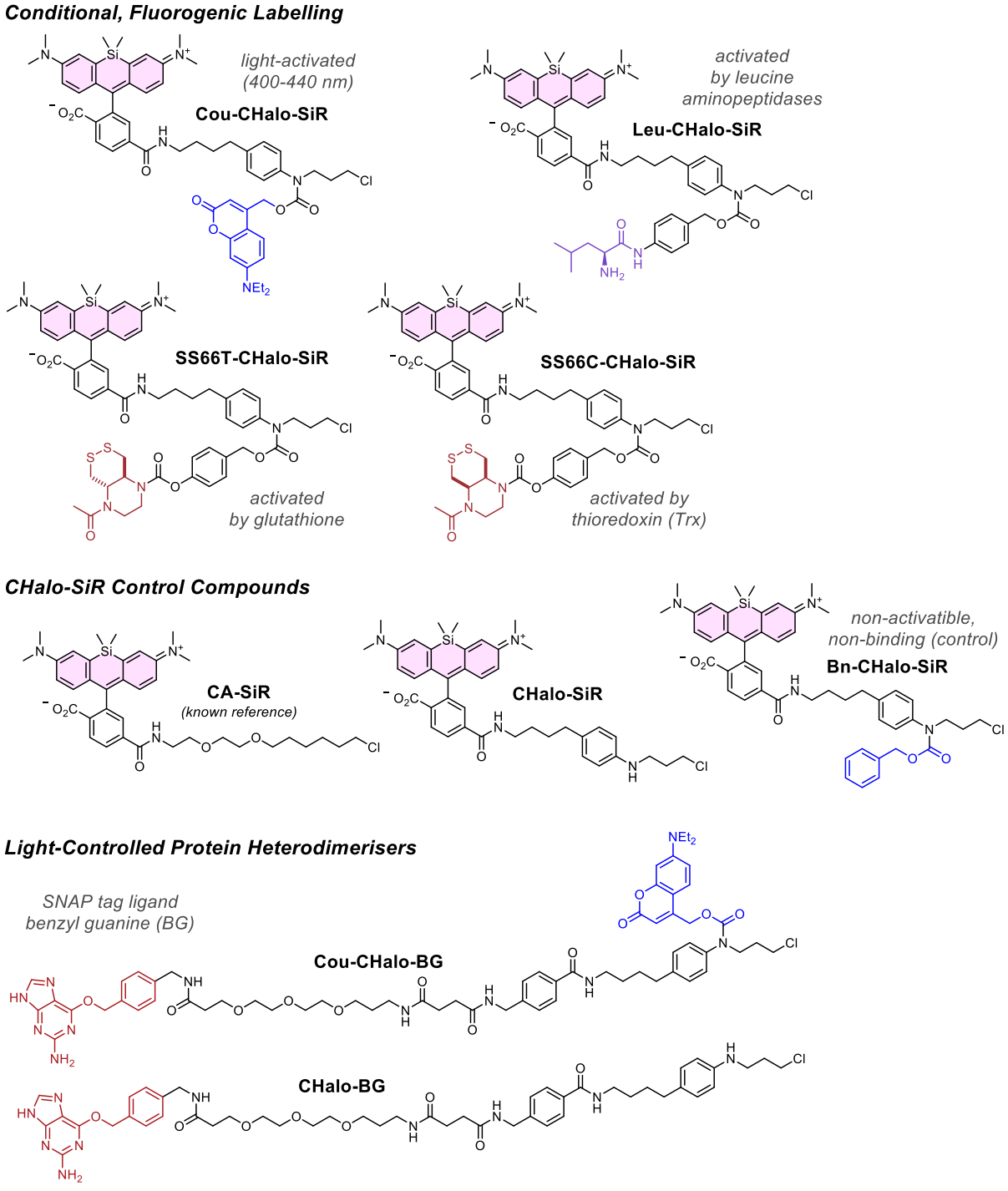

Figure S4: Chemical structures of **CHalo** reagents.

2.2 Design Optimisation: proof-of-concept fluorescein conjugates

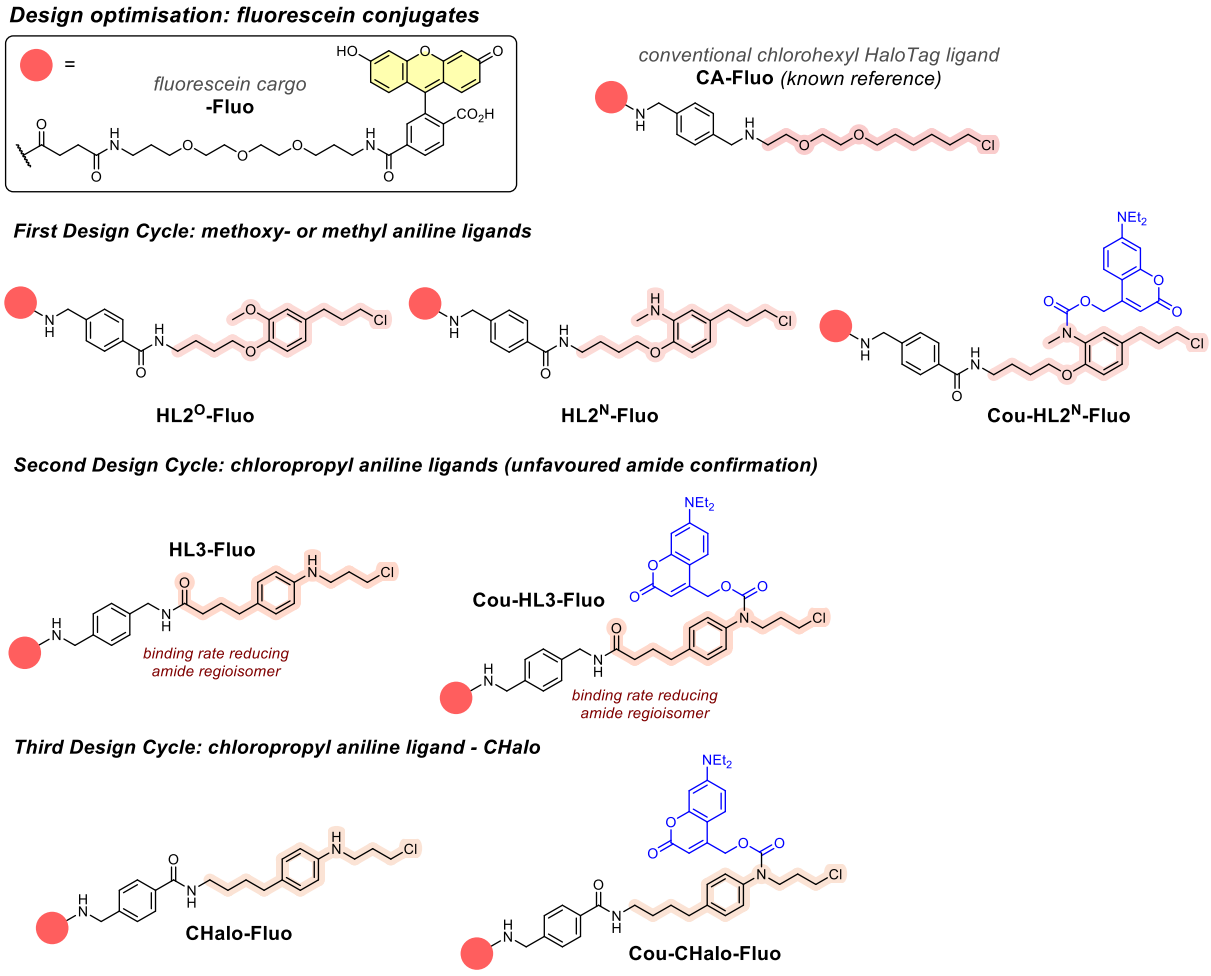

Figure S5: Chemical structures of initial HaloTag ligand designs as fluorescein conjugates which were iteratively optimised before arriving at the **CHalo** Design.

3 Supplementary Note 1: Ligand Design (Fig S6-S8)

3.1 Initial Design (HL2^N Ligand)

The HaloTag protein has been evolved to accept long, linear substrates like the classic chloroalkane motif (CA, **Fig. S6b**), with which it reacts at outstanding speed. The CA motif is used almost[1] exclusively for HaloTag reagents, so little is known about what structural changes are needed to make a CA derivative that *cannot* ligate to HaloTag. Since CA must insert down a long and seemingly narrow protein tunnel for ligation (**Fig. S6a**: crystal structure with CA-TMR[2]), it seemed likely that installing a bulky caging group on the chain, ≤10 atoms away from the reactive chlorine, would block ligation. However, the ethylene glycol ether backbone of the CA motif is chemically featureless, and does not offer a caging site, so we needed to install one. This site must be easy to derivatise with a range of stimulus-responsive cages in biochemically stable but easily uncaged form, which suggested installing an amine for caging as a carbamate since many such cage types are well known (for enzyme[3], light[4,5], or biochemical[6,7] uncaging). Yet, after uncaging this site, the motif must ligate HaloTag as efficiently as possible: which we imagined would be problematic for an aliphatic amine (e.g. as an isosteric replacement for one of the ether oxygens) due to its basicity and polarity.

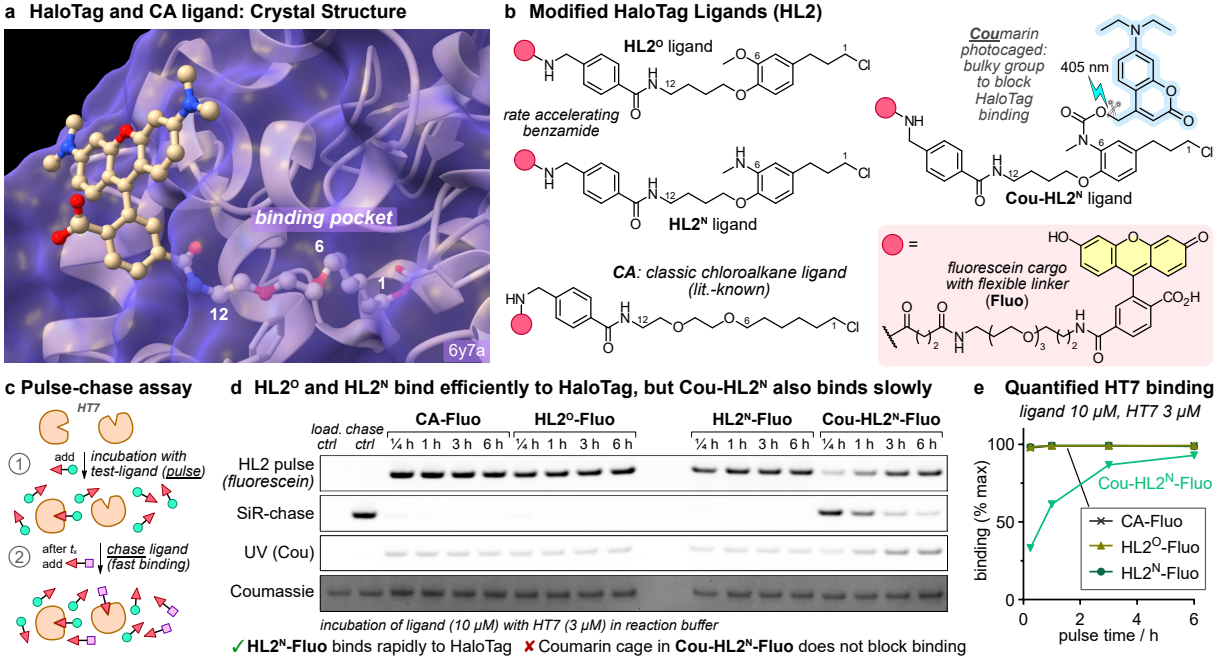

Figure S6: Design of HaloTag ligand HL2^N and its coumarin-photocaged version Cou-HL2^N for light-induced HaloTag binding. (a) Crystal structure of CA-rhodamine bound to HaloTag7 protein (HT7) with the chromophore positioned on the protein surface and the chloroalkane chain buried inside the protein *(pdb code: 6y7a)*; **(b)** Chemical structures of HL2-type fluorescein conjugates; **(c)** Schematic representation of the "pulse-chase" assay used to determine the binding efficiency of our ligands to HT7: (i) incubation with test-ligand (pulse), then (ii) addition of excess of **CA-SiR** which is known to rapidly bind HT7 (chase); **(d)** SDS-PAGE gel showing the binding efficiencies of **CA-Fluo** compared to **HL2^O-Fluo**, **HL2^N-Fluo** and **Cou-HL2^N-Fluo** (10 µM) each after incubation with purified HT7 (3 µM) for different times (15 min, 1 h, 3 h, 6 h); all rows show the HT7 band: (i) fluorescein fluorescence, (ii) SiR fluorescence, (iii) UV fluorescence (365 nm), (iv) Coumassie staining; **(e)** Quantified HT7-binding of HL2-type fluorescein conjugates (quantified from SiR-chase channel from panel d; quantification from fluorescein channel in panel d).

Thus, we seized on a recent report by Tadross *et al.*[8] who showed that a methoxybenzene is well tolerated as part of the HaloTag-ligating chain of **HTL.2** reagents (**Fig. 1e**). We exchanged the methoxy group for an only weakly basic *N*-methylaniline, yielding **HL2^N** where the carbamate-cageable nitrogen is six atoms away from the chlorine (**Fig. 1b**). We synthesised the fluorescein conjugate of the **HL2^N** ligand (**HL2^N-Fluo**), and its diethylaminocoumarin-photocaged derivative (**Cou-HL2^N-Fluo**), as well as the Tadross-inspired non-cageable analogue **HL2^O-Fluo** (which we expected should benchmark the rate penalty for installing an *N*-methylaniline instead of the **HTL.2**-type methoxybenzene). We performed pulse-chase assays (**Fig. S6c**) to assess their ability to ligate to the HaloTag protein: typically, a reagent ("pulse reagent") is incubated with purified HaloTag 7 protein (HT7) for a specific time ("pulse time") for ligation to take place, then an excess of a rapidly-ligating "chase ligand" (**CA-MaP555**[9] or **CA-SiR**[10]) is applied to saturate the remaining fraction of non-ligated HT7 so that the pulse labelling is essentially stopped after the given pulse time. The degree of labelling can be quantified by several methods, where different fluorophore wavelengths are used to quantify the pulse and the chase labels, e.g. by in-gel fluorescence analysis of an SDS-PAGE gel (which proves covalent attachment of the dye to the protein, otherwise the fluorescence signal would not overlap with the HT7 protein band). In

our experience, pulse quantification is more reliably interpretable at low pulse labelling, with chase quantification becoming more reliably quantifiable with high pulse labelling.

Pleasingly, **HL2^{N}-Fluo** ligated very effectively to HaloTag (full binding within 15 min, like **HL2^{O}-Fluo**), which supported the aniline-type design logic. However surprisingly, caging it as a carbamate (**Cou-HL2^{N}**) did not stop the ligation reaction (binding half time $t_{½}$ ca. 0.5 h; **Fig. S6de**). We concluded that caging must be performed closer to the HaloTag ligation reaction site chlorine.

3.2 CHalo Ligand Design

We now moved the cageable nitrogen as close as possible to the HaloTag ligation site. To avoid the potential for cytotoxic aziridine formation, we decided to place the cageable nitrogen not two but three methylenes away from the reactive chlorine, i.e. extending the chloroalkyl chain by one methylene unit from the Tadross design. This yielded **CHalo**, a simple substrate that is conveniently accessible from cheap starting materials yet surprisingly was never reported before in chemical literature for any purpose. The syntheses of caged cargo-bearing CHalo reagents were also simple and high-yielding (e.g. caging by reaction with a chloroformate, cargo attachment by amide coupling, **Fig. S7ab**). We anticipated that the potentially non-optimal positioning of the aryl ring might reduce ligation kinetics: but we now tested this for both free and caged analogues.

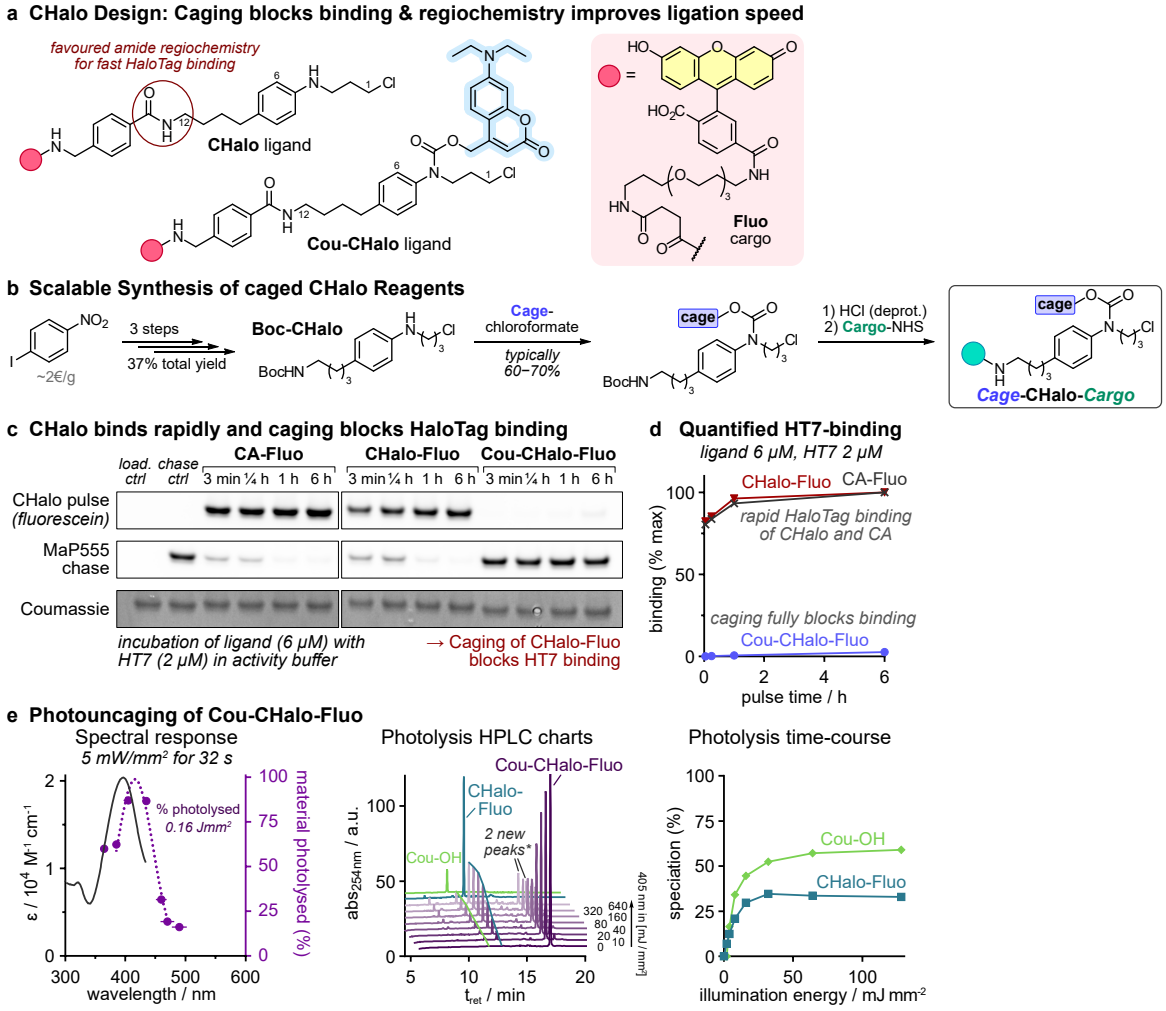

Figure S7: CHalo Design: fast HaloTag Ligation and full binding suppression for caged Cou-CHalo ligand. (a) Chemical structures of **CHalo-** and **Cou-CHalo-Fluo**; **(b)** Synthetic access to CHalo reagents; **(c)** SDS-PAGE gel showing the binding efficiencies of **CHalo-Fluo** and **Cou-CHalo-Fluo** (6 µM) each after incubation with purified HT7 (2 µM) for different times (3 min, 15 min, 1 h, 6 h); all rows show HT7 band: (i) fluorescein fluorescence, (ii) MaP555 chase fluorescence, (iii) Coumassie staining (full gel and quantification from SiR-chase channel in **Fig S14**); **(d)** Quantified HT7 binding of CHalo fluorescein conjugates (quantified from fluorescein channel in panel b); **(e) Cou-CHalo-Fluo** can be uncaged efficiently with blue light (ideal: 400−440 nm) and GFP orthogonally (no uncaging >470 nm; 50 µM sample in DMSO:water 7:3; illumination with the same integrated light intensity for each "wavelength" (horizontal error bars show FWHM of these quasi-Gaussian excitation light source LED "wavelengths"); HPLC speciation and photolysis time-course (50 µM in MeCN:water 1:1; illumination with 405 nm light, 5 mW/mm^2, applied for times from 1 to 128 seconds (factor 2 steps)); **the species in the "2 new peaks" close to the Cou-CHalo-SiR signal include the coumaryl-CHalo alkyl aniline which is a non-physiological byproduct of the high concentrations used in this assay (after an aniline has been photoliberated, it can trap another photogenerated coumarinyl unit: byproduct mass lacks CO_2).*

Free **CHalo** ligated rapidly to HaloTag protein with the fluorescein conjugates displaying similar ligation rates as the optimised linear CA substrate (**Fig. S7c**). Crucially though, the binding of carbamate-**caged-CHalo** was fully suppressed (under 1% after 100 minutes incubation, see **Supplementary Note 2** for analysis). Importantly, the CHalo ligand retains its HaloTag specificity and does not show off-target labelling of other proteins (**Fig. S16**). This now motivated us to create caged, logic-gated CHalo reagents for some of the applications that are impossible with any of the known, unconditional, HaloTag-ligating motifs; and began with the photoactivatable **Cou-CHalo-Fluo** which showed an expected uncaging action spectrum profile[11] with efficient uncaging from 380 to 450 nm (but no uncaging above 470 nm: which allows GFP imaging with lasers or filtered sources to be performed *in situ* without photouncaging), that converts **Cou-CHalo-Fluo** to free **CHalo-Fluo** with ca. >35% uncaging yield (expected for coumarin photocaged substrates[11], **Fig S7e**).

3.3 Amide regiochemistry strongly effects ligation kinetics

Due to even easier synthetic accessibility, we had initially synthesised a cageable aniline ligand **HL3**, with flipped amide connectivity compared to the benzamide in the **CHalo** design (**Fig. S8a**). Caging **HL3** equally effectively blocked the HaloTag ligation, but the labelling speed of free **HL3** was significantly slower than free **CHalo** (**Fig. S8b**): showing the strong influence of amide regiochemistry on ligation kinetics.

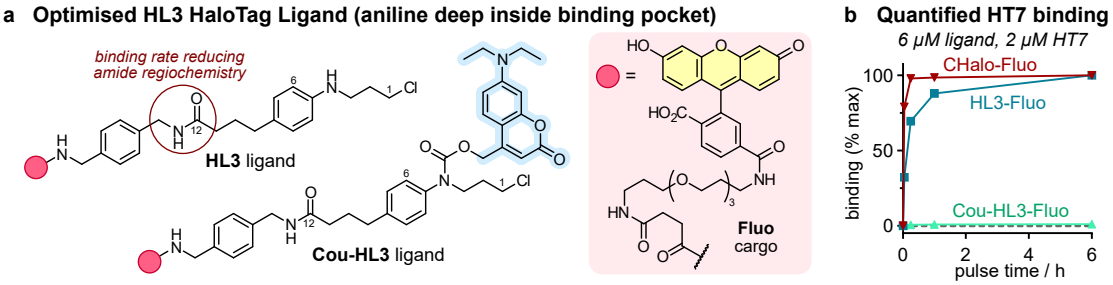

Figure S8: HL3 Design shows that amide regiochemistry strongly effects HaloTag ligation kinetics. (a) Chemical structures of **HL3-** and **Cou-HL3-Fluo**; **(b)** Quantified HT7 binding of **HL3** and **CHalo** fluorescein conjugates (quantified from fluorescein channel in SDS-PAGE gel from **Fig. S12**).

4 Supplementary Note 2: Rates & corrections for non-ligating compounds

In the text, for simplicity we state “less than 1% of **caged-CHalo** ligated within 100 minutes”. In reality, this useful guide is also a broad generalisation: ligation is a bimolecular reaction, so the apparent rate depends largely on protein and ligand concentrations, as well as assay setup (temperature, medium, etc). But in practice, the more important question is: what was the real ligating species, when "caged ligation" was seen?

We believe that the caged-CHalo reagents actually *do not* ligate at all; and where ligation develops over time without a specific stimulus, what is occurring is an *in situ* hydrolysis or adventitious cleavage of the cage. The rates of those cleavages depend greatly upon assay settings and experimenters (hence e.g. our warning in the "user guide" **Supplementary Note 1**, to use red-emissive lights when handling Cou-caged reagents).

We do not want to under-sell the caging performance by falsely interpreting background signal as caged-ligation, but we also do not want to over-sell ligand performance by restricting the analysis to specific cage chemotypes and unusual assay settings (or by discussing only the quasi-non-existant caged-ligated fraction). Thus, in order to give a useful guideline about the real, in-practice utility of caged-CHalo reagents we gave this 1% figure, on the understanding that it essentially reflects their *O*-alkyl-*N*-aryl-*N*-alkyl carbamates’ robustness, and should not be misinterpreted as "1% of the caged reagent will be found ligated onto HaloTag".

The “<1% in 100 minutes” figure is taken from our **Cou-CHalo-Fluo** assay with 6 µM ligand and 2 µM HaloTag, as used in standard benchmarking papers[12]: noting that Cou is a not-particularly-hydrolytically-resistant cage [compare: **Bn-CHalo-SiR** reaches 1% apparent signal only after 6 hours]; and though free **CHalo-Fluo** is also not the fastest-ligating substrate (compare to e.g. **CHalo-SiR**), the protein excess conditions ought to ensure that this “<1% in 6 hours” reflects rather a worst case scenario - **we believe that most experimenters will experience better stability and lower "unwanted ligation" in practice**.

Data acquisition and correction for non-ligating compounds

These assays were especially designed to test the *absence* of signal from caged compounds that are synthesised from a highly-signal-active precursor which can convert *in situ* to the signal-active form (by benzylic hydrolysis, and for the Cou reagents also by photouncaging from background lighting during assay setup and stop reagent addition). We chose to work in “typical” conditions that would be careful, but not overly controlled, hoping that these would reflect the experience of a typical experimenter in a real assay setup.

(1) As is typical for testing inactivity from a caged target, we expected the inevitable small amount of residual uncaged compound present at time zero in the assay to rapidly generate a signal plateau in our experiments, that might be minor (when roughly 1:1 ligand:protein are used) or significant (when vast excess of ligand is used). Therefore, when estimating the resistance to ligation of the caged compounds, we excluded a portion of this residual signal source, in a relatively bias-free way (that underestimates the likely residual signal by a factor ca. 2).

For the assays with 3:1 ligand:protein ratio, the direct ligand signal at the 5 min timepoint (fluorescein channel) was interpreted as the residual; for example, a loading-corrected gel band fluorescence value of 0.0053 (**Cou-CHalo-Fluo**) was interpreted as arising from 0.2% residual free **CHalo-Fluo**, and this value subtracted from all subsequent assay values (no adjustments for increasing reaction over time).

For the assays with 100:1 ligand:protein ratio that used the same **Cou-CHalo-Fluo** stock but were prepared on a different day, we expected only a slight difference in residual fit. Indeed, the fitted residual percentage was 0.1%.

For the assays that used **Bn-CHalo-SiR** and were prepared by the same final step purification as for **Cou-CHalo-Fluo**, we also expected a similar residual fit. Indeed, the fitted residual percentage was 0.1%.

(2) Both reagents are theoretically capable of uncaging over time inside the assay, by benzylic hydrolysis (expect: Cou much faster than Bn) and/or by photouncaging from stray light (Cou only). These uncaging modes should generate linear signal increases over time at low labelling percentages, since HaloTag protein will always be in vast excess compared to the *in situ* uncaged fraction.

For the Bn reagent assay (only run at 100:1 ratio, only readout by MaP555 chase), we saw only very small signal increase over time, and it was indeed apparently linear (fluorescence reaches 0.2% of theoretical maximum after 1 hour, 1% of theoretical maximum after 6 hours: i.e. *in situ* uncaging of only 0.01% of the applied **Bn-CHalo** reagent). These are very small numbers in an absolute sense and argue for the general stability and utility of the *O*-alkyl-*N*-aryl-*N*-alkyl carbamate caging strategies that CHalo was designed to harness.

For the Cou reagents, we believe that hydrolytic uncaging may be a more significant ongoing process, since the signal increases were concentration-dependent, and proportional to ligand concentration; but (a) the uncaging is still slow, such that the reagents can be useful binary indicators in photo-triggered applications in biology; and (b) we believe that its rate is specific to the Cou group, and need not be a feature of other photocages or enzyme cages. The 6 µM ligand : 2 µM HaloTag assays show a roughly linear signal increase (0.6% at 1 hour, 2.8% at 6 hours); the 20 µM : 0.2 µM assay has higher increase which is unsurprising from its higher concentration if free ligand is the limiting factor (1.4% at 1 hour, 18% at 6 hours, in the direct readout channel). We believe that our assay setup and quenching steps are the ones that apply light to the sample,

whereas the incubation protected in the dark excludes it, therefore we believe that *in situ* uncaging does not reflect Cou photouncaging.

Although we used MaP555 chase as a counter-readout, we considered it ***not suitable for quantifying low ligation*** data, because in our benchmarking experiments the chase channel had assay-to-assay variability of typically ±15% of readout maximum when used to assess conversions at low CHalo ligation percentages. Therefore the MaP chase data are not shown on graphs for **Cou-CHalo-Fluo** systems because their intrinsic Fluo channel readout is more reliable (though we quantified e.g. 25% readout at 6 hours for **Cou-CHalo-Fluo** which roughly matches the 18% from intrinsic readout), and MaP chase data are only graphed for the 100:1 **Bn-CHalo-SiR** run which has no intrinsic channel but should have the maximum possible parasitic labelling.

(3) Once these overly simplified corrections for 0.1-0.2% residual free ligand were introduced, the caged-reagent assay data are much more plausibly interpretable than before.

The 3:1 assay now has a linear fit appropriate to e.g. an ongoing pseudo-first-order reaction where the availability of *in situ* uncaged **CHalo-Fluo** is the limiting factor, rather than its previous form (a saturation curve form with half-conversion by ~2 hours but plateauing at just 3.5%).

The same is true for the 100:1 assay with **Bn-CHalo-SiR** (now ongoing linear; previously a saturation curve with half-conversion after about 5 minutes [similar to the kinetic for free **CHalo-SiR**] but plateauing at just 11%); and the 100:1 assay with **Cou-CHalo-Fluo** (previously pausing at 10% conversion from 15 min to 1 hour, then reaching 30% at 6 hours; now nearly linear increase at approx. 3% per hour).

Plausibility: In all caged-reagent assays, the residual free ligand corrections applied only alter the signal curves by subtracting a value that is less than the uncorrected signal developed within 15 minutes. If signals specific to the actual reagent species had been developing, they would simply appear to be delayed by about 15 minutes as a result of these corrections, without changing their form. Instead, the form of these data now match plausible expectations for their mechanism (caged forms never ligate, tiny portions that get uncaged are what ligates effectively): confirming the suitability of this correction.

Caged-Ligation with HL2^{N} reagents?

We had been surprised that **HL2^{N}** reagents apparently ligated even when caged, so checked the plausibility of caged-ligation with different methods than just the standard pulse/chase imaging channels. In the end, we found reliable confirmation by imaging the in-gel Cou motif fluorescence from ***HaloTag-ligated Cou-HL2^{N}-Fluo*** reagents using a broad "UV excitation" setting (filtering for roughly 365 nm excitation, 450 emission) which acquires signal more intensively from the Cou group than from the fluorescein group (approx ratio 75:25, determined after using an SiR chase to confirm the percentage occupancy, then assuming that fluorescein motif UV intensity within ligated **Cou-HL2^{N}-Fluo** is identical to the motif UV intensity for **HL2^{N}-Fluo** and subtracting the occupancy-adjusted partial contribution of the fluorescein motif).

In that reagent case, the efficiency of caged ligation was so high (ca. 1/3 the rate of uncaged **HL2^{N}-Fluo**) that the levels of (residual plus *in situ*) uncaged **HL2^{N}-Fluo** ligating to HaloTag proved much smaller than the level of caged-reagent ligation, which both allows robust confirmation that the caged-reagent was really the ligating species, and allows robust analysis of its binding kinetics by the "UV channel" signal intensity (the fluorescein motif component does not even need to be normalised away since the stoichiometry is enforced as 1:1). Additional corrections that might be desired for fine quantification, e.g. for fluorescence intensity modulation due to the dual chromophore ligand, were considered superfluous because the main effect, that the caged reagent ligates, was already visible as confirmed by the 3-fold higher fluorescence intensity (from the Cou motif) which dominates the UV band and which is not a feature of the free **HL2^{N}-Fluo** comparator (**Fig. S6**). (Future experimenters interested in this phenomenon might consider using an isosteric coumarinyl-propionamide rather than coumarinyl-hydroxymethylcarbamate, to prevent photolability of the product and allow for e.g. MS-based quantification).

This observation seems in line with recently emerging results that argue that HaloTag is rather more tolerant for alkylator ligands than had previously been assumed (viz. the assumption that the linearity and length of the classic chloroalkane linker is strongly required so that a reagent can dock and ligate); and suggests additional modes of functionalising HaloTag-reactive ligands with two orthogonal cargos, while preserving decent to very good ligation kinetics (probably the aryl ring and substituent disposition that the **HL2^{N}** design inherited from Tadross and coworkers, is crucial in this respect, since it provides a very fast basis for ligation).

5 Supplementary Note 3: Harnessing known cage reactivities with CHalo

The CHalo system can in principle harness a variety of useful cages to allow ligation after different stimuli. Such caging groups have been broadly developed in prior literature, e.g. for triggering uncaging with light (photocages), enzymatically, or with a biochemical stimulus; and these caging groups can easily be introduced onto the CHalo ligand as carbamates (**Fig. S9a**) allowing straightforward implementation of diverse gating applications - a crucial flexibility advantage of small molecule reagents versus genetic tools.

A variety of **photocages** are available with tuned uncaging wavelengths (**Fig. S9b**). The most commonly used *ortho*-nitrobenzyl (*o*-NB) photocages are cleaved with UV light, with some modifications up to 380 nm (disadvantageous: relatively high phototoxicity). Dialkylaminocoumarins (e.g. DEACM) can be activated with violet light and we used the DEACM cage since it allows parallel GFP imaging (490 nm excitation) without photo-cleavage. Depending on the application, blue/green/yellow-responsive coumarins or other cage types such as BODIPYs or xanthenes[4] could be designed instead; and even far-red to near-infrared uncaging by cyanine cages[13,14] or SiR-assisted cleavage of *o*-NB cages[15] are feasible: i.e. the whole visible light range is conceptually accessible for CHalo. For more literature examples we refer the readers to this review[5].

Enzyme cages are widely used for fluorogenic enzyme activity probes (**Fig. S9c**), with a broad range of target enzymes such as nitroreductases, peptidases, esterases, glucosidases or oxidoreductases.[3,16,17] Such probes enable the sensitive detection of enzyme turnover (instead of just enzyme expression level) and can reveal changes in enzyme activity (e.g. in disease) rendering them invaluable research tools. **Biochemical** cages for sensing stimuli such as hydrogen sulfide or hydrogen peroxide are also known (**Fig. S9d**).[6,7]

All these cages are well known for releasing either phenols or anilines (optionally with the use of chemical adapters[18]), so they can conceptually be used straightforwardly to cage the CHalo ligand and thus create diverse photo-/enzyme-/biochemically-caged probes. For more examples we refer the readers to this review[3].

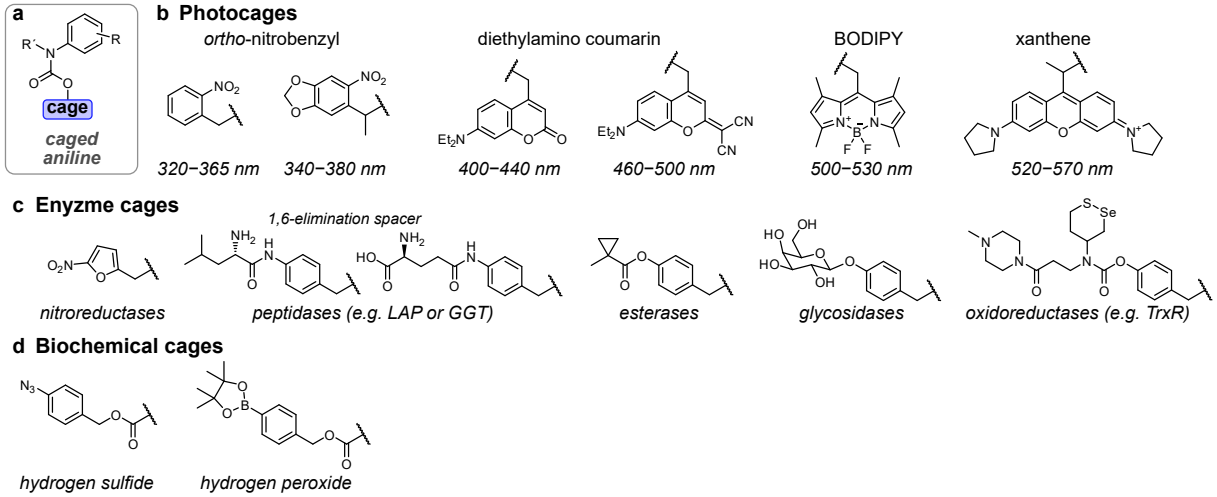

Figure S9: A selection of known caging groups that should be chemically compatible with the CHalo motif, and could in the future be applied to harness photo-, enzyme- or biochemical uncaging (optionally using chemical adaptors).

6 Supplementary Note 4: CHalo Ligation and CHalo-SiR Fluorogenicity

Conclusions: (1) CHalo's intrinsic ligation rate (ca. 1/10 that of CA) as well as its cell permeability are "good enough" to perform strongly in cells in settings where normal CA reagents succeed. The target protein choice and the CHalo reagent cargo's barrier crossing ability will be the key determinants of any given reagent's *actual* labelling speed in biology. (2) **CHalo-SiR** is a powerful fluorogenic label, much like SiR-CA. (3) **Caged-CHalo-SiR** reagents are cage-conditional fluorogenic labels that inherit the uncaging features known for their chosen cage, then (when uncaged) give the ligation and fluorogenicity known for CHalo-SiR.

Background: Fluorogenic chloroalkane-siliconrhodamine ligands are perhaps the most widely used of all HaloTag reagents (sold as SiR-Halo, SiR-CA, Halo-JF646, etc). These ligands excel for low-background, low-photodamage, far-red imaging of HaloTag fusion proteins, since their fluorescence in the cell environment is low until they ligate to HaloTag (typically quoted: 5 to 20-fold fluorescence turn-on upon ligation)[10]. While the bimolecular reaction rate for TMR/CPY-chloroalkane ligating to HaloTag protein can be incredibly fast in purified cell-free conditions (up to ca. 10^8 $M^{-1}s^{-1}$)[12], this is not the rate-limiting aspect for performance in biology: because the ligation reaction requires first that the reagent encounters its target protein, i.e. typically it must cross at least the plasma membrane, while remaining soluble and bioavailable, and the rate of crossing barriers is almost always much slower than the rate of ligation once they are crossed.[9] The assay setting and the cellular location of the HaloTag fusion protein determine what barriers must be crossed and therefore greatly control how fast the overall crossing-then-ligation can proceed: e.g. very low hindrance for extracellular labelling in 2D cell culture following reagent addition to the medium (very fast fluorogenicity), high hindrance for intracellular labelling in the brain *in vivo* following i.v. administration (very slow fluorogenicity). The structure of the cargo attached to the chloroalkane (or CHalo) motif also greatly controls barrier crossing rates: e.g. high membrane permeability for "MaP" dyes that favour a spirocyclised unligated state, vs low membrane permeability for permanently open (zwitterionic) dyes.

Goals: Given that target encounter rate (restricted by barrier crossing rate e.g. by cell permeability) is usually rate-limiting for HaloTag ligation in live biology, we consider that the best outcomes for the CHalo motif *as a conditional ligation motif* would be that (a) neither CHalo nor typical caged-CHalo motifs make their reagents dramatically less permeable than the known chloroalkane motif; and (b) CHalo reagents are not dramatically slower to ligate than chloroalkane reagents. We expected that if our (intentionally) simple CHalo reagents had slow apparent labelling rates in live biology, the first point of improvement would be to switch cargos to the known faster-cell-penetrating dyes (like the MaP series) as cargos; and we would only consider the apparent intracellular labelling rates or the apparent cell-free labelling rates as problematic features of the CHalo motif *if* those rates were >100x slower than the rates for cognate chloroalkane compounds.

To determine what performance both **CHalo-Cargo** and **Caged-CHalo-Cargo** reagents could have, as compared to known CA-SiR, we also used silicon-rhodamine as the cargo, and made **CHalo-SiR** as well as caged **Cou-CHalo-SiR** and **Bn-CHalo-SiR** as testbed reagents.

Solubility and aggregation problems call for caution about ligation rate and fluorogenicity assays: At least in our hands, SiR-Halo, **CHalo-SiR**, **caged-CHalo-SiR**, and presumably other similarly-sized reagents with high $logD_{7.4}$ values (e.g. expected for those with CPY as cargo), seem prone to aggregation in biological media even at low concentrations (e.g. 500 nM), and presumably also to adsorption effects (e.g. onto the plastic of well plate or cuvette walls or pipette tips depending on the solvent, as well as onto e.g. albumin protein). This may be reflected in the choice of high BSA concentrations (10 µM) as a standard component of the "activity buffer" used for much development work around dye ligands for HaloTag. At least in our hands, the strong tendency to aggregation is coupled with large variation in how much aggregation is actually ongoing (increases over time, also depends on ligand concentration, buffer / cosolvent, assay temperature, handling and dilution steps, other assay components, etc) as well as how reversible the aggregation is, as well as how problematic that aggregation is (depending on readout).

For example, we knew already from work with well-water-soluble and permanently-fluorescent **Caged-CHalo-Fluo** reagents that caged CHalo species should not ligate to HaloTag over even 6 hours (**Fig S7cd**, **Supplementary Note 2**). Indeed, with caged-CHalo-SiR (which we expected would have low fluorescence in cellular environments, due to its preferred biolocalisation into apolar environments where the non-red-absorbing and hence non-fluorescent spirocyclised form would dominate), cellular assays did not show strong fluorescence: so we were confident that no spontaneous ligation or uncaging-then-ligation was occurring (since this would lock the SiR into place on the HaloTag protein such that the fluorescent zwitterionic form now dominates). Cell-free assays are coherent with this lack of spontaneous ligation or uncaging-then-ligation: the caged-CHalo-SiR reagent has very low UV-Vis absorption and very low fluorescence (**Fig S10fg**). In our assays, CA-SiR had apparently 9-fold lower absorbance and 5-fold lower fluorescence emission intensity in cuvette (aqueous activity buffer, including 10 µM BSA) in the absence of HaloTag protein, than when HaloTag protein was supplied in excess and ligation was allowed to plateau (**Fig S10b**). Under the same conditions, CHalo-SiR had apparently 40-fold lower absorbance and 400-fold lower fluorescence emission intensity in the absence of HaloTag protein as compared to the presence of HaloTag (**Fig S10c**). Notably, the UV-Vis absorbances of CHalo-SiR and CA-SiR incubated with excess HaloTag protein were essentially identical (scaling by a factor 0.85, which is within assay variation limits, **Fig S10bc**); and even the raw data values of their fluorescence emission spectra were essentially identical (**Fig S10bc**: although each emission spectrum is technically

on an arbitrary unit scale, the experiments were acquired under otherwise identical conditions, and the raw value scaling was by only 0.91).

We trust the conclusions that ligated CHalo-dye reagents will have similar or identical fluorescence intensity and spectrum as their ligated chloroalkane-dye counterparts; and that non-ligated CHalo-dye *or* caged-CHalo-dye reagents will have similar or identical fluorescence properties as their non-ligated chloroalkane-dye counterparts. **However, we caution against** simplistic claims on the basis of this assay type that e.g. "CHalo-SiR is 400-fold fluorogenic upon target binding whereas CA-SiR is only 5-fold fluorogenic", and we caution against interpreting the without-vs-with HaloTag data in terms of open/closed ratios and/or fluorescence quantum yields. The absorbance is entirely dependent on the open/closed ratio, which depends on the microenvironment (e.g. should have one value if the dye is ligated to protein; but if not it will depend on the solvent nature and its dielectric if the dye is not ligated but is in molecular solution, or else it will depend on how the dye is part of an aggregate/adsorbate/precipitate if not in molecular solution); and the fluorescence depends both on the absorption as well as on additional microenvironment features that affect e.g. quantum yield. Therefore, when there is low or no ligation, the measured fluorescence values in cell-free settings may actually have more to do with whether the unligated reagent is in molecular solution or part of an aggregate/adsorbate (extrinsic features of the cell-free assay setup that do not translate to cellular settings), rather than reflecting intrinsic parameters that do translate to any possible cell assay setting.

D_{50} values: Those solubility-related problems were raised previously[9], with the recommendation that determining open/closed ratios across a range of solvent dielectrics is a better way to characterise the ability of a dye to be fluorogenic in cells thanks to ligation-induced de-lactonisation.[9] For example, D_{50} values can be defined as the dielectric constant at which a dye has 50:50 open:closed ratio when all of the dye is in true molecular solution. SiR reagents are reported to have D_{50} values ca. 30−35,[10] showing that this dye has a high tendency to spirocyclise even in somewhat polar environments: and due to most SiR reagents' overall hydrophobicity, this should ensure that in cells, most unligated SiR-bearing compounds will be nonfluorescent lactones since they will preferentially partition into hydrophobic environments with low dielectrics (**Fig. S10e**). We measured the absorbance of CHalo-SiR in water-dioxane mixtures; at high dielectrics (<20% dioxane) we saw a drop in solubility which compromised the high-end of titration and made it uncertain whether a plateau was reached (all-zwitterionic state), however we could confidently determine that its D_{50} value by this method was ≥53: so it likewise favours dielectric-and-partitioning-based fluorogenicity in the cellular setting.

Ligation Rates? Given that the data so far support caging-control of ligation as well as ligation-control over the open/closed ratio and fluoresecence, and given the arguments about fusion protein and barrier crossing determining biological performance more than cell-free ligation rates, we felt it would be necessary but also sufficient for typical performance in cellular settings that uncaged CHalo-SiR should show somewhat similar ligation rate as SiR-CA in reasonably robust cell-free settings; and we did **not** attempt to measure cell-free ligation rates under any particular conditions with high precision.

We screened several cell-free parameter choices until we were satisfied with the robustness of our analysis. For example, under standard conditions from the literature ("activity buffer" with 10 µM BSA, 4 µM HaloTag, 2 µM ligand, 1% DMSO), we found that apparent ligation rates were drastically affected by changing the DMSO percentage and handling procedure in ways that indicate that aggregation/insolubility of CHalo-SiR (and also of SiR-CA) were compromising the actual ligation rates (e.g. easily making ligation seem 10-100 fold slower than when solubility was ensured by using higher cosolvent percentage, lower ligand concentrations, etc). We approximated the **CHalo-SiR** ligation rate particularly by using minimal dye concentrations and by varying DMSO concentrations until the apparent rate was stable (**Fig. S10i**; 1-10% DMSO).

Using the conditions we feel were reliable, we found that **CHalo-SiR ligated to HaloTag with a bimolecular reaction rate constant of ca. 10^6 $M^{-1}s^{-1}$ at 23°C in cell-free assays** (**Fig S10i**: 5 nM dye, 200 nM HaloTag, 3-10% DMSO), indicating that the rate constant would be higher still at physiological 37°C. This is about 20-fold slower than typical values quoted for SiR-CA ligation at 37 °C;[12] and although in our hands SiR-CA ligated too fast to be well-resolved by the measurement techniques we employed for CHalo compounds, our estimate for the SiR-CA ligation rate was **10-fold faster** than CHalo-SiR ligation rate (**Fig S10h**), which we assume reflects an intrinsic 10-fold slower ligation of the CHalo than the CA motif. We feel that this intrinsic ligation rate difference is molecularly plausible (given the change of ligand structure compared to the optimised Tadross scaffold that the need for conditional ligation had enforced). Also, since CA reagents are considered useful over a vast range of ligation kinetics (from 10^4 to 10^8 M^{-1} s^{-1} depending on their cargo), we considered that (a) the only 10-fold difference would not make CHalo reagents useless, especially when the cargo is one that favours higher reaction rates; (b) the cell-free ligation rate difference would still be irrelevant in almost all biological practical applications since it leaves the CHalo ligation rate as being much faster than the other rate steps we expected to be important or rate-determining for practical performance.

Indeed, **cellular assays** showed much slower CHalo and CA labelling rates (half-lives 0.6-3 hours, **Fig S10j**) than in cell-free assays (seconds to minutes). They were also only 5-fold different from each other.

Finally, to validate the principle of **CHalo uncaging**, we studied the aminocoumarin-photocaged fluorogenic reagent **Cou-CHalo-SiR**. The reagent inherited the expected properties known for its cage: it was efficiently uncaged with blue light (50% conversion with 10 mJ/mm^2 at 380-440 nm, **Fig. S10k**), yet unaffected by wavelengths used for typical GFP imaging (no uncaging above 470 nm). Incubation with purified HaloTag protein

showed no ligation (and therefore no fluorescence generation) before uncaging light, but rapidly generated fluorescence after being illuminated with 405 nm light (**Fig. S10l**).

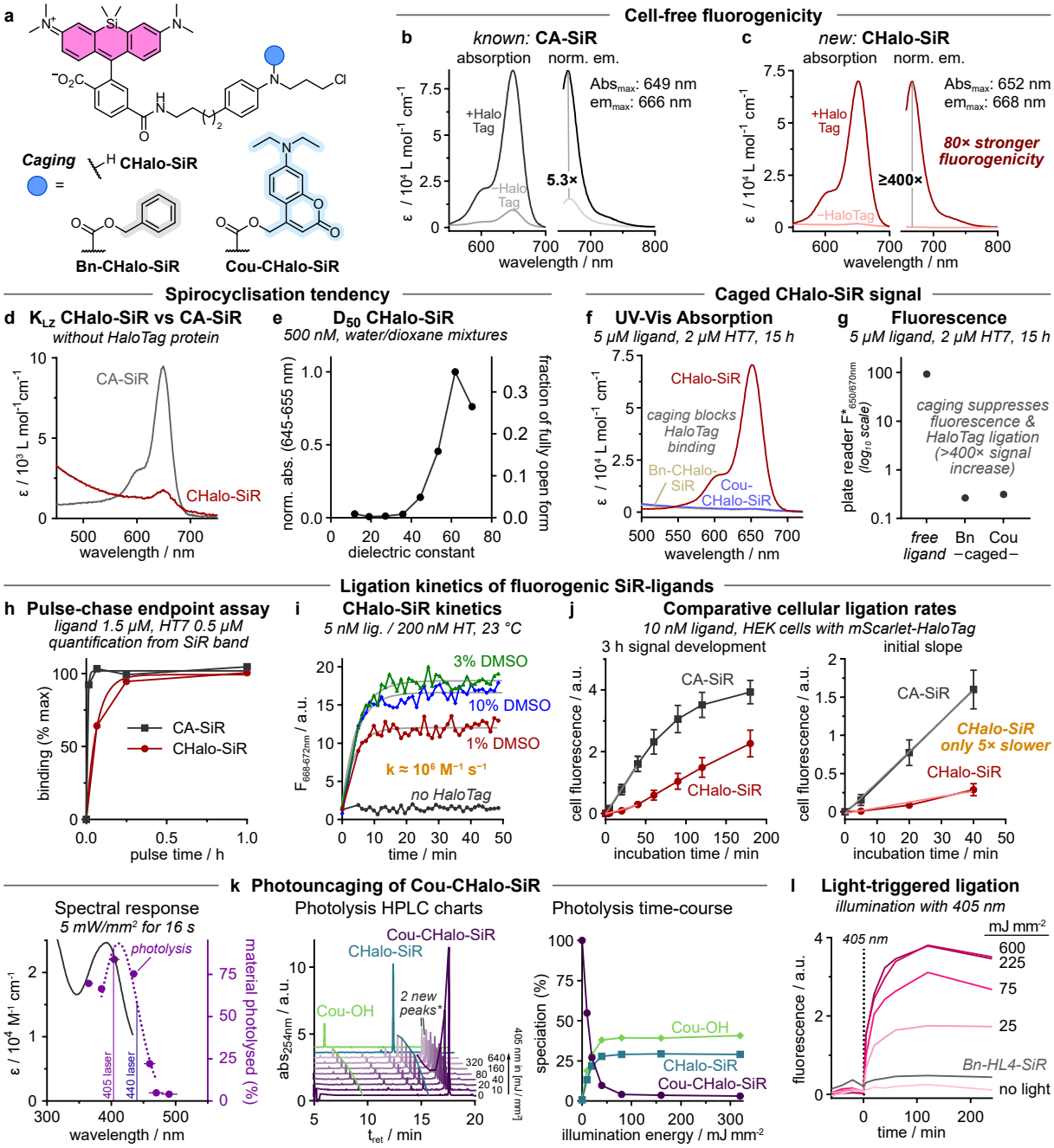

Figure S10: Absorbance, fluorogenicity and photouncaging properties of Cou-CHalo-SiR. (a) Chemical structures of **CHalo-SiR** and its caged derivatives **Bn-** and **Cou-CHalo-SiR**; **(b-c) CHalo-SiR** has 400-fold far-red fluorescence turn-on upon HaloTag binding (2 µM ligand ± 4 µM HaloTag7). **(d)** Investigation of the lactone-zwitterion equilibria of non-ligated **CHalo-SiR** and **CA-SiR** (UV-vis spectra without HaloTag protein). **(e)** CHalo-SiR absorbance as a function of the dielectric constant (absorbance normalised to maximum absorbance, measured in water/1,4-dioxane mixtures; 0.5 µM CHalo-SiR); aggregation effects cause low absorbance value at high dielectric constant. **(fg)** Visible region absorption spectra and fluorescence emission of free **CHalo-SiR**, and caged **Bn-** and **Cou-CHalo-SiR** after incubation with HaloTag protein (5 µM ligand, 2 µM HT7, 15 h); **(h)** Ligation kinetics of CHalo-SiR compared to CA-SiR quantified from SiR in-gel fluorescence (SDS-PAGE gel and quantification in **Fig. S13**); **(i)** Binding kinetics of **CHalo-SiR** determined by fluorescence increase upon HaloTag binding (5 nM ligand, 200 nM HT7, in PBS with 1−10% DMSO, 23 °C); **(j)** Cellular ligation rates of **CHalo-SiR** and **CA-SiR** (10 nM) in HEK cells transfected with cytosolic Halo-mScarlet (quantification from microscopy images; *n*=3). **(k) Cou-CHalo-Fluo** can be uncaged efficiently with blue light (ideal: 400−440 nm) and GFP orthogonally (no uncaging >470 nm; 50 µM sample in DMSO:water 7:3; illumination with the same light intensity for each wavelength, *horizontal error bars: FWHM of excitation light*; HPLC speciation and photolysis time-course (50 µM in MeCN:water 1:1; illumination with 405 nm LED light, 5 mW/mm^2, applied for times from 2 to 128 seconds (factor 2 steps)); **the species in the "2 new peaks" close to the Cou-CHalo-SiR signal include the coumaryl-CHalo alkyl aniline which is a nonphysiological byproduct of the high concentrations used in this assay (after an aniline has been photoliberated, it can trap another photogenerated coumarinyl unit: byproduct mass lacks CO_2)*; **(l) Cou-CHalo-SiR** generates fluorescence upon photouncaging followed by HaloTag binding (5 µM ligand with 2 µM HT7; 1 h pre-incubation, then 405 nm, 5 mW/mm^2).

7 Supplementary Note 5: HaloTag as an anchor; and biological background

§1: Biological Background for prior usage of SLPs (expanded from the main text's Introduction)

The HaloTag[19,20], SNAP-tag[21,22], and CLIP-tag[21,23] self-labelling proteins (SLPs) have enormously expanded the possibilities of *chemical biology* because they offer a high-specificity, orthogonal connection, latching the functionality of very diverse *chemical* reagents onto very diverse *biological* targets. The HaloTag has been broadly used,[24] especially for fluorescently labelling proteins of interest (POIs) with typically fluorogenic, small molecule fluorophores[9,10,25,26] (**Fig 1a**) that have been applied for studying protein localisation[27], movement and trafficking[28], intracellular protein concentrations,[29] or protein turnover,[1] in living cells; or for ultrafast staining of thick tissues after fixation[30]. Other major fields of application are chemically induced protein dimerisation (CID)[31–33], targeted localisation of biosensors (e.g. for calcium)[34], specific protein degradation,[35] or for increasing the local concentration of a reagent to enforce binding or reaction, through tethering (DART,[36] T-REX[37]). Conceptually, HaloTag has been the most attractive SLP since (1) its ligation rate to its conventional ligands can be up to 1000 times faster than that of SNAP and CLIP to theirs[38], (2) it is reported to be entirely monomeric, rather than introducing partial aggregation tendency due to its uniform negative surface charge[39], (3) it is reported to have no organelle localisation preference, (4) its classic HaloTag-reactive motif, i.e. the 6-chlorohexyl bisether **CA** (**Fig. 1a**) is more apolar than SNAP/CLIP motifs which generally favours the passive cell entry of Halo ligands over those of SNAP and CLIP[40].

§2: General features for and against "using HaloTag as an All-Purpose Anchor"

Using HaloTag as an "all-purpose anchor protein" to durably mark cells or proteins with molecular reporters at a specific time or region, or upon specific stimuli, potentially against a non-emissive background, is an attractive prospect for tracing cell dynamics, trafficking, history, and fate. (1) The HaloTag system is very broadly **established** - it is available in many model systems, with many tissue / cell-type specificities and subcellular compartmentalisations. (2) The covalent ligation of the ligand with the HaloTag protein prevents post-ligation diffusion of the small molecule from the protein (either localised at cellular structures or compartementalised with the HaloTag-POI), thus allowing **durable** labelling and in the case of enzyme-cages enables reliable signal integration as a real-time and cumulative readout for the enzyme activity. (3) Using the **conditional ligation** approach (instead of ligation followed by conditional activation) has a number of unique advantages, which are covered in detail in the paragraphs below: from multiplexing and multipurpose assays (§3), through to successfully harnessing enzyme substrate probe designs (§5-6). (4) The recent disclosure of "xHTL" exchangeable HaloTag ligands (moderate to high affinity but without ligation reactivity[41]) hints at noncovalent **exchangeable CHalo** (XCHalo) systems, simply by replacing its chlorine with e.g. a trifluoromethanesulfonamide, which may be particularly effective in multipurpose assays (e.g. sequential recruitment to different targets).

§3: Multiplexing: Multicolour and Multipurpose uses of CHalo/HaloTag

By **multiplexing CHalo reagents**, their conditional ligation after activation can, at least conceptually, be used for e.g. **multi-target multi-colour imaging** (e.g. Cage^{n}-CHalo-Dye^{n} panels with five channels separable via intensiometric imaging (blue, green, yellow, red, far-red), or, more by FLIM). This should durably capture the activities of different enzymes in parallel with single-cell resolution, such that the **relative enzyme activities are quantitatively reflected** in the relative HaloTag-recorded reporter signals (expecting proportionality factors *between* enzymes, which crucially however are *invariant* between different cells at least in 2D cell culture assays). Such relative activity assays have been previously impossible with known small-molecule enzyme activity probes (that suffer from post-activation signal loss by diffusion or export out of cells) or genetic intensiometric sensors (which give signals dependent on their expression levels, and therefore make absolute and relative quantification difficult). These multicolour CHalo/HaloTag assays may also be useful e.g. for fingerprinting to distinguish correlated vs non-correlated enzyme activities within or outside networks, as a marker of normal or dysregulated functions. The multicolour reporters can be direct live cell reporters (fluorogenic reagents), or endpoint readouts (if permanently fluorescent reagents are used, since these need washout before quantification). Our ongoing research aims at multicolour panels to fingerprint and record the relative activities of related oxidoreductases with quantitative accuracy at single cell resolution, that we believe will be able to harness the *in vivo* applicability of HaloTag protein systems to allow panel translation from cell culture to live animal settings.

Multiplexing can also include applications beyond just imaging, e.g. including both reporter reagents and effector reagents (well beyond the one phototriggered heterodimeriser we have shown here) for **multipurpose assays**: e.g. a 550 nm photouncaged XCHalo-based recruiter to CLIP-Tag and a 450 nm photouncaged CHalo-based recruiter to SNAP-tag, for two-colour-two-target sequential recruitments, applied in parallel with 460 nm and 580 nm emissive reporters whose ligations are dependent on enzyme activities and with a 650 nm emissive reporter dependent on a reactive small molecule. Such multipurpose assays can leverage the many suitable "channels" of photocage as well as the diversity of click chemistry, biochemical, and enzymatic cage groups for the CHalo uncaging step, married to the broad range of functional cargos.

§4: Side note on SLPs in the context of photo-triggered fluorogenic labels (expanded from main text):

Photo-triggered (or photoactivated, or photoconvertible) fluorescent proteins are widely used throughout biology, e.g. paGFP. Chemigenetic counterparts of these protein-only tools have only recently been developed, driven by the need for vastly more photostable and higher-performance fluorophores at custom wavelength regions [which are feasible for small molecule chemistry to access]: but so far these have been restricted to *unconditionally-ligating but photoactivated-fluorescence reagents* (HaloTag-reactive caged-fluorophores, e.g. PaX[42]). Yet, outside their target uses in high-resolution structural imaging of the SLPs' fusion protein targets, these approaches have several limitations for broader chemical biology: e.g., they prevent more powerful assays because all ligation sites are saturated with the pre-fluorophore, so HaloTag becomes a single-purpose anchor; and, during photoactivation, background from non-ligated but photoactivated forms can lower the signal-to-noise, and can diffuse unchecked (all cells' binding sites saturated). A minor point too is that conditional ligation keeps the target protein and fluorophore spatially separate during uncaging, which may reduce on-target photodamage during photouncaging (or, equivalently, while imaging ongoing enzymatic uncaging). The comparative advantages and unique applications of photoactivated-ligation rather than post-ligation-photoactivated-fluorescence systems, with their focus on revealing or harnessing a stimulus or stimulus-defined spatiotemporal location, parallel those discussed above for other prior ligation vs downstream ligation reagent designs.

§5: Generalities on molecular imaging

Fluorogenic probes are crucial tools for visualising and quantifying bioactivity by linearly generating fluorescence upon biological stimuli, from zero background. They are often used for non-invasive bioactivity imaging for enzymes (e.g. peptidases, esterases, phosphatases, glycosidases, and oxidoreductases[3,43–48]) or reactive analytes[3] such as hydrogen peroxide and hydrogen sulfide.[6,7] However, **post-activation signal loss** problematically impairs cell-resolved activity imaging, since it lowers the sensitivity and reliability of signal quantification. There are only a few generalised methods that can increase the **cellular signal retention**: mainly, charge trapping[7,49–51], fluorophore precipitation,[52] or non-specific electrophilic labelling of impermeable biomolecules (SPiDER probes[53]). Each has its specific **disadvantages and limitations**[51], e.g. with charge-trapping, retention is often only moderately improved (ion exporters[54]) and probes require additional delivery strategies; whereas precipitation- or electrophilic-trapping are pro-inflammatory and cell toxic in the longer term (crystal formation / protein alkylation[55]).

The **ideal enzyme activity integrating probe** would be as non-invasive / non-toxic as typical non-retained (soluble) probes but have long-term retention across a range of different cell lines (variable exporter expression profiles etc). We propose that clean, specific, efficient (quantitative), bioorthogonal reaction of a probe product with an introduced innocent intracellular protein target like HaloTag should achieve full product retention without disturbing the *activating target enzyme* or without nonspecific / off-target cell-toxic effects (signal now protected from loss due to small molecule transporters, bioorthogonal reaction allows high dosage without toxic side effects, and the system is immediately *in vivo* compatible since many examples have been shown for expressing HaloTag *in vivo*).

We use CHalo as a modular basis for reagents to image and integrate the bioactivity of an enzyme or reactive biochemical, since *the step which is cell-retaining is the same as the step which is signal generating* (HaloTag ligation step with SiR cargo), and that step is efficient, and entirely conditional on prior CHalo uncaging. This should then allow high-sensitivity imaging and integration with e.g. caged CHalo-SiR fluorogenic reagents. Advantageously, since CHalo's aniline carbamate caging chemistry is compatible with auto-immolative spacers that act as chemical adapters allowing a diversity of chemical reaction types and biochemical / enzyme activators to act as the upstream trigger for uncaging[56] and thus bioactivity integration. The proof of concept for this design principle will be a demonstration via a leucine aminopeptidase (LAP) probe.

§6: SLPs in the context of enzyme-triggered fluorogenic labels and molecular imaging / recording

There are no generally useful platforms for sensitive fluorogenic chemical probes that allow quantitative *in vivo* enzyme activity integration and localisation, and are cell-retained without impacting native biology. Failings often include e.g. limited signal retention, and biological non-innocence (see ref[51]). A similar concept, briefly mentioned in the main text, has been the use of single-purpose protein-based integrators, like CaProLa[57], that transduce macromolecular rearrangements of the sensor (e.g. a cpHaloTag) which have been caused by cellular activity (e.g. analyte binding) into durable ligation events that can be read out later. These sensors are however laborious to construct and to translate between model systems; they seem adapted to only one activity readout per sensor; and the space of "activity" that they can sense is, probably, mostly separate from the activity space that classic small molecule enzyme substrates can reveal.

CHalo's principle of **triggered ligation** uses enzyme activity to allow a probe product to ligate cleanly and durably to HaloTag: which seems an ideally quantitative, non-invasive, high-sensitivity approach that could harness the diverse HaloTag-expressing animal models already available. The CHalo design could ensure that the enzyme reaction proceeds *unimpeded* on the free Caged-CHalo substrate, resulting in a *rapidly ligating uncaged CHalo product* that is then irreversibly trapped by HaloTag (for accumulating readout and/or sensitive endpoint analysis). This seems a reliable way to convert the decades of knowledge on freely-

diffusing small molecule enzyme probes[3] into biologically innocent quantitative integrators. The successful performance of **Leu-CHalo-SiR**, which contains a common PABA 1,6-elimination spacer as a chemical adapter, also promises that other types of chemical adapters (benzylic or other elimination, or cyclisation, etc) which access a huge diversity of enzymatic or chemical reactivities,[56] can be used to patch a diversity of enzyme-uncaged motifs onto the CHalo system without case-by-case needs to re-assess compounds for potential instability or kinetic problems with their uncaging or ligation steps (**Fig. 2ef**).

It is not otherwise obvious how enzyme activity should be used to gate a different step of the process without introducing major problems. The only easily conceivable alternative approach is one that we call **prior ligation**: anchoring a small-molecule activity probe onto HaloTag then generating fluorescence upon reaction of the target enzyme with the HaloTag-probe conjugate. Prior ligation reagents could in principle be created very easily with molecularly simple substrate designs using modules that have been known for decades (e.g. CA-fluorescein-*O*-esters). However, we are unaware of any probes utilising prior ligation of a pro-fluorophore to HaloTag that managed to be effective fluorogenic sensors for enzyme activity. A prior ligation concept would require the activating enzyme to have equally good recognition of the protein-bound substrate motif, as for the freely-diffusing small molecule substrate: which seems highly unlikely. More probably, the HaloTag protein would block or restrict enzyme access to the protein-bound motif, whereas unligated pro-fluorophore would react without hindrance: so suppressing specific bound signal while giving a freely diffusing unwanted background, and in turn, reducing probe sensitivity and utility. Even more problematically, pre-activation anchoring requires the HaloTag and the activating enzyme to reside in the same cellular compartment (since proteins cannot cross intracellular membranes) and even if they are accessible for one another, diffusion of a HaloTag-probe construct to e.g. a plasma membrane bound enzyme of interest would be much slower than a freely diffusible small molecule probe limiting the turnover and thus the sensitivity.

§7: SLPs in the context of chemically induced protein dimerisation (CID)

Simple reagent examples have tested spontaneous (unconditional) HaloTag-to-SNAP-tag dimerisers that could be cleaved upon illumination,[31] or unconditional HaloTag-to-SNAP-tag dimerisers that target exofacial proteins.[58] Although we did not find assays in those reports that characterise the degree of non-productive monovalent labelling depending on ligand : SNAP : Halo stoichoimetry (also known as the "hook effect" for bifunctional molecules), it seems impossible that those designs would escape this otherwise entirely general problem for saturable systems, which is particularly problematic when stoichiometries are far from equal and the overall concentration is low (i.e. in all but a few special cases).

To overcome the hook effect, photo-activatable protein ligation motifs have instead proven to be invaluable tools in applications around and towards chemically induced dimerisation (CID) reagents. Some early examples tested benzylguanine caging for conditional SNAP-tag ligation[59] (which although not done for SNAP-to-Halo designs, is still conceptually on the same level: see below). However, benzylguanine (BG) caging designs were then essentially abandoned, with few "tool creation" reports and so far without followup "tool use" papers: likely due to the problems of benzylguanine caging chemistry and slow post-uncaging kinetics which have recently been discussed[60] (although the recent report of "second generation" SNAP-tag substrates may revitalise design efforts leveraging SNAP-caged reagents[61]). Matching that analysis, most studies using phototriggered heterodimerisers in the last decade have focused instead on unconditional HaloTag labelling followed by trimethoprim (TMP) photouncaging for noncovalent recruitment of *Escherichia coli* dihydrofolate reductase (eDHFR), allowing conditional protein dimerisation: since the TMP ligand can be more easily caged than benzylguanine[60] and results in very rapid, good-affinity binding to eDHFR (even if it is noncovalent and technically reversible). Such photo-activatable dimerisers and photosplitters (which incorporate an additional photocleavable group in the linker between the two ligand motifs) were used for applications ranging from light-induced recruitment of cytosolic proteins to kinetochores or mitochondria, to controlling peroxisome transport and mitotic checkpoint signalling, to molecular activity painting and studying signalling processes.[33,62–65]

However, to the best of our knowledge, no photocaged double-covalent heterodimeriser has yet been reported. Conceptually, while uncaging Halo ligation had been impossible, photouncaged-Halo-to-SNAP heterodimerisation could have been done before since the SNAP-tag ligand offers not only an aniline-type nitrogen that could be suitable for caging, but also imidazole-type nitrogens that have already been explored for caging, even if both are considered difficult[60] caging sites (and we had indeed worked towards Halo-to-SNAP reagents in early stages of this project before abandoning them). However, any such SNAP-to-Halo designs would have had to photouncage the SNAP ligation step (10-100 fold slower ligation than HaloTag ligation[38]) which seems unpromising for tool utility; and in any case, no photouncaged-SNAP-to-Halo designs were reported to be successful. **Cou-CHalo-BG** instead can perform the slower[38] SNAP-ligation first; then, after washout of unligated reagent, photouncaging unleashes the expectedly faster HaloTag-ligation to complete the heterodimerisation (**Fig. 2j-l**): a labelling order that best retains the spatiotemporal resolution of photouncaging, and which may in the future be adaptable to work with *fluorogenic* HaloTag ligation (i.e. fluorescent turn-on reports on the successful completion of heterodimerisation).

8 Additional Data

8.1 SDS-PAGE Gels and Quantification

For full discussion of (caged) $HL2^N$ ligands see **Fig. S6**. In **Fig. S11** we additionally show the quantification of in-gel fluorescence from $HL2^{O/N}$ ligands from the SiR-chase and the fluorescein channels as well as the increase of the UV fluorescence (ex.: 365 nm) proving the undesired binding of the caged **Cou-$HL2^N$-Fluo**.

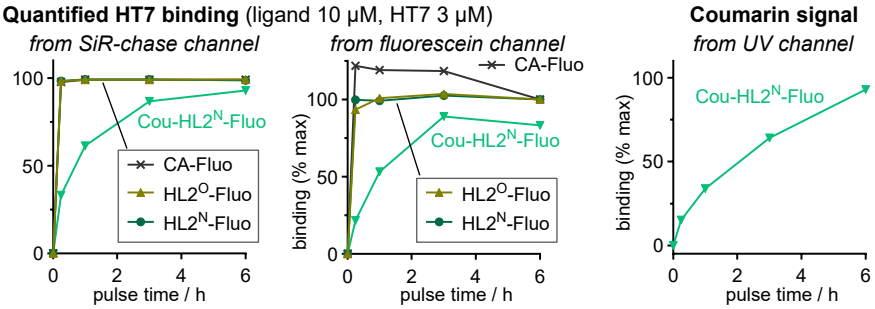

Figure S11: $HL2^N$-Fluo efficiently ligates to HaloTag but ligation of Cou-$HL2^N$-Fluo is not blocked by caging: additional in-gel fluorescence quantification from SiR-chase and fluorescein channel for SDS-PAGE gel shown in **Fig. S6**; the coumarin signal increases upon ligation of **Cou-$HL2^N$-Fluo** while no signal increase occurs from free **$HL2^N$-Fluo** which is not coumarin-caged (quantified from UV channel, normalised to 93% at 6 h from SiR-chase; incubation with 10 µM ligand and purified HT7 (3 µM) for different times (15 min, 1 h, 3 h, 6 h)).

For full discussion of the HL3 ligand see **Fig. S8**. **Fig. S12** shows the SDS-PAGE gel used for quantifying the HL3 binding and the signal quantification from both the fluorescein and the SiR-chase channels.

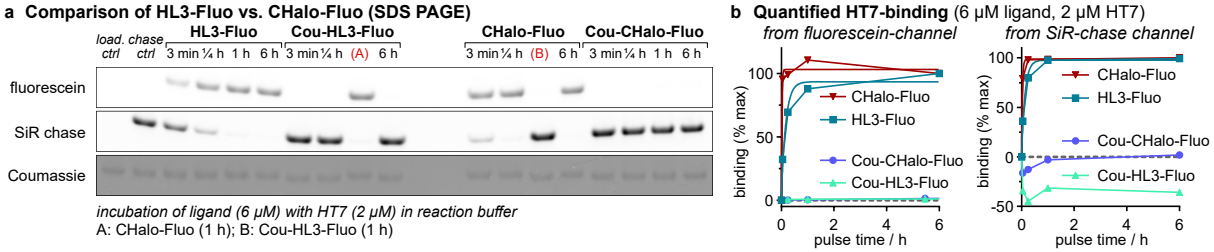

Figure S12: HL3-Ligand shows slower HaloTag ligation kinetics than CHalo. (a) SDS-PAGE gel showing the binding efficiencies of **HL3-Fluo** and **Cou-HL3-Fluo** compared to **CHalo-Fluo**, and **Cou-CHalo-Fluo** (6 µM) each after incubation with purified HT7 (2 µM) for different times (3 min, 15 min, 1 h, 6 h); A: **CHalo-Fluo**, 1 h; B: **Cou-HL3-Fluo**, 1 h; all rows show HT7 band: (i) fluorescein fluorescence, (ii) SiR chase fluorescence, (iii) Coumassie staining; **(b)** Quantified HT7-binding of HL3/4-type fluorescein conjugates (quantified from fluorescein or SiR channel in panel b).

The development of the CHalo ligand is discussed in detail at **Fig. S7** together with SDS-PAGE data showing rapid binding of CHalo reagents and fully blocked binding of caged CHalo reagents. In **Fig. S13** we additionally show comparative SDS-PAGE data for CA- and CHalo- conjugates with fluorescein and silicon-rhodamine SiR to assess the relative binding speed by in-gel fluorescence (quantification from fluorescein or SiR fluorescence as well as from MaP555 chase fluorescence). Despite incubation of ligand and HaloTag protein at low concentrations (1.5 : 0.5 µM) the ligation is still too fast to reliably resolve it by in-gel fluorescence (>60% ligation after 3 min) supporting that the CHalo ligand gives very rapid HaloTag ligation (detailed kinetics discussion at **Fig. S10ef**).

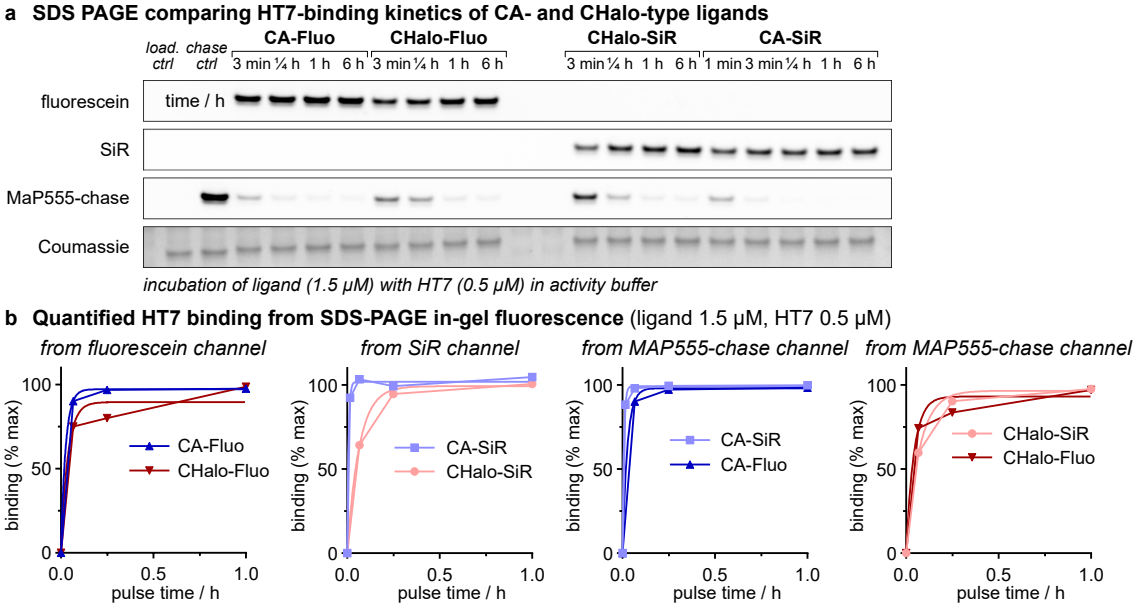

Figure S13: CHalo-Fluo and CHalo-SiR efficiently ligate to HaloTag (comparison to CA reagents). (a) SDS-PAGE gel for determining the binding kinetics of the fluorescein conjugates **CA-Fluo** and **CHalo-Fluo** and the SiR conjugates **CA-SiR** and **CHalo-SiR** (1.5 μM) each after incubation with purified HT7 (0.5 μM) for different times (3 min, 15 min, 1 h, 6 h, and after 1 min for **CA-SiR**); all rows show the HT7 band: (i) fluorescein fluorescence, (ii) SiR fluorescence, (iii) MaP555 fluorescence, (iv) Coumassie staining; **(b)** HT7-binding quantified from fluorescein, SiR, and MaP555-chase channel in panel a).

For full discussion of the CHalo binding and how caging blocks binding see **Supplementary Note 2** and discussion at **Fig. S7**. **Fig. S14** shows the SDS-PAGE analysis and in-gel fluorescence quantification of (caged) CHalo fluorescein conjugates (quantified from fluorescein channel and MaP555 chase channel).

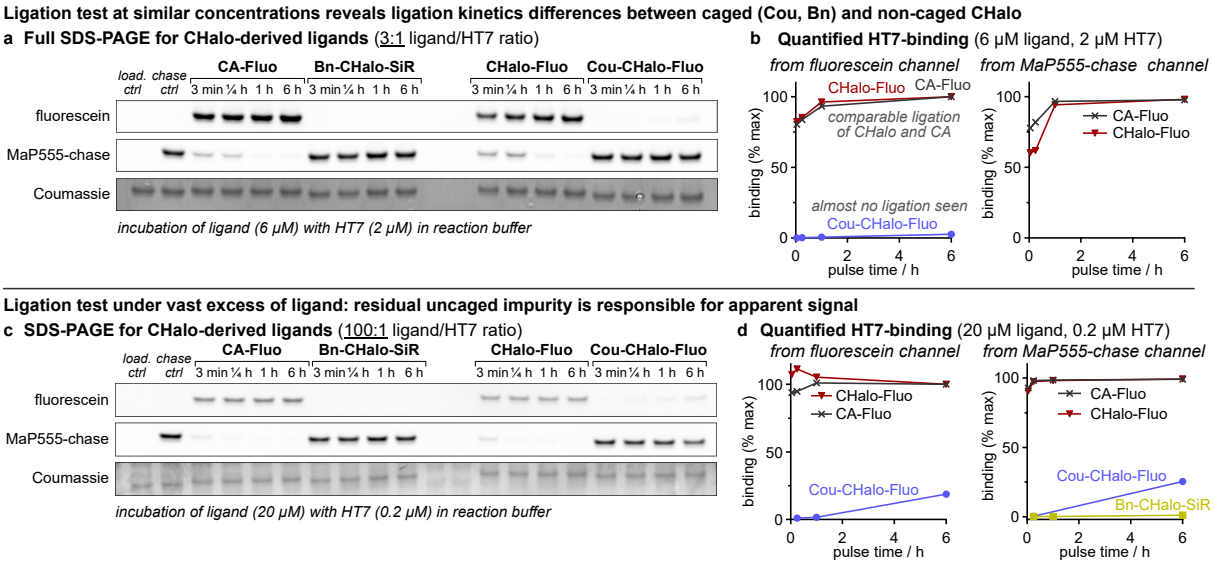

Figure S14: Caging of CHalo ligand effectively blocks HaloTag ligation. (a) SDS-PAGE gel showing the binding efficiencies of **CA-Fluo** compared to **Bn-CHalo-SiR**, **CHalo-Fluo**, and **Cou-CHalo-Fluo** (6 μM) each after incubation with purified HT7 (2 μM, *ratio = 3:1*) for different times (3 min, 15 min, 1 h, 6 h); all rows show HT7 band: (i) fluorescein fluorescence, (ii) MaP555 fluorescence, (iii) Coumassie staining (parts of gel shown in **Fig S7c**); **(b)** Quantified HT7-binding of CHalo-type fluorescein conjugates (quantified from MaP555 channel from panel b); **(c)** SDS-PAGE gel showing the binding efficiencies of **CA-Fluo** compared to **Bn-CHalo-SiR**, **CHalo-Fluo**, and **Cou-CHalo-Fluo** (20 μM) each after incubation with purified HT7 (0.2 μM, *ratio = 100:1*) for different times (3 min, 15 min, 1 h, 6 h); all rows show HT7 band: (i) fluorescein fluorescence, (ii) MaP555 fluorescence, (iii) Coumassie staining; **(d)** Quantified HT7-binding quantified from fluorescein and MaP555 chase channel from panel d).

8.2 Fluorescence Properties of Fluorescein Conjugates

For the proof-of-concept studies, we conjugated fluorescein to the HaloTag ligands as permanently fluorescent markers to trace ligation by in-gel fluorescence. All conjugates show the expected absorption and emission maxima (ca. 500/520 nm) with extinction coefficients 40−80·10^3 M^{-1} cm^{-1} (**Fig. S15**, **Table S1**). The quantum yields, however, strongly differed: highest fluorescence is observed for the ethylene glycol ligand **CA** (Φ = 0.83) which is strongly reduced for the phenyl group containing ligand **HL2^O** (Φ = 0.28) and even lower for the aniline ligands **HL2^N** and **CHalo** (Φ ca. 0.15) which might be explained by photoinduced electron transfer partially quenching the fluorescence.[66] The quenching seems even stronger when another quencher is installed in the **Cou-HL2^N** and **Cou-CHalo** ligands (Φ ca. 0.05) giving a 15-fold lower quantum yield compared to **CA-Fluo**. Interestingly, our fluorescein aryl-chain conjugates revealed small fluorogenicity upon HaloTag ligation that is coherent with suppressed PET quenching efficiency once ligation fixes the chain arene out of contact with the fluorophore (reminiscent of the larger unquenching seen with rhodamines), whereas alkyl-chain **CA-Fluo** shows reduced fluorescence upon binding (potentially due to unfavourable interactions of the normally anionic fluorescein with the protein surface that is best evolved for cationic rhodamines).

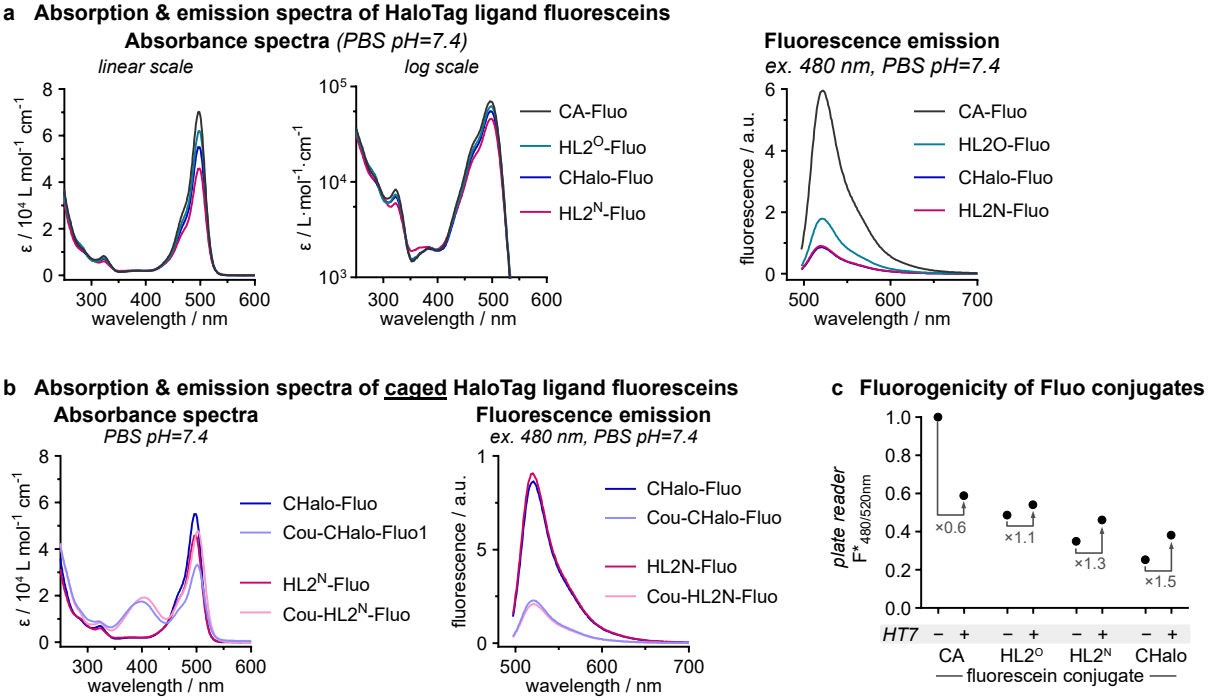

Figure S15: Absorption and fluorescence properties of HaloTag ligand fluorescein conjugates. (a) Absorption and emission spectra of **CA-**, **HL2^O-**, **HL2^N-** and **CHalo-Fluo** (10 µM, PBS, pH = 7.4); **(b)** Absorption and emission spectra of coumarin-caged conjugates **Cou-HL2^N-Fluo** and **Cou-CHalo-Fluo** (10 µM, PBS, pH = 7.4); **(c)** Fluorescence emission differences of free and HaloTag-bound Fluo-conjugates (2 µM ligand, 4 µM HT7, activity buffer, 15 h).

Fluorophore	$\lambda_{Abs,max}$ / nm	$\lambda_{emission,max}$ / nm	Stokes Shift / nm	$\varepsilon_{\lambda,max}$ / L mol^{-1} cm^{-1}	Φ_{FL}	brightness / L mol^{-1} cm^{-1}
CA-Fluo	497	522	25	70·10^3	0.83	59·10^3
HL2^O-Fluo	498	521	23	62·10^3	0.28	17·10^3
HL2^N-Fluo	498	520	22	46·10^3	0.17	7.7·10^3
Cou-HL2^N-Fluo	502	521	19	48·10^3	0.04	1.9·10^3
CHalo-Fluo	498	521	23	55·10^3	0.14	7.8·10^3
Cou-CHalo-Fluo	501	520	19	33·10^3	0.06	1.8·10^3

Table S1: Fluorescence properties of fluorescein conjugates **as free (unbound) ligands, in aqueous buffer** (PBS, pH = 7.4).

Quantum yields of the novel fluorophores were determined the following equation (Resch-Genger and coworkers[67]), albeit with the refractive indices cancelling each other (same medium):

$$\Phi_{f,x} = \Phi_{f,st} \cdot \frac{F_x}{F_{st}} \cdot \frac{1 - 10^{-A_{st}(\lambda_{ex})}}{1 - 10^{-A_x(\lambda_{ex})}} \cdot \frac{n_x(\lambda_{em})^2}{n_{st}(\lambda_{em})^2}$$

Fluorescein was used as a reference fluorophore with a quantum yield of $\Phi_{f,st}$ = 0.85 (in PBS, pH=7.4).[68]

8.3 HaloTag specificity

We supported the HaloTag-specificity of **CHalo-Fluo** ligation by competitive incubations of the ligand (5 µM) with HaloTag (0.1 µg, 0.5 µM) and cell lysates (up to 10 µg cellular protein). In-gel fluorescence indicated that the ligand only binds to HaloTag even though at least 4.5 µM of unreacted ligand remains exposed to cell lysate proteins (**Fig S16a**).

Relatedly, incubating the fluorogenic **CHalo-SiR** with cell lysate only (no HaloTag protein) shows no unwanted fluorescence generation, supporting that no undesired covalent or non-covalent interactions with the SiR conjugate occur that would generate off-target fluorescence (**Fig S16b**).

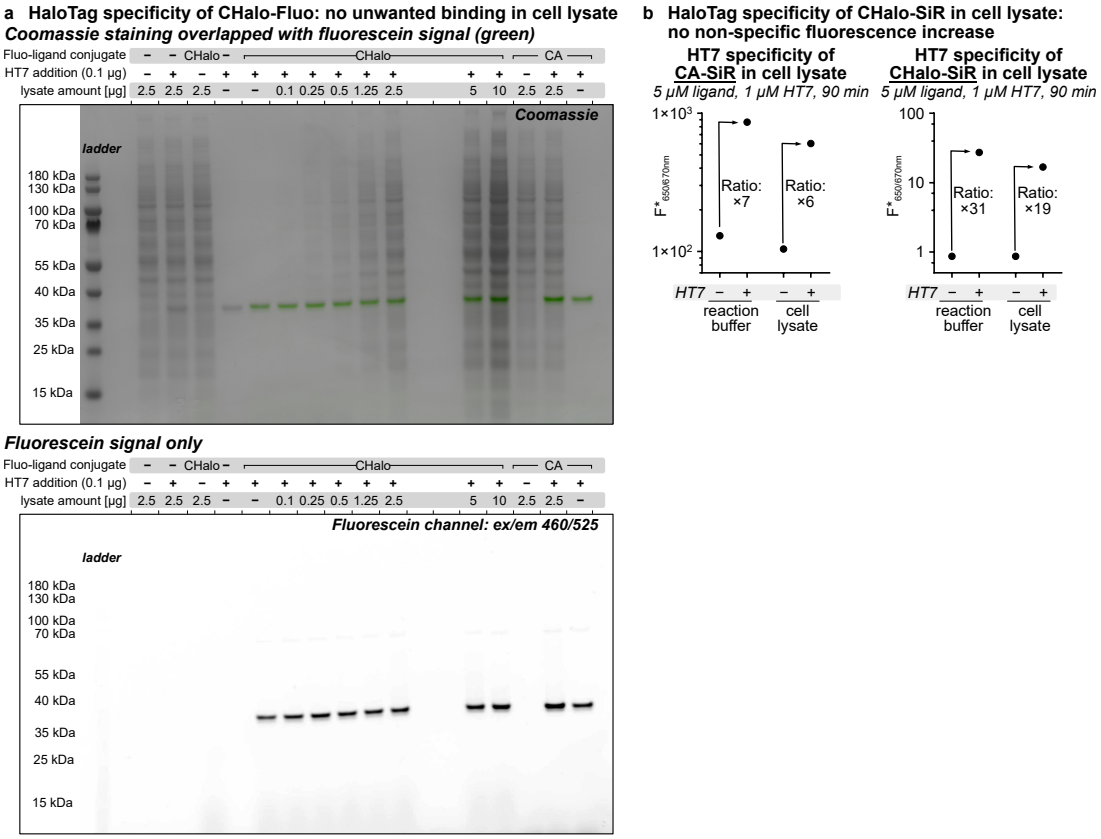

Figure S16: HaloTag specific binding of CHalo-Fluo in cell lysate. (a) SDS-PAGE gel of **CHalo-Fluo** with different amounts of HeLa cell lysate with and without HT7 (treatment of 5 µM **CHalo-Fluo** for 1 h with or without HT7 (0.5 µM), comparison: **CA-Fluo**); **(b)** Fluorescence generation of **CA-SiR** and **CHalo-SiR** with reaction buffer or with HeLa cell lysate with and without HT7 (treatment of 5 µM ligands for 1.5 h with 1 µM HT7).

8.4 Localisation of non-specific CHalo-SiR background in cells

The fluorescence of **CHalo-SiR** reagents is mostly, but not entirely, suppressed before ligation to HaloTag. Live cell imaging experiments showed minor non-specific background fluorescence of **CHalo-SiR** reagents in cells without HaloTag ligation (compare **Fig S18**: Leu-CHalo-SiR without HaloTag). Treatment of U2OS cells without HaloTag showed SiR signal in mitochondria, nucleus, and endoplasmic reticulum (ER) (**Fig. S17**). This localisation stems from the SiR dye cargo (not an intrinsic feature of the CHalo motif logic gate), which is logical since lipophilic, delocalised cations like rhodamines and triphenylphosphoniums are known as mitochondrial targeting groups with some ER localisation.[69]

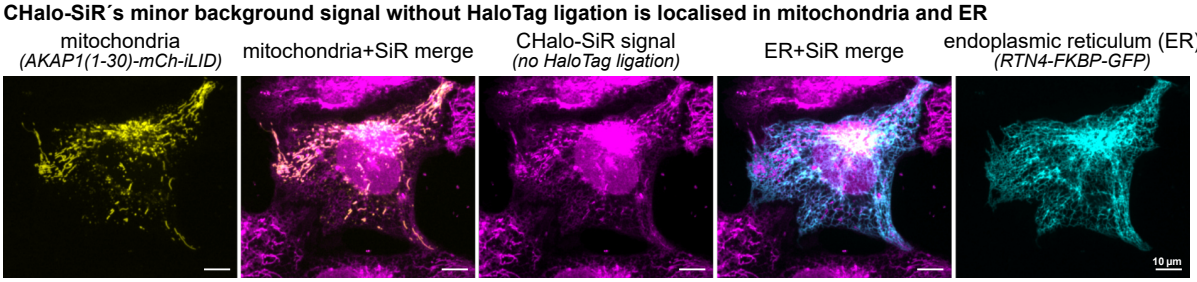

Figure S17: CHalo-SiR gives minor non-specific fluorescence (no HaloTag ligation) in cells that is localised in mitochondria and ER. Incubation of U2OS cells (no HaloTag) with **CHalo-SiR** (5 µM) for 20 min.

8.5 Additional Data for Leu-CHalo-SiR

8.5.1 HaloTag dependent signal generation and post-wash retention

We used the CHalo system for durable enzyme-activity imaging by uncaging **Leu-CHalo-SiR** with leucine aminopeptidase (LAP) followed by fluorogenic HaloTag ligation of the released **CHalo-SiR**. **Leu-CHalo-SiR** enables very sensitive detection due to its full fluorescence suppression before binding and the >400-fold fluorogenicity upon ligation (**Fig. 1h-j**). Cruicially, **caged-CHalo-SiR** cannot ligate to HaloTag (**Fig. 2f:** no signal for **Bn-CHalo-SiR**) and the signal generation from the released probe is fully dependent on the ligation to HaloTag (**Fig S18a**: no signal in cells not expressing HaloTag). After LAP activation (leucine peptidolysis, then spontaneous 1,6-elimination of the carbamic acid anion from the *para*-aminobenzyl spacer, then its spontaneous CO_2 evolution to give the uncaged CHalo-SiR reagent) followed by ligation to HaloTag protein, the HaloTag----CHalo-SiR conjugate is now membrane-impermeable and intracellularly retained. The actual SiR signal is limited by the rate of degradation of the HaloTag fusion protein employed, which depends on the cell line and protein target.[1] Nonetheless, signal integration by HaloTag ligation over hours to days is a feasible approach, even *in vivo* as shown by the calcium signal recorder CaProLa in flies.[70]

Fig. S18b shows the post-wash retention of the SiR signal in the specific settings we used (cytosolic HaloTag-mScarlet target, HEK cells): both unconditional ligators (CA-SiR and **CHalo-SiR**) are well retained for 2 h; but their signal decreases by 85% over the course of 24 h. We conjecture that the HaloTag-mScarlet fusion protein has a turnover half-life of ca. 8 h, explaining that signal loss (plausible rate). Such signal reduction was not observed for **Leu-CHalo-SiR** which showed bright cellular signal even after 48 h. We do not attribute that observation to retaining the ligated product from time zero, but rather to retention of the unligated probe that ligated later, allowing continuous signal generation after washing - although this still indicates remarkable detection sensitivity at presumably very low concentrations (although the retention is likely here fostered by the leucine trigger, and therefore cannot be expected with other trigger-CHalo probes). Nonetheless, since protein half-life can be tuned or chosen to fit desired applications, we see clear potential for more-stable (or faster-turnover) HaloTag protein anchors. (*Images used in quantification are shown in **Figs. S20−25***).

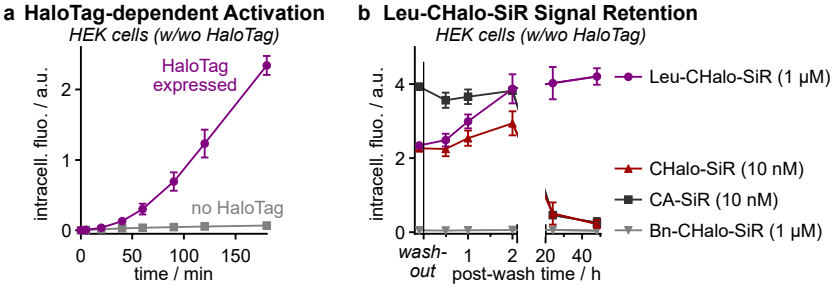

Figure S18: **(a)** HaloTag dependent **Leu-CHalo-SiR** signal generation in cells (1 µM, HEK cells with or without cytosolic HaloTag-mScarlet protein; data quantified from microscopy images); **(b)** Intracellular signal retention after removing the SiR reagent (2× medium change, pre-incubation of HEK cells with cytosolic HaloTag-mScarlet with each ligand for 3 h; data quantified from microscopy images; *n*=3).

8.5.2 Full data for Figure 2e

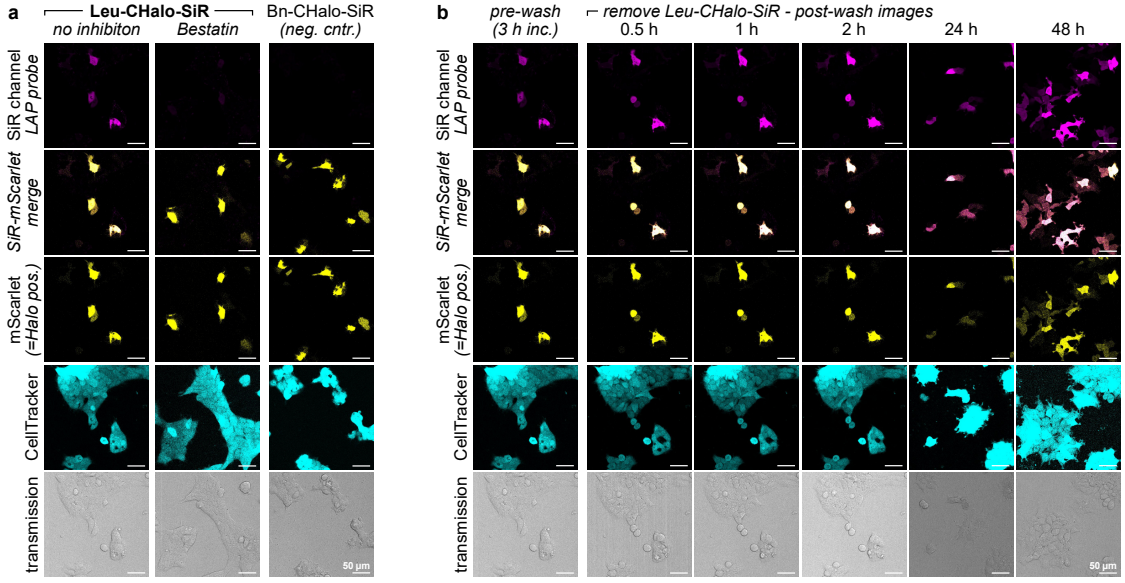

Figure S19: Full microscopy data for main **Fig. 2e** (HEK cells, 1 µM probe, 3 h, then 2× wash; optional pre-treatment with bestatin (LAP inhibitor, 100 µM, 30 min)).

8.5.3 Microscopy images for fluorescence quantification

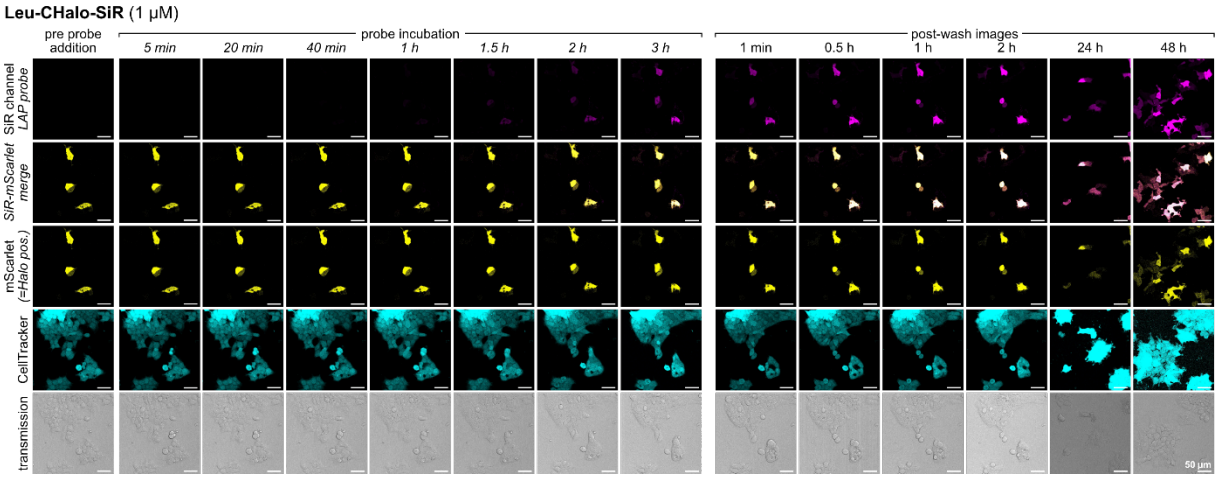

Figure S20: Microscopy images for fluorescence quantification for **Leu-CHalo-SiR** (1 µM probe in HEK cells transfected with cytosolic HaloTag-mScarlet; 3 h probe incubation, then 2× wash and post-wash imaging for 48 h; images from one of three replicates which were used for quantification).

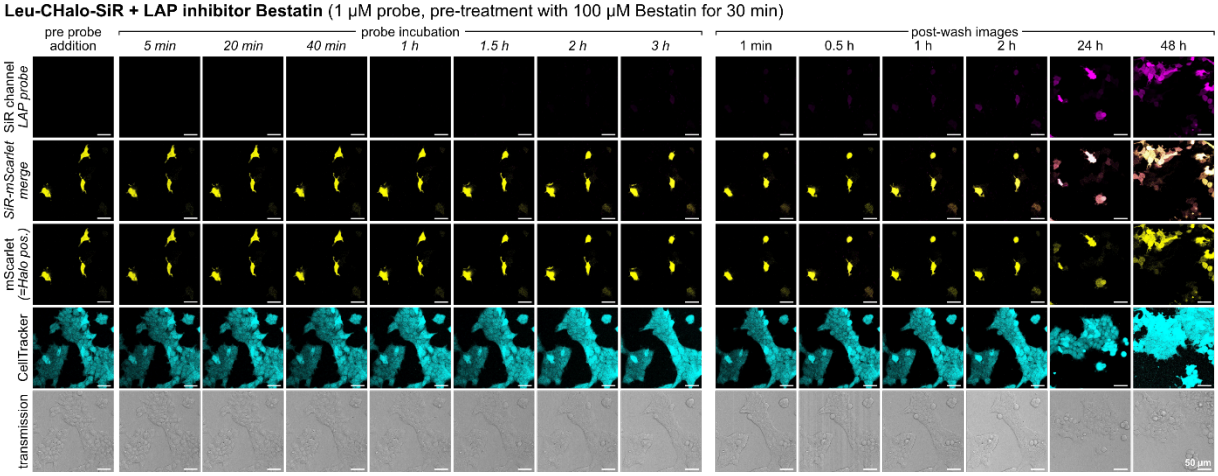

Figure S21: Microscopy images for fluorescence quantification for **Leu-CHalo-SiR with LAP inhibitor bestatin** (pre-treatment with bestatin (100 µM, 30 min); then 1 µM probe in HEK cells transfected with cytosolic HaloTag-mScarlet; 3 h probe incubation, then 2× wash and post-wash imaging for 48 h; images from one of three replicates which were used for quantification). These can be interpreted as: washout removes bestatin, but only partially removes **Leu-CHalo-SiR**.

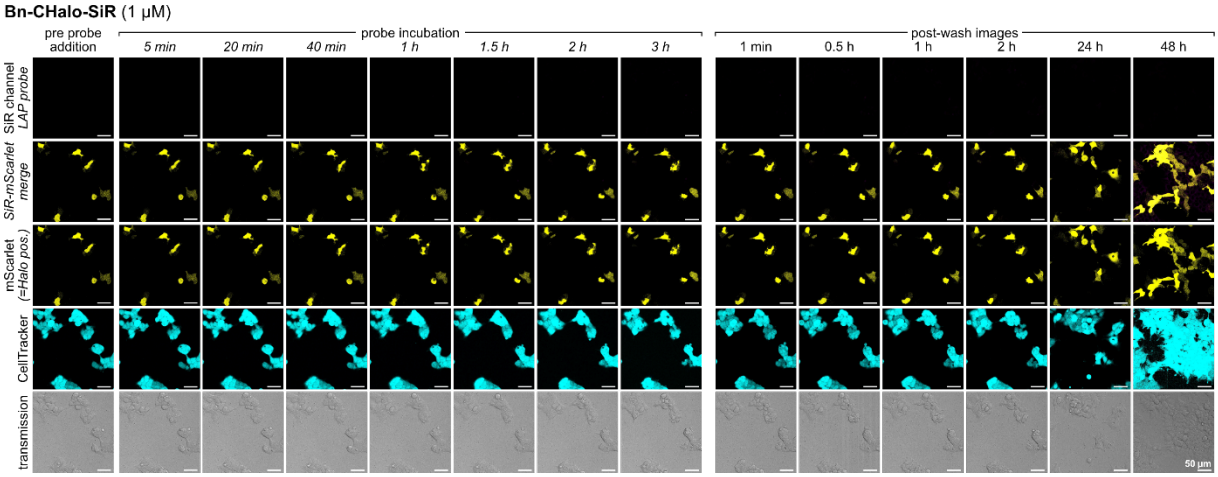

Figure S22: Microscopy images for fluorescence quantification for **non-activatable Bn-CHalo-SiR** (1 µM probe in HEK cells transfected with cytosolic HaloTag-mScarlet; 3 h probe incubation, then 2× wash and post-wash imaging for 48 h; images from one of three replicates which were used for quantification).

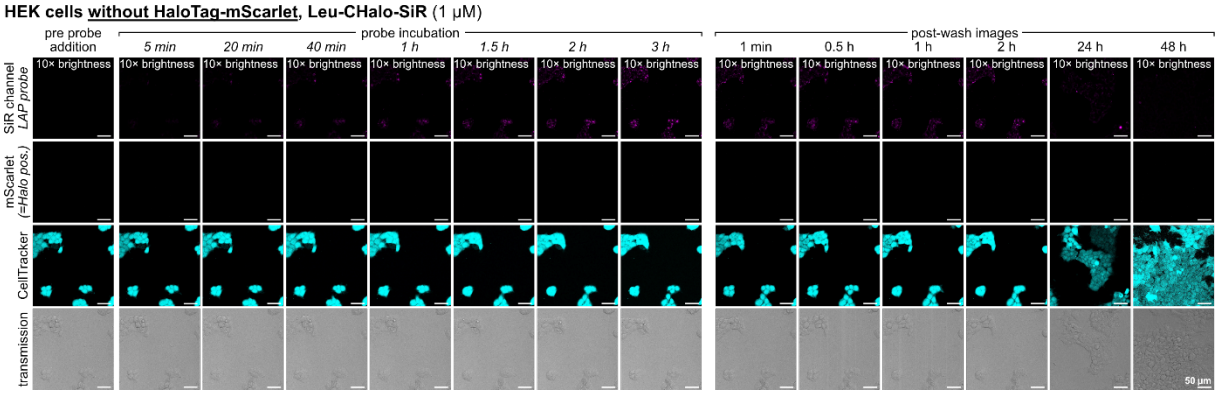

Figure S23: Microscopy images for fluorescence quantification for **Leu-CHalo-SiR in HEK cells without HaloTag-mScarlet** (1 µM probe; 3 h probe incubation, then 2× wash and post-wash imaging for 48 h; SiR brightness 10× enhanced compared to the images for the other probes to make the minor background fluorescence visible; images from one of three replicates which were used for quantification).

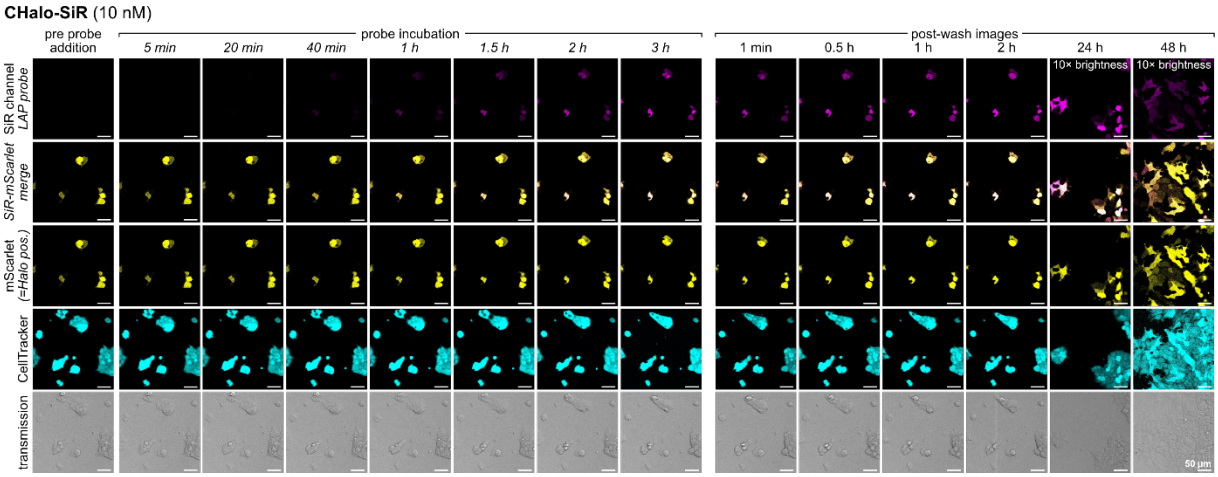

Figure S24: Microscopy images for fluorescence quantification for **free CHalo-SiR** (10 nM probe in HEK cells transfected with cytosolic HaloTag-mScarlet; 3 h probe incubation, then 2× wash and post-wash imaging for 48 h; images from one of three replicates which were used for quantification).

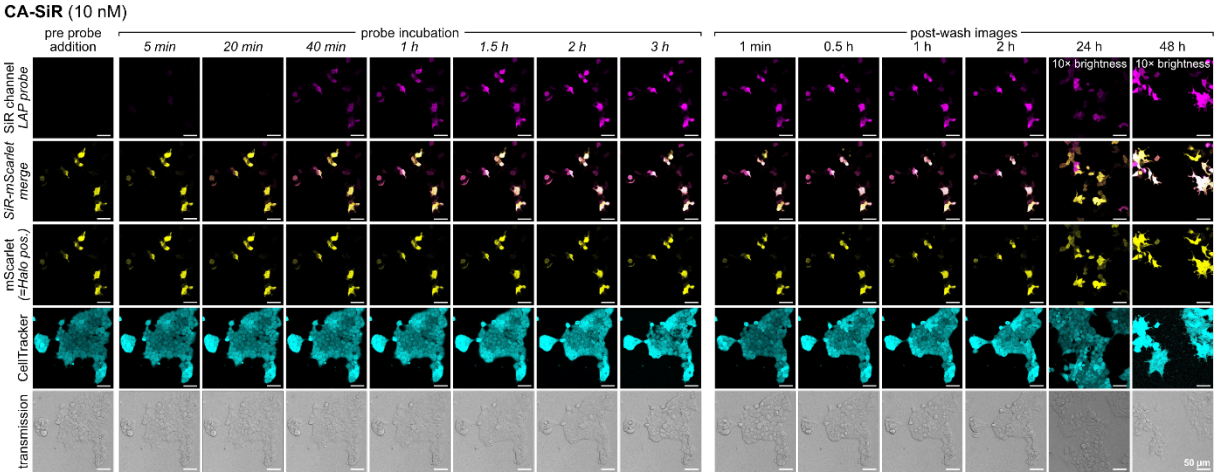

Figure S25: Microscopy images for fluorescence quantification for **known CA-SiR** (10 nM probe in HEK cells transfected with cytosolic HaloTag-mScarlet; 3 h probe incubation, then 2× wash and post-wash imaging for 48 h; images from one of three replicates which were used for quantification).

8.6 Additional Data for Cou-CHalo-BG

Cou-CHalo-BG can be efficiently uncaged with violet/blue light (ca. 50% conversion with 10 mJ/mm^2 at 405 nm, **Fig. S26a**, panel 3) while being unaffected by GFP imaging (no uncaging above 470 nm) as expected for aminocoumarin cages.

We quantified the co-localisation upon SNAP-Halo dimerisation (see main **Fig. 2l**) using Mander's coefficient (**Fig. S26b**) showing rapid and strong increase of the signal co-localisation upon light-activation of SNAP-ligated **Cou-CHalo-BG** (pre-incubation for 1 h, then light-activation, imaging after 5 min).

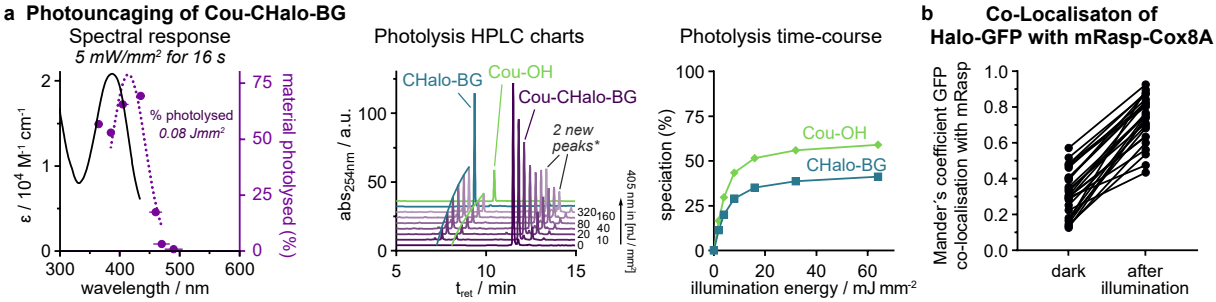

Figure S26: (a) Cou-CHalo-BG can be uncaged efficiently with blue light (ideal: 400−440 nm) and GFP orthogonally (no uncaging >470 nm; 50 µM sample in DMSO:water 7:3; illumination with the same light intensity for each wavelength, *horizontal error bars: FWHM of excitation light*; HPLC speciation and photolysis time-course (50 µM in MeCN:water 1:1; illumination with 405 nm light, 5 mW/mm^2, applied for times from 1 to 64 seconds (factor 2 steps)); **the species in the "2 new peaks" close to the Cou-CHalo-SiR signal include the coumaryl-CHalo alkyl aniline which is a nonphysiological by-product of the high concentrations used in this assay (after an aniline has been photoliberated, it can trap another photo-generated coumarinyl unit: byproduct mass lacks CO_2)*; **(b)** Halo-SNAP dimerisation efficiency quantified by Mander´s coefficient of GFP co-localisation with mRaspberry (quantification for main **Fig. 2l**; each data point represents one cell; *n* = 3).

9 Methods: photochemical and biological characterisation

9.1 Photochemical characterisation

Absorption spectroscopy

(several figures, indicated at specific methods section)

UV-Vis spectra were recorded on a Cary 60 UV-Vis spectrophotometer from *Agilent Technologies Inc.*, Santa Clara (USA) using 1 cm quartz or PMMA cuvettes. The scan rate was set to 600 nm/min and 2.5 nm slit width was used. Unless stated otherwise, the probes and fluorophores were dissolved in PBS (pH = 7.4, ≤1 % DMSO). All spectra of CHalo ligands with purified HaloTag7 protein were performed in reaction buffer (25 mM PBS (PanReac AppliChem, A0965.9010), 150 mM NaCl (Bernd Kraft, 04610.2600), 0.5 g/l BSA (Carl Roth, 3737.2) (pH = 7.5)).

Fluorescence spectroscopy

(several figures, indicated at specific methods section)

Fluorescence spectroscopy was performed on a Cary Eclipse Fluorescence Spectrometer from *Agilent Technologies Inc.*, Santa Clara (USA) using quartz cuvettes (scan rate: 120 nm/min, 5 nm slit width) or on a Tecan Infinite M1000 plate reader. All spectra of CHalo ligands with purified HaloTag7 protein were performed in reaction buffer (25 mM PBS (PanReac AppliChem, A0965.9010), 150 mM NaCl (Bernd Kraft, 04610.2600), 0.5 g/l BSA (Carl Roth, 3737.2) (pH = 7.5)).

Photouncaging efficiency (HPLC analysis)

(Figures: S7e, S10k, S26)

Instrument: Analytical HPLC analysis was conducted using an Agilent 1100 SL system equipped with a binary pump to deliver water:acetonitrile eluent mixtures containing 0.1% formic acid at a 1 mL/min flow rate, an Agilent 1100 series diode array detector, and a Hypersil Gold HPLC column. The eluent was a mixture of water (analytical grade, 0.1 % formic acid) and MeCN (analytical grade, 0.1 % formic acid).

The samples were illuminated in 384-well plate wells (50 µM, 50 µL, solvent: mixtures of acetonitrile/water 1:1 or DMSO/water 7:3) using a pE-4000 illumination system (CoolLED) set to 5 mW/cm^2. The pE-4000 illumination system was attached to a liquid light guide for light output that enables convenient handling and output uniformity in the illuminated wells. The liquid light guide was placed directly over the well to ensure uniform and comparable illumination conditions.

9.2 Cell-free biological characterisation

SDS-PAGE

(several figures, indicated at methods for pulse-chase assay & HaloTag specificity)

Samples were denatured in NuPAGE LDS-buffer 4× (Invitrogen, NP0007) and NuPAGE DTT buffer 10× (Invitrogen, NP0004) at appropriate volumes and heated to 70 °C in a Biometra TSC ThermoShaker (Analytik Jena) for 10 min. Gels (NuPage 4−12%, Bis-Tris Midi-Protein-Gel (Invitrogen, WG1402BOX)) were run using a SureLock Tandem Midi Gel Tank (Thermo Fisher, STM1001) and NuPAGE MES running buffer (Invitrogen, NP0002) at 165V for 40 min using a PowerEase Touch 350W Power Supply (Thermo Fisher, PS0350). 5 µL of PageRuler protein ladder (thermos scientific, 26616) and 10 µL of the samples were added to the wells. The in-gel fluorescence was imaged on an Amersham ImageQuant 800 Fluor (Cytiva) using the Cy2-channel (ex: 460 nm, em: 525bp20) for fluorescein ligands, Cy3-channel (ex: 535 nm, em: 605bp40) for MaP555-ligand and Cy5-channel (ex: 635 nm, em: 705bp40) for SiR-ligands; UV (ex. 365 nm, Cy3(UV)-filter) was used for coumarin fluorescence. The total protein stain was imaged after staining the gel with InstantBlue (abcam, ab119211) for 1 h.

Gels were evaluated using Bio-Rad Image Lab Software (quantification of absorption/fluorescence intensity), Microsoft Excel and GraphPad Prism. Quantified fluorescence intensities were corrected for the total protein amount quantified from InstantBlue staining to account for differences in the loaded amount protein. The quantified values from the fluorescein channel were normalised to the value after 6 h incubation (to the corresponding free ligand for Cou-caged fluoresceins), values from the chase channel gave the percentage of chase binding and were transformed to percentage of fluorescein ligand binding (100%−[percentage chase]). The coumarin binding of **Cou-HL2^{N}-Fluo** was quantified from the UV signal (subtracted by background from fluorescein determined from **HL2^{N}-Fluo**, normalisation of 6 h time-point to percentage calculated from chase-channel). For low ligation of Cou-CHalo reagents, further corrections were performed (see **Supplementary Note 2**).

HaloTag7 expression and purification

(preparation for all experiments using purified HaloTag7 protein)

Method A: The HT7 plasmid pET51b-His-TEV-HaloTag7 was a gift from Kai Johnsson (Addgene plasmid # 167266; http://n2t.net/addgene:167266 ; RRID:Addgene_167266), transformed into C41 (DE3) E. coli (Sigma-Aldrich, CMC0017) and plated onto 2xYT agar (Carl Roth, X967.1) with 100 µg/mL ampicillin (Carl Roth, K029.1). After incubation at 37 °C overnight a single colony was picked, inoculated in 13 mL tubes (Sarstedt, 62.515.006) with 8 mL 2xYT medium (Carl Roth, X966.1) supplemented with 100 µg/mL ampicillin (Carl Roth, K029.1) and incubated at 37 °C 200 RPM overnight. 100 µL were then added into 10 mL 2xYT medium supplemented with 100 µg/mL ampicillin in 100 mL Erlenmeyer flasks. Expression was induced by adding 0.5 mM IPTG (Carl Roth, 2316.4) and 1 mM $MgCl_2$ (Merck, M8266) at an OD_{600} of 0.8. After incubation at 37 °C overnight cultures were pelleted for 10 min (4800g). Bacteria were lysed for 20 min in protease inhibitor cocktail buffer (Sigma-Aldrich, I3911), DNAse (PanReac, A3778), lysozyme (Carl Roth, 8259.2) and Bugbuster 10× protein extraction reagent (Merck Millipore, 70921) and the lysate clarified by centrifuging for 15 min (20.000g). The proteins were purified using a HisTrap HP 1 mL (Cytiva, GE29-0510-221) on an Äkta Pure 25 M (Cytiva) with 50 mM Tris (Carl Roth, 4855.2), 500 mM NaCl (Bernd Kraft, 04610.2600), 250 mM imidazole (tcichemicals, I0001) elution buffer (pH = 7.5) and a HiLoad Superdex 200 PG 16/600 column (Cytiva, GE28-9893-35) with 25 mM Tris (Carl Roth, 4855.2), 1 mM EDTA (VWR, 7125.1000), 1 M NaCl (Bernd Kraft, 04610.2600) elution buffer. Proteins were assessed by SDS-PAGE and then transferred into 25mM PBS (PanReac AppliChem, A0965.9010), 150 mM NaCl (Bernd Kraft, 04610.2600) buffer (pH = 7.5) using zeba 7k MWCO spin columns (thermo scientific, 89882), concentrated using an Amicon Ultra centrifugational filter (merck Millipore, UFC8010) and stored at 4°C until use.

Method B: *E. coli BL21* were transformed with pET51b-His-TEV-HaloTag7 (Addgene #167266; gift from Kai Johnsson) and plated on LB agar supplemented with 100 µg/mL ampicillin. After overnight incubation at 37 °C, a single colony was used to inoculate 30 mL of LB medium containing 100 µg/mL ampicillin and grown at 37 °C, 200 rpm. 10 mL of the culture was put into 700 mL LB medium containing 100 µg/mL ampicillin and grown at 37 °C, 200 rpm until OD600 of 0.6. Protein expression was induced with 0.5 mM IPTG and cultures were incubated overnight at 28 °C. Cells were harvested by centrifugation (6.000 × g, 10 min) and pellets were resuspended in Lysis buffer (50 mM HEPES, 300 mM NaCl, 10 mM Imidazol, pH 7.4) and the slurry was subjected to cell lysis (LM10 microfluidizer; 15000 PSI, 5 passes, on ice). The lysate was clarified by centrifugation (10,000 × g, 20 min). The supernatant was applied to Ni-NTA Sepharose Fast Flow resin (Qiagen) and bound proteins were eluted with buffer containing 280 mM imidazole, 50 mM Tris, 300 mM NaCl, pH 7.4. Fractions containing the target protein were pooled and subjected to size exclusion chromatography (SEC) on a HiLoad Superdex 200 16/60 column (Cytiva) equilibrated in 25 mM HEPES, 150 mM NaCl, pH 7.5. The major elution peak, corresponding to HaloTag7, was identified by SDS-PAGE. Peak fractions were concentrated using 10 kDa MWCO centrifugal filters and further purified on a Superdex 75 Increase 10/300 GL column (Cytiva). Final peak fractions were pooled, concentrated, aliquoted, and stored at 4 °C. Protein purity was confirmed by SDS-PAGE. Thermal stability was assessed by nanoDSF (Prometheus NT.48, NanoTemper), giving a melting temperature (T_m) of ~63°C.

HaloTag dependent fluorogenicity

(Figures: SiR: S10b−d; fluoresceins: S15a−c)

The fluorogenicity of the ligand-**SiR** conjugates was determined using a Cary Eclipse Fluorescence Spectrometer (excitation: 652 nm, scan rate: 120 nm/min, 5 nm slit width). Purified HaloTag 7 protein (4 µM) and the respective ligand (**CA-SiR** and **CHalo-SiR**, 2 µM respectively) were mixed in reaction buffer (25 mM PBS (PanReac AppliChem, A0965.9010), 150 mM NaCl (Bernd Kraft, 04610.2600), 0.5 g/l BSA (Carl Roth, 3737.2) (pH = 7.5)) and incubated until binding was completed (maximum fluorescence intensity is reached: 15 min for **CA-SiR**, 8 h for **CHalo-SiR**). Then the ligand-SiR conjugates were incubated in reaction buffer (2 µM) without HaloTag 7 protein for the same time and the fluorescence was measured. The turn-on ratio was determined by the fluorescence difference of dye with or without HaloTag 7 at emission 665−672 nm. Absorption spectra were measured on a Cary 60 UV-Vis spectrophotometer as described above.

The fluorogenicity of the ligand-**fluorescein** conjugates was determined using a Tecan Infinite M1000 plate reader (ex: 480 nm; em: 488−700 nm). The fluorescein ligand-conjugates (**HL1-Fluo**, **HL2^{O}-Fluo**, **HL2^{N}-Fluo** and **CHalo-Fluo**, 2 µM concentration) were incubated for 15 h with or without purified HaloTag 7 protein (4 µM) in reaction buffer (25 mM PBS (PanReac AppliChem, A0965.9010), 150 mM NaCl (Bernd Kraft, 04610.2600), 0.5 g/l BSA (Carl Roth, 3737.2) (pH = 7.5)). The fluorescence emission was normalised to the signal of HL1-Fluo at 520 nm and the turn-on ratio was determined from the signal ratio of dye with or without HaloTag 7 at 520 nm. Absorption and emission spectra (ex: 480 nm) in PBS (pH = 7.4) were recorded as described above.

Dielectric constant dependent UV-Vis absorbance

(Figure S10e)

CHalo-SiR (0.5 µM) was dissolved in water/1,4-dioxane mixtures containing 10−80vol% 1,4-dioxane (1% DMSO) and the absorbance at 645−655 nm was measured at ambient temperature (23 °C). The absorbance was normalised to the highest value and plotted against the dielectric constant of the solvent mixture.[71] The fraction of the fully open (zwitterionic) form was calculated as the fraction of the HaloTag ligated CHalo-SiR absorbance ($7.3 \cdot 10^4$ M^{-1} cm^{-1}).

Pulse-chase assays

(Figures: S6de, S7cd, S8b, S10h, S11, S12ab, S13ab, S14a−d)

HaloTag7 (HT7) protein was incubated with the tested ligand for different times, after which a commercially available, fast-binding HT7 ligand was added in excess to stop the reaction and bind to the remaining unbound HT7 protein. All assays working with photocaged ligands were performed in a darkened room and whenever possible covered with aluminium foil. To compare the binding kinetics of **Cou-CHalo-Fluo** (photocaged), **CHalo-Fluo**, **CA-Fluo** and **BnCHalo-SiR** to HT7 protein, assays were performed with 2 µM HT7 and 6 µM ligand or with 0.2 µM HT7 and 20 µM ligand. Protein and ligand were mixed in reaction buffer (25 mM PBS (PanReac AppliChem, A0965.9010), 150 mM NaCl (Bernd Kraft, 04610.2600), 0.5 g/l BSA (Carl Roth, 3737.2) (pH = 7.5)) and incubated at room temperature for 3, 15, 60 and 360 min respectively. To compare the binding kinetics of CA and CHalo as fluorescein and SiR conjugates, a ratio of 1:3 protein:ligand (0.5 µM:1.5 µM) was mixed in reaction buffer and incubated for 1 (only **CA-SiR**), 4, 15, 60 and 240 min respectively. After incubation, the chase ligand (**MaP555**[9] or **CA-SiR**[10]), was added at 10 µM concentration for 1 h to bind remaining HT7. The samples were analysed by SDS-PAGE as described above. Controls: HT7 protein only; HT7 protein with chase ligand. The unused SDS-PAGE pockets were filled with reaction buffer.

Binding & fluorogenicity of caged SiR ligands

(Figure S10fg)

The ligand SiR conjugates (free **CHalo-SiR** and caged **Bn-CHalo-SiR** and **Cou-CHalo-SiR**, 5 µM respectively) were incubated with HT7 (2 µM) in reaction buffer (25 mM PBS (PanReac AppliChem, A0965.9010), 150 mM NaCl (Bernd Kraft, 04610.2600), 0.5 g/L BSA (Carl Roth, 3737.2) (pH = 7.5)) for 15 h to complete binding. The fluorescence intensity was determined using a Tecan Infinite M1000 plate reader (ex: 650 nm; em: 665 nm). Absorption spectra were recorded as described above.

Binding kinetics

(Figure S10i)

The ligand-SiR binding kinetics was determined from the fluorescence turn-on kinetics upon HaloTag binding at ambient temperature (23 °C). HaloTag protein (200 nM final concentration) and the ligand (**CA-SiR** or **CHalo-SiR**, 5 nM final concentration) were prepared as 2X stocks in PBS (pH = 7.5) with varying DMSO concentration in both stock solutions (1, 3 and 10% DMSO) to assess solubility / aggregation effects with different DMSO content. Both components were mixed 1:1 (25 µL ligand + 25 µL HaloTag) and the fluorescence intensity (ex: 645 nm; em: 668−672 nm) was measured every 1.2 s for 60 s (delay from mixing HaloTag and the ligand to first measurement: 5 s ±1 s) using a Cary Eclipse Fluorescence Spectrometer (scan rate: 300 nm/min, 5 nm slit width).

The emission values were averaged and plotted against the incubation time and fitted with a “one-phase association fit” which provided the “plateau value” with GraphPad Prism (version 10.4.2). The approximated rate constant k was determined by plotting ln(F*(t)) against the first 10 s of incubation time and applying a linear fit ($F^*(t) = ([plateau]-[F_{668\text{-}672nm}(t)])/([plateau]-[S_0])$; S_0 = fluorescence emission of ligand without HaloTag). The rate constants were calculated as k = −slope(ln(F*(t))) / c(HaloTag).

Light dependent binding of Cou-CHalo-SiR with purified HT7

(Figure S10l)

Under light exclusion, **Cou-CHalo-SiR** (5 µM) was incubated with purified HT7 (2 µM) in reaction buffer (25 mM PBS (PanReac AppliChem, A0965.9010), 150 mM NaCl (Bernd Kraft, 04610.2600), 0.5 g/L BSA (Carl Roth, 3737.2) (pH = 7.5)) for 1 h (fluorescence measurement after 20, 40 and 60 min). Then, the samples were illuminated with 405 nm light (using a pE-4000 illumination system (CoolLED) set to 5 mW/cm^2) for different times (5, 15, 45, 120 s) and the fluorescence intensities were measured after 5 min, 20 min, 1 h, 2 h and 4 h using a Tecan Infinite M1000 plate reader (ex: 650 nm; em: 665 nm).

HT7 specific protein binding

(Figure S16ab)

Cell culturing and lysis: HeLa cells were obtained from German Collection of Microorganisms and Cell Cultures (DSMZ Cat No. ACC57) and grown in Dulbecco’s modified Eagle’s medium (DMEM, Sigma-Aldrich, D1145) supplemented with 10% heat-inactivated fetal bovine serum (Biochrom S0615), 1% L-glutamine (Sigma-Aldrich, G7513), 1 mM Sodium Pyruvate (Sigma-Aldrich, S8636) and 100 nM sodium selenite (Sigma-Aldrich, 214485-5G) at 37°C and 5% CO_2. Washing was performed with Dulbecco’s PBS (Sigma-Aldrich, D8537), cell detachment was performed using Trypsin-EDTA solution (Sigma-Aldrich, T4174) diluted to 1x Dulbecco’s PBS (Sigma-Aldrich, D8537). Cell growth was monitored using an inverted microscope (Nikon Eclipse Ti), passage was kept between 2 and 20. Cells are tested regularly for mycoplasma contamination and only mycoplasma negative cells were used in assays. HeLa cells were lysed using M-PER reagent (thermos scientific, 78501) according to the manufacturer’s protocol and protein concentration was measured using the Pierce BCA Protein Assay Kit (Thermo Scientific, 23227), afterwards the lysate was stored on ice until used (2.8 mg protein / mL).

In-gel fluorescence of fluorescein conjugates: 0.5 µM HT7 protein and 5 µM of **CA-Fluo** or **CHalo-Fluo** ligand with differing amounts of HeLa cell lysate (0.1–10 µg, prepared as described above) were mixed in reaction buffer (25 mM PBS (PanReac AppliChem, A0965.9010), 150 mM NaCl (Bernd Kraft, 04610.2600), 0.5 g/L BSA (Carl Roth, 3737.2) (pH = 7.5)) and incubated for typically 1 h (or times as specified) at room temperature. The samples were analysed by SDS-PAGE as described above. Controls: lysate only; HaloTag7 only; ligands only; HT7 protein with ligand. The unused SDS-PAGE pockets were filled with reaction buffer.

Fluorescence measurement of SiR conjugates: HT7 (1 µM) and the ligand SiR conjugate (5 µM; **CA-SiR** or **CHalo-SiR**) were incubated with HeLa cell lysate or reaction buffer (25 mM PBS (PanReac AppliChem, A0965.9010), 150 mM NaCl (Bernd Kraft, 04610.2600), 0.5 g/L BSA (Carl Roth, 3737.2) (pH = 7.5)) and incubated at room temperature for typically 90 min (full binding was not reached for CHalo reagents). The fluorescence intensity was determined using a Tecan Infinite M1000 plate reader (ex: 650 nm; em: 665 nm).

9.3 Cellular characterisation

9.3.1 Cellular ligation rate

(Figure S10j)

HEK 293T cells were grown in DMEM (ThermoFisher 21885108) supplemented with 10% FBS (Biochrom S0615) and 1% Penicillin/Streptomycin (ThermoFisher 15140122) at 37 °C and 5% CO_2. Cell growth was monitored using an inverted microscope (Leica DMi1). Assays were performed in 8-well glass bottom chambered coverslips (ibidi 80827). These were coated two days before experiment by applying a 0.1 mg/mL Poly-D-Lysine (Sigma-Aldrich P7280) solution for 2 h at 37 °C and HEK cells seeded into the coated wells at a density of 20.000 cells per cm².

Transfection with Halo-mScarlet plasmid (kind gift from Kai Johnsson (Addgene plasmid # 167266 ; http://n2t.net/addgene:167266 ; RRID:Addgene_167266)) was performed 6 h after seeding. Per well (1 cm²) to be transfected, 26 µL of DMEM were combined with 0.26 µg of plasmid DNA and 0.78 µL of TransIT-LT1 transfection reagent (Mirus Bio MIR 2304), incubated at room temperature for 15–30 min, then added to cells dropwise. 27 µL of DMEM only were added to non-transfected control wells.

Confocal live cell imaging was performed at the Core Facility Bioimaging of the Biomedical Center with an inverted Leica SP8X microscope, equipped with Argon laser, WLL2 laser (470−670 nm) and acusto-optical beam splitter. Live cells were treated and recorded at 37 °C. For the duration of the assay, cells were kept in Hank’s Balanced Salt Solution (HBSS, ThermoFisher 14025092) to allow incubation without CO_2 atmosphere.

Experiments were performed with the following timeline: Cells were stained with 0.5 µM CMFDA (green cell tracker dye (abcam ab145459)) at 37 °C for 15 min. The medium was then changed to 250 µL HBSS and 50 µL of 6x concentrated solutions of CA-SiR and CHalo-SiR were added to achieve 10 nM final concentration. Images were acquired after 5, 20, 40, 60, 90, 120 and 180 min of incubation.

The microscope was programmed to take three images of different fields of view per condition and time point tested, which were focused using reflection-based adaptive focus control. Bias deriving from time delays between probes imaged in different wells was minimized by permutation of the positioning of probes between replicates. Images were acquired with a 20× 0.75 objective and additional 2× optical zoom. Image pixel size was 569 nm. The following fluorescence settings were used: CMFDA excitation 488 nm (Argon), emission 500–540 nm; mScarlet excitation 569 nm (WLL), emission 580–600 nm; SiR excitation 652 nm (WLL), emission 665–705 nm. Recording was performed sequentially to avoid bleed-through. CMFDA, mScarlet and SiR were recorded with hybrid photo detectors (HyDs), a transmitted light image was generated with a conventional photomultiplier tube. (Note: the represented brightness of the CMFDA CellTracker images was increased for the time-points 24 and 48 h due to signal loss after long incubations.)

Images were analysed using Fiji ImageJ. Images of transfected cells were segmented by thresholding on the mScarlet channel. Images of non-transfected cells were segmented by thresholding on the CMFDA channel. The resulting masks were then applied to the SiR channel to obtain a mean fluorescence intensity value. Analysed images were in focus and field of view outliers were excluded from analysis (for each biological replicate at least two field of view images were evaluated, otherwise the replicate was repeated). Data was plotted using GraphPad Prism.

9.3.2 Spatiotemporally controlled cellular microtubule labelling: Cou-CHalo-SiR

(Figures: labelling of stable microtubules: 2bc, Movie S1; localisation to endomembranes: S17)

Cell culture

U2OS cells (ATCC, CVCL_0224) were cultured in Dulbecco's Modified Eagle Medium (DMEM, Sigma) supplemented with 10% Fetal Bovine Serum (FBS, Corning), 100 U/mL penicillin and 100 µg/mL streptomycin (1% Penstrep, Sigma) at 37 °C with 5% CO_2.

DNA constructs

StableMARK-Halo-2xFKBP was cloned into a pSIN-TRE vector described in Noordstra *et al*.[72] with a puromycin resistance cassette by Gibson assembly. Prior to this a StableMARK-Halo-2xFKBP construct was cloned into a pB80 vector from Nijenhuis *et al*.[73] (gift from L. Kapitein, UU, Utrecht, Netherlands; Addgene, #174625) with flexible GS linkers between all the domains by Gibson assembly, using the StableMARK from StableMARK-2xmNeon (Jansen *et al*.[74], gift from L. Kapitein, UU, Utrecht, Netherlands; Addgene, #174649) and FKBP from Vim-mCh-FKBP (Pasolli *et al*.[75], Addgene; #240423) and Halo from Halo-Rab6A (Meiring *et al*.[76], Addgene; #190171). Lentiviral packaging constructs pMD2.G (Addgene, #12259) and psPAX2 (Addgene, #12260) were gifts from D. Trono, EPFL, Lausanne, Switzerland. EB3-GFP (Addgene, #190164) was described in Stepanova *et al*.[77]. RTN4-FKBP-GFP (Farias *et al*.[78]) was a gift from G.G. Farias, UU, Utrecht, Netherlands) and AKAP1(1-30)-mCh-iLID was a gift from L. Kapitein, UU, Utrecht, Netherlands.

Lentivirus production

HEK293T cells at 90% confluency were transfected with 15 µg pSIN-TRE StableMARK-Halo-2xFKBP, 5 µg pMD2.G and 10 µg psPAX2 using 90 µL MaxPEI (1 mg/mL Polyethylenimine, Polysciences) in optiMEM (1.2 mL final volume). Transfection mix was vortexed at low speed and pre-incubated at room temperature for 10 min before adding to HEK293T cells. Medium was refreshed the following 3 days, only collected for virus harvest on the last 2 days. Medium was filtered through a 0.045 µm filter before applying to a Amicon Ultra-15 filter column (Merck, UFC903029) and centrifuging for 25 min at 1400×g to purify virus. Supernatant was aliquoted and stored at −80 °C until used for cell transduction.

Cell line transduction and selection

U2OS cells were transduced with virus when they were at 40% confluency, medium was refreshed the following day and 3 µg/mL puromycin was added 48 h after transduction for 20 h to select for pSIN-TRE StableMARK-Halo-2xFKBP containing cells. From here single cells were plated and expanded to make a clonal cell line, subsequently selected for optimal expression levels upon 16 h treatment with 500 ng/mL doxycycline (Doxycycline-hyclate, Abcam, ab141091).

Cell transfection

U2OS cells were transfected with EB3-GFP or RTN4-FKBP-GFP and AKAP1(1-30)-mCh-iLID using Fugene 6 (Promega, #E2691) according to manufacturer's instructions at a ratio of 1 µg DNA to 3 µL Fugene 6.

Cou-CHalo-SiR uncaging to label stable microtubules in U2OS

pSIN StableMARK-Halo-2xFKBP U2OS were seeded into an 8 well labtek chamber (Thermo Scientific, #155409) at 40% together with EB3-GFP Fugene 6 transfection mix and 500 ng/mL doxycycline the day

before the experiment. At the day of the experiment, the medium on the cells was replaced with 200 µL fresh medium. In a dark room without blue/UV light a 2x **Cou-Chalo-SiR** solution (10 µM **Cou-Chalo-SiR**, 2% DMSO in cell media) was prepared and prewarmed to 37 °C. Samples were imaged on a custom spinning disc confocal microscope with a Nikon Eclipse Ti2-E body with Perfect Focus, a Yokogawa CSU-X1-A1 spinning disc unit, an ASI MS-2000-XYZ stage with Piezo Top plate and STXG-PLAMX-SETZ21L TokaiHit incubation chamber keeping sample at 37 °C with 5% CO_2 during the experiment. The sample was imaged using a Plan Apo VC 100x / 1.40 oil objective and Prime BSI sCMOS camera (Teledyne Photometrics). Voltran Stradus lasers 405 (wavelength for uncaging), 488 (GFP: microtubule marker) and 642 nm (SiR) were used to illuminate sample in combination with ET460/50m, ET525/50m and ET700/75m Chroma filters respectively. MetaMorph 7.10 software was used to control the microscope. 200 µL of the 2x **Cou-Chalo-SiR** solution was added to a well such that the final concentration was 5 µM **Cou-Chalo-SiR** and 1% DMSO, 5 min prior to commencing imaging. EB3-GFP (488 nm, 50 µW, 0.1 W/cm^2) and **Cou-Chalo-SiR** (642 nm, 0.52 mW, 1 W/cm^2) were imaged every 10 s using 500 ms exposure times. A single 2 s long pulse of 405 nm (0.74 mW, 2 W/cm^2) was applied to the sample to uncage **Cou-Chalo-SiR** at the indicated time points, spaced 2 min apart. *(Figures: 2bc; Movie S1)*

Localization of CHalo-SiR to ER and mitochondria

WT U2OS were seeded at 15% onto 25 mm glass #1.5 coverslips in a 6 well cell culture plate. The following day cells were transfected with RTN4-FKBP-GFP and AKAP1(1-30)-mCh-iLID. One day after transfection, the coverslips with cells were mounted in Attofluor cell chambers (Invitrogen, #A7816) with fresh medium. Samples were imaged on a custom spinning disc confocal microscope with a Nikon Eclipse Ti2-E body with perfect focus, a Yokogawa CSU-W1-T1 spinning disc unit, ASI MS-2000-XYZ stage with Piezo Top plate and STXG-PLAMX-SETZ21L TokaiHit incubation chamber keeping sample at 37 °C with 5% CO_2 during the experiment. Sample was imaged using a Plan Apo λD 100x / 1.45 objective and Prime BSI sCMOS camera (Teledyne Photometrics). Voltran Stradus lasers 488 (GFP: ER marker) and 642 nm (SiR) and Coherent OBIS 561 nm (mCherry: mitochondrial marker) lasers were used to illuminate sample in combination with ET525/50m, ET700/75m and ET630/75m Chroma filters respectively. MetaMorph 7.10 software was used to control the microscope. RTN4-FKBP-GFP, AKAP1(1-30)-mCh-iLID and **CHalo-SiR** were imaged once every 1 min for 20 min after addition. **CHalo-SiR** (5 µM, 1% DMSO in cell medium) was applied to cells immediately after the acquisition started.

9.3.3 Live cell imaging of enzyme activity: Leu-CHalo-SiR

(Figures: 2ef, S18ab, S19−25)

Bestatin is both a broad-acting ***aminopeptidase inhibitor*** (reason why we employ it to transiently chemically inhibit the function of peptidases: this is a way to test the cellular enzyme-specificity and activity-responsiveness of our leucine-anilide-caged model probe; the unnatural substrate design of leucine anilides makes them primarily processed in human cells only by the more tolerant enzyme leucine aminopeptidase), and an inhibitor of cellular inhibitor of apoptosis protein 1 (cIAP1, an E3 ligase i.e. having roles in the proteosomal degradation of other proteins). In the conditions we use and with the readout that we are monitoring, we do not expect that its cIAP1 inhibiting effects are relevant to assay outcomes or conclusions.

HEK 293T cells were grown in DMEM (ThermoFisher 21885108) supplemented with 10% FBS (Biochrom S0615) and 1% Penicillin/Streptomycin (ThermoFisher 15140122) at 37 °C and 5% CO_2. Cell growth was monitored using an inverted microscope (Leica DMi1). Assays were performed in 8-well glass bottom chambered coverslips (ibidi 80827). These were coated two days before experiment by applying a 0.1 mg/mL Poly-D-Lysine (Sigma-Aldrich P7280) solution for 2 h at 37 °C and HEK cells seeded into the coated wells at a density of 20.000 cells per cm².

Transfection with Halo-mScarlet plasmid (kind gift from Kai Johnsson (Addgene plasmid # 167266 ; http://n2t.net/addgene:167266 ; RRID:Addgene_167266)) was performed 6 h after seeding. Per well (1 cm²) to be transfected, 26 µL of DMEM were combined with 0.26 µg of plasmid DNA and 0.78 µL of TransIT-LT1 transfection reagent (Mirus Bio MIR 2304), incubated at room temperature for 15–30 min, then added to cells dropwise. 27 µL of DMEM only were added to non-transfected control wells.

Confocal live cell imaging was performed at the Core Facility Bioimaging of the Biomedical Center with an inverted Leica SP8X microscope, equipped with Argon laser, WLL2 laser (470−670 nm) and acusto-optical beam splitter. Live cells were treated and recorded at 37 °C. For the duration of the assay, cells were kept in Hank's Balanced Salt Solution (HBSS, ThermoFisher 14025092) to allow incubation without CO_2 atmosphere.

Experiments were performed with the following timeline: Cells were stained with 0.5 µM CMFDA (green cell tracker dye (abcam ab145459)) at 37 °C for 15 min. The medium was then changed to 250 µL HBSS with or without 100 µM bestatin (Carl Roth 2937.1). After 25 min of bestatin incubation, pre-treatment images were recorded. After 30 min of bestatin incubation, 50 µL of 6x concentrated solutions of the different silicon-rhodamine (SiR) HaloTag ligand dyes were added on top of the wells to achieve the final concentrations of 10 nM (for **CA-SiR**, **CHalo-SiR**) or 1 µM (for **Leu-CHalo-SiR**, **Bn-CHalo-SiR** and all ligands on non-transfected cells) respectively. Images were acquired after 5, 20, 40, 60, 90, 120 and 180 min of incubation. All wells

were then washed twice with HBSS and post-wash images acquired at 0, 30, 60 and 120 min thereafter. Cells were then returned to the incubator (37°C, 5% CO_2) in DMEM (+FCS, +Penicillin/Streptomycin) supplemented with 100 µg/mL primocin (invivogen ant-pm) and again transferred to the microscope for image acquisition at 24 h (± 1.5 h) and 48 h (± 1.5 h) post washing.

The microscope was programmed to take three images of different fields of view per condition and time point tested, which were focused using reflection-based adaptive focus control. Bias deriving from time delays between probes imaged in different wells was minimized by permutation of the positioning of probes between replicates. Images were acquired with a 20× 0.75 objective and additional 2× optical zoom. Image pixel size was 569 nm. The following fluorescence settings were used: CMFDA excitation 488 nm (Argon), emission 500–540 nm; mScarlet excitation 569 nm (WLL), emission 580–600 nm; SiR excitation 652 nm (WLL), emission 665–705 nm. Recording was performed sequentially to avoid bleed-through. CMFDA, mScarlet and SiR were recorded with hybrid photo detectors (HyDs), a transmitted light image was generated with a conventional photomultiplier tube. (Note: the represented brightness of the CMFDA CellTracker images was increased for the time-points 24 and 48 h due to signal loss after long incubations.)

Images were analysed using Fiji ImageJ. Images of transfected cells were segmented by thresholding on the mScarlet channel. Images of non-transfected cells were segmented by thresholding on the CMFDA channel. The resulting masks were then applied to the SiR channel to obtain a mean fluorescence intensity value. Analysed images were in focus and field of view outliers were excluded from analysis (for each biological replicate at least two field of view images were evaluated, otherwise the replicate was repeated). Data was plotted using GraphPad Prism.

9.3.4 Pulse-chase quantification of integrated enzyme activity: SS66T/C-CHalo-SiR

U2OS cells with stable GFP-NUP98 marker (nuclear pore complex) and transient HaloTag7-Sec61 fusion protein (ER-localised protein transport complex) as recorder were cultured and passaged in DMEM with penicillin (100 U/mL) and streptomycin (100 µg/mL), 10% FCS, 100 nM Na_2SeO_3 (for optimal functional translation of selenoproteins, relevant for TrxR-dependent redox biology), and 300 µg/mL G418 (selection for HaloTag-Sec61). 10 k cells were seeded per well in Greiner µ-clear 96 well plate, in 100 µL medium, one day before treatment; cells were then treated with caged-CHalo-SiR pulse ligands (10 µL of 10X probe stocks that had been freshly prepared from addition of 9 µL of DMEM to 1 µL of pulse ligand solution in 100% DMSO) establishing 1% DMSO final concentration. After 16 h incubation, JF525-HTL was added (chase ligand; 1 µM final concentration, by directly adding 1 µL of 100X stock in pure DMSO). GFP channel imaging showed image intensities stabilised after 15 min (saturation of remaining HaloTag binding sites by JF525). Imaging was then conducted with a BioTek Cytation 5 Cell Imaging Multimode Reader (epifluorescence microscope), using CY5 filter cube for SiR imaging ("623" nm LED with 628/40 bandpass excitation filter and 685/40 bandpass emission filter, red channel in **Fig 2h**) and YFP filter cube for GFP and JF525 imaging ("505" nm LED with 500/24 bandpass excitation filter and 542/27 bandpass emission filter, green channel in **Fig 2h**). Images were analysed using Fiji. ROIs containing the ER, excluding the nucleus and the cell periphery, were used to quantify the SiR/JF525 pulse/chase ratios; (minor) contributions from extracellular background to the per-pixel fluorescence were first subtracted from the average ROI fluorescence values in each channel, then the SiR/JF525 intensity ratios were calculated.

9.3.5 Spatiotemporally controlled protein heterodimerisation: Cou-CHalo-BG

(Figures: 2l, S26b; Movie S2)

Primary Neuronal Cultures

C57BL/6 mice were obtained from the animal facility at the Max Planck Institute for Biological Intelligence in Martinsried, Germany. All procedures involving mice were performed in compliance with the Government of Upper Bavaria, approved by the license number ROB-55.2-2532.Vet_02-23-213. Primary neurons were collected as previously described.[79–81] E16.5 timed-pregnant dams were euthanized by CO_2 and the mouse embryos were rapidly collected and decapitated in ice-cold dissection media (Hank´s Balanced Salt Solution supplemented with 100 mM of $MgCl_2$, 100 mM of HEPES and 10 mM kynurenic acid (Sigma-Aldrich, K3375)). The brains were dissected and stripped of meninges. Hippocampi were collected in ice-cold dissection media and dissociated into a single-cell suspension using of papain (0.2 mg/mL; Roche, 10108014001) for 5 min at 37 °C. Enzyme digestion was quenched using ovomucoid trypsin inhibitor (1 mg/mL; Abnova, P5243), followed by washes and trituration in complete media: Neurobasal (Gibco, 21103049) with B27 (Gibco, 17504044), penicillin/streptomycin and *L*-glutamine (Gibco, 10378016). Cells were then counted and 10^5 cells were plated onto glass-bottom 24-well plates previously coated with poly-*L*-lysine and laminin. Neurons were maintained in a humidified incubator at 37 °C and 5% CO_2 with a half-media change on DIV 5 and 7 (DIV = days *in vitro*).

Treatments, Microscopy and analysis

On DIV 5-7, neurons were co-transfected with 50 ng of GFP-Halo (subcloned from Addgene #67764 by removing the PEX3 sequence using MfeI and AscI digestion followed by T4 re-ligation (all enzymes from New

England Biolabs) and transformation), 400 ng of SNAP-OMM (Addgene, #69599) and 50 ng of mito-mRaspberry (Addgene, #55931) per well, using Lipofectamine 2000 (Invitrogen, 11668019). The transfection ratio of GFP-Halo and SNAP-OMM was found to be optimal between 1:4 and 1:8. Cells were treated and imaged at least 48 h post-transfection (DIV 7-9).

Neurons were imaged on an inverted laser-scanning confocal microscope Stellaris DMI8 (Leica), controlled by the LAS-X software (Leica) using a HC PL APO CS2 63×/1.40 OIL objective, kept at 37 °C by a Okolab black cage incubator. Imaging settings: excitation with a white light laser (GFP: 489 nm and mRaspberry: 598 nm) and emission collection in a single sequence using 2 hybrid detectors for the GFP (500–530 nm) and mRaspberry (609–653 nm) channels.

The neurons were treated with **Cou-CHalo-BG** (final concentration: 5 µM, 0.5% DMSO) or DMSO only (negative control) for 1 h in complete media (Neurobasal with B27, penicillin/streptomycin and *L*-glutamine). The excess of the **Cou-CHalo-BG** was removed by medium change and incubation for 5 min (the wash cycle was repeated 3×), then the medium was changed to Hibernate E without phenol red for imaging (Transnetyx Tissue, HEPR500). The acquisitions for the timelapse experiments were performed under the Lightning mode at 598 Hz on 50 × 50 µm (1176 × 1176 px) frames at 30 s intervals (1 frame before illumination, then "uncaging frame", then imaging for 5 min). Uncaging was performed using a 405 nm laser diode (16.1−213 µW, 45.6−603 kW/cm^2) during the acquisition of the "uncaging frame" (pixel dwell time of 750 ns).

The re-localisation of the GFP signal to the mitochondrial mRaspberry signal was quantified by comparing the images before uncaging and 5 min after uncaging. The images were analyzed with JaCoP in FIJI/ImageJ (version 1.54) and the Mander´s coefficient for the ratio of GFP overlapping mitochondria was calculated.

10 Synthetic Chemistry

10.1 Chemistry methods and techniques

10.1.1 Analytical methods

High resolution mass spectrometry (**HRMS**) was conducted on the following instruments: (1) a *Thermo Finnigan LTQ FT Ultra FourierTransform* ion cyclotron resonance spectrometer from *ThermoFisher Scientific GmbH* applying electron spray ionisation (ESI) with a spray capillary voltage of 4 kV at temperature 250 °C with a method dependent range from 50 to 2000 u;(2) a *Finnigan MAT 95 from Thermo Fisher Scientific* applying electron ionisation (EI) at a source temperature of 250 °C and an electron energy of 70 eV with a method dependent range from 40 to 1040 u; and (3) a Waters Xevo G2-XS Q-TOF applying electron spray ionisation (ESI) with a spray capillary voltage of 2 kV at a source temperature of 140 °C with a method dependent range from 50 to 1200 u.

Nuclear magnetic resonance (**NMR**) spectroscopy was performed using the following instruments: (1) a *Bruker Avance* (600/150 MHz, with TCI cryoprobe) or (2) a *Bruker Avance III HD Biospin* (400/100 MHz, with BBFO cryoprobe^{TM}) from Bruker Corp. or (3) a Bruker Avance III HD (800 MHz, with cryoprobe) or (4) a Bruker Avance Neo (600/150 MHz, with cryoprobe). NMR-spectra were measured at 298 K, unless stated otherwise, and were analysed with the program *MestreNova 12* developed by *MestreLab Ltd.* ^{1}H-NMR spectra chemical shifts (δ) in parts per million (ppm) relative to tetramethylsilane (δ = 0 ppm) are reported using the residual protic solvent ($CHCl_3$ in $CDCl_3$: δ = 7.26 ppm, DMSO-d_5 in DMSO-d_6: δ = 2.50 ppm, CHD_2OD in CD_3OD: δ = 3.31 ppm) as an internal reference. For ^{13}C-NMR spectra, chemical shifts in ppm relative to tetramethylsilane (δ = 0 ppm) are reported using the central resonance of the solvent signal ($CDCl_3$: δ = 77.16 ppm, DMSO-d_6: δ = 39.52 ppm, CD_3OD: δ = 49.00 ppm) as an internal reference. For ^{1}H-NMR spectra in addition to the chemical shift the following data is reported in parenthesis: multiplicity, coupling constant(s) and number of hydrogen atoms. The abbreviations for multiplicities and related descriptors are s = singlet, d = doublet, t = triplet, q = quartet, or combinations thereof, m = multiplet and br = broad. When rotamers were observed in the NMR spectra, the corresponding signals are separated by a slash ("/"). Where known products matched literature analysis data, only selected data acquired are reported.

Analytical high performance liquid chromatography (**HPLC**) analysis was conducted either using an *Agilent 1100* system from *Agilent Technologies Corp.,* Santa Clara (USA) equipped with a DAD detector and a *Hypersil Gold* HPLC column from *ThermoFisher Scientific GmbH*, Dreieich (Germany) or a *Agilent 1200 SL* system *Agilent Technologies Corp.,* Santa Clara (USA) equipped with a DAD detector, a *Hypersil Gold* HPLC column from *ThermoFisher Scientific GmbH*, Dreieich (Germany) and consecutive low-resolution mass detection using a LC/MSD IQ mass spectrometer applying ESI from *Agilent Technologies Corp.,* Santa Clara (USA). For both systems mixtures of water and MeCN (both analytical grade, 0.1 % formic acid) were used as eluent systems.

10.1.2 Synthetic techniques

Unless stated otherwise, all reactions were performed without precautions regarding potential air- and moisture-sensitivity and were stirred with Teflon-coated magnetic stir bars. For work under inert gas (nitrogen) atmosphere, a Schlenk apparatus and a high vacuum pump from Vacuubrand GmbH, Wertheim (Germany) were used. For solvent evaporation a *Laborota 400* from Heidolph GmbH, Schwabach (Germany) equipped

with a vacuum pump was used. Flash column chromatography was conducted with a Biotage® Isolera One Chromatograph with Biotage® Sfär Silica D columns (10 g or 25 g silica) for normal-phase (np) chromatography or with Biotage® Sfär C18 D columns (12 g or 30 g silica) for reversed-phase (rp) chromatography. Reactions were monitored by thin layer chromatography (TLC) on TLC plates (*Si 60 F254 on aluminium sheets*) provided by Merck GmbH and visualised by UV irradiation and by analytical HPLC-MS. The procedures and yields are not optimised.

10.1.3 Chemicals

All chemicals, which were obtained from BLDpharm, Sigma-Aldrich, TCI, Alfa Aesar, Acros, abcr or carbolution were used as received and without purification. Tetrahydrofuran (THF), dichloromethane (DCM) and dimethylformamide (DMF) were provided by Acros and were stored under argon atmosphere and dried over molecular sieves. TLC control, extractions and column chromatography were conducted using distilled, technical grade solvents. Whenever the term *hexanes (Hex)* is used, the applied solvent actually comprised isomeric mixtures of hexane (2-methylpentane, 3-methylpentane, 2,2-dimethylbutane, 2,3-dimethylbutane).

10.2 Synthetic procedures

10.2.1 General Procedures

General Procedure A: deprotection of Boc-amines

The Boc-amines were dissolved in anhydrous DCM (0.02 M–0.25 M) and hydrogen chloride in dioxane (4 M) was added to give 2 M HCl concentration in the mixture. The reaction mixture was stirred at room temperature for 1 h, the volatiles were removed *in vacuo* and the product was used without further purification for the next synthetic step.

General Procedure B: amide coupling with HATU

The carboxylic acid (1.0 eq) was dissolved in anhydrous DMF (0.02 M–0.25 M), DIPEA (5.0 eq) and *O*-(7-Azabenzotriazol-1-yl)-*N*,*N*,*N*′,*N*′-tetramethyluronium-hexafluorphosphat (HATU, 1.0 eq–1.2 eq) were added and the mixture was stirred at room temperature for 20 min. Then the amine (0.5 eq–2.0 eq, equivalents varied depending on the synthetic accessibility of respective carboxylate and amine) was added and the reaction mixture was stirred at room temperature for 1–12 h until completion (monitored by HPLC-MS). The solvent was removed *in vacuo* and the crude product was diluted with ethyl acetate and a half-saturated solution of sodium bicarbonate. The layers were separated, the aqueous layer was extracted with ethyl acetate (3×) and the combined organic layers were washed with brine and dried over sodium sulfate. The crude product was purified by flash column chromatography.

General Procedure C: DEACM-carbamate formation with triphosgene

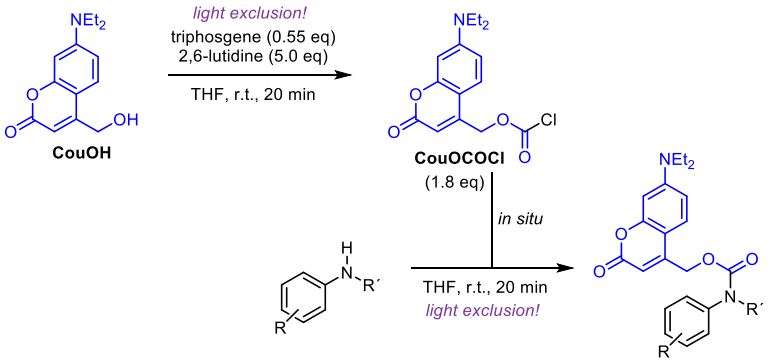

Note: the reaction must be performed under light exclusion.

Adaptation from previously described procedure.[82] Under nitrogen atmosphere, **CouOH** (1.0 eq) was dissolved in anhydrous THF (0.1 M). Triphosgene (0.55 eq) and 2,6-lutidine (5.0 eq) were added and the reaction mixture was stirred at room temperature for 20 min (HPLC-MS analysis of the reaction progress by quenching with methyl piperazine in acetonitrile).

In a separate flask, the aniline was dissolved in anhydrous THF (0.02 M–0.2 M) under nitrogen atmosphere. Then the reaction mixture with the **CouOCOCl** (1.8 eq) was added dropwise and the mixture was stirred at room temperature for 20 min. Upon full conversion of the aniline, the excess of the **CouOCOCl** was reacted with a secondary amine (piperidine or methyl piperazine depending on the desired polarity for the following purification). The mixture was diluted with ethyl acetate and water, extracted (3×), the organic layers were washed with brine (1x) and the crude product was purified by flash column chromatography.

Note 1: the chloroformate formation shows unwanted chloride formation (giving CouCl) with tertiary amine bases like DIPEA. A previously described procedure[82] solved the problem by reacting CouOH and phosgene

without a base in THF, which requires at least 6 h reaction time for decent conversion. We found that using the sterically hindered pyridine base 2,6-lutidine enables selective formation to CouOCOCl within minutes.

Note 2: the carbamate formation with CouOCOCl is much cleaner than the reaction with CouO-PFPC (see General Procedure D) which mostly gives the hydrolysed byproduct CouOH and minor amounts of CouCl. We still used an excess of the chloroformate to ensure full conversion of the aniline since we often observed partial hydrolysis of the chloroformate during the reaction.

General Procedure D: DEACM-carbamate formation with bis(pentafluorophenyl)carbonate

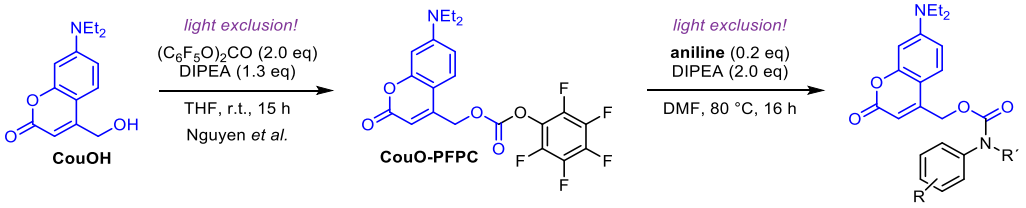

Note: the reaction must be performed under light exclusion.

CouO-PFPC was prepared according to a previously described procedure (Nguyen *et al.*[82], compound 14) using bis(pentafluorophenyl)-carbonate to afford the coumarin pentafluorophenylcarbonate (PFPC) which can be purified and stored at −20 °C.[82] For photocaging (secondary) anilines, the aniline (0.2 eq) was dissolved in anhydrous DMF (0.05 M–0.2 M), DIPEA (2.0 eq) and **CouO-PFPC** (1.0 eq) were added and the reaction mixture was heated to 80 °C for 16 h. The solvent was removed in vacuo and the crude product was purified by flash column chromatography.

Note: while the CouO-PFPC is a convenient reagent due to its stability, the carbamate formation reaction gives unwanted side products (ether CouO-C_6F_5, carbonate $(CouO)_2CO$ and the hydrolysis product CouOH, therefore CouO-PFPC is used in excess). Separation of these byproducts from the desired product is often inconvenient without prep-HPLC purification, thus, for larger scale reactions the use of triphosgene is more advantageous.

General Procedure E: Siliconrhodamine (SiR) conjugation

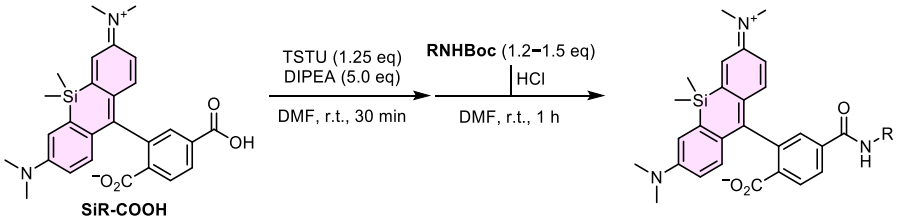

6-Carboxy tetramethyl siliconrhodamine (**SiR-COOH**) was dissolved in anhydrous DMF (4.2 mM), DIPEA (5.0 eq) and TSTU (50 mM in DMF, 1.6 eq) were added and the reaction mixture was stirred at room temperature for 30 min. In parallel the Boc-amine was deprotected following General Procedure A, subsequently added to the SiR-NHS ester and stirred at room temperature for 1 h. The mixture was purified by preparative HPLC.

10.2.2 CHalo Ligand building blocks

Synthetic route for CHalo-Boc

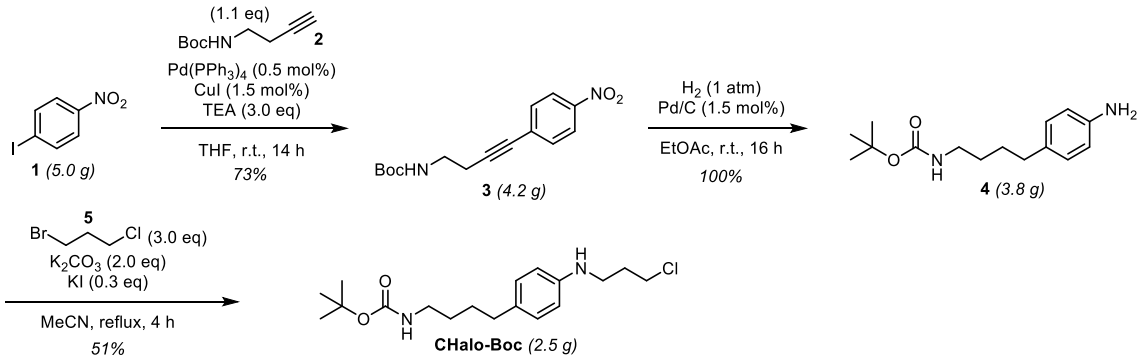

Compound 3

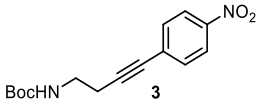

1-Iodo-4-nitrobenzene (**1**, 5.00 g, 19.9 mmol, 1.0 eq) was dissolved in anhydrous THF (50 mL, 0.4 M), triethylamine (8.3 mL, 60 mmol, 3.0 eq) and *tert*-butyl but-3-yn-1-ylcarbamate (**2**, 3.83 g, 21.5 mmol, 1.1 eq) were added and the solution was degassed by bubbling nitrogen through the mixture for 10 min. Copper iodide (57 mg, 0.30 mmol, 1.5 mol%) and tetrakis(triphenylphosphine)palladium(0) (0.12 g, 99 µmol, 0.50 mol%) were added and the reaction mixture was stirred at room temperature for 14 h. The volatiles were removed *in vacuo*, the residue was diluted with water (50 mL), brine (10 mL) and diethyl ether (50 mL), the layers were separated and the aqueous layer was extracted with diethyl ether (3 × 30 mL). The combined organic layers were dried over sodium sulfate and the solvent was removed *in vacuo*. The crude product was purified by flash column chromatography (*iso*-hexanes/ethyl acetate; 5→25% EtOAc) affording **3** (4.23 g, 14.6 mmol, 73%) as an orange solid.

TLC Rf = 0.10 (*np*, Hex:EtOAc 9:1); Rf of **1** = 0.62
^{1}H-NMR (600 MHz, $CDCl_3$): *δ* (ppm) = 8.16 (d, J = 8.8 Hz, 2H), 7.53 (d, J = 8.9 Hz, 2H), 4.85 (s, 1H), 3.38 (s, 2H), 2.65 (t, J = 6.6 Hz, 2H), 1.45 (s, 9H).
^{13}C-NMR (151 MHz, $CDCl_3$): *δ* (ppm) = 155.8, 147.0, 132.5, 130.6, 123.7, 93.4, 80.6, 79.8, 39.4, 28.5, 21.4.
HRMS (ESI+): m/z calc. for $C_{10}H_{11}N_2O_2^+$ $[M-Boc+H]^+$: 191.0815, found: 191.0822.

Compound 4

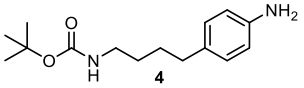

3 (4.18 g, 14.4 mmol, 1.0 eq) was dissolved in ethyl acetate (30 mL, 0.5 M) under nitrogen atmosphere, palladium on charcoal (Pd/C, 0.26 g, 0.22 mmol, 1.5 mol%) was added and the reaction was stirred under hydrogen atmosphere (1 atm) for 17 h. The Pd/C was removed by filtration over Celite (washed with ethyl acetate (7×) and the filtrate was concentrated under reduce pressure affording **4** (3.81 g, 14.4 mmol, 100%) as a colourless solid.

TLC Rf = 0.15 (*np*, Hex:EtOAc 3:1); Rf of **3** = 0.47
^{1}H-NMR (600 MHz, $CDCl_3$): *δ* (ppm) = 6.96 (d, J = 8.3 Hz, 2H), 6.63 (d, J = 8.3 Hz, 2H), 4.50 (s, 1H), 3.45 (s, br, 2H), 3.12 (d, J = 6.3 Hz, 2H), 2.51 (t, J = 7.6 Hz, 2H), 1.62 – 1.54 (m, 2H), 1.48 (dt, J = 13.5, 6.6 Hz, 2H), 1.44 (s, 9H).
^{13}C-NMR (151 MHz, $CDCl_3$): *δ* (ppm) = 156.1, 144.0, 132.7, 129.3, 115.5, 79.1, 40.6, 34.7, 29.7, 29.0, 28.6.
HRMS (ESI+): m/z calc. for $C_{15}H_{24}N_2NaO_2^+$ $[M+Na]^+$: 287.1730, found: 287.1733.

CHalo-Boc

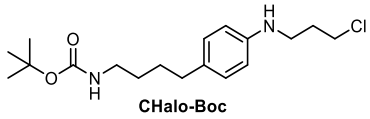

4 (3.74 g, 14.1 mmol, 1.0 eq) was dissolved in anhydrous acetonitrile (40 mL, 0.35 M) under nitrogen atmosphere. Potassium carbonate (3.91 g, 28.3 mmol, 2.0 eq), potassium iodide (0.71 g, 4.2 mmol, 0.30 eq) and 1-bromo-3-chloropropane (**5**, 4.2 mL, 42 mmol, 3.0 eq) were added and the reaction mixture was heated to reflux for 4 h. The volatiles were removed under reduced pressure and the residue was diluted with water (50 mL), brine (30 mL) and ethyl acetate (30 mL). The layers were separated and the aqueous layer was extracted with ethyl acetate (2 × 30 mL). The combined organic layers were washed with brine (40 mL), dried over sodium sulfate and the solvent was removed *in vacuo*. The crude product was purified by flash column chromatography (*iso*-hexanes/ethyl acetate; 0→25% EtOAc) affording **CHalo-Boc** (2.45 g, 7.19 mmol, 51%) as an off-white solid. The starting material **4** was partially recovered (0.92 g, 3.5 mmol, 25%).

Note: Although the reaction did not proceed to full conversion, longer reaction times and more equivalents of 1-bromo-3-chloropropane were avoided due to increasing double alkylation.

TLC *Rf* = 0.43 (*np*, Hex:EtOAc 3:1); Rf of **4** = 0.15
^{1}H-NMR (600 MHz, $CDCl_3$): *δ* (ppm) = 6.99 (d, J = 8.4 Hz, 2H), 6.56 (d, J = 8.4 Hz, 2H), 4.52 (s, 1H), 3.65 (t, J = 6.3 Hz, 2H), 3.31 (t, J = 6.6 Hz, 2H), 3.12 (q, J = 6.7 Hz, 2H), 2.51 (t, J = 7.4 Hz, 2H), 2.06 (p, J = 6.5 Hz, 2H), 1.63 – 1.53 (m, 2H), 1.53 – 1.46 (m, 2H), 1.44 (s, 9H).
^{13}C-NMR (151 MHz, $CDCl_3$): *δ* (ppm) = 156.1, 146.0, 131.4, 129.3, 113.0, 79.1, 42.8, 41.3, 40.6, 34.6, 32.1, 29.7, 29.0, 28.5.
HRMS (ESI+): m/z calc. for $C_{18}H_{29}ClN_2NaO_2^+$ [M+Na]$^+$: 363.1810, found: 363.1812.

Cou-CHalo-Boc

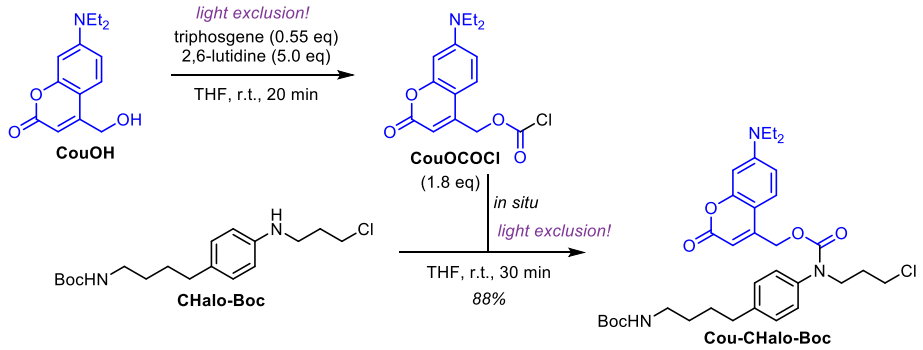

Note: the reaction must be performed under light exclusion.

According to General Procedure C: **CouOH** (71 mg, 0.29 mmol, 1.0 eq) was dissolved in anhydrous THF. Triphosgene (47 mg, 0.16 mmol, 0.55 eq) was added, then 2,6-lutidine (0.17 mL, 1.4 mmol, 5.0 eq) was added dropwise and the reaction mixture was stirred at room temperature for 20 min to give **CouOCOCl**.

In a separate flask, **CHalo-Boc** (54 mg, 0.16 mmol, 1.0 eq) was dissolved in anhydrous THF and the reaction mixture of the **CouOCOCl** (1.8 eq) was added dropwise. The mixture was stirred at room temperature for 30 min. *N*-Methylpiperazine (53 µL, 0.48 mmol, 3.0 eq) was added to react with the excess **CouOCOCl** and the mixture was stirred for 10 min. The volatiles were removed *in vacuo* and the residue was diluted with water (15 mL), brine (10 mL) and ethyl acetate (15 mL). The layers were separated and the aqueous layer was extracted with ethyl acetate (2 × 15 mL). The combined organic layers were washed with brine (20 mL), dried over sodium sulfate and the solvent was removed *in vacuo*. The crude product was purified by flash column chromatography (*iso*-hexanes/ethyl acetate; 5→25% EtOAc) affording **Cou-CHalo-Boc** (86 mg, 0.14 mmol, 88%) as a yellow solid.

TLC *Rf* = 0.27 (*np*, Hex:EtOAc 2:1); Rf of **CHalo-Boc** = 0.66
^{1}H-NMR (600 MHz, $CDCl_3$): *δ* (ppm) = 7.21 (d, J = 8.1 Hz, 3H), 7.13 (d, J = 6.9 Hz, 2H), 6.59 (s, 1H), 6.52 (s, 1H), 5.69 (s, 1H), 5.22 (s, 2H), 4.73 (s, 1H), 3.85 (s, 2H), 3.56 (t, J = 6.3 Hz, 2H), 3.40 (q, J = 7.0 Hz, 4H), 3.15 (d, J = 6.3 Hz, 2H), 2.66 (t, J = 7.4 Hz, 2H), 2.07 (p, J = 6.6 Hz, 2H), 1.67 (p, J = 7.7 Hz, 2H), 1.55 – 1.47 (m, 2H), 1.43 (s, 9H), 1.20 (t, J = 7.1 Hz, 6H).
^{13}C-NMR (151 MHz, $CDCl_3$): *δ* (ppm) = 161.9, 156.2, 154.9, 150.2, 142.0, 138.6, 129.6, 127.4, 124.4, 109.2, 98.4, 79.1, 62.6, 48.6, 45.2, 42.2, 40.6, 35.2, 31.3, 29.8, 29.2, 28.6, 12.5.
HRMS (ESI+): m/z calc. for $C_{33}H_{44}ClN_3NaO_6^+$ [M+Na]$^+$: 636.2811, found: 636.2793

10.2.3 Fluorogenic CHalo-SiR conjugates

SiR-COOH

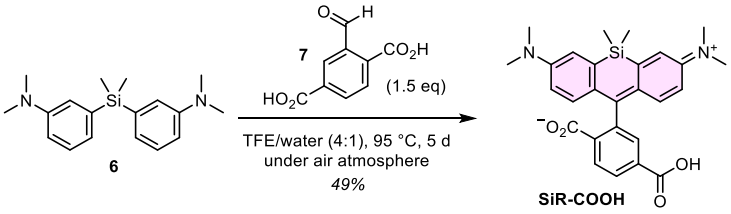

6 (previously described[83]) was reacted with **7** (previously described[84]) adapting known procedures for xanthene synthesis.[84,85]

6 (0.17 g, 0.58 mmol, 1.0 eq) was dissolved in trifluoroethanol/water (4:1, 4 mL), **7** (0.17 g, 0.88 mmol, 1.5 eq) was added and the reaction was heated to 95 °C in a pressure tube for 5 d. The volatiles were removed under reduced pressure and the crude product was purified by *rp*-flash column chromatography (acetonitrile/water; 25→60% MeCN) to give **SiR-COOH** (0.13 g, 0.28 mmol, 49%) as a blue solid. Analytical data matched literature values.[10]

CA-SiR was synthesised according to a previously described procedure (Lukinavičius *et al*.[10], compound SiR-Halo).

CHalo-SiR

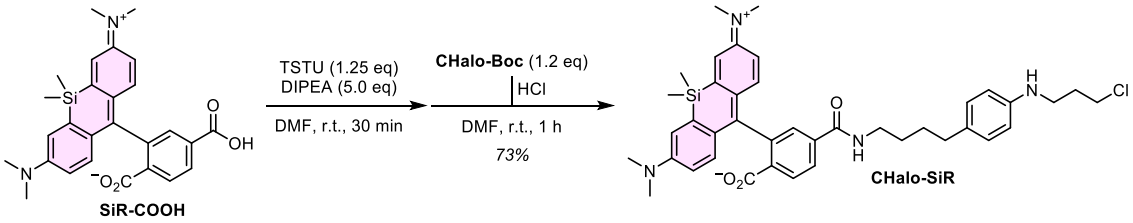

CHalo-Boc (13 mg, 38 µmol, 1.2 eq) was coupled with **SiR-COOH** following General Procedure E. Purification by *rp*-flash column chromatography (acetonitrile/water; 20→70% MeCN) affording **CHalo-SiR** (16 mg, 23 µmol, 73%) as a light-blue solid.

^{1}H-NMR (600 MHz, $CDCl_3$): δ (ppm) = 7.97 (dd, J = 8.0, 0.8 Hz, 1H), 7.88 (dd, J = 8.0, 1.4 Hz, 1H), 7.61 (dd, J = 1.4, 0.8 Hz, 1H), 6.98 – 6.94 (m, 4H), 6.76 (d, J = 8.9 Hz, 2H), 6.56 (dd, J = 9.0, 2.9 Hz, 2H), 6.52 (d, J = 8.5 Hz, 2H), 6.10 (t, J = 5.8 Hz, 1H), 3.64 (t, J = 6.3 Hz, 2H), 3.43 – 3.36 (m, 2H), 3.29 (t, J = 6.6 Hz, 2H), 2.97 (s, 12H), 2.52 (t, J = 7.1 Hz, 2H), 2.04 (p, J = 6.5 Hz, 2H), 1.66 – 1.54 (m, 4H), 0.67 (s, 3H), 0.59 (s, 3H).
^{13}C-NMR (151 MHz, $CDCl_3$): δ (ppm) = 170.1, 166.3, 155.4, 149.5, 146.2, 140.1, 136.9, 131.2, 131.0, 129.3, 129.2, 128.3, 127.7, 126.0, 122.9, 116.6, 113.6, 113.0, 92.1, 42.8, 41.2, 40.4, 40.3, 34.6, 32.1, 29.1, 29.0, 0.5, -1.1.
HRMS (ESI+): m/z calc. for $C_{40}H_{48}ClN_4O_3Si^+$ $[M]^+$: 695.3179, found: 695.3162

Synthetic route for Bn-CHalo-SiR

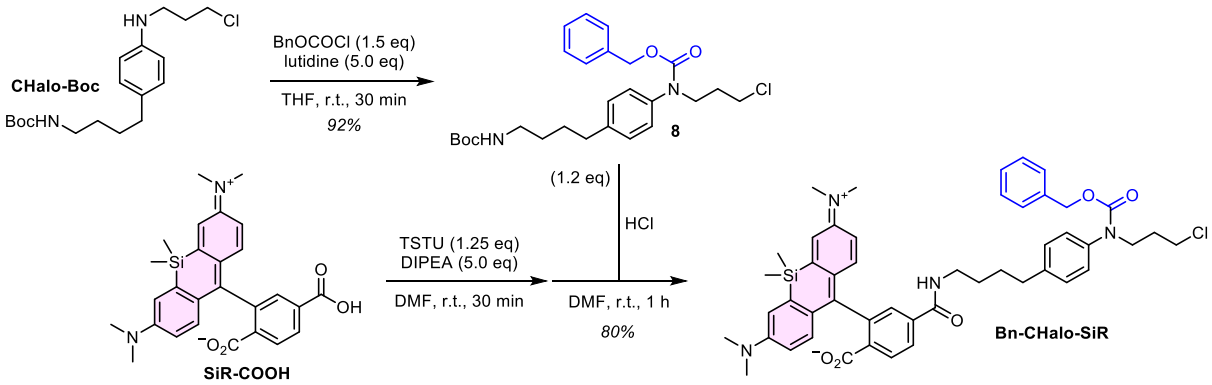

Compound 8

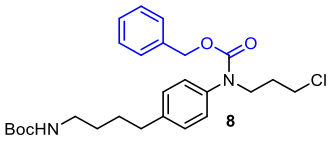

Adaptation from previously described procedure.[82] Under nitrogen atmosphere, **CHalo-Boc** (50 mg, 0.15 mmol, 1.0 eq) was dissolved in anhydrous THF (3 mL). 2,6-Lutidine (85 µL, 0.73 mmol, 5.0 eq) and benzyl chloroformate (32 µL, 0.22 mmol, 1.5 eq) were added and the reaction mixture was stirred at room temperature for 30 min. The solvent was removed under reduced pressure, water (20 mL) was added and the mixture was extracted with ethyl acetate (3 × 15 mL). The organic layer was dried over sodium sulfate, the desiccant was filtered off and the solvent was removed *in vacuo*. The crude product was purified by *np*-flash column chromatography (*iso*-hexanes/ethyl acetate; 0→40% EtOAc) to give **8** (64 mg, 0.14 mmol, 92%) as a colourless solid.

TLC *Rf* = 0.33 (n*p*, Hex:EtOAc 3:1); Rf of **CHalo-Boc** = 0.43
^{1}H-NMR (400 MHz, $CDCl_3$): *δ* (ppm) = 7.35 – 7.21 (m, 5H), 7.16 (d, *J* = 8.3 Hz, 2H), 7.09 (d, *J* = 7.7 Hz, 2H), 5.14 (s, 2H), 4.50 (s, 1H), 3.85 – 3.78 (m, 2H), 3.53 (t, *J* = 6.5 Hz, 2H), 3.18 – 3.10 (m, 2H), 2.62 (t, *J* = 7.6 Hz, 2H), 2.04 (p, *J* = 6.6 Hz, 2H), 1.69 – 1.63 (m, 2H), 1.56 – 1.48 (m, 2H), 1.44 (s, 9H).
^{13}C-NMR (101 MHz, $CDCl_3$): *δ* (ppm) = 156.1, 155.7, 141.1, 139.4, 136.7, 129.2, 128.5, 128.0, 127.4, 127.1, 79.3, 67.3, 48.3, 42.4, 40.5, 35.2, 31.5, 29.8, 28.6.
HRMS (ESI+): m/z calc. for $C_{26}H_{35}ClN_2NaO_4^+$ $[M+Na]^+$: 497.2178, found: 497.2161

Bn-CHalo-SiR

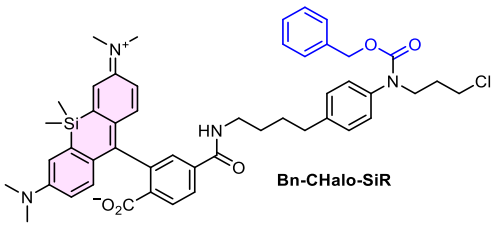

8 (18 mg, 38 µmol, 1.2 eq) was coupled with **SiR-COOH** following General Procedure E. Purification by *rp*-flash column chromatography (acetonitrile/water; 25→85% MeCN) affording **Bn-CHalo-SiR** (16 mg, 23 µmol, 73%) as a light-blue solid.

^{1}H-NMR (600 MHz, $CDCl_3$): *δ* (ppm) = 7.96 (dd, J = 8.0, 0.7 Hz, 1H), 7.89 (dd, J = 8.0, 1.4 Hz, 1H), 7.62 (s, 1H), 7.36 – 7.19 (m, 5H), 7.12 (d, J = 8.0 Hz, 2H), 7.06 (d, J = 8.0 Hz, 2H), 6.96 (d, J = 2.9 Hz, 2H), 6.76 (d, J = 9.0 Hz, 2H), 6.55 (dd, J = 9.0, 2.9 Hz, 2H), 6.28 (s, 1H), 5.12 (s, 2H), 3.82 – 3.77 (m, 2H), 3.51 (t, J = 6.5 Hz, 2H), 3.39 (q, J = 6.8 Hz, 2H), 2.96 (s, 12H), 2.61 (t, J = 7.4 Hz, 2H), 2.02 (p, J = 6.7 Hz, 2H), 1.65 (p, J = 7.9 Hz, 2H), 1.58 (q, J = 7.2 Hz, 2H), 0.66 (s, 3H), 0.59 (s, 3H).
^{13}C-NMR (151 MHz, $CDCl_3$): *δ* (ppm) = 170.1, 166.3, 155.6, 155.4, 149.5, 140.8, 140.0, 139.5, 136.8, 136.7, 131.2, 129.2, 129.1, 128.5, 128.3, 128.0, 127.7, 127.1, 126.0, 123.0, 116.6, 113.6, 92.1, 67.3, 48.3, 42.3, 40.3, 40.2, 35.1, 31.5, 29.2, 28.6, 0.4, -1.1.
HRMS (ESI+): m/z calc. for $C_{48}H_{54}ClN_4O_5Si^+$ $[M+H]^+$: 829.3547, found: 829.3532

Cou-CHalo-SiR

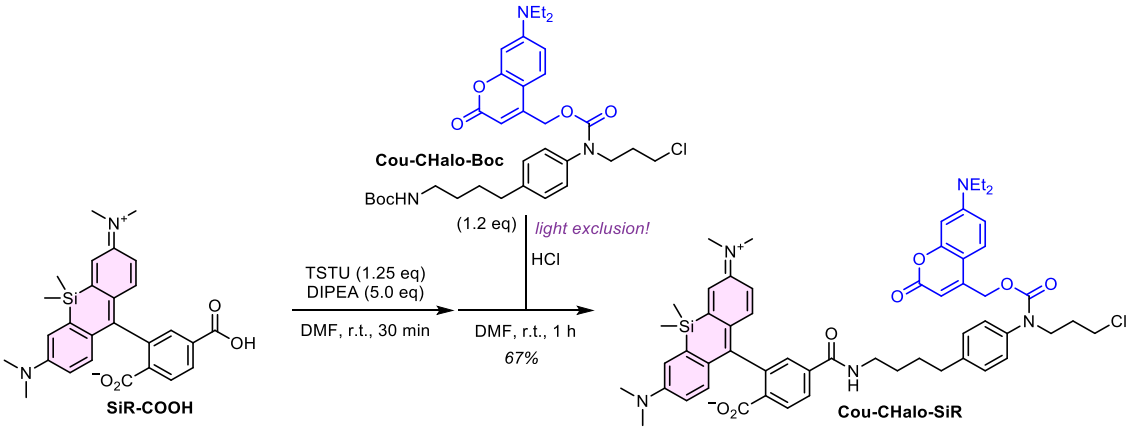

Note: the reaction must be performed under light exclusion.

Cou-CHalo-Boc (32 mg, 52 µmol, 1.2 eq) was coupled with **SiR-COOH** following General Procedure E. Purification by *rp*-flash column chromatography (acetonitrile/water; 30→90% MeCN) followed by *np*-flash column chromatography (DCM/MeOH; 0→3% MeOH) affording **Cou-CHalo-SiR** (28 mg, 29 µmol, 67%) as a yellow solid.

TLC *Rf* = 0.44 (*np*, DCM:MeOH 19:1)
^{1}H-NMR (400 MHz, DMSO-d_6): *δ* (ppm) = 8.73 (t, J = 5.5 Hz, 1H), 8.06 (d, J = 8.8 Hz, 1H), 8.01 (d, J = 8.0 Hz, 1H), 7.64 (s, 1H), 7.42 – 7.34 (m, 1H), 7.26 – 7.17 (m, 5H), 7.01 (d, J = 1.7 Hz, 2H), 6.66 – 6.60 (m, 5H), 6.50 (s, 1H), 5.24 (s, 2H), 3.78 – 3.73 (m, 2H), 3.63 (t, J = 6.4 Hz, 2H), 3.41 (q, J = 6.9 Hz, 4H), 3.27 – 3.21 (m, 2H), 2.90 (s, 12H), 2.62 – 2.55 (m, 2H), 1.90 (p, J = 6.6 Hz, 2H), 1.63 – 1.45 (m, 4H), 1.10 (t, J = 7.0 Hz, 6H), 0.63 (s, 3H), 0.51 (s, 3H).
^{13}C-NMR (151 MHz, $CDCl_3$): *δ* (ppm) = 170.1, 166.4, 162.3, 156.0, 154.8, 154.3, 150.8, 150.4, 149.4, 141.9, 140.2, 138.6, 137.2, 131.7, 129.7, 129.1, 128.2, 127.8, 127.6, 125.7, 124.3, 123.9, 116.8, 113.3, 108.9, 105.6, 104.5, 97.7, 92.4, 62.4, 48.2, 44.8, 42.2, 40.3, 35.1, 31.2, 28.7, 12.5, 0.6, -1.5.
HRMS (ESI+): m/z calc. for $C_{55}H_{63}ClN_5O_7Si^+$ $[M+H]^+$: 968.4180, found: 968.4176

Synthetic route for Leu-CHalo-SiR

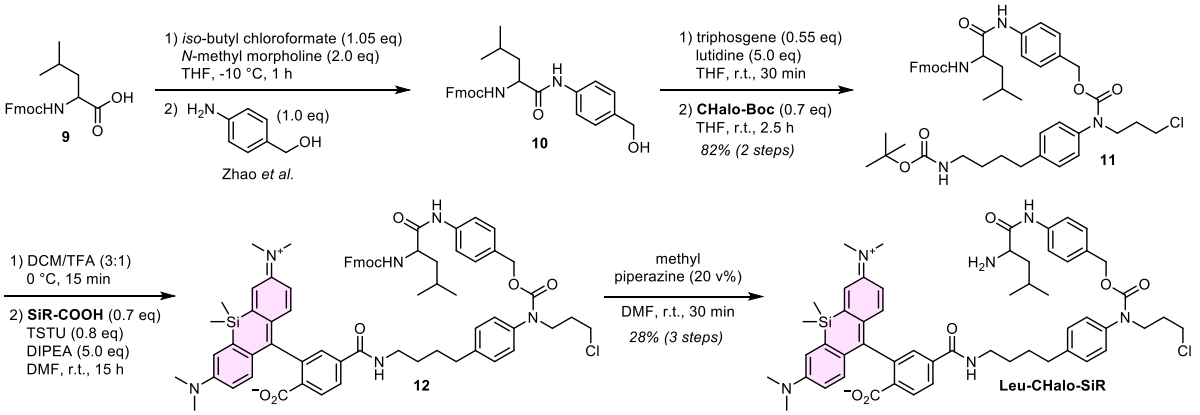

Compound **10** was prepared according to a previously described procedure (Zhao *et al*.[86], compound 3).

Compound 11

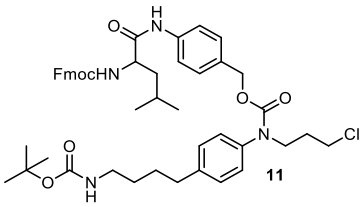

Adaptation from previously described procedure.[82] Under nitrogen atmosphere, **10** (10 mg, 22 µmol, 1.0 eq) was dissolved in anhydrous THF (1 mL). Triphosgene (0.6 eq) and 2,6-lutidine (5.0 eq) were added and the reaction mixture was stirred at room temperature for 15 min. In a separate flask, **CHalo-Boc** (2 mg, 6 µmol, 0.7 eq) was dissolved in anhydrous THF (0.5 mL) under nitrogen atmosphere, the **10**-chloroformate was added. dropwise and the reaction mixture was stirred at room temperature for 20 min. Methyl piperazine (2 µL, 18 µmol, 3.0 eq) was added to react with the excess of the chloroformate. The mixture was diluted with water (10 mL) and extracted with ethyl acetate (3 × 10 mL). The organic layer was dried over sodium sulfate, the desiccant was filtered off and the solvent was removed *in vacuo*. The crude product was purified by *rp*-flash column chromatography (acetonitrile/water; 20→100% MeCN) to give **11** (4 mg, 5 µmol, 82% over 2 steps) as a colourless solid.

TLC *Rf* = 0.69 (*np*, Hex:EtOAc 1:1)
^{1}H-NMR (600 MHz, $CDCl_3$): *δ* (ppm) = 8.14 (s, 1H), 7.76 (d, J = 7.4 Hz, 2H), 7.57 (t, J = 7.0 Hz, 2H), 7.43 (s, 2H), 7.38 (t, J = 7.3 Hz, 2H), 7.29 – 7.27 (m, 2H), 7.14 (d, J = 8.2 Hz, 2H), 7.08 (d, J = 8.3 Hz, 4H), 5.30 (s, 1H), 5.05 (s, 2H), 4.57 (s, 1H), 4.48 – 4.38 (m, 2H), 4.29 (s, 1H), 4.20 (t, J = 6.7 Hz, 1H), 3.80 (t, J = 6.9 Hz, 2H), 3.53 (s, 2H), 3.13 (s, 2H), 2.62 (t, J = 7.5 Hz, 2H), 2.06 – 1.99 (m, 2H), 1.70 (s, 1H), 1.66 – 1.58 (m, 4H), 1.55 – 1.46 (m, 2H), 1.43 (s, 9H), 1.01 – 0.91 (m, 6H).
^{13}C-NMR (151 MHz, $CDCl_3$): *δ* (ppm) = 155.6, 143.8, 141.4, 139.3, 132.7, 129.2, 127.9, 127.2, 127.2, 125.1, 120.2, 119.9, 67.2, 54.4, 48.1, 47.3, 42.4, 40.8, 40.5, 35.2, 31.5, 29.9, 29.8, 28.7, 28.6, 24.9, 23.1, 22.1.
HRMS (ESI+): m/z calc. for $C_{47}H_{57}ClN_4NaO_7^+$ $[M+Na]^+$: 847.3808, found: 847.3806.

Leu-CHalo-SiR

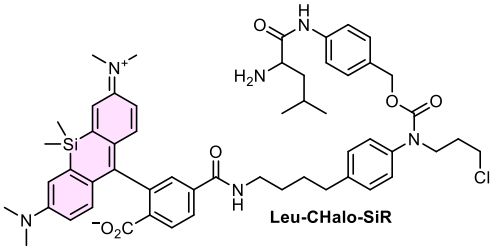

11 (2 mg, 2 µmol, 1.3 eq) was Boc-deprotected in DCM / trifluoroacetic acid (3:1, 1.33 mL) at 0 °C for 15 min. The trifluoroacetic acid was quenched by slowly adding aqueous sodium carbonate solution until no gas development was observed upon addition. The intermediate was coupled with the NHS ester of **SiR-COOH** (1.0 eq) following General Procedure E to give **12** which was Fmoc-deprotected by adding methyl piperazine (20 vol%) to the coupling reaction mixture in DMF which was stirred at room temperature for 30 min. The crude product was purified by preparative HPLC (acetonitrile/water, 0.1% formic acid; 15→70% MeCN, 20 min) affording **Leu-CHalo-SiR** (0.37 mg, 0.39 µmol, 28% over 3 steps) as a light-blue solid.

Note regarding the Boc-deprotection: 2M HCl in DCM/dioxane (1:1) decomposed the carbamate to the undesired benzyl chloride; DCM/TFA (1:1) at r.t. gave the benzylic TFA-adduct.

Note regarding the Fmoc-deprotection: methyl piperazine was used instead of the standard protocol with piperidine for easier separation of the fluorenyl deprotection side product.

^{1}H-NMR (600 MHz, DMSO-d_6): δ (ppm) = 8.74 (d, J = 5.7 Hz, 1H), 8.43 (s, 4H), 8.06 (dd, J = 8.1, 1.3 Hz, 1H), 8.01 (d, J = 8.1 Hz, 1H), 7.64 (s, 1H), 7.58 (d, J = 7.4 Hz, 1H), 7.17 (d, J = 8.5 Hz, 2H), 7.13 (d, J = 8.5 Hz, 2H), 7.01 (d, J = 2.6 Hz, 2H), 6.66 – 6.60 (m, 4H), 4.99 (s, 2H), 3.74 – 3.68 (m, 2H), 3.60 (t, J = 6.4 Hz, 2H), 2.91 (s, 12H), 2.68 (t, J = 4.8 Hz, 3H), 2.58 – 2.53 (m, 4H), 2.53 – 2.51 (m, 4H), 1.91 – 1.83 (m, 2H), 1.59 – 1.52 (m, 2H), 1.50 (d, J = 6.8 Hz, 2H), 0.89 (d, J = 6.6 Hz, 3H), 0.87 (d, J = 6.6 Hz, 3H), 0.63 (s, 3H), 0.52 (s, 3H).
HRMS (ESI+): m/z calc. for $C_{55}H_{63}ClN_5O_7Si^+$ $[M+H]^+$: 968.4180, found: 968.4176

Synthetic route for SS66T-CHalo-SiR (GSH activation)

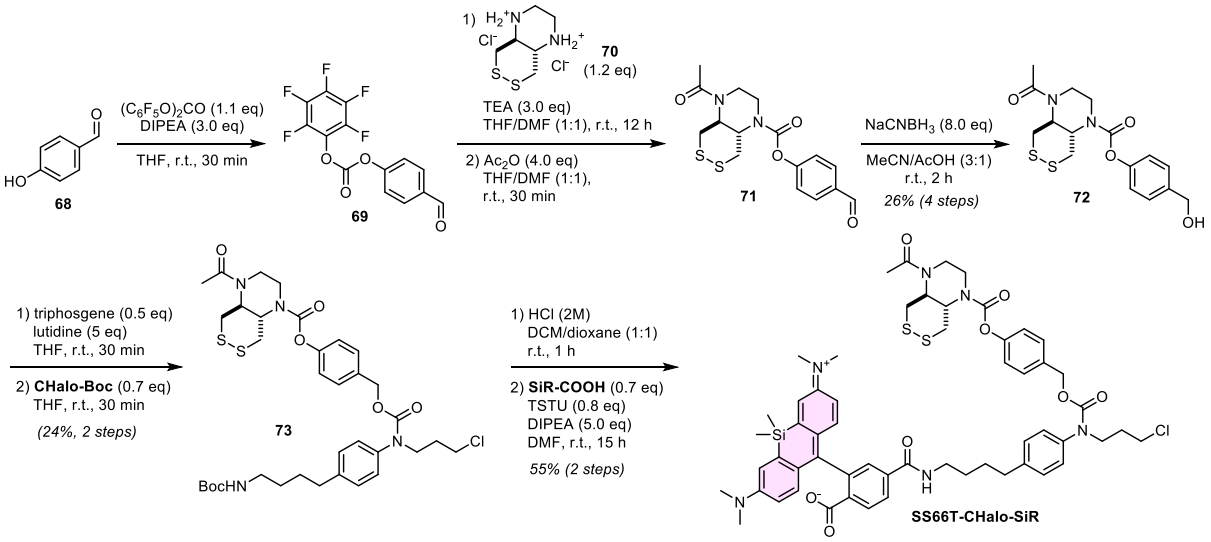

Compound 72

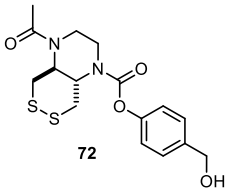

4-Hydroxybenzaldehyde (**68**, 37 mg, 0.30 mmol, 1.0 eq) was dissolved in anhydrous THF (1.1 mL). DIPEA (0.15 mL, 0.90 mmol, 3.0 eq) and bis(pentafluorophenyl)carbonate (201 mg, 0.51 mmol, 1.7 eq) were added and the reaction mixture was stirred at room temperature for 30 min. Diamine **70** (90 mg, 0.36 mmol, 1.2 eq), DIPEA (0.15 mL, 0.90 mmol, 3.0 eq) and anhydrous DMF (1.1 mL) were added and the mixture stirred at

room temperature for 12 h. Then, acetic anhydride (0.11 mL, 1.2 mmol, 4.0 eq) was added, the mixture was stirred at room temperature for 30 min and the excess of the acetic anhydride was removed upon addition of *N*-methyl piperazine (0.20 mL, 1.8 mmol, 6.0 eq). The volatiles were removed *in vacuo* and the crude product was semi-purified by *rp*- flash column chromatography (acetonitrile/water; 5→50% MeCN). **71** was dissolved in acetonitrile (1.5 mL) and acetic acid (0.5 mL), sodium cyanoborohydride (75 mg, 1.2 mmol, 4.0 eq) was added and the reaction mixture was stirred at room temperature for 2 h. DCM (10 mL) and a half-saturated solution of sodium bicarbonate (15 mL) were added, the layers were separated and the aqueous layer was extracted with DCM (2 ×10 mL). The organic layer was dried over sodium sulfate, the desiccant was filtered off and the solvent was removed *in vacuo*. The crude product was purified by *rp*-flash column chromatography (acetonitrile/water; 5→35% MeCN) to give **72** (29 mg, 79 µmol, 26% over 4 steps) as a colourless oil.

TLC *Rf* = 0.37 (*np*, DCM:MeOH 19:1)
^{1}H-NMR (400 MHz, $CDCl_3$): *δ* (ppm) = 7.35 (d, *J* = 8.5 Hz, 2H), 7.05 (d, *J* = 8.0 Hz, 2H), 4.66 (d, *J* = 2.7 Hz, 2H), 4.29 (s, 1H), 4.16 – 3.81 (m, 2H), 3.80 – 3.41 (m, 4H), 3.30 (dd, *J* = 13.6, 2.6 Hz, 1H), 3.24 – 2.84 (m, 1H), 2.11 (s, 3H), 2.02 (s, 1H).
HRMS (ESI+): m/z calc. for $C_{16}H_{20}N_2NaO_4S_2^+$ [M+Na]$^+$: 391.0757, found: 391.0749.

Compound 73

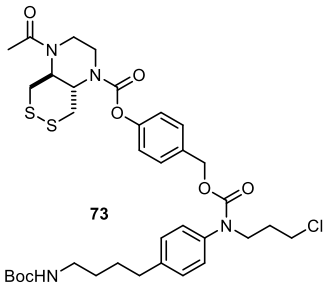

Under nitrogen atmosphere, **72** (5.0 mg, 14 µmol, 1.2 eq) was dissolved in anhydrous THF (0.25 mL). Triphosgene (2.8 mg, 9.5 µmol, 0.8 eq) was added from a fresh stock solution, then 2,6-lutidine (7.9 µL, 68 µmol, 6.0 eq) was added and the reaction mixture was stirred at room temperature for 20 min to form the chloroformate (HPLC-MS analysis of the reaction progress by quenching with piperidine in acetonitrile).

In a separate flask, **CHalo-Boc** (3.9 mg, 11 µmol, 1.0 eq) was dissolved in anhydrous THF (0.3 mL) under nitrogen atmosphere, added to the chloroformate and the reaction mixture was stirred at room temperature for 30 min. The mixture was diluted with DCM (10 mL) and water (15 mL), the layers were separated and the aqueous layer was extracted with DCM (2 ×10 mL). The organic layer was dried over sodium sulfate, the desiccant was filtered off and the solvent was removed *in vacuo*. The crude product was purified by *rp*-flash column chromatography (acetonitrile/water; 20→100% MeCN) to give **73** (2 mg, 3 µmol, 24% over 2 steps) as a colourless solid.

TLC *Rf* = 0.74 (*np*, DCM/MeOH 47:3)
^{1}H-NMR (400 MHz, $CDCl_3$): *δ* (ppm) = 7.23 (d, *J* = 8.3 Hz, 2H), 7.16 (d, *J* = 8.4 Hz, 2H), 7.07 (d, *J* = 7.8 Hz, 2H), 7.04 – 6.98 (m, 2H), 5.10 (s, 2H), 4.71 – 4.17 (m, 2H), 3.98 (d, *J* = 48.0 Hz, 1H), 3.84 – 3.76 (m, 2H), 3.67 (s, 3H), 3.53 (t, *J* = 6.5 Hz, 2H), 3.34 – 2.88 (m, 5H), 2.63 (t, *J* = 7.6 Hz, 2H), 2.12 (s, 3H), 2.08 – 1.98 (m, 2H), 1.70 – 1.57 (m, 4H), 1.57 – 1.47 (m, 2H), 1.44 (s, 9H).
HRMS (ESI+): m/z calc. for $C_{35}H_{47}ClN_4NaO_7S_2^+$ [M+Na]$^+$: 757.2467, found: 757.2438.

SS66T-CHalo-SiR

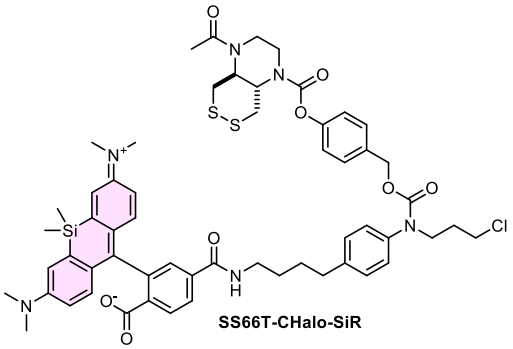

73 (2 mg, 3 µmol, 1.7 eq) was coupled with **SiR-COOH** following General Procedure E. Purification by reparative HPLC (acetonitrile/water, 0.1% formic acid; 20→80% MeCN, 20 min) affording **SS66T-CHalo-SiR** (0.99 mg, 0.91 µmol, 57%) as a light-blue solid.

HRMS (ESI+): m/z calc. for $C_{57}H_{66}ClN_6O_8S_2Si^+$ [M+H]$^+$: 1089.384, found: 1089.382.

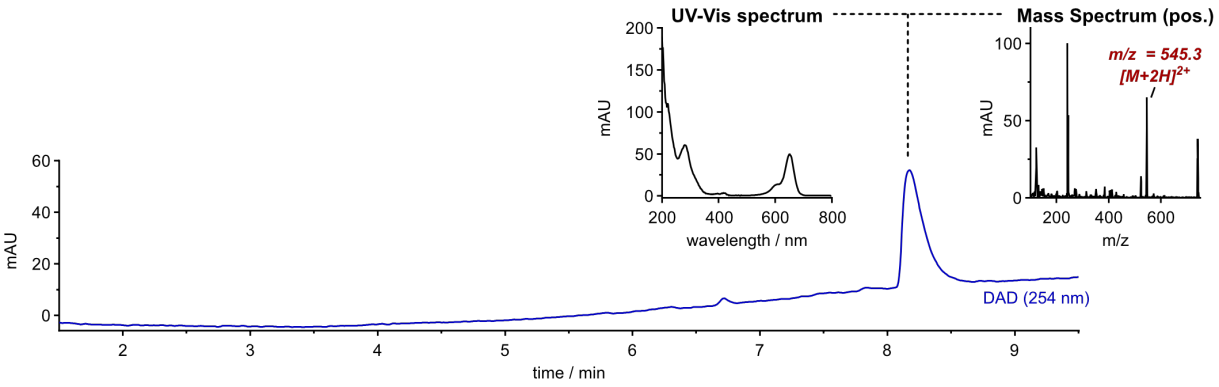

Synthetic route for SS66C-CHalo-SiR (thioredoxin (Trx) activation)

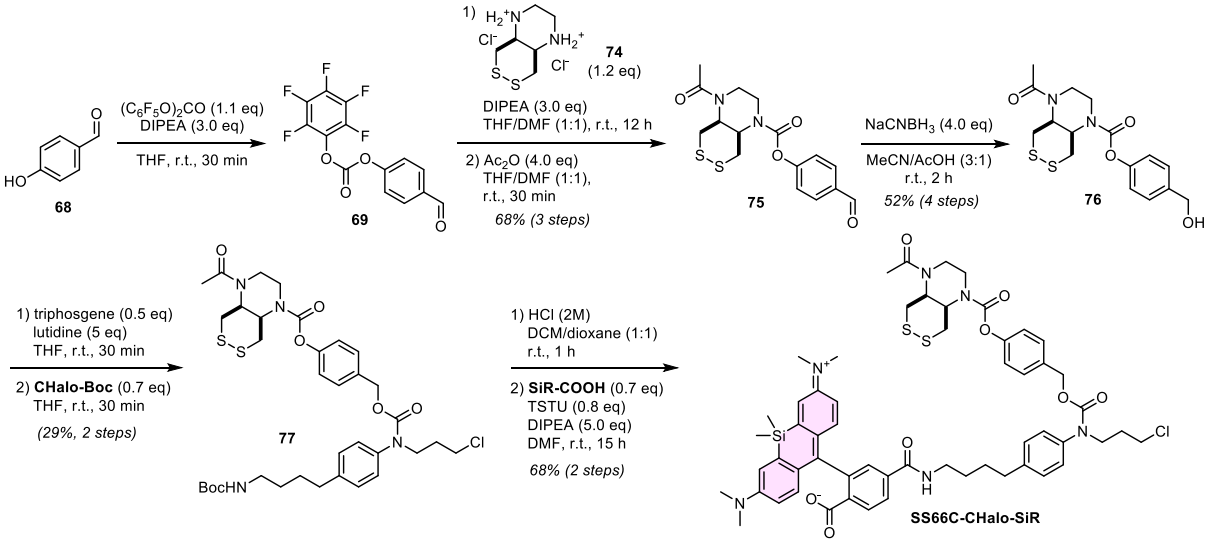

Compound 76

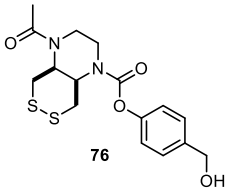

4-Hydroxybenzaldehyde (**68**, 12 mg, 0.10 mmol, 1.0 eq) was dissolved in anhydrous THF (0.4 mL). DIPEA (0.05 mL, 0.30 mmol, 3.0 eq) and bis(pentafluorophenyl)carbonate (67 mg, 0.17 mmol, 1.7 eq) were added and the reaction mixture was stirred at room temperature for 30 min. Diamine **74** (30 mg, 0.12 mmol, 1.2 eq), DIPEA (0.05 mL, 0.30 mmol, 3.0 eq) and anhydrous DMF (0.4 mL) were added and the mixture stirred at room temperature for 12 h. Then, acetic anhydride (38 µL, 0.40 mmol, 4.0 eq) was added, the mixture was stirred at room temperature for 30 min and the excess of the acetic anhydride was removed upon addition of *N*-methyl piperazine (67 µL, 0.60 mmol, 6.0 eq). The volatiles were removed *in vacuo* and the crude product was semi-purified by *rp*- flash column chromatography (acetonitrile/water; 5→50% MeCN). **75** was dissolved in acetonitrile (1.5 mL) and acetic acid (0.5 mL), sodium cyanoborohydride (25 mg, 0.40 mmol, 4.0 eq) was added and the reaction mixture was stirred at room temperature for 2 h. DCM (10 mL) and a half-saturated solution of sodium bicarbonate (15 mL) were added, the layers were separated and the aqueous layer was extracted with DCM (2 ×10 mL). The organic layer was dried over sodium sulfate, the desiccant was filtered off and the solvent was removed *in vacuo*. The crude product was purified by *rp*-flash column chromatography (acetonitrile/water; 5→35% MeCN) to give **72** (19 mg, 52 µmol, 52% over 4 steps) as a colourless oil.

TLC *Rf* = 0.37 (*np*, DCM:MeOH 19:1)
^{1}H-NMR (400 MHz, $CDCl_3$): *δ* (ppm) = 7.38 (d, *J* = 8.5 Hz, 2H), 7.10 (d, *J* = 8.6 Hz, 2H), 4.69 (s, 2H), 4.40 (td, *J* = 6.1, 3.4 Hz, 1H), 4.23 (s, 1H), 3.90 – 3.80 (m, 2H), 3.79 – 3.65 (m, 2H), 3.50 (dd, *J* = 14.0, 9.0 Hz, 1H), 3.16 (dd, *J* = 14.4, 3.4 Hz, 1H), 2.97 (dd, *J* = 13.5, 4.1 Hz, 1H), 2.15 (s, 3H), 1.83 (d, *J* = 11.5 Hz, 1H).
^{13}C-NMR (151 MHz, $CDCl_3$): *δ* (ppm) = 170.3, 154.0, 150.2, 138.5, 128.1, 121.7, 64.7, 51.3, 43.3, 42.0, 38.6, 36.2, 21.9; *one expected carbon peak not observed.*
HRMS (ESI+): m/z calc. for $C_{16}H_{20}N_2NaO_4S_2^+$ [M+Na]$^+$: 391.0757, found: 391.0746.

Compound 77

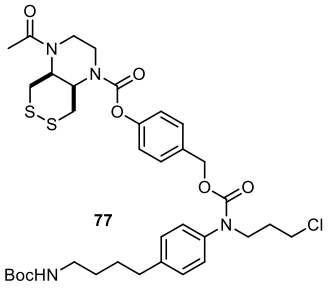

Under nitrogen atmosphere, **76** (6.3 mg, 17 µmol, 1.2 eq) was dissolved in anhydrous THF (0.25 mL). Triphosgene (3.6 mg, 12 µmol, 0.8 eq) was added from a fresh stock solution, then 2,6-lutidine (10 µL, 86 µmol, 6.0 eq) was added and the reaction mixture was stirred at room temperature for 20 min to form the chloroformate (HPLC-MS analysis of the reaction progress by quenching with piperidine in acetonitrile).

In a separate flask, **CHalo-Boc** (4.9 mg, 14 µmol, 1.0 eq) was dissolved in anhydrous THF (0.3 mL) under nitrogen atmosphere, added to the chloroformate and the reaction mixture was stirred at room temperature for 30 min. The mixture was diluted with DCM (10 mL) and water (15 mL), the layers were separated and the aqueous layer was extracted with DCM (2 ×10 mL). The organic layer was dried over sodium sulfate, the desiccant was filtered off and the solvent was removed *in vacuo*. The crude product was purified by *rp*-flash column chromatography (acetonitrile/water; 20→100% MeCN) to give **77** (3 mg, 4 µmol, 29% over 2 steps) as a colourless solid.

TLC *Rf* = 0.74 (*np*, DCM/MeOH 47:3)
^{1}H-NMR (400 MHz, $CDCl_3$): *δ* (ppm) = 7.23 (d, *J* = 8.4 Hz, 2H), 7.15 (d, *J* = 8.3 Hz, 2H), 7.07 (t, *J* = 7.3 Hz, 4H), 5.11 (s, 2H), 4.40 (td, *J* = 6.1, 3.3 Hz, 1H), 4.28 – 4.17 (m, 1H), 3.90 – 3.63 (m, 6H), 3.60 – 3.45 (m, 3H), 3.19 – 3.07 (m, 3H), 3.03 – 2.93 (m, 1H), 2.66 – 2.59 (m, 2H), 2.15 (s, 3H), 2.07 – 1.98 (m, 2H), 1.72 – 1.57 (m, 4H), 1.57 – 1.47 (m, 2H), 1.44 (s, 9H).
HRMS (ESI+): m/z calc. for $C_{35}H_{47}ClN_4NaO_7S_2^+$ [M+Na]$^+$: 757.2467, found: 757.2452.

SS66C-CHalo-SiR

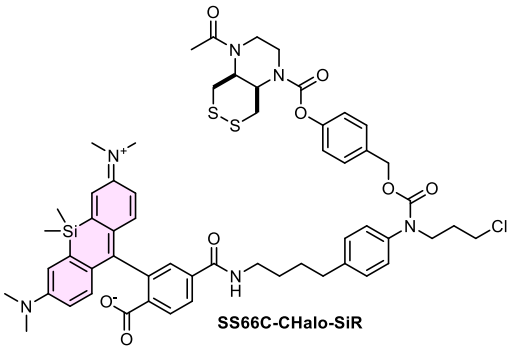

77 (3 mg, 4 µmol, 2.6 eq) was coupled with **SiR-COOH** following General Procedure E. Purification by reparative HPLC (acetonitrile/water, 0.1% formic acid; 20→80% MeCN, 20 min) affording **SS66T-CHalo-SiR** (1.2 mg, 1.1 µmol, 68%) as a light-blue solid.

HRMS (ESI+): m/z calc. for $C_{57}H_{66}ClN_6O_8S_2Si^+$ [M+H]$^+$: 1089.384, found: 1089.382.

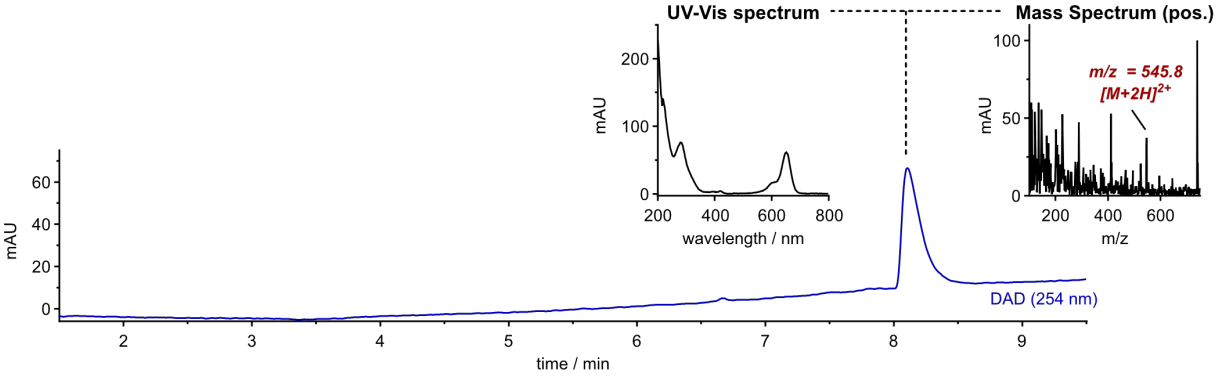

10.2.4 Light-controlled protein heterodimeriser Cou-CHalo-BG

Synthetic route for Cou-CHalo-BG

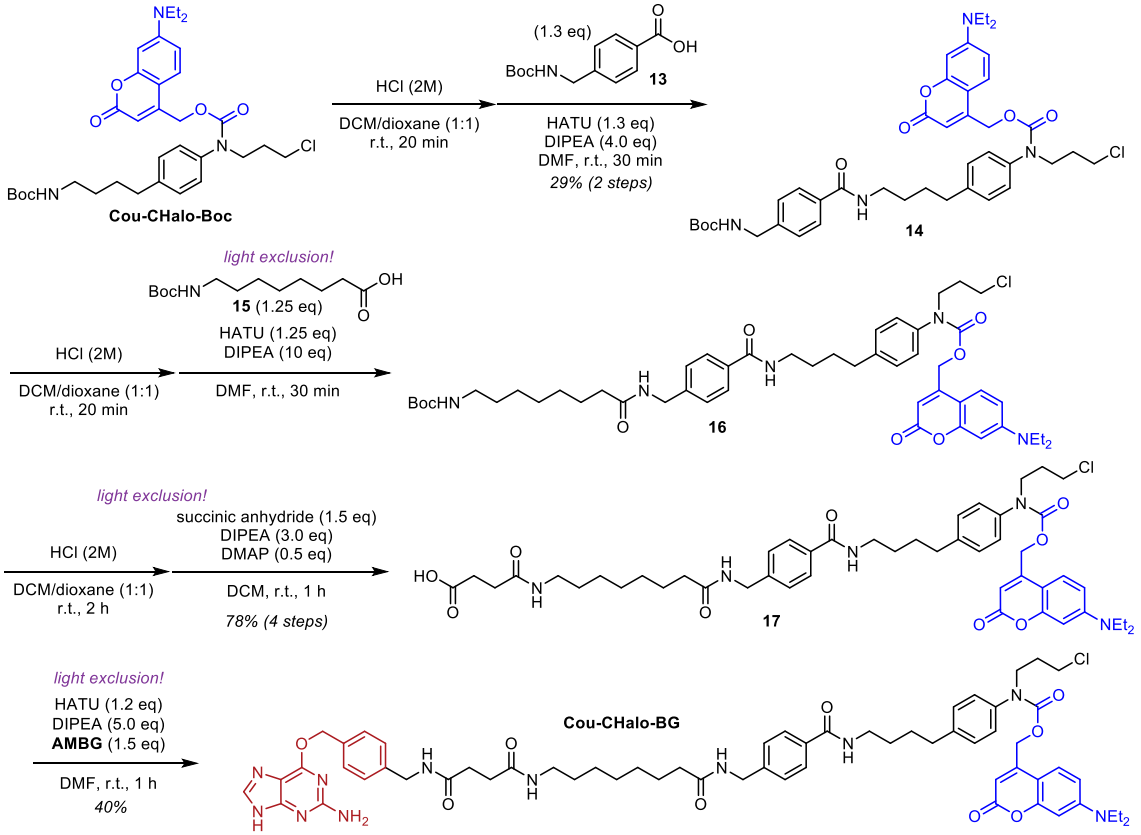

Compound 14

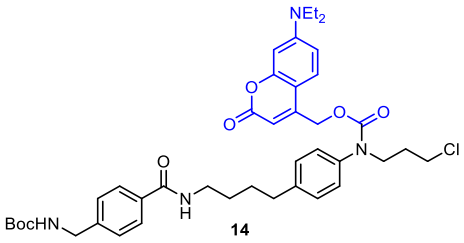

Note: the reaction must be performed under light exclusion.

Cou-CHalo-Boc (29 mg, 47 µmol, 1.0 eq) was deprotected according to General Procedure A (0.1 M) and coupled with carboxylate **13** (16 mg, 61 µmol, 1.3 eq, 0.02 M) following General Procedure B (1.0 eq HATU, 30 min reaction time). Piperidine (6 µL, 0.06 mmol, 1.3 eq) was added to react with excess carboxylate. The volatiles were removed *in vacuo*, the residue was diluted with water (15 mL) and brine (10 mL) and extracted with ethyl acetate (3 × 10 mL). The organic layer was dried over sodium sulfate, the desiccant was filtered off and the solvent was removed *in vacuo*. The crude product was purified by flash *np*-column chromatography (*iso*-hexanes/ethyl acetate; 10→70% EtOAc) to give **14** (31 mg, 42 µmol, 88%) as a yellow solid.

TLC *Rf* = 0.17 (*np*, Hex:EtOAc 1:1); 0.47 (*np*, DCM:MeOH 19:1)
^{1}H-NMR (600 MHz, $CDCl_3$/MeOD (4:1)): *δ* (ppm) = 7.70 (s, 2H), 7.24 (d, J = 7.9 Hz, 2H), 7.17 (d, J = 7.6 Hz, 3H), 7.07 (d, J = 7.6 Hz, 2H), 6.54 (s, 1H), 6.43 (s, 1H), 5.48 (s, 1H), 5.14 (s, 2H), 4.23 (s, 2H), 3.81 – 3.75 (m, 2H), 3.51 (t, J = 5.9 Hz, 2H), 3.40 – 3.31 (m, 6H), 2.66 – 2.61 (m, 2H), 2.00 (p, J = 6.6 Hz, 2H), 1.72 – 1.63 (m, 2H), 1.58 – 1.51 (m, 2H), 1.37 (s, 9H), 1.13 (t, J = 7.0 Hz, 6H).
^{13}C-NMR (151 MHz, $CDCl_3$/MeOD (4:1)): *δ* (ppm) = 167.9, 162.5, 156.3, 155.9, 154.9, 150.6, 142.4, 141.9, 138.4, 133.5, 129.6, 127.4, 127.3, 124.2, 109.1, 105.8, 104.7, 97.7, 79.8, 62.5, 48.3, 44.9, 44.1, 42.1, 39.9, 35.0, 31.0, 28.8, 28.6, 28.3, 12.3.
HRMS (ESI+): m/z calc. for $C_{41}H_{52}ClN_4O_7^+$ $[M+H]^+$: 747.3519, found: 747.3524.

Compound 17

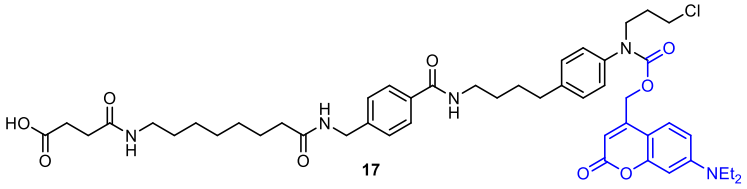

17

Note: the reaction must be performed under light exclusion.

14 (31 mg, 42 µmol, 1.0 eq) was deprotected according to General Procedure A (0.04 M) and coupled with carboxylate **15** (14 mg, 52 µmol, 1.25 eq, 0.04 M) following General Procedure B (1.0 eq HATU, 30 min reaction time). The volatiles were removed *in vacuo* to give crude **16** which was Boc-deprotected according to General Procedure A (0.05 M) and dissolved in anhydrous DCM (2 mL). DIPEA (35 µL, 0.21 mmol, 5.0 eq), DMAP (3 mg, 0.02 mmol, 0.5 eq) and succinic anhydride (6 mg, 0.06 mmol, 1.5 eq) were added and the reaction mixture was stirred at room temperature for 20 min. The volatiles were removed *in vacuo* and the crude product was purified by *rp*-flash column chromatography (acetonitrile/water; 10→70% MeCN) to give **17** (28 mg, 32 µmol, 76% over 4 steps) as a yellow solid.

^{1}H-NMR (600 MHz, $CDCl_3$/MeOD (1:1)): *δ* (ppm) = 7.72 (d, J = 7.8 Hz, 2H), 7.27 (d, J = 8.3 Hz, 2H), 7.21 (d, J = 7.8 Hz, 3H), 7.11 (d, J = 7.9 Hz, 2H), 6.59 (s, 1H), 6.47 (s, 1H), 5.58 (s, 1H), 5.34 – 5.10 (m, 2H), 4.36 (s, 2H), 3.81 (s, 2H), 3.53 (t, J = 6.1 Hz, 2H), 3.40 (q, J = 6.1 Hz, 6H), 3.12 (t, J = 7.1 Hz, 2H), 2.70 – 2.63 (m, 2H), 2.57 (t, J = 6.9 Hz, 2H), 2.41 (t, J = 7.0 Hz, 2H), 2.18 (t, J = 7.5 Hz, 2H), 2.03 (p, J = 6.5 Hz, 2H), 1.70 (s, 2H), 1.60 (dq, J = 14.5, 7.4 Hz, 4H), 1.42 (q, J = 7.0 Hz, 2H), 1.27 (s, 6H), 1.17 (t, J = 7.1 Hz, 6H).
^{13}C-NMR (151 MHz, $CDCl_3$/MeOD (1:1)): *δ* (ppm) = 209.5, 175.4, 174.9, 173.0, 168.6, 163.1, 156.2, 155.2, 151.3, 150.8, 142.4, 142.0, 138.6, 133.6, 129.7, 127.8, 127.6, 127.5, 124.7, 109.5, 62.8, 45.2, 43.1, 42.2, 40.1, 39.6, 36.3, 35.3, 31.3, 30.9, 29.9, 29.3, 29.1, 29.1, 28.9, 28.8, 26.7, 25.8.
HRMS (ESI+): m/z calc. for $C_{48}H_{62}ClN_5NaO_9^+$ $[M+Na]^+$: 910.4128, found: 910.4131.

Cou-CHalo-BG

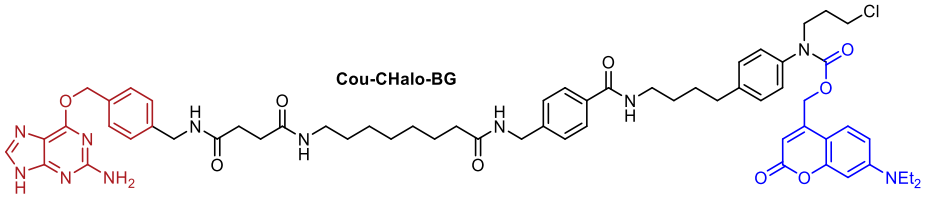

Note: the reaction must be performed under light exclusion.

6-((4-(aminomethyl)benzyl)oxy)-9H-purin-2-amine (**AMBG**, 13 mg, 47 µmol, 1.5 eq) was coupled with carboxylate **17** (28 mg, 32 µmol, 1.0 eq, 0.01 M) following General Procedure B (1.2 eq HATU, 1 h reaction time). The reaction mixture was filtered over Celite to remove the insoluble **AMBG**, the volatiles were removed under reduced pressure and the crude product was purified by *rp*-flash column chromatography (acetonitrile/water; 20→70% MeCN) followed by *np*-flash column chromatography (DCM/MeOH; 0.5→15% MeOH) affording **Cou-CHalo-BG** (14.4 mg, 13 µmol, 40%) as a yellow solid.

TLC *Rf* = 0.27 (*np*, DCM:MeOH 9:1)
^{1}H-NMR (600 MHz, DMSO-d_6): *δ* (ppm) = 12.49 (s, 1H), 8.41 (t, J = 5.7 Hz, 1H), 8.35 (td, J = 6.0, 3.5 Hz, 2H), 7.83 – 7.76 (m, 4H), 7.43 (d, J = 8.1 Hz, 2H), 7.37 (s, 1H), 7.28 (d, J = 8.1 Hz, 2H), 7.27 – 7.23 (m, 6H), 6.67 – 6.62 (m, 1H), 6.51 (s, 1H), 6.26 (s, 2H), 5.45 (s, 2H), 5.25 (s, 2H), 4.28 (d, J = 6.0 Hz, 2H), 4.25 (d, J = 5.9 Hz, 2H), 3.77 (s, 2H), 3.64 (t, J = 6.4 Hz, 2H), 3.41 (q, J = 7.0 Hz, 4H), 3.28 (q, J = 6.6 Hz, 2H), 3.00 (q, J = 6.6 Hz, 2H), 2.61 (t, J = 7.5 Hz, 2H), 2.36 (ddd, J = 7.8, 6.2, 1.7 Hz, 2H), 2.31 (ddd, J = 8.6, 6.3, 1.7 Hz, 2H), 2.13 (t, J = 7.4 Hz, 2H), 1.92 (p, J = 6.6 Hz, 2H), 1.65 – 1.58 (m, 2H), 1.57 – 1.53 (m, 2H), 1.52 – 1.47 (m, 2H), 1.35 (p, J = 7.0 Hz, 2H), 1.23 (d, J = 4.3 Hz, 6H), 1.10 (t, J = 7.0 Hz, 6H).
^{13}C-NMR (151 MHz, DMSO-d_6): *δ* (ppm) = 172.2, 171.4, 171.1, 165.9, 160.6, 159.6, 155.7, 154.0, 151.2, 150.4, 142.9, 141.1, 139.5, 138.6, 135.2, 133.1, 129.0, 128.5, 127.2, 127.2, 126.8, 125.4, 108.7, 105.1, 96.8, 66.5, 62.5, 47.6, 44.0, 42.6, 42.6, 41.8, 41.7, 38.9, 38.5, 35.3, 34.4, 30.9, 30.9, 30.7, 29.1, 28.9, 28.6, 28.5, 28.4, 26.3, 25.3, 12.3.
HRMS (ESI+): m/z calc. for $C_{61}H_{74}ClN_{11}NaO_9^+$ $[M+Na]^+$: 1162.525, found: 1162.526.

Synthetic route for CHalo-BG

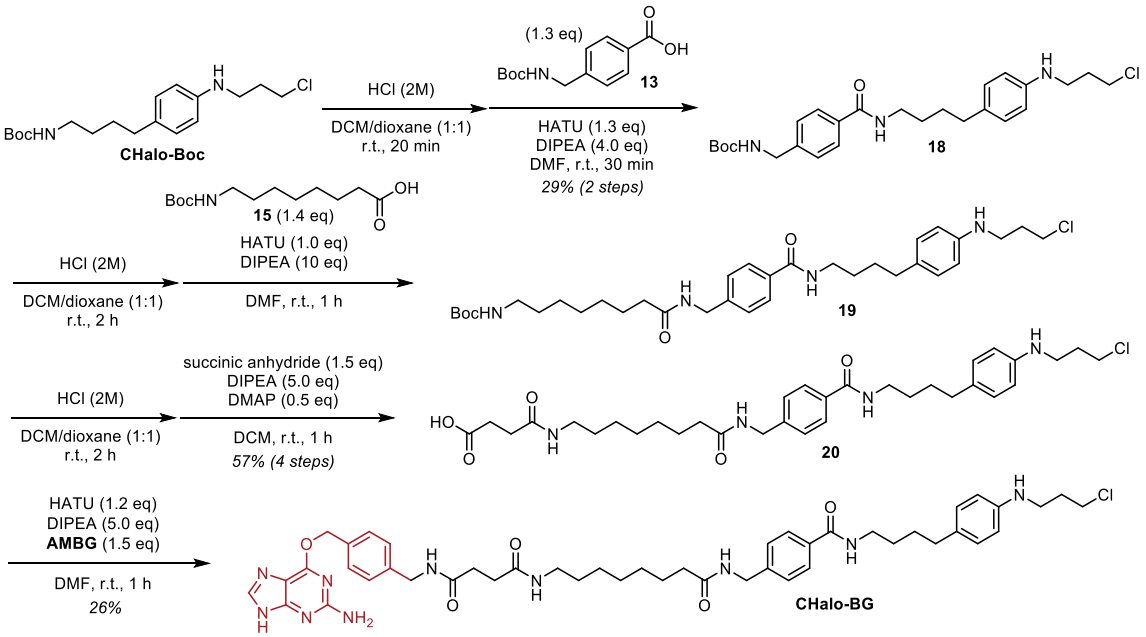

Compound 18

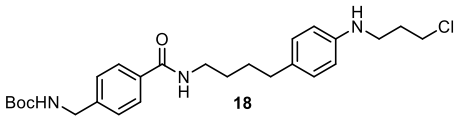

CHalo-Boc (0.16 g, 0.48 mmol, 1.0 eq) was deprotected according to General Procedure A (0.02 M) and coupled with carboxylate **13** (0.15 g, 0.59 mmol, 1.3 eq, 0.25 M) following General Procedure B (1.0 eq HATU, 30 min reaction time). *N*-methyl piperazine (66 µL, 0.59 mmol, 1.3 eq) was added to react with excess carboxylate. The volatiles were removed *in vacuo*, the residue was diluted with water (15 mL) and extracted with ethyl acetate (3 × 10 mL). The organic layer was dried over sodium sulfate, the desiccant was filtered off and the solvent was removed *in vacuo*. The crude product was purified by flash *rp*-column chromatography (acetonitrile/water; 10→80% MeCN) to give **18** (72 mg, 0.15 mmol, 29% over 2 steps) as a light-yellow solid.

^{1}H-NMR (400 MHz, $CDCl_3$): δ (ppm) = 7.69 (d, J = 8.1 Hz, 2H), 7.31 (d, J = 8.0 Hz, 2H), 6.99 (d, J = 8.3 Hz, 2H), 6.56 (d, J = 8.4 Hz, 2H), 6.14 (s, 1H), 4.97 (s, 1H), 4.33 (d, J = 5.6 Hz, 2H), 3.65 (t, J = 6.3 Hz, 2H), 3.44 (q, J = 6.4 Hz, 2H), 3.31 (t, J = 6.6 Hz, 2H), 2.54 (t, J = 6.8 Hz, 2H), 2.06 (p, J = 6.5 Hz, 2H), 1.68 – 1.59 (m, 4H), 1.46 (s, 9H).
^{13}C-NMR (101 MHz, $CDCl_3$): δ (ppm) = 167.3, 156.0, 146.1, 142.6, 133.8, 131.3, 129.4, 127.5, 127.3, 113.1, 79.9, 44.4, 42.8, 41.3, 40.1, 34.6, 32.1, 29.3, 29.1, 28.5.
HRMS (ESI+): m/z calc. for $C_{26}H_{37}ClN_3O_3^+$ $[M+H]^+$: 474.2518, found: 474.2501

Compound 20

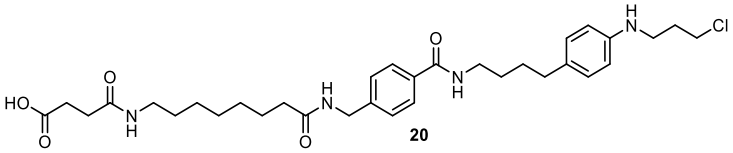

18 (11 mg, 23 µmol, 1.0 eq) was deprotected according to General Procedure A (0.02 M) and coupled with carboxylate **15** (8 mg, 32 µmol, 1.4 eq, 0.03 M) following General Procedure B (1.0 eq HATU, 1 h reaction time). The volatiles were removed *in vacuo* to give crude **19** which was Boc-deprotected according to General Procedure A (0.02 M) and dissolved in anhydrous DCM (2 mL). DIPEA (20 µL, 0.12 mmol, 5.0 eq), DMAP (1.4 mg, 12 µmol, 0.5 eq) and succinic anhydride (2.8 mg, 28 µmol, 1.2 eq) were added and the reaction mixture was stirred at room temperature for 2 h. The volatiles were removed *in vacuo* and the crude product was purified by *rp*-flash column chromatography (acetonitrile/water; 5→50% MeCN) to give **20** (8 mg, 13 µmol, 57% over 4 steps) as a colourless solid.

^{1}H-NMR (600 MHz, MeOD/$CDCl_3$ (4:1)): δ (ppm) = 7.72 (d, J = 8.3 Hz, 2H), 7.30 (d, J = 8.4 Hz, 2H), 6.96 (d, J = 8.5 Hz, 2H), 6.57 (d, J = 8.5 Hz, 2H), 4.38 (s, 2H), 3.63 (t, J = 6.4 Hz, 2H), 3.36 (t, J = 6.5 Hz, 2H), 3.24 (t, J = 6.7 Hz, 2H), 3.13 (t, J = 7.1 Hz, 2H), 2.57 (t, J = 7.1 Hz, 2H), 2.52 (t, J = 6.9 Hz, 2H), 2.43 (t, J = 7.1 Hz, 2H), 2.21 (t, J = 7.5 Hz, 2H), 2.02 (p, J = 6.6 Hz, 2H), 1.65 – 1.57 (m, 6H), 1.45 (p, J = 7.2 Hz, 2H), 1.30 (s, 6H).

^{13}C-NMR (151 MHz, MeOD/$CDCl_3$ (4:1)): δ (ppm) = 175.8, 175.5, 173.6, 169.2, 146.9, 142.9, 134.0, 131.9, 129.7, 128.0, 127.9, 113.9, 43.3, 43.1, 41.9, 40.5, 39.9, 36.6, 35.1, 32.6, 31.2, 30.1, 29.7, 29.7, 29.5, 29.5, 29.3, 27.1, 26.2.
HRMS (ESI+): m/z calc. for $C_{33}H_{48}ClN_4O_5^+$ $[M+H]^+$: 615.3308, found: 615.3308.

CHalo-BG

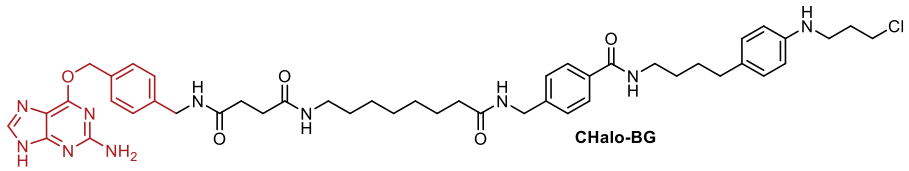

6-((4-(aminomethyl)benzyl)oxy)-9*H*-purin-2-amine (**AMBG**, 5 mg, 20 µmol, 1.5 eq) was coupled with carboxylate **20** (8 mg, 13 µmol, 1.0 eq, 0.05 M) following General Procedure B (1.2 eq HATU, 1 h reaction time). The crude product was purified by preparative HPLC (acetonitrile/water, 0.1% formic acid; 5→50% MeCN, 20 min) affording **CHalo-BG** (3.0 mg, 3.4 µmol, 26%) as a colourless solid.

^{1}H-NMR (600 MHz, DMSO-d_6): δ (ppm) = 12.42 (s, 1H), 8.39 (t, J = 5.6 Hz, 1H), 8.37 – 8.32 (m, 2H), 7.79 (d, J = 3.3 Hz, 2H), 7.76 (d, J = 8.3 Hz, 2H), 7.43 (d, J = 7.8 Hz, 2H), 7.28 (d, J = 8.3 Hz, 2H), 7.25 (d, J = 8.1 Hz, 2H), 6.89 (d, J = 8.4 Hz, 2H), 6.48 (d, J = 8.5 Hz, 2H), 6.29 (s, 2H), 5.44 (s, 2H), 5.42 (t, J = 5.6 Hz, 1H), 4.28 (d, J = 5.9 Hz, 2H), 4.24 (d, J = 5.9 Hz, 2H), 3.72 (t, J = 6.5 Hz, 2H), 3.24 (q, J = 6.4 Hz, 2H), 3.09 (q, J = 6.3 Hz, 2H), 3.00 (q, J = 6.8 Hz, 2H), 2.43 (t, J = 6.9 Hz, 2H), 2.36 (dd, J = 11.0, 4.6 Hz, 2H), 2.31 (dd, J = 11.1, 4.6 Hz, 2H), 2.13 (t, J = 7.4 Hz, 2H), 1.95 (p, J = 6.6 Hz, 2H), 1.56 – 1.45 (m, 6H), 1.39 – 1.31 (m, 2H), 1.23 (s, 6H).
^{13}C-NMR (151 MHz, DMSO-d_6): δ (ppm) = 172.3, 171.4, 171.1, 165.8, 159.9, 159.7, 155.2, 146.8, 142.9, 137.8, 135.2, 133.1, 129.2, 128.8, 128.5, 127.2, 127.2, 126.8, 113.5, 112.1, 66.5, 43.4, 41.8, 41.7, 40.1, 39.1, 38.5, 35.3, 34.0, 31.7, 30.9, 30.9, 29.1, 28.9, 28.8, 28.6, 28.5, 26.3, 25.3.
HRMS (ESI+): m/z calc. for $C_{46}H_{59}ClN_{10}NaO_5^+$ $[M+Na]^+$: 889.4251, found: 889.4246.

10.2.5 Light-controlled & reporting protein heterodimeriser Cou-CHalo-SiR-BG

Synthetic route for Cou-CHalo-SiR-BG

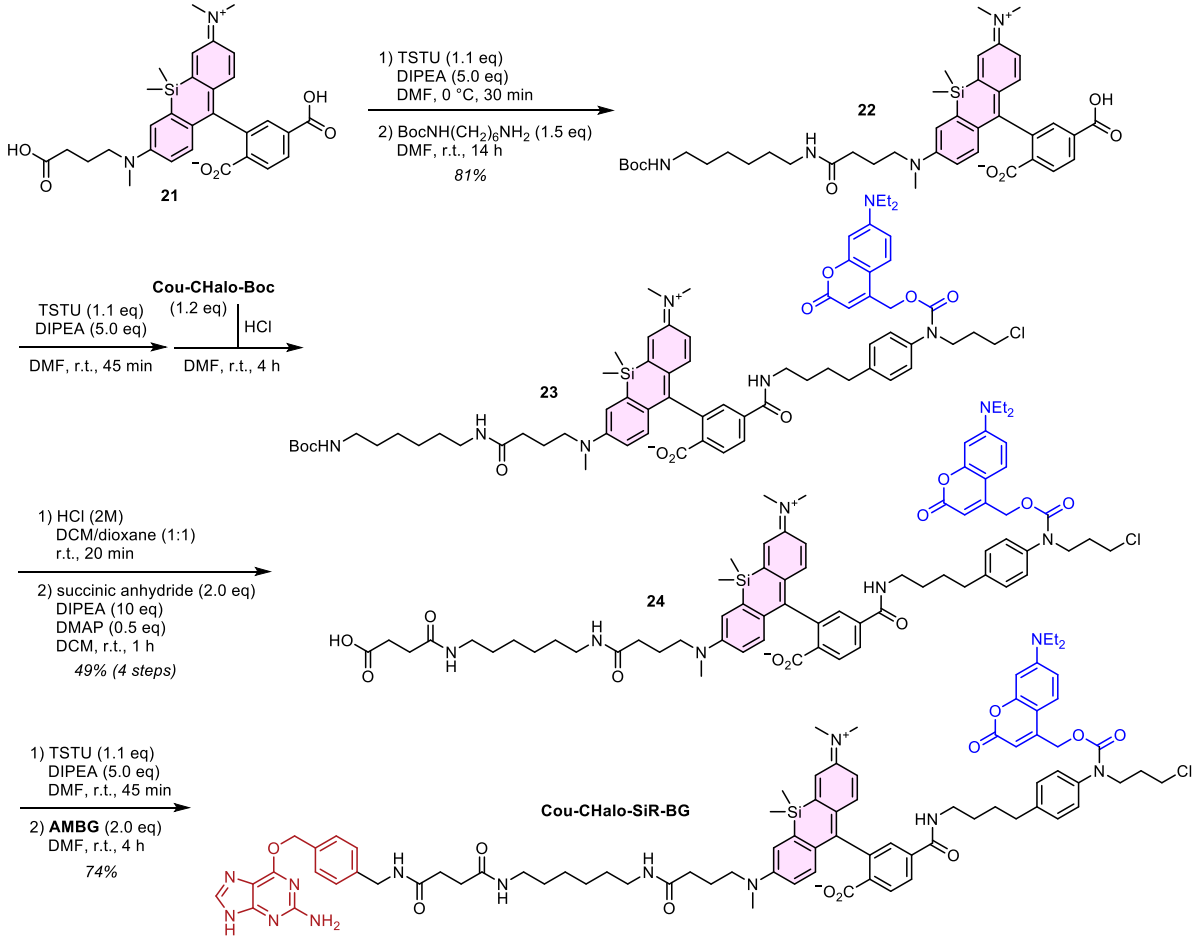

Compound 22

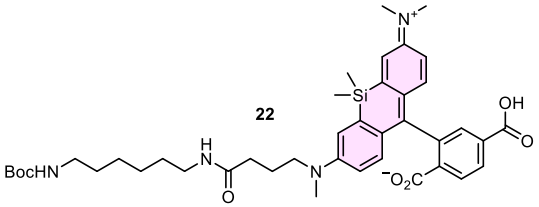

21 was a kind gift from the laboratory of Kai Johnsson.

21 (10 mg, 19 µmol, 1.0 eq) was dissolved in anhydrous DMF (0.3 mL), DIPEA (16 µL, 92 µmol, 5.0 eq) was added and the mixture was cooled to 0 °C. TSTU (6.1 mg, 20 µmol, 1.1 eq) was dissolved in anhydrous DMF (0.4 mL), added to the solution of **21** and the mixture was stirred at 0 °C for 45 min. Then, Boc-1,6-hexanediamine (6.0 mg, 28 µmol, 1.5 eq) was added and the mixture was stirred at room temperature for 45 min. The solvent was removed *in vacuo* and the crude product was purified by *rp*-flash column chromatography (acetonitrile/water; 10→80% MeCN) to give **22** (11 mg, 15 µmol, 81%) as a blue solid.

^{1}H-NMR (600 MHz, $CDCl_3$/MeOD 2:1): *δ* (ppm) = 7.91 (d, J = 8.0 Hz, 1H), 7.67 (d, J = 8.0 Hz, 1H), 7.63 (s, 1H), 6.67 (d, J = 2.7 Hz, 1H), 6.65 (d, J = 2.7 Hz, 1H), 6.40 (d, J = 8.9 Hz, 1H), 6.38 (d, J = 9.0 Hz, 1H), 6.27 – 6.23 (m, 2H), 3.06 – 3.02 (m, 2H), 2.79 (t, J = 7.1 Hz, 2H), 2.68 (t, J = 7.0 Hz, 2H), 2.64 (s, 6H), 2.63 (s, 3H), 1.85 (t, J = 7.3 Hz, 2H), 1.54 (p, J = 7.3 Hz, 2H), 1.11 (dd, J = 14.2, 7.2 Hz, 4H), 1.08 (s, 9H), 0.98 – 0.94 (m, 4H), 0.33 (s, 3H), 0.25 (s, 3H).
^{13}C-NMR (151 MHz, $CDCl_3$/MeOD 2:1): *δ* (ppm) = 173.4, 170.4, 166.9, 156.7, 154.0, 149.3, 148.1, 136.9, 136.8, 136.0, 130.5, 130.0, 129.8, 129.5, 127.9, 127.8, 125.7, 125.1, 116.4, 116.0, 113.1, 112.7, 78.5, 51.1, 39.7, 39.4, 38.8, 37.3, 32.7, 29.2, 28.6, 27.6, 25.9, 25.8, 22.5, -0.6, -2.4.
HRMS (ESI+): m/z calc. for $C_{41}H_{55}N_4O_7Si^+$ $[M+H]^+$: 743.3835, found: 743.3843.

Compound 24

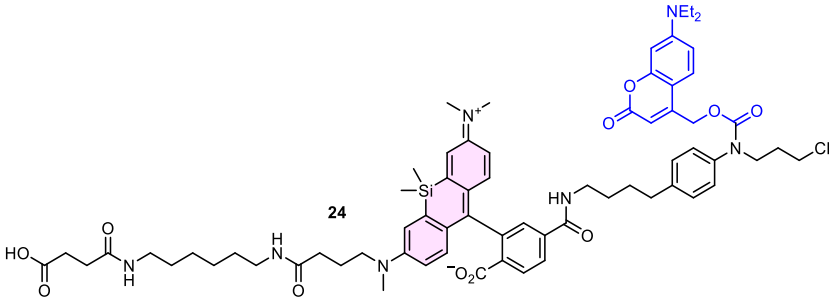

22 (11 mg, 15 µmol, 1.0 eq) was dissolved in anhydrous DMF (0.5 mL) and DIPEA (13 µL, 74 µmol, 5.0 eq) was added. TSTU (5.4 mg, 18 µmol, 1.2 eq) was dissolved in anhydrous DMF (0.4 mL), added to the solution of **22** and the mixture was stirred at room temperature for 30 min. **Cou-CHalo-Boc** (10 mg, 17 µmol, 1.2 eq) was deprotected according to General Procedure A, dissolved in anhydrous DMF (0.4 mL) and added to the reaction mixture, the resulting mixture was stirred at room temperature for 4 h. The solvent was removed *in vacuo* and the crude product was semi-purified by *rp*-flash column chromatography (acetonitrile/water; 20→100% MeCN) to give **23** (12 mg) as green solid. **23** (12 mg, 10 µmol, 1.0 eq) was deprotected according to General Procedure A (0.01 M) and dissolved in anhydrous DCM (1 mL). DIPEA (8.2 µL, 48 µmol, 5.0 eq), DMAP (0.6 mg, 5 µmol, 0.5 eq) and succinic anhydride (2 mg, 19 µmol, 2.0 eq) were added and the reaction mixture was stirred at room temperature for 1 h. The volatiles were removed *in vacuo* and the crude product was purified by *rp*-flash column chromatography (acetonitrile/water; 20→80% MeCN) to give **24** (9 mg, 7 µmol, 49% over 4 steps) as a green solid.

^{1}H-NMR (600 MHz, $CDCl_3$/MeOD 4:1): *δ* (ppm) = 7.97 (s, 2H), 7.93 (d, J = 7.9 Hz, 1H), 7.74 (s, 1H), 7.19 (d, J = 7.9 Hz, 3H), 7.07 (d, J = 7.0 Hz, 2H), 6.91 (d, J = 2.4 Hz, 1H), 6.89 (d, J = 2.8 Hz, 1H), 6.68 (d, J = 8.9 Hz, 1H), 6.66 (d, J = 9.0 Hz, 1H), 6.55 (d, J = 7.8 Hz, 1H), 6.50 – 6.42 (m, 2H), 6.35 (s, 1H), 5.42 (s, 1H), 5.14 (s, 2H), 3.80 (s, 2H), 3.53 (t, J = 5.8 Hz, 2H), 3.40 – 3.33 (m, 6H), 3.28 (d, J = 7.1 Hz, 2H), 3.13 – 3.07 (m, 4H), 2.88 (s, 9H), 2.68 – 2.63 (m, 2H), 2.54 (t, J = 6.9 Hz, 2H), 2.39 (t, J = 6.9 Hz, 2H), 2.13 (t, J = 7.3 Hz, 2H), 2.02 (p, J = 6.5 Hz, 2H), 1.82 (p, J = 7.3 Hz, 2H), 1.69 (s, 2H), 1.56 (p, J = 7.5 Hz, 2H), 1.44 – 1.37 (m, 4H), 1.23 (dq, J = 11.6, 5.8 Hz, 6H), 1.15 (t, J = 7.1 Hz, 6H), 0.60 (s, 3H), 0.53 (s, 3H).
^{13}C-NMR (151 MHz, $CDCl_3$/MeOD 4:1): *δ* (ppm) = 175.8, 173.7, 173.2, 171.0, 167.3, 167.2, 163.0, 151.1, 149.7, 148.5, 142.0, 140.5, 138.6, 137.5, 131.2, 130.8, 129.7, 128.8, 128.4, 128.3, 127.5, 125.8, 124.4, 124.2, 116.9, 116.4, 113.5, 113.2, 109.3, 97.6, 93.5, 62.7, 51.7, 48.4, 44.9, 42.2, 40.4, 40.3, 39.3, 39.3, 38.1, 35.2, 33.5, 31.2, 31.1, 30.2, 29.8, 29.2, 29.2, 28.9, 28.8, 26.4, 26.3, 23.1, 12.5, 0.4, -1.6.
HRMS (ESI+): m/z calc. for $C_{68}H_{85}ClN_7O_{11}Si^+$ $[M+H]^+$: 1238.5759, found: 1238.5757.

Cou-CHalo-SiR-BG

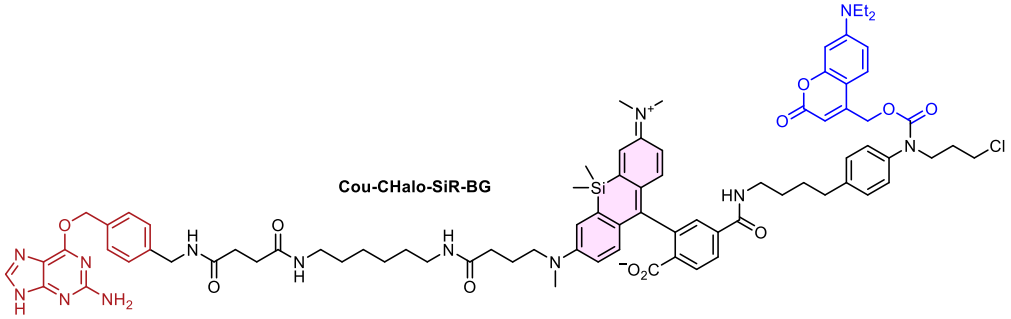

24 (9 mg, 7 µmol, 1.0 eq) was dissolved in anhydrous DMF (0.3 mL), DIPEA (6.2 µL, 36 µmol, 5.0 eq) and TSTU (50 mM in DMF, 0.17 mL, 8.7 µmol, 1.2 eq) were added and the reaction mixture was stirred at room temperature for 30 min. 6-((4-(aminomethyl)benzyl)oxy)-9*H*-purin-2-amine (**AMBG**, 4 mg, 15 µmol, 2.0 eq) was added and the solution was sonicated to disperse the hardly soluble AMBG. The reaction mixture was stirred for 45 min, the mixture was filtered over celite and the crude product was purified by preparative HPLC (acetonitrile/water, 0.1% formic acid; 25→75% MeCN, 20 min) to give **Cou-CHalo-SiR-BG** (8.0 mg, 5.4 µmol, 74%) as a green solid.

^{1}H-NMR (600 MHz, $CDCl_3$/MeOD 2:1): δ (ppm) = 8.28 (t, J = 5.6 Hz, 1H), 8.13 (s, 1H), 8.06 (t, J = 5.7 Hz, 1H), 8.00 (d, J = 7.4 Hz, 1H), 7.95 (d, J = 8.0 Hz, 1H), 7.75 (s, 1H), 7.71 (s, 1H), 7.57 (d, J = 4.9 Hz, 1H), 7.43 – 7.38 (m, 3H), 7.25 – 7.17 (m, 5H), 7.08 (s, 2H), 6.96 – 6.92 (m, 1H), 6.91 (d, J = 2.7 Hz, 1H), 6.68 (d, J = 9.0 Hz, 1H), 6.66 (d, J = 9.1 Hz, 1H), 6.58 (s, 1H), 6.48 (s, 2H), 6.35 (s, 1H), 5.47 (s, 2H), 5.15 (s, 2H), 4.33 (d, J = 4.8 Hz, 2H), 3.80 (s, 2H), 3.54 (t, J = 5.8 Hz, 2H), 3.44 – 3.34 (m, 6H), 3.30 – 3.26 (m, 2H), 3.10 (q, J = 6.5 Hz, 4H), 2.90 (s, 9H), 2.66 (s, 2H), 2.48 (t, J = 6.1 Hz, 2H), 2.46 – 2.41 (m, 2H), 2.15 (t, J = 7.3 Hz, 2H), 2.02 (p, J = 6.5 Hz, 2H), 1.82 (p, J = 7.2 Hz, 2H), 1.74 – 1.66 (m, 2H), 1.58 (p, J = 7.2 Hz, 2H), 1.44 – 1.38 (m, 4H), 1.29 – 1.21 (m, 4H), 1.17 (t, J = 6.7 Hz, 6H), 0.62 (s, 3H), 0.54 (s, 3H).
^{13}C-NMR (151 MHz, $CDCl_3$/MeOD 2:1): δ (ppm) = 174.3, 174.2, 173.6, 173.6, 173.6, 171.3, 167.8, 160.3, 156.4, 155.5, 151.7, 150.1, 148.9, 140.8, 138.8, 137.8, 135.8, 131.4, 131.0, 130.0, 129.0, 128.9, 128.8, 128.6, 128.0, 127.8, 126.1, 124.8, 124.5, 117.2, 116.8, 113.8, 113.5, 109.6, 97.9, 68.2, 63.1, 52.0, 48.7, 45.1, 43.5, 42.4, 40.7, 40.4, 39.9, 39.7, 38.3, 35.4, 33.6, 31.9, 31.9, 31.5, 29.5, 29.5, 29.2, 29.1, 26.8, 26.8, 23.4, 12.6, 0.5, -1.5.
HRMS (ESI+): m/z calc. for $C_{81}H_{97}ClN_{13}O_{11}Si^+$ $[M+H]^+$: 1490.6883, found: 1490.6895.

10.2.6 Proof-of-Concept and Design Optimisation

Synthetic route for 6-Carboxyfluorescein conjugation precursor (Fluo)

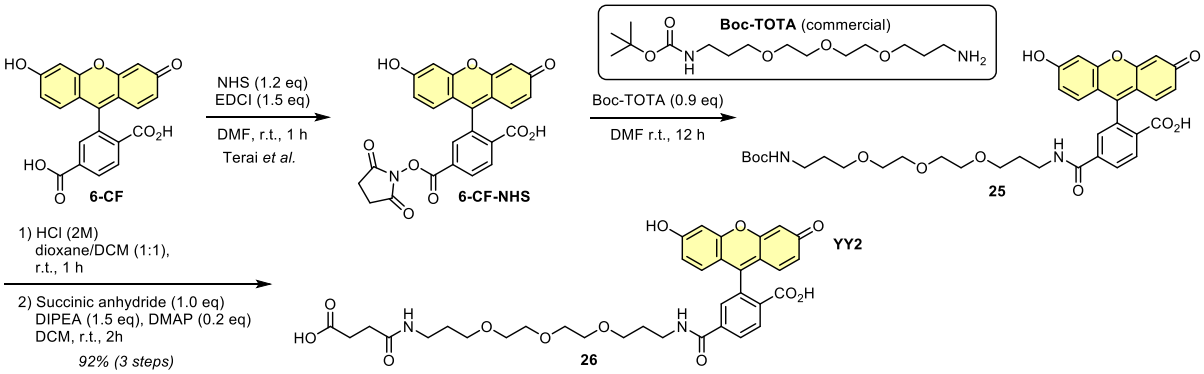

6-CF-NHS was prepared according to a previously described procedure (Terai *et al.*[87], first synthetic step for compound 25).

Compound 26

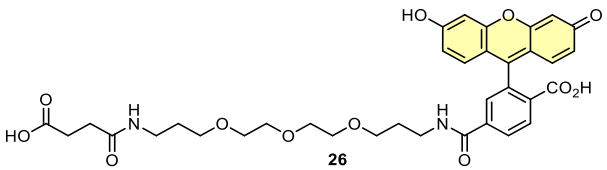

6-CF-NHS (51 mg, 0.11 mmol, 1.1 eq) was dissolved in anhydrous DMF (2 mL). **Boc-TOTA** (31 mg, 98 µmol, 1.0 eq) was added and the reaction was stirred at room temperature for 12 h. The volatiles were removed *in vacuo* to afford crude **25** which was used for the next synthetic step without purification.

25 was deprotected according to General Procedure A (0.03 M) and dissolved in anhydrous DMF (1.5 mL). DIPEA (50 µL, 0.29 mmol, 3.0 eq), 4-(dimethylamino)pyridine (6 mg, 50 µmol, 0.5 eq) and succinic anhydride (10 mg, 98 µmol, 1.0 eq) were added and the reaction mixture was stirred at room temperature for 2 h. The volatiles were removed *in vacuo* and the crude product was purified by *rp*-flash column chromatography (acetonitrile/water, 0.1% formic acid; 5→60% MeCN) affording **26** (61 mg, 90 µmol, 92% over 3 steps) as an orange solid.

TLC *Rf* = 0.81 (*rp*, 50% MeCN).
^{1}H-NMR (400 MHz, MeOD): *δ* (ppm) = 8.14 (dd, J = 8.0, 1.4 Hz, 1H), 8.08 (dd, J = 8.0, 0.6 Hz, 1H), 7.64 (dd, J = 1.2, 0.7 Hz, 1H), 6.69 (d, J = 2.3 Hz, 2H), 6.61 (d, J = 8.7 Hz, 2H), 6.55 (dd, J = 8.7, 2.4 Hz, 2H), 3.50 (d, J = 7.6 Hz, 8H), 3.44 – 3.37 (m, 6H), 3.19 (t, J = 6.8 Hz, 2H), 2.58 – 2.53 (m, 2H), 2.42 (t, J = 6.8 Hz, 2H), 1.80 (p, J = 6.3 Hz, 2H), 1.67 (p, J = 6.6 Hz, 2H).
^{13}C-NMR (101 MHz, MeOD): *δ* (ppm) = 176.2, 174.4, 170.6, 167.9, 161.4, 154.7, 154.0, 142.4, 130.4, 130.3, 130.3, 126.1, 123.9, 113.7, 110.9, 103.6, 85.7, 71.3, 71.2, 71.1, 70.9, 70.2, 69.7, 39.1, 37.8, 31.6, 30.3, 30.1.
HRMS (ESI+): m/z calc. for $C_{35}H_{39}N_2O_{12}^+$ [M+H]$^+$: 679.2498, found: 679.2484.

Synthetic route for CA-Fluo

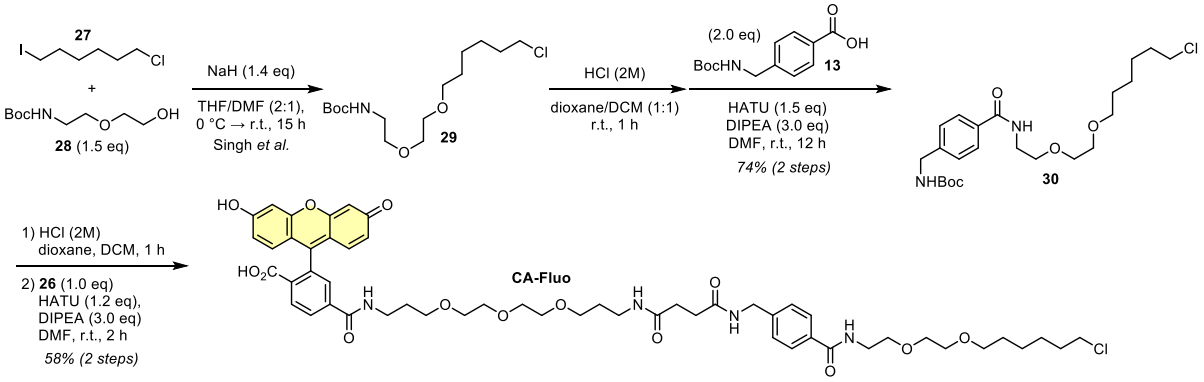

Compound **29** was prepared according to a previously described procedure (Singh *et al.*[88], compound A3).

Compound 30

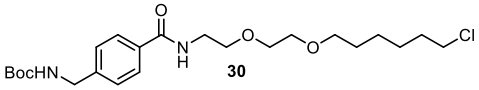

30 was previously described in a patent by PROMEGA (US9702824[89]). **29** (50 mg, 0.15 mmol, 1.0 eq) was deprotected according to General Procedure A (0.08 M) and coupled with carboxylate **13** (40 mg, 0.15 mmol, 2.0 eq, 0.1 M) following General Procedure B (1.1 eq HATU, 12 h reaction time). The crude product was purified by *np*-flash column chromatography (*iso*-hexanes/ethyl acetate; 20→70% EtOAc) affording **30** (52 mg, 0.11 mmol, 74%) as an off-white solid.

TLC *Rf* = 0.70 (*np*, DCM:MeOH 9:1)
^{1}H-NMR (400 MHz, $CDCl_3$): *δ* (ppm) = 7.71 (d, J = 8.2 Hz, 2H), 7.29 (d, J = 8.0 Hz, 2H), 6.82 – 6.75 (m, 1H), 5.12 – 5.04 (m, 1H), 4.32 (d, J = 5.8 Hz, 2H), 3.66 – 3.60 (m, 6H), 3.58 – 3.54 (m, 2H), 3.48 (t, J = 6.7 Hz, 2H), 3.43 (t, J = 6.7 Hz, 2H), 1.71 (p, J = 6.7 Hz, 2H), 1.61 – 1.49 (m, 2H), 1.47 – 1.25 (m, 13H)
^{13}C-NMR (101 MHz, $CDCl_3$): *δ* (ppm) = 167.3, 156.0, 142.8, 133.5, 127.4, 127.4, 79.7, 71.3, 70.3, 70.0, 69.8, 45.1, 44.3, 39.7, 32.5, 29.5, 28.5, 26.7, 25.4
HRMS (ESI+): m/z calc. for $C_{23}H_{38}ClN_2O_5^+$ [M+H]$^+$: 457.2464, found: 457.2458

CA-Fluo

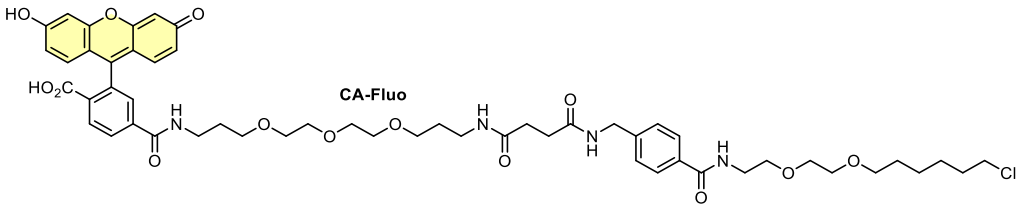

30 (10 mg, 22 µmol, 1.0 eq) was deprotected according to General Procedure A (0.02 M) and coupled with carboxylate **26** (15 mg, 22 µmol, 1.0 eq, 0.02 M) following General Procedure B (1.1 eq HATU, 12 h reaction time). The crude product was purified by preparative HPLC (acetonitrile/water, 0.1% formic acid; 5→65% MeCN, 20 min) affording **CA-Fluo** (13 mg, 13 µmol, 58% over 2 steps) as an orange solid.

TLC *Rf* = 0.49 (*rp*, 50% MeCN); *Rf* = 0.17 (*np*, DCM:MeOH 9:1)
^{1}H-NMR (400 MHz, DMSO-d_6): *δ* (ppm) = 10.16 (s, 2H), 8.67 (t, J = 5.5 Hz, 1H), 8.46 (t, J = 5.6 Hz, 1H), 8.39 (t, J = 6.0 Hz, 1H), 8.16 (dd, J = 8.0, 1.3 Hz, 1H), 8.07 (d, J = 8.1 Hz, 1H), 7.82 – 7.75 (m, 3H), 7.67 (s, 1H), 7.30 (d, J = 8.3 Hz, 2H), 6.69 (d, J = 2.1 Hz, 2H), 6.59 (d, J = 8.7 Hz, 2H), 6.55 (dd, J = 8.7, 2.2 Hz, 2H), 4.29 (d, J = 5.9 Hz, 2H), 3.60 (t, J = 6.6 Hz, 2H), 3.55 – 3.49 (m, 4H), 3.48 – 3.32 (m, 18H), 3.25 (q, J = 6.7 Hz, 2H), 3.05 (q, J = 6.7 Hz, 2H), 2.41 – 2.35 (m, 2H), 2.35 – 2.28 (m, 2H), 1.73 – 1.63 (m, 4H), 1.58 (p, J = 6.6 Hz, 2H), 1.45 (p, J = 6.7 Hz, 2H), 1.39 – 1.21 (m, 4H)
^{13}C-NMR (101 MHz, DMSO-d_6): *δ* (ppm) = 171.5, 171.2, 168.1, 166.0, 164.4, 159.8, 152.5, 151.9, 142.9, 140.7, 132.8, 129.4, 129.3, 128.3, 127.2, 126.8, 124.9, 122.3, 112.9, 109.2, 102.3, 83.9, 70.2, 69.7, 69.6, 69.5, 69.5, 69.5, 69.4, 68.9, 68.2, 68.0, 45.4, 41.7, 39.2, 36.9, 35.8, 32.0, 30.8, 30.7, 29.4, 29.1, 29.1, 26.1, 24.9
HRMS (ESI+): m/z calc. for $C_{53}H_{66}ClN_4O_{14}^+$ $[M+H]^+$: 1017.426, found: 1017.425

Synthetic route for HL2^{O}-Fluo

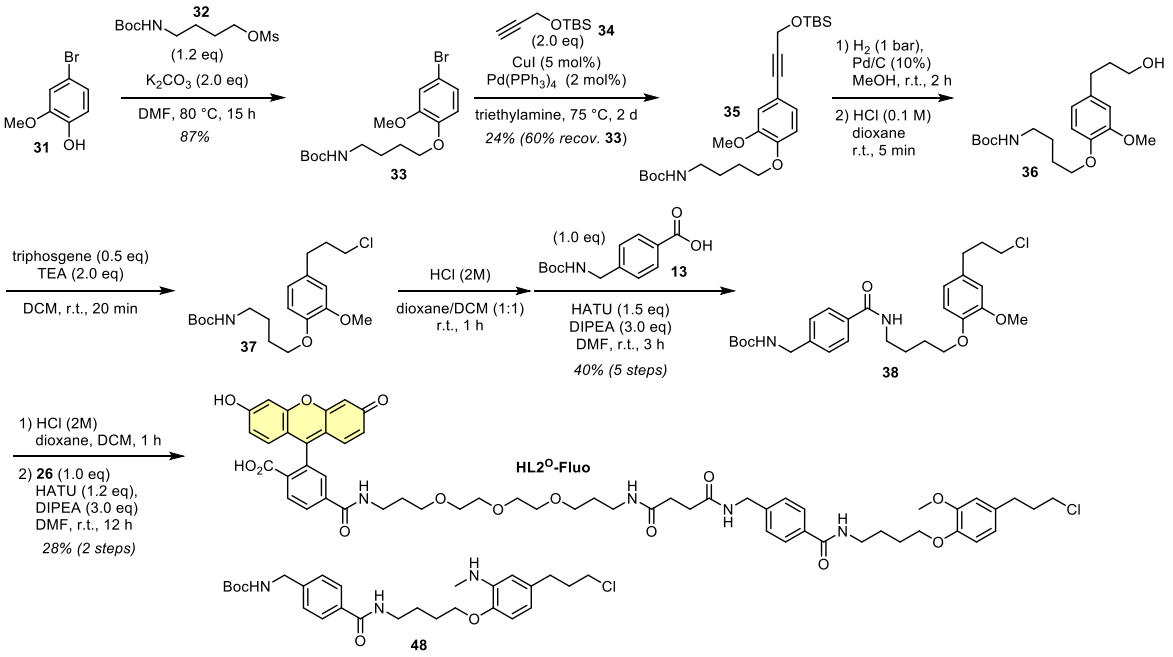

Compound **32** was prepared according to a previously described procedure (Rafiq *et al.*[90], compound 25).

Compound 33

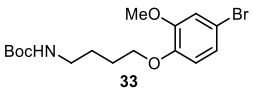

31 (1.00 g, 4.93 mmol, 1.0 eq) was dissolved in anhydrous DMF (40 mL; *Note*: the mixture becomes very viscous if too concentrated) under nitrogen atmosphere. Potassium carbonate (1.36 g, 9.86 mmol, 2.0 eq) and **32** (1.58 g, 5.92 mmol, 1.2 eq) were added and the reaction mixture heated to 80 °C for 15 h. The solvent was removed *in* vacuo, then a half-saturated solution of sodium bicarbonate (50 mL) was added and the mixture was extracted with ethyl acetate (3 × 50 mL). The organic layer was dried over sodium sulfate, the desiccant was filtered off and the solvent was removed *in vacuo*. The crude product was purified by *np*-flash column chromatography (*iso*-hexanes/ethyl acetate; 5→30% EtOAc) affording **33** (1.60 g, 4.27 mmol, 87%) as a colourless solid.

TLC *Rf* = 0.37 (*np*, Hex:EtOAc 4:1)
^{1}H-NMR (400 MHz, $CDCl_3$): *δ* (ppm) = 7.00 (dd, J = 8.5, 2.3 Hz, 1H), 6.97 (d, J = 2.3 Hz, 1H), 6.72 (d, J = 8.5 Hz, 1H), 4.81 (s, 1H), 3.99 (t, J = 6.3 Hz, 2H), 3.85 (s, 3H), 3.19 (q, J = 6.4 Hz, 2H), 1.91 – 1.81 (m, 2H), 1.67 (p, J = 7.0 Hz, 2H), 1.44 (s, 9H)
^{13}C-NMR (101 MHz, $CDCl_3$): *δ* (ppm) = 156.2, 150.2, 147.7, 123.5, 115.1, 114.2, 113.0, 79.2, 68.8, 56.2, 40.2, 28.6, 26.9, 26.4
HRMS (ESI+): m/z calc. for $C_{16}H_{24}BrNNaO_4^+$ [M+Na]$^+$: 396.0781, found: 396.0785

Compound 35

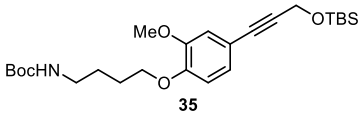

35

33 (0.55 g, 1.5 mmol, 1.0 eq) was dissolved in triethylamine under nitrogen atmosphere. The solution was degassed by bubbling nitrogen through the mixture for 10 min (ca. half solvent evaporated). Tetrakis(triphenylphosphine)palladium(0) (34 mg, 29 µmol, 2 mol%), copper iodide (14 mg, 74 µmol, 5 mol%) and TBS-propargyl alcohol **34** (commercial, 0.60 mL, 2.9 mmol, 2.0 eq) were added and the reaction mixture was heated to 75 °C for 2 d. The volatiles were removed *in vacuo*, the crude product was diluted with water (20 mL) and extracted with ethyl acetate (3 × 20 mL). The combined organic layers were dried over sodium sulfate, the desiccant was filtered off and the solvent was removed *in vacuo*. The crude product was purified by *rp*-flash column chromatography (acetonitrile/water, 0.1% formic acid; 50→100% MeCN) affording **35** (0.17 g, 0.36 mmol, 24%) as a brown oil and recovering the starting material **33** (0.33 g, 0.88 mmol, 60%).

TLC *Rf* = 0.74 (*np*, Hex:EtOAc 7:3)
^{1}H-NMR (400 MHz, $CDCl_3$): *δ* (ppm) = 7.00 (dd, J = 8.2, 1.9 Hz, 1H), 6.93 (d, J = 1.9 Hz, 1H), 6.77 (d, J = 8.3 Hz, 1H), 4.85 (s, 1H), 4.53 (s, 2H), 4.02 (t, J = 6.3 Hz, 2H), 3.84 (s, 3H), 3.19 (q, J = 6.6 Hz, 2H), 1.92 – 1.83 (m, 2H), 1.71 – 1.63 (m, 2H), 1.44 (s, 9H), 0.94 (s, 9H), 0.16 (s, 6H)
^{13}C-NMR (101 MHz, $CDCl_3$): *δ* (ppm) = 156.2, 148.9, 148.9, 125.0, 115.3, 114.7, 112.4, 86.5, 85.0, 79.1, 68.6, 56.0, 52.5, 40.2, 28.6, 26.9, 26.3, 26.0, 18.5, -4.9
HRMS (ESI+): m/z calc. for $C_{25}H_{41}NNaO_5Si^+$ [M+Na]$^+$: 486.2646, found: 486.2642

Compound 38

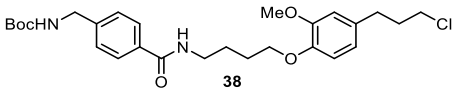

38

38 was prepared in five synthetic steps without purification of the intermediate products.

35 (82 mg, 0.18 mmol, 1.0 eq) was dissolved in methanol (3 mL) under nitrogen atmosphere, palladium on charcoal (Pd/C, 21 mg, 18 µmol, 10 mol%) was added and the reaction was stirred under hydrogen atmosphere (1 atm) for 2 h. The Pd/C was removed by filtration over Celite (washed with methanol (3×) and ethyl acetate (3×)), the filtrate was concentrated under reduce pressure, redissolved in dioxane (0.1 M HCl, 3 mL) and stirred at room temperature for 5 min for selective TBS-deprotection. The crude product was semi-purified by *np*-flash column chromatography (*iso*-hexanes/ethyl acetate; 20→80% EtOAc) to give **36** (40 mg, ca. 64% over 2 steps).

Alcohol **36** was converted to the alkyl chloride **37** adapting a previously described protocol by Ayala *et al.*[91] **36** was dissolved in anhydrous DCM (1 mL) under nitrogen atmosphere and triethylamine (31 µL, 0.23 mmol, 2.0 eq) was added. A solution of triphosgene (17 mg, 57 µmol, 0.5 eq) in anhydrous DCM (0.4 mL) was added dropwise and the reaction mixture was stirred at room temperature for 20 min. The mixture was diluted with a half-saturated solution of sodium bicarbonate (20 mL) and extracted with DCM (3 × 15 mL) to give **37**.

37 was Boc-deprotected according to General Procedure A (0.11 M) and coupled with carboxylate **13** (29 mg, 0.11 mmol, 1.0 eq, 0.11 M) following General Procedure B (1.1 eq HATU, 3 h reaction time). The crude product was purified by *np*-flash column chromatography (*iso*-hexanes/ethyl acetate; 20→70% EtOAc) to give **38** (36 mg, 71 µmol, 40% over 5 steps) as a colourless solid.

TLC *Rf* = 0.50 (*np*, Hex:EtOAc 1:2)
^{1}H-NMR (400 MHz, $CDCl_3$): *δ* (ppm) = 7.76 (d, J = 8.1 Hz, 2H), 7.28 (d, J = 8.1 Hz, 2H), 7.10 – 7.05 (m, 1H), 6.79 (d, J = 8.0 Hz, 1H), 6.74 – 6.68 (m, 2H), 5.04 (s, 1H), 4.32 (d, J = 5.7 Hz, 2H), 4.04 (t, J = 5.7 Hz, 2H), 3.70 (s, 3H), 3.56 – 3.48 (m, 4H), 2.71 (t, J = 7.4 Hz, 2H), 2.09 – 2.00 (m, 2H), 1.92 (p, J = 6.2 Hz, 2H), 1.82 (p, J = 6.6 Hz, 2H), 1.45 (s, 9H)
^{13}C-NMR (101 MHz, $CDCl_3$): *δ* (ppm) = 167.4, 156.0, 149.1, 146.5, 142.5, 133.8, 133.6, 127.4, 127.3, 120.6, 112.6, 112.0, 79.8, 68.7, 55.7, 44.3, 44.3, 39.3, 34.2, 32.4, 28.5, 26.6, 26.1
HRMS (ESI+): m/z calc. for $C_{27}H_{38}ClN_2O_5^+$ [M+H]$^+$: 505.2464, found: 505.2458

HL2^{O}-Fluo

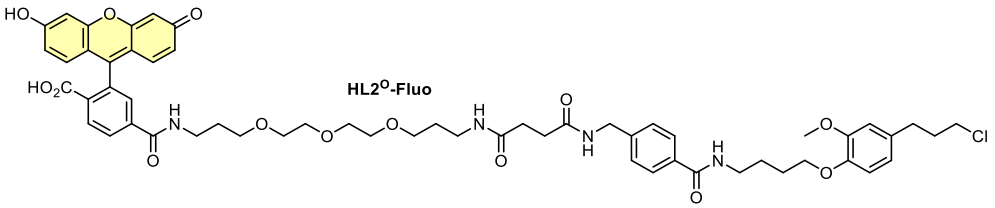

38 (5.5 mg, 11 µmol, 1.0 eq) was deprotected according to General Procedure A (0.02 M) and coupled with carboxylate **26** (7.6 mg, 11 µmol, 1.0 eq, 0.02 M) following General Procedure B (1.1 eq HATU, 12 h reaction time). The crude product was purified by preparative HPLC (acetonitrile/water, 0.1% formic acid; 10→75% MeCN, 20 min) affording **HL2^{O}-Fluo** (3.3 mg, 3.1 µmol, 29% over 2 steps) as an orange solid.

TLC *Rf* = 0.41 (*rp*, 50% MeCN); *Rf* = 0.19 (*np*, DCM:MeOH 9:1)
^{1}H-NMR (800 MHz, DMSO-d_6): *δ* (ppm) = 10.18 (s, br, 2H), 8.65 (t, J = 5.6 Hz, 1H), 8.43 (t, J = 5.6 Hz, 1H), 8.38 (t, J = 6.0 Hz, 1H), 8.15 (dd, J = 8.1, 1.1 Hz, 1H), 8.07 (d, J = 8.1 Hz, 1H), 7.81 – 7.76 (m, 3H), 7.66 (s, 1H), 7.30 (d, J = 8.3 Hz, 2H), 6.84 (d, J = 8.2 Hz, 1H), 6.80 (d, J = 1.9 Hz, 1H), 6.68 (d, J = 8.1 Hz, 3H), 6.59 (d, J = 8.7 Hz, 2H), 6.55 (dd, J = 8.7, 2.0 Hz, 2H), 4.29 (d, J = 5.9 Hz, 2H), 3.92 (t, J = 6.4 Hz, 2H), 3.73 (s, 3H), 3.60 (t, J = 6.5 Hz, 2H), 3.46 – 3.44 (m, 4H), 3.44 – 3.40 (m, 4H), 3.38 (t, J = 6.2 Hz, 2H), 3.37 – 3.33 (m, 2H), 3.30 (q, J = 6.8 Hz, 2H), 3.24 (q, J = 6.6 Hz, 2H), 3.05 (q, J = 6.8 Hz, 2H), 2.64 – 2.61 (m, 2H), 2.37 (t, J = 7.2 Hz, 2H), 2.31 (t, J = 7.2 Hz, 2H), 2.00 – 1.96 (m, 2H), 1.73 (dt, J = 14.6, 6.5 Hz, 2H), 1.67 (dp, J = 21.7, 6.7 Hz, 4H), 1.57 (p, J = 6.6 Hz, 2H)
^{13}C-NMR (201 MHz, DMSO-d_6): *δ* (ppm) = 171.5, 171.1, 168.1, 165.9, 164.4, 159.9, 152.4, 151.9, 149.0, 146.4, 142.8, 140.6, 133.2, 133.1, 129.3, 129.3, 128.5, 127.1, 126.8, 125.0, 122.3, 120.1, 113.3, 112.9, 112.4, 109.3, 102.3, 84.4, 69.7, 69.7, 69.5, 69.5, 68.2, 68.0, 68.0, 55.4, 44.8, 41.7, 38.8, 36.9, 35.8, 33.9, 31.8, 30.8, 30.7, 29.3, 29.1, 26.4, 25.9
HRMS (ESI+): m/z calc. for $C_{57}H_{66}ClN_4O_{14}^+$ $[M+H]^+$: 1065.426, found: 1065.424

Synthetic route for HL2^{N}-Fluo

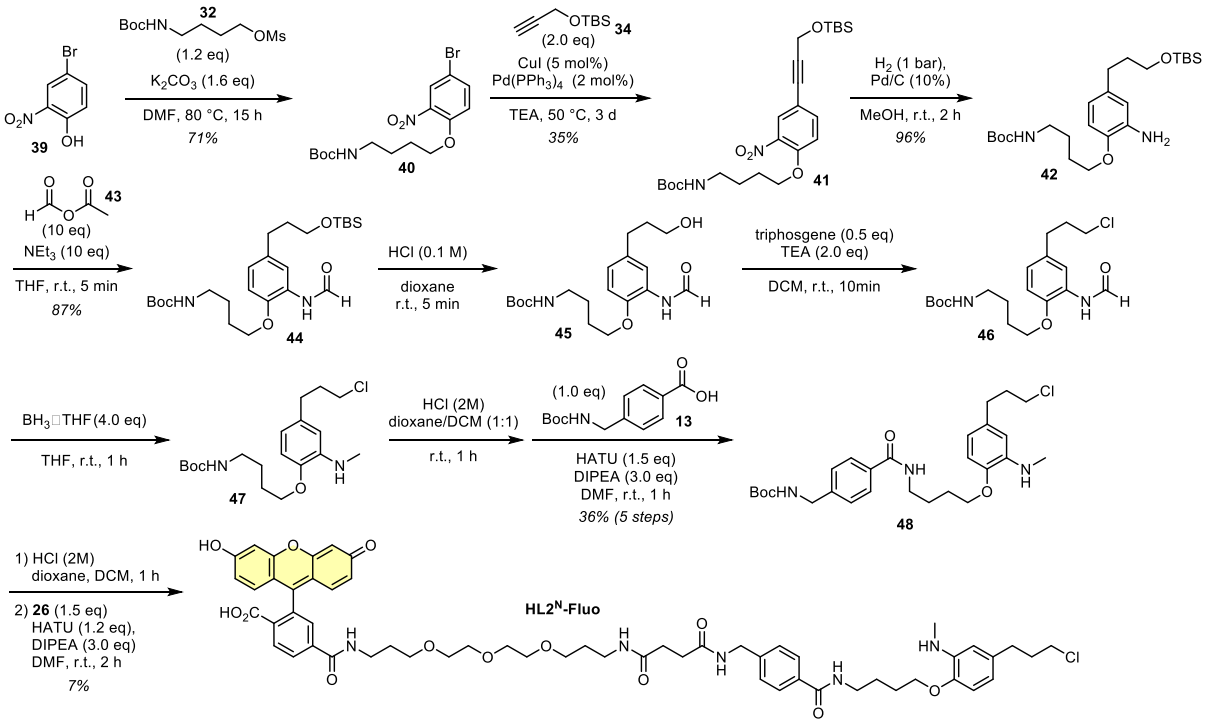

Compound 40

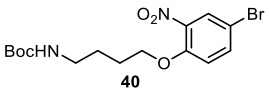

39 (1.50 g, 6.88 mmol, 1.0 eq) was dissolved in anhydrous DMF (40 mL; *Note*: the mixture becomes very viscous if too concentrated) under nitrogen atmosphere. Potassium carbonate (1.90 g, 13.8 mmol, 2.0 eq) and mesylate **32** (2.21 g, 8.26 mmol, 1.2 eq) were added and the reaction mixture was heated to 80 °C for 15 h. The solvent was removed *in* vacuo, then a half-saturated solution of sodium bicarbonate (50 mL) was

added and the mixture was extracted with ethyl acetate (3 × 50 mL). The organic layer was dried over sodium sulfate, the desiccant was filtered off and the solvent was removed *in vacuo*. The crude product was purified by *np*-flash column chromatography (*iso*-hexanes/ethyl acetate; 5→35% EtOAc) affording **40** (1.26 g, 3.24 mmol, 71%) as a light-yellow solid.

TLC *Rf* = 0.18 (*np*, Hex:EtOAc 4:1)
^{1}H-NMR (400 MHz, $CDCl_3$): *δ* (ppm) = 7.95 (d, J = 2.5 Hz, 1H), 7.60 (dd, J = 8.9, 2.5 Hz, 1H), 6.96 (d, J = 9.0 Hz, 1H), 4.63 (s, 1H), 4.10 (t, J = 6.1 Hz, 2H), 3.18 (q, J = 6.7 Hz, 2H), 1.90 – 1.81 (m, 2H), 1.73 – 1.64 (m, 2H), 1.43 (s, 9H)
^{13}C-NMR (101 MHz, $CDCl_3$): *δ* (ppm) = 156.2, 151.6, 140.3, 136.9, 128.4, 116.2, 111.8, 79.3, 69.5, 40.0, 28.5, 26.6, 26.2
HRMS (ESI+): m/z calc. for $C_{15}H_{21}BrN_2NaO_5^+$ [M+Na]$^+$: 411.0526, found: 411.0528

Compound 41

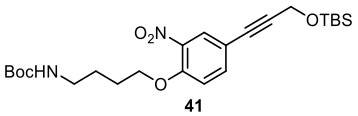

41

40 (1.00 g, 2.57 mmol, 1.0 eq) was dissolved in triethylamine under nitrogen atmosphere. The solution was degassed by bubbling nitrogen through the mixture for 10 min (ca. half solvent evaporated). Tetrakis(triphenylphosphine)palladium(0) (59 mg, 51 µmol, 2 mol%), copper iodide (25 mg, 0.13 mmol, 5 mol%) and TBS-propargyl alcohol **34** (commercial, 1.04 mL, 5.14 mmol, 2.0 eq) were added and the reaction mixture was heated to 50 °C for 3 d. The volatiles were removed *in vacuo*, the crude product was diluted with water (40 mL) and extracted with ethyl acetate (3 × 25 mL). The combined organic layers were dried over sodium sulfate, the desiccant was filtered off and the solvent was removed *in vacuo*. The crude product was purified by *rp*-flash column chromatography (acetonitrile/water, 0.1% formic acid; 50→100% MeCN) affording **41** (0.44 g, 0.91 mmol, 36%) as a brown oil.

TLC *Rf* = 0.59 (*np*, Hex:EtOAc 7:3)
^{1}H-NMR (400 MHz, $CDCl_3$): *δ* (ppm) = 7.88 (d, J = 2.1 Hz, 1H), 7.55 (dd, J = 8.7, 2.1 Hz, 1H), 6.99 (d, J = 8.8 Hz, 1H), 4.63 (s, 1H), 4.52 (s, 2H), 4.12 (t, J = 6.1 Hz, 2H), 3.19 (q, J = 6.7 Hz, 2H), 1.92 – 1.82 (m, 2H), 1.74 – 1.65 (m, 2H), 1.43 (s, 9H), 0.93 (s, 9H), 0.16 (s, 6H)
^{13}C-NMR (101 MHz, $CDCl_3$): *δ* (ppm) = 156.2, 152.2, 139.6, 137.2, 128.8, 115.5, 114.4, 88.7, 82.3, 79.4, 69.4, 52.3, 40.1, 28.5, 26.7, 26.2, 26.0, 18.5, -4.9
HRMS (ESI+): m/z calc. for $C_{24}H_{38}N_2NaO_6Si^+$ [M+Na]$^+$: 501.2391, found: 501.2387

Compound 42

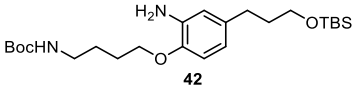

42

41 (0.40 g, 0.84 mmol, 1.0 eq) was dissolved in methanol (3 mL) under nitrogen atmosphere, palladium on charcoal (Pd/C, 50 mg, 42 µmol, 10 mol%) was added and the reaction was stirred under hydrogen atmosphere (1 atm) for 2.5 h. The Pd/C was removed by filtration over Celite (washed with methanol (3×) and ethyl acetate (3×)), the volatiles were removed *in vacuo* giving **42** (0.36 g, 0.80 mmol, 96%) as a colourless oil.

TLC *Rf* = 0..52 (*np*, Hex:EtOAc 2:1)
^{1}H-NMR (400 MHz, $CDCl_3$): *δ* (ppm) = 6.68 (d, J = 8.2 Hz, 1H), 6.58 (s, 1H), 6.53 (d, J = 8.1 Hz, 1H), 4.58 (s, 1H), 3.98 (t, J = 6.2 Hz, 2H), 3.61 (t, J = 6.4 Hz, 2H), 3.19 (q, J = 6.7 Hz, 2H), 2.56 – 2.50 (m, 2H), 1.87 – 1.73 (m, 4H), 1.72 – 1.62 (m, 2H), 1.44 (s, 9H), 0.90 (s, 9H), 0.05 (s, 6H)
^{13}C-NMR (101 MHz, $CDCl_3$): *δ* (ppm) = 145.0, 135.2, 118.5, 115.8, 111.6, 79.3, 68.0, 62.6, 40.5, 34.8, 31.6, 28.6, 27.1, 26.8, 26.1, 18.5, -5.1
HRMS (ESI+): m/z calc. for $C_{24}H_{45}N_2O_4Si^+$ [M+H]$^+$: 453.3143, found: 453.3137

Compound 44

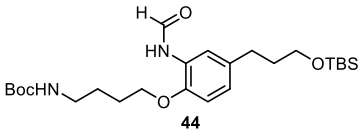

44

Adaptation from previously described procedure.[92] First, mixed anhydride **43** was prepared: Formic acid (0.17 mL, 4.5 mmol, 1.5 eq) and acetic anhydride (0.28 mL, 3.0 mmol, 1.0 eq) were heated to 50 °C for 2.5 h to form the mixed anhydride.

In a separate flask, **42** (90 mg, 0.20 mmol, 1.0 eq) was dissolved in anhydrous THF (3 mL), triethylamine (0.28 mL, 2.0 mmol, 10 eq) and **43** (0.16 mL, 2.0 mmol, 10 eq) were added and the reaction was stirred at room temperature for 1 h. The volatiles were removed *in vacuo*, the crude product was diluted with a half-saturated solution of sodium bicarbonate (20 mL) and the mixture was extracted with ethyl acetate (3 × 15 mL). The organic layer was dried over sodium sulfate, the desiccant was filtered off and the solvent was removed *in vacuo*. The crude product was purified by *np*-flash column chromatography (*iso*-hexanes/ethyl acetate; 10→50% EtOAc) affording **44** (83 mg, 0.17 mmol, 87%) as a light-red oil.

Note: the product might partially TBS-deprotected during silica column chromatography.

TLC *Rf* = 0.32 (*np*, Hex:EtOAc 2:1)
^{1}H-NMR (400 MHz, $CDCl_3$), *rotamers observed*: *δ* (ppm) = 8.73 (d, J = 11.7 Hz, 0.2H), 8.50 (d, J = 1.4 Hz, 0.6H), 8.38 (s, 0.5H), 8.25 (d, J = 1.7 Hz, 0.6H), 8.16 (s, 0.1H), 7.68 (d, J = 10.8 Hz, 0.2H), 7.12 – 7.01 (m, 0.4H), 6.95 – 6.89 (m, 0.3H), 6.86 (dd, J = 8.2, 1.8 Hz, 0.7H), 6.81 (d, J = 8.4 Hz, 0.3H), 6.77 (d, J = 8.3 Hz, 0.7H), 4.59 (s, 1H), 4.01 (dt, J = 20.9, 6.3 Hz, 2H), 3.62 (t, J = 6.4 Hz, 2H), 3.31 – 3.13 (m, 2H), 2.64 – 2.58 (m, 2H), 1.89 – 1.75 (m, 4H), 1.67 (dq, J = 12.8, 6.7 Hz, 2H), 1.44 (s, 9H), 0.90 (s, 9H), 0.05 (s, 6H)
HRMS (ESI−): m/z calc. for $C_{25}H_{43}N_2O_5Si^-$ $[M-H]^-$: 479.2947, found: 479.2945

Compound 48

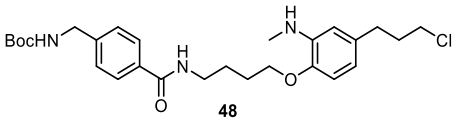

48

48 was prepared in five synthetic steps without purification of the intermediate products.

44 (53 mg, 0.11 mmol, 1.0 eq) dissolved in dioxane with HCl (0.1 M HCl, 2 mL) and stirred at room temperature for 5 min for selective TBS-deprotection. The volatiles were removed *in vacuo* and the crude product was diluted with a half-saturated solution of sodium bicarbonate (20 mL) and extracted with ethyl acetate (3 × 15 mL) affording alcohol **45** which was used without further purification.

Alcohol **45** was converted to the alkyl chloride **46** adapting a previously described protocol by Ayala *et al.*[91] **45** was dissolved in anhydrous DCM (1 mL) under nitrogen atmosphere and triethylamine (30 µL, 0.22 mmol, 2.0 eq) was added. A solution of triphosgene (16 mg, 55 µmol, 0.5 eq) in anhydrous DCM (0.4 mL) was added dropwise and the reaction mixture was stirred at room temperature for 20 min. The mixture was diluted with a half-saturated solution of sodium bicarbonate (20 mL) and extracted with DCM (3 × 15 mL). The organic layer was dried over sodium sulfate and the solvent was removed *in vacuo* to give **46** which was used without further purification.

46 was dissolved in anhydrous THF (3 mL) under nitrogen atmosphere and cooled to 0 °C. Borane-tetrahydrofuane complex (1 M in THF, 0.44 mL, 0.44 mmol, 4.0 eq) was added and the reaction mixture was stirred at room temperature for 1 h. Citric acid (0.12 g, 0.55 mmol, 5.0 eq) was dissolved in water (2 mL) and added to the reaction mixture dropwise to quench the excess of the borane. The resulting mixture was diluted with water (20 mL), a saturated solution of bicarbonate (5 mL) and extracted with ethyl acetate (3 × 15 mL). The organic layer was dried over sodium sulfate and the solvent was removed *in vacuo* to give **47** which was used without further purification.

47 was deprotected according to General Procedure A (0.09 M) and coupled with carboxylate **13** (28 mg, 0.11 mmol, 1.0 eq, 0.09 M) following General Procedure B (1.1 eq HATU, 2 h reaction time). The crude product was purified by flash column chromatography (*iso*-hexanes/ethyl acetate; 20→70% EtOAc) to give **48** (16 mg, 32 µmol, 36% over 5 steps) as a colourless solid.

TLC *Rf* = 0.54 (*np*, Hex:EtOAc 1:2); *Rf* = 0.76 (*np*, DCM:MeOH 9:1)
^{1}H-NMR (400 MHz, $CDCl_3$): *δ* (ppm) = 7.69 (d, J = 8.2 Hz, 2H), 7.30 (d, J = 8.2 Hz, 2H), 6.66 (d, J = 8.0 Hz, 1H), 6.46 (dd, J = 8.0, 2.0 Hz, 1H), 6.43 (d, J = 2.0 Hz, 1H), 6.35 – 6.27 (m, 1H), 4.99 – 4.90 (m, 1H), 4.34 (d, J = 5.8 Hz, 2H), 4.01 (t, J = 5.9 Hz, 2H), 3.57 – 3.49 (m, 4H), 2.85 (s, 3H), 2.69 (t, J = 7.3 Hz, 2H), 2.10 – 2.02 (m, 2H), 1.89 (dq, J = 10.7, 5.9 Hz, 2H), 1.81 (dt, J = 13.5, 6.2 Hz, 2H), 1.46 (s, 9H)
^{13}C-NMR (101 MHz, $CDCl_3$): *δ* (ppm) = 167.4, 156.0, 144.6, 142.7, 139.3, 133.8, 133.7, 127.5, 127.3, 116.3, 110.3, 110.1, 79.9, 67.9, 44.6, 44.4, 39.9, 34.5, 32.7, 30.6, 28.5, 26.9, 26.8
HRMS (ESI+): m/z calc. for $C_{27}H_{39}ClN_3O_4^+$ $[M+H]^+$: 504.2624, found: 504.2617

HL2^N-Fluo

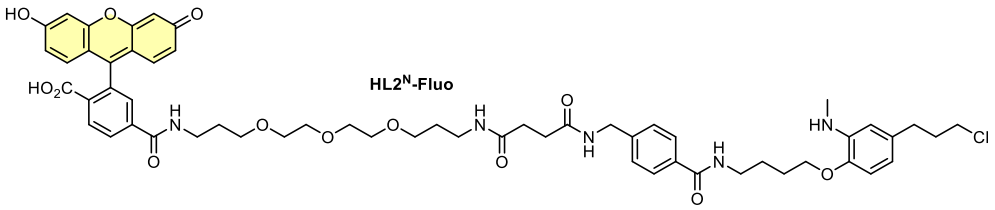

48 (8.0 mg, 16 µmol, 1.0 eq) was deprotected according to General Procedure A (0.02 M) and coupled with carboxylate **26** (16 mg, 24 µmol, 1.5 eq, 0.04 M) following General Procedure B (1.1 eq HATU, 3 h reaction time). The crude product was purified by preparative HPLC (acetonitrile/water, 0.1% formic acid; 10→50% MeCN, 20 min) affording **HL2^N-Fluo** (1.2 mg, 1.2 µmol, 7% over 2 steps) as an orange solid.

^{1}H-NMR (400 MHz, DMSO-d$_6$): δ (ppm) = 8.64 (t, *J* = 5.4 Hz, 1H), 8.49 – 8.39 (m, 2H), 8.13 (d, *J* = 8.9 Hz, 1H), 8.07 (d, *J* = 8.1 Hz, 1H), 7.81 (dd, *J* = 16.3, 6.9 Hz, 3H), 7.65 (s, 1H), 7.30 (d, *J* = 8.3 Hz, 2H), 6.67 (d, *J* = 8.0 Hz, 1H), 6.61 (d, *J* = 8.8 Hz, 3H), 6.51 (d, *J* = 8.0 Hz, 2H), 6.33 (dd, *J* = 7.9, 2.0 Hz, 1H), 6.31 (d, *J* = 1.9 Hz, 1H), 4.89 – 4.84 (m, 1H), 4.29 (d, *J* = 5.9 Hz, 2H), 3.93 (t, *J* = 6.0 Hz, 2H), 3.60 (t, *J* = 6.5 Hz, 2H), 3.51 – 3.38 (m, 16H), 3.28 – 3.22 (m, 4H), 3.05 (q, *J* = 6.8 Hz, 2H), 2.70 (d, *J* = 4.8 Hz, 2H), 2.60 – 2.55 (m, 2H), 2.42 – 2.36 (m, 2H), 2.33 (d, *J* = 5.8 Hz, 3H), 1.97 (dt, *J* = 13.7, 6.6 Hz, 2H), 1.73 (dq, *J* = 19.8, 6.6 Hz, 6H), 1.58 (p, *J* = 6.6 Hz, 2H)
HRMS (ESI+): m/z calc. for $C_{57}H_{67}ClN_5O_{13}^+$ [M+H]$^+$: 1064.442, found: 1064.441.

Synthetic route for Cou-HL2^N-Fluo

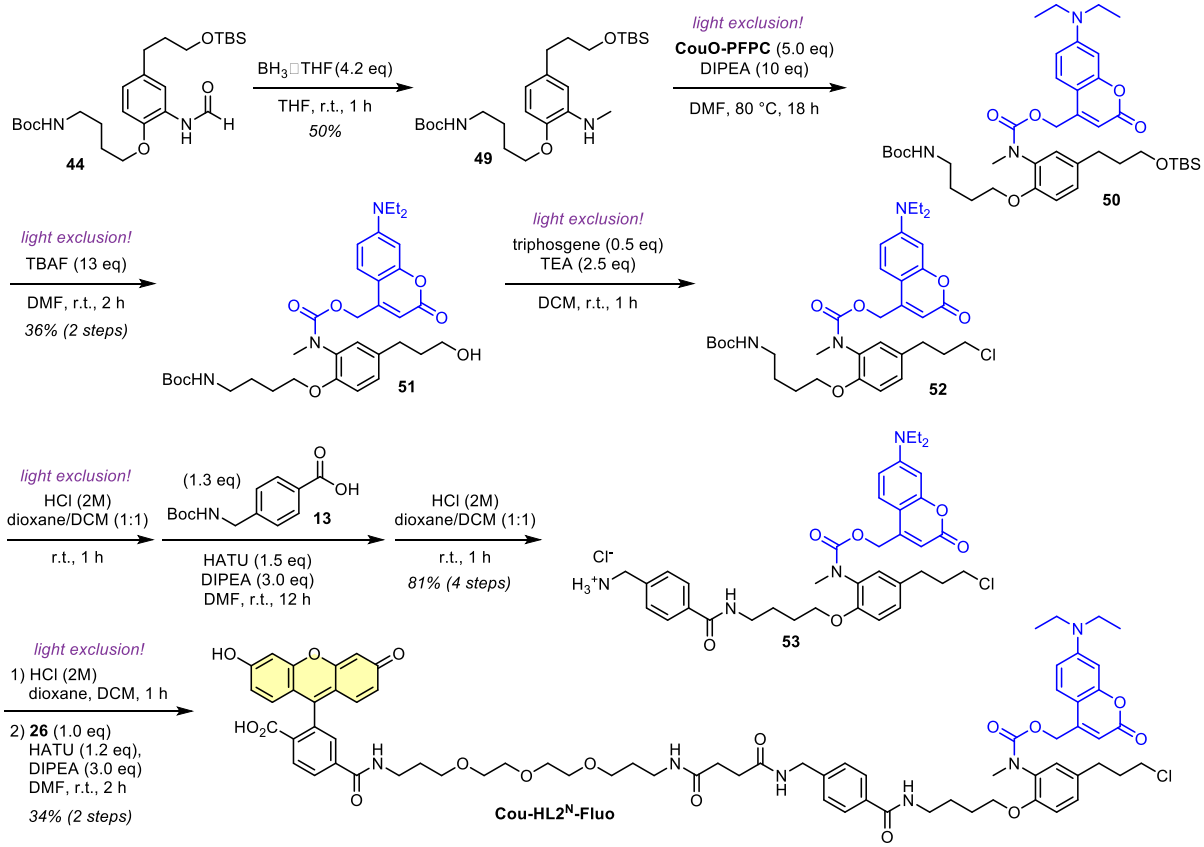

Compound 49

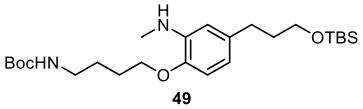

44 (40 mg, 83 µmol, 1.0 eq) was dissolved in anhydrous THF (1.5 mL) under nitrogen atmosphere and cooled to 0 °C. Borane-tetrahydrofuane complex (1 M in THF, 0.35 mL, 0.35 mmol, 4.2 eq) was added and the reaction mixture was stirred at room temperature for 1 h. Citric acid (87 g, 0.42 mmol, 5.0 eq) was dissolved in water (1 mL) and added to the reaction mixture dropwise to quench the excess of the borane. The resulting mixture was diluted with water (20 mL), a saturated solution of bicarbonate (5 mL) and extracted with ethyl

acetate (3 × 15 mL). The organic layer was dried over sodium sulfate, the desiccant was filtered off and the solvent was removed *in vacuo*. The crude product was purified by flash column chromatography (*iso*-hexanes/ethyl acetate; 5→30% EtOAc) to give **49** (19 mg, 41 µmol, 50%) as a colourless oil.

TLC *Rf* = 0.47 (*np*, Hex:EtOAc 3:1)
^{1}H-NMR (400 MHz, $CDCl_3$): *δ* (ppm) = 6.64 (d, J = 7.8 Hz, 1H), 6.48 – 6.43 (m, 2H), 4.58 (s, 1H), 3.97 (t, J = 6.2 Hz, 2H), 3.64 (t, J = 6.4 Hz, 2H), 3.19 (q, J = 6.7 Hz, 2H), 2.86 (s, 3H), 2.62 – 2.54 (m, 2H), 1.86 – 1.77 (m, 4H), 1.70 – 1.61 (m, 2H), 1.44 (s, 9H), 0.91 (s, 9H), 0.06 (s, 6H)
^{13}C-NMR (101 MHz, $CDCl_3$): *δ* (ppm) = 156.1, 144.5, 139.3, 135.4, 116.0, 110.2, 110.1, 79.3, 67.9, 62.8, 40.5, 34.9, 32.0, 30.6, 28.6, 27.1, 26.8, 26.1, 18.5, -5.1
HRMS (ESI+): m/z calc. for $C_{25}H_{47}N_2O_4Si^+$ $[M+H]^+$: 467.3300, found: 467.3296

Compound 51

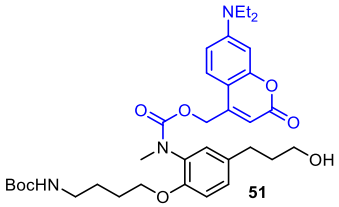

Note: the reaction must be performed under light exclusion.

49 (25 mg, 54 µmol, 1.0 eq) was dissolved in anhydrous DMF (1 mL) and transformed to **50** following General Procedure D (0.05 M) which was TBS-deprotected by addition of tetrabutylammonium fluoride (1 M in THF, 0.70 mL, 0.70 mmol, 13 eq) into the reaction mixture. The mixture was diluted with water (20 mL) and extracted with ethyl acetate (4 × 15 mL). The organic layer was washed with brine (30 mL), dried over sodium sulfate and the volatiles were removed *in vacuo*. The crude product was purified by reversed-phase flash column chromatography (acetonitrile/water, 0.1% formic acid; 20→90% MeCN) affording **51** (12 mg, 19 µmol, 36% over 2 steps) as a yellow solid.

TLC *Rf* = 0.33 (*np*, Hex:EtOAc 1:2); *Rf* = 0.65 (*np*, DCM:MeOH 9:1)
HRMS (ESI+): m/z calc. for $C_{34}H_{48}N_3O_8^+$ $[M+H]^+$: 626.3436, found: 626.3438.

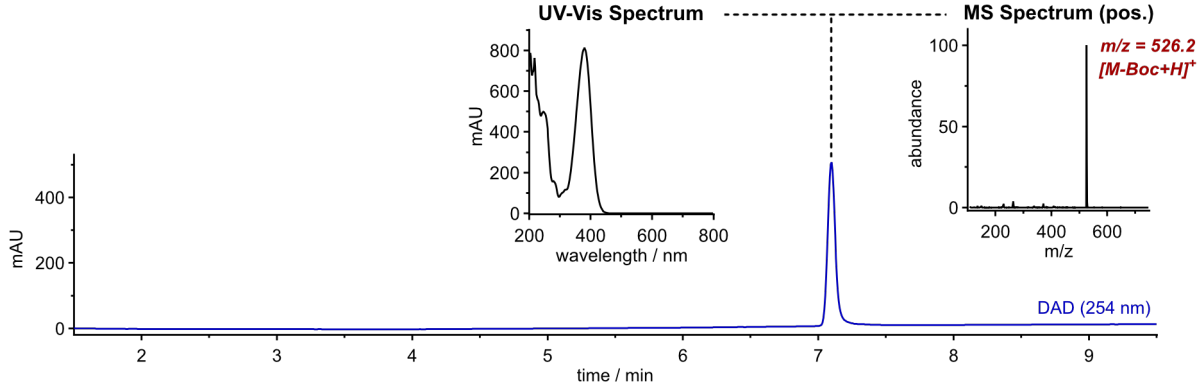

Compound 53

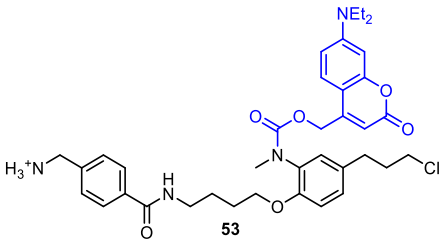

Note: the reaction must be performed under light exclusion.

Alcohol **51** was converted to the alkyl chloride **52** adapting a previously described protocol by Ayala *et al.*[91] **51** (12 mg, 19 µmol, 1.0 eq) was dissolved in anhydrous DCM (2 mL) under nitrogen atmosphere and triethylamine (6.7 µL, 48 µmol, 2.5 eq) was added. A solution of triphosgene (2.9 mg, 9.6 µmol, 0.5 eq) in anhydrous DCM (0.1 mL) was added dropwise and the reaction mixture was stirred at room temperature for 20 min. The mixture was diluted with a half-saturated solution of sodium bicarbonate (20 mL) and extracted with DCM (3 × 15 mL). The organic layer was dried over sodium sulfate and the solvent was removed *in vacuo* to give **52** which was used without further purification.

52 was deprotected according to General Procedure A (0.02 M) and coupled with carboxylate **13** (6.4 mg, 25 µmol, 1.3 eq, 0.02 M) following General Procedure B (1.1 eq HATU, 2 h reaction time). The crude product was purified by *np*-flash column chromatography (*iso*-hexanes/ethyl acetate; 30→80% EtOAcwhich was directly converted to **53** following General Procedure A (0.02 M) affording the product (11 mg, 15 µmol, 81% over 4 steps) as a colourless solid.

LRMS (ESI+): m/z calc. for $C_{37}H_{46}ClN_4O_6^+$ [M+H]$^+$: 677.3, found: 677.3.

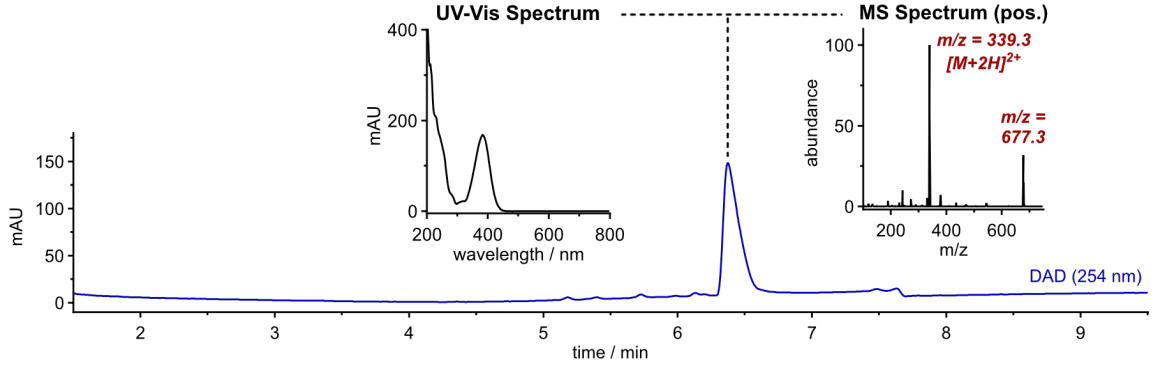

HL2^N-Fluo

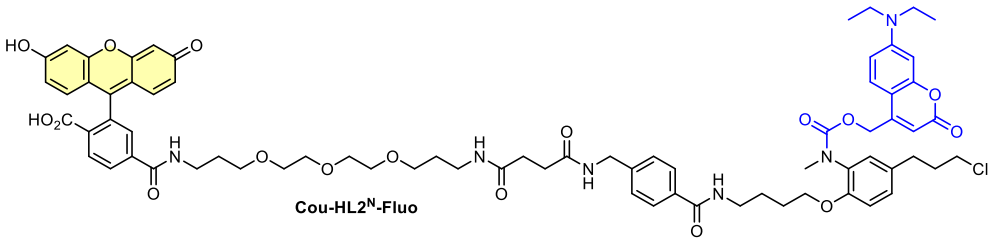

Note: the reaction must be performed under light exclusion.

53 (11 mg, 15 µmol, 1.0 eq) coupled with carboxylate **2** (11 mg, 15 µmol, 1.0 eq, 0.03 M) following General Procedure B (1.1 eq HATU, 12 h reaction time). The crude product was purified by preparative HPLC (acetonitrile/water, 0.1% formic acid; 20→85% MeCN, 20 min) affording **Cou-HL2^N-Fluo** (7.1 mg, 5.3 µmol, 34% over 2 steps) as an orange solid.

TLC *Rf* = 0.19 (*rp*, 50% MeCN); *Rf* = 0.27 (*np*, DCM:MeOH 9:1)

^{1}H-NMR (800 MHz, DMSO-d_6): *δ* (ppm) = 10.21 (s, 2H), 8.66 (t, J = 5.5 Hz, 1H), 8.42 (t, J = 5.3 Hz, 1H), 8.38 (t, J = 5.7 Hz, 1H), 8.16 (d, J = 8.1 Hz, 1H), 8.07 (d, J = 8.1 Hz, 1H), 7.80 (t, J = 5.4 Hz, 1H), 7.76 (d, J = 8.1 Hz, 2H), 7.67 (s, 1H), 7.30 (dd, J = 12.9, 8.6 Hz, 3H), 7.15 – 7.09 (m, 2H), 7.03 (d, J = 8.3 Hz, 1H), 6.69 (s, 2H), 6.62 – 6.57 (m, 3H), 6.56 (d, J = 7.1 Hz, 2H), 6.50 (s, 1H), 5.67 (s, 1H), 5.34 – 5.13 (m, 2H), 4.29 (d, J = 5.6 Hz, 2H), 4.01 (t, J = 6.2 Hz, 2H), 3.59 (t, J = 6.4 Hz, 2H), 3.49 – 3.45 (m, 4H), 3.45 – 3.34 (m, 12H), 3.30 – 3.27 (m, 2H), 3.27 – 3.23 (m, 2H), 3.12 (s, 3H), 3.06 (q, J = 6.6 Hz, 2H), 2.67 – 2.62 (m, 2H), 2.38 (t, J = 7.2 Hz, 2H), 2.32 (t, J = 7.2 Hz, 2H), 1.98 (p, J = 6.6 Hz, 2H), 1.74 (s, 2H), 1.69 (p, J = 6.6 Hz, 2H), 1.66 – 1.61 (m, 2H), 1.58 (p, J = 6.6 Hz, 2H), 1.11 (t, J = 6.9 Hz, 6H)

^{13}C-NMR (201 MHz, DMSO-d_6): *δ* (ppm) = 171.5, 171.1, 168.1, 165.9, 164.4, 160.6, 159.9, 155.7, 154.5, 152.5, 152.2, 151.9, 151.4, 150.3, 142.7, 140.6, 133.1, 132.9, 130.6, 129.3, 129.3, 128.6, 128.6, 127.1, 126.8, 125.2, 125.0, 122.3, 113.0, 113.0, 112.9, 109.3, 108.5, 105.1, 104.1, 102.3, 96.8, 82.8, 69.7, 69.7, 69.5, 69.5, 68.2, 68.0, 67.6, 62.1, 44.7, 44.0, 41.7, 38.8, 37.3, 36.9, 35.8, 33.6, 31.1, 30.8, 30.7, 29.3, 29.1, 26.2, 25.8, 12.3

HRMS (ESI+): m/z calc. for $C_{72}H_{82}ClN_6O_{17}^+$ [M+H]$^+$: 1337.542, found: 1337.539.

Synthetic route for HL3-Fluo

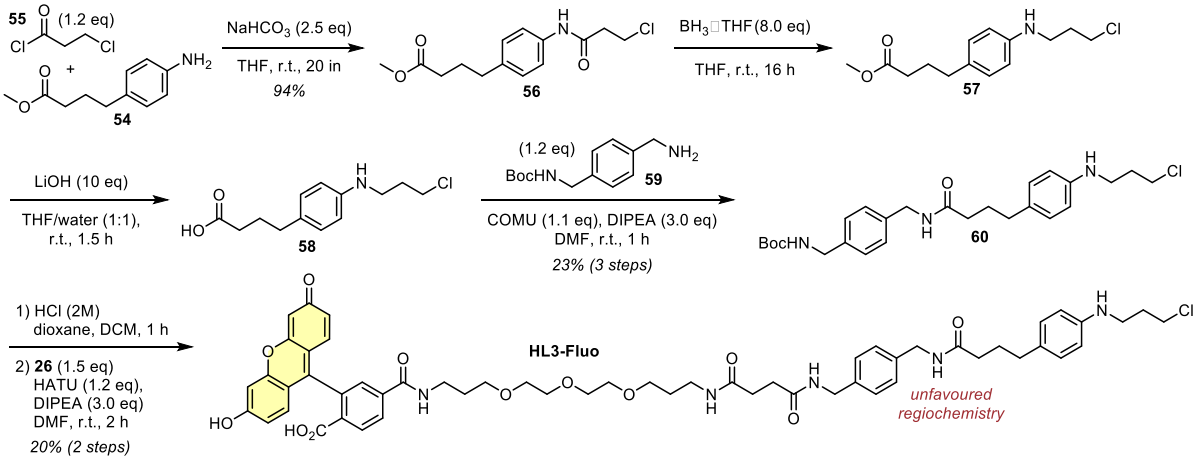

Compound 56

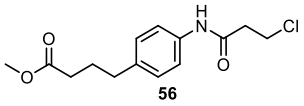

Methyl 4-(4-aminophenyl)butanoate (**54**, 50 mg, 0.26 mmol, 1.0 eq) was dissolved in anhydrous THF. Sodium bicarbonate (54 mg, 0.65 mmol, 2.5 eq) and 3-chloropropionyl chloride (**55**, 30 µL, 0.31 mmol, 1.2 eq) were added and the reaction mixture was stirred at room temperature for 20 min. The mixture was diluted with a half-saturated solution of sodium bicarbonate (20 mL) and extracted with ethyl acetate (3 × 15 mL). The organic layer was washed with brine (30 mL), dried over sodium sulfate and the solvent was removed *in vacuo* affording **56** (69 mg, 0.24 mmol, 94%) as a colourless solid.

TLC *Rf* = 0.25 (*np*, Hex:EtOAc 3:1)
^{1}H-NMR (400 MHz, $CDCl_3$): *δ* (ppm) = 7.43 (d, J = 8.4 Hz, 2H), 7.28 (s, 1H), 7.14 (d, J = 8.4 Hz, 2H), 3.88 (t, J = 6.4 Hz, 2H), 3.66 (s, 3H), 2.80 (t, J = 6.4 Hz, 2H), 2.62 (t, J = 7.6 Hz, 2H), 2.32 (t, J = 7.5 Hz, 2H), 1.93 (p, J = 7.5 Hz, 2H).
^{13}C-NMR (101 MHz, $CDCl_3$): *δ* (ppm) = 174.1, 167.7, 138.0, 135.5, 129.2, 120.3, 51.7, 40.7, 40.1, 34.6, 33.4, 26.6.
HRMS (ESI+): m/z calc. for $C_{14}H_{19}ClNO_3^+$ $[M+H]^+$: 284.1048, found: 284.1051

Compound 60

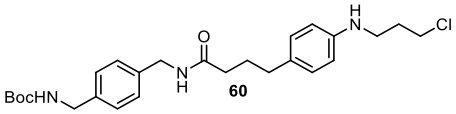

56 (50 mg, 0.18 µmol, 1.0 eq) was dissolved in anhydrous THF (1 mL) under nitrogen atmosphere and cooled to 0 °C. Borane-tetrahydrofuane complex (1 M in THF, 1.4 mL, 1.4 mmol, 8.0 eq) was added and the reaction mixture was stirred at room temperature for 16 h. Citric acid (370 g, 1.8 mmol, 10 eq) was dissolved in water (4 mL) and added to the reaction mixture dropwise to quench the excess of the borane. The resulting mixture was diluted with water (20 mL) and extracted with ethyl acetate (3 × 15 mL). The organic layer was dried over sodium sulfate, the desiccant was filtered off and the solvent was removed *in vacuo*. The crude product was semi-purified by *np*-flash column chromatography (*iso*-hexanes/ethyl acetate; 0→40% EtOAc) to give **57** (15 mg, ≤56 µmol) which was used without further purification.

Crude **57** (15 mg) was dissolved in THF (2 mL) and water (2 mL), lithium hydroxide (23 mg, 0.56 mmol, 10 eq) was added and the reaction mixture was stirred at room temperature for 1.5 h. The mixture was acidified with hydrochloric acid (2 M, 0.33 mL, 0.67 mmol, 12 eq), the volatiles were removed under reduced pressure and the crude product was dried under high vacuum for 14 h affording **58** which was used without further purification.

Carboxylate **58** was dissolved in anhydrous DMF (0.03 M) and coupled with amine **59** (16 mg, 67 µmol, 1.2 eq) following General Procedure B (1.2 eq COMU, 2 h reaction time). The Crude product was purified by flash column chromatography (*iso*-hexanes/ethyl acetate; 20→80% EtOAc) affording **60** (19 mg, 40 µmol, 23% over 3 steps) as a colourless solid.

TLC *Rf* = 0.35 (*np*, Hex:EtOAc 1:1)
^{1}H-NMR (400 MHz, $CDCl_3$): *δ* (ppm) = 7.22 (s, 4H), 6.97 (d, J = 8.4 Hz, 2H), 6.56 (d, J = 8.4 Hz, 2H), 5.73 (s, 1H), 4.87 (s, 1H), 4.39 (d, J = 5.7 Hz, 2H), 4.28 (d, J = 5.7 Hz, 2H), 3.65 (t, J = 6.3 Hz, 2H), 3.31 (t, J = 6.6 Hz, 2H), 2.54 (t, J = 7.4 Hz, 2H), 2.19 (t, J = 7.5 Hz, 2H), 2.06 (p, J = 6.5 Hz, 2H), 1.92 (p, J = 7.5 Hz, 2H), 1.45 (s, 9H).
^{13}C-NMR (101 MHz, $CDCl_3$): *δ* (ppm) = 172.9, 156.0, 145.9, 138.4, 137.6, 130.8, 129.5, 128.2, 127.9, 113.3, 79.7, 44.4, 43.4, 42.8, 41.5, 36.0, 34.4, 32.0, 28.5, 27.6.
LRMS (ESI+): m/z calc. for $C_{26}H_{37}ClN_3O_3^+$ $[M+H]^+$: 474.3, found: 474.3.

HL3-Fluo

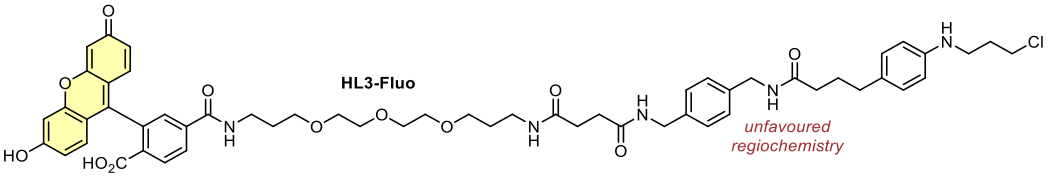

60 (5 mg, 11 µmol, 1.0 eq) was deprotected according to General Procedure A (0.02 M) and coupled with carboxylate **26** (11 mg, 16 µmol, 1.5 eq, 0.03 M) following General Procedure B (1.2 eq COMU, 3 h reaction time). The crude product was purified by preparative HPLC (acetonitrile/water, 0.1% formic acid; 10→65% MeCN, 20 min) affording **HL3-Fluo** (2.1 mg, 2.1 µmol, 20% over 2 steps) as an orange solid.

^{1}H-NMR (400 MHz, DMSO-d_6): *δ* (ppm) = 8.66 (t, *J* = 5.5 Hz, 1H), 8.30 (t, *J* = 6.1 Hz, 1H), 8.26 (t, *J* = 5.8 Hz, 1H), 8.15 (dd, *J* = 8.0, 1.2 Hz, 1H), 8.07 (d, *J* = 8.1 Hz, 1H), 7.79 (t, *J* = 5.5 Hz, 1H), 7.66 (s, 1H), 7.16 (s, 4H), 6.88 (d, *J* = 8.4 Hz, 2H), 6.67 (s, 2H), 6.59 (d, *J* = 8.7 Hz, 2H), 6.54 (dd, *J* = 8.7, 2.1 Hz, 2H), 6.48 (d, *J* = 8.5 Hz, 2H), 5.45 (t, *J* = 5.4 Hz, 1H), 4.20 (dd, *J* = 5.8, 2.0 Hz, 4H), 3.73 (t, *J* = 6.5 Hz, 2H), 3.48 – 3.39 (m, 10H), 3.27 – 3.21 (m, 2H), 3.10 (q, *J* = 6.4 Hz, 2H), 3.04 (q, *J* = 6.8 Hz, 2H), 2.42 – 2.36 (m, 3H), 2.31 (dt, *J* = 10.3, 5.1 Hz, 5H), 2.13 – 2.06 (m, 2H), 1.95 (p, *J* = 6.6 Hz, 2H), 1.70 (tt, *J* = 13.2, 7.1 Hz, 4H), 1.57 (p, *J* = 6.6 Hz, 2H).
HRMS (ESI+): m/z calc. for $C_{56}H_{65}ClN_5O_{12}^+$ $[M+H]^+$: 1034.431, found: 1034.434.

Synthetic route for Cou-HL3-Fluo

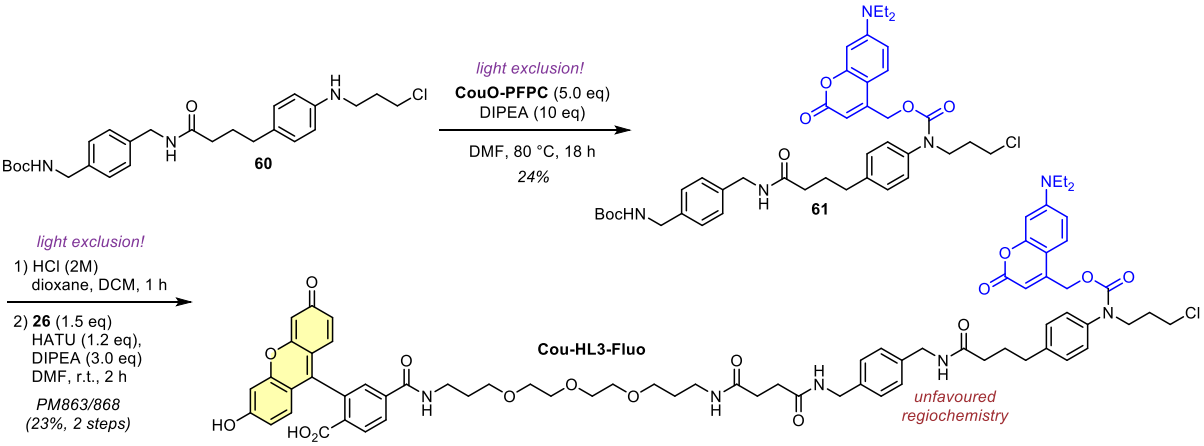

Compound 61

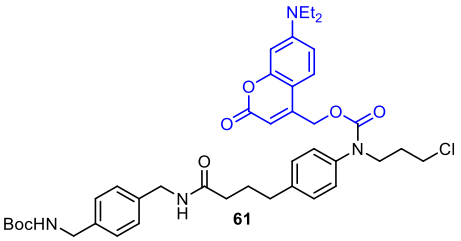

Note: the reaction must be performed under light exclusion.

60 (12 mg, 25 µmol, 1.0 eq) was dissolved in anhydrous DMF (1 mL) transformed to **61** following General Procedure D. The product was semi-purified by *rp*-flash column chromatography (acetonitrile/water, 0.1% formic acid; 20→80% MeCN) affording **61** (4.5 mg, 6.0 µmol, 24%) as a yellow solid.

TLC *Rf* = 15 (*np*, Hex:EtOAc 1:1)
HRMS (ESI+): m/z calc. for $C_{41}H_{52}ClN_4O_7^+$ $[M+H]^+$: 747.3519, found: 747.3536

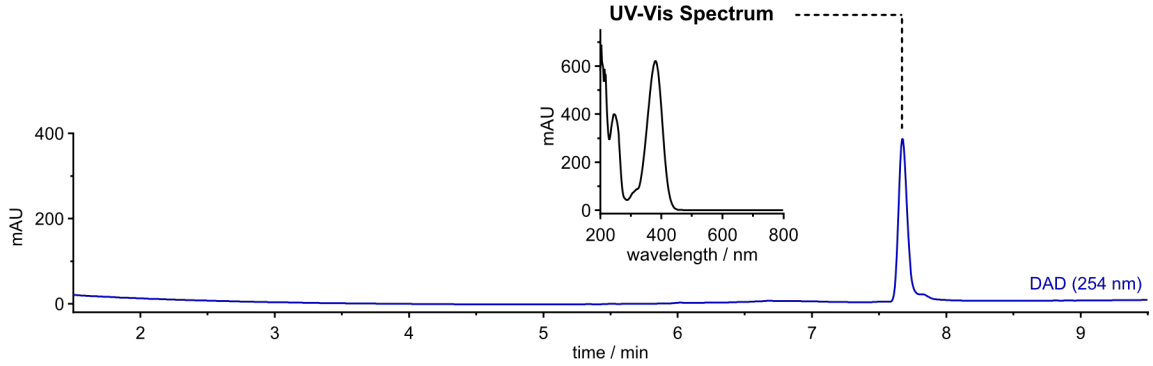

Cou-HL3-Fluo

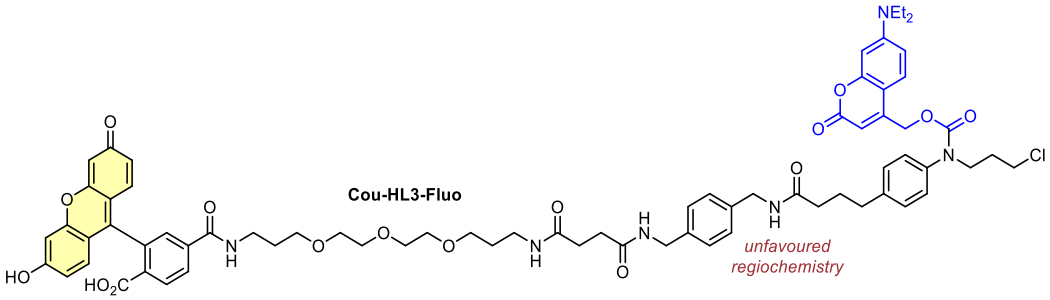

Note: the reaction must be performed under light exclusion.

61 (4.5 mg, 6.0 µmol, 1.0 eq) was deprotected according to General Procedure A (0.02 M) and coupled with carboxylate **26** (6.2 mg, 9.0 µmol, 1.5 eq, 0.03 M) following General Procedure B (1.0 eq HATU, 1 h reaction time). The crude product was purified by preparative HPLC (acetonitrile/water, 0.1% formic acid; 20→70% MeCN, 20 min) affording **Cou-HL3-Fluo** (1.9 mg, 1.4 µmol, 23% over 2 steps) as an orange solid.

^{1}H-NMR (400 MHz, DMSO-d_6): δ (ppm) = 8.65 (t, J = 5.5 Hz, 1H), 8.31 (t, J = 5.7 Hz, 2H), 8.13 (d, J = 8.0 Hz, 1H), 8.06 (d, J = 8.1 Hz, 1H), 7.79 (t, J = 5.5 Hz, 1H), 7.65 (s, 1H), 7.37 (s, 1H), 7.25 (t, J = 6.4 Hz, 4H), 7.17 (s, 4H), 6.64 (s, 3H), 6.59 (d, J = 8.7 Hz, 3H), 6.52 (d, J = 7.2 Hz, 3H), 5.26 (s, 2H), 4.21 (dd, J = 8.8, 6.0 Hz, 4H), 3.77 (s, 2H), 3.64 (t, J = 6.4 Hz, 2H), 3.43 (ddt, J = 14.1, 7.3, 2.9 Hz, 16H), 3.04 (q, J = 6.7 Hz, 2H), 2.61 – 2.55 (m, 4H), 2.31 (dt, J = 10.2, 4.3 Hz, 4H), 2.16 (t, J = 7.3 Hz, 2H), 1.92 (p, J = 6.5 Hz, 2H), 1.82 (p, J = 7.5 Hz, 2H), 1.69 (q, J = 6.6 Hz, 2H), 1.57 (p, J = 6.7 Hz, 2H), 1.10 (t, J = 7.0 Hz, 6H).
HRMS (ESI+): m/z calc. for $C_{71}H_{80}ClN_6O_{16}^+$ [M+H]$^+$: 1307.531, found: 1307.533.

Initial synthetic route for CHalo building block (improved procedure above)

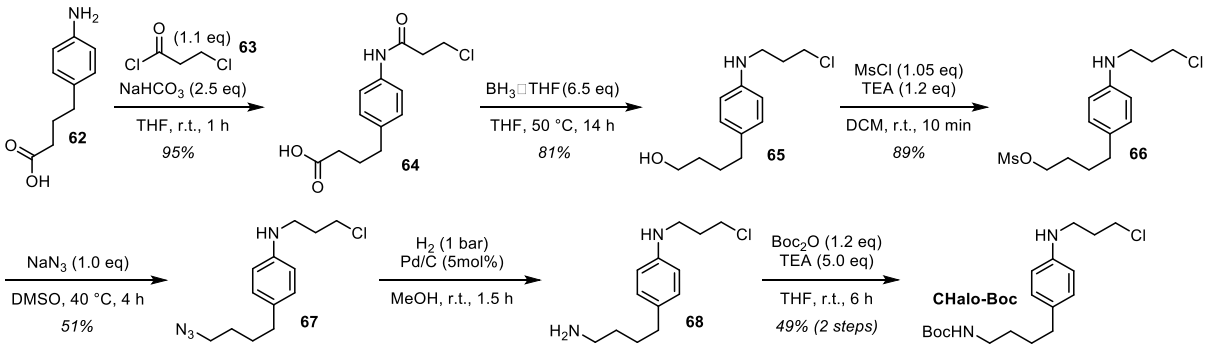

Compound 64

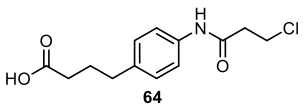

4-Aminobenzenebutanoic acid (**62**, 1.50 g, 7.95 mmol, 1.0 eq) was dissolved in anhydrous THF (30 mL). Sodium hydrogen carbonate (1.67 g, 19.9 mmol, 2.5 eq) and 3-chloropropionyl chloride (**63**, 0.835 mL, 8.75 mmol, 1.1 eq) were added and the reaction mixture was stirred at room temperature for 1 h. The solvent was removed *in vacuo* and the residue was diluted with water (15 mL) and hydrochloric acid (2 M, 20 mL, 5.0 eq) and extracted with ethyl acetate (3 × 25 mL). The organic layer was washed with brine (30 mL), dried

over sodium sulfate, the desiccant was filtered off and the solvent was removed *in vacuo* affording **64** (2.03 g, 7.53 mmol, 95%) as a colourless solid.

^{1}H-NMR (600 MHz, DMSO-d_6): δ (ppm) = 10.00 (s, 1H), 7.50 (d, J = 8.5 Hz, 2H), 7.11 (d, J = 8.5 Hz, 2H), 3.87 (t, J = 6.3 Hz, 2H), 2.79 (t, J = 6.3 Hz, 2H), 2.56 – 2.51 (m, 2H), 2.19 (t, J = 7.4 Hz, 2H), 1.76 (p, J = 7.5 Hz, 2H).
^{13}C-NMR (151 MHz, DMSO-d_6): δ (ppm) = 174.4, 167.8, 136.9, 136.6, 128.6, 119.2, 41.0, 39.2, 33.9, 33.1, 26.4.
HRMS (ESI+): m/z calc. for $C_{13}H_{16}ClNNaO_3^+$ $[M+Na]^+$: 202.0711, found: 292.0711.

Compound 65

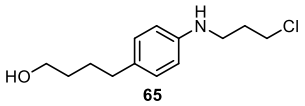

65

64 (2.00 g, 7.41 mmol, 1.0 eq) was dissolved in anhydrous THF (10 mL) under nitrogen atmosphere and borane tetrahydrofurane complex (1 M in THF, 48.2 mL, 48.2 mmol, 6.5 eq) was added. The reaction mixture was heated to 50 °C for 14 h. Methanol (ca. 10 mL) was added slowly until no gas development was observed upon addition any more to quench the excess of the borane and the volatiles were removed *in vacuo*. The crude product was purified by flash column chromatography (DCM/MeOH; 0→2% MeOH) to give **65** (1.46 g, 6.04 mmol, 81%) as a light-yellow oil.

TLC *Rf* = 0.18 (*np*, DCM:MeOH 99:1)
^{1}H-NMR (400 MHz, MeOD): δ (ppm) = 6.95 (d, J = 8.4 Hz, 2H), 6.59 (d, J = 8.4 Hz, 2H), 3.67 (t, J = 6.4 Hz, 2H), 3.55 (t, J = 6.4 Hz, 2H), 3.23 (t, J = 6.7 Hz, 2H), 2.50 (t, J = 7.3 Hz, 2H), 2.03 (p, J = 6.6 Hz, 2H), 1.65 – 1.48 (m, 4H).
^{13}C-NMR (101 MHz, MeOD): δ (ppm) = 148.0, 132.4, 130.0, 114.4, 62.9, 43.6, 42.4, 35.8, 33.3, 33.2, 29.2.
HRMS (ESI+): m/z calc. for $C_{13}H_{21}ClNO^+$ $[M+H]^+$: 242.1306, found: 242.1310.

Compound 66

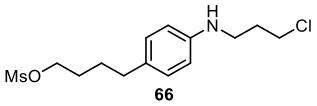

66

65 (0.17 g, 0.70 mmol, 1.0 eq) was dissolved in anhydrous DCM (4 mL) under nitrogen atmosphere, triethylamine (0.17 mL, 0.84 mmol, 1.2 eq) was added and the reaction was cooled to 0 °C. Methanesulfonyl chloride (57 µL, 0.74 mmol, 1.05 eq) was added, the reaction was allowed to warm to room temperature, stirred for 10 min and then diluted with ethyl acetate (15 mL). The organic layer was washed with water (3 × 10 mL), dried over sodium sulfate and the solvent was removed *in vacuo* affording **66** (0.20 g, 0.62 mmol, 89%) as a colourless oil.

TLC *Rf* = 0.71 (*np*, DCM:MeOH 99:1)
^{1}H-NMR (400 MHz, $CDCl_3$): δ (ppm) = 6.99 (d, J = 8.4 Hz, 2H), 6.60 (d, J = 8.4 Hz, 2H), 4.22 (t, J = 6.3 Hz, 2H), 3.65 (t, J = 6.3 Hz, 2H), 3.32 (t, J = 6.6 Hz, 2H), 2.98 (s, 3H), 2.55 (t, J = 7.3 Hz, 2H), 2.07 (p, J = 6.5 Hz, 2H), 1.81 – 1.73 (m, 2H), 1.73 – 1.63 (m, 2H).
LRMS (ESI+): m/z calc. for $C_{14}H_{23}ClNO_3S^+$ $[M+H]^+$: 320.1, found: 320.1.

Compound 67

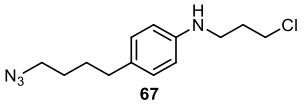

67

66 (1.69 g, 5.28 mmol, 1.0 eq) was dissolved in anhydrous DMSO (6 mL) under nitrogen atmosphere, sodium azide (0.34 g, 5.28 mmol, 1.0 eq) was added and the reaction mixture was heated to 40 °C for 4 h. The mixture was diluted with water (15 mL), brine (40 mL) and extracted with ethyl acetate (40 mL). The organic layer was washed with a 1:1 mixture of water and brine (30 mL), dried over sodium sulfate and the solvent was removed *in vacuo*. The crude product was purified by flash column chromatography (*iso*-hexanes /ethyl acetate; 0→10% EtOAc) to give **67** (0.72 g, 2.7 mmol, 51%) as a colourless oil.

Note: azide substitution of the alkyl chloride is observed as a side reaction.

TLC *Rf* = 0.71 (*np*, Hex:EtOAc 4:1)
^{1}H-NMR (400 MHz, $CDCl_3$): δ (ppm) = 7.01 (d, J = 8.1 Hz, 2H), 6.63 (d, J = 8.1 Hz, 2H), 3.65 (t, J = 6.2 Hz, 2H), 3.33 (t, J = 6.6 Hz, 2H), 3.27 (t, J = 6.1 Hz, 2H), 2.54 (t, J = 6.6 Hz, 2H), 2.08 (p, J = 6.3 Hz, 2H), 1.70 – 1.57 (m, 4H).

^{13}C-NMR (101 MHz, $CDCl_3$): δ (ppm) = 145.4, 131.8, 129.4, 113.7, 51.5, 42.7, 41.8, 34.6, 31.9, 28.9, 28.5.
HRMS (ESI+): m/z calc. for $C_{13}H_{20}ClN_4^+$ [M+H]$^+$: 267.1371, found: 267.1376.

Compound CHalo-Boc

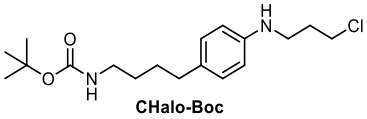

Note: here we report the initial synthetic procedure towards **CHalo-Boc**, an optimised preparation is described above.

67 (50 mg, 0.19 mmol, 1.0 eq) was dissolved in methanol (2 mL) under nitrogen atmosphere, palladium on charcoal (Pd/C, 11 mg, 9.4 µmol, 5 mol%) was added and the reaction was stirred under hydrogen atmosphere (1 atm) for 1.5 h. The Pd/C was removed by filtration over Celite (washed with methanol (4×)) and the filtrate was concentrated under reduce pressure. The intermediate product **68** was suspended in anhydrous THF (2.5 mL), triethylamine (0.13 mL, 0.94 mmol, 5.0 eq) and di-*tert*-butyl dicarbonate (51 mg, 0.22 mmol, 1.2 eq) were added and the reaction mixture was stirred at room temperature for 6 h. The mixture was diluted with water (15 mL) and extracted with DCM (3 × 10 mL). The organic layer was dried over sodium sulfate and the solvent was removed *in vacuo*. The crude product was purified by flash column chromatography (*iso*-hexanes/ethyl acetate; 0→30% EtOAc) to give **CHalo-Boc** (31 mg, 91 µmol, 49% over 2 steps) as a colourless oil.

TLC *Rf* = 0.34 (*np*, Hex:EtOAc 9:1)
^{1}H-NMR (600 MHz, $CDCl_3$): δ (ppm) = 6.99 (d, J = 8.4 Hz, 2H), 6.56 (d, J = 8.4 Hz, 2H), 4.52 (s, 1H), 3.65 (t, J = 6.3 Hz, 2H), 3.31 (t, J = 6.6 Hz, 2H), 3.12 (q, J = 6.7 Hz, 2H), 2.51 (t, J = 7.4 Hz, 2H), 2.06 (p, J = 6.5 Hz, 2H), 1.63 – 1.53 (m, 2H), 1.53 – 1.46 (m, 2H), 1.44 (s, 9H).
^{13}C-NMR (151 MHz, $CDCl_3$): δ (ppm) = 156.1, 146.0, 131.4, 129.3, 113.0, 79.1, 42.8, 41.3, 40.6, 34.6, 32.1, 29.7, 29.0, 28.5.
HRMS (ESI+): m/z calc. for $C_{18}H_{29}ClN_2NaO_2^+$ [M+Na]$^+$: 363.1810, found: 363.1812.

CHalo-Fluo

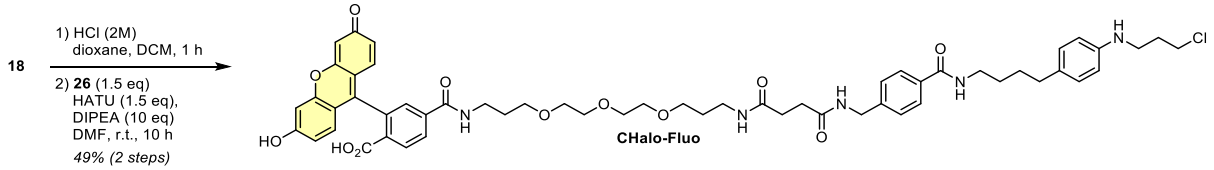

18 (3 mg, 6 µmol, 1.0 eq) was deprotected according to General Procedure A (0.02 M) and coupled with carboxylate **26** (7 mg, 10 µmol, 1.5 eq, 0.05 M) following General Procedure B (1.0 eq HATU, 10 h reaction time). The crude product was purified by preparative HPLC (acetonitrile/water, 0.1% formic acid; 10→60% MeCN, 20 min) affording **CHalo-Fluo** (3.2 mg, 4.1 µmol, 49% over 2 steps) as an orange solid.

^{1}H-NMR (800 MHz, DMSO-d_6): δ (ppm) = 10.16 (s, 2H), 8.66 (t, J = 5.4 Hz, 1H), 8.38 (t, J = 5.5 Hz, 2H), 8.16 (d, J = 8.1 Hz, 1H), 8.07 (d, J = 8.1 Hz, 1H), 7.79 (t, J = 5.3 Hz, 1H), 7.76 (d, J = 8.1 Hz, 2H), 7.66 (s, 1H), 7.29 (d, J = 8.0 Hz, 2H), 6.89 (d, J = 8.2 Hz, 2H), 6.69 (d, J = 1.8 Hz, 2H), 6.58 (d, J = 8.7 Hz, 2H), 6.55 (dd, J = 8.7, 1.9 Hz, 2H), 6.48 (d, J = 8.2 Hz, 2H), 5.42 (s, 1H), 4.30 – 4.26 (m, 2H), 3.72 (t, J = 6.5 Hz, 2H), 3.47 – 3.44 (m, 4H), 3.44 – 3.40 (m, 4H), 3.38 (t, J = 6.2 Hz, 2H), 3.36 – 3.34 (m, 2H), 3.26 – 3.22 (m, 4H), 3.09 (q, J = 6.2 Hz, 2H), 3.05 (q, J = 6.6 Hz, 2H), 2.43 (t, J = 6.9 Hz, 2H), 2.37 (t, J = 7.2 Hz, 2H), 2.31 (t, J = 7.2 Hz, 2H), 1.95 (p, J = 6.5 Hz, 2H), 1.68 (p, J = 6.5 Hz, 2H), 1.57 (p, J = 6.6 Hz, 2H), 1.54 – 1.46 (m, 4H).
^{13}C-NMR (201 MHz, DMSO-d_6): δ (ppm) = 171.5, 171.2, 168.1, 165.8, 164.4, 159.6, 152.7, 151.8, 146.8, 142.7, 140.8, 133.1, 129.4, 129.3, 129.2, 128.8, 128.1, 127.1, 126.8, 124.9, 122.2, 112.7, 112.1, 109.2, 102.2, 83.3, 69.7, 69.7, 69.5, 69.5, 68.2, 68.0, 43.4, 41.7, 40.1, 39.0, 36.9, 35.8, 34.0, 31.7, 30.8, 30.7, 29.4, 29.1, 28.9, 28.8.
HRMS (ESI+): m/z calc. for $C_{56}H_{65}ClN_5O_{12}^+$ [M+H]$^+$: 1034.431, found: 1034.431.

Cou-CHalo-Fluo

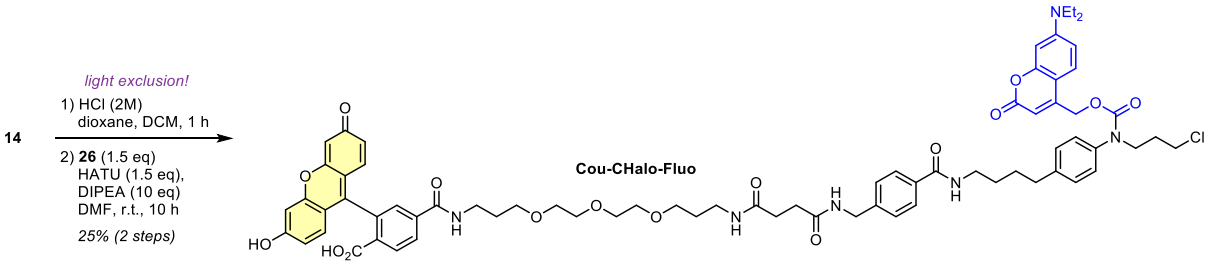

Note: the reaction must be performed under light exclusion.

14 (3 mg, 4 µmol, 1.0 eq) was deprotected according to General Procedure A (0.02 M) and coupled with carboxylate **26** (4 mg, 6 µmol, 1.5 eq, 0.05 M) following General Procedure B (1.0 eq HATU, 10 h reaction time). The crude product was purified by preparative HPLC (acetonitrile/water, 0.1% formic acid; 10→75% MeCN, 20 min) affording **Cou-CHalo-Fluo** (1.3 mg, 1.0 µmol, 25% over 2 steps) as an orange solid.

^{1}H-NMR (400 MHz, DMSO-d_6): δ (ppm) = 10.17 (s, 2H), 8.67 (t, J = 5.5 Hz, 1H), 8.40 (q, J = 5.9 Hz, 2H), 8.16 (d, J = 8.1 Hz, 1H), 8.07 (d, J = 8.0 Hz, 1H), 7.78 (dd, J = 15.0, 6.8 Hz, 3H), 7.66 (s, 1H), 7.43 – 7.34 (m, 1H), 7.29 (d, J = 8.2 Hz, 2H), 7.25 (s, 4H), 6.69 (d, J = 1.9 Hz, 2H), 6.65 (d, J = 8.6 Hz, 1H), 6.60 – 6.55 (m, 4H), 6.55 – 6.49 (m, 2H), 5.25 (s, 2H), 4.28 (d, J = 5.8 Hz, 2H), 3.80 – 3.73 (m, 2H), 3.64 (t, J = 6.4 Hz, 2H), 3.42 (tt, J = 11.9, 5.6 Hz, 16H), 3.26 (dq, J = 13.3, 6.6 Hz, 4H), 3.05 (q, J = 6.7 Hz, 2H), 2.64 – 2.59 (m, 2H), 2.40 – 2.34 (m, 2H), 2.32 (d, J = 6.3 Hz, 2H), 1.91 (p, J = 6.5 Hz, 2H), 1.68 (p, J = 6.4 Hz, 2H), 1.57 (dt, J = 12.6, 6.2 Hz, 6H), 1.10 (t, J = 6.9 Hz, 6H).
HRMS (ESI+): m/z calc. for $C_{71}H_{80}ClN_6O_{16}^+$ $[M+H]^+$: 1307.531, found: 1307.533.

11 References

(1) Merrill, R. A.; Song, J.; Kephart, R. A.; Klomp, A. J.; Noack, C. E.; Strack, S. A Robust and Economical Pulse-Chase Protocol to Measure the Turnover of HaloTag Fusion Proteins. *J. Biol. Chem.* **2019**, *294* (44), 16164–16171. https://doi.org/10.1074/jbc.RA119.010596.

(2) Los, G. V.; Encell, L. P.; McDougall, M. G.; Hartzell, D. D.; Karassina, N.; Zimprich, C.; Wood, M. G.; Learish, R.; Ohana, R. F.; Urh, M.; Simpson, D.; Mendez, J.; Zimmerman, K.; Otto, P.; Vidugiris, G.; Zhu, J.; Darzins, A.; Klaubert, D. H.; Bulleit, R. F.; Wood, K. V. HaloTag: A Novel Protein Labeling Technology for Cell Imaging and Protein Analysis. *ACS Chem. Biol.* **2008**, *3* (6), 373–382. https://doi.org/10.1021/cb800025k.

(3) Chyan, W.; Raines, R. T. Enzyme-Activated Fluorogenic Probes for Live-Cell and in Vivo Imaging. *ACS Chem. Biol.* **2018**, *13* (7), 1810–1823. https://doi.org/10.1021/acschembio.8b00371.

(4) Egyed, A.; Németh, K.; Molnár, T. Á.; Kállay, M.; Kele, P.; Bojtár, M. Turning Red without Feeling Embarrassed─Xanthenium-Based Photocages for Red-Light-Activated Phototherapeutics. *J. Am. Chem. Soc.* **2023**. https://doi.org/10.1021/jacs.2c11499.

(5) Weinstain, R.; Slanina, T.; Kand, D.; Klán, P. Visible-to-NIR-Light Activated Release: From Small Molecules to Nanomaterials. *Chem. Rev.* **2020**, *120* (24), 13135–13272. https://doi.org/10.1021/acs.chemrev.0c00663.

(6) Messina, M. S.; Quargnali, G.; Chang, C. J. Activity-Based Sensing for Chemistry-Enabled Biology: Illuminating Principles, Probes, and Prospects for Boronate Reagents for Studying Hydrogen Peroxide. *ACS Bio Med Chem Au* **2022**, *2* (6), 548–564. https://doi.org/10.1021/acsbiomedchemau.2c00052.

(7) Fosnacht, K. G.; Hammers, M. D.; Earp, M. S.; Gilbert, A. K.; Pluth, M. D. A Cell Trappable Methyl Rhodol-Based Fluorescent Probe for Hydrogen Sulfide Detection. *Chem. Asian J.* **2022**, *17* (16), e202200426. https://doi.org/10.1002/asia.202200426.

(8) Shields, B. C.; Yan, H.; Lim, S. S. X.; Burwell, S. C. V.; Cammarata, C. M.; Fleming, E. A.; Yousefzadeh, S. A.; Goldenshtein, V. Z.; Kahuno, E. W.; Vagadia, P. P.; Loughran, M. H.; Zhiquan, L.; McDonnell, M. E.; Scalabrino, M. L.; Thapa, M.; Hawley, T. M.; Field, G. D.; Hull, C.; Schiltz, G. E.; Glickfeld, L. L.; Reitz, A. B.; Tadross, M. R. DART.2: Bidirectional Synaptic Pharmacology with Thousandfold Cellular Specificity. *Nat. Methods* **2024**, *21* (7), 1288–1297. https://doi.org/10.1038/s41592-024-02292-9.

(9) Wang, L.; Tran, M.; D'Este, E.; Roberti, J.; Koch, B.; Xue, L.; Johnsson, K. A General Strategy to Develop Cell Permeable and Fluorogenic Probes for Multicolour Nanoscopy. *Nat. Chem.* **2019**, 1–8. https://doi.org/10.1038/s41557-019-0371-1.

(10) Lukinavičius, G.; Umezawa, K.; Olivier, N.; Honigmann, A.; Yang, G.; Plass, T.; Mueller, V.; Reymond, L.; Corrêa Jr, I. R.; Luo, Z.-G.; Schultz, C.; Lemke, E. A.; Heppenstall, P.; Eggeling, C.; Manley, S.; Johnsson, K. A Near-Infrared Fluorophore for Live-Cell Super-Resolution Microscopy of Cellular Proteins. *Nat. Chem.* **2013**, *5* (2), 132–139. https://doi.org/10.1038/nchem.1546.

(11) Schmitt, C.; Mauker, P.; Vepřek, N. A.; Gierse, C.; Meiring, J. C. M.; Kuch, J.; Akhmanova, A.; Dehmelt, L.; Thorn-Seshold, O. A Photocaged Microtubule-Stabilising Epothilone Allows Spatiotemporal Control of Cytoskeletal Dynamics. *Angew. Chem. Int. Ed.* **2024**, *63* (43), e202410169. https://doi.org/10.1002/anie.202410169.

(12) Wilhelm, J.; Kühn, S.; Tarnawski, M.; Gotthard, G.; Tünnermann, J.; Tänzer, T.; Karpenko, J.; Mertes, N.; Xue, L.; Uhrig, U.; Reinstein, J.; Hiblot, J.; Johnsson, K. Kinetic and Structural Characterization of the Self-Labeling Protein Tags HaloTag7, SNAP-Tag, and CLIP-Tag. *Biochemistry* **2021**, *60* (33), 2560–2575. https://doi.org/10.1021/acs.biochem.1c00258.

(13) Russo, M.; Janeková, H.; Meier, D.; Generali, M.; Štacko, P. Light in a Heartbeat: Bond Scission by a Single Photon above 800 Nm. *J. Am. Chem. Soc.* **2024**, *146* (12), 8417–8424. https://doi.org/10.1021/jacs.3c14197.

(14) Gorka, A. P.; Yamamoto, T.; Zhu, J.; Schnermann, M. J. Cyanine Photocages Enable Spatial Control of Inducible Cre-Mediated Recombination. *ChemBioChem* **2018**, *19* (12), 1239–1243. https://doi.org/10.1002/cbic.201800061.

(15) Yan, X.; Zhao, J.-H.; Wang, Q.; Wang, W.; Ding, Y.; Zhou, Y.; Chen, G.; Du, J.; Huang, W.; Chu, L. Silicon Rhodamine-Catalyzed Near-Infrared Light-Induced Photodecaging of Ortho-Nitrobenzyl Groups In Vitro and In Vivo. *J. Am. Chem. Soc.* **2025**, *147* (24), 20957–20966. https://doi.org/10.1021/jacs.5c04942.

(16) Zeisel, L.; Felber, J. G.; Scholzen, K. C.; Poczka, L.; Cheff, D.; Maier, M. S.; Cheng, Q.; Shen, M.; Hall, M. D.; Arnér, E. S. J.; Thorn-Seshold, J.; Thorn-Seshold, O. Selective Cellular Probes for Mammalian Thioredoxin Reductase TrxR1: Rational Design of RX1, a Modular 1,2-Thiaselenane Redox Probe. *Chem* **2022**, *8* (5), 1493–1517. https://doi.org/10.1016/j.chempr.2022.03.010.

(17) Zeisel, L.; Felber, J. G.; Scholzen, K. C.; Schmitt, C.; Wiegand, A. J.; Komissarov, L.; Arnér, E. S. J.; Thorn-Seshold, O. Piperazine-Fused Cyclic Disulfides Unlock High-Performance Bioreductive Probes of Thioredoxins and Bifunctional Reagents for Thiol Redox Biology. *J. Am. Chem. Soc.* **2024**, *146* (8), 5204–5214. https://doi.org/10.1021/jacs.3c11153.

(18) Papot, S.; Tranoy, I.; Tillequin, F.; Florent, J.-C.; Gesson, J.-P. Design of Selectively Activated Anticancer Prodrugs: Elimination and Cyclization Strategies. *Curr. Med. Chem. Anticancer Agents* **2002**, *2* (2), 155–185. https://doi.org/10.2174/1568011023354173.

(19) Jasim, S. Development of a Dehalogenase-Based Protein Fusion Tag Capable of Rapid, Selective and Covalent Attachment to Customizable Ligands. *AACE Clin. Case Rep.* **2021**, *7* (1), 1.
(20) Los, G. V.; Encell, L. P.; McDougall, M. G.; Hartzell, D. D.; Karassina, N.; Zimprich, C.; Wood, M. G.; Learish, R.; Ohana, R. F.; Urh, M.; Simpson, D.; Mendez, J.; Zimmerman, K.; Otto, P.; Vidugiris, G.; Zhu, J.; Darzins, A.; Klaubert, D. H.; Bulleit, R. F.; Wood, K. V. HaloTag: A Novel Protein Labeling Technology for Cell Imaging and Protein Analysis. *ACS Chem. Biol.* **2008**, *3* (6), 373–382. https://doi.org/10.1021/cb800025k.
(21) Sun, X.; Zhang, A.; Baker, B.; Sun, L.; Howard, A.; Buswell, J.; Maurel, D.; Masharina, A.; Johnsson, K.; Noren, C. J.; Xu, M.-Q.; Corrêa Jr., I. R. Development of SNAP-Tag Fluorogenic Probes for Wash-Free Fluorescence Imaging. *ChemBioChem* **2011**, *12* (14), 2217–2226. https://doi.org/10.1002/cbic.201100173.
(22) Gronemeyer, T.; Chidley, C.; Juillerat, A.; Heinis, C.; Johnsson, K. Directed Evolution of O6-Alkylguanine-DNA Alkyltransferase for Applications in Protein Labeling. *Protein Eng. Des. Sel.* **2006**, *19* (7), 309–316. https://doi.org/10.1093/protein/gzl014.
(23) Gautier, A.; Juillerat, A.; Heinis, C.; Corrêa, I. R.; Kindermann, M.; Beaufils, F.; Johnsson, K. An Engineered Protein Tag for Multiprotein Labeling in Living Cells. *Chem. Biol.* **2008**, *15* (2), 128–136. https://doi.org/10.1016/j.chembiol.2008.01.007.
(24) Porzberg, N.; Gries, K.; Johnsson, K. Exploiting Covalent Chemical Labeling with Self-Labeling Proteins. *Annu. Rev. Biochem.* **2025**, *94* (Volume 94, 2025), 29–58. https://doi.org/10.1146/annurev-biochem-030222-121016.
(25) Deo, C.; Abdelfattah, A. S.; Bhargava, H. K.; Berro, A. J.; Falco, N.; Farrants, H.; Moeyaert, B.; Chupanova, M.; Lavis, L. D.; Schreiter, E. R. The HaloTag as a General Scaffold for Far-Red Tunable Chemigenetic Indicators. *Nat. Chem. Biol.* **2021**, *17* (6), 718–723. https://doi.org/10.1038/s41589-021-00775-w.
(26) Grimm, J. B.; Tkachuk, A. N.; Xie, L.; Choi, H.; Mohar, B.; Falco, N.; Schaefer, K.; Patel, R.; Zheng, Q.; Liu, Z.; Lippincott-Schwartz, J.; Brown, T. A.; Lavis, L. D. A General Method to Optimize and Functionalize Red-Shifted Rhodamine Dyes. *Nat. Methods* **2020**, *17* (8), 815–821. https://doi.org/10.1038/s41592-020-0909-6.
(27) Schwenzer, N.; Teiwes, N. K.; Kohl, T.; Pohl, C.; Giller, M. J.; Lehnart, S. E.; Steinem, C. CaV1.3 Channel Clusters Characterized by Live-Cell and Isolated Plasma Membrane Nanoscopy. *Commun. Biol.* **2024**, *7* (1), 1–11. https://doi.org/10.1038/s42003-024-06313-3.
(28) Roed, S. N.; Wismann, P.; Underwood, C. R.; Kulahin, N.; Iversen, H.; Cappelen, K. A.; Schäffer, L.; Lehtonen, J.; Hecksher-Soerensen, J.; Secher, A.; Mathiesen, J. M.; Bräuner-Osborne, H.; Whistler, J. L.; Knudsen, S. M.; Waldhoer, M. Real-Time Trafficking and Signaling of the Glucagon-like Peptide-1 Receptor. *Mol. Cell. Endocrinol.* **2014**, *382* (2), 938–949. https://doi.org/10.1016/j.mce.2013.11.010.
(29) Komatsubara, A. T.; Goto, Y.; Kondo, Y.; Matsuda, M.; Aoki, K. Single-Cell Quantification of the Concentrations and Dissociation Constants of Endogenous Proteins. *J. Biol. Chem.* **2019**, *294* (15), 6062–6072. https://doi.org/10.1074/jbc.RA119.007685.
(30) Kohl, J.; Ng, J.; Cachero, S.; Ciabatti, E.; Dolan, M.-J.; Sutcliffe, B.; Tozer, A.; Ruehle, S.; Krueger, D.; Frechter, S.; Branco, T.; Tripodi, M.; Jefferis, G. S. X. E. Ultrafast Tissue Staining with Chemical Tags. *Proc. Natl. Acad. Sci. U.S.A.* **2014**, *111* (36), E3805–E3814. https://doi.org/10.1073/pnas.1411087111.
(31) Zimmermann, M.; Cal, R.; Janett, E.; Hoffmann, V.; Bochet, C. G.; Constable, E.; Beaufils, F.; Wymann, M. P. Cell-Permeant and Photocleavable Chemical Inducer of Dimerization. *Angew. Chem. Int. Ed.* **2014**, *53* (18), 4717–4720. https://doi.org/10.1002/anie.201310969.
(32) Erhart, D.; Zimmermann, M.; Jacques, O.; Wittwer, M. B.; Ernst, B.; Constable, E.; Zvelebil, M.; Beaufils, F.; Wymann, M. P. Chemical Development of Intracellular Protein Heterodimerizers. *Chem. Biol.* **2013**, *20* (4), 549–557. https://doi.org/10.1016/j.chembiol.2013.03.010.
(33) Ballister, E. R.; Aonbangkhen, C.; Mayo, A. M.; Lampson, M. A.; Chenoweth, D. M. Localized Light-Induced Protein Dimerization in Living Cells Using a Photocaged Dimerizer. *Nat. Commun.* **2014**, *5* (1), 5475. https://doi.org/10.1038/ncomms6475.
(34) Deo, C.; Sheu, S.-H.; Seo, J.; Clapham, D. E.; Lavis, L. D. Isomeric Tuning Yields Bright and Targetable Red Ca2+ Indicators. *J. Am. Chem. Soc.* **2019**, *141* (35), 13734–13738. https://doi.org/10.1021/jacs.9b06092.
(35) Neklesa, T. K.; Tae, H. S.; Schneekloth, A. R.; Stulberg, M. J.; Corson, T. W.; Sundberg, T. B.; Raina, K.; Holley, S. A.; Crews, C. M. Small-Molecule Hydrophobic Tagging–Induced Degradation of HaloTag Fusion Proteins. *Nat. Chem. Biol.* **2011**, *7* (8), 538–543. https://doi.org/10.1038/nchembio.597.
(36) Shields, B. C.; Kahuno, E.; Kim, C.; Apostolides, P. F.; Brown, J.; Lindo, S.; Mensh, B. D.; Dudman, J. T.; Lavis, L. D.; Tadross, M. R. Deconstructing Behavioral Neuropharmacology with Cellular Specificity. *Science* **2017**, *356* (6333), eaaj2161. https://doi.org/10.1126/science.aaj2161.
(37) Lin, H.-Y.; Haegele, J. A.; Disare, M. T.; Lin, Q.; Aye, Y. A Generalizable Platform for Interrogating Target- and Signal-Specific Consequences of Electrophilic Modifications in Redox-Dependent Cell Signaling. *J. Am. Chem. Soc.* **2015**, *137* (19), 6232–6244. https://doi.org/10.1021/ja5132648.
(38) Wilhelm, J.; Kühn, S.; Tarnawski, M.; Gotthard, G.; Tünnermann, J.; Tänzer, T.; Karpenko, J.; Mertes, N.; Xue, L.; Uhrig, U.; Reinstein, J.; Hiblot, J.; Johnsson, K. Kinetic and Structural Characterization of

the Self-Labeling Protein Tags HaloTag7, SNAP-Tag, and CLIP-Tag. *Biochemistry* **2021**, *60* (33), 2560–2575. https://doi.org/10.1021/acs.biochem.1c00258.

(39) Ohana, R. F.; Encell, L. P.; Zhao, K.; Simpson, D.; Slater, M. R.; Urh, M.; Wood, K. V. HaloTag7: A Genetically Engineered Tag That Enhances Bacterial Expression of Soluble Proteins and Improves Protein Purification. *Protein Expression Purif.* **2009**, *68* (1), 110–120. https://doi.org/10.1016/j.pep.2009.05.010.

(40) R. Correa, I.; Baker, B.; Zhang, A.; Sun, L.; R. Provost, C.; Lukinavicius, G.; Reymond, L.; Johnsson, K.; Xu, M.-Q. Substrates for Improved Live-Cell Fluorescence Labeling of SNAP-Tag. *Curr. Pharm. Des.* **2013**, *19* (30), 5414–5420.

(41) Kompa, J.; Bruins, J.; Glogger, M.; Wilhelm, J.; Frei, M. S.; Tarnawski, M.; D'Este, E.; Heilemann, M.; Hiblot, J.; Johnsson, K. Exchangeable HaloTag Ligands for Super-Resolution Fluorescence Microscopy. *J. Am. Chem. Soc.* **2023**, *145* (5), 3075–3083. https://doi.org/10.1021/jacs.2c11969.

(42) Lincoln, R.; Bossi, M. L.; Remmel, M.; D'Este, E.; Butkevich, A. N.; Hell, S. W. A General Design of Caging-Group-Free Photoactivatable Fluorophores for Live-Cell Nanoscopy. *Nat. Chem.* **2022**, *14* (9), 1013–1020. https://doi.org/10.1038/s41557-022-00995-0.

(43) Lippert, A. R.; Van de Bittner, G. C.; Chang, C. J. Boronate Oxidation as a Bioorthogonal Reaction Approach for Studying the Chemistry of Hydrogen Peroxide in Living Systems. *Acc. Chem. Res.* **2011**, *44* (9), 793–804. https://doi.org/10.1021/ar200126t.

(44) Albers, A. E.; Dickinson, B. C.; Miller, E. W.; Chang, C. J. A Red-Emitting Naphthofluorescein-Based Fluorescent Probe for Selective Detection of Hydrogen Peroxide in Living Cells. *Bioorg. Med. Chem. Lett.* **2008**, *18* (22), 5948–5950. https://doi.org/10.1016/j.bmcl.2008.08.035.

(45) Gruber, T. D.; Krishnamurthy, C.; Grimm, J. B.; Tadross, M. R.; Wysocki, L. M.; Gartner, Z. J.; Lavis, L. D. Cell-Specific Chemical Delivery Using a Selective Nitroreductase–Nitroaryl Pair. *ACS Chem. Biol.* **2018**, *13* (10), 2888–2896. https://doi.org/10.1021/acschembio.8b00524.

(46) Li, L.; Ge, J.; Wu, H.; Xu, Q.-H.; Yao, S. Q. Organelle-Specific Detection of Phosphatase Activities with Two-Photon Fluorogenic Probes in Cells and Tissues. *J. Am. Chem. Soc.* **2012**, *134* (29), 12157–12167. https://doi.org/10.1021/ja3036256.

(47) Ito, H.; Kawamata, Y.; Kamiya, M.; Tsuda-Sakurai, K.; Tanaka, S.; Ueno, T.; Komatsu, T.; Hanaoka, K.; Okabe, S.; Miura, M.; Urano, Y. Red-Shifted Fluorogenic Substrate for Detection of lacZ-Positive Cells in Living Tissue with Single-Cell Resolution. *Angew. Chem. Int. Ed.* **2018**, *57* (48), 15702–15706. https://doi.org/10.1002/anie.201808670.

(48) Tian, L.; Yang, Y.; Wysocki, L. M.; Arnold, A. C.; Hu, A.; Ravichandran, B.; Sternson, S. M.; Looger, L. L.; Lavis, L. D. Selective Esterase–Ester Pair for Targeting Small Molecules with Cellular Specificity. *Proc. Natl. Acad. Sci. U.S.A.* **2012**, *109* (13), 4756–4761. https://doi.org/10.1073/pnas.1111943109.

(49) Turnbull, J. L.; Benlian, B. R.; Golden, R. P.; Miller, E. W. Phosphonofluoresceins: Synthesis, Spectroscopy, and Applications. *J. Am. Chem. Soc.* **2021**, *143* (16), 6194–6201. https://doi.org/10.1021/jacs.1c01139.

(50) Dickinson, B. C.; Peltier, J.; Stone, D.; Schaffer, D. V.; Chang, C. J. Nox2 Redox Signaling Maintains Essential Cell Populations in the Brain. *Nat. Chem. Biol.* **2011**, *7* (2), 106–112. https://doi.org/10.1038/nchembio.497.

(51) Mauker, P.; Dessen-Weissenhorn, L.; Zecha, C.; Vepřek, N. A.; Brandmeier, J. I.; Beckmann, D.; Kitowski, A.; Kernmayr, T.; Thorn-Seshold, J.; Kerschensteiner, M.; Thorn-Seshold, O. Cellularly-Retained Fluorogenic Probes for Sensitive Cell-Resolved Bioactivity Imaging. bioRxiv April 20, 2025, p 2025.04.17.649302. https://doi.org/10.1101/2025.04.17.649302.

(52) Huang, Z.; Terpetschnig, E.; You, W.; Haugland, R. P. 2-(2′-Phosphoryloxyphenyl)-4(3*H*)-Quinazolinone Derivatives as Fluorogenic Precipitating Substrates of Phosphatases. *Anal.Biochem.* **1992**, *207* (1), 32–39. https://doi.org/10.1016/0003-2697(92)90495-S.

(53) Doura, T.; Kamiya, M.; Obata, F.; Yamaguchi, Y.; Hiyama, T. Y.; Matsuda, T.; Fukamizu, A.; Noda, M.; Miura, M.; Urano, Y. Detection of LacZ-Positive Cells in Living Tissue with Single-Cell Resolution. *Angew. Chem. Int. Ed.* **2016**, *55* (33), 9620–9624. https://doi.org/10.1002/anie.201603328.

(54) Sun, H.; Johnson, D. R.; Finch, R. A.; Sartorelli, A. C.; Miller, D. W.; Elmquist, W. F. Transport of Fluorescein in MDCKII-MRP1 Transfected Cells and Mrp1-Knockout Mice. *Biochem. Biophys. Res. Commun.* **2001**, *284* (4), 863–869. https://doi.org/10.1006/bbrc.2001.5062.

(55) Iwashita, H.; Castillo, E.; Messina, M. S.; Swanson, R. A.; Chang, C. J. A Tandem Activity-Based Sensing and Labeling Strategy Enables Imaging of Transcellular Hydrogen Peroxide Signaling. *Proc. Natl. Acad. Sci. U.S.A.* **2021**, *118* (9), e2018513118. https://doi.org/10.1073/pnas.2018513118.

(56) Papot, S.; Tranoy, I.; Tillequin, F.; Florent, J. C.; Gesson, J. P. Design of Selectively Activated Anticancer Prodrugs: Elimination and Cyclization Strategies. *Current Medicinal Chemistry -Anti-Cancer Agents* **2002**, *2* (2), 155–185. https://doi.org/10.2174/1568011023354173.

(57) Huppertz, M.-C.; Wilhelm, J.; Grenier, V.; Schneider, M. W.; Falt, T.; Porzberg, N.; Hausmann, D.; Hoffmann, D. C.; Hai, L.; Tarnawski, M.; Pino, G.; Slanchev, K.; Kolb, I.; Acuna, C.; Fenk, L. M.; Baier, H.; Hiblot, J.; Johnsson, K. Recording Physiological History of Cells with Chemical Labeling. *Science* **2024**, *383* (6685), 890–897. https://doi.org/10.1126/science.adg0812.

(58) Broichhagen, J.; Trumpp, M.; Gatin-Fraudet, B.; Bruckmann, K.; Burdzinski, W.; Roßmann, K.; Levitz, J.; Knaus, P.; Jatzlau, J. Developing HaloTag and SNAP-Tag Chemical Inducers of Dimerization to

Probe Receptor Oligomerization and Downstream Signaling. *Angewandte Chemie International Edition* **2025**, *n/a* (n/a), e202506830. https://doi.org/10.1002/anie.202506830.
(59) Banala, S.; Arnold, A.; Johnsson, K. Caged Substrates for Protein Labeling and Immobilization. *ChemBioChem* **2008**, *9* (1), 38–41. https://doi.org/10.1002/cbic.200700472.
(60) Caldwell, S. E.; Demyan, I. R.; Falcone, G. N.; Parikh, A.; Lohmueller, J.; Deiters, A. Conditional Control of Benzylguanine Reaction with the Self-Labeling SNAP-Tag Protein. *Bioconjugate Chem.* **2025**, *36* (3), 540–548. https://doi.org/10.1021/acs.bioconjchem.5c00002.
(61) Kühn, S.; Nasufovic, V.; Wilhelm, J.; Kompa, J.; de Lange, E. M. F.; Lin, Y.-H.; Egoldt, C.; Fischer, J.; Lennoi, A.; Tarnawski, M.; Reinstein, J.; Vlijm, R.; Hiblot, J.; Johnsson, K. SNAP-Tag2 for Faster and Brighter Protein Labeling. *Nature Chemical Biology* **2025**. https://doi.org/10.1038/s41589-025-01942-z.
(62) Chen, X.; Wu, Y.-W. Tunable and Photoswitchable Chemically Induced Dimerization for Chemo-Optogenetic Control of Protein and Organelle Positioning. *Angew. Chem. Int. Ed.* **2018**, *57* (23), 6796–6799. https://doi.org/10.1002/anie.201800140.
(63) Aonbangkhen, C.; Zhang, H.; Wu, D. Z.; Lampson, M. A.; Chenoweth, D. M. Reversible Control of Protein Localization in Living Cells Using a Photocaged-Photocleavable Chemical Dimerizer. *J. Am. Chem. Soc.* **2018**, *140* (38), 11926–11930. https://doi.org/10.1021/jacs.8b07753.
(64) Zhang, H.; Aonbangkhen, C.; Tarasovetc, E. V.; Ballister, E. R.; Chenoweth, D. M.; Lampson, M. A. Optogenetic Control of Kinetochore Function. *Nat. Chem. Biol.* **2017**, *13* (10), 1096–1101. https://doi.org/10.1038/nchembio.2456.
(65) Chen, X.; Venkatachalapathy, M.; Kamps, D.; Weigel, S.; Kumar, R.; Orlich, M.; Garrecht, R.; Hirtz, M.; Niemeyer, C. M.; Wu, Y.-W.; Dehmelt, L. "Molecular Activity Painting": Switch-like, Light-Controlled Perturbations inside Living Cells. *Angew. Chem. Int. Ed.* **2017**, *56* (21), 5916–5920. https://doi.org/10.1002/anie.201611432.
(66) Escudero, D. Revising Intramolecular Photoinduced Electron Transfer (PET) from First-Principles. *Acc. Chem. Res.* **2016**, *49* (9), 1816–1824. https://doi.org/10.1021/acs.accounts.6b00299.
(67) Würth, C.; Grabolle, M.; Pauli, J.; Spieles, M.; Resch-Genger, U. Relative and Absolute Determination of Fluorescence Quantum Yields of Transparent Samples. *Nat. Protoc.* **2013**, *8* (8), 1535–1550. https://doi.org/10.1038/nprot.2013.087.
(68) Zhang, X.-F.; Zhang, J.; Liu, L. Fluorescence Properties of Twenty Fluorescein Derivatives: Lifetime, Quantum Yield, Absorption and Emission Spectra. *J. Fluoresc.* **2014**, *24* (3), 819–826. https://doi.org/10.1007/s10895-014-1356-5.
(69) Dessolin, J.; Schuler, M.; Quinart, A.; De Giorgi, F.; Ghosez, L.; Ichas, F. Selective Targeting of Synthetic Antioxidants to Mitochondria: Towards a Mitochondrial Medicine for Neurodegenerative Diseases? *Eur. J. Pharmacol.* **2002**, *447* (2), 155–161. https://doi.org/10.1016/S0014-2999(02)01839-3.
(70) Huppertz, M.-C.; Wilhelm, J.; Grenier, V.; Schneider, M. W.; Falt, T.; Porzberg, N.; Hausmann, D.; Hoffmann, D. C.; Hai, L.; Tarnawski, M.; Pino, G.; Slanchev, K.; Kolb, I.; Acuna, C.; Fenk, L. M.; Baier, H.; Hiblot, J.; Johnsson, K. Recording Physiological History of Cells with Chemical Labeling. *Science* **2024**, *383* (6685), 890–897. https://doi.org/10.1126/science.adg0812.
(71) Critchfield, F. E.; Gibson, J. A. Jr.; Hall, J. L. Dielectric Constant for the Dioxane—Water System from 20 to 35°. *J. Am. Chem. Soc.* **1953**, *75* (8), 1991–1992. https://doi.org/10.1021/ja01104a506.
(72) Noordstra, I.; Liu, Q.; Nijenhuis, W.; Hua, S.; Jiang, K.; Baars, M.; Remmelzwaal, S.; Martin, M.; Kapitein, L. C.; Akhmanova, A. Control of Apico–Basal Epithelial Polarity by the Microtubule Minus-End-Binding Protein CAMSAP3 and Spectraplakin ACF7. *J. Cell Sci.* **2016**, *129* (22), 4278–4288. https://doi.org/10.1242/jcs.194878.
(73) Nijenhuis, W.; van Grinsven, M. M. P.; Kapitein, L. C. An Optimized Toolbox for the Optogenetic Control of Intracellular Transport. *J. Cell Biol.* **2020**, *219* (4), e201907149. https://doi.org/10.1083/jcb.201907149.
(74) Jansen, K. I.; Iwanski, M. K.; Burute, M.; Kapitein, L. C. A Live-Cell Marker to Visualize the Dynamics of Stable Microtubules throughout the Cell Cycle. *J. Cell Biol.* **2023**, *222* (5), e202106105. https://doi.org/10.1083/jcb.202106105.
(75) Pasolli, M.; Meiring, J. C. M.; Conboy, J. P.; Koenderink, G. H.; Akhmanova, A. Optogenetic and Chemical Genetic Tools for Rapid Repositioning of Vimentin Intermediate Filaments. *J. Cell Biol.* **2025**, *224* (9), e202504004. https://doi.org/10.1083/jcb.202504004.
(76) Meiring, J. C. M.; Grigoriev, I.; Nijenhuis, W.; Kapitein, L. C.; Akhmanova, A. Opto-Katanin, an Optogenetic Tool for Localized, Microtubule Disassembly. *Curr. Biol.* **2022**, *32* (21), 4660-4674.e6. https://doi.org/10.1016/j.cub.2022.09.010.
(77) Stepanova, T.; Slemmer, J.; Hoogenraad, C. C.; Lansbergen, G.; Dortland, B.; Zeeuw, C. I. D.; Grosveld, F.; Cappellen, G. van; Akhmanova, A.; Galjart, N. Visualization of Microtubule Growth in Cultured Neurons via the Use of EB3-GFP (End-Binding Protein 3-Green Fluorescent Protein). *J. Neurosci.* **2003**, *23* (7), 2655–2664. https://doi.org/10.1523/JNEUROSCI.23-07-02655.2003.
(78) Farías, G. G.; Fréal, A.; Tortosa, E.; Stucchi, R.; Pan, X.; Portegies, S.; Will, L.; Altelaar, M.; Hoogenraad, C. C. Feedback-Driven Mechanisms between Microtubules and the Endoplasmic Reticulum Instruct Neuronal Polarity. *Neuron* **2019**, *102* (1), 184-201.e8. https://doi.org/10.1016/j.neuron.2019.01.030.

(79) Shlevkov, E.; Kramer, T.; Schapansky, J.; LaVoie, M. J.; Schwarz, T. L. Miro Phosphorylation Sites Regulate Parkin Recruitment and Mitochondrial Motility. *Proc. Natl. Acad. Sci. U.S.A.* **2016**, *113* (41), E6097–E6106. https://doi.org/10.1073/pnas.1612283113.
(80) Harbauer, A. B.; Hees, J. T.; Wanderoy, S.; Segura, I.; Gibbs, W.; Cheng, Y.; Ordonez, M.; Cai, Z.; Cartoni, R.; Ashrafi, G.; Wang, C.; Perocchi, F.; He, Z.; Schwarz, T. L. Neuronal Mitochondria Transport *Pink1* mRNA via Synaptojanin 2 to Support Local Mitophagy. *Neuron* **2022**, *110* (9), 1516-1531.e9. https://doi.org/10.1016/j.neuron.2022.01.035.
(81) Hees, J. T.; Wanderoy, S.; Lindner, J.; Helms, M.; Murali Mahadevan, H.; Harbauer, A. B. Insulin Signalling Regulates Pink1 mRNA Localization via Modulation of AMPK Activity to Support PINK1 Function in Neurons. *Nat. Metab.* **2024**, *6* (3), 514–530. https://doi.org/10.1038/s42255-024-01007-w.
(82) Nguyen, H. P.; Stewart, S.; Kukwikila, M. N.; Jones, S. F.; Offenbartl-Stiegert, D.; Mao, S.; Balasubramanian, S.; Beck, S.; Howorka, S. A Photo-Responsive Small-Molecule Approach for the Opto-Epigenetic Modulation of DNA Methylation. *Angew. Chem. Int. Ed.* **2019**, *58* (20), 6620–6624. https://doi.org/10.1002/anie.201901139.
(83) Grimm, J. B.; Brown, T. A.; Tkachuk, A. N.; Lavis, L. D. General Synthetic Method for Si-Fluoresceins and Si-Rhodamines. *ACS Cent. Sci.* **2017**, *3* (9), 975–985. https://doi.org/10.1021/acscentsci.7b00247.
(84) Dwight, S. J.; Levin, S. Scalable Regioselective Synthesis of Rhodamine Dyes. *Org. Lett.* **2016**, *18* (20), 5316–5319. https://doi.org/10.1021/acs.orglett.6b02635.
(85) Zhou, Y.; Bi, T.; Wang, R.; Liang, P.; Lai, J.; Luo, Q.; Wang, H.; Shen, H.; Liu, Z.; Yang, S.; Ren, W. Optimization of the Procedure for Gram Scale Synthesis of Silicon Rhodamine and Its Application in Labeling BRD4 Kinase Inhibitor. *J. Anal. Test.* **2024**, *8* (4), 569–574. https://doi.org/10.1007/s41664-024-00309-y.
(86) Zhao, T.; Zhang, J.; Tang, M.; Ma, L. Z.; Lei, X. Development of an Effective Fluorescence Probe for Discovery of Aminopeptidase Inhibitors to Suppress Biofilm Formation. *J. Antibiot.* **2019**, *72* (6), 461–468. https://doi.org/10.1038/s41429-019-0166-z.
(87) Terai, T.; Kohno, M.; Boncompain, G.; Sugiyama, S.; Saito, N.; Fujikake, R.; Ueno, T.; Komatsu, T.; Hanaoka, K.; Okabe, T.; Urano, Y.; Perez, F.; Nagano, T. Artificial Ligands of Streptavidin (ALiS): Discovery, Characterization, and Application for Reversible Control of Intracellular Protein Transport. *J. Am. Chem. Soc.* **2015**, *137* (33), 10464–10467. https://doi.org/10.1021/jacs.5b05672.
(88) Singh, V.; Wang, S.; Kool, E. T. Genetically Encoded Multispectral Labeling of Proteins with Polyfluorophores on a DNA Backbone. *J. Am. Chem. Soc.* **2013**, *135* (16), 6184–6191. https://doi.org/10.1021/ja4004393.
(89) Cong, M.; Corona, C.; Mcdougall, M. G.; Zimprich, C. pH Sensors. US9702824B2, July 11, 2017.
(90) Taj, R.; Sorensen, J. L. Synthesis of Actinomycetes Natural Products JBIR-94, JBIR-125, and Related Analogues. *Tetrahedron Lett.* **2015**, *56* (51), 7108–7111. https://doi.org/10.1016/j.tetlet.2015.11.020.
(91) Ayala, C. E.; Villalpando, A.; Nguyen, A. L.; McCandless, G. T.; Kartika, R. Chlorination of Aliphatic Primary Alcohols via Triphosgene–Triethylamine Activation. *Org. Lett.* **2012**, *14* (14), 3676–3679. https://doi.org/10.1021/ol301520d.
(92) Nakagawa, Y.; Irie, K.; Masuda, A.; Ohigashi, H. Synthesis, Conformation and PKC Isozyme Surrogate Binding of New Lactone Analogues of Benzolactam-V8s. *Tetrahedron* **2002**, *58* (11), 2101–2115. https://doi.org/10.1016/S0040-4020(02)00099-6.

12 NMR spectra

Compound 3

^{1}H-NMR

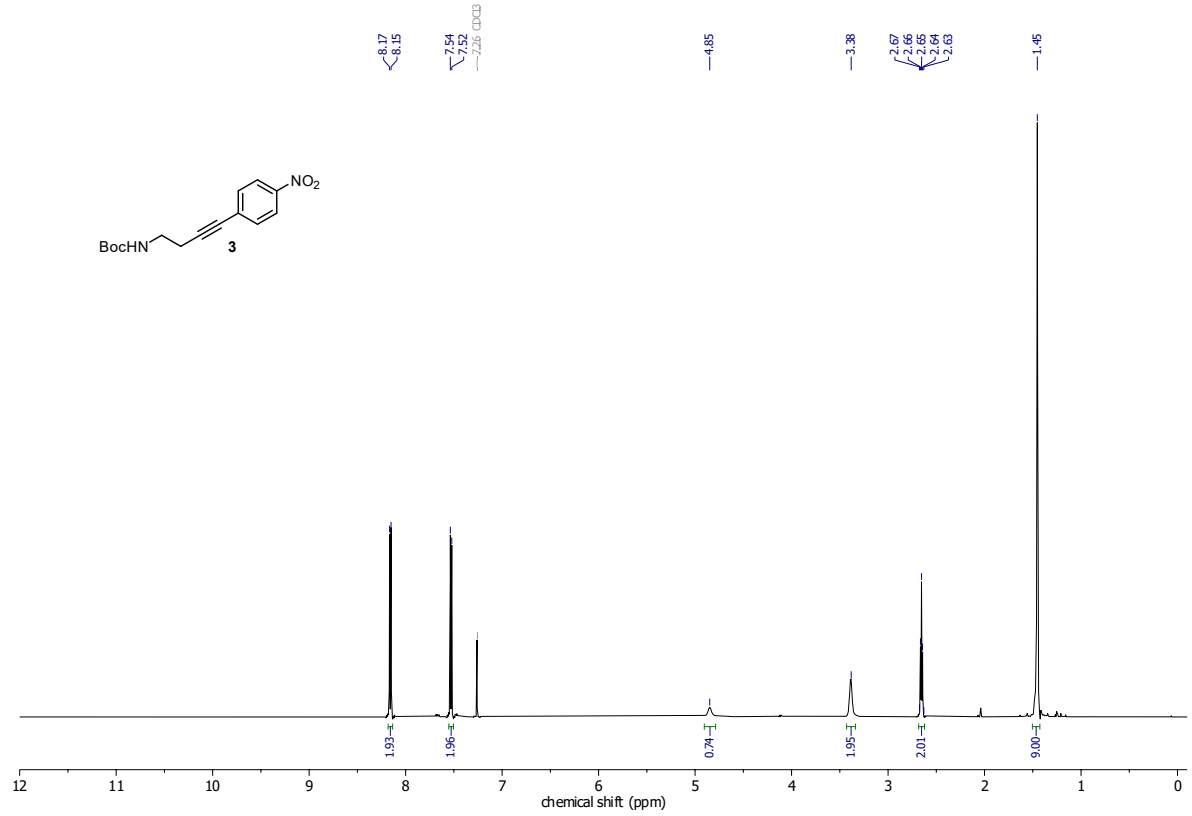

^{13}C-NMR

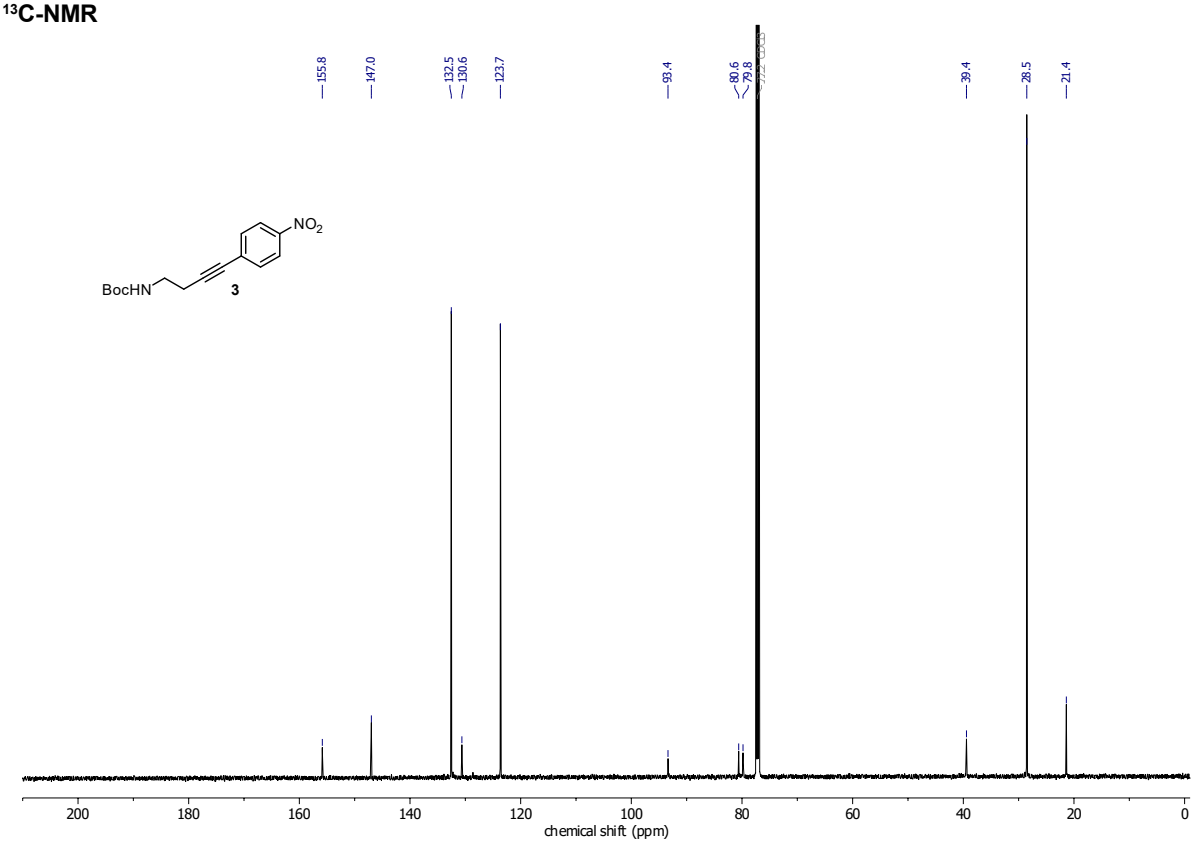

Compound 4

^{1}H-NMR

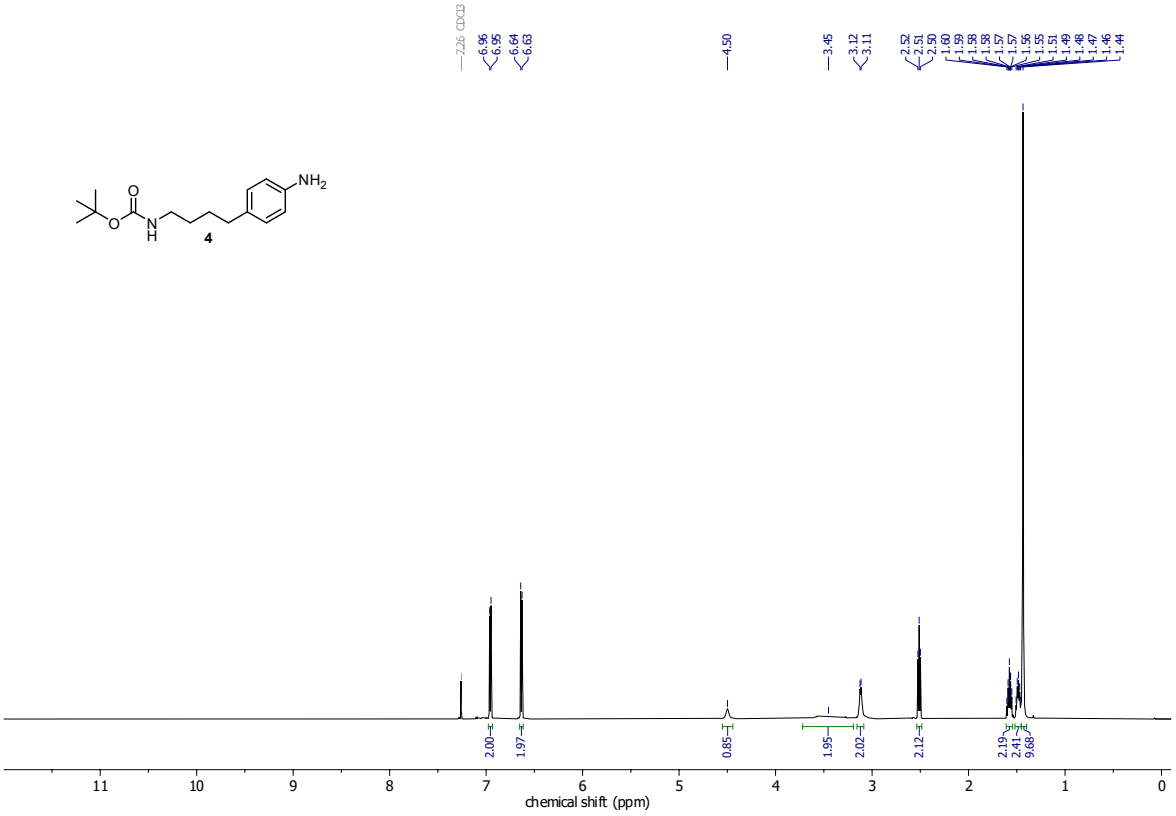

^{13}C-NMR

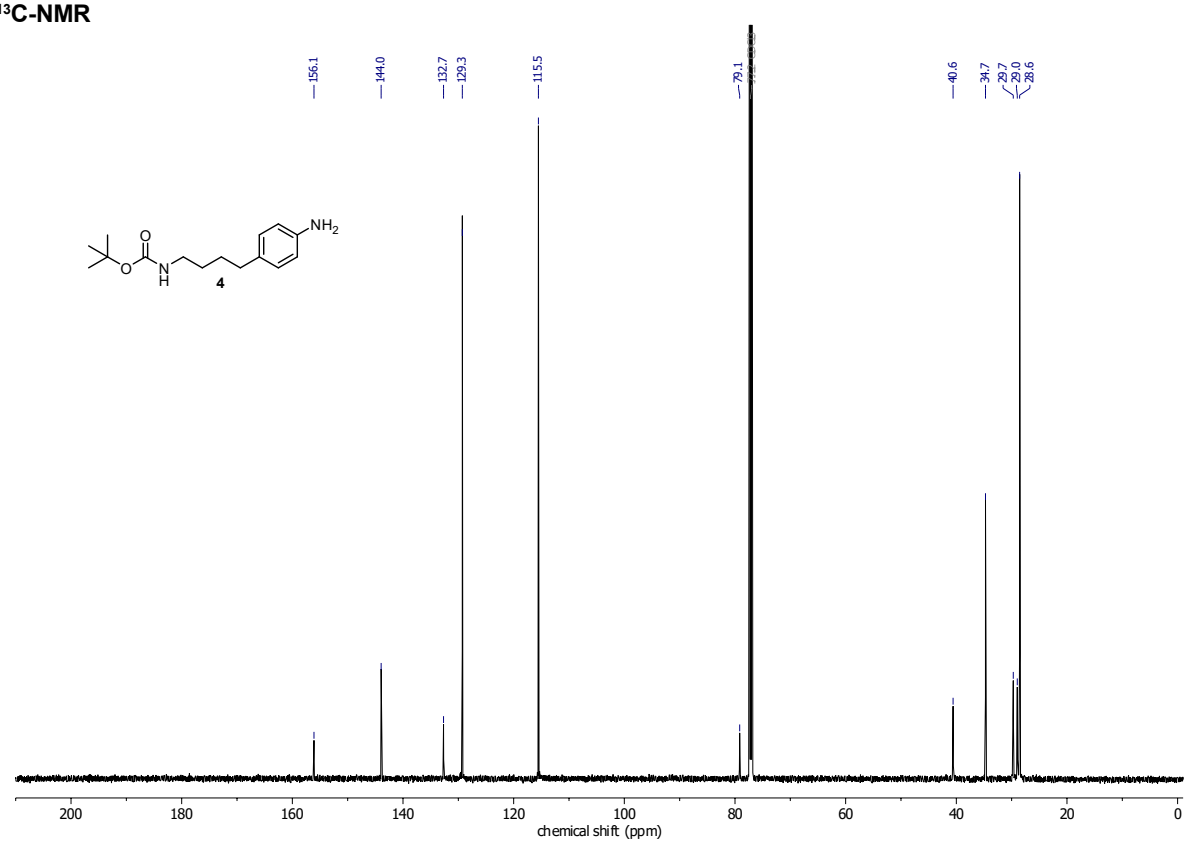

CHalo-Boc

^{1}H-NMR

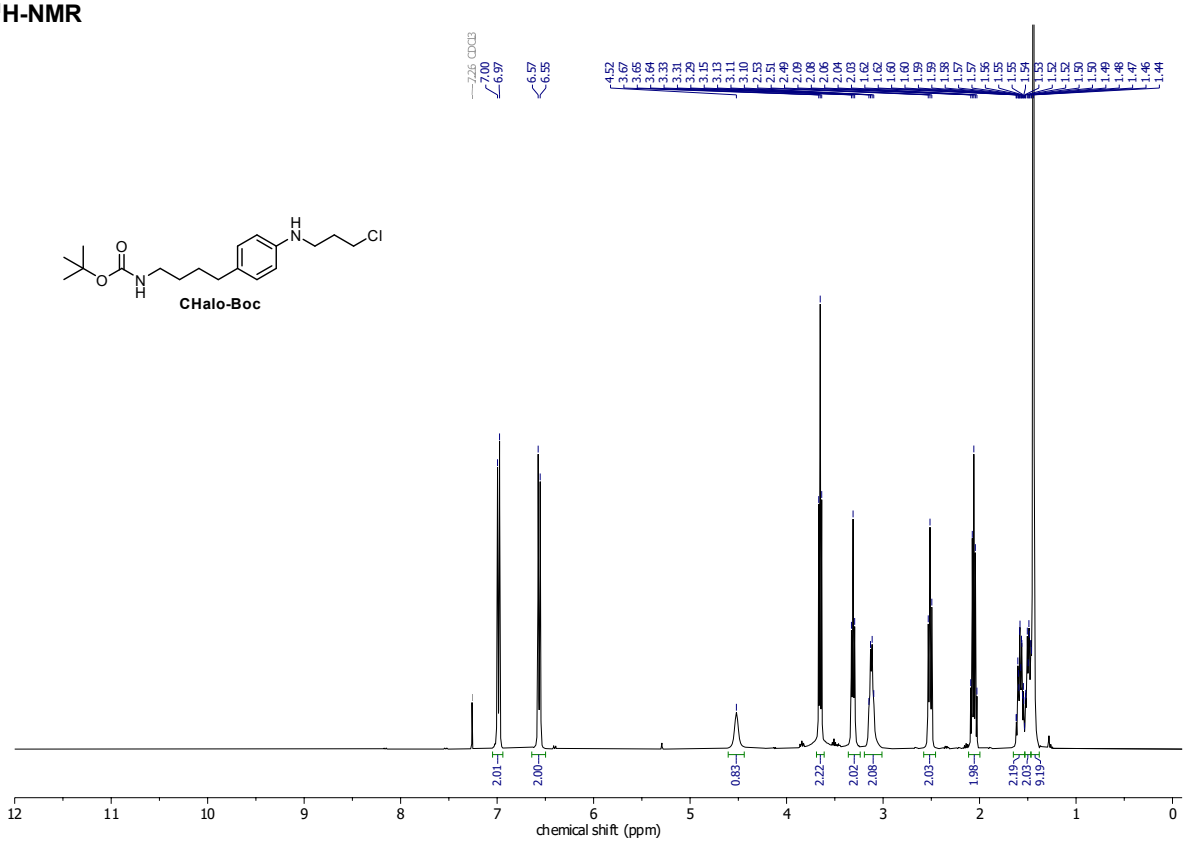

^{13}C-NMR

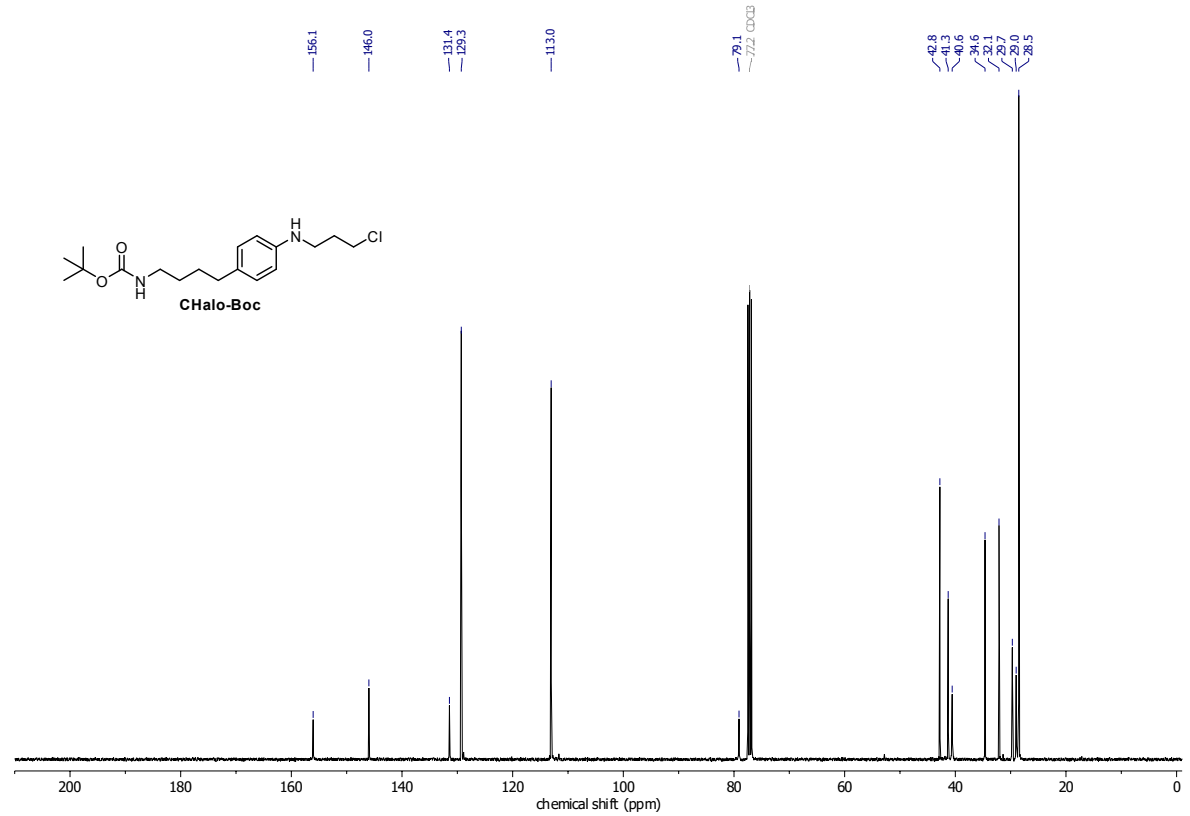

Cou-CHalo-Boc

^{1}H-NMR

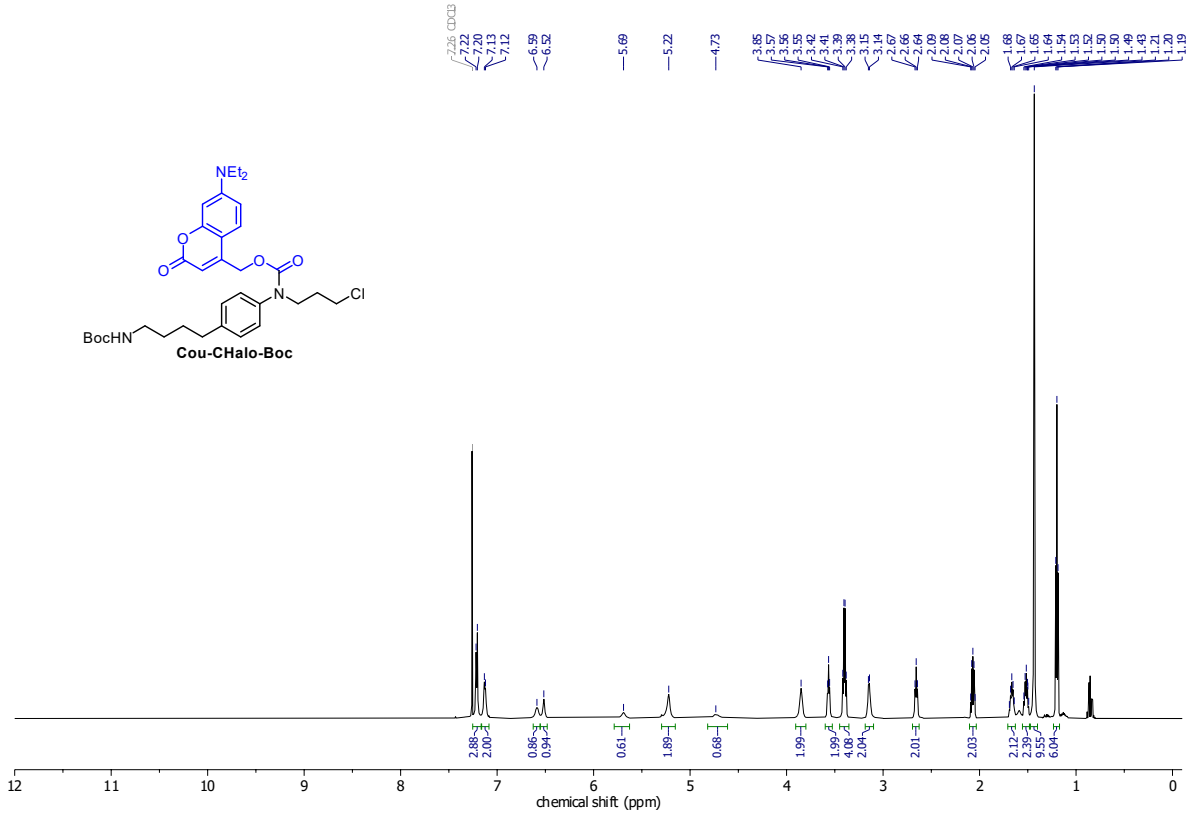

^{13}C-NMR

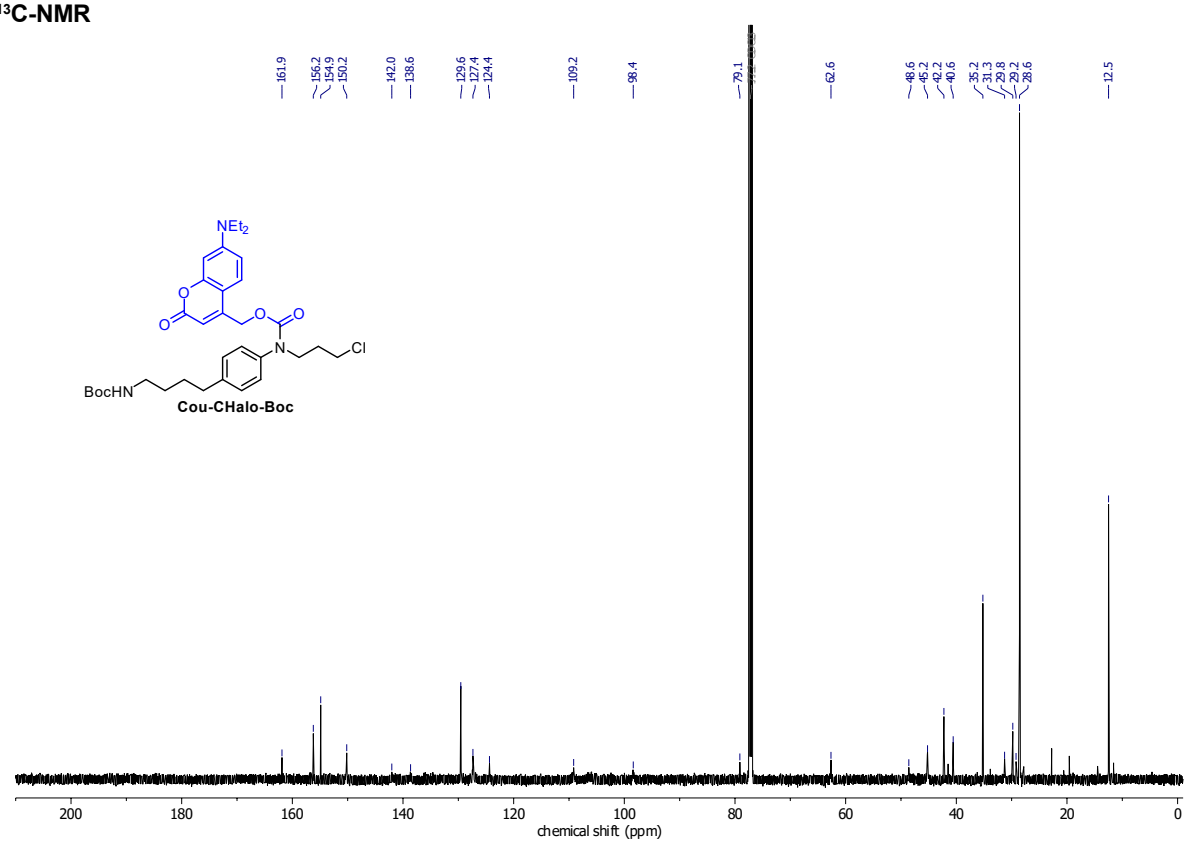

HSQC

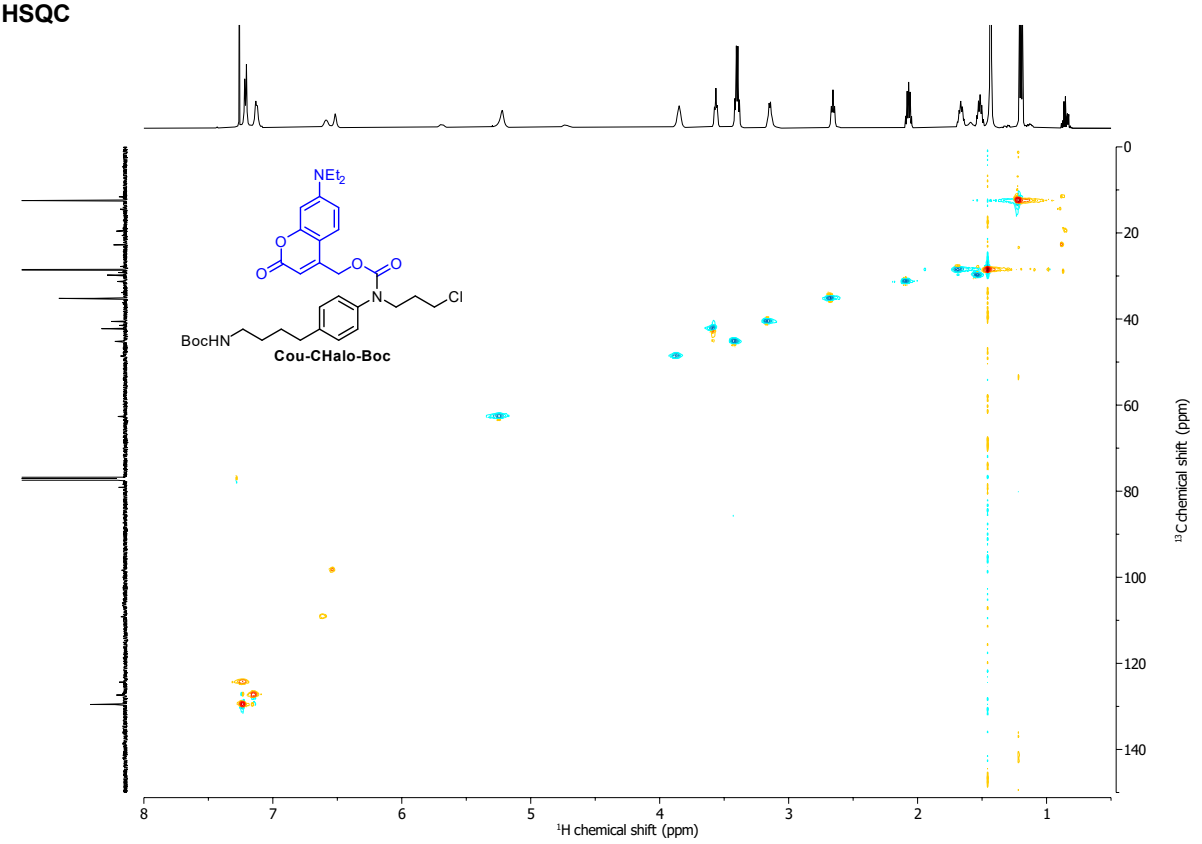
NEt2
O
O
O
O
N
Cl
BocHN
Cou-CHalo-Boc
8
7
6
5
4
3
2
1
¹H chemical shift (ppm)
0
20
40
60
80
100
120
140
¹³C chemical shift (ppm)

CHalo-SiR

^{1}H-NMR

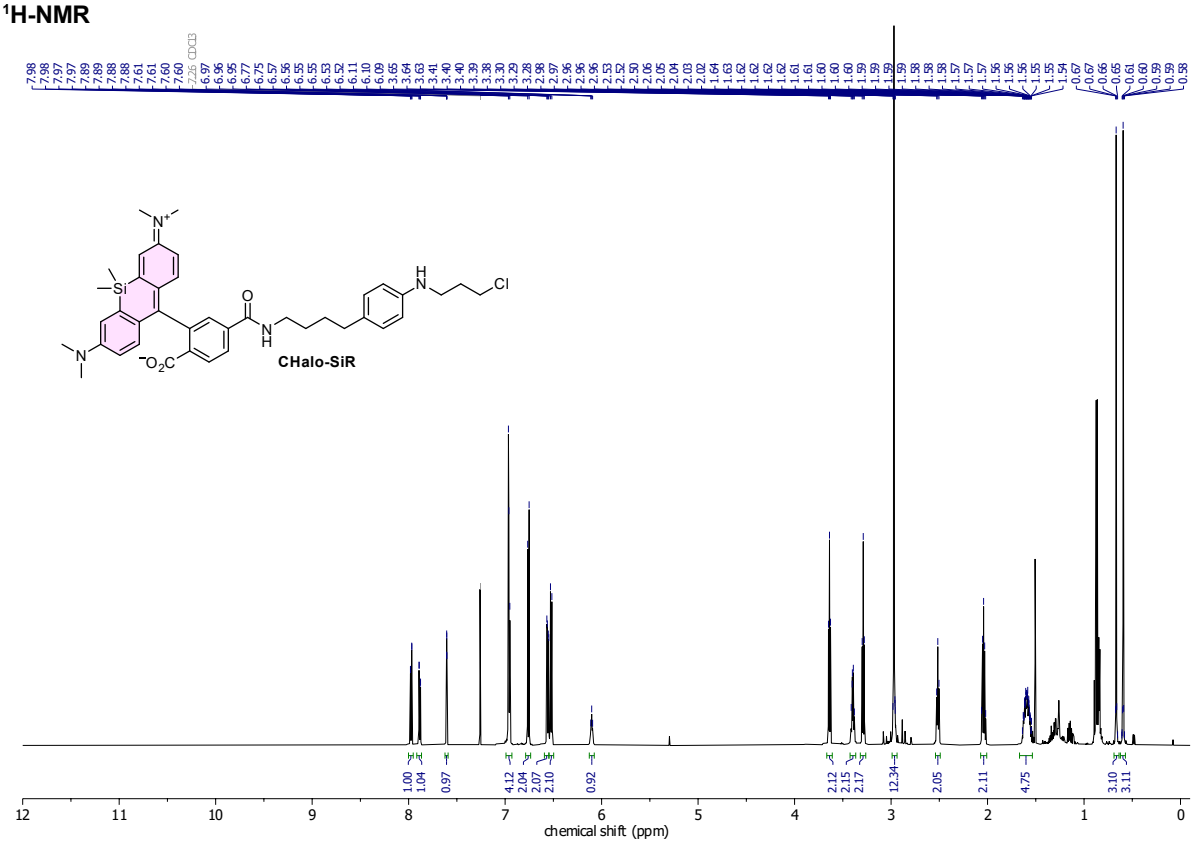

^{13}C-NMR

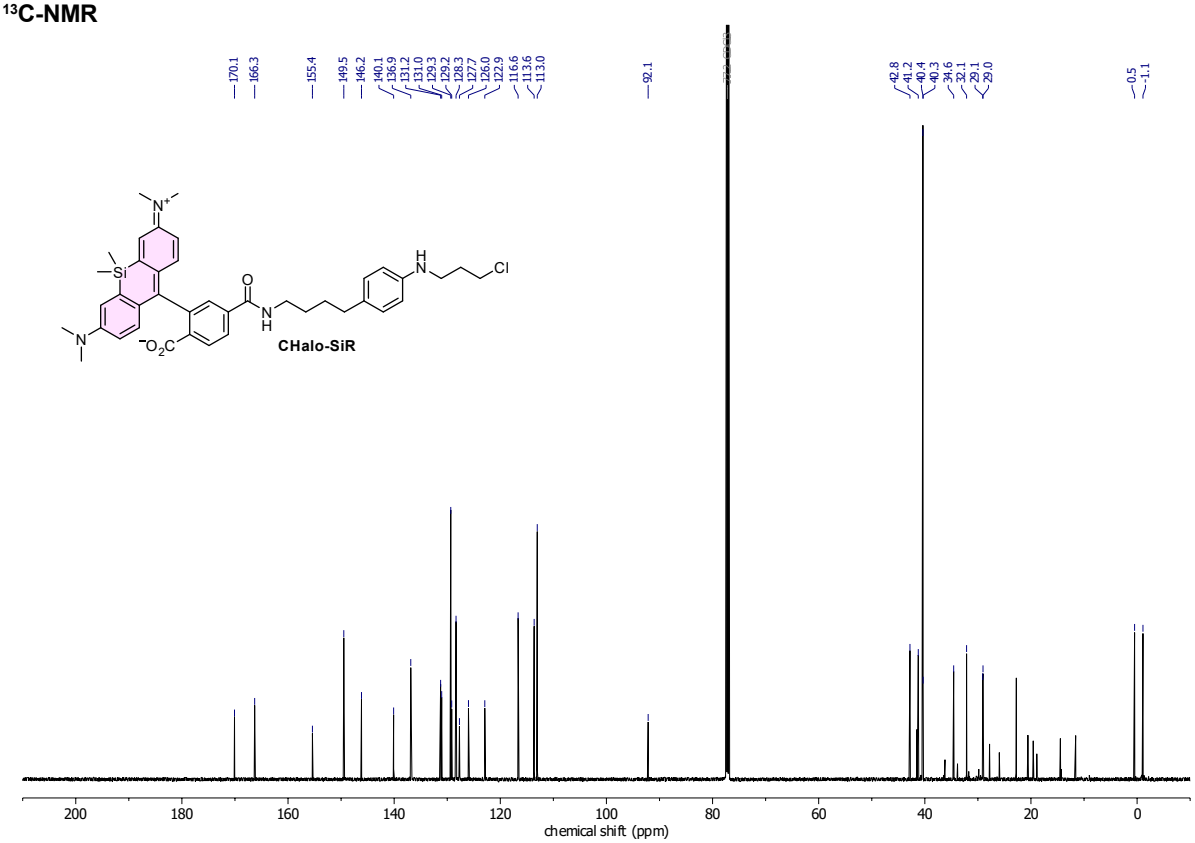

**minor H-grease impurities*

HSQC

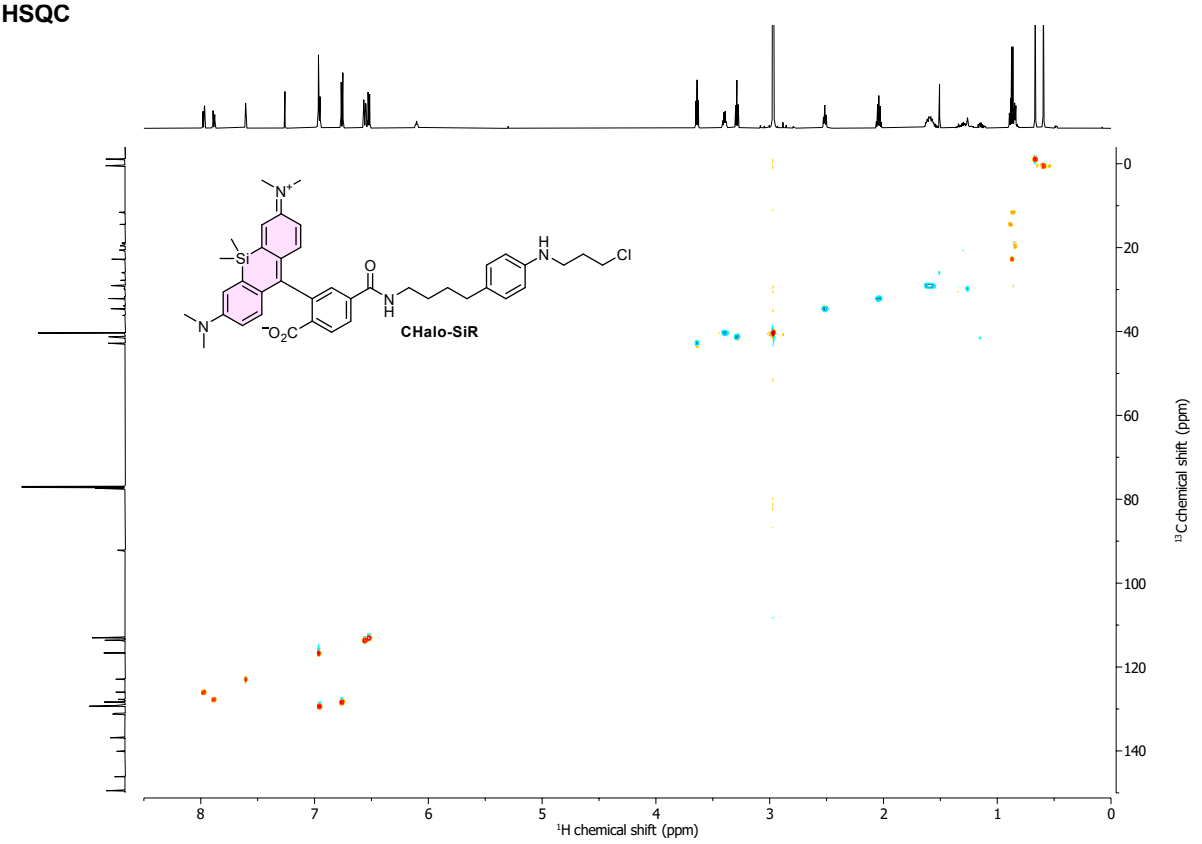
CHalo-SiR
^{1}H chemical shift (ppm)
^{13}C chemical shift (ppm)

HMBC

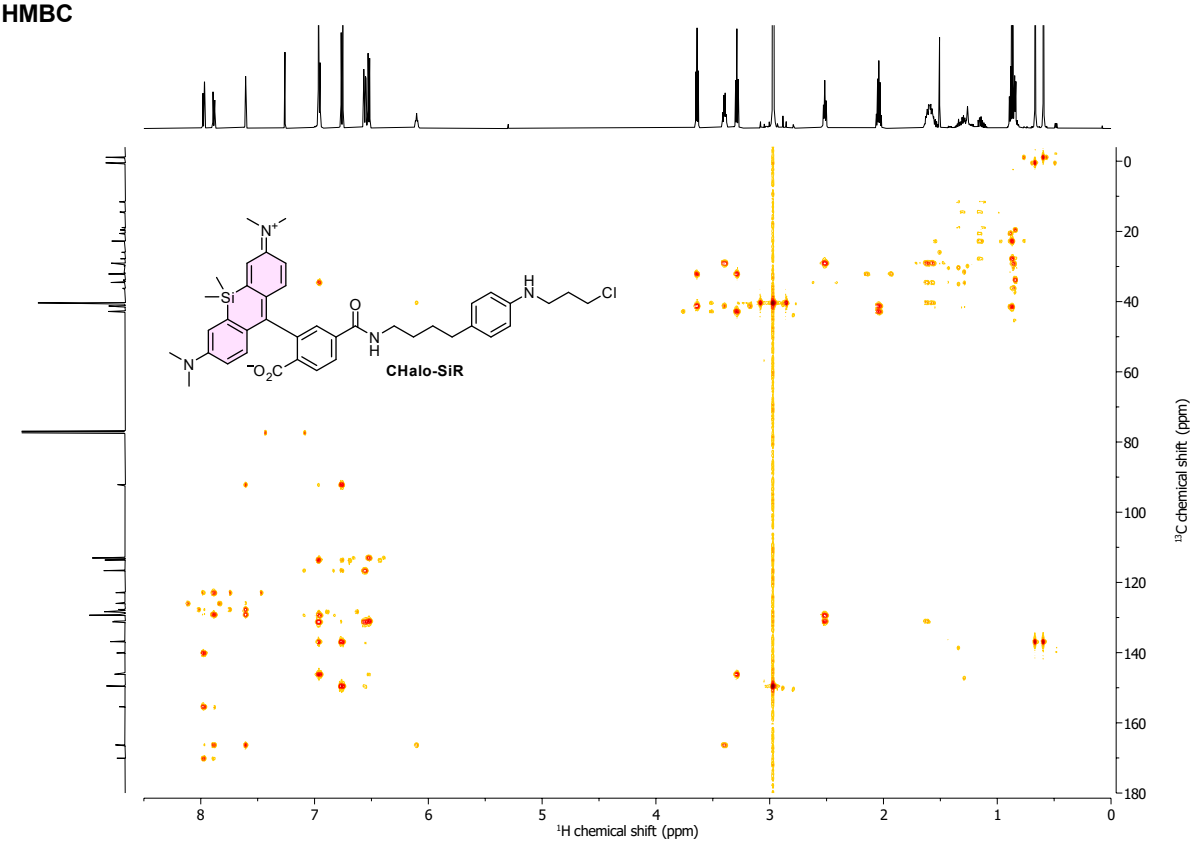
CHalo-SiR
^{1}H chemical shift (ppm)
^{13}C chemical shift (ppm)

Compound 8

^{1}H-NMR

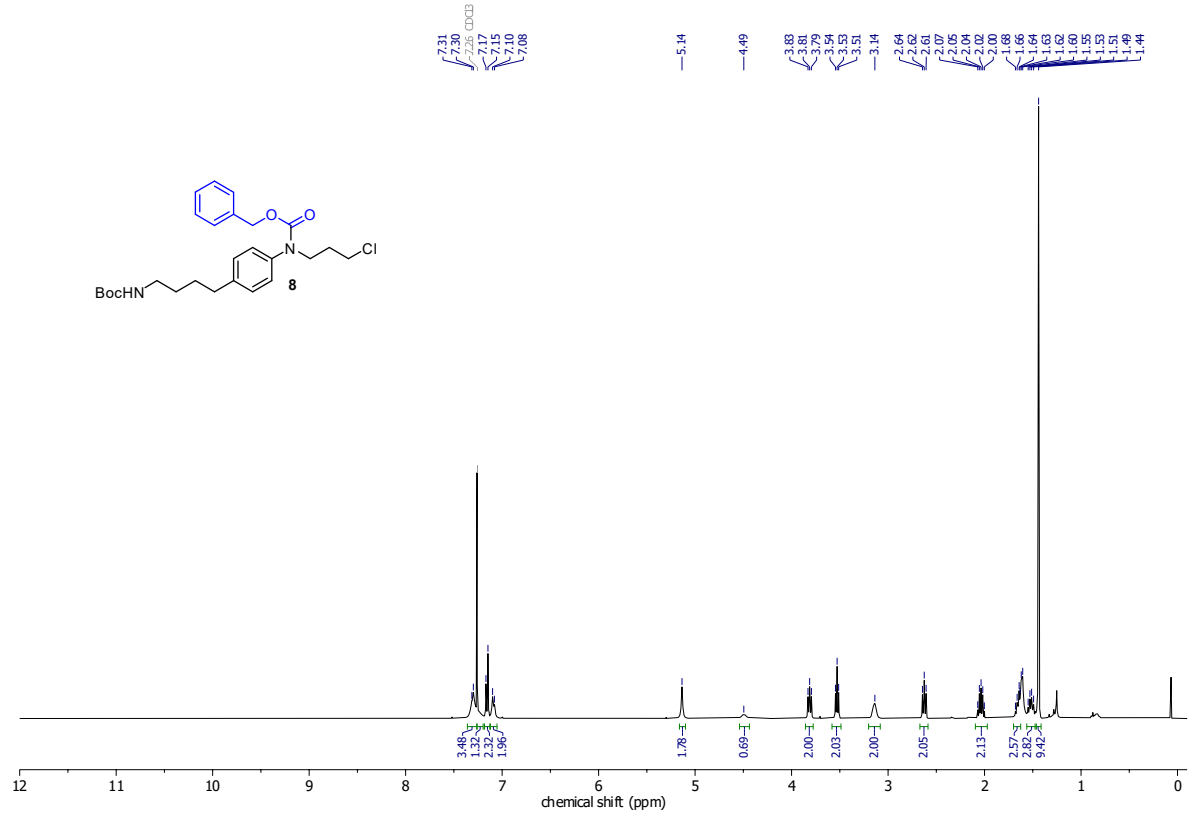

^{13}C-NMR

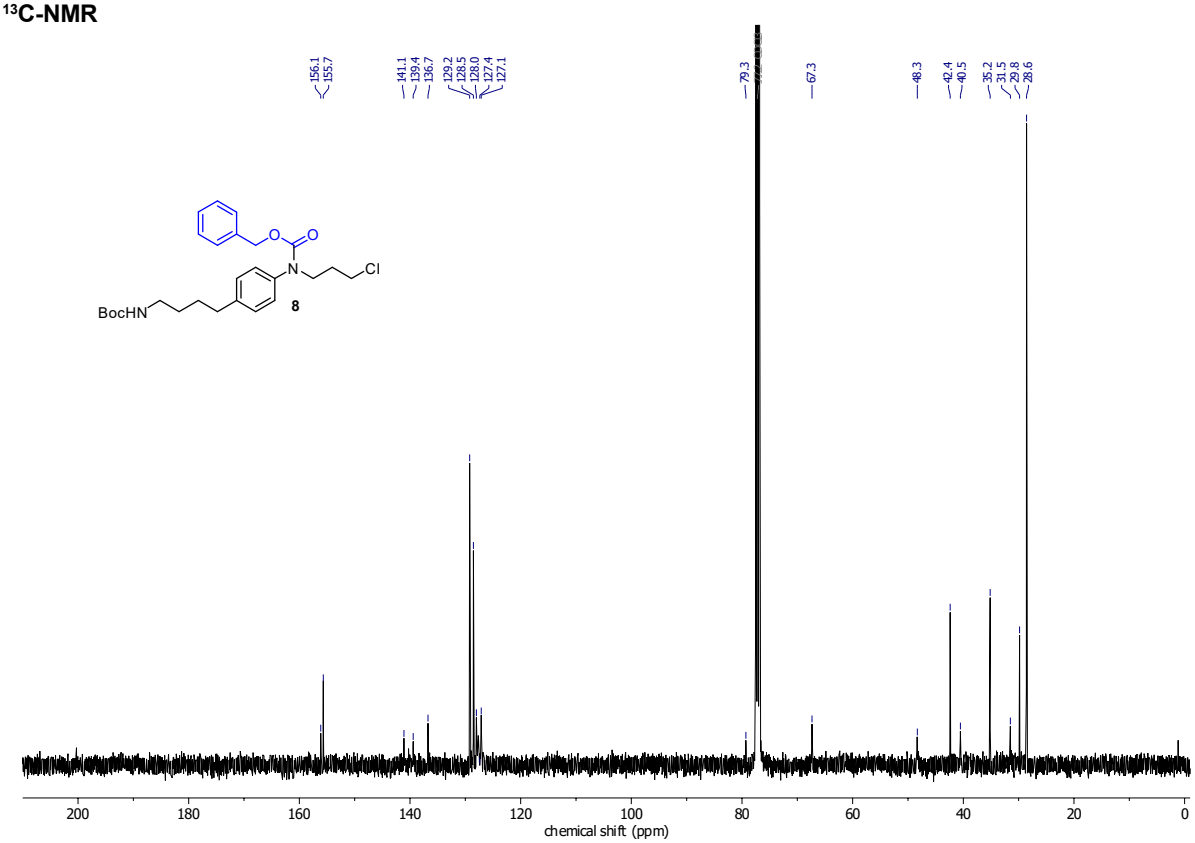

Bn-CHalo-SiR

^{1}H-NMR

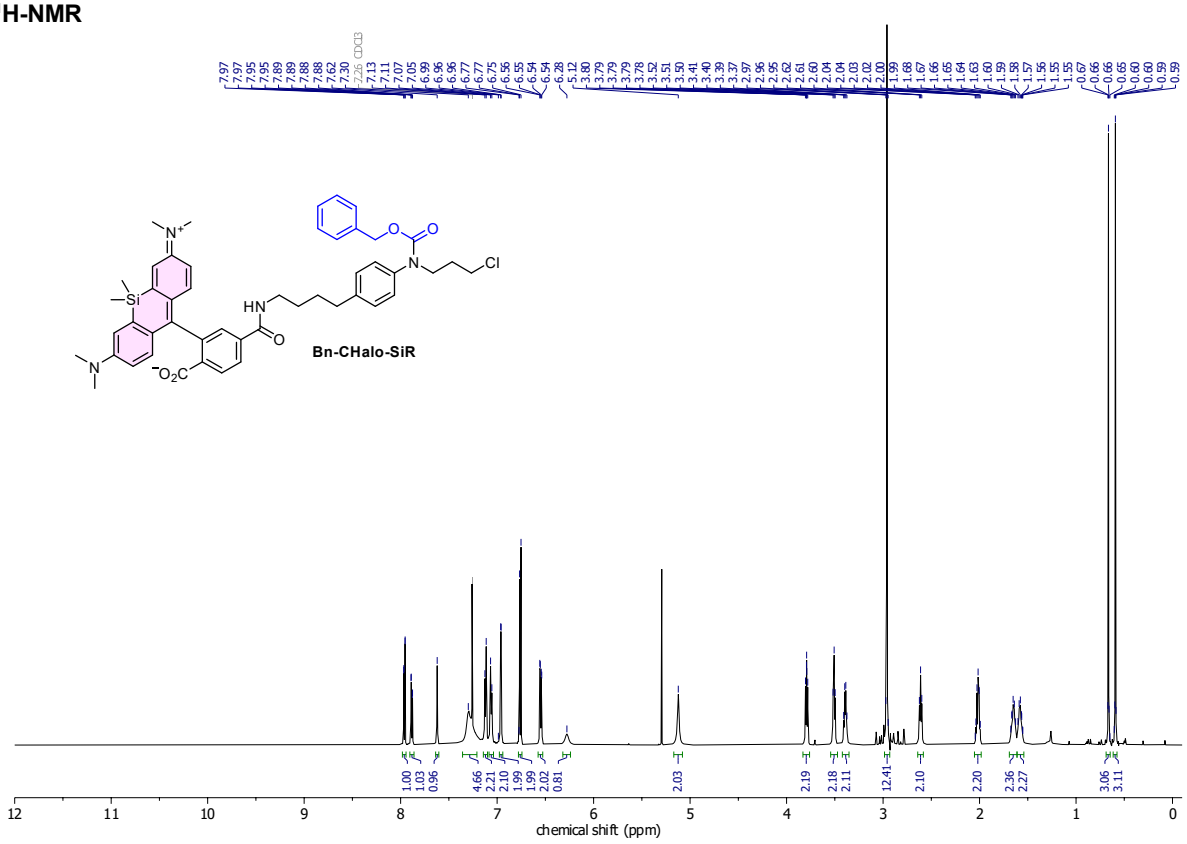

^{13}C-NMR

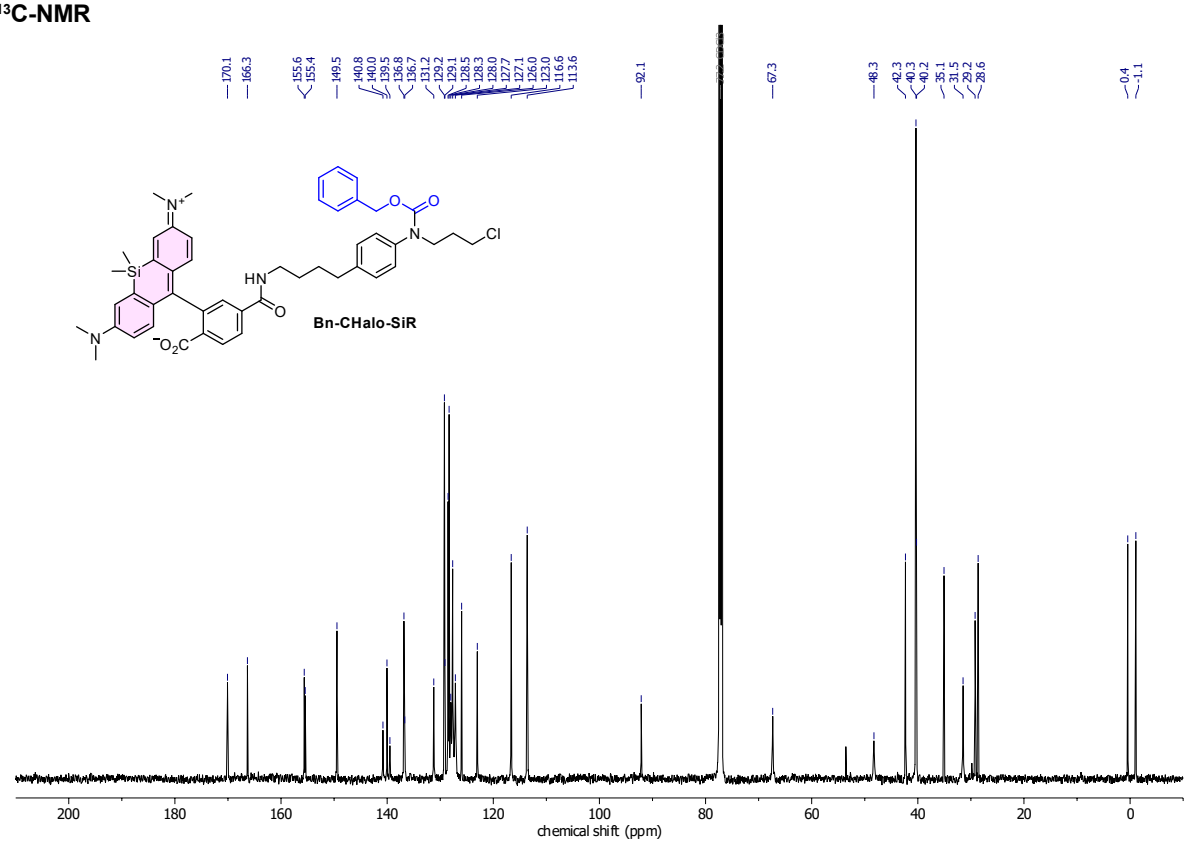

Cou-CHalo-SiR

^{1}H-NMR

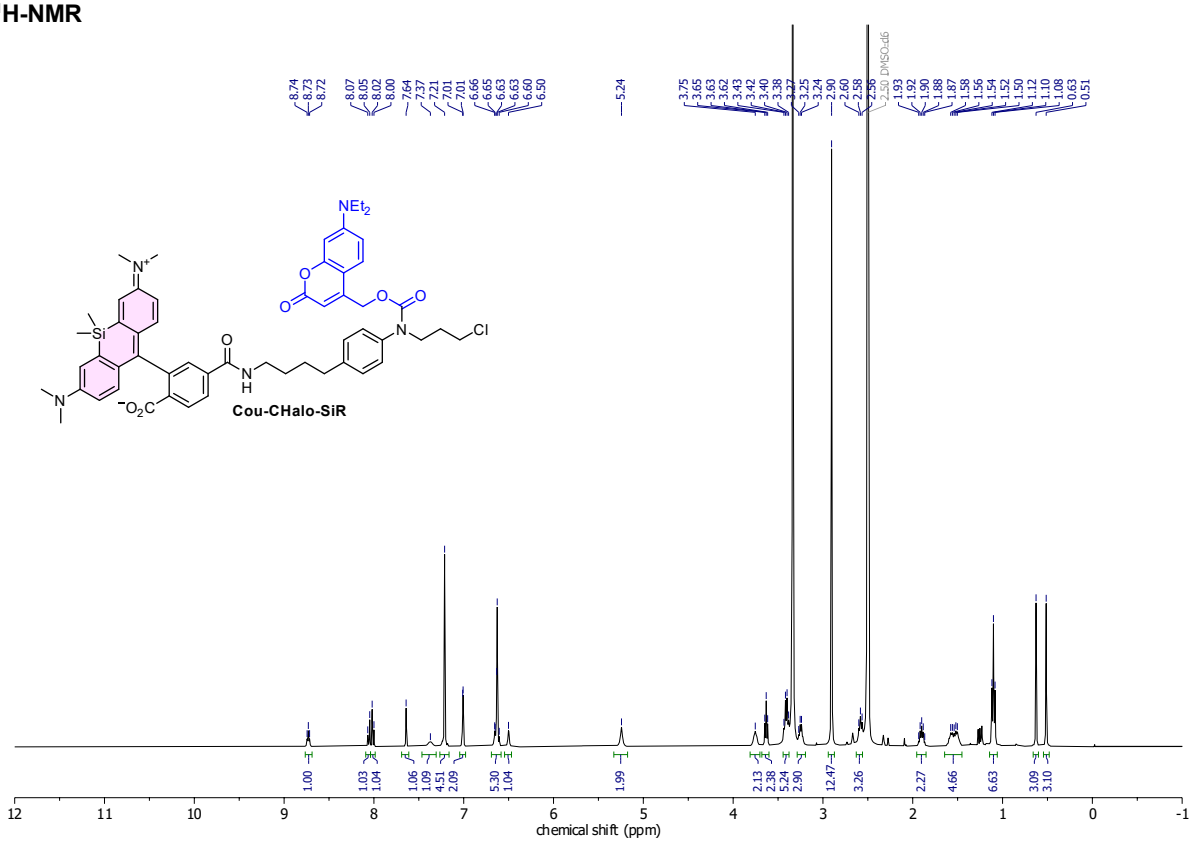

^{13}C-NMR

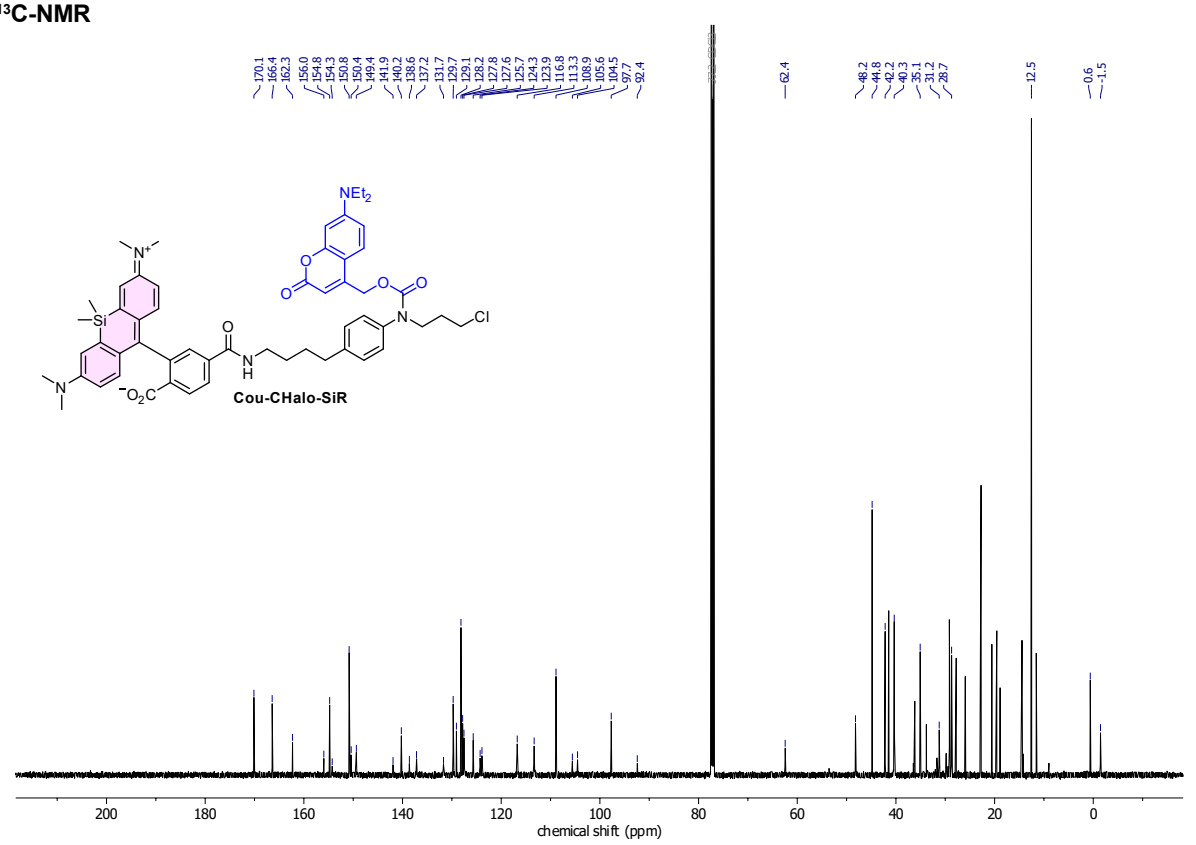

**minor H-grease impurities in ^{13}C-spectrum*

HSQC

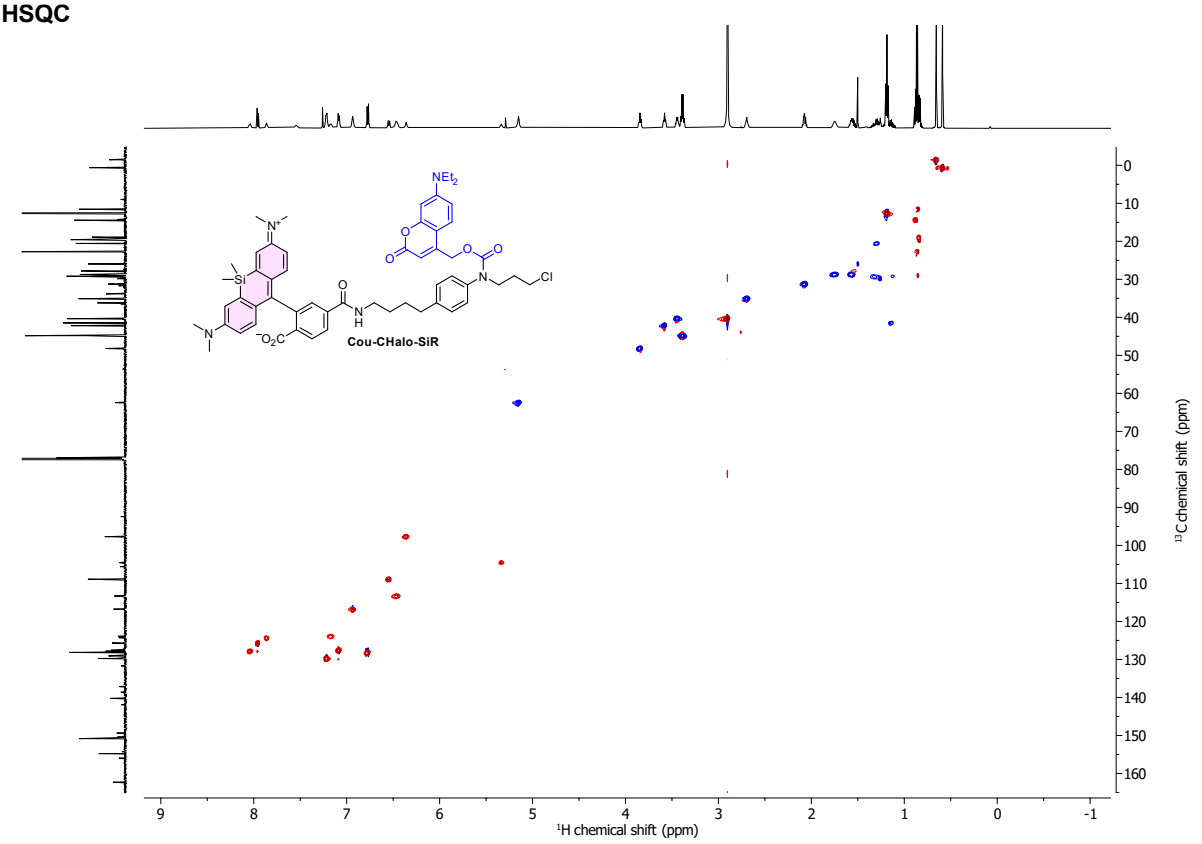
Cou-CHalo-SiR
^{1}H chemical shift (ppm)
^{13}C chemical shift (ppm)

HMBC

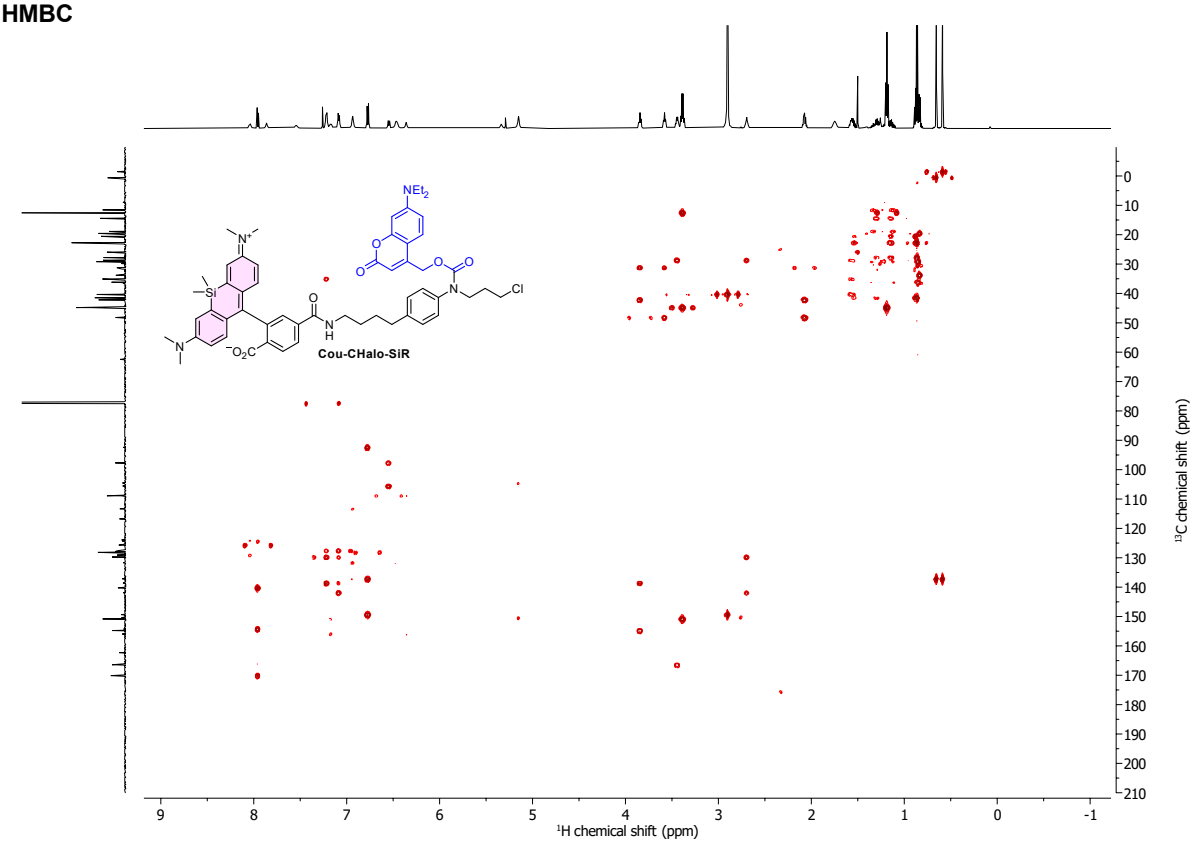
Cou-CHalo-SiR
^{1}H chemical shift (ppm)
^{13}C chemical shift (ppm)

Compound 11

^{1}H-NMR

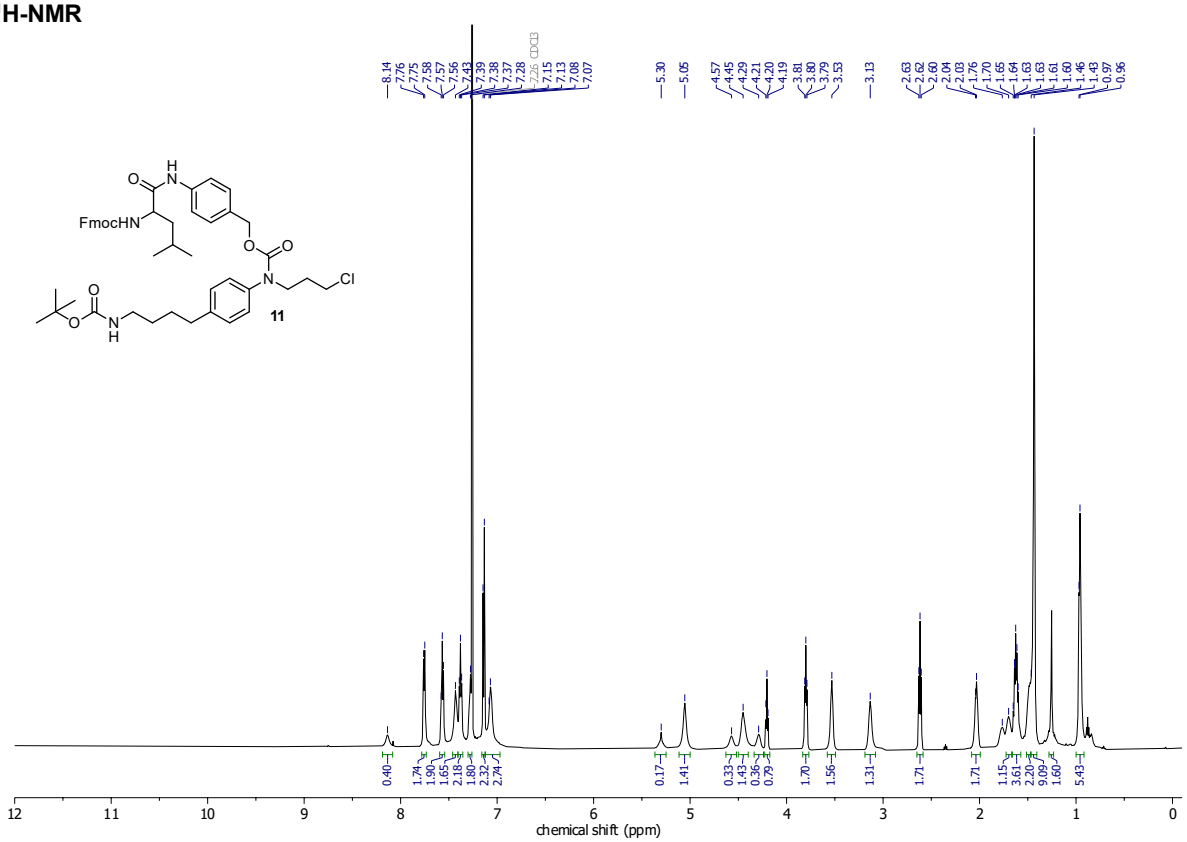

^{13}C-NMR

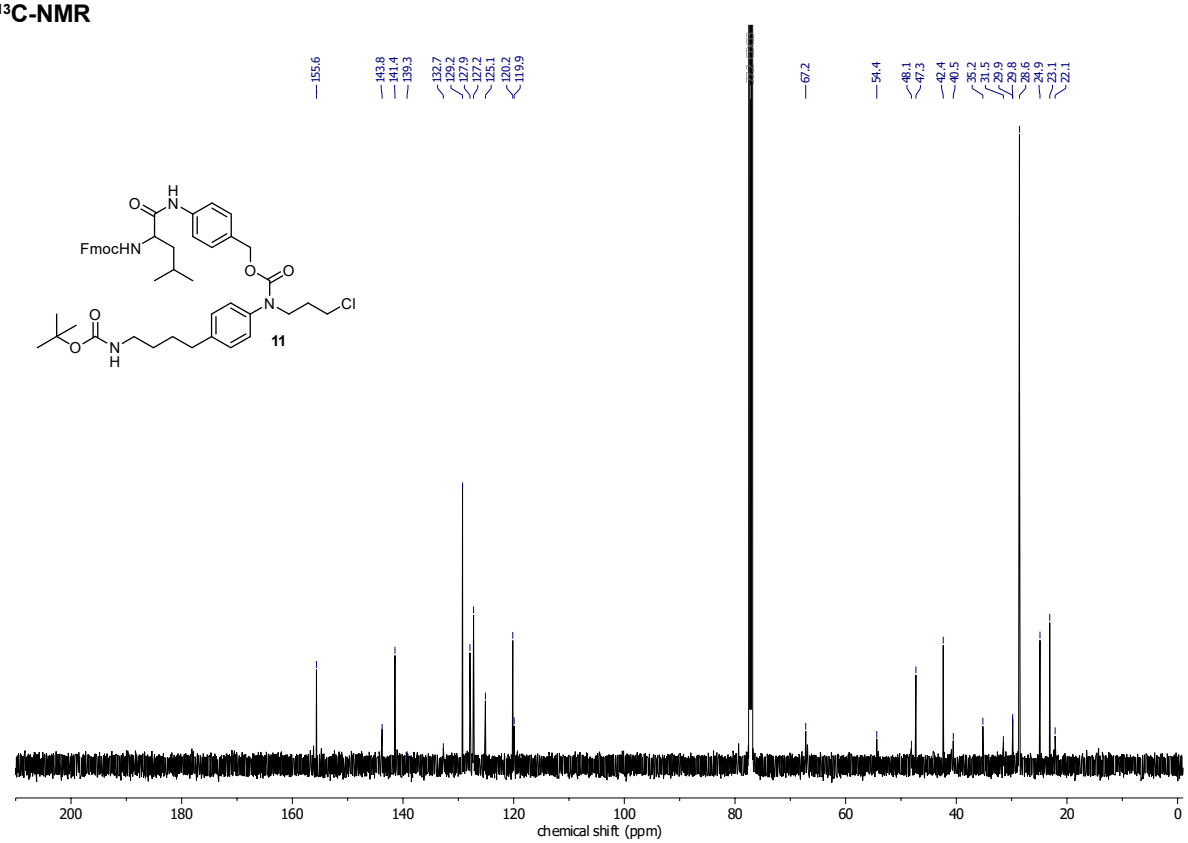

HSQC

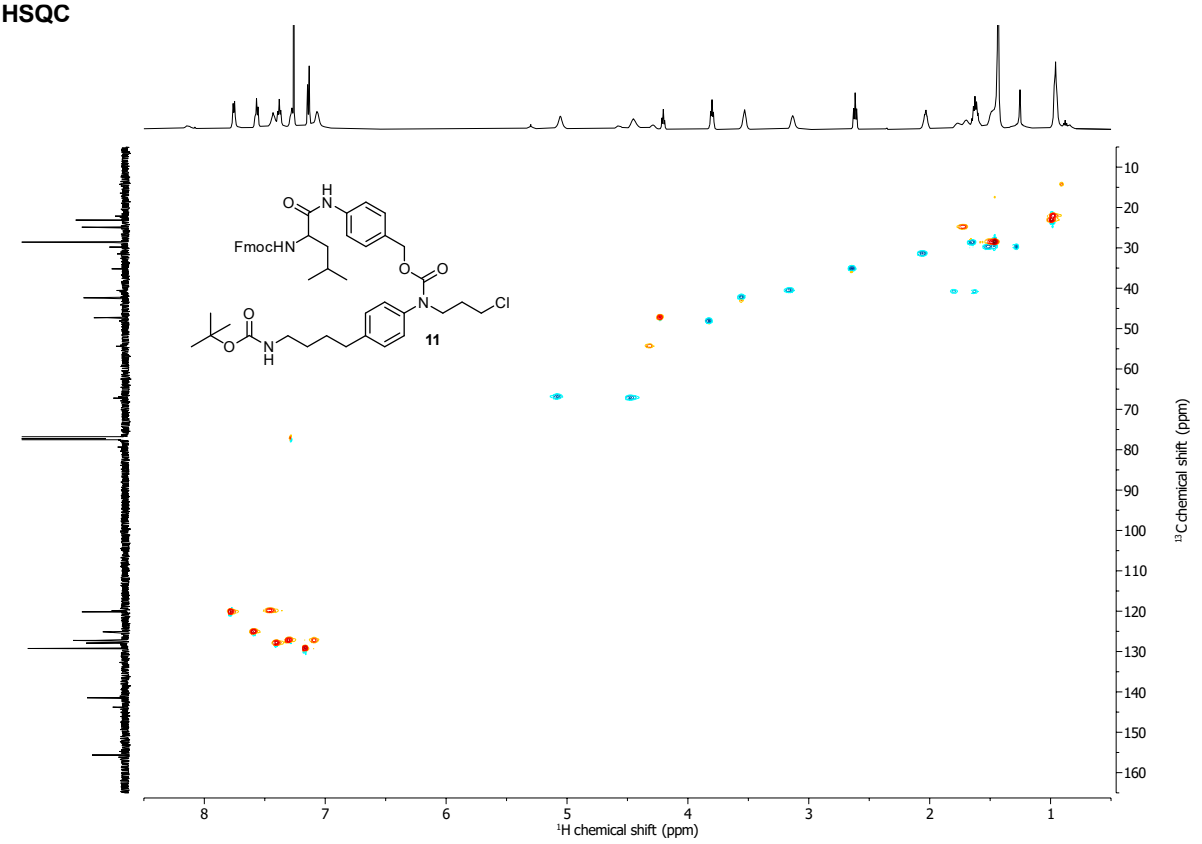
FmocHN
Cl
11
^{13}C chemical shift (ppm)
^{1}H chemical shift (ppm)

HMBC

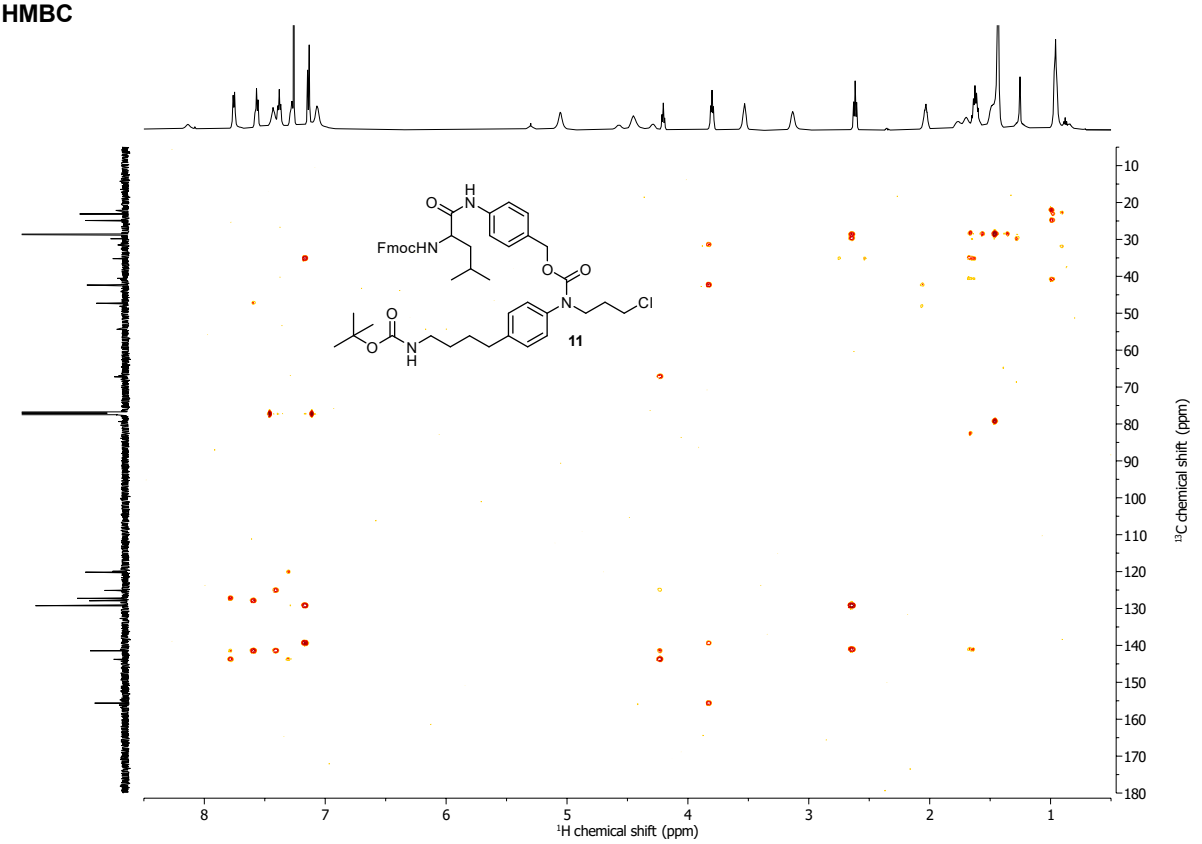
FmocHN
Cl
11
^{13}C chemical shift (ppm)
^{1}H chemical shift (ppm)

Leu-CHalo-SiR

^{1}H-NMR

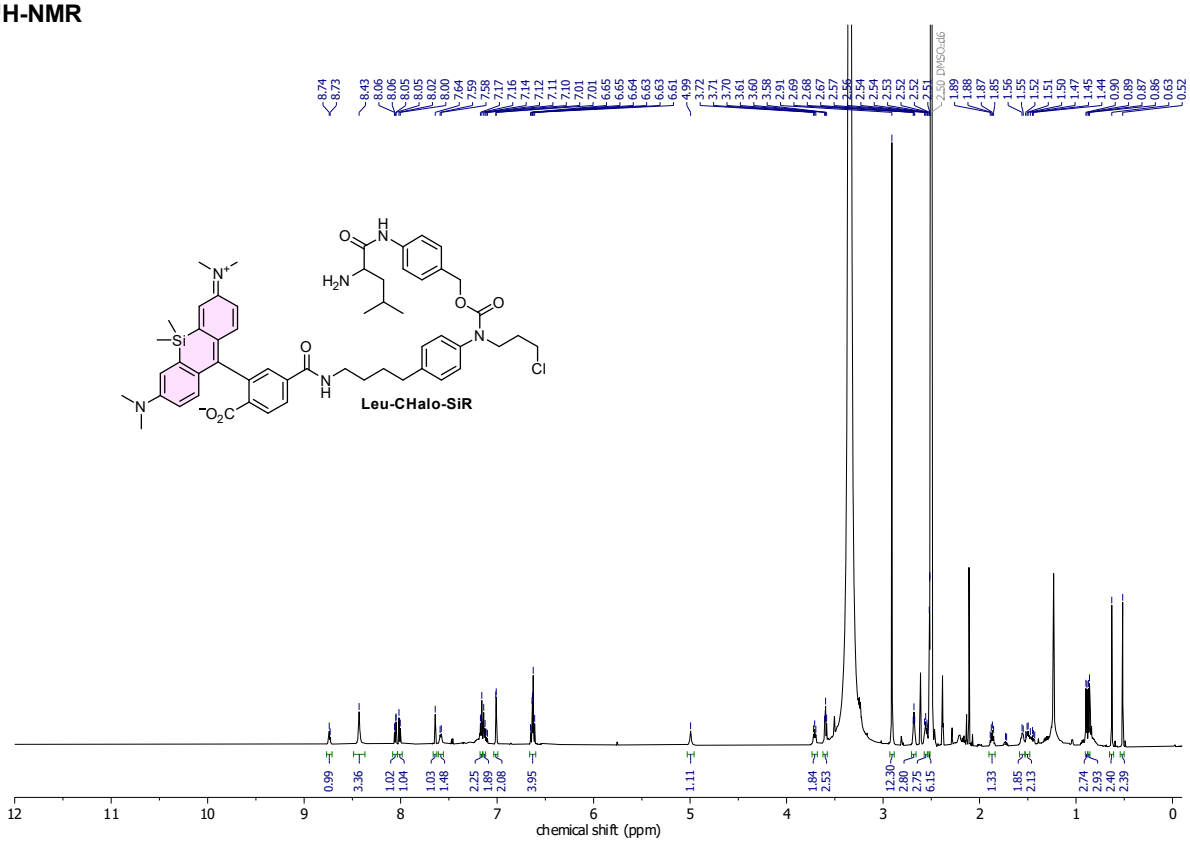

Compound 72
^{1}H-NMR

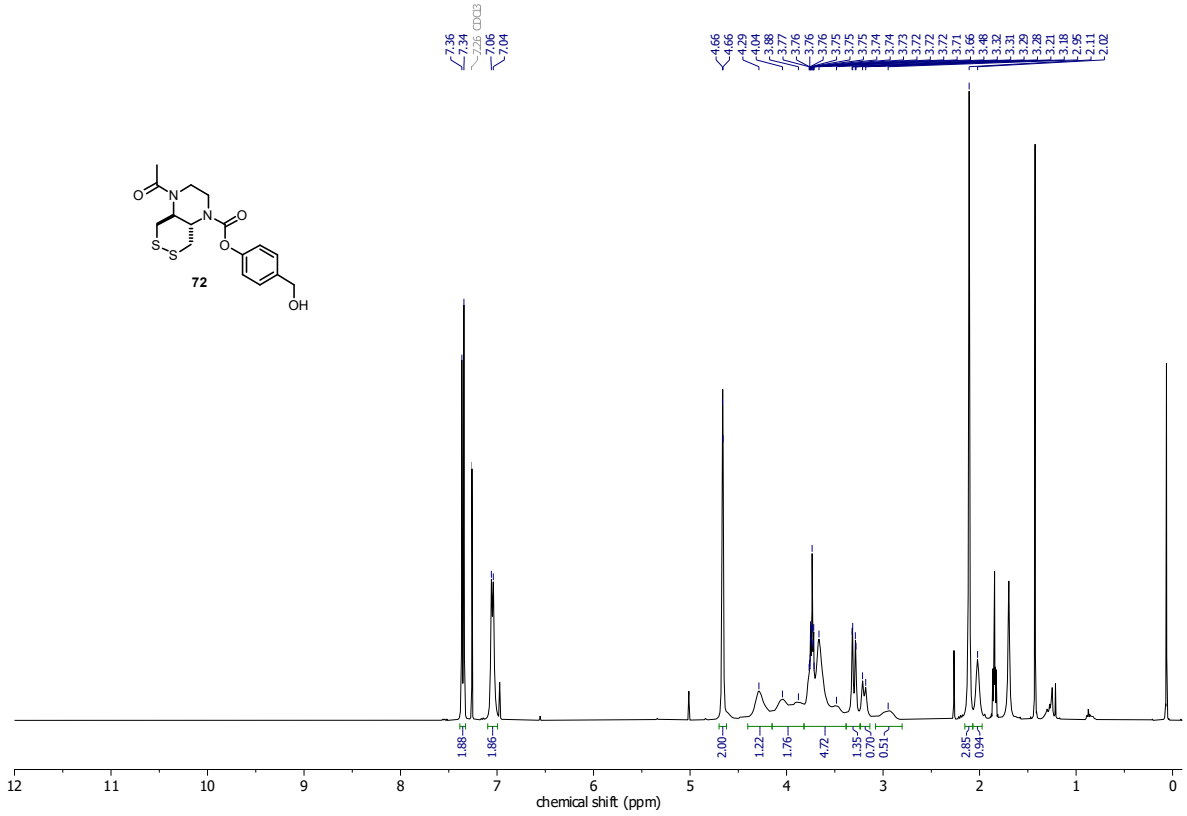

**minor silicon grease impurity*

Compound 73
^{1}H-NMR

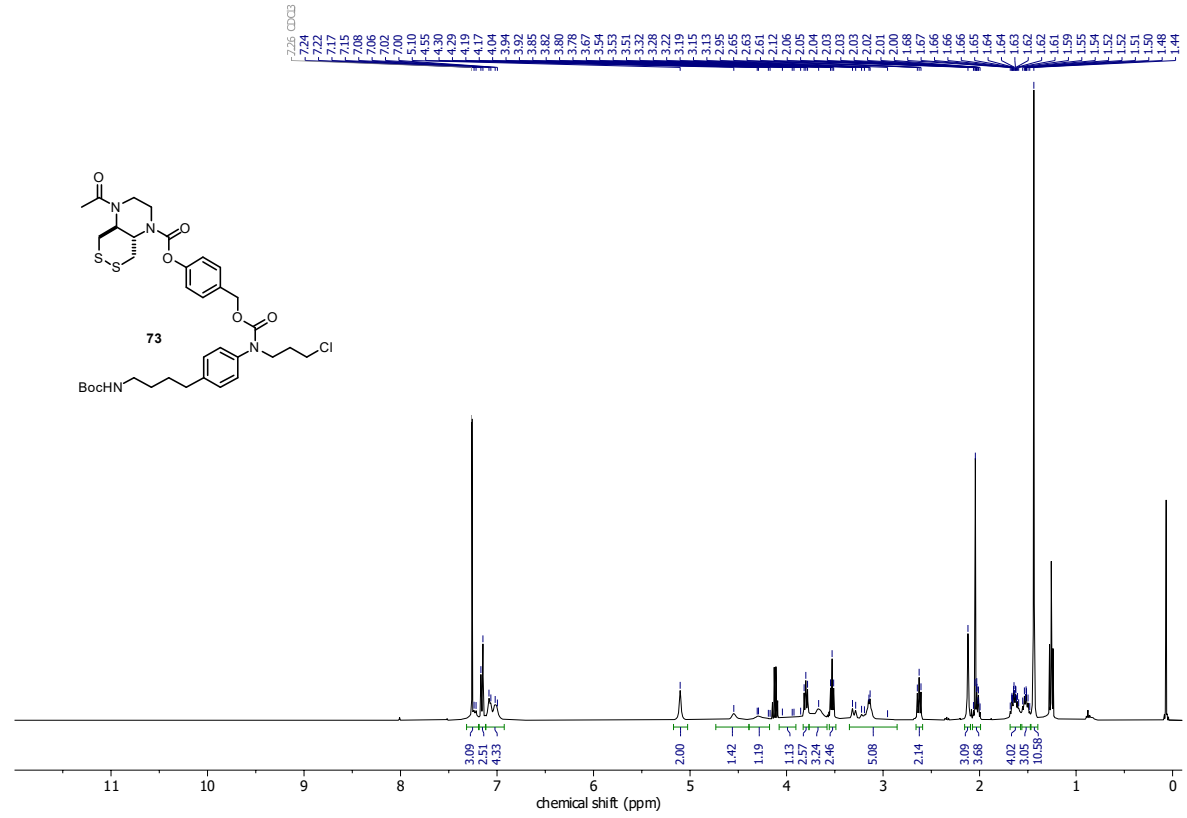

**ethyl acetate and silicon grease impurities*

Compound 76

^{1}H-NMR

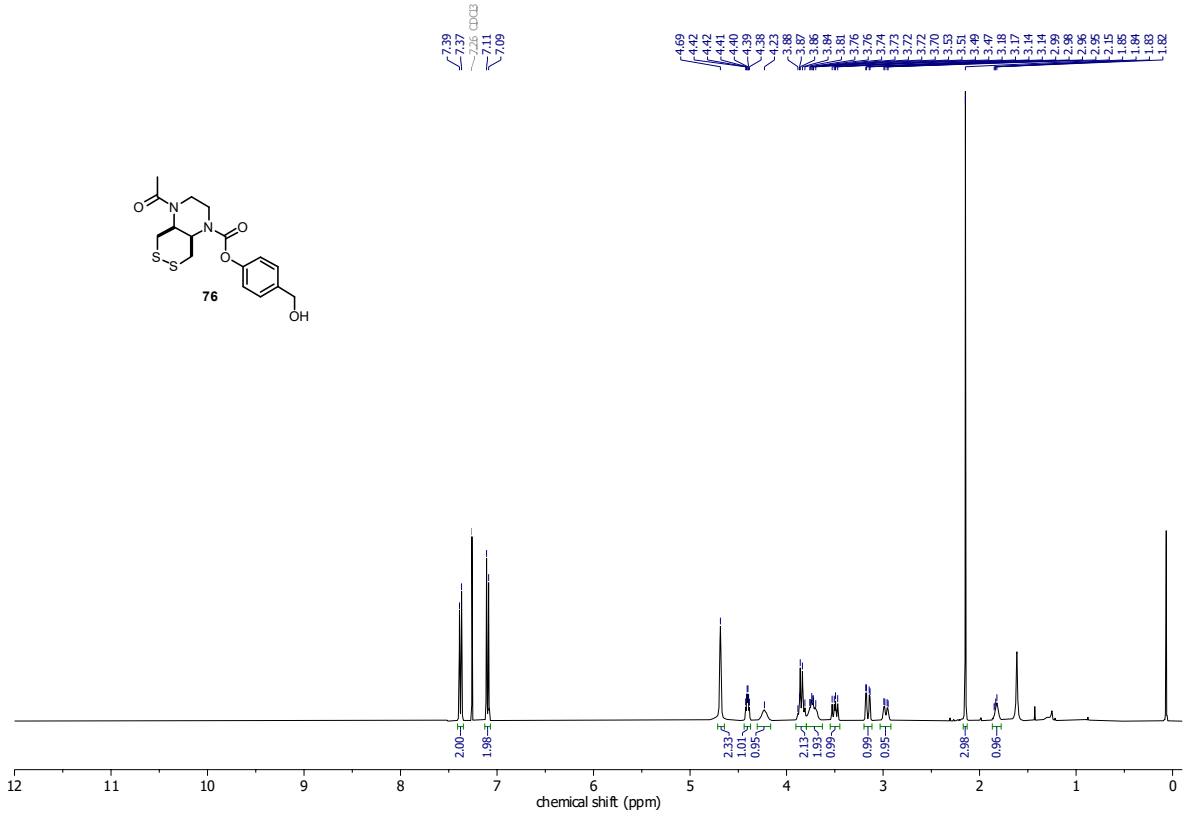

^{13}C-NMR

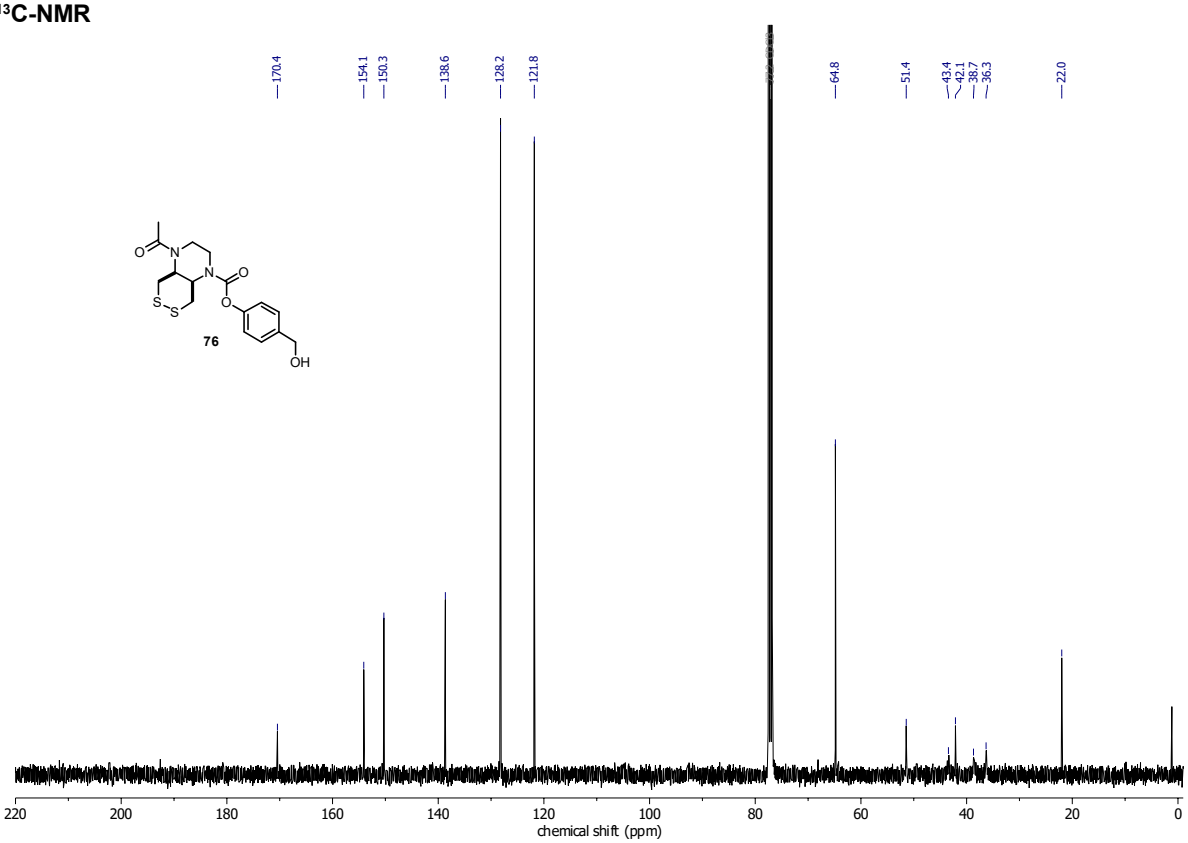

**minor silicon grease impurity*

Compound 77
^{1}H-NMR

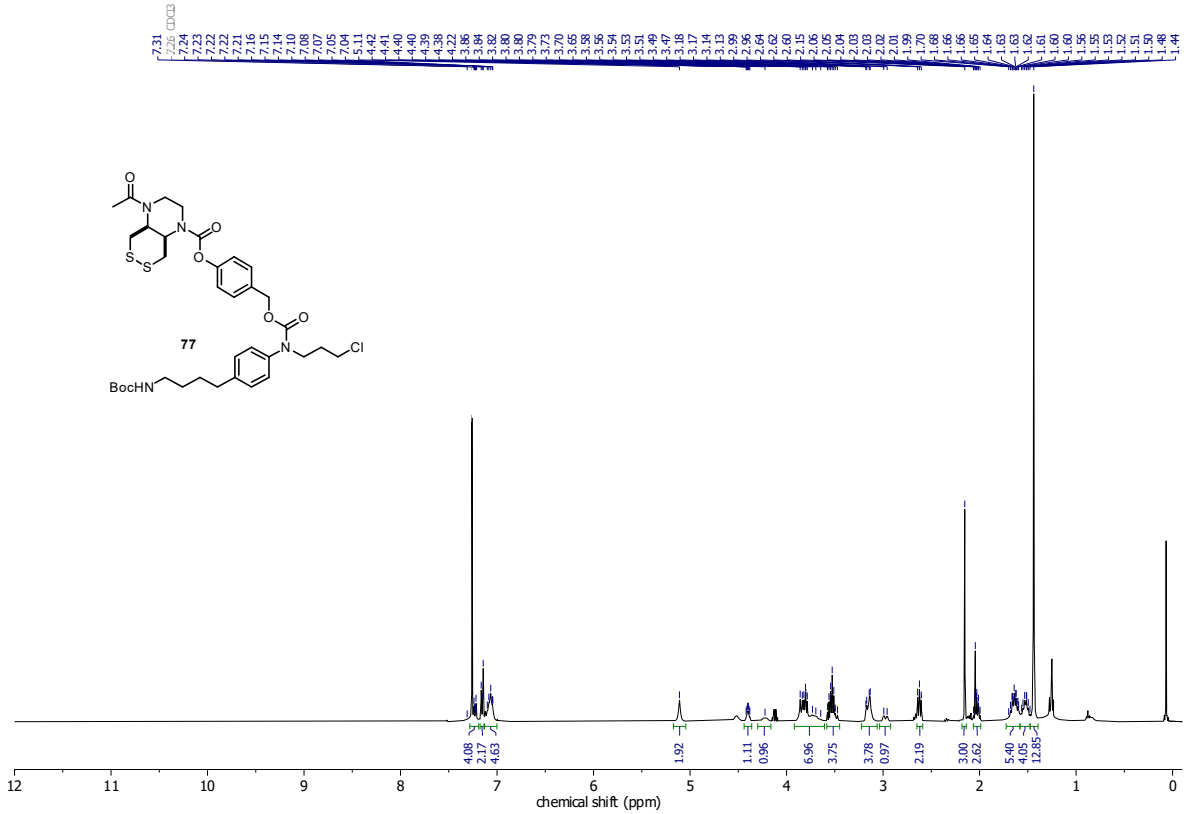

**ethyl acetate and silicon grease impurities*

Compound 14

^{1}H-NMR

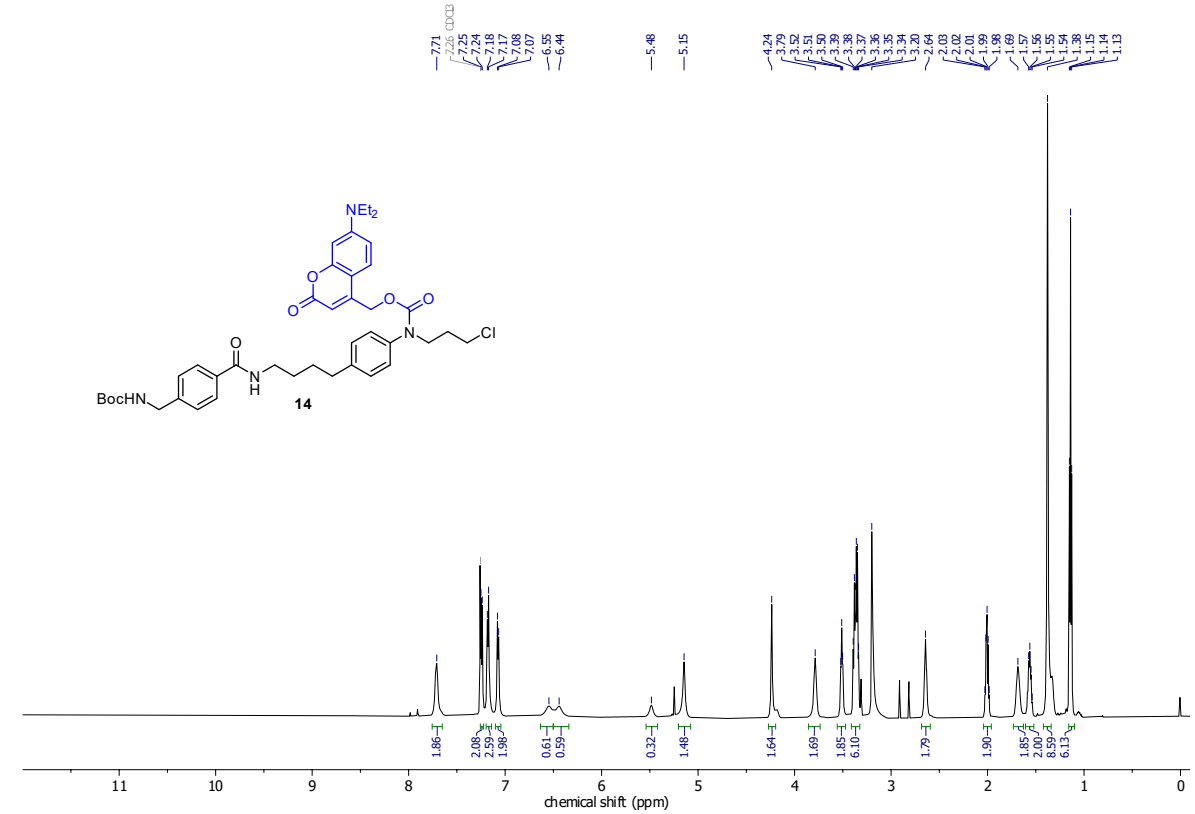

^{13}C-NMR

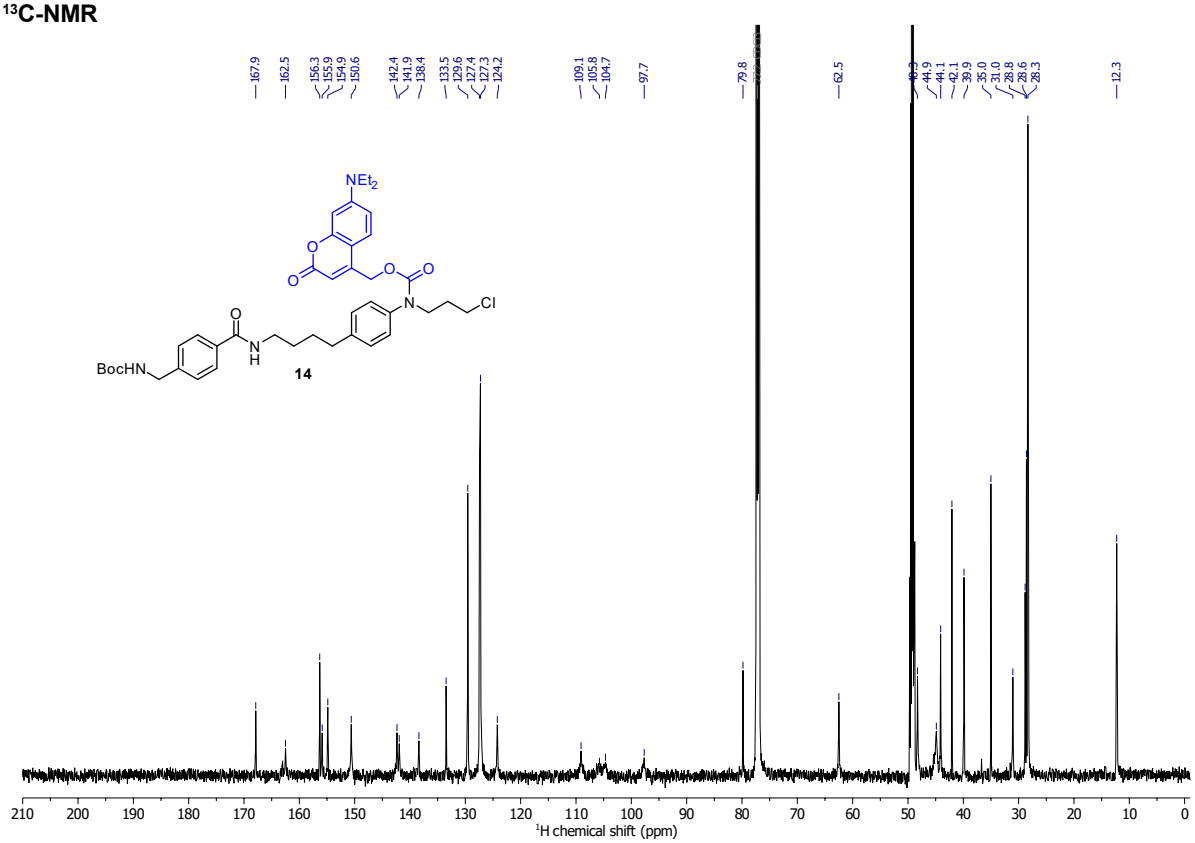

HSQC

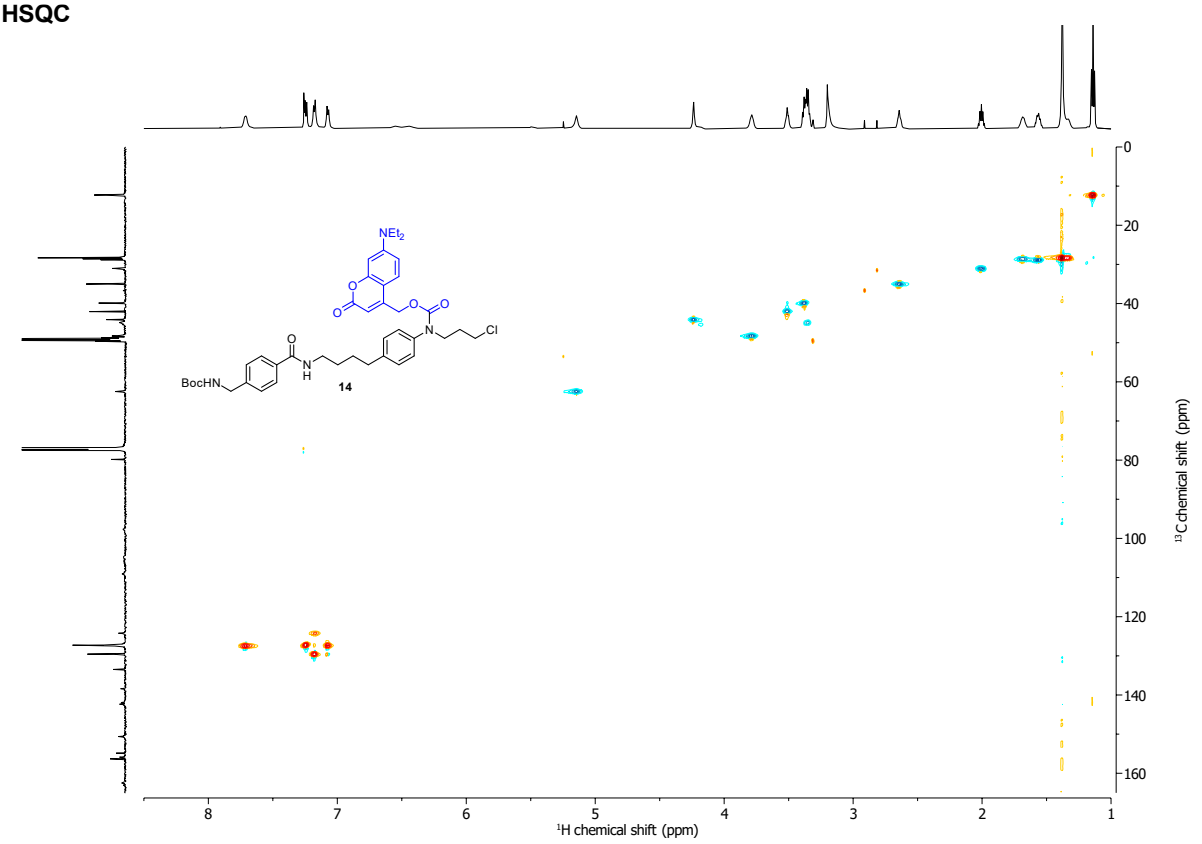
NEt2
O
O
O
O
N
Cl
O
N
H
BocHN
14
0
20
40
60
80
100
120
140
160
13C chemical shift (ppm)
8
7
6
5
4
3
2
1
1H chemical shift (ppm)

HMBC

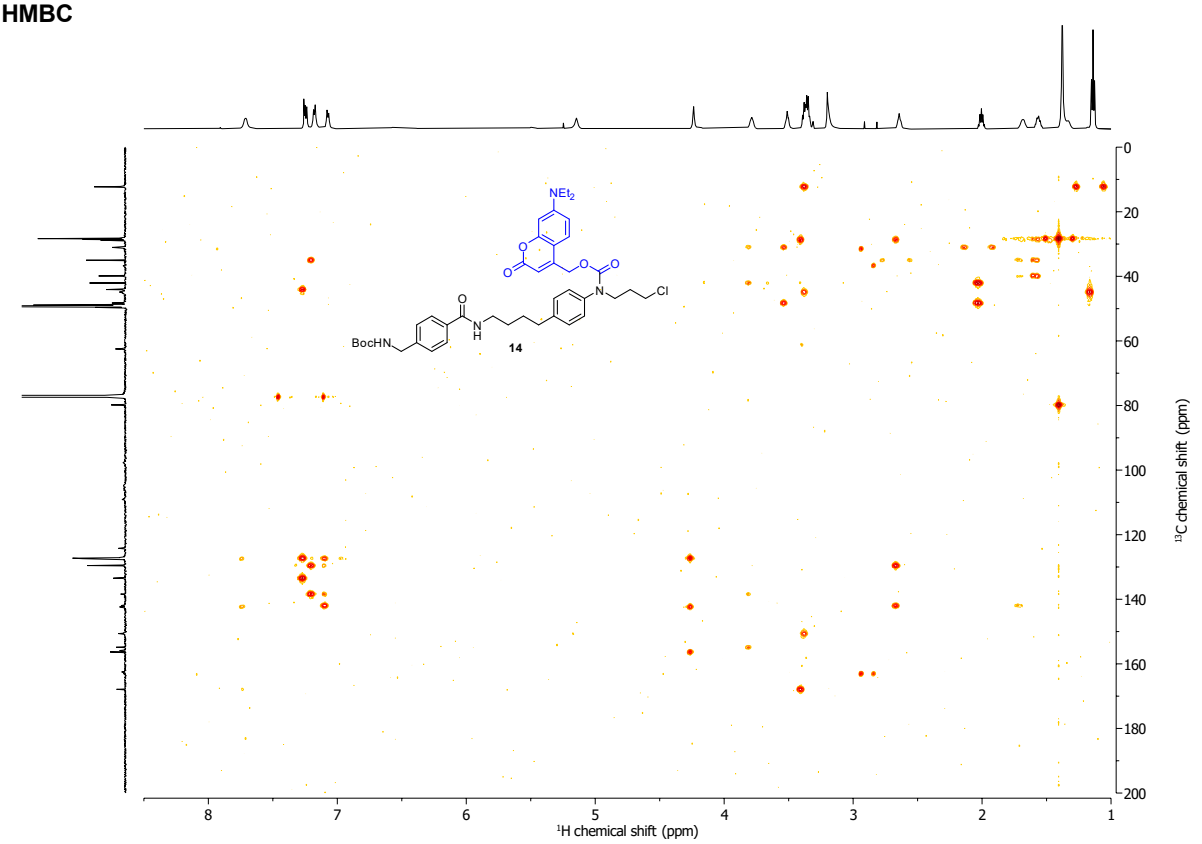
NEt2
O
O
O
O
N
Cl
O
N
H
BocHN
14
0
20
40
60
80
100
120
140
160
180
200
13C chemical shift (ppm)
8
7
6
5
4
3
2
1
1H chemical shift (ppm)

Compound 17

^{1}H-NMR

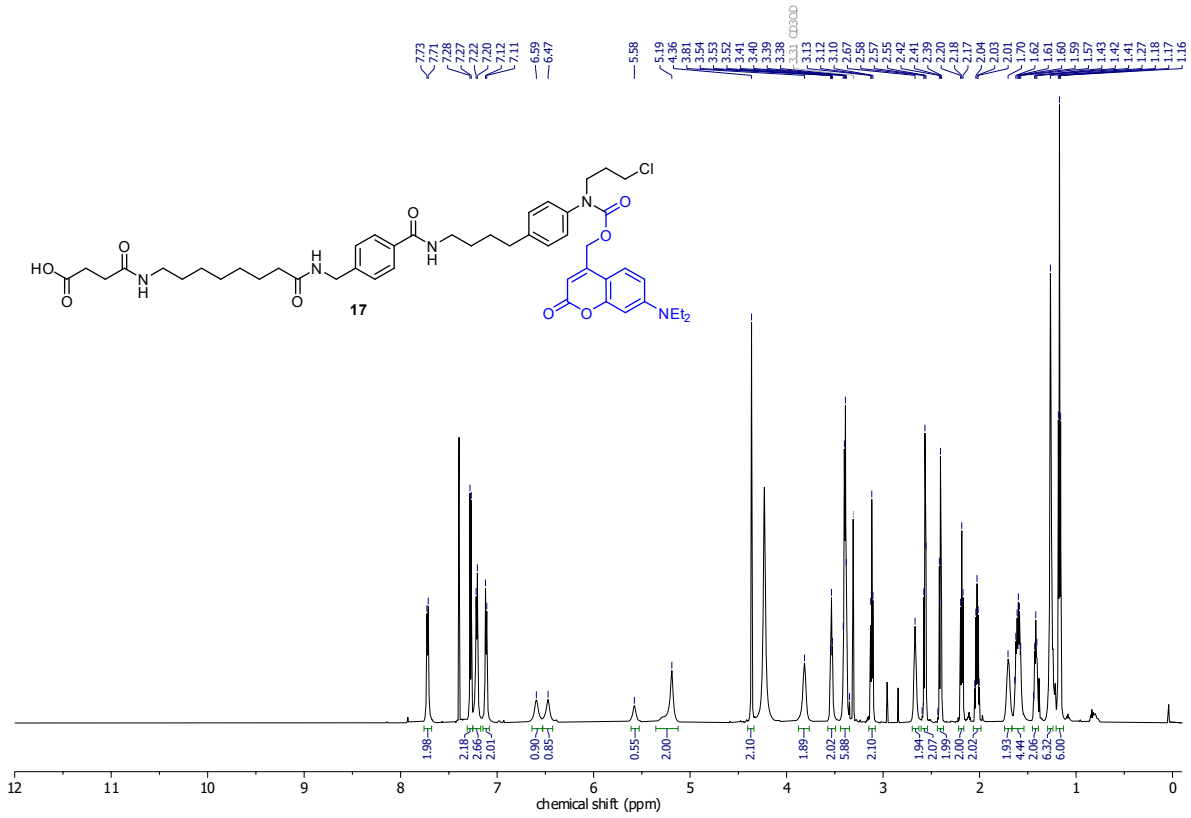

^{13}C-NMR

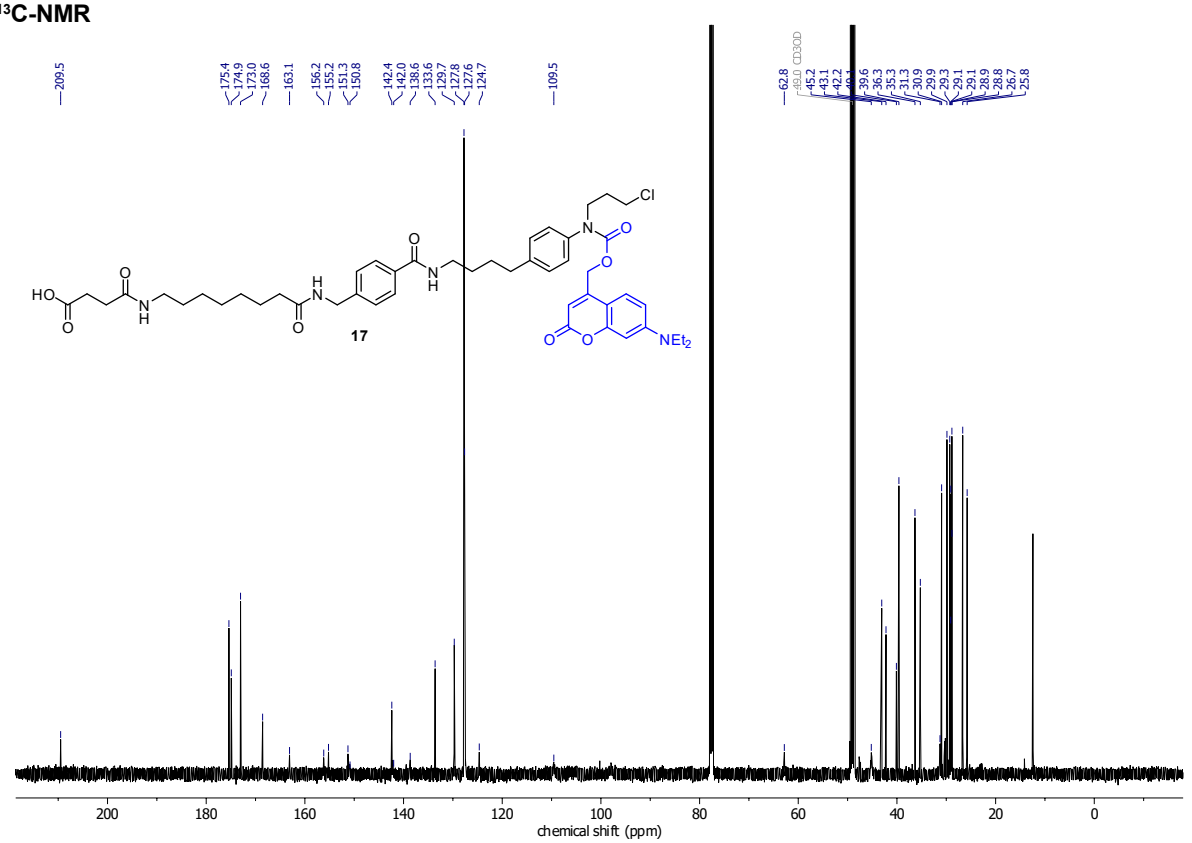

Cou-CHalo-BG

^{1}H-NMR

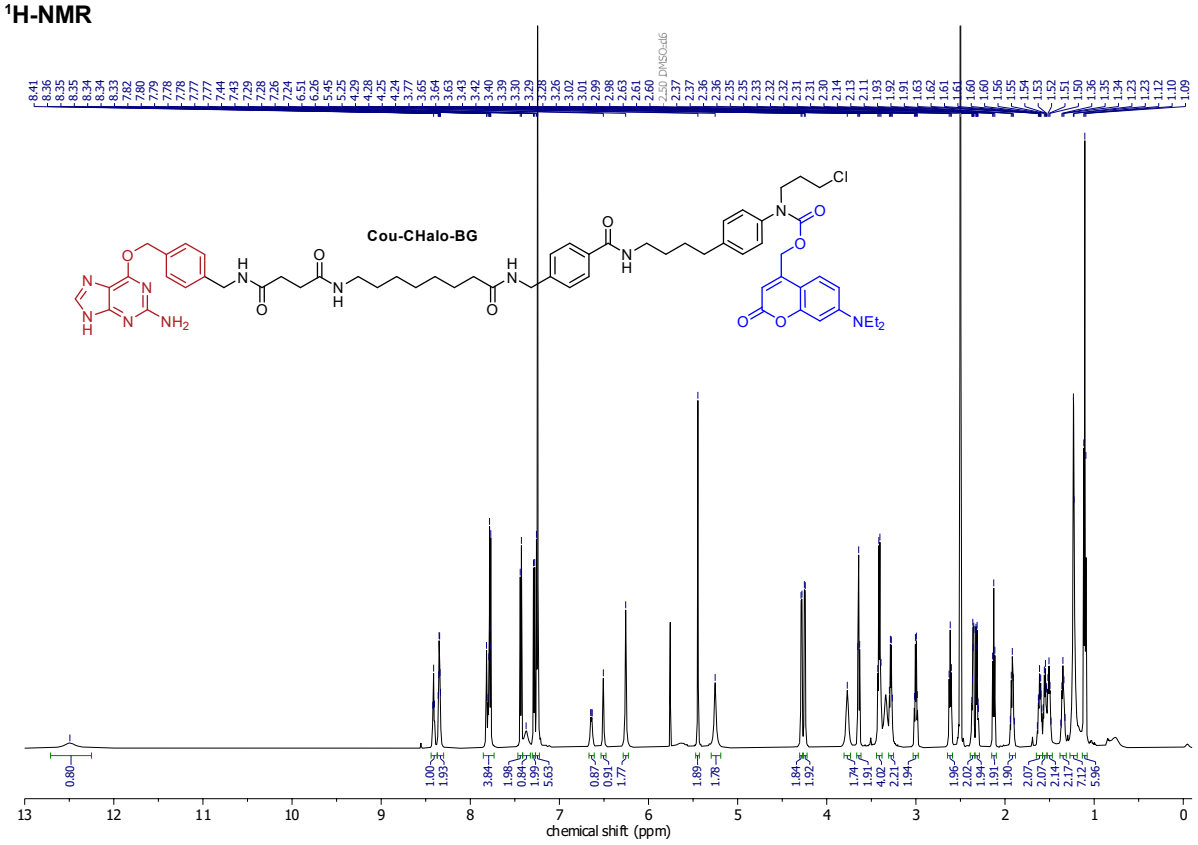

^{13}C-NMR

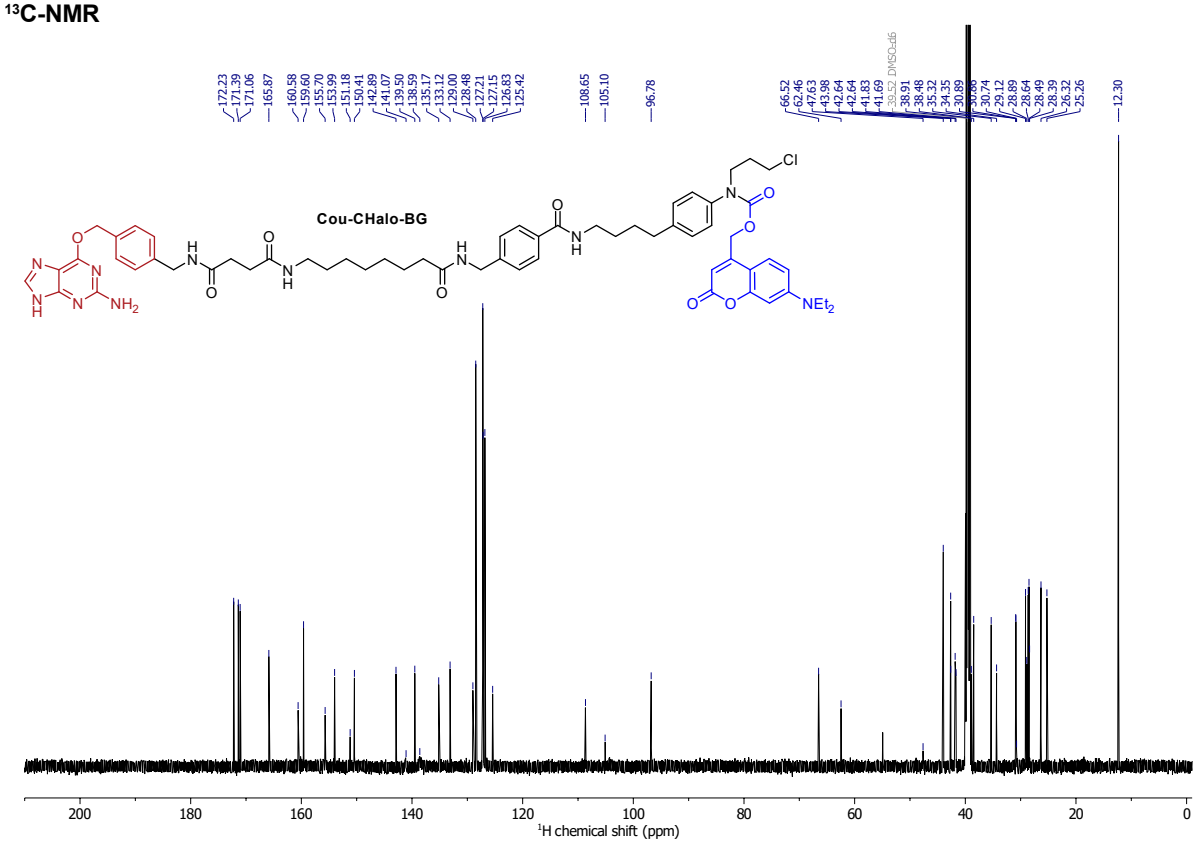

Compound 18

^{1}H-NMR

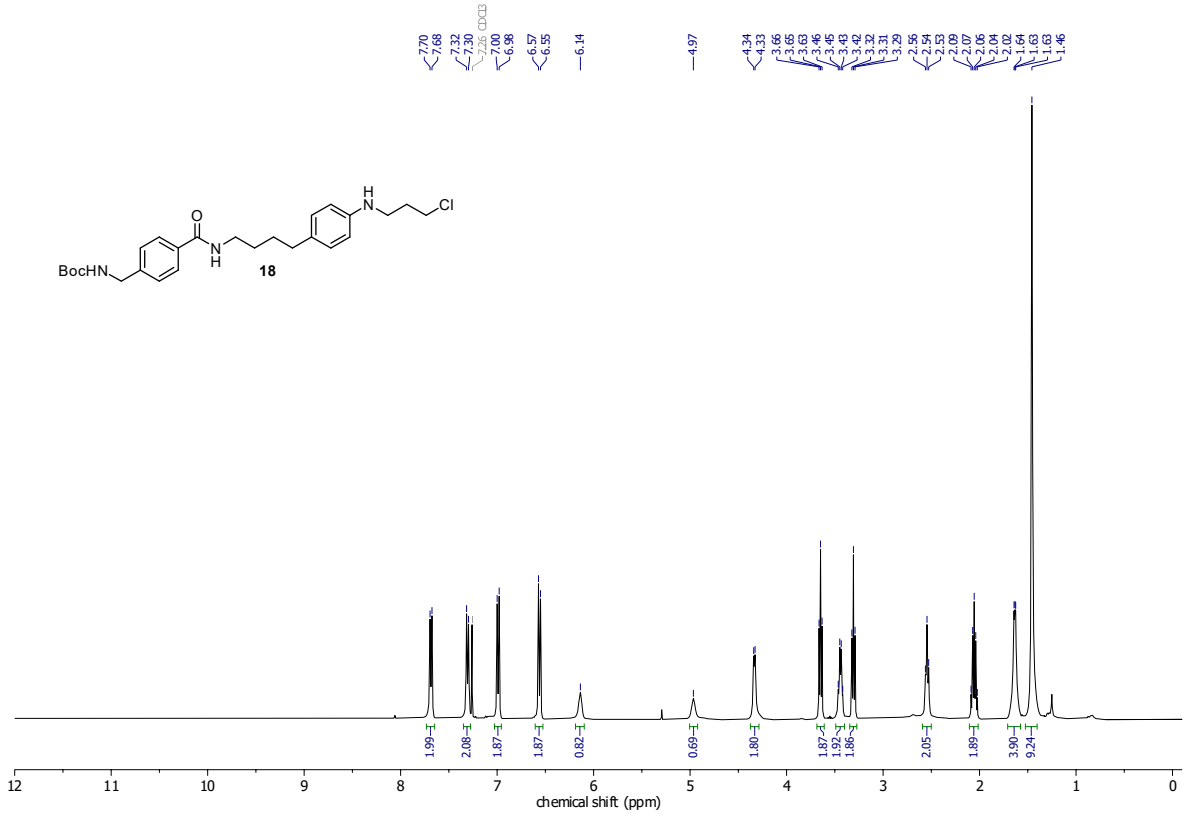

^{13}C-NMR

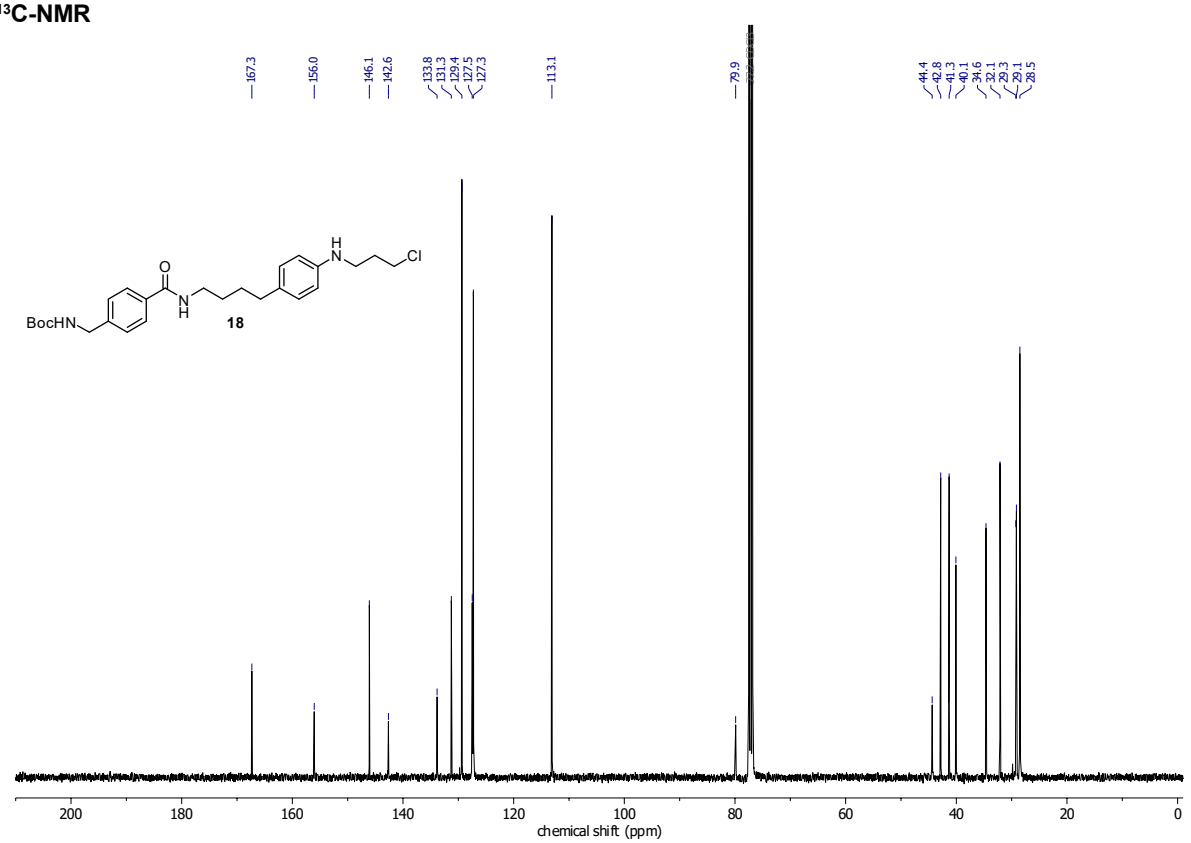

Compound 20

^{1}H-NMR

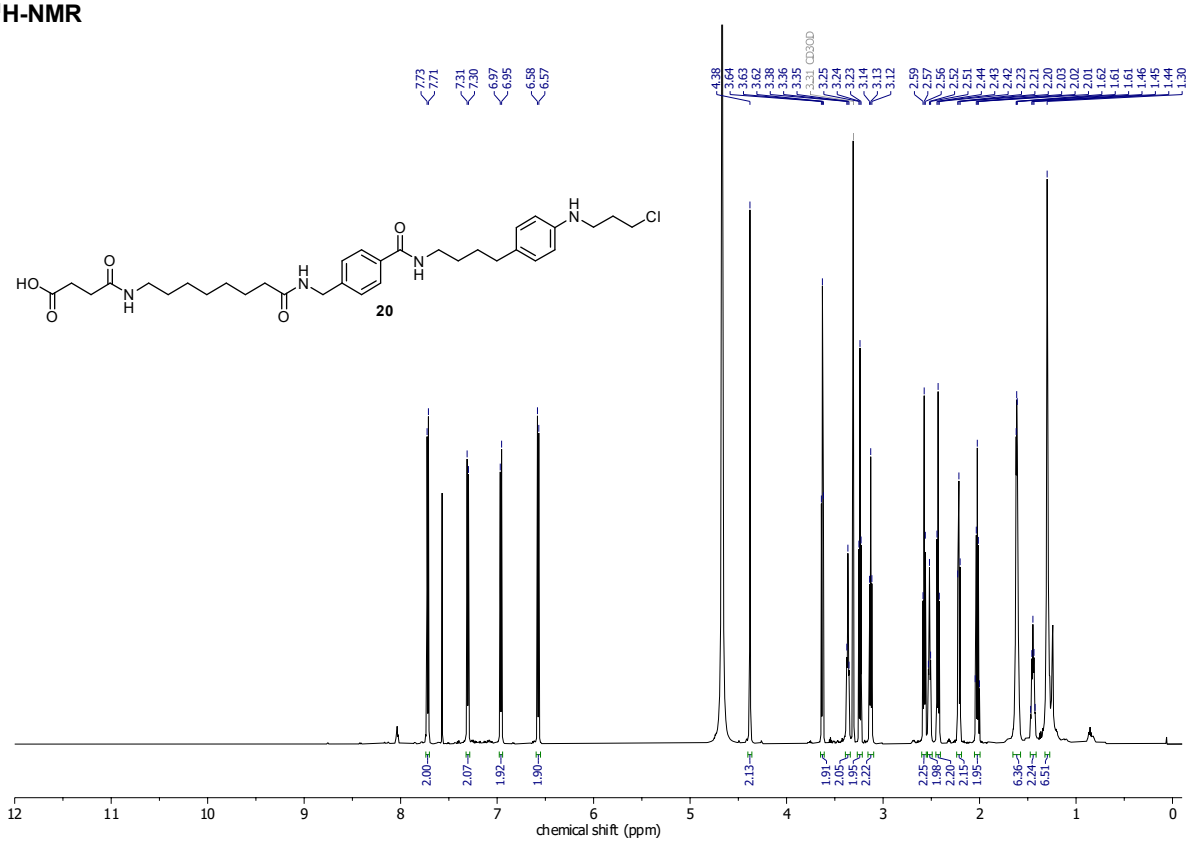

^{13}C-NMR

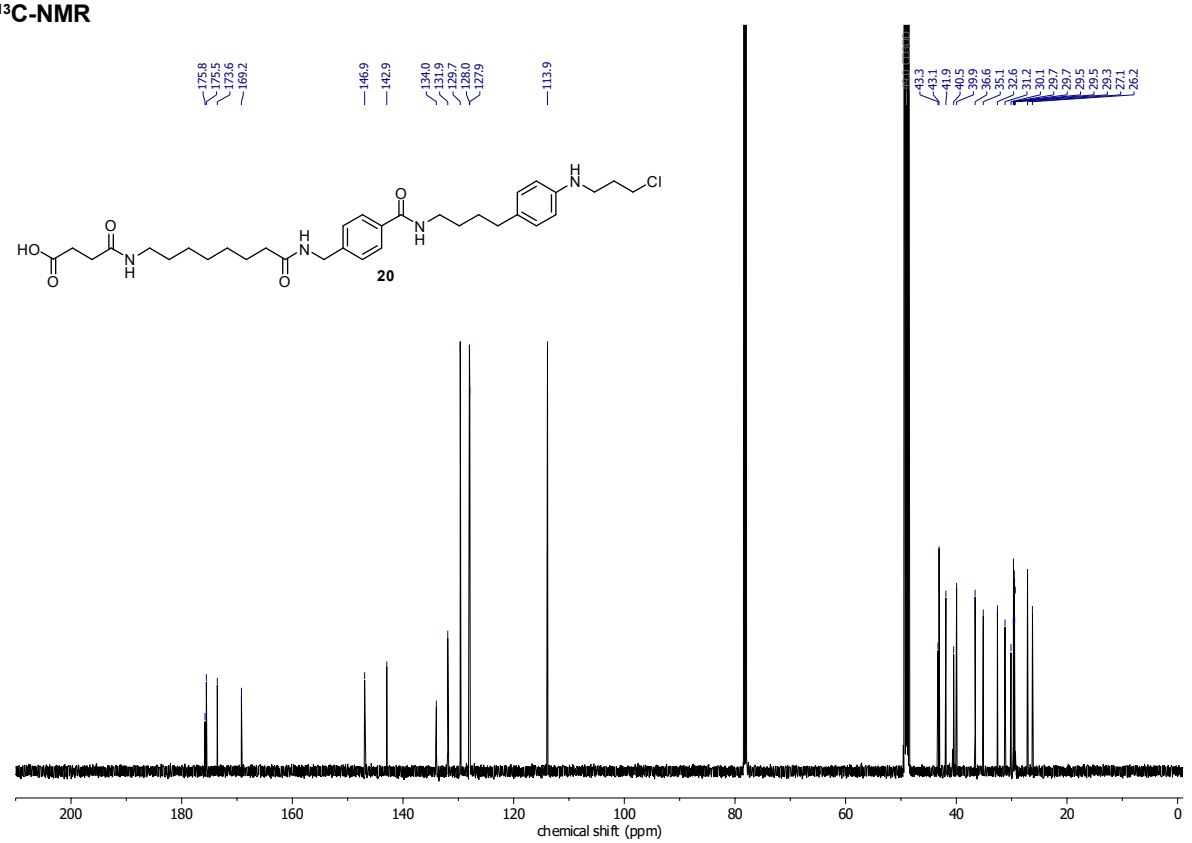

CHalo-BG

^{1}H-NMR

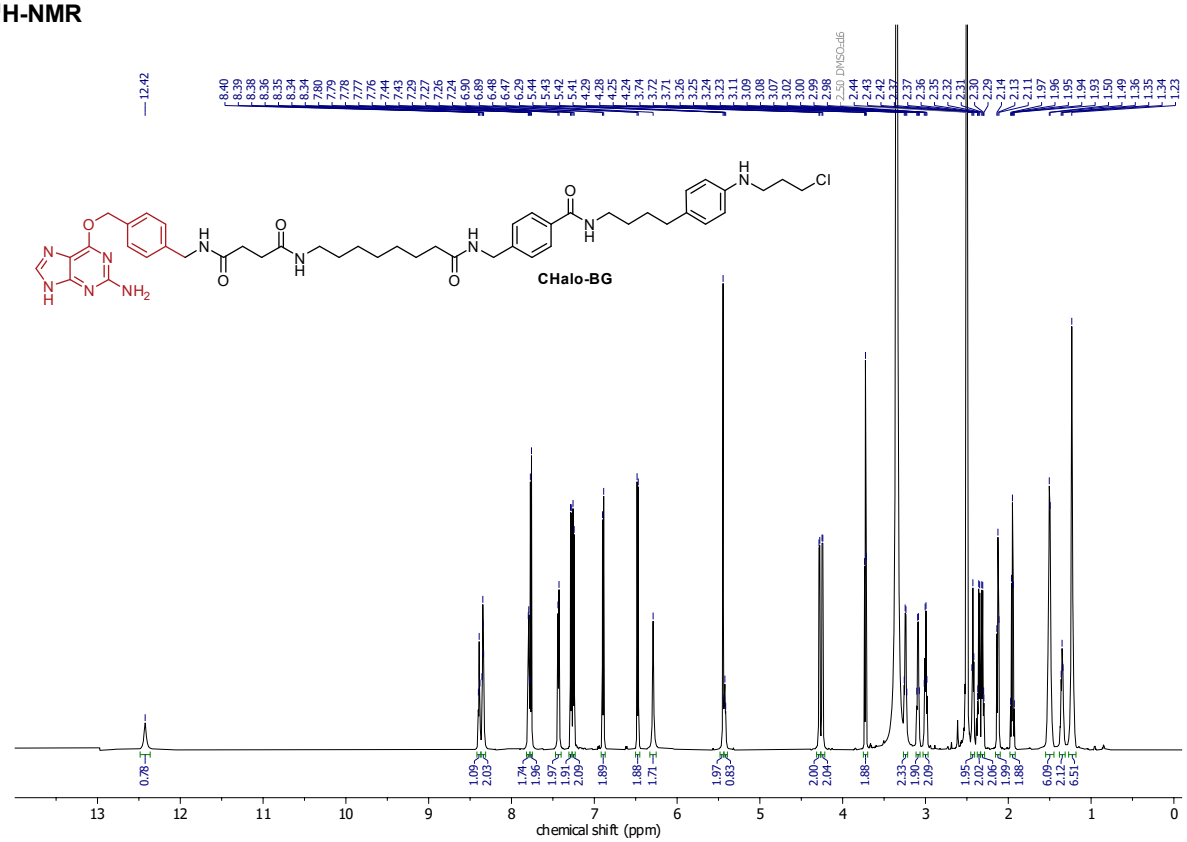

^{13}C-NMR

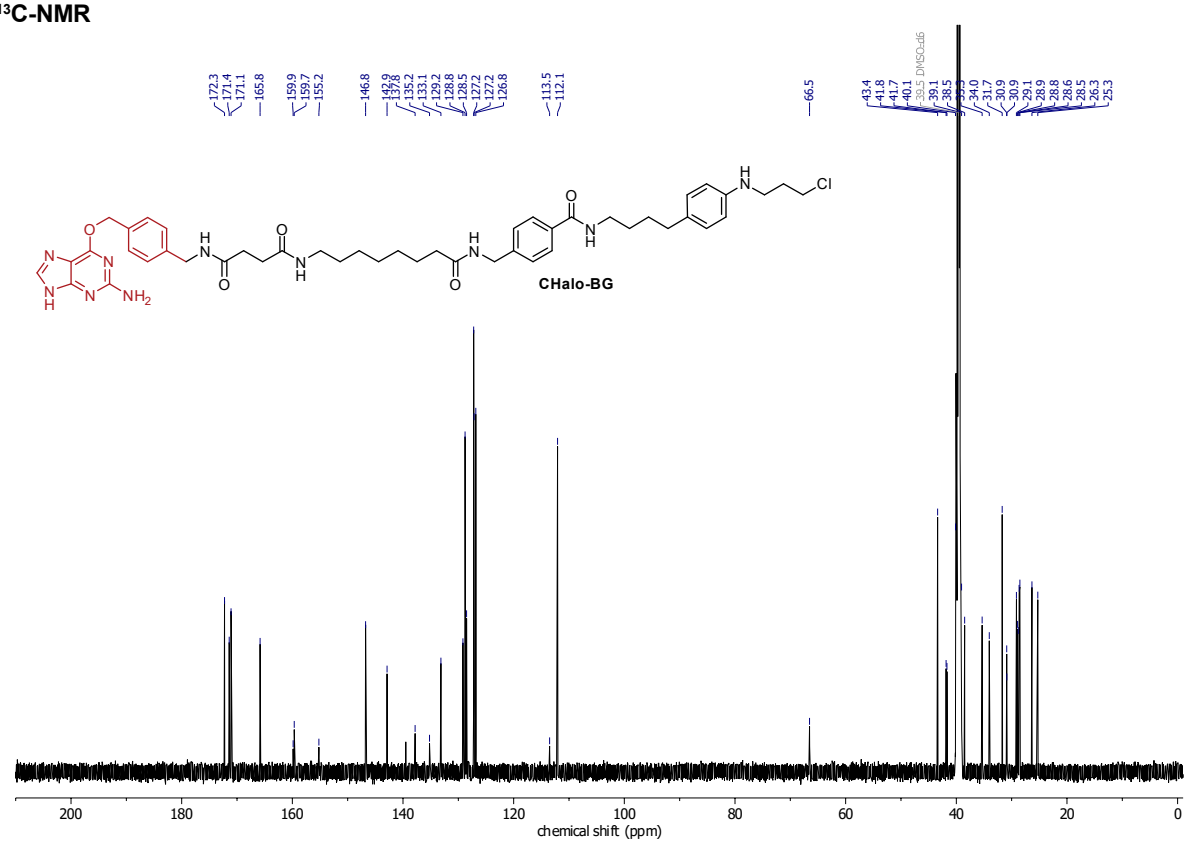

Compound 22

^{1}H-NMR

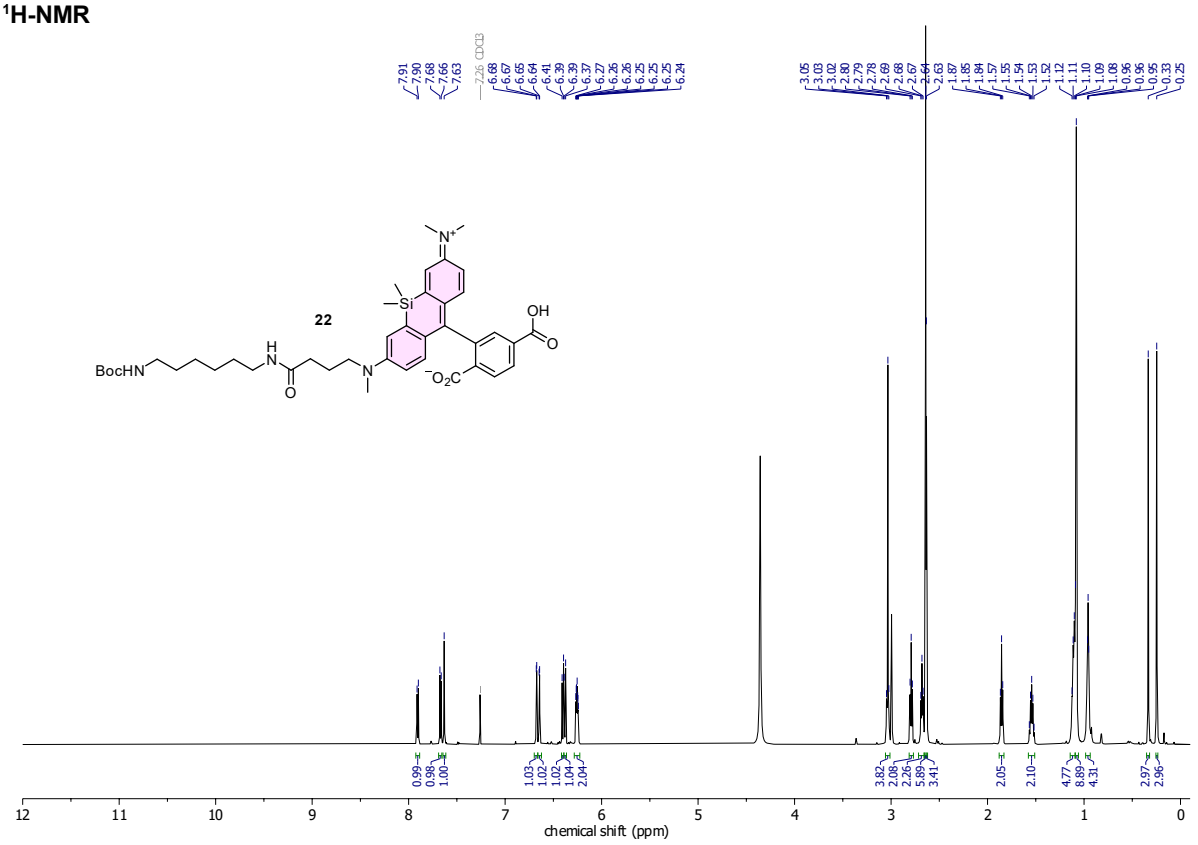

^{13}C-NMR

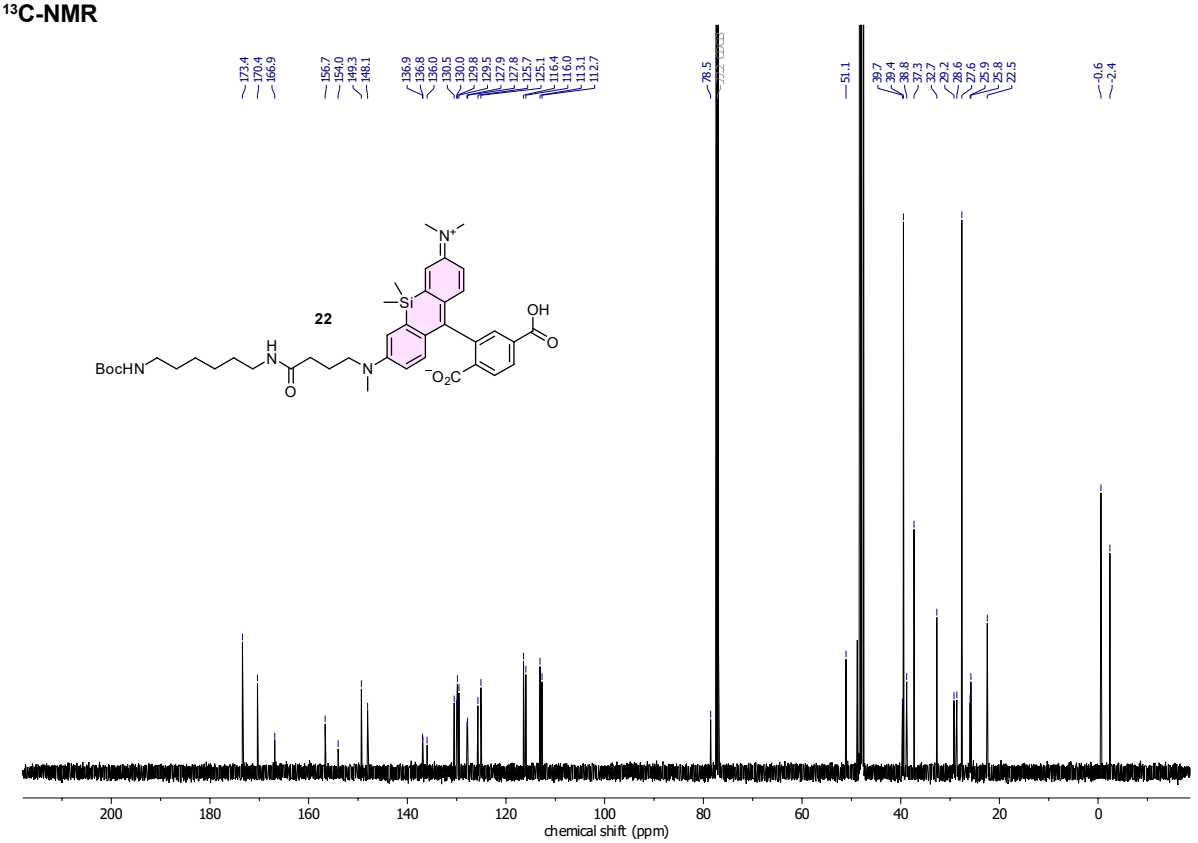

HSQC

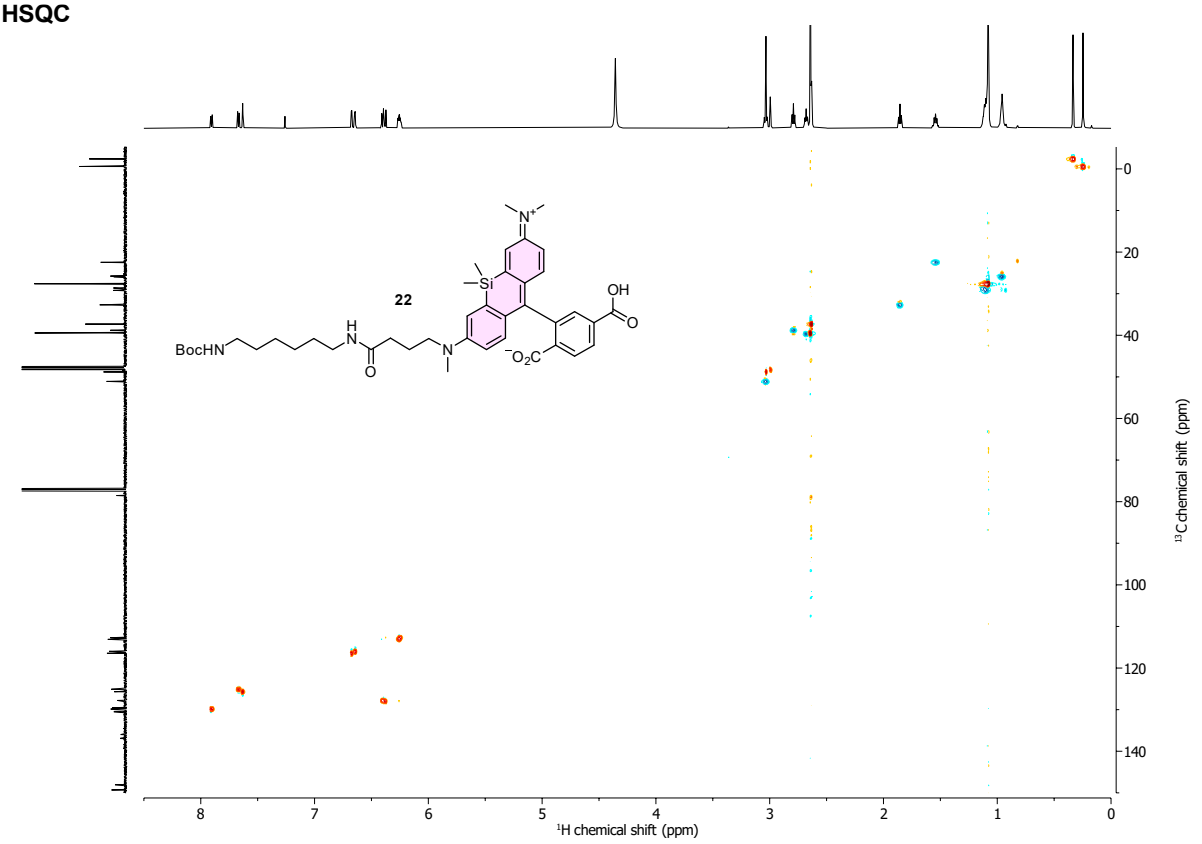
22
BocHN
H
N
O
N
O2C
Si
N+
OH
O
0
20
40
60
80
100
120
140
13C chemical shift (ppm)
8
7
6
5
4
3
2
1
0
1H chemical shift (ppm)

HMBC

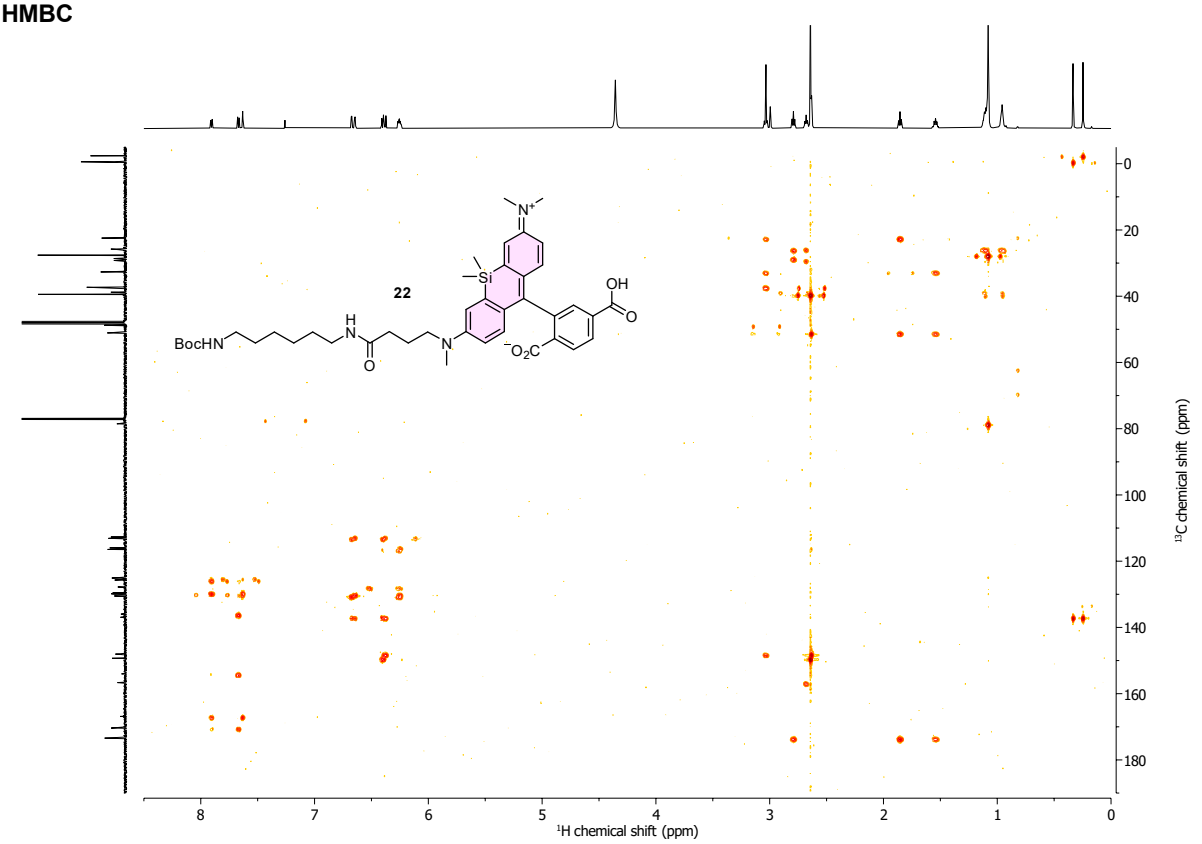
22
BocHN
H
N
O
N
O2C
Si
N+
OH
O
0
20
40
60
80
100
120
140
160
180
13C chemical shift (ppm)
8
7
6
5
4
3
2
1
0
1H chemical shift (ppm)

Compound 24

^{1}H-NMR

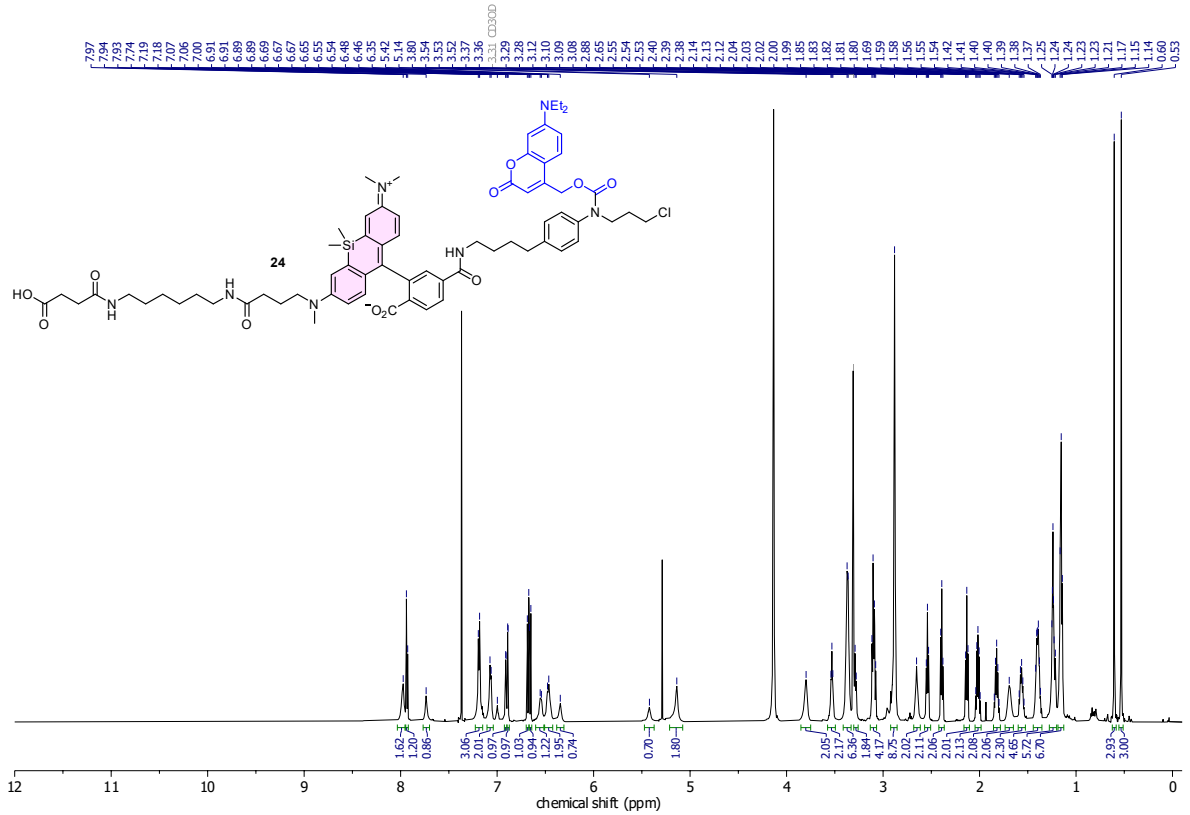

^{13}C-NMR

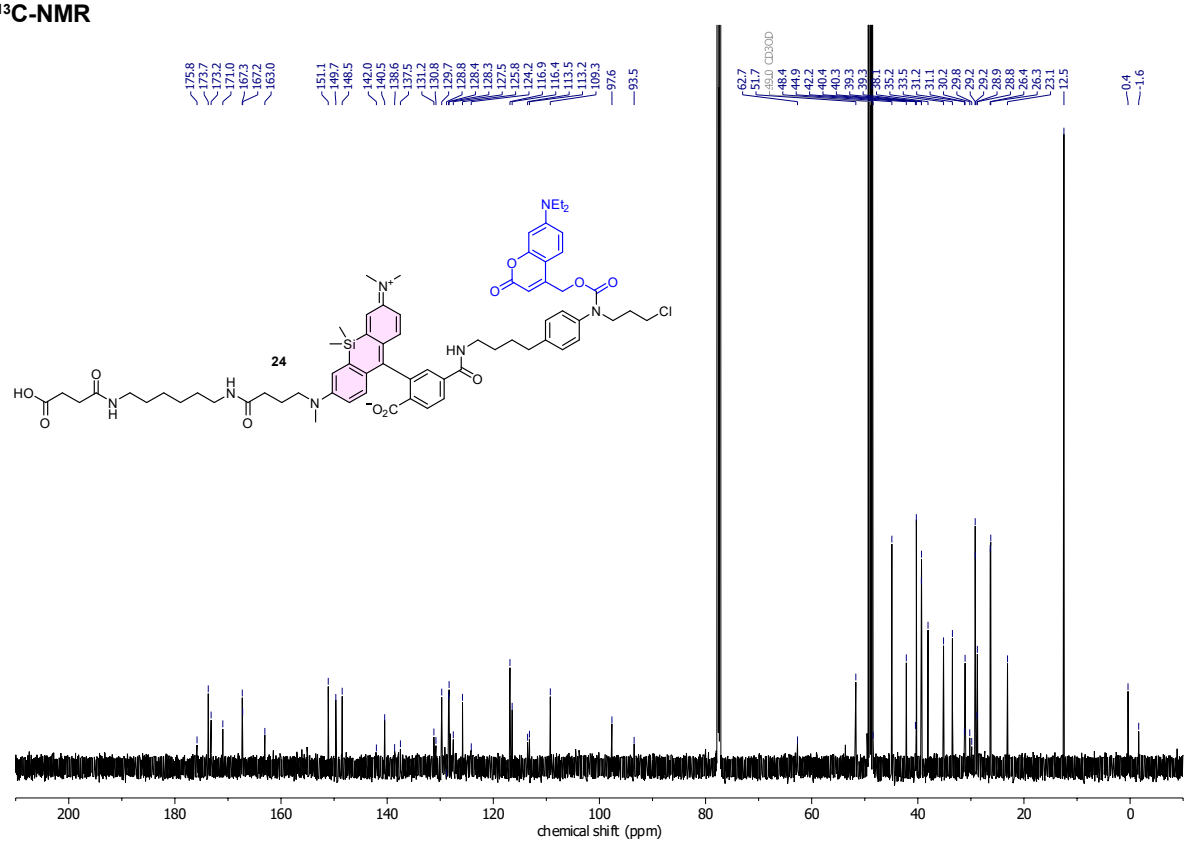

HSQC

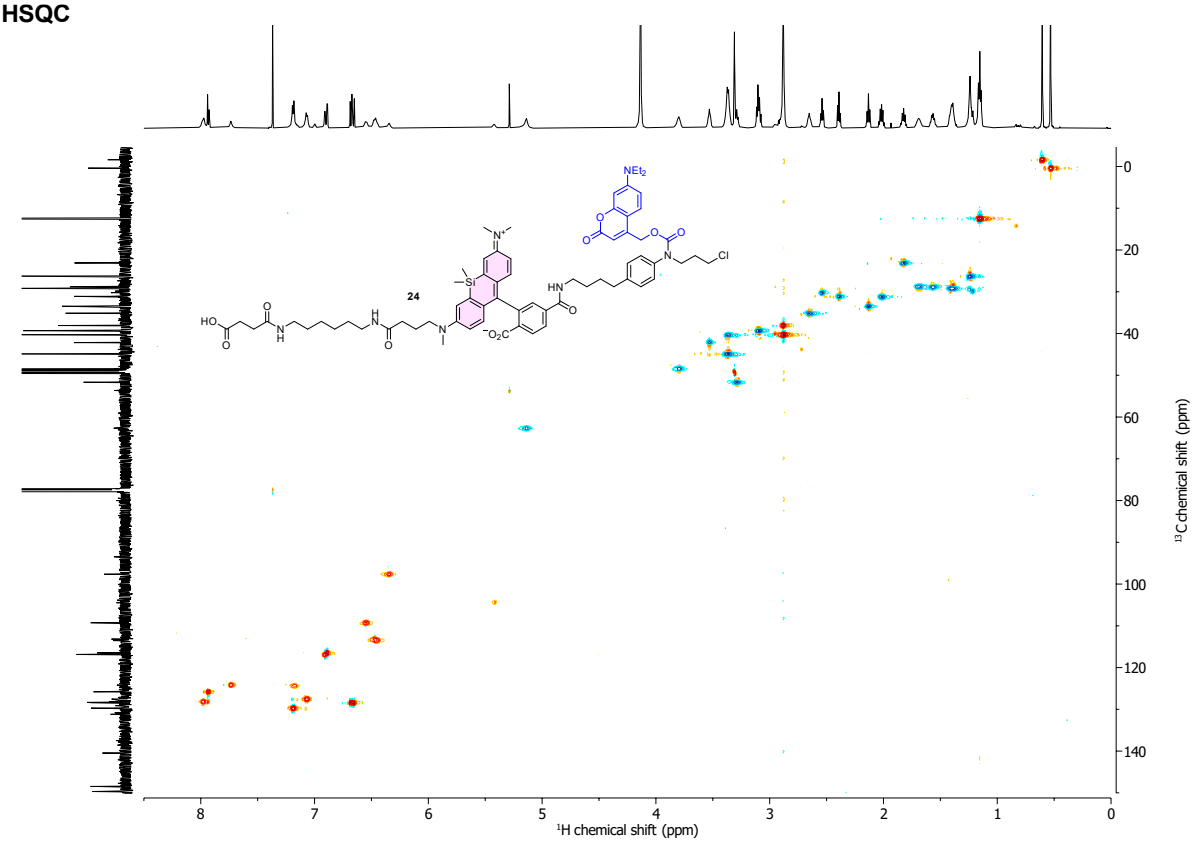
24
^{1}H chemical shift (ppm)
^{13}C chemical shift (ppm)

HMBC

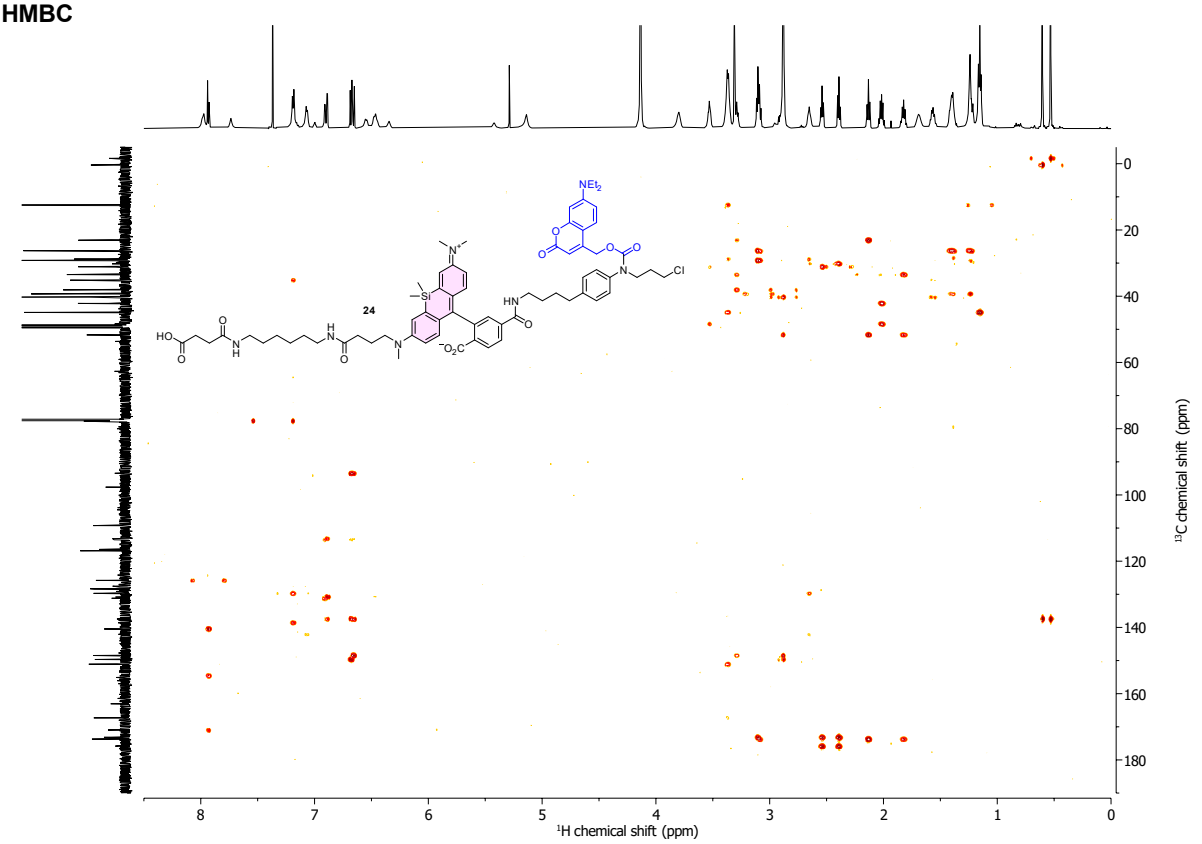
24
^{1}H chemical shift (ppm)
^{13}C chemical shift (ppm)

Cou-CHalo-SiR-BG

^{1}H-NMR

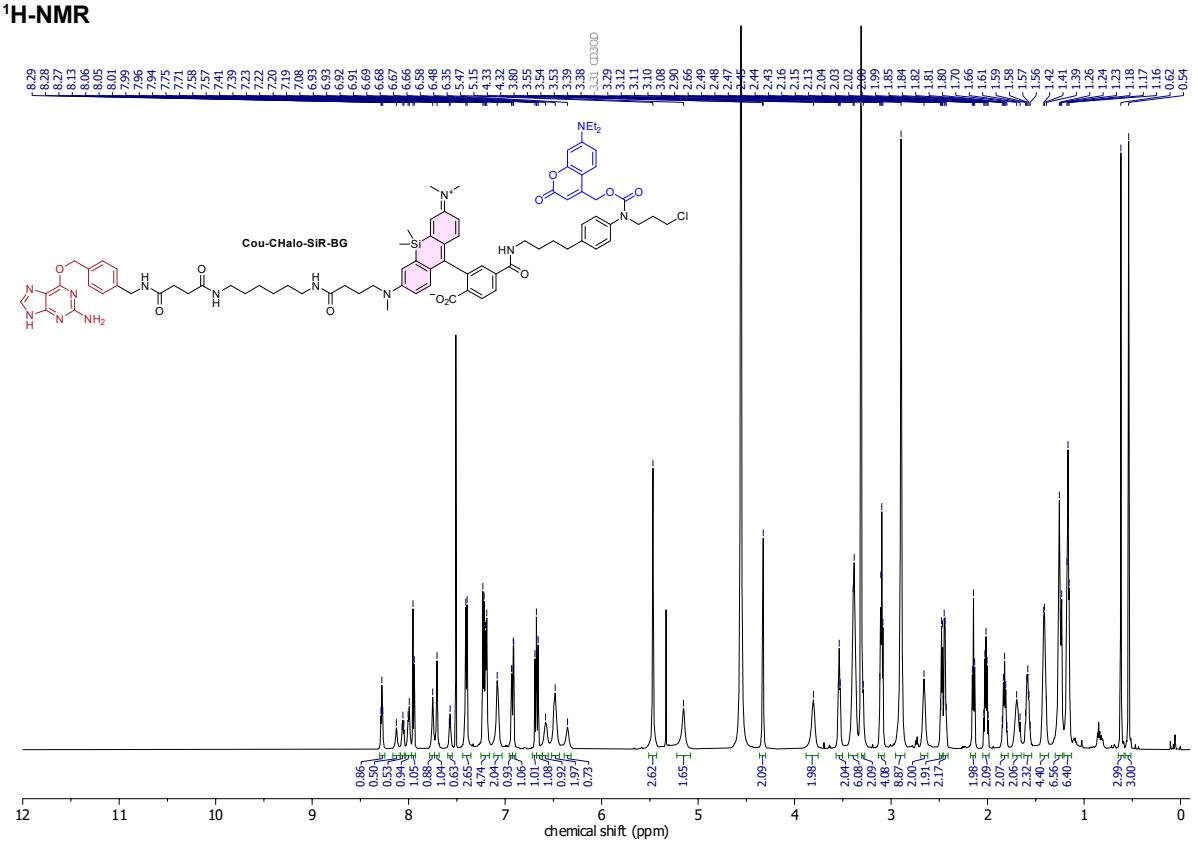

^{13}C-NMR

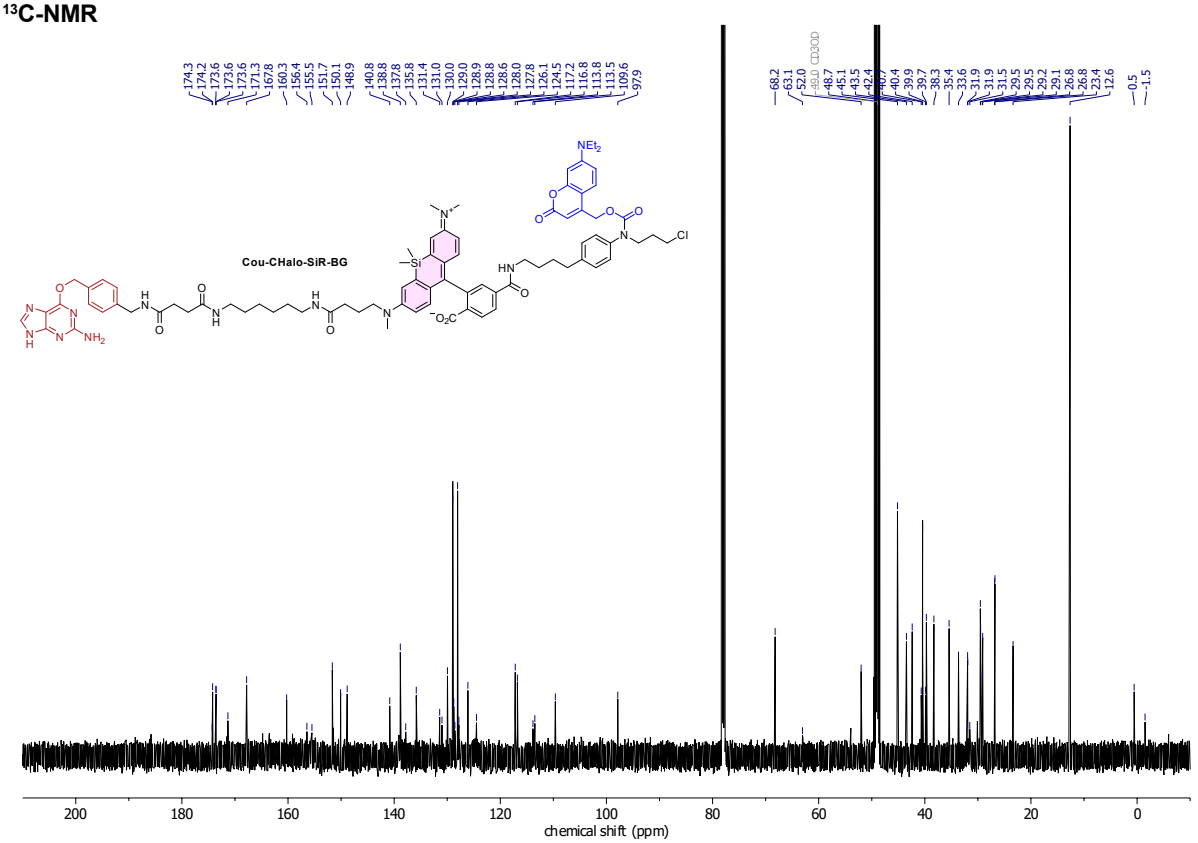

HSQC

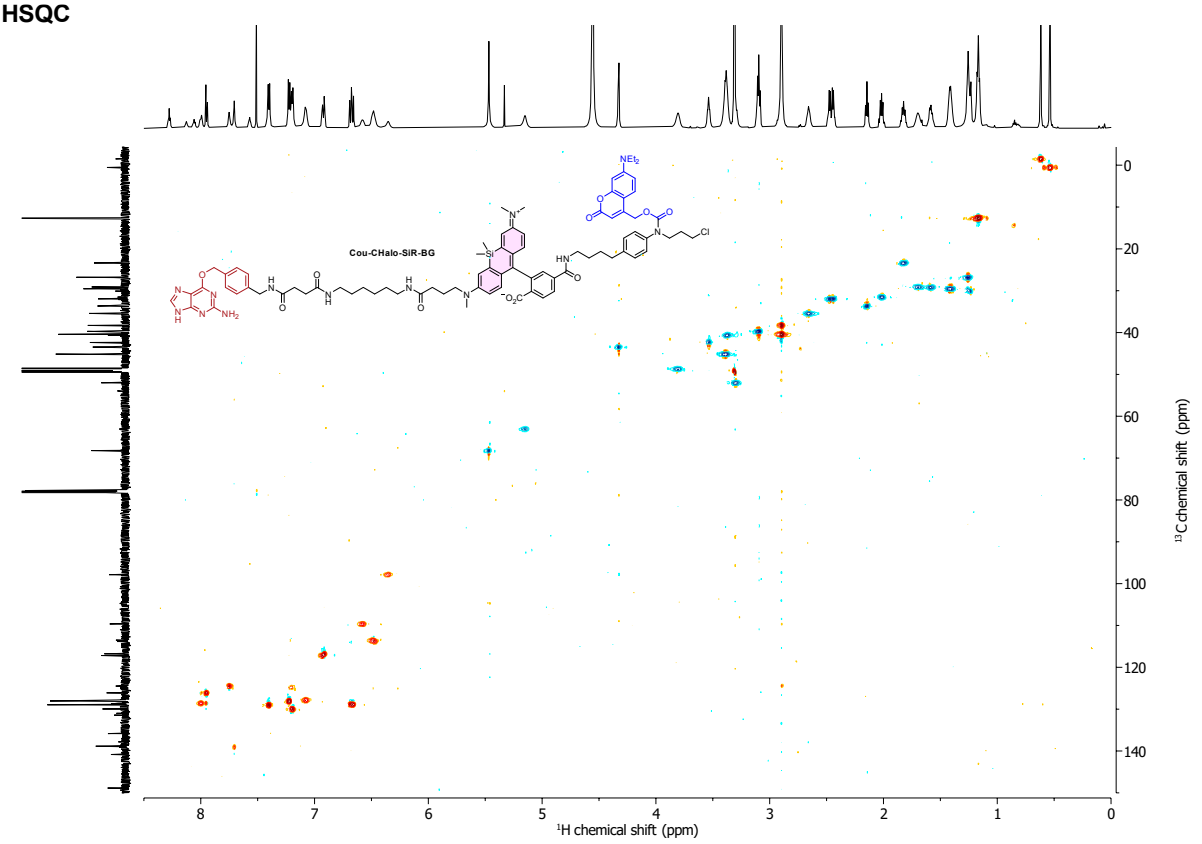
Cou-CHalo-SiR-BG
^{1}H chemical shift (ppm)
^{13}C chemical shift (ppm)

HMBC

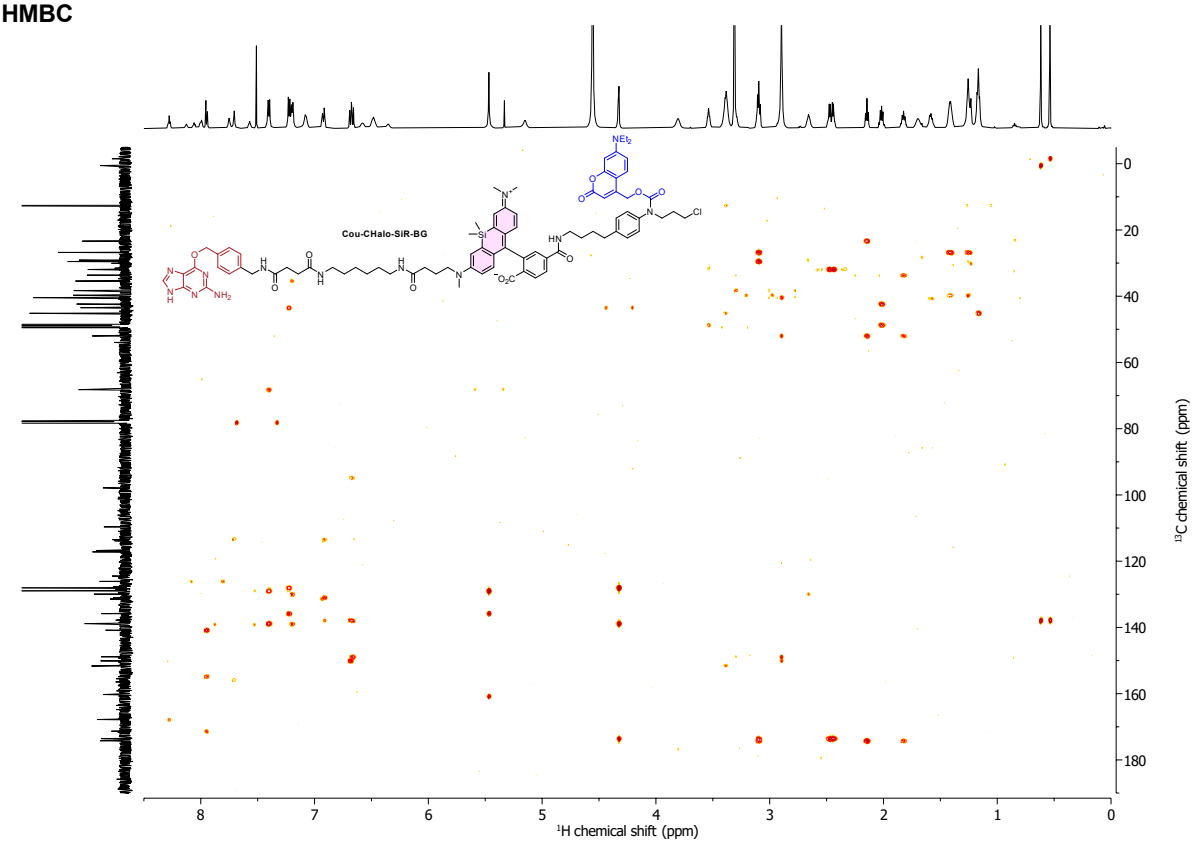
Cou-CHalo-SiR-BG
^{1}H chemical shift (ppm)
^{13}C chemical shift (ppm)

Compound 26

^{1}H-NMR

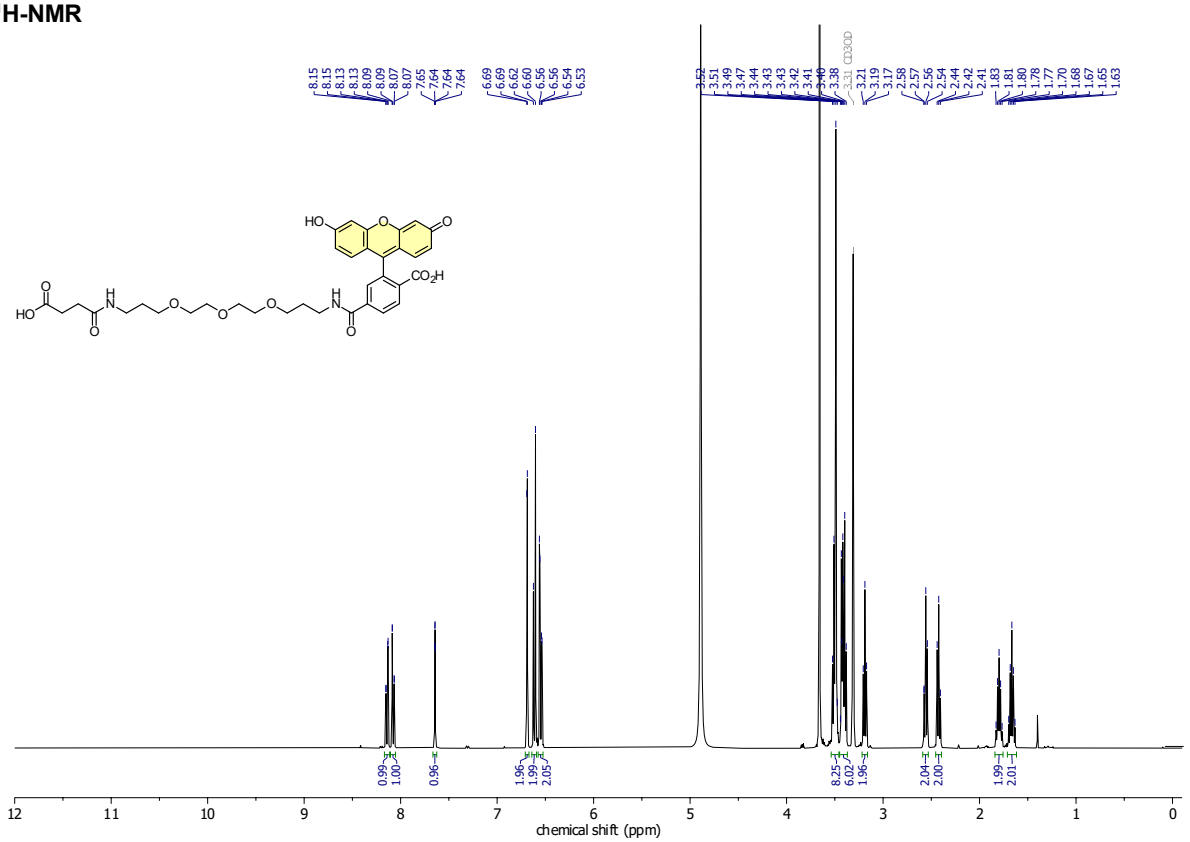

^{13}C-NMR

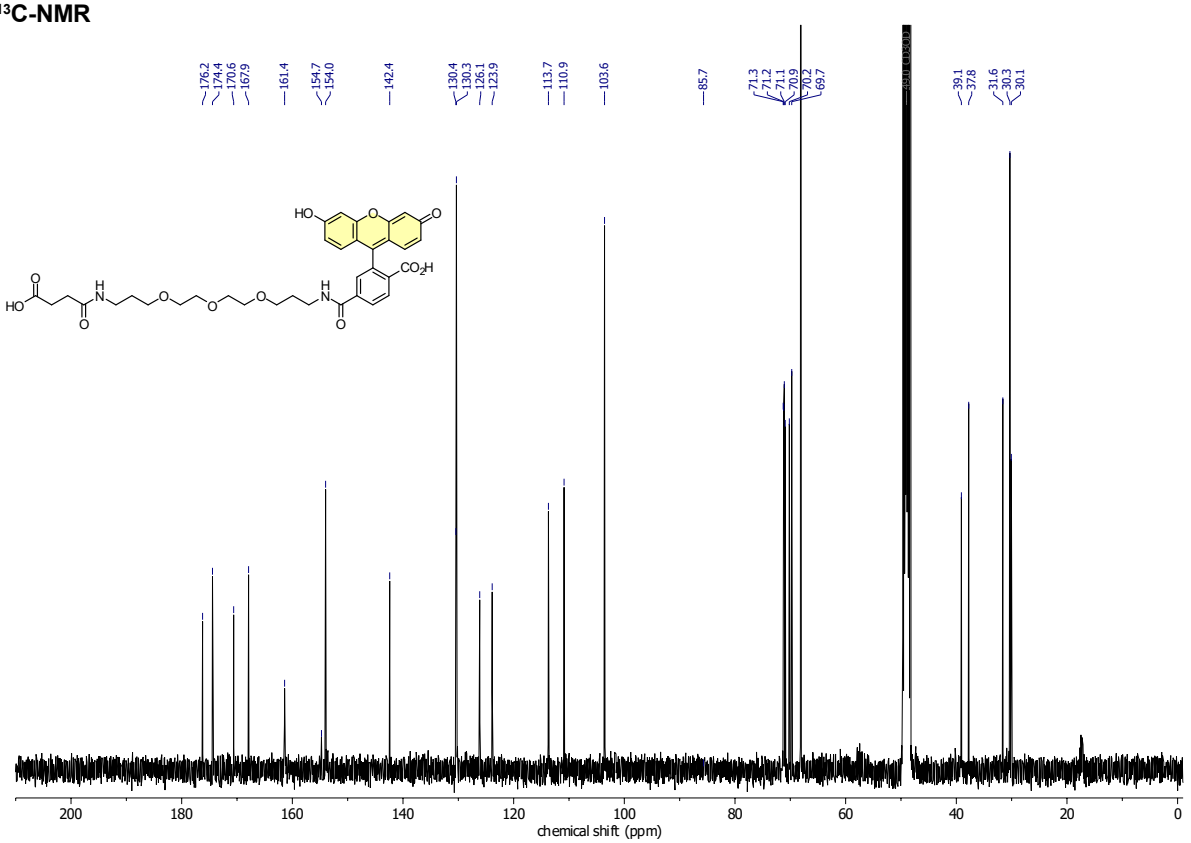

Compound 30

^{1}H-NMR

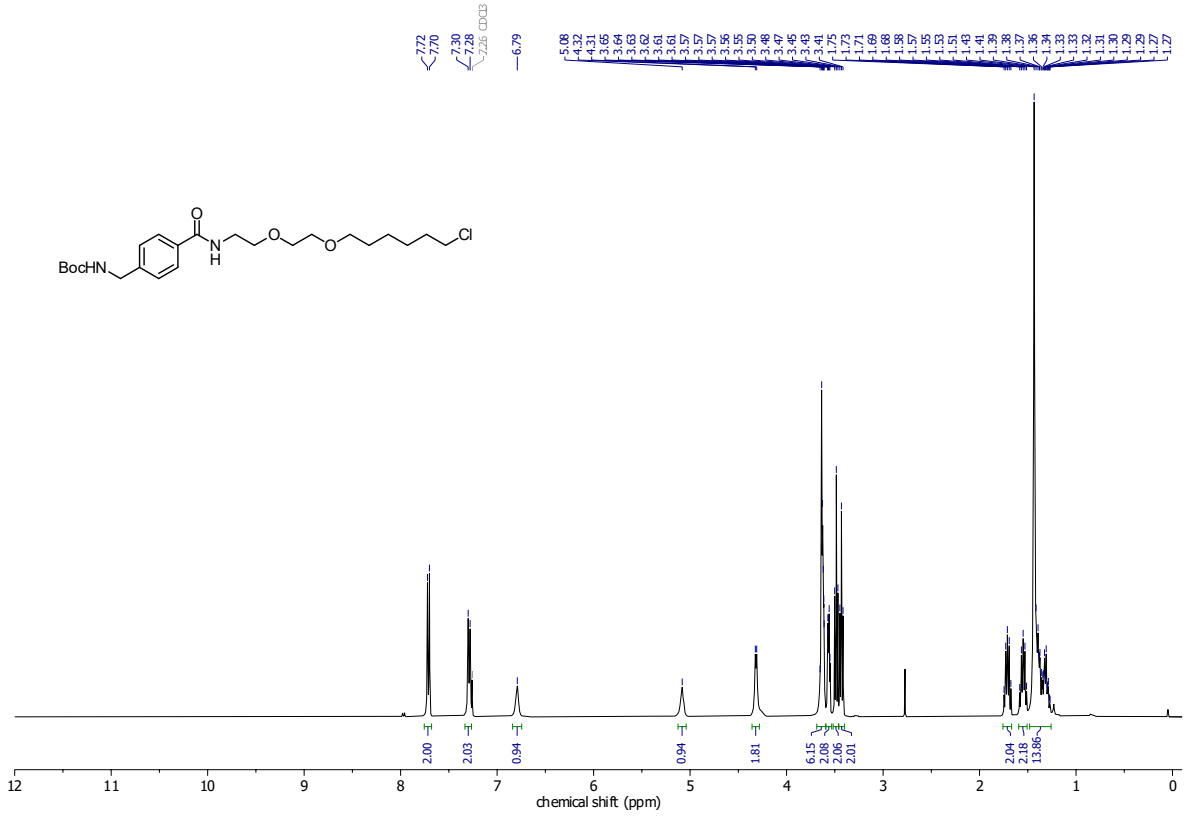

^{13}C-NMR

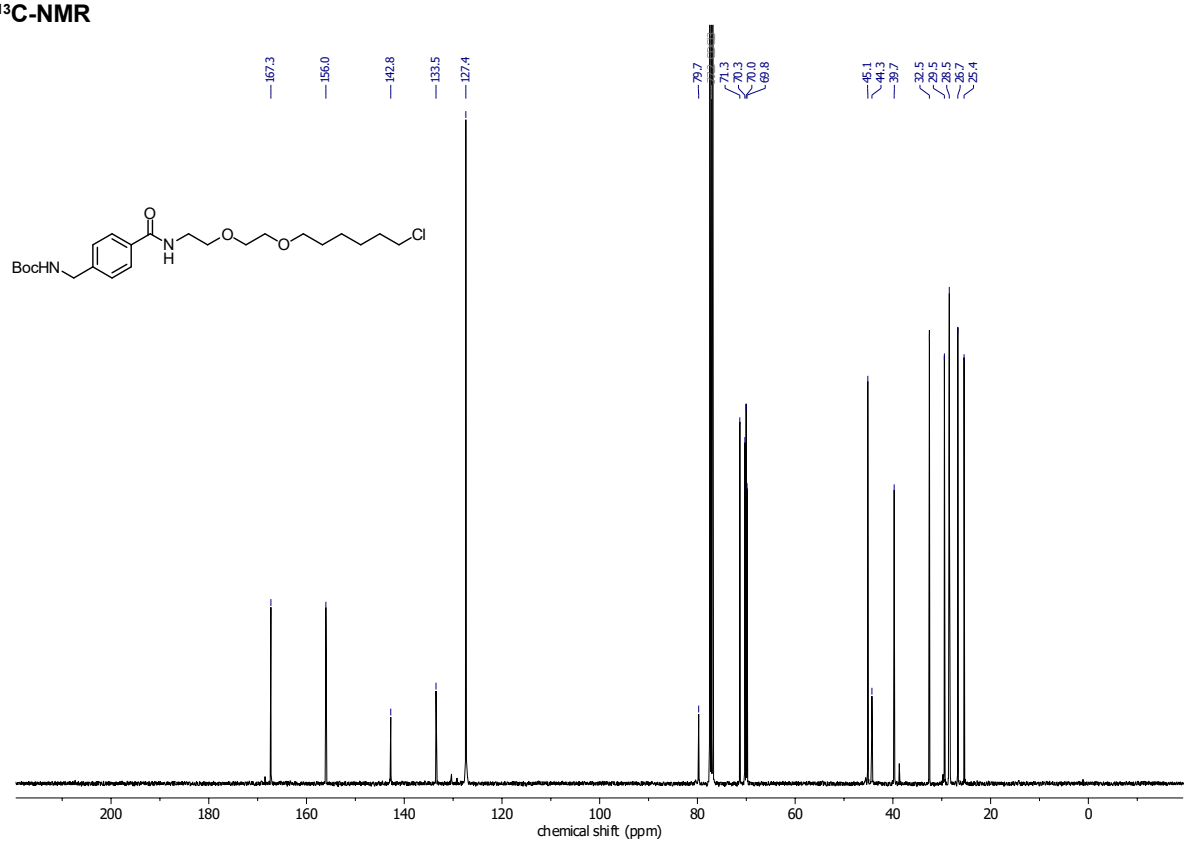

CA-Fluo

^{1}H-NMR

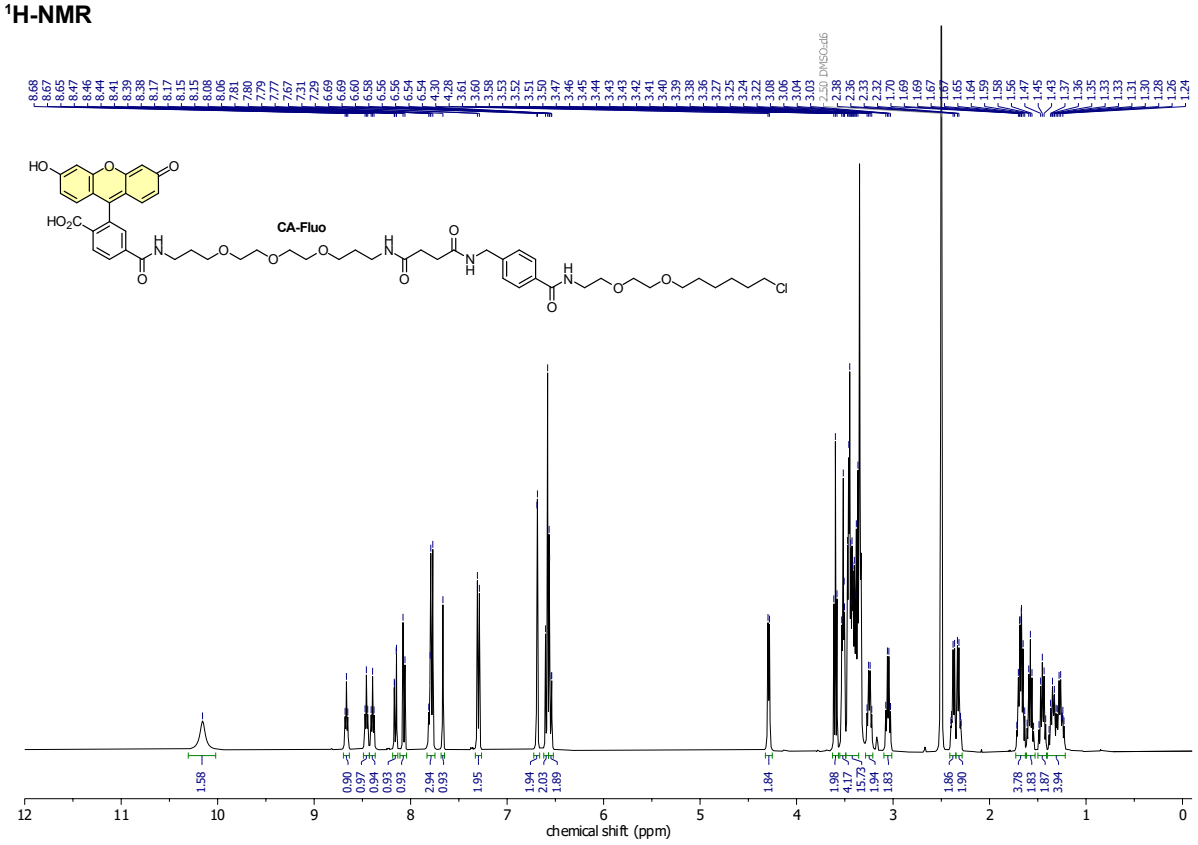

^{13}C-NMR

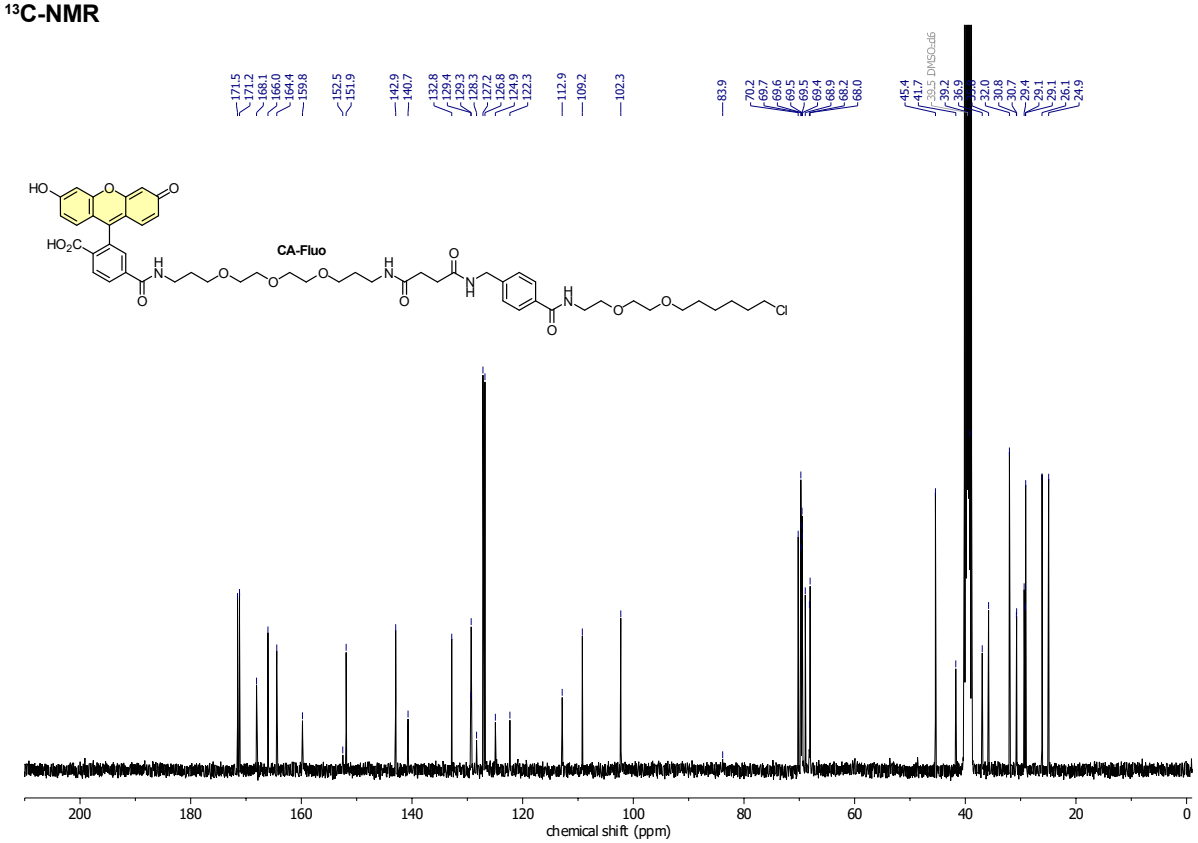

Compound 33

^{1}H-NMR

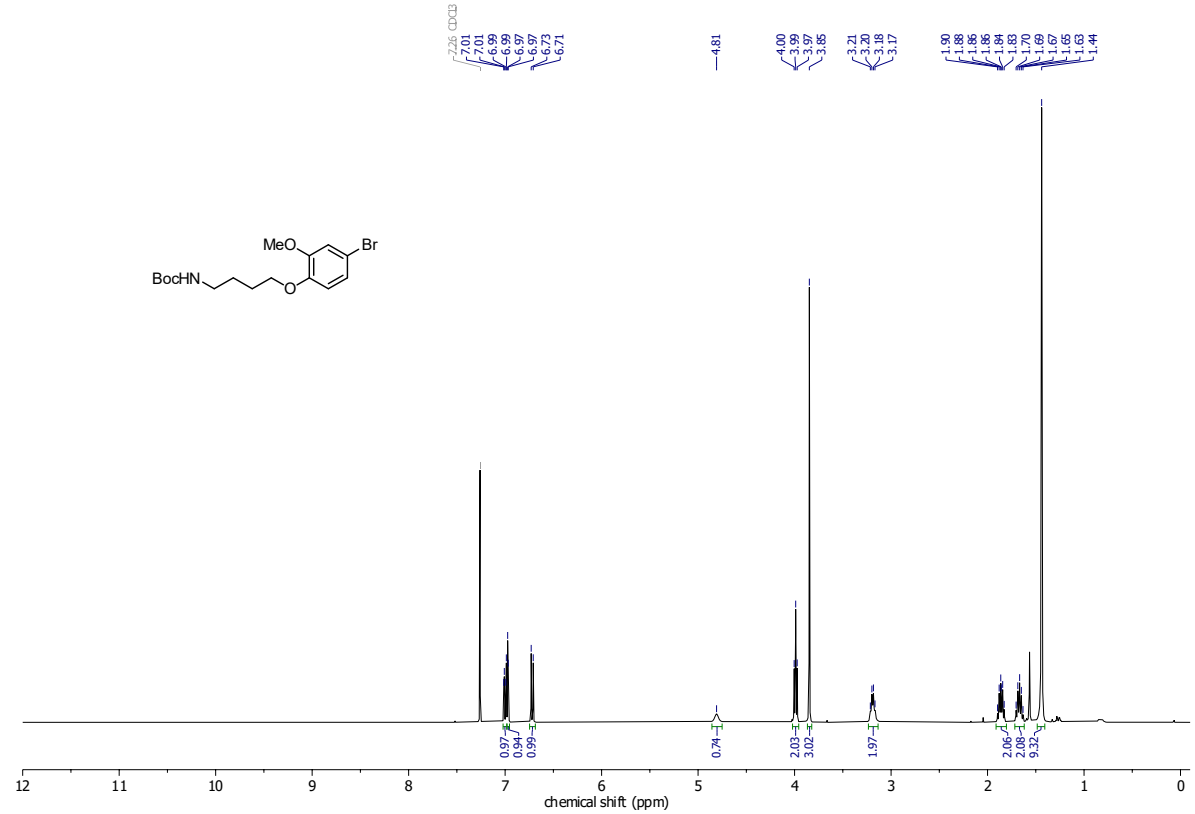

^{13}C-NMR

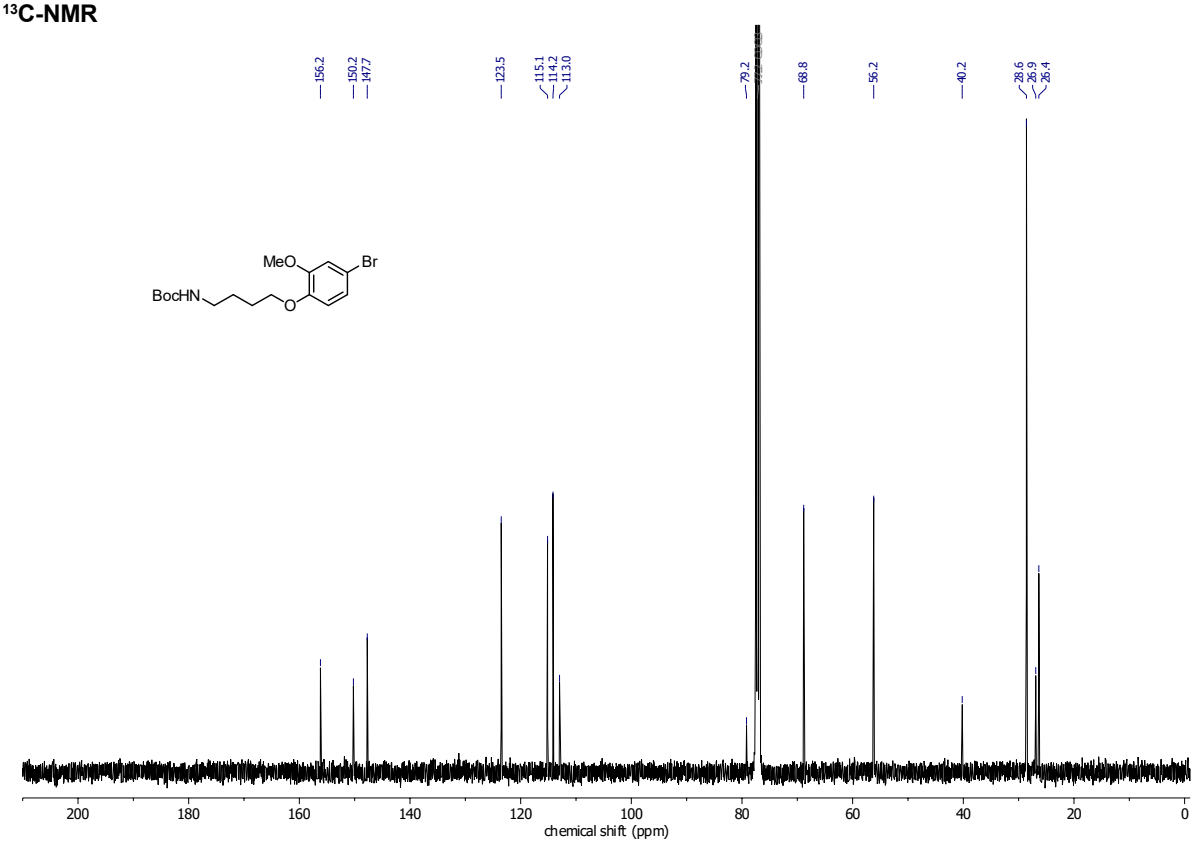

Compound 35

^{1}H-NMR

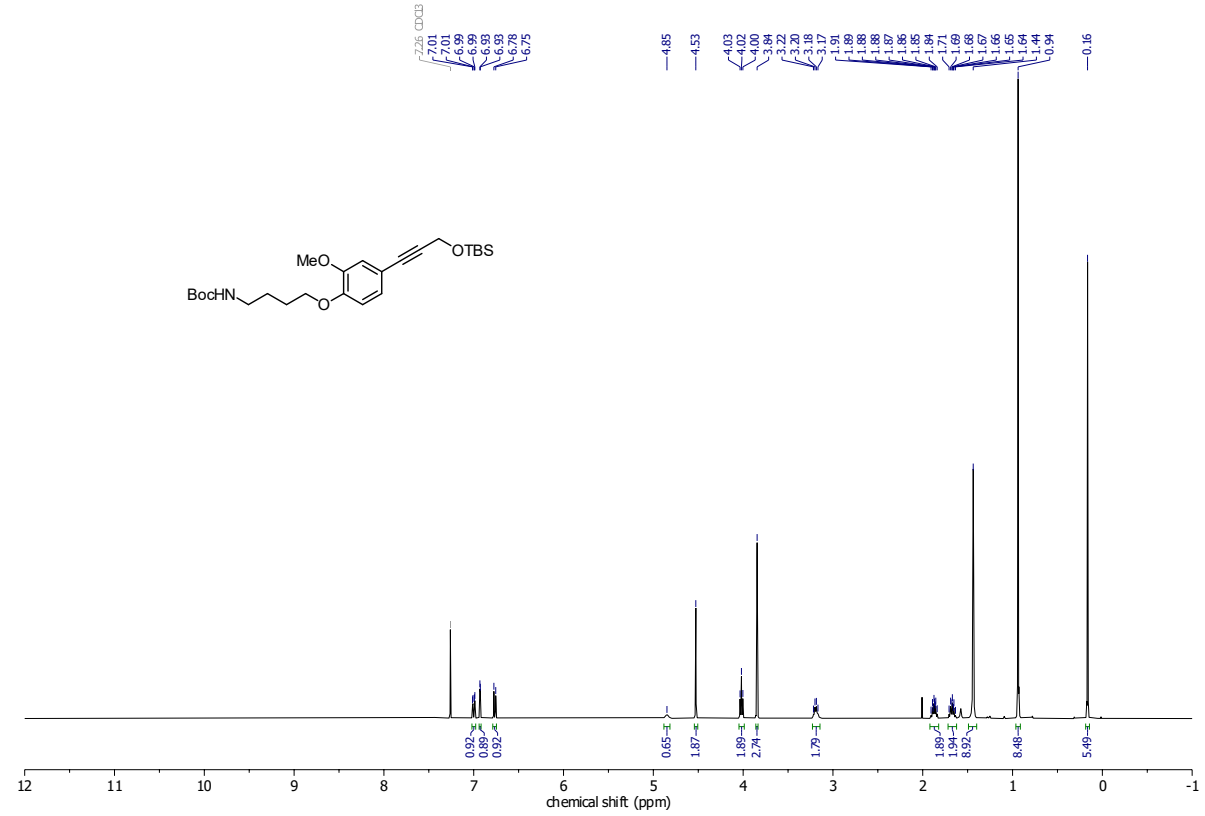

^{13}C-NMR

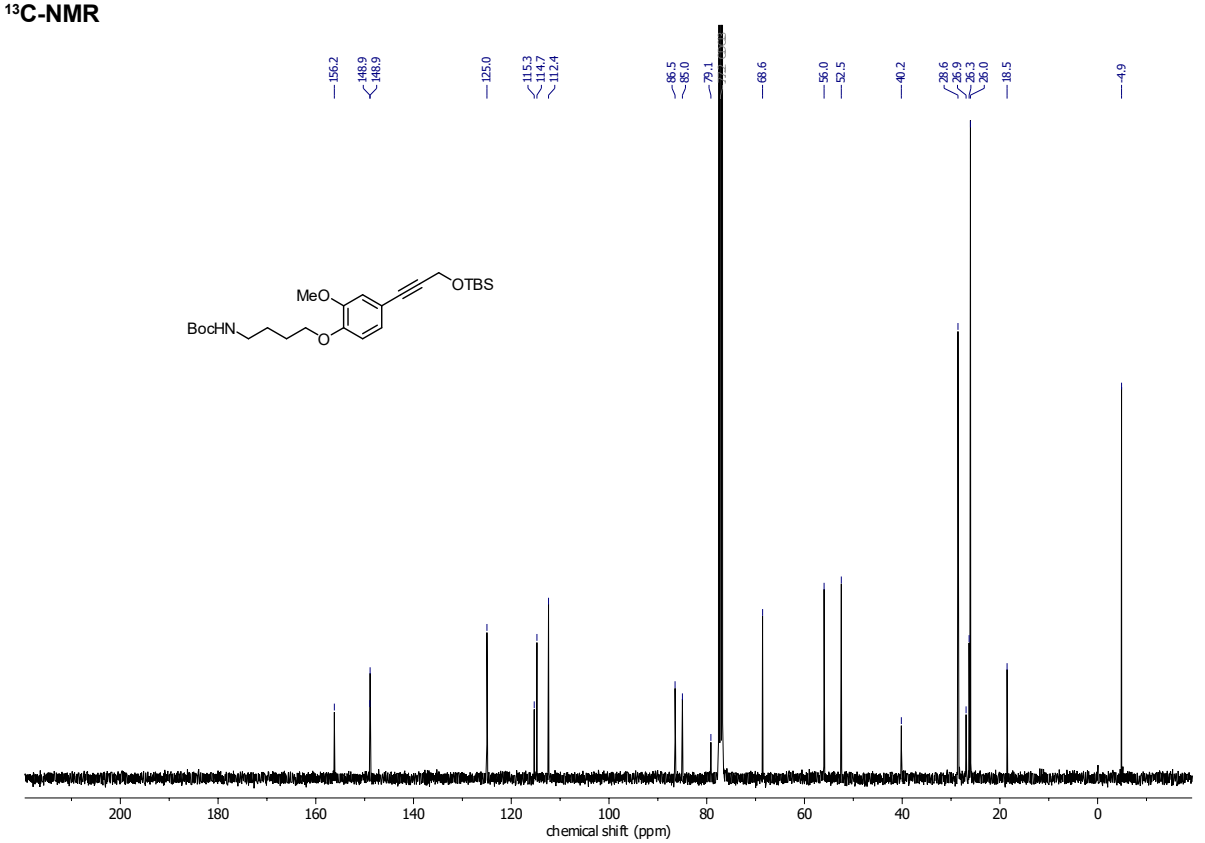

Compound 38

^{1}H-NMR

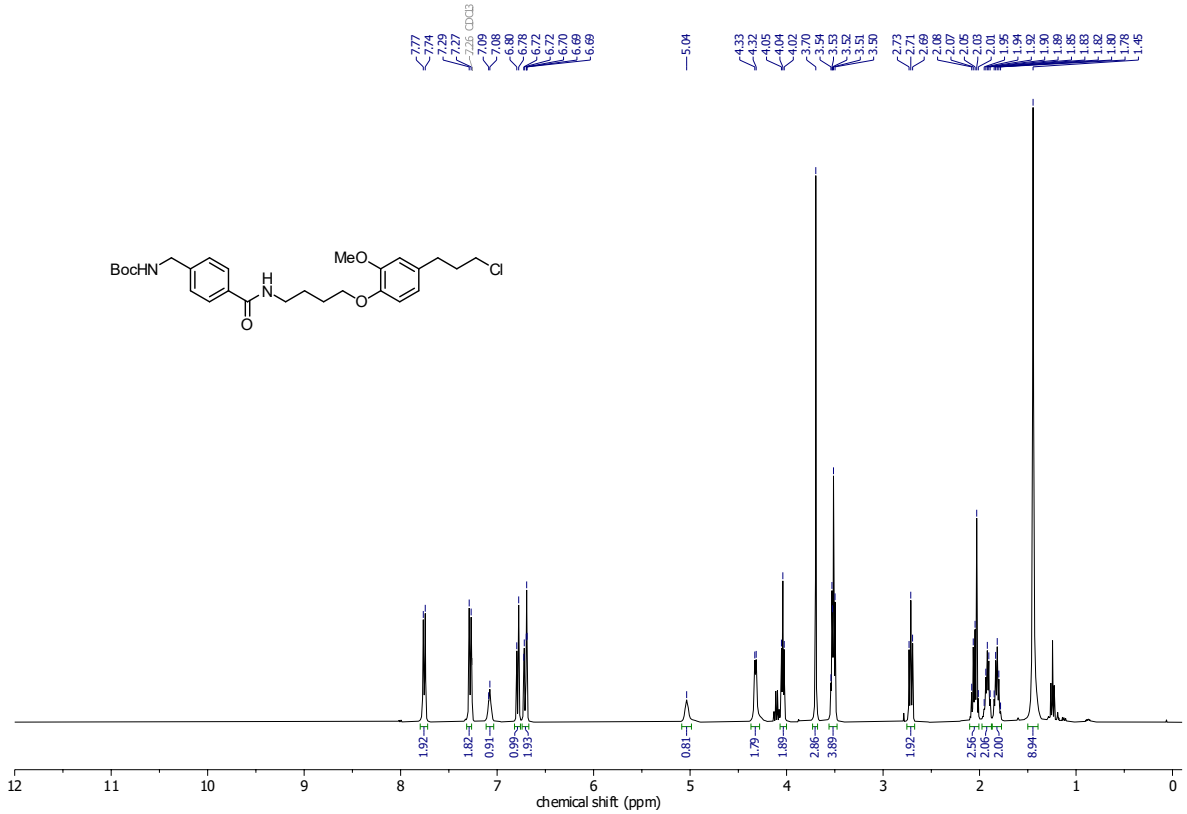

^{13}C-NMR

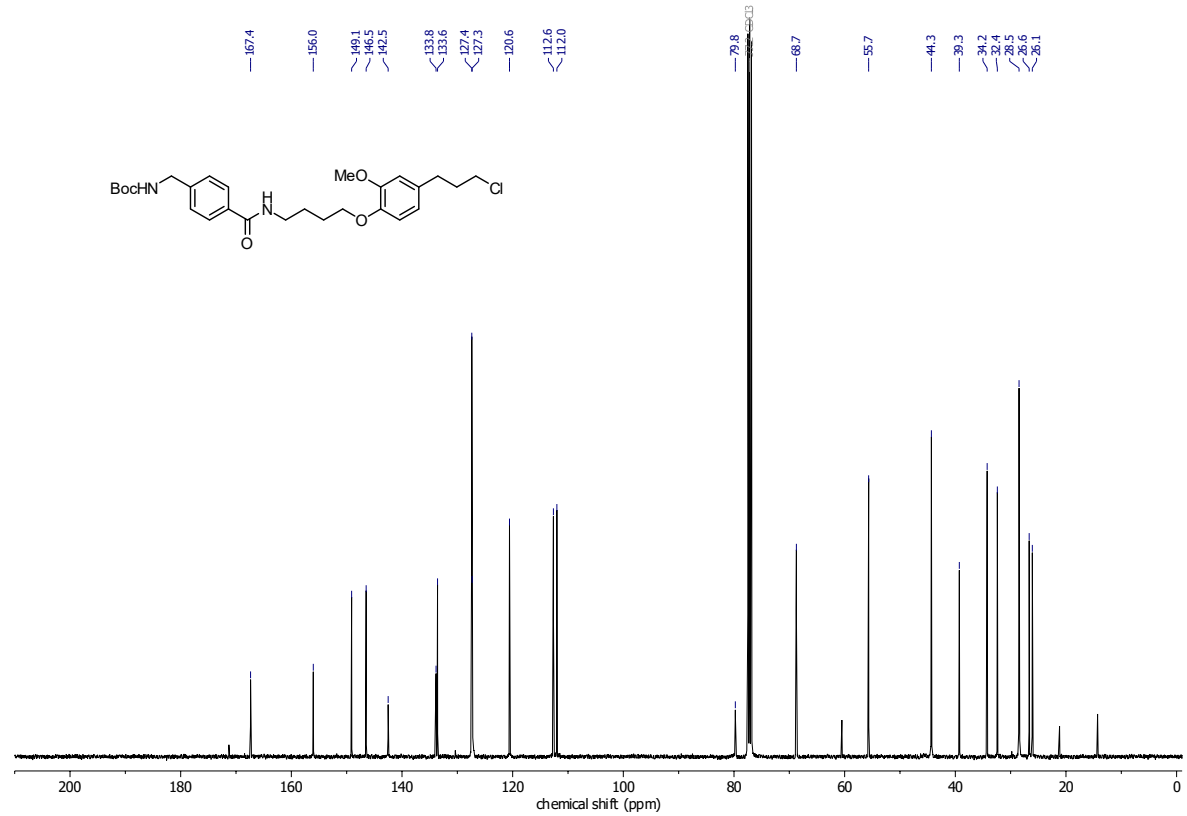

HL2^{O}-Fluo

^{1}H-NMR

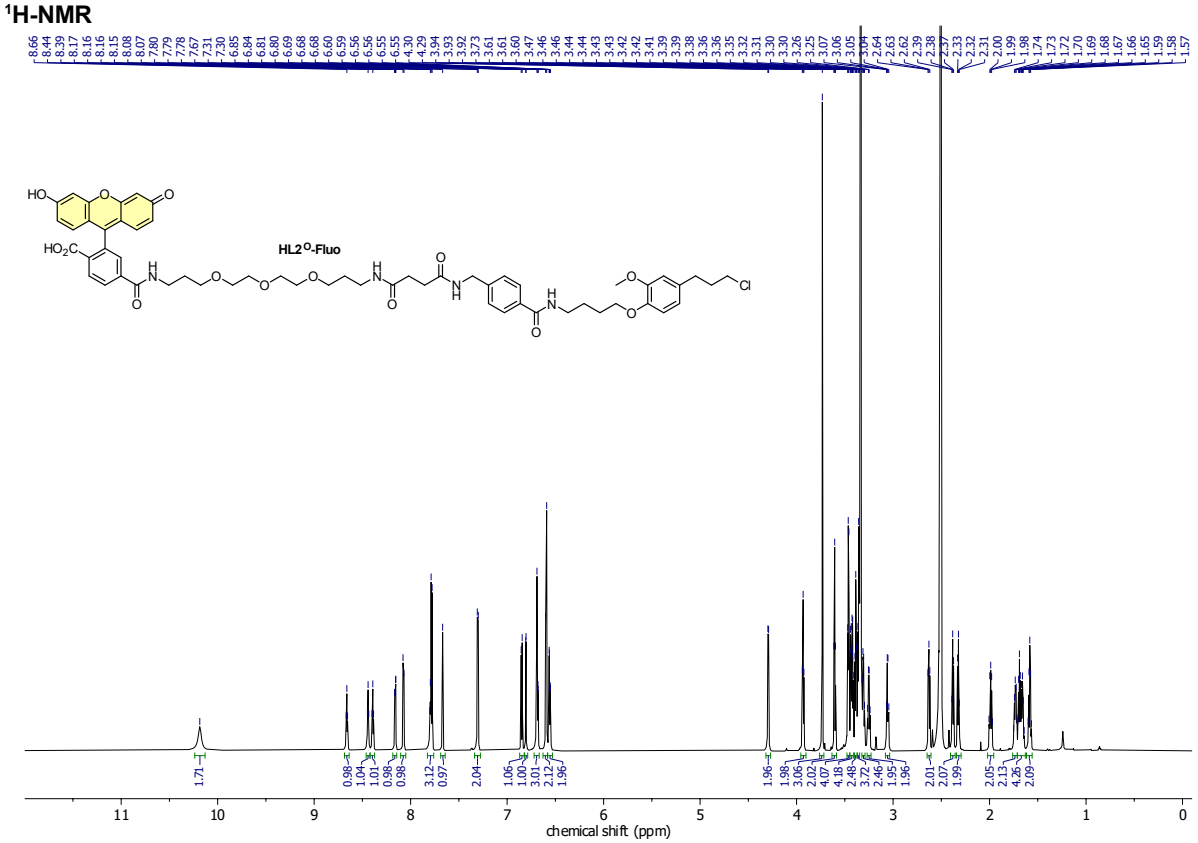

^{13}C-NMR

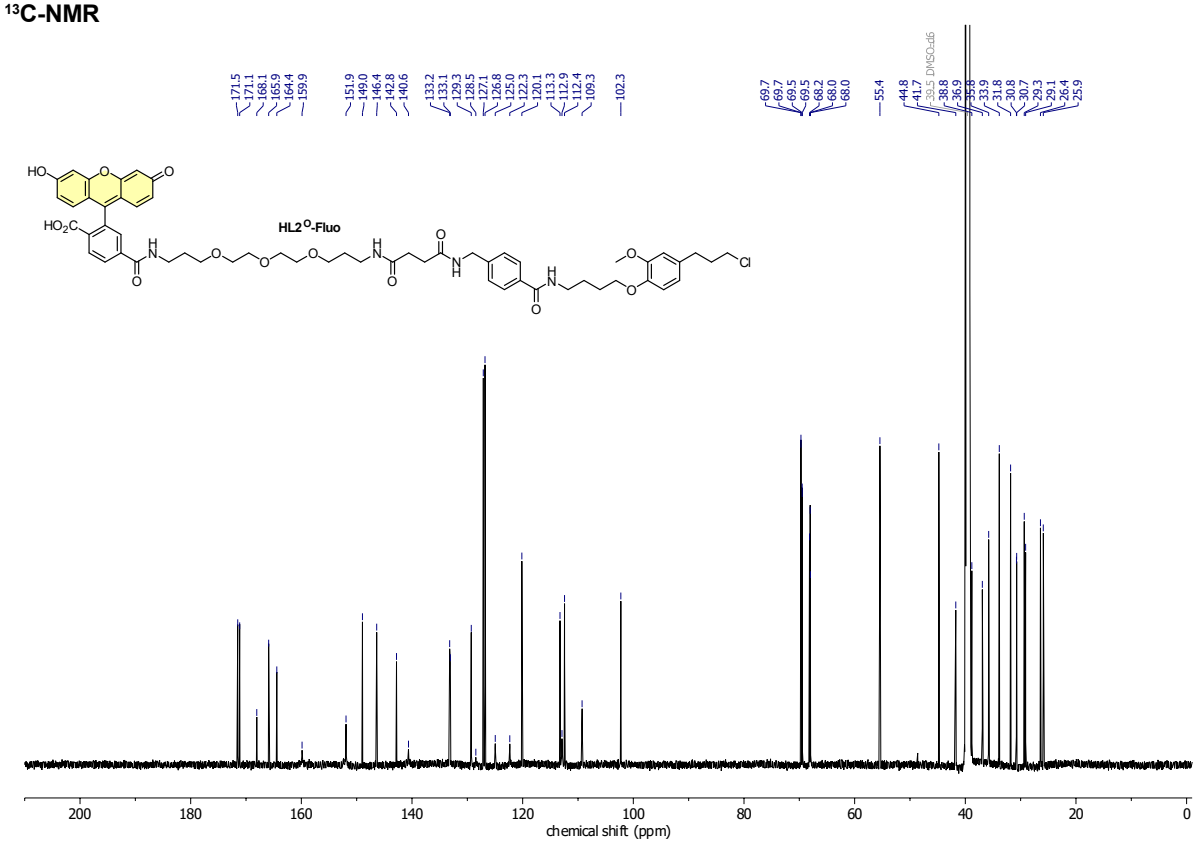

HSQC

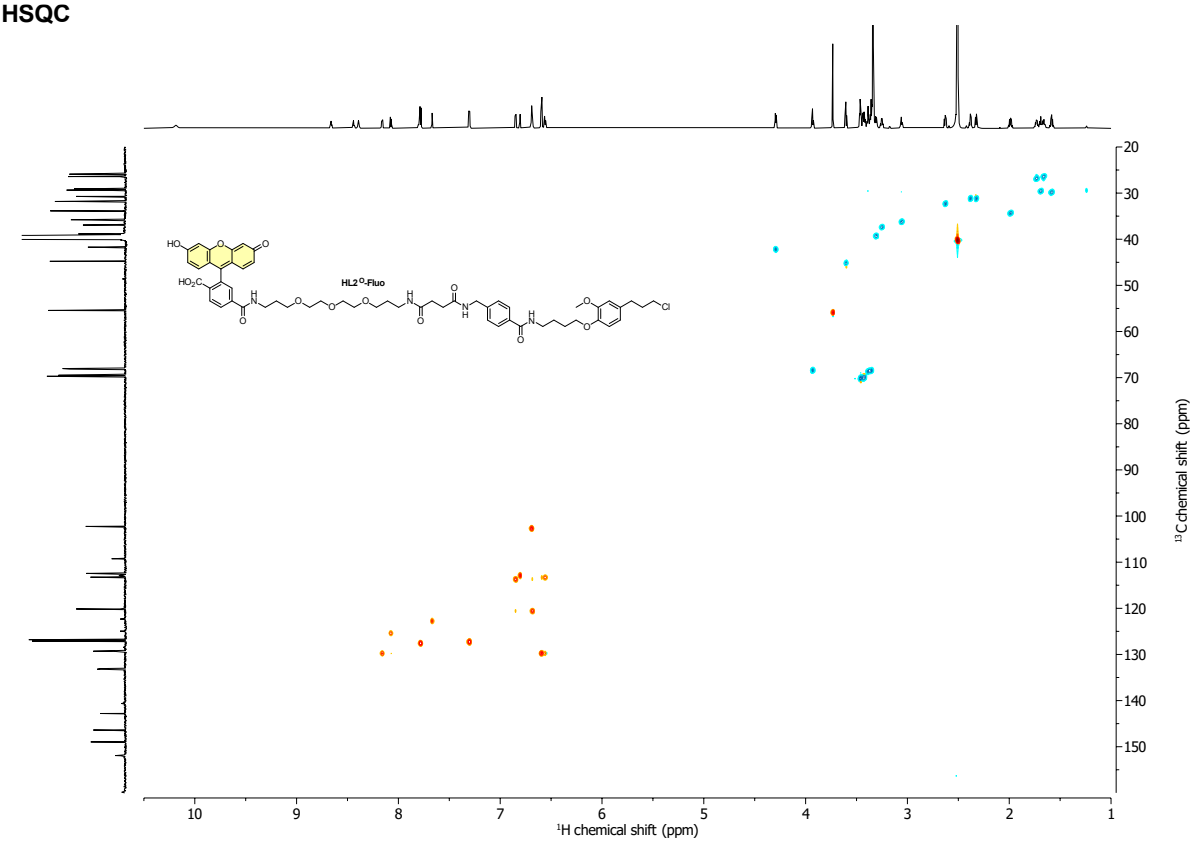
HL2 O-Fluo
^{13}C chemical shift (ppm)
^{1}H chemical shift (ppm)

HMBC

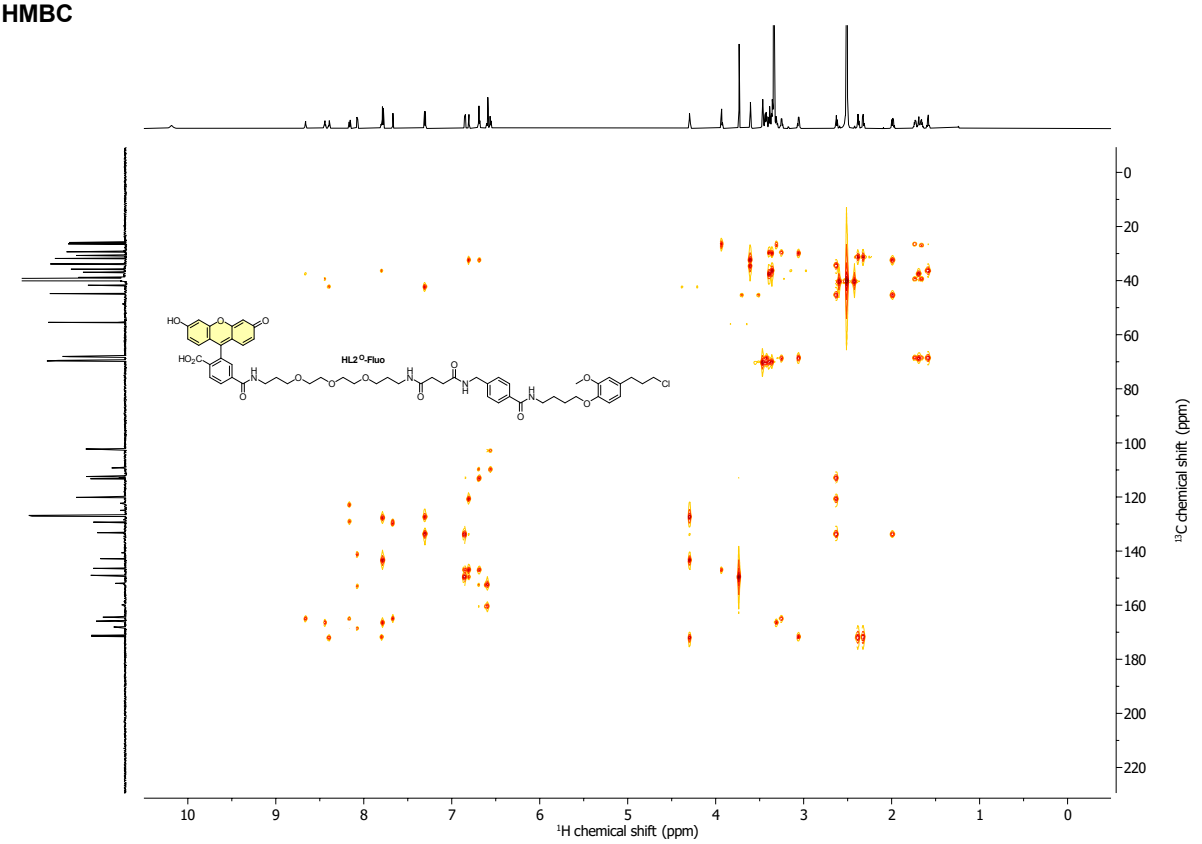
HL2 O-Fluo
^{13}C chemical shift (ppm)
^{1}H chemical shift (ppm)

Compound 40

^{1}H-NMR

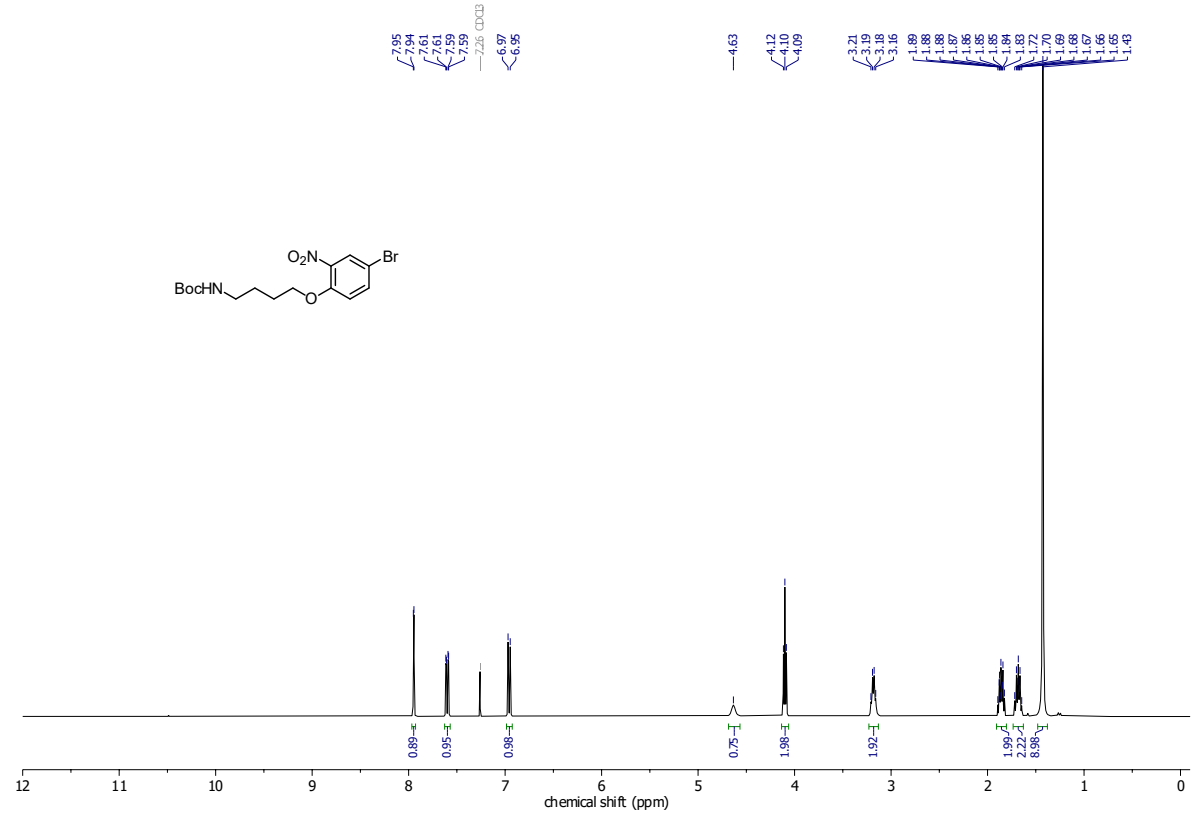

^{13}C-NMR

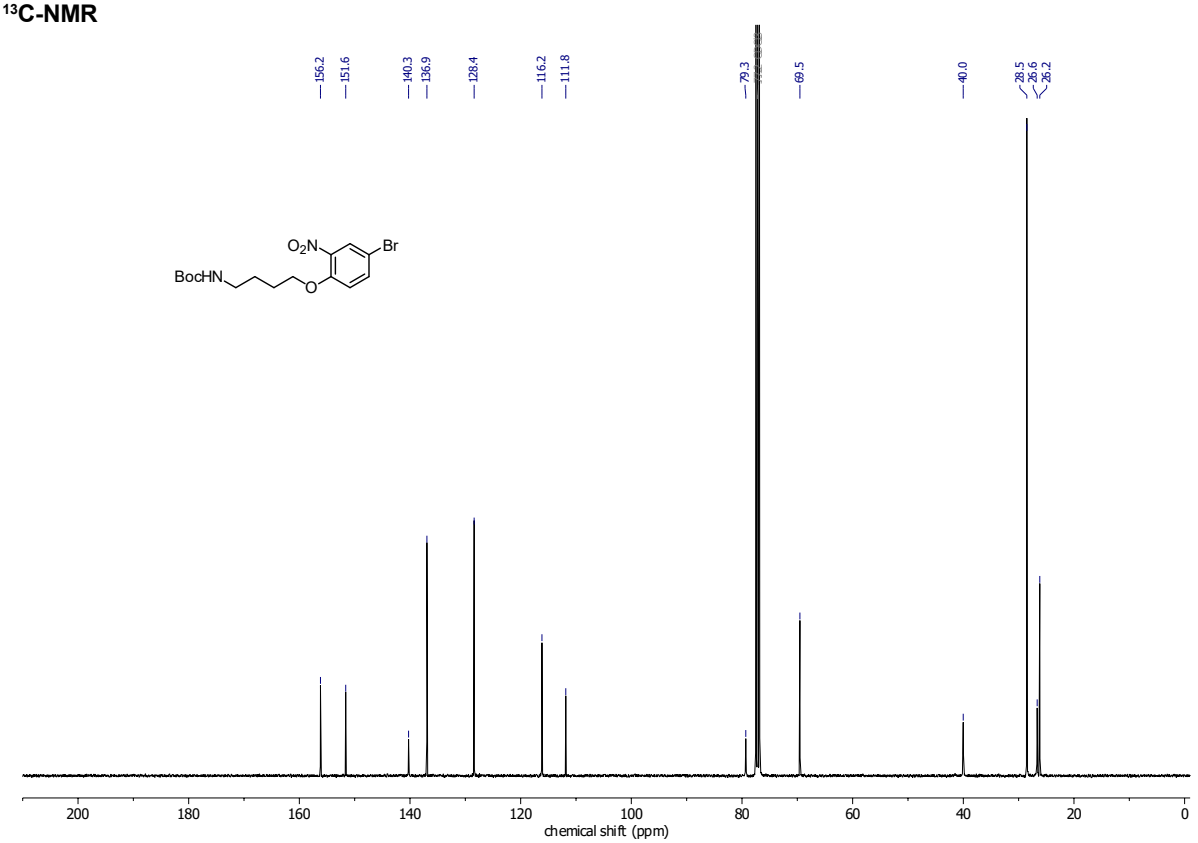

Compound 41

^{1}H-NMR

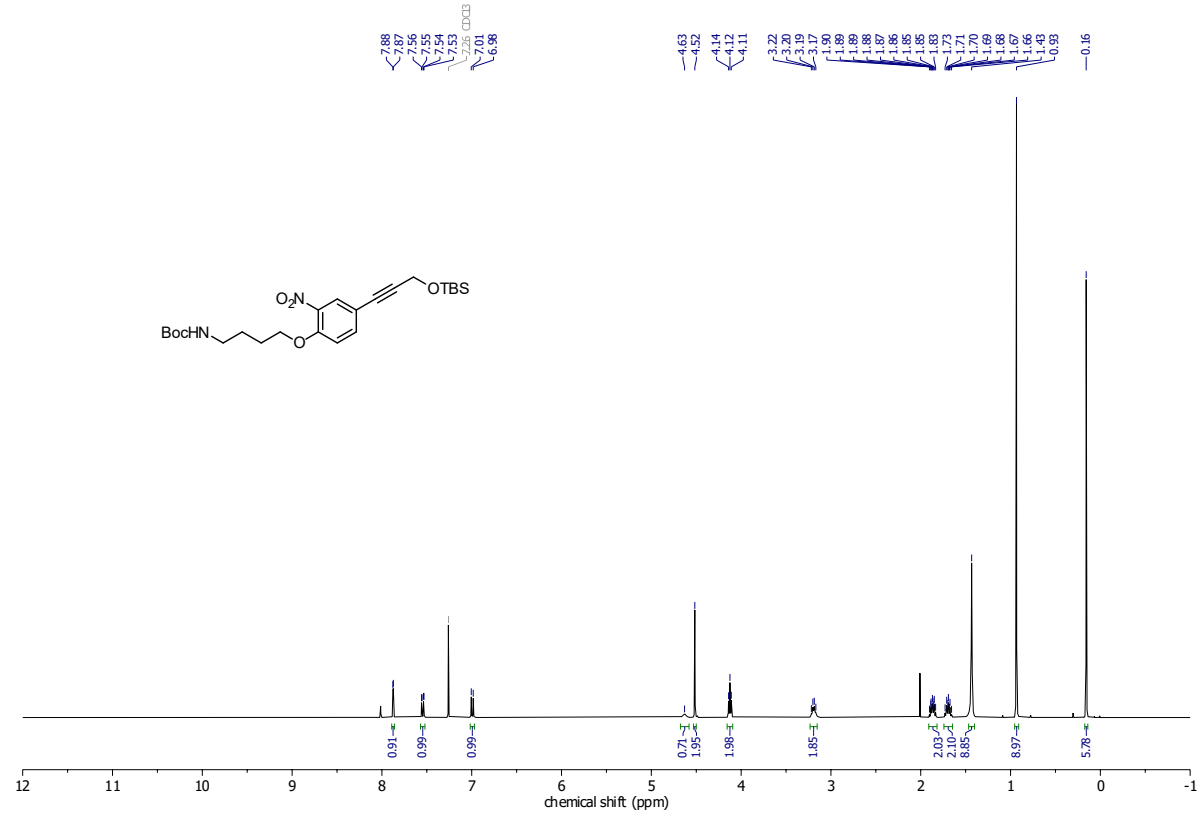

^{13}C-NMR

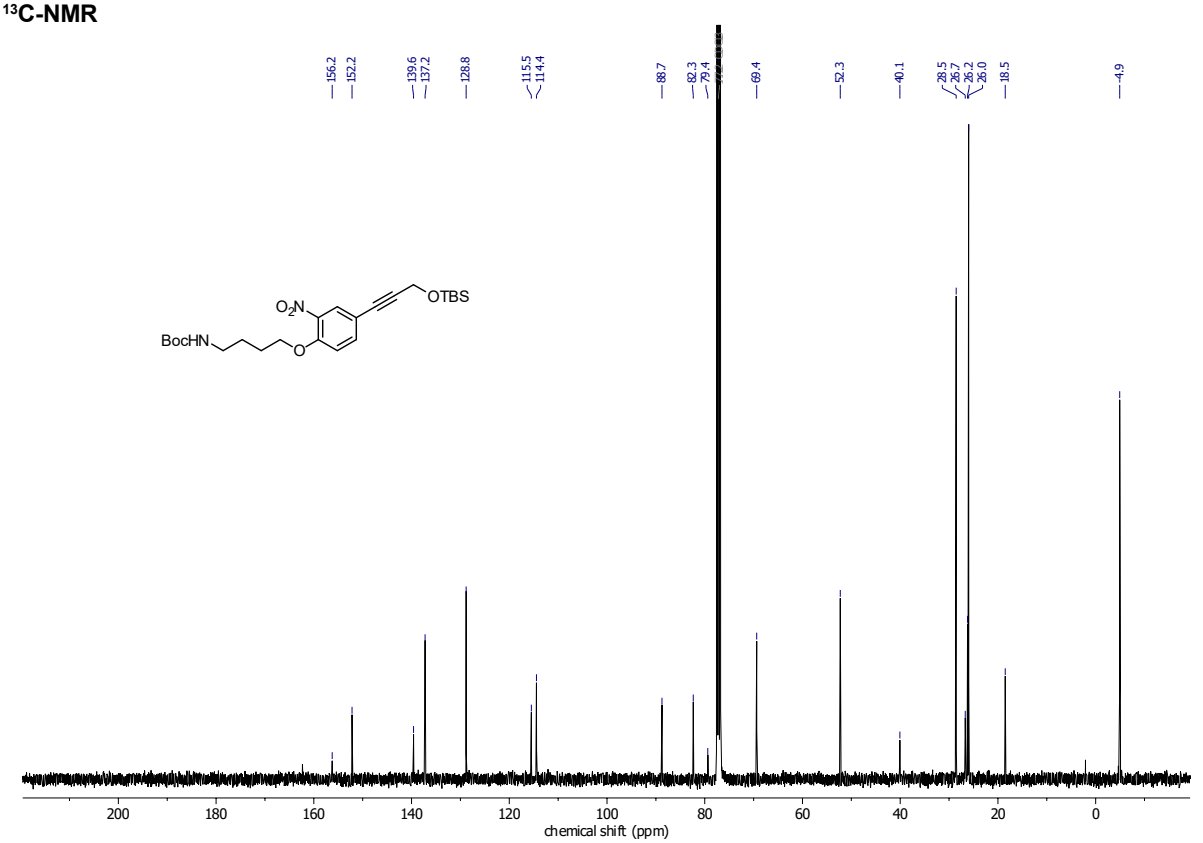

Compound 42

^{1}H-NMR

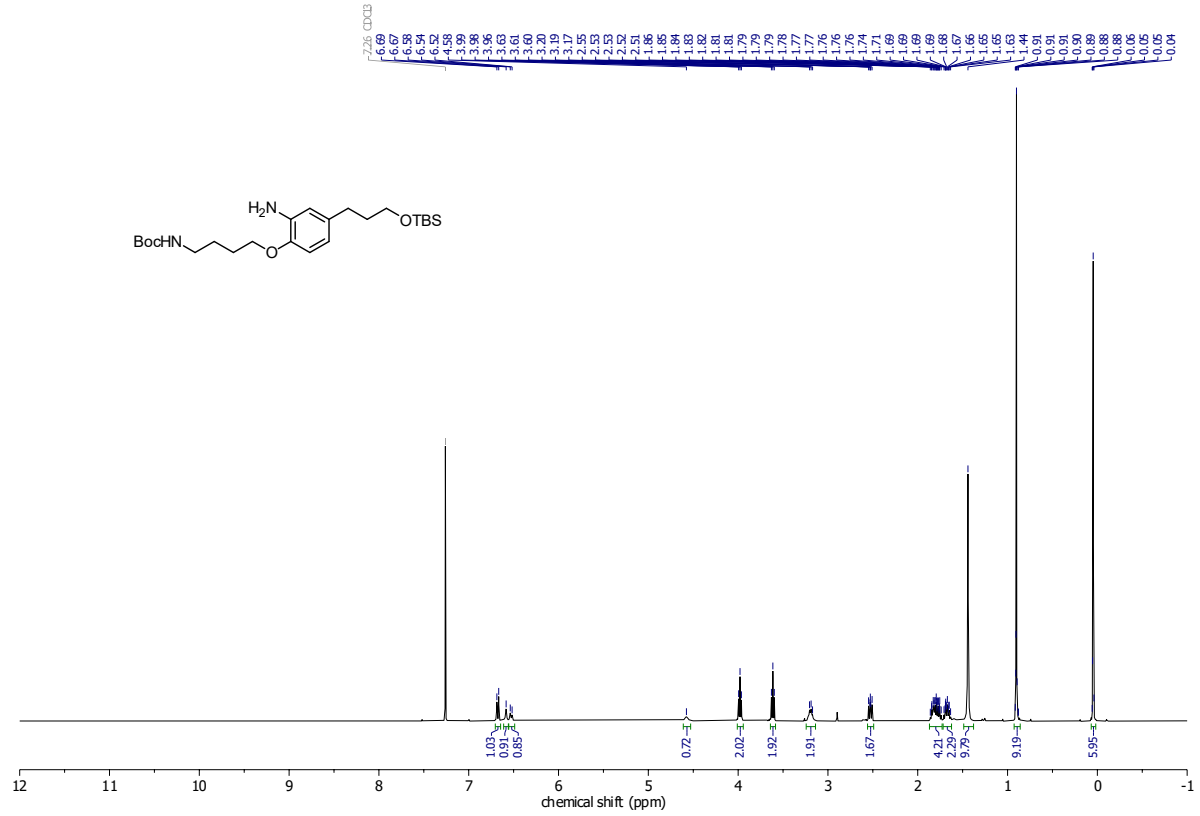

^{13}C-NMR

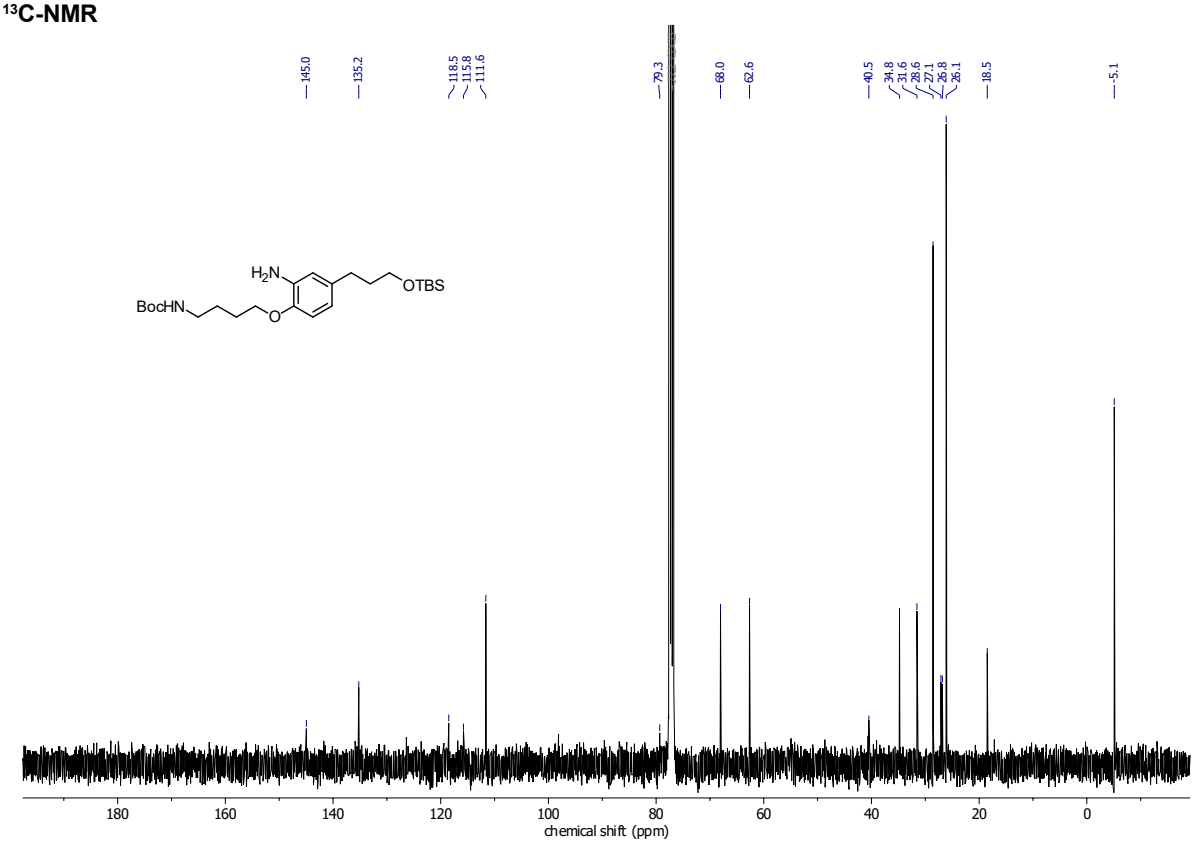

Compound 44
^{1}H-NMR

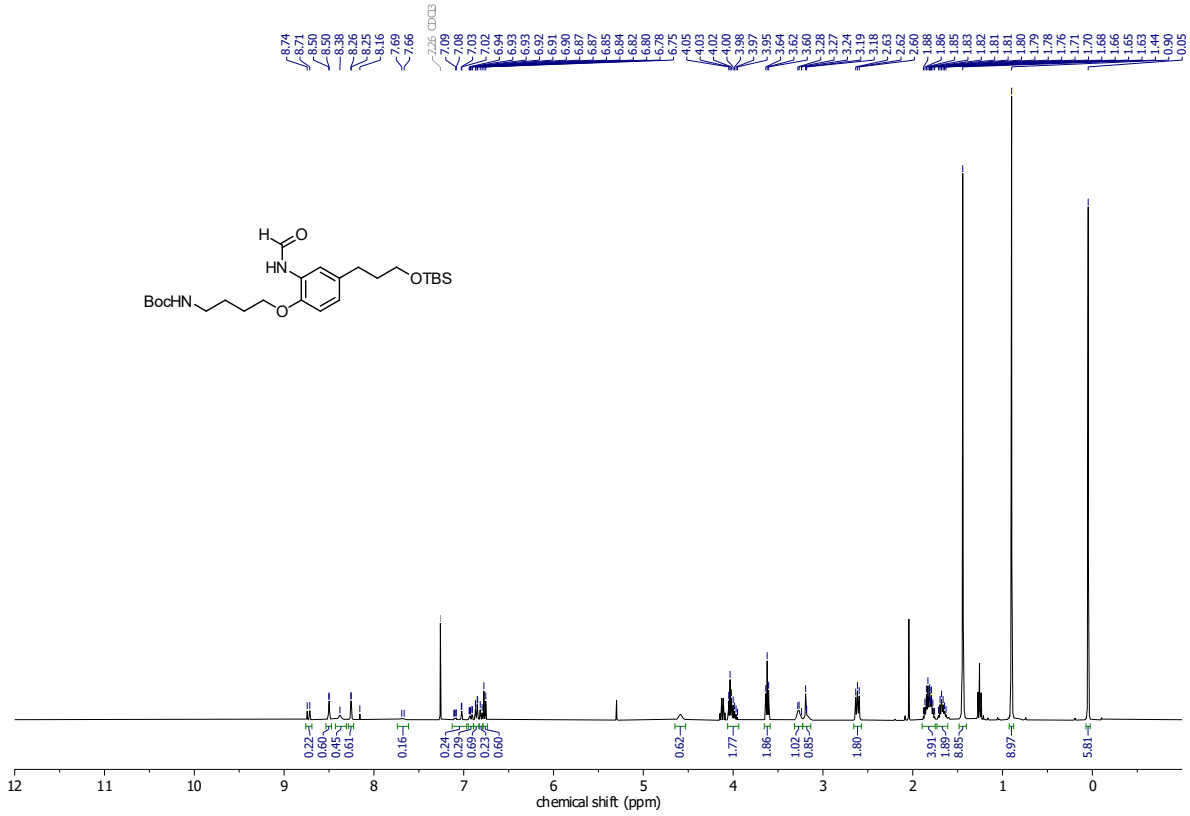

Compound 48

^{1}H-NMR

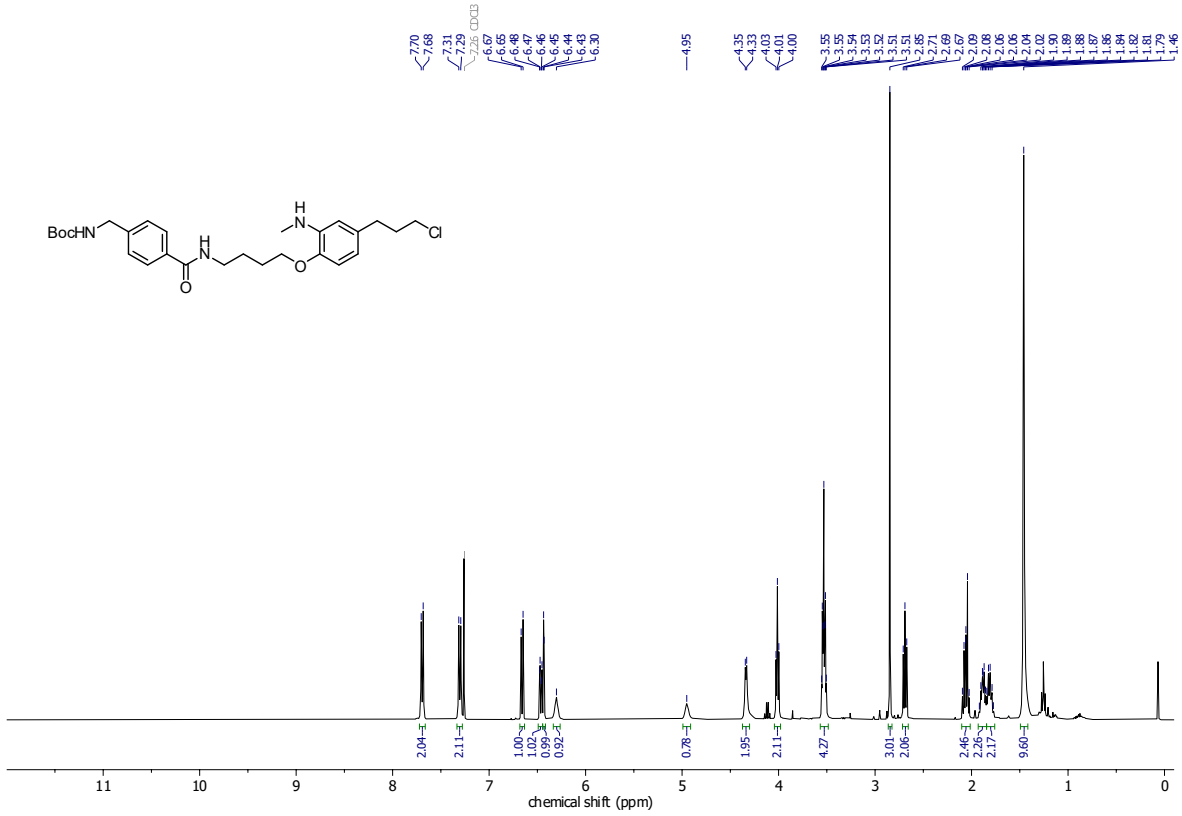

^{13}C-NMR

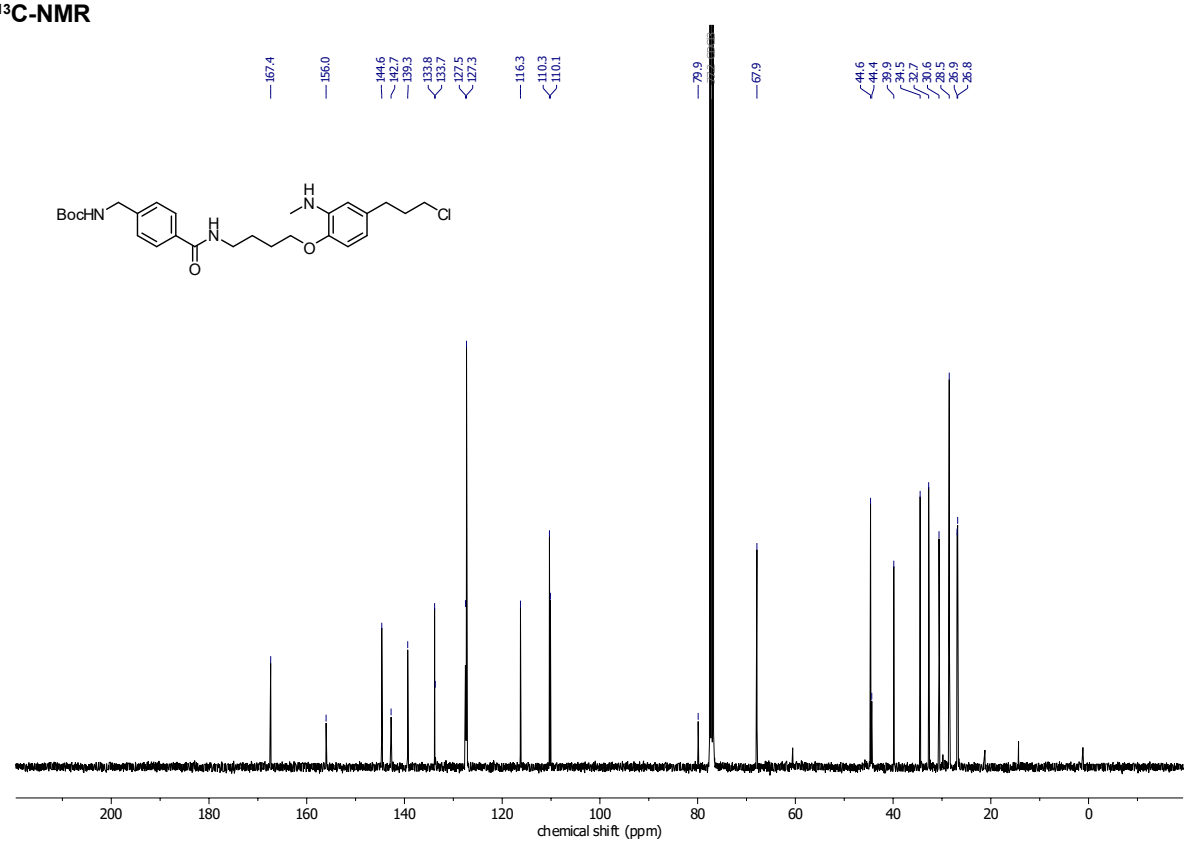

HL2^{N}-Fluo
^{1}H-NMR

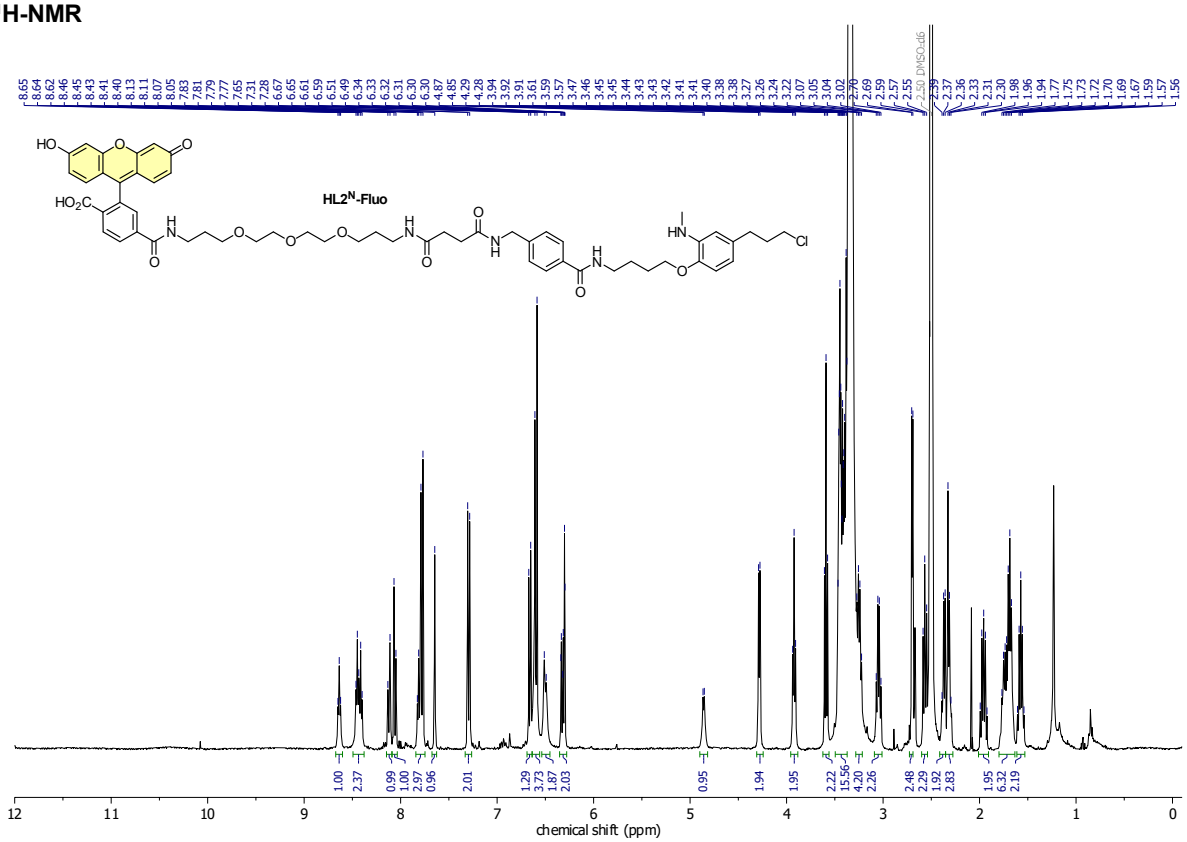

Compound 49

^{1}H-NMR

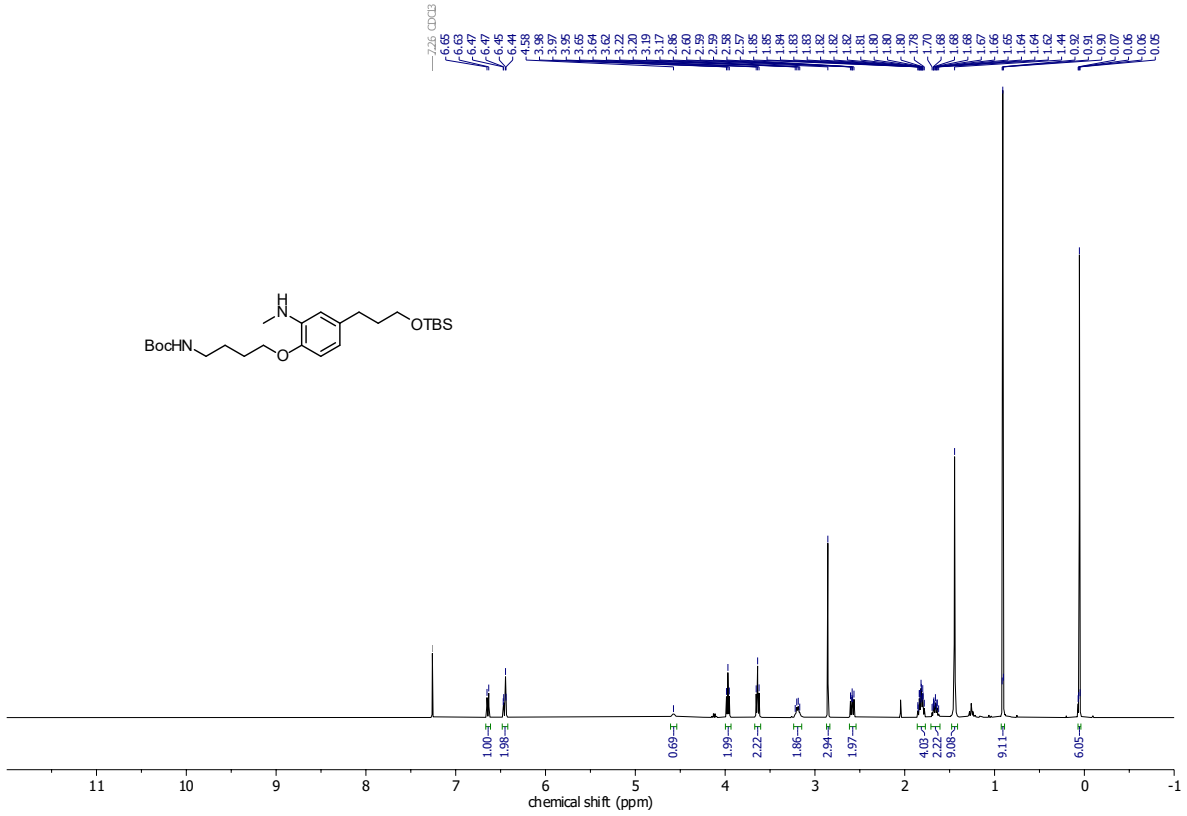

^{13}C-NMR

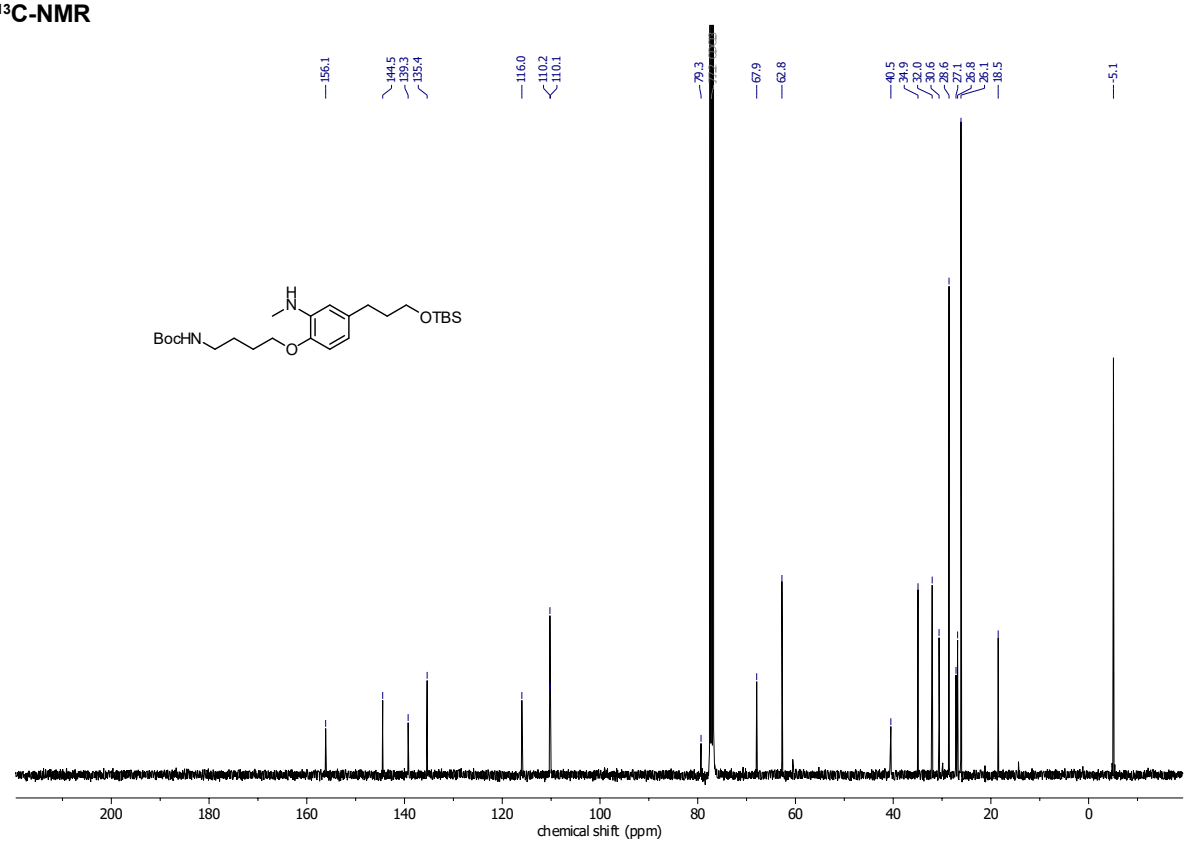

Cou-HL2^{N}-Fluo

^{1}H-NMR

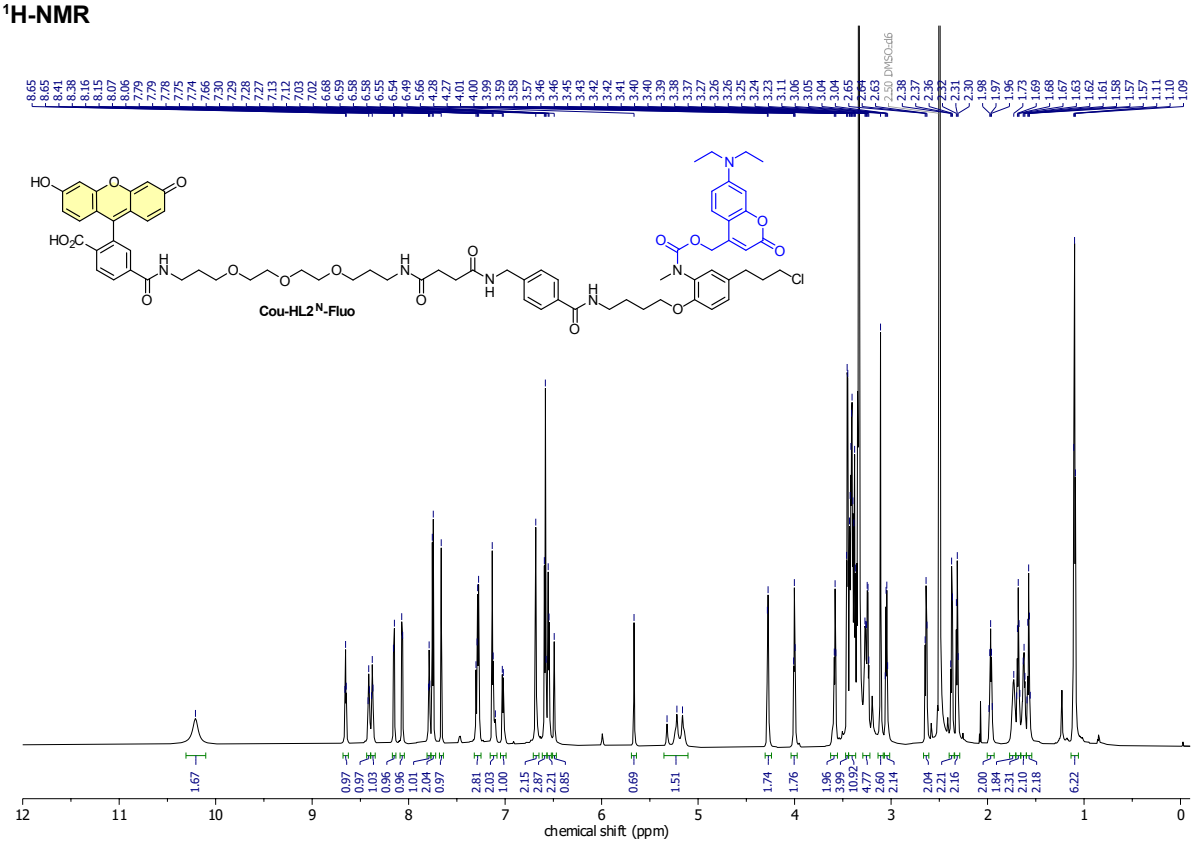

^{13}C-NMR

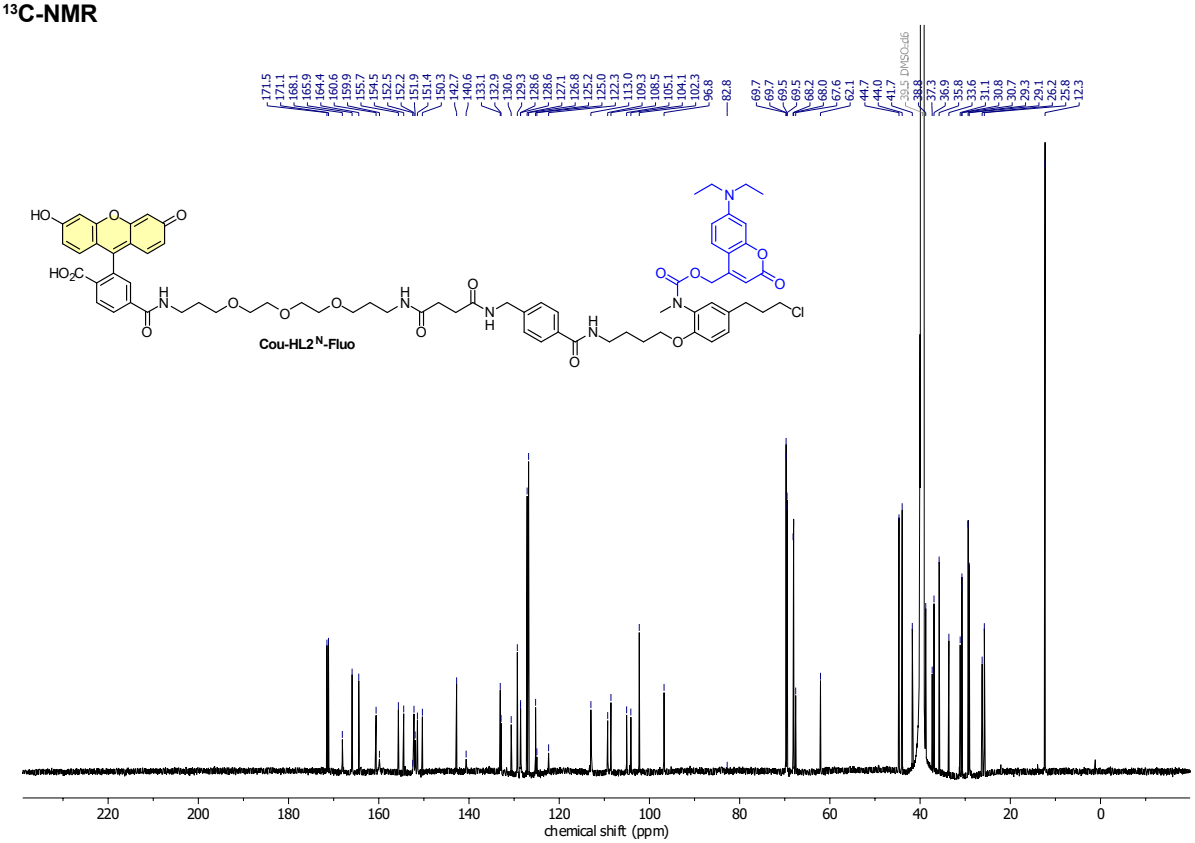

HSQC

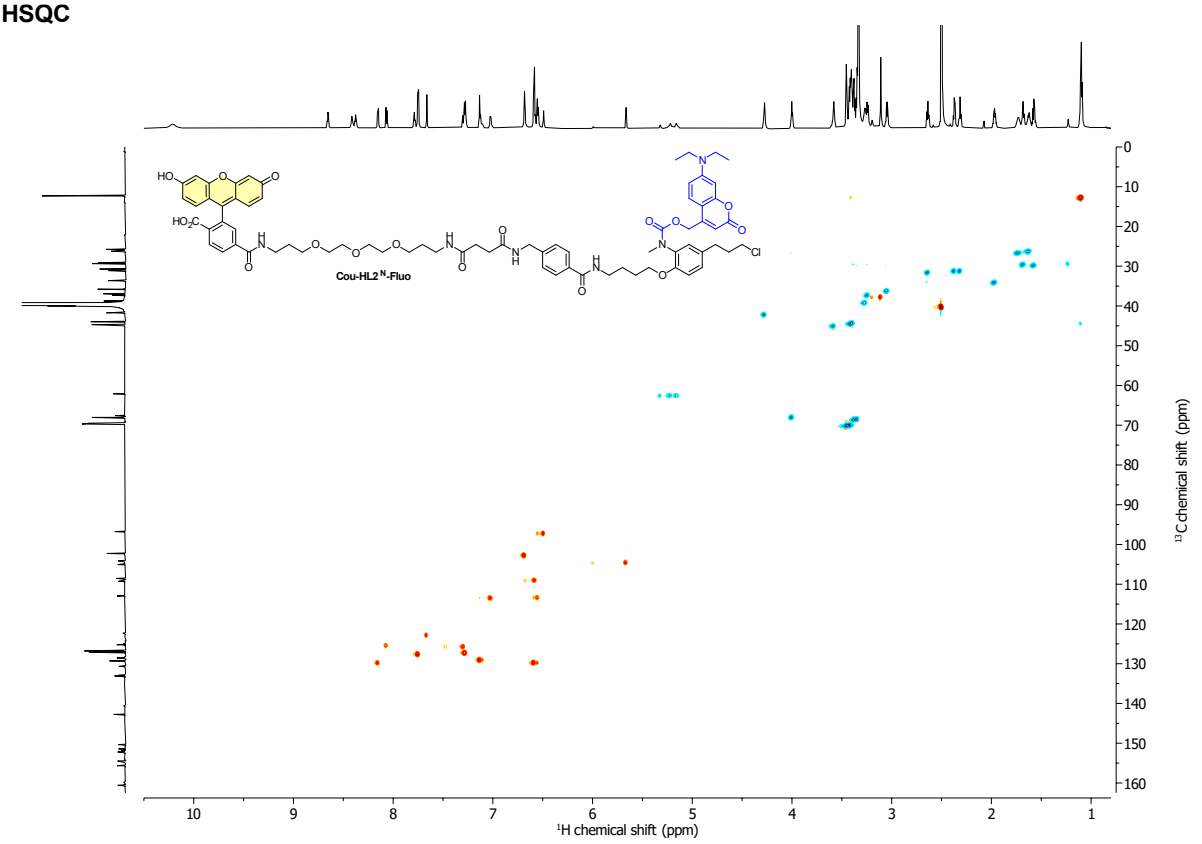
Cou-HL2 N-Fluo
^{1}H chemical shift (ppm)
^{13}C chemical shift (ppm)

HMBC

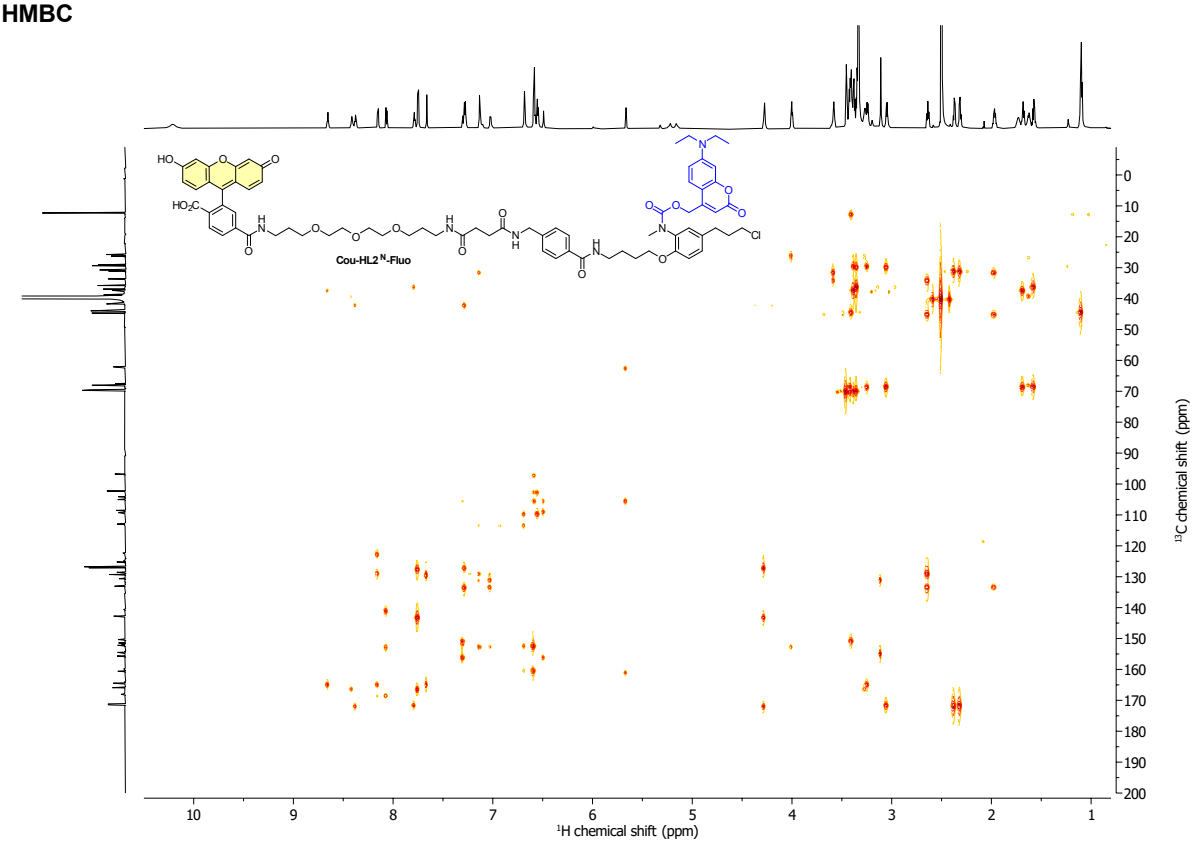
Cou-HL2 N-Fluo
^{1}H chemical shift (ppm)
^{13}C chemical shift (ppm)

Compound 56

^{1}H-NMR

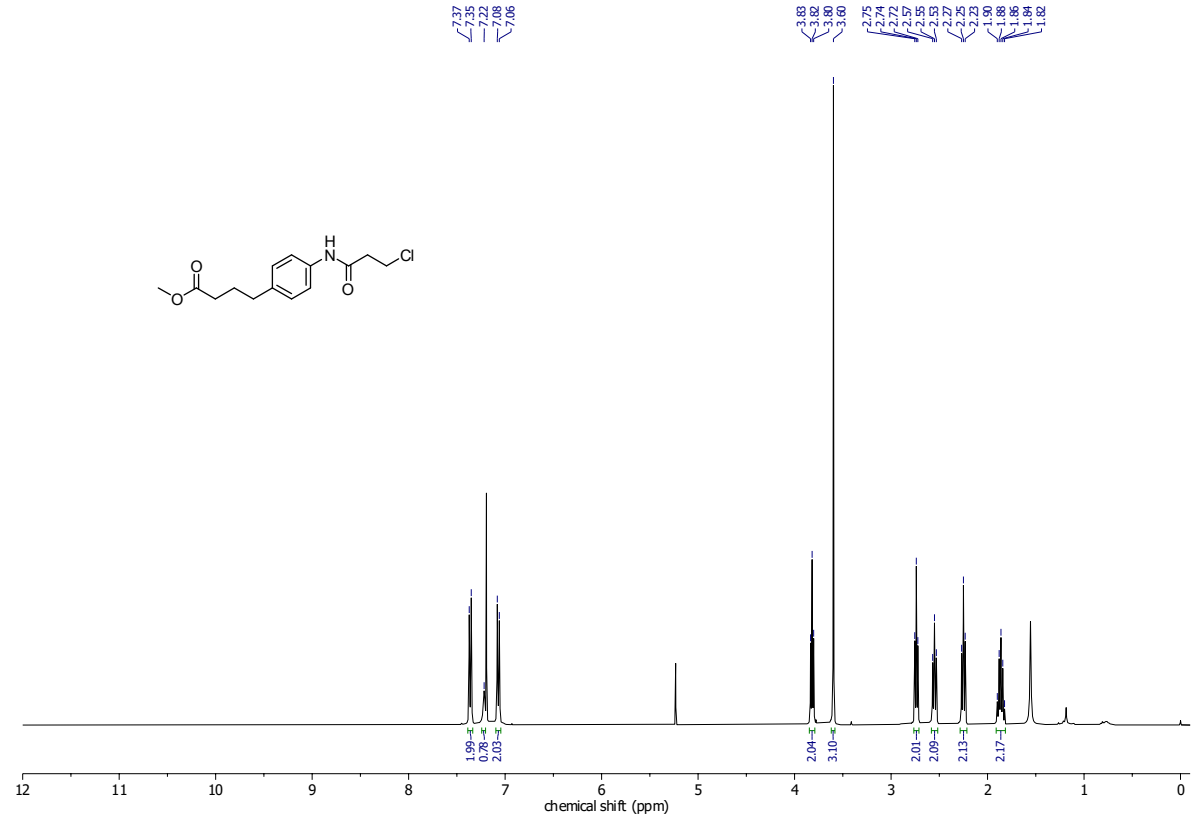

^{13}C-NMR

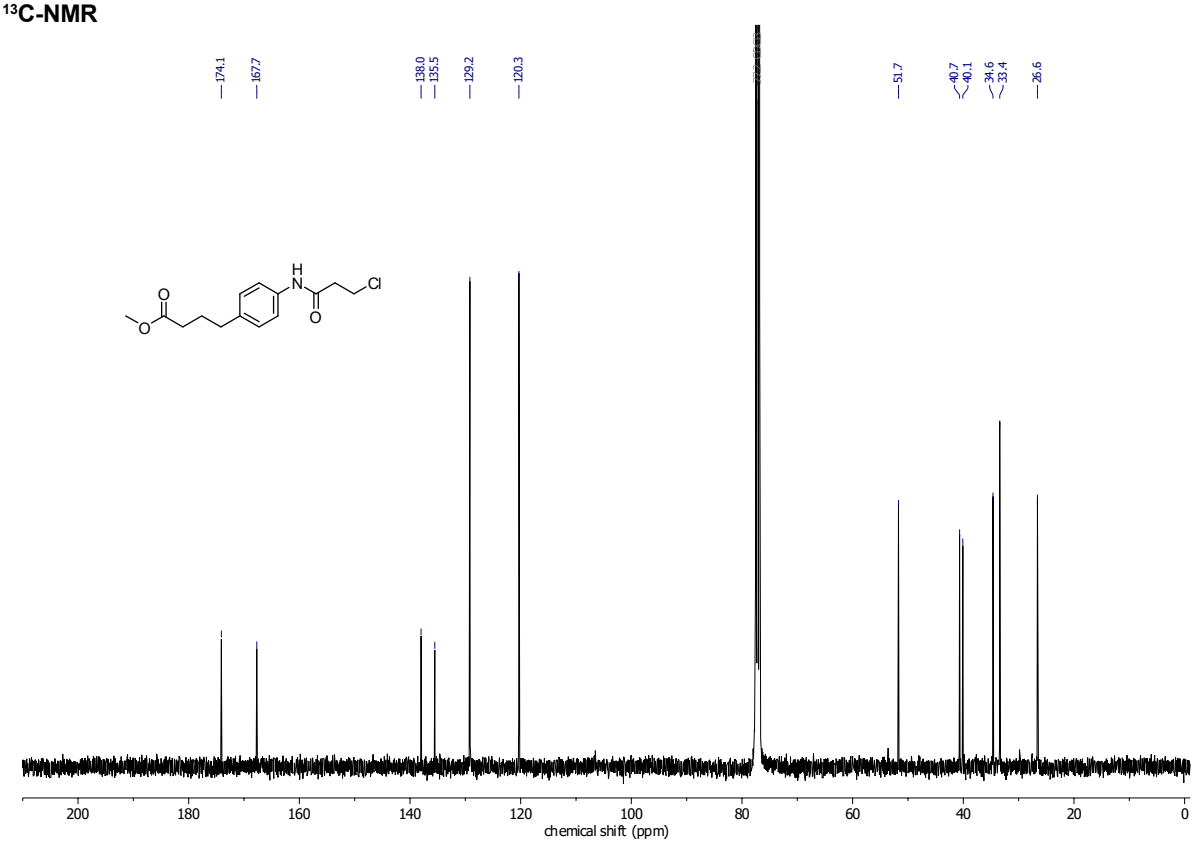

Compound 60

^{1}H-NMR

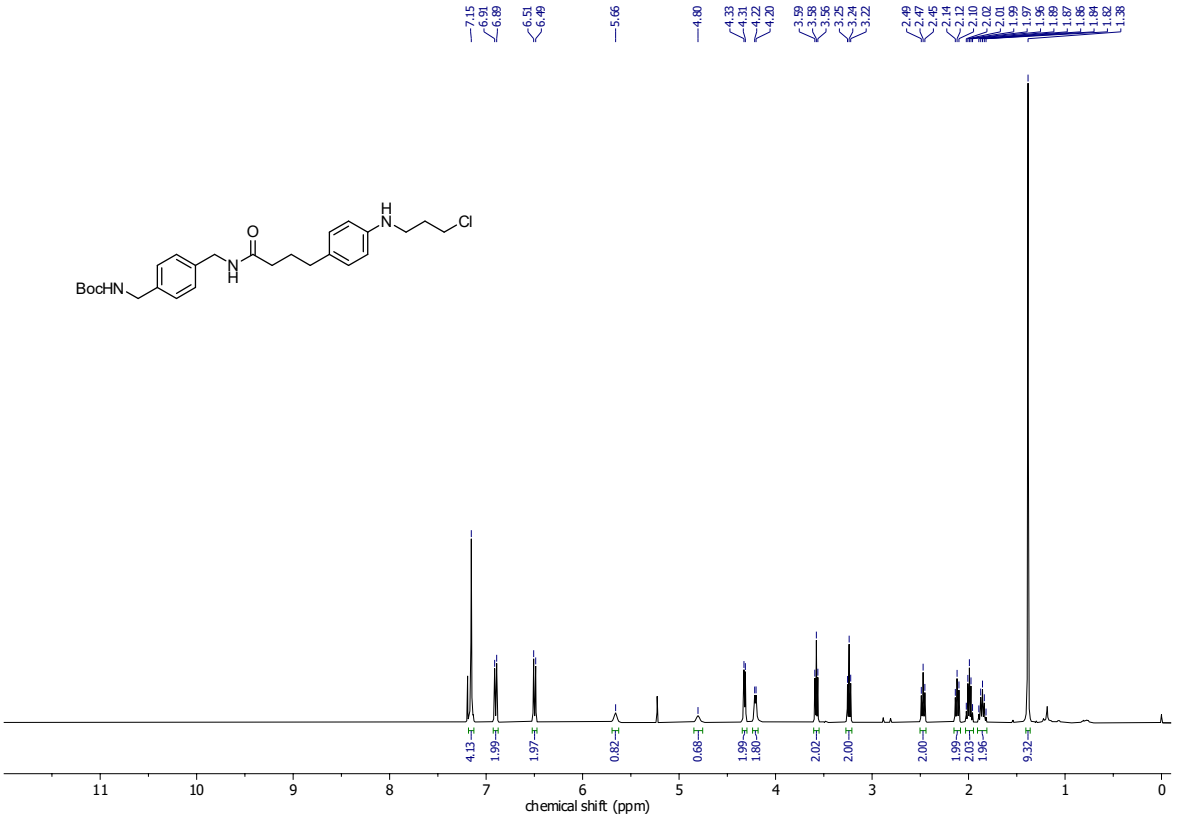

^{13}C-NMR

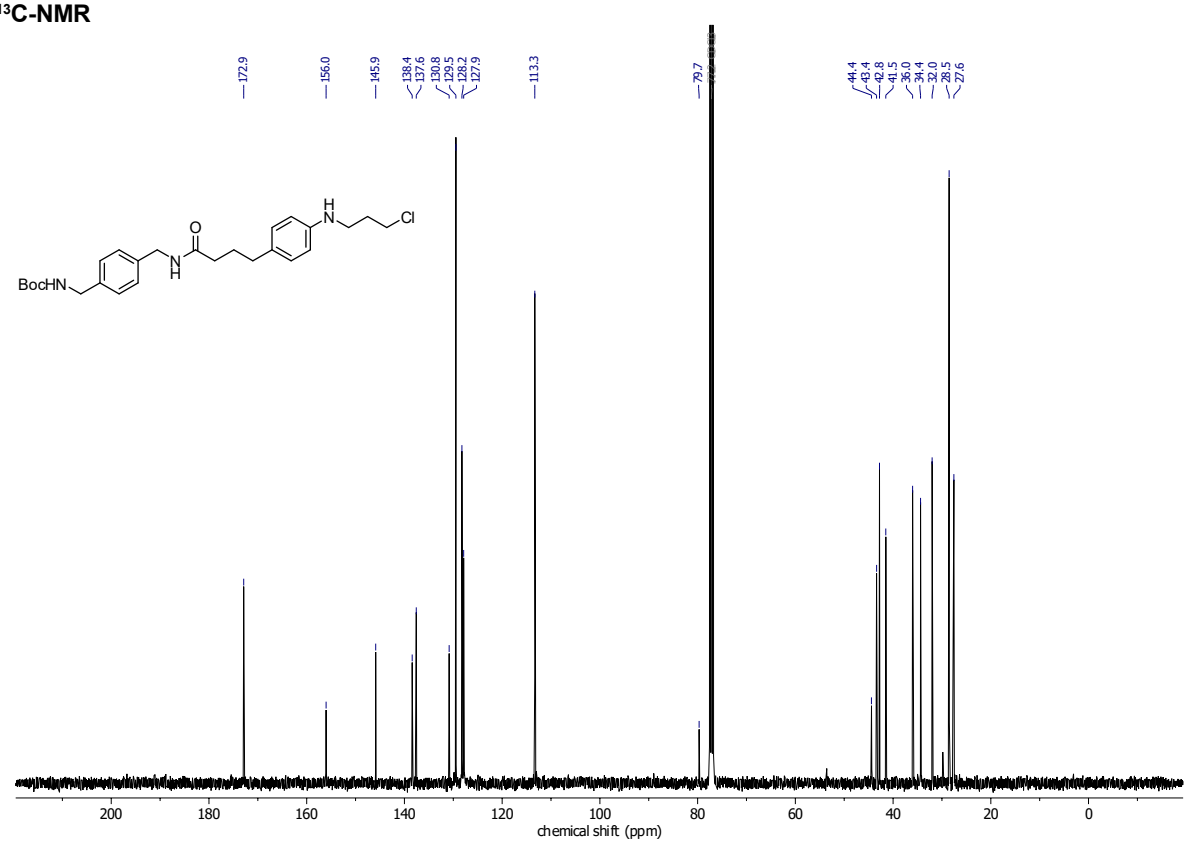

HL3-Fluo

^{1}H-NMR

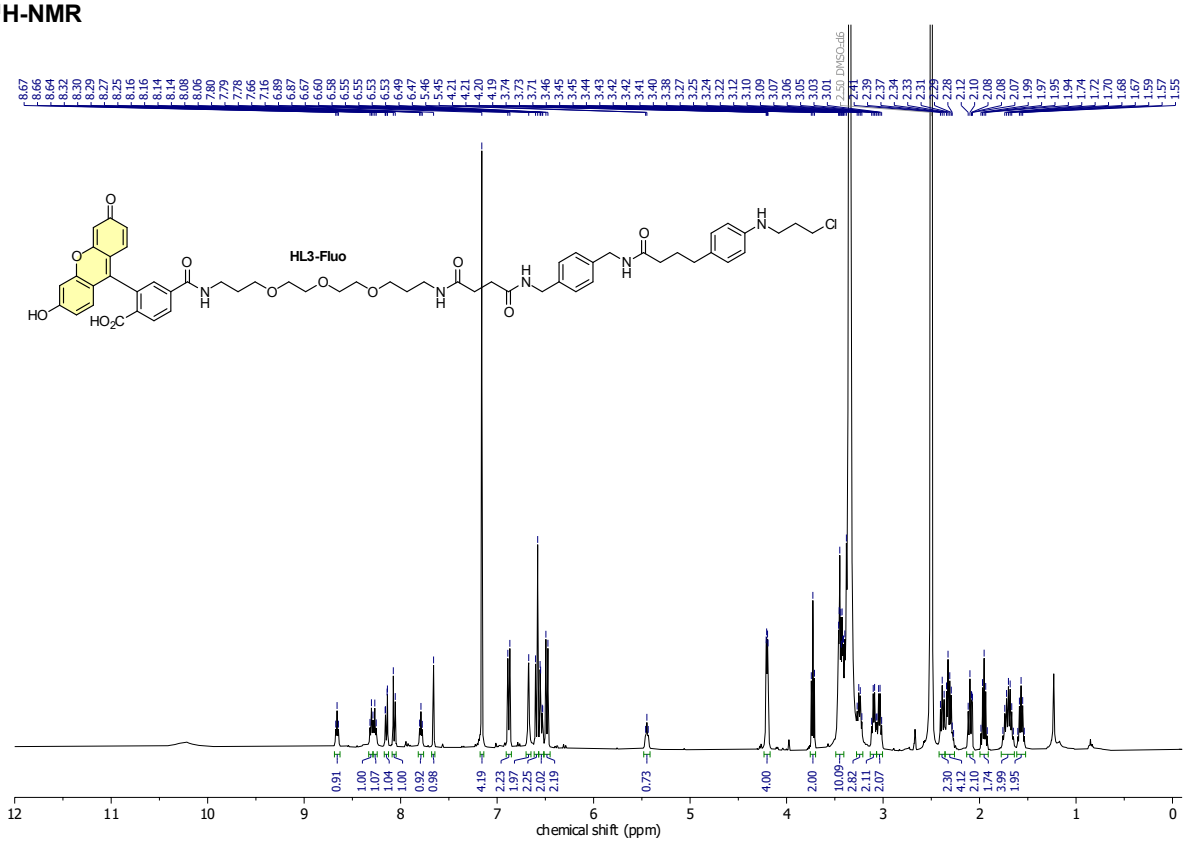

Cou-HL3-Fluo

^{1}H-NMR

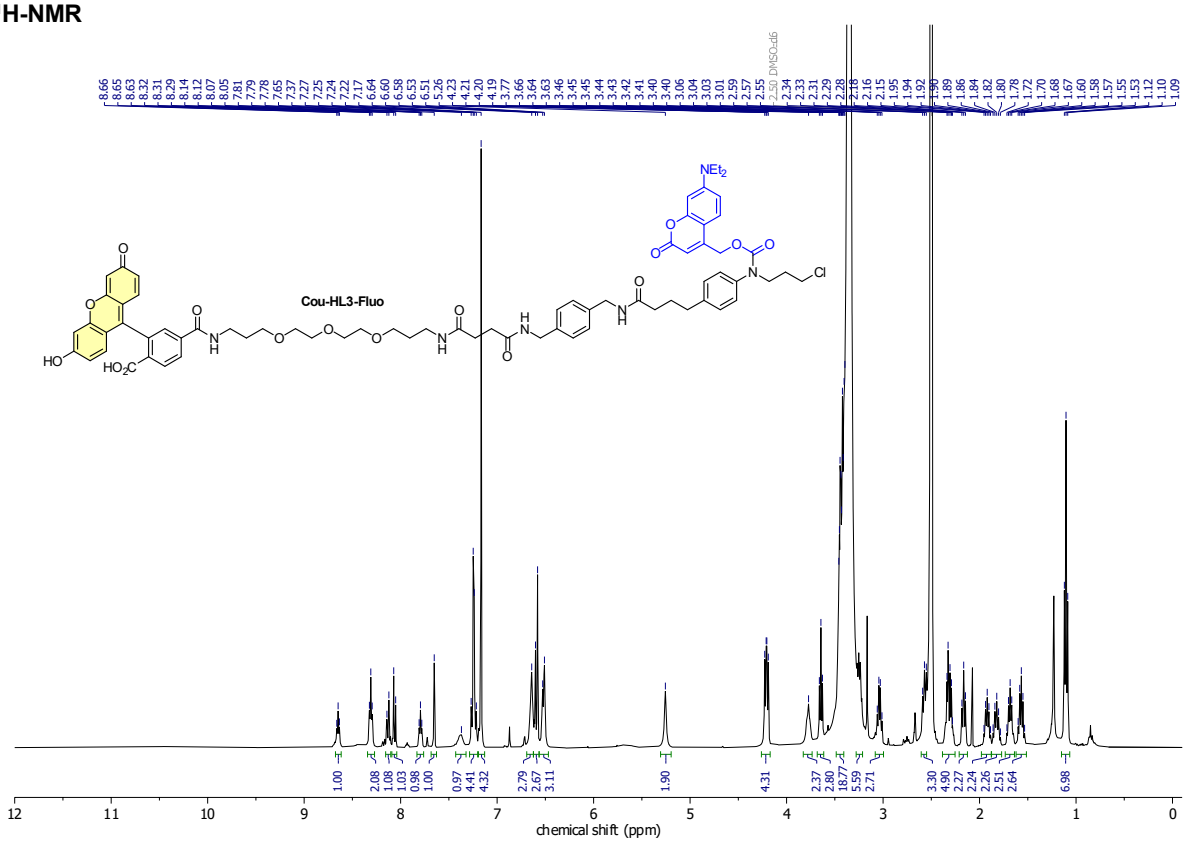

Compound 64

^{1}H-NMR

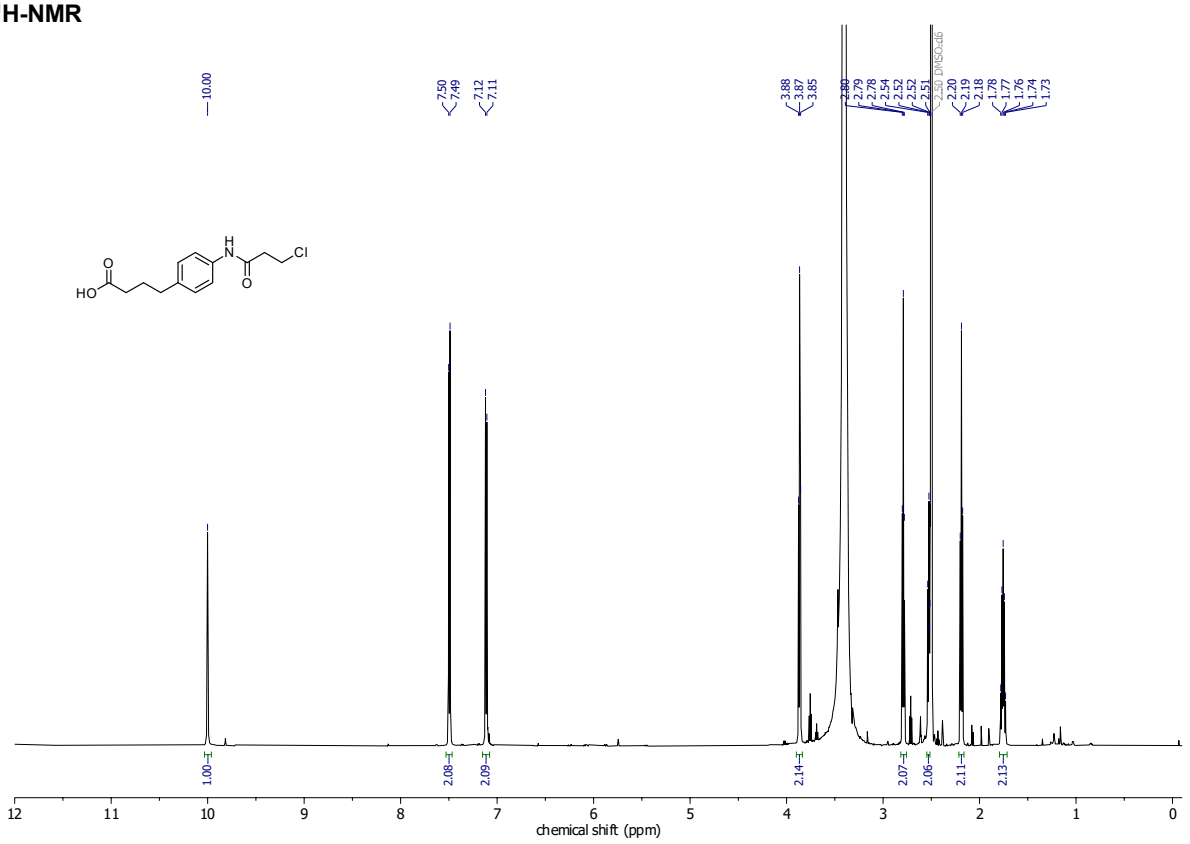

^{13}C-NMR

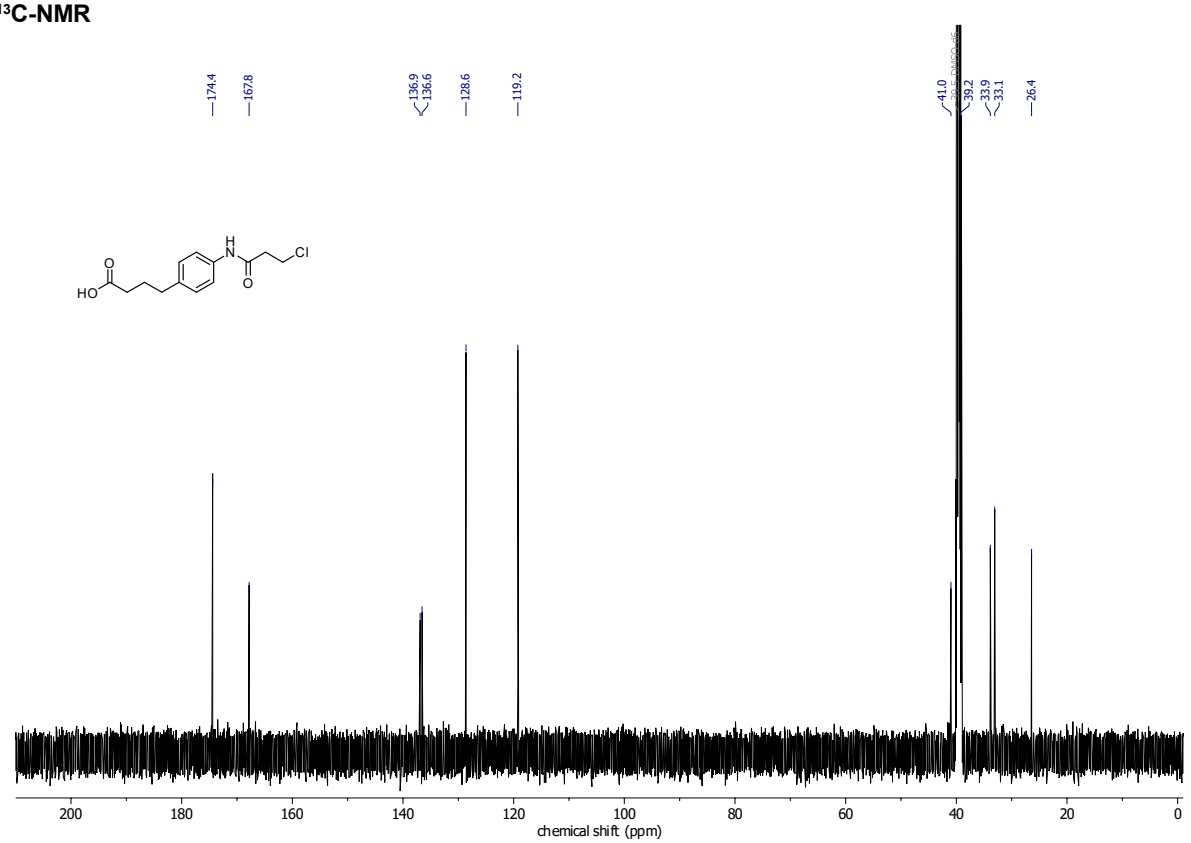

HSQC

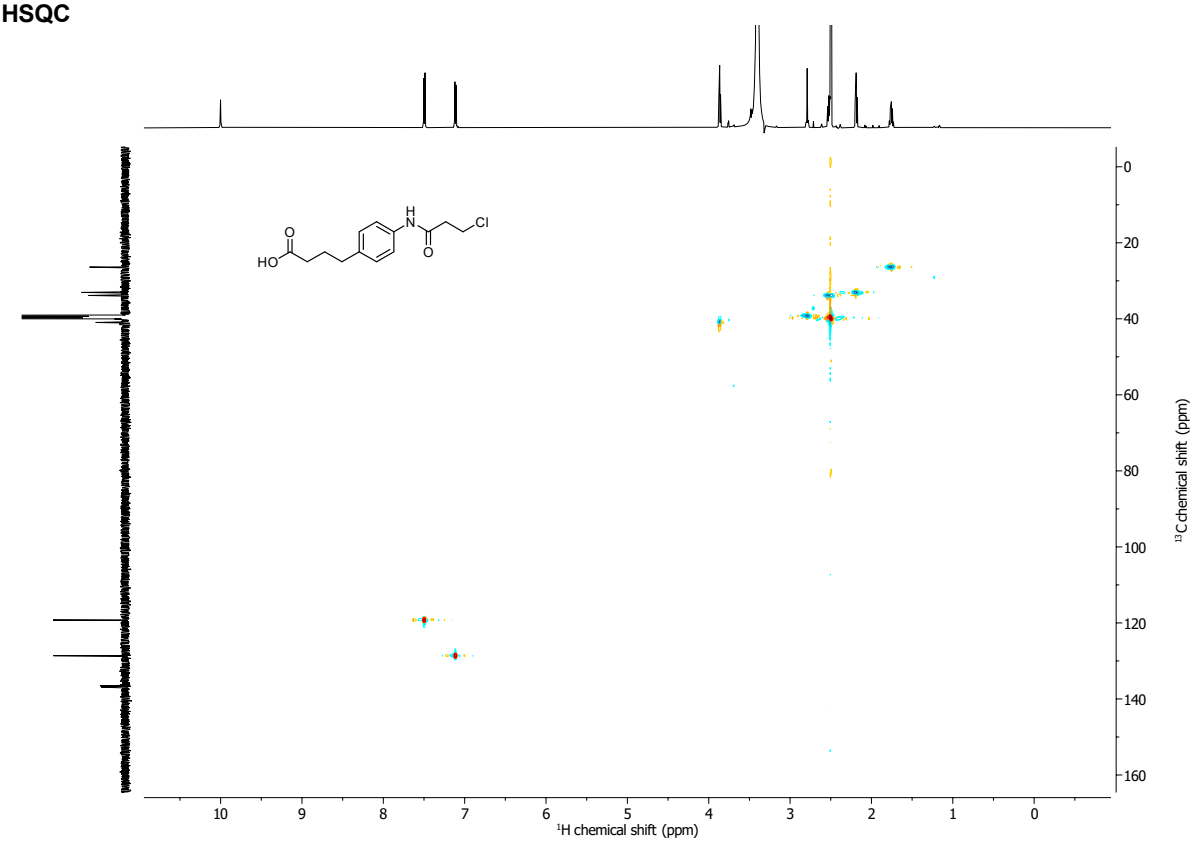
HO
O
H
N
O
Cl
0
20
40
60
80
100
120
140
160
13C chemical shift (ppm)
10
9
8
7
6
5
4
3
2
1
0
1H chemical shift (ppm)

Compound 65

^{1}H-NMR

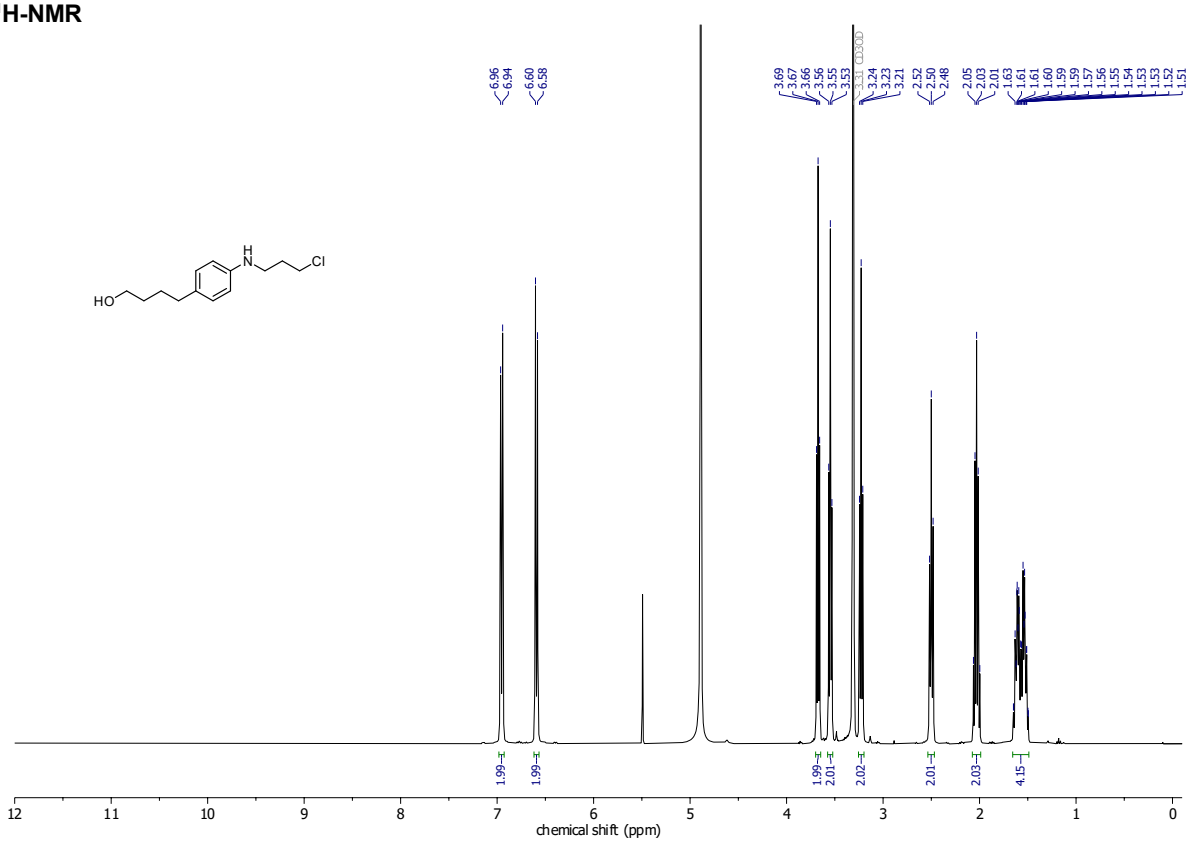

^{13}C-NMR

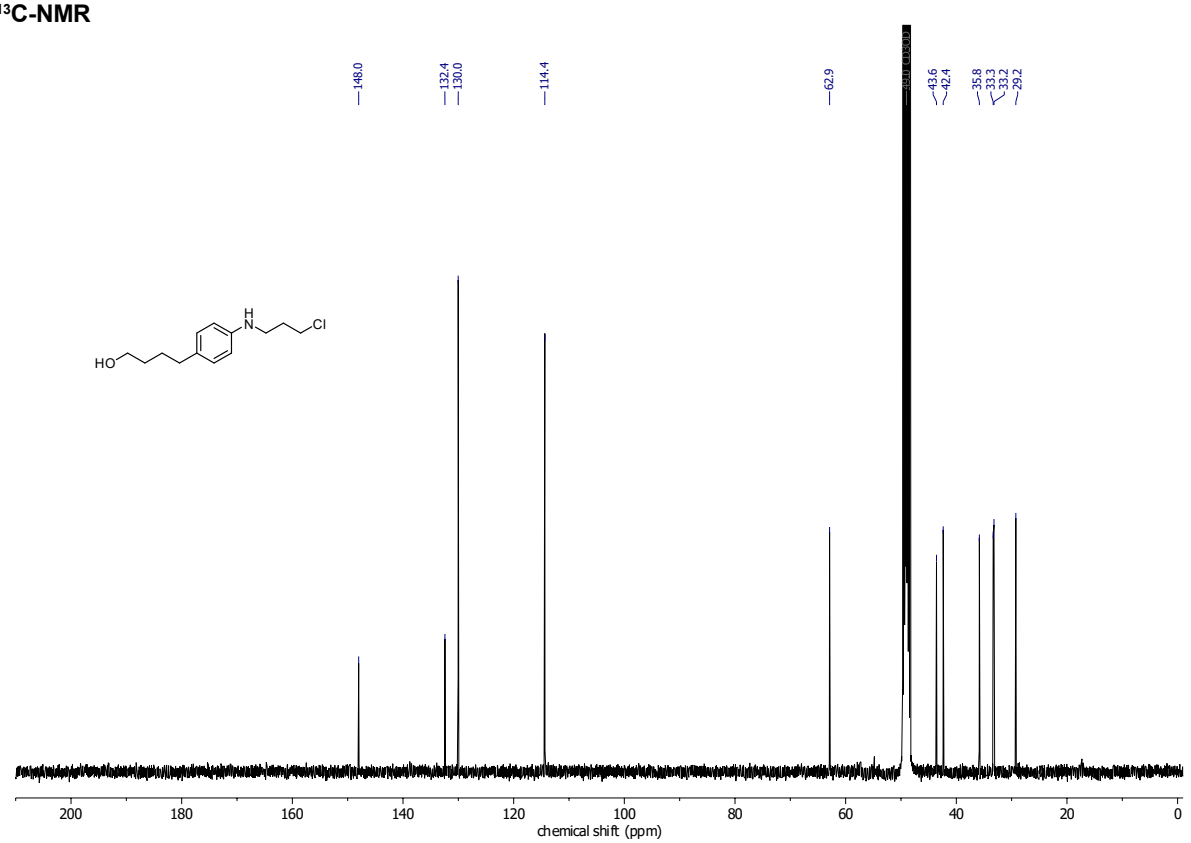

Compound 66

^{1}H-NMR

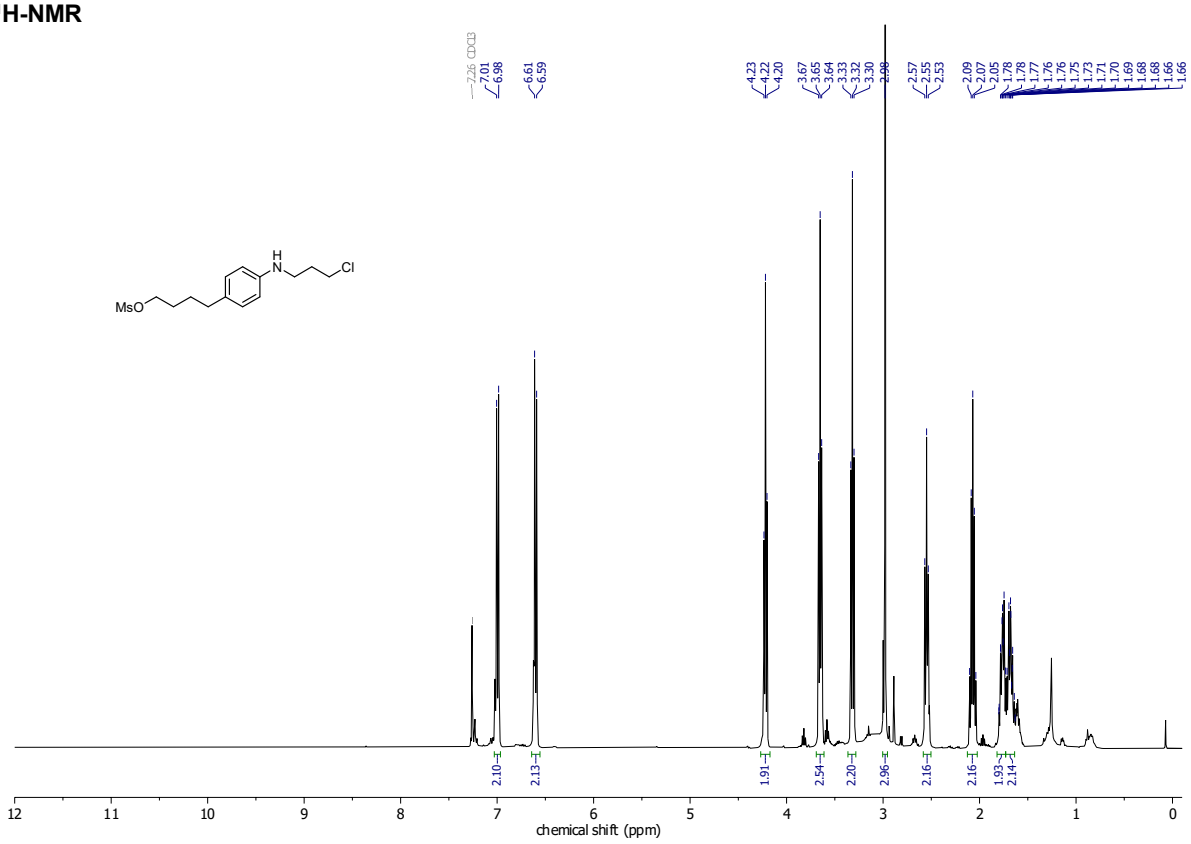

Compound 67

^{1}H-NMR

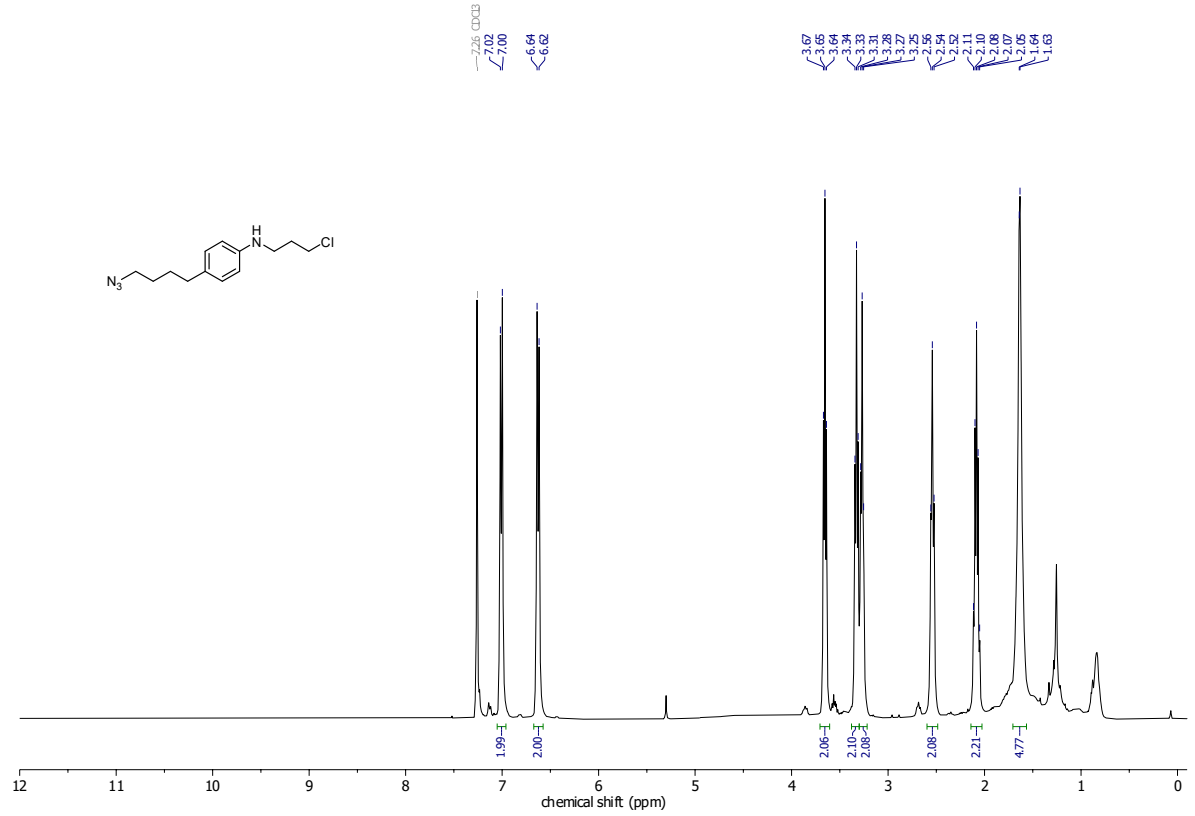

^{13}C-NMR

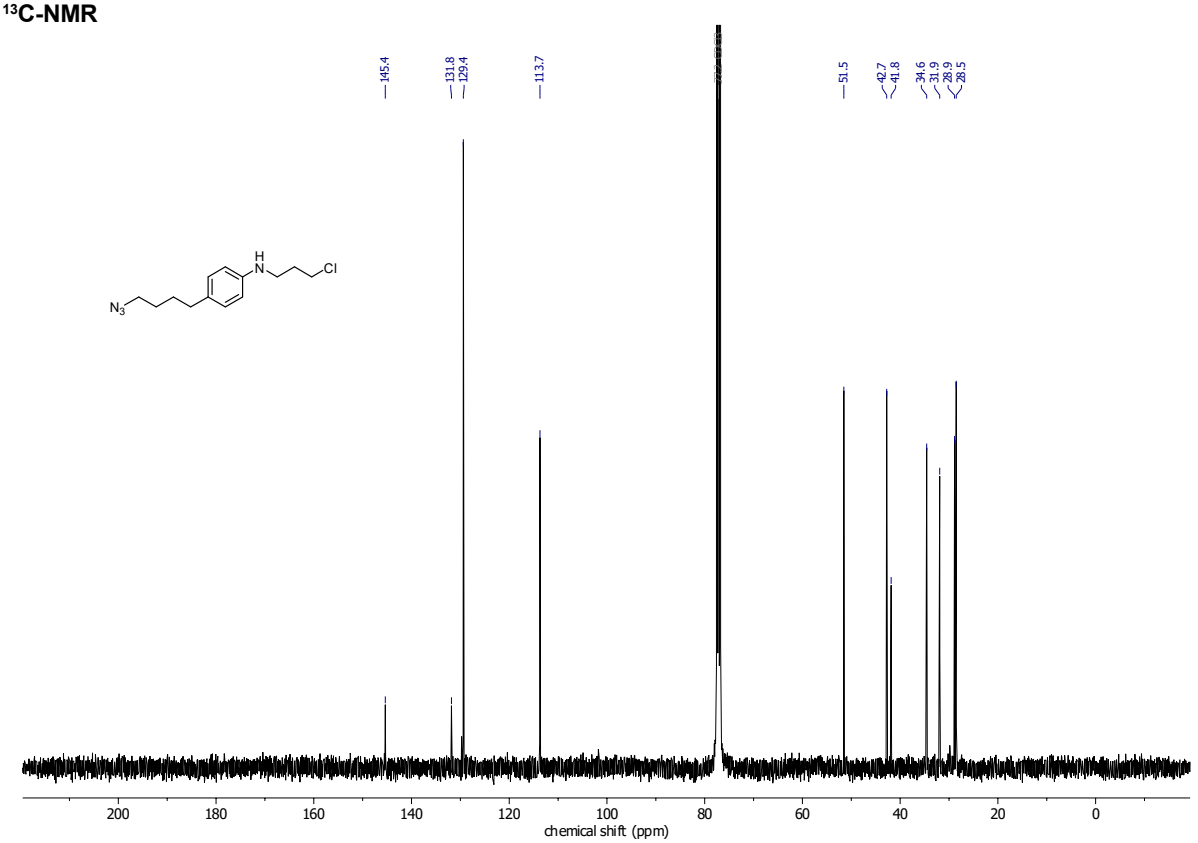

CHalo-Fluo

^{1}H-NMR

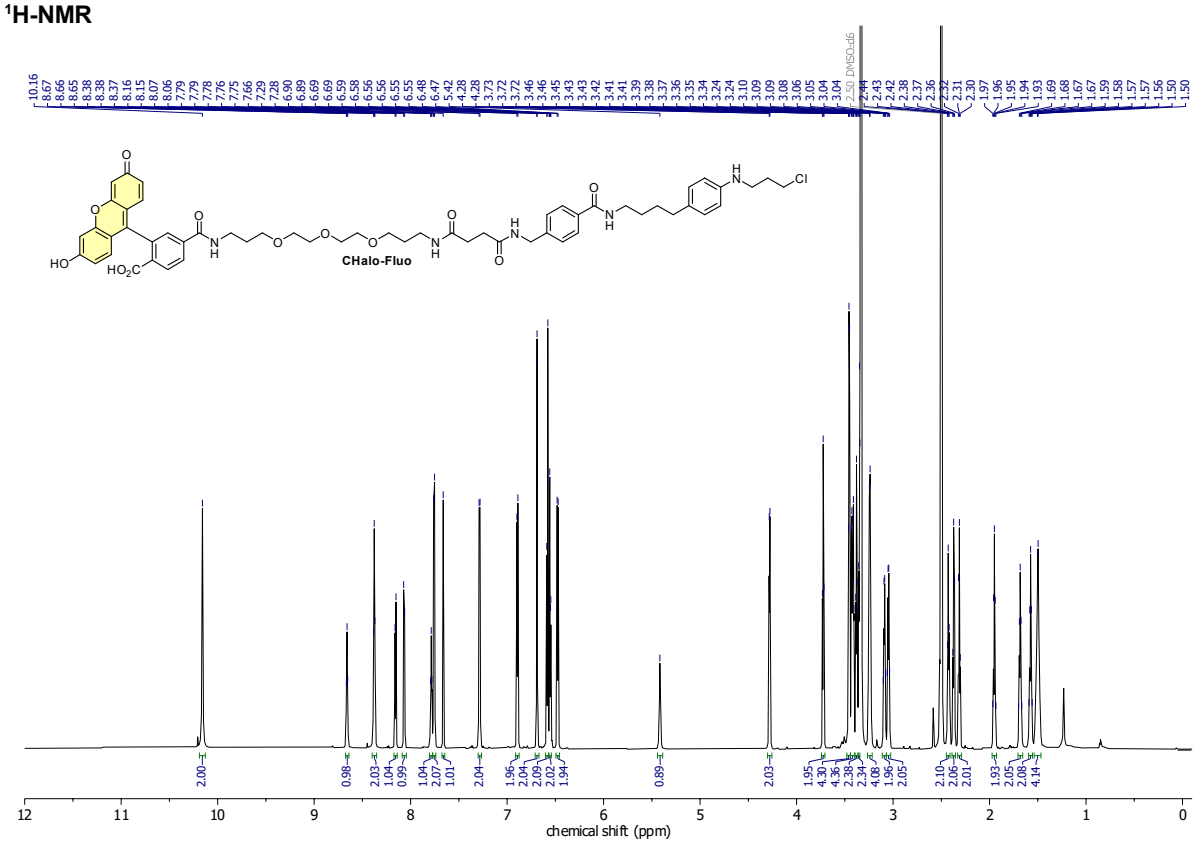

^{13}C-NMR

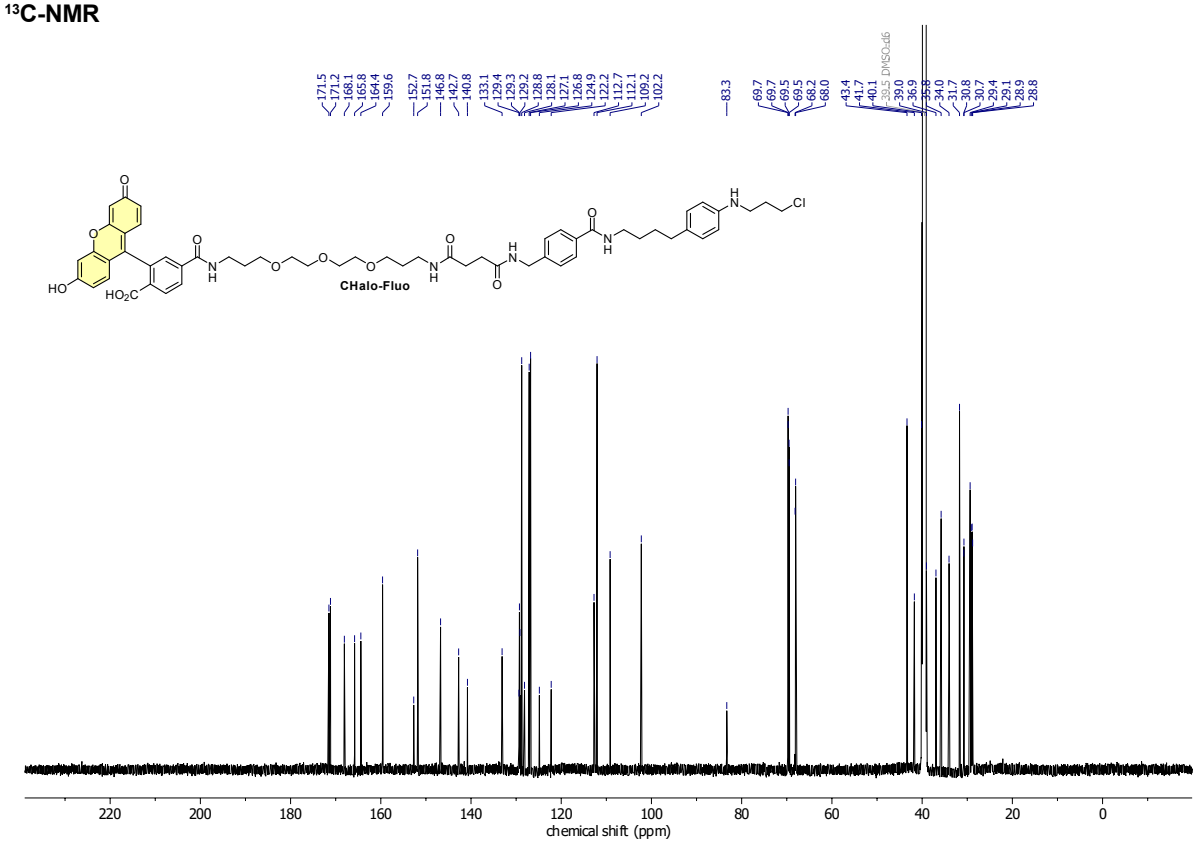

Cou-CHalo-Fluo

^{1}H-NMR

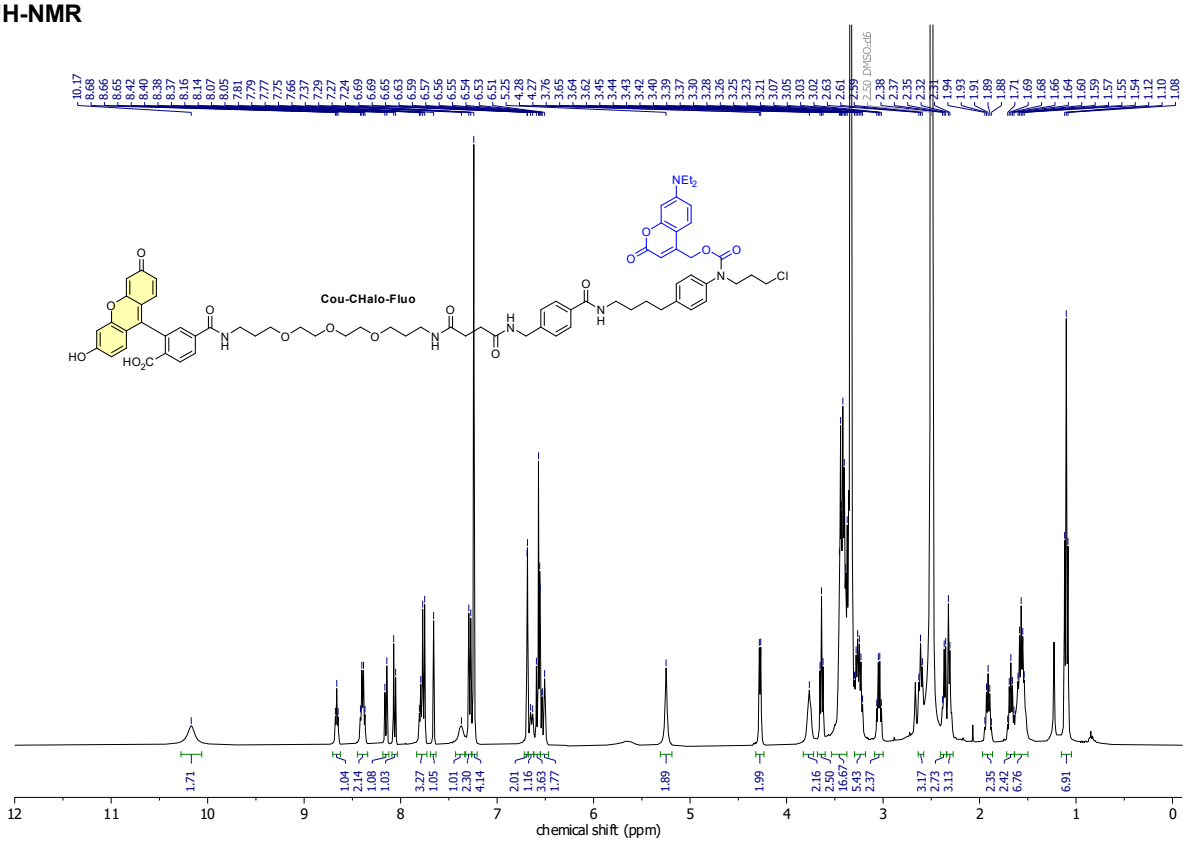

11 List of Abbreviations

A549	human lung carcinoma cell line
ABPP	activity-based protein profiling
BAPTA	calcium binder: 1,2-bis(*ortho*-aminophenoxy)ethane-*N,N,N′,N′*-tetraacetic acid
BC	O^2-benzylcytosine (CLIP-tag ligand)
BG	O^6-benzyl guanine (SNAP-tag ligand)
BODIPY	boron-dipyrromethene (chromophore class)
CA	chloroalkane ligand for HaloTag
calc.	calculated
Caprola	calcium dependent protein labelling system
CID	chemically induced dimerisation
CP	O^4-benzyl-6-chloropyrimidine-2-amine (SNAP-tag ligand)
DART	drug acutely restricted by tethering
DCM	dichloromethane
DIPEA	*N*,*N*-diisopropylethylamine
DMAP	*N*,*N*-dimethylaminopyridine
DMEM	Dulbecco's modified Eagle's medium (cell culture medium)
DMF	*N*,*N*-dimethylformamide
DPP-IV	dipeptidylpeptidase IV
EI	electron ionisation (mass spectrometry)
eq	equivalents
ESI	electrospray ionisation (mass spectrometry)
ESIPT	excited-state intramolecular proton transfer
FP	fluorescent protein
FRET	fluorescence resonance energy transfer
GFP	green fluorescent protein
GGT	γ-glutamyl transferase
HBSS	Hank's balanced salt solution
HEK	human embryonic kidney cell line (we used HEK293t)
HeLa	human cervical cancer cell line (named after Henrietta Lacks)
Hex	*iso*-hexanes (mixture)
hNQO1	human NAD(P)H:quinone oxidoreductase isozyme 1
HOMO	highest occupied molecular orbital
HPLC	high-performance liquid chromatography
HPQ	(2-(2'-hydroxyphenyl)-4(3*H*)-quinazolinone
HRMS	high resolution mass spectrometry
J	Coupling constant in NMR spectroscopy (in Hz)
LAP	leucine aminopeptidase
LC/MS	liquid chromatography mass spectrometry
LG	leaving group
LUMO	lowest unoccupied molecular orbital
LXR	nuclear liver X receptor
MDG	membrane damage green (probe developed in this thesis)
MT	microtubule
NADPH	reduced form of nicotinamide adenine dinucleotide phosphate
NHS	*N*-hydroxy succinimide
NIR	near-infrared
NMR	nuclear magnetic resonance
np	normal phase (chromatography)
NTR	nitroreductase enzyme
PBS	phosphate buffered saline

PeT	photo-induced electron transfer
PG	protecting group
PHOTAC	PHOtochemically TArgeting Chimeras
POI	protein of interest
PORTL	photoswitchable orthogonal remotely tethered ligand
PROTAC	PROteolysis TArgeting Chimeras
r.t.	room temperature
R_f	retardation factor
rp	reversed-phase (chromatography)
SiR	silicon-rhodamine fluorophore
SLP	self-labelling protein
SRM	super-resolution microscopy
TBAF	tetrabutyl ammonium fluoride
TEA	triethylamine
TF	trifluoromethyl fluorobenzyl pyrimidine ligand for SNAP-tag2
THF	tetrahydrofuran
TICT	twisted intramolecular charge transfer
TLC	thin-layer chromatography
TML	trimethyl lock
TMP	trimethoprim
TRP	transient receptor potential
Trx	the mammalian redox protein thioredoxin 1
TrxR	the mammalian selenoenzyme thioredoxin reductase 1
xHTL	exchangeable HaloTag ligand
δ	chemical shift (NMR)

12 Software use

Affinity Designer (version 2.6.3): figure design and assembly.

ChatGPT (GPT-5): spelling checks, translation, text-shortening, and improving thesis readability.

ChemDraw Professional (version 23.1.2.7): chemical structures.

Excel (version 2507, Microsoft Office 365): data analysis.

GraphPad Prism (version 10.4.2): data analysis and graph plotting.

Word (version 2507, Microsoft Office 365): writing the paper manuscripts and this thesis.

13 References

(1) Kapitein, L. C.; Hoogenraad, C. C. Building the Neuronal Microtubule Cytoskeleton. *Neuron* **2015**, *87* (3), 492–506. https://doi.org/10.1016/j.neuron.2015.05.046.

(2) Etienne-Manneville, S. Microtubules in Cell Migration. *Annu. Rev. Cell Dev. Biol.* **2013**, *29*, 471–499. https://doi.org/10.1146/annurev-cellbio-101011-155711.

(3) Burute, M.; Kapitein, L. C. Cellular Logistics: Unraveling the Interplay Between Microtubule Organization and Intracellular Transport. *Annu. Rev. Cell Dev. Biol.* **2019**, *35*, 29–54. https://doi.org/10.1146/annurev-cellbio-100818-125149.

(4) Forth, S.; Kapoor, T. M. The Mechanics of Microtubule Networks in Cell Division. *J. Cell Biol.* **2017**, *216* (6), 1525–1531. https://doi.org/10.1083/jcb.201612064.

(5) Dumontet, C.; Jordan, M. A. Microtubule-Binding Agents: A Dynamic Field of Cancer Therapeutics. *Nat. Rev. Drug Discov.* **2010**, *9* (10), 790–803. https://doi.org/10.1038/nrd3253.

(6) Peterson, J. R.; Mitchison, T. J. Small Molecules, Big Impact: A History of Chemical Inhibitors and the Cytoskeleton. *Chem. Biol.* **2002**, *9* (12), 1275–1285. https://doi.org/10.1016/S1074-5521(02)00284-3.

(7) Borowiak, M.; Nahaboo, W.; Reynders, M.; Nekolla, K.; Jalinot, P.; Hasserodt, J.; Rehberg, M.; Delattre, M.; Zahler, S.; Vollmar, A.; Trauner, D.; Thorn-Seshold, O. Photoswitchable Inhibitors of Microtubule Dynamics Optically Control Mitosis and Cell Death. *Cell* **2015**, *162* (2), 403–411. https://doi.org/10.1016/j.cell.2015.06.049.

(8) Gao, L.; Meiring, J. C. M.; Varady, A.; Ruider, I. E.; Heise, C.; Wranik, M.; Velasco, C. D.; Taylor, J. A.; Terni, B.; Weinert, T.; Standfuss, J.; Cabernard, C. C.; Llobet, A.; Steinmetz, M. O.; Bausch, A. R.; Distel, M.; Thorn-Seshold, J.; Akhmanova, A.; Thorn-Seshold, O. In Vivo Photocontrol of Microtubule Dynamics and Integrity, Migration and Mitosis, by the Potent GFP-Imaging-Compatible Photoswitchable Reagents SBTubA4P and SBTub2M. *J. Am. Chem. Soc.* **2022**, *144* (12), 5614–5628. https://doi.org/10.1021/jacs.2c01020.

(9) Gao, L.; Meiring, J. C. M.; Kraus, Y.; Wranik, M.; Weinert, T.; Pritzl, S. D.; Bingham, R.; Ntouliou, E.; Jansen, K. I.; Olieric, N.; Standfuss, J.; Kapitein, L. C.; Lohmüller, T.; Ahlfeld, J.; Akhmanova, A.; Steinmetz, M. O.; Thorn-Seshold, O. A Robust, GFP-Orthogonal Photoswitchable Inhibitor Scaffold Extends Optical Control over the Microtubule Cytoskeleton. *Cell Chem. Biol.* **2021**, *28* (2), 228-241.e6. https://doi.org/10.1016/j.chembiol.2020.11.007.

(10) Sailer, A.; Meiring, J. C. M.; Heise, C.; Pettersson, L. N.; Akhmanova, A.; Thorn-Seshold, J.; Thorn-Seshold, O. Pyrrole Hemithioindigo Antimitotics with Near-Quantitative Bidirectional Photoswitching That Photocontrol Cellular Microtubule Dynamics with Single-Cell Precision. *Angew. Chem. Int. Ed.* **2021**, *60* (44), 23695–23704. https://doi.org/10.1002/anie.202104794.

(11) Sailer, A.; Ermer, F.; Kraus, Y.; Bingham, R.; Lutter, F. H.; Ahlfeld, J.; Thorn-Seshold, O. Potent Hemithioindigo-Based Antimitotics Photocontrol the Microtubule Cytoskeleton in Cellulo. *Beilstein J. Org. Chem.* **2020**, *16* (1), 125–134. https://doi.org/10.3762/bjoc.16.14.

(12) Sailer, A.; Ermer, F.; Kraus, Y.; Lutter, F. H.; Donau, C.; Bremerich, M.; Ahlfeld, J.; Thorn-Seshold, O. Hemithioindigos for Cellular Photopharmacology: Desymmetrised Molecular Switch Scaffolds Enabling Design Control over the Isomer-Dependency of Potent Antimitotic Bioactivity. *ChemBioChem* **2019**, *20* (10), 1305–1314. https://doi.org/10.1002/cbic.201800752.

(13) Noguchi, M.; Skwarczynski, M.; Prakash, H.; Hirota, S.; Kimura, T.; Hayashi, Y.; Kiso, Y. Development of Novel Water-Soluble Photocleavable Protective Group and Its Application for Design of Photoresponsive Paclitaxel Prodrugs. *Bioorg. Med. Chem.* **2008**, *16* (10), 5389–5397. https://doi.org/10.1016/j.bmc.2008.04.022.

(14) Skwarczynski, M.; Noguchi, M.; Hirota, S.; Sohma, Y.; Kimura, T.; Hayashi, Y.; Kiso, Y. Development of First Photoresponsive Prodrug of Paclitaxel. *Bioorganic & Medicinal Chemistry Letters* **2006**, *16* (17), 4492–4496. https://doi.org/10.1016/j.bmcl.2006.06.030.

(15) Gropeanu, R. A.; Baumann, H.; Ritz, S.; Mailänder, V.; Surrey, T.; Campo, A. del. Phototriggerable 2',7-Caged Paclitaxel. *PLoS One* **2012**, *7* (9), e43657. https://doi.org/10.1371/journal.pone.0043657.

(16) Carling, C.-J.; Olejniczak, J.; Foucault-Collet, A.; Collet, G.; Viger, M. L.; Huu, V. A. N.; Duggan, B. M.; Almutairi, A. Efficient Red Light Photo-Uncaging of Active Molecules in Water upon Assembly into Nanoparticles. *Chem. Sci.* **2016**, *7* (3), 2392–2398. https://doi.org/10.1039/C5SC03717D.

(17) Müller-Deku, A.; Meiring, J. C. M.; Loy, K.; Kraus, Y.; Heise, C.; Bingham, R.; Jansen, K. I.; Qu, X.; Bartolini, F.; Kapitein, L. C.; Akhmanova, A.; Ahlfeld, J.; Trauner, D.; Thorn-Seshold, O. Photoswitchable Paclitaxel-Based Microtubule Stabilisers Allow Optical Control over the Microtubule Cytoskeleton. *Nat. Commun.* **2020**, *11* (1), 4640. https://doi.org/10.1038/s41467-020-18389-6.

(18) Gao, L.; Meiring, J. C. M.; Heise, C.; Rai, A.; Müller-Deku, A.; Akhmanova, A.; Thorn-Seshold, J.; Thorn-Seshold, O. Photoswitchable Epothilone-Based Microtubule Stabilisers Allow GFP-Imaging-Compatible, Optical Control over the Microtubule Cytoskeleton. *Angew. Chem. Int. Ed.* **2022**, *61* (10), e202114614. https://doi.org/10.1002/anie.202114614.

(19) Ojima, I.; Das, M. Recent Advances in the Chemistry and Biology of New Generation Taxoids. *J. Nat. Prod.* **2009**, *72* (3), 554–565. https://doi.org/10.1021/np8006556.

(20) Baker, S. A.; Rutter, J. Metabolites as Signalling Molecules. *Nat. Rev. Mol. Cell. Biol.* **2023**, *24* (5), 355–374. https://doi.org/10.1038/s41580-022-00572-w.

(21) Fletcher, D. A.; Mullins, R. D. Cell Mechanics and the Cytoskeleton. *Nature* **2010**, *463* (7280), 485–492. https://doi.org/10.1038/nature08908.

(22) Bar-Peled, L.; Kory, N. Principles and Functions of Metabolic Compartmentalization. *Nat. Metab.* **2022**, *4* (10), 1232–1244. https://doi.org/10.1038/s42255-022-00645-2.

(23) Payen, A.; Persoz, J. F. Mémoire Sur La Diastase, Les Principaux Produits de Ses Réactions et Leurs Applications Aux Arts Industriels. *Annales de chimie et de physique* **1833**, *2* (53), 73–92.

(24) de Crécy-Lagard, V.; Haas, D.; Hanson, A. D. Newly-Discovered Enzymes That Function in Metabolite Damage-Control. *Curr. Opin. Chem. Biol.* **2018**, *47*, 101–108. https://doi.org/10.1016/j.cbpa.2018.09.014.

(25) Singh, D. Targeting the Unexplored "Dark Proteome": Novel Approaches in Drug Discovery. *Curr. Proteomics* **2025**, *22* (3), 100020. https://doi.org/10.1016/j.curpro.2025.100020.

(26) Niphakis, M. J.; Cravatt, B. F. Enzyme Inhibitor Discovery by Activity-Based Protein Profiling. *Annu. Rev. Biochem.* **2014**, *83* (Volume 83, 2014), 341–377. https://doi.org/10.1146/annurev-biochem-060713-035708.

(27) Giandomenico, S. L.; Schuman, E. M. Genetic Manipulation and Targeted Protein Degradation in Mammalian Systems: Practical Considerations, Tips and Tricks for Discovery Research. *FEBS Open Bio* **2023**, *13* (7), 1164–1176. https://doi.org/10.1002/2211-5463.13581.

(28) Heinrich, L.; Bennett, D.; Ackerman, D.; Park, W.; Bogovic, J.; Eckstein, N.; Petruncio, A.; Clements, J.; Pang, S.; Xu, C. S.; Funke, J.; Korff, W.; Hess, H. F.; Lippincott-Schwartz, J.; Saalfeld, S.; Weigel, A. V. Whole-Cell Organelle Segmentation in Volume Electron Microscopy. *Nature* **2021**, *599* (7883), 141–146. https://doi.org/10.1038/s41586-021-03977-3.

(29) Su, J.; Song, Y.; Zhu, Z.; Huang, X.; Fan, J.; Qiao, J.; Mao, F. Cell–Cell Communication: New Insights and Clinical Implications. *Sig. Transduct. Target. Ther.* **2024**, *9* (1), 196. https://doi.org/10.1038/s41392-024-01888-z.

(30) Fujita, K.; Urano, Y. Activity-Based Fluorescence Diagnostics for Cancer. *Chem. Rev.* **2024**, *124* (7), 4021–4078. https://doi.org/10.1021/acs.chemrev.3c00612.

(31) Chyan, W.; Raines, R. T. Enzyme-Activated Fluorogenic Probes for Live-Cell and in Vivo Imaging. *ACS Chem. Biol.* **2018**, *13* (7), 1810–1823. https://doi.org/10.1021/acschembio.8b00371.

(32) Hananya, N.; Shabat, D. Recent Advances and Challenges in Luminescent Imaging: Bright Outlook for Chemiluminescence of Dioxetanes in Water. *ACS Cent. Sci.* **2019**, *5* (6), 949–959. https://doi.org/10.1021/acscentsci.9b00372.

(33) Tannous, R.; Shelef, O.; Gutkin, S.; David, M.; Leirikh, T.; Ge, L.; Jaber, Q.; Zhou, Q.; Ma, P.; Fridman, M.; Spitz, U.; Houk, K. N.; Shabat, D. Spirostrain-Accelerated Chemiexcitation of Dioxetanes Yields Unprecedented Detection Sensitivity in Chemiluminescence Bioassays. *ACS Cent. Sci.* **2024**, *10* (1), 28–42. https://doi.org/10.1021/acscentsci.3c01141.

(34) Yang, M.; Huang, J.; Fan, J.; Du, J.; Pu, K.; Peng, X. Chemiluminescence for Bioimaging and Therapeutics: Recent Advances and Challenges. *Chem. Soc. Rev.* **2020**, *49* (19), 6800–6815. https://doi.org/10.1039/D0CS00348D.

(35) Liu, J.; Wu, F.; Wang, M.; Tao, M.; Liu, Z.; Hai, Z. Caspase-3-Responsive Fluorescent/Photoacoustic Imaging of Tumor Apoptosis. *Anal. Chem.* **2023**, *95* (25), 9404–9408. https://doi.org/10.1021/acs.analchem.3c01387.

(36) Arrowsmith, C. H.; Audia, J. E.; Austin, C.; Baell, J.; Bennett, J.; Blagg, J.; Bountra, C.; Brennan, P. E.; Brown, P. J.; Bunnage, M. E.; Buser-Doepner, C.; Campbell, R. M.; Carter, A. J.; Cohen, P.; Copeland, R. A.; Cravatt, B.; Dahlin, J. L.; Dhanak, D.; Edwards, A. M.; Frederiksen, M.; Frye, S. V.; Gray, N.; Grimshaw, C. E.; Hepworth, D.; Howe, T.; Huber, K. V. M.; Jin, J.; Knapp, S.; Kotz, J. D.; Kruger, R. G.; Lowe, D.; Mader, M. M.; Marsden, B.; Mueller-Fahrnow, A.; Müller, S.; O'Hagan, R. C.; Overington, J. P.; Owen, D. R.; Rosenberg, S. H.; Ross, R.; Roth, B.; Schapira, M.; Schreiber, S. L.; Shoichet, B.; Sundström, M.; Superti-Furga, G.; Taunton, J.; Toledo-Sherman, L.; Walpole, C.; Walters, M. A.; Willson, T. M.; Workman, P.; Young, R. N.; Zuercher, W. J. The Promise and Peril of Chemical Probes. *Nat. Chem. Biol.* **2015**, *11* (8), 536–541. https://doi.org/10.1038/nchembio.1867.

(37) Hong, C.; Tontonoz, P. Liver X Receptors in Lipid Metabolism: Opportunities for Drug Discovery. *Nat. Rev. Drug Discov.* **2014**, *13* (6), 433–444. https://doi.org/10.1038/nrd4280.

(38) Collins, J. L.; Fivush, A. M.; Watson, M. A.; Galardi, C. M.; Lewis, M. C.; Moore, L. B.; Parks, D. J.; Wilson, J. G.; Tippin, T. K.; Binz, J. G.; Plunket, K. D.; Morgan, D. G.; Beaudet, E. J.; Whitney, K. D.; Kliewer, S. A.; Willson, T. M. Identification of a Nonsteroidal Liver X Receptor Agonist through Parallel Array Synthesis of Tertiary Amines. *J. Med. Chem.* **2002**, *45* (10), 1963–1966. https://doi.org/10.1021/jm0255116.

(39) Ranjitkar, P.; Perera, B. G. K.; Swaney, D. L.; Hari, S. B.; Larson, E. T.; Krishnamurty, R.; Merritt, E. A.; Villén, J.; Maly, D. J. Affinity-Based Probes Based on Type II Kinase Inhibitors. *J. Am. Chem. Soc.* **2012**, *134* (46), 19017–19025. https://doi.org/10.1021/ja306035v.

(40) Wang, L.; Tran, M.; D'Este, E.; Roberti, J.; Koch, B.; Xue, L.; Johnsson, K. A General Strategy to Develop Cell Permeable and Fluorogenic Probes for Multicolour Nanoscopy. *Nat. Chem.* **2019**, 1–8. https://doi.org/10.1038/s41557-019-0371-1.

(41) Chang, C. J. Introduction: Fluorescent Probes in Biology. *Chem. Rev.* **2024**, *124* (21), 11639–11640. https://doi.org/10.1021/acs.chemrev.4c00552.

(42) Minoshima, M.; Reja, S. I.; Hashimoto, R.; Iijima, K.; Kikuchi, K. Hybrid Small-Molecule/Protein Fluorescent Probes. *Chem. Rev.* **2024**, *124* (10), 6198–6270. https://doi.org/10.1021/acs.chemrev.3c00549.

(43) Wang, L.; Frei, M. S.; Salim, A.; Johnsson, K. Small-Molecule Fluorescent Probes for Live-Cell Super-Resolution Microscopy. *J. Am. Chem. Soc.* **2019**, *141* (7), 2770–2781. https://doi.org/10.1021/jacs.8b11134.

(44) Porzberg, N.; Gries, K.; Johnsson, K. Exploiting Covalent Chemical Labeling with Self-Labeling Proteins. *Annu. Rev. Biochem.* **2025**, *94*, 29–58. https://doi.org/10.1146/annurev-biochem-030222-121016.

(45) Frazier, C. C. Photodynamic Therapy in Dermatology. *Int. J. Dermatol.* **1996**, *35* (5), 312–316. https://doi.org/10.1111/j.1365-4362.1996.tb03629.x.

(46) Ash, C.; Dubec, M.; Donne, K.; Bashford, T. Effect of Wavelength and Beam Width on Penetration in Light-Tissue Interaction Using Computational Methods. *Lasers Med. Sci.* **2017**, *32* (8), 1909–1918. https://doi.org/10.1007/s10103-017-2317-4.

(47) Karton-Lifshin, N.; Segal, E.; Omer, L.; Portnoy, M.; Satchi-Fainaro, R.; Shabat, D. A Unique Paradigm for a Turn-ON Near-Infrared Cyanine-Based Probe: Noninvasive Intravital Optical Imaging of Hydrogen Peroxide. *J. Am. Chem. Soc.* **2011**, *133* (28), 10960–10965. https://doi.org/10.1021/ja203145v.

(48) Gatin-Fraudet, B.; Ottenwelter, R.; Le Saux, T.; Norsikian, S.; Pucher, M.; Lombès, T.; Baron, A.; Durand, P.; Doisneau, G.; Bourdreux, Y.; Iorga, B. I.; Erard, M.; Jullien, L.; Guianvarc'h, D.; Urban, D.; Vauzeilles, B. Evaluation of Borinic Acids as New, Fast Hydrogen Peroxide–Responsive Triggers. *Proc. Natl. Acad. Sci. U.S.A.* **2021**, *118* (50), e2107503118. https://doi.org/10.1073/pnas.2107503118.

(49) Zhang, X.-X.; Wu, H.; Li, P.; Qu, Z.-J.; Tan, M.-Q.; Han, K.-L. A Versatile Two-Photon Fluorescent Probe for Ratiometric Imaging E. Coli β-Galactosidase in Live Cells and in Vivo. *Chem. Commun.* **2016**, *52* (53), 8283–8286. https://doi.org/10.1039/C6CC04373A.

(50) Baeyer, A. Ueber Eine Neue Klasse von Farbstoffen. *Berichte der deutschen chemischen Gesellschaft* **1871**, *4* (2), 555–558. https://doi.org/10.1002/cber.18710040209.

(51) Grimm, J. B.; Tkachuk, A. N.; Xie, L.; Choi, H.; Mohar, B.; Falco, N.; Schaefer, K.; Patel, R.; Zheng, Q.; Liu, Z.; Lippincott-Schwartz, J.; Brown, T. A.; Lavis, L. D. A General Method to Optimize and Functionalize Red-Shifted Rhodamine Dyes. *Nat. Methods* **2020**, *17* (8), 815–821. https://doi.org/10.1038/s41592-020-0909-6.

(52) Ye, H.; Sun, L.; Pang, Z.; Ji, X.; Jiao, Y.; Tu, X.; Huang, H.; Tang, X.; Xi, Z.; Yi, L. Cell-Trappable BODIPY-NBD Dyad for Imaging of Basal and Stress-Induced H2S in Live Biosystems. *Anal. Chem.* **2022**, *94* (3), 1733–1741. https://doi.org/10.1021/acs.analchem.1c04324.

(53) Thivierge, C.; Bandichhor, R.; Burgess, K. Spectral Dispersion and Water Solubilization of BODIPY Dyes via Palladium-Catalyzed C−H Functionalization. *Org. Lett.* **2007**, *9* (11), 2135–2138. https://doi.org/10.1021/ol0706197.

(54) Baumgartner, B.; Glembockyte, V.; Mayer, R.; Gonzalez-Hernandez, A.; Kindler, R.; Valavalkar, A.; Wiegand, A.; Müller-Deku, A.; Grubert, L.; Steiner, F.; Gross, C.; Reynders, M.; Grenier, V.; Broichhagen, J.; Hecht, S.; Tinnefeld, P.; Ofial, A.; Dietzek-Ivanšic, B.; Levitz, J.; Thorn-Seshold, O. Azobenzenes Can Achieve Near-Infrared Photocontrol in Biological Systems, with Quantitative Z→E Photoisomerization, via Singlet Manifold Photoredox. ChemRxiv September 14, 2023. https://doi.org/10.26434/chemrxiv-2023-37sv4.

(55) Chen, J.-A.; Pan, H.; Wang, Z.; Gao, J.; Tan, J.; Ouyang, Z.; Guo, W.; Gu, X. Imaging of Ovarian Cancers Using Enzyme Activatable Probes with Second Near-Infrared Window Emission. *Chem. Commun.* **2020**, *56* (18), 2731–2734. https://doi.org/10.1039/C9CC09158K.

(56) Grimm, J. B.; Sung, A. J.; Legant, W. R.; Hulamm, P.; Matlosz, S. M.; Betzig, E.; Lavis, L. D. Carbofluoresceins and Carborhodamines as Scaffolds for High-Contrast Fluorogenic Probes. *ACS Chem. Biol.* **2013**, *8* (6), 1303–1310. https://doi.org/10.1021/cb4000822.

(57) Grimm, J. B.; Brown, T. A.; Tkachuk, A. N.; Lavis, L. D. General Synthetic Method for Si-Fluoresceins and Si-Rhodamines. *ACS Cent. Sci.* **2017**, *3* (9), 975–985. https://doi.org/10.1021/acscentsci.7b00247.

(58) Daly, H. C.; Matikonda, S. S.; Steffens, H. C.; Ruehle, B.; Resch-Genger, U.; Ivanic, J.; Schnermann, M. J. Ketone Incorporation Extends the Emission Properties of the Xanthene Scaffold Beyond 1000 Nm. *Photochemistry and Photobiology* **2022**, *98* (2), 325–333. https://doi.org/10.1111/php.13544.

(59) Chyan, W.; Kilgore, H. R.; Gold, B.; Raines, R. T. Electronic and Steric Optimization of Fluorogenic Probes for Biomolecular Imaging. *J. Org. Chem.* **2017**, *82* (8), 4297–4304. https://doi.org/10.1021/acs.joc.7b00285.

(60) Tachibana, R.; Kamiya, M.; Suzuki, S.; Morokuma, K.; Nanjo, A.; Urano, Y. Molecular Design Strategy of Fluorogenic Probes Based on Quantum Chemical Prediction of Intramolecular Spirocyclization. *Commun. Chem.* **2020**, *3* (1), 82. https://doi.org/10.1038/s42004-020-0326-x.

(61) Hanaoka, K.; Ikeno, T.; Iwaki, S.; Deguchi, S.; Takayama, K.; Mizuguchi, H.; Tao, F.; Kojima, N.; Ohno, H.; Sasaki, E.; Komatsu, T.; Ueno, T.; Maeda, K.; Kusuhara, H.; Urano, Y. A General Fluorescence off/on Strategy for Fluorogenic Probes: Steric Repulsion-Induced Twisted Intramolecular Charge Transfer (Sr-TICT). *Sci. Adv.* **2024**, *10* (7), eadi8847. https://doi.org/10.1126/sciadv.adi8847.

(62) Chen, J.-A.; Pan, H.; Wang, Z.; Gao, J.; Tan, J.; Ouyang, Z.; Guo, W.; Gu, X. Imaging of Ovarian Cancers Using Enzyme Activatable Probes with Second Near-Infrared Window Emission. *Chem. Commun.* **2020**, *56* (18), 2731–2734. https://doi.org/10.1039/C9CC09158K.

(63) Faucher, F. F.; Liu, K. J.; Cosco, E. D.; Widen, J. C.; Sorger, J.; Guerra, M.; Bogyo, M. Protease Activated Probes for Real-Time Ratiometric Imaging of Solid Tumors. *ACS Cent. Sci.* **2023**, *9* (5), 1059–1069. https://doi.org/10.1021/acscentsci.3c00261.

(64) Ogasawara, A.; Kamiya, M.; Sakamoto, K.; Kuriki, Y.; Fujita, K.; Komatsu, T.; Ueno, T.; Hanaoka, K.; Onoyama, H.; Abe, H.; Tsuji, Y.; Fujishiro, M.; Koike, K.; Fukayama, M.; Seto, Y.; Urano, Y. Red Fluorescence Probe Targeted to Dipeptidylpeptidase-IV for Highly Sensitive Detection of Esophageal Cancer. *Bioconjugate Chem.* **2019**, *30* (4), 1055–1060. https://doi.org/10.1021/acs.bioconjchem.9b00198.

(65) Lukinavičius, G.; Umezawa, K.; Olivier, N.; Honigmann, A.; Yang, G.; Plass, T.; Mueller, V.; Reymond, L.; Corrêa Jr, I. R.; Luo, Z.-G.; Schultz, C.; Lemke, E. A.; Heppenstall, P.; Eggeling, C.; Manley, S.; Johnsson, K. A Near-Infrared Fluorophore for Live-Cell Super-Resolution Microscopy of Cellular Proteins. *Nat. Chem.* **2013**, *5* (2), 132–139. https://doi.org/10.1038/nchem.1546.

(66) Urano, Y.; Sakabe, M.; Kosaka, N.; Ogawa, M.; Mitsunaga, M.; Asanuma, D.; Kamiya, M.; Young, M. R.; Nagano, T.; Choyke, P. L.; Kobayashi, H. Rapid Cancer Detection by Topically Spraying a γ-Glutamyltranspeptidase–Activated Fluorescent Probe. *Sci. Transl. Med.* **2011**, *3* (110), 110ra119-110ra119. https://doi.org/10.1126/scitranslmed.3002823.

(67) Sakabe, M.; Asanuma, D.; Kamiya, M.; Iwatate, R. J.; Hanaoka, K.; Terai, T.; Nagano, T.; Urano, Y. Rational Design of Highly Sensitive Fluorescence Probes for Protease and Glycosidase Based on Precisely Controlled Spirocyclization. *J. Am. Chem. Soc.* **2013**, *135* (1), 409–414. https://doi.org/10.1021/ja309688m.

(68) Hanaoka, K.; Iwaki, S.; Yagi, K.; Myochin, T.; Ikeno, T.; Ohno, H.; Sasaki, E.; Komatsu, T.; Ueno, T.; Uchigashima, M.; Mikuni, T.; Tainaka, K.; Tahara, S.; Takeuchi, S.; Tahara, T.; Uchiyama, M.; Nagano, T.; Urano, Y. General Design Strategy to Precisely Control the Emission of Fluorophores via a Twisted Intramolecular Charge Transfer (TICT) Process. *J. Am. Chem. Soc.* **2022**. https://doi.org/10.1021/jacs.2c06397.

(69) Urano, Y.; Kamiya, M.; Kanda, K.; Ueno, T.; Hirose, K.; Nagano, T. Evolution of Fluorescein as a Platform for Finely Tunable Fluorescence Probes. *J. Am. Chem. Soc.* **2005**, *127* (13), 4888–4894. https://doi.org/10.1021/ja043919h.

(70) Carter, K. P.; Young, A. M.; Palmer, A. E. Fluorescent Sensors for Measuring Metal Ions in Living Systems. *Chem. Rev.* **2014**, *114* (8), 4564–4601. https://doi.org/10.1021/cr400546e.

(71) Obara, R.; Kamiya, M.; Tanaka, Y.; Abe, A.; Kojima, R.; Kawaguchi, T.; Sugawara, M.; Takahashi, A.; Noda, T.; Urano, Y. γ-Glutamyltranspeptidase (GGT)-Activatable Fluorescence Probe for Durable Tumor Imaging. *Angew. Chem. Int. Ed.* **2021**, *133* (4), 2153–2157. https://doi.org/10.1002/ange.202013265.

(72) Zhou, Z.; Wang, F.; Yang, G.; Lu, C.; Nie, J.; Chen, Z.; Ren, J.; Sun, Q.; Zhao, C.; Zhu, W.-H. A Ratiometric Fluorescent Probe for Monitoring Leucine Aminopeptidase in Living Cells and Zebrafish Model. *Anal. Chem.* **2017**, *89* (21), 11576–11582. https://doi.org/10.1021/acs.analchem.7b02910.

(73) Kitagawa, Y.; Tanaka, S.; Kamiya, M.; Kuriki, Y.; Yamamoto, K.; Shimizu, T.; Nejo, T.; Hana, T.; Matsuura, R.; Koike, T.; Yamazawa, E.; Kushihara, Y.; Takahashi, S.; Nomura, M.; Takami, H.; Takayanagi, S.; Mukasa, A.; Urano, Y.; Saito, N. A Novel Topical Fluorescent Probe for Detection of Glioblastoma. *Clin. Cancer Res.* **2021**, *27* (14), 3936–3947. https://doi.org/10.1158/1078-0432.CCR-20-4518.

(74) Kuriki, Y.; Yoshioka, T.; Kamiya, M.; Komatsu, T.; Takamaru, H.; Fujita, K.; Iwaki, H.; Nanjo, A.; Akagi, Y.; Takeshita, K.; Hino, H.; Hino, R.; Kojima, R.; Ueno, T.; Hanaoka, K.; Abe, S.; Saito, Y.; Nakajima, J.; Urano, Y. Development of a Fluorescent Probe Library Enabling Efficient Screening of Tumour-Imaging Probes Based on Discovery of Biomarker Enzymatic Activities. *Chem. Sci.* **2022**, *13* (16), 4474–4481. https://doi.org/10.1039/D1SC06889J.

(75) Matsuzaki, H.; Kamiya, M.; Iwatate, R. J.; Asanuma, D.; Watanabe, T.; Urano, Y. Novel Hexosaminidase-Targeting Fluorescence Probe for Visualizing Human Colorectal Cancer. *Bioconjugate Chem.* **2016**, *27* (4), 973–981. https://doi.org/10.1021/acs.bioconjchem.6b00037.

(76) Fujita, K.; Kamiya, M.; Yoshioka, T.; Ogasawara, A.; Hino, R.; Kojima, R.; Ueo, H.; Urano, Y. Rapid and Accurate Visualization of Breast Tumors with a Fluorescent Probe Targeting α-Mannosidase 2C1. *ACS Cent. Sci.* **2020**, *6* (12), 2217–2227. https://doi.org/10.1021/acscentsci.0c01189.

(77) Ito, H.; Kawamata, Y.; Kamiya, M.; Tsuda-Sakurai, K.; Tanaka, S.; Ueno, T.; Komatsu, T.; Hanaoka, K.; Okabe, S.; Miura, M.; Urano, Y. Red-Shifted Fluorogenic Substrate for Detection of lacZ-Positive Cells in Living Tissue with Single-Cell Resolution. *Angew. Chem. Int. Ed.* **2018**, *57* (48), 15702–15706. https://doi.org/10.1002/anie.201808670.

(78) Zhang, X.; Chen, X.; Liu, K.; Zhang, Y.; Gao, G.; Huang, X.; Hou, S. Near-Infrared Ratiometric Probe with a Self-Immolative Spacer for Rapid and Sensitive Detection of Alkaline Phosphatase Activity and Imaging *in Vivo*. *Analytica Chimica Acta* **2020**, *1094*, 113–121. https://doi.org/10.1016/j.aca.2019.10.001.

(79) Coleman, J. E. Structure and Mechanism of Alkaline Phosphatase. *Annu. Rev. Biophys.* **1992**, *21*, 441–483. https://doi.org/10.1146/annurev.bb.21.060192.002301.

(80) Tian, L.; Yang, Y.; Wysocki, L. M.; Arnold, A. C.; Hu, A.; Ravichandran, B.; Sternson, S. M.; Looger, L. L.; Lavis, L. D. Selective Esterase–Ester Pair for Targeting Small Molecules with Cellular Specificity. *Proc. Natl. Acad. Sci. U.S.A.* **2012**, *109* (13), 4756–4761. https://doi.org/10.1073/pnas.1111943109.

(81) Tallman, K. R.; Levine, S. R.; Beatty, K. E. Profiling Esterases in Mycobacterium Tuberculosis Using Far-Red Fluorogenic Substrates. *ACS Chem. Biol.* **2016**, *11* (7), 1810–1815. https://doi.org/10.1021/acschembio.6b00233.

(82) Dirak, M.; Chan, J.; Kolemen, S. Optical Imaging Probes for Selective Detection of Butyrylcholinesterase. *J. Mater. Chem. B* **2024**, *12* (5), 1149–1167. https://doi.org/10.1039/D3TB02468G.

(83) Ross, D.; Kepa, J. K.; Winski, S. L.; Beall, H. D.; Anwar, A.; Siegel, D. NAD(P)H:Quinone Oxidoreductase 1 (NQO1): Chemoprotection, Bioactivation, Gene Regulation and Genetic Polymorphisms. *Chem. Biol. Interact.* **2000**, *129* (1), 77–97. https://doi.org/10.1016/S0009-2797(00)00199-X.

(84) Silvers, W. C.; Prasai, B.; Burk, D. H.; Brown, M. L.; McCarley, R. L. Profluorogenic Reductase Substrate for Rapid, Selective, and Sensitive Visualization and Detection of Human Cancer Cells That Overexpress NQO1. *J. Am. Chem. Soc.* **2013**, *135* (1), 309–314. https://doi.org/10.1021/ja309346f.

(85) Zeisel, L.; Weissenhorn, L. D.; Scholzen, K. C.; Madabeni, A.; Orian, L.; Arnér, E. S. J.; Thorn-Seshold, O. Bicyclic Selenenyl Sulfides with Tuned Bioreductive Step Rates Reveal Constraints for Probes Targeting Thioredoxin Reductase. *Angew. Chem. Int. Ed.* **2025**, *64* (35), e202508911. https://doi.org/10.1002/anie.202508911.

(86) Zeisel, L.; Felber, J. G.; Scholzen, K. C.; Poczka, L.; Cheff, D.; Maier, M. S.; Cheng, Q.; Shen, M.; Hall, M. D.; Arnér, E. S. J.; Thorn-Seshold, J.; Thorn-Seshold, O. Selective Cellular Probes for Mammalian Thioredoxin Reductase TrxR1: Rational Design of RX1, a Modular 1,2-Thiaselenane Redox Probe. *Chem* **2022**, *8* (5), 1493–1517. https://doi.org/10.1016/j.chempr.2022.03.010.

(87) Zeisel, L.; Felber, J. G.; Scholzen, K. C.; Schmitt, C.; Wiegand, A. J.; Komissarov, L.; Arnér, E. S. J.; Thorn-Seshold, O. Piperazine-Fused Cyclic Disulfides Unlock High-Performance Bioreductive Probes of Thioredoxins and Bifunctional Reagents for Thiol Redox Biology. *J. Am. Chem. Soc.* **2024**, *146* (8), 5204–5214. https://doi.org/10.1021/jacs.3c11153.

(88) Felber, J. G.; Zeisel, L.; Poczka, L.; Scholzen, K.; Busker, S.; Maier, M. S.; Theisen, U.; Brandstädter, C.; Becker, K.; Arnér, E. S. J.; Thorn-Seshold, J.; Thorn-Seshold, O. Selective, Modular Probes for Thioredoxins Enabled by Rational Tuning of a Unique Disulfide Structure Motif. *J. Am. Chem. Soc.* **2021**, *143* (23), 8791–8803. https://doi.org/10.1021/jacs.1c03234.

(89) Wang, S.; Tan, W.; Lang, W.; Qian, H.; Guo, S.; Zhu, L.; Ge, J. Fluorogenic and Mitochondria-Localizable Probe Enables Selective Labeling and Imaging of Nitroreductase. *Anal. Chem.* **2022**, *94* (20), 7272–7277. https://doi.org/10.1021/acs.analchem.2c00512.

(90) Jin, C.; Zhang, Q.; Lu, W. Selective Turn-on near-Infrared Fluorescence Probe for Hypoxic Tumor Cell Imaging. *RSC Advances* **2017**, *7* (30), 18217–18223. https://doi.org/10.1039/C7RA01466J.

(91) Sies, H.; Belousov, V. V.; Chandel, N. S.; Davies, M. J.; Jones, D. P.; Mann, G. E.; Murphy, M. P.; Yamamoto, M.; Winterbourn, C. Defining Roles of Specific Reactive Oxygen Species (ROS) in Cell Biology and Physiology. *Nat. Rev. Mol. Cell Bio.* **2022**, *23* (7), 499–515. https://doi.org/10.1038/s41580-022-00456-z.

(92) Lin, M. T.; Beal, M. F. Mitochondrial Dysfunction and Oxidative Stress in Neurodegenerative Diseases. *Nature* **2006**, *443* (7113), 787–795. https://doi.org/10.1038/nature05292.

(93) Forman, H. J.; Zhang, H. Targeting Oxidative Stress in Disease: Promise and Limitations of Antioxidant Therapy. *Nat. Rev. Drug Discov.* **2021**, *20* (9), 689–709. https://doi.org/10.1038/s41573-021-00233-1.

(94) Cheung, E. C.; Vousden, K. H. The Role of ROS in Tumour Development and Progression. *Nat. Rev. Cancer* **2022**, *22* (5), 280–297. https://doi.org/10.1038/s41568-021-00435-0.

(95) Messina, M. S.; Quargnali, G.; Chang, C. J. Activity-Based Sensing for Chemistry-Enabled Biology: Illuminating Principles, Probes, and Prospects for Boronate Reagents for Studying Hydrogen Peroxide. *ACS Bio & Med Chem Au* **2022**, *2* (6), 548–564. https://doi.org/10.1021/acsbiomedchemau.2c00052.

(96) Kolluru, G. K.; Shen, X.; Bir, S. C.; Kevil, C. G. Hydrogen Sulfide Chemical Biology: Pathophysiological Roles and Detection. *Nitric Oxide* **2013**, *35*, 5–20. https://doi.org/10.1016/j.niox.2013.07.002.

(97) Xuan, W.; Sheng, C.; Cao, Y.; He, W.; Wang, W. Fluorescent Probes for the Detection of Hydrogen Sulfide in Biological Systems. *Angew. Chem. Int. Ed.* **2012**, *51* (10), 2282–2284. https://doi.org/10.1002/anie.201107025.

(98) Fosnacht, K. G.; Hammers, M. D.; Earp, M. S.; Gilbert, A. K.; Pluth, M. D. A Cell Trappable Methyl Rhodol-Based Fluorescent Probe for Hydrogen Sulfide Detection. *Chem. Asian J.* **2022**, *17* (16), e202200426. https://doi.org/10.1002/asia.202200426.

(99) Wu, Q.; Zhou, Q.-H.; Li, W.; Ren, T.-B.; Zhang, X.-B.; Yuan, L. Evolving an Ultra-Sensitive Near-Infrared β-Galactosidase Fluorescent Probe for Breast Cancer Imaging and Surgical Resection Navigation. *ACS Sens.* **2022**, *7* (12), 3829–3837. https://doi.org/10.1021/acssensors.2c01752.

(100) G. Gavriel, A.; R. Sambrook, M.; T. Russell, A.; Hayes, W. Recent Advances in Self-Immolative Linkers and Their Applications in Polymeric Reporting Systems. *Polym. Chem.* **2022**, *13* (22), 3188–3269. https://doi.org/10.1039/D2PY00414C.

(101) Papot, S.; Tranoy, I.; Tillequin, F.; Florent, J.-C.; Gesson, J.-P. Design of Selectively Activated Anticancer Prodrugs: Elimination and Cyclization Strategies. *Curr. Med. Chem. Anticancer Agents* **2002**, *2* (2), 155–185. https://doi.org/10.2174/1568011023354173.

(102) Thorn-Seshold, O.; Vargas-Sanchez, M.; McKeon, S.; Hasserodt, J. A Robust, High-Sensitivity Stealth Probe for Peptidases. *Chem. Commun.* **2012**, *48* (50), 6253–6255. https://doi.org/10.1039/C2CC32227G.

(103) Alouane, A.; Labruère, R.; Le Saux, T.; Schmidt, F.; Jullien, L. Self-Immolative Spacers: Kinetic Aspects, Structure–Property Relationships, and Applications. *Angew. Chem. Int. Ed.* **2015**, *54* (26), 7492–7509. https://doi.org/10.1002/anie.201500088.

(104) Komatsu, T.; Kikuchi, K.; Takakusa, H.; Hanaoka, K.; Ueno, T.; Kamiya, M.; Urano, Y.; Nagano, T. Design and Synthesis of an Enzyme Activity-Based Labeling Molecule with Fluorescence Spectral Change. *J. Am. Chem. Soc.* **2006**, *128* (50), 15946–15947. https://doi.org/10.1021/ja0657307.

(105) Beesley, R. M.; Ingold, C. K.; Thorpe, J. F. CXIX.—The Formation and Stability of Spiro-Compounds. Part I. Spiro-Compounds from Cyclohexane. *J. Chem. Soc., Trans.* **1915**, *107* (0), 1080–1106. https://doi.org/10.1039/CT9150701080.

(106) Greenwald, R. B.; Choe, Y. H.; Conover, C. D.; Shum, K.; Wu, D.; Royzen, M. Drug Delivery Systems Based on Trimethyl Lock Lactonization: Poly(Ethylene Glycol) Prodrugs of Amino-Containing Compounds. *J. Med. Chem.* **2000**, *43* (3), 475–487. https://doi.org/10.1021/jm990498j.

(107) King, M. M.; Cohen, L. A. Stereopopulation Control. VII. Rate Enhancement in the Lactonization of 3-(o-Hydroxyphenyl)Propionic Acids: Dependence on the Size of Aromatic Ring Substituents. *J. Am. Chem. Soc.* **1983**, *105* (9), 2752–2760. https://doi.org/10.1021/ja00347a040.

(108) -Takbhate, B. P. A Narrative Review on Confocal Laser Scanning Microscopy: Principle, Applications, Advancements and Challenges. *JCDR* **2024**, *18* (11). https://doi.org/10.7860/JCDR/2024/73869.20245.

(109) Picot, J.; Guerin, C. L.; Le Van Kim, C.; Boulanger, C. M. Flow Cytometry: Retrospective, Fundamentals and Recent Instrumentation. *Cytotechnology* **2012**, *64* (2), 109–130. https://doi.org/10.1007/s10616-011-9415-0.

(110) Croce, A. C.; Bottiroli, G. Autofluorescence Spectroscopy and Imaging: A Tool for Biomedical Research and Diagnosis. *Eur. J. Histochem.* **2014**, *58* (4). https://doi.org/10.4081/ejh.2014.2461.

(111) Bretscher, M. S.; Raff, M. C. Mammalian Plasma Membranes. *Nature* **1975**, *258* (5530), 43–49. https://doi.org/10.1038/258043a0.

(112) Yang, N. J.; Hinner, M. J. Getting Across the Cell Membrane: An Overview for Small Molecules, Peptides, and Proteins. *Methods Mol. Biol.* **2015**, *1266*, 29–53. https://doi.org/10.1007/978-1-4939-2272-7_3.

(113) Yang, N. J.; Hinner, M. J. Getting Across the Cell Membrane: An Overview for Small Molecules, Peptides, and Proteins. *Methods Mol. Biol.* **2015**, *1266*, 29–53. https://doi.org/10.1007/978-1-4939-2272-7_3.

(114) Rosser, B. G.; Powers, S. P.; Gores, G. J. Calpain Activity Increases in Hepatocytes Following Addition of ATP. Demonstration by a Novel Fluorescent Approach. *J. Biol. Chem.* **1993**, *268* (31), 23593–23600. https://doi.org/10.1016/S0021-9258(19)49504-5.

(115) Sun, H.; Johnson, D. R.; Finch, R. A.; Sartorelli, A. C.; Miller, D. W.; Elmquist, W. F. Transport of Fluorescein in MDCKII-MRP1 Transfected Cells and Mrp1-Knockout Mice. *Biochem. Biophys. Res. Commun.* **2001**, *284* (4), 863–869. https://doi.org/10.1006/bbrc.2001.5062.

(116) Bresler, S. E.; Bresler, V. M.; Kazbekov, E. N.; Nikiforov, A. A.; Vasilieva, N. N. On the Active Transport of Organic Acids (Fluorescein) in the Choroid Plexus of the Rabbit. *Biochim. Biophys. Acta, Biomembr.* **1979**, *550* (1), 110–119. https://doi.org/10.1016/0005-2736(79)90119-6.

(117) Fukuda, T.; Yokomizo, S.; Casa, S.; Monaco, H.; Manganiello, S.; Wang, H.; Lv, X.; Ulumben, A. D.; Yang, C.; Kang, M.-W.; Inoue, K.; Fukushi, M.; Sumi, T.; Wang, C.; Kang, H.; Bao, K.; Henary, M.; Kashiwagi, S.; Soo Choi, H. Fast and Durable Intraoperative Near-Infrared Imaging of Ovarian Cancer Using Ultrabright Squaraine Fluorophores. *Angew. Chem. Int. Ed.* **2022**, *61* (17), e202117330. https://doi.org/10.1002/anie.202117330.

(118) Jia, S.; Lin, E. Y.; Mobley, E. B.; Lim, I.; Guo, L.; Kallepu, S.; Low, P. S.; Sletten, E. M. Water-Soluble Chromenylium Dyes for Shortwave Infrared Imaging in Mice. *Chem* **2023**, *9* (12), 3648–3665. https://doi.org/10.1016/j.chempr.2023.08.021.

(119) Izumi, S.; Urano, Y.; Hanaoka, K.; Terai, T.; Nagano, T. A Simple and Effective Strategy To Increase the Sensitivity of Fluorescence Probes in Living Cells. *J. Am. Chem. Soc.* **2009**, *131* (29), 10189–10200. https://doi.org/10.1021/ja902511p.

(120) Turnbull, J. L.; Benlian, B. R.; Golden, R. P.; Miller, E. W. Phosphonofluoresceins: Synthesis, Spectroscopy, and Applications. *J. Am. Chem. Soc.* **2021**, *143* (16), 6194–6201. https://doi.org/10.1021/jacs.1c01139.

(121) Caldwell, S. T.; O'Byrne, S. N.; Wilson, C.; Cvetko, F.; Murphy, M. P.; McCarron, J. G.; Hartley, R. C. Photoactivated Release of Membrane Impermeant Sulfonates inside Cells. *Chem. Commun.* **2021**, *57* (32), 3917–3920. https://doi.org/10.1039/D0CC07713E.

(122) Rusha, L.; Miller, S. C. Design and Application of Esterase-Labile Sulfonate Protecting Groups. *Chem. Commun.* **2011**, *47* (7), 2038–2040. https://doi.org/10.1039/C0CC04796A.

(123) Li, X.; Higashikubo, R.; Taylor, J.-S. Use of Multiple Carboxylates to Increase Intracellular Retention of Fluorescent Probes Following Release From Cell Penetrating Fluorogenic Conjugates. *Bioconjugate Chem.* **2008**, *19* (1), 50–56. https://doi.org/10.1021/bc070079y.

(124) Dickinson, B. C.; Peltier, J.; Stone, D.; Schaffer, D. V.; Chang, C. J. Nox2 Redox Signaling Maintains Essential Cell Populations in the Brain. *Nat. Chem. Biol.* **2011**, *7* (2), 106–112. https://doi.org/10.1038/nchembio.497.

(125) Jiang, G.; Lou, X.-F.; Zuo, S.; Liu, X.; Ren, T.-B.; Wang, L.; Zhang, X.-B.; Yuan, L. Tuning the Cellular Uptake and Retention of Rhodamine Dyes by Molecular Engineering for High-Contrast Imaging of Cancer Cells. *Angew. Chem. Int. Ed.* **2023**, e202218613. https://doi.org/10.1002/anie.202218613.

(126) Huang, Z.; Terpetschnig, E.; You, W.; Haugland, R. P. 2-(2′-Phosphoryloxyphenyl)-4(3*H*)-Quinazolinone Derivatives as Fluorogenic Precipitating Substrates of Phosphatases. *Anal. Biochem.* **1992**, *207* (1), 32–39. https://doi.org/10.1016/0003-2697(92)90495-S.

(127) Liu, H.-W.; Li, K.; Hu, X.-X.; Zhu, L.; Rong, Q.; Liu, Y.; Zhang, X.-B.; Hasserodt, J.; Qu, F.-L.; Tan, W. In Situ Localization of Enzyme Activity in Live Cells by a Molecular Probe Releasing a Precipitating Fluorochrome. *Angew. Chem. Int. Ed.* **2017**, *56* (39), 11788–11792. https://doi.org/10.1002/anie.201705747.

(128) Liu, Y.; Xu, C.; Liu, H.-W.; Teng, L.; Huan, S.; Yuan, L.; Zhang, X.-B. Precipitated Fluorophore-Based Molecular Probe for In Situ Imaging of Aminopeptidase N in Living Cells and Tumors. *Anal. Chem.* **2021**, *93* (16), 6463–6471. https://doi.org/10.1021/acs.analchem.1c00280.

(129) Mulay, S. R.; Desai, J.; Kumar, S. V.; Eberhard, J. N.; Thomasova, D.; Romoli, S.; Grigorescu, M.; Kulkarni, O. P.; Popper, B.; Vielhauer, V.; Zuchtriegel, G.; Reichel, C.; Bräsen, J. H.; Romagnani, P.; Bilyy, R.; Munoz, L. E.; Herrmann, M.; Liapis, H.; Krautwald, S.; Linkermann, A.; Anders, H.-J. Cytotoxicity of Crystals Involves RIPK3-MLKL-Mediated Necroptosis. *Nat. Commun.* **2016**, *7* (1), 10274. https://doi.org/10.1038/ncomms10274.

(130) Doura, T.; Kamiya, M.; Obata, F.; Yamaguchi, Y.; Hiyama, T. Y.; Matsuda, T.; Fukamizu, A.; Noda, M.; Miura, M.; Urano, Y. Detection of LacZ-Positive Cells in Living Tissue with Single-Cell Resolution. *Angew. Chem. Int. Ed.* **2016**, *55* (33), 9620–9624. https://doi.org/10.1002/anie.201603328.

(131) Iwashita, H.; Castillo, E.; Messina, M. S.; Swanson, R. A.; Chang, C. J. A Tandem Activity-Based Sensing and Labeling Strategy Enables Imaging of Transcellular Hydrogen Peroxide Signaling. *Proc. Natl. Acad. Sci. U.S.A.* **2021**, *118* (9), e2018513118. https://doi.org/10.1073/pnas.2018513118.

(132) Kashima, H.; Kamiya, M.; Obata, F.; Kojima, R.; Nakano, S.; Miura, M.; Urano, Y. Photoactivatable Fluorophores for Durable Labelling of Individual Cells. *Chem. Commun.* **2021**, *57* (47), 5802–5805. https://doi.org/10.1039/D1CC01488A.

(133) Friese, M. A.; Schattling, B.; Fugger, L. Mechanisms of Neurodegeneration and Axonal Dysfunction in Multiple Sclerosis. *Nat. Rev. Neurol.* **2014**, *10* (4), 225–238. https://doi.org/10.1038/nrneurol.2014.37.

(134) Cheng, H.-C.; Ulane, C. M.; Burke, R. E. Clinical Progression in Parkinson Disease and the Neurobiology of Axons. *Ann. Neurol.* **2010**, *67* (6), 715–725. https://doi.org/10.1002/ana.21995.

(135) Witte, M. E.; Schumacher, A.-M.; Mahler, C. F.; Bewersdorf, J. P.; Lehmitz, J.; Scheiter, A.; Sánchez, P.; Williams, P. R.; Griesbeck, O.; Naumann, R.; Misgeld, T.; Kerschensteiner, M. Calcium Influx through Plasma-Membrane Nanoruptures Drives Axon Degeneration in a Model of Multiple Sclerosis. *Neuron* **2019**, *101* (4), 615-624.e5. https://doi.org/10.1016/j.neuron.2018.12.023.

(136) Williams, P. R.; Marincu, B.-N.; Sorbara, C. D.; Mahler, C. F.; Schumacher, A.-M.; Griesbeck, O.; Kerschensteiner, M.; Misgeld, T. A Recoverable State of Axon Injury Persists for Hours after Spinal Cord Contusion in Vivo. *Nat. Commun.* **2014**, *5* (1), 5683. https://doi.org/10.1038/ncomms6683.

(137) Köster, S.; van Pee, K.; Hudel, M.; Leustik, M.; Rhinow, D.; Kühlbrandt, W.; Chakraborty, T.; Yildiz, Ö. Crystal Structure of Listeriolysin O Reveals Molecular Details of Oligomerization and Pore Formation. *Nat. Commun.* **2014**, *5* (1), 3690. https://doi.org/10.1038/ncomms4690.

(138) Turpin, C.; Catan, A.; Guerin-Dubourg, A.; Debussche, X.; Bravo, S. B.; Álvarez, E.; Elsen, J. V. D.; Meilhac, O.; Rondeau, P.; Bourdon, E. Enhanced Oxidative Stress and Damage in Glycated Erythrocytes. *PLoS One* **2020**, *15* (7), e0235335. https://doi.org/10.1371/journal.pone.0235335.

(139) Mohandas, N.; An, X. Malaria and Human Red Blood Cells. *Med Microbiol Immunol* **2012**, *201* (4), 593–598. https://doi.org/10.1007/s00430-012-0272-z.

(140) Raymond, M. H.; Davidson, A. J.; Shen, Y.; Tudor, D. R.; Lucas, C. D.; Morioka, S.; Perry, J. S. A.; Krapivkina, J.; Perrais, D.; Schumacher, L. J.; Campbell, R. E.; Wood, W.; Ravichandran, K. S. Live Cell Tracking of Macrophage Efferocytosis during Drosophila Embryo Development in Vivo. *Science* **2022**, *375* (6585), 1182–1187. https://doi.org/10.1126/science.abl4430.

(141) Suzuki, T.; Fujikura, K.; Higashiyama, T.; Takata, K. DNA Staining for Fluorescence and Laser Confocal Microscopy. *J. Histochem. Cytochem.* **1997**, *45* (1), 49–53. https://doi.org/10.1177/002215549704500107.

(142) Strober, W. Trypan Blue Exclusion Test of Cell Viability. *Curr. Protoc. Immunol.* **1997**, *21* (1), A.3B.1-A.3B.2. https://doi.org/10.1002/0471142735.ima03bs21.

(143) Biebricher, A. S.; Heller, I.; Roijmans, R. F. H.; Hoekstra, T. P.; Peterman, E. J. G.; Wuite, G. J. L. The Impact of DNA Intercalators on DNA and DNA-Processing Enzymes Elucidated through Force-Dependent Binding Kinetics. *Nat Commun* **2015**, *6* (1), 7304. https://doi.org/10.1038/ncomms8304.

(144) Snaidero, N.; Möbius, W.; Czopka, T.; Hekking, L. H. P.; Mathisen, C.; Verkleij, D.; Goebbels, S.; Edgar, J.; Merkler, D.; Lyons, D. A.; Nave, K.-A.; Simons, M. Myelin Membrane Wrapping of CNS Axons by PI(3,4,5)P3-Dependent Polarized Growth at the Inner Tongue. *Cell* **2014**, *156* (1), 277–290. https://doi.org/10.1016/j.cell.2013.11.044.

(145) Beharry, A. A.; Woolley, G. A. Azobenzene Photoswitches for Biomolecules. *Chem. Soc. Rev.* **2011**, *40* (8), 4422–4437. https://doi.org/10.1039/C1CS15023E.

(146) Jia, S.; Sletten, E. M. Spatiotemporal Control of Biology: Synthetic Photochemistry Toolbox with Far-Red and Near-Infrared Light. *ACS Chem. Biol.* **2022**, *17* (12), 3255–3269. https://doi.org/10.1021/acschembio.1c00518.

(147) Kowalik, L.; Chen, J. K. Illuminating Developmental Biology through Photochemistry. *Nat Chem Biol* **2017**, *13* (6), 587–598. https://doi.org/10.1038/nchembio.2369.

(148) Murale, D. P.; Hong, S. C.; Haque, Md. M.; Lee, J.-S. Photo-Affinity Labeling (PAL) in Chemical Proteomics: A Handy Tool to Investigate Protein-Protein Interactions (PPIs). *Proteome Sci.* **2017**, *15* (1), 14. https://doi.org/10.1186/s12953-017-0123-3.

(149) Alvarez-Lorenzo, C.; Bromberg, L.; Concheiro, A. Light-Sensitive Intelligent Drug Delivery Systems. *Photochemistry and Photobiology* **2009**, *85* (4), 848–860. https://doi.org/10.1111/j.1751-1097.2008.00530.x.

(150) Hüll, K.; Morstein, J.; Trauner, D. In Vivo Photopharmacology. *Chem. Rev.* **2018**, *118* (21), 10710–10747. https://doi.org/10.1021/acs.chemrev.8b00037.

(151) Thorn-Seshold, O. Photoswitchable Cytotoxins. In *Molecular Photoswitches*; John Wiley & Sons, Ltd, 2022; pp 873–919. https://doi.org/10.1002/9783527827626.ch36.

(152) Velema, W. A.; Szymanski, W.; Feringa, B. L. Photopharmacology: Beyond Proof of Principle. *J. Am. Chem. Soc.* **2014**, *136* (6), 2178–2191. https://doi.org/10.1021/ja413063e.

(153) Zhang, F.; Wang, L.-P.; Brauner, M.; Liewald, J. F.; Kay, K.; Watzke, N.; Wood, P. G.; Bamberg, E.; Nagel, G.; Gottschalk, A.; Deisseroth, K. Multimodal Fast Optical Interrogation of Neural Circuitry. *Nature* **2007**, *446* (7136), 633–639. https://doi.org/10.1038/nature05744.

(154) Weinstain, R.; Slanina, T.; Kand, D.; Klán, P. Visible-to-NIR-Light Activated Release: From Small Molecules to Nanomaterials. *Chem. Rev.* **2020**, *120* (24), 13135–13272. https://doi.org/10.1021/acs.chemrev.0c00663.

(155) Klán, P.; Šolomek, T.; Bochet, C. G.; Blanc, A.; Givens, R.; Rubina, M.; Popik, V.; Kostikov, A.; Wirz, J. Photoremovable Protecting Groups in Chemistry and Biology: Reaction Mechanisms and Efficacy. *Chem. Rev.* **2013**, *113* (1), 119–191. https://doi.org/10.1021/cr300177k.
(156) Barltrop, J. A.; Plant, P. J.; Schofield, P. Photosensitive Protective Groups. *Chem. Commun. (London)* **1966**, No. 22, 822–823. https://doi.org/10.1039/C19660000822.
(157) Il'ichev, Y. V.; Wirz, J. Rearrangements of 2-Nitrobenzyl Compounds. 1. Potential Energy Surface of 2-Nitrotoluene and Its Isomers Explored with Ab Initio and Density Functional Theory Methods. *J. Phys. Chem. A* **2000**, *104* (33), 7856–7870. https://doi.org/10.1021/jp000261v.
(158) Pease, A. C.; Solas, D.; Sullivan, E. J.; Cronin, M. T.; Holmes, C. P.; Fodor, S. P. Light-Generated Oligonucleotide Arrays for Rapid DNA Sequence Analysis. *Proc. Natl. Acad. Sci. U.S.A.* **1994**, *91* (11), 5022–5026. https://doi.org/10.1073/pnas.91.11.5022.
(159) Corrie, J. E. T.; Barth, A.; Munasinghe, V. R. N.; Trentham, D. R.; Hutter, M. C. Photolytic Cleavage of 1-(2-Nitrophenyl)Ethyl Ethers Involves Two Parallel Pathways and Product Release Is Rate-Limited by Decomposition of a Common Hemiacetal Intermediate. *J. Am. Chem. Soc.* **2003**, *125* (28), 8546–8554. https://doi.org/10.1021/ja034354c.
(160) Josa-Culleré, L.; Llebaria, A. In the Search for Photocages Cleavable with Visible Light: An Overview of Recent Advances and Chemical Strategies. *ChemPhotoChem* **2021**, *5* (4), 296–314. https://doi.org/10.1002/cptc.202000253.
(161) Schade, B.; Hagen, V.; Schmidt, R.; Herbrich, R.; Krause, E.; Eckardt, T.; Bendig, J. Deactivation Behavior and Excited-State Properties of (Coumarin-4-Yl)Methyl Derivatives. 1. Photocleavage of (7-Methoxycoumarin-4-Yl)Methyl-Caged Acids with Fluorescence Enhancement. *J. Org. Chem.* **1999**, *64* (25), 9109–9117. https://doi.org/10.1021/jo9910233.
(162) Schulte, A. M.; Alachouzos, G.; Szymanski, W.; Feringa, B. L. The Fate of the Contact Ion Pair Determines the Photochemistry of Coumarin-Based Photocleavable Protecting Groups. *Chem. Sci.* **2024**. https://doi.org/10.1039/D3SC05725A.
(163) Eckardt, T.; Hagen, V.; Schade, B.; Schmidt, R.; Schweitzer, C.; Bendig, J. Deactivation Behavior and Excited-State Properties of (Coumarin-4-Yl)Methyl Derivatives. 2. Photocleavage of Selected (Coumarin-4-Yl)Methyl-Caged Adenosine Cyclic 3',5'-Monophosphates with Fluorescence Enhancement. *J. Org. Chem.* **2002**, *67* (3), 703–710. https://doi.org/10.1021/jo010692p.
(164) Fournier, L.; Aujard, I.; Le Saux, T.; Maurin, S.; Beaupierre, S.; Baudin, J.-B.; Jullien, L. Coumarinylmethyl Caging Groups with Redshifted Absorption. *Chem. Eur. J.* **2013**, *19* (51), 17494–17507. https://doi.org/10.1002/chem.201302630.
(165) Egyed, A.; Németh, K.; Molnár, T. Á.; Kállay, M.; Kele, P.; Bojtár, M. Turning Red without Feeling Embarrassed─Xanthenium-Based Photocages for Red-Light-Activated Phototherapeutics. *J. Am. Chem. Soc.* **2023**. https://doi.org/10.1021/jacs.2c11499.
(166) Peterson, J. A.; Wijesooriya, C.; Gehrmann, E. J.; Mahoney, K. M.; Goswami, P. P.; Albright, T. R.; Syed, A.; Dutton, A. S.; Smith, E. A.; Winter, A. H. Family of BODIPY Photocages Cleaved by Single Photons of Visible/Near-Infrared Light. *J. Am. Chem. Soc.* **2018**, *140* (23), 7343–7346. https://doi.org/10.1021/jacs.8b04040.
(167) Rubinstein, N.; Liu, P.; Miller, E. W.; Weinstain, R. Meso-Methylhydroxy BODIPY: A Scaffold for Photo-Labile Protecting Groups. *Chem. Commun.* **2015**, *51* (29), 6369–6372. https://doi.org/10.1039/C5CC00550G.
(168) Goswami, P. P.; Syed, A.; Beck, C. L.; Albright, T. R.; Mahoney, K. M.; Unash, R.; Smith, E. A.; Winter, A. H. BODIPY-Derived Photoremovable Protecting Groups Unmasked with Green Light. *J. Am. Chem. Soc.* **2015**, *137* (11), 3783–3786. https://doi.org/10.1021/jacs.5b01297.
(169) Russo, M.; Janeková, H.; Meier, D.; Generali, M.; Štacko, P. Light in a Heartbeat: Bond Scission by a Single Photon above 800 Nm. *J. Am. Chem. Soc.* **2024**, *146* (12), 8417–8424. https://doi.org/10.1021/jacs.3c14197.
(170) Gorka, A. P.; Yamamoto, T.; Zhu, J.; Schnermann, M. J. Cyanine Photocages Enable Spatial Control of Inducible Cre-Mediated Recombination. *ChemBioChem* **2018**, *19* (12), 1239–1243. https://doi.org/10.1002/cbic.201800061.
(171) Yan, X.; Zhao, J.-H.; Wang, Q.; Wang, W.; Ding, Y.; Zhou, Y.; Chen, G.; Du, J.; Huang, W.; Chu, L. Silicon Rhodamine-Catalyzed Near-Infrared Light-Induced Photodecaging of Ortho-Nitrobenzyl Groups In Vitro and In Vivo. *J. Am. Chem. Soc.* **2025**, *147* (24), 20957–20966. https://doi.org/10.1021/jacs.5c04942.
(172) Takahashi, H.; Kamiya, M.; Kawatani, M.; Umezawa, K.; Ukita, Y.; Niwa, S.; Oda, T.; Urano, Y. Neural and Behavioral Control in Caenorhabditis Elegans by a Yellow-Light–Activatable Caged Compound. *Proc. Natl. Acad. Sci. U.S.A.* **2021**, *118* (6), e2009634118. https://doi.org/10.1073/pnas.2009634118.
(173) Sitkowska, K.; Hoes, M. F.; Lerch, M. M.; Lameijer, L. N.; Meer, P. van der; Szymański, W.; Feringa, B. L. Red-Light-Sensitive BODIPY Photoprotecting Groups for Amines and Their Biological Application in Controlling Heart Rhythm. *Chem. Commun.* **2020**, *56* (41), 5480–5483. https://doi.org/10.1039/D0CC02178D.
(174) Elamri, I.; Heumüller, M.; Herzig, L.-M.; Stirnal, E.; Wachtveitl, J.; Schuman, E. M.; Schwalbe, H. A New Photocaged Puromycin for an Efficient Labeling of Newly Translated Proteins in Living Neurons. *ChemBioChem* **2018**, *19* (23), 2458–2464. https://doi.org/10.1002/cbic.201800408.
(175) Klöcker, N.; Weissenboeck, F. P.; van Dülmen, M.; Špaček, P.; Hüwel, S.; Rentmeister, A. Photocaged 5′ Cap Analogues for Optical Control of mRNA Translation in Cells. *Nat. Chem.* **2022**, *14* (8), 905–913. https://doi.org/10.1038/s41557-022-00972-7.
(176) Štacko, P.; Muchová, L.; Vítek, L.; Klán, P. Visible to NIR Light Photoactivation of Hydrogen Sulfide for Biological Targeting. *Org. Lett.* **2018**, *20* (16), 4907–4911. https://doi.org/10.1021/acs.orglett.8b02043.
(177) Palao, E.; Slanina, T.; Muchová, L.; Šolomek, T.; Vítek, L.; Klán, P. Transition-Metal-Free CO-Releasing BODIPY Derivatives Activatable by Visible to NIR Light as Promising Bioactive Molecules. *J. Am. Chem. Soc.* **2016**, *138* (1), 126–133. https://doi.org/10.1021/jacs.5b10800.
(178) Butkevich, A. N.; Weber, M.; Cereceda Delgado, A. R.; Ostersehlt, L. M.; D'Este, E.; Hell, S. W. Photoactivatable Fluorescent Dyes with Hydrophilic Caging Groups and Their Use in Multicolor Nanoscopy. *J. Am. Chem. Soc.* **2021**, *143* (44), 18388–18393. https://doi.org/10.1021/jacs.1c09999.
(179) Gautier, A.; Deiters, A.; Chin, J. W. Light-Activated Kinases Enable Temporal Dissection of Signaling Networks in Living Cells. *J. Am. Chem. Soc.* **2011**, *133* (7), 2124–2127. https://doi.org/10.1021/ja1109979.
(180) Olson, J. P.; Banghart, M. R.; Sabatini, B. L.; Ellis-Davies, G. C. R. Spectral Evolution of a Photochemical Protecting Group for Orthogonal Two-Color Uncaging with Visible Light. *J. Am. Chem. Soc.* **2013**, *135* (42), 15948–15954. https://doi.org/10.1021/ja408225k.
(181) Nägele, T.; Hoche, R.; Zinth, W.; Wachtveitl, J. Femtosecond Photoisomerization of *Cis*-Azobenzene. *Chem. Phys. Lett.* **1997**, *272* (5), 489–495. https://doi.org/10.1016/S0009-2614(97)00531-9.
(182) Kobauri, P.; Dekker, F. J.; Szymanski, W.; Feringa, B. L. Rational Design in Photopharmacology with Molecular Photoswitches. *Angew. Chem. Int. Ed.* **2023**, *62* (30), e202300681. https://doi.org/10.1002/anie.202300681.
(183) Hartley, G. S. The Cis-Form of Azobenzene. *Nature* **1937**, *140* (3537), 281–281. https://doi.org/10.1038/140281a0.
(184) Fliegl, H.; Köhn, A.; Hättig, C.; Ahlrichs, R. Ab Initio Calculation of the Vibrational and Electronic Spectra of Trans- and Cis-Azobenzene. *J. Am. Chem. Soc.* **2003**, *125* (32), 9821–9827. https://doi.org/10.1021/ja034433o.
(185) Fuchter, M. J. On the Promise of Photopharmacology Using Photoswitches: A Medicinal Chemist's Perspective. *J. Med. Chem.* **2020**, *63* (20), 11436–11447. https://doi.org/10.1021/acs.jmedchem.0c00629.
(186) Hüll, K.; Morstein, J.; Trauner, D. In Vivo Photopharmacology. *Chem. Rev.* **2018**, *118* (21), 10710–10747. https://doi.org/10.1021/acs.chemrev.8b00037.
(187) Banghart, M.; Borges, K.; Isacoff, E.; Trauner, D.; Kramer, R. H. Light-Activated Ion Channels for Remote Control of Neuronal Firing. *Nat. Neurosci.* **2004**, *7* (12), 1381–1386. https://doi.org/10.1038/nn1356.
(188) Laprell, L.; Hüll, K.; Stawski, P.; Schön, C.; Michalakis, S.; Biel, M.; Sumser, M. P.; Trauner, D. Restoring Light Sensitivity in Blind Retinae Using a Photochromic AMPA Receptor Agonist. *ACS Chem. Neurosci.* **2016**, *7* (1), 15–20. https://doi.org/10.1021/acschemneuro.5b00234.

(189) Frank, J. A.; Moroni, M.; Moshourab, R.; Sumser, M.; Lewin, G. R.; Trauner, D. Photoswitchable Fatty Acids Enable Optical Control of TRPV1. *Nat. Commun.* **2015**, *6* (1), 7118. https://doi.org/10.1038/ncomms8118.

(190) Müller, M.; Niemeyer, K.; Ojha, N. K.; Porav, S. A.; Vinayagam, D.; Urban, N.; Büchau, F.; Oleinikov, K.; Makke, M.; Bauer, C. C.; Johnson, A. V.; Muench, S. P.; Zufall, F.; Bruns, D.; Schwarz, Y.; Raunser, S.; Leinders-Zufall, T.; Bon, R. S.; Schaefer, M.; Thorn-Seshold, O. Ideal Efficacy Photoswitches for TRPC4/5 Channels Harness High Potency for Spatiotemporally-Resolved Control of TRPC Function in Live Tissues. bioRxiv July 13, 2024, p 2024.07.12.602451. https://doi.org/10.1101/2024.07.12.602451.

(191) Reynders, M.; Matsuura, B. S.; Bérouti, M.; Simoneschi, D.; Marzio, A.; Pagano, M.; Trauner, D. PHOTACs Enable Optical Control of Protein Degradation. *Sci. Adv.* **2020**, *6* (8), eaay5064. https://doi.org/10.1126/sciadv.aay5064.

(192) Ko, T.; Oliveira, M. M.; Alapin, J. M.; Morstein, J.; Klann, E.; Trauner, D. Optical Control of Translation with a Puromycin Photoswitch. *J. Am. Chem. Soc.* **2022**, *144* (47), 21494–21501. https://doi.org/10.1021/jacs.2c07374.

(193) Weston, C. E.; Richardson, R. D.; Haycock, P. R.; White, A. J. P.; Fuchter, M. J. Arylazopyrazoles: Azoheteroarene Photoswitches Offering Quantitative Isomerization and Long Thermal Half-Lives. *J. Am. Chem. Soc.* **2014**, *136* (34), 11878–11881. https://doi.org/10.1021/ja505444d.

(194) Siewertsen, R.; Neumann, H.; Buchheim-Stehn, B.; Herges, R.; Näther, C.; Renth, F.; Temps, F. Highly Efficient Reversible Z−E Photoisomerization of a Bridged Azobenzene with Visible Light through Resolved S1(Nπ*) Absorption Bands. *J. Am. Chem. Soc.* **2009**, *131* (43), 15594–15595. https://doi.org/10.1021/ja906547d.

(195) Baumgartner, B.; Glembockyte, V.; Gonzalez-Hernandez, A. J.; Valavalkar, A.; Mayer, R. J.; Fillbrook, L. L.; Müller-Deku, A.; Zhang, J.; Steiner, F.; Gross, C.; Reynders, M.; Munguba, H.; Arefin, A.; Ofial, A.; Beves, J. E.; Lohmueller, T.; Dietzek-Ivanšic, B.; Broichhagen, J.; Tinnefeld, P.; Levitz, J.; Thorn-Seshold, O. A General Method for Near-Infrared Photoswitching in Biology, Demonstrated by the >700 Nm Photocontrol of GPCR Activity in Brain Slices. ChemRxiv April 30, 2024. https://doi.org/10.26434/chemrxiv-2024-vm4n3.

(196) Konrad, D. B.; Savasci, G.; Allmendinger, L.; Trauner, D.; Ochsenfeld, C.; Ali, A. M. Computational Design and Synthesis of a Deeply Red-Shifted and Bistable Azobenzene. *J. Am. Chem. Soc.* **2020**, *142* (14), 6538–6547. https://doi.org/10.1021/jacs.9b10430.

(197) Posa, L.; Romano, G.; Ji, X.; Khan, S.; Paz, B. M.; Han, G. W.; Nazarova, A. L.; Zaidi, S. A.; Ranjbar, M.; Pleil, K.; Katritch, V.; Gati, C.; Trauner, D.; Levitz, J. An Opioid Efficacy Switch for Reversible Optical Control of Peripheral Analgesia. bioRxiv February 13, 2025, p 2024.12.16.628735. https://doi.org/10.1101/2024.12.16.628735.

(198) Schmitt, C.; Mauker, P.; Vepřek, N. A.; Gierse, C.; Meiring, J. C. M.; Kuch, J.; Akhmanova, A.; Dehmelt, L.; Thorn-Seshold, O. A Photocaged Microtubule-Stabilising Epothilone Allows Spatiotemporal Control of Cytoskeletal Dynamics. *Angew. Chem. Int. Ed.* **2024**, *63* (43), e202410169. https://doi.org/10.1002/anie.202410169.

(199) Keppler, A.; Gendreizig, S.; Gronemeyer, T.; Pick, H.; Vogel, H.; Johnsson, K. A General Method for the Covalent Labeling of Fusion Proteins with Small Molecules in Vivo. *Nat. Biotechnol.* **2003**, *21* (1), 86–89. https://doi.org/10.1038/nbt765.

(200) Juillerat, A.; Heinis, C.; Sielaff, I.; Barnikow, J.; Jaccard, H.; Kunz, B.; Terskikh, A.; Johnsson, K. Engineering Substrate Specificity of O6-Alkylguanine-DNA Alkyltransferase for Specific Protein Labeling in Living Cells. *ChemBioChem* **2005**, *6* (7), 1263–1269. https://doi.org/10.1002/cbic.200400431.

(201) Gronemeyer, T.; Chidley, C.; Juillerat, A.; Heinis, C.; Johnsson, K. Directed Evolution of O6-Alkylguanine-DNA Alkyltransferase for Applications in Protein Labeling. *Protein Eng. Des. Sel.* **2006**, *19* (7), 309–316. https://doi.org/10.1093/protein/gzl014.

(202) Sun, X.; Zhang, A.; Baker, B.; Sun, L.; Howard, A.; Buswell, J.; Maurel, D.; Masharina, A.; Johnsson, K.; Noren, C. J.; Xu, M.-Q.; Corrêa Jr., I. R. Development of SNAP-Tag Fluorogenic Probes for Wash-Free Fluorescence Imaging. *ChemBioChem* **2011**, *12* (14), 2217–2226. https://doi.org/10.1002/cbic.201100173.

(203) Bodor, D. L.; Rodríguez, M. G.; Moreno, N.; Jansen, L. E. T. Analysis of Protein Turnover by Quantitative SNAP-Based Pulse-Chase Imaging. *Curr. Protoc. Cell Biol.* **2012**, *55* (1), 8.8.1-8.8.34. https://doi.org/10.1002/0471143030.cb0808s55.

(204) Wilhelm, J.; Kühn, S.; Tarnawski, M.; Gotthard, G.; Tünnermann, J.; Tänzer, T.; Karpenko, J.; Mertes, N.; Xue, L.; Uhrig, U.; Reinstein, J.; Hiblot, J.; Johnsson, K. Kinetic and Structural Characterization of the Self-Labeling Protein Tags HaloTag7, SNAP-Tag, and CLIP-Tag. *Biochemistry* **2021**, *60* (33), 2560–2575. https://doi.org/10.1021/acs.biochem.1c00258.

(205) R. Correa, I.; Baker, B.; Zhang, A.; Sun, L.; R. Provost, C.; Lukinavicius, G.; Reymond, L.; Johnsson, K.; Xu, M.-Q. Substrates for Improved Live-Cell Fluorescence Labeling of SNAP-Tag. *Curr. Pharm. Des.* **2013**, *19* (30), 5414–5420.

(206) Kühn, S.; Nasufovic, V.; Wilhelm, J.; Kompa, J.; de Lange, E. M. F.; Lin, Y.-H.; Egoldt, C.; Fischer, J.; Lennoi, A.; Tarnawski, M.; Reinstein, J.; Vlijm, R.; Hiblot, J.; Johnsson, K. SNAP-Tag2 for Faster and Brighter Protein Labeling. *Nat. Chem. Biol.* **2025**, 1–8. https://doi.org/10.1038/s41589-025-01942-z.

(207) Los, G. V.; Encell, L. P.; McDougall, M. G.; Hartzell, D. D.; Karassina, N.; Zimprich, C.; Wood, M. G.; Learish, R.; Ohana, R. F.; Urh, M.; Simpson, D.; Mendez, J.; Zimmerman, K.; Otto, P.; Vidugiris, G.; Zhu, J.; Darzins, A.; Klaubert, D. H.; Bulleit, R. F.; Wood, K. V. HaloTag: A Novel Protein Labeling Technology for Cell Imaging and Protein Analysis. *ACS Chem. Biol.* **2008**, *3* (6), 373–382. https://doi.org/10.1021/cb800025k.

(208) Jasim, S. Development of a Dehalogenase-Based Protein Fusion Tag Capable of Rapid, Selective and Covalent Attachment to Customizable Ligands. *AACE Clin. Case Rep.* **2021**, *7* (1), 1.

(209) Erdmann, R. S.; Baguley, S. W.; Richens, J. H.; Wissner, R. F.; Xi, Z.; Allgeyer, E. S.; Zhong, S.; Thompson, A. D.; Lowe, N.; Butler, R.; Bewersdorf, J.; Rothman, J. E.; Johnston, D. S.; Schepartz, A.; Toomre, D. Labeling Strategies Matter for Super-Resolution Microscopy: A Comparison between HaloTags and SNAP-Tags. *Cell Chem. Biol.* **2019**, *26* (4), 584-592.e6. https://doi.org/10.1016/j.chembiol.2019.01.003.

(210) Los, G. V.; Encell, L. P.; McDougall, M. G.; Hartzell, D. D.; Karassina, N.; Zimprich, C.; Wood, M. G.; Learish, R.; Ohana, R. F.; Urh, M.; Simpson, D.; Mendez, J.; Zimmerman, K.; Otto, P.; Vidugiris, G.; Zhu, J.; Darzins, A.; Klaubert, D. H.; Bulleit, R. F.; Wood, K. V. HaloTag: A Novel Protein Labeling Technology for Cell Imaging and Protein Analysis. *ACS Chem. Biol.* **2008**, *3* (6), 373–382. https://doi.org/10.1021/cb800025k.

(211) Shields, B. C.; Yan, H.; Lim, S. S. X.; Burwell, S. C. V.; Cammarata, C. M.; Fleming, E. A.; Yousefzadeh, S. A.; Goldenshtein, V. Z.; Kahuno, E. W.; Vagadia, P. P.; Loughran, M. H.; Zhiquan, L.; McDonnell, M. E.; Scalabrino, M. L.; Thapa, M.; Hawley, T. M.; Field, G. D.; Hull, C.; Schiltz, G. E.; Glickfeld, L. L.; Reitz, A. B.; Tadross, M. R. DART.2: Bidirectional Synaptic Pharmacology with Thousandfold Cellular Specificity. *Nat. Methods* **2024**, *21* (7), 1288–1297. https://doi.org/10.1038/s41592-024-02292-9.

(212) Kompa, J.; Bruins, J.; Glogger, M.; Wilhelm, J.; Frei, M. S.; Tarnawski, M.; D'Este, E.; Heilemann, M.; Hiblot, J.; Johnsson, K. Exchangeable HaloTag Ligands for Super-Resolution Fluorescence Microscopy. *J. Am. Chem. Soc.* **2023**, *145* (5), 3075–3083. https://doi.org/10.1021/jacs.2c11969.

(213) Gautier, A.; Juillerat, A.; Heinis, C.; Corrêa, I. R.; Kindermann, M.; Beaufils, F.; Johnsson, K. An Engineered Protein Tag for Multiprotein Labeling in Living Cells. *Chem. Biol.* **2008**, *15* (2), 128–136. https://doi.org/10.1016/j.chembiol.2008.01.007.

(214) Miller, L. W.; Cai, Y.; Sheetz, M. P.; Cornish, V. W. In Vivo Protein Labeling with Trimethoprim Conjugates: A Flexible Chemical Tag. *Nat. Methods* **2005**, *2* (4), 255–257. https://doi.org/10.1038/nmeth749.

(215) Gallagher, S. S.; Sable, J. E.; Sheetz, M. P.; Cornish, V. W. An In Vivo Covalent TMP-Tag Based on Proximity-Induced Reactivity. *ACS Chem. Biol.* **2009**, *4* (7), 547–556. https://doi.org/10.1021/cb900062k.

(216) Mo, J.; Chen, J.; Shi, Y.; Sun, J.; Wu, Y.; Liu, T.; Zhang, J.; Zheng, Y.; Li, Y.; Chen, Z. Third-Generation Covalent TMP-Tag for Fast Labeling and Multiplexed Imaging of Cellular Proteins. *Angew. Chem. Int. Ed.* **2022**, *134* (36), e202207905. https://doi.org/10.1002/ange.202207905.

(217) Grimm, J. B.; Muthusamy, A. K.; Liang, Y.; Brown, T. A.; Lemon, W. C.; Patel, R.; Lu, R.; Macklin, J. J.; Keller, P. J.; Ji, N.; Lavis, L. D. A General Method to Fine-Tune Fluorophores for Live-Cell and in Vivo Imaging. *Nat. Methods* **2017**, *14* (10), 987–994. https://doi.org/10.1038/nmeth.4403.

(218) Hirano, M.; Ando, R.; Shimozono, S.; Sugiyama, M.; Takeda, N.; Kurokawa, H.; Deguchi, R.; Endo, K.; Haga, K.; Takai-Todaka, R.; Inaura, S.; Matsumura, Y.; Hama, H.; Okada, Y.; Fujiwara, T.; Morimoto, T.; Katayama, K.; Miyawaki, A. A Highly Photostable and Bright Green Fluorescent Protein. *Nat. Biotechnol.* **2022**, *40* (7), 1132–1142. https://doi.org/10.1038/s41587-022-01278-2.

(219) Gadella, T. W. J.; van Weeren, L.; Stouthamer, J.; Hink, M. A.; Wolters, A. H. G.; Giepmans, B. N. G.; Aumonier, S.; Dupuy, J.; Royant, A. mScarlet3: A Brilliant and Fast-Maturing Red Fluorescent Protein. *Nat. Methods* **2023**, *20* (4), 541–545. https://doi.org/10.1038/s41592-023-01809-y.

(220) Kohl, J.; Ng, J.; Cachero, S.; Ciabatti, E.; Dolan, M.-J.; Sutcliffe, B.; Tozer, A.; Ruehle, S.; Krueger, D.; Frechter, S.; Branco, T.; Tripodi, M.; Jefferis, G. S. X. E. Ultrafast Tissue Staining with Chemical Tags. *Proc. Natl. Acad. Sci. U.S.A.* **2014**, *111* (36), E3805–E3814. https://doi.org/10.1073/pnas.1411087111.

(221) Shaner, N. C.; Steinbach, P. A.; Tsien, R. Y. A Guide to Choosing Fluorescent Proteins. *Nat. Methods* **2005**, *2* (12), 905–909. https://doi.org/10.1038/nmeth819.

(222) Schwenzer, N.; Teiwes, N. K.; Kohl, T.; Pohl, C.; Giller, M. J.; Lehnart, S. E.; Steinem, C. CaV1.3 Channel Clusters Characterized by Live-Cell and Isolated Plasma Membrane Nanoscopy. *Commun. Biol.* **2024**, *7* (1), 1–11. https://doi.org/10.1038/s42003-024-06313-3.

(223) Damenti, M.; Coceano, G.; Pennacchietti, F.; Bodén, A.; Testa, I. STED and Parallelized RESOLFT Optical Nanoscopy of the Tubular Endoplasmic Reticulum and Its Mitochondrial Contacts in Neuronal Cells. *Neurobiol. Dis.* **2021**, *155*, 105361. https://doi.org/10.1016/j.nbd.2021.105361.

(224) Roed, S. N.; Wismann, P.; Underwood, C. R.; Kulahin, N.; Iversen, H.; Cappelen, K. A.; Schäffer, L.; Lehtonen, J.; Hecksher-Soerensen, J.; Secher, A.; Mathiesen, J. M.; Bräuner-Osborne, H.; Whistler, J. L.; Knudsen, S. M.; Waldhoer, M. Real-Time Trafficking and Signaling of the Glucagon-like Peptide-1 Receptor. *Mol. Cell. Endocrinol.* **2014**, *382* (2), 938–949. https://doi.org/10.1016/j.mce.2013.11.010.

(225) Komatsubara, A. T.; Goto, Y.; Kondo, Y.; Matsuda, M.; Aoki, K. Single-Cell Quantification of the Concentrations and Dissociation Constants of Endogenous Proteins. *J. Biol. Chem.* **2019**, *294* (15), 6062–6072. https://doi.org/10.1074/jbc.RA119.007685.

(226) Bojkowska, K.; Santoni de Sio, F.; Barde, I.; Offner, S.; Verp, S.; Heinis, C.; Johnsson, K.; Trono, D. Measuring In Vivo Protein Half-Life. *Chem. Biol.* **2011**, *18* (6), 805–815. https://doi.org/10.1016/j.chembiol.2011.03.014.

(227) Merrill, R. A.; Song, J.; Kephart, R. A.; Klomp, A. J.; Noack, C. E.; Strack, S. A Robust and Economical Pulse-Chase Protocol to Measure the Turnover of HaloTag Fusion Proteins. *J. Biol. Chem.* **2019**, *294* (44), 16164–16171. https://doi.org/10.1074/jbc.RA119.010596.

(228) Shields, B. C.; Kahuno, E.; Kim, C.; Apostolides, P. F.; Brown, J.; Lindo, S.; Mensh, B. D.; Dudman, J. T.; Lavis, L. D.; Tadross, M. R. Deconstructing Behavioral Neuropharmacology with Cellular Specificity. *Science* **2017**, *356* (6333), eaaj2161. https://doi.org/10.1126/science.aaj2161.

(229) Broichhagen, J.; Damijonaitis, A.; Levitz, J.; Sokol, K. R.; Leippe, P.; Konrad, D.; Isacoff, E. Y.; Trauner, D. Orthogonal Optical Control of a G Protein-Coupled Receptor with a SNAP-Tethered Photochromic Ligand. *ACS Cent. Sci.* **2015**, *1* (7), 383–393. https://doi.org/10.1021/acscentsci.5b00260.

(230) Donthamsetti, P.; Winter, N.; Hoagland, A.; Stanley, C.; Visel, M.; Lammel, S.; Trauner, D.; Isacoff, E. Cell Specific Photoswitchable Agonist for Reversible Control of Endogenous Dopamine Receptors. *Nat. Commun.* **2021**, *12* (1), 4775. https://doi.org/10.1038/s41467-021-25003-w.

(231) Donthamsetti, P. C.; Broichhagen, J.; Vyklicky, V.; Stanley, C.; Fu, Z.; Visel, M.; Levitz, J. L.; Javitch, J. A.; Trauner, D.; Isacoff, E. Y. Genetically Targeted Optical Control of an Endogenous G Protein-Coupled Receptor. *J. Am. Chem. Soc.* **2019**, *141* (29), 11522–11530. https://doi.org/10.1021/jacs.9b02895.

(232) Parvez, S.; Long, M. J. C.; Lin, H.-Y.; Zhao, Y.; Haegele, J. A.; Pham, V. N.; Lee, D. K.; Aye, Y. T-REX on-Demand Redox Targeting in Live Cells. *Nat. Protoc.* **2016**, *11* (12), 2328–2356. https://doi.org/10.1038/nprot.2016.114.

(233) Lin, H.-Y.; Haegele, J. A.; Disare, M. T.; Lin, Q.; Aye, Y. A Generalizable Platform for Interrogating Target- and Signal-Specific Consequences of Electrophilic Modifications in Redox-Dependent Cell Signaling. *J. Am. Chem. Soc.* **2015**, *137* (19), 6232–6244. https://doi.org/10.1021/ja5132648.

(234) Mertes, N.; Busch, M.; Huppertz, M.-C.; Hacker, C. N.; Wilhelm, J.; Gürth, C.-M.; Kühn, S.; Hiblot, J.; Koch, B.; Johnsson, K. Fluorescent and Bioluminescent Calcium Indicators with Tuneable Colors and Affinities. *J. Am. Chem. Soc.* **2022**, *144* (15), 6928–6935. https://doi.org/10.1021/jacs.2c01465.

(235) Deo, C.; Abdelfattah, A. S.; Bhargava, H. K.; Berro, A. J.; Falco, N.; Farrants, H.; Moeyaert, B.; Chupanova, M.; Lavis, L. D.; Schreiter, E. R. The HaloTag as a General Scaffold for Far-Red Tunable Chemigenetic Indicators. *Nat. Chem. Biol.* **2021**, *17* (6), 718–723. https://doi.org/10.1038/s41589-021-00775-w.

(236) Deo, C.; Sheu, S.-H.; Seo, J.; Clapham, D. E.; Lavis, L. D. Isomeric Tuning Yields Bright and Targetable Red Ca2+ Indicators. *J. Am. Chem. Soc.* **2019**, *141* (35), 13734–13738. https://doi.org/10.1021/jacs.9b06092.

(237) Tsao, K. K.; Imai, S.; Chang, M.; Hario, S.; Terai, T.; Campbell, R. E. The Best of Both Worlds: Chemigenetic Fluorescent Sensors for Biological Imaging. *Cell Chem. Biol.* **2024**, *31* (9), 1652–1664. https://doi.org/10.1016/j.chembiol.2024.08.002.

(238) Farrants, H.; Shuai, Y.; Lemon, W. C.; Monroy Hernandez, C.; Zhang, D.; Yang, S.; Patel, R.; Qiao, G.; Frei, M. S.; Plutkis, S. E.; Grimm, J. B.; Hanson, T. L.; Tomaska, F.; Turner, G. C.; Stringer, C.; Keller, P. J.; Beyene, A. G.; Chen, Y.; Liang, Y.; Lavis, L. D.; Schreiter, E. R. A Modular Chemigenetic Calcium Indicator for Multiplexed in Vivo Functional Imaging. *Nat. Methods* **2024**, *21* (10), 1916–1925. https://doi.org/10.1038/s41592-024-02411-6.

(239) Broichhagen, J.; Trumpp, M.; Gatin-Fraudet, B.; Bruckmann, K.; Burdzinski, W.; Roßmann, K.; Levitz, J.; Knaus, P.; Jatzlau, J. Developing HaloTag and SNAP-Tag Chemical Inducers of Dimerization to Probe Receptor Oligomerization and Downstream Signaling. *Angew. Chem. Int. Ed.* **2025**, *64* (35), e202506830. https://doi.org/10.1002/anie.202506830.

(240) Gautier, A.; Nakata, E.; Lukinavičius, G.; Tan, K.-T.; Johnsson, K. Selective Cross-Linking of Interacting Proteins Using Self-Labeling Tags. *J. Am. Chem. Soc.* **2009**, *131* (49), 17954–17962. https://doi.org/10.1021/ja907818q.

(241) Ballister, E. R.; Aonbangkhen, C.; Mayo, A. M.; Lampson, M. A.; Chenoweth, D. M. Localized Light-Induced Protein Dimerization in Living Cells Using a Photocaged Dimerizer. *Nat. Commun.* **2014**, *5* (1), 5475. https://doi.org/10.1038/ncomms6475.

(242) Zimmermann, M.; Cal, R.; Janett, E.; Hoffmann, V.; Bochet, C. G.; Constable, E.; Beaufils, F.; Wymann, M. P. Cell-Permeant and Photocleavable Chemical Inducer of Dimerization. *Angew. Chem. Int. Ed.* **2014**, *53* (18), 4717–4720. https://doi.org/10.1002/anie.201310969.

(243) Erhart, D.; Zimmermann, M.; Jacques, O.; Wittwer, M. B.; Ernst, B.; Constable, E.; Zvelebil, M.; Beaufils, F.; Wymann, M. P. Chemical Development of Intracellular Protein Heterodimerizers. *Chem. Biol.* **2013**, *20* (4), 549–557. https://doi.org/10.1016/j.chembiol.2013.03.010.

(244) Voß, S.; Klewer, L.; Wu, Y.-W. Chemically Induced Dimerization: Reversible and Spatiotemporal Control of Protein Function in Cells. *Curr. Opin. Chem. Biol.* **2015**, *28*, 194–201. https://doi.org/10.1016/j.cbpa.2015.09.003.

(245) Buckley, D. L.; Raina, K.; Darricarrere, N.; Hines, J.; Gustafson, J. L.; Smith, I. E.; Miah, A. H.; Harling, J. D.; Crews, C. M. HaloPROTACS: Use of Small Molecule PROTACs to Induce Degradation of HaloTag Fusion Proteins. *ACS Chem. Biol.* **2015**, *10* (8), 1831–1837. https://doi.org/10.1021/acschembio.5b00442.

(246) Neklesa, T. K.; Tae, H. S.; Schneekloth, A. R.; Stulberg, M. J.; Corson, T. W.; Sundberg, T. B.; Raina, K.; Holley, S. A.; Crews, C. M. Small-Molecule Hydrophobic Tagging–Induced Degradation of HaloTag Fusion Proteins. *Nat. Chem. Biol.* **2011**, *7* (8), 538–543. https://doi.org/10.1038/nchembio.597.

(247) Yoshii, T.; Oki, C.; Watahiki, R.; Nakamura, A.; Tahara, K.; Kuwata, K.; Furuta, T.; Tsukiji, S. Chemo-Optogenetic Protein Translocation System Using a Photoactivatable Self-Localizing Ligand. *ACS Chem. Biol.* **2021**, *16* (8), 1557–1565. https://doi.org/10.1021/acschembio.1c00416.

(248) Rudd, A. K.; Valls Cuevas, J. M.; Devaraj, N. K. SNAP-Tag-Reactive Lipid Anchors Enable Targeted and Spatiotemporally Controlled Localization of Proteins to Phospholipid Membranes. *J. Am. Chem. Soc.* **2015**, *137* (15), 4884–4887. https://doi.org/10.1021/jacs.5b00040.

(249) Aonbangkhen, C.; Zhang, H.; Wu, D. Z.; Lampson, M. A.; Chenoweth, D. M. Reversible Control of Protein Localization in Living Cells Using a Photocaged-Photocleavable Chemical Dimerizer. *J. Am. Chem. Soc.* **2018**, *140* (38), 11926–11930. https://doi.org/10.1021/jacs.8b07753.

(250) Chen, X.; Venkatachalapathy, M.; Kamps, D.; Weigel, S.; Kumar, R.; Orlich, M.; Garrecht, R.; Hirtz, M.; Niemeyer, C. M.; Wu, Y.-W.; Dehmelt, L. "Molecular Activity Painting": Switch-like, Light-Controlled Perturbations inside Living Cells. *Angew. Chem. Int. Ed.* **2017**, *56* (21), 5916–5920. https://doi.org/10.1002/anie.201611432.

(251) Chang, D.; Feng, S.; Girik, V.; Riezman, H.; Winssinger, N. Luciferase Controlled Protein Interactions. *J. Am. Chem. Soc.* **2021**, *143* (10), 3665–3670. https://doi.org/10.1021/jacs.0c11016.

(252) Caldwell, S. E.; Demyan, I. R.; Falcone, G. N.; Parikh, A.; Lohmueller, J.; Deiters, A. Conditional Control of Benzylguanine Reaction with the Self-Labeling SNAP-Tag Protein. *Bioconjugate Chem.* **2025**, *36* (3), 540–548. https://doi.org/10.1021/acs.bioconjchem.5c00002.

(253) Ishikawa, H.; Meng, F.; Kondo, N.; Iwamoto, A.; Matsuda, Z. Generation of a Dual-Functional Split-Reporter Protein for Monitoring Membrane Fusion Using Self-Associating Split GFP. *Protein Eng. Des. Sel.* **2012**, *25* (12), 813–820. https://doi.org/10.1093/protein/gzs051.

(254) Huppertz, M.-C.; Wilhelm, J.; Grenier, V.; Schneider, M. W.; Falt, T.; Porzberg, N.; Hausmann, D.; Hoffmann, D. C.; Hai, L.; Tarnawski, M.; Pino, G.; Slanchev, K.; Kolb, I.; Acuna, C.; Fenk, L. M.; Baier, H.; Hiblot, J.; Johnsson, K. Recording Physiological History of Cells with Chemical Labeling. *Science* **2024**, *383* (6685), 890–897. https://doi.org/10.1126/science.adg0812.

(255) Lavis, L. D.; Chao, T.-Y.; Raines, R. T. Synthesis and Utility of Fluorogenic Acetoxymethyl Ethers. *Chem. Sci.* **2011**, *2* (3), 521–530. https://doi.org/10.1039/C0SC00466A.

(256) Liu, C.; Pan, J.; Li, S.; Zhao, Y.; Wu, L. Y.; Berkman, C. E.; Whorton, A. R.; Xian, M. Capture and Visualization of Hydrogen Sulfide by a Fluorescent Probe. *Angew. Chem. Int. Ed.* **2011**, *50* (44), 10327–10329. https://doi.org/10.1002/anie.201104305.

(257) Poronik, Y. M.; Vygranenko, K. V.; Gryko, D.; Gryko, D. T. Rhodols – Synthesis, Photophysical Properties and Applications as Fluorescent Probes. *Chem. Soc. Rev.* **2019**, *48* (20), 5242–5265. https://doi.org/10.1039/C9CS00166B.

(258) Culbertson, C. T.; Jacobson, S. C.; Michael Ramsey, J. Diffusion Coefficient Measurements in Microfluidic Devices. *Talanta* **2002**, *56* (2), 365–373. https://doi.org/10.1016/S0039-9140(01)00602-6.

(259) Birke, R.; Ast, J.; Roosen, D. A.; Lee, J.; Roßmann, K.; Huhn, C.; Mathes, B.; Lisurek, M.; Bushiri, D.; Sun, H.; Jones, B.; Lehmann, M.; Levitz, J.; Haucke, V.; Hodson, D. J.; Broichhagen, J. Sulfonated Red and Far-Red Rhodamines to Visualize SNAP- and Halo-Tagged Cell Surface Proteins. *Org. Biomol. Chem.* **2022**, *20* (30), 5967–5980. https://doi.org/10.1039/D1OB02216D.

(260) Roßmann, K.; Sun, S.; Olesen, C. H.; Kowald, M.; Tapp, E.; Pabst, U.; Bieck, M.; Birke, R.; Shields, B. C.; Jeong, P.; Hong, J.; Tadross, M. R.; Levitz, J.; Lehmann, M.; Lipstein, N.; Broichhagen, J. A One-Step Protocol to Generate Impermeable Fluorescent HaloTag Substrates for in Situ Live Cell Application and Super-Resolution Imaging. bioRxiv September 23, 2024, p 2024.09.20.614087. https://doi.org/10.1101/2024.09.20.614087.

(261) Sednev, M. V.; Wurm, C. A.; Belov, V. N.; Hell, S. W. Carborhodol: A New Hybrid Fluorophore Obtained by Combination of Fluorescein and Carbopyronine Dye Cores. *Bioconjugate Chem.* **2013**, *24* (4), 690–700. https://doi.org/10.1021/bc3006732.

(262) Grimm, J. B.; Gruber, T. D.; Ortiz, G.; Brown, T. A.; Lavis, L. D. Virginia Orange: A Versatile, Red-Shifted Fluorescein Scaffold for Single- and Dual-Input Fluorogenic Probes. *Bioconjugate Chem.* **2016**, *27* (2), 474–480. https://doi.org/10.1021/acs.bioconjchem.5b00566.

(263) David, M.; Leirikh, T.; Kopp, T.; Shabat, D. Phenylamine-1,2-Dioxetanes: Superior Class of Chemiluminescent Luminophores for Aqueous Sensing and Bioimaging. ChemRxiv July 17, 2025. https://doi.org/10.26434/chemrxiv-2025-crj7n.

(264) Wu, Y.; Huang, S.; Wang, J.; Sun, L.; Zeng, F.; Wu, S. Activatable Probes for Diagnosing and Positioning Liver Injury and Metastatic Tumors by Multispectral Optoacoustic Tomography. *Nat. Commun.* **2018**, *9* (1), 3983. https://doi.org/10.1038/s41467-018-06499-1.

(265) Müller, M.; Valavalkar, A.; Gujrati, V.; Prohaska, J. P.; Shelar, D.; Kaltenegger, M.; Ivanšić, B. D.-; Ntziachristos, V.; Thorn-Seshold, O. Molecular Rotors Are Loud, Highly Photostable, NIR/SWIR-Active Molecular Optoacoustic Contrast Agents. ChemRxiv November 25, 2024. https://doi.org/10.26434/chemrxiv-2024-t6zqq.

(266) Siewertsen, R.; Neumann, H.; Buchheim-Stehn, B.; Herges, R.; Näther, C.; Renth, F.; Temps, F. Highly Efficient Reversible Z−E Photoisomerization of a Bridged Azobenzene with Visible Light through Resolved S1(Nπ*) Absorption Bands. *J. Am. Chem. Soc.* **2009**, *131* (43), 15594–15595. https://doi.org/10.1021/ja906547d.

(267) Trads, J. B.; Hüll, K.; Matsuura, B. S.; Laprell, L.; Fehrentz, T.; Görldt, N.; Kozek, K. A.; Weaver, C. D.; Klöcker, N.; Barber, D. M.; Trauner, D. Sign Inversion in Photopharmacology: Incorporation of Cyclic Azobenzenes in Photoswitchable Potassium Channel Blockers and Openers. *Angew. Chem. Int. Ed.* **2019**, *58* (43), 15421–15428. https://doi.org/10.1002/anie.201905790.

(268) Hammerich, M.; Schütt, C.; Stähler, C.; Lentes, P.; Röhricht, F.; Höppner, R.; Herges, R. Heterodiazocines: Synthesis and Photochromic Properties, Trans to Cis Switching within the Bio-Optical Window. *J. Am. Chem. Soc.* **2016**, *138* (40), 13111–13114. https://doi.org/10.1021/jacs.6b05846.

(269) Dong, M.; Babalhavaeji, A.; Samanta, S.; Beharry, A. A.; Woolley, G. A. Red-Shifting Azobenzene Photoswitches for in Vivo Use. *Acc. Chem. Res.* **2015**, *48* (10), 2662–2670. https://doi.org/10.1021/acs.accounts.5b00270.

14 Acknowledgements

This thesis would not have been possible without the support from many people. First and foremost, I want to thank my **supervisor Oliver** for his constant support during my PhD, for all the great scientific discussions we had, his trust and for giving me the freedom to develop my own ideas and set my own priorities on the various projects I worked on. I highly appreciate how you enabled my scientific and professional development, with research retreats, supporting the attendance of so many conferences, and the research stay in Tokyo – experiences that non only shaped me as a professional but also as a person. Thank you for showing me what I am capable of by always pushing me to the limits.

I want to thank my **thesis committee**: my second examiner Dr. Pavel Kielkowski as well as Prof. Dr. Andrea Rentmeister, Prof. Dr. Martin Kerschensteiner, Prof. Dr. Oliver Trapp and Prof. Dr. Ivan Huc.

Also, I am grateful to **Prof. Dr. Yasuteru Urano** for the great opportunity to join his research group in Tokyo as a visiting scientist, where I gained invaluable insights into the frontiers of medicinal probe and prodrug development and the Japanese culture. Thanks to Sascha, for his support and for showing me so many great (food) places and to all the lab mates and new friends I made: Kimiko, Kunitake, Shimada, Ito, Seike, Winnie, Hata, Abe, Fujita, Kiji, Tachibana, and Yijing – it was great to meet you, monosugoi!

All my projects could not have been realised without the support from many **great collaborators** from different research areas on all my interdisciplinary projects. Thank you not only for your contributions and the many exciting discussions but also for your patience with my questions or multiple requests for changing figures etc. There would be no meaningful applications from this thesis if it wasn't for you. I thank Daniela, for kick-starting the membrane-damage project when we both had just started the PhD and first had to learn how to swim with this challenging project and for all the successful and failed follow-up projects throughout my PhD; Luciano, for your support and many discussion on the CHalo dimeriser; Louise, for discussing and collaborating on the fluorogenic CHalo-labelling in mouse embryos; Joyce, for microtubule imaging with CHalo-SiR and explaining Fiji to me; Kristina, for many discussions and optimisations during the initial CHalo experiments; and Andrew, Chantal and Simone for the application experiments that greatly enhanced the impact of the Membrane-Damage Paper.

Mein besonderer Dank gilt der **CHalo Sub-Group**: Luc und Carmen, wir haben dieses Projekt gemeinsam aus der Wiege gehoben und durch zahlreiche Höhen und Tiefen getragen und ohne Eure Unterstützung hätte ich es nie so umsetzen können. Danke, dass ihr mit eurer positiven Art und euren klugen Ideen zur Lösung der Herausforderungen die Rückschläge erträglicher gemacht habt. Danke auch den anderen helfenden Händen bei diesem Projekt: Brandy, für deine Synthese-Unterstützung in einer Zeit, in der jeder Tag gezählt hat, sodass wir vor dem Laborumzug alle Proof-of-Concept Ergebnisse zusammenhatten; JP, für deine Unterstützung seit August, welche die Grundlage für neue Anwendungen gelegt hat und dafür, dass wir trotz des Zeitdrucks immer gut(gelaunt) zusammengearbeitet haben; und Martin, für die synthetische Unterstützung mit den Ester Probes.

Ich möchte mich bei all meinen **Praktikantinnen und Praktikanten** bedanken, die mich bei meinen Projekten unterstützt haben und den Laboralltag bereichert haben: Brandy, für die Untersuchung der Phosphonate als Membrane-Damage Probes; Tobi, für die Synthese der ersten erfolgversprechenden Lipid-Fluoresceine für das Cell Retention Projekt; Jürgen, für die Unterstützung bei den Photocage-Taxanen; Lara, für erste Tests mit Membrane-Damage Prodrugs; Julia, für die zahlreichen Tests zum Photocagen von SLP Liganden; und Hannah, für die Membrane-Damage Prodrug Synthese und die ersten Schritte zur Synthese eines aktivierbaren HaloTag Liganden, was den Start des CHalo Projekts markierte. Ich freue mich, dass ich mit euch allen zusammenarbeiten durfte.

Außerdem danke ich meinen **ehemaligen Betreuerinnen und Betreuern**, die mich im Verlauf meiner Ausbildung wesentlich geprägt haben: meiner ehemaligen Chemie-Lehrerin Susanne, die meine Faszination für die Chemie geweckt hat; Kerstin, die als Betreuerin meiner Bachelorarbeit meine ersten Schritte in einem Forschungslabor begleitet hat; Max, der mir im OC-Forschungspraktikum die wichtigsten Grundlagen in der organischen Synthese beigebracht hat; Michael, bei dem ich in Newcastle zum ersten Mal eigenständig forschen durfte; und Andreas, für die Betreuung meines Industriepraktikums bei Bayer. Mit diesen Eindrücken habt ihr die Grundlage für meine weitere Entwicklung gelegt.

Riesiger Dank geht an alle meine **Lab-Mates in der TS Group**, mit denen ich tagtäglich im Labor stand: nicht zuletzt dank euch hatte ich in den letzten Jahren so eine herausragende Zeit. Danke für das wissenschaftsbegeisterte Umfeld, in dem jeder zu jeder Zeit gerne über Science geredet und immer wertvollen Input gegeben hat, wenn ich selbst nicht weiterkam. Und danke für all die anderen Erlebnisse, im Labor oder privat, sei es bei spannenden Mittagspausen-Diskussionen, Halbmarathon im passenden Outfit, beim Laborumbau mit Blisterfolie, Rap-Duellen, interessanten Dokumentarfilmen, ziemlich unlustigen Sticker-Aktionen, in Kroatien am Pool, in den Bergen, beim Angeln am Forellenteich, bei dem einen oder anderen Feierabendbierchen mit gelegentlichem Milchbarausflug, oder oder oder – ich könnte diese Liste unendlich fortsetzen. Egal wie alles andere lief, wegen euch bin ich jeden Tag gerne ins Labor gekommen und ich hoffe, dass diese Freundschaften die Promotionszeit noch lange überdauern werden. Ich danke allen aktuellen und ehemaligen OTS-Mitgliedern, ganz besonders Adi, Alex, Annabel, Ben, Brandy, Carina, Carmen, Elena, Jan, Janni (Secret OTS-Member), Jimmy, Julia, Lena, Li, JP, Luc, Lukas, Markus, Martin, Michaela.

Auch danke ich den vielen anderen Menschen, die das **Leben auf dem Campus** bereichert haben: der Konrad-Gruppe, Konsti, Bene, Anna und Irene, für zahlreiche gemeinsame (Wiesn-)Ausflüge; Janin, für die gemeinsame Praktikumsbetreuung; dem Networking-Planungsteam, Lukas, Janni, Yassi, Johanna und Alex; den Menschen, die mit ihrer freundlichen Art das Leben auf dem Campus so viel angenehmer machen: Michi von der Entsorgung, Claudia vom NMR-Service in der Pharmazie in München und Tilo vom NMR in Dresden sowie den Damen aus der Chemikalienausgabe in München. Außerdem danke ich Alejandro, Annika, Benny, Felix, Isi, Jonathan, Laura, Leonie, Nicole, Thomas, Sabrina, Samy, Sophie und Patricia für die gute Zeit während des Studiums.

Diese Dissertation wurde zu großen Teilen auch durch den Rückhalt und die Unterstützung von Menschen aus **meinem persönlichen Umfeld** möglich. Ganz besonderer Dank gilt meinen Eltern Ruth und Thies – danke für eure unschätzbare Unterstützung über mein gesamtes Leben hinweg, für alle Fähigkeiten, die ihr mir mitgegeben habt und dafür, dass ihr meine Vorbilder seid. Ihr habt den Weg bereitet für alles, was ich bis jetzt erreicht habe und noch erreichen werde, ohne euch wäre ich heute nicht hier. Danke, dass ihr immer hinter mir steht und egal wo ich auf der Welt gerade bin, immer nur einen Anruf entfernt seid. Danke Daniel für die vielen gemeinsamen Unternehmungen und die Projekte, die wir als Brüder zusammen umgesetzt haben. Danke Sina, für die gemeinsamen Erlebnisse, die Ablenkung nach anstrengenden Labortagen und deine Unterstützung und Geduld in der Abschlussphase meiner Promotion. Danke Sophie für die langjährige Freundschaft seit dem ersten Semester, die tiefgründigen Gespräche über Gott und die Welt, die spannenden Diskussionen und Projekte und deinen bedingungslosen Support. Danke Lukas für das gemeinsame Durchhalten in der Abschlussphase in der Dresden-WG, die zahlreichen und oft wunderbar herausfordernden Outdoor-Erlebnisse und die unzähligen guten Gespräche. Danke Li, dass du als Gruppenältester nicht nur die Grundlage für alle PhD Students nach dir gelegt hast, sondern auch mein Senpai seit Beginn der Masterarbeit warst, womit du mir den Start in die Promotion wesentlich erleichtert hast (und sorry nochmal, dass ich dich aus deinem Revier vertrieben habe). Danke Sally für die wundervolle gemeinsame Zeit. Danke Janni für alle gemeinsamen Aktivitäten, bei denen wir die Berge und Straßen unsicher machen. Danke Alejandro für die lange Freundschaft seit Studienbeginn und die vielen Erlebnisse seitdem. Danke Michi für die Zeit seit Newcastle und in unserer WG. Und danke allen anderen wundervollen Menschen, mit denen ich in den letzten Jahrzehnten Zeit verbringen durfte. Ihr habt mich zu dem Menschen gemacht, der ich heute bin.